Challenges and Advances
in Computational Chemistry and Physics 15
Series Editor: Jerzy Leszczynski

Tigran V. Shahbazyan
Mark I. Stockman *Editors*

Plasmonics: Theory and Applications

Springer

Plasmonics: Theory and Applications

CHALLENGES AND ADVANCES IN COMPUTATIONAL CHEMISTRY AND PHYSICS

Volume 15

Series Editor:

JERZY LESZCZYNSKI
Jackson State University, Jackson, Mississippi, USA

For further volumes:
http://www.springer.com/series/6918

Plasmonics: Theory and Applications

Edited by

Tigran V. Shahbazyan
Department of Physics, Jackson State University, Jackson, MS, USA

Mark I. Stockman
Department of Physics and Astronomy, Georgia State University, Atlanta, GA, USA

Springer

Editors
Tigran V. Shahbazyan
Department of Physics
Jackson State University
Jackson, MS
USA

Mark I. Stockman
Department of Physics and Astronomy
Georgia State University
Atlanta, GA
USA

ISBN 978-94-007-7804-7 ISBN 978-94-007-7805-4 (eBook)
DOI 10.1007/978-94-007-7805-4
Springer Dordrecht Heidelberg New York London

Library of Congress Control Number: 2013955251

© Springer Science+Business Media Dordrecht 2013
This work is subject to copyright. All rights are reserved by the Publisher, whether the whole or part of the material is concerned, specifically the rights of translation, reprinting, reuse of illustrations, recitation, broadcasting, reproduction on microfilms or in any other physical way, and transmission or information storage and retrieval, electronic adaptation, computer software, or by similar or dissimilar methodology now known or hereafter developed. Exempted from this legal reservation are brief excerpts in connection with reviews or scholarly analysis or material supplied specifically for the purpose of being entered and executed on a computer system, for exclusive use by the purchaser of the work. Duplication of this publication or parts thereof is permitted only under the provisions of the Copyright Law of the Publisher's location, in its current version, and permission for use must always be obtained from Springer. Permissions for use may be obtained through RightsLink at the Copyright Clearance Center. Violations are liable to prosecution under the respective Copyright Law.
The use of general descriptive names, registered names, trademarks, service marks, etc. in this publication does not imply, even in the absence of a specific statement, that such names are exempt from the relevant protective laws and regulations and therefore free for general use.
While the advice and information in this book are believed to be true and accurate at the date of publication, neither the authors nor the editors nor the publisher can accept any legal responsibility for any errors or omissions that may be made. The publisher makes no warranty, express or implied, with respect to the material contained herein.

Printed on acid-free paper

Springer is part of Springer Science+Business Media (www.springer.com)

Preface

Plasmonics is a rapidly developing field that blends together fundamental research and applications ranging across physics, chemistry, biology, medicine, engineering, defense, environmental sciences, etc. It dates back to 1950s when surface plasmon polaritons were discovered [1, 2]. Its development received a new impetus in mid-1970s with the discovery of surface-enhanced Raman scattering (SERS) [3–5], and again following the observation of giant single-molecule SERS [6, 7]. However, it was during the past decade that plasmonics experienced a truly explosive growth. This book is a snapshot of current developments in various areas of plasmonics presented in several reviews written by leading researchers in the field.

The material is arranged in 15 chapters starting with an overview by one of the Editors followed by topical reviews. It is assumed that the reader is familiar with the fundamentals; a number of excellent recent introductory texts are available [8–11]. Naturally, the included topics do not nearly cover the incredible breadth of current plasmonics research and applications, but hopefully will give readers an interesting summary of this exciting field.

Tigran V. Shahbazyan
Mark I. Stockman

References

1. R.H. Ritchie, Phys. Rev. **106**, 874 (1957)
2. A.W. Blackstock, R.H. Ritchie, R.D. Birkhoff, Phys. Rev. **100**, 1078 (1955)
3. M. Fleischman, P.J. Hendra and A.J. McQuillan, Chem. Phys. Lett. **26**, 163 (1974)
4. D.L. Jeanmaire, R.P. Van Duyne, J. Electroanal. Chem. **84**, 1 (1977)
5. M.G. Albrecht, J.A. Creighton, J. Am. Chem. Soc. **99**, 5215 (1977)
6. S. Nie, S.R. Emory, Science **275**, 1102 (1997)
7. K. Kneipp, Y. Wang, H. Kneipp, L.T. Perelman, I. Itzkan, R.R. Dasari, M.S. Feld, Phys. Rev. Lett. **78**, 1667 (1997)
8. S.A. Maier, *Plasmonics: Fundamentals and Applications*, (Springer, New York, 2007)

9. D. Sarid, W. Challener, *Modern Introduction to Surface Plasmons: Theory, Mathematica Modeling, and Applications*, (Cambridge University Press, New York, 2010)
10. L. Novotny, B. Hecht, *Principles of Nano-Optics*, 2nd edn., (Cambridge University Press, New York, 2012)
11. M. Pelton, G.W. Bryant, *Introduction to Metal-Nanoparticle Plasmonics*, (Willey, Hoboken, 2013)

Contents

1 Nanoplasmonics: From Present into Future 1
Mark I. Stockman
1.1 Introduction 1
1.1.1 Preamble 1
1.1.2 Composition of the Chapter 2
1.2 Basics of Nanoplasmonics 3
1.2.1 Fundamentals 3
1.2.2 Nanoantennas 8
1.2.3 Radiative Loss 9
1.2.4 Other Important Issues of Plasmonics in Brief 12
1.3 Nanolocalized Surface Plasmons (SPs) and Their Hot Spots 16
1.3.1 SPs as Eigenmodes 16
1.3.2 Inhomogeneous Localization of SPs and Hot Spots of Local Fields 18
1.3.3 Retarded Green's Function and Field Equation Solution 22
1.3.4 SP Modes as Resonances 24
1.3.5 Examples of Local Fields and Their Hot Spots 26
1.3.6 Experimental Examples of Nanoplasmonic Hot Spots 29
1.4 Ultrafast Plasmonics and Coherent Control on Nanoscale 33
1.4.1 Introduction 33
1.4.2 Time-Reversal Solution for Coherent Control 36
1.4.3 Qualitative Description of Time-Reversal Coherent Control 37
1.4.4 Numerical Results for Time-Reversal Coherent Control 40
1.4.5 Coherent Control by Spatiotemporal Pulse Shaping 46
1.4.6 Experimental Demonstrations of Coherent Control on the Nanoscale 50

1.5 Quantum Nanoplasmonics: Spaser and Nanoplasmonics with Gain 55
1.5.1 Introduction to Spasers and Spasing 55
1.5.2 Spaser Fundamentals. 56
1.5.3 Brief Overview of Latest Progress in Spasers 59
1.5.4 Equations of Spaser 64
1.5.5 Spaser in CW Mode 69
1.5.6 Spaser as Ultrafast Quantum Nanoamplifier. 72
1.5.7 Compensation of Loss by Gain and Spasing 77
1.5.8 Conditions of Loss Compensation by Gain and Spasing. 81
References 88

2 Plasmonics for Enhanced Vibrational Signatures 103
Katrin Kneipp, Harald Kneipp and Janina Kneipp
2.1 Introduction 104
2.2 "Normal" and "Surface Enhanced" Vibrational Spectroscopy 105
2.2.1 Surface Enhanced Raman Scattering. 106
2.2.2 Surface Enhanced Infrared Absorption 108
2.2.3 Surface Enhanced Raman Scattering Using Two-Photon Excitation: Surface Enhanced Hyper Raman Scattering 108
2.2.4 Surface Enhanced Pumped Anti-Stokes Raman Scattering 110
2.2.5 Surface Enhanced Coherent or Stimulated Raman Scattering Methods 111
2.3 Plasmonic Nanstructures for Supporting Vibrational Spectroscopy 113
2.4 Selected Applications of Surface Enhanced Vibrational Spectroscopy 116
2.4.1 SERS for Probing Catalytic Reactions. 116
2.4.2 Vibrational Spectroscopy of Protein Monolayers Using SEIRA 118
2.4.3 New Labels for Linear and Non-Linear Vibrational Probing and Imaging. 119
2.5 Brief Summary and Outlook 120
References 121

3 Plasmonically Enhanced Dye-Sensitized Solar Cells 125
Michael B. Ross, Martin G. Blaber and George C. Schatz
3.1 Introduction 126

3.2 Plasmon Enhanced Dye-Sensitized Solar Cells 128
3.2.1 Mechanism of Enhanced Dye Absorption 129
3.2.2 Calculating Solar Enhancement 130
3.3 Enhancing the Solar Spectrum 132
3.3.1 Metal Composition 133
3.3.2 Shape 135
3.3.3 Polarization-Independent Resonances 135
3.3.4 Dielectric Core—Metal Shell Particles 138
3.3.5 Polarization-Dependent Resonances in Anisotropic Particles 138
3.3.6 Other Geometries 139
3.4 Challenges and Outlook 139
3.4.1 Ensembles 140
3.4.2 Excited State Lifetime of Plasmons 142
3.4.3 Metal Losses 142
3.5 Conclusion. 144
References 144

4 Silicon Plasmonics 149
Ilya Goykhman, Boris Desiatov and Uriel Levy
4.1 Introduction 149
4.2 Silicon Plasmonics Components 151
4.2.1 Motivation 151
4.2.2 Passive Devices 151
4.2.3 Active Devices 156
4.3 Concluding Remarks 163
References 164

5 Ultrafast Nonlinear Plasmonics 167
Fabrice Vallée and Natalia Del Fatti
5.1 Introduction 167
5.2 Dielectric Function of Metals and Metal Nanoparticles 169
5.3 Electron-Light Interaction and Electron Kinetics 172
5.3.1 Coherent Electron-Light Coupling 173
5.3.2 Ultrafast Electron Kinetics. 174
5.4 Time Dependent Metal Dielectric Function Change 183
5.4.1 Electronic Contribution 183
5.4.2 Lattice Contribution 187
5.5 Ultrafast Nonlinear Optical Response 188
5.5.1 Metal Film. 189
5.5.2 Single Plasmonic Nanoparticle 190
5.5.3 Plasmonic Material: Ensemble of Metal Nanoparticles 198

5.6 Conclusion. 201
References 202

6 Second-Order Nonlinear Optical Properties of Plasmonic Nanostructures 207
Martti Kauranen, Hannu Husu, Jouni Mäkitalo, Robert Czaplicki, Mariusz Zdanowicz, Joonas Lehtolahti, Janne Laukkanen and Markku Kuittinen
6.1 Introduction 208
6.2 Theoretical Background. 209
6.2.1 Nonlinear Response Tensor 209
6.2.2 Extension to Multipole Effects 211
6.3 Experimental Techniques. 212
6.3.1 Samples and Fabrication 212
6.3.2 Experimental Setup. 213
6.4 Early Work 214
6.4.1 Basic Results 214
6.4.2 Multipole Effects 214
6.4.3 Related Work. 215
6.5 Local-Field Issues. 216
6.5.1 Gap Dependence 216
6.5.2 Chiral Symmetry Breaking of Dimers 217
6.6 Improved Samples 219
6.6.1 Key Improvement in Fabrication 219
6.6.2 Dipole Limit 220
6.7 Tailored Nonlinear Response 220
6.7.1 Resonance Domain Effects 220
6.7.2 Tailored SHG Response 221
6.8 Numerical Modeling 222
6.8.1 Challenges in Modeling. 222
6.8.2 General Approach for Nonlinear Problems 223
6.8.3 Recent Approaches for Modeling SHG 224
6.8.4 Boundary-Element Method 224
6.9 Outlook. 227
References 229

7 Ultrafast and Nonlinear Plasmon Dynamics. 237
Markus B. Raschke, Samuel Berweger and Joanna M. Atkin
7.1 Electronic Excitation at Metal Surfaces: Surface Modes 237
7.1.1 Introduction 237
7.1.2 Linear Optical Polarization 238
7.1.3 Time Domain Description 239
7.1.4 Electronic Properties of Metals 240
7.1.5 Drude-Sommerfeld Model 241

7.1.6 Interband Transition and Hybridization 242
7.1.7 Optics at Metal Interfaces 244
7.1.8 Propagating Surface Plasmon Polaritons 245
7.1.9 Localized SPP in Small Metal Particles. 246
7.2 Damping of Surface Plasmon Polaritons 249
7.2.1 Theory of Radiative and Nonradiative Decay. 249
7.2.2 Experimental Studies of Plasmon Lifetimes. 253
7.3 Nonlinear Plasmon Optics 255
7.3.1 Second-Order Nonlinear Optics 258
7.3.2 SHG Response at Metal Surfaces 260
7.3.3 Nonlinear Wavemixing with Surface Plasmons 262
7.3.4 Surface-Enhanced Nonlinear Processes 264
7.3.5 Nonlinear Light Scattering. 266
7.3.6 Nonlinear Optical Antennas. 269
7.4 Femtosecond Time-Domain Measurement of Plasmon Dynamics 270
7.5 Ultrafast Spatio-Temporal Control with Plasmonic Antennas 274
7.6 Outlook. 278
References 279

8 Controlling Thermal Radiation with Surface Waves 283
Philippe Ben-Abdallah, François Marquier and Jean-Jacques Greffet
8.1 Surface-Waves Assisted Thermal Emission 283
8.1.1 Introduction to Thermal Emission. 283
8.1.2 Spatially-Coherent Thermal Emission: Surface-Phonons Assisted Directional Thermal Emission 291
8.1.3 Surface-Phonons Assisted Isotropic Thermal Emission 293
8.1.4 Surface-Plasmons Assisted Thermal Emission 295
8.1.5 Polarization Effects: Coupling of s-Polarized Propagating Waves and Surface Waves. 296
8.1.6 Crossed Gratings 298
8.1.7 Metamaterials with Controlled Emission Spectrum . . . 298
8.1.8 Multilayers and Photonic Crystals for Controlled Emission 299
8.2 Radiative Heat Transfer at the Nanoscale 300
8.2.1 Heat Flux Exchanged Between Two Planar Media . . . 301
8.2.2 A Mesoscopic Analysis of the Heat Transfer at the Nanoscale. 304
8.2.3 Heat Transfer Mediated by Photon Tunneling 308

8.2.4 Beyond SPPs Coupling: Toward a Near-Field Analog of Blackbody 312
8.2.5 Applications. 315
References 322

9 Aperiodic Order in Nanoplasmonics 329
Luca Dal Negro, Carlo Forestiere, Nathaniel Lawrence, Sylvanus Lee, Jacob Trevino and Gary Walsh
9.1 Introduction 330
9.2 Fundamentals of Deterministic Aperiodic Order. 331
9.2.1 Periodic and Quasi-Periodic Order 331
9.2.2 Aperiodic Order and Substitutions 333
9.2.3 Plasmonic Chains: Collective Excitations and Energy Gaps 336
9.2.4 Rotational Symmetry: Aperiodic Tilings and Vogel Spirals. 339
9.2.5 Aperiodic Order and Number Theory 345
9.2.6 Hot Spot Engineering with Aperiodic Plasmon Arrays 348
9.3 Engineering Applications of Aperiodic Plasmon Arrays 352
9.3.1 Nanofabrication of Aperiodic Plasmon Arrays 352
9.3.2 Applications to Surface Enhanced Raman Biosensing. 356
9.3.3 Applications to Colorimetric Optical Sensing. 360
9.3.4 Applications to Light Emission Enhancement 363
9.3.5 Applications to Thin-Film Solar Cell Enhancement 367
9.4 Outlook and Conclusions. 370
References 372

10 Waves on Subwalength Metallic Surfaces: A Microscopic View Point 379
Philippe Lalanne and Haitao Liu
10.1 Introduction 379
10.2 Waves on Metal Surfaces: Historical Background. 381
10.3 Fano's Microscopic Model of Wood Anomaly. 382
10.4 Field Scattered on Metal Surfaces by Subwavelength Indentations 384
10.4.1 The Quasi-Cylindrical Wave 384
10.4.2 SPP and Quasi-CW Launched by a Dipole Point-Source on a Metal Surface (3D case) 388
10.5 Fano-Like Model of the Extraordinary Optical Transmission 389

10.6 Generalized Microscopic Model with Surface Plasmon Polaritons and Quasi-Cylindrical Waves 393
10.6.1 Cross Conversion from Quasi-Cylindrical Wave to Surface Plasmon Polariton 393
10.6.2 Multiple-Scattering Model with Surface Plasmon Polaritons and Quasi-Cylindrical Waves 394
10.7 Conclusion. 397
References 398

11 Plasmonic Functionalities Based on Detuned Electrical Dipoles 401
Anders Pors, Michael G. Nielsen and Sergey I. Bozhevolnyi
11.1 Introduction 401
11.2 Detuned Electrical Dipole Metamaterials: Optical Transparency and Slow Light. 403
11.2.1 The Two-Nanorod System. 405
11.2.2 The Three-Nanorod System 410
11.2.3 Experimental Study of Detuned Electrical Dipole Metamaterials 412
11.3 Applications. 415
11.3.1 Plasmonic Sensing 415
11.3.2 Metamaterial Wave Retarders in Reflection. 421
11.4 Conclusion. 426
References 427

12 Plasmonics with a Twist: Taming Optical Tornadoes on the Nanoscale 431
Svetlana V. Boriskina
12.1 Introduction 431
12.2 Energy Transport and Dissipation in Plasmonic Materials 436
12.3 How can a Particle Absorb more than the Light Incident on it? 437
12.4 Nanoparticle-Generated Optical Tornadoes 440
12.5 Molding the River of Light in Vortex Nanogear Transmissions 444
12.6 Hydrodynamics of Light Flow in Plasmonic Nanostructures 449
12.7 Applications of Plasmonically-Integrated Tornadoes 451
12.8 Conclusions and Outlook. 456
References 457

13 Spinoptics in Plasmonics. 463
Erez Hasman and Vladimir Kleiner
13.1 Introduction 463

13.2 Spin-Based Plasmonic Effect in Nanoscale Structures 464
13.3 Optical Spin Symmetry Breaking in Nanoapertures 470
13.4 Plasmonic Aharonov-Bohm Effect 475
13.5 Spin-Dependent Plasmonics: Interfering Topological Defects 480
13.6 Optical Spin-Hall Effect from Plasmonic Nanoapertures 484
13.7 Coupled Thermal Antenna Lattices and Rashba-like Spin Degeneracy Violation 492
References 496

14 Plasmonics and Super-Hydrophobicity: A New Class of Nano-Bio-Devices 501
F. Gentile, M. L. Coluccio, A. Toma, A. Alabastri, R. Proietti Zaccaria, G. Das, F. De Angelis, P. Candeloro, C. Liberale, G. Perozziello, L. Tirinato, M. Leoncini and E. Di Fabrizio
14.1 Introduction 502
14.2 Super-Hydrophobicity: The Physical Model 504
14.2.1 The Physics of Drops and Surfaces 504
14.2.2 Lattice Packings and SHSs 506
14.2.3 Vanishingly Small Friction Coefficients of SHSs and Evaporation Dynamics 508
14.2.4 Consideration for an Optimal Design 509
14.3 Materials and Methods 511
14.3.1 Fabrication of the Devices 511
14.3.2 Samples SEM Characterization 512
14.3.3 Samples AFM Characterization 512
14.3.4 Fluorescence Microscopy Characterization of Rhodamine deposits 513
14.3.5 Raman Characterization of Rhodamine Deposits 513
14.4 Results 513
14.5 Discussion 520
14.6 Conclusion 522
References 523

15 Cooperative Effects in Plasmonics 525
Vitaliy N. Pustovit and Tigran V. Shahbazyan
15.1 Plasmon-Mediated Superradiance Near Metal Nanostructures 525
15.1.1 Introduction 525
15.1.2 Plasmonic Coupling of Radiating Dipoles 528
15.1.3 Radiated Energy of an Ensemble of Dipoles Near Nanoparticle 533
15.1.4 Discussion and Numerical Results 534

15.2 Resonance Energy Transfer Near Metal Nanostructures Mediated by Surface Plasmons 544
15.2.1 Introduction 544
15.2.2 Energy Transfer from a Single Donor to an Acceptor Near Plasmonic Nanostructure 546
15.2.3 Numerical Results for Plasmon-Assisted Single-Donor Energy Transfer Near Metal Nanoparticle 551
15.2.4 Cooperative Plasmon-Assisted Resonance Energy Transfer from an Ensemble of Donor to an Acceptor 553
15.2.5 Numerical Results for Cooperative Energy Transfer. 557
References 564

Index 567

Chapter 1
Nanoplasmonics: From Present into Future

Mark I. Stockman

Abstract A review of nanoplasmonics is given. This includes fundamentals, nanolocalization of optical energy and hot spots, ultrafast nanoplasmonics and control of the spatiotemporal nanolocalization of optical fields, and quantum nanoplasmonics (spaser and gain plasmonics). This chapter reviews both fundamental theoretical ideas in nanoplasmonics and selected experimental developments. It is designed both for specialists in the field and general physics readership.

Keywords Plasmon · Spaser · Stimulated emission · Generation threshold

1.1 Introduction

1.1.1 Preamble

This is a review chapter on fundamentals of nanoplasmonics. Admittedly, the selection of the included subjects reflects the interests and expertise of the author.

We have made a conscious decision not to include such important and highly developed subject as SERS (Surface Enhanced Raman Scattering). The reason is that this subject is too large and too specialized for this chapter. There is an extensive literature devoted to SERS. This includes both reviews and original publications—see, e.g., Refs. [1–5] and a representative collective monograph [6]. Another important subject that we do not include in this review is the extraordinary transmission of light through subwavelength holes—there are extensive literature and excellent reviews

M. I. Stockman (✉)
Ludwig Maximilian University, Munich, Germany

Max Plank Institute for Quantum Optics, Garching at Munich, Germany · Georgia State University, Atlanta, GA30340, USA
e-mail: mstockman@gsu.edu

T. V. Shahbazyan and M. I. Stockman (eds.), *Plasmonics: Theory and Applications*, Challenges and Advances in Computational Chemistry and Physics 15,
DOI: 10.1007/978-94-007-7805-4_1, © Springer Science+Business Media Dordrecht 2013

on this subject—see, e.g., [7–11]. Also, due to limitations of time and space we do not cover systematically a subject of particular interest to us: the adiabatic nanoconcentration of optical energy [12]. There are many important experimental developments and promising applications of this phenomenon [12–22]. This field by itself is large enough to warrant a dedicated review. We only briefly touch this subject in Sect. 1.4.5.

Another important class of questions that we leave mostly outside of this review chapter are concerned with applications of nanoplasmonics. Among this applications are sensing, biomedical diagnostics, labels for biomedical research, nanoantennas for light-emitting diodes, etc. There exist a significant number of reviews on the applications of nanopalsmonics, of which we mention just a few below, see also a short feature article [23]. Especially promising and important are applications to cancer treatment [24, 25], sensing and solar energy conversion to electricity [26], and photo-splitting of hydrogen [27] and water [28] ("artificial photosynthesis" for solar production of clean fuels).

Presently, nanoplasmonics became a highly developed and advanced science. It would have been an impossible task to review even a significant part of it. We select some fundamental subjects in plasmonics of high and general interest. We hope that our selection reflects the past, shows the modern state, and provides an attempt to glimpse into the future. Specifically, our anticipation is that the ultrafast nanoplasmonics, nanoplasmonics in strong field, and the spaser as a necessary active element will be prominently presented in this future. On the other hand, it is still just a glimpse into it.

1.1.2 Composition of the Chapter

In Sect. 1.2, we present an extended introduction to nanoplasmonics. Then we consider selected subfields of nanoplasmonics in more detail. Nanoplasmonics is presently a rather developed science with a number of effects and rich applications [23]. In the center of our interest and, in our opinion, the central problem of nanoplasmonics is control and monitoring of the localization of optical energy in space on the nanometer scale and in time on the femtosecond or even attosecond scale.

In Sect. 1.3, we consider ultimately small nanoplasmonic systems with size less or on the order of skin depth l_s where we employ the so-called quasistatic approximation to describe in an analytical form the nanolocalized optical fields, their eigenmodes and hot spots, and introduce the corresponding Green's functions and solutions. This section is focused on the spatial nanoconcentration of the local optical fields.

In Sect. 1.4 we present ideas and results of ultrafast nanoplasmonics and coherent control of nanoscale localization of the optical fields, including control in time with femtosecond resolution. We will describe both theoretical ideas and some experimental results.

One of the most important problems of the nanoplasmonics, where only recently solutions and first experimental results have been obtained, is the active and gain nanoplasmonics. Its major goal is to create nanoscale quantum generators and

amplifiers of optical energy. In Sect. 1.5, we present theory and a significant number of experimental results available to date regarding the spaser and related polaritonic spasers (nanolasers or plasmonic lasers). We also consider a related problem of loss compensation in metamaterials.

1.2 Basics of Nanoplasmonics

1.2.1 Fundamentals

Nanoplasmonics is a branch of optical condensed matter science devoted to optical phenomena on the nanoscale in nanostructured metal systems. A remarkable property of such systems is their ability to keep the optical energy concentrated on the nanoscale due to modes called surface plasmons (SPs). It is well known [29] and reviewed below in this chapter that the existence of SPs depends entirely on the fact that dielectric function ε_m has a negative real part, $\mathrm{Re}\,\varepsilon_m < 0$. The SPs are well pronounced as resonances when the losses are small enough, i.e., $\mathrm{Im}\,\varepsilon_m \ll -\mathrm{Re}\,\varepsilon_m$. This is a known property of a good plasmonic metal, valid, e.g., for silver in the most of the visible region. We will call a substance a good plasmonic metal if these two properties

$$\mathrm{Re}\,\varepsilon_m < 0, \quad \mathrm{Im}\,\varepsilon_m \ll -\mathrm{Re}\,\varepsilon_m \tag{1.1}$$

are satisfied simultaneously.

There is a limit to which an electromagnetic wave can be concentrated. We immediately note that, as we explain below, nanoplasmonics is about concentration of *electromechanical* energy at optical frequencies (in contrast to electromagnetic energy) on the nanoscale.

The scale of the concentration of electromagnetic energy is determined by the wavelength and can be understood from Fig. 1.1a. Naively, let us try to achieve the strongest light localization using two parallel perfect mirrors forming an ideal Fabry-Perot resonator. A confined wave (resonator mode) should propagate normally to the surface of the mirrors. In this case, its electric field $\mathbf{E}$ is parallel to the surface of the mirror. The ideal mirror can be thought of as a metal with a zero skin depth that does not allow the electric field of the wave $\mathbf{E}$ to penetrate inside. Therefore the field is zero inside the mirror and, due to the Maxwell boundary conditions, must be zero on the surface of the mirror. The same condition should be satisfied at the surface of the second mirror. Thus, length L of this Fabry-Perot cavity should be equal an integer number n of the half-wavelengths of light in the inner dielectric, $L = n\lambda/2$. The minimum length of this resonator is, obviously $\lambda/2$. This implies that light cannot be confined tighter than to a length of $\lambda/2$ in each direction, with the minimum modal volume of $\lambda^3/8$.

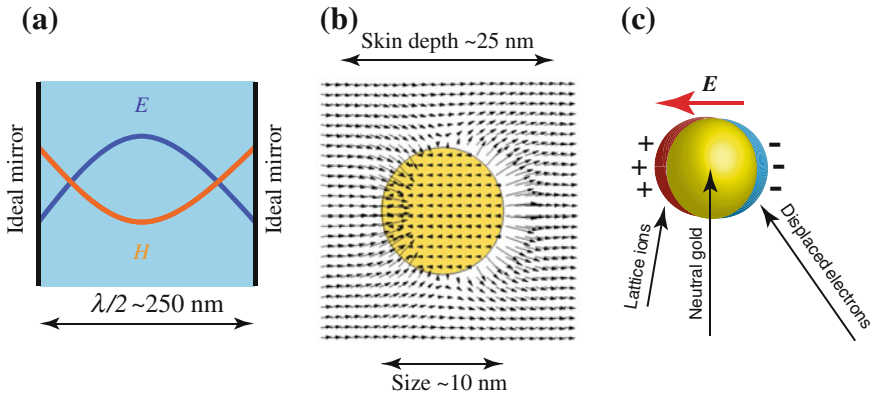

Fig. 1.1 **a** Localization of optical fields by ideal mirrors and **b** by a gold nanoparticle. **c** Schematic of charge separation

One may think that it is impossible to achieve a localization of the optical energy to smaller volume than $\lambda^3/8$ by any means, because the ideal mirrors provide the best confinement of electromagnetic waves. There are two implied assumptions: (i) The optical energy is electromagnetic energy, and (ii) The best confinement is provided by ideal mirrors. Both these assumptions must be abandoned to achieve nanolocalization of optical energy.

Consider a nanoplasmonic system whose size is less than or comparable to the skin depth

$$l_s = \lambda\!\!\!^{-}\left[\mathrm{Re}\left(\frac{-\varepsilon_m^2}{\varepsilon_m+\varepsilon_d}\right)^{1/2}\right]^{-1}, \tag{1.2}$$

where $\lambda\!\!\!^{-} = \lambda/(2\pi) = \omega/c$ is the reduced vacuum wavelength. For single-valence plasmonic metals (silver, gold, copper, alkaline metals) $l_s \approx 25\,\mathrm{nm}$ in the entire optical region.

For such a plasmonic nanosystem with $R \lesssim l_s$, the optical electric field penetrates the entire system and drives oscillations of the metal electrons. The total energy of the system in this case is a sum of the potential energy of the electrons in the electric field and their mechanical kinetic energy. While the magnetic field is present, non-relativistic electrons' interaction with it is weak proportional to a small parameter $v_F/c \sim \alpha \sim 10^{-2}$, where v_F is the electron speed at the Fermi surface, c is speed of light, and $\alpha = e^2/\hbar c$ is the fine structure constant. Thus in this limit, which is conventionally called quasistatic, the effects of the magnetic component of the total energy is relatively small. Hence, this total energy is mostly *electromechanical* (and not electromagnetic) energy. [At this point, it may be useful to refer to Eq. (1.107), which expresses the Brillouin formula for total energy $\mathscr{E}$ of a system in such a quasistatic case.] This is why the wavelength, which determines the length

scale of the energy exchange between the electric and magnetic components of an electromagnetic wave, does not define the limit of the spatial localization of energy. Because the size of the system R is smaller than any electromagnetic length scale, of which smallest is l_s, it is R that defines the spatial scale of the optical energy localization. Thus the optical fields are confined on the nanoscale, and their spatial distribution scales with the system's size. This physical picture is at the heart of the nanoplasmonics.

Consider as an example a gold nanosphere of radius $R < l_s$, e.g., $R \sim 10\,\text{nm}$, subjected to a plane electromagnetic wave, as shown in Fig. 1.1b. The field penetrates the metal and causes displacement of electrons with respect to the lattice resulting in the opposite charges appearing at the opposing surfaces, as illustrated in Fig. 1.1c. The attraction of these charges causes a restoring force that along with the (effective) mass of the electrons defines an electromechanical oscillator called a SP. When the frequency ω_{sp} of this SP is close to the frequency of the excitation light wave, a resonance occurs leading to the enhanced local field at the surface, as illustrated in Fig. 1.1b.

This resonant enhancement has also an adverse side: loss of energy always associated with a resonance. The rate of this loss is proportional to $\text{Im}\,\varepsilon_m$ [30]. This leads to a finite lifetime of SPs. The decay rate of the plasmonic field γ is $\propto (\text{Im}\,\varepsilon_m)^{-1}$. In fact, it is given below in this chapter as Eq. (1.49) in Sect. 1.3.4. This expression has originally been obtained in Ref. [31] and is also reproduced below for convenience,

$$\gamma = \frac{\text{Im}\, s(\omega)}{\frac{\partial \text{Re}\, s(\omega)}{\partial \omega}} \approx \frac{\text{Im}\, \varepsilon_m(\omega)}{\frac{\partial \text{Re}\varepsilon_m(\omega)}{\partial \omega}}, \tag{1.3}$$

where

$$s(\omega) = \frac{\varepsilon_d}{\varepsilon_d - \varepsilon_m(\omega)} \tag{1.4}$$

is Bergman's spectral parameter [29]. Note that γ does not explicitly depend on the system geometry but only on the optical frequency ω and the permittivities. However, the system's geometry determines the SP frequency ω and, thus, implicitly enters these equations. The approximate equality in Eq. (1.3) is valid for relatively small relaxation rates, $\gamma \ll \omega$. Apart from γ, an important parameter is the so-called quality factor

$$Q = \frac{\omega}{2\gamma} \approx \frac{\omega \frac{\partial \text{Re}\varepsilon_m(\omega)}{\partial \omega}}{2\text{Im}\,\varepsilon_m(\omega)} \tag{1.5}$$

The quality factor determines how many optical periods free SP oscillations occur before field decays. It also shows how many times the local optical field at the surface of a plasmonic nanoparticle exceeds the external field.

Note that another definition of the quality factor, which is often used, is

$$Q = \frac{-\text{Re}\,\varepsilon_m(\omega)}{\text{Im}\,\varepsilon_m(\omega)}. \tag{1.6}$$

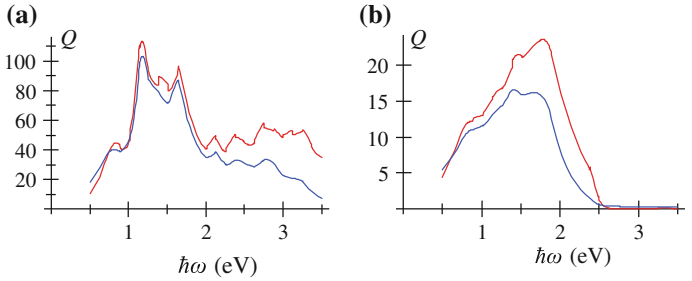

Fig. 1.2 **a** Quality factor Q for silver and **b** for gold calculated according to Eq. (1.5) (*red*) and Eq. (1.6) (*blue*) as a function of frequency ω

The SP quality factors Q calculated according to Eqs. (1.5)–(1.6) for gold and silver using the permittivity data of Ref. [32] are shown in Fig. 1.2. The Q-factors found from these two definitions agree reasonably well in the red to near-infrared (near-ir) region but not in the yellow to blue region of the visible spectrum. The reason is that these two definitions would be equivalent if metals' permittivity were precisely described by a Drude-type formula $\mathrm{Re}\,\varepsilon_m(\omega) = -\omega_p^2/\omega^2$, where ω_p is the bulk plasma frequency; $\hbar\omega_p \approx 9\,\mathrm{eV}$ for one-electron metals such as silver, copper, gold, and alkaline metals. This formula is reasonably well applicable in the red and longer wavelength part of the spectrum, but not in the yellow to blue part where the D-band transitions are important. Note that silver is a much better plasmonic metal than gold: its Q-factor is several-fold of that of gold.

The finite skin depth of real metals leads to an effect related to nanoplasmonic confinement: a phase shift $\Delta\varphi$ for light reflected from a metal mirror deviates from a value of $\Delta\varphi = \pi$ characteristic of an ideal metal. As suggested in Ref. [33], this allows for ultrasmall cavities whose length $L \ll \lambda$. While generally this is a valid idea, there two problems with Ref. [33] that affect the validity of its specific results. First, the Fresnel reflection formulas used in this article to calculate $\Delta\varphi$ are only valid for infinite surfaces but not for the "nanomirrors" in a nanocavity. Second, Eq. (1.1) of this article expressing Q is incorrect: it contains in the denominator a quantity $\partial\,[\omega\mathrm{Im}\varepsilon_m(\omega)]/\partial\omega$ instead of $2\mathrm{Im}\,\varepsilon_m(\omega)$ as in Eq. (1.5). The correct expression [30] for Ohmic losses defining the Q-factor, which we reproduce as Eq. (1.108), is proportional to $\mathrm{Im}\,\varepsilon_m(\omega)$ as in Eq. (1.5) and not to $\partial\,[\omega\mathrm{Im}\varepsilon_m(\omega)]/\partial\omega$, which constitutes a significant difference.

The lifetime τ of the SPs is related to the spectral width as

$$\tau = \frac{1}{2\gamma}. \tag{1.7}$$

Note that the SP spectral width γ, quality factor Q, and lifetime τ depend explicitly only on frequency ω and the type of the metal (permittivity ε_m) but not on the nanosystem's geometry or surrounding dielectric. However, this geometry and

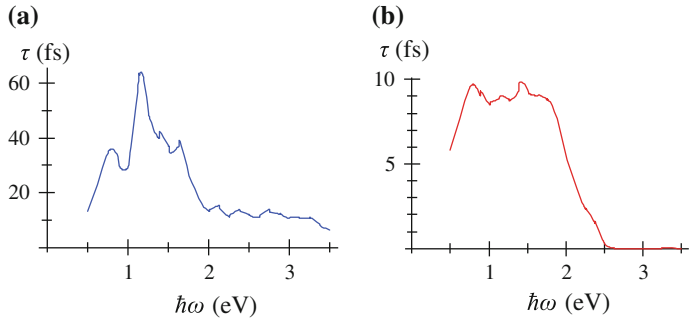

Fig. 1.3 **a** Lifetime τ of SPs for silver and **b** for gold calculated according to Eq. (1.7) as a function of frequency ω

the ambient-dielectric permittivity ε_d do affect the modal frequency and enter the corresponding Eqs. (1.3), (1.5), and (1.7) implicitly via ω.

The dependence of the SP lifetime τ on frequency ω calculated for gold and silver using permittivity [32] is illustrated in Fig. 1.3. This lifetime is in the range 10–60 fs for silver and 1–10 fs for gold in the plasmonic region. These data show that nanoplasmonic phenomena are ultrafast (femtosecond).

However, the fastest linear response time τ_c of SPs, as any other linear response system, depends not on the relaxation time but solely on the bandwidth. In fact, it can be calculated as a quarter period (i.e., a time interval between zero and the maximum field) of the beating between the extreme spectral components of the plasmonic oscillations,

$$\tau_c = \frac{1}{4}\frac{2\pi}{\Delta\omega}, \tag{1.8}$$

where $\Delta\omega$ is the spectral bandwidth of the plasmonic spectrum. For gold and silver, this bandwidth is the entire optical spectrum, i.e., $\hbar\Delta\omega \approx 3.5\,\text{eV}$. If aluminum is included among system's plasmonic metals, this bandwidth is increased to $\hbar\Delta\omega \approx 9\,\text{eV}$. This yields this coherent reaction time $\tau_c \sim 100\,\text{as}$. Thus nanoplasmonics is potentially attosecond science.

While the characteristic size of a nanoplasmonic system should be limited from the top by the skin depth, $R \ll l_s$, it is also limited from the bottom by the so called nonlocality length l_{nl}—see, e.g., [34, 35]. This nonlocality length is the distance that an electron with the Fermi velocity v_F moves in space during a characteristic period of the optical field,

$$l_{nl} \sim v_F/\omega \sim 1\,\text{nm}, \tag{1.9}$$

where an estimate is shown for the optical spectral region. For metal nanoparticles smaller than l_{nl}, the spatial dispersion of the dielectric response function and the related Landau damping cause broadening and disappearance of SP resonances [34, 35].

Thus, we have arrived at the basic understanding of the qualitative features of nanoplasmonics. Consider a plasmonic nanosystem whose size R satisfies a condition $l_{nl} \ll R \ll l_s$. This nanosystem is excited by an external field in resonance. In this case, the local optical field in the vicinity of such a nanosystem is enhanced by a factor $\sim Q$, which does not depend on R. The spatial extension of the local field scales with the size of the nanosystem $\propto R$. This is because $R \ll l_s$, and l_s is the smallest electromagnetic length; thus there is no length in the system that R can be comparable to. When the external field changes, the local field relaxes with the relaxation time Q/ω that does not depend on R; the lifetimes of the SP are in the femtosecond range.

In many cases of fundamental and applied significance, the size of a nanosystem can be comparable to or even greater than l_s but still subwavelength, $\lambda \gg R \gtrsim l_s$. In such a case, the coupling to far-field radiation and radiative losses may greatly increase as we will discuss below in Sects. 1.2.2 and 1.2.3. Another important subfield of nanoplasmonics that is related to extended systems is the surface plasmon polaritons—see, e.g., a collective monograph [36]. We consider some polaritonic phenomena relevant to coherent control below in Sect. 1.4.5.

1.2.2 Nanoantennas

Consider a molecule situated in the near-field of a metal plasmonic nanosystem. Such a molecule interacts not with the external field but with the local optical field $\mathbf{E}(\mathbf{r})$ at its location $\mathbf{r}$. The interactions Hamiltonian of such a molecule with the optical field is $H' = -\mathbf{E}(\mathbf{r})\mathbf{d}$, where $\mathbf{d}$ is the dipole operator of this molecule. Note that a modal expansion of the quantized local field operator is given below in this chapter by Eq. (1.64).

Consequently, the enhanced local fields cause enhancement of radiative and nonradiative processes in which such a molecule participate. In particular, the rates of both the excitation and emission are enhanced proportionality to the local field intensity, i.e., by a factor of $\sim Q^2$. This effect is often referred to as nanoantenna effect [37–64] in analogy with the common radio-frequency antennas. For the recent review of the concept and applications of optical nanoantennas see Ref. [65]. Currently, the term nanoantenna or optical antenna is used so widely that it has actually became synonymous with the entire field of nanoplasmonics: any enhancement in nanoplasmonic systems is called a nanoantenna effect.

General remarks about the terms "nanoantenna" or "optical antenna" are due. The term "antenna" has originated in the conventional radio-frequency technology where it is used in application to receivers for devices that convert the wave energy of far-field radio waves into local (near-field) electric power used to drive the input circuitry. For transmitters, antennas perform the inverse transformation: from the local field electric power to that of the emitted radio waves. Due to the general properties of time reversal symmetry there is no principal difference between the receiving and transmitting antennas: any receiving antenna can work as a transmitting one and

vice versa. The mechanism of the efficiency enhancement in the radio frequency range is a combination of spatial focusing (e.g., for parabolic antennas) and resonant enhancement (e.g., for a dipole antenna). In all cases, the size of the radio antenna is comparable to or greater than the wavelength. Thus one may think that a receiving antenna collects energy from a large geometric cross and concentrates it in a small, subwalength area.

The receiving antennas in radio and microwave technology are loaded by matched impedance loads that effectively withdraw the energy from them. This suppresses the radiation by such antennas but simultaneously dampens their resonances and makes them poor resonators.

In majority of cases, the optical antennas are not matched-loaded because they are designed not to transduce energy efficiently but to create high local fields interacting with molecules or atoms, which do not load these antennas significantly. (There are exceptions though: for instance, the nanoantenna in Ref. [66] is loaded with an adiabatic nanofocusing waveguide.) The unloaded antennas efficiently loose energy to radiation (scattering), which also dampens their resonances.

A question is whether this concept of collecting energy form a large geometric cross section is a necessary paradigm also in nanoplasmonics. The answer is no, which is clear already from the fact that the enhancement of the rates of both the excitation and emission of a small chromophore (molecule, rear earth ion, etc.) in the near field of a small ($R \lesssim l_s$) plasmonic nanoparticle is $\sim Q^2$ and *does not depend* on the nanoparticle size R. This enhancement is due to the coherent resonant accumulation of the energy of the SPs during $\sim Q$ plasmonic oscillations and has nothing to do with the size of the nanoparticle. Thus such an enhancement does not quite fit into the concept of antennas as established in the radio or microwave technology.

Another test of the nanoantenna concept is whether the efficiency of a nanoantenna is necessarily increased with its size. The answer to this question is generally no. This is because for plasmonic nanoparticles, with the increase of size there is also an increased radiative loss—see below Sect. 1.2.3. In contrast, for many types of radio-frequency antennas (dish antennas or microwave-horn antennas, for instance), the efficiency does increase with the size.

1.2.3 Radiative Loss

As we described above in conjunction with Fig. 1.1c, the interaction of optical radiation with a nanoplasmonic system occurs predominantly via the dipole oscillations. The radiative decay of SPs occur via spontaneous emission of photons, which is a process that does not exist in classical physics and requires a quantum-mechanical treatment. To find the radiative life time of a SP state quantum-mechanically, we need to determine the transitional dipole matrix element $\mathbf{d}_{0p}$ between the ground state $|0\rangle$ and a single-plasmon excited state $|p\rangle$. To carry out such a computation consistently,

one needs to quantize the SPs, which we have originally done in Ref. [31] and present below in Sect. 1.5.4.1.

However, there is a general way to do it without the explicit SP quantization, which we present below in this section. We start with the general expression for polarizability α of a nanosystem obtained using quantum mechanics—see. e.g., Ref. [67], which near the plasmon frequency has a singular form,

$$\alpha = \frac{1}{\hbar}\frac{\left|\mathbf{d}_{0p}\right|^2}{\omega - \omega_{sp}}, \tag{1.10}$$

where ω_{sp} is the frequency of the resonant SP mode. This can compared with the corresponding pole expression of the polarizability of a nanoplasmonic system, which is given below as Eq. (1.55), to find absolute value of the matrix element $\left|\mathbf{d}_{0p}\right|$.

Here, for the sake of simplicity, we will limit ourselves to a particular case of a nanosphere whose polarizability is given by a well-known expression

$$\alpha = R^3 \frac{\varepsilon_m(\omega) - \varepsilon_d}{\varepsilon_m(\omega) + 2\varepsilon_d}, \tag{1.11}$$

where R is the radius of the nanosphere. The SP frequency $\omega = \omega_{sp}$ corresponds to the pole of α, i.e., it satisfies an equation

$$\mathrm{Re}\,\varepsilon_m(\omega_{sp}) = -2\varepsilon_d, \tag{1.12}$$

where we neglect $\mathrm{Im}\,\varepsilon_m$. In the same approximation, near $\omega = \omega_{sp}$, we obtain from Eq. (1.11),

$$\alpha = -3R^3\varepsilon_d \left[\left(\omega - \omega_{sp}\right)\frac{\partial \mathrm{Re}\,\varepsilon_m(\omega_{sp})}{\partial \omega_{sp}}\right]^{-1}. \tag{1.13}$$

Comparing the two pole approximations of Eqs. (1.10) and (1.13), we obtain the required expression for the dipole moment of a quantum transition between the ground state and the SP state,

$$\left|\mathbf{d}_{0p}\right|^2 = \hbar 3R^3\varepsilon_d \left[\frac{\partial \mathrm{Re}\,\varepsilon_m(\omega_{sp})}{\partial \omega_{sp}}\right]^{-1}. \tag{1.14}$$

Consider the well-known quantum-mechanical expression for the dipole-radiation rate (see, e.g., Ref. [67]),

$$\gamma^{(r)} = \frac{4}{3}\frac{\omega^3\sqrt{\varepsilon_d}}{\hbar c^3}\left|\mathbf{d}_{0p}\right|^2. \tag{1.15}$$

Substituting Eq. (1.14) into (1.15), we obtain the desired expression for the quantum-mechanical rate of the radiative decay of the SP state as

$$\gamma^{(r)} = 4\varepsilon_d^{3/2}\left(\frac{\omega_{sp}R}{c}\right)^3\left[\frac{\partial \mathrm{Re}\,\varepsilon_m(\omega_{sp})}{\partial\omega_{sp}}\right]^{-1}. \tag{1.16}$$

Note that for losses not very large (which is the case in the entire plasmonic region for noble metals), the Kramers-Kronig relations for $\varepsilon_m(\omega)$ predict [30] that

$$\frac{\partial \mathrm{Re}\,\varepsilon_m(\omega_{sp})}{\partial\omega_{sp}} > 0, \tag{1.17}$$

which guarantees that $\gamma^{(r)} > 0$ in Eq. (1.16).

Comparing this expression to Eq. (1.3) [see also Eq. (1.49)], we immediately conclude that, in contrast to the internal (radiationless) loss rate γ, the radiative rate is proportional to the volume of the system (i.e., the number of the conduction electrons in it), which is understandable. Thus for systems small enough, the radiative rate can be neglected. The quality factor of the SP resonance is actually defined by the total decay rate $\gamma^{(\mathrm{tot})}$ [cf. Eq. (1.5)],

$$Q = \frac{\omega_{sp}}{2\gamma^{(tot)}}, \quad \gamma^{(tot)} = \gamma + \gamma^{(r)}. \tag{1.18}$$

Therefore, Q is lower for larger nanoparticles, tending to a constant for small R. To quantify it, we find a ratio

$$\frac{\gamma^{(\mathrm{tot})}}{\gamma} = 1 + \frac{4}{\mathrm{Im}\,\varepsilon_m(\omega_{sp})}\left(\frac{\sqrt{\varepsilon_d}\omega_{sp}R}{c}\right)^3. \tag{1.19}$$

We illustrate behavior of this rate ratio of the total to internal loss, $\gamma^{(\mathrm{tot})}/\gamma$, in Fig. 1.4. General conclusion is that the radiative loss for silver is not very important for nanospheres in the true quasistatic regime, i.e., for $R < l_s \approx 25$ nm but is a dominant mechanism of loss for $R > 30$ nm, especially in high-permittivity environments. In contrast, for gold the radiative loss is not very important in the quasistatic regime due to the much higher intrinsic losses, except for a case of a relatively high ambient permittivity, $\varepsilon_d = 5$.

Though it is outside of the scope of this chapter, we would like to point out that there is a general approach to combat radiative losses in relatively large nanoparticles. This is related to the well-known Fano resonances originally discovered by Ugo Fano in atomic spectra [68]. These resonances can be described in the following way. In certain cases of optical excitation, when two quantum paths lead to the same final quantum state of the system, the resonance peaks have specific asymmetric line shapes due to the interference of these quantum paths.

An analogous phenomenon is also known in nanoplasmonics and metamaterials [69–77]. It can be explained in the following way [77]. Apart from bright plasmonic resonances with high transitional dipole moment, there are also dark ones [78], which by themselves are not very prominent in optical spectra. However, if a bright

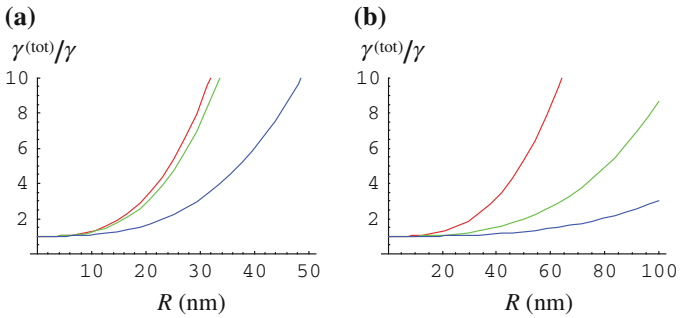

Fig. 1.4 Ratio of the rates of the total to internal loss, $\gamma^{(\mathrm{tot})}/\gamma$, for a nanosphere as a function of its radius R for **a** silver and **b** gold. The *blue*, *green*, and *red lines* correspond to the embedding dielectric with $\varepsilon_d = 1, 2$, and 5, respectively. The computations are made at the SP frequency ω_{sp}, which for these value of ε_d is for silver $\hbar\omega_{sp} = 3.5, 3.2, 2.5\,\mathrm{eV}$, and for gold $\hbar\omega_{sp} = 2.6, 2.4, 2.0\,\mathrm{eV}$, correspondingly

resonance and a dark resonance coexist in a certain spectral range—which is not unlikely, because the bright resonances are spanning relatively wide wavelength ranges—then their optical fields interfere. This interference significantly enhances the manifestation of the dark resonance: it acquires strength from the bright resonance and shows itself as an asymmetric peak-and-dip profile characteristic of a Fano resonance. An important, albeit counterintuitive, property of the Fano resonances is that, exactly at the frequency of the Fano dip, the hot spots of the nanolocalized optical fields in the nanosystem are strongest. This is because at this frequency the nanosystem emits minimal light intensity and, consequently, it does not wastefully deplete the energy of the plasmon oscillations. This leads to a decreased radiative loss and a high resonance quality factor.

Thus at the frequency of a Fano resonance, the radiative loss is significantly suppressed. The width of the Fano resonances is ultimately determined by the internal (Ohmic) losses described by $\mathrm{Im}\,\varepsilon_m$. Summarizing, the Fano resonances enable one using relatively large nanoplasmonic particles or plasmonic metamaterials to achieve narrow spectral features with high local fields. These can be applied to plasmonic sensing and to produce spasers and nanolasers—see Sect. 1.5.

1.2.4 Other Important Issues of Plasmonics in Brief

There are other very important issues and directions of investigation in plasmonics that we will not be able to review in any details in this chapter due to the limitations of time and space. Below we will briefly list some of them.

1.2.4.1 Enhanced Mechanical Forces in Nanoplasmonic Systems

The resonantly enhanced local fields in the vicinity of plasmonic nanoparticles lead to enhanced nanolocalized forces acting between the nanoparticles, see, e.g., Refs. [79–85]. A perspective application of plasmonically-enhanced forces is optical manipulation (tweezing) of micro- and nanoparticles [86–92].

Another direction of research is opened up by the recently introduced theoretically surface-plasmon-induced drag-effect rectification (SPIDER) [93], which is based on transfer of the linear momentum from decaying surface-plasmon polaritons (SPPs) to the conduction electrons of a metal nanowire. The SPIDER effect bears a promise to generate very high terahertz fields in the vicinity of the metal nanowire.

1.2.4.2 Interaction Between Electrons and Surface Plasmons

The surface plasmonics, as it is called today, originated by a prediction of electron energy losses for an electron beam in thin metal films below the energy of the bulk plasmons [94]. This is how coherent electronic excitations called SPPs today were predicted. Soon after this prediction, the SPP-related energy losses were experimentally confirmed [95, 96]. Presently, the electron energy loss spectroscopy (EELS) in nanopalsmonics is a thriving field of research. We refer to a recent review [97] for further detail.

A distinct and original direction of research is control of mechanical motion of metal nanoparticles using electron beams [98]. It is based on the same principles as optically-induced forces. The difference in this case is that the SP oscillations in nanoparticles are excited locally, with an angstrom precision, by a beam of fast electrons—see also Sect. 1.2.4.1 above.

There are other important phenomena in plasmonics based on electron-SP interaction called nonlocality [99]. One of them is dephasing of plasmons causing their decay into electron-hole pairs, which is called Landau damping, contributing to $\mathrm{Im}\,\varepsilon_m$. There is necessarily a related phenomenon of spatial dispersion contributing to $\mathrm{Re}\,\varepsilon_m$. These become important for plasmonics when the size of the nanosystem become too small, $R \lesssim l_{nl}$—see Eq. (1.9). The nonlocality and Landau damping degrade plasmonic effects. The nonlocal effects lead to an increased decay rate of dipolar emitters at metal surfaces [34] and limits resolution of plasmonic imaging, making the so-called "perfect" lens [100] rather imperfect [35]. In aggregates, the nonlocality of dielectric responses causes reduction of local fields and widening of plasmonic resonances [101]. These broadening effects have initially been taken into account purely phenomenologically by adding an additional contribution to the width of plasmonic resonances $\sim A/\tau_{nl}$, where $A = const$ [102]. Practically, if the size of a nanoparticle is less then 3 nm, the non-local broadening of the SP resonances is very significant; otherwise, it can be neglected in a reasonable approximation.

The above-mentioned publications [34, 35, 99, 101] on the nonlocality phenomena are based on a semi-phenomenological approach where the nonlocality is treated via applying additional boundary conditions stemming from the electron scattering

by the boundaries of the plasmonic system. A more advanced approach to nonlocality in nanoplasmonics, albeit treatable only for very small, $R \lesssim 1$ nm, nanoparticles, is based on an *ab initio* quantum-chemical approach of time-dependent density functional theory (usually abbreviated as TD-DFT) [103–109].

It shows that while for larger particles and relatively large spacing between them ($\gtrsim$1 nm), the semi-phenomenological models work quite well; for smaller nanoparticles and gaps the predicted local fields are significantly smaller. This is understandable because in *ab initio* theories there are phenomena that are important in the extremely small nanosystem such as a significant dephasing due to the stronger coupling between the collective plasmon and one-particle electron degrees of freedom, discreetness of the one-electron spectrum, spill-out of the conduction-band electrons (extension of their wave function outside of the lattice region) and the corresponding undescreening of the d-band electrons, and simply the discreetness of the lattice.

In the latest set of publications, e.g., [108, 109], this approach is called quantum nanoplasmonics. We would argue that this approach is traditionally called quantum chemistry because what is found from the TD-DFT quantum-mechanically is the dielectric response (susceptibility or polarizability) of the nanosystems. However, even to calculate theoretically the permittivity of a bulk method, one has to employ quantum-mechanical many-body approaches such as the random-phase approximation, self-consistent random-phase approximation (or GW-aproximation), or TD-DFT, etc. The only difference from the above-sited works is that for bulk metals the size effects are absent. Therefore permittivities can be adopted from experimental measurements such as Ref. [32, 110].

Based on the arguments of the preceding paragraph, we would reserve the therm "quantum plasmonics" for the subfields of nanoplasmonics studying phenomena related to quantum nature and behavior SPs and SPPs. This term has been proposed in our 2003 paper [31] introducing the spaser as a quantum generator of nanolocalized optical fields—see Sect. 1.5 and references sited therein. A related field of studies devoted to quantum behavior of single SPPs also can reasonably be called quantum plasmonics as proposed later in Refs. [111, 112].

While the decay of SP excitations is usually a parasitic phenomenon, there are some effects that completely depend on it. One of them is the SPIDER [93] mentioned above in Sect. 1.2.4.1. It is based on the transfer of the energy and momentum from SPPs to the conduction electrons, which microscopically occurs through the decay of the SPPs into electron-hole pairs leading to production of hot electrons.

Yet another range of phenomena associated with a plasmon-dephasing decay into incoherent electron-hole pairs (Landau damping) has come to the forefront recently. This is the plasmon-assisted and enhanced generation of a dc electric current due to rectification in Schottky diodes involving hot electrons [61, 113–115]. This phenomenon is promising for applications to photodetection and solar energy conversion. Note that the use of the Schottky contacts between the plasmonic metal and a semiconductor permits one to eliminate a requirement that the photon energy $\hbar\omega$ is greater that the band gap. This is replaced by a much weaker requirement that $\hbar\omega$ is greater than a significantly lower Schottky-barrier potential [116].

1.2.4.3 Nonlinear Photoprocesses in Nanoplasmonics

As became evident from the first steps of what now is called nanoplasmonics, the enhanced local fields in resonant metal nanosystems bring about strongly enhanced nonlinear responses [117–120].

Nonlinear nanoplasmonics is presently a very large and developed field. Some of its phenomena related to coherent control and spasing are discussed in Sects. 1.4, and 1.5. Here we will give a classification of the nonlinear nanoplasmonic phenomena and provide some examples, not attempting at being comprehensive.

Nonlinearities in nanoplasmonics can occur in the nanostructured plasmonic metal, in the embedding medium (dielectric), or in both. Correspondingly, we classify them as intrinsic, extrinsic, or combined. As an independent classification, these nonlinearities can be classified as weak (perturbative) or strong (nonperturbative). The perturbative nonlinearities can be coherent (or parametric), characterized by nonlinear polirizabilities [121] and incoherent such as nonlinear absorption, two-photon fluorescence, surface-enhanced hyper-Raman scattering (SEHRS) [122], nonlinear photo-modification, two-photon electron emission [123], etc.

Here are some examples illustrating a variety of nonlinear photoprocesses in nanoplasmonics.

- Second-harmonic generation from nanostructured metal surfaces and metal nanoparticles [57, 124–132] is a coherent, perturbative (second-order or three-wave mixing), intrinsic nonlinearity.
- Enhanced four wave mixing (sum- or difference frequency generation) at metal surfaces [133] is a coherent, perturbative (third-order or four-wave), intrinsic nonlinearity.
- Another four-wave mixing process in a hybrid plasmonic-photonic waveguide involves nonlinearities in both metal and dielectric [134] and, therefore, is classified as a coherent, combined, perturbative third-order nonlinear process.
- An all-optical modulator consisting of a plasmonic waveguide covered with CdSe quantum dots [135] is based on a perturbative third-order, combined nonlinearity. To the same class belongs a nanoscale-thickness metamaterial modulator [136].
- An ultrafast all-optical modulator using polaritons in an aluminum plasmonic waveguide is based on perturbative third-order, intrinsic nonlinearity [137]. There are arguments that this nonlinearity is incoherent, based on interband population transfer of carriers [137].
- Nonperturbative (strong-field), coherent, extrinsic nonlinearity is plasmon-enhanced generation of high harmonics [138] where the enhanced nanoplasmonic fields excite argon atoms in the surrounding medium. Spaser [31] belongs to the same class where the nonlinearity is the saturation of the gain medium by the coherent plasmonic field [139]. The same is true for the loss compensation by gain [140, 141].
- Intrinsic perturbative nonlinearities in nanoplasmonics stemming from a redistribution of the electron density caused by the ponderomotive forces of nanoplasmonic fields have been predicted for surface plasmon polaritons [93, 142]. An intrinsic

nonperturbative nonlinear process is the predicted plasmon soliton [143] where strong local optical fields in a plasmonic waveguide cause a significant redistribution of the conduction-electron density.

- There are also relevant strongly-nonlinear processes in non-plasmonic materials that are based on nanolocalized fields and are very similar to those in plasmonics. Among them are near-field enhanced electron acceleration from dielectric nanospheres with intense few-cycle laser fields [144]. Another such a process is a strong optical-field electron emission from tungsten nanotips controlled with an attosecond precision [145].
- Finally, a recently predicted phenomenon of metallization of dielectrics by strong optical fields [146, 147] belongs to a new class of highly-nonlinear phenomena where strong optical fields bring a dielectric nanofilm into a plasmonic metal-like state.

1.3 Nanolocalized Surface Plasmons (SPs) and Their Hot Spots

1.3.1 SPs as Eigenmodes

Assuming that a nanoplasmonic system is small enough, $R \ll \lambda\!\!\!^{-}$, $R \lesssim l_s$, we employ the so-called quasistatic approximation where the Maxwell equations reduce to the continuity equation for electrostatic potential $\varphi(\mathbf{r})$,

$$\frac{\partial}{\partial \mathbf{r}} \varepsilon(\mathbf{r}) \frac{\partial}{\partial \mathbf{r}} \varphi(\mathbf{r}) = 0. \tag{1.20}$$

The systems permittivity (dielectric function) varying in space is expressed as

$$\varepsilon(\mathbf{r}) = \varepsilon_m(\omega)\Theta(\mathbf{r}) + \varepsilon_d[1 - \Theta(\mathbf{r})]. \tag{1.21}$$

Here $\Theta(\mathbf{r})$ is the so-called characteristic function of the nanosystem, which is equal to 1 when $\mathbf{r}$ belongs to the metal and 0 otherwise. We solve this equation following the spectral theory developed in Refs. [29, 78, 148].

Consider a nanosystem excited by an external field with potential $\varphi_0(\mathbf{r})$ at an optical frequency ω. This potential is created by external charges and, therefore, satisfies the Laplace equation within the system,

$$\frac{\partial^2}{\partial \mathbf{r}^2} \varphi_0(\mathbf{r}) = 0. \tag{1.22}$$

We present the field potential as

$$\varphi(\mathbf{r}) = \varphi_0(\mathbf{r}) + \varphi_1(\mathbf{r}), \tag{1.23}$$

where $\varphi_1(\mathbf{r})$ is the local field.

Substituting Eq. (1.23) into (1.20) and taking Eqs. (1.21) and (1.22) into account, we obtain a second-order elliptic equation with the right-hand side that describes the external excitation source,

$$\frac{\partial}{\partial \mathbf{r}} \Theta(\mathbf{r}) \frac{\partial}{\partial \mathbf{r}} \varphi_1(\mathbf{r}) - s(\omega) \frac{\partial^2}{\partial \mathbf{r}^2} \varphi_1(\mathbf{r}) = -\frac{\partial}{\partial \mathbf{r}} \Theta(\mathbf{r}) \frac{\partial}{\partial \mathbf{r}} \varphi_0(\mathbf{r}), \tag{1.24}$$

where $s(\omega)$ is Bergman's spectral parameter [29] defined by Eq. (1.4).

As a convenient basis to solve this field equation we introduce eigenmodes (SPs) with eigenfunctions $\varphi_n(\mathbf{r})$ and the corresponding eigenvalues, s_n, where n is the full set of indices that identify the eigenmodes. These eigenmodes are defined by the following generalized eigenproblem,

$$\frac{\partial}{\partial \mathbf{r}} \Theta(\mathbf{r}) \frac{\partial}{\partial \mathbf{r}} \varphi_n(\mathbf{r}) - s_n \frac{\partial^2}{\partial \mathbf{r}^2} \varphi_n(\mathbf{r}) = 0, \tag{1.25}$$

where eigenfunctions $\varphi_n(\mathbf{r})$ satisfy the homogeneous Dirichlet-Neumann boundary conditions on a surface S surrounding the system. These we set as

$$\varphi_1(\mathbf{r})|_{\mathbf{r}\in S} = 0, \quad \text{or} \quad \mathbf{n}(\mathbf{r}) \frac{\partial}{\partial \mathbf{r}} \varphi_1(\mathbf{r}) \Big|_{\mathbf{r}\in S} = 0, \tag{1.26}$$

with $\mathbf{n}(\mathbf{r})$ denoting a normal to the surface S at a point of $\mathbf{r}$. These boundary conditions (1.26) are essential and necessary to define the eigenproblem.

From Eqs. (1.25)–(1.26) applying the Gauss theorem, we find

$$s_n = \frac{\int_V \Theta(\mathbf{r}) \left| \frac{\partial}{\partial \mathbf{r}} \varphi_n(\mathbf{r}) \right|^2 \mathrm{d}^3 r}{\int_V \left| \frac{\partial}{\partial \mathbf{r}} \varphi_n(\mathbf{r}) \right|^2 \mathrm{d}^3 r}. \tag{1.27}$$

From this equation, it immediately follows that all the eigenvalues are real numbers and

$$1 \geq s_n \geq 0. \tag{1.28}$$

Physically, as one can judge from Eq. (1.27), an eigenvalue of s_n is the integral fraction of the eigenmode (surface plasmon) intensity $|\partial \varphi_n(\mathbf{r}) / \partial \mathbf{r}|^2$ that is localized within the metal.

Because the SP eigenproblem is real, and all the eigenvalues s_n are all real, the eigenfunctions φ_n can also be chosen real, though are not required to be chosen in such a way. Physically, it means that the quasistatic nanoplasmonic eigenproblem is time-reversible.

For the eigenproblem (1.25)–(1.26), we can introduce a scalar product of any two functions ψ_1 and ψ_2 as

$$(\psi_2 \mid \psi_1) = \int_V \left[\frac{\partial}{\partial \mathbf{r}}\psi_2^*(\mathbf{r})\right]\left[\frac{\partial}{\partial \mathbf{r}}\psi_1(\mathbf{r})\right] d^3r, \tag{1.29}$$

This construct possesses all the necessary and sufficient properties of a scalar product: it is a binary, Hermitian self-adjoined, and positive-defined operation. It is easy to show that the eigenfunctions of Eqs. (1.25)–(1.26) are orthogonal. They can be normalized as

$$(\varphi_n \mid \varphi_m) = \delta_{nm}, \tag{1.30}$$

1.3.2 Inhomogeneous Localization of SPs and Hot Spots of Local Fields

One of the most fundamental properties of eigenmodes is their localization. By nature, the SP eigenmodes of small nanoplasmonic systems are localized and non-propagating. This generally follows from the fact that the eigenproblem (1.25) is real and has real eigenvalues, implying time-reversal invariance and, consequently, zero current carried by any eigenmode.

From the early days of nanoplasmonics, there has been keen attention paid to the localization of SP eigenmodes, because it was immediately clear that absence of any characteristic wavelength of the localized SPs leads to the possibility of their concentration in nanoscopic volumes of the space [117, 120, 149]. Many early publications claimed that the SPs in disordered nanoplasmonics systems, e.g., fractal clusters, experience Anderson localization [150–156].

However, a different picture of the SP localization, named inhomogeneous localization, has been introduced [78, 157–160]. In this picture of inhomogeneous localization, eigenmodes of very close frequencies with varying degree of localization, from strongly localized at the minimum scale of the system to delocalized over the entire nanosystem coexist. This phenomenon of inhomogeneous localization has been experimentally confirmed recently [161]. The eigenmodes experiencing the Anderson localization are dark, corresponding to dipole-forbidden transitions, and thus can only be excited from the near field [78].

A related phenomenon is the formation of hot spots in local fields of nanoplasmonic system that we introduced in Refs. [157, 158, 162, 163]. As characteristic of the inhomogeneous localization, the energy is localized by different SP eigenmodes at vastly different scales. However, it is the localization at the minimum scale that gives the highest local fields and energy density; these tightly-localized modes are the most conspicuous in the near-field intensity distributions as the hot spots. The hot spots exist in all kind of nanoplasmonic system but they are especially strongly pronounced in disordered and aperiodic systems [164].

We will illustrate the hot spots and the inhomogeneous localization of the SP eigenmodes using the results of the original works that established the phenomena [157, 158] using plasmonic-metal fractal clusters as objects. The model of these fractals were the so-called cluster-cluster aggregates (CCA) [165, 166]. In Fig. 1.5,

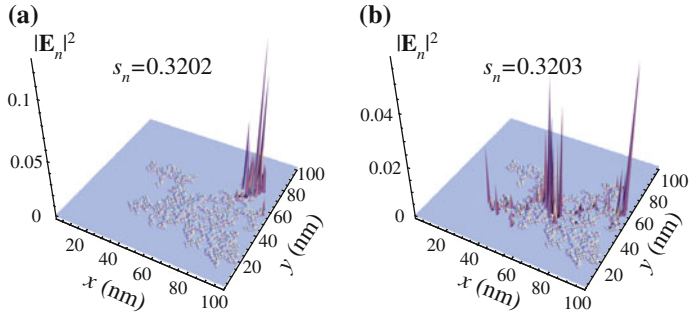

Fig. 1.5 Near-field intensity of eigenmodes computed for cluster-cluster aggregate (CCA) cluster. Square of the eigenmode electric field $|\mathbf{E_n}|^2$ is displayed against the projection of the cluster for two eigenmodes with close eigenvalues: **a** $s_n = 0.3202$ and **b** $s_n = 0.3203$. For silver embedding medium with a permittivity $\varepsilon_d \approx 2.0$, which is an approximate value for water, these modes correspond to a *blue* spectral range with $\hbar\omega \approx 3.13$ eV. Adapted from Ref. [157]

we show two representative eigenmodes with Bergman's eigenvalues of $s_n = 0.3202$ and $s_n = 0.3203$, which are very close in frequency (the blue spectral range for the case of silver in water). Both the eigenmodes are highly singular and are represented by sharp peaks—hot spots—that may be separated by the distances from the minimum scale of the system to the maximum scale that is on the order of the total size of the entire system. These eigenmodes possess very different topologies but very close eigenvalues and, consequently, have almost the same frequency $\hbar\omega \approx 3.13$ eV. This coexistence of the very different eigenmodes at the same frequency was called the inhomogeneous localization [157, 158].

The formation of host spots by the SP eigenmodes and the inhomogeneous localization of the eigenmodes are very pronounced for the fractal clusters. However, the same phenomena also take place in all dense random plasmonic systems. Physically, this phenomena is related to the absence of the characteristic length scale for SPs: the smallest electromagnetic scale is the skin depth $l_s \approx 25$ nm, which is too large on the scale of the system to affect the SP localization. The inhomogeneous localization implies that eigenmodes can be localized on all scales but this localization is always singular. The hot spots are the concentration regions of the optical energy: sharp peaks on the minimum scale ("fine grain" size) of the system are most visible.

Note that there is a fundamental difference between the plasmonic hot spots and their counterpart in the wave optics: speckles produced by scattering of laser light from a random medium. In the speckle case, there is a characteristic size of the speckles on the order of a character distance L_s between them that is determined by diffraction:

$$L_s \sim \lambda D/A, \tag{1.31}$$

where λ is wavelength of light, A is an aperture (cross-size of the coherent spot of light on the scattering system), and D is the distance from the scatterer to the observation screen.

One of the plasmonic system models studied in significant detail is a random planar composite (RPC) also called a semi-continuous metal film [78, 128, 148, 155, 161, 167–170]. This is a planar system where metal occupies a given fill fraction f of the system's volume. At a low f, the RPC is a system of remote randomly positioned metal particles. For high values of f, it is an almost continuous film with rare holes in it. For $f \approx 0.5$, there are percolation phenomena: there is a large connected random cluster of the metal extending between the boundaries of the system [171]. This connected percolation cluster is known to possess a fractal geometry.

To consider statistical measures of the SP localization, we introduce the localization radius L_n of an eigenmode, which is defined as the gyration radius of its electric field intensity $|\mathbf{E}_n(\mathbf{r})|^2$, where

$$E_n(\mathbf{r}) = -\frac{\partial}{\partial \mathbf{r}}\varphi_n(\mathbf{r}) \tag{1.32}$$

is the eigenmode electric field, as

$$L_n^2 = \int_V \mathbf{r}^2 |\mathbf{E}_n(\mathbf{r})|^2 \mathrm{d}^3 r - \left(\int_V \mathbf{r} |\mathbf{E}_n(\mathbf{r})|^2 \mathrm{d}^3 r \right)^2 . \tag{1.33}$$

We remind that due to Eq. (1.30), the eigenmode fields are normalized

$$\int_V |\mathbf{E}_n(\mathbf{r})|^2 \mathrm{d}^3 r = 1, \tag{1.34}$$

so Eq. (1.33) is a standard definition of the gyration radius.

In Fig. 1.6a, we show the smoothed, discretized nanostructure of one particular sample of a RPC. This system is generated in the following way. We consider a volume of size, in our case, $32 \times 32 \times 32$ grid steps. In the central xz plane of this cube we randomly fill a cell of size 2×2 grid steps with metal with some probability

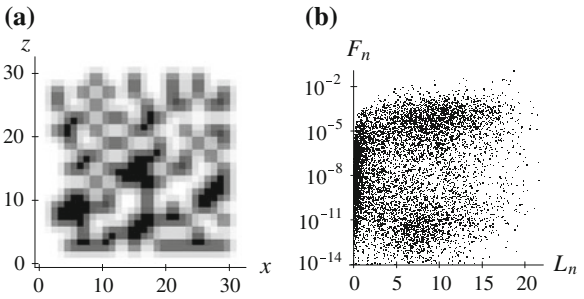

Fig. 1.6 For a planar random composite (in the xz-plane), the density of the metal component (panel **a**) and all eigenmodes plotted in the coordinates of oscillator strength F_n versus localization radius L_n (panel **b**)

f (fill factor or filling factor). Then we repeat this procedure with other 2×2 cells in that central xz plane. As a result, we arrive at a thin planar layer of thickness 2 grid steps in the y direction and fill factor of f in the central xz plane.

In Fig. 1.6b, we display all of the eigenmodes (SPs) of the above-described RPC in a plot of oscillator strength F_n *versus* localization length L_n. These eigenmodes are strikingly unusual.

First, there is a large number of eigenmodes with negligible oscillator strengths $F_n \lesssim 10^{-5}$. Note that the rounding-up relative error in our computations is $\sim 10^{-6}$, so these eigenmodes' oscillator strengths do not significantly differ from zero. Such eigenmodes do not couple to the far-field electromagnetic waves, and they can be neither observed nor excited from the far-field (wave) zone. We call them *dark modes*. They can, however, be excited and observed by NSOM (near-field scanning optical microscope) type probes in the near-field region. Such eigenmodes are also important from the computational-mathematical point of view because they are necessary for the completeness of the eigenmode set.

Second, in Fig. 1.6b, there also are many eigenmodes with relatively large oscillator strengths, $F_n \gtrsim 10^{-4}$, which we call *luminous* or *bright* modes. These do couple efficiently to the far-zone fields.

Third, both the luminous and the dark modes have localization radii L_n with all possible values, from zero to one half of the diagonal system size, and with very little correlation between F_n and L_n, except for the superlocalized (zero-size) eigenmodes that are all dark. This wide range of L_n shows that *the Anderson localization does not occur for most of the modes, including all the luminous modes*. Similar to these findings in certain respects, deviations from the simple Anderson localization have been seen in some studies of the spatial structure of vibrational modes [172, 173], dephasing rates [174] in disordered solids induced by long-range (dipole- type) interactions. A direct confirmation of this picture of the inhomogeneous localization has been obtained in experiments studying fluctuations of the local density of states of localized SPs on disordered metal films [161].

To gain more insight, we show in Fig. 1.7 the local electric field intensities $|\mathbf{E}_n(\mathbf{r})|^2$ for particular eigenmodes of four extreme types, all with eigenvalues very close to $s_n = 0.2$. As a measure of the eigenmode oscillator strength, we show a normalized oscillator strength F_n. The data of Fig. 1.7 confirm the above-discussed absence of correlation between the localization length and oscillator strength, and also show that there is no correlation between the topology of the local field intensity and the oscillator strength—compare the pairs of eigenmodes: $s_n = 0.1996$ with $s_n = 0.2015$, and $s_n = 0.2$ with $s_n = 0.2011$. Note that the large and random changes of the intensities between the close eigenmodes evident in Fig. 1.7 is an underlying cause of the giant fluctuations [175] and chaos [157–159] of local fields.

A fundamental property of the SP eigenmodes, whether localized or delocalized, is that they may be thought of as consisting of hot spots. While the localized eigenmodes possess a single tight hot spot, the delocalized ones consist of several or many host spots. Note that the fields in the hot spots constituting a single eigenmode are coherent. In a sense, the hot spots are somewhat analogous to speckles produced by laser light scattered from a random system. However, such speckles are limited by

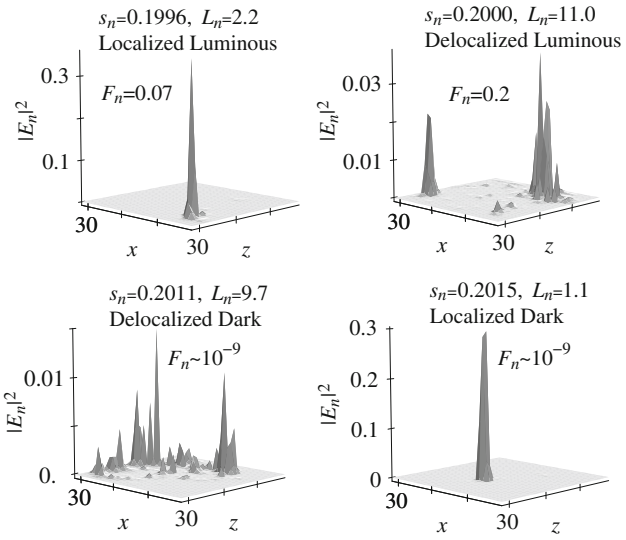

Fig. 1.7 Hot spots: Local field intensities $|\mathbf{E}_n(\mathbf{r})|^2$ of eigenmodes at the surface of the system shown in Fig. 1.6, versus spatial coordinates in the xz plane

the half-wavelength of light and cannot be smaller than that. In contrast, there is no wavelength limitations for the SP hot spots. They are limited only by the minimum scale of the underlying plasmonic system.

1.3.3 Retarded Green's Function and Field Equation Solution

Retarded Green's function $G^r(\mathbf{r}, \mathbf{r}'; \omega)$ of field equation (1.24), by definition, satisfies the same equation with the Dirac δ-function on the right-hand side,

$$\left[\frac{\partial}{\partial \mathbf{r}}\Theta(\mathbf{r})\frac{\partial}{\partial \mathbf{r}} - s(\omega)\frac{\partial^2}{\partial \mathbf{r}^2}\right] G^r(\mathbf{r}, \mathbf{r}'; \omega) = \delta(\mathbf{r} - \mathbf{r}'), \tag{1.35}$$

We expand this Green's function over the eigenfunctions φ_n using the orthonormality Eq. (1.30), obtaining

$$G^r(\mathbf{r}, \mathbf{r}'; \omega) = \sum_n \frac{\varphi_n(\mathbf{r})\,\varphi_n(\mathbf{r}')^*}{s(\omega) - s_n}. \tag{1.36}$$

This expression for Green's function is exact (within the quasistatic approximation) and contains the maximum information on the linear responses of a nanosystem to an arbitrary excitation field at any frequency. It satisfies all the general properties

of Green's functions due to the analytical form of Eq. (1.36) as an expansion over the eigenmodes (surface plasmons). This result demonstrates separation of geometry of a nanosystem from its material properties and the excitation field. The eigenfunctions $\varphi_n(\mathbf{r})$ and eigenvalues s_n in Eq. (1.36) depend only on geometry of the nanosystem, but not on its material composition or the optical excitation frequency. In contrast, the spectral parameter $s(\omega)$ depends only on the material composition and the excitation frequency, but not on the system's geometry. One of the advantages of this approach is in its applications to numerical computations: the eigenproblem has to be solved only once, and then the optical responses of the nanosystem are determined by Green's function that can be found by a simple summation in Eq. (1.36).

This Green's function is called retarded because it describes responses that occur necessarily at later time moments with respect to the forces that cause them. (Note that this name and property have nothing to do with the electromagnetic retardation, which is due to the finite speed of light and is absent in the quasistatic approximation.) This property, also called Kramers-Kronig causality, is mathematically equivalent to all singularities of $G^r(\mathbf{r}, \mathbf{r}'; \omega)$ as a function of complex ω being situated in the lower half-plane. Consequently, $G^r(\mathbf{r}, \mathbf{r}'; \omega)$ as a function of ω satisfies the Kramers-Kronig dispersion relations [30]. By the mere form of the spectral expansion (1.36), this Green's function satisfies all other exact analytical properties. This guarantees that in numerical simulations it will possess these properties irrespectively of the numerical precision with which the eigenproblem is solved. This insures an exceptional numerical stability of computational Green's function approaches.

Once the Green's function is found from Eq. (1.36), the local optical field potential is found as contraction of this Green's function with the excitation potential $\varphi_0(\mathbf{r})$ as

$$\varphi_1(\mathbf{r}) = -\int_V G^r(\mathbf{r}, \mathbf{r}'; \omega) \frac{\partial}{\partial \mathbf{r}'} \Theta(\mathbf{r}') \frac{\partial}{\partial \mathbf{r}'} \varphi_0(\mathbf{r}') \, \mathrm{d}^3 r'. \tag{1.37}$$

From Eqs. (1.23) and (1.37) using the Gauss theorem, we obtain an expression for the field potential $\varphi(\mathbf{r})$ as a functional of the external (excitation) potential $\varphi_0(\mathbf{r})$,

$$\varphi(\mathbf{r}) = \varphi_0(\mathbf{r}) - \int_V \varphi_0(\mathbf{r}') \frac{\partial}{\partial \mathbf{r}'} \Theta(\mathbf{r}') \frac{\partial}{\partial \mathbf{r}'} G^r(\mathbf{r}, \mathbf{r}'; \omega) \, \mathrm{d}^3 r'. \tag{1.38}$$

Finally, differentiating this, we obtain a closed expression for the optical electric field $\mathbf{E}(\mathbf{r})$ as a functional of the excitation (external) field $\mathbf{E}^{(0)}(\mathbf{r})$ as

$$E_\alpha(\mathbf{r}) = E_\alpha^{(0)}(\mathbf{r}) + \int_V G^r_{\alpha\beta}(\mathbf{r}, \mathbf{r}'; \omega) \Theta(\mathbf{r}') E_\beta^{(0)}(\mathbf{r}') \, \mathrm{d}^3 r', \tag{1.39}$$

where $\alpha, \beta, \ldots$ are Euclidean vector indices ($\alpha, \beta, \ldots = x, y, z$) with summation over repeated indices implied; the fields are

$$\mathbf{E}(\mathbf{r}) = -\frac{\partial \varphi(\mathbf{r})}{\partial \mathbf{r}}, \quad \mathbf{E}^{(0)}(\mathbf{r}) = -\frac{\partial \varphi_0(\mathbf{r})}{\partial \mathbf{r}}, \tag{1.40}$$

and the tensor (dyadic) retarded Green's function is defined as

$$G^r_{\alpha\beta}(\mathbf{r},\mathbf{r}';\omega) = \frac{\partial^2}{\partial r_\alpha \partial r'_\beta} G^r(\mathbf{r},\mathbf{r}';\omega). \tag{1.41}$$

One of the exact properties of this Green's function is its Hermitian symmetry,

$$G^r_{\alpha\beta}(\mathbf{r},\mathbf{r}';\omega) = G^r_{\beta\alpha}(\mathbf{r}',\mathbf{r};-\omega)^*. \tag{1.42}$$

If the excitation is an optical field, its wave front is flat on the scale of the nanosystem, i.e., $\mathbf{E}^{(0)} = \text{const}$. Then from Eq. (1.39) we get

$$E_\alpha(\mathbf{r}) = \left[\delta_{\alpha\beta} + g_{\alpha\beta}(\mathbf{r},\omega)\right] E^{(0)}_\beta, \tag{1.43}$$

where the local field enhancement (tensorial) factor is a contraction of the retarded dyadic Green's function,

$$g_{\alpha\beta}(\mathbf{r},\omega) = \int_V G^r_{\alpha\beta}(\mathbf{r},\mathbf{r}';\omega)\Theta(\mathbf{r}')\,\mathrm{d}^3 r'. \tag{1.44}$$

1.3.4 SP Modes as Resonances

Each physical eigenmode is described by the corresponding pole of Green's function (1.36). Close to such a pole, Green's function and, consequently, local fields (1.43) become large, which describes the surface plasmon resonance of the nanosystem. A complex frequency of such a resonance can be found from the position of the corresponding pole in the complex plane of frequency,

$$s(\omega_n - i\gamma_n) = s_n, \tag{1.45}$$

where ω_n is the real frequency of the surface plasmon, and γ_n is its spectral width (relaxation rate).

Note that we presume $\gamma_n > 0$, i.e., a negative sign of the imaginary part of the physical surface frequency. This a presumption, which is confirmed by the solution presented below in this section, is based on the standard convention of the sign of an exponential in the field temporal evolution,

$$\mathbf{E}_n(\mathbf{r},t) \propto \exp\left[-i(\omega_n - i\gamma_n)t\right] \propto \exp(-\gamma_n t), \tag{1.46}$$

which decays exponentially for $t \to +\infty$, as should be. The wave functions of physical surface plasmons are the familiar eigenfunctions $\varphi_n(\mathbf{r})$, i.e., those of the

geometric eigenmodes. However, their physical frequencies, of course, depend on the material composition of the system.

For weak relaxation, $\gamma_n \ll \omega_n$, one finds that this real surface plasmon frequency satisfies an equation

$$\mathrm{Re}[s(\omega_n)] = s_n, \tag{1.47}$$

and that the surface plasmon spectral width is expressed as

$$\gamma_n = \frac{\mathrm{Im}[s(\omega_n)]}{s_n'}, \quad s_n' \equiv \left.\frac{\partial \mathrm{Re}[s(\omega)]}{\partial \omega}\right|_{\omega=\omega_n}. \tag{1.48}$$

In terms of the dielectric permittivity as functions of frequency

$$s'(\omega) = \frac{\varepsilon_d}{|\varepsilon_d - \varepsilon(\omega)|^2}\mathrm{Re}\frac{\partial \varepsilon_m(\omega)}{\partial \omega}, \quad \gamma(\omega) = \frac{\mathrm{Im}\varepsilon_m(\omega)}{\mathrm{Re}\frac{\partial \varepsilon_m(\omega)}{\partial \omega}}. \tag{1.49}$$

This expression has been given in Sect. 1.2.1 as Eq. (1.3). Importantly, the spectral width γ is a universal function of frequency ω and does not explicitly depend on the eigenmode wave function $\varphi_n(\mathbf{r})$ or system's geometry. However, the system's geometry does, of course, define the plasmon eigenfrequencies ω_n. This property has been successfully used in Ref. [176] where a method of designing nanoplasmonic systems with desired spectra has been developed. Note also that the classical SPs have been quantized in Ref. [31] in connection with the prediction of spaser, a nanoscale counterpart of laser (see Sect. 1.5).

As follows from Eq. (1.28), external frequency ω is within the range of the physical surface plasmon frequencies and, therefore, can be close to a surface plasmon resonance [pole of Green's function (1.36) as given by Eq. (1.45)] under the following conditions

$$0 \le \mathrm{Re}\, s(\omega) \le 1, \quad \mathrm{Im}\, s(\omega) \ll \mathrm{Re}\, s(\omega). \tag{1.50}$$

These conditions are equivalent to

$$\varepsilon_d > 0, \quad 0 \le \mathrm{Re}\, \varepsilon_m(\omega) < 0, \quad \mathrm{Im}\, \varepsilon_m(\omega) \ll |\mathrm{Re}\, \varepsilon_m(\omega)|\,. \tag{1.51}$$

These conditions, in fact, constitute a definition of a plasmonic system, i.e., a system where a position of surface plasmon resonance can be physically approached: the dielectric permittivity of the metal component should be negative and almost real, while the permittivity of the second constituent (dielectric) should be positive, as assumed.

It is useful to write down an expression for Green's function (1.36) that is asymptotically valid near its poles, which can be obtained from Eqs. (1.47) and (1.48) as

$$G^r(\mathbf{r}, \mathbf{r}'; \omega) = \frac{1}{s'(\omega)} \sum_n \frac{\varphi_n(\mathbf{r})\, \varphi_n(\mathbf{r}')^*}{\omega - \omega_n + i\gamma_n}, \tag{1.52}$$

where γ_n is given above by Eqs. (1.48) or (1.49). This expression constitutes what is called the singular approximation or pole approximation of the Green's function. When an excitation frequency is in resonance with an SP frequency, i.e., $\omega = \omega_n$, the Green's function (1.52) increases in magnitude by $\sim\omega_n/\gamma_n \sim Q$ times, where the quality factor Q is given by Eq. (1.5).

Below, for the sake of reference, we give a modal expansion for the polarizability α of a nanoplasmonic system as a tensor,

$$\alpha_{\alpha\beta} = -\frac{\varepsilon_d}{4\pi}\sum_n \frac{1}{s_n(s-s_n)} M_{n\alpha} M^*_{n\beta}, \tag{1.53}$$

where the indexes α, β denote Cartesian components, and $\mathbf{M}_n$ is a coupling vector defined as

$$\mathbf{M}_n = -\int_V \Theta(\mathbf{r}) \frac{\partial \varphi_n(\mathbf{r})}{\partial \mathbf{r}} \, \mathrm{d}^3 r. \tag{1.54}$$

Near a SP frequency, $\omega \approx \omega_n$, a singular part of the polarizability (1.53) acquires a form

$$\alpha_{\alpha\beta} = -\frac{\varepsilon_d}{4\pi s_n' s_n} \frac{M_{n\alpha} M^*_{n\beta}}{\omega - \omega_n + i\gamma_n}. \tag{1.55}$$

Also, for the reference sake, we give a general expression for the SP radiative decay rate, $\gamma_n^{(r)}$. This can be obtained from Eq. (1.55) taking into account Eqs. (1.10) and (1.15) as

$$\gamma_n^{(r)} = \frac{\varepsilon_d^{3/2}\omega^3 |\mathbf{M}_n|^2}{9\pi c^3 s_n' s_n}. \tag{1.56}$$

Note that $|\mathbf{M}_n|^2 \sim V_n$, where V_n is the modal volume of the n-th eigenmode. Thus Eq. (1.56) is consistent with Eq. (1.16) obtained earlier in this chapter.

1.3.5 Examples of Local Fields and Their Hot Spots

Let us give an example of local fields computed using Eq. (1.39). We start with the results of the original publications Ref. [157, 158] where the hot spots of the plasmonic local fields have been predicted. This prediction was made for fractal clusters because the fractals were expected to possess highly inhomogeneous and fluctuating local optical fields as was shown in pioneering papers in a subfield of physical optics that today is called nanoplasmonics [117, 149, 177].

In Fig. 1.8 adapted from Ref. [157], we illustrate the local-field hot spots for a silver CCA cluster of $N = 1500$ identical nanospheres embedded in water. We show local field intensity $I = |\mathbf{E}(\mathbf{r}, \omega)|^2$ relative to the excitation field intensity I_0 at

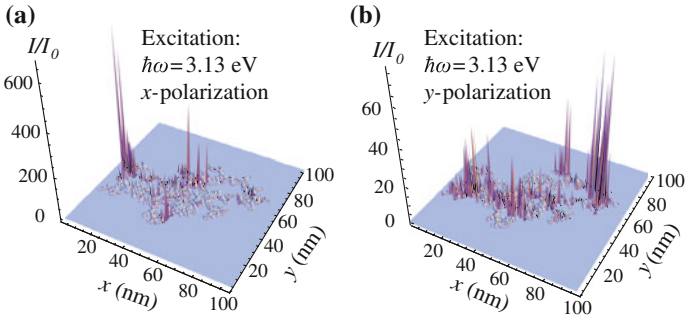

Fig. 1.8 Spatial distributions of local field intensity I relative to the external intensity I_0 for an individual CCA cluster of $N = 1500$ silver nanospheres in water ($\varepsilon_d = 2.0$) for the frequency $\hbar\omega = 3.13\,\text{eV}$. The polarizations of the excitation radiation is x (**a**) and y (**b**), as indicated in the panels. The projection of the cluster nanospheres to the xy plane is also shown. Adapted from Ref. [157]

the surface of the silver nanospheres at a relatively high frequency $\hbar\omega = 3.13\,\text{eV}$ corresponding to vacuum wavelength $\lambda = 390\,\text{nm}$ in the far blue end of the visible spectrum. We can clearly see that the local intensity is highly non-uniform, exhibiting pronounced singular hot spots. These hot spots are localized at the minimum scale of the system (on the order of the radius of the nanospheres). The local intensity in the hot spots is greatly enhanced (by a factor of up to ~600) as one would expect from an estimate $I/I_0 \sim Q^2$—cf. Fig. 1.2.

This hot spotting is nothing else as random nanofocusing. It is similar in this respect to the formation of speckles in the wave optics, as we have discussed above in conjunction with Fig. 1.5. However, reflecting the properties of the corresponding SP eigenmodes, there is no characteristic wavelength that limits this hot spot singularity by defining the characteristic size L_s of the speckles, which is also a characteristic separation between them—see Eq. (1.31).

Another property of the local fields of a great significance is the dramatic dependence of the intensity distribution on the polarization: the local distributions or the x-polarization (Fig. 1.8a) and y-polarization (panel b) are completely different. An experimental observation of this effect has been obtained in Ref. [118] already at a very early stage of the development of nanoplasmonics.

Note that the SP eigenmode geometry is also strongly dependent on its frequency—see Fig. 1.5. However, in externally-excited local fields, this frequency dependence is obscured by the resonance broadening due to the losses, as is evident from the expression for the resonant part of the Green's function

We will present below spectral and statistical properties of the local fields using a model of random planar composite (RPC). A specific RPC system used in the computation is shown in Fig. 1.9a. To improve numerical accuracy, we smooth the unit-step characteristic function $\Theta(\mathbf{r})$ with a Gaussian filter with a radius of 1 grid step: this dramatically improves numerical accuracy of a grid method that we use to solve the eigenproblem. Such a smoothing is clearly seen in Fig. 1.9a.

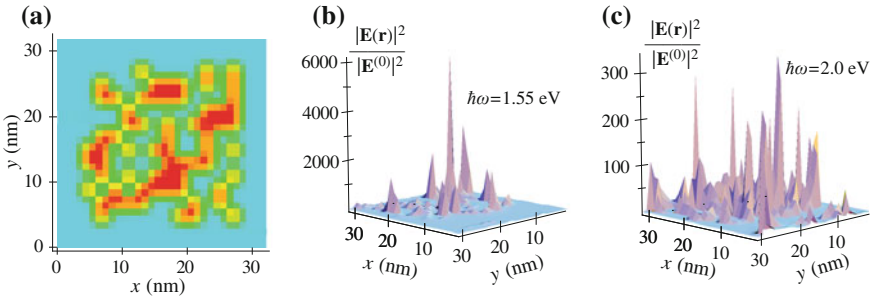

Fig. 1.9 **a** Geometry of nanostructured random planar composite (RPC): characteristic function $\Theta(\mathbf{r})$ is displayed in the xz plane of the RPC. Axes unit is nm; thickness of the system in the y direction (normal to its plane) is 2 nm. The fill factor is $p = 0.5$. Characteristic function $\Theta(\mathbf{r})$ is smoothed by a Gaussian filter with a radius of 1 nm to improve numerical accuracy (shown in the panel by the halftone density). **b** Local field intensity $|\mathbf{E}(\mathbf{r})|^2$ in the plane of the nanostructure displayed relative to the excitation field intensity $|\mathbf{E}^{(0)}|^2$; excitation frequency $\hbar\omega = 1.55$ eV; computed using Eq. (1.38). The metal is silver embedded in the dielectric with $\varepsilon_d = 2$. **c** Same as (**b**) but for $\hbar\omega = 2.0$ eV. Adapted from data computed for Ref. [178]

In Fig. 1.9b, c, we display the spatial distribution of the local field intensity $|\mathbf{E}(\mathbf{r})|^2$ in the plane of the nanostructure at the surface of the metal. These computations are described in Ref. [178]. They are done for silver whose dielectric function is adopted from Ref. [32]; the embedding dielectric has permittivity is set as $\varepsilon_d = 2.0$. This intensity is plotted relative to the excitation field intensity $|\mathbf{E}_0|^2$; thus the quantity displayed is the enhancement factor of the local field intensity. Panel (b) shows the intensity computed from Eq. (1.38). The maximum of the local intensity enhancement of $\approx$6000 is in a reasonable agreement with the estimate $\sim Q^2 \sim 10^4$, where Q is displayed in Fig. 1.2.

Dependence of the local fields on frequency is dramatic: cf. Figs. 1.9b, c. As frequency increases from the near-IR (1.55 eV) to visible (2.0 eV), the distribution becomes much more delocalized and its magnitude dramatically decreases, which cannot be explained by some decrease of quality factor Q alone. Most importantly, at all frequencies these near-field intensity distributions are dominated by the pronounced hots spots. These are manifestation of the hot spots of the SP eigenmodes—see Fig. 1.7.

Generally, the intensity distribution of local field intensity in Fig. 1.9b, c is highly singular: it consists of relatively narrow peaks (hot spots [158, 163]) separated by regions of a low intensity. This is a typical distribution of intensity in plasmonic nanosystems, which is a reflection of the inhomogeneous localization of the SP eigenmodes.

1.3.6 Experimental Examples of Nanoplasmonic Hot Spots

There has been a significant number of experimental studies of near-field distributions of optical fields in plasmonic nanostructures. In all cases, a pronounced picture of the hots spots [157, 158] has been exhibited, see, e.g., Refs. [123, 155, 168]. The inhomogeneous localization of the SP eigenmodes (see Sect. 1.3.2), which is inherently related to hot spots, has recently been confirmed experimentally [161].

The photoemission electron microscope (PEEM) is a powerful tool of analyzing the distribution of the local field intensity without perturbing it in any way. In the PEEM approach, the plasmonic nanosystem to be analyzed serves as a cathode and an object of an electron microscope. The electron emission is caused by the local field $\mathbf{E}(\mathbf{r}, \omega)$ of the plasmonic system. The photoelectrons are analyzed by the electron optics of the PEEM that creates a magnified image of the system in "light" of the photo-emitted electrons.

For silver, the work function W_f (i.e., the minimum energy needed to excite an electron from the Fermi surface to the zero energy that is the energy in vacuum outside of the metal) is approximately 4.2 eV. The highest energy of an optical quantum (at the vacuum wavelength of 390 nm) is 3.2 eV, i.e., it is significantly less than W_f. Thus, a single optical photon cannot emit an electron from a silver surface. Such an emission can, however, occur through two-photon absorption, leaving for the emitted electron the kinetic energy at infinity of $E_\infty \leq 2\hbar\omega - W_f$. Such a two-photon electron photoemission is in the foundation of the so-called two-photon photoemission PEEM (or, 2PP-PEEM). On the other hand, for ultraviolet radiation (say, from a Hg lamp), the energy of a photon is sufficient for the one-photon photoemission PEEM (1PP-PEEM). The 2PP-PEEM electron intensity mirrors the distribution of $I_2 = |\mathbf{E}(\mathbf{r}, \omega)|^4$.

A model system to illustrate the hot spots used in a 2PP-PEEM experiment of Ref. [123] is shown in Fig. 1.10a. This is a diffraction grating covered with a silver layer with roughness of a < 10 nm RMS grain size, as the scanning electron micrograph (SEM) shows in the insert. The Hg lamp illumination (the energy of the quantum $\hbar\omega = 4.89$ eV exceeds $W_f = 4.2$ eV, thus allowing one-photon photoemission, 1PP-PEEM) shows a smooth image of the underlying diffraction grating with the resolution of the PEEM ($\lesssim$100 nm).

A dramatically different picture is observed in Fig. 1.10b. In this case, the irradiation is with femtosecond laser pulses of $\lambda = 400$ nm vacuum wavelength. The corresponding energy of the quantum is below the work function, $\hbar\omega = 3\,\text{eV} < W_f = 4.2\,\text{eV}$. Thus the electron photoemission is two-photon. The corresponding 2PP-PEEM image in Fig. 1.10b exhibits a pronounced picture of the hot spots due to the fact that in this case the optical frequency is in the plasmonic range. These hot spots are localized SPs that are excited by the p-polarized radiation with a significantly greater efficiency than by an s-polarized one. This suggests that SPPs excitation may play a role as an intermediate process for the localized SP excitation. In a full qualitative agreement with theory (see Sect. 1.3.2), these hot spots are

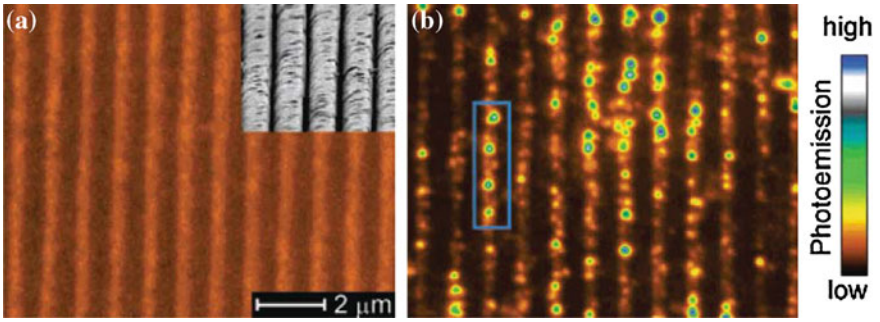

Fig. 1.10 PEEM micrographs of the same region on the silver grating obtained with **a** 254-nm line of a Hg lamp (1PP-PEEM) and **b** p-polarized 400-nm femtosecond laser excitation (2PP-PEEM). A scanning electron micrograph (SEM) of the silver grating in (**a**) is superimposed with the 1PP-PEEM image to show correspondence in the >100 nm scale topographical contrast. The surface roughness with <10 nm RMS distribution in the SEM image, which is too fine to resolve with the PEEM, gives rise to excitation of the localized SP modes seen as the hot spots in the 2PP-PEEM image of (**b**). The blue rectangle locates the four hot spots that were used for a coherent control experiment. Adapted from Ref. [123]

singular, highly localized, and randomly distributed in space. The local fields in these hot spots are highly enhanced as witnessed by their dominance in the 2PP process.

Formation of the hot spots for random nanostructured plasmonic systems is a universal phenomenon whose physics is defined by the absence of the characteristic wavelength of the localized SPs, which localize at all available scales and whose fields are highly singular and highest at the minimum scale [78, 157, 158, 179].

One of the most convincing and comprehensive studies of geometry and statistics of the plasmonic hots spots is recently published Ref. [180] performed using PEEM and semicontinuous gold film whose model is RPC. Adapted from this, in Fig. 1.11, we show spatial distributions of the hot spots for a semicontinuous film with a fill factor (percentage of the area occupied by metal) $f = 0.53$. At this f, the film is close to the percolation threshold for static conductivity. The connected clusters in such a film have a fractal nature where we expect giant fluctuations and inhomogeneous localization of the SP fields [157, 158]. In fact, the distributions in Fig. 1.11 do demonstrate

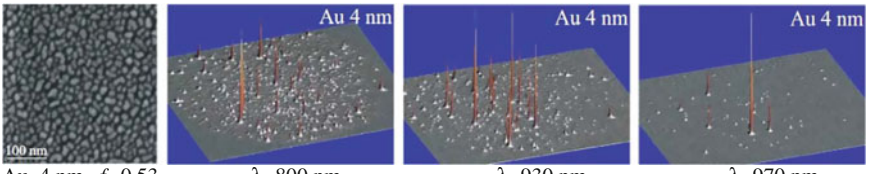

Fig. 1.11 *Left* column, scanning electron microscope images of the gold/glass films for the 4 nm grain size (filling factor $f = 0.53$). *Right*, PEEM distributions corresponding to gold/glass films for three different wavelengths. For each PEEM image, excitation wavelength λ is indicated. Adapted from Ref. [180]

pronounced hot-spot behavior with inhomogeneous localization, giant fluctuations in space, where the distributions and intensities of individual hot spots strongly and randomly change with frequency. These distributions are in a full qualitative agreement with the theoretical predictions for the hot spots of local nanoplasmonic fields [157, 158]—cf. above Figs. 1.8, 1.9.

We emphasize again that the PEEM-based observation of the plasmonic hot spots is completely non-perturbing. The photo-emitted electrons that are used in the PEEM fly away from the metal surface naturally, no matter whether they are used for imaging or not.

There has also been a series of research dealing with the observation of the plasmonic hot spots using the scanning near-field optical microscope (NSOM or SNOM) [155, 162, 168]. In fact, the first experimental evidence of the nanoplasmonic hot spots has been obtained [162] using an aperture-type NSOM, which is a based a tapered optical fiber with the tip covered by a metal. A general concern about such observation is that they are perturbative: the tip of NSOM (or nanoscope, as it is often called) is typically much larger than a hot spot. Made of metal, it can, in principle, modify the host spot by both shifting its resonant frequency and decreasing the quality factor.

As an example, we present Fig. 1.12 adapted from Ref. [168]. This study is done on the semicontinuous metal film (random planar composite, or RPC). At relatively low values of the fill factor, $f = 0.36$ and $f = 0.45$, the local intensity distribution $I(\mathbf{r})$ shows relatively delocalized regions elongated normally to the direction of propagation (vertical axis in the figure). These are analogous to the caustics of the usual 3d optics. Relatively close to the percolation point, $f = 0.66$ and $f = 0.73$, the distribution $I(\mathbf{r})$ becomes highly localized exhibiting singular hot spots. The behavior of $I(\mathbf{r})$ at a relatively high fill factor of $f = 0.83$ again reminds that for the low f showing delocalized caustics but not singular hot spots. This is understandable because in this case the system is basically a smooth film with a few defects. This film supports SPPs that are weakly scattered by the relatively few defects.

As we have discussed above in this section, NSOM measurements of hot spots are inherently perturbative. While PEEM is nonperturbative, the spatial resolution so far has been insufficient (due to aberrations in the electron optics and large spread of the

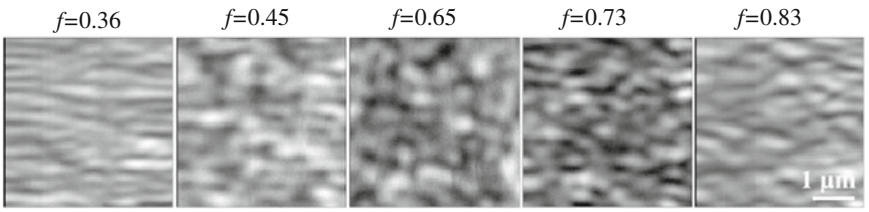

Fig. 1.12 NSOM images of $4 \times 4\,\mu\text{m}^2$ semi-continuous silver films with different metal filling fractions f as indicated above the graphs. Local intensity distribution is displayed as a function of the spatial coordinates in the plane of the film. The *white areas* correspond to higher intensities. Adapted from Ref. [168]

emitted electrons over their energies). Additionally, PEEM requires clean surfaces in high vacuum.

A fundamentally different non-perturbing approach to studying nanoplasmonic hot spots has been pioneered in Refs. [181, 182]. It is based on the so-called photon-localization super-resolution far-field microscopy. This method of far-field super-resolution has originally been developed in application to biological imaging [183].

This method's fundamentals can be very briefly described as the following. Assume that there is a *single* radiating chromophore (say, fluorescing molecule) in the view field of an optical microscope. Alternatively, there may be a number of such chromophores but their concentration should be low enough so they are resolved separately by the microscope (i.e., the distance between these molecules are greater than the microscope's resolution). The center of the emission of such a single (or separately resolved) emitter can be found with any precision that is only limited by statistical fluctuations of the number of the recorded photons but not by the resolution of the microscope provided that this microscope or the system under study does not change in the course of the observation.

After the position and brightness of a given single molecule are recorded, this molecule is naturally bleached. Then another molecule comes into the hot spot and its position and brightness are recorded until it is bleached. The process is repeated until the distribution of the brightness of emitters is built with a sufficient statistical precision.

It is assumed that the emission brightness of a single chromophore is proportional to the local field intensity of the hot spot at its position and that this chromophore exerts a negligibly weak perturbation on the local field of the hot spot. Thus this photon-localization nanoscopy is a non-perturbative method allowing one to find the intensity distribution at the hot spot on the nanoscale limited only by the statistical fluctuations (inversely proportional to the accumulation time) and the size of the chromophore itself, which is negligible in realistic situations.

The results of the hot spot local intensity-distribution measurements for an aluminum surface are shown in Fig. 1.13a. This distribution is a narrow peak with the width of $\approx$20 nm. The observed fine structure of this distribution is attributed to statistical fluctuations [181]. The cross section through this distribution displayed in Fig. 1.13b suggests an exponential decay of this distribution function in space with the FWHM $= 20$ nm.

Very similar results are obtained for the silver colloid clusters as shown in Figs. 1.13c, d. Note that the aluminum surface studied is nominally smooth and contains only random roughness while the silver colloid clusters are fractals whose density fundamentally possesses large and correlated fluctuations.

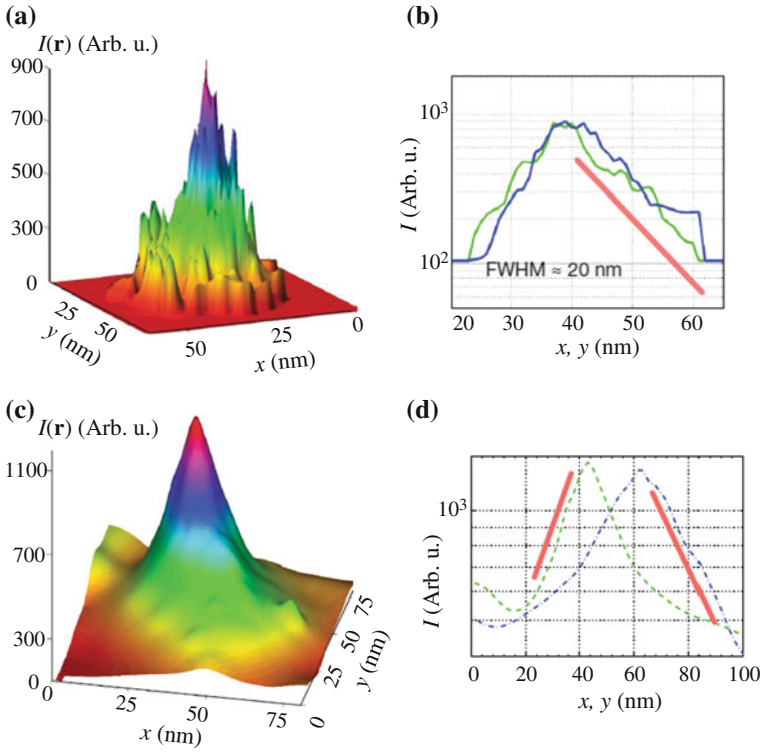

Fig. 1.13 Hot spots at the surfaces of metals measured by the photon localization method (see the text). **a**, **b** Distribution of the local intensity for a hot spot at the surface of aluminum. The kernel window size is 2.1 nm; this small window size makes the image appear noisy. The dye is Chromeo-542 with excitation at 532 nm and the emission centered around 580 nm. **b** An exponential decay field profile is visible, and is more evident on a log scale, shown as almost a decade of straight line (*red solid line*). The *blue* and *green curves* are two *cross sections* of the hot spot along x and y directions through the peak. The FWHM of the spot is ∼20 nm. **c** and **d** is the same as (**a**) and (**b**), respectively, but for the case of a silver metal colloid cluster precipitated on a surface. A Chromeo-642 dye (Active Motif)—whose emission centers around 660 nm—is used. Adapted from Ref. [181]

1.4 Ultrafast Plasmonics and Coherent Control on Nanoscale

1.4.1 Introduction

The nanoplasmonic processes can potentially be the fastest in optics: their shortest evolution times are defined by the inverse spectral width of the region of the plasmonic resonances and are on the order of 100 as [184], see also Sect. 1.2.1. The relaxation times of the SP excitations are also ultrashort, in the 10–100 fs range [185–189]. See also the SP relaxation times for gold and silver displayed in Fig. 1.3. The

nanolocalization and such ultrafast kinetics make plasmonic nanostructures promising for various applications, especially for the ultrafast computations, data control and storage on the nanoscale.

These and potentially many other applications require precise control over the optical excitations of the nanostructures in time and space on the femtosecond-nanometer scale. Such a control cannot be imposed by far-field focusing of the optical radiation because the diffraction limits its dimension to greater than half wavelength. In other words, the optical radiation does not have spatial degrees of freedom on the nanoscale. There is a different class of approaches to control a system on nanoscale based on plasmonic nanoparticles or waveguides brought to the *near-field* region of the system. Among these we mention: the tips of scanning near-field optical microscopes [190], adiabatic plasmonic waveguides [12], nanowires [191, 192], plasmonic superlenses [193] or hyperlenses [194]. In all these cases, massive amount of metal is brought to the vicinity of the plasmonic nanosystem, which will produce strong perturbations of its spectrum and SP eigenmodes, cause additional optical losses, and adversely affect the ultrafast dynamics and energy nanolocalization in the system. This nanowaveguide approach also may not work because of the excitation delocalization due to the strong interaction (capacitive coupling) at the nanoscale distances for optical frequencies.

We have proposed [195] a principally different approach to ultrafast optical control on the nanoscale based on the general idea of coherent control. The coherent control of the quantum state of atom and molecules is based on the directed interference of the different quantum pathways of the optical excitation [196–205], which is carried out by properly defining the phases of the corresponding excitation waves. This coherent control can also be imposed by an appropriate phase modulation of the excitation ultrashort (femtosecond) pulse [202, 206–208]. Shaping the polarization of a femtosecond pulse has proven to be a useful tool in controlling quantum systems [209].

Our idea of the coherent control on the nanoscale by the phase modulation of the excitation pulse can be explained with a schematic shown in Fig. 1.14. Phase modulation of the excitation pulse can be thought of as changing the frequency (color) of light as the pulse progresses in time. For the sake of argument, let us assume, as shown in Fig. 1.14, that initially the pulse contains blue colors that gradually change to red with the time progression. At earlier times, the dominating blue component of the pulse will excite the SP eigenmodes with corresponding high optical frequencies. As the pulse progresses, the lower-frequency eigenmodes are excited. It is assumed that the total duration τ_p of the pulse is less than the decay (decoherence) time $\tau = \gamma^{-1}$ of the SPs , i.e., $\tau_p \lesssim \tau$ [for the decay rates and life times of the SPs see Eq. (1.3) or (1.49) and Fig. 1.3]. In such a case, the SPs of different frequencies will coexist simultaneously, and their fields will interfere. This interference depends on the relative phases and amplitudes of the SPs of different frequencies which, in turn, are determined by the relative phases of different spectral components of the excitation pulse. The ultimate goal of the spatio-temporal coherent control on the nanoscale is to have a hot spot of the local fields at a given nanosite at a given

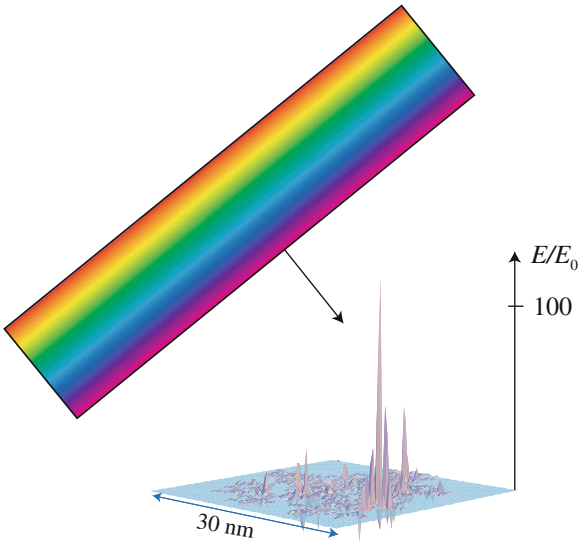

Fig. 1.14 Schematic of the fundamentals of the coherent control of nanoscale optical energy distribution. An excitation pulse is phase-modulated (shown by *different colors* changing with the progression of the pulse), which may be qualitatively thought of as different frequencies (*colors*) are incident on the nanosystem at different times, in a certain sequence. The system (a fractal cluster) is indicated by its projection on the horizontal coordinate plane. In response to this pulse, different SP eigenmodes are excited in a sequence. As time progresses, these eigenmodes interfere between themselves leading to a hot spot appearing at a required position at a given time. This leads to a large enhancement of the local field E relative to the excitation field E_0

femtosecond temporal interval. Below in this chapter we show how this problem is solved both theoretically and experimentally.

Another approach that we have proposed [210] invokes spatial modulation of the excitation field on the microscale in a polaritonic system. This field excites SPPs whose phases are determined by those of the original field. This determines the wave fronts of the SPP waves that focus on the nanoscale at the targeted nanofoci at the required times with femtosecond temporal resolution. The spatial-phase coherent control of the SPPs has been demonstrated experimentally by different groups [211, 212].

Our initial idea [195] has been subsequently developed theoretically [148, 209, 213, 214] and experimentally [123, 215–217]. In this coherent control approach, one sends from the far-field zone a shaped pulse (generally, modulated by phase, amplitude, and polarization) that excites a wide-band packet of SP excitations in the entire nanosystem. The phases, amplitudes, and polarizations of these modes are forced by this shaped excitation pulse in such a manner that at the required moment of time and at the targeted nanosite, these modes' oscillations add in phase while at the other sites and different moments of time they interfere destructively, which brings about the desired spatio-temporal localization.

Theoretically, the number of the effective degrees of freedom that a shaped femtosecond pulse may apply to a nanoplasmonic system can be estimated in the following way. The number of the independent frequency bands is $\sim\Delta\omega/\gamma$, where $\Delta\omega$ is the bandwidth of the plasmonic system. For each such a band, there are two degrees of freedom: amplitude and phase. Thus, the total number N_{DF} of the degrees of freedom for coherent control can be estimated as

$$N_{DF} \sim 2\frac{\Delta\omega}{\gamma}. \tag{1.57}$$

For a plasmonic system with the maximum bandwidth $\Delta\omega \sim \omega$, and Eq. (1.57) becomes

$$N_{DF} \sim 4Q, \tag{1.58}$$

where we took into account Eq. (1.5). In the optical region for noble metals $Q \sim 100$ (see Fig. 1.2), providing a rich, ~100-dimensional space of controlling parameters. The coherent control approach is non-invasive: in principle, it does not perturb or change the nanosystem's material structure in any way.

However, how to actually determine a shaped femtosecond pulse that compels the optical fields in the nanosystem to localize at a targeted nanosite at the required femtosecond time interval is a formidable problem to which until now there has been no general and efficient approach. To compare, our original chirped pulses possessed only two effective degrees of freedom (carrier frequency ω_0 and chirp), which allowed one to concentrate optical energy at the tip of a V-shape structure versus its opening [148, 195]. Similarly, the two unmodulated pulses with the regulated delay τ between them used in the interferometric coherent control [123, 213, 216] also possess only two degrees of freedom (τ and ω_0) and can only select one of any two local-field hot spots against the other; it is impossible, in particular, to select one desired hot spot against *several* others.

There exists another method based on the adaptive genetic algorithms [202]. However, its application to the spatial-temporal localization in nanosystem is difficult due to the complexity of the problem. To date, the only example is the spatial concentration of the excitation on one arm of the three-pronged metal nanostar [215] where the obtained controlling pulses are very complicated and difficult to interpret though the nanosystem itself is rather simple. A general problem with this method is that the adaptive genetic algorithms are actually refined trial-and-error methods; they do not allow one to obtain the required controlling pulses as a result of the solution of a set of deterministic equations or an application of any regular deterministic procedure such as Green's function integration.

1.4.2 Time-Reversal Solution for Coherent Control

Our solution of this major problem of the coherent control, which is proposed and theoretically developed in Ref. [218], is based on an idea of time-reversal that has

originally been proposed and used to control the focusing of acoustic waves and microwave radiation [219–221]. Some of these studies required use of a reverberating chamber to cause multiple interactions of the waves with the system needed to transfer the information to the far field. The electromagnetic subwavelength focusing also required a subwavelength-scale metal structure (a metal wire brush) to be positioned in the vicinity of the target system as a focusing antenna. In contrast, in nanoplasmonics there is no need for the reverberating chamber or the metal brush antenna, because the plasmonic nanosystem plays the roles of both of them. It confines the plasmonic modes for long times relative to their oscillation periods and also nano-localizes these modes.

1.4.3 Qualitative Description of Time-Reversal Coherent Control

The idea of the time-reversal solution of the nanoscale coherent control can be described using a schematic of Fig. 1.15. Consider a metal plasmonic nanosystem, indicated by blue in Fig. 1.15a, which may be embedded in a host dielectric (or

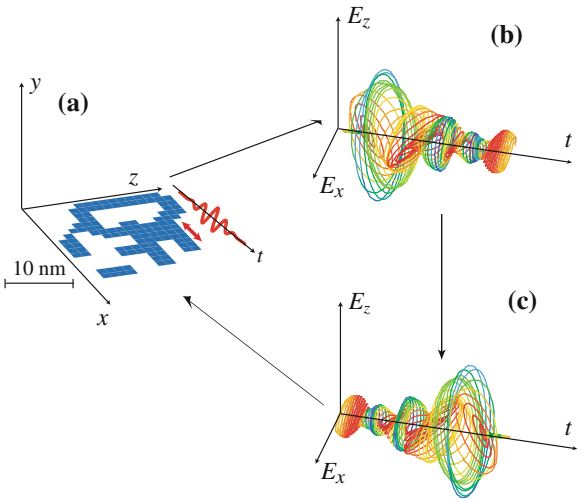

Fig. 1.15 **a** Geometry of nanosystem, initial seed oscillating dipole and its oscillation waveform. The nanosystem as a thin nanostructured silver film is depicted in *blue*. A position of the oscillating dipole that initially excites the system is indicated by a *double red arrow*, and its oscillation in time is shown by a *bold red waveform*. **b** Field in the far-field zone that is generated by the system following the excitation by the local oscillating dipole: vector $\{E_x(t), E_z(t)\}$ is shown as a function of the observation time t. The *color* corresponds to the instantaneous ellipticity as explained in the text in connection with **c** Same as in panel (**b**) but for a time-reversed pulse in the far zone that is used as an excitation pulse to drive the optical energy nanolocalization at the position of the initial dipole

be in vacuum). The nanosystem is excited by an external ultrafast (femtosecond) nanosource of radiation at its surface. As such we choose an oscillating dipole indicated by a double red arrow. This dipole generates a local optical electric field shown by a bold red waveform. This field excites SP oscillations of the system in its vicinity. In turn these oscillations excite other, more distant regions, and so forth until the excitation spreads out over the entire system. The relatively long relaxation time of these SP modes leads to the long "reverberations" of the plasmonic fields and the corresponding far-zone optical electric field. The latter is shown in Fig. 1.15b where one can see that a complicated vector waveform is predicted. This waveform is time reversed, as shown in panel (c), and send back to the system as an excitation plane wave from the *far-field* zone. If the entire field, in the whole space including the near-field (evanescent) zone, were time reversed and the system would have been completely time-reversible, which would imply the absence of any dielectric losses, then the system would have been compelled by this field exactly to back-trace its own evolution in time. This would have lead to the concentration of the local optical energy exactly at the position of the initial dipole at a time corresponding to the end of the excitation pulse.

Indeed, the system is somewhat lossy, which means that it is not exactly time reversible. Nevertheless, these losses are small, and one may expect that they will not fundamentally change the behavior of the system. Another problem appear to be more significant: the evanescent fields contain the main information of the nanodistribution of the local fields in the system, and they cannot be time reversed from the far zone because they are exponentially small, practically lost there. However, our idea is that the nanostructured metal system itself plays the role of the metal brush of Ref. [221] continuously coupling the evanescent fields to the far zone. Therefore the fields in the far zone actually contain, in their reverberations, most information about the evanescent fields that will be regenerated in the process of the time reversal.

We will illustrate this idea by considering a random planar composite (RPC) whose geometry is shown in gray in the center of Fig. 1.16. In specific computations, as the plasmonic metal, we consider silver whose dielectric permittivity ε_m we adopt from bulk data [32]. This system has been generated by randomly positioning $2 \times 2 \times 2\,\mathrm{nm}^3$ metal cubes on a plane, which for certainty we will consider as the xz coordinate plane. The random system shown in the center of Fig. 1.16 has filling factor of $f = 0.5$.

The interaction of a nanosystem with electromagnetic pulses is described in Green's function approach using quasistatic approximation [148, 195, 222]—see Sect. 1.3.3. It is known that the optical excitation energy in random plasmonic nanostructures localizes in "hot spots" whose size is on the nanoscale and is determined by the minimum scale of the system inhomogeneities [78, 158, 159, 223]—see Sect. 1.3.5.

Initially, to find positions of these hot spots in our system, we apply an ultrashort near-infrared (near-ir) pulse whose spectral width was very large, covering a frequency band from 1.1 to 1.7 eV. The pulse polarization is along the z axis (the incidence direction is normal to the plane of the nanostructure, i.e. along the y axis). The resulting optical electric field $\mathbf{E}$ is expressed in terms of the external electric

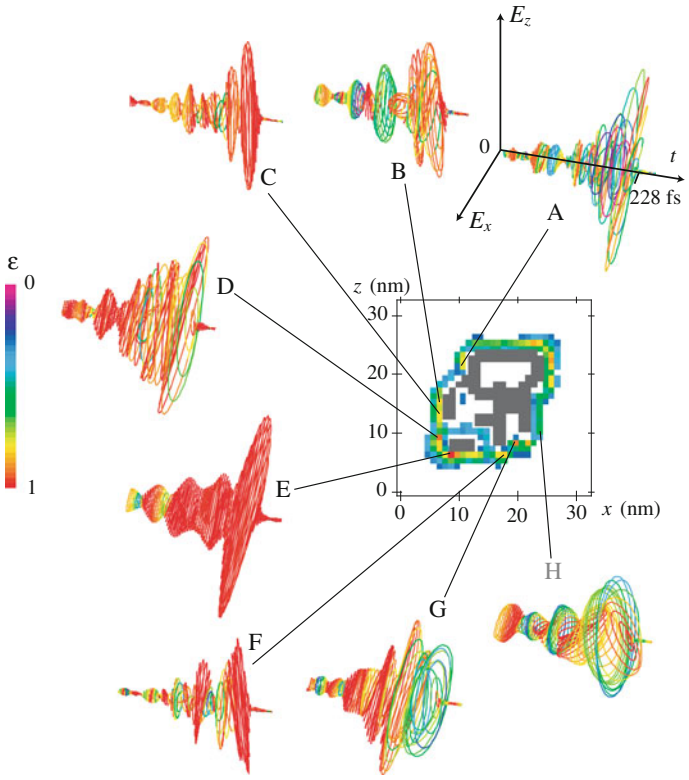

Fig. 1.16 Schematic of plasmonic-nanosystem geometry, local fields, and pulses generated in the far field. *Central insert* The geometry of a nanosystem is shown by *dark gray*, and the local fields in the region surrounding it are shown by *colors*. The highest local field intensity is depicted by *red* and the lowest intensity is indicated by *blue* (in the *rainbow sequence of colors*). Panels A–H: The excitation waveforms in the far fields obtained as described in the text by positioning the initial excitation dipole at the metal surface at the locations indicated by the corresponding lines. Coordinate vectors $\boldsymbol{\rho}$ of points A–H in the xz plane are (in nm): $\boldsymbol{\rho}_A = (11, 22)$, $\boldsymbol{\rho}_B = (7, 16)$, $\boldsymbol{\rho}_C = (7, 14)$, $\boldsymbol{\rho}_D = (7, 10)$, $\boldsymbol{\rho}_E = (9, 7)$, $\boldsymbol{\rho}_F = (18, 7)$, $\boldsymbol{\rho}_G = (20, 9)$, and $\boldsymbol{\rho}_H = (24, 11)$. The instantaneous degree of linear polarization ε is calculated as the eccentricity of an instantaneous ellipse found from an fit to a curve formed by vector $\{E_x(t), E_y(t)\}$ during an instantaneous optical period. The pure circular polarization corresponds to $\varepsilon = 0$ and is denoted by *blue-violet* color; the pure linear polarization is for $\varepsilon = 1$ indicated by *red*. The corresponding polarization *color-coding bar* is shown at the *left edge* of the figure

field of the excitation optical wave $\mathbf{E}_0$ and retarded dyadic Green's function $\mathbf{G}^r$, as given by Eqs. (1.43)–(1.44).

The hot spots are always localized at the surface of the metal, predominantly at the periphery of the system. Their intensities found as the result of these computations are depicted by colors in the center of Fig. 1.16. The highest local intensity is indicated by red, and the lowest by blue in the region surrounding the metal. We have selected

eight of these hot spots for our computations as denoted by letters A to H in the figure.

To generate the field in the far zone, we take a point dipole and position it at a surface of the metal at point $\mathbf{r}_0$ at such a hot spot, as described in the discussion of Fig. 1.15. The near-zone field $\mathbf{E}^L(\mathbf{r}, t)$ generated in response to this point dipole is found from Green's function relation

$$\mathbf{E}^L(\mathbf{r}, t) = \frac{4\pi}{\varepsilon_d} \int dt' \mathbf{G}^r(\mathbf{r}, \mathbf{r}_0; t - t')\, \mathbf{d}(\mathbf{r_0}, t'). \tag{1.59}$$

Knowing this local electric field, we calculate the total radiating optical dipole moment of the nanosystem in the frequency domain as

$$\mathbf{D}(\omega) = \frac{1}{4\pi} \int d^3r\, [\varepsilon_m(\omega) - \varepsilon_d]\, \Theta(\mathbf{r}) \mathbf{E}^L(\mathbf{r}, \omega). \tag{1.60}$$

Here and below, the frequency- and time-domain quantities, as indicated by their arguments ω and t, are Fourier transforms of each other. The field in the far zone produced by this radiating dipole is given by standard electrodynamic formula—see, e.g. Sect. 67 in Ref. [224]. The time-reversed field is generated by time-reversed dipole $\mathbf{D}^T(t)$ that is complex-conjugated in the frequency domain, $\mathbf{D}^T(\omega) = \mathbf{D}(\omega)^*$.

The dependence on time of the initial excitation dipole, $\mathbf{d}(\mathbf{r}_0, t)$ is set as an ultrashort Gaussian-shaped pulse of 12 fs duration with the carrier frequency $\hbar\omega_0 = 1.2$ eV. Following the procedure described above, the fields shown in Figs. 1.15 and 1.16 have been calculated for the radiation propagating in the y direction (normal to the plane of the nanostructure). These fields simply copy the retarded time evolution of the emitting dipole.

At the completing stage of our calculations, the time-reversed excitation pulse is sent back to the system as a plane wave propagating along the y direction (normal to the nanosystem plane). To calculate the resulting local fields, we again use Green's function Eq. (1.43) where the shaped excitation pulse substitutes for field $\mathbf{E}_0$.

1.4.4 Numerical Results for Time-Reversal Coherent Control

The electric field of the excitation wave is chosen as a modulated waveform (including amplitude, phase, and polarization modulation) that has been computed as described above in the previous subsection. The optical excitation energy can only be concentrated at sites where SP eigenmodes localize. For the present system, these are the hot spots shown by color in the central insert of Fig. 1.16, labeled A–H. The corresponding calculated excitation waveforms are displayed in panels as vector plots shown as functions of time $\{E_x(t), E_z(t)\}$.

There are several important features of these waveforms deserving our attention and discussion. First, these waveforms are rather long in duration: much longer than

the excitation-dipole 12 fs pulses. This confirms our understanding that the initial dipole field excites local SP fields that, in a cascade manner, excite a sequence of the system SPs, which ring down relatively long time (over 200 fs, as shown in the figure). This long ring-down process is exactly what is required for the nanostructure to transfer to the far-field zone the information on the near-zone local (evanescent) fields as is suggested by our idea presented above in the introduction. The obtained fields are by shape resembling the controlling pulses for the microwave radiation [221]. However, a fundamental difference is that in the microwave case the long ringing-down is due to the external reverberation chamber, while for the nanoplasmonic systems it is due to the intrinsic evolution of the highly resonant SP eigenmodes that possess high Q-factors (setting a reverberation chamber around a nanosystem would have been, indeed, unrealistic).

Second, one can see that the pulses in Fig. 1.16 have a very nontrivial polarization properties ranging from the pure linear polarization (indicated by red as explained in the caption to Fig. 1.16) to the circular polarization indicated by blue, including all intermediate degrees of circularity. The temporal-polarization structure of pulses A–H in Fig. 1.16 is very complicated, somewhat reminding that of Ref. [215], which was obtained by a genetic adaptive algorithm. However, in our case these pulses are obtained in a straightforward manner, by applying the well-known, deterministic Green's function of the system, which is a highly efficient and fast method.

Third, and most important, feature of the waveforms in Fig. 1.16 is that they are highly site-specific: pulses generated by the initial dipole in different positions are completely different. This is a very strong indication that they do transfer to the far far-field zone the information about the complicated spatio-temporal structure of the local, near-zone fields. This creates a pre-requisite for studying a possibility to use these pulses for the coherently-controlled nano-targeting.

Now we turn to the crucial test of the nanofocusing induced by the excitation pulses discussed above in conjunction with Fig. 1.16. Because of the finite time window ($T = 228$ fs) used for the time reversal, all these excitation pulses end and should cause the concentration of the optical energy (at the corresponding sites) at the same time, $t = T = 228$ fs (counted from the moment the excitation pulse starts impinging on the system). After this concentration instant, the nanofocused fields can, in principle, disappear (dephase) during a very short period on the order of the initial dipole pulse length, i.e. $\sim$12 fs. Thus this nanofocusing is a dynamic, transient phenomenon.

Note that averaging (or, integration) of the local-field intensity $I(\mathbf{r}, t) = |\mathbf{E}(\mathbf{r}, t)|^2$ over time t would lead to the loss of the effects of the phase modulation. This is due to a mathematical equality $\int_{-\infty}^{\infty} I(\mathbf{r}, t)dt = \int_{-\infty}^{\infty} |\mathbf{E}(\mathbf{r}, \omega)|^2 d\omega/(2\pi)$, where the spectral-phase modulation of the field certainly eliminates from the expression in the right-hand side. Thus the averaged intensity of the local fields is determined only by the local power spectrum of the excitation $|\mathbf{E}(\mathbf{r}, \omega)|^2$ and, consequently, is not coherently controllable. Very importantly, such a cancellation does not take place for nonlinear phenomena. In particular, two-photon processes such as two-photon fluorescence or two-photon electron emission that can be considered as proportional to the squared intensity $I^2(\mathbf{r}, t) = |\mathbf{E}(\mathbf{r}, t)|^4$ are coherently controllable even after time

averaging (integration), as we have argued earlier [148, 213]. Note the distributions measured in nonlinear optical experiments with the detection by the PEEM [123, 215, 216, 225] and in the fluorescence upconversion experiments [226] can be modeled as such nonlinear processes that yield distributions $\langle I^n(\mathbf{r})\rangle = \int_{-\infty}^{\infty} I^n(\mathbf{r},t)dt/T$, where $n \geq 2$. Inspired by this, we will consider below, in particular, the coherent control of the two-photon process averaged intensity $\langle I^2(\mathbf{r})\rangle$.

Let us investigate how precisely one can achieve the spatio-temporal focusing of the optical excitation at a given nanosite of a plasmonic nanostructure using the full shaping (amplitude, phase, and polarization) of the excitation pulses found from the time-reversal method. The results for the present nanostructure, targeting sites A–H, are shown in Fig. 1.17. For each excitation pulse, the spatial distribution of the local field intensity is displayed for the moment of time when this local intensity acquires its global (highest) maximum. The most important conclusion that one can draw from comparing panels (a)–(h) is that for each pulse A–H this global maximum corresponds to the maximum concentration of the optical energy at the corresponding targeted nanosite A–H. This obtained spatial resolution is as good as 4 nm, which is determined by the spatial size of inhomogeneities of the underlying plasmonic metal nanosystem. It is very important that this localization occurs not only at the desired nanometer-scale location but also very close to the targeted time that in our case is $t = 228$ fs. Thus the full shaping of femtosecond pulses by the time reversal is an efficient method of controlling the spatio-temporal localization of energy at the fs–nm scale.

Let us turn to the temporal dynamics of intensity of the nanoscale local fields at the targeted sites A–H, which is shown in Fig. 1.18a–h. As we can see, in each of the panels there is a sharp spike of the local fields very close to the target time of $t = 228$. The duration of this spike in most panels (a–f) is close to that of the initial dipole, i.e., 12 fs. This shows a trend to the reproduction of the initial excitation state due to the evolution of the time-reversed SP packet induced by the shaped pulses. There is also a pedestal that shows that this reproduction is not precise, which is expected due to the fact that the time reversal is incomplete: only the far-zone field propagating in one direction (along the y axis) is reversed. Nevertheless, as the discussion of Fig. 1.17 shows, this initial excitation-state reproduction is sufficient to guarantee that the targeted (initial excitation) site develops the global maximum (in time and space) of the local-field intensity. Interesting enough, the trend to reproduce the initial excitation state is also witnessed by almost symmetric (with respect to the maximum points $t = 228$ fs) shapes of all waveforms, which occurs in spite of the very asymmetric shapes of the excitation waveforms (cf. Fig. 1.16).

Apart from the ultrafast (femtosecond) dynamics of the nanolocalized optical fields discussed above in conjunction with Figs. 1.17 and 1.18, there is a considerable interest in its the time-integrated or averaged distributions, in particular, the mean squared intensity $\langle I^2(\mathbf{r})\rangle$. This quantity defines the nanoscale spatial distribution of the incoherent two-photon processes such as two-photon electron emission or two-photon luminescence. For example, in some approximation, the spatial distribution of the two-photon electron emission recorded by PEEM [123, 215, 216, 225] is determined by $\langle I^2(\mathbf{r})\rangle$.

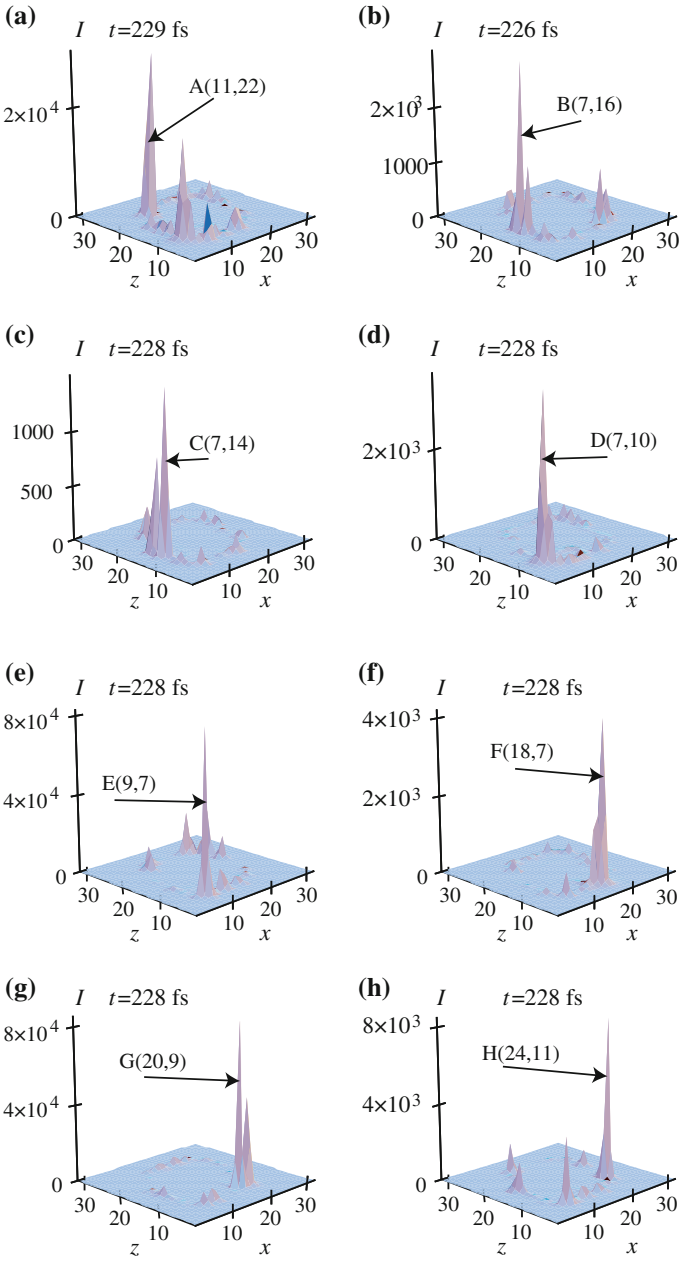

Fig. 1.17 Spatial distributions of the local optical field intensities at the surface of the metal nanostructure. Panels **a**–**h** correspond to the excitation with pulses A–H. Each such a distribution is displayed for the instance t at which the intensity for a given panel reaches its global maximum in space and time. This time t is displayed at the *top* of the corresponding panels. The corresponding targeted sites are indicated by arrows and labeled by the corresponding letters A–H and the coordinates (x, z). No special normalization has been applied so the distribution within any given panel is informative but not necessarily the magnitudes of the intensities between the panels

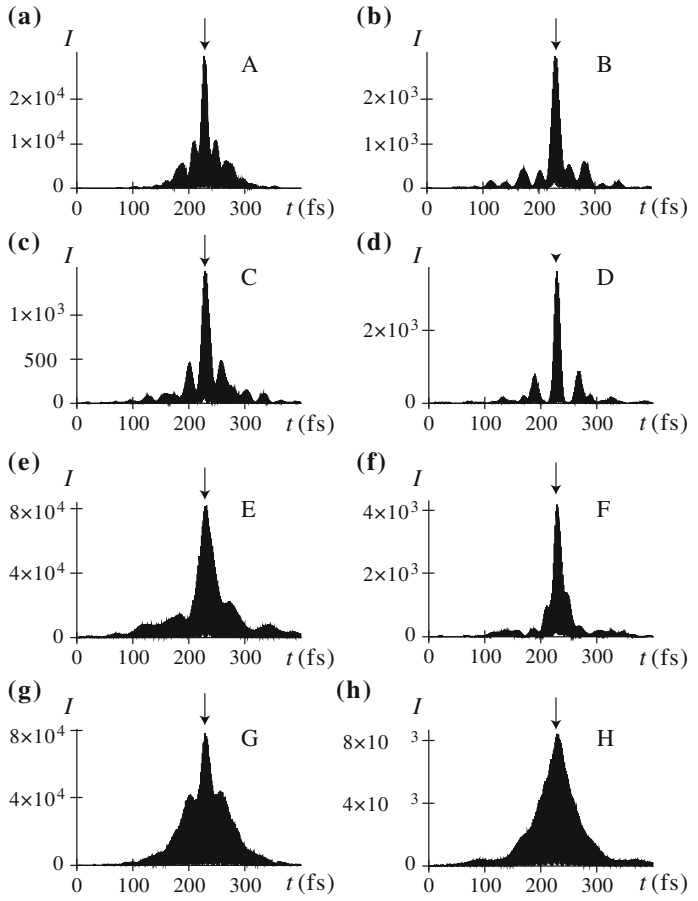

Fig. 1.18 **a–h** Temporal dynamics of the local field Intensity $I(\mathbf{r}, t) = \mathbf{E}^2(\mathbf{r}, t)$ at the corresponding hot spots A–H. The *down-arrows mark* the target time $t = 228$ fs where the local energy concentration is expected to occur

Now we test the spatial concentration of time-averaged mean-squared intensity $\langle I^2(\mathbf{r})\rangle$ for all sites, which is displayed in Fig. 1.19. As clearly follows from this figure, in all cases, there are leading peaks at the targeted sites. Thus the two-photon excitation, even after the time averaging, can be concentrated at desired sites using the coherent-control by the time-reversed shaped pulses.

We point out that there has recently been an experimental demonstration of a coherent spatiotemporal control on the nanoscale by polarization and phase pulse shaping [217]. The optical energy concentration at a given site on a ∼50 nm spatial scale at a given time on a ∼100 fs temporal scale has been demonstrated. Since this time scale is comparable to or longer than the SP dephasing time, the time-reversal method could not have been employed.

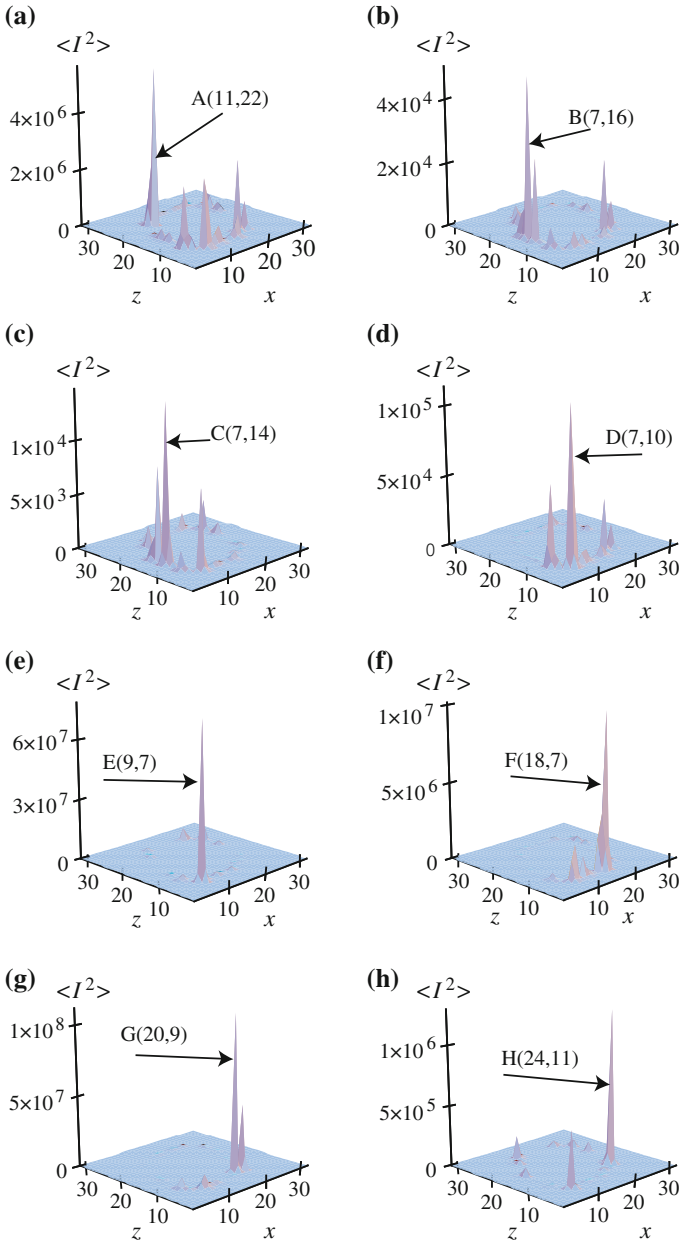

Fig. 1.19 Spatial distributions of the time-averaged mean-squared intensity $\langle I^2(\mathbf{r})\rangle$ in the near-field. This represents, in particular, the spatial distribution of the two-photon excited photocurrent density. Panels **a**–**h** correspond to the excitation with pulses A–H. The corresponding targeted sites are indicated by arrows and labeled by the corresponding letters A–H and coordinates (x, z). No special normalization has been applied so the distribution within any given panel is informative but not necessarily the magnitudes of the intensities between the panels can be compared

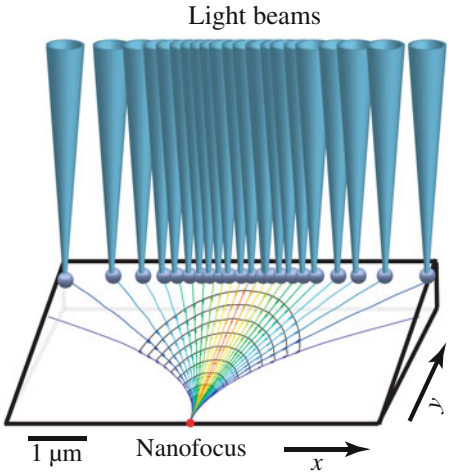

Fig. 1.20 Schematic of spatiotemporal coherent control on nanoscale. Adapted from Ref. [210]. Independently controlled light beams (shown by *blue* cones) are focused on launch pads depicted as silver spheres that are positioned on a thick edge of a wedge. SPP wavelets generated by the launchpads are shown by *black* arcs. Normal to them are rays (SPP trajectories) that are displayed by color lines coded accordingly to their origination points. These wavefronts and trajectories converge at the nanofocus indicated by the *red* dot

1.4.5 Coherent Control by Spatiotemporal Pulse Shaping

For coherent control on the nanoscale, as we have described above in Sect. 1.4, the phase of the excitation waveform along with its polarization provide functional degrees of freedom to control the nanoscale distribution of energy [123, 148, 195, 209, 213–215, 217, 225, 227]. Spatiotemporal pulse shaping permits one to generate dynamically predefined waveforms modulated both in frequency and in space to focus ultrafast pulses in the required microscopic spatial and femtosecond temporal domains [228, 229]. Here we follow Ref. [210] that has introduced a method of full coherent control on the nanoscale where a temporally and *spatially* modulated waveform is launched in a graded nanostructured system, specifically a wedge—see schematic of Fig. 1.20. Its propagation from the thick (macroscopic) to the thin (nanoscopic) edge of the wedge and the concurrent adiabatic concentration provide a possibility to focus the optical energy in nanoscale spatial and femtosecond temporal regions.

This method unifies three components that individually have been developed and experimentally tested. The coupling of the external radiation to the surface plasmon polaritons (SPPs) propagating along the wedge occurs through an array of nanoobjects (nanoparticles or nanoholes) that is situated at the thick edge of the wedge. The phases of the SPPs emitted (scattered) by individual nanoobjects are determined by a spatio-temporal modulator. The nanofocusing of the SPPs occurs due to their

propagation toward the nanofocus and the concurrent adiabatic concentration [12, 230, 231].

The coupling of the external radiation to SPPs and their nanofocusing have been observed—see, e.g., Refs. [232, 233]. The second component of our approach, the spatio-temporal coherent control of such nanofocusing has been developed [228, 229]. The third component, the adiabatic concentration of SPPs also has been observed and extensively studied experimentally [13–16, 18, 19, 22].

The adiabatic concentration (nanofocusing) is based on adiabatic following by a propagating SPP wave of a graded plasmonic waveguide, where the phase and group velocities decrease while the propagating SPP wave is adiabatically transformed into a standing, localized SP mode. A new quality that is present in this approach is a possibility to arbitrary move the nanofocus along the nanoedge of the wedge. Moreover, it is possible to superimpose any number of such nanofoci simultaneously and, consequently, create any distribution of the nanolocalized fields at the thin edge of the wedge.

To illustrate this idea of the full spatiotemporal coherent control, now let us turn to a wedge that contains a line of nanosize scatterers (say, nanoparticles or nanoholes) located at the thick edge and parallel to it, i.e. in the x direction in Fig. 1.20. Consider first monochromatic light incident on these nanoparticles or nanoholes that scatter and couple it into SPP wavelets. Every such a scatterer emits SPPs in all directions; there is, of course, no favored directionality of the scattering.

At this point, we assume that the excitation radiation and, correspondingly, the scattered wavelets of the SPP are coherent, and their phases vary in space along the thick edge, i.e., in the x direction. Then the SPP wavelets emitted by different scatterers will interfere, which in accord with the Huygens-Fresnel principle leads to formation of a smooth wavefront of the SPP wave at some distance from the scatterers in the "far SPP field", i.e., at distances much greater than the SPP wavelength $2\pi/k_{SPP}$.

Such wavefronts are shown in Fig. 1.20 with concave black curves. The energy of the SPP is transferred along the rays, which are the lines normal to the wavefronts, shown by the colored lines. By the appropriate spatial phase modulation of the excitation radiation along the line of scatterers (in the x direction) over distances of many SPP wavelengths, these wavefronts can be formed in such a way that the rays intersect at a given point, forming a nanofocus at the thin (sharp) edge of the wedge, as shown schematically in Fig. 1.20. Diffraction of the SPP waves will lead to a finite size of this focal spot.

By changing the spatial phase profile of the excitation radiation, this focal spot can be arbitrarily moved along the thin edge. This focusing and adiabatic concentration, as the SPPs slow down approaching the sharp edge, will lead to the enhancement of the intensity of the optical fields in the focal region. This dynamically-controlled concentration of energy is a plasmonic counterpart of a large phased antenna array (also known as an aperture synthesis antenna), widely used in radar technology (synthetic aperture radar or SAR) and radio astronomy [234].

Now we can consider excitation by spatiotemporally shaped ultrashort pulses independently in space. Such pulses are produced by spatio-temporal modulators

[228, 229]. The field produced by them is a coherent superposition of waves with different frequencies whose amplitudes and phases can arbitrarily vary in space and with frequency. This modulation can be chosen so that all the frequency components converge at the same focal spot at the same time forming an ultrashort pulse of the nanolocalized optical fields.

As an example we consider a silver [32] nanowedge illustrated in Fig. 1.20 whose maximum thickness is $d_m = 30\,\text{nm}$, the minimum thickness is $d_f = 4\,\text{nm}$, and whose length (in the y direction) is $L = 5\,\mu\text{m}$. Trajectories calculated by the Wentzel-Kramers-Brillouin (WKB) method in Ref. [210] for $\hbar\omega = 2.5\,\text{eV}$ are shown by lines (color used only to guide eye); the nanofocus is indicated by a bold red dot. In contrast to focusing by a conventional lens, the SPP rays are progressively bent toward the wedge slope direction.

Now consider the problem of coherent control. The goal is to excite a spatiotemporal waveform at the thick edge of the wedge in such a way that the propagating SPP rays converge at an arbitrary nanofocus at the sharp edge where an ultrashort pulse is formed. To solve this problem, we use the idea of back-propagation or time-reversal [220, 221, 235]. We generate rays at the nanofocus as an ultrashort pulse containing just several oscillations of the optical field. Propagating these rays, we find amplitudes and phases of the fields at the thick edge at each frequency as given by the complex propagation phase (eikonal) $\Phi(\boldsymbol{\rho})$, where $\boldsymbol{\rho}$ is a 2-d coordinate vector in the plane of the wedge. Then we complex conjugate the amplitudes of frequency components, which corresponds to the time reversal. We also multiply these amplitudes by $\exp(2\text{Im}\,\Phi)$, which pre-compensates for the Ohmic losses. This provides the required phase and amplitude modulation at the thick edge of the wedge.

We show an example of such calculations in Fig. 1.21. Panel (a) displays the trajectories of SPPs calculated [210] by the WKB method. The trajectories for different frequencies are displayed by colors corresponding to their visual perception. There is a very significant spectral dispersion: trajectories with higher frequencies are much more curved. The spatial-frequency modulation that we have found succeeds in bringing all these rays (with different frequencies and emitted at different x points) to the same nanofocus at the sharp edge.

The required waveforms at different x points of the thick edge of the wedge are shown in Fig. 1.21b–d where the corresponding longitudinal electric fields are shown. The waves emitted at large x, i.e., at points more distant from the nanofocus, should be emitted significantly earlier to pre-compensate for the longer propagation times. They should also have different amplitudes due to the differences in the adiabatic compression along the different rays. Finally, there is clearly a negative chirp (gradual decrease of frequency with time). This is due to the fact that the higher frequency components propagate more slowly and therefore must be emitted earlier to form a coherent ultrashort pulse at the nanofocus.

In Fig. 1.21e we display together all three of the representative waveforms at the thick edge to demonstrate their relative amplitudes and positions in time. The pulse at the extreme point in x (shown by blue) has the longest way to propagate and therefore is the most advanced in time. The pulse in the middle point (shown by green) is intermediate, and the pulse at the center ($x = 0$, shown by red) is last. One can

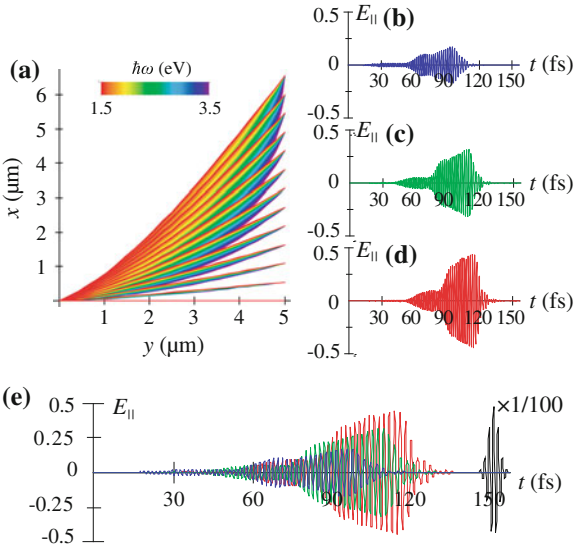

Fig. 1.21 **a** Trajectories (*rays*) of SPP packets propagating from the thick edge to the nanofocus displayed in the *x y* plane of the wedge. The frequencies of the individual rays in a packet are indicated by *color* as coded by the *bar* at the *top*. **b–d** Spatiotemporal modulation of the excitation pulses at the thick edge of the wedge required for nanofocusing. The temporal dependencies (waveforms) of the electric field for the phase-modulated pulses for three points at the thick edge boundary: two extreme points and one at the *center*, as indicated, aligned with the corresponding *x* points at panel **a**. **e** The three excitation pulses of panels **b–d** (as shown by their *colors*), superimposed to elucidate the phase shifts, delays, and shape changes between these pulses. The resulting ultrashort pulse at the nanofocus is shown by the *black line*. The scale of the electric fields is arbitrary but consistent throughout the figure

notice also a counterintuitive feature: the waves propagating over longer trajectories are smaller in amplitude though one may expect the opposite to compensate for the larger losses. The explanation is that the losses are actually insignificant for the frequencies present in these waveforms, and the magnitudes are determined by adiabatic concentration factor.

Figure 1.21e also shows the resulting ultrashort pulse in the nanofocus. This is a transform-limited, Gaussian pulse. The propagation along the rays completely compensates the initial phase and amplitude modulation, exactly as intended. As a result, the corresponding electric field of the waveform is increased by a factor of 100. Taking the other component of the electric field and the magnetic field into account, the corresponding increase of the energy density is by a factor $\sim 10^4$ with respect to that of the SPPs at the thick edge.

To briefly conclude, an approach [210] to full coherent control of spatiotemporal energy localization on the nanoscale has been presented. From the thick edge of a plasmonic metal nanowedge, SPPs are launched, whose phases and amplitudes are independently modulated for each constituent frequency of the spectrum and at each

spatial point of the excitation. This pre-modulates the departing SPP wave packets in such a way that they reach the required point at the sharp edge of the nanowedge in phase, with equal amplitudes forming a nanofocus where an ultrashort pulse with required temporal shape is generated. This system constitutes a "nanoplasmonic portal" connecting the incident light field, whose features are shaped on the microscale, with the required point or features at the nanoscale.

1.4.6 Experimental Demonstrations of Coherent Control on the Nanoscale

The ideas of the coherent control of the nanoscale distribution of ultrafast optical fields both space and in time, which have been introduced theoretically in Refs. [148, 195, 210, 214, 218, 236, 237], have been investigated and confirmed experimentally. Using the full phase and amplitude modulation of the excitation-pulse wavefront in both polarizations (the so-called polarization pulse shaping), the experiments have achieved both spatial control [123, 215] and spatiotemporal control [217] on nm–fs scale.

Recently spatiotemporal nanofocusing via the adiabatic concentration along the lines of ideas presented above in Sect. 1.4.5 has been successfully demonstrated experimentally [21]. In this work, a shaped femtosecond pulse has been coupled by a grating to a TM_0 SPP mode on the surface of an adiabatically-tapered nanocone. The spatiotemporal concentration of optical energy in space to a $\sim$10 nm region and in time to a 15 fs duration (Fourier-transform limited, i.e., the shortest possible at a given bandwidth). Indeed the position of the nanofocus in Ref. [21] is always the tip of the nanocone; so the possibility of moving the nanofocus in space is not available.

The ideas of employing the spatial modulation of the excitation wavefront [210] described above in Sect. 1.4.5 have been experimentally tested and confirmed for continuous wave (CW) excitation [211, 212]. We will present some of these experimental results below in this section.

We start with experiments on polarization-shaping coherent control that we adapt from Ref. [215]. The corresponding experimental approach is schematically illustrated in Fig. 1.22. Polarization-shaped ultrashort laser pulses illuminate a planar nanostructure, with two-photon photoemission electron microscopy (PEEM) [238] providing the feedback signal from the nanoscale field distribution that is essential for adaptive near-field control.

The spatial resolution of two-photon PEEM ($\sim$50 nm) is determined by its electron optics and is, thus, independent of the electromagnetic light-field diffraction limit. The sensitivity of the two-photon PEEM patterns to the optical field intensities arises from the nonlinear two-photon photoemission process whose intensity is proportional to the time-integrated fourth power of the local electric-field amplitude. With these elements in place, a user-specified nanoscopic optical field distribution is realized by processing recorded photoemission patterns in an evolutionary algorithm that directs the iterative optimization of the irradiating laser pulse shape.

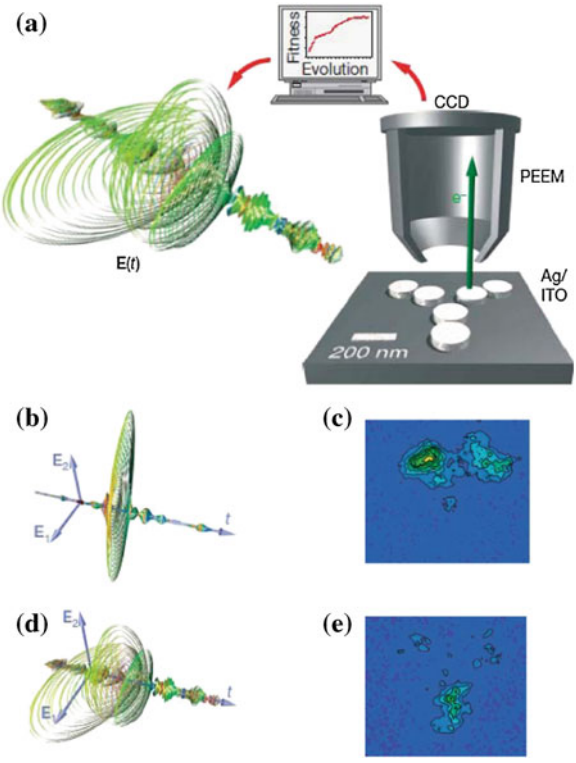

Fig. 1.22 Schematic and experimental results of coherent control with polarization shaping. Adapted from Ref. [215]. **a** Schematic of the experiment. A polarization shaper for ultrashort laser pulses controls the temporal evolution of the vectorial electric field $E(t)$ on a femtosecond timescale. These pulses illuminate a planar nanostructure in an ultrahigh-vacuum chamber that is equipped with a photoemission electron microscope (PEEM). The nanostructure consists of six circular Ag islands on an indium-tin oxide (ITO) film and a quartz substrate. A computer-controlled charge-coupled device (CCD) camera records the photoemission image and provides a feedback signal for an evolutionary learning algorithm. Iterative optimization of the pulse-shaper settings leads to an increase in the fitness value and correspondingly allows control over the nanooptical fields. **b**, **c** The optimal laser pulses, as experimentally characterized, display complex temporal electric-field evolution for the objectives of **b** minimizing and **d** maximizing the concentration of the excitation on the lower branch. E_1 and E_2 indicate the two field components that are phase-modulated in the polarization pulse shaper in the first and second LCD layer, respectively. They are at 45° angles with respect to the p-polarization. The overall time window shown is 2 ps. **c** The experimental PEEM image after adaptive maximization of the *upper region* intensity using complex polarization-shaped laser pulses (fittest individual of the final generation) shows predominant emission from the *upper region*. **e** Photoemission after minimization of the intensity in the *upper region* is concentrated in the *lower region*

The basic idea of the experiment is that the measured PEEM pattern identifies the origin of ejected photoelectrons and hence the regions of high local field intensity. A controlled variation of the PEEM pattern then proves the spatial control over the

nanoscopic field distribution. We have already discussed such an approach above—see Fig. 1.10 [123] and the corresponding discussion in Sect. 1.3.6.

The nanostructure used consists of circular Ag disks with 180 nm diameter and 30 nm height, fabricated by electron-beam lithography on a conductive, 40-nm-thick indium-tin oxide (ITO) film grown on a quartz substrate. The disks are arranged into three dimers that form the arms of a star-like shape (Fig. 1.22a, lower right). The whole nanostructure is about 800 nm across, while the gap between two of the dimer disks is ∼10 nm wide. After inspection by scanning-electron microscopy (SEM), the sample is mounted in the ultrahigh-vacuum PEEM set-up. The deposition of a small amount of caesium (∼0.1 monolayers) reduces the work function of the Ag nanostructure to about 3.1 eV, that is, just below the threshold for two-photon photoemission with 790 nm photons.

The PEEM pattern obtained after maximization of the photoemission from the upper two arms of the Ag nanostructure in shown in Fig. 1.22c. It shows strong emission from these two upper arms and almost no emission from the bottom arm. Analogously, the photoemission after minimization of the upper part PEEM brightness (Fig. 1.22e) occurs mainly in the lower area while the contribution from the upper two arms is extremely weak. The adaptively determined solution to each optimization problem has been proven to be robust with respect to slight imperfections in the experimental nanostructures. These successful optimizations demonstrate that polarization pulse shaping allows adaptive control of the spatial distribution of photoelectrons on a subwavelength scale, and thus of the nanoscopic optical fields that induce photoemission.

The optimally polarization-shaped laser pulses after adaptive maximization and minimization described above are shown in Figs. 1.22b, d, respectively, as determined by dual-channel spectral interferometry [239, 240]. In this representation, the shape of the quasi-three-dimensional figure indicates the temporal evolution of the polarization state of the electric field, with the color representing the instantaneous oscillation frequency. Contributions from both transverse polarization components are visible in each of the two cases. Whereas the upper-region photoemission maximization is achieved with a comparatively simple time evolution, the corresponding minimization requires a more complex field with varying degrees of ellipticity, orientation and temporal amplitudes.

Our idea [210] of the coherent control on the nanoscale by spatial modulation (shaping) of the excitation waveform has been developed theoretically [237] and experimentally [211, 212]. The coherent control of nanoscale distribution of local optical fields based on CW excitation aimed at achieving a deterministic control of plasmonic fields by using the spatial shaping of high order beams such as Hermite-Gaussian (HG) and Laguerre-Gaussian (LG) beams has been carried out in Ref. [211]. It has been shown experimentally that the spatial phase shaping of the excitation field provides an additional degree of freedom to drive optical nanoantennas and consequently control their near field response.

An example of such a deterministic coherent control is illustrated in Fig. 1.23. It shows a double gap antenna formed by three 500 nm aligned gold bars forming two identical 50 nm air gaps separated by 500 nm. For reference, in panel (a) it displays

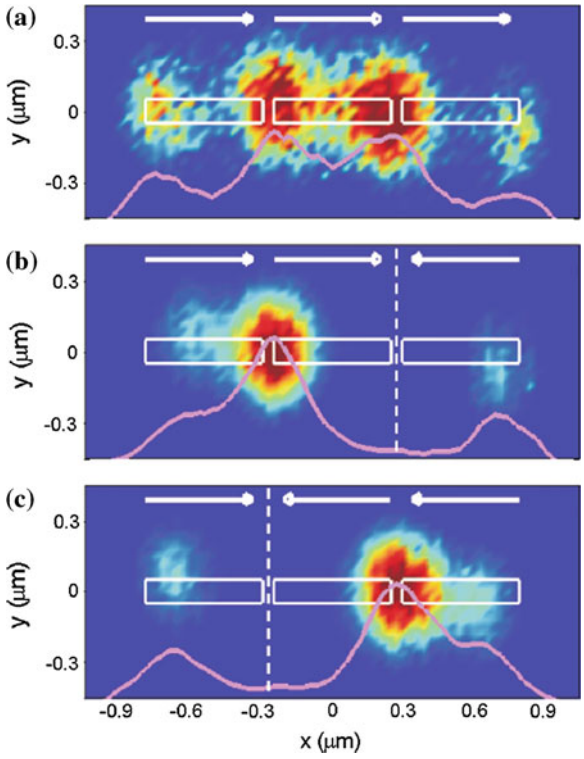

Fig. 1.23 Experimental results on spatial coherent control of nanoantennas. Adapted from Ref. [211]. Experimental two-photon luminescence (TPL) maps recorded for **a** a Gaussian beam and **b**, **c** a Hermite-Gaussian (HG10) beam whom phase shift (indicated by the *vertical dashed line*) coincides with (**b**) the *right* gap and (**c**) the *left* gap

a measured two-photon luminescence (TPL) map when driving the whole antenna with a Gaussian beam linearly polarized along the x-axis. Note that similar to what has been discussed above in Sect. 1.4.4, in particular, in conjunction with Fig. 1.19, the TPL reflects the time-averaged distribution of the local field intensity $\langle I^2(\mathbf{r})\rangle$. As we see from Fig. 1.23a and as expected, a field concentration is observed in both gaps. Figure 1.23b, c shows TPL maps recorded when the π-phase shift of a HG10 beam coincides, respectively, with the right and left gaps. These data demonstrate how a suitable positioning of the phase jump over the double antenna enables us to selectively switch on and off one of the two hot-spot sites.

Even closer to the original idea [210] that a plasmonic wavefront can be shaped and focused at a predetermined spot by a spatial phase modulation of the excitation waveform incident on optically-addressable launch pads is a recent publication [212]. This article achieves controlled launching and propagation of SPPs by spatially designing the amplitude and phase of the incident light. The chosen amplitude profile, consisting of four bright ("on") SPP launching platforms and one central

dark ("off") arena, fully separates plasmonic effects from photonic effects and in addition is the necessary starting point for later focusing and scanning experiments. Any intensity detected inside the arena is purely plasmonic.

Adapting from Ref. [212], we present the achieved SPP focusing in Fig. 1.24. A phase optimization loop is used to focus SPPs at a pre-chosen target. This loop yields the optimal phase for each launching pad ("superpixel") as well as the relative intensity to focus. The amplitude profile is the same in all cases including the bare gold case, with four launching areas and a central dark arena where only SPPs can propagate. The incident polarization is diagonal in relation to the grating lines so as to have all available angles (2π range) contributing to the focus, thereby maximizing the numerical aperture and resolution.

Successful focusing at the center of the SPP arena is shown in Fig. 1.24a. The structured SPP wavefront produces an intensity in the designated target that is at least 20 times higher than the average SPP background of an unstructured wavefront. The measured size of the plasmonic focus is 420 nm, consistent with the diffraction limit of the SPPs. The flexibility of the method (scanning the focus) is demonstrated in Figs. 1.24b, c, which shows the SPP focus relocated without mechanical motion to controlled positions in the plasmonic arena.

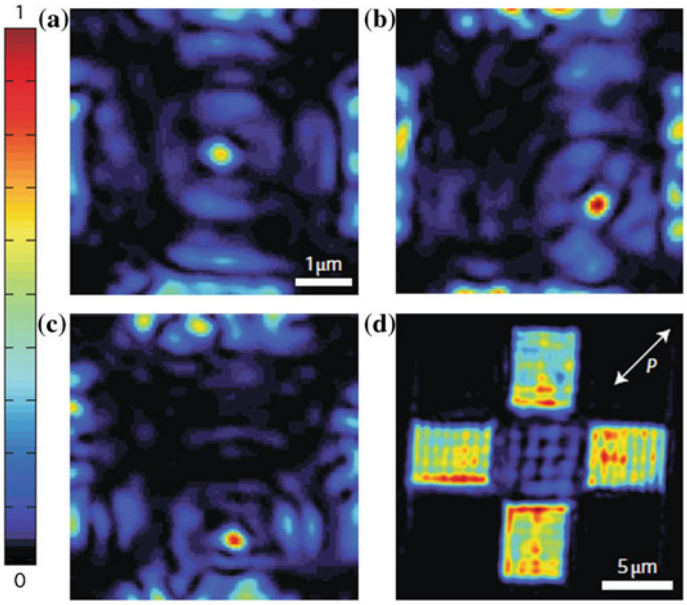

Fig. 1.24 Experiment on coherent control (dynamic focusing) of SPPs. Adapted from Ref. [212]. **a** Relative phases of the superpixels are optimized to focus SPPs at the *center* of the SPP arena. The intensity in the target spot is purely plasmonic and 20 times higher than the average background of an unstructured plasmonic wavefront. The focus size is diffraction limited by the detecting optics. **b**, **c**, Demonstration of SPP focusing on freely chosen targets in the SPP arena. **d** Background reference of an unstructured SPP wavefront (uniform phase profile)

The work of Ref. [212] has fully implemented the idea of Ref. [210] on the spatial-phase-modulation control of the SPP wavefronts to position a SPP nanofocus at a desired location at the surface. However, it employs only CW excitation and does not exploit a potential femtosecond temporal degree of freedom to achieve such a nanofocusing at a predetermined moment of time as in Ref. [210].

1.5 Quantum Nanoplasmonics: Spaser and Nanoplasmonics with Gain

1.5.1 Introduction to Spasers and Spasing

Not just a promise anymore [241], nanoplasmonics has delivered a number of important applications: ultrasensing [242], scanning near-field optical microscopy [190, 243], SP-enhanced photodetectors [53], thermally assisted magnetic recording [244], generation of extreme uv [138], biomedical tests [242, 245], SP-assisted thermal cancer treatment [246], plasmonic enhanced generation of extreme ultraviolet (EUV) pulses [138] and extreme ultraviolet to soft x-ray (XUV) pulses [247], and many others—see also Ref. [23].

To continue its vigorous development, nanoplasmonics needs an active device—near-field generator and amplifier of nanolocalized optical fields, which has until recently been absent. A nanoscale amplifier in microelectronics is the metal-oxide-semiconductor field effect transistor (MOSFET) [248, 249], which has enabled all contemporary digital electronics, including computers and communications and enabled the present day technology as we know it. However, the MOSFET is limited by frequency and bandwidth to $\lesssim$100 GHz, which is already a limiting factor in further technological development. Another limitation of the MOSFET is its high sensitivity to temperature, electric fields, and ionizing radiation, which limits its use in extreme environmental conditions and nuclear technology and warfare.

An active element of nanoplasmonics is the spaser (Surface Plasmon Amplification by Stimulated Emission of Radiation), which was proposed [31, 250] as a nanoscale quantum generator of nanolocalized coherent and intense optical fields. The idea of spaser has been further developed theoretically [139–141, 251]. Spaser effect has recently been observed experimentally [252]. Also a number of SPP spasers (also called nanolasers) have been experimentally observed [253–256].

Spaser is a nanoplasmonic counterpart of laser: it is a quantum generator and nanoamplifier where photons as the generated quanta are replaced by SPs. Spaser consists of a metal nanoparticle, which plays a role of the laser cavity (resonator), and the gain medium. Figure 1.25 schematically illustrates geometry of a spaser introduced in the original article [31], which contains a V-shaped metal nanoparticle surrounded by a layer of semiconductor nanocrystal quantum dots.

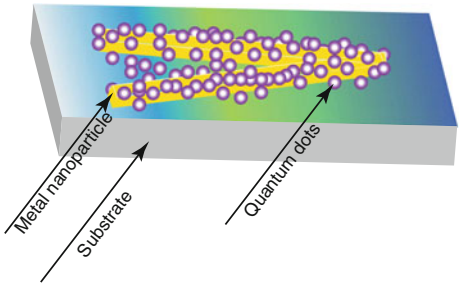

Fig. 1.25 Schematic of the spaser as originally proposed in Ref. [31]. The resonator of the spaser is a metal nanoparticle shown as a gold V-shape. It is covered by the gain medium depicted as nanocrystal quantum dots. This active medium is supported by a substrate

1.5.2 Spaser Fundamentals

As we have already mentioned, the spaser is a nanoplasmonic counterpart of the laser [31, 251]. The laser has two principal elements: resonator (or cavity) that supports photonic mode(s) and the gain (or active) medium that is population-inverted and supplies energy to the lasing mode(s). An inherent limitation of the laser is that the size of the laser cavity in the propagation direction is at least half wavelength and practically more than that even for the smallest lasers developed [253, 254, 257]. In the spaser [31] this limitation is overcome. The spasing modes are surface plasmons (SPs) whose localization length is on the nanoscale [78] and is only limited by the minimum inhomogeneity scale of the plasmonic metal and the nonlocality radius [35] $l_{nl} \sim 1$ nm. So, the spaser is truly nanoscopic—its minimum total size can be just a few nanometers.

The resonator of a spaser can be any plasmonic metal nanoparticle whose total size R is much less than the wavelength λ and whose metal thickness is between l_{nl} and l_s, which supports a SP mode with required frequency ω_n. This metal nanoparticle should be surrounded by the gain medium that overlaps with the spasing SP eigenmode spatially and whose emission line overlaps with this eigenmode spectrally [31]. As an example, we consider a model of a nanoshell spaser [139, 251, 258], which is illustrated in Fig. 1.26. Panel (a) shows a silver nanoshell carrying a single SP (plasmon population number $N_n = 1$) in the dipole eigenmode. It is characterized by a uniform field inside the core and hot spots at the poles outside the shell with the maximum field reaching $\sim 10^6$ V/cm. Similarly, Fig. 1.26b shows the quadrupole mode in the same nanoshell. In this case, the mode electric field is non-uniform, exhibiting hot spots of $\sim 1.5 \times 10^6$ V/cm of the modal electric field at the poles. These high values of the modal fields is the underlying physical reason for a very strong feedback in the spaser. Under our conditions, the electromagnetic retardation within the spaser volume can be safely neglected. Also, the radiation of such a spaser is a weak effect: the decay rate of plasmonic eigenmodes is dominated

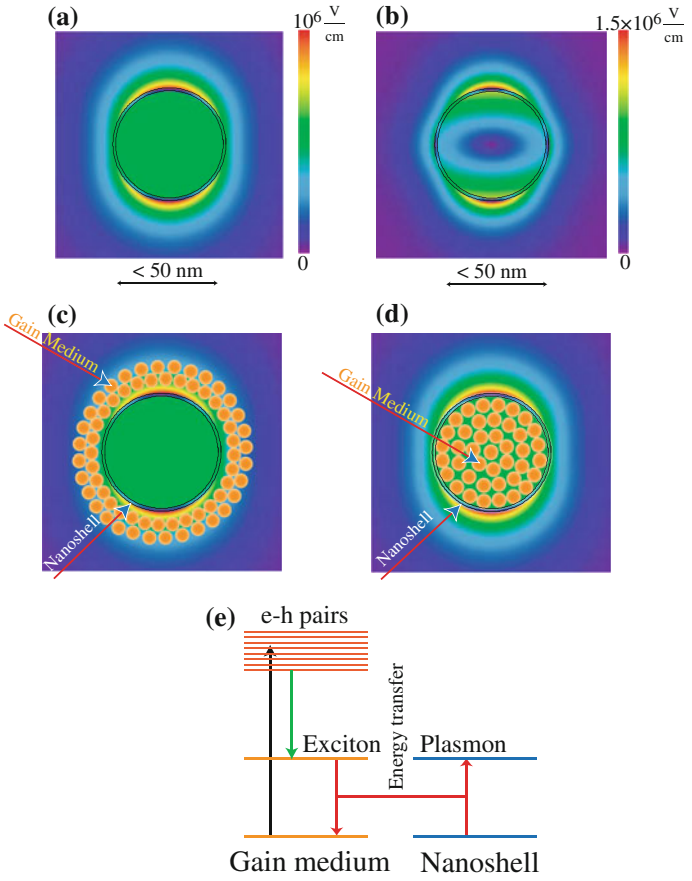

Fig. 1.26 Schematic of spaser geometry, local fields, and fundamental processes leading to spasing. Adapted from Ref. [139]. **a** Nanoshell geometry and the local optical field distribution for one SP in an axially-symmetric dipole mode. The nanoshell has aspect ratio $\eta = 0.95$. The local field magnitude is color-coded by the scale bar in the *right-hand side* of the panel. **b** The same as (**a**) but for a quadrupole mode. **c** Schematic of a nanoshell spaser where the gain medium is outside of the shell, on the background of the dipole-mode field. **d** The same as (**c**) but for the gain medium inside the shell. **e** Schematic of the spasing process. The gain medium is excited and population-inverted by an external source, as depicted by the *black arrow*, which produces electron-hole pairs in it. These pairs relax, as shown by the *green arrow*, to form the excitons. The excitons undergo decay to the ground state emitting SPs into the nanoshell. The plasmonic oscillations of the nanoshell stimulates this emission, supplying the feedback for the spaser action

by the internal loss in the metal. Therefore, it is sufficient to consider only quasistatic eigenmodes [29, 78] and not their full electrodynamic counterparts [259].

For the sake of numerical illustrations of our theory, we will use the dipole eigenmode (Fig. 1.26a). There are two basic ways to place the gain medium: (i) outside the nanoshell, as shown in panel (c), and (ii) in the core, as in panel (d), which

was originally proposed in Ref. [258]. As we have verified, these two designs lead to comparable characteristics of the spaser. However, the placement of the gain medium inside the core illustrated in Fig. 1.26d has a significant advantage because the hot spots of the local field are not covered by the gain medium and are sterically available for applications.

Note that any l-multipole mode of a spherical particle is, indeed, $2l + 1$-times degenerate. This may make the spasing mode to be polarization unstable, like in lasers without polarizing elements. In reality, the polarization may be clamped and become stable due to deviations from the perfect spherical symmetry, which exist naturally or can be introduced deliberately. More practical shape for a spaser may be a nanorod, which has a mode with the stable polarization along the major axis. However, a nanorod is a more complicated geometry for theoretical treatment, and we will consider it elsewhere.

The level diagram of the spaser gain medium and the plasmonic metal nanoparticle is displayed in Fig. 1.26e along with a schematic of the relevant energy transitions in the system. The gain medium chromophores may be semiconductor nanocrystal quantum dots [31, 260], dye molecules [261, 262], rare-earth ions [258], or electron-hole excitations of an unstructured semiconductor [253, 257]. For certainty, we will use a semiconductor-science language of electrons and holes in quantum dots.

The pump excites electron-hole pairs in the chromophores (Fig. 1.26e), as indicated by the vertical black arrow, which relax to form excitons. The excitons constitute the two-level systems that are the donors of energy for the SP emission into the spasing mode. In vacuum, the excitons would recombine emitting photons. However, in the spaser geometry, the photoemission is strongly quenched due to the resonance energy transfer to the SP modes, as indicated by the red arrows in the panel. The probability of the radiativeless energy transfer to the SPs relative to that of the radiative decay (photon emission) is given by the so-called Purcell factor

$$\sim \frac{\lambda\!\!\!^{-3} Q}{R^3} \gg 1, \tag{1.61}$$

where R is a characteristic size of the spaser metal core. Thus this radiativeless energy transfer to the spaser mode is the dominant process whose probability is by orders of magnitude greater than that of the free-space (far-field) emission.

The plasmons already in the spaser mode create the high local fields that excite the gain medium and stimulate more emission to this mode, which is the feedback mechanism. If this feedback is strong enough, and the life time of the spaser SP mode is long enough, then an instability develops leading to the avalanche of the SP emission in the spasing mode and spontaneous symmetry breaking, establishing the phase coherence of the spasing state. Thus the establishment of spasing is a non-equilibrium phase transition, as in the physics of lasers.

1.5.3 Brief Overview of Latest Progress in Spasers

After the original theoretical proposal and prediction of the spaser [31], there has been an active development in this field, both theoretical and experimental. There has also been a US patent issued on spaser [250].

Among theoretical developments, a nanolens spaser has been proposed [263], which possesses a nanofocus ("the hottest spot") of the local fields. In Refs. [31, 263], the necessary condition of spasing has been established on the basis of the perturbation theory.

There have been theories published describing the SPP spasers (or, "nanolasers" as sometimes they are called) phenomenologically, on the basis of classic linear electrodynamics by considering the gain medium as a dielectric with a negative imaginary part of the permittivity, e.g., [258]. Very close fundamentally and technically are works on the loss compensation in metamaterials [264–267]. Such linear-response approaches do not take into account the nature of the spasing as a non-equilibrium phase transition, at the foundation of which is spontaneous symmetry breaking: establishing coherence with an arbitrary but sustained phase of the SP quanta in the system [139]. Spaser is necessarily a deeply-nonlinear (nonperturbative) phenomenon where the coherent SP field always saturates the gain medium, which eventually brings about establishment of the stationary (or, continuous wave, CW) regime of the spasing [139]. This leads to principal differences of the linear-response results from the microscopic quantum-mechanical theory in the region of spasing, as we discuss below in conjunction with Fig. 1.29.

There has also been a theoretical publication on a bowtie spaser (nanolaser) with electrical pumping [268]. It is based on balance equations and only the CW spasing generation intensity is described. Yet another theoretical development has been a proposal of the lasing spaser [269], which is made of a plane array of spasers.

There have also been a theoretical proposal of a spaser ("nanolaser") consisting of a metal nanoparticle coupled to a single chromophore [270]. In this paper, a dipole–dipole interaction is illegitimately used at very small distances r where it has a singularity (diverging for $r \to 0$), leading to a dramatically overestimated coupling with the SP mode. As a result, a completely unphysical prediction of CW spasing due to single chromophore has been obtained [270]. In contrast, our theory [139] is based on the full (exact) field of the spasing SP mode without the dipole (or, any multipole) approximation. As our results of Sect. 1.5.5 below show, hundreds of chromophores per metal nanoparticle are realistically requited for the spasing even under the most favorable conditions.

There has been a vigorous experimental investigation of the spaser and the concepts of spaser. Stimulated emission of SPPs has been observed in a proof-of-principle experiment using pumped dye molecules as an active (gain) medium [261]. There have also been later experiments that demonstrated strong stimulated emission compensating a significant part of the SPP loss [262, 271–274]. As a step toward the lasing spaser, the first experimental demonstration has been reported of a partial compensation of the Joule losses in a metallic photonic metamaterial using optically

pumped PbS semiconductor quantum dots [260]. There have also been experimental investigations reporting the stimulated emission effects of SPs in plasmonic metal nanoparticles surrounded by gain media with dye molecules [275, 276].

The full loss compensation and amplification of the long-range SPPs at $\lambda = 882\,\text{nm}$ in a gold nanostrip waveguide with a dyes solution as a gain medium has been observed [277]. Another example of full loss compensation has recently been obtained for thin ($\sim$20 nm thickness) gold stripes (width $\sim 1\,\mu\text{m}$) surrounded by a gain medium containing donor–acceptor with a Fögrster energy transfer to increase the Stokes shift and decrease absorption at the probe frequency.

At the present time, there have been a number of the successful experimental observations of the spaser and SPP spasers (the so-called nanolasers). An electrically-pumped nanolaser with semiconductor gain medium have been demonstrated [253] where the lasing modes are SPPs with a one-dimensional confinement to a $\sim$50 nm size. Other electrically-pumped nanolasers (SPP spasers) have recently been fabricated and their lasing observed based on a diode with an intrinsic InGaAs gain media and silver nanocavities as plasmonic cores [278–280]. The latest of these nanolasers [280] operates at a room temperature and has a relatively small cavity volume $V_c \approx 0.67\lambda^3$, where vacuum wavelength $\lambda = 1591\,\text{nm}$. This volume is still much larger than the modal volumes of the spasers with tighter confinement, especially SP-mode spasers—see below.

A nanolaser with an optically-pumped semiconductor gain medium and a hybrid semiconductor/metal (CdS/Ag) SPP waveguide has been demonstrated with an extremely tight transverse (two-dimensional) mode confinement to $\sim$10 nm size [254]. This has been followed by the development of CdS/Ag nanolasers generating a visible single mode at a room temperature with a tight one-dimensional confinement ($\sim$20 nm) and a two-dimensional confinement in the plane of the structure to an area $\sim 1\,\mu\text{m}^2$ [255]. A highly efficient SPP spaser in the communication range ($\lambda = 1.46\,\mu\text{m}$) with an optical pumping based on a gold film and an InGaAs semiconductor quantum-well gain medium has recently been reported [256].

Another class of spasers observed are random spasers comprised of a rough metal nanofilm as a plasmonic component and a dye-doped polymeric film as a gain medium [281]. The spasing in such systems competes with loss compensation for SPPs propagating at the interface—see also Sect. 1.5.7.

Historically, the first spaser observed was a nanoparticle spaser [252]. This spaser is a chemically synthesized gold nanosphere of radius 7 nm surrounded by a dielectric shell of a 21 nm outer radius containing immobilized dye molecules. Under nanosecond optical pumping in the absorption band of the dye, this spaser develops a relatively narrow-spectrum and intense visible emission that exhibits a pronounced threshold in pumping intensity. The observed characteristics of this spaser are in an excellent qualitative agreement and can be fully understood on the basis of the corresponding theoretical results described below in Sect. 1.5.5.

1.5.3.1 Nanospaser with Semiconductor Gain Media

It is of both fundamental and applied importance to develop nanoscale-size spasers (nanospasers) with semiconductor gain media. The photochemical and electrochemical stability of the semiconductor gain media is the main attraction of such a design. Belonging to this class, spasers have recently been fabricated and their operation observed, comprised of a InGaN-core/InN-shell semiconductor-nanorod gain medium and silver film as a plasmonic component [282, 283]. They generate on ocalized SP modes. One of these [283] is a nanospaser with a deeply sub-wavelength mode size based on an epitaxial silver nanofilm [283]. Such a design bears a promise of practical applications due to its stability and small modal volume leading to high operational speed—see below Sect. 1.5.6.

In Fig. 1.27, we display geometry of this InGaN-core/InN-shell nanorod spaser and properties of its spasing mode. The active region of the spaser (Fig. 1.27a, left panel) is a core-shell nanocylinder with a 30-nm diameter core of InGaN surrounded by think shell if GaN. The latter is a wide band-gap semiconductor that plays a role of insulator. The active nanorod is separated by the metal by a 5-nm layer of silica. The plasmonic component of this spaser is a flat layer of epitaxial silver. The high monocrystalline quality of the silver film is instrumental in reducing the threshold of the spaser and increasing its output. The calculated intensity for the spasing eigenmode is shown in the right panel of Fig. 1.27a. Similar to the gap modes introduced in Ref. [284], this eigenmode is concentrated in the thin layer of a low-permittivity dielectric (silica) between the two high-permittivity media: GaN and silver. The modal fields do penetrate sufficiently into the gain medium providing the feedback necessary for the spaser functioning.

Under 8.3 kW/cm^2 optical pumping with frequency above the band gap of InGaN, a series of the emission spectra of a single spaser is displayed in Fig. 1.27b, At a room temperature, $T = 300$ K, the emission is a spontaneous fluorescence in a wide yellow–green spectral band near the band gap of InGaN. The first evidence of the spasing appears at $T = 120$ K as a small notch at the green side of the spectrum. As the temperature decreases to $T = 8$ K, the narrow line at $\lambda \approx 500$ nm becomes dominant and narrow. This change of the spectrum over the threshold is in a qualitative agreement with theory—see below Sect. 1.5.5 and, in particular, Figs. 1.29d–f.

The light–line (L–L) line is the dependence of the light intensity out (the intensity of the radiation emitted by the spaser within the linewidth spectral range) versus the intensity of the pumping radiation. The theoretical prediction for the spaser is that after reaching the spasing threshold, the L–L line becomes linear with universally unit slope—see Fig. 1.29a and its discussion in Sect. 1.5.5.

The experimentally obtained L–L line of the nanorod spaser shown in Fig. 1.27c is in an excellent agreement with this prediction. Note that this figure is presented in the double-logarithmic scale. There are two curves in this figure taken at different temperatures, which are similar though at a lower temperature the intensity out is higher and the threshold is lower. The parts of the curves at lower pumping intensities are also unit-slope straight lines corresponding to spontaneous fluorescence. With the increased intensity, the curves enter a transitional regime of amplified spontaneous

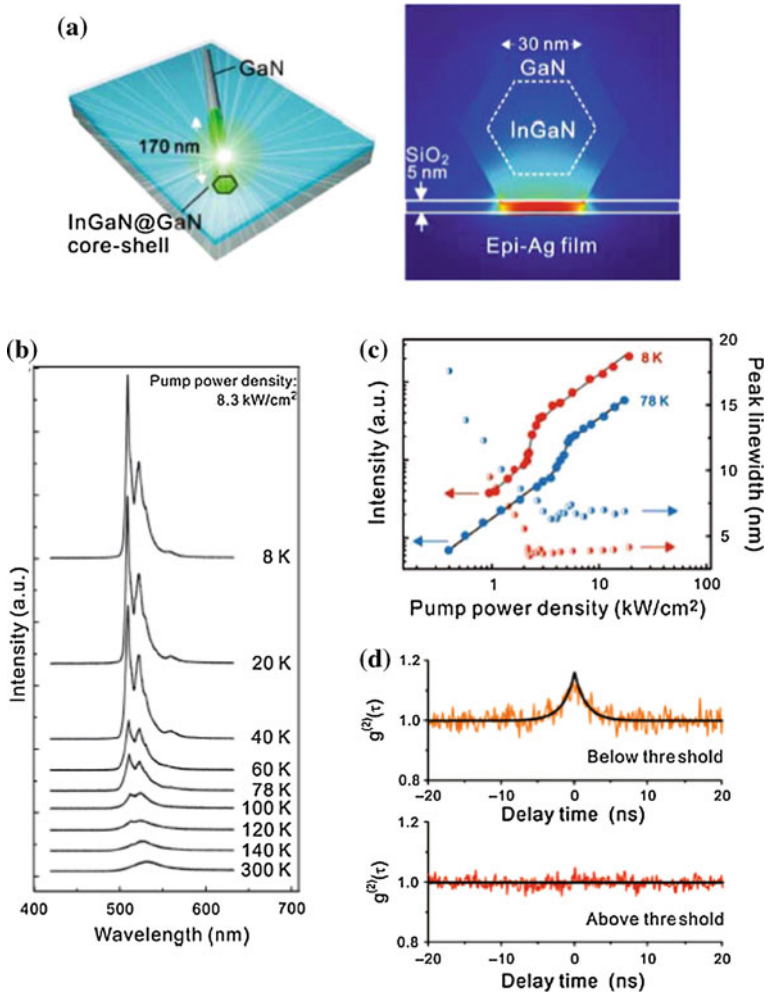

Fig. 1.27 InGaN nanospaser and its properties. **a** Schematics of geometry of InGaN/GaN core-shell nanospaser (*left*) and theoretical intensity of its spasing eigenmode. **b** Series of emission spectra: Temperature-dependent spasing behavior from 8 to 300 K. The spasing threshold at 140 K is clearly visible. **c** The L–L (light–light) plots at the main lasing peak (510 nm) are shown with the corresponding linewidth-narrowing behavior when the spaser is measured at 8 K (*red*) and 78 K (*blue*), with lasing thresholds of 2.1 and 3.7 kW/cm^2, respectively. **d** Second-order photon correlation function $g^{(2)}(\tau)$ measured at 8 K. The *upper curve* is recorded below the spasing threshold, and the lower above the threshold. Adapted from Ref. [283]

emission where the slopes are greater than one. The regime of developed spasing takes place at high intensities where the L–L curves become unit-slope straight lines without a saturation. As have already been mentioned above, this is a universal behavior.

This universal unsaturable behavior can be very simply understood qualitatively—cf. Ref. [285]. The excitation rate $\dot{N}_e$ of the upper spasing level is linearly proportional to pumping intensity I_p, $\dot{N}_e = \sigma_e I_p$, where σ_e is the total excitation cross section into the conduction band of the semiconductor gain medium. In the developed spasing regime, plasmon population N_n of the spasing eigenmode becomes large, asymptotically $N_n \to \infty$. Correspondingly, the stimulated decay rate, which is $\propto N_n$, becomes large and dominates over any spontaneous decay rate. Thus, all the excitation events to the conduction band end up with the emission of a SP into the spasing mode whose SP population becomes $N_n = \dot{N}_e/\gamma_n$, where γ_n is the SP decay rate—see above Eq. (1.48). Finally, radiation rate $\dot{N}_r$ for a spaser becomes

$$\dot{N}_r = \sigma_e \gamma^{(r)} \Big/ \gamma_n, \tag{1.62}$$

where $\gamma^{(r)}$ is the SP radiative decay rate, which for a plasmonic metal sphere is given by Eq. (1.16) and in, general case, by Eq. (1.56). Of course. in reality the straight-line, unsaturable L–L curves will end when the pumping intensities become so high that the nonlinearity in the spaser metal develops (including, but not limited to, thermal nonlinearity), or optical breakdown occurs, or heat production will physically damage the spaser.

As theory shows (see below Sect. 1.5.6.1 and Fig. 1.30a), under steady pumping, the generating spaser reaches its stationary regime within ~100 fs. Correspondingly, we expect that any fluctuation in the emission radiated by the generating spaser relaxes back to the mean level within the same time. A measure of the fluctuations of the spaser-radiation intensity $I(t)$ with time t is the second-order autocorrelation function

$$g^{(2)}(\tau) = \frac{\langle I(t+\tau) I(t) \rangle}{\langle I(t) \rangle^2}, \tag{1.63}$$

where τ is the delay time, and $\langle \cdots \rangle$ denotes quantum-mechanical (theory) or temporal (experiment) averaging.

Experimentally, $g^{(2)}(\tau)$ has been measured for a single spaser in Ref. [283]. The result is reproduced in Fig. 1.27d. The upper curve is recorded below the spasing threshold; at the zero delay, it shows a peak, which is characteristic of incoherent radiation. If such radiation is produced by many independent emitters, it has Gaussian statistics, and the peak value should be $g^{(2)}(0) = 2$—this effect was introduced by Hanbury Brown and Twiss and used by them for stellar interferometry [286]. For the upper curve of Fig. 1.27d, $g^{(2)}(0)$ is significantly less. This may be due to various reasons, in particular, insufficient temporal resolution of the photodetection or partial coherence between the individual emitters of the gain medium induced by their interaction via plasmonic fields.

In sharp contrast, above the spasing threshold, the autocorrelation function in Fig. 1.27d is a constant at all delays. As we have already pointed out this is due to the fact that after an emission of a photon, the number of plasmons in the spaser is restored within ~100 fs, while the temporal resolution of the photodetection in

Ref. [283] is $\Delta\tau \gtrsim 100\,\text{ps}$, i.e., three orders of magnitude coarser. The physical reason for $g^{(2)}(\tau) = \text{const}$ is that the spaser under steady-state pumping tends to keep a constant plasmon population. After the emission of a photon, this population is decreased by one. However, very rapidly, within $\sim$100 fs, it restores to the pre-emission level. This transitional restoration process is too fast and the photodetectors of Ref. [283] miss it, producing $g^{(2)}(\tau) = \text{const}$.

1.5.4 Equations of Spaser

1.5.4.1 Quantum Density Matrix Equations (Optical Bloch Equations) for Spaser

The SP eigenmodes $\varphi_n(\mathbf{r})$ are described by a wave equation (1.25) [31, 78]. The electric field operator of the quantized SPs is an operator [31]

$$\hat{\mathbf{E}}(\mathbf{r}) = -\sum_n A_n \nabla\varphi_n(\mathbf{r})(\hat{a}_n + \hat{a}_n^\dagger), \quad A_n = \left(\frac{4\pi\hbar s_n}{\varepsilon_d s_n'}\right)^{1/2}, \tag{1.64}$$

where $\hat{a}_n^\dagger$ and $\hat{a}_n$ are the SP creation and annihilation operators, $-\nabla\varphi_n(\mathbf{r}) = \mathbf{E}_n(\mathbf{r})$ is the modal field of an nth mode, and $s_n' = \text{Re}\,[ds(\omega_n)/d\omega_n]$. Note that we have corrected a misprint in Ref. [31] by replacing the coefficient 2π by 4π.

The spaser Hamiltonian has the form

$$\hat{H} = \hat{H}_g + \hbar\sum_n \omega_n \hat{a}_n^\dagger \hat{a}_n - \sum_p \hat{\mathbf{E}}(\mathbf{r}_p)\hat{\mathbf{d}}^{(p)}, \tag{1.65}$$

where $\hat{H}_g$ is the Hamiltonian of the gain medium, p is a number (label) of a gain medium chromophore, $\mathbf{r}_p$ is its coordinate vector, and $\hat{\mathbf{d}}^{(p)}$ is its dipole moment operator. In this theory, we treat the gain medium quantum mechanically but the SPs quasiclassically, considering $\hat{a}_n$ as a classical quantity (c-number) a_n with time dependence as $a_n = a_{0n}\exp(-i\omega t)$, where a_{0n} is a slowly-varying amplitude. The number of coherent SPs per spasing mode is then given by $N_p = |a_{0n}|^2$. This approximation neglects the quantum fluctuations of the SP amplitudes. However, when necessary, we will take into account these quantum fluctuations, in particular, to describe the spectrum of the spaser.

Introducing $\rho^{(p)}$ as the density matrix of a pth chromophore, we can find its equation of motion in a conventional way by commutating it with the Hamiltonian (1.65) as

$$i\hbar\dot{\rho}^{(p)} = [\rho^{(p)}, \hat{H}], \tag{1.66}$$

where the dot denotes temporal derivative. We use the standard rotating wave approximation (RWA), which only takes into account the resonant interaction between the

optical field and chromophores. We denote $|1\rangle$ and $|2\rangle$ as the ground and excited states of a chromophore, with the transition $|2\rangle \rightleftharpoons |1\rangle$ resonant to the spasing plasmon mode n. In this approximation, the time dependence of the nondiagonal elements of the density matrix is $\left(\rho^{(p)}\right)_{12} = \bar{\rho}_{12}^{(p)} \exp(i\omega t)$, and $\left(\rho^{(p)}\right)_{21} = \bar{\rho}_{12}^{(p)*} \exp(-i\omega t)$, where $\bar{\rho}_{12}^{(p)}$ is an amplitude slowly varying in time, which defines the coherence (polarization) for the $|2\rangle \rightleftharpoons |1\rangle$ spasing transition in a pth chromophore of the gain medium.

Introducing a rate constant Γ_{12} to describe the polarization relaxation and a difference $n_{21}^{(p)} = \rho_{22}^{(p)} - \rho_{11}^{(p)}$ as the population inversion for this spasing transition, we derive an equation of motion for the non-diagonal element of the density matrix as

$$\dot{\bar{\rho}}_{12}^{(p)} = -\left[i\left(\omega - \omega_{12}\right) + \Gamma_{12}\right] \bar{\rho}_{12}^{(p)} + i a_{0n} n_{21}^{(p)} \tilde{\Omega}_{12}^{(p)*}, \tag{1.67}$$

where

$$\tilde{\Omega}_{12}^{(p)} = -A_n \mathbf{d}_{12}^{(p)} \nabla \varphi_n(\mathbf{r}_p)/\hbar \tag{1.68}$$

is the one-plasmon Rabi frequency for the spasing transition in a pth chromophore, and $\mathbf{d}_{12}^{(p)}$ is the corresponding transitional dipole element. Note that always $\mathbf{d}_{12}^{(p)}$ is either real or can be made real by a proper choice of the quantum state phases, making the Rabi frequency $\tilde{\Omega}_{12}^{(p)}$ also a real quantity.

An equation of motion for n_{21}^{p} can be found in a standard way by commutating it with $\hat{H}$. To provide conditions for the population inversion ($n_{21}^{p} > 0$), we imply existence of a third level. For simplicity, we assume that it very rapidly decays into the excited state $|2\rangle$ of the chromophore, so its own populations is negligible. It is pumped by an external source from the ground state (optically or electrically) with some rate that we will denote g. In this way, we obtain the following equation of motion:

$$\dot{\bar{n}}_{21}^{(p)} = -4\mathrm{Im}\left[a_{0n} \bar{\rho}_{12}^{(p)} \tilde{\Omega}_{21}^{(p)}\right] - \gamma_2 \left(1 + n_{21}^{(p)}\right) + g\left(1 - n_{21}^{(p)}\right), \tag{1.69}$$

where γ_2 is the decay rate $|2\rangle \rightarrow |1\rangle$.

The stimulated emission of the SPs is described as their excitation by the coherent polarization of the gain medium. The corresponding equation of motion can be obtained using Hamiltonian (1.65) and adding the SP relaxation with a rate of γ_n as

$$\dot{a}_{0n} = \left[i\left(\omega - \omega_n\right) - \gamma_n\right] a_{0n} + i a_{0n} \sum_p \rho_{12}^{(p)*} \tilde{\Omega}_{12}^{(p)}. \tag{1.70}$$

As an important general remark, the system of Eqs. (1.67), (1.69), and (1.70) is highly nonlinear: each of these equations contains a quadratic nonlinearity: a product of the plasmon-field amplitude a_{0n} by the density matrix element ρ_{12} or population inversion n_{21}. Altogether, this is a six-order nonlinearity. This nonlinearity is a fundamental property of the spaser equations, which makes the spaser generation

always an essentially nonlinear process that involves a noneqilibrium phase transition and a spontaneous symmetry breaking: establishment of an arbitrary but sustained phase of the coherent SP oscillations.

A relevant process is spontaneous emission of SPs by a chromophore into a spasing SP mode. The corresponding rate $\gamma_2^{(p)}$ for a chromophore at a point $\mathbf{r}_p$ can be found in a standard way using the quantized field (1.64) as

$$\gamma_2^{(p)} = 2\frac{A_n^2}{\hbar\gamma_n}\left|\mathbf{d}_{12}\nabla\varphi_n(\mathbf{r}_p)\right|^2 \frac{(\Gamma_{12}+\gamma_n)^2}{(\omega_{12}-\omega_n)^2+(\Gamma_{12}+\gamma_n)^2}. \tag{1.71}$$

As in Schawlow-Towns theory of laser-line width [287], this spontaneous emission of SPs leads to the diffusion of the phase of the spasing state. This defines width γ_s of the spasing line as

$$\gamma_s = \frac{\sum_p \left(1+n_{21}^{(p)}\right)\gamma_2^{(p)}}{2(2N_p+1)}. \tag{1.72}$$

This width is small for a case of developed spasing when $N_p \gg 1$. However, for $N_p \sim 1$, the predicted width may be too high because the spectral diffusion theory assumes that $\gamma_s \lesssim \gamma_n$. To take into account this limitation in a simplified way, we will interpolate to find the resulting spectral width Γ_s of the spasing line as $\Gamma_s = \left(\gamma_n^{-2}+\gamma_s^{-2}\right)^{-1/2}$.

We will also examine the spaser as a bistable (logical) amplifier. One of the ways to set the spaser in such a mode is to add a saturable absorber. This is described by the same Eqs. (1.67)–(1.70) where the chromophores belonging to the absorber are not pumped by the external source directly, i.e., for them in Eq. (1.69) one has to set $g = 0$.

Numerical examples are given for a silver nanoshell where the core and the external dielectric have the same permittivity of $\varepsilon_d = 2$; the permittivity of silver is adopted from Ref. [32]. The following realistic parameters of the gain medium are used (unless indicated otherwise): $d_{12} = 1.5 \times 10^{-17}$ esu, $\hbar\Gamma_{12} = 10$ meV, $\gamma_2 = 4 \times 10^{12}\,\mathrm{s}^{-1}$ (this value takes into account the spontaneous decay into SPs), and density of the gain medium chromophores is $n_c = 2.4 \times 10^{20}\,\mathrm{cm}^{-3}$, which is realistic for dye molecules but may be somewhat high for semiconductor quantum dots that were proposed as the chromophores [31] and used in experiments [260]. We will assume a dipole SP mode and chromophores situated in the core of the nanoshell as shown in Fig. 1.26d. This configuration are of advantage both functionally (because the region of the high local fields outside the shell is accessible for various applications) and computationally (the uniformity of the modal fields makes the summation of the chromophores trivial, thus greatly facilitating numerical procedures).

1.5.4.2 Equations for CW Regime

Physically, the spaser action is a result of spontaneous symmetry breaking when the phase of the coherent SP field is established from the spontaneous noise. Mathematically, the spaser is described by homogeneous differential Eqs. (1.67)–(1.70). These equations become homogeneous algebraic equations for the CW case. They always have a trivial, zero solution. However, they may also possess a nontrivial solution describing spasing. An existence condition of such a nontrivial solution is

$$(\omega_s - \omega_n + i\gamma_n)^{-1} \times (\omega_s - \omega_{21} + i\Gamma_{12})^{-1} \sum_p \left|\tilde{\Omega}_{12}^{(p)}\right|^2 n_{21}^{(p)} = -1. \tag{1.73}$$

The population inversion of a pth chromophore $n_{21}^{(p)}$ is explicitly expressed as

$$n_{21}^{(p)} = (g - \gamma_2) \times \left\{ g + \gamma_2 + 4N_n \left|\tilde{\Omega}_{12}^{(p)}\right|^2 / \left[(\omega_s - \omega_{21})^2 + \Gamma_{12}^2\right] \right\}^{-1}. \tag{1.74}$$

From the imaginary part of Eq. (1.73) we immediately find the spasing frequency ω_s,

$$\omega_s = \left(\gamma_n \omega_{21} + \Gamma_{12}\omega_n\right) / \left(\gamma_n + \Gamma_{12}\right), \tag{1.75}$$

which generally does not coincide with either the gain transition frequency ω_{21} or the SP frequency ω_n, but is between them (this is a frequency walk-off phenomenon similar to that of laser physics). Substituting Eq. (1.75) back into (1.73)–(1.74), we obtain a system of equations

$$\frac{(\gamma_n + \Gamma_{12})^2}{\gamma_n \Gamma_{12}\left[(\omega_{21} - \omega_n)^2 + (\Gamma_{12} + \gamma_n)^2\right]} \times \sum_p \left|\tilde{\Omega}_{12}^{(p)}\right|^2 n_{21}^{(p)} = 1, \tag{1.76}$$

$$n_{21}^{(p)} = (g - \gamma_2) \times \left[g + \gamma_2 + \frac{4N_n \left|\tilde{\Omega}_{12}^{(p)}\right|^2 (\Gamma_{12} + \gamma_n)}{(\omega_{12} - \omega_n)^2 + (\Gamma_{12} + \gamma_n)^2} \right]^{-1}. \tag{1.77}$$

This system defines the stationary (CW-generation) number of SPs per spasing mode, N_n.

Since $n_{21}^{(p)} \leq 1$, from Eqs. (1.76), (1.77) we immediately obtain a necessary condition of the existence of spasing,

$$\frac{(\gamma_n + \Gamma_{12})^2}{\gamma_n \Gamma_{12}\left[(\omega_{21} - \omega_n)^2 + (\Gamma_{12} + \gamma_n)^2\right]} \sum_p \left|\tilde{\Omega}_{12}^{(p)}\right|^2 \geq 1. \tag{1.78}$$

This expression is fully consistent with Ref. [31]. The following order of magnitude estimate of this spasing condition has a transparent physical meaning and is of heuristic value,

$$\frac{d_{12}^2 Q N_c}{\hbar \Gamma_{12} V_n} \gtrsim 1, \tag{1.79}$$

where $Q = \omega/\gamma_n$ is the quality factor of SPs, V_n is the volume of the spasing SP mode, and N_c is the of number of the gain medium chromophores within this volume. Deriving this estimate, we have neglected the detuning, i.e., set $\omega_{21} - \omega_n = 0$. We also used the definitions of A_n of Eq. (1.64) and $\tilde{\Omega}_{12}^{(p)}$ given by Eq. (1.68), and the estimate $|\nabla\varphi_n(\mathbf{r})|^2 \sim 1/V$ following from the normalization of the SP eigenmodes $\int |\nabla\varphi_n(\mathbf{r})|^2 \, d^3r = 1$ of Ref. [78]. The result of Eq. (1.79) is, indeed, in agreement with Ref. [31] where it was obtained in different notations.

It follows from Eq. (1.79) that for the existence of spasing it is beneficial to have a high quality factor Q, a high density of the chromophores, and a large transition dipole (oscillator strength) of the chromophore transition. The small modal volume V_n (at a given number of the chromophores N_c) is beneficial for this spasing condition: physically, it implies strong feedback in the spaser. Note that for the given density of the chromophores $n_c = N_c/V_n$, this spasing condition does not explicitly depend on the spaser size, which opens up a possibility of spasers of a very small size limited from the bottom by only the nonlocality radius $l_{nl} \sim 1\,\text{nm}$. Another important property of Eq. (1.79) is that it implies the quantum-mechanical nature of spasing and spaser amplification: this condition essentially contains the Planck constant $\hbar$ and, thus, does not have a classical counterpart. Note that in contrast to lasers, the spaser theory and Eqs. (1.78), (1.79) in particular do not contain speed of light, i.e., they are quasistatic.

Now we will examine the spasing condition and reduce it to a requirement for the gain medium. First, we substitute all the definitions and assume the perfect resonance between the generating SP mode and the gain medium, i.e., $\omega_n = \omega_{21}$. As a result, we obtain from Eq. (1.78),

$$\frac{4\pi}{3} \frac{s_n |\mathbf{d}_{12}|^2}{\hbar \gamma_n \Gamma_{12} \varepsilon_d s_n'} \int_V [1 - \Theta(\mathbf{r})] \, |\mathbf{E}_n(\mathbf{r})|^2 \, d^3r \geq 1, \tag{1.80}$$

where the integral is extended over the volume V of the system, and the Θ-function takes into account a simplifying realistic assumption that the gain medium occupies the entire space free from the core's metal. We also assume that the orientations of the transition dipoles $\mathbf{d}_{12}^{(p)}$ are random and average over them, which results in the factor of 3 in the denominator in Eq. (1.80). From Eqs. (1.27) and (1.34), it follows that

$$\int_V [1 - \Theta(\mathbf{r})] \, |\mathbf{E}_n(\mathbf{r})|^2 \, d^3r = 1 - s_n. \tag{1.81}$$

Next, we give approximate expressions for the spectral parameter (1.4), which are very accurate for the realistic case of $Q \gg 1$,

$$\mathrm{Im}\, s(\omega) = \frac{s_n^2}{\varepsilon_d} \mathrm{Im}\, \varepsilon_m(\omega) = \frac{1}{Q} s_n (1 - s_n), \tag{1.82}$$

where definition (1.6) is used. Taking into account Eqs. (1.47), (1.48) and (1.81), (1.82), we obtain from Eq. (1.80) a necessary condition of spasing at a frequency ω as

$$\frac{4\pi}{3} \frac{|\mathbf{d}_{12}|^2 n_c [1 - \mathrm{Re}\, s(\omega)]}{\hbar \Gamma_{12} \mathrm{Re}\, s(\omega) \mathrm{Im}\, \varepsilon_m(\omega)} \geq 1, \tag{1.83}$$

For the sake of comparison, consider a continuous gain medium comprised of the same chromophores as the gain shell of the spaser. Its gain g (whose dimensionality is cm^{-1}) is given by a standard expression

$$g = \frac{4\pi}{3} \frac{\omega}{c} \frac{\sqrt{\varepsilon_d}\, |\mathbf{d}_{12}|^2 n_c}{\hbar \Gamma_{12}}. \tag{1.84}$$

Substituting it into Eq. (1.83), we obtain the spasing criterion in terms of the gain as

$$g \geq g_{th}, \quad g_{th} = \frac{\omega}{c\sqrt{\varepsilon_d}} \frac{\mathrm{Re}\, s(\omega)}{1 - \mathrm{Re}\, s(\omega)} \mathrm{Im}\, \varepsilon_m(\omega), \tag{1.85}$$

where g_{th} has a meaning of the threshold gain needed for spasing. Importantly, this gain depends only on the dielectric properties of the system and spasing frequency but not on the geometry of the system or the distribution of the local fields of the spasing mode (hot spots, etc.) explicitly. However note that the system's geometry (along with the permittivities) does define the spasing frequencies.

In Figs. 1.28a, b, correspondingly, we illustrate the analytical expression (1.85) for gold and silver embedded in a dielectric with $\varepsilon_d = 2$ (simulating a light glass) and $\varepsilon_d = 10$ (simulating a semiconductor), correspondingly. These are computed from Eq. (1.85) assuming that the metal core is embedded into the gain medium with the real part of the dielectric function equal to ε_d. As we see from Fig. 1.28, the spasing is possible for silver in the near-ir communication range and the adjacent red portion of the visible spectrum for a gain $g < 3000\,\mathrm{cm}^{-1}$ (regions below the red line in Fig. 1.28), which is realistically achievable with direct band-gap semiconductors (DBDSs).

1.5.5 Spaser in CW Mode

The "spasing curve" (a counterpart of the light–light curve, or L–L curve, for lasers), which is the dependence of the coherent SP population N_n on the excitation rate

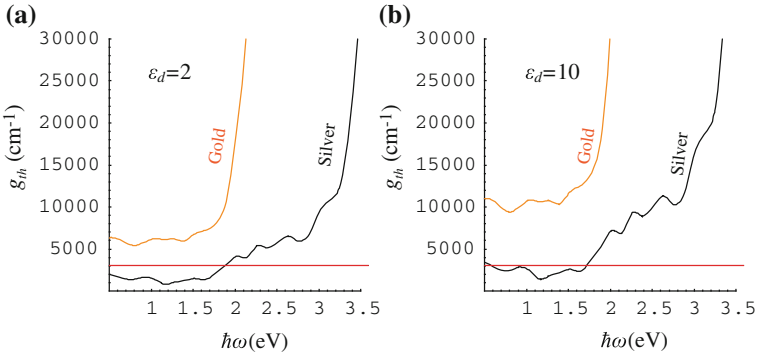

Fig. 1.28 Threshold gain for spasing g_{th} for silver and gold, as indicated in the graphs, as a function of the spasing frequency ω. The *red line* separates the area $g_{th} < 3 \times 10^3$ cm^{-1}, which can relatively easily be achieved with direct band-gap semiconductors (DBGSs). The real part of the gain medium permittivity is denoted in the corresponding panels as ε_d

g, obtained by solving Eqs. (1.76), (1.77), is shown in Fig. 1.29a for four types of the silver nanoshells with the frequencies of the spasing dipole modes as indicated, which are in the range from near-ir ($\hbar\omega_s = 1.2$ eV) to mid-visible ($\hbar\omega_s = 2.2$ eV). In all cases, there is a pronounced threshold of the spasing at an excitation rate $g_{th} \sim 10^{12}$ s^{-1}. Soon after the threshold, the dependence $N_n(g)$ becomes linear, which means that every quantum of excitation added to the active medium with a high probability is stimulated to be emitted as a SP, adding to the coherent SP population.

While this is similar to conventional lasers, there is a dramatic difference for the spaser. In lasers, a similar relative rate of the stimulated emission is achieved at a photon population of $\sim 10^{18}$–10^{20}, while in the spaser the SP population is $N_n \lesssim 100$. This is due to the much stronger feedback in spasers because of the much smaller modal volume V_n—see discussion of Eq. (1.79). The shape of the spasing curves of Fig. 1.29a (the well-pronounced threshold with the linear dependence almost immediately above the threshold) is in a qualitative agreement with the experiment [252].

The population inversion number n_{21} as a function of the excitation rate g is displayed in Fig. 1.29b for the same set of frequencies (and with the same color coding) as in panel (a). Before the spasing threshold, n_{21} increases with g to become positive with the onset of the population inversion just before the spasing threshold. For higher g, after the spasing threshold is exceeded, the inversion n_{21} becomes constant (the inversion clamping). The clamped levels of the inversion are very low, $n_{21} \sim 0.01$, which again is due to the very strong feedback in the spaser.

The spectral width Γ_s of the spaser generation is due to the phase diffusion of the quantum SP state caused by the noise of the spontaneous emission of the SPs into the spasing mode, as described by Eq. (1.72). This width is displayed in Fig. 1.29c as a function of the pumping rate g. At the threshold, Γ_s is that of the SP line γ_n but for stronger pumping, as the SPs accumulate in the spasing mode, it decreases

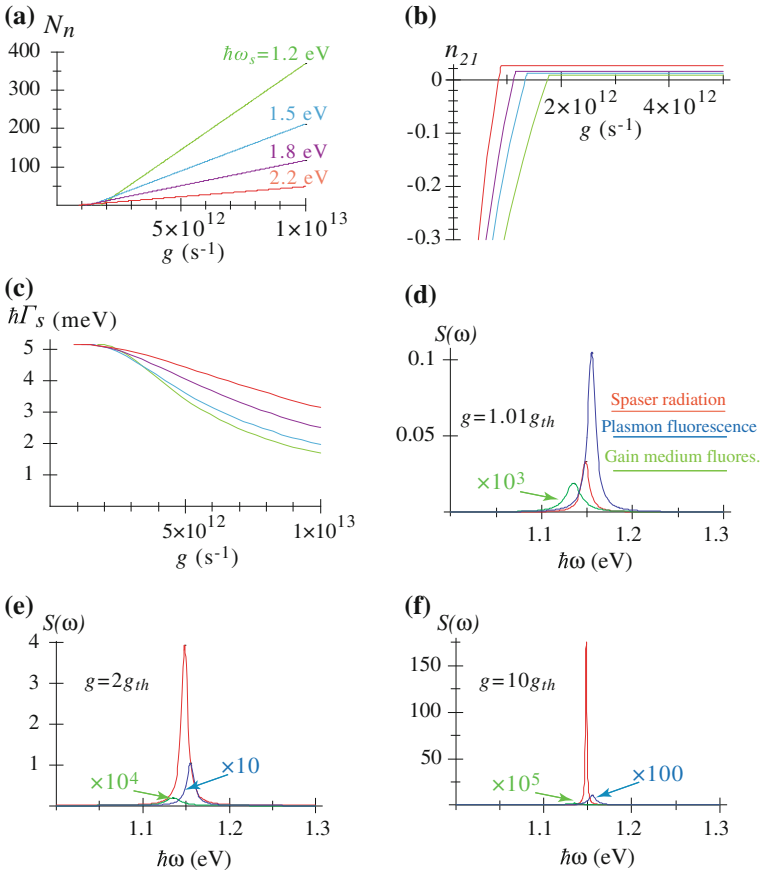

Fig. 1.29 Spaser SP population and spectral characteristics in the stationary state. The computations are done for a silver nanoshell with the external radius $R_2 = 12$ nm; the detuning of the gain medium from the spasing SP mode is $\hbar(\omega_{21} - \omega_n) = -0.02$ eV. The other parameters are indicated in Sect. 1.5.4. **a** Number N_n of plasmons per spasing mode as a function of the excitation rate g (per one chromophore of the gain medium). Computations are done for the dipole eigenmode with the spasing frequencies ω_s as indicated, which were chosen by the corresponding adjustment of the nanoshell aspect ratio. **b** Population inversion n_{12} as a function of the pumping rate g. The *color coding of the lines* is the same as in panel (**a**). **c** The spectral width Γ_s of the spasing line (expressed as $\hbar\Gamma_s$ in meV) as a function of the pumping rate g. The *color coding of the lines* is the same as in panel (**a**). **d–f** Spectra of the spaser for the pumping rates g expressed in the units of the threshold rate g_{th}, as indicated in the panels. The *curves* are color coded and scaled as indicated

$\propto N_n^{-1}$, as given by Eq. (1.72). This decrease of Γ_s reflects the higher coherence of the spasing state with the increased number of SP quanta and, correspondingly, lower quantum fluctuations. As we have already mentioned, this is similar to the lasers as described by the Schawlow-Townes theory [287].

The developed spasing in a dipole SP mode will show itself in the far field as an anomalously narrow and intense radiation line. The shape and intensity of this line in relation to the lines of the spontaneous fluorescence of the isolated gain medium and its SP-enhanced fluorescence line in the spaser is illustrated in Figs. 1.29d–f. Note that for the system under consideration, there is a 20 meV red shift of the gain medium fluorescence with respect to the SP line center. It is chosen so to illustrate the spectral walk-off of the spaser line. For one percent in the excitation rate above the threshold of the spasing (panel d), a broad spasing line (red color) appears comparable in intensity to the SP-enhanced spontaneous fluorescence line (blue color). The width of this spasing line is approximately the same as of the fluorescence, but its position is shifted appreciably (spectral walk-off) toward the isolated gain medium line (green color). For the pumping twice more intense (panel e), the spaser-line radiation dominates, but its width is still close to that of the SP line due to significant quantum fluctuations of the spasing state phase. Only when the pumping rate is an order of magnitude above the threshold, the spaser line strongly narrows (panel f), and it also completely dominates the spectrum of the radiation. This is a regime of small quantum fluctuations, which is desired in applications.

These results in the spasing region are different in the most dramatic way from previous phenomenological models, which are based on linear electrodynamics where the gain medium that has negative imaginary part of its permittivity plus lossy metal nanosystem, described purely electrodynamically [258, 265]. For instance, in a "toy model" [265], the width of the resonance line tends to zero at the threshold of spasing and then broadens up again. This distinction of the present theory is due the nature of the spasing as a spontaneous symmetry breaking (nonequilibrium phase transition with a randomly established but sustained phase) leading to the establishment of a coherent SP state. This non-equilibrium phase transition to spasing and the spasing itself are contained in the present theory due to the fact that the fundamental equations of the spasing (1.67), (1.69), and (1.70) are nonlinear, as we have already discussed above in conjunction with these equations—see the text after Eq. (1.70). The previous publications on gain compensation by loss [258, 265, 267] based on linear electrodynamic equations do not contain spasing. Therefore, they are not applicable in the region of the complete loss compensation and spasing, though their results are presented for that region.

1.5.6 Spaser as Ultrafast Quantum Nanoamplifier

1.5.6.1 Problem of Setting Spaser as an Amplifier

As we have already mentioned in Sect. 1.5.1, a fundamental and formidable problem is that, in contrast to the conventional lasers and amplifiers in quantum electronics, the spaser has an inherent feedback that typically cannot be removed. Such a spaser will develop generation and accumulation of the macroscopic number of coherent SPs in the spasing mode. This leads to the population inversion clamping in the CW

regime at a very low level—cf. Fig. 1.29b. This CW regime corresponds to the net amplification equal zero, which means that the gain exactly compensates the loss, which condition is expressed by Eq. (1.76). This is a consequence of the nonlinear gain saturation. This holds for any stable CW generator (including any spaser or laser) and precludes using them as amplifiers.

There are several ways to set a spaser as a quantum amplifier. One of them is to reduce the feedback, i.e., to allow some or most of the SP energy in the spaser to escape from the active region, so the spaser will not generate in the region of amplification. Such a root has successfully been employed to build a SPP plasmonic amplifier on the long-range plasmon polaritons [277]. A similar root for the SP spasers would be to allow some optical energy to escape either by a near-field coupling or by a radiative coupling to far-field radiation. The near-field coupling approach is promising for building integrated active circuits out of the spasers. Another root has been used in Ref. [288], which employed symmetric SPP modes in a thin gold strip. Such modes have much lower loss that the antisymmetric modes at the expense of much weaker confinement (transverse modal area $\sim\lambda^2$). The lower loss allows one to use the correspondingly lower gain and, therefore, avoid both spasing at localized SP modes and random lasing due to back-scattering from gold imperfections.

Following Ref. [139], we consider here two distinct approaches for setting the spasers as quantum nanoamplifiers. The first is a transient regime based on the fact that the establishment of the CW regime and the consequent inversion clamping and the total gain vanishing require some time that is determined mainly by the rate of the quantum feedback and depends also on the relaxation rates of the SPs and the gain medium. After the population inversion is created by the onset of pumping and before the spasing spontaneously develops, as we show below in this section, there is a time interval of approximately 250 fs, during which the spaser provides usable (and as predicted, quite high) amplification—see Sect. 1.5.6.2 below.

The second approach to set the spaser as a logical quantum nanoamplifier is a bistable regime that is achieved by introducing a saturable absorber into the active region, which prevents the spontaneous spasing. Then injection of a certain above-threshold amount of SP quanta will saturate the absorber and initiate the spasing. Such a bistable quantum amplifier will be considered in Sect. 1.5.6.3.

The temporal behavior of the spaser has been found by direct numerical solution of Eqs. (1.67)–(1.70). This solution is facilitated by the fact that in the model under consideration all the chromophores experience the same local field inside the nanoshell, and there are only two types of such chromophores: belonging to the gain medium and the saturable absorber, if it is present.

1.5.6.2 Monostable Spaser as a Nanoamplifier in Transient Regime

Here we consider a monostable spaser in a transient regime. This implies that no saturable absorber is present. We will consider two pumping regimes: stationary and pulse.

Starting with the stationary regime, we assume that the pumping at a rate (per one chromophore) of $g = 5 \times 10^{12}\,\mathrm{s}^{-1}$ starts at a moment of time $t = 0$ and stays constant after that. Immediately at $t = 0$, a certain number of SPs are injected into the spaser. We are interested in its temporal dynamics from this moment on.

The dynamical behavior of the spaser under this pumping regime is illustrated in Figs. 1.30a, b. As we see, the spaser, which starts from an arbitrary initial population N_n, rather rapidly, within a few hundred femtoseconds approaches the same stationary ("logical") level. At this level, an SP population of $N_n = 67$ is established, while the inversion is clamped at a low level of $n_{21} = 0.02$. On the way to this stationary state, the spaser experiences relaxation oscillations in both the SP numbers and inversion, which have a trend to oscillate out of phase (compare panels a and b). This temporal dynamics of the spaser is quite complicated and highly nonlinear (unharmonic). It is controlled not by a single relaxation time but by a set of the relaxation rates. Clearly, among these are the energy transfer rate from the gain medium to the SPs and the relaxation rates of the SPs and the chromophores.

In this mode, the main effect of the initial injection of the SPs (described theoretically as different initial values of N_n) is in the interval of time it is required for the spaser to reach the final (CW) state. For very small N_n, which in practice can be supplied by the noise of the spontaneous SP emission into the mode, this time is approximately 250 fs (cf.: the corresponding SP relaxation time is less then 50 fs). In contrast, for the initial values of $N_n = 1$–5, this time shortens to 150 fs.

Now consider the second regime: pulse pumping. The gain-medium population of the spaser is inverted at $t = 0$ to saturation with a short (much shorter than 100 fs) pump pulse. Simultaneously, at $t = 0$, some number of plasmons are injected (say, by an external nanoplasmonic circuitry). In response, the spaser should produce an amplified pulse of the SP excitation. Such a function of the spaser is illustrated in Figs. 1.30c, d.

As we see from panel (c), independently from the initial number of SPs, the spaser always generates a series of SP pulses, of which only the first pulse is large (at or above the logical level of $N_n \sim 100$). (An exception is a case of little practical importance when the initial $N_n = 120$ exceeds this logical level, when two large pulses are produced.) The underlying mechanism of such a response is the rapid depletion of the inversion seen in panel (d), where energy is dissipated in the metal of the spaser. The characteristic duration of the SP pulse ~100 fs is defined by this depletion, controlled by the energy transfer and SP relaxation rates. This time is much shorter than the spontaneous decay time of the gain medium. This acceleration is due to the stimulated emission of the SPs into the spasing mode (which can be called a "stimulated Purcell effect"). There is also a pronounced trend: the lower is initial SP population N_n, the later the spaser produces the amplified pulse. In a sense, this spaser functions as a pulse-amplitude to time-delay converter.

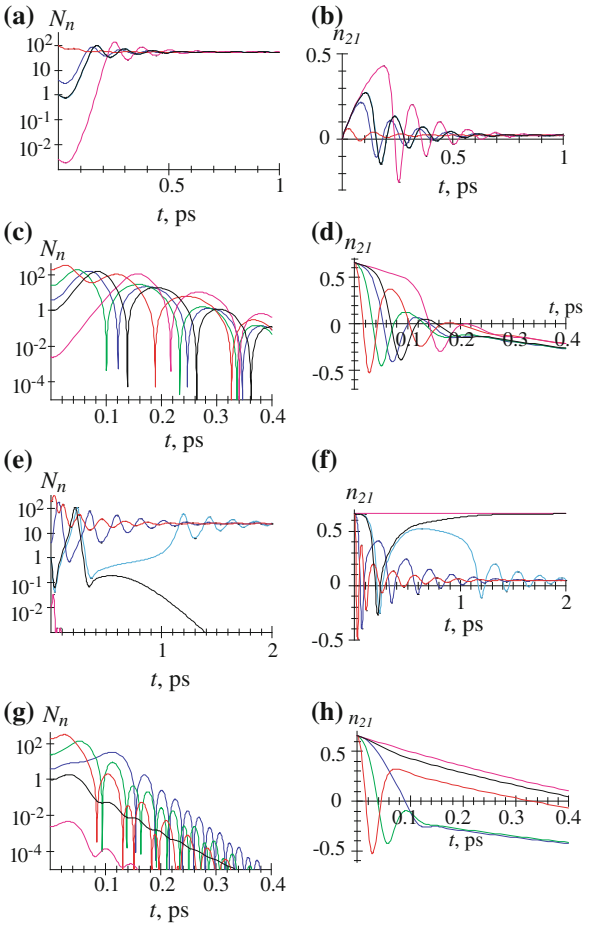

Fig. 1.30 Ultrafast dynamics of spaser. **a** For monostable spaser (without a saturable absorber), dependence of SP population in the spasing mode N_n on time t. The spaser is stationary pumped at a rate of $g = 5 \times 10^{12}\,\mathrm{s}^{-1}$. The *color-coded curves* correspond to the initial conditions with the different initial SP populations, as shown in the graphs. **b** The same as (**a**) but for the temporal behavior of the population inversion n_{21}. **c** Dynamics of a monostable spaser (no saturable absorber) with the pulse pumping described as the initial inversion $n_{21} = 0.65$. Coherent SP population N_n is displayed as a function of time t. Different initial populations are indicated by *color-coded curves*. **d** The same as (**c**) but for the corresponding population inversion n_{21}. **e** The same as (**a**) but for bistable spaser with the saturable absorber in concentration $n_a = 0.66 n_c$. **f** The same as (**b**) but for the bistable spaser. **g** The same as (**e**) but for the pulse pumping with the initial inversion $n_{21} = 0.65$. **h** The same as (**g**) but for the corresponding population inversion n_{21}

1.5.6.3 Bistable Spaser with Saturable Absorber as an Ultrafast Nanoamplifier

Now let us consider a bistable spaser as a quantum threshold (or, logical) nanoamplifier. Such a spaser contains a saturable absorber mixed with the gain medium with parameters indicated at the end of Sect. 1.5.4.1 and the concentration of the saturable absorber $n_a = 0.66n_c$. This case of a bistable spaser amplifier is of a particular interest because in this regime the spaser comes as close as possible in its functioning to the semiconductor-based (mostly, MOSFET-based) digital nanoamplifiers. As in the previous subsection, we will consider two cases: the stationary and short-pulse pumping.

We again start with the case of the stationary pumping at a rate of $g = 5\times10^{12}\ \mathrm{s}^{-1}$. We show in Figs. 1.30e, f the dynamics of such a spaser. For a small initial population $N_n = 5 \times 10^{-3}$ simulating the spontaneous noise, the spaser is rapidly (faster than in 50 fs) relaxing to the zero population (panel e), while its gain-medium population is equally rapidly approaching a high level (panel f) $n_{21} = 0.65$ that is defined by the competition of the pumping and the enhanced decay into the SP mode (the purple curves). This level is so high because the spasing SP mode population vanishes and the stimulated emission is absent. After reaching this stable state (which one can call, say, "logical zero"), the spaser stays in it indefinitely long despite the continuing pumping.

In contrast, for initial values N_n of the SP population large enough (for instance, for $N_n = 5$, as shown by the blue curves in Figs. 1.30e, f), the spaser tends to the "logical one" state where the stationary SP population reaches the value of $N_n \approx 60$. Due to the relaxation oscillations, it actually exceeds this level within a short time of $\lesssim$100 fs after the seeding with the initial SPs. As the SP population N_n reaches its stationary (CW) level, the gain medium inversion n_{21} is clamped down at a low level of a few percent, as typical for the CW regime of the spaser. This "logical one" state salso persists indefinitely, as long as the inversion is supported by the pumping.

There is a critical curve (separatrix) that divide the two stable dynamics types (leading to the logical levels of zero and one). For the present set of parameters this separatrix starts with the initial population of $N_n \approx 1$. For a value of the initial N_n slightly below 1, the SP population N_n experiences a slow (hundreds fs in time) relaxation oscillation but eventually relaxes to zero (Fig. 1.30e, black curve), while the corresponding chromophore population inversion n_{21} relaxes to the high value $n_{21} = 0.65$ (panel f, black curve). In contrast, for a value of N_n slightly higher than 1 (light blue curves in panels e and f), the dynamics is initially close to the separatrix but eventually the initial slow dynamics tends to the high SP population and low chromophore inversion through a series of the relaxation oscillations. The dynamics close to the separatrix is characterized by a wide range of oscillation times due to its highly nonlinear character. The initial dynamics is slowest (the "decision stage" of the bistable spaser that lasts $\gtrsim$1 ps). The "decision time" is diverging infinitesimally close to the separatrix, as is characteristic of any threshold (logical) amplifier.

The gain (amplification coefficient) of the spaser as a logical amplifier is the ratio of the high CW level to the threshold level of the SP population N_n. For this

specific spaser with the chosen set of parameters, this gain is ≈60, which is more than sufficient for the digital information processing. Thus this spaser can make a high-gain, ∼10 THz-bandwidth logical amplifier or dynamical memory cell with excellent prospects of applications.

The last but not the least regime to consider is that of the pulse pumping in the bistable spaser. In this case, the population inversion ($n_{21} = 0.65$) is created by a short pulse at $t = 0$ and simultaneously initial SP population N_n is created. Both are simulated as the initial conditions in Eqs. (1.67)–(1.70). The corresponding results are displayed in Figs. 1.30g, h.

When the initial SP population exceeds the critical one of $N_n = 1$ (the blue, green, and red curves), the spaser responds with generating a short (duration less than 100 fs) pulse of the SP population (and the corresponding local fields) within a time $\lesssim$100 fs (panel g). Simultaneously, the inversion is rapidly (within ∼100 fs) exhausted (panel h).

In contrast, when the initial SP population N_n is less than the critical one (i.e., $N_n < 1$ in this specific case), the spaser rapidly (within a time $\lesssim$100 fs) relaxes as $N_n \to 0$ through a series of realaxation oscillations—see the black and magenta curves in Fig. 1.30g. The corresponding inversion decays in this case almost exponentially with a characteristic time ∼1 ps determined by the enhanced energy transfer to the SP mode in the metal—see the corresponding curves in panel (h). Note that the SP population decays faster when the spaser is above the generation threshold due to the stimulated SP emission leading to the higher local fields and enhanced relaxation.

1.5.7 Compensation of Loss by Gain and Spasing

1.5.7.1 Introduction to Loss Compensation by Gain

A problem for many applications of plasmonics and metamaterials is posed by losses inherent in the interaction of light with metals. There are several ways to bypass, mitigate, or overcome the detrimental effects of these losses, which we briefly discuss below.

(i) The most common approach consists in employing effects where the losses are not fundamentally important such as surface plasmon polariton (SPP) propagation used in sensing [23], ultramicroscopy [16, 19], and solar energy conversion [26]. For realistic losses, there are other effects and applications that are not prohibitively suppressed by the losses and useful, in particular, sensing based on SP resonances and surface enhanced Raman scattering (SERS) [23, 178, 242, 289, 290].

(ii) Another promising idea is to use superconducting plasmonics to dramatically reduce losses [74, 291–293]. However, this is only applicable for frequencies below the superconducting gaps, i.e., in the terahertz region.

(iii) Yet another proposed direction is using highly doped semiconductors where the Ohmic losses can be significantly lower due to much lower free carrier concentrations [294]. However, a problem with this approach may lie in the fact that the usefulness of plasmonic modes depends not on the loss *per se* but on the quality factor Q, which for doped semiconductors may not be higher than for the plasmonic metals.

(iv) One of the alternative approaches to low-loss plasmonic metamaterials is based on our idea of the spaser: it is using a gain to compensate the dielectric (Ohmic) losses [295, 296]. In this case the gain medium is included into the metamaterials. It surrounds the metal plasmonic component in the same manner as in the spasers. The idea is that the gain will provide quantum amplification compensating the loss in the metamaterials quite analogously to the spasers.

We will consider theory of the loss compensation in the plasmonic metamaterials using gain [140, 141]. Below we show that the full compensation or overcompensation of the optical loss in a dense resonant gain metamaterial leads to an instability that is resolved by its spasing (i.e., by becoming a generating spaser). We further show analytically that the conditions of the complete loss compensation by gain and the threshold condition of spasing—see Eqs. (1.83) and (1.85)—are identical. Thus the full compensation (overcompensation) of the loss by gain in such a metamaterial will cause spasing. This spasing limits (clamps) the gain—see Sect. 1.5.5—and, consequently, inhibits the complete loss compensation (overcompensation) at any frequency.

1.5.7.2 Permittivity of Nanoplasmonic Metamaterial

We will consider, for certainty, an isotropic and uniform metamaterial that, by definition, in a range of frequencies ω can be described by the effective permittivity $\bar{\varepsilon}(\omega)$ and permeability $\bar{\mu}(\omega)$. We will concentrate below on the loss compensation for the optical electric responses; similar consideration with identical conclusions for the optical magnetic responses is straightforward. Our theory is applicable for the true three-dimensional (3d) metamaterials whose size is much greater than the wavelength λ (ideally, an infinite metamaterial).

Consider a small piece of such a metamaterial with sizes much greater that the unit cell but much smaller than λ. Such a piece is a metamaterial itself. Let us subject this metamaterial to a uniform electric field $\mathbf{E}(\omega) = -\nabla\phi(\mathbf{r}, \omega)$ oscillating with frequency ω. Note that $\mathbf{E}(\omega)$ is the amplitude of the macroscopic electric field inside the metamaterial. We will denote the local field at a point $\mathbf{r}$ inside this metamaterial as $\mathbf{e}(\mathbf{r}, \omega) = -\nabla\varphi(\mathbf{r}, \omega)$. We assume standard boundary conditions

$$\varphi(\mathbf{r}, \omega) = \phi(\mathbf{r}, \omega), \tag{1.86}$$

for $\mathbf{r}$ belonging to the surface S of the volume under consideration.

To present our results in a closed form, we first derive a homogenization formula used in Ref. [297] (see also references cited therein). By definition, the electric displacement in the volume V of the metamaterial is given by a formula

$$\mathbf{D}(\mathbf{r}, \omega) = \frac{1}{V} \int_V \varepsilon(\mathbf{r}, \omega)\mathbf{e}(\mathbf{r}, \omega) dV, \tag{1.87}$$

where $\varepsilon(\mathbf{r}, \omega)$ is a position-dependent permittivity. This can be identically expressed (by multiplying and dividing by the conjugate of the macroscopic field E^*) and, using the Gauss theorem, transformed to a surface integral as

$$\begin{aligned} D &= \frac{1}{V E^*(\omega)} \int_V \mathbf{E}^*(\omega)\varepsilon(\mathbf{r}, \omega)\mathbf{e}(\mathbf{r}, \omega) dV \\ &= \frac{1}{V E^*(\omega)} \int_S \phi^*(\mathbf{r}, \omega)\varepsilon(\mathbf{r}, \omega)\mathbf{e}(\mathbf{r}, \omega) d\mathbf{S}, \end{aligned} \tag{1.88}$$

where we took into account the Maxwell continuity equation $\nabla [\varepsilon(\mathbf{r}, \omega)\mathbf{e}(\mathbf{r}, \omega)] = 0$. Now, using the boundary conditions of Eq. (1.86), we can transform it back to the volume integral as

$$\begin{aligned} D &= \frac{1}{V E^*(\omega)} \int_S \varphi^*(\mathbf{r})\varepsilon(\mathbf{r}, \omega)\mathbf{e}(\mathbf{r}, \omega) d\mathbf{S} \\ &= \frac{1}{V E^*(\omega)} \int_V \varepsilon(\mathbf{r}, \omega) \left|\mathbf{e}(\mathbf{r}, \omega)\right|^2 dV. \end{aligned} \tag{1.89}$$

From the last equality, we obtain the required homogenization formula as an expression for the effective permittivity of the metamaterial:

$$\bar{\varepsilon}(\omega) = \frac{1}{V \left|E(\omega)\right|^2} \int_V \varepsilon(\mathbf{r}, \omega) \left|\mathbf{e}(\mathbf{r}, \omega)\right|^2 dV. \tag{1.90}$$

1.5.7.3 Plasmonic Eigenmodes and Effective Resonant Permittivity of Metamaterials

This piece of the metamaterial with the total size $R \ll \lambda$ can be treated in the quasistatic approximation. The local field inside the nanostructured volume V of the metamaterial is given by the eigenmode expansion [78, 148, 218]

$$\mathbf{e}(\mathbf{r}, \omega) = \mathbf{E}(\omega) - \sum_n \frac{a_n}{s(\omega) - s_n} \mathbf{E}_n(\mathbf{r}), \tag{1.91}$$

$$a_n = \mathbf{E}(\omega) \int_V \theta(\mathbf{r})\mathbf{E}_n(\mathbf{r}) dV,$$

where we remind that $\mathbf{E}(\omega)$ is the macroscopic field. In the resonance, $\omega = \omega_n$, only one term at the pole of in Eq. (1.91) dominates, and it becomes

$$\mathbf{e}(\mathbf{r}, \omega) = \mathbf{E}(\omega) + i \frac{a_n}{\operatorname{Im} s(\omega_n)} \mathbf{E}_n(\mathbf{r}). \tag{1.92}$$

The first term in this equation corresponds to the mean (macroscopic) field and the second one describes the deviations of the local field from the mean field containing contributions of the hot spots [158]. The mean root square ratio of the second term (local field) to the first (mean field) is estimated as

$$\sim \frac{f}{\operatorname{Im} s(\omega_n)} = \frac{f Q}{s_n(1 - s_n)}, \tag{1.93}$$

where we took into account that, in accord with Eq. (1.34), $E_n \sim V^{-1/2}$, and

$$f = \frac{1}{V} \int_V \theta(\mathrm{r}) dV, \tag{1.94}$$

where f is the metal fill factor of the system, and Q is the plasmonic quality factor. Deriving expression (1.93), we have also taken into account an equality $\operatorname{Im} s(\omega_n) = s_n(1 - s_n)/Q$, which is valid in the assumed limit of the high quality factor, $Q \gg 1$ (see the next paragraph).

For a good plasmonic metal $Q \gg 1$—see Fig. 1.2. For most metal-containing metamaterials, the metal fill factor is not small, typically $f \gtrsim 0.5$. Thus, keeping Eq. (1.28) in mind, it is very realistic to assume the following condition

$$\frac{f Q}{s_n(1 - s_n)} \gg 1. \tag{1.95}$$

If so, the second (local) term of the field (1.92) dominates and, with a good precision, the local field is approximately the eigenmode's field:

$$\mathbf{e}(\mathbf{r}, \omega) = i \frac{a_n}{\operatorname{Im} s(\omega_n)} \mathbf{E}_n(\mathbf{r}). \tag{1.96}$$

Substituting this into Eq. (1.90), we obtain a homogenization formula

$$\bar{\varepsilon}(\omega) = b_n \int_V \varepsilon(\mathbf{r}, \omega) \left[\mathbf{E}_n(\mathbf{r})\right]^2 dV, \tag{1.97}$$

where $b_n > 0$ is a real positive coefficient whose specific value is

$$b_n = \frac{1}{3V} \left(\frac{Q \int_V \theta(\mathbf{r}) \mathbf{E}_n(\mathbf{r}) dV}{s_n (1 - s_n)} \right)^2 \tag{1.98}$$

Using Eqs. (1.97) and (1.27), (1.34), it is straightforward to show that the effective permittivity (1.97) simplifies exactly to

$$\bar{\varepsilon}(\omega) = b_n \left[s_n \varepsilon_m(\omega) + (1 - s_n)\varepsilon_h(\omega) \right]. \tag{1.99}$$

1.5.8 Conditions of Loss Compensation by Gain and Spasing

In the case of the full inversion (maximum gain) and in the exact resonance, the host medium permittivity acquires the imaginary part describing the stimulated emission as given by the standard expression

$$\varepsilon_h(\omega) = \varepsilon_d - i \frac{4\pi}{3} \frac{|\mathbf{d}_{12}|^2 n_c}{\hbar \Gamma_{12}}, \tag{1.100}$$

where $\varepsilon_d = \mathrm{Re}\, \varepsilon_h$, $\mathbf{d}_{12}$ is a dipole matrix element of the gain transition in a chromophore center of the gain medium, Γ_{12} is a spectral width of this transition, and n_c is the concentration of these centers (these notations are consistent with those used above in Sects. 1.5.4.1–1.5.6.3). Note that if the inversion is not maximum, then this and subsequent equations are still applicable if one sets as the chromophore concentration n_c the inversion density: $n_c = n_2 - n_1$, where n_2 and n_1 are the concentrations of the chromophore centers of the gain medium in the upper and lower states of the gain transition, respectively.

The condition for the full electric loss compensation in the metamaterial and amplification (overcompensation) at the resonant frequency $\omega = \omega_n$ is

$$\mathrm{Im}\, \bar{\varepsilon}(\omega) \leq 0 \tag{1.101}$$

Taking Eq. (1.99) into account, this reduces to

$$s_n \mathrm{Im}\, \varepsilon_m(\omega) - \frac{4\pi}{3} \frac{|\mathbf{d}_{12}|^2 n_c (1 - s_n)}{\hbar \Gamma_{12}} \leq 0. \tag{1.102}$$

Finally, taking into account Eqs. (1.28), (1.47) and that $\mathrm{Im}\, \varepsilon_m(\omega) > 0$, we obtain from Eq. (1.102) the condition of the loss (over)compensation as

$$\frac{4\pi}{3} \frac{|\mathbf{d}_{12}|^2 n_c \left[1 - \mathrm{Re}\, s(\omega) \right]}{\hbar \Gamma_{12} \mathrm{Re}\, s(\omega) \mathrm{Im}\, \varepsilon_m(\omega)} \geq 1, \tag{1.103}$$

where the strict inequality corresponds to the overcompensation and net amplification. In Eq. (1.100) we have assumed non-polarized gain transitions. If these transitions are all polarized along the excitation electric field, the concentration n_c should be multiplied by a factor of 3.

Equation (1.103) is a fundamental condition, which is precise [assuming that the requirement (1.95) is satisfied, which is very realistic for metamaterials] and general. Moreover, it is fully analytical and, actually, very simple. Remarkably, it depends only on the material characteristics and does not contain any geometric properties of the metamaterial system or the local fields. (Note that the system's geometry does affect the eigenmode frequencies and thus enters the problem implicitly.) In particular, the hot spots, which are prominent in the local fields of nanostructures [78, 158], are completely averaged out due to the integrations in Eqs. (1.90) and (1.97).

The condition (1.103) is completely non-relativistic (quasistatic)—it does not contain speed of light c, which is characteristic of also of the spaser. It is useful to express this condition also in terms of the total stimulated emission cross section $\sigma_e(\omega)$ (where ω is the central resonance frequency) of a chromophore of the gain medium as

$$\frac{c\sigma_e(\omega)\sqrt{\varepsilon_d}n_c\,[1-\mathrm{Re}\,s(\omega)]}{\omega \mathrm{Re}\,s(\omega)\mathrm{Im}\,\varepsilon_m(\omega)} \geq 1. \tag{1.104}$$

We see that Eq. (1.103) *exactly* coincides with a spasing condition expressed by Eq. (1.83). This brings us to an important conclusion: the full compensation (overcompensation) of the optical losses in a metamaterial [which is resonant and dense enough to satisfy condition (1.95)] and the spasing occur under precisely the same conditions.

We have considered above in Sect. 1.5.4.2 the conditions of spasing, which are equivalent to (1.104). These are given by one of equivalent conditions of Eqs. (1.83), (1.85), (1.103). It is also illustrated in Fig. 1.28. We stress that exactly the same conditions are for the full loss compensation (overcompensation) of a dense resonant plasmonic metamaterial with gain.

We would like also to point out that the criterion given by the equivalent conditions of Eqs. (1.83), (1.85), (1.103), or (1.104) is derived for localized SPs, which are describable in the quasistatic approximation, and is not directly applicable to the propagating plasmonic modes (SPPs). However, we expect that very localized SPPs, whose wave vector $k \lesssim l_s$, can be described by these conditions because they are, basically, quasistatic. For instance, the SPPs on a thin metal wire of a radius $R \lesssim l_s$ are described by a dispersion relation [12]

$$k \approx \frac{1}{R}\left[-\frac{\varepsilon_m}{2\varepsilon_d}\left(\ln\sqrt{-\frac{4\varepsilon_m}{\varepsilon_d}}-\gamma\right)\right]^{-1/2}, \tag{1.105}$$

where $\gamma \approx 0.57721$ is the Euler constant. This relation is obviously quasistatic because it does not contain speed of light c.

1.5.8.1 Discussion of Spasing and Loss Compensation by Gain

This fact of the equivalence of the full loss compensation and spasing is intimately related to the general criteria of the thermodynamic stability with respect to small fluctuations of electric and magnetic fields—see Chap. IX of Ref. [30],

$$\mathrm{Im}\,\bar{\varepsilon}(\omega) > 0, \quad \mathrm{Im}\,\bar{\mu}(\omega) > 0, \tag{1.106}$$

which must be *strict* inequalities for all frequencies for electromagnetically stable systems. For systems in thermodynamic equilibrium, these conditions are automatically satisfied.

However, for the systems with gain, the conditions (1.106) can be violated, which means that such systems can be electromagnetically unstable. The first of conditions (1.106) is opposite to Eqs. (1.101) and (1.103). This has a transparent meaning: the electrical instability of the system is resolved by its spasing.

The significance of these stability conditions for gain systems can be elucidated by the following *gedanken* experiment. Take a small isolated piece of such a metamaterial (which is a metamaterial itself). Consider that it is excited at an optical frequency ω either by a weak external optical field $\mathbf{E}$ or acquires such a field due to fluctuations (thermal or quantum). The energy density $\mathscr{E}$ of such a system is given by the Brillouin formula [30]

$$\mathscr{E} = \frac{1}{16\pi}\frac{\partial \omega \mathrm{Re}\,\bar{\varepsilon}}{\partial \omega}|\mathbf{E}|^2 . \tag{1.107}$$

Note that for the energy of the system to be definite, it is necessary to assume that the loss is not too large, $|\mathrm{Re}\,\bar{\varepsilon}| \gg \mathrm{Im}\,\bar{\varepsilon}$. This condition is realistic for many metamaterials, including all potentially useful ones.

The internal optical energy-density loss per unit time Q (i.e., the rate of the heat-density production in the system) is [30]

$$Q = \frac{\omega}{8\pi}\mathrm{Im}\,\bar{\varepsilon}\,|\mathbf{E}|^2 . \tag{1.108}$$

Assume that the internal (Ohmic) loss dominates over other loss mechanisms such as the radiative loss, which is also a realistic assumption since the Ohmic loss is very large for the experimentally studied systems and the system itself is very small (the radiative loss rate is proportional to the volume of the system). In such a case of the dominating Ohmic losses, we have $d\mathscr{E}/dt = Q$. Then Eqs. (1.107) and (1.108) can be resolved together yielding the energy $\mathscr{E}$ and electric field $|\mathbf{E}|$ of this system to evolve with time t exponentially as

$$|\mathbf{E}| \propto \sqrt{\mathscr{E}} \propto e^{-\Gamma t}, \quad \Gamma = \omega \mathrm{Im}\,\bar{\varepsilon} \Big/ \frac{\partial(\omega \mathrm{Re}\,\bar{\varepsilon})}{\partial \omega}. \tag{1.109}$$

We are interested in a resonant case when the metamaterial possesses a resonance at some eigenfrequency $\omega_n \approx \omega$. For this to be true, the system's behavior must be plasmonic, i.e., $\mathrm{Re}\,\bar{\varepsilon}(\omega) < 0$. Then the dominating contribution to $\bar{\varepsilon}$ comes from a resonant SP eigenmode n with a frequency $\omega_n \approx \omega$. In such a case, the dielectric function [78] $\bar{\varepsilon}(\omega)$ has a simple pole at $\omega = \omega_n$. As a result, $\partial\left(\omega \mathrm{Re}\,\bar{\varepsilon}\right)/\partial\omega \approx \omega\partial \mathrm{Re}\,\bar{\varepsilon}/\partial\omega$ and, consequently, $\Gamma = \gamma_n$, where γ_n is the SP decay rate given by Eqs. (1.3) or (1.48), and the metal dielectric function ε_m is replaced by the effective permittivity $\bar{\varepsilon}$ of the metamaterial. Thus, Eq. (1.109) is fully consistent with the spectral theory of SPs—see Sect. 1.3.4.

If the losses are not very large so that energy of the system is meaningful, the Kramers-Kronig causality requires [30] that $\partial(\omega \mathrm{Re}\,\bar{\varepsilon})/\partial\omega > 0$. Thus, $\mathrm{Im}\,\bar{\varepsilon} < 0$ in Eq. (1.109) would lead to a negative decrement,

$$\Gamma < 0, \tag{1.110}$$

implying that the initial small fluctuation starts exponentially grow in time in its field and energy, which is an instability. Such an instability is indeed not impossible: it will result in spasing that will eventually stabilize $|\mathbf{E}|$ and $\mathscr{E}$ at finite stationary (CW) levels of the spaser generation.

Note that the spasing limits (clamps) the gain and population inversion making *the net gain to be precisely zero* [139] in the stationary (continuous wave or CW) regime see Sect. 1.5.6 and Fig. 1.29b. Above the threshold of the spasing, the population inversion of the gain medium is clamped at a rather low level $n_{21} \sim 1\,\%$. The corresponding net amplification in the CW spasing regime is exactly zero, which is a condition for the CW regime. This makes the complete loss compensation and its overcompensation impossible in a dense resonant metamaterial where the feedback is created by the internal inhomogeneities (including its periodic structure) and the facets of the system.

Because the loss (over) compensation condition (1.103), which is also the spasing condition, is geometry-independent, it is useful to illustrate it for commonly used plasmonic metals, gold and silver whose permittivity we adopt from Ref. [32]. For the gain medium chromophores, we will use a reasonable set of parameters: $\Gamma_{12} = 5 \times 10^{13}\,\mathrm{s}^{-1}$ and $d_{12} = 4.3 \times 10^{-18}$ esu. The results of computations are shown in Fig. 1.31. (Note that this figure expresses a condition of spasing equivalent to that of Fig. 1.28). For silver as a metal and $n_c = 6 \times 10^{18}\,\mathrm{cm}^{-3}$, the corresponding lower (black) curve in panel (a) does not reach the value of 1, implying that no full loss compensation is achieved. In contrast, for a higher but still very realistic concentration of $n_c = 2.9 \times 10^{19}\,\mathrm{cm}^{-3}$, the upper curve in Fig. 1.31a does cross the threshold line in the near-infrared region. Above the threshold area, there will be the instability and the onset of the spasing. As Fig. 1.31b demonstrates, for gold the spasing occurs at higher, but still realistic, chromophore concentrations.

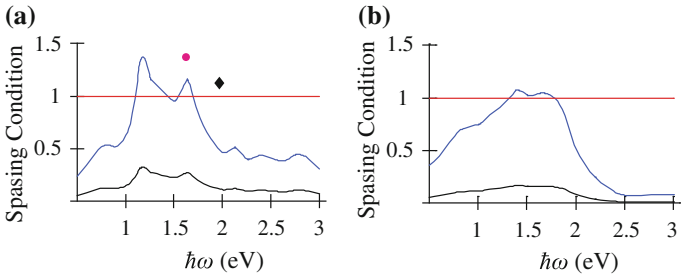

Fig. 1.31 Spasing criterion as a function of optical frequency ω. The *straight line* (*red on line*) represents the threshold for the spasing and full loss compensation, which take place for the curve segments above it. **a** Computations for silver. The chromophore concentration is $n_c = 6\times 10^{18}\,\mathrm{cm}^{-3}$ for the lower curve (*black*) and $n_c = 2.9\times 10^{19}\,\mathrm{cm}^{-3}$ for the *upper curve* (*blue on line*). The *black diamond* shows the value of the spasing criterion for the conditions of Ref. [262]—see the text. **b** Computations for gold. The chromophore concentration is $n_c = 3\times 10^{19}\,\mathrm{cm}^{-3}$ for the *lower curve* (*black*) and $n_c = 2\times 10^{20}\,\mathrm{cm}^{-3}$ for the *upper curve* (*blue on line*)

1.5.8.2 Discussion of Published Research on Spasing and Loss Compensations

Now let us discuss the implications of these results for the research published recently on the gain metamaterials. To carry out a quantitative comparison with Ref. [267], we turn to Fig. 1.31a where the lower (black) curve corresponds to the nominal value of $n_c = 6\times 10^{18}\,\mathrm{cm}^{-3}$ used in Ref. [267]. There is no full loss compensation and spasing. This is explained by the fact that Ref. [267] uses, as a close inspection shows, the gain dipoles parallel to the field (this is equivalent to increasing n_c by a factor of 3) and the local field enhancement [this is equivalent to increasing n_c by a factor of $(\varepsilon_h + 2)/3$. Because the absorption cross section of dyes is measured in the appropriate host media (liquid solvents or polymers), it already includes the Lorentz local-field factor. To compare to the results of Ref. [267], we increase in our formulas the concentration n_c of the chromophores by a factor of $\varepsilon_h + 2$ to $n_c = 2.9\times 10^{19}\,\mathrm{cm}^{-3}$, which corresponds to the upper curve in Fig. 1.31a. This curve rises above the threshold line exactly in the same (infra)red region as in Ref. [267].

This agreement of the threshold frequencies between our analytical theory and numerical theory [267] is not accidental: inside the region of stability (i.e., in the absence of spasing) both theories should and do give close results, provided that the gain-medium transition alignment is taken into account, and the local field-factor is incorporated. However, above the threshold (in the region of the overcompensation), there should be spasing causing the population inversion clamping and zero net gain, and not a loss compensation.

The complete loss compensation is stated in a recent experimental paper [298], where the system is actually a nanofilm rather than a 3d metamaterial, to which our theory would have been applicable. For the Rhodamine 800 dye used with extinction cross section [299] $\sigma = 2\times 10^{-16}\,\mathrm{cm}^2$ at 690 nm in concentration $n_c = 1.2\times 10^{19}\,\mathrm{cm}^{-3}$, realistically assuming $\varepsilon_d = 2.3$, for frequency $\hbar\omega = 1.7\,\mathrm{eV}$,

we calculate from Eq. (1.104) a point shown by the magenta solid circle in Fig. 1.31a, which is significantly above the threshold. Because in such a nanostructure the local fields are very non-uniform and confined near the metal similar to the spaser, they likewise cause a feedback. The condition of Eq. (1.95) is likely to be well-satisfied for Ref. [298]. Thus, the system may spase, which would cause the clamping of inversion and loss of gain.

In contrast to these theoretical arguments, there is no evidence of spasing indicated in the experiment [298], which can be explained by various factors. Among them, the system of Ref. [298] is a gain-plasmonic nanofilm and not a true 3d material. This system is not isotropic. Also, the size of the unit cell $a \approx 280$ nm is significantly greater than the reduced wavelength $\lambda\!\!\!^{-}$, which violates the quasistatic conditions and makes the possibility of homogenization and considering this system as an optical metamaterial problematic. This circumstance may lead to an appreciable spatial dispersion. It may also cause a significant radiative loss and prevent spasing for some modes.

We would also like to point out that the fact that the unit cell of the negative-refracting (or, double-negative) metamaterial of Ref. [298] is relatively large, $a \approx 280$ nm, is not accidental. As follows from theoretical consideration of Ref. [300], optical magnetism and, consequently, negative refraction for metals is only possible if the minimum scale of the conductor feature (the diameter d of the nanowire) is greater then the skin depth, $d \gtrsim l_s \approx 25$ nm, which allows one to circumvent Landau-Lifshitz's limitation on the existence of optical magnetism [30, 300]. Thus, a ring-type resonator structure would have a size $\gtrsim 2l_s$ (two wires forming a loop) and still the same diameter for the hole in the center, which comes to the total of $\gtrsim 4l_s \approx 100$ nm. Leaving the same distance between the neighboring resonator wires, we arrive at an estimate of the size of the unit cell $a \gtrsim 8l_s = 200$ nm, which is, indeed, the case for Ref. [298] and other negative-refraction "metamaterials" in the optical region. This makes our theory not directly applicable to them. Nevertheless, if the spasing condition (1.83) [or (1.85), or (1.104)] is satisfied, the system still may spase on the hot-spot defect modes.

In an experimental study of the lasing spaser [260], a nanofilm of PbS quantum dots (QDs) was positioned over a two-dimensional metamaterial consisting of an array of negative split ring resonators. When the QDs were optically pumped, the system exhibited an increase of the transmitted light intensity on the background of a strong luminescence of the QDs but apparently did not reach the lasing threshold. The polarization-dependent loss compensation was only $\sim$1 %. Similarly, for an array of split ring resonators over a resonant quantum well, where the inverted electron-hole population was excited optically [301], the loss compensation did not exceed $\sim$8 %. The relatively low loss compensation in these papers may be due either to random spasing and/or spontaneous or amplified spontaneous emission enhanced by this plasmonic array, which reduces the population inversion.

A dramatic example of possible random spasing is presented in Ref. [262]. The system studied was a Kretschmann-geometry SPP setup [302] with an added $\sim$1 μm polymer film containing Rodamine 6G dye in the $n_c = 1.2 \times 10^{19}$ cm^{-3} concentration. When the dye was pumped, there was outcoupling of radiation in a range

of angles. This was a threshold phenomenon with the threshold increasing with the Kretschmann angle. At the maximum of the pumping intensity, the widest range of the outcoupling angles was observed, and the frequency spectrum at every angle narrowed to a peak near a single frequency $\hbar\omega \approx 2.1\,\mathrm{eV}$.

These observations of Ref. [262] can be explained by the spasing where the feedback is provided by roughness of the metal. At the high pumping, the localized SPs (hots spots), which possess the highest threshold, start to spase in a narrow frequency range around the maximum of the spasing criterion—the left-hand side of Eq. (1.103). Because of the sub-wavelength size of these hot spots, the Kretschmann phase-matching condition is relaxed, and the radiation is outcoupled into a wide range of angles.

The SPPs of Ref. [262] excited by the Kretschmann coupling are short-range SPPs, very close to the antisymmetric SPPs. They are localized at subwavelength distances from the surface, and their wave length in the plane is much shorter the ω/c. Thus they can be well described by the quasistatic approximation and the present theory is applicable to them. Substituting the above-given parameters of the dye and the extinction cross section $\sigma_e = 4\times10^{-16}\,\mathrm{cm}^2$ into Eq. (1.104), we obtain a point shown by the black diamond in Fig. 1.31, which is clearly above the threshold, supporting our assertion of the spasing. Likewise, the amplified spontaneous emission and, possibly spasing, appear to have prevented the full loss compensation in a SPP system of Ref. [274]. Note that recently, random spasing for rough surfaces surrounded by dye gain media was shown experimentally in two independent observations [281, 303].

Note that the long-range SPPs of Ref. [277] are localized significantly weaker (at distances $\sim\lambda$) than those excited in Kretschmann geometry. Thus the long-range SPPs experience a much weaker feedback, and the amplification instead of the spasing can be achieved. Generally, the long-range SPPs are fully electromagnetic (non-quasistatic) and are not describable in the present theory. Similarly, relatively weakly confined, full electromagnetic are symmetric SPP modes on thin gold strips in Ref. [288] where the amplification has been demonstrated.

As we have already discussed in conjunction with Fig. 1.28, the spasing is readily achievable with the gain medium containing common DBGSs or dyes. There have been numerous experimental observations of the spaser. Among them is a report of a SP spaser with a 7-nm gold nanosphere as its core and a laser dye in the gain medium [252], observations of the SPP spasers (also known as nanolasers) with silver as a plasmonic-core metal and DBGS as the gain medium with a 1d confinement [253, 256], a tight 2d confinement [254], and a 3d confinement [255]. There also has been a report on observation of a SPP microcylinder spaser [304]. A high efficiency room-temperature semiconductor spaser with a DBGS InGaAS gain medium operating near 1.5 μm (i.e., in the communication near-ir range) has been reported [256].

The research and development in the area of spasers as quantum nano-generators is very active and will undoubtedly lead to further rapid advances. The next in line is the spaser as an ultrafast nanoamplifier, which is one of the most important tasks in nanotechnology.

In contrast to this success and rapid development in the field of spasing and spasers, there has so far been a comparatively limited progress in the field of loss

compensation by gain in metamaterials, which is based on the same principles of quantum amplification as the spaser. This status exists despite a significant effort in this direction and numerous theoretical publications, e.g., [267, 305]. There has been so far a single, not yet confirmed independently, observation of the full loss compensation in a plasmonic metamaterial with gain [298].

In large periodic metamaterials, plasmonic modes generally are propagating waves (SPPs) that satisfy Bloch theorem [306] and are characterized by quasi-wavevector **k**. These are propagating waves except for the band edges where $\mathbf{ka} = \pm\pi$, where **a** is the lattice vector. At the band edges, the group velocity v_g of these modes is zero, and these modes are localized, i.e., they are SPs. Their wave function is periodic with period $2a$, which may be understood as a result of the Bragg reflection from the crystallographic planes. Within this $2a$ period, these band-edge modes can, indeed, be treated quasistatically because $2a \ll l_s, \lambda$. If any of the band-edge frequencies is within the range of compensation [where the condition (1.83) [or, (1.85)] is satisfied], the system will spase. In fact, at the band edge, this metamaterial with gain is similar to a distributed feedback (DFB) laser [307]. It actually is a DFB spaser, which, as all the DFB lasers, generates in a band-edge mode.

Moreover, not only the SPPs, which are exactly at the band edge, will be localized. Due to unavoidable disorder caused by fabrication defects in metamaterials, there will be scattering of the SPPs from these defects. Close to the band edge, the group velocity becomes small, $v_g \to 0$. Because the scattering cross section of any wave is $\propto v_g^{-2}$, the corresponding SPPs experience Anderson localization [308]. Also, there always will be SPs nanolocalized at the defects of the metamaterial, whose local fields are hot spots—see Fig. 1.10 and, generally, Sect. 1.3.5 and the publications referenced therein. Each of such hot spots within the bandwidth of conditions (1.83) or (1.85) will be a generating spaser, which clamps the inversion and precludes the full loss compensation.

Note that for a 2d metamaterial (metasurface), the amplification of the spontaneous emission and spasing may occur in SPP modes propagating *in plane* of the structure, unlike the signal that propagates normally to it as in Ref. [298].

Acknowledgments This work was supported by Grant No. DEFG02-01ER15213 from the Chemical Sciences, Biosciences and Geosciences Division and by Grant No. DE-FG02-11ER46789 from the Materials Sciences and Engineering Division of the Office of the Basic Energy Sciences, Office of Science, U.S. Department of Energy.

References

1. M. Moskovits, Surface-enhanced spectroscopy. Rev. Mod. Phys. **57**, 783–826 (1985)
2. M.I. Stockman, V.M. Shalaev, M. Moskovits, R. Botet, T.F. George, Enhanced Raman scattering by fractal clusters: scale invariant theory. Phys. Rev. B **46**, 2821–2830 (1992)
3. L. Gunnarsson, S. Petronis, B. Kasemo, H. Xu, J. Bjerneld, M. Kall, Optimizing nanofabricated substrates for surface enhanced Raman scattering. Nanostruct. Mater. **12**, 783–788 (1999)

4. H.X. Xu, E.J. Bjerneld, M. Kall, L. Borjesson, Spectroscopy of single hemoglobin molecules by surface enhanced Raman scattering. Phys. Rev. Lett. **83**, 4357–4360 (1999)
5. H. Xu, J. Aizpurua, M. Kall, P. Apell, Electromagnetic contributions to single-molecule sensitivity in surface-enhanced Raman scattering. Phys. Rev. E **62**, 4318–4324 (2000)
6. K. Kneipp, M. Moskovits, H. Kneipp (eds.), *Electromagnetic Theory of SERS*, vol. 103 (Springer, Heidelberg, 2006)
7. T.W. Ebbesen, H.J. Lezec, H.F. Ghaemi, T. Thio, P.A. Wolff, Extraordinary optical transmission through sub-wavelength hole arrays. Nature **391**, 667–669 (1998)
8. H.J. Lezec, A. Degiron, E. Devaux, R.A. Linke, L. Martin-Moreno, F.J. Garcia-Vidal, T.W. Ebbesen, Beaming light from a subwavelength aperture. Science **297**, 820–822 (2002)
9. L. Martin-Moreno, F.J. Garcia-Vidal, H.J. Lezec, A. Degiron, T.W. Ebbesen, Theory of highly directional emission from a single subwavelength aperture surrounded by surface corrugations. Phys. Rev. Lett. **90**, 167401-1-4 (2003)
10. C. Genet, T.W. Ebbesen, Light in tiny holes. Nature **445**, 39–46 (2007)
11. F.J. Garcia-Vidal, L. Martin-Moreno, T.W. Ebbesen, L. Kuipers, Light passing through subwavelength apertures. Rev. Mod. Phys. **82**, 729–787 (2010)
12. M.I. Stockman, Nanofocusing of optical energy in tapered plasmonic waveguides. Phys. Rev. Lett. **93**, 137404-1-4 (2004)
13. E. Verhagen, A. Polman, L. Kuipers, Nanofocusing in laterally tapered plasmonic waveguides. Opt. Express **16**, 45–57 (2008)
14. E. Verhagen, M. Spasenovic, A. Polman, L. Kuipers, Nanowire plasmon excitation by adiabatic mode transformation. Phys. Rev. Lett. **102**, 203904-1-4 (2009)
15. F. de Angelis, M. Patrini, G. Das, I. Maksymov, M. Galli, L. Businaro, L.C. Andreani, E. Di Fabrizio, A hybrid plasmonic-photonic nanodevice for label-free detection of a few molecules. Nano Lett. **8**, 2321–2327 (2008)
16. F. de Angelis, G. Das, P. Candeloro, M. Patrini, M. Galli, A. Bek, M. Lazzarino, I. Maksymov, C. Liberale, L.C. Andreani, E. Di Fabrizio, Nanoscale chemical mapping using three-dimensional adiabatic compression of surface plasmon polaritons. Nat. Nanotechnol. **5**, 67–72 (2009)
17. F. de Angelis, F. Gentile, F.M.G. Das, M. Moretti, P. Candeloro, M.L. Coluccio, G. Cojoc, A. Accardo, C. Liberale, R.P. Zaccaria, G. Perozziello, L. Tirinato, A. Toma, G. Cuda, R. Cingolani, E.D. Fabrizio, Breaking the diffusion limit with super-hydrophobic delivery of molecules to plasmonic nanofocusing sers structures. Nat. Photonics **5**, 682–687 (2011)
18. C. Ropers, C.C. Neacsu, T. Elsaesser, M. Albrecht, M.B. Raschke, C. Lienau, Grating-coupling of surface plasmons onto metallic tips: a nano-confined light source. Nano Lett. **7**, 2784–2788 (2007)
19. C.C. Neacsu, S. Berweger, R.L. Olmon, L.V. Saraf, C. Ropers, M.B. Raschke, Near-field localization in plasmonic superfocusing: a nanoemitter on a tip. Nano Lett. **10**, 592–596 (2010)
20. M.B. Raschke, S. Berweger, J.M. Atkin, R.L. Olmon, Adiabatic tip-plasmon focusing for nano-Raman spectroscopy. J. Phys. Chem. Lett. **1**, 3427–3432 (2010)
21. S. Berweger, J.M. Atkin, X.G. Xu, R.L. Olmon, M.B. Raschke, Femtosecond nanofocusing with full optical waveform control. Nano Lett. **11**, 4309–4313 (2011)
22. D. Sadiq, J. Shirdel, J.S. Lee, E. Selishcheva, N. Park, C. Lienau, Adiabatic nanofocusing scattering-type optical nanoscopy of individual gold nanoparticles. Nano Lett. **11**, 1609–1613 (2011)
23. M.I. Stockman, Nanoplasmonics: the physics behind the applications. Phys. Today **64**, 39–44 (2011)
24. S. Lal, S.E. Clare, N.J. Halas, Nanoshell-enabled photothermal cancer therapy: impending clinical impact. Acc. Chem. Res. **41**, 1842–1851 (2008)
25. X.H. Huang, S. Neretina, M.A. El-Sayed, Gold nanorods: from synthesis and properties to biological and biomedical applications. Adv. Mater. **21**, 4880–4910 (2009)
26. H.A. Atwater, A. Polman, Plasmonics for improved photovoltaic devices. Nat. Mater. **9**, 205–213 (2010)

27. S. Mukherjee, F. Libisch, N. Large, O. Neumann, L.V. Brown, J. Cheng, J.B. Lassiter, E.A. Carter, P. Nordlander, N.J. Halas, Hot electrons do the impossible: plasmon-induced dissociation of H_2 on au. Nano Lett. **13**, 240–247 (2012)
28. S. Mubeen, J. Lee, N. Singh, S. Kramer, G.D. Stucky, M. Moskovits, An autonomous photosynthetic device in which all charge carriers derive from surface plasmons. Nat. Nano **8**, 247–251 (2013)
29. D.J. Bergman, D. Stroud, Properties of macroscopically inhomogeneous media, in *Solid State Physics*, vol. 46, ed. by H. Ehrenreich, D. Turnbull (Academic, Boston, 1992), pp. 148–270
30. L.D. Landau, E.M. Lifshitz, *Electrodynamics of Continuous Media* (Pergamon, Oxford, 1984)
31. D.J. Bergman, M.I. Stockman, Surface plasmon amplification by stimulated emission of radiation: quantum generation of coherent surface plasmons in nanosystems. Phys. Rev. Lett. **90**, 027402-1-4 (2003)
32. P.B. Johnson, R.W. Christy, Optical constants of noble metals. Phys. Rev. B **6**, 4370–4379 (1972)
33. E. Feigenbaum, M. Orenstein, Ultrasmall volume plasmons, yet with complete retardation effects. Phys. Rev. Lett. **101**, 163902-1-4 (2008)
34. I.A. Larkin, M.I. Stockman, M. Achermann, V.I. Klimov, Dipolar emitters at nanoscale proximity of metal surfaces: giant enhancement of relaxation in microscopic theory. Phys. Rev. B **69**, 121403(R)-1-4 (2004)
35. I.A. Larkin, M.I. Stockman, Imperfect perfect lens. Nano Lett. **5**, 339–343 (2005)
36. S.I. Bozhevolny (ed.), *Plasmonic Nanoguides and Circuits* (World Scientific Publishing, Singapore, 2008)
37. A. Kramer, F. Keilmann, B. Knoll, R. Guckenberger, The coaxial tip as a nano-antenna for scanning near-field microwave transmission microscopy. Micron **27**, 413–417 (1996)
38. S.J. Oldenburg, G.D. Hale, J.B. Jackson, N.J. Halas, Light scattering from dipole and quadrupole nanoshell antennas. Appl. Phys. Lett. **75**, 1063–1065 (1999)
39. T. Kalkbrenner, U. Hkanson, A. Schadle, S. Burger, C. Henkel, V. Sandoghdar, Optical microscopy via spectral modifications of a nanoantenna. Phys. Rev. Lett. **95**, 200801-1-4 (2005)
40. P. Muhlschlegel, H.J. Eisler, O.J.F. Martin, B. Hecht, D.W. Pohl, Resonant optical antennas. Science **308**, 1607–1609 (2005)
41. P.J. Schuck, D.P. Fromm, A. Sundaramurthy, G.S. Kino, W.E. Moerner, Improving the mismatch between light and nanoscale objects with gold bowtie nanoantennas. Phys. Rev. Lett. **94**, 017402-1-4 (2005)
42. S. Kuhn, U. Hakanson, L. Rogobete, V. Sandoghdar, Enhancement of single-molecule fluorescence using a gold nanoparticle as an optical nanoantenna. Phys. Rev. Lett. **97**, 017402-1-4 (2006)
43. L. Novotny, Effective wavelength scaling for optical antennas. Phys. Rev. Lett. **98**, 266802-1-4 (2007)
44. T.H. Taminiau, F.B. Segerink, R.J. Moerland, L. Kuipers, N.F. van Hulst, Near-field driving of a optical monopole antenna. J. Opt. A **9**, S315–S321 (2007)
45. T.H. Taminiau, F.B. Segerink, N.F. van Hulst, A monopole antenna at optical frequencies: single-molecule near-field measurements. IEEE Trans. Antennas Propag. **55**, 3010–3017 (2007)
46. N. Behr, M.B. Raschke, Optical antenna properties of scanning probe tips: plasmonic light scattering, tip-sample coupling, and near-field enhancement. J. Phys. Chem. C **112**, 3766–3773 (2008)
47. G.W. Bryant, F.J.G. de Abajo, J. Aizpurua, Mapping the plasmon resonances of metallic nanoantennas. Nano Lett. **8**, 631–636 (2008)
48. P. Ghenuche, S. Cherukulappurath, T.H. Taminiau, N.F. van Hulst, R. Quidant, Spectroscopic mode mapping of resonant plasmon nanoantennas. Phys. Rev. Lett. **101**, 116805-1-4 (2008)
49. H.C. Guo, T.P. Meyrath, T. Zentgraf, N. Liu, L.W. Fu, H. Schweizer, H. Giessen, Optical resonances of bowtie slot antennas and their geometry and material dependence. Opt. Express **16**, 7756–7766 (2008)

50. R.M. Bakker, H.K. Yuan, Z.T. Liu, V.P. Drachev, A.V. Kildishev, V.M. Shalaev, R.H. Pedersen, S. Gresillon, A. Boltasseva, Enhanced localized fluorescence in plasmonic nanoantennae. Appl. Phys. Lett. **92**, 043101-1-3 (2008)
51. R.L. Olmon, P.M. Krenz, A.C. Jones, G.D. Boreman, M.B. Raschke, Near-field imaging of optical antenna modes in the mid-infrared. Opt. Express **16**, 20295–20305 (2008)
52. T.H. Taminiau, F.D. Stefani, F.B. Segerink, N.F.V. Hulst, Optical antennas direct single-molecule emission. Nat. Photonics **2**, 234–237 (2008)
53. L. Tang, S.E. Kocabas, S. Latif, A.K. Okyay, D.S. Ly-Gagnon, K.C. Saraswat, D.A.B. Miller, Nanometre-scale germanium photodetector enhanced by a near-infrared dipole antenna. Nat. Photonics **2**, 226–229 (2008)
54. P. Bharadwaj, B. Deutsch, L. Novotny, Optical antennas. Adv. Opt. Photonics **1**, 438–483 (2009)
55. H. Eghlidi, K.G. Lee, X.W. Chen, S. Gotzinger, V. Sandoghdar, Resolution and enhancement in nanoantenna-based fluorescence microscopy. Nano Lett. **9**, 4007–4011 (2009)
56. T. Hanke, G. Krauss, D. Trauetlein, B. Wild, R. Bratschitsch, A. Leitenstorfer, Efficient nonlinear light emission of single gold optical antennas driven by few-cycle near-infrared pulses. Phys. Rev. Lett. **103**, 257404-1-4 (2009)
57. S. Palomba, M. Danckwerts, L. Novotny, Nonlinear plasmonics with gold nanoparticle antennas. J. Opt. A **11**, 114030 (2009)
58. L.Y. Cao, J.S. Park, P.Y. Fan, B. Clemens, M.L. Brongersma, Resonant germanium nanoantenna photodetectors. Nano Lett. **10**, 1229–1233 (2010)
59. V. Giannini, G. Vecchi, J.G. Rivas, Lighting up multipolar surface plasmon polaritons by collective resonances in arrays of nanoantennas. Phys. Rev. Lett. **105**, 266801-1-4 (2010)
60. A. Weber-Bargioni, A. Schwartzberg, M. Schmidt, B. Harteneck, D.F. Ogletree, P.J. Schuck, S. Cabrini, Functional plasmonic antenna scanning probes fabricated by induced-deposition mask lithography. Nanotechnology **21**, 065306-1-6 (2010)
61. M.W. Knight, H. Sobhani, P. Nordlander, N.J. Halas, Photodetection with active optical antennas. Science **332**, 702–704 (2011)
62. W.-D. Li, F. Ding, J. Hu, S.Y. Chou, Three-dimensional cavity nanoantenna coupled plasmonic nanodots for ultrahigh and uniform surface-enhanced Raman scattering over large area. Opt. Express **19**, 3925–3936 (2011)
63. N. Liu, M.L. Tang, M. Hentschel, H. Giessen, A.P. Alivisatos, Nanoantenna-enhanced gas sensing in a single tailored nanofocus. Nat. Mater. **10**, 631–636 (2011)
64. I.S. Maksymov, A.E. Miroshnichenko, Active control over nanofocusing with nanorod plasmonic antennas. Opt. Express **19**, 5888–5894 (2011)
65. L. Novotny, N. van Hulst, Antennas for light. Nat. Photonics **5**, 83–90 (2011)
66. M. Schnell, P.A. Gonzalez, L. Arzubiaga, F. Casanova, L.E. Hueso, A. Chuvilin, R. Hillenbrand, Nanofocusing of mid-infrared energy with tapered transmission lines. Nat. Photonics **5**, 283–287 (2011)
67. V.B. Berestetskii, E.M. Lifshits, L.P. Pitaevskii, *Quantum Electrodynamics* (Pergamon Press, Oxford, 1982)
68. U. Fano, On the absorption spectrum of noble gases at the arc spectrum limit. Nuovo Cimento **12**, 154–161 (1935)
69. V.A. Fedotov, M. Rose, S.L. Prosvirnin, N. Papasimakis, N.I. Zheludev, Sharp trapped-mode resonances in planar metamaterials with a broken structural symmetry. Phys. Rev. Lett. **99**, 147401-1-4 (2007)
70. F. Hao, Y. Sonnefraud, P.V. Dorpe, S.A. Maier, N.J. Halas, P. Nordlander, Symmetry breaking in plasmonic nanocavities: subradiant LSPR sensing and a tunable Fano resonance. Nano Lett. **8**, 3983–3988 (2008)
71. N.A. Mirin, K. Bao, P. Nordlander, Fano resonances in plasmonic nanoparticle aggregates. J. Phys. Chem. A **113**, 4028–4034 (2009)
72. L.V. Brown, H. Sobhani, J.B. Lassiter, P. Nordlander, N.J. Halas, Heterodimers: plasmonic properties of mismatched nanoparticle pairs. ACS Nano **4**, 819–832 (2010)

73. J.A. Fan, C.H. Wu, K. Bao, J.M. Bao, R. Bardhan, N.J. Halas, V.N. Manoharan, P. Nordlander, G. Shvets, F. Capasso, Self-assembled plasmonic nanoparticle clusters. Science **328**, 1135–1138 (2010)
74. V.A. Fedotov, A. Tsiatmas, J.H. Shi, R. Buckingham, P. de Groot, Y. Chen, S. Wang, N.I. Zheludev, Temperature control of Fano resonances and transmission in superconducting metamaterials. Opt. Express **18**, 9015–9019 (2010)
75. M. Hentschel, M. Saliba, R. Vogelgesang, H. Giessen, A.P. Alivisatos, N. Liu, Transition from isolated to collective modes in plasmonic oligomers. Nano Lett. **10**, 2721–2726 (2010)
76. B. Luk'yanchuk, N.I. Zheludev, S.A. Maier, N.J. Halas, P. Nordlander, H. Giessen, C.T. Chong, The Fano resonance in plasmonic nanostructures and metamaterials. Nat. Mater. **9**, 707–715 (2010)
77. M.I. Stockman, Dark-hot resonances. Nature **467**, 541–542 (2010)
78. M.I. Stockman, S.V. Faleev, D.J. Bergman, Localization versus delocalization of surface plasmons in nanosystems: can one state have both characteristics? Phys. Rev. Lett. **87**, 167401-1-4 (2001)
79. L. Novotny, Forces in optical near-fields, in *Near-Field Optics and Surface Plasmon Polaritons*, vol. 81, ed. by S. Kawata (Springer, Berlin, 2001), pp. 123–141
80. F.V. Ignatovich, L. Novotny, Experimental study of nanoparticle detection by optical gradient forces. Rev. Sci. Instrum. **74**, 5231–5235 (2003)
81. K. Joulain, J.-P. Mulet, F. Marquier, R. Carminati, J.-J. Greffet, Surface electromagnetic waves thermally excited: Radiative heat transfer, coherence properties and Casimir forces revisited in the near field. Surf. Sci. Rep. **57**, 59–112 (2005)
82. X.T. Li, D.J. Bergman, D. Stroud, Electric forces among nanospheres in a dielectric host. Europhys. Lett. **69**, 1010–1016 (2005)
83. G. Volpe, R. Quidant, G. Badenes, D. Petrov, Surface plasmon radiation forces. Phys. Rev. Lett. **96**, 238101 (2006)
84. A.S. Zelenina, R. Quidant, M. Nieto-Vesperinas, Enhanced optical forces between coupled resonant metal nanoparticles. Opt. Lett. **32**, 1156–1158 (2007)
85. I. Takuya, I. Hajime, Theory of resonant radiation force exerted on nanostructures by optical excitation of their quantum states: from microscopic to macroscopic descriptions. Phys. Rev. B **77**, 245319-1-16 (2008)
86. R. Quidant, S. Zelenina, M. Nieto-Vesperinas, Optical manipulation of plasmonic nanoparticles. Appl. Phys. A **89**, 233–239 (2007)
87. M. Righini, A.S. Zelenina, C. Girard, R. Quidant, Parallel and selective trapping in a patterned plasmonic landscape. Nat. Phys. **3**, 477–480 (2007)
88. R. Quidant, C. Girard, Surface-plasmon-based optical manipulation. Laser Photonics Rev. **2**, 47–57 (2008)
89. M. Righini, G. Volpe, C. Girard, D. Petrov, R. Quidant, Surface plasmon optical tweezers: tunable optical manipulation in the femtonewton range. Phys. Rev. Lett. **100**, 186804-1-4 (2008)
90. M.L. Juan, R. Gordon, Y.J. Pang, F. Eftekhari, R. Quidant, Self-induced back-action optical trapping of dielectric nanoparticles. Nat. Phys. **5**, 915–919 (2009)
91. M. Righini, P. Ghenuche, S. Cherukulappurath, V. Myroshnychenko, F.J.G. de Abajo, R. Quidant, Nano-optical trapping of Rayleigh particles and *Escherichia coli* bacteria with resonant optical antennas. Nano Lett. **9**, 3387–3391 (2009)
92. L.M. Tong, M. Righini, M.U. Gonzalez, R. Quidant, M. Kall, Optical aggregation of metal nanoparticles in a microfluidic channel for surface-enhanced Raman scattering analysis. Lab Chip **9**, 193–195 (2009)
93. M. Durach, A. Rusina, M.I. Stockman, Giant surface-plasmon-induced drag effect in metal nanowires. Phys. Rev. Lett. **103**, 186801-1-4 (2009)
94. R.H. Ritchie, Plasma losses by fast electrons in thin films. Phys. Rev. **106**, 874–881 (1957)
95. A.W. Blackstock, R.H. Ritchie, R.D. Birkhoff, Mean free path for discrete electron energy losses in metallic foils. Phys. Rev. **100**, 1078 (1955)

96. N. Swanson, C.J. Powell, Inelastic scattering cross sections for 20-kev electrons in Al, Be, and polystyrene. Phys. Rev. **145**, 195 (1966)
97. F.J.G. de Abajo, Optical excitations in electron microscopy. Rev. Mod. Phys. **82**, 209 (2010)
98. A. Reyes-Coronado, R.G. Barrera, P.E. Batson, P.M. Echenique, A. Rivacoba, J. Aizpurua, Electromagnetic forces on plasmonic nanoparticles induced by fast electron beams. Phys. Rev. B **82**, 235429-1-19 (2010)
99. B.B. Dasgupta, R. Fuchs, Polarizability of a small sphere including nonlocal effects. Phys. Rev. B **24**, 554–561 (1981)
100. J.B. Pendry, Negative refraction makes a perfect lens. Phys. Rev. Lett. **85**, 3966–3969 (2000)
101. F.J.G. de Abajo, Nonlocal effects in the plasmons of strongly interacting nanoparticles, dimers, and waveguides. J. Phys. Chem. C **112**, 17983–17987 (2008)
102. U. Kreibig, M. Vollmer, *Optical Properties of Metal Clusters* (Springer, New York, 1995)
103. V.N. Pustovit, T.V. Shahbazyan, Quantum-size effects in SERS from noble-metal nanoparticles. Microelectron. J. **36**, 559–563 (2005)
104. V.N. Pustovit, T.V. Shahbazyan, Finite-size effects in surface-enhanced Raman scattering in noble-metal nanoparticles: a semiclassical approach. J. Opt. Soc. Am. A **23**, 1369–1374 (2006)
105. V.N. Pustovit, T.V. Shahbazyan, Surface-enhanced Raman scattering on the nanoscale: a microscopic approach. J. Opt. A **8**, S208–S212 (2006)
106. V.N. Pustovit, T.V. Shahbazyan, SERS from molecules adsorbed on small Ag nanoparticles: a microscopic model. Chem. Phys. Lett. **420**, 469–473 (2006)
107. V.N. Pustovit, T.V. Shahbazyan, Microscopic theory of surface-enhanced Raman scattering in noble-metal nanoparticles. Phys. Rev. B **73**, 085408-1-7 (2006)
108. J. Zuloaga, E. Prodan, P. Nordlander, Quantum description of the plasmon resonances of a nanoparticle dimer. Nano Lett. **9**, 887–891 (2009)
109. P. Nordlander, J. Zuloaga, E. Prodan, Quantum plasmonics: Optical properties and tunability of metallic nanorods. ACS Nano **4**, 5269–5276 (2010)
110. E.D. Palik, *Handbook of Optical Constants of Solids* (Academic, San Diego, 1998)
111. D.E. Chang, A.S. Sorensen, P.R. Hemmer, M.D. Lukin, Quantum optics with surface plasmons. Phys. Rev. Lett. **97**, 053002-1-4 (2006)
112. A.V. Akimov, A. Mukherjee, C.L. Yu, D.E. Chang, A.S. Zibrov, P.R. Hemmer, H. Park, M.D. Lukin, Generation of single optical plasmons in metallic nanowires coupled to quantum dots. Nature **450**, 402–406 (2007)
113. P. Berini, A. Akbari, R.N. Tait, Surface plasmon waveguide Schottky detector. Opt. Express **18**, 8505–8514 (2010)
114. C. Scales, I. Breukelaar, P. Berini, Surface-plasmon Schottky contact detector based on a symmetric metal stripe in silicon. Opt. Lett. **35**, 529–531 (2010)
115. U. Levy, I. Goykhman, B. Desiatov, J. Khurgin, J. Shappir, Locally oxidized silicon surface-plasmon Schottky detector for telecom regime. Nano Lett. **11**, 2219–2224 (2011)
116. S.M. Sze, *Physics of Semiconductor Devices* (Wiley-Interscience, Hoboken, 2007)
117. A.V. Butenko, V.M. Shalaev, M.I. Stockman, Giant impurity nonlinearities in optics of fractal clusters. Sov. Phys. JETP **67**, 60–69 (1988)
118. A.V. Karpov, A.K. Popov, S.G. Rautian, V.P. Safonov, V.V. Slabko, V.M. Shalaev, M.I. Stockman, Observation of a wavelength- and polarization-selective photomodification of silver clusters. JETP Lett. **48**, 571–573 (1988)
119. S.G. Rautian, V.P. Safonov, P.A. Chubakov, V.M. Shalaev, M.I. Stockman, Surface-enhanced parametric scattering of light by silver clusters. JETP Lett. **47**, 243–246 (1988)
120. V.M. Shalaev, M.I. Stockman, R. Botet, Resonant excitations and nonlinear optics of fractals. Physica A **185**, 181–186 (1992)
121. R.W. Boyd, *Nonlinear Optics* (Academic, London, 2003)
122. J. Kneipp, H. Kneipp, K. Kneipp, Two-photon vibrational spectroscopy for biosciences based on surface-enhanced hyper-Raman scattering. Proc. Natl. Acad. Sci. USA **103**, 17149–17153 (2006)

123. A. Kubo, K. Onda, H. Petek, Z. Sun, Y.S. Jung, H.K. Kim, Femtosecond imaging of surface plasmon dynamics in a nanostructured silver film. Nano Lett. **5**, 1123–1127 (2005)
124. A.V. Zayats, I.I. Smolyaninov, C.C. Davis, Observation of localized plasmonic excitations in thin metal films with near-field second-harmonic microscopy. Opt. Commun. **169**, 93–96 (1999)
125. A. Bouhelier, M. Beversluis, A. Hartschuh, L. Novotny, Near-field second-harmonic generation induced by local field enhancement. Phys. Rev. Lett. **90**, 13903-1-4 (2003)
126. S.I. Bozhevolnyi, J. Beermann, V. Coello, Direct observation of localized second-harmonic enhancement in random metal nanostructures. Phys. Rev. Lett. **90**, 197403-1-4 (2003)
127. M. Labardi, M. Allegrini, M. Zavelani-Rossi, D. Polli, G. Cerullo, S.D. Silvestri, O. Svelto, Highly efficient second-harmonic nanosource for near-field optics and microscopy. Opt. Lett. **29**, 62–64 (2004)
128. M.I. Stockman, D.J. Bergman, C. Anceau, S. Brasselet, J. Zyss, Enhanced second-harmonic generation by metal surfaces with nanoscale roughness: nanoscale dephasing, depolarization, and correlations. Phys. Rev. Lett. **92**, 057402-1-4 (2004)
129. N.I. Zheludev, V.I. Emelyanov, Phase matched second harmonic generation from nanostructured metal surfaces. J. Opt. A **6**, 26–28 (2004)
130. R.C. Jin, J.E. Jureller, H.Y. Kim, N.F. Scherer, Correlating second harmonic optical responses of single Ag nanoparticles with morphology. J. Am. Chem. Soc. **127**, 12482–12483 (2005)
131. B.K. Canfield, H. Husu, J. Laukkanen, B.F. Bai, M. Kuittinen, J. Turunen, M. Kauranen, Local field asymmetry drives second-harmonic generation in noncentrosymmetric nanodimers. Nano Lett. **7**, 1251–1255 (2007)
132. M. Zdanowicz, S. Kujala, H. Husu, M. Kauranen, Effective medium multipolar tensor analysis of second-harmonic generation from metal nanoparticles. New J. Phys. **13**, 023025-1-12 (2011)
133. J. Renger, R. Quidant, N. van Hulst, L. Novotny, Surface-enhanced nonlinear four-wave mixing. Phys. Rev. Lett. **104**, 046803-1-4 (2010)
134. T. Utikal, M.I. Stockman, A.P. Heberle, M. Lippitz, H. Giessen, All-optical control of the ultrafast dynamics of a hybrid plasmonic system. Phys. Rev. Lett. **104**, 113903-1-4 (2010)
135. D. Pacifici, H.J. Lezec, H.A. Atwater, All-optical modulation by plasmonic excitation of CdSe quantum dots. Nat. Photonics **1**, 402–406 (2007)
136. Z.L. Samson, K.F. MacDonald, F. de Angelis, B. Gholipour, K. Knight, C.C. Huang, E. Di Fabrizio, W. Hewak, N.I. Zheludev, Metamaterial electro-optic switch of nanoscale thickness. Appl. Phys. Lett. **96**, 143105-1-3 (2010)
137. K.F. MacDonald, Z.L. Samson, M.I. Stockman, N.I. Zheludev, Ultrafast active plasmonics. Nat. Photonics **3**, 55–58 (2009)
138. S. Kim, J.H. Jin, Y.J. Kim, I.Y. Park, Y. Kim, S.W. Kim, High-harmonic generation by resonant plasmon field enhancement. Nature **453**, 757–760 (2008)
139. M.I. Stockman, The spaser as a nanoscale quantum generator and ultrafast amplifier. J. Opt. **12**, 024004-1-13 (2010)
140. M.I. Stockman, Spaser action, loss compensation, and stability in plasmonic systems with gain. Phys. Rev. Lett. **106**, 156802-1-4 (2011)
141. M.I. Stockman, Loss compensation by gain and spasing. Phil. Trans. R. Soc. A **369**, 3510–3524 (2011)
142. P. Ginzburg, A. Hayat, N. Berkovitch, M. Orenstein, Nonlocal ponderomotive nonlinearity in plasmonics. Opt. Lett. **35**, 1551–1553 (2010)
143. E. Feigenbaum, M. Orenstein, Plasmon–soliton. Opt. Lett. **32**, 674–676 (2007)
144. S. Zherebtsov, T. Fennel, J. Plenge, E. Antonsson, I. Znakovskaya, A. Wirth, O. Herrwerth, F. Suessmann, C. Peltz, I. Ahmad, S.A. Trushin, V. Pervak, S. Karsch, M.J.J. Vrakking, B. Langer, C. Graf, M.I. Stockman, F. Krausz, E. Ruehl, M.F. Kling, Controlled near-field enhanced electron acceleration from dielectric nanospheres with intense few-cycle laser fields. Nat. Phys. **7**, 656–662 (2011)
145. M. Kruger, M. Schenk, P. Hommelhoff, Attosecond control of electrons emitted from a nanoscale metal tip. Nature **475**, 78–81 (2011)

146. M. Durach, A. Rusina, M.F. Kling, M.I. Stockman, Metallization of nanofilms in strong adiabatic electric fields. Phys. Rev. Lett. **105**, 086803-1-4 (2010)
147. M. Durach, A. Rusina, M.F. Kling, M.I. Stockman, Predicted ultrafast dynamic metallization of dielectric nanofilms by strong single-cycle optical fields. Phys. Rev. Lett. **107**, 086602-1-5 (2011)
148. M.I. Stockman, D.J. Bergman, T. Kobayashi, Coherent control of nanoscale localization of ultrafast optical excitation in nanosystems. Phys. Rev. B **69**, 054202-1-10 (2004)
149. V.M. Shalaev, M.I. Stockman, Optical properties of fractal clusters (susceptibility, surface enhanced Raman scattering by impurities). Sov. Phys. JETP **65**, 287–294 (1987)
150. V.M. Shalaev, R. Botet, A.V. Butenko, Localization of collective dipole excitations on fractals. Phys. Rev. B **48**, 6662–6664 (1993)
151. V.M. Shalaev, R. Botet, D.P. Tsai, J. Kovacs, M. Moskovits, Fractals: localization of dipole excitations and giant optical polarizabilities. Phys. A **207**, 197–207 (1994)
152. A.K. Sarychev, V.A. Shubin, V.M. Shalaev, Anderson localization of surface plasmons and Kerr nonlinearity in semicontinuous metal films. Phys. B **279**, 87–89 (2000)
153. S.I. Bozhevolnyi, V.A. Markel, V. Coello, W. Kim, V.M. Shalaev, Direct observation of localized dipolar excitations on rough nanostructured surfaces. Phys. Rev. B **58**, 11441–11448 (1998)
154. A.K. Sarychev, V.A. Shubin, V.M. Shalaev, Anderson localization of surface plasmons and nonlinear optics of metal-dielectric composites. Phys. Rev. B **60**, 16389–16408 (1999)
155. S. Gresillon, L. Aigouy, A.C. Boccara, J.C. Rivoal, X. Quelin, C. Desmarest, P. Gadenne, V.A. Shubin, A.K. Sarychev, V.M. Shalaev, Experimental observation of localized optical excitations in random metal-dielectric films. Phys. Rev. Lett. **82**, 4520–4523 (1999)
156. V.M. Shalaev, *Nonlinear Optics of Random Media : Fractal Composites and Metal-Dielectric Films* (Springer, Berlin, 2000)
157. M.I. Stockman, Inhomogeneous eigenmode localization, chaos, and correlations in large disordered clusters. Phys. Rev. E **56**, 6494–6507 (1997)
158. M.I. Stockman, L.N. Pandey, T.F. George, Inhomogeneous localization of polar eigenmodes in fractals. Phys. Rev. B **53**, 2183–2186 (1996)
159. M.I. Stockman, Chaos and spatial correlations for dipolar eigenproblems. Phys. Rev. Lett. **79**, 4562–4565 (1997)
160. M.I. Stockman, Giant attosecond fluctuations of local optical fields in disordered nanostructured media. Phys. Rev. B **62**, 10494–10497 (2000)
161. V. Krachmalnicoff, E. Castanie, Y.D. Wilde, R. Carminati, Fluctuations of the local density of states probe localized surface plasmons on disordered metal films. Phys. Rev. Lett. **105**, 183901-1-4 (2010)
162. D.P. Tsai, J. Kovacs, Z. Wang, M. Moskovits, V.M. Shalaev, J.S. Suh, R. Botet, Photon scanning tunneling microscopy images of optical excitations of fractal metal colloid clusters. Phys. Rev. Lett. **72**, 4149–4152 (1994)
163. M.I. Stockman, L.N. Pandey, L.S. Muratov, T.F. George, Photon scanning-tunneling-microscopy images of optical-excitations of fractal metal colloid clusters: comment. Phys. Rev. Lett. **75**, 2450–2450 (1995)
164. L.D. Negro, S.V. Boriskina, Deterministic aperiodic nanostructures for photonics and plasmonics applications. Laser Photonics Rev. **6**, 178–218 (2012)
165. M. Kolb, R. Botet, J. Julienne, Scaling of kinetically growing clusters. Phys. Rev. Lett. **51**, 1123–1126 (1983)
166. D.A. Weitz, M. Oliveria, Fractal structures formed by kinetic aggregation of aqueous gold colloids. Phys. Rev. Lett. **52**, 1433–1436 (1984)
167. S.L. Westcott, N.J. Halas, Electron relaxation dynamics in semicontinuous metal films on nanoparticle surfaces. Chem. Phys. Lett. **356**, 207–213 (2002)
168. K. Seal, A.K. Sarychev, H. Noh, D.A. Genov, A. Yamilov, V.M. Shalaev, Z.C. Ying, H. Cao, Near-field intensity correlations in semicontinuous metal-dielectric films. Phys. Rev. Lett. **94**, 226101-1-4 (2005)

169. M.I. Stockman, Giant fluctuations of second harmonic generation on nanostructured surfaces. Chem. Phys. **318**, 156–162 (2005)
170. E. Fort, S. Gresillon, Surface enhanced fluorescence. J. Phys. D **41**, 013001-1-31 (2008)
171. A.L. Efros, *Physics and Geometry of Disorder: Percolation Theory* (Mir, Moscow, 1986)
172. L.S. Levitov, Delocalization of vibrational modes caused by electric dipole interaction. Phys. Rev. Lett. **64**, 547–550 (1990)
173. D.A. Parshin, H.R. Schober, Multifractal structure of eigenstates in the Anderson model with long-range off-diagonal disorder. Phys. Rev. B **57**, 10232–10235 (1998)
174. A.L. Burin, Y. Kagan, L.A. Maksimov, I.Y. Polischuk, Dephasing rate in dielectric glasses at ultralow temperatures. Phys. Rev. Lett. **80**, 2945–2948 (1998)
175. M.I. Stockman, L.N. Pandey, L.S. Muratov, T.F. George, Giant fluctuations of local optical fields in fractal clusters. Phys. Rev. Lett. **72**, 2486–2489 (1994)
176. P. Ginzburg, N. Berkovitch, A. Nevet, I. Shor, M. Orenstein, Resonances on-demand for plasmonic nano-particles. Nano Lett. **11**, 2329–2333 (2011)
177. V.A. Markel, L.S. Muratov, M.I. Stockman, T.F. George, Theory and numerical simulation of optical properties of fractal clusters. Phys. Rev. B **43**, 8183 (1991)
178. M.I. Stockman, Electromagnetic theory of SERS, in *Surface Enhanced Raman Scattering*, vol. 103, ed. by M.M.K. Kneipp, H. Kneipp (Springer, Heidelberg, 2006), pp. 47–66
179. M.I. Stockman, T. George, Photon tunneling microscope reveals local hot-spots. Phys. World **7**, 27–28 (1994)
180. C. Awada, G. Barbillon, L. Douillard, J.J. Greffet, Experimental study of hot spots in gold/glass nanocomposite films by photoemission electron microscopy. Phys. Rev. B **85**, 045438-1-6 (2012)
181. H. Cang, A. Labno, C.G. Lu, X.B. Yin, M. Liu, C. Gladden, Y.M. Liu, X. Zhang, Probing the electromagnetic field of a 15-nanometre hotspot by single molecule imaging. Nature **469**, 385–388 (2011)
182. A. McLeod, A. Weber-Bargioni, Z. Zhang, S. Dhuey, B. Harteneck, J.B. Neaton, S. Cabrini, P.J. Schuck, Nonperturbative visualization of nanoscale plasmonic field distributions via photon localization microscopy. Phys. Rev. Lett. **106**, 037402 (2011)
183. A. Yildiz, J.N. Forkey, S.A. McKinney, T. Ha, Y.E. Goldman, P.R. Selvin, Myosin v walks hand-over-hand: single fluorophore imaging with 1.5-nm localization. Science **300**, 2061–2065 (2003)
184. M.I. Stockman, M.F. Kling, U. Kleineberg, F. Krausz, Attosecond nanoplasmonic field microscope. Nat. Photonics **1**, 539–544 (2007)
185. T. Klar, M. Perner, S. Grosse, G. von Plessen, W. Spirkl, J. Feldman, Surface-plasmon resonances in single metallic nanoparticles. Phys. Rev. Lett. **80**, 4249–4252 (1998)
186. J. Lehmann, M. Merschdorf, W. Pfeiffer, A. Thon, S. Voll, G. Gerber, Surface plasmon dynamics in silver nanoparticles studied by femtosecond time-resolved photoemission. Phys. Rev. Lett. **85**, 2921–2924 (2000)
187. J. Bosbach, C. Hendrich, F. Stietz, T. Vartanyan, F. Trager, Ultrafast dephasing of surface plasmon excitation in silver nanoparticles: influence of particle size, shape, and chemical surrounding. Phys. Rev. Lett. **89**, 257404-1-4 (2002)
188. C. Hendrich, J. Bosbach, F. Stietz, F. Hubenthal, T. Vartanyan, F. Trager, Chemical interface damping of surface plasmon excitation in metal nanoparticles: A study by persistent spectral hole burning. Appl. Phys. B **76**, 869–875 (2003)
189. T. Zentgraf, A. Christ, J. Kuhl, H. Giessen, Tailoring the ultrafast dephasing of quasiparticles in metallic photonic crystals. Phys. Rev. Lett. **93**, 243901-1-4 (2004)
190. L. Novotny, B. Hecht, *Principles of Nano-Optics* (Cambridge University Press, Cambridge, 2006)
191. A. Ono, J. Kato, S. Kawata, Subwavelength optical imaging through a metallic nanorod array. Phys. Rev. Lett. **95**, 267407-1-4 (2005)
192. G. Shvets, S. Trendafilov, J.B. Pendry, A. Sarychev, Guiding, focusing, and sensing on the subwavelength scale using metallic wire arrays. Phys. Rev. Lett. **99**, 053903-1-4 (2007)
193. J.B. Pendry, Perfect cylindrical lenses. Opt. Express **11**, 755–760 (2003)

194. Z. Liu, H. Lee, Y. Xiong, C. Sun, X. Zhang, Far-field optical hyperlens magnifying sub-diffraction-limited objects. Science **315**, 1686–1686 (2007)
195. M.I. Stockman, S.V. Faleev, D.J. Bergman, Coherent control of femtosecond energy localization in nanosystems. Phys. Rev. Lett. **88**, 067402-1-4 (2002)
196. D.J. Tannor, S.A. Rice, Control of selectivity of chemical reaction via control of wave packet evolution. J. Chem. Phys. **83**, 5013–5018 (1985)
197. P. Brumer, M. Shapiro, *Principles of the Quantum Control of Molecular Processes* (Wiley, New York, 2003)
198. R.S. Judson, H. Rabitz, Teaching lasers to control molecules. Phys. Rev. Lett. **68**, 1500 (1992)
199. G. Kurizki, M. Shapiro, P. Brumer, Phase-coherent control of photocurrent directionality in semiconductors. Phys. Rev. B **39**, 3435–3437 (1989)
200. T.C. Weinacht, J. Ahn, P.H. Bucksbaum, Controlling the shape of a quantum wavefunction. Nature **397**, 233–235 (1999)
201. P. Brumer, M. Shapiro, Laser control of molecular processes. Ann. Rev. Phys. Chem. **43**, 257–282 (1992)
202. H. Rabitz, R. de Vivie-Riedle, M. Motzkus, K. Kompa, Chemistry: whither the future of controlling quantum phenomena? Science **288**, 824–828 (2000)
203. J.M. Geremia, H. Rabitz, Optimal identification of Hamiltonian information by closed-loop laser control of quantum systems. Phys. Rev. Lett. **89**, 263902-1-4 (2002)
204. N.A. Nguyen, B.K. Dey, M. Shapiro, P. Brumer, Coherent control in nanolithography: Rydberg atoms. J. Phys. Chem. A **108**, 7878–7888 (2004)
205. M. Shapiro, P. Brumer, Quantum control of bound and continuum state dynamics. Phys. Rep. **425**, 195–264 (2006)
206. A. Assion, T. Baumert, M. Bergt, T. Brixner, B. Kiefer, V. Seyfried, M. Strehle, G. Gerber, Control of chemical reactions by feedback-optimized phase-shaped femtosecond laser pulses. Science **282**, 919–922 (1998)
207. R. Bartels, S. Backus, E. Zeek, L. Misoguti, G. Vdovin, I.P. Christov, M.M. Murnane, H.C. Kapteyn, Shaped-pulse optimization of coherent emission of high-harmonic soft x-rays. Nature **406**, 164–166 (2000)
208. N. Dudovich, D. Oron, Y. Silberberg, Single-pulse coherently controlled nonlinear Raman spectroscopy and microscopy. Nature **418**, 512–514 (2002)
209. T. Brixner, G. Krampert, T. Pfeifer, R. Selle, G. Gerber, M. Wollenhaupt, O. Graefe, C. Horn, D. Liese, T. Baumert, Quantum control by ultrafast polarization shaping. Phys. Rev. Lett. **92**, 208301-1-4 (2004)
210. M. Durach, A. Rusina, K. Nelson, M.I. Stockman, Toward full spatio-temporal control on the nanoscale. Nano Lett. **7**, 3145–3149 (2007)
211. G. Volpe, S. Cherukulappurath, R.J. Parramon, G. Molina-Terriza, R. Quidant, Controlling the optical near field of nanoantennas with spatial phase-shaped beams. Nano Lett. **9**, 3608–3611 (2009)
212. B. Gjonaj, J. Aulbach, P.M. Johnson, A.P. Mosk, L. Kuipers, A. Lagendijk, Active spatial control of plasmonic fields. Nat. Photonics **5**, 360–363 (2011)
213. M.I. Stockman, P. Hewageegana, Nanolocalized nonlinear electron photoemission under coherent control. Nano Lett. **5**, 2325–2329 (2005)
214. M. Sukharev, T. Seideman, Phase and polarization control as a route to plasmonic nanodevices. Nano Lett. **6**, 715–719 (2006)
215. M. Aeschlimann, M. Bauer, D. Bayer, T. Brixner, F.J.G. Abajo de, W. Pfeiffer, M. Rohmer, C. Spindler, F. Steeb, Adaptive subwavelength control of nano-optical fields. Nature **446**, 301–304 (2007)
216. M. Bauer, C. Wiemann, J. Lange, D. Bayer, M. Rohmer, M. Aeschlimann, Phase propagation of localized surface plasmons probed by time-resolved photoemission electron microscopy. Appl. Phys. A **88**, 473–480 (2007)
217. M. Aeschlimann, M. Bauer, D. Bayer, T. Brixner, S. Cunovic, F. Dimler, A. Fischer, W. Pfeiffer, M. Rohmer, C. Schneider, F. Steeb, C. Struber, D.V. Voronine, Spatiotemporal control of nanooptical excitations. Proc. Natl. Acad. Sci. USA **107**, 5329–5333 (2010)

218. X. Li, M.I. Stockman, Highly efficient spatiotemporal coherent control in nanoplasmonics on a nanometer-femtosecond scale by time reversal. Phys. Rev. B **77**, 195109-1-10 (2008)
219. A. Derode, A. Tourin, J. de Rosny, M. Tanter, S. Yon, M. Fink, Taking advantage of multiple scattering to communicate with time-reversal antennas. Phys. Rev. Lett. **90**, 014301-1-4 (2003)
220. G. Lerosey, J. de Rosny, A. Tourin, A. Derode, G. Montaldo, M. Fink, Time reversal of electromagnetic waves. Phys. Rev. Lett. **92**, 193904-1-3 (2004)
221. G. Lerosey, J. de Rosny, A. Tourin, M. Fink, Focusing beyond the diffraction limit with far-field time reversal. Science **315**, 1120–1122 (2007)
222. M.I. Stockman, Electromagnetic theory of SERS, in *Surface Enhanced Raman Scattering: Physics and Applications*, ed. by K. Kneipp, M. Moskovits, H. Kneipp (Springer, Heidelberg, 2006), pp. 47–66
223. M.I. Stockman, L.N. Pandey, L.S. Muratov, T.F. George, Optical-absorption and localization of eigenmodes in disordered clusters. Phys. Rev. B **51**, 185–195 (1995)
224. L.D. Landau, E.M. Lifshitz, *The Classical Theory of Fields* (Pergamon Press, Oxford, 1975)
225. A. Kubo, N. Pontius, H. Petek, Femtosecond microscopy of surface plasmon polariton wave packet evolution at the silver/vacuum interface. Nano Lett. **7**, 470–475 (2007)
226. E. Verhagen, L. Kuipers, A. Polman, Enhanced nonlinear optical effects with a tapered plasmonic waveguide. Nano Lett. **7**, 334–337 (2007)
227. M. Sukharev, T. Seideman, Coherent control of light propagation via nanoparticle arrays. J. Phys. B **40**, S283–S298 (2007)
228. M.M. Wefers, K.A. Nelson, Programmable phase and amplitude femtosecond pulse shaping. Opt. Lett. **18**, 2032–2034 (1993)
229. T. Feurer, J.C. Vaughan, K.A. Nelson, Spatiotemporal coherent control of lattice vibrational waves. Science **299**, 374–377 (2003)
230. A.J. Babajanyan, N.L. Margaryan, K.V. Nerkararyan, Superfocusing of surface polaritons in the conical structure. J. Appl. Phys. **87**, 3785–3788 (2000)
231. D.K. Gramotnev, M.W. Vogel, M.I. Stockman, Optimized nonadiabatic nanofocusing of plasmons by tapered metal rods. J. Appl. Phys. **104**, 034311-1-8 (2008)
232. W. Nomura, M. Ohtsu, T. Yatsui, Nanodot coupler with a surface plasmon polariton condenser for optical far/near-field conversion. Appl. Phys. Lett. **86**, 181108-1-3 (2005)
233. L.L. Yin, V.K. Vlasko-Vlasov, J. Pearson, J.M. Hiller, J. Hua, U. Welp, D.E. Brown, C.W. Kimball, Subwavelength focusing and guiding of surface plasmons. Nano Lett. **5**, 1399–1402 (2005)
234. R.J. Mailloux, *Phased Array Antenna Handbook* (Artech House, Boston, 2005)
235. G. Lerosey, J. de Rosny, A. Tourin, A. Derode, M. Fink, Time reversal of wideband microwaves. Appl. Phys. Lett. **88**, 154101-1-3 (2006)
236. M.I. Stockman, Ultrafast nanoplasmonics under coherent control. New J. Phys. **10**, 025031-1-20 (2008)
237. T.S. Kao, S.D. Jenkins, J. Ruostekoski, N.I. Zheludev, Coherent control of nanoscale light localization in metamaterial: creating and positioning isolated subwavelength energy hot spots. Phys. Rev. Lett. **106**, 085501-1-4 (2011)
238. M. Bauer, O. Schmidt, C. Wiemann, R. Porath, M. Scharte, O. Andreyev, G. Schonhense, M. Aeschlimann, Time-resolved two photon photoemission electron microscopy. Appl. Phys. B **74**, 223–227 (2002)
239. T. Brixner, G. Gerber, Femtosecond polarization pulse shaping. Opt. Lett. **26**, 557–559 (2001)
240. T. Brixner, G. Krampert, P. Niklaus, G. Gerber, Generation and characterization of polarization-shaped femtosecond laser pulses. Appl. Phys. B **74**, S133–S144 (2002)
241. H.A. Atwater, The promise of plasmonics. Sci. Am. **296**, 56–63 (2007)
242. J.N. Anker, W.P. Hall, O. Lyandres, N.C. Shah, J. Zhao, R.P.V. Duyne, Biosensing with plasmonic nanosensors. Nat. Mater. **7**, 442–453 (2008)
243. A. Israel, M. Mrejen, Y. Lovsky, M. Polhan, S. Maier, A. Lewis, Near-field imaging probes electromagnetic waves. Laser Focus World **43**, 99–102 (2007)

244. W.A. Challener, C. Peng, A.V. Itagi, D. Karns, W. Peng, Y. Peng, X. Yang, X. Zhu, N.J. Gokemeijer, Y.T. Hsia, G. Ju, R.E. Rottmayer, M.A. Seigler, E.C. Gage, Heat-assisted magnetic recording by a near-field transducer with efficient optical energy transfer. Nat. Photonics **3**, 220–224 (2009)
245. N. Nagatani, R. Tanaka, T. Yuhi, T. Endo, K. Kerman, Y. Takamura, E. Tamiya, Gold nanoparticle-based novel enhancement method for the development of highly sensitive immunochromatographic test strips. Sci. Technol. Adv. Mater. **7**, 270–275 (2006)
246. L.R. Hirsch, R.J. Stafford, J.A. Bankson, S.R. Sershen, B. Rivera, R.E. Price, J.D. Hazle, N.J. Halas, J.L. West, Nanoshell-mediated near-infrared thermal therapy of tumors under magnetic resonance guidance. Proc. Natl. Acad. Sci. USA **100**, 13549–13554 (2003)
247. I.-Y. Park, S. Kim, J. Choi, D.-H. Lee, Y.-J. Kim, M.F. Kling, M.I. Stockman, S.-W. Kim, Plasmonic generation of ultrashort extreme-ultraviolet light pulses. Nat. Photonics **5**, 677–681 (2011)
248. D. Kahng, Electric field controlled semiconductor device, United States Patent 3,102,230 (1963)
249. Y. Tsividis, *Operation and Modeling of the MOS Transistor* (McGraw-Hill, New York, 1999)
250. M.I. Stockman, D.J. Bergman, Surface plasmon amplification by stimulated emission of radiation (spaser), US Patent 7,569,188 (2009)
251. M.I. Stockman, Spasers explained. Nat. Photonics **2**, 327–329 (2008)
252. M.A. Noginov, G. Zhu, A.M. Belgrave, R. Bakker, V.M. Shalaev, E.E. Narimanov, S. Stout, E. Herz, T. Suteewong, U. Wiesner, Demonstration of a spaser-based nanolaser. Nature **460**, 1110–1112 (2009)
253. M.T. Hill, M. Marell, E.S.P. Leong, B. Smalbrugge, Y. Zhu, M. Sun, P.J. van Veldhoven, E.J. Geluk, F. Karouta, Y.-S. Oei, R. Ntzel, C.-Z. Ning, M.K. Smit, Lasing in metal-insulator-metal sub-wavelength plasmonic waveguides. Opt. Express **17**, 11107–11112 (2009)
254. R.F. Oulton, V.J. Sorger, T. Zentgraf, R.-M. Ma, C. Gladden, L. Dai, G. Bartal, X. Zhang, Plasmon lasers at deep subwavelength scale. Nature **461**, 629–632 (2009)
255. R.-M. Ma, R.F. Oulton, V.J. Sorger, G. Bartal, X. Zhang, Room-temperature sub-diffraction-limited plasmon laser by total internal reflection. Nat. Mater. **10**, 110–113 (2010)
256. R.A. Flynn, C.S. Kim, I. Vurgaftman, M. Kim, J.R. Meyer, A.J. Mäkinen, K. Bussmann, L. Cheng, F.S. Choa, J.P. Long, A room-temperature semiconductor spaser operating near 1.5 micron. Opt. Express **19**, 8954–8961 (2011)
257. M.T. Hill, Y.-S. Oei, B. Smalbrugge, Y. Zhu, T. de Vries, P.J. van Veldhoven, F.W.M. van Otten, T.J. Eijkemans, J.P. Turkiewicz, H. de Waardt, E.J. Geluk, S.-H. Kwon, Y.-H. Lee, R. Noetzel, M.K. Smit, Lasing in metallic-coated nanocavities. Nat. Photonics **1**, 589–594 (2007)
258. J.A. Gordon, R.W. Ziolkowski, The design and simulated performance of a coated nanoparticle laser. Opt. Express **15**, 2622–2653 (2007)
259. D.J. Bergman, D. Stroud, Theory of resonances in the electromagnetic scattering by macroscopic bodies. Phys. Rev. B **22**, 3527–3539 (1980)
260. E. Plum, V.A. Fedotov, P. Kuo, D.P. Tsai, N.I. Zheludev, Towards the lasing spaser: controlling metamaterial optical response with semiconductor quantum dots. Opt. Express **17**, 8548–8551 (2009)
261. J. Seidel, S. Grafstroem, L. Eng, Stimulated emission of surface plasmons at the interface between a silver film and an optically pumped dye solution. Phys. Rev. Lett. **94**, 177401-1-4 (2005)
262. M.A. Noginov, G. Zhu, M. Mayy, B.A. Ritzo, N. Noginova, V.A. Podolskiy, Stimulated emission of surface plasmon polaritons. Phys. Rev. Lett. **101**, 226806-1-4 (2008)
263. K. Li, X. Li, M.I. Stockman, D.J. Bergman, Surface plasmon amplification by stimulated emission in nanolenses. Phys. Rev. B **71**, 115409-1-4 (2005)
264. Z.G. Dong, H. Liu, T. Li, Z.H. Zhu, S.M. Wang, J.X. Cao, S.N. Zhu, X. Zhang, Resonance amplification of left-handed transmission at optical frequencies by stimulated emission of radiation in active metamaterials. Opt. Express **16**, 20974–20980 (2008)

265. M. Wegener, J.L. Garcia-Pomar, C.M. Soukoulis, N. Meinzer, M. Ruther, S. Linden, Toy model for plasmonic metamaterial resonances coupled to two-level system gain. Opt. Express **16**, 19785–19798 (2008)
266. A. Fang, T. Koschny, M. Wegener, C.M. Soukoulis, Self-consistent calculation of metamaterials with gain. Phys. Rev. B (Rapid Commun.) **79**, 241104(R)-1-4, (2009)
267. S. Wuestner, A. Pusch, K.L. Tsakmakidis, J.M. Hamm, O. Hess, Overcoming losses with gain in a negative refractive index metamaterial. Phys. Rev. Lett. **105**, 127401-1-4 (2010)
268. S.W. Chang, C.Y.A. Ni, S.L. Chuang, Theory for bowtie plasmonic nanolasers. Opt. Express **16**, 10580–10595 (2008)
269. N.I. Zheludev, S.L. Prosvirnin, N. Papasimakis, V.A. Fedotov, Lasing spaser. Nat. Photonics **2**, 351–354 (2008)
270. I.E. Protsenko, A.V. Uskov, O.A. Zaimidoroga, V.N. Samoilov, E.P. O'Reilly, Dipole nanolaser. Phys. Rev. A **71**, 063812 (2005)
271. M. Ambati, S.H. Nam, E. Ulin-Avila, D.A. Genov, G. Bartal, X. Zhang, Observation of stimulated emission of surface plasmon polaritons. Nano Lett. **8**, 3998–4001 (2008)
272. Z.K. Zhou, X.R. Su, X.N. Peng, L. Zhou, Sublinear and superlinear photoluminescence from Nd doped anodic aluminum oxide templates loaded with Ag nanowires. Opt. Express **16**, 18028–18033 (2008)
273. M.A. Noginov, V.A. Podolskiy, G. Zhu, M. Mayy, M. Bahoura, J.A. Adegoke, B.A. Ritzo, K. Reynolds, Compensation of loss in propagating surface plasmon polariton by gain in adjacent dielectric medium. Opt. Express **16**, 1385–1392 (2008)
274. P.M. Bolger, W. Dickson, A.V. Krasavin, L. Liebscher, S.G. Hickey, D.V. Skryabin, A.V. Zayats, Amplified spontaneous emission of surface plasmon polaritons and limitations on the increase of their propagation length. Opt. Lett. **35**, 1197–1199 (2010)
275. M.A. Noginov, G. Zhu, M. Bahoura, J. Adegoke, C. Small, B.A. Ritzo, V.P. Drachev, V.M. Shalaev, The effect of gain and absorption on surface plasmons in metal nanoparticles. Appl. Phys. B **86**, 455–460 (2007)
276. M.A. Noginov, Compensation of surface plasmon loss by gain in dielectric medium. J. Nanophotonics **2**, 021855-1-17 (2008)
277. I.D. Leon, P. Berini, Amplification of long-range surface plasmons by a dipolar gain medium. Nat. Photonics **4**, 382–387 (2010)
278. K. Ding, Z.C. Liu, L.J. Yin, M.T. Hill, M.J.H. Marell, P.J. van Veldhoven, R. Noetzel, C.Z. Ning, Room-temperature continuous wave lasing in deep-subwavelength metallic cavities under electrical injection. Phys. Rev. B **85**, 041301-1-5 (2012)
279. K. Ding, L. Yin, M.T. Hill, Z. Liu, P.J. van Veldhoven, C.Z. Ning, An electrical injection metallic cavity nanolaser with azimuthal polarization. Appl. Phys. Lett. **102**, 041110-1-4 (2013)
280. K. Ding, M.T. Hill, Z.C. Liu, L.J. Yin, P.J. van Veldhoven, C.Z. Ning, Record performance of electrical injection sub-wavelength metallic-cavity semiconductor lasers at room temperature. Opt. Express **21**, 4728–4733 (2013)
281. J.K. Kitur, G. Zhu, A.B. Yu, M.A. Noginov, Stimulated emission of surface plasmon polaritons on smooth and corrugated silver surfaces. J. Opt. **14**, 114015-1-8 (2012)
282. C.Y. Wu, C.T. Kuo, C.Y. Wang, C.L. He, M.H. Lin, H. Ahn, S. Gwo, Plasmonic green nanolaser based on a metal-oxide-semiconductor structure. Nano Lett. **11**, 4256–4260 (2011)
283. Y.-J. Lu, J. Kim, H.-Y. Chen, C. Wu, N. Dabidian, C.E. Sanders, C.-Y. Wang, M.-Y. Lu, B.-H. Li, X. Qiu, W.-H. Chang, L.-J. Chen, G. Shvets, C.-K. Shih, S. Gwo, Plasmonic nanolaser using epitaxially grown silver film. Science **337**, 450–453 (2012)
284. R.F. Oulton, V.J. Sorger, D.A. Genov, D.F.P. Pile, X. Zhang, A hybrid plasmonic waveguide for subwavelength confinement and long-range propagation. Nat. Photonics **2**, 496–500 (2008)
285. D. Li, M.I. Stockman, Electric spaser in the extreme quantum limit. Phys. Rev. Lett. **110**, 106803-1-5 (2013)
286. R.H. Brown, R.Q. Twiss, A test of a new type of stellar interferometer on sirius. Nature **178**, 1046–1048 (1956)
287. A.L. Schawlow, C.H. Townes, Infrared and optical masers. Phys. Rev. **112**, 1940 (1958)

288. S. Kna-Cohen, P.N. Stavrinou, D.D.C. Bradley, S.A. Maier, Confined surface plasmon-polariton amplifiers. Nano Lett. **13**, 1323–1329 (2013)
289. K. Kneipp, M. Moskovits, H. Kneipp (eds.), *Surface Enhanced Raman Scattering: Physics and Applications* (Springer, Heidelberg, 2006)
290. J. Kneipp, H. Kneipp, B. Wittig, K. Kneipp, Novel optical nanosensors for probing and imaging live cells. Nanomed.: Nanotechnol. Biol. Med. **6**, 214–226 (2010)
291. F.J. Dunmore, D.Z. Liu, H.D. Drew, S. Dassarma, Q. Li, D.B. Fenner, Observation of below-gap plasmon excitations in superconducting $YBa_2Cu_3O_7$ films. Phys. Rev. B **52**, R731–R734 (1995)
292. D. Schumacher, C. Rea, D. Heitmann, K. Scharnberg, Surface plasmons and Sommerfeld-Zenneck waves on corrugated surfaces: application to High-T_c superconductors. Surf. Sci. **408**, 203–211 (1998)
293. A. Tsiatmas, A.R. Buckingham, V.A. Fedotov, S. Wang, Y. Chen, P.A.J. de Groot, N.I. Zheludev, Superconducting plasmonics and extraordinary transmission. Appl. Phys. Lett. **97**, 111106-1-3 (2010)
294. A. Boltasseva, H.A. Atwater, Low-loss plasmonic metamaterials. Science **331**, 290–291 (2011)
295. V.M. Shalaev, Optical negative-index metamaterials. Nat. Photonics **1**, 41–48 (2007)
296. N.I. Zheludev, A roadmap for metamaterials. Opt. Photonics News **22**, 30–35 (2011)
297. M.I. Stockman, K.B. Kurlayev, T.F. George, Linear and nonlinear optical susceptibilities of Maxwell Garnett composites: dipolar spectral theory. Phys. Rev. B **60**, 17071–17083 (1999)
298. S. Xiao, V.P. Drachev, A.V. Kildishev, X. Ni, U.K. Chettiar, H.-K. Yuan, V.M. Shalaev, Loss-free and active optical negative-index metamaterials. Nature **466**, 735–738 (2010)
299. Z. Gryczynski, O.O. Abugo, J.R. Lakowicz, Polarization sensing of fluorophores in tissues for drug compliance monitoring. Anal. Biochem. **273**, 204–211 (1999)
300. R. Merlin, Metamaterials and the Landau-Lifshitz permeability argument: large permittivity begets high-frequency magnetism. Proc. Natl. Acad. Sci. USA **106**, 1693–1698 (2009)
301. N. Meinzer, M. Ruther, S. Linden, C.M. Soukoulis, G. Khitrova, J. Hendrickson, J.D. Olitzky, H.M. Gibbs, M. Wegener, Arrays of Ag split-ring resonators coupled to InGaAs single-quantum-well gain. Opt. Express **18**, 24140–24151 (2010)
302. E. Kretschmann, H. Raether, Radiative decay of nonradiative surface plasmons excited by light. Z. Naturforsch. A **23**, 2135–2136 (1968)
303. E. Heydari, R. Flehr, J. Stumpe, Influence of spacer layer on enhancement of nanoplasmon-assisted random lasing. Appl. Phys. Lett. **102**, 133110–4 (2013)
304. J.K. Kitur, V.A. Podolskiy, M.A. Noginov, Stimulated emission of surface plasmon polaritons in a microcylinder cavity. Phys. Rev. Lett. **106**, 183903-1-4 (2011)
305. O. Hess, S. Wuestner, A. Pusch, K.L. Tsakmakidis, J.M. Hamm, Gain and plasmon dynamics in active negative-index metamaterials. Phil. Trans. R. Soc. A **369**, 3525–3550 (2011)
306. F. Bloch, Über die quantenmechanik der elektronen in kristallgittern. Z. Phys. A **52**, 555–600 (1929)
307. H. Ghafouri-Shiraz, *Distributed Feedback Laser Diodes and Optical Tunable Filters* (Wiley, West Sussex, 2003)
308. P.W. Anderson, Absence of diffusion in certain random lattices. Phys. Rev. **109**, 1492–1505 (1958)

Chapter 2
Plasmonics for Enhanced Vibrational Signatures

Katrin Kneipp, Harald Kneipp and Janina Kneipp

Abstract Vibrational signatures provide key information on the molecular composition of matter and on molecular structure and structural changes. Vibrational transitions in molecules can be probed optically by infrared absorption (IRA) and Raman scattering (RS). Exploiting local optical fields in the vicinity of plasmonic nanostructures has revolutionized optics and spectroscopy and opens up exciting new capabilities, particularly also for vibrational spectroscopy. The basic prerequisites for plasmon-supported spectroscopy are strongly enhanced and highly confined local optical fields in the wavelength range applied in the respective spectroscopic method. Here, we review plasmon supported linear and non-linear vibrational spectroscopies. Our discussion includes incoherent effects such as surface enhanced Raman scattering (SERS), surface enhanced pumped anti-Stokes Raman scattering (SEPARS), surface enhanced hyper Raman scattering (SEHRS), and surface enhanced infrared absorption (SEIRA), as well as coherent Raman techniques such as surface enhanced coherent anti-Stokes Raman scattering (SECARS) and surface enhanced stimulated Raman scattering (SESRS). Emphasis will be placed on materials and nanostructures that efficiently support various vibrational spectroscopic methods. Selected applications of surface enhanced vibrational spectroscopy for chemical probing and sensing will be discussed.

Keywords Surface plasmon · Raman scattering · SERS

K. Kneipp (✉) · H. Kneipp
Physics Department, Danmarks Tekniske Universitet, 2800 Lyngby, Denmark
e-mail: kneipp@usa.net

J. Kneipp
Chemistry Department, Humboldt Universität zu Berlin, 12489 Berlin, Germany
e-mail: janina.kneipp@chemie.hu-berlin.de

J. Kneipp
BAM Federal Institute for Materials Research and Testing, 12489 Berlin, Germany

T. V. Shahbazyan and M. I. Stockman (eds.), *Plasmonics: Theory and Applications*,
Challenges and Advances in Computational Chemistry and Physics 15,
DOI: 10.1007/978-94-007-7805-4_2, © Springer Science+Business Media Dordrecht 2013

2.1 Introduction

Building blocks of matter such as atoms in a molecule are in periodic motion and exhibit intrinsic vibrational modes. Typical vibrational frequencies range from approximately 10^{14} Hz ($\sim$3,000 cm^{-1}) for vibrations involving light atoms such as C-H groups down to the THz range ($<$100 cm^{-1}) corresponding, for example, to motions of sub-domains in proteins [1, 2]. Spectroscopic observation of vibrational modes provides a non-invasive key to the chemical composition and structure of matter. Applying vibrational spectroscopies to small quantities of matter at nanoscale dimensions and at single molecule level is a great challenge [3]. It can be met by combining vibrational spectroscopy with plasmonics and performing vibrational spectroscopy in enhanced local fields in the vicinity of plasmonic structures [4–7].

Figure 2.1 shows different processes that can be employed in vibrational spectroscopy. Molecular vibrations accompanied by changes of a dipole moment can be directly accessed by the absorption of infrared photons at the energy of the molecular vibration $h\nu_M$. Alternatively, photons can be scattered inelastically on the vibrational quantum states. As a consequence of this so-called Raman scattering process incident photons $h\nu_L$ lose energy by exciting vibrational quanta at energy $h\nu_M$, and the scattered light appears at a lower (Stokes) frequency $\nu_S = \nu_L - \nu_M$. By interacting with a molecule in an excited vibrational state, incoming photons gain energy from molecular vibrations, and the scattering signal appears at higher (anti-Stokes) frequency $\nu_{aS} = \nu_L + \nu_M$. Probing of vibrational modes by Raman scattering requires changes of polarizability α with the vibrational coordinate Q. At extremely high intensities, two photons can be simultaneously scattered by a molecular vibration. This scattering process, called hyper Raman scattering (HRS) results in an incoherent Raman signal ν_{hS} shifted relative to the twice of the excitation frequency ν_L with $\nu_{hS} = 2\nu_L - \nu_M$ or, for anti-Stokes hyper Raman scattering $\nu_{haS} = 2\nu_L + \nu_M$ [8, 9]. Following one- and two-photon excitation, respectively, the spontaneous Raman- and hyper Raman scattering processes generate an incoherent Raman signal.

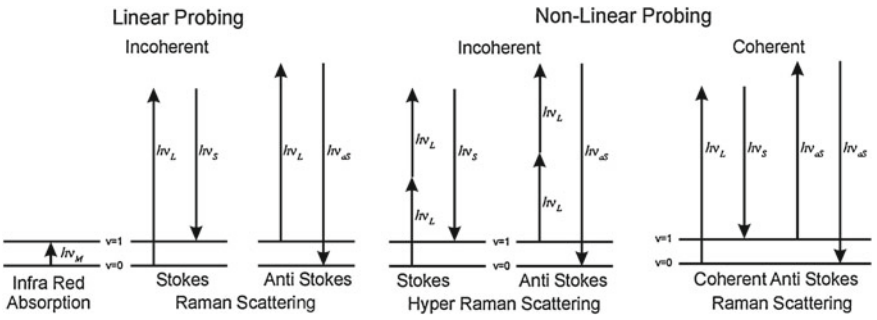

Fig. 2.1 Spectoscopic methods for probing vibrational transitions displayed in an energy level diagram, v= 0 and v= 1 are vibrational ground and first excited vibrational states

In addition to incoherent, spontaneous Raman scattering, vibrational modes can be probed by coherent Raman processes, also called stimulated, Raman scattering. There, molecular vibrations are coherently driven by two interacting fields at frequency differences that match vibrational transitions [10, 11]. In coherent Raman probing, vibrational information appears in strong and directed coherent optical signals. This makes coherent Raman scattering attractive for fast collection of vibrational information and for vibrational imaging [12]. Moreover, time resolved coherent Raman techniques, such as impulsive stimulated Raman spectroscopy or femtosecond stimulated Raman spectroscopy can provide information on the pathways and dynamics of chemical reactions, as they allow to monitor vibrational signatures of intermediate structures with ultrafast time resolution [13–16].

In this article, we focus on *surface enhanced* vibrational spectroscopy exploiting enhanced local fields of plasmonic structures. In Sect. 2.2, we introduce the incoherent effects of surface enhanced Raman scattering (SERS), surface enhanced infrared-absorption SEIRA, surface enhanced pumped anti- Stokes scattering (SEPARS), and surface enhanced hyper Raman scattering (SEHRS). There, we also explain the coherent Raman techniques of surface enhanced coherent anti-Stokes Raman scattering (SECARS) and surface enhanced stimulated Raman scattering (SESRS), and summarize some important features of these plasmonic supported optical effects. In Sect. 2.3, we discuss important properties of plasmonic nanostructures and conditions suitable for enhancing different vibrational spectra obtained in different wavelength ranges. In Sect. 2.4, we illustrate the capabilities of plasmon supported vibrational spectroscopy by selected applications, in particular ultrasensitive SEIRA of protein monolayers, monitoring of catalytic reactions on composite nanostructures with SERS, and a new class of nanosensors and labels based on SERS-, SEHRS- or SECARS signals. These examples illustrate how plasmonics transforms vibrational spectroscopy from a method for chemical structure analysis to a versatile tool providing information on chemical structures and processes along with ultrasensitive detection limits and nanoscale confinement of spectroscopic information. Section 2.5 gives a brief summary and outlook to potential future developments in the field.

2.2 “Normal” and “Surface-Enhanced” Vibrational Spectroscopy

Vibrational modes can be probed based on absorption and inelastic scattering of photons, as discussed above. Due to the Raman scattering process, vibrational information occurring in the infrared range of the spectrum is transferred to the visible, NIR, or UV range, respectively, depending on the excitation wavelength applied. Figure 2.1 illustrates some of the different spectroscopic methods for vibrational probing in an energy level diagram. Usually, in Raman scattering, excitation and/or scattered photons are not in resonance with any real molecular electronic transition (see Fig. 2.1). In contrast, in resonance Raman scattering (RRS), the excitation laser,

and often also the Raman scattered photons, match electronic transitions in the molecule. This gives rise to a stronger Raman signal for those vibrational modes which are related to the electronic transition. But, fluorescence may be excited at the same time, together with the Raman scattering, and the strong fluorescence signal can interfere with the Raman Stokes light.

A critical parameter that determines the applicability of a spectroscopic effect for structural probing is its cross section. Raman cross sections range from 10^{-31} to 10^{-29} cm^2 per molecule. In the case of RRS, cross sections become typically 2–6 orders of magnitude larger. Infrared absorption appears at cross sections from 10^{-22} up to 10^{-20} cm^2, i.e. about 10 orders of magnitude larger than non-resonant Raman cross sections. Overall, even the best cross sections achievable for vibrational spectroscopy are still orders of magnitude below those used in electronic absorption and in fluorescence which can be typically obtained at cross sections of 10^{-17}–10^{-16} cm^2. Despite the high molecular structural information content in vibrational spectra, the low cross sections, particularly those of Raman scattering, represent a considerable disadvantage for all applications of vibrational spectroscopy. This applies particularly for two-photon excitation. Cross sections on the order of 10^{-65} cm^4 s/photon for HRS—compared to 10^{-50} cm^4 s/photon typical of two-photon fluorescence—make the utilization of HRS as a practical spectroscopic tool nearly impossible. This situation has changed dramatically during the last 15 years. Exciting opportunities for gaining and improving vibrational signals arise, when spectroscopy takes place in strongly enhanced local optical fields of plasmonic nanostructures [4, 17, 18]. Field enhancement in such metal structures can be understood in terms of resonant excitation of high-Q-factor surface plasmon polaritons or/and by field concentration due to the lightening rod effect [19]. Some effects and observations exploiting enhanced optical fields, can be explained by looking at metal nanostructures as optical nanoantenna which can direct and further enhance local optical fields. [20, 21]. We discuss "surface enhancement" for different vibrational spectroscopic methods in more detail in the following sections.

2.2.1 Surface Enhanced Raman Scattering

Surface-enhanced Raman scattering (SERS) is probably the most prominent observation to demonstrate the capabilities of plasmon supported spectroscopy.

In analogy to normal, non-surface–enhanced Raman scattering, the number of Stokes photons per second n_S^{SERS} in surface-enhanced Raman scattering can be calculated as

$$n_S^{SERS} = N_0 \sigma^{SERS} n_L \tag{2.1}$$

where σ_S^{SERS} describes an effective cross section of the surface enhanced Raman process, S denotes the Stokes scattering. n_L is the Photon flux density of the excitation laser. N_0 is the number of molecules in the vibrational ground state, which are involved in the SERS Stokes process. The cross section for Raman scattering is

proportional to the square of the change of polarizability α with the vibrational coordinate Q. It is generally agreed that both so-called "electromagnetic" field enhancement effects and "chemical first layer" effects contribute to surface enhanced Raman signals [22]. The chemical effects include enhancement mechanism(s) of the Raman signal that can be explained in terms of specific interactions, i.e. electronic coupling between molecule and metal [23–25], resulting in a larger Raman cross section of the adsorbed molecule $\sigma^{RS}{}_{ads}$ compared to that of the molecule without coupling to the metal $\sigma^{RS}{}_{free}$. The electromagnetic field enhancement arises from the enhanced local optical field at the location of the molecule in the vicinity of a plasmonic nanostructure [18, 26, 27]. It can be described by field enhancement factors A(ν). Using these field enhancement factors for the excitation and scattered fields, an effective SERS cross section can be written as

$$\sigma^{SERS} = \sigma^{RS}_{ads} \left|A\left(\nu_L\right)\right|^2 \left|A\left(\nu_S\right)\right|^2 \tag{2.2}$$

with

$$\left|A\left(\nu\right)\right|^2 = \frac{\left|E\left(\nu\right)\right|^2}{\left|E^{(0)}\left(\nu\right)\right|^2} \tag{2.2a}$$

where E(ν) is the local optical field (laser and the scattered field, respectively), and $E^{(0)}(\nu)$ are the same fields in the absence of the metal nanostructures.

The SERS enhancement factor G_{SERS} for Stokes scattering is determined by the ratio of the effective SERS cross section σ^{SERS} to the normal Raman cross section $\sigma^{RS}{}_{free}$

$$G_{SERS} = \frac{\sigma^{RS}_{ads}}{\sigma^{RS}_{free}} \left|A\left(\nu_L\right)\right|^2 \left|A\left(\nu_S\right)\right|^2 \tag{2.3}$$

The first term in formula (2.3), $\sigma^{RS}{}_{ads}/\sigma^{RS}{}_{free}$, describes the chemical enhancement effect. Chemical SERS enhancement factors may contribute to the total SERS enhancement at a factor of 10 to 1,000. The second two terms describe the local field enhancement effect for the excitation and scattered fields, respectively. Both incoming excitation light and scattered light are enhanced, and—assuming the field enhancement being roughly the same for the excitation and scattering frequency—the electromagnetic enhancement scales roughly with the field enhancement factor to the power of four. Numerous experimental and theoretical studies show that local field enhancement constitutes the major contribution to the SERS effects by providing enhancement factors up to 10^{12}. With a contribution of an enhancement factor of $\sim 10^2$ due to a chemical SERS effect, total SERS enhancement factors can be on the order of 10^{14}. This brings typical non-resonant Raman cross sections to effective SERS cross sections on the order of 10^{16} cm^2.

2.2.2 Surface Enhanced Infrared Absorption

In principle, all photon-driven processes should benefit from enhanced local optical fields, and in fact, successful attempts to increase IR absorption signals were reported only a few years after the discovery of SERS [28]. The sensitivity of infrared (IR) vibration spectroscopy can be enhanced by several orders of magnitude if plasmonic electromagnetic nearfield enhancement is exploited. In contrast to scattering, where at least two photons are involved, SEIRA signals, as the result of a one-photon absorption process, benefit from local field enhancement $A(\nu)$ only to the power of two. The enhancement factor for infrared absorption can be written as

$$G_{SEIRA} = \frac{\sigma_{ads}^{abs}}{\sigma_{free}^{abs}} \left| A\left(\nu_M\right) \right|^2 \tag{2.4}$$

with infrared absorption cross sections $\sigma^{abs}{}_{ads}$ and $\sigma^{abs}{}_{free}$ for the free and adsorbed molecule, respectively. $A(\nu_M)$ describes the enhancement of the infrared optical field at the frequency of the vibrational transition. The cross section of IR absorption is proportional to the square of the change of the dipole moment μ with the vibrational coordinate Q. By analogy with Raman scattering, we take into account that also IR absorption cross sections may differ for adsorbed and free molecules, i.e. there may exist also a chemical contribution to SEIRA. The key prerequisites for exploiting SEIRA in practical spectroscopy are structures which provide field enhancement also in the IR range. With the concept of a novel resonant mechanism involving the interference of a broadband plasmon with the narrowband vibration from molecules, enormous enhancement of the vibrational signals from less than one attomol of molecules on individual gold nanowires was experimentally demonstrated [29, 30]. The tailored gold nanowires act as plasmonic nanoantennas in the infrared. It was demonstrated that field enhancement in the IR range can be generated by nanoparticle arrays that display shifted and broad plasmon resonances in the near to mid-IR [7, 31, 32]. Best SEIRA enhancement factors have been reported to be $10^4 - 10^5$ [7, 30]. Another approach for generating enhanced and confined local fields in the IR range exploits resonances with phonon polaritons [33, 34]. Enhancement factors of 100 for IR absorption on polar dielectric silicon carbide nanoparticles have been reported [34].

2.2.3 Surface Enhanced Raman Scattering Using Two-Photon Excitation: Surface Enhanced Hyper Raman Scattering

Hyper Raman scattering results in incoherent Raman signals shifted relative to twice the excitation frequency (see also Fig. 2.1). Hyper Raman scattering is related to higher order terms in the induced dipole moment which become operative at high

optical field strength

$$P_{ind} = \alpha E + \beta EE + \cdots \tag{2.5}$$

with β as hyper polarizability. The first linear term including α describes linear Raman and Rayleigh scattering, the second term describes *hyper* Rayleigh and *hyper* Raman scattering. Hyper Raman scattering follows symmetry selection rules different from Raman scattering. Therefore, it can probe vibrations hat are forbidden in Raman scattering [8, 9].

As a non-linear, two-photon excited process, HRS depends on the excitation photon flux density n_{L} to the power of two. In analogy to Eq. (2.1) , the number of surface-enhanced hyper Raman Stokes photons n^{SEHRS} can be calculated as

$$n^{SEHRS} = N_0 \sigma^{SEHRS} n_L^2 \tag{2.6}$$

where σ^{SEHRS} is the effective cross section of the surface-enhanced hyper Raman process.

HRS can be enhanced in an analogous fashion to normal Raman scattering by a chemical effect and by enhancement of the optical fields when the molecule is in close proximity of metallic nanostructures. The effective surface-enhanced hyper Raman cross section can be written as

$$\sigma^{SEHRS} = \sigma_{ads}^{HRS} \left|A\left(\nu_L\right)\right|^4 \left|A\left(\nu_{hS}\right)\right|^2 \tag{2.7}$$

where $\sigma^{\mathrm{HRS}}{}_{\mathrm{ads}}$ describes an "chemically" enhanced hyper Raman cross section compared to that of a "free" molecule, $\mathrm{A}(\nu)$ describe the enhancement of the optical fields at the excitation and hyper Raman scattered wavelengths, respectively. We can write an enhancement factor for SEHRS as

$$G_{SEHRS} = \frac{\sigma_{ads}^{HRS}}{\sigma_{free}^{HRS}} \left|A(\nu_L)\right|^4 \left|A(\nu_{HS})\right|^2 \tag{2.8}$$

Strong surface enhancement corresponding to the field enhancement factor to the power of six can overcome the inherently weak nature of hyper-Raman scattering and enable to measure hyper Raman spectra also at the anti-Stokes side [35].

Figure 2.2 displays Stokes and anti-Stokes hyper Raman spectra and illustrates the dependence of non-linear SEHRS signals on the excitation intensity to the power of two. Effective cross sections of SEHRS have shown to be on the order of $10^{-46} - 10^{-45}\,\mathrm{cm}^4\,\mathrm{s}$, comparable or even better than the best cross sections for two-photon fluorescence obtained so far. These cross sections enable the measurement of SEHRS spectra at excitation intensities of $10^6 - 10^7\,\mathrm{W}\,/\,\mathrm{cm}^{-2}$, conditions that can be easily achieved with mode-locked picosecond lasers under weak focusing conditions [36], and also in tightly focused continuous wave (cw) [37] or low-energy pulsed lasers [38].

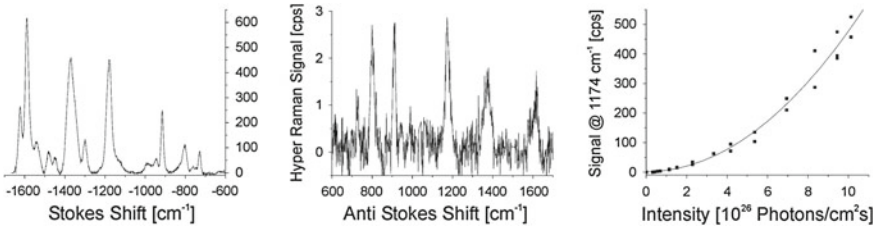

Fig. 2.2 **a** SEHRS Stokes and anti-Stokes spectra of crystal violet attached to silver nanoaggregates. The spectra were measured using 1,064 nm mode locked ps pulses at an average power of 40 mW. Anti-Stokes HRS can be observed because of the extremely high effective cross section of SEHRS. **b** The square-law dependence of the hyper Raman scattering signal on the excitation intensity verifies the two-photon process. *cps* counts per second (Reprinted with permission from [35])

2.2.4 Surface Enhanced Pumped Anti-Stokes Raman Scattering

Anti-Stokes Raman scattering starts from the first excited vibrational levels (see Fig. 2.1) and is proportional to the number of molecules in the first excited vibrational state N_1. This number N_1, relative to the number of molecules in the vibrational ground state N_0 is determined by the Boltzmann factor. This results in much weaker anti-Stokes Raman signals than Stokes signals. A strong surface-enhanced Raman Stokes process with an effective cross section σ^{SERS} populates the first excited vibrational levels in addition to thermal population [39–42], and results in an increase of anti- Stokes signals. Under stationary conditions and in a weakly saturating intensity regime ($\exp(-h\nu_M/kT) \leq \sigma_S^{\mathrm{SERS}}\, \tau_1\, n_L << 1$), the anti-Stokes signal n_{aS}^{SERS} can be estimated according to

$$n_{aS}^{SERS} = N_0 e^{-\frac{h\nu_M}{kT}} \sigma^{SERS} n_L + N_0 \left(\sigma^{SERS}\right)^2 \tau_1 n_L^2 \tag{2.9}$$

The first term describes anti-Stokes scattering related to thermal population of the first excited vibrational state. The second term describes an anti-Stokes signal related to a population of the first excited vibrational state due to "pumping" by a spontaneous Raman Stokes process, τ_1 is the lifetime of the excited vibrational state. Pumping of vibrational levels by a surface-enhanced Stokes process in the weakly saturating intensity regime gives rise to a quadratic dependence of the anti-Stokes signal on the excitation intensity. This nonlinear pumped anti- Stokes scattering can be described by an effective two-photon cross section σ^{SEPARS}.

$$\sigma^{SEPARS} = \left(\sigma^{SERS}\right)^2 \tau_1 \tag{2.10}$$

Assuming a SERS cross section of approximately $10^{-16}\,\mathrm{cm}^2$ and a vibrational life time on the order of 10 picoseconds, effective two-photon cross sections can be up to $10^{-43}\,\mathrm{cm}^4\,\mathrm{s}$. This is about seven orders of magnitude larger than typical cross sections for two-photon excited fluorescence. Moreover, anti-Stokes spectra provide

vibrational information at the high energy side of the excitation laser, which is free from disturbing fluorescence.

SEPARS generates an incoherent anti-Stokes signal. The large effective cross section can be explained by the nature of the process, which is a two-photon process using the vibrational level as a real intermediate state. The effective Raman cross section strongly benefits from enhanced local fields. In an analogous fashion to formula (2.2), we can split chemical and electromagnetic enhancement and write the effective surface-enhanced cross section for pumped anti-Stokes scattering as

$$\sigma^{SEPARS} = \left(\sigma_{ads}^{RS}\right)^2 \tau_1 \left|A\left(\nu_L\right)\right|^4 \left|A\left(\nu_S\right)\right|^2 \left|A\left(\nu_{aS}\right)\right|^2 \tag{2.11}$$

Pumped anti-Stokes Raman scattering benefits from enhanced local fields to the power of eight. Observing the effects of vibrational pumping without support of plasmonics means dealing with an effective cross section of 10^{-71} cm^4 s. Excitation intensities on the order of 10^{20} W/cm^2 would be required in order to bring the pumped anti-Stokes signal to the level of anti-Stokes scattering from thermally (room temperature) populated vibrational modes.

2.2.5 *Surface Enhanced Coherent or Stimulated Raman Scattering Methods*

The development of lasers has triggered the field of stimulated or coherent Raman spectroscopy, also called "active Raman spectroscopy" , in the seventies of the last century [43]. Coherent Raman methods came back to the focus of interest during the recent decade [10, 11, 44].

In stimulated or coherent Raman probing, two optical fields coherently drive a vibrational mode while one of these fields, or another third one, probes this coherent molecular vibration. The third-order non-linear susceptibility $X^{(3)}$, which enables the process, has resonances at the vibrational frequencies and therefore, by tuning the frequency differences between the lasers, on can probe the vibrational spectrum of a molecule.

There are different ways to perform coherent nonlinear Raman probing. The two mostly prominent coherent Raman methods are coherent anti-Stokes Raman spectroscopy (CARS) and stimulated Raman spectroscopy (SRS): During CARS, an excitation laser (v_L) and a Stokes laser (v_S) generate a coherent molecular vibration. The excitation laser is scattered again on this vibration and produces a coherent anti-Stokes signal. The nonlinear polarization, which is responsible for CARS can be written as

$$P^{CARS} \propto X^{(3)} E_L\left(\nu_L\right) E_L\left(\nu_L\right) E_S^*\left(-\nu_S\right) \tag{2.12a}$$

In contrast, so-called stimulated Raman spectroscopy (SRS) measures changes in the signal levels of the two lasers which occur due to their non-linear interaction.

The nonlinear polarization, which generates SRS is

$$P^{SRS} \propto \mathrm{X}^{(3)} E_L\,(\nu_L)\, E_L^*\,(-\nu_L)\, E_S\,(\nu_S) \tag{2.12b}$$

Stimulated Raman spectroscopy can be used in an enhancing or depletion modus by measuring an enhancement in the lower frequency "Stokes" laser field (stimulated Raman gain), or a depletion in the higher frequency "anti-Stokes" laser field (stimulated Raman loss or inverse Raman scattering), respectively [11, 14]. Whereas CARS requires additionally phase matching conditions between the interacting lasers, stimulated Raman spectroscopy always fulfills this momentum conservation automatically.

In the discussed coherent Raman processes, four interacting coherent optical fields can benefit from plasmonic enhancement. The enhancement factor for the coherent non-linear Raman processes can be written as

$$G_{SECARS} = \frac{(\mathrm{X}^{(3)}_{ads})^2}{(\mathrm{X}^{(3)}_{free})^2}\, |A\,(\nu_L)|^4\, |A\,(\nu_S)|^2\, |A\,(\nu_{aS})|^2 \tag{2.13a}$$

$$G_{SESRS} = \frac{|\mathrm{X}^{(3)}_{ads}|^2}{|\mathrm{X}^{(3)}_{free}|^2}\, |A\,(\nu_L)|^4\, |A\,(\nu_S)|^4 \tag{2.13b}$$

Here we consider that also the non-linear susceptibility can be different for adsorbed and "free" molecules.

There are some reports on experimental demonstration of surface enhanced coherent Raman spectroscopy (SECARS) [45–50]. Silver nanoparticle aggregates, silver films and nanostructured gold surfaces were used as plasmonic enhancing structures. SECARS enhancement factors exceeding five orders of magnitude have been observed [49]. Recently, surface enhanced femtosecond stimulated Raman spectroscopy has been reported exploiting gold nanoantenna with embedded Raman molecules. Using a picosecond Raman and femtosecond probe pulse, the time- and ensemble averaged enhancement factor was estimated in the range from $10^4 - 10^6$ [51].

Figure 2.3 summarizes different plasmon supported spectroscopic methods for vibrational probing. Note that in incoherent probing, spectroscopic signals linearly depend on the number of molecules while coherent Raman signals show a quadratic dependence. In general, field enhancement factors $\mathrm{A}(\nu)$ depend on frequency. However, Raman shifts are relatively small and therefore, we can assume for SERS, SEPAS and SECARS that $\mathrm{A}(\mathrm{v_L}) \sim \mathrm{A}(\mathrm{v_S}) \sim \mathrm{A}(\mathrm{v_{aS}}) = \mathrm{A}(\nu)$. SEIRA, SERS and SEHRS depend on field enhancement factors $\mathrm{A}(\nu)$ to the power of two, four and six respectively, while SEPARS, SECARS, and SESRS benefit from $\mathrm{A}(\nu)$ to the power of eight.

For supporting different vibrational spectroscopic methods, field enhancement is required within very different wavelength ranges including IR and THz frequencies

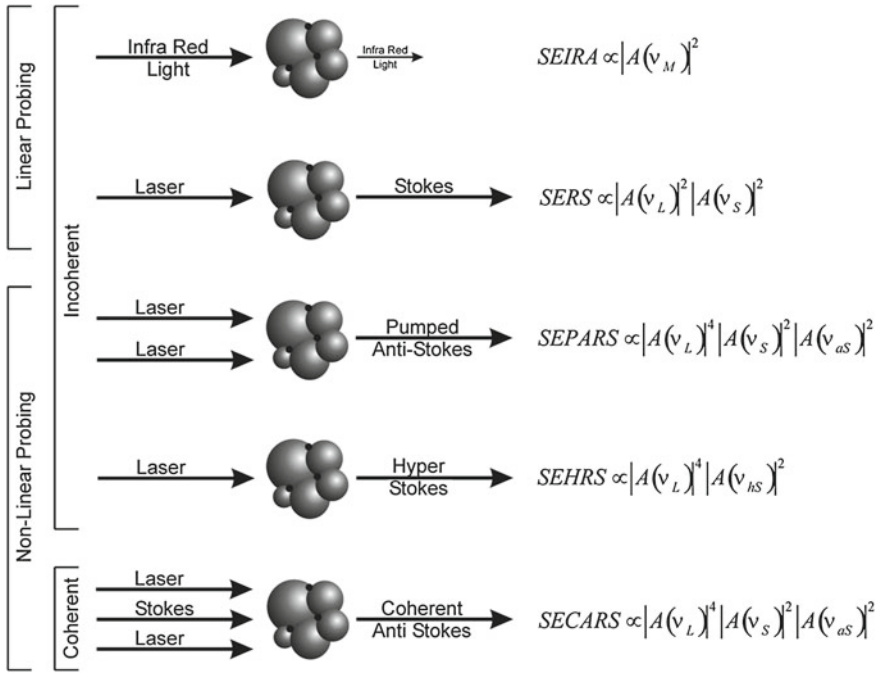

Fig. 2.3 Surface enhanced vibrational spectroscopies and their dependence on field enhancement factors A(ν)

for SEIRA and near infrared, visible or near ultraviolet frequencies for linear and non-linear (resonance) Raman scattering. For SEHRS, optimum structures should provide high enhancement in two relatively widely separated ranges of the electromagnetic spectrum. In the Sect. 2.3, we discuss basic requirements for plasmonic nanostructures suitable for surface enhanced vibrational spectroscopy.

2.3 Plasmonic Nanstructures for Supporting Vibrational Spectroscopy

The basic property of enhancing plasmonic structures is their capability to generate spatially confined and enhanced fields due to resonances with the collective oscillations of the free conduction electrons in the metal, so-called surface plasmons. This requires nanostructures with plasmon resonances in different ranges in the electromagnetic spectrum. Moreover, in order to achieve high enhancement levels, the plasmonic elements should have high Q-factors. For a modern summary about the field of nanoplasmonics, see e.g. [19, 52–55]. The existence of surface plasmons strongly depends on the dielectric constants of the metal ε_m and requires negative

real part of the complex dielectric constant, $\mathrm{Re}\,\varepsilon_m < 0$. High Q-factors, i.e. small damping requires small imaginary parts of ε_m. Gold, silver and also copper fulfil these requirements in the visible and near infrared range. Silver and gold are the most common materials in plasmon supported optics and spectroscopy. There is a strong interest in extending the working range of plasmonics by looking for new materials. For an overview of plasmonic materials see [56].

Properties of surface plasmons and related local optical fields in the vicinity of plasmonic structures are not only determined by their material properties, but also by the morphology of the structures. For example, so-called hot spots which provide extremely strong SERS enhancement always exist for aggregates formed by silver or gold nanoparticles but not for isolated particles [57, 58]. For illustration, Fig. 2.4 compares SERS experiments performed on isolated gold nanospheres and on small aggregates formed by these spheres.

In agreement with theory, enhancement factors for isolated gold spheres have been inferred to be $10^3 - 10^4$ by comparing surface enhanced Raman signals with non-surface enhanced standards. These SERS enhancement factors are too small to measurably populate the first excited vibrational state and the anti-Stokes spectrum appears at the expected relatively low signal level (Fig. 2.4b). In particular, the high frequency modes are not seen on the anti-Stokes side due to their low thermal population. This situation changes when the particles form aggregates. Now a strong anti-Stokes signals appears, in particular also for higher frequency Raman modes. This is an indication of a very strong Raman process that populates the first excited vibrational state. The difference in SERS enhancement levels for isolated

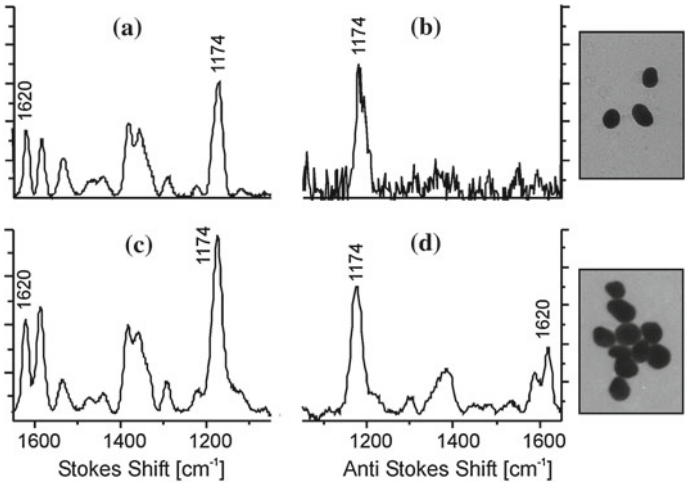

Fig. 2.4 Stokes and anti-Stokes SERS spectra of crystal violet attached to isolated and aggregated gold nanospheres. Strong anti-Stokes signals for aggregated spheres indicate population of first excited vibrational states beyond Boltzmann distribution. This population pumping due to a very strong SERS Stokes process indicates a dramatic increase in local field enhancement for nanoparticle aggregates versus isolated particles (Reprinted with permission from [58])

gold nanoparticles and aggregates can be up to 10 orders of magnitude. Isolated silver nanoparticles and silver nanoaggregates show basically the same behavior [59, 60]. The dramatic increase in field enhancement level can be explained by the interaction and hybridization of plasmons in adjacent nanoparticles [55]. Plasmonic field enhancement exhibits particularly exciting properties for fractal metallic nanostructures [61–64].

Surface plasmon resonances for isolated particles strongly depend on their shape and size. Advances in a controlled production of gold and silver nanoparticles make it possible to tune their plasmon resonances over wide ranges in the visible and NIR. Figure 2.5 summarizes representative tuning ranges for selected gold- and silver nanostructures [65].

While plasmon resonances mainly cover the range between near ultraviolet (UV) and near IR, further developing of SEIRA as a spectroscopic tool requires nanostructures which provide high field enhancement in the IR range. Nanoshells are very interesting "single-particle" plasmonic structures exhibiting well-defined tunable plasmon resonances over wide energy ranges down to the IR [66]. These structures are of particular interest for the design of enhancing structures for SEIRA experiments [31, 55, 67]. Also metal nanowires provide sufficiently strong antenna-like plasmonic resonances in the IR [29]. The resonance of the antenna can be adjusted to the molecular vibration frequencies by changing the wire length. Arrays where antennae can couple via nanogaps have been suggested and demonstrated as structures which provide strong electromagnetic enhancement in the IR range [7, 30]. Vibration-signal enhancement up to 500,000 have been obtained for molecular monolayers adsorbed on gold nanowires.

Another methodological challenge in vibrational spectroscopy is plasmonic supported (resonance) Raman scattering using ultraviolet light for excitation. The exten-

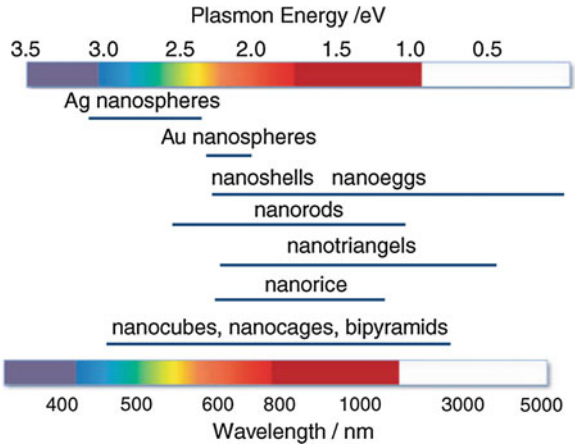

Fig. 2.5 Spectral dependence of the plasmon resonance of differently shaped silver and gold nanoparticles (Reprinted with permission from [65])

sion of SERS studies to the ultraviolet region, i.e. UV-SERS would offer interesting capabilities, particularly for supporting UV resonance Raman studies in biosciences [68, 69]. Aluminium has been considered as one of the best candidates for enhancing local fields in the UV region [70]. It has been experimentally demonstrated that Al triangular nanoparticle arrays can support plasmon resonances that are tunable throughout the visible and into the UV portion of the spectrum [71]. UV-SERS using ordered Al nanohole arrays are theoretically proposed and simulated by using FDTD method [72]. SERS spectra observed from crystal violet on aluminium using 244 nm excitation have been reported [73]. Surface-enhanced Raman scattering in the ultraviolet spectral region was also observed on rhodium and ruthenium electrodes [74].

Non-linear vibrational probing, such as hyper Raman spectroscopy can require plasmonic support in very different frequency ranges since the scattering signals appears shifted relatively to the second harmonic frequency of the excitation laser. The problem can be addressed by using enhancing structure that exhibit plasmon excitations over a wide spectral range. For example, silver aggregate structures can show a broad plasmon spectrum from 400 to 1,200 nm which covers all optical fields participating in the non-linear Raman effect [75, 76]. Another approach for dealing with different optical frequencies in non-linear effects employs antenna elements with different resonance wavelength matching the interacting optical fields [77]. The application of multifrequency gold nanowire antennas has been demonstrated in frequency conversion experiments.

2.4 Selected Applications of Surface Enhanced Vibrational Spectroscopy

2.4.1 SERS for Probing Catalytic Reactions

High molecular structural selectivity along with high detection sensitivity suggests surface enhanced vibrational spectroscopies as powerful methods for monitoring chemical processes and reactions.

Application of SERS for insight into catalytic processes requires bifunctional nanostructures that provide both plasmonic properties and the ability to act as catalyst. Direct observations of catalytic reactions have been reported by using composite nanoparticles with gold for plasmonic and Pt or Pd for catalytic function [78, 79].

In another experiment, gold nannoparticles and catalytic active Pt nanoparticles have been simultaneous immobilization on a glass surface, see schema a in Fig. 2.6 [80]. This approach combines the advantages of easy preparation without the need for synthesis of composite nanoparticles and high versatility regarding the choice of catalyst. The proximity of both types of nanoparticles enables interaction of the molecules with the platinum nanoparticles while they reside in the local optical fields provided by the localized surface plasmons of the gold nanoparticles. The

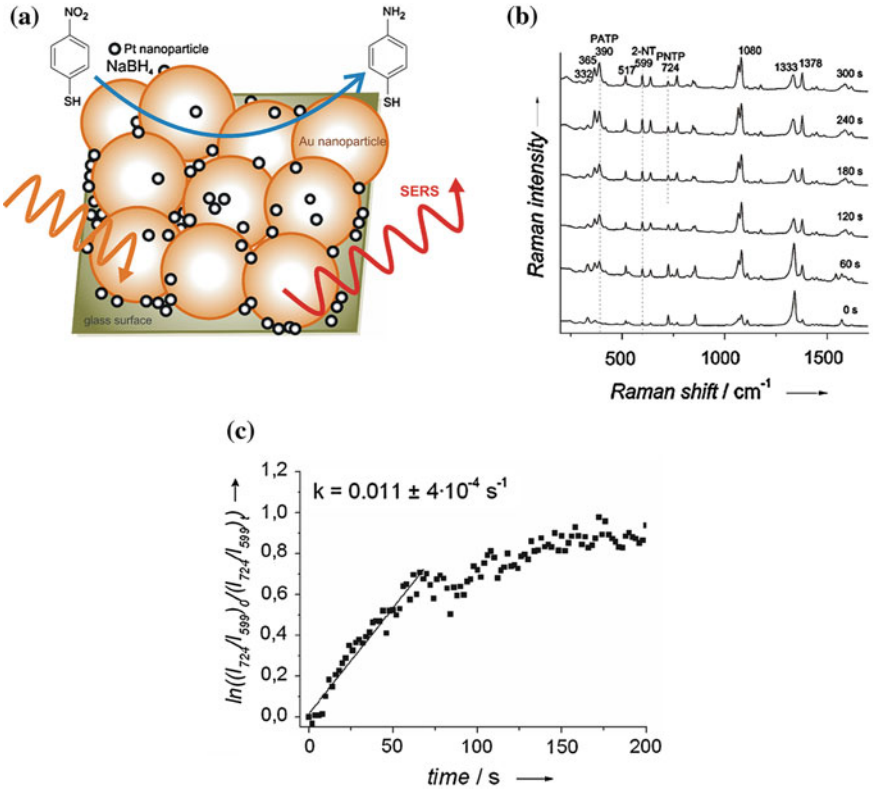

Fig. 2.6 SERS for probing the kinetics of nanoparticle-catalyzed reactions. **a** Schematic of a mix-and-match surface with immobilized gold and platinum nanoparticles. The reaction is catalyzed by the platinum nanoparticles, while the surface-enhanced Raman scattering (SERS) signal is brought about by local optical fields of the gold nanoparticles **b** SERS spectra for monitoring the reduction of *p*-nitrothiophenol (PNTP) by sodium borohydride to *p*-aminothiophenol (PATP), spectra were measured at different time points after the addition of sodium borohydride **c** Determination of rate constants for the reduction based on the intensity ratio of the band of PNTP at 724 cm^1 and of 2-NT at 599 cm^1 (Reprinted with permission from [80])

chemical species involved in the catalytic process can be characterized by their SERS features, see also Fig. 2.6b. To monitor the reaction over time, the relative intensity of typical SERS bands of the starting compound and the end product can be used for quantification, see Fig. 2.6c. Structural characterization of the species in the reaction and the rate constants are thus determined in the same experiment.

2.4.2 *Vibrational Spectroscopy of Protein Monolayers Using SEIRA*

Compared to SERS and particularly also compared to non-linear Raman methods, the electromagnetic contribution for SEIRA signals is "modest" since the effect is only proportional to the square of the field enhancement (see Fig. 2.3). However, IR absorption and Raman scattering follow different symmetry selection rules and can therefore probe different vibrational modes. For a comprehensive vibrational characterization, Raman scattering *and* IR absorption spectra are of interest.

As we have discussed, infrared absorption can be efficiently supported by nanoantenna arrays. The collective resonant excitation of the nanoantenna ensemble results in signal enhancement factors of $10^4 - 10^5$. This "collectively enhanced IR absorption" (CEIRA) spectroscopy technique allows direct identification of vibrational signatures of single protein monolayers of silk fibroin, see Fig. 2.7a. The ability to control the thickness of the silk protein films from several nanometers to several micrometers provides an opportunity to probe the near field behavior of the nanorod antenna by varying the film thickness. Due to the rapid decaying of the strongly enhanced near fields with distance from the nanorod surfaces saturation of the enhancement is expected to occur for films as thin as 40 nm. Figure 2.7b illustrates Amide-I and II vibrational modes of the protein back bone. These two vibrations also appear in the reflectance spectra shown in Fig. 2.7c. CEIRA is based on collective plasmonic excitations created by tailoring of the dipolar interactions in engineered nano-antenna arrays. The method allows detection of 300 zeptomoles of proteins for the entire array, corresponding to 145 molecules per antenna.

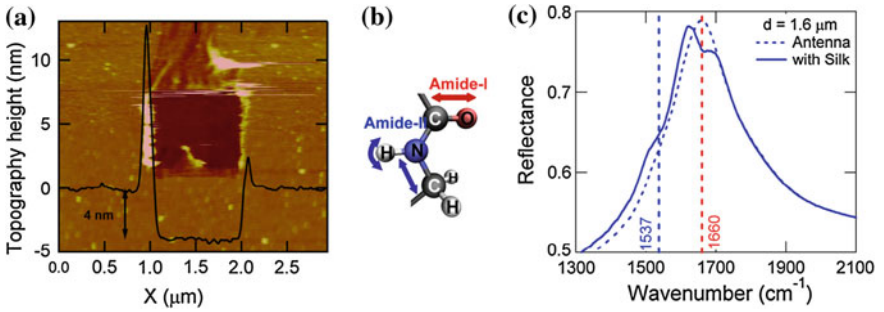

Fig. 2.7 Surface enhanced IR reflection absorption spectroscopy (IRRAS) of a single silk protein monolayer **a** Silk film thickness is measured by atomic force microscope for a 4 nm thick film. **b** Amide-I and II vibrational modes of the protein back bone. **c** Reflectance spectra from the nanoantenna array before (*dashed line*) and after coating of 2 nm thick protein film (*solid line*). *Dashed vertical lines* indicate the positions of the protein amide-I and II absorption peaks (Reprinted with permission from [7])

2.4.3 New Labels for Linear and Non-Linear Vibrational Probing and Imaging

During recent years, it has been demonstrated that surface-enhanced Raman scattering opens up exciting capabilities for creating new labels particularly for biosciences. Applications of SERS tags have been demonstrated for labeling DNA strands and proteins [81, 82], for in vivo imaging in a mice [83] and for probing and imaging in life cells [84, 85].

SERS labels consist of gold or silver nanoaggregates with an attached reporter species, e.g. a dye, see also Fig. 2.8. The labels are detected based on the SERS signature of the reporter molecule. Distinguishable spectral signatures even for similar reporter molecules enable a large pool of spectrally non-overlapping labels [3]. Since SERS works well with molecular non-resonant excitation, all labels can be used at the same excitation wavelength. Therefore, SERS labels benefit from real multiplexing capabilities.

As a particular advantage, SERS labels do not only highlight targeted structures through the specific reporter spectrum, SERS in the local optical fields of the gold or silver nanostructures also provides sensitive and spatially localized molecular

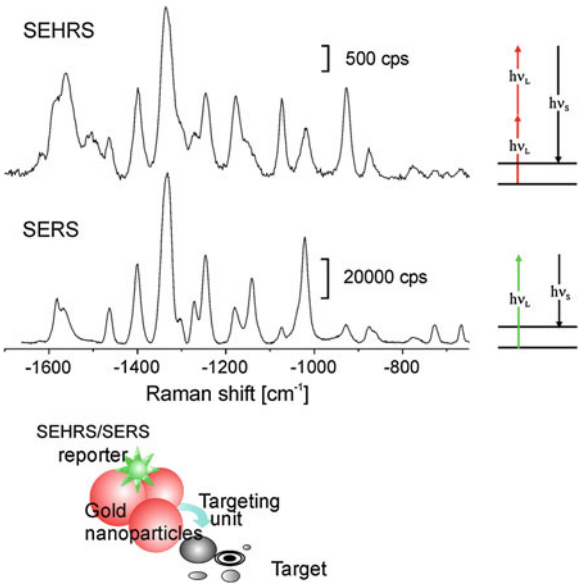

Fig. 2.8 Schematic of a multifunctional SERS label built from gold or silver nanoaggregates with an reporter molecule attached along with its one and two-photon excited spectral signature. The example shows SEHRS and SERS spectra from a label built from silver nanoaggregates with rose bengal as reporter molecule. Two-photon excited SEHRS spectra were measured using 1,064 nm mode locked ps pulses, one-photon excited SERS spectra were collected using 785 nm cw light (Reprinted with permission from [35])

structural information on the environment of the label [86]. Moreover, the SERS signature of a reporter molecule, attached to the gold nanoparticle, which exhibits a pH-sensitive Raman spectrum, can deliver information on the local pH-value in the surrounding of the label [87]. SERS labels can be functionalized (targeting unit) using specific linker in order to address specific molecules or structures.

Due to the plasmonic support, SERS appears at high signal level. This suggests SERS signatures for vibrational imaging.

Two-photon excitation is gaining rapidly in interest and significance in spectroscopy and optical imaging. The development of optical labels that are suitable also for two-photon excitation and non-linear imaging is an important task in advancing methods for vibrational probing and imaging. Effective plasmonic supported cross sections of SERS and SEHRS can be on the order of $10^{-17} - 10^{-16}\,\mathrm{cm}^2$ and $10^{-46} - 10^{-45}\,\mathrm{cm}^4\,\mathrm{s}$, respectively. This suggests versatile optical SERS/ SEHRS labels suitable for both one- and two-photon probing and imaging. Figure 2.8 shows the schematic of a SEHRS/SERS label along with its spectral signatures, for this label, SEHRS and SERS spectra of the reporter molecule rose bengal. Plasmonic supported Raman labels have also been employed in CARS imaging for immunohistochemistry [50].

2.5 Brief Summary and Outlook

Plasmonics supported vibrational spectroscopy can transform vibrational spectroscopy from a method for chemical structural analysis requiring relatively large amounts of matter to a tool for nanosciences providing at the same time high molecular structural selectivity and ultrasensitive detection limits. Vibrational spectra collected by surface enhanced Raman scattering (SERS), by surface enhanced infrared absorption (SEIRA), and by surface enhanced two-photon excited hyper Raman scattering (SEHRS) allow a comprehensive structural characterization of matter and monitoring of chemical processes. Sophisticated nanoantenna structures and arrays advance the field of surface enhanced IR absorption. Here, the extension to the THz range might be of particular interest. A combination of the confined probed volumes and the enhancement of vibratinal signatures in plasmonic fields with scanning probe capabilities of an atomic force microscope as it is employed in tip enhanced Raman spectroscopy enables simultaneous morphological-topological and molecular structural information at the nanoscale.

In particular, *non-linear* coherent and incoherent Raman scattering benefits from plasmonic support. Further progress in theoretical understanding of plasmonic enhancement as well as advanced technologies for making taylored plasmonic nanostructures will allow us to take advantage of all the potential capabilities of plasmonic supported non-linear vibrational spectroscopy. First observation of surface enhanced femtosecond stimulated Raman scattering opens up exciting new ways for probing ultrafast processes that might occur in plasmon-mediated interaction between molecules and light. Methods such as SEHRS, SEPARS and SECARS combine structural

sensitivity and selectivity of vibrational spectroscopy, methodological advantages of multiphoton and coherent spectroscopy, as well as high signal levels and confined probed volumes inherent to plasmon supported spectroscopy. Employing these advantages opens up exciting capabilities for vibrational probing and imaging.

References

1. B. Schrader, *Infrared and Raman Spectroscopy: Methods and Applications* (Wiley, Chichester, 1995)
2. D. Mitleman, *Sensing with Terahertz Radiation* (Springer, Berlin, 2003)
3. K. Kneipp, H. Kneipp, I. Itzkan, R.R. Dasari, M.S. Feld, Ultrasensitive chemical analysis by Raman spectroscopy. Chem. Rev. **99**, 2957–2975 (1999)
4. K. Kneipp, Surface-enhanced Raman scattering. Phys. Today **60**, 40–46 (2007)
5. P.L. Stiles, J.A. Dieringer, N.C. Shah, R.R. Van Duyne, Surface-enhanced Raman spectroscopy. Annu. Rev. Anal. Chem. **1**, 601–626 (2008)
6. J. Kneipp, H. Kneipp, K. Kneipp, SERS–a single-molecule and nanoscale tool for bioanalytics. Chem. Soc. Rev. **37**, 1052–1060 (2008)
7. R. Adato, A.A. Yanik, J.J. Amsden, D.L. Kaplan, F.G. Omenetto, M.K. Hong, S. Erramilli, H. Altug, Ultra-sensitive vibrational spectroscopy of protein monolayers with plasmonic nanoantenna arrays. Proc. Nat. Acad. Sci. U.S.A. **106**, 19227–19232 (2009)
8. V.N. Denisov, B.N. Mavrin, V.B. Podobedov, Hyper Raman scattering. Phys. Rep. **151**, 1 (1987)
9. A.M. Kelley, *Hyper-Raman scattering by molecular vibrations, in Annual Review of Physical Chemistry*, vol. 61 (Annual Reviews, Palo Alto, 2010), pp. 41–61
10. J.X. Cheng, X.S. Xie, Coherent anti-Stokes Raman scattering microscopy: instrumentation, theory, and applications. J. Phys. Chem. B **108**, 827–840 (2004)
11. C.W. Freudiger, W. Min, G.R. Holtom, B.W. Xu, M. Dantus, X.S. Xie, Highly specific label-free molecular imaging with spectrally tailored excitation-stimulated Raman scattering (STE-SRS) microscopy. Nat. Photonics **5**, 103–109 (2011)
12. C.L. Evans, X.S. Xie, Coherent anti-stokes Raman scattering microscopy: chemical imaging for biology and medicine. Annu. Rev. Anal. Chem. **1**, 883–909 (2008)
13. L. Dhar, J.A. Rogers, K.A. Nelson, Time-resolved vibrational spectroscopyin the impulsive limit. Chem. Rev. **94**, 157–193 (1994)
14. S. Umapathy, A. Lakshmanna, B. Mallick, Ultrafast Raman loss spectroscopy. J. Raman Spectrosc. **40**, 235–237 (2009)
15. A. Weigel, N.P. Ernsting, Excited Stilbene: intramolecular vibrational redistribution and solvation studied by femtosecond stimulated Raman spectroscopy. J. Phys. Chem. B **114**, 7879–7893 (2010)
16. R.R. Frontiera, R.A. Mathies, Femtosecond stimulated Raman spectroscopy. Laser Photonics Rev. **5**, 102–113 (2011)
17. M. Moskovits, *Surface-enhanced Raman spectroscopy: a brief perspective, in Surface-Enhanced Raman Scattering: Physics and Applications* (Springer-Verlag Berlin, Berlin, 2006), pp. 1–17
18. P. Johansson, H.X. Xu, M. Kall, Surface-enhanced Raman scattering and fluorescence near metal nanoparticles. Phys. Rev. B **72**, 035427 (2005)
19. M.I. Stockman, Nanoplasmonics: past, present, and glimpse into future. Opt. Express **19**, 22029–22106 (2011)
20. L. Novotny, N. van Hulst, Antennas for light. Nat. Photonics **5**, 83–90 (2011)
21. A. Ahmed, R. Gordon, Single molecule directivity enhanced Raman scattering using nanoantennas. Nano Lett. **12**, 2625–2630 (2012)
22. K. Kneipp, M. Moskovits, H. Kneipp, *in Surface-Enhanced Raman Scattering- Physics and Applications* (Springer, Berlin, 2006)

23. A. Otto, Surface- enhanced Raman scattering: 'classical' and 'chemical' origins, in *Light Scattering in Solids IV. Electronic Scattering, Spin Effects, SERS and Morphic Effects*, ed. by M. Cardona, G. Guntherodt (Springer, Berlin, 1984), pp. 289–418
24. A. Campion, P. Kambhampati, Surface-enhanced Raman scattering. Chem. Soc. Rev. **27**, 241–250 (1998)
25. J.R. Lombardi, R.L. Birke, Time-dependent picture of the charge-transfer contributions to surface enhanced Raman spectroscopy. J. Chem. Phys. **126**, 244709 (2007)
26. M.I. Stockman, *Electromagnetic theory of SERS, in Surface-Enhanced Raman Scattering: Physics and Applications* (Springer, Berlin, 2006), pp. 47–65
27. G.C. Schatz, M.A. Young, R.P. Van Duyne, *Electromagnetic mechanism of SERS, in Surface-Enhanced Raman Scattering: Physics and Applications* (Springer, Berlin, 2006), pp. 19–45
28. R.F. Aroca, D.J. Ross, C. Domingo, Surface-enhanced infrared spectroscopy. Appl. Spectrosc. **58**, 324A–338A (2004)
29. F. Neubrech, A. Pucci, T.W. Cornelius, S. Karim, A. Garcia-Etxarri, J. Aizpurua, Resonant plasmonic and vibrational coupling in a Tailored nanoantenna for infrared detection. Phys. Rev. Lett. **101**, 4 (2008)
30. A. Pucci, F. Neubrech, D. Weber, S. Hong, T. Toury, M.L. de la Chapelle, Surface enhanced infrared spectroscopy using gold nanoantennas. Phys. Status Solidi B Basic Solid State Phys. **247**, 2071–2074 (2010)
31. F. Le, D.W. Brandl, Y.A. Urzhumov, H. Wang, J. Kundu, N.J. Halas, J. Aizpurua, P. Nordlander, Metallic nanoparticle arrays: a common substrate for both surface-enhanced Raman scattering and surface-enhanced infrared absorption. ACS Nano **2**, 707–718 (2008)
32. V. Liberman, R. Adato, T.H. Jeys, B.G. Saar, S. Erramilli, H. Altug, Rational design and optimization of plasmonic nanoarrays for surface enhanced infrared spectroscopy. Opt. Express **20**, 11953–11966 (2012)
33. R. Hillenbrand, T. Taubner, F. Keilmann, Phonon-enhanced light-matter interaction at the nanometre scale. Nature **418**, 159–162 (2002)
34. M.S. Anderson, Enhanced infrared absorption with dielectric nanoparticles. Appl. Phys. Lett. **83**, 2964–2966 (2003)
35. J. Kneipp, H. Kneipp, K. Kneipp, Two-photon vibrational spectroscopy for biosciences based on surface-enhanced hyper-Raman scattering. Proc. Nat. Acad. Sci. U.S.A. **103**, 17149–17153 (2006)
36. H. Kneipp, K. Kneipp, F. Seifert, Surface-enhanced hyper-Raman scattering (SEHRS) and surface-enhanced Raman scattering (SERS) by means of mode-locked Ti:sapphire laser excitation. Chem. Phys. Lett. **212**, 374–378 (1993)
37. T. Itoh, Y. Ozaki, H. Yoshikawa, T. Ihama, H. Masuhara, Hyper-Rayleigh scattering and hyper-Raman scattering of dye-adsorbed silver nanoparticles induced by a focused continuous-wave near-infrared laser. Appl. Phys. Lett. **88**, 084102 (2006)
38. L. Weinan, A. Meyers-Kelley, SEHRS spectra on Ag films at pulse energies below 2 pJ. J. Am. Chem. Soc. **128**, 3492–3493 (2006)
39. K. Kneipp, Y. Wang, H. Kneipp, I. Itzkan, R.R. Dasari, M.S. Feld, Population pumping of ecited vibrational states by spontaneous surface-enhanced Raman scattering. Phys. Rev. Lett. **76**, 2444 (1996)
40. K. Kneipp, H. Kneipp, P. Corio, S.D.M. Brown, K. Shafer, J. Motz, L.T. Perelman, E.B. Hanlon, A. Marucci, G. Dresselhaus, M.S. Dresselhaus, Surface-enhanced and normal Stokes and anti-Stokes Raman spectroscopy of single-walled carbon nanotubes. Phys. Rev. Lett. **84**, 3470–3473 (2000)
41. K. Kneipp, H. Kneipp, R. Manoharan, I. Itzkan, R.R. Dasari, M.S. Feld, Surface-enhanced Raman scattering (SERS)—a new tool for single molecule detection and identification. Bioimaging **6**, 104–110 (1998)
42. K. Kneipp, H. Kneipp, I. Itzkan, R.R. Dasari, M.S. Feld, M.S. Dresselhaus, *Nonlinear Raman Probe of Single Molecules Attached to Colloidal Silver and Gold Clusters, in Optical Properties of Nanostructured Random Media* (Springer, Berlin, 2002)

43. W. Kiefer, D.A. Long, *Non-Linear Raman Spectroscopy and its Chemical Application* (Reider, Dordrecht, 1982)
44. A. Volkmer, J.X. Cheng, X.S. Xie, Vibrational imaging with high sensitivity via epidetected coherent anti-Stokes Raman scattering microscopy. Phys. Rev. Lett. **87**, 3901 (2001)
45. E. Liang, A. Weippert, J. Funk, A. Materny, W. Kiefer, Experimental observation of surface-enhanced coherent anti-Stokes Raman scattering. Chem. Phys. Lett. **227**, 115–120 (1994)
46. I. Baltog, M. Baibarac, S. Lefrant, Coherent anti-Stokes Raman scattering on single-walled carbon nanotubes and copper phthalocyanine thin films excited through surface plasmons. J. Opt. Pure Appl. Opt. **7**, 632–639 (2005)
47. I. Baltog, M. Baibarac, S. Lefrant, "Single-beam pumped" coherent anti-Stokes Raman scattering on carbon nanotubes thin films excited through surface plasmons. Physica E Low Dimensional Syst. Nanostruct. **40**, 2380–2385 (2008)
48. C.J. Addison, S.O. Konorov, A.G. Brolo, M.W. Blades, R.F.B. Turner, Tuning gold nanoparticle self-assembly for optimum coherent anti-stokes Raman scattering and second harmonic generation response. J. Phys. Chem. C **113**, 3586–3592 (2009)
49. C. Steuwe, C.F. Kaminski, J.J. Baumberg, S. Mahajan, Surface enhanced coherent anti-stokes Raman scattering on nanostructured gold surfaces. Nano Lett. **11**, 5339–5343 (2011)
50. S. Schlucker, M. Salehi, G. Bergner, M. Schutz, P. Strobel, A. Marx, I. Petersen, B. Dietzek, J. Popp, Immuno-surface-enhanced coherent anti-stokes Raman scattering microscopy: immunohistochemistry with target-specific metallic nanoprobes and nonlinear Raman microscopy. Anal. Chem. **83**, 7081–7085 (2011)
51. R.R. Frontiera, A.I. Henry, N.L. Gruenke, R.P. Van Duyne, Surface-enhanced femtosecond stimulated Raman spectroscopy. J. Phys. Chem. Lett. **2**, 1199–1203 (2011)
52. Y. Sonnefraud, A.L. Koh, D.W. McComb, S.A. Maier, Nanoplasmonics: engineering and observation of localized plasmon modes. Laser Photonics Rev. **6**, 277–295 (2012)
53. M.I. Stockman, Nanoplasmonics: the physics behind the applications. Phys. Today **64**, 39–44 (2011)
54. L. Novotny, From near-field optics to optical antennas. Phys. Today **64**, 47–52 (2011)
55. S. Lal, N.K. Grady, J. Kundu, C.S. Levin, J.B. Lassiter, N.J. Halas, Tailoring plasmonic substrates for surface enhanced spectroscopies. Chem. Soc. Rev. **37**, 898–911 (2008)
56. P.R. West, S. Ishii, G.V. Naik, N.K. Emani, V.M. Shalaev, A. Boltasseva, Searching for better plasmonic materials. Laser Photonics Rev. **4**, 795–808 (2010)
57. K. Kneipp, W. Yang, H. Kneipp, L.T. Perelman, I. Itzkan, R.R. Dasari, M.S. Feld, Single molecule detection using surface-enhanced Raman scattering (SERS). Phys. Rev. Lett. **78**, 1667–70 (1997)
58. K. Kneipp, H. Kneipp, J. Kneipp, Surface-enhanced Raman scattering in local optical fields of silver and gold nanoaggregatess–from single-molecule Raman spectroscopy to ultrasensitive probing in live cells. Acc. Chem. Res. **39**, 443–450 (2006)
59. K. Kneipp, H. Kneipp, R. Manoharan, E.B. Hanlon, I. Itzkan, R.R. Dasari, M.S. Feld, Extremely large enhancement factors in surface-enhanced Raman scattering for molecules on colloidal gold clusters. Appl. Spectrosc. **52**, 1493–1497 (1998)
60. K. Kneipp, H. Kneipp, V.B. Kartha, R. Manoharan, G. Deinum, I. Itzkan, R.R. Dasari, M.S. Feld, Detection and identification of a single DNA base molecule using surface–enhanced Raman scattering (SERS). Phys. Rev. E **57**, R6281–R6284 (1998)
61. M.I. Stockman, V.M. Shalaev, M. Moskovits, R. Botet, T.F. George, Enhanced Raman scattering by fractal clusters: scale-invariant theory. Phys. Rev. B **46**, 2821–2830 (1992)
62. V.A. Podolskiy, V.M. Shalaev, Giant optical responses in microcavity-fractal composites. Laser Phys. **11**, 26–30 (2001)
63. K.R. Li, M.I. Stockman, D.J. Bergman, Self-similar chain of metal nanospheres as an efficient nanolens. Phys. Rev. Lett. **91**, 227–402 (2003)
64. J. Kneipp, X.T. Li, M. Sherwood, U. Panne, H. Kneipp, M.I. Stockman, K. Kneipp, Gold nanolenses generated by laser ablation-efficient enhancing structure for surface enhanced Raman scattering analytics and sensing. Anal. Chem. **80**, 4247–4251 (2008)

65. C. Hoppener, L. Novotny, Exploiting the light-metal interaction for biomolecular sensing and imaging. Q. Rev. Biophys. **45**, 209–255 (2012)
66. N.J. Halas, S. Lal, W.S. Chang, S. Link, P. Nordlander, Plasmons in strongly coupled metallic nanostructures. Chem. Rev. **111**, 3913–3961 (2011)
67. J. Kundu, F. Le, P. Nordlander, N.J. Halas, Surface enhanced infrared absorption (SEIRA) spectroscopy on nanoshell aggregate substrates. Chem. Phys. Lett. **452**, 115–119 (2008)
68. V. Jayaraman, K.R. Rodgers, I. Mukeriji, T.G. Spiro, Hemoglobin allostery—resonance Raman spectroscopy of kinetic intermediates. Science **269**, 1843–1848 (1995)
69. K.R. Rodgers, T.G. Spiro, Nanosecond dynamics of the R–>T transition in hemoglobin-ultreviolet raman studies. Science **265**, 1697–1699 (1994)
70. E.J. Zeman, G.C. Schatz, An acurate electromagnetic theory study of surface enhancement factors for AG, AU, CU, LI, NA, AL, GA, IN, ZN and CD. J. Phy. Chem. **91**, 634–643 (1987)
71. G.H. Chan, J. Zhao, G.C. Schatz, R.P. Van Duyne, Localized surface plasmon resonance spectroscopy of triangular aluminum nanoparticles. J. Phys. Chem. C **112**, 13958–13963 (2008)
72. Z.L. Yang, Q.H. Li, B. Ren, Z.Q. Tian, Tunable SERS from aluminium nanohole arrays in the ultraviolet region. Chem. Commun. **47**, 3909–3911 (2011)
73. T. Dorfer, M. Schmitt, J. Popp, Deep-UV surface-enhanced Raman scattering. J. Raman Spectrosc. **38**, 1379–1382 (2007)
74. B. Ren, X.F. Lin, Z.L. Yang, G.K. Liu, R.F. Aroca, B.W. Mao, Z.Q. Tian, Surface-enhanced Raman scattering in the ultraviolet spectral region: UV-SERS on rhodium and ruthenium electrodes. J. Am. Chem. Soc. **125**, 9598–9599 (2003)
75. K. Kneipp, H. Kneipp, *Two-Photon Excited Surface-Enhanced Raman Scattering, Surface-Enhanced Raman Scattering: Physics and Applications* (Springer, Berlin, 2006)
76. K. Kneipp, H. Kneipp, SERS signals at the anti Stokes side of the excitation laser in extremely high local optical fields of silver and gold nanoclusters. Faraday Discuss. **132**, 27–33 (2006)
77. H. Harutyunyan, G. Volpe, R. Quidant, L. Novotny, Enhancing the nonlinear optical response using multifrequency gold-nanowire antennas. Phys. Rev. Lett. **108**, 4 (2012)
78. K.N. Heck, B.G. Janesko, G.E. Scuseria, N.J. Halas, M.S. Wong, Observing metal-catalyzed chemical reactions in situ using surface-enhanced Raman spectroscopy on Pd-Au nanoshells. J. Am. Chem. Soc. **130**, 16592–16600 (2008)
79. W. Xie, C. Herrmann, K. Kompe, M. Haase, S. Schlucker, Synthesis of bifunctional Au/Pt/Au Core/Shell nanoraspberries for in situ SERS monitoring of platinum-catalyzed reactions. J. Am. Chem. Soc. **133**, 19302–19305 (2011)
80. V. Joseph, C. Engelbrekt, J. Zhang, U. Gernert, J. Ulstrup, J. Kneipp, Characterizing the kinetics of nanoparticle-catalyzed reactions by surface-enhanced Raman scattering. Angew. Chem. Int. Ed. **51**, 7592–7596 (2012)
81. Y.W.C. Cao, R.C. Jin, C.A. Mirkin, Nanoparticles with Raman spectroscopic fingerprints for DNA and RNA detection. Science **297**, 1536–1540 (2002)
82. Y.C. Cao, R.C. Jin, J.M. Nam, C.S. Thaxton, C.A. Mirkin, Raman dye-labeled nanoparticle probes for proteins. J. Am. Chem. Soc. **125**, 14676–14677 (2003)
83. X.M. Qian, X.H. Peng, D.O. Ansari, Q. Yin-Goen, G.Z. Chen, D.M. Shin, L. Yang, A.N. Young, M.D. Wang, S.M. Nie, In vivo tumor targeting and spectroscopic detection with surface-enhanced Raman nanoparticle tags. Nat. Biotechnol. **26**, 83–90 (2008)
84. J. Kneipp, H. Kneipp, A. Rajadurai, R.W. Redmond, K. Kneipp, Optical probing and imaging of live cells using SERS labels. J. Raman Spectrosc. **40**, 1–5 (2009)
85. J. Kneipp, H. Kneipp, B. Wittig, K. Kneipp, Novel optical nanosensors for probing and imaging live cells. Nanomed. Nanotechnol. Bio. Med. **6**, 214–226 (2010)
86. J. Kneipp, *Nanosensors Based on SERS for Applications in Living Cells, Surface-Enhanced Raman Scattering: Physics and Applications* (Springer, Berlin, 2006)
87. J. Kneipp, H. Kneipp, B. Wittig, K. Kneipp, One and two photon excited optical pH probing for cells using surface enhanced Raman and hyper Raman nanosensors. Nano Lett. **103**, 17149–17153 (2007)

Chapter 3
Plasmonically Enhanced Dye-Sensitized Solar Cells

Michael B. Ross, Martin G. Blaber and George C. Schatz

Abstract The unique absorption and scattering properties of metallic (typically silver or gold) nanoscale structures are dominated by their localized surface plasmon resonances, leading to strongly confined electromagnetic fields and unprecedented control over light at the nanoscale. The scattering properties of metal nanoparticles have recently been used to trap light within thin film inorganic solar cell devices to increase the effective optical density of the absorbing layer. Enhanced local fields have been utilized to enhance the photo-absorption cross-section of dye molecules in dye-sensitized solar cells. Here we will review the current state of the art in plasmon-enhanced dye-sensitized solar cells and comment on the challenges that must be addressed for the realization of next generation devices.

Keywords Surface plasmon · Photovoltaics · Solar cells

Acronyms

DSSC	Dye-sensitized solar cell
FTO	Fluorine doped Tin Oxide
LSPR	Localized surface plasmon resonance
NIR	Near infrared
PV	Photovoltaic
UV	Ultraviolet

M. B. Ross · M. G. Blaber · G. C. Schatz (✉)
Department of Chemistry, and International Institute for Nanotechnology, Northwestern University, 2145 Sheridan Road, Evanston, IL 60208-3113, USA
e-mail: schatz@chem.northwestern.edu

T. V. Shahbazyan and M. I. Stockman (eds.), *Plasmonics: Theory and Applications*, Challenges and Advances in Computational Chemistry and Physics 15,
DOI: 10.1007/978-94-007-7805-4_3, © Springer Science+Business Media Dordrecht 2013

3.1 Introduction

Increasing population and economic growth continue to drive global energy consumption. Though fossil fuels, including natural gas, coal, tar sands, and oil, could meet these demands; increasing concern about the sustainability of these energy sources has led to the invigoration of support for renewable energy sources. Solar energy provides an alternative and abundant source of energy. More solar energy is transferred to the surface of the earth each hour than is consumed globally each year [1]. However, module costs for solar cells must decrease to approximately US$ 0.50 per peak Watt without subsidies for solar to be competitive with traditional fossil fuels [2].

The efficiency of single-junction photovoltaic (PV) cells is intrinsically limited by the band gap of the absorbing medium. In the case of silicon, with a band gap of 1.1 eV, much of the energy of ultraviolet (UV) and visible wavelength photons is lost to the mismatch between photon energy and the band gap, limiting the maximum efficiency to about 34 % [3]. Multi-junction cells can be used to improve the match between photon energy and the band gap of the absorber. The efficiency record as of 2012 for a multi-junction p-n photovoltaic is 43.5 % for a 3-junction InGa cell with a 306× solar concentrator [4].

An alternative to increasing efficiency is a dramatic reduction in manufacturing cost for low efficiency devices; this has led to a steady increase in thinfilm PV research, with recent devices utilizing hydrogen ion implantation and annealing to produce 20 μm thick single crystal silicon substrates. The optical density of thin film PV systems is low and efficiency drops with reduced thickness. Both localized surface plasmons and surface plasmon polaritons have been utilized in thin film PV devices to scatter light into the absorbing semiconductor and confine it there, thereby increasing the path length of light in the cell, increasing the optical density and photoelectron generation [5].

Dye-sensitized solar cells (DSSCs) present an attractive alternative to traditional inorganic devices because the components can be of low purity and the manufacturing process is conducive to high throughput printing. The basic components of a DSSC are presented in Fig. 3.1. A sensitizing dye is chemisorbed to a mesoporous film of wide band gap semiconductor, usually TiO_2, which is attached to a transparent conducting oxide film. Light is absorbed by the dye and a photoexcited electron is transferred to the semiconductor and then to the electrode. A redox couple (usually iodide/tri-iodide) then reduces the dye to the ground state and carries the hole to the counter electrode.

Since the first DSSC by O'Regan and Grätzel in 1991, the field has expanded greatly; however, until recently, efficiencies had stalled at around 9 % [6]. This is in part due to the complexity of having separate materials responsible for the light absorption and the electron/hole transport. However, the diversity of components is attractive because novel materials can easily be incorporated into a variety of photo-collection systems to understand and maximize their effect. For a review of the diversity of dyes and electron/hole transport materials, see Ref. [4]. Recent ad-

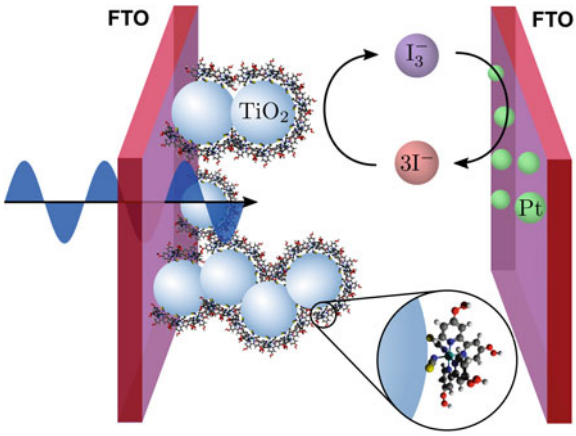

Fig. 3.1 Scheme of a dye-sensitized solar cell. The transparent electrodes are generally composed of fluorine-doped tin oxide (FTO)

vances in nanotechnology and robust dyes have boosted efficiencies of DSSCs to over 12 % [7].

Substantial progress has been made in understanding the chemistry and physics of DSSCs, with most suggesting that the primary way to increase DSSC efficiency is by increasing the photo-voltage.[4, 8] Recent work on alternatives to the iodide/trioidide redox mediator has vetted increases in cell efficiency by decreasing the dye regeneration overpotential. Dye engineering can be used to reduce the injection overpotential (which is the energy difference between the molecule excited state and the TiO_2 conduction band). The other way to increase the photovoltage is by decreasing the dark current of the cell, which is a measure of the electron-hole recombination pathways in the DSSC. Even in cells with high charge-collection efficiencies, significant photocurrent density loss is seen due to resistance in the cell and charge exchange at the TiO_2/electrolyte interface [9].

The total resistance is dependent on the electron-transport resistance and the rate of recombination. Recombination comes in three forms: decay of the excited state of the dye prior to electron injection, recombination of electrons in the mesoporous semiconductor with oxidized dyes, and recombination of electrons with the redox mediator. Fewer recombination events and faster electron transport in TiO_2 would reduce loss. The charge recombination rate in DSSCs is proportional to the surface area of the mesoporous titania network [10], and therefore, the thickness of the film [9]. Ideally, the film thickness should be ten times shorter, $\sim$100 nm, than the electron diffusion length in TiO_2 [9]. Thus, decreasing the thickness of the oxide layer and/or increasing the carrier length will increase photocurrents in DSSCs. As the film thickness is decreased, the optical density decreases and hence there is a reduction in photon capture, which subsequently reduces photocurrent generation. To offset the decrease in optical density, plasmonic nanoparticles can be incorporated into the DSSC to provide increased dye absorption.

More importantly, a thinner cell greatly decreases carrier recombination in the oxide layer. As seen in Fig. 3.2, the carrier recombination efficiency varies inversely

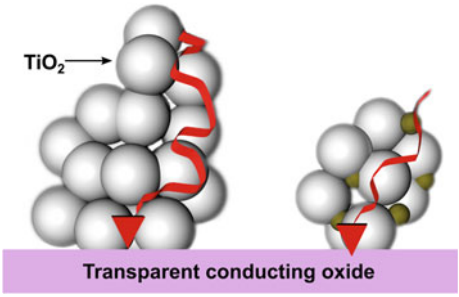

Fig. 3.2 Comparison of carrier paths in DSSCs without(*left*) and with (*right*) plasmonic nanoparticle inclusions

with the length of the oxide layer. The further an electron has to travel, the more likely it is to encounter an oxidized dye and be lost. Each electron that does not reach the Pt electrode can be considered a wasted photon absorption event. Thus, plasmonic nanoparticles can lead to lower recombination frequencies *via* shorter path lengths in the cell. This can also allow the use of cheaper materials with shorter carrier mean free paths [11]. Solar conversion efficiencies could increase with diminished material needs in terms of both scarcity and cost. DSSCs would become easier to implement on larger scales as they became more economically feasible.

3.2 Plasmon Enhanced Dye-Sensitized Solar Cells

Localized surface plasmon resonances (LSPRs) are characteristic excitations of the conduction electrons in small metal nanoparticles. They are seen when a, the dimension of the particle, is less than the excitation wavelength, when $a < \lambda$. Photons travelling in media with a positive dielectric constant ($\varepsilon_d > 0$) couple with LSPRs with varying efficiencies based on the nanoparticle shape, size and the relationship between the medium dielectric constant and the dielectric function of the metal ($\varepsilon_m(\omega) = \varepsilon_r(\omega) + i\varepsilon_i(\omega)$) [12]. The coupling efficiency between photons and the LSPR is described by the absorption and scattering cross-sections (C_{abs} and C_{sca} respectively) of the nanoparticles. The values of C_{abs} and C_{sca} can be many times larger than the geometric cross-section of the nanoparticle, indicating in the case of C_{abs} that the electric field in and around the nanoparticle can be many times the strength of the incident field. This strong localization of electromagnetic energy around metal particles is of primary importance to increasing the absorption cross-section of dyes.

In the following, we will discuss the mechanism of enhanced dye absorption due to LSPRs: including ways to enhance dye absorption over the solar spectrum by utilizing nanoparticles of various shapes, mitigating Ohmic losses in the metal due to surface plasmon excitation, and coupling of the particle electromagnetic fields with the dye.

3.2.1 Mechanism of Enhanced Dye Absorption

In contrast to inorganic p-n junction type cells where plasmonically active metal nanostructures are used to scatter light into the photoabsorbing layer [5], metal nanoparticles directly increase photoabsorption of the dye in DSSCs by near-field coupling [13]. The local electric field felt by a dye molecule absorbed on or near a metal nanoparticle can be hundreds (or even thousands) of times the strength of the incident field [14]. The strength of the near-field around a nanoparticle depends upon the energy stored in the plasmon mode and the number and placement of sharp features in the nanostructure. The stored energy is approximately related to the absorption cross-section of the particle, which in the quasi-static limit (where the particles are very small compared to the incident photon wavelength) is given by:

$$C_{\text{abs}} = k\text{Im}(\alpha), \tag{3.1}$$

where k is the free space wavevector ($2\pi/\lambda$) and α is the polarizability of the nanoparticle. The polarizability of a sphere is given by:

$$\alpha = 4\pi a^3 \frac{\varepsilon_{\text{m}} - \varepsilon_{\text{d}}}{\varepsilon_{\text{m}} + 2\varepsilon_{\text{d}}}, \tag{3.2}$$

where a is the radius of the sphere and ε_{m} and ε_{d} are the dielectric constants of the metal and surrounding dielectric, respectively. When the real part of the metal dielectric constant is equal to $-2\varepsilon_{\text{d}}$, the denominator of (3.2) approaches zero and the system is resonant. Increasing the dielectric constant of the surrounding medium causes the resonance to move to a higher wavelength, or 'red-shift'. For metals such as silver and gold, the red-shift moves the resonance away from interband transitions in the metal. If a plasmonic structure is designed such that the LSPR is near the interband transitions, the LSPR will be heavily damped due to decay into electron-hole pairs. Thus, red-shifting the resonance from interband transitions increases the polarizability and hence the absorption cross-section of the nanoparticle.

Although the introduction of bare Au nanoparticles into a DSSC has been shown to increase the cell photocurrent [15], in most DSSCs the use of corrosive redox mediators such as the iodide/triiodide redox couple requires that the nanoparticles be protected with a capping layer. Both TiO_2 [16] and SiO_2 [17] capping layers have been investigated on gold and silver nanoparticles incorporated into DSSCs. Depending on the thickness of the capping layer, the particle experiences an effective dielectric environment in between the value of ε_{c} for the capping layer and the value of ε_{d} for the solution. As the thickness increases the proportion of effective medium dielectric constant tends towards ε_{c}, and the resonance red-shifts (if ε_{c} is greater than ε_{d}) in accordance with Eq. 3.2. Additionally, as the thickness of the capping layer increases, the distance between the adsorbed dye and the metal particle increases. Because the electric field associated with the plasmon resonance on the nanoparticle decays exponentially away from the metal surface, the observed photocurrent decreases. For

example, Standridge, *et al*. showed that the observed overall cell efficiency decreased by 40 % when the thickness of the TiO_2 capping layer was increased from 2.0 nm to 4.9 nm [18].

To demonstrate the effect of capping layer thickness, Mie theory [19] can be used to calculate the optical properties of a spherical nanoparticle with a 20 nm radius silver core and a TiO_2 shell of varying thickness (Fig. 3.3). The absorption efficiency of the bare silver particle has a maximum value of nine, indicating that the absorption cross-section of the particle is nine times larger than the area of the particle (Fig. 3.3a). To put this in perspective, typical DSSC dye molecules have absorption cross-sections which are smaller than their geometric cross-sections [20], generally of the order of one $Å^2$. The typical density of molecules on the surface of the titania is between 0.5 and 1 dye molecule per nm^2 [21]. The effective cross-section of a dye molecule adsorbed to the nanoparticle surface is approximately:

$$C_{\text{eff}} = \left\langle |\mathbf{E}|^2 \right\rangle C_{\text{dye}}, \tag{3.3}$$

where $\langle\,\rangle$ indicates averaging over the surface of the nanoparticle and C_{dye} is the absorption cross-section of an isolated dye molecule. The surface-average fields for silver/titania nanoparticles are shown in Fig. 3.3b, it is clear that the surface-averaged fields decrease dramatically with increased TiO_2 thickness which, alongside experimental observations [18], suggests that near-field enhancement is the primary enhancement mechanism.

To demonstrate the increase in the effective dye cross-section due to the near-field, Fig. 3.3d shows the result of Eq. (3.3) for a dye with a frequency independent absorption cross-section of 0.01 nm^2 multiplied by the number of dye molecules on the surface N_{dye} (assuming one molecule per nm^2). For the bare silver particle, N_{dye} is 5,000 and the total cross-section of all of the dye molecules increases from 50 nm^2 to 7,500 nm^2, in line with the 150× increase predicted by the strong local-field. The reduction in field enhancement with increasing TiO_2 thickness is partially compensated by the increase in the surface area of the nanoparticle, which increases with radius. For a 12 nm layer of TiO_2, N_{dye} is 13,000 and the total dye absorption cross section increases from 130 nm^2 to 2,500 nm^2.

3.2.2 Calculating Solar Enhancement

Above, we note that the cross-section of a plasmonically enhanced dye is just the product of the surface-averaged near-field on the plasmonically active component and the non-enhanced dye cross-section. To calculate the solar-weighted dye enhancement factor, the product of the dye absorption spectrum, the solar spectrum and the local-field strength must be integrated over a relevant fraction of the solar spectrum:

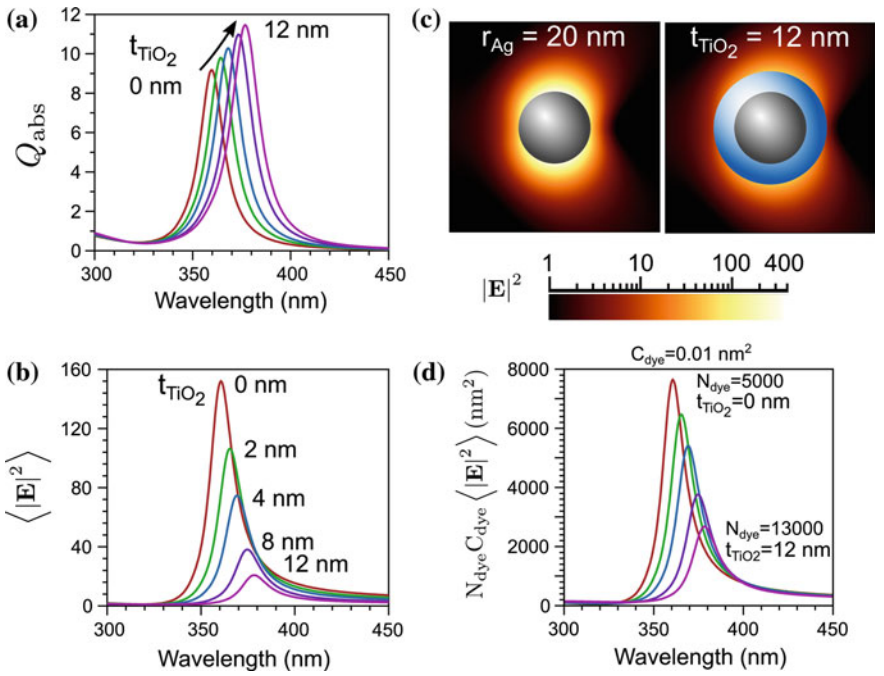

Fig. 3.3 Optical Response of a Ag nanosphere coated with a TiO_2 capping layer of varying thickness (0 nm – 12 nm). **a** The absorption efficiency (total particle cross-section divided by the cross-sectional area of the *silver core*) showing the red-shift of the resonance. **b** The surface-averaged electric field enhancement (measured 0.25 nm from the TiO_2 surface). **c** The electric field enhancement around the Ag/TiO_2 structure showing that the field enhancement around the particle is lower for increased TiO_2 thickness. Light is polarized in the vertical direction and propagates left to right in the figure. **d** The total cross-section of a monolayer of dyes absorbed to the structures in (**a**) and (**b**). The cross-section of the isolated dye is 0.01 nm^2

$$C_{EF} = \int_{1.5eV}^{4.1eV} D(\omega) S(\omega) \left\langle |\mathbf{E}(\omega)|^2 \right\rangle d\omega. \tag{3.4}$$

With D and S as the dye absorption cross-section and AM 1.5 G solar spectrum, respectively, normalized according to:

$$\int_{1.5eV}^{4.1eV} f(\omega) d\omega = 1. \tag{3.5}$$

An example calculation of C_{EF} is presented in Fig. 3.4. The normalized absorption cross-section for the N3 dye was used for D, and the nanoparticle was a 30 nm radius silver sphere coated with 10 nm of AgO and 2 nm of amorphous TiO_2. The

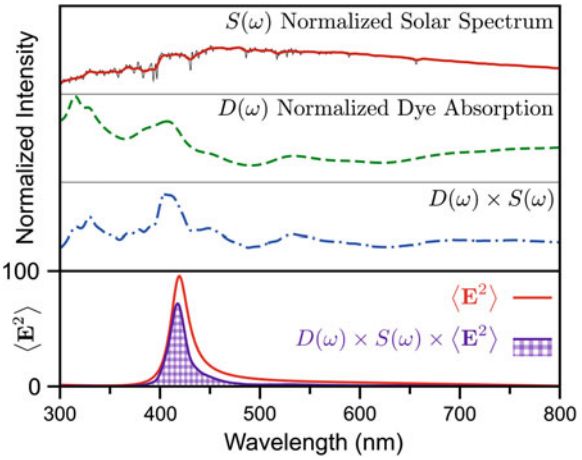

Fig. 3.4 Method for calculating solar integrated N3 dye absorption enhancement factor C_{EF}. The solar spectrum and N3 dye absorption spectra are normalized according to Eq. 3.5, and then multiplied by the surface-average field, the result is then integrated (purple hatched area, bottom panel). For this example (30 nm radius silver sphere coated with 10 nm of AgO and 2 nm amorphous TiO_2), $C_{EF} = 12.9$

result is an integrated cross-section enhancement of $C_{EF} = 12.9$. Silver is readily oxidized at ambient conditions and thus this layer of oxide must be considered as it changes the dielectric environment of the particle. Figure 3.5 shows the results of the same analysis for a wide range of silver particle sizes and AgO coating thicknesses. The AgO has a dielectric constant of 6.25, and so increasing the thickness causes a dramatic red-shift in the plasmon resonance as is expected (Eq. 3.2). For example, for the $r_{Ag} = 5$ nm case, when no AgO is present, the LSPR peaks at 366 nm, whereas for 20 nm of AgO it peaks at 550 nm. For a particle of this size, the field enhancement drops off rapidly with increased oxide layer thickness. When the silver radius is increased to 30 nm, this tunability causes the resonance to cross the maximum dye absorption cross-section (around 400 nm), and the reduction in the field enhancement is not as severe as in the small particle case. These factors combine to form a region of optimum geometry when the silver radius is 30 nm and the oxide coating is about 10 nm. Although this enhances the dye absorption by a factor of almost 13, the enhancement covers only a small fraction of the solar spectrum.

3.3 Enhancing the Solar Spectrum

A majority of the energy in the solar spectrum resides in the spectral range 300 nm–1,750 nm. Capturing the largest possible fraction of this spectrum is essential for any solar application. The tunability of the absorption efficiency of metal nanoparticles with size, shape and composition is particularly important for dye-based cells;

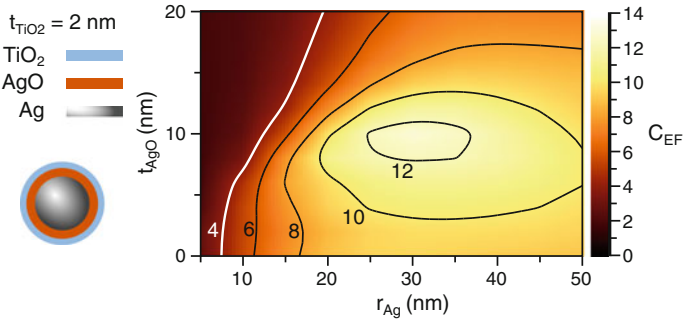

Fig. 3.5 Dye absorption enhancement factor as a function of *silver sphere* radius and AgO thickness. The Ag/AgO particle has a constant 2 nm amorphous TiO_2 coating. The N3 dye was used in Eq. 3.4

especially considering the difficulty in developing strongly absorbing dyes approaching and reaching into the near-infrared [22, 23]. In the following section, we will discuss the properties of the LSPR in terms of nanoparticle composition, shape, and size.

3.3.1 Metal Composition

The strength and wavelength position of the LSPR depends on the dielectric function of the metal, which can be split into two terms:

$$\varepsilon_{\mathrm{m}}(\omega) = 1 - \frac{\omega_{\mathrm{p}}^2}{\omega(\omega + i\gamma)} + \varepsilon_{\mathrm{IB}}(\omega). \tag{3.6}$$

The first term is the so-called 'Drude' contribution, which describes intraband processes unique to metals. The Drude contribution is described by the density of free electrons in the metal *via* the plasma frequency, $\omega_{\mathrm{p}} = ((Ne^2)/(m_e\varepsilon_0))^{1/2}$, where N is the free electron density e is the charge on the electron, m_e is electron mass, and ε_0, the dielectric function of free space. The damping constant, γ, describes the electron relaxation processes in the metal, which at room temperature is dominated by electron-phonon scattering. The second term is the interband contribution, which describes quasiparticle excitations from the occupied to unoccupied bands in the metal. As mentioned previously, in metals such as silver, gold and copper, interband transitions become allowed for frequencies above the band edge of the metal and in these regions the LSPR is severely damped. Figure. 3.6a shows the regions where interband transitions occur in these three metals, as well as aluminum.

The strength of interband transitions in the noble metals follows the trend Cu > Au > Ag, and the band edge follows the inverse trend with Ag > Au > Cu. Because

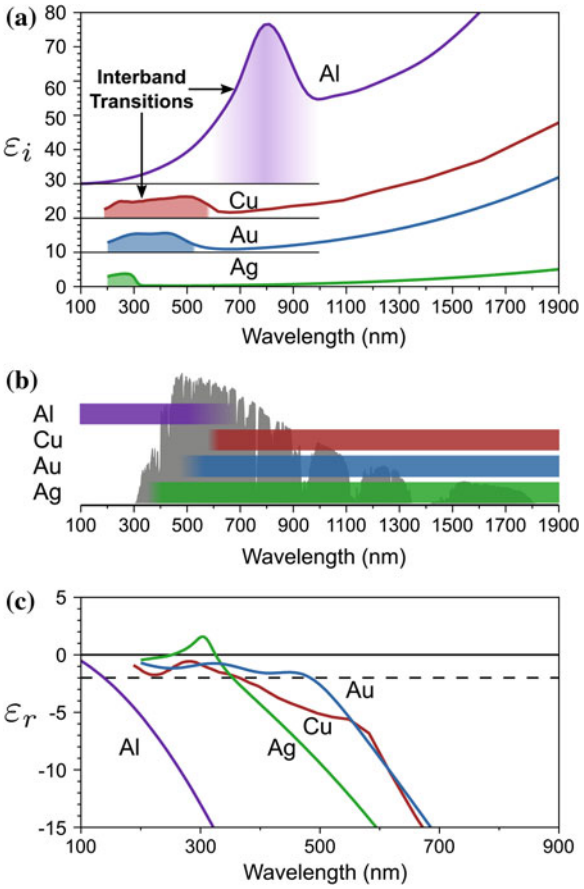

Fig. 3.6 Dielectric functions of plasmonics metals. **a** The imaginary part of the dielectric functions of Al, Cu, Ag and Au with shaded sections indicating the presence of interband transitions. **b** The energy flux AM 1.5 G solar spectrum (*gray*) overlayed with the regions where the metals have good plasmonic properties. **c** The real part of the dielectric function. The *dashed line* indicates the resonance condition for a sphere at -2

of these trends, copper is not a widely used plasmonic material. Conversely, both silver and gold are both excellent plasmonic materials, with silver having slightly lower loss ($i\varepsilon_i(\omega)$), and gold having lower reactivity. In Fig. 3.6b, the spectral range of the metals is considered: *i.e.* over what range of the solar spectrum can they be expected to be strong absorbers.

The band structure of aluminum is such that the frequency of the band edge is small (0.8 eV), and interband transitions occur both in the visible and the near infrared (NIR). However, there are no interband transitions in the 100–500 nm regime, indicating that aluminum nanoparticles may be of some utility in the 300–400 nm wavelength range that is only partially covered by silver. Because of interband tran-

sitions, copper and gold are poor plasmonic materials in the wavelength range of 300–550 nm; silver is poor below about 350 nm. This suggests that a combination of silver, gold, and aluminum particles of various sizes could allow for LSPRs from the UV to the NIR whilst minimizing the interference of interband transitions.

In light of recent methods to cap metal nanoparticles with protective layers, it is clear that silver is the optimum choice for plasmon enhanced DSSCs. Local surface plasmon resonances can be excited on silver nanostructures over a majority of the solar spectrum.

3.3.2 Shape

The variety of shapes available *via* recent wet chemistry synthetic methods is large and includes spheres [24], dielectric core-metallic shell particles [25], rods [26–30], cubes [31, 32], concave cubes [33], octahedra [31], hollow octahedra [34], rhombic dodecahedra [35], disks [36, 37], triangular prisms [38] and hollow triangular prisms [39] to name but a few. Of these myriad shapes, only a small fraction have been incorporated into DSSC devices. Here we will discuss the general properties of these shapes as they apply to DSSCs and review current progress in incorporating these structures into DSSCs.

3.3.3 Polarization-Independent Resonances

Spheres, core-shell particles, and, to some extent, cubes exhibit polarization-independent resonances because of their high symmetries. This is ideal for DSSCs, as the particles can be readily combined with the semiconductor and deposited onto the conducting oxide with no regard for the orientation of the nanoparticles in the structure. Lower symmetry structures, such as rods and prisms, have polarization- and orientation- dependent resonances and care must be taken to optimize the deposition mechanics to ensure that the long axis of the structures is perpendicular to the incident sunlight. The inclusion of spherical metal nanoparticles has so far been the dominant method to investigate the effect of plasmons on the photovoltage and photocurrent of DSSCs. A summary of DSSC device setups presented in the literature is shown in Fig. 3.7.

The first example of plasmonically enhanced DSSCs in the literature was in 1997, where it was shown that 0.3 and 1 % by volume of silver spheres could increase the photocurrent in a Rose bengal dye-sensitized TiO_2 cell. Here the majority of the photocurrent comes from direct electron injection from the silver into the TiO_2 (type A cell, Fig. 3.7) [40]. The same cell showed a decrease in photocurrent upon inclusion of 3 % by volume gold spheres. This was explained by noting that a majority of the photocurrent in the silver case arose from UV in the irradiation source, where gold exhibits interband transitions.

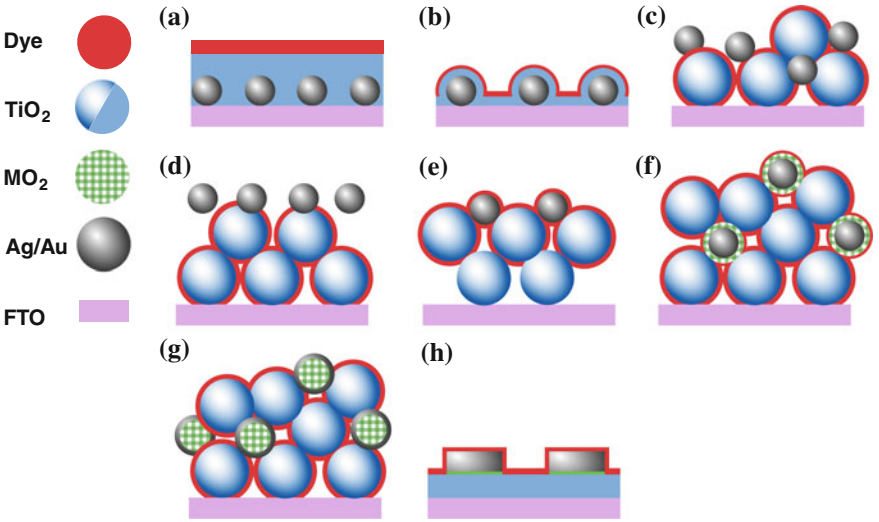

Fig. 3.7 Summary of plasmonically enhanced DSSC geometries that have been investigated in the literature. Each geometry is discussed in detail on the subsequent few pages

Another type A cell was the first to report that there exists an optimum concentration of metal inclusions in the DSSCs; they showed that a silver island film with an effective thickness of 3.3 nm gave enhanced photocurrent compared to an island film with effective thickness of 6.0 nm [41]. They attribute the difference in cell performance to fluctuations in the surface states of the TiO_2 and increased trapping of carriers with increased silver concentration. Many variations on the type A style cells have been made, with many of them relying purely on direct electron injection from the nanoparticle to the TiO_2; from here we will focus on dye-mediated absorption processes.

As mentioned earlier, silver nanoparticles are susceptible to oxidation and thus need to be protected to maintain their plasmonic properties. The formation of an oxide layer has been shown to affect the metal dielectric response at the interface [42, 43]. Type B cells were made using atomic layer deposition (ALD) to coat 36 nm silver nanoparticles in a layer of either amorphous or anatase TiO_2 in order to study the effect of the TiO_2 thickness on the enhancement of dye absorption [18]. Anatase is TiO_2's most conductive crystalline form, but it requires a minimum thickness of 6.5 nm to prevent oxidation of coated silver particles. Amorphous TiO_2 can be deposited at lower thicknesses but the cells degrade over time. Depositing 7.7 nm of TiO_2 was shown to fully protect the nanoparticles [18]. However the near-field coupling decays with distance from the surface, resulting in low plasmon-enhanced dye absorption at 7.7 nm (see Fig. 3.3). Adding a more chemically robust intermediary between the metal and the semiconductor can decrease the thickness of the TiO_2 coating needed. Depositing 0.2 nm of Al_2O_3 (sapphire) was shown to reduce the

necessary TiO_2 thickness to ~5 nm [16], and allowing for higher coupling, and absorption, by the dyes.

A comparison of the position of unprotected gold particles (type C, D and E) showed that cells of type C exhibit twice the photocurrent of a metal-free cell, and types D and E have reduced photocurrent compared to metal-free cells [44].

Du et al. [45] note that the size of the TiO_2 particles affects the electron injection dynamics in a Au sphere/TiO_2 type D system, with larger TiO_2 particles reducing recombination due to a longer diffusion length. Additionally, charging of the Ag in a Ag/TiO_2 cell was shown to prevent recombination of the charge carriers due to a large screening effect by the metal [46]. But the same effect also doubles the time for the redox mediator to regenerate the dye [46].

Recent advances in growing the TiO_2 directly on the metal nanoparticles using wet chemistry has allowed for the creation of type F cells [47]. It was found that as little as 0.1 wt. % of core-shell particles improved efficiency from 7.8 to 9 % while decreasing the thickness of the cell by 25 %. This decreased carrier distance is one of the main appeals of incorporating plasmonic nanoparticles into photovoltaics.

Choi et al. performed measurements on DSSCs including both TiO_2 and SiO_2 coated Au nanospheres (type D) and noted that the TiO_2 coated particles increased the overall cell efficiency from 9.29 % without Au to 9.78 % with Au, whilst the SiO_2 coated Au increased the cell efficiency to 10.21 % [17]. The difference was caused by charge accumulation on the Au cores in the Au/TiO_2 case, which modifies the Fermi level of the composite film [48]. This did not, however, explain the observation that the Au/SiO_2 only increases the cell efficiency for particle loadings of less than 0.70 wt. %, above which the cell efficiency decreases.

The optimum particle loading that has been reported by reference [17] can be explained by noting that a majority of light absorption in a metal loaded cell occurs at the top of the cell, even for modest particle loadings. Take for example a 1 μm thick cell loaded with 20 nm radius silver spheres. The cross-section of such spheres is 0.013 μm^2. Beer's law relates the absorption cross-section, optical path length (l) and number density of absorbers (N) to the transmission through the cell *via* $T = \exp(-C_{abs} l N)$. For a 1 μm thick cell, a particle loading of $N = 400\ \mu m^{-3}$ is required to achieve an optical density (1-T) of 99 %. There are therefore 7.4 layers of silver spheres in the cell with an areal density of 55 particles per square micron. The top layer of spheres absorbs 49 % of the initial intensity of the incident light, which is approximately 5×10^5 photons $\mu m^{-2} s^{-1}$, with each subsequent layer absorbing 49 % of the remaining light, *i.e.* the first layer of spheres absorbs 49 % of the photons, and the remaining 6.4 layers absorb the remaining 50 %. It is easy to imagine that the top layer of particles excites many more dye molecules than the redox couple can reduce per second, resulting in lost photon absorption opportunities. This highlights the importance of varying the density of the particle loading through the thickness of the cell. It is vital that no single layer absorbs dramatically more photons than the other layers, and therefore the particle positions in the cell must be optimized to follow an exponential loading density that minimizes bleaching.

3.3.4 Dielectric Core—Metal Shell Particles

So far we have only discussed essentially spherical metal particles with various dielectric coatings. In order to cover a large fraction of the solar spectrum, geometries that allow for large shifts in the LSPR wavelength must be used. One example of this is the dielectric core—metal shell geometry. The polarizability of this geometry is given by:

$$\alpha = V \frac{(\varepsilon_\mathrm{m} - \varepsilon_\mathrm{d})(\varepsilon_\mathrm{c} + 2\varepsilon_\mathrm{m}) + f(\varepsilon_\mathrm{c} - \varepsilon_\mathrm{m})(\varepsilon_\mathrm{d} + 2\varepsilon_\mathrm{m})}{(\varepsilon_\mathrm{m} + 2\varepsilon_\mathrm{d})(\varepsilon_\mathrm{c} + 2\varepsilon_\mathrm{m}) + 2f(\varepsilon_\mathrm{m} - \varepsilon_\mathrm{d})(\varepsilon_\mathrm{c} - 2\varepsilon_\mathrm{m})}, \tag{3.7}$$

where ε_c, ε_m and ε_d are the dielectric functions of the core, metal and surrounding dielectric respectively. The fill fraction, f, is the fraction of the volume occupied by the core: $f = (r_\mathrm{c}/r_\mathrm{m})^3$. As the fraction approaches one, the resonance condition in terms of ε_m moves to more negative values, and the LSPR red-shifts.

SiO_2-core-silver-shell, type G, particles have been introduced into DSSCs, where they show a broad absorption band from approximately 450–700 nm [49]. Incorporating 22 vol. % of these core-shell particles resulted in an increase in overall cell efficiency from 2.7 to over 4 %. The authors note that the core-shell particles reduce the dye available surface area by 21 % and dye adsorption by the same amount. With this considered, the near-field enhancement of dye absorption for the 22 vol. % is over 1.8 [49]. Upon inclusion of 33 vol. % core-shell particles, the efficiency of the cell decreased, possibly due to a reduction in the dye accessible surface area [49].

3.3.5 Polarization-Dependent Resonances in Anisotropic Particles

Asymmetry in the geometry of a nanoparticle gives rise to polarization-dependent resonances. These can vary from highly anisotropic particles, such as prisms and rods, to more isotropic ones, like cubes and dodecahedra. As a simple example, let us consider a rod, which typically has two distinct resonances. The longitudinal resonance occurs when the polarization of light is parallel to the long axis of the particle, and is always red of the sphere resonance. The transverse resonance occurs when the polarization is parallel to the short axis and occurs at approximately the same frequency as the sphere resonance. The polarizability of a rod-like prolate-spheroid is given by:

$$\alpha = V \frac{\varepsilon_\mathrm{m} - \varepsilon_\mathrm{d}}{\varepsilon_\mathrm{d} + L(\varepsilon_\mathrm{m} - \varepsilon_\mathrm{d})}, \tag{3.8}$$

where L is a depolarization factor that takes the form:

$$L_\mathrm{Long} = \frac{1 - e^2}{e^2}\left(-1 + \frac{1}{2e}\ln\frac{1+e}{1-e}\right), \tag{3.9}$$

for the longitudinal resonance and

$$L_{\text{Trans}} = \frac{1 - L_{\text{Long}}}{2}, \tag{3.10}$$

for the transverse resonance. The eccentricity, e, of the spheroid is:

$$e = \sqrt{1 - (b^2/a^2)}, \tag{3.11}$$

where a and b are the radii of the long and short axes, respectively.

Hägglund et al. directly showed increased carrier generation rates in dyes from polarization-dependent LSPR's in rod-like gold particles [50]. This was done by lithographically patterning an array of particles onto a TiO_2 film (type H, note the green layer, Al_2O_3, separating the gold from the TiO_2, thereby preventing modification of the Fermi level and direct electron injection). By changing the polarization of incident light, one can excite two different resonances in the particle, allowing for discrimination of the LSPR enhancement. Photocurrent enhancement shows a strong dependence on the polarization of incident light; both axes show positive enhancement with the transverse resonance showing a more pronounced effect due to better overlap with the dye absorption spectrum. This led the authors to conclude that the dye injection rate is increased by the LSPR.

3.3.6 Other Geometries

Most methods of incorporating plasmons into DSSCs involve discrete nanoparticles. In light of advances in optical trapping in p–n junction cells, it is worth noting work has been done on incorporating nano-patterned silver back reflectors into solid-state-DSSCs [51]. The intent of the study was to illustrate that even cells with strongly absorbing dyes, such as the state-of-the-art Z907-Ru dye, can be enhanced.

3.4 Challenges and Outlook

This young field has seen a variety of creative geometries and materials advances needed to increase efficiencies and decrease the materials used in dye-sensitized solar cells. Some have simply involved changing the placement of the plasmonic nanoparticles relative to the mesoporous oxide carrier. Others involve more intricate fabrication, coating, and particle geometries chosen to minimize loss and scattering while maximizing absorbance and thus enhancement.

Because the solar spectrum spans a broad wavelength range, it is unlikely that a single size or shape of nanoparticle will offer optimal broadband absorption. Thus, creative combinations of sizes, shapes, and nanoparticle compositions are likely to give the best absorption enhancements. In thin film silicon cells, ~95% absorption

efficiencies have been reached with a combination of Al substrate and Au nanoparticles [52]. Additionally, nucleated silver nanoparticles showed a large increase in scattering resulting in a ∼5 % increase in photocurrent [53]. The nucleated large particles were essentially 200 nm Ag particles covered in many smaller 20–40 nm particles. The small particles scatter red light and the large particles scatter blue light, maximizing the total scattered radiation into the cell. Though this study was formulated for thin film silicon cells, similar principles with different particles involving absorption and field concentration could be incorporated into DSSCs.

To elucidate some of possibilities for local field enhancement offered by various nanoparticle shapes (Fig. 3.8), we have calculated the optical response of silver cubes, prisms and rods within the discrete dipole approximation (See [54, 55] for details and [56] for an overview). For simplicity, the particles were not coated in a capping layer in the simulation. The cubes have a rounding on the corners of 10 % of the edge length, which is comparable to what is seen experimentally. They offer strong enhancement in the UV for particles with an edge length of less than 60 nm, with the 40 nm edge length cubes offering field enhancements above 200. The prisms also have a radius of curvature on the corners of 10 % of the edge length. Increasing the aspect ratio of the prism (edge length: thickness) rapidly red-shifts the resonance and causes a large increase in the field enhancement from approximately 1,000 for 5:1 prisms, to 4,500 for 15:1 and larger. The enhancement for rods is even more dramatic, reaching nearly 20,000 for 8:1 (length:width) aspect ratio rods. It is clear from these brief calculations that massively-enhanced fields can be observed across the entire solar spectrum by modifying the geometry of the nanoparticles in a system.

3.4.1 Ensembles

Thus far we have only discussed nanoparticle attributes on a single particle level. However, nanoparticles are usually implemented in ensembles where proximity allows for optical-mode coupling. The coupling of these modes leads to very large field enhancement in the gaps between particles. Many applications have arisen because of this strong enhancement, particularly in the field of surface enhanced Raman scattering (SERS), where the Raman scattering scales with the fourth power of the local electric field ($\langle \mathbf{E}^4/\mathbf{E}_0^4 \rangle$). This has resulted in reports of enhancement factors of up to 10^{10} [57, 58]. As of yet, there have been no reports of particle dimers or aggregates being used systematically to enhance absorption in DSSCs. To demonstrate the possible increase in dye absorption provided by dimerized particle structures, we have calculated the electric field enhancement around a dimer of 20 nm radius silver spheres with a 2 nm TiO_2 capping layer. Even with the presence of the capping layer, the field enhancement can be increased from 160 in the case where the particles are separated by 5 nm, to 360 when they are separated by 1 nm. The approximate factor of two change in enhancement due to the gap is much smaller than arises in Raman scattering, which means that dimers with small gaps are less important in solar energy than in Raman, however the results in Fig. 3.9 suggest that dimer

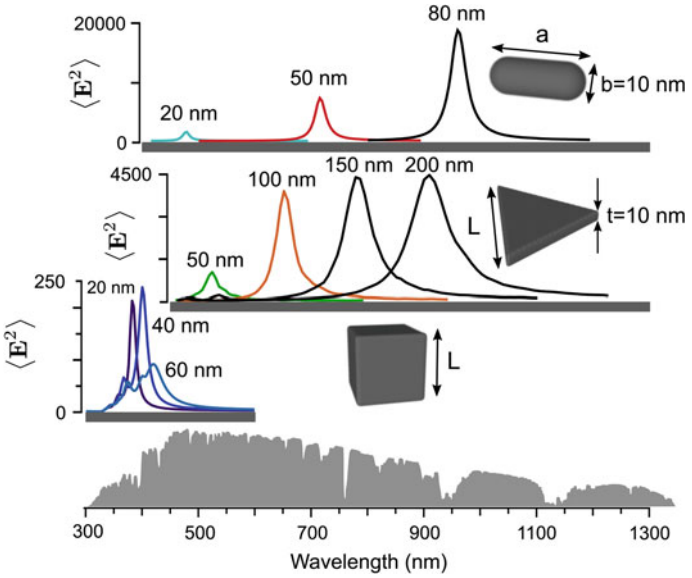

Fig. 3.8 Surface-averaged electric fields for a variety of *silver* nanoparticles. The bottom panel in gray is the AM 1.5G solar spectrum

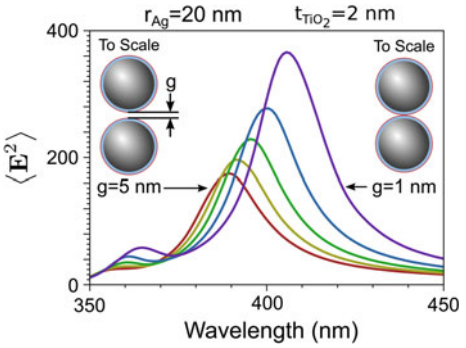

Fig. 3.9 The effect of interparticle gap on the surface-averaged fields. The system is a dimer of 20 nm radius *silver spheres* coated with 2 nm of TiO_2. A 0.5 nm layer of dye is included in the images to scale, but was not present in the simulation, which was performed using generalized Mie theory [59]

structures and other small aggregates can be useful if easily fabricated. The result for 1 nm separation probably represents a limit on how small the interparticle gap can be assuming that the TiO_2 is uniformly covered by dye molecules. The possibility arises in this case that the redox couple may not have access to molecules in the confined region between particles, resulting in lost photocurrent. The high enhancement in nanoparticle gaps is markedly more pronounced with anisotropic structures, thus similar enhancement could be gained with larger gaps that still allow for diffusion of the redox electrolyte.

3.4.2 Excited State Lifetime of Plasmons

The utility of plasmonically enhanced DSSCs relies on the premise that electron injection from the dye to the TiO_2 occurs on a timescale that is more rapid than the lifetime of the plasmon. There have been many studies on electron injection dynamics (see [60] for a review), with many reports suggesting that the charge injection occurs on the sub-100 fs timescale. However, there have been reports of injection half-times ranging from sub-3 fs [61] to 200 ps [62]. For small nanoparticles (in the quasi-static limit, where there is minimal scattering), the excited state lifetime of a LSPR is related to the full-width at half-maximum (Γ) *via*

$$T = 2\hbar/\Gamma, \tag{3.12}$$

the minimum non-radiative contribution to Γ depends on the frequency of the LSPR and is given by:

$$\Gamma(\omega) = 2\varepsilon_{\mathrm{i}}(\omega)\left(\frac{\mathrm{d}\varepsilon_{\mathrm{r}}(\omega)}{\mathrm{d}\omega}\right)^{-1} \tag{3.13}$$

In Eq. 3.13, ε_{r} and ε_{i} are the real and imaginary parts of the dielectric function of the metal. Dephasing times calculated using Eqs. 3.12 and 3.13 for silver and gold are shown in Fig. 3.10. For particles that cannot be considered in the quasi-static regime (for spheres, a radius of about 30 nm) there is a contribution to Γ from radiative effects, such as scattering, which reduces the lifetime of the state. There are several noteworthy features of Fig. 3.10, the first is that the lifetime of LSPRs on silver particles is at least twice that of gold across all frequencies, and the second is that interband transitions result in very low lifetimes at high frequencies.

There have also been reports that the injection dynamics depend on the nature of the excited state of the dye, with singlet injection dynamics on the N719 dye occurring on time scales almost two orders of magnitude faster than triplet injection [63]. In this case, a combination of finely tuning the plasmon resonance of nanoparticles and dye engineering could assist in promoting singlet excitation to aid electron injection dynamics.

3.4.3 Metal Losses

It is well known that metal nanoparticles get hot under irradiation, a characteristic that has resulted in their use in fields as diverse as tumor therapy [64]. The rate of energy loss inside a metal particle (due to scattering of the electrons on phonons) is the product of the imaginary part of the dielectric constant of the metal and the volume integral of the internal electric field strength (see [65, Sect. 80]):

$$\frac{\mathrm{d}q}{\mathrm{d}t} = \frac{\omega}{2}\varepsilon_{\mathrm{i}}(\omega)\int \mathbf{E}(\omega)^2 \mathrm{d}V \tag{3.14}$$

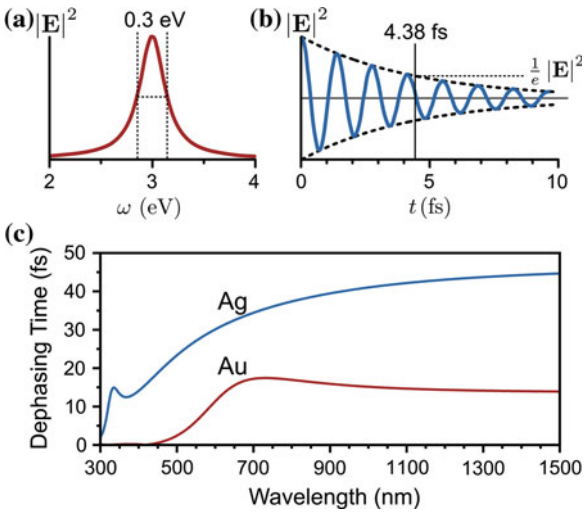

Fig. 3.10 Lifetime of plasmonic states. **a** A typical plasmon resonance showing the strength of the electric field and the full width at half maximum of the resonance. **b** The Fourier transform of (**a**), showing the decay of the field strength with time. The dephasing time of 4.38 fs is related to the FWHM of 0.3 eV *via* Eq. 3.12. **c** Dephasing times of silver and gold calculated using Eqs. 3.12 and 3.13.

This loss poses the immediate problem that the larger the strength of the internal field (which to a first approximation is proportional to the surface field) the larger the energy loss to the metal. Additionally, as particle size increases, the ratio of volume to surface area increases, indicating that a larger fraction of the field will reside in the metal than at the surface, compounding energy loss. There are two reasonably straightforward remedies to this issue. The first is to keep the volume of individual particles reasonably low. The second is to observe that the dye molecules obey the same expression as the metal, except the internal field of the dye molecule is entirely due to the surface field of the particle, and the obvious solution becomes to increase the imaginary part of the dielectric constant of the dye to compensate for the lack of field strength. This idea has been investigated [66], and it was noted that, although the relationship between loss in the dye versus loss in the metal is geometry-dependent, if the imaginary part of the dielectric function of the dye is above two, the fraction of energy loss to the dye can approach 90 % of the total energy loss [66]. Despite these results, dyes with low absorption cross sections (such as the N3 dye) have been shown to be enhanced by metal nanoparticle inclusions. Some progress has been made using hybrid electrodynamics/quantum mechanics techniques to study plasmonically enhanced dye absorption [67], but as of yet, the dynamics of energy transfer between nanoparticles and dye molecules remains largely unexplored.

3.5 Conclusion

Plasmonic enhancement of dye sensitized solar cells is a young field with a promising future; only a handful of cells have been built and tested, with those incorporating only a small selection of the available dyes and nanoparticle shapes. We have shown that there is a bright future for enhancing dye absorption across the entire solar spectrum. Coupled with research into the energetics and dynamics of particle-dye interactions, we expect that plasmon-enhanced dye-sensitized solar cells will help to reduce the cost and improve the efficiency of next generation solar cells.

Acknowledgments This work was supported by the Department of Energy, Office of Basic Energy Science, grant DE-SC0004752. M.B.R. acknowledges the National Defense Science and Engineering Graduate Fellowship.

References

1. N.S. Lewis, D.G. Nocera, Powering the planet: chemical challenges in solar energy utilization. Proc. Natl. Acad. Sci. USA **104**, 20142 (2007)
2. D.M. Powell, M.T. Winkler, H.J. Choi, C.B. Simmons, D.B. Needleman, T. Buonassisi, Crystalline silicon photovoltaics: a cost analysis framework for determining technology pathways to reach baseload electricity costs. Energy Environ. Sci. **5**, 5874 (2012)
3. W. Shockley, H.J. Queisser, Detailed balance limit of efficiency of P–N junction solar cells. J. Appl. Phys. **32**, 510 (1961)
4. A. Hagfeldt, G. Boschloo, L.C. Sun, L. Kloo, H. Pettersson, Dye-sensitized solar cells. Chem. Rev. **110**, 6595 (2010)
5. H.A. Atwater, A. Polman, Plasmonics for improved photovoltaic devices. Nat. Mater. **9**, 205 (2010)
6. B. O'Regan, M. Gratzel, A low-cost, high-efficiency solar-cell based on dye-sensitized colloidal TiO2 films. Nature **353**, 737 (1991)
7. A. Yella, H.W. Lee, H.N. Tsao, C.Y. Yi, A.K. Chandiran, M.K. Nazeeruddin, E.W.G. Diau, C.Y. Yeh, S.M. Zakeeruddin, M. Gratzel, Porphyrin-sensitized solar cells with cobalt (II/III)-based redox electrolyte exceed 12 percent efficiency. Science **334**, 629 (2011)
8. M. Gratzel, Photoelectrochemical cells. Nature **414**, 338 (2001)
9. K. Zhu, S.R. Jang, A.J. Frank, Impact of high charge-collection efficiencies and dark energy-loss processes on transport, recombination, and photovoltaic properties of dye-sensitized solar cells. J. Phys. Chem. Lett. **2**, 1070 (2011)
10. K. Zhu, N. Kopidakis, N.R. Neale, J. van de Lagemaat, A.J. Frank, Influence of surface area on charge transport and recombination in dye-sensitized TiO2 solar cells. J. Phys. Chem. B **110**, 25174 (2006)
11. C. Hagglund, S.P. Apell, Plasmonic near-field absorbers for ultrathin solar cells. J. Phys. Chem. Lett. **3**, 1275 (2012)
12. K.L. Kelly, E. Coronado, L.L. Zhao, G.C. Schatz, The optical properties of m nanoparticles: The influence of size, shape, and dielectric environment. J. Phys. Chem. B **107**, 668 (2003)
13. C. Nahm, H. Choi, J. Kim, D.R. Jung, C. Kim, J. Moon, B. Lee, B. Park, The effects of 100 nm-diameter Au nanoparticles on dye-sensitized solar cells. Appl. Phys. Lett. **99**, 253107 (2011)
14. M.G. Blaber, G.C. Schatz, Extending SERS into the infrared with gold nanosphere dimers. Chem. Commun. **47**, 3769 (2011)

15. K. Ishikawa, C.J. Wen, K. Yamada, T. Okubo, The photocurrent of dye-sensitized solar cells enhanced by the surface plasmon resonance. J. Chem. Eng. Jpn. **37**, 645 (2004)
16. S.D. Standridge, G.C. Schatz, J.T. Hupp, Toward Plasmonic Solar Cells: Protection of silver nanoparticles via atomic layer deposition of TiO2. Langmuir **25**, 2596 (2009)
17. H. Choi, W.T. Chen, P.V. Kamat, Know Thy Nano Neighbor. Plasmonic versus electron charging effects of metal nanoparticles in dye-sensitized solar cells. ACS Nano **6**, 4418 (2012)
18. S.D. Standridge, G.C. Schatz, J.T. Hupp, Distance dependence of plasmon-enhanced photocurrent in dye-sensitized solar cells. J. Am. Chem. Soc. **131**, 8407 (2009)
19. G. Mie, Beiträge zur Optik trüber Medien, speziell kolloidaler Metallösungen. Ann. Phys. **25**, 377 (1908)
20. M. Gratzel, Solar energy conversion by dye-sensitized photovoltaic cells. Inorg. Chem. **44**, 6841 (2005)
21. M. Grätzel, Conversion of sunlight to electric power by nanocrystalline dye-sensitized solar cells. J. Photochem. Photobiol. A **164**, 3 (2004)
22. S. Altobello, R. Argazzi, S. Caramori, C. Contado, S. Da Fre, P. Rubino, C. Chone, G. Larramona, C.A. Bignozzi, Sensitization of nanocrystalline TiO2 with black absorbers based on Os and Ru polypyridine complexes. J. Am. Chem. Soc. **127**, 15342 (2005)
23. L. Macor, F. Fungo, T. Tempesti, E.N. Durantini, L. Otero, E.M. Barea, F. Fabregat-Santiago, J. Bisquert, Near-IR sensitization of wide band gap oxide semiconductor by axially anchored Si-naphthalocyanines. Energy Environ. Sci. **2**, 529 (2009)
24. S. Link, M.A. El-Sayed, Spectral properties and relaxation dynamics of surface plasmon electronic oscillations in gold and silver nanodots and nanorods. J. Phys. Chem. B **103**, 8410 (1999)
25. C. Graf, A. van Blaaderen, Metallodielectric colloidal core-shell particles for photonic applications. Langmuir **18**, 524 (2002)
26. M. Ahmed, R. Narain, Rapid synthesis of gold nanorods using a one-step photochemical strategy. Langmuir **26**, 18392 (2010)
27. N.R. Jana, L. Gearheart, C.J. Murphy, Wet chemical synthesis of high aspect ratio cylindrical gold nanorods. J. Phys. Chem. B **105**, 4065 (2001)
28. N.R. Jana, L. Gearheart, C.J. Murphy, Wet chemical synthesis of silver nanorods and nanowires of controllable aspect ratio. Chem. Comm. **37**, 617 (2001)
29. F. Kim, J.H. Song, P.D. Yang, Photochemical synthesis of gold nanorods. J. Am. Chem. Soc. **124**, 14316 (2002)
30. T.K. Sau, C.J. Murphy, Seeded high yield synthesis of short Au nanorods in aqueous solution. Langmuir **20**, 6414 (2004)
31. D. Seo, J.C. Park, H. Song, Polyhedral gold nanocrystals with O-h symmetry: from octahedra to cubes. J. Am. Chem. Soc. **128**, 14863 (2006)
32. A. Tao, P. Sinsermsuksakul, P.D. Yang, Polyhedral silver nanocrystals with distinct scattering signatures. Angew. Chem. Int. Edit. **45**, 4597 (2006)
33. J.A. Zhang, M.R. Langille, M.L. Personick, K. Zhang, S.Y. Li, C.A. Mirkin, Concave cubic gold nanocrystals with high-index facets. J. Am. Chem. Soc. **132**, 14012 (2010)
34. M.R. Langille, M.L. Personick, J. Zhang, C.A. Mirkin, Bottom-Up Synthesis of gold octahedra with tailorable hollow features. J. Am. Chem. Soc. **133**, 10414 (2011)
35. M.L. Personick, M.R. Langille, J. Zhang, C.A. Mirkin, Shape control of gold nanoparticles by silver underpotential deposition. Nano Lett. **11**, 3394 (2011)
36. M. Maillard, S. Giorgio, M.P. Pileni, Tuning the size of silver nanodisks with similar aspect ratios: Synthesis and optical properties. J. Phys. Chem. B **107**, 2466 (2003)
37. G.P. Lee, A.I. Minett, P.C. Innis, G.G. Wallace, A new twist: controlled shape-shifting of silver nanoparticles from prisms to discs. J. Mater. Chem. **19**, 8294 (2009)
38. R.C. Jin, Y.W. Cao, C.A. Mirkin, K.L. Kelly, G.C. Schatz, J.G. Zheng, Photoinduced conversion of silver nanospheres to nanoprisms. Science **294**, 1901 (2001)
39. H.J. Yoo, J.E. Millstone, S.Z. Li, J.W. Jang, W. Wei, J.S. Wu, G.C. Schatz, C.A. Mirkin, Core-shell triangular bifrustums. Nano Lett. **9**, 3038 (2009)

40. G.L. Zhao, H. Kozuka, T. Yoko, Effects of the incorporation of silver and gold nanoparticles on the photoanodic properties of rose bengal sensitized TiO2 film electrodes prepared by sol-gel method. Solar Energy Mater. Solar Cells **46**, 219 (1997)
41. C. Wen, K. Ishikawa, M. Kishima, K. Yamada, Effects of silver particles on the photovoltaic properties of dye-sensitized TiO2 thin films. Solar Energy Mater. Solar Cells **61**, 339 (2000)
42. P. Wismann, R.E. Hummell (ed.), Handbook of Optical Properties:*Optics of small particles, interfaces, and surfaces*, vol II. (CRC Press: Boca Raton, FL), (1997). ISBN 13: 978-0849324857
43. M.D. Malinsky, K.L. Kelly, G.C. Schatz, R.P. Van Duyne, Nanosphere lithography: effect of substrate on the localized surface plasmon resonance spectrum of silver nanoparticles. J. Phys. Chem. B **105**, 2343 (2001)
44. W. Hou, P. Pavaskar, Z. Liu, J. Theiss, M. Aykol, S.B. Cronin, Plasmon resonant enhancement of dye sensitized solar cells. Energy Environ. Sci. **4**, 4650 (2011)
45. L.C. Du, A. Furube, K. Yamamoto, K. Hara, R. Katoh, M. Tachiya, Plasmon-induced charge separation and recombination dynamics in gold-TiO2 nanoparticle systems: dependence on TiO2 particle size. J. Phys. Chem. C **113**, 6454 (2009)
46. P.K. Sudeep, K. Takechi, P.V. Kamat, Harvesting photons in the infrared. Electron injection from excited tricarbocyanine dye (IR-125) into TiO2 and Ag@TiO2 core-shell nanoparticles. J. Phys. Chem. C **111**, 488 (2007)
47. J.F. Qi, X.N. Dang, P.T. Hammond, A.M. Belcher, Highly efficient plasmon-enhanced dye-sensitized solar cells through metal@oxide core-shell nanostructure. ACS Nano **5**, 7108 (2011)
48. V. Subramanian, E.E. Wolf, P.V. Kamat, Catalysis with TiO2/gold nanocomposites. Effect of metal particle size on the fermi level equilibration. J. Am. Chem. Soc. **126**, 4943 (2004)
49. B. Ding, B.J. Lee, M.J. Yang, H.S. Jung, J.K. Lee, Surface-plasmon assisted energy conversion in dye-sensitized solar cells. Adv. Energy Mater. **1**, 415 (2011)
50. C. Hagglund, M. Zach, B. Kasemo, Enhanced charge carrier generation in dye sensitized solar cells by nanoparticle plasmons. Appl. Phys. Lett. **92**, 013113 (2008)
51. I.K. Ding, J. Zhu, W.S. Cai, S.J. Moon, N. Cai, P. Wang, S.M. Zakeeruddin, M. Gratzel, M.L. Brongersma, Y. Cui, M.D. McGehee, Plasmonic dye-sensitized solar cells. Adv. Energy Mater. **1**, 52 (2011)
52. A. Pors, A.V. Uskov, M. Willatzen, I.E. Protsenko, Control of the input efficiency of photons into solar cells with plasmonic nanoparticles. Opt. Commun. **284**, 2226 (2011)
53. X. Chen, B.H. Jia, J.K. Saha, B.Y. Cai, N. Stokes, Q. Qiao, Y.Q. Wang, Z.R. Shi, M. Gu, Broadband enhancement in thin-film amorphous silicon solar cells enabled by nucleated silver nanoparticles. Nano Lett. **12**, 2187 (2012)
54. B.T. Draine, P.J. Flatau, Discrete-dipole approximation for scattering calculations. J. Opt. Soc. Am. A **11**, 1491 (1994)
55. P.J. Flatau, B.T. Draine, Fast near field calculations in the discrete dipole approximation for regular rectilinear grids. Opt. Express **20**, 1247 (2012)
56. J. Zhao, A.O. Pinchuk, J.M. Mcmahon, S.Z. Li, L.K. Ausman, A.L. Atkinson, G.C. Schatz, Methods for describing the electromagnetic properties of silver and gold nanoparticles. Acc. Chem. Res. **41**, 1710 (2008)
57. E. Le, C. Ru, E. Blackie, M. Meyer, P. G. Etchegoin, Surface enhanced Raman scattering enhancement factors: A comprehensive study. J. Phys. Chem. C **111**, 13794 (2007)
58. J.M. McMahon, S. Li, L.K. Ausman, G.C. Schatz, Modeling the effect of small gaps in surface-enhanced Raman spectroscopy. J. Phys. Chem. C **116**, 1627 (2012)
59. Xu, Y.-l., Electromagnetic scattering by an aggregate of spheres. Appl. Opt. **34**, 4573 (1995).
60. N.A. Anderson, T.Q. Lian, Ultrafast electron transfer at the molecule-semiconductor nanoparticle interface. Annu. Rev. Phys. Chem. **56**, 491 (2005)
61. J. Schnadt, P.A. Bruhwiler, L. Patthey, J.N. O'Shea, S. Sodergren, M. Odelius, R. Ahuja, O. Karis, M. Bassler, P. Persson, H. Siegbahn, S. Lunell, N. Martensson, Experimental evidence for sub-3-fs charge transfer from an aromatic adsorbate to a semiconductor. Nature **418**, 620 (2002)

62. S.E. Koops, B.C. O'Regan, P.R.F. Barnes, J.R. Durrant, Parameters influencing the efficiency of electron injection in dye-sensitized solar cells. J. Am. Chem. Soc. **131**, 4808 (2009)
63. J.J.H. Pijpers, R. Ulbricht, S. Derossi, J.N.H. Reek, M. Bonn, Picosecond electron injection dynamics in dye-sensitized oxides in the presence of electrolyte. J. Phys. Chem. C **115**, 2578 (2011)
64. L.R. Hirsch, R.J. Stafford, J.A. Bankson, S.R. Sershen, B. Rivera, R.E. Price, J.D. Hazle, N.J. Halas, J.L. West, Nanoshell-mediated near-infrared thermal therapy of tumors under magnetic resonance guidance. Proc. Natl. Acad. Sci. USA **100**, 13549 (2003)
65. L.D. Landau, E.M. Lifshitz, *Electrodynamics of Continuous Media*, 2nd edn. (Butterworth-Heinemann, Oxford, 1984), p. 8
66. R. Watanabe, K. Miyano, Metal nanoparticles in a photovoltaic cell: effect of metallic loss. AIP Adv. **1**, 042154 (2011)
67. H.N. Chen, M.G. Blaber, S.D. Standridge, E.J. DeMarco, J.T. Hupp, M.A. Ratner, G.C. Schatz, Computational modeling of plasmon-enhanced light absorption in a multicomponent dye sensitized solar cell. J. Phys. Chem. C **116**, 10215 (2012)

Chapter 4
Silicon Plasmonics

Ilya Goykhman, Boris Desiatov and Uriel Levy

Abstract The implementation of plasmonic components using silicon platform holds a great promise for the development of advanced nanoscale on-chip photonic functionalities. The combination of high optical mode confinement offered by plasmonics together with mature and well established CMOS technology makes the field of silicon plasmonics a promising technological solution for intra-chip integration of nanoscale optical and opto-electronic devices operating side by side with modern electronics. The great opportunity of the silicon plasmonic platform resides in bridging the dimensionality gap between the photonic and electronic components on-chip, while moderating the loss-confinement limitation of plasmonic structures. In this section we refer to the fundamental problems of silicon-plasmonic integration and review the current state of the art demonstrations in the field with special emphasis on the advantages of using plasmonics for the purpose of constructing of novel nanoscale devices such as modern plasmonic modulators, concentrators and photodetectors for on-chip applications.

Keywords Silicon · Plasmonics · Integrated devices · Nanotechnology

4.1 Introduction

In the past few decades we have been witnessing a revolution in electronics, in which computation capacity has been increasing very rapidly, following Moore's law that was originally declared over 45 years ago. However, the improvement in performance of VLSI circuits is now saturating, primarily because of fundamental limitations in device scaling, signal delay, signal distortion and heat dissipation. In order to allow further growth in data rates, there is an urgent need for a paradigm

I. Goykhman · B. Desiatov · U. Levy (✉)
Department of Applied Physics, The Benin School of Engineering and Computer Science, The Center for Nanoscience and Nanotechnology, The Hebrew University of Jerusalem, 91904 Jerusalem, Israel
e-mail: ulevy@mail.huji.ac.il

T. V. Shahbazyan and M. I. Stockman (eds.), *Plasmonics: Theory and Applications*, Challenges and Advances in Computational Chemistry and Physics 15,
DOI: 10.1007/978-94-007-7805-4_4, © Springer Science+Business Media Dordrecht 2013

shift from present integrated circuit technology towards what is coined "post CMOS era". The need for future emerging technologies that could play a role in shaping this post CMOS era is now well recognized by the electronics industry. For example, the report of the international technology roadmap for semiconductors indicates the following: "Proposed post-CMOS replacement devices are very different from their CMOS counterparts, and often pass computational state variables (or tokens) other than charge. Alternative state variables include collective or single spin, excitonic, plasmonic, photonic,… " [1].

Among the variety of potential technological solutions, photonics seems to be a promising candidate since it offers advantages in bandwidth, delay, cross-talk and power. Indeed, optics is already being used for long range communication, and is now being considered for shorter range applications including board-to-board and even chip-to-chip level [2]. In particular, the challenge of constructing short range photonics based communication can be mitigated by the use of the technology of silicon photonics. Over the years, large variety of silicon photonics based devices were demonstrated, including waveguides, splitters, combiners, filters, modulators, switches, and more. The wealth of silicon photonics devices and components, together with the mature CMOS compatible fabrication technology makes the field of silicon photonics an excellent candidate for being integrated in short range communication systems already in the very near future.

Side by side with the great promise of silicon photonics, it has also several limitations one needs to overcome in order to facilitate on chip integration of photonic and electronic systems. In particular, a major concern is the dimensionality mismatch between silicon photonics based devices and electronics components. A fundamental reason for this mismatch is the concept of diffraction limit. While electronic structures are nowadays much below 100 nm in size and are not limited by the wavelength of electron, being orders of magnitude smaller, the photonic mode size in dielectric structures cannot be scaled down much below the wavelength of light in the material. Indeed, typical dimensions of modern silicon waveguides are in the order of 500 nm wide and about 250 nm thick. This size mismatch between photonics and electronics is a major barrier, preventing the integration of silicon photonic devices such as waveguides, optical switches and optical modulators with electronic components on the same chip.

Recent progress in plasmonics may allow circumventing this obstacle. Plasmonic modes (either surface plasmon polaritons, or localized plasmons) can be confined at the nanoscale owing to the possibility of having short effective wavelength (in the U.V and even in the X-ray) at optical frequencies. An example for high mode confinement is the use of metal-insulator-metal (MIM) structures, which does not exhibit a cutoff for the fundamental mode. Therefore, by reducing the width of the insulator section high mode confinement is obtained because the metal does not allow the mode to extend much beyond its boundary with the insulator. The combination of nanoscale confinement and high frequencies makes the field of plasmonics an attractive candidate for "bridging the gap" between photonic components and modern electronics.

While plasmonics may become an attractive platform for supporting the operation of CMOS electronics, it is not expected to fully replace the silicon integrated circuits in the foreseeable future. The maturity, reliability, and wealth of electronic devices as well as the massive accumulated know-how in silicon science and technology—these are all clear indicators that silicon is here to stay, at least to some degree. Therefore, a growing effort is recently devoted for the development of a new platform, combining the concepts of silicon photonics with the advantages offered by the use of plasmonics. This hybrid approach, now coined as "silicon plasmonics" is the focus of this chapter. Along the text we review the recent achievements in the field and provide a forecast for future progress.

4.2 Silicon Plasmonics Components

4.2.1 Motivation

A modern optoelectronic circuit consists of passive and active devices (e.g. optical on chip waveguides or fibers, splitters, combiners, couplers, filters, modulators, switches, light sources and detectors). The great challenge of the silicon plasmonic platform is to facilitate the realization and the integration of such components on a chip, while mitigating challenges as loss and nanoscale confinement. In the following sub sections we review the current state of the art in this field with special emphasis on our work at the Hebrew University of Jerusalem.

4.2.2 Passive Devices

A major passive building block in an on chip optoelectronic circuit is obviously the optical waveguide linking between the various on chip components. Over the years, there has been a tremendous progress in the field of silicon based waveguides. It is now possible to routinely demonstrate light guiding such silicon waveguides having a submicron cross sectional dimensions. Typical propagation loss values are in the range of 2 dB/cm although it is possible to reduce loss even further e.g. by defining a waveguide structure by local oxidation of silicon (LOCOS) rather than using aggressive reactive ion etching (RIE) [3, 4]. While propagation loss of silicon waveguides is no longer a major concern, mode size is still far too large compared with typical dimensions of on chip electronic components. To further reduce the mode size, plasmonic guiding should be considered. Naively, one would think of constructing a silicon plasmonic waveguide by depositing a metal layer on top of a silicon waveguide. Unfortunately such a structure does not provide a satisfactory solution. Figure 4.1 (top) shows the dispersion diagram of an SPP mode propagating along a single silver-silicon interface, whereas Fig. 4.1 (bottom) shows corresponding

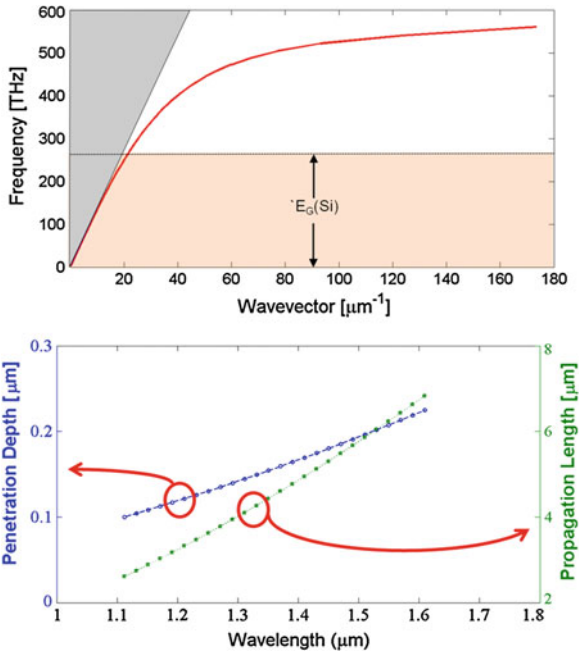

Fig. 4.1 *Top* Dispersion diagram, *bottom* mode size and propagation length of a single interface silicon-Ag plasmonic waveguide. Mode size is defined as the distance in the transverse direction (into the silicon) in which the intensity decays to 1/e compared with its value on the interface. Propagation length is defined as the distance along the propagation direction in which the intensity decays to 1/e of its original value

penetration depth into the silicon layer and the propagation length as a function of the excitation wavelength. As can be seen, in the case of high index dielectric (e.g. silicon) the propagation length of the SPP mode at telecom wavelengths is only few microns. At the same time, the mode size still extends few hundreds of nanometers into the silicon. This is due to the fact that in telecom regime the operation frequencies are significantly lower than the plasma frequency of electrons in the metal, and therefore the dispersion curve the SPP mode at this spectral range is very close to the silicon light line, thus offering very little advantage in terms of mode confinement.

According to data presented in Fig. 4.1, the challenge of deep nanoscale confinement cannot be achieved by constructing a single interface of silicon and metal. Indeed, it is possible to further reduce the mode size by using a symmetric double interface structure in which a thin layer of silicon is sandwiched between two layers of metal. Yet, while providing high confinement, the propagation loss of this structure is even worse than its single interface counterpart. Although the fundamental mode of such structure does not exhibit a cut off [5, 6], ohmic loss plays a major role due to the increased interaction of the mode with the metal. Therefore, such structures can be considered only for very short propagation length, with the goal of deep

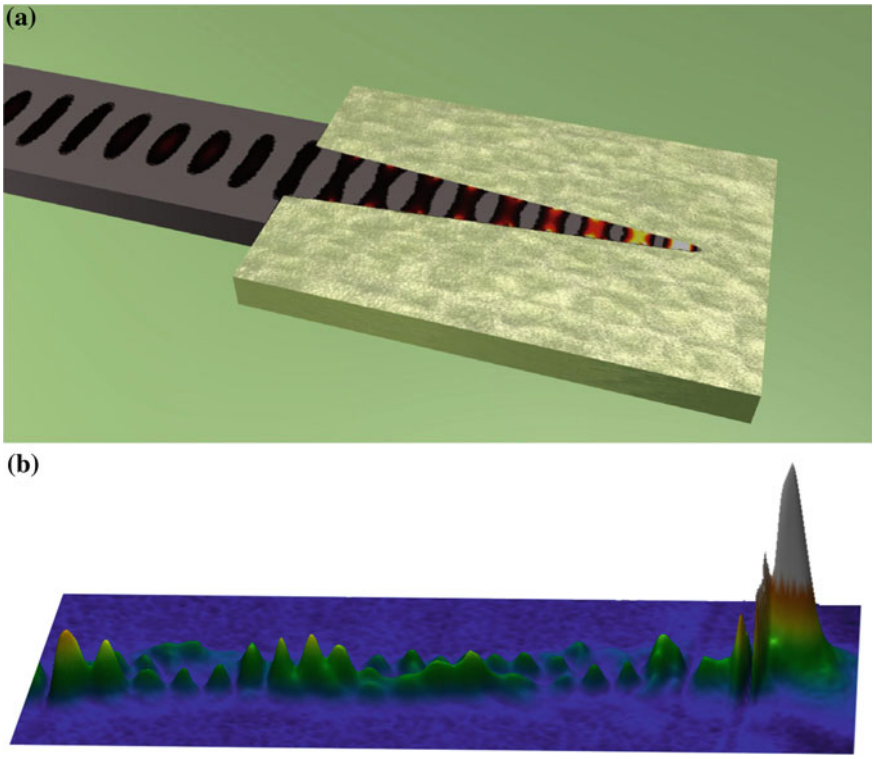

Fig. 4.2 **a** Schematic representation of nano-tip focusing device, with metal surrounding the silicon tip and the calculated electric field intensity distribution in the device. The confinement of energy at the apex of the silicon tip is clearly evident. **b** 3D representation of the near-field signal measurement results, showing strong field enhancement at the apex of the tip

subwavelength confinement of electromagnetic energy distribution. Applications of these devices are primarily in the area of enhancing light matter interactions, e.g. enhancing non-linearities, spontaneous emission and detection of light via the mechanism of enhancement in Purcell factor. Very recently, such high mode confinement in a silicon tip surrounded by metal was demonstrated by Desiatov et al. [7]. In this work, light was coupled from a silicon waveguide into a metal-silicon-metal structure where the silicon was tapered down to about 20 nm in size. A schematic drawing of the device, together with a full wave simulation showing the field enhancement at the apex of the tip is presented in Fig. 4.2. Using a near field scanning optical microscope (NSOM), the authors demonstrated the confinement of plasmons excited at the wavelength of 1.55 μm into dimensions smaller than 50 nm, i.e. more than 30 times smaller than the excitation wavelength.

While the direct interface between metal and silicon does not allow surface plasmons to propagate a substantial distance of over few microns before decaying, propagation length can be significantly enhanced by placing a thin layer of low index

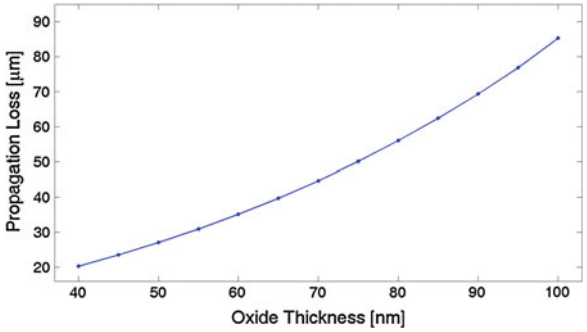

Fig. 4.3 Calculated propagation length as a function of the oxide thickness in a layered structure consisting of silver-silicon dioxide-silicon

dielectric material in between the metal and the high index dielectric (e.g. silicon). This way, the photonic mode in the high index dielectric and the plasmonic mode resides at the metal-low index dielectric interface are coupled, forming a hybrid mode which is mostly confined at the thin low index layer. This approach, now known as the "hybrid waveguide", was first proposed by Oulton et al. [8] and later demonstrated for guiding and nanolasing in a Ag-MgF_2-CdS platform [9]. Recently, several structures consisting of metal-oxide-silicon were demonstrated [10–12]. Varieties of configurations with different oxide thickness as well as several metals, including CMOS compatible metals (e.g. Cu and Al) were investigated. Similar to other plasmonic structures, typical trade-off between high confinement of the hybrid mode and the unavoidable propagation loss is observed in these devices. Figure 4.3 shows the calculated propagation loss of a strip silver-oxide-silicon waveguide as a function of the oxide layer thickness. As expected, a thinner oxide spacer which provides higher confinement of the electromagnetic mode gives rise to enhanced interaction of electromagnetic field with the metal resulting in a lower propagation length. Therefore, one can control the loss and the confinement by tuning the oxide layer thickness. This capability to compromise between nanoscale confinement and low loss characteristic makes the hybrid structure an attractive tool for future design of dense opto-electronic circuitry on-chip. In addition, owing to the presence of low index spacer layer in the hybrid configuration, the propagation loss can be also compensated by introducing a gain medium in the low index material see e.g. [13].

To date, the longest propagation length of a hybrid silicon plasmonic waveguide was demonstrated by Goykhman et al. [14], where a self aligned approach for the fabrication of hybrid waveguide based on the LOCOS technique was demonstrated. The fabrication process is depicted in Fig. 4.4. Starting with silicon on insulator (SOI) substrate consisting of 360 nm-thick crystalline silicon layer on top of a 2 μm thick buried oxide, a 100 nm thick silicon nitride layer (SiN) was deposited by low-pressure chemical vapor deposition (LPCVD). Next, the mask defining the optical structure consisting of the a hybrid plasmonic waveguide, the input/output photonic waveguides and a 1 μm length tapered couplers for adiabatic conversion between the

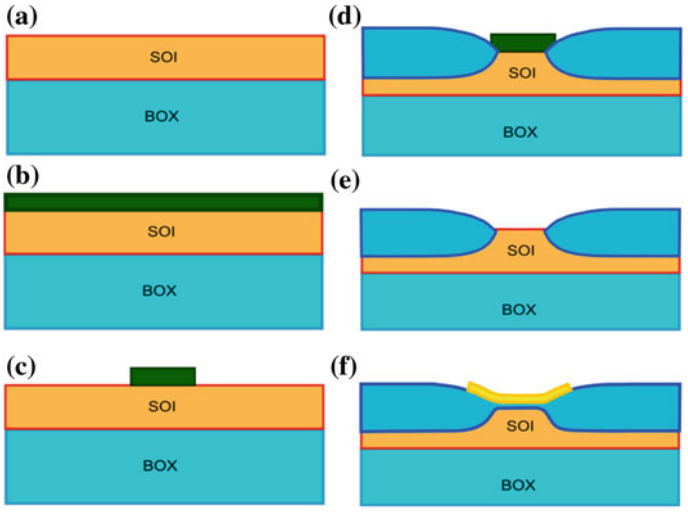

Fig. 4.4 Fabrication process flow of the locally-oxidized hybrid plasmonic waveguide. **a** Planar substrate; **b** Nitride layer deposition; **c** Nitride patterning; **d** Local oxidation; **e** Nitride strip; **f** Formation of thin oxide gap and metal deposition. Reprinted with permission from [14]. Copyright 2010 American Institute of Physics

photonic and the hybrid mode was patterned in protective SiN layer using standard electron-beam lithography followed by inductively coupled reactive ion etching. To transfer the defined pattern into the silicon, the chip was oxidized where the nitride layer serves as a mask preventing the oxygen diffusion. After local oxidation, the SiN mask was etched out and a 75 nm thick silicon oxide was thermally grown to serve as low index spacer between the silicon waveguide and the metal. Finally, after second lithographic step of opening a metallization window, a 50 nm-thick gold layer was deposited onto the chip followed by a lift-off process to lay down the metallic strip of the hybrid plasmonic structure. It should be noted, that the metal surface is self-aligned with respect to the thin oxide layer and the silicon waveguide underneath, because the hybrid region is isolated and separated from the rest of the structure by thick oxide spacers defined with the LOCOS process.

A scanning-electron microscope (SEM) micrograph of this hybrid plasmonic waveguide prior the metal deposition, is shown in Fig. 4.5a. The structure consists of a silicon rib waveguide (310 nm width, 325 nm height) with a thin oxide gap of 75 nm. The height of the rib is 150 nm. A calculated mode profile of the device is shown in Fig. 4.5b. According to the simulation, the effective index of the hybrid mode and its propagation loss parameter were found to be 2.58 and 102 cm^{-1} respectively. The reported measured propagation length was very similar, $105 \pm 5\,cm^{-1}$. Additionally, the coupling loss between the silicon photonic waveguide and the hybrid waveguide was found to be 1.7 ± 0.2dB.

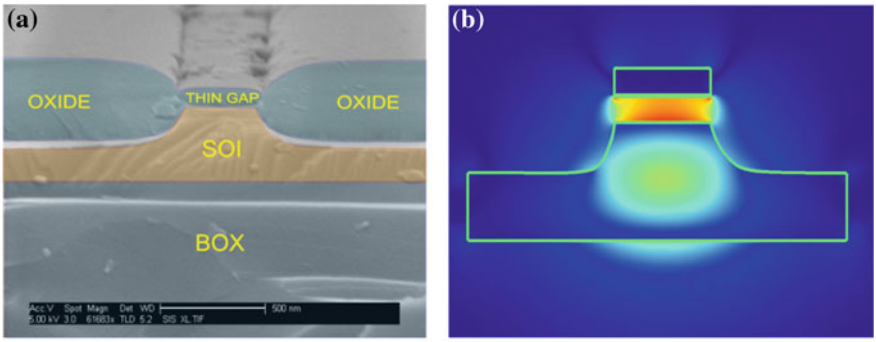

Fig. 4.5 **a** SEM image of the hybrid plasmonic structure with highlighted different material layers. **b** Electromagnetic simulation showing the intensity profile of the mode in the hybrid plasmonic waveguide. Reprinted with permission from [14]. Copyright 2010 American Institute of Physics

In addition to its application for plasmonic guiding, the hybrid approach can be used for the construction of hybrid plasmonic-photonic passive devices such as couplers, splitters and filters [15–19]. Very recently, this platform was also used for the demonstration of a micro ring resonator with a very small radius of 1–2 μm, having Q factor of $\sim$275 [20]. While significant progress has been demonstrated in the design and the experimental demonstration of silicon plasmonic passive devices, there is still a room for further improvement. Advanced designs should be implemented such that trade off between confinement and loss will be optimized depending on the specific application. This will provide on chip system designers with a complete toolkit of passive components to choose from.

4.2.3 Active Devices

In parallel with the growing work on passive devices, we are experiencing a substantial progress in the field of active silicon plasmonic devices. As mentioned earlier, the major active devices of interest include lasers, modulators and detectors. The plasmonic laser (SPASER) attracts significant research efforts starting from the pioneering work of Bergman and Stockman [21]. Unfortunately, as of this date there is no clear path towards the construction of silicon based SPASERS. Not only the demonstration of SPASERS and other nano lasers is still challenging, primarily owing to high ohmic loss in the metal [22], selecting silicon which is a bad gain material by itself further jeopardizing this effort. This is because of the indirect energy band of silicon, resulting relatively low radiation recombination rate compared with non radiative processes.

While the realization of a silicon plasmonic laser seems to be out of reach, at least in the near future, there has been a significant progress towards the realization of the two other active plasmonic devices, namely silicon plasmonic modulators (SPMs) and silicon plasmonic detectors (SPDs). These last two devices are the focus of the following sections.

4.2.3.1 Silicon Plasmonic Modulators

Similarly to their silicon photonics counterparts, advanced SPMs need to satisfy a long list of features, such as low power consumption (typically measured as energy per bit), high rate, high extinction ratio, relatively low loss, small foot print, linear transfer function and more. However, unlike silicon photonic modulators, where the required phase modulation can be achieved over a long propagation distance (typically few millimeters, [23–26]), or alternatively via the use of resonators with decent Q factors [27–32], the SPMs cannot rely on accumulating phase over a large distances owing to the large propagation loss of the optical signals. Moreover, to support on chip communication functionalities, the foot print of such SPMs should not go beyond few microns.

A step towards the realization of SPMs is the demonstration of the PlasMOStor [33]. The PlasMOStor is based on field-effect modulation of plasmon waveguide modes in a metal-oxide-semiconductor (MOS) geometry, which is very similar to that of the hybrid silicon plasmonic waveguides discussed in the previous section. In the PlasMOStor configuration, near-infrared optical transmission between a source and a drain is controlled by a gate voltage that drives the device into accumulation mode. Using the gate oxide as an optical channel, electro-optic modulation is achieved in device volumes of half of a cubic wavelength. A schematic drawing of the device is shown in Fig. 4.6.

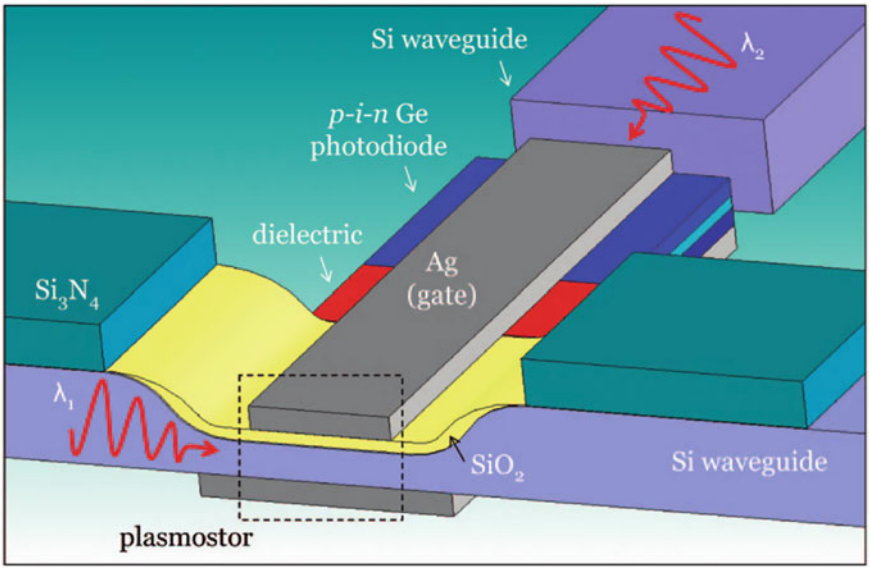

Fig. 4.6 Schematic drawing of the PlasMOStor configuration. Reprinted with permission from [33]. Copyright 2009 American Chemical Society

The device consists of a silicon waveguide covered by a thin silicon dioxide layer. A metal electrode is positioned on top of the oxide. Two modes (photonic and plasmonic) are supported by the structure. By properly designing the dimensions of the structure, the photonic mode can be brought to a near cut-off condition for the wavelength of operation around 1550 nm. If no voltage is applied, both modes propagate in the waveguide and can interfere destructively if the length of the device is chosen such that both modes are in anti-phase at the output. Due to the destructive interference, a small output signal is measured. Upon the application of voltage to the gate, the photonic mode is brought to cut-off such that it can no longer interfere with the plasmonic mode. As a result, higher output signal is obtained. Using this approach, a substantial modulation was obtained with very low power consumption, in the range of femtojoules per bit. Although high speed operation was not demonstrated, the device has the potential for gigahertz modulation frequencies owing to its small dimensions allowing the obtaining of small RC time constants.

While the PlasMOStor concept has the potential for becoming a viable candidate as an SPM, there is still a long way to go before it can replace current technologies. First, on chip coupling schemes need to be employed in order to facilitate the demonstration of a low loss device. Additionally, the coupling of signals to both modes needs to be precisely controlled such that the extinction ratio of the device will be high under varying operation conditions. Finally, in spite of the low power consumption, heat issues related to generating power within a very small volume need to be addressed.

Another approach for demonstrating SPM devices is by using the hybrid structure of metal - oxide-silicon (MOS) and exploring accumulation or inversion operation of this MOS capacitor for the realization of an electro-absorption SPM. This concept was demonstrated by several authors [34–37]. For example, Kwong et al. [34] demonstrated about 6 dB attenuation under the application of 7 V for a device length of about 3 μm. The demonstration by Leuthold et al. [36] is based on integrating an active section consisting of a stack of silver (Ag), indium tin oxide (ITO), and SiO_2 layers into a silicon waveguide platform. This structure supports a strongly confined asymmetric SPP in the 1.55 μm telecommunication wavelength window. The absorption coefficient of the SPP is modulated by applying a voltage between the two silver electrodes, generating free carriers in the ITO layer. This configuration is expected to operate at rates faster than 100 Gbit/s owing to the ultra small RC time constant. Finally, SPM which is based on all optical modulation was demonstrated as well [37]. In this work, a gold-silicon grating coupler is used to couple pump pulses (800 fs pulse width, central wavelength around 775 nm). The pump signal generates free carriers in the silicon which in turn modifies the effective refractive index of the silicon. As a result, the coupling of a probe signal (in the spectral regime of 1300–1700 nm) into SPP mode on the gold-silicon interface can be controlled. The authors demonstrate resonance shift larger than the resonance linewidth by using a pump energy density of 2.2 mJ/cm^2, with time response of about 100 ps, practically limited by the recombination time of the free carriers in silicon. Time response can be further enhanced by generating free carriers in the metal, as previously demonstrated by Zheludev et al. [38].

4.2.3.2 Silicon Plasmonic Detectors

At the end of each photonic/plasmonic communication link there is a need for a detector which "converts" photons to electrons. While silicon detectors are widely used in everyday life, they are not efficient for the detection of near-infrared signals in the telecom regime. This is because the energy band gap of silicon is in the order of 1.1 eV, whereas the energy of a photon in the telecom regime is only about 0.8 eV. In other words, while the transparency of silicon at the telecom frequency band allows its deployment as the material of choice for guiding, modulation and other manipulations of light, its very same property prohibit silicon from being used as an active absorbing material for detection of infrared optical signals. Over the years, the silicon photonics industry developed approaches for circumventing this deficiency by considering solutions such as the integration of germanium active layer with silicon platform [39–41], and fabrication of InGaAs/Si avalanche photodetectors using wafer bonding technology [42, 43]. While these approaches provide a path towards detection of light at the telecom wavelength regime, there is still a clear advantage in developing monolithic CMOS compatible devices for the detection of light in silicon, without the need to rely on other material systems. Recently, several approaches were proposed and demonstrated along these lines including two-photon absorption [44, 45], insertion of midbandgap defect states into silicon lattice [46], using a polysilicon active layer [47] and cavity enhanced photocurrent generation [45, 47, 48]. Yet, another promising approach to detect infrared sub-bandgap optical radiation in silicon is to employ the internal photoemission (IPE) process using a Schottky barrier (SB) photodetector [49, 50]. In its simplest form, such a detector consists of metal film on a lightly doped semiconductor (e.g. silicon) forming a Schottky contact at metal-semiconductor interface with potential barrier Φ_B and rectifying electrical characteristics. Typically, the obtained Schottky barrier (Φ_B) is lower than the energy bandgap of silicon [50], thus allowing detection of long-wavelength (infrared) photons via the internal photoemission process. More specifically, when optical radiation below the bandgap is applied to the metal-silicon contact by top (trough the metal) or back (through the semiconductor) illumination, the conduction electrons in the metal absorb infrared photons with energy $h\nu$ exceeding the potential barrier at the interface Φ_B (see Fig. 4.7). Gaining sufficient energy, these excited (hot) electrons are able to cross over the SB [50], sweep out the depletion region of the semiconductor and be collected as a photocurrent under reverse bias (photoconductive mode) operation.

A fundamental deficiency of the conventional SB based photodetector is related to the fact that the volume in which the photons interact with electrons in the metal is very small, namely only a small fraction of the incident photons actually causes photoemission. Clearly, there is a need to confine the optical power at the boundary between the materials forming the Schottky contact, thereby increasing the interaction of light with the metal in the vicinity of the interface where the photoemission process takes place. This light localization could significantly improve the detection capability of the system and potentially pave the way for device miniaturization and realization of on-chip photodetectors on the nanoscale. As early as in 1970s the con-

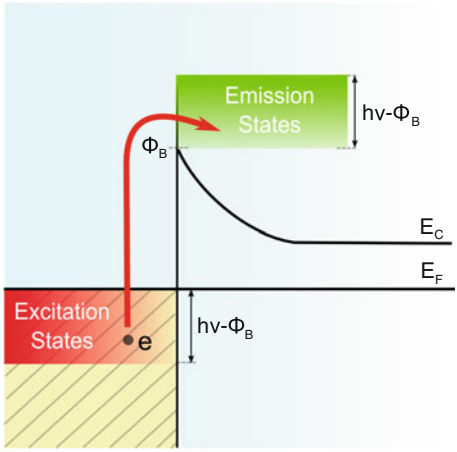

Fig. 4.7 Energy band diagram of metal-semiconductor Schottky contact. The *red arrow* corresponds to the transition of a hot electron from the vicinity of the Fermi level in the metal to the conduction band of the semiconductor. Reprinted with permission from [51]. Copyright 2011 American Chemical Society

cept of using SPPs on the metal-air interface for improving the efficiency of external photoemission in photo-cathodes has been explored [52, 53] and recently, it had been successfully applied to the enhancement of internal photoemission for infrared photodetection in silicon-based plasmonic structures [54–57, 51].

Two major configurations are being developed in recent years. One is geared towards the construction of photodetectors in guided mode configuration, where the other relies on free space illumination. The efficiency of the latter configuration can be enhanced by the use of a nanoantenna array in order to confine the electromagnetic energy at the interface between the metal and the silicon, as was recently demonstrated by a research group from Rice University [58]. By illuminating their structure from the top in free space configurations, responsivity in the order of few nA/mW for operation wavelength of 1.55 μm was reported. Another option for improving the efficiency of SB based photodetectors in free space configuration is by using the concept of cavity enhanced photodetection, where light at the wavelength of resonance travels several times across the Schottky interface [59].

Guided mode configuration, on the other hand, offers long interaction length between the propagating SPP signal and the Schottky photodetector. As such, it can provide higher efficiency because most of the signal is absorbed and excite hot electrons, some of which can cross over the SB and be collected as a photocurrent. This guided wave configuration in silicon plasmonic platform was first demonstration by the group of Berini [56, 60]. Their device consists of a metal stripe on silicon forming a Schottky contact thereon and supporting a surface plasmon polariton mode that is strongly confined and localized to the metal–semiconductor interface. Detection of optical radiation below the bandgap of silicon (at infrared wavelengths) occurs through internal photoemission. Responsivities of 0.38 and 1.04 mA/W were measured at a wavelength of 1280 nm for gold and aluminum stripes on n-type silicon respectively. A later work reported even higher responsivity by the use of metal nanodisks embedded in the silicon [61].

A different geometry was developed by our group at the Hebrew University [51]. Our approach is based on a self-aligned fabrication approach of local-oxidation of silicon (LOCOS) on SOI substrate, where nanoscale waveguide structure is defined by oxide spacers. Implementation of the LOCOS process provides compatibility with standard CMOS technology and permits a precise control over the shape and the dimensions of the waveguide [4]. Additionally, the LOCOS technique enables the fabrication of low-loss bus photonic waveguide (ca. 0.3 dB/cm) and the detector in the same process step, where the oxide spacers effectively define the area of metal-silicon interface and thus allow avoiding lateral misalignment between the silicon surface and the metal layer to form a Schottky contact.

Our device was fabricated by depositing a 100 nm of silicon nitride (SiN) on top of a 340 nm-thick, silicon device layer which is separated from the handle wafer by a 2 μm-thick buried oxide. Next, the mask defining the optical and electrical structures including the photonic bus waveguide, the detection region and the contacts area were patterned into the protective SiN layer using standard electron-beam lithography (EBL) followed by reactive ion etching (RIE). The defined pattern was next transferred to the silicon layer by wet oxidation process where the nitride layer serves as a mask preventing the oxygen diffusion. After oxidation the nitride mask was removed by an additional RIE step. To make the Schottky plasmonic photodetector we firstly realized an ohmic contact to the silicon layer by evaporating an aluminum pad and alloying the structure at 450 °C. Finally, a 50 nm-thick Au layer was deposited onto the chip followed by a lift-off process to lay down the metallic strip of the plasmonic structure to form a Schottky contact.

The cross sectional profile of the structures following the LOCOS process is shown by an SEM image of the photonic waveguide prior to metallization (Fig. 4.8), indicating waveguide dimensions of 310 nm width by 340 nm height. Such a structure supports the fundamental TM polarized (out of plane) optical mode. A thin rib (60 nm thickness) was kept to facilitate electrical contact to the silicon. According to Fig. 4.8, the oxide spacers formed by the LOCOS process smooth the profile of the waveguide

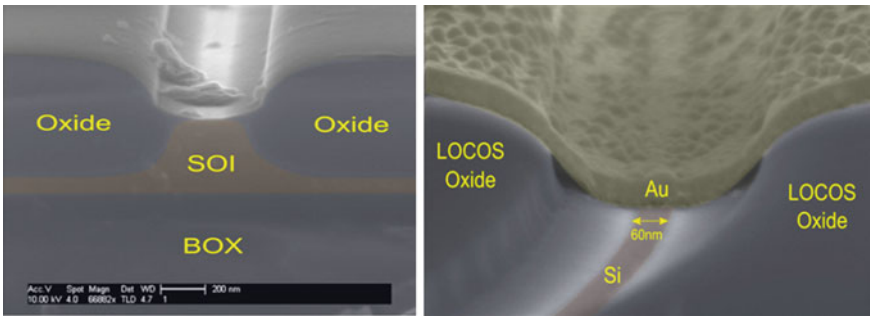

Fig. 4.8 SEM micrographs of the photonic bus waveguide after local-oxidation process before the metallization step and of Schottky contact. Reprinted with permission from [51]. Copyright 2011 American Chemical Society

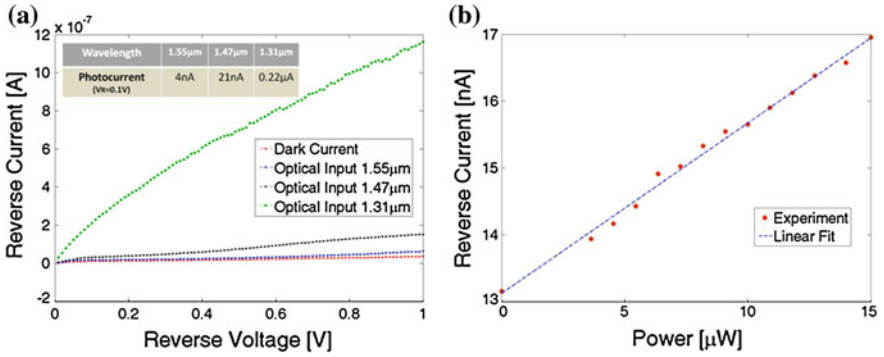

Fig. 4.9 **a** I-V curve in reverse bias for three different wavelength in the near infrared regime. **b** Representative result of responsivity measurement for wavelength of 1.55 μm. The current is measured under reverse bias of 0.1 V as a function of optical power in the Schottky detector. Reprinted with permission from [51]. Copyright 2011 American Chemical Society

and provide an electrical isolation between the regions of high electric field generated at the sharp edges of metal and silicon, thereby minimizing the leakage current of the device. Based on Fig. 4.9, we found the effective width of the detector to be 60 nm.

Using finite element mode solver (COMSOL) the modes in both the photonic and the plasmonic waveguide were calculated. According to the simulation results the effective refractive index of the photonic and plasmonic modes were found to be 2.29 and 3.25 + 0.02i respectively, indicating absorption loss of 0.7/μm in the plasmonic waveguide. The length of the Schottky detector was chosen to be 30 μm, practically ensuring the absorption of the optical signal within the structure.

By measuring the I-V characteristics of the device for different temperatures the barrier height (Φ_B) and the effective Richardson constant (A^{**}) were found to be $\Phi_B = 0.315$ V and $A^{**} = 32\,A/cm^2K^2$, very similar to the values presented in the literature [52] for p-type silicon-Au Schottky contact.

The detection functionality of the device at different telecom wavelengths was demonstrated by measuring the I-V characteristics of the Schottky diode at the presence of an optical signal. Figure 4.9a represents the measurement results of the Schottky photodetector for optical signals at several wavelengths under constant incident optical power. The observed spectral response reveals an increased responsivity for shorter wavelengths. This is expected due to the enhanced quantum efficiency of the internal photoemission process for energetic incident photons according to the modified Fowler equation [61, 62]:

$$\eta_e = C\frac{(h\nu - \Phi_B)^2}{h\nu}$$

where η_e is the quantum efficiency of photoemission process (number of carriers that contribute to the photocurrent per incident photon) and C is the photoemission coefficient. The obtained voltage dependence of the current in reverse bias can be related

to the combined effect of SB lowering due to the image force and the space-charge-limited nature of the photocurrent [52]. Responsivity was extracted by measuring the current across the Schottky contact under weak reverse bias of 0.1 V as a function of the incident optical power. A representative measurement result at the wavelength of 1.55 μm is shown in Fig. 4.9b. Indeed, the measured photocurrent showed linear dependence in the incident optical power. The obtained internal responsivity of the device was found to be 0.25, 1.4 and 13.3 mA/W for optical wavelengths of 1.55, 1.47 and 1.31 μm respectively. External responsivity was actually lower due to fiber to photonic waveguide and photonic waveguide to plasmonic waveguide coupling loss. Very recently, quantum efficiency was improved by nearly two orders of magnitude using the concept of roughness engineering, suppressing the reflection of electrons from the metal-silicon boundary [63].

4.3 Concluding Remarks

Being compatible with CMOS technology on one hand and allowing true subwavelength confinement on the other, the field of silicon plasmonics holds a great promise. Currently, the integration between plasmonics and silicon technology is still at its infancy. Keeping in mind that silicon plasmonic based devices have been emerged only over the last five years it would be reasonable to believe that plenty of opportunities for exploring advanced components, functionalities and configurations are available. However, in order to make a significant breakthrough in the field one should first be aware of the opportunities and not of lesser importance—the limitations of this platform.

To start, it is unlikely that silicon plasmonics will be used for guiding of signals over long distances, owing to the large propagation loss involved. The attempts to compete with dielectric guiding for centimeters scale range do not show a great promise. If silicon plasmonics is to be used for guiding, it is most likely be in the local interconnect level (micrometers length scale), interfacing between single elements and units on a chip. On the other hand, this very same nature of high propagation loss makes the silicon plasmonic platform an attractive choice for the construction of advanced photodetectors with enhanced wavelength photo response, as was shown for example by the several demonstrations of plasmonic enhanced Schottky detectors. The strong absorption and the high confinement may also play a positive role in the construction of silicon plasmonic modulators based on the effect of electro absorption, owing to the small device footprint and the relatively low number of carriers required to achieve a significant modulation. This may lead to ultra low energy per bit modulations at high rates.

Another promising direction is related to light matter interactions. The capability of plasmonics to concentrate electromagnetic energy into deep subwavelength scale volumes makes it attractive for enhancing spontaneous emission from silicon. While silicon based SPASERS are not expected to emerge in the near future, it may be sufficient to replace some of their functionalities using nanoscale silicon based

incoherent light emitting devices. This may be turn true if extraction efficiencies in the range of few percents will be achieved, together with modulation rates in the gigahertz regime.

Finally, from nowadays perspective, silicon plasmonics is probably the only technologically compatible platform which can provide the need integrate between optics and electronics at the level of a chip scale. Will it actually be the case or would it remains another unrealized promise? It is probably too soon to tell. One thing is for sure—it is surely worth trying.

References

1. ITRS 2009
2. D.A.B. Miller, Device requirements for optical interconnects to silicon chips. Proc. IEEE **97**, 1166–1185 (2009)
3. J. Cardenas, C.B. Poitras, J.T. Robinson, K. Preston, L. Chen, M. Lipson, Low loss etchless silicon photonic waveguides. Opt. Express **17**(6), 4752–4757 (2009)
4. B. Desiatov, I. Goykhman, U. Levy, Demonstration of submicron square-like silicon waveguide using optimized LOCOS process. Opt. Express **18**(18), 18592–18597 (2010)
5. S.A. Maier, *Plasmonics: Fundamentals and Applications* (Springer, Berlin, 2007)
6. P. Ginzburg, D. Arbel, M. Orenstein, Gap plasmon polariton structure for very efficient microscale-to-nanoscale interfacing. Opt. Lett. **31**(22), 3288–3290 (2006)
7. B. Desiatov, I. Goykhman, U. Levy, Plasmonic nanofocusing of light in an integrated silicon photonics platform. Opt. Express **19**(14), 13150–13157 (2011)
8. R.F. Oulton, V.J. Sorger, D.A. Genov, D.F.P. Pile, X. Zhang, A hybrid plasmonic waveguide for subwavelength confinement and long-range propagation. Nat. Photonics **2**(8), 496–500 (2008)
9. R.F. Oulton, V.J. Sorger, T. Zentgraf, R.-M. Ma, C. Gladden, L. Dai, G. Bartal, X. Zhang, Plasmon lasers at deep subwavelength scale. Nature **461**, 629–632 (2009)
10. D. Dai, S. He, A silicon-based hybrid plasmonic waveguide with a metal cap for a nano-scale light confinement. Opt. Express **17**(19), 16646–16653 (2009)
11. M. Wu, Z. Han, V. Van, Conductor-gap-silicon plasmonic waveguides and passive components at subwavelength scale. Opt. Express **18**(11),11728–11736 (2010)
12. S. Zhu, T.Y. Liow, G.Q. Lo, D.L. Kwong, Silicon-based horizontal nanoplasmonic slot waveguides for on-chip integration. Opt. Express **19**(9), 8888–8902 (2011)
13. D. Dai, Y. Shi, S. He, L. Wosinski, L. Thylen, Gain enhancement in a hybrid plasmonic nano-waveguide with a low-index or high-index gain medium. Opt. Express **19**(14), 925–12936 (2011)
14. I. Goykhman, B. Desiatov, U. Levy, Experimental demonstration of locally oxidized hybrid silicon-plasmonic waveguide. Appl. Phys. Lett. **97**(14), 141106+ (2010)
15. H.S. Chu, E.P. Li, P. Bai, R. Hegde, Optical performance of single-mode hybrid dielectric-loaded plasmonic waveguide-based components. Appl. Phys. Lett. **96**(22), 221103+ (2010)
16. H.-S. Chu, Y.A. Akimov, P. Bai, E.-P. Li, Hybrid dielectric-loaded plasmonic waveguide and wavelength selective components for efficiently controlling light at subwavelength scale. J. Opt. Soc. Am. B **28**(12), 2895–2901 (2011)
17. Y. Song, J. Wang, Q. Li, M. Yan, M. Qiu, Broadband coupler between silicon waveguide and hybrid plasmonic waveguide. Opt. Express **18**(12), 13173–13179 (2010)
18. J. Wang, X. Guan, Y. He, Y. Shi, Z. Wang, S. He, P. Holmströ m, L. Wosinski, L. Thylen, D. Dai, Sub-μm^2 power splitters by using silicon hybrid plasmonic waveguides. Opt. Express **19**(2), 838–847 (2011)
19. M.Z. Alam, J.S. Aitchison, M. Mojahedi, Compact and silicon-on-insulator-compatible hybrid plasmonic TE-pass polarizer. Opt. Lett. **37**(1), 55–57 (2012)

20. S. Zhu, G.Q. Lo, D.L. Kwong, Components for silicon plasmonic nanocircuits based on horizontal Cu-SiO2-Si-SiO2-cu nanoplasmonic waveguides. Opt. Express **20**(6), 5867–5881 (2012)
21. D.J. Bergman, M.I. Stockman, Surface plasmon amplification by stimulated emission of radiation: quantum generation of coherent surface plasmons in nanosystems. Phys. Rev. Lett. **90**(2), 027402+ (2003)
22. J.B. Khurgin, G. Sun, Injection pumped single mode surface plasmon generators: threshold, linewidth, and coherence. Opt. Express **20**(14), 15309–15325 (2012)
23. W M. Green, M.J. Rooks, L. Sekaric, Y.A. Vlasov, Ultra-compact, low RF power, 10 gb/s silicon Mach-zehnder modulator. Opt. Express **15**(25), 17106–17113 (2007)
24. A. Liu, L. Liao, D. Rubin, H. Nguyen, B. Ciftcioglu, Y. Chetrit, N. Izhaky, M. Paniccia, High-speed optical modulation based on carrier depletion in a silicon waveguide. Opt. Express **15**(2), 660–668 (2007)
25. F.Y. Gardes, D.J. Thomson, N.G. Emerson, G.T. Reed, 40 gb/s silicon photonics modulator for TE and TM polarisations. Opt. Express **19**(12), 11804–11814 (2011)
26. G.T. Reed, G. Mashanovich, F.Y. Gardes, D.J. Thomson, Silicon optical modulators. Nat. Photonics **4**(8), 518–526 (2010)
27. Q. Xu, B. Schmidt, S. Pradhan, M. Lipson, Micrometre-scale silicon electro-optic modulator. Nature **435**, 325–327 (2005)
28. V.R. Almeida, C.A. Barrios, R.R. Panepucci, M. Lipson, All-optical control of light on a silicon chip. Nature **431**, 1081–10842 (2004)
29. L. Zhou, A.W. Poon, Silicon electro-optic modulators using p-i-n diodes embedded 10-micron-diameter microdisk resonators. Opt. Express **14**(15), 6851–6857 (2006)
30. M.R. Watts, D.C. Trotter, R.W. Young, A.L. Lentine, Ultralow power silicon microdisk modulators and switches. Group IV Photonics IEEE, 4–6 (2008)
31. W. Bogaerts, P. De Heyn, T. Van Vaerenbergh, K. De Vos, S. Kumar Selvaraja, T. Claes, P. Dumon, P. Bienstman, D. Van Thourhout, R. Baets, Silicon microring resonators. Laser & Photon. Rev. **6**(1), 47–73 (2012)
32. S. Feng, T. Lei, H. Chen, H. Cai, X. Luo, A.W. Poon, Silicon photonics: from a microresonator perspective. Laser & Photon. Rev. **6**(2), 145–177 (2012)
33. J.A. Dionne, K. Diest, L.A. Sweatlock, H.A. Atwater, PlasMOStor: a metal-oxide-si field effect plasmonic modulator. Nano Lett. **9**(2), 897–902 (2009)
34. S. Zhu, G.Q. Lo, D.L. Kwong, Electro-absorption modulation in horizontal metal-insulator-silicon-insulator-metal nanoplasmonic slot waveguides. Appl. Phys. Lett. **99**(15), 151114+ (2011)
35. T. Hirata, K. Kajikawa, T. Tabei, H. Sunami, Proposal of a metal-oxide-semiconductor silicon optical modulator based on inversion-carrier absorption. J. Appl. Phys. **47**, 2906–2909 (2008)
36. A. Melikyan, N. Lindenmann, S. Walheim, P.M. Leufke, S. Ulrich, J. Ye, P. Vincze, H. Hahn, T. Schimmel, C. Koos, W. Freude, J. Leuthold, Surface plasmon polariton absorption modulator. Opt. Express **19**(9), 8855–8869 (2011)
37. J.N. Caspers, N. Rotenberg, H.M. van Driel, Ultrafast silicon-based active plasmonics at telecom wavelengths. Opt. Express **18**(19), 19761–19769 (2010)
38. K.F. MacDonald, Z.L. Samson, M.I. Stockman, N.I. Zheludev, Ultrafast active plasmonics. Nat. Photon. **3**(1), 55–58 (2009)
39. Y. Kang, H.-D. Liu, M. Morse, M.J. Paniccia, M. Zadka, S. Litski, G. Saridm, A. Pauchard, Y.-H. Kuo, H.-W. Chen, W.S. Zaoui, J.E. Bowers, A. Beling, D.C. McIntosh, X. Zheng, J.C. Campbell, Monolithic germanium/silicon avalanche photodiodes with 340 GHz gain-bandwidth product. Nat. Photon. **3**(1), 59–63 (2009)
40. J. Michel, J. Liu, L.C. Kimerling, High-performance Ge-on-Si photodetectors. Nat. Photon. **4**(8), 527–534 (2010)
41. S. Assefa, F. Xia, Y.A. Vlasov, Reinventing germanium avalanche photodetector for nanophotonic on-chip optical interconnects. Nature **464**, 80–84 (2010)
42. A.R. Hawkins, W. Wu, P. Abraham, K. Streubel, J.E. Bowers, High gain-bandwidth-product silicon heterointerface photodetector. Appl. Phys. Lett. **70**, 303–305 (1997)

43. Y. Kang et al., Fused InGaAs/Si avalanche phototodiodes with low noise performance. IEEE Photon. Tech. Lett. **14**, 1593–1595 (2002)
44. T.K. Liang, H.K. Tsang, I.E. Day, J. Drake, A.P. Knights, M. Asghari, Silicon waveguide two-photon absorption detector at 1.5 μm wavelength for autocorrelation measurements. Appl. Phys. Lett. **81**(7), 1323–1325 (2002)
45. T. Tanabe, H. Sumikura, H. Taniyama, A. Shinya, M. Notomi, All-silicon sub-Gb/s telecom detector with low dark current and high quantum efficiency on chip. Appl. Phys. Lett. **96**(10), 101103+ (2010)
46. J.D.B. Bradley, P.E. Jessop, A.P. Knights, Silicon waveguide-integrated optical power monitor with enhanced sensitivity at 1550 nm. Appl. Phys. Lett. **86**(24), 241103+ (2005)
47. K. Preston, Y.H. Lee, M. Zhang, M. Lipson, Waveguide-integrated telecom-wavelength photodiode in deposited silicon. Opt. Lett. **36**(1), 52–54 (2011)
48. H. Chen, X. Luo, A.W. Poon, Cavity-enhanced photocurrent generation by 1.55 μm wavelengths linear absorption in a p-i-n diode embedded silicon microring resonator. Appl. Phys. Lett. **95**(17), 171111+ (2009)
49. D.W. Peters, An infrared detector utilizing internal photoemission. Proc. IEEE **55**(5), 704–705 (1967)
50. S.M. Sze, K.K. Ng, *Physics of Semiconductor Devices* (Wiley, New York, 2006)
51. I. Goykhman, B. Desiatov, J. Khurgin, J. Shappir, U. Levy, Locally oxidized silicon Surface-Plasmon schottky detector for telecom regime. Nano Lett. **11**(6), 2219–2224 (2011)
52. J.E. Sipe, J. Becher, Surface-plasmon-assisted photoemission. J. Opt. Soc. Am. **71**(10), 1286–1288 (1981)
53. J.G. Endriz, Surface waves and grating-tuned photocathodes. Appl. Phys. Lett. **25**(5), 261–262 (1974)
54. S. Zhu, M.B. Yu, G.Q. Lo, D.L. Kwong, Near-infrared waveguide-based nickel silicide Schottky-barrier photodetector for optical communications. Appl. Phys. Lett. **92**(8), 081103+ (2008)
55. Y. Wang, X. Su, Y. Zhu, Q. Wang, D. Zhu, J. Zhao, S. Chen, W. Huang, S. Wu, Photocurrent in Ag-Si photodiodes modulated by plasmonic nanopatterns. Appl. Phys. Lett. **95**(24), 241106+ (2009)
56. A. Akbari, R.N. Tait, P. Berini, Surface plasmon waveguide schottky detector. Opt. Express **18**(8), 8505–8514 (2010)
57. M. Casalino, L. Sirleto, M. Iodice, N. Saffioti, M. Gioffrè, I. Rendina, G. Coppola, Cu/p-Si schottky barrier-based near infrared photodetector integrated with a silicon-on-insulator waveguide. Appl. Phys. Lett. **96**(24), 241112+ (2010)
58. M.W. Knight, H. Sobhani, P. Nordlander, N.J. Halas, Photodetection with active optical antennas. Science **332**, 702–704 (2011)
59. M. Casalino, L. Sirleto, L. Moretti, M. Gioffrè, G. Coppola, I. Rendina, Silicon resonant cavity enhanced photodetector based on the internal photoemission effect at 1.55 μm: fabrication and characterization. Appl. Phys. Lett. **92**(25), 251104+ (2008)
60. A. Akbari, P. Berini, Schottky contact surface-plasmon detector integrated with an asymmetric metal stripe waveguide. Appl. Phys. Lett. **95**(2), 021104+ (2009)
61. S. Zhu, H.S. Chu, G.Q. Lo, P. Bai, D.L. Kwong, Waveguide-integrated near-infrared detector with self-assembled metal silicide nanoparticles embedded in a silicon p-n junction. Appl. Phys. Lett. **100**(6), 061109+ (2012)
62. R.H. Fowler, The analysis of photoelectric sensitivity curves for clean metals at various temperatures. Phys. Rev. Online Arch. (Prola) **38**, 45–56 (1931)
63. I. Goykhman, B. Desiatov, J. Khurgin, J. Shappir, U. Levy, Waveguide based compact silicon Schottky photodetector with enhanced responsivity in the telecom spectral band. Opt. Express **20**, 28594–28602 (2012)

Chapter 5
Ultrafast Nonlinear Plasmonics

Fabrice Vallée and Natalia Del Fatti

Abstract The mechanisms at the origin of the ultrafast third-order optical nonlinearity of metallic and plasmonic materials are described focusing on the dominant resonant processes associated to energy absorption. Optical nonlinearity is discussed in terms of ultrafast modifications of the dielectric function of the constituting metal as a consequence of electron and lattice heating, using a bulk-like model. Based on this description, the time- and spectral-dependent nonlinear changes of the optical response of plasmonic materials due to interaction with a femtosecond light pulse are modeled. The results are illustrated in the case of an individual gold nanoparticle for different shapes (sphere, ellipsoid, and rod), and for an ensemble of gold nanoparticles dispersed in a dielectric matrix. The same approach can be extended to more complex plasmonic materials or meta-materials.

Keywords Surface plasmon · Nonlinear optics · Ultrafast dynamics

5.1 Introduction

Experimental and theoretical investigations of the new properties of nanoobjects and nanomaterials have been an intense field of researches during the last decade. They are motivated by the possibility of modifying and controlling the physical and chemical properties of nanomaterials, playing with the size, shape, structure or composition of the nanoobjects they are formed of, and with their organization

F. Vallée (✉)
FemtoNanoOptics Group, LASIM, CNRS and Universtié Lyon 1, 43 Bd. du 11 November, 69622 Villeurbanne, France
e-mail: fabrice.vallee@univ-lyon1.fr

N. Del Fatti
Institut Lumière Matière, CNRS and Universtié Lyon 1, 43 Bd. du 11 November, 69622 Villeurbanne, France

T. V. Shahbazyan and M. I. Stockman (eds.), *Plasmonics: Theory and Applications*, Challenges and Advances in Computational Chemistry and Physics 15,
DOI: 10.1007/978-94-007-7805-4_5, © Springer Science+Business Media Dordrecht 2013

and interactions in the material. This versatility opens a broad field of technological applications but also raises many fundamental questions on the involved processes at the origin of the observed properties. In the optical domain, a large interest has been devoted to plasmonic effects in metallic nanoparticles or nanomaterials. They show-up by the appearance of new optical resonances in their linear and nonlinear optical responses [1–6]. These are associated to localized or propagating surface plasmon resonances (SPR) depending of the system dimensionality, e.g., in metal nanoparticles or in nanowires and at surfaces, respectively. SPR are concomitant with strong enhancement and spatial localization of the electromagnetic field in and around metallic nanostructures due to dielectric confinement or local field effect. Their spectral properties, wavelength, width, and amplitude reflect the characteristics of the nanoobjects (composition, size, shape), of their environment, and of their coupling in a nanomaterial [3, 5, 7–11]. They have been exploited to design new optical devices, with many applications, as in sensing [12, 13], and also offers a large potential for sub-wavelength light manipulation and guiding in plasmonic metamaterials [14–17].

The optical response of a plasmonic material being directly connected to those of its nano-components, it can be actively modified and controlled modifying their dielectric function. This can be done optically with a light pulse exploiting the optical nonlinearities component materials, and in particular the large nonlinearity of metals. Using femtosecond pulses, it opens the way to ultrafast active control of light propagation or transmission [18–24]. The ultrafast optical nonlinearity of metal nanostructures also provides a unique way to investigate their electronic and vibrational properties. Time-resolved spectroscopy has been extensively used in this context, first in metal films [25–31], and, subsequently, in metal nanostructures [32–37], and in single nanoparticles [38–45]. It has provided information on electronic motion coherence losses or SPR polarization decay [46–49], on electron energy redistribution in nanoobjects (electron-electron scattering and electron-lattice energy transfer) [33, 50–53], on their acoustic vibrations [33, 37, 44, 54–57] and on metal-environment energy exchanges [58, 59]. These studies also yield information on the physical origins of the third order nonlinearity of metallic materials, disentangling them using their different spectral and temporal signatures [60].

Fully exploiting the potentialities offered by the optical nonlinearities of metallic nanomaterials requires modeling of their nonlinear optical response at a nanoscale including plasmonic effects. In this chapter we describe ultrafast third order Kerr-type nonlinearity of metallic nanomaterials and its impact of their observable optical response, e.g., light absorption, transmission, or reflection. It is based on modeling ultrafast modification of the dielectric function of metal due to its interaction with a short light pulse. Even for pulses as short as 20 fs, this is dominated by resonant incoherent processes associated to energy absorption by the electrons of the metal [26, 37, 43, 47, 61]. Note that it is not the case for optical nonlinearity leading to creation of new frequencies, such as second, third or high-harmonic generations, that mostly involves coherent processes [48, 62–64]. The nonlinear mechanisms considered here are associated to energy absorption by the material and show a time dependence following its electronic, vibrational and thermal relaxation. The

impact of the different mechanisms on modification of the metal dielectric function on different time-scales will be first introduced, based on a modeling developed for bulk metals [26, 29, 52, 61, 65]. The induced changes of the observable optical properties of the material will then be discussed, focusing to the case of single metal nanoparticles and composite nanomaterials formed by an ensemble of nanoparticles dispersed in a dielectric matrix.

5.2 Dielectric Function of Metals and Metal Nanoparticles

The response of a bulk or nanostructured system in the optical domain directly reflects interaction of the electrons of the constituting material with the electromagnetic field. It is described via the dielectric functions of the material components, possibly modified by quantum confinement effects and material coupling. In the case of a bulk metal, the dielectric function ε^{bulk} can be separated into two types of contributions: a quasi-free electron one due to electrons in the conduction band and an interband one due to transitions between electronic bands. The former, related to intraband optical absorption, is well described by a Drude expression (free electron response), so that ε^{bulk} can be written [66]:

$$\varepsilon^{bulk}(\omega) = \varepsilon^{ib}(\omega) - \frac{\omega_p^2}{\omega\left[\omega + i\gamma_{bulk}(\omega)\right]}, \tag{5.1}$$

where ω_p is the plasma frequency ($\omega_p^2 = n_e e^2/\varepsilon_0 m_e$, with n_e the density of conduction electrons and m_e their mass). The intraband contribution is associated to optical transitions in the conduction band (i.e., without modification of n_e). Absorption of a photon by a conduction electron has to be assisted by a third particle, e.g., a phonon or another electron, or by a defect to conserve energy and momentum. The imaginary part of the Drude part of ε^{bulk} is thus proportional to the electron optical scattering rate $\gamma_{bulk}(\omega)$. It is determined by electron-phonon and electron-electron scattering (neglecting electron-defect scattering) with simultaneous exchange of the energy $\hbar\omega$ of a photon [67–69]. It *a priori* depends on the frequency ω, on the lattice temperature T_L and on the electron temperature T_e (or more generally on the electron distribution function f in a non-equilibrium situation). It can thus be written:

$$\gamma_{bulk}(\omega, T_e, T_L) = \gamma_{e-ph}(\omega, T_L, T_e) + \gamma_{e-e}(\omega, T_e). \tag{5.2}$$

The electron-phonon contribution γ_{e-ph} has been computed modeling electron-phonon interaction via deformation potential interaction [68, 70]. A simplified expression is obtained assuming a parabolic conduction band and $\hbar\omega$ much smaller than the Fermi energy E_F:

$$\gamma_{e-ph}(\omega, T_L, T_e) = \frac{G_{ph}}{\hbar\omega}\int_0^\infty \sqrt{E}\sqrt{E+\hbar\omega}\, f(E)\,(1-f(E+\hbar\omega))dE, \quad (5.3)$$

where G_{ph} depend on the lattice temperature T_L via the occupation number of the phonon states. If T_L is much larger than the Debye temperature, G_{ph} and thus γ_{e-ph} are proportional to T_L.

As for DC scattering describing metal conductivity (i.e., $\omega = 0$ case), only umklapp electron-electron scattering contribute to γ_{e-e}. Its expression has been computed for thermalized conduction electron and is given by [67]:

$$\gamma_{e-e}(\omega, T_e) = \frac{\omega^2}{4\pi^2\,\omega_p}\left[1+\left(\frac{2\pi k_B T_e}{\hbar\omega}\right)^2\right]. \quad (5.4)$$

Note that the amplitudes of γ_{e-ph} and γ_{e-e} are not precisely reproduced by these expressions (Eqs. 5.3 and 5.4), that will be further used only to discuss their relative changes with the electron and lattice temperature (Sects. 4.1.2 and 4.2.2).

For particles smaller than the electron mean free path, 20–40 nm in noble metals, the presence of surfaces cannot be neglected. For not too small particles (larger than about 2 nm), the impact of confinement on the interband contribution is weak [71]. Its main consequence is modification of the collision rate of the conduction electrons [3, 60, 72]. The dielectric function of the metal in a nanoparticle takes a similar form as in the bulk:

$$\varepsilon(\omega) = \varepsilon^{ib}(\omega) - \frac{\omega_p^2}{\omega\left[\omega + i\gamma_n(\omega)\right]}, \quad (5.5)$$

where γ_n is the electron scattering rate in the confined metal. Its correction as compared to the bulk rate γ_{bulk} is due to modification of the intrinsic electron collision rates [42, 50, 51] and, in a classical model, to additional electron scattering off the particle surfaces. Both effects are consequences of electron quantum confinement in the nanoparticles and depend on its size and geometry [2, 3, 6, 33, 73–75]. For a sphere of diameter D, one can simply write:

$$\gamma_n(\omega, T_L, T_e) = \gamma_{nano}(\omega, T_L, T_e) + 2g(\omega, T_e)v_F/D, \quad (5.6)$$

v_F being the Fermi velocity. γ_{nano} is the intrinsic optical scattering rate of the electrons in a nanoparticle, due to electron–electron and electron–vibration interactions [73, 75]. From a classical standpoint, the last term introduces electron–surface collisions which provide a new way of conserving momentum during photon absorption. From a quantum standpoint, it is due to the appearance of allowed optical transitions between confined states, k no longer being a good quantum number. Its amplitude, given by the g value in Eq. 5.6, thus depends on the confinement potential of the conduction electrons in the particle [2, 3, 6, 74, 75]. In the simplest model, the electrons are assumed to be in the periodic potential of the crystal, bounded by an infinite spherical potential well corresponding to the outer surface of the sphere. For

not too small particle, a continuum of conduction band states is recovered and one obtains [26, 76]:

$$g(\omega, T_e) = \frac{1}{\hbar\,\omega\, E_F^2} \int_0^\infty E^{3/2}\sqrt{E+\hbar\,\omega} f(E)[1-f(E+\hbar\,\omega)]dE. \tag{5.7}$$

For noble metals, $g \approx 0.7$ at room temperature in the optical domain (g varies weakly with frequency), consistent with experimental results obtained in single nanoparticles [73]. Note that, for not too small particles, γ_{nano} shows a 1/D correction as compared to γ_{bulk} [73]. This is the same size dependence as the surface term (Eq. 5.6) and the two effects cannot be distinguished so that γ_n can be rewritten:

$$\gamma_n(\omega, T_L, T_e) = \gamma_{bulk}(\omega, T_L, T_e) + 2g_{eff}(\omega, T_e)v_F/D, \tag{5.8}$$

where g_{eff} is a modified g factor lumping all confinement effects.

In noble metal, in the visible range, ε^{ib} is associated to interband transitions from the full d-bands to empty states, above the Fermi energy, E_F, in the conduction band, and to absorption from latter to empty band states of higher energy. The formers dominate with a threshold at $\hbar\,\omega_{ib} \approx 4.1$eV and 1.9 eV in silver and gold, respectively, interband absorption increasing more importantly above about 2.3 eV in gold (Fig. 5.1). The absorption rise in the vicinity of ω_{ib} can be well reproduced in gold and silver using the models developed for thermomodulation studies [77–79]. In gold, only d-band to conduction band (d $\rightarrow$ c) transitions are taking place close to ω_{ib}, with a dominant contribution around the L point of the Brillouin zone and a weaker one at lower energy around the X point. In the constant transition matrix element approximation and neglecting the width of the electronic states, the interband contribution to the imaginary part of the gold dielectric function can then be written:

$$\varepsilon_2^{ib}(\omega) = \frac{A}{\omega^2}\left[\int_{E_{dc,L}^m}^{E_{dc,L}^M} D_{d\rightarrow c}^L(E,\omega) f(E)dE - K_{XL}^2 \int_{E_{dc,X}^m}^{E_{dc,X}^M} D_{d\rightarrow c}^X(E,\omega) f(E)dE\right]. \tag{5.9}$$

$D_{d\rightarrow c}^{L,X}(E,\omega)$ is the energy dependent joint density of state for the d $\rightarrow$ c transition around the L and X points as given in [78] using band structure calculations [80]. K_{XL} is their relative amplitude. The two parameters, K_{XL} and the amplitude A, are obtained by fitting the experimental ε_2^{ib} values deduced by subtracting the Drude contribution to the measured ε_2^{bulk}, Eq. 5.1 [38, 65, 81, 82]. Different value of K_{XL} are obtained using different set of measured ε_2^{bulk}. For the data of [81] one obtains $K_{XL} \approx 0.37$ (Fig. 5.1), while for the data of [83] $K_{XL} \approx 0.84$ (note that these different values yield similar nonlinear spectra, the X point influence on $\Delta\varepsilon^{ib}$ being weak). A similar approach can be used for silver, absorption mostly taking place around the L point of the Brillouin zone, with a main contribution due to transitions from the d-bands to the conduction band and, a weaker one, due to transition from the conduction band to a higher energy empty s-band [77, 79] as shown by band structure modeling [84].

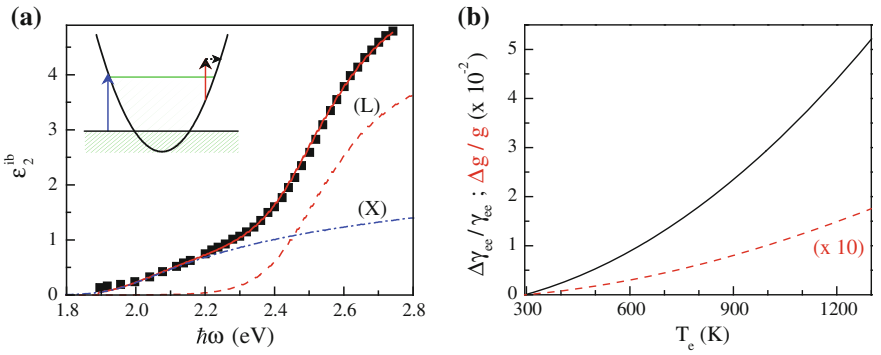

Fig. 5.1 **a** Experimental and computed interband contributions to the imaginary part of the gold dielectric function ε_2. The experimental values are obtained from [81] after subtracting the Drude contribution (obtained by fitting the near infrared part of ε_2). The dashed and dash-dotted lines show the contributions around the L and X points of the Brillouin zone (Eq. 5.9). The inset shows a schematic band structure of noble metals. **b** Relative change of the electron-electron scattering rate g_{e-e} (Eq. 5.4) and electron-surface scattering coefficient g (Eq. 5.7) in gold as a function of the electronic temperature T_e (the initial temperature is $T_0 = 295$ K)

5.3 Electron-Light Interaction and Electron Kinetics

When a light pulse is incident on a metal coherent interaction with the electron first takes place followed by electron excitation and relaxation with lattice heating. The different time-scale of the excitation and relaxation processes are illustrated in Fig. 5.2. The created coherent polarization decays on a sub 10–20 fs time scale leading to light-metal energy transfer [46, 47, 49]. As it is much faster than electron-electron and electron-lattice energy redistributions, a strongly nonequilibrium electron distribution is thus created [29, 37]. The injected energy is subsequently redistributed among the electrons by electron-electron (e-e) scattering establishing a Fermi-Dirac distribution in few hundred femtoseconds [26, 29], transferred to the lattice by electron-phonon (e-ph) interaction on a slightly longer time scale, typically one picosecond [26, 29, 85], and eventually damped to the environment in few to few hundred picoseconds [58, 59]. Material acoustic vibration (Lamb mode vibration, shock waves, acoustic echoes, …) are indirectly launched and are observed in the time domain on picosecond to few hundred picosecond time scales [55, 86–88, 56]. These different processes all translate in time-dependent changes of the metal dielectric function on different time scales. Their relative importance depends on the pulse duration (relative to the kinetics of the considered process in the investigated material), and will be described in the following assuming femtosecond pulses.

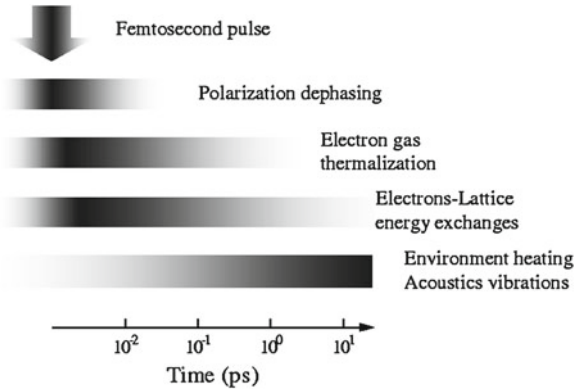

Fig. 5.2 Time scale of the different nonequilibrium electron relaxation processes in a metal film or nanoparticle after excitation by a femtosecond pulse: coherent polarization decay (few to 10 fs), electron-electron energy exchanges (establishment of the electron temperature in few hundred fs), electron-lattice energy transfer (on a picosecond scale) and damping of the nanoparticle energy to its environment (in few to few hundred ps). Acoustic vibrations take place on a picosecond to few tens of picosecond scale depending on the film thickness or nanoparticle size and geometry

5.3.1 Coherent Electron-Light Coupling

In a bulk metal, the optical electric field couples with the electrons in the conduction band inducing their forced oscillation at the optical frequency ω_e. The electron motion generates a polarization (or equivalently a current) that radiates an electromagnetic field, this simple picture leading to the Drude expression for the quasi-free electron dielectric function (Eq. 5.1). Light absorption takes place with polarization decay due to electron scattering, leading to excitation of single electron-hole pairs in the conduction band (Landau damping, where an electron is excited in a E energy state above the Fermi energy, E_F, leaving a hole in the $E - \hbar\omega_e$ energy state below E_F). It can be globally interpreted in the quasi-particle interaction model of the free electron absorption: one photon is absorbed by one conduction band electron with assistance of a third quasi-particle [66], the time scale for this process being then the electron scattering time $\tau_{bulk} = 1/\gamma_{bulk}$ (Eq. 5.1).

In metal nanoparticles a similar process takes place, taking into account nanoscale electron localization. The optical field induces oscillation of the electron density at the optical frequency ω_e in the nanoparticles. This electron movement generates an oscillating dipole in each particle that radiates at the same frequency (which is at the origin of the particle Rayleigh scattering). A coherent superposition of material polarization and electromagnetic field is created, light absorption taking place with decay of the induced material polarization. As discussed by Kawabata and Kubo, this decay takes place with single electron excitation, which is similar to Landau damping of the collective plasmon mode in a plasma [2]. As in bulk metal, decay is induced by electron scattering in each nanoparticle, the relevant time being then $\tau_n = 1/\gamma_n$ (Eq. 5.5).

This polarization decay, frequently discussed in terms of surface plasmon resonance dephasing in nanoparticles has been investigated using time-resolved second and third harmonic generation in large noble-metal plasmonic objects [46, 48, 49, 89]. Sub-10 to -20 fs decay times have been deduced, consistent with the estimated bulk scattering times τ_{bulk} in noble metals (confinement effects are negligible for the investigated sizes). In the spectral domain hole burning measurements have been performed to estimate the homogeneous SPR linewidth as a function of the size, shape and environment of oblate particles. Dephasing times in the same ranges are inferred by these spectral results [90–92]. More generally, for optical pulses down to 15–20 fs, no deviation from "instantaneous" single electron excitation has been observed in metal film consistent with polarization decay with the electron scattering time τ_{bulk} [26]. Similar results were obtained in metal nanoparticles, where this decay is expected to be even faster, due to increase of the intrinsic scattering rates and additional electron surface scattering (Eq. 5.5). In particular, ultrafast sub-10 fs Landau decay has been confirmed probing the induced depopulation of electronic states well below the Fermi energy in few nanometer silver nanoparticles [47]. For optical frequencies larger than the interband threshold, $\omega_e \geq \omega_{ib}$, interband interaction with light also takes place. It corresponds mostly to excitation of an electron from the d-band to the conduction band. Ultrafast dephasing of the conduction electron-d band hole pair is also expected due to ultrafast few-fs dephasing of carriers in metal [93, 94].

Electronic nonlinear coherent polarization due to interaction with an intense electromagnetic pulse is at the origin of the observed nonlinearity of metal nano-materials leading to emission of new frequencies radiated by the nonlinear dipoles, such as in harmonic generation [48, 62–64]. It also contributes to excitation of high energy states leading to new frequency creation by anti-Stokes photoluminescence [95, 96], multi-step nonlinear absorption due to electronic state excitation also taking place. However, its damping involves similar processes as for the linear coherent polarization and is thus expected to also take place on a few to a few tens of femtoseconds. Due to this ultrafast damping, this coherent contribution is usually weaker than incoherent ones when they are involved. This is the case in nonlinear processes where no new frequency is created such as those leading to optical Kerr effect. This has been confirmed by the absence of coherent response in pump-probe experiments with pulses in the 20 fs range [26, 52, 53]. In the following only resonant incoherent contributions due to metal absorption, and the associated electron and lattice relaxation kinetics, will thus be considered.

5.3.2 Ultrafast Electron Kinetics

If only intraband excitation is considered, in both bulk and confined metallic materials optical absorption leads to excitation of single electrons, each of them increasing its energy by $\hbar\omega$ (i.e., an electron hole-pair is created in the conduction band). Electrons with an energy E between $E_F - \hbar\omega_e$ and E_F are excited above the Fermi energy

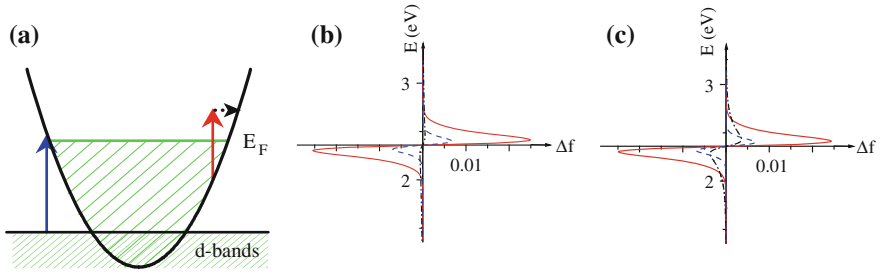

Fig. 5.3 **a** Schematic band structure of gold with a parabolic conduction band and undispersed d-bands. The left and right arrows indicate interband and intraband transitions. **b** and **c** Change of the distribution function f of the conduction band electron in gold after absorption of a light pulse with $\hbar\omega_e = 1.5\,\text{eV}$ and duration $t_p = 25\,\text{fs}$ **b** and 250 fs **c**. The dash-dotted, full and dashed lines correspond to time $t = 0$ fs, 500 fs and 3 ps, respectively, after the maximum of the excitation pulse at $t = 0\,\text{fs}$). The same energy is absorbed by the electrons: $\Delta T_e^{me} = 100\,\text{K}$

with a final energy between E_F and $E_F + \hbar\omega_e$ (Fig. 5.3). Describing the conduction electron distribution by a one-particle function f and assuming an isotropic parabolic conduction band, the induced distribution change $\Delta f(E) = f(E) - f_0(E)$ in the constant transition matrix element approximation and weak excitation limit, is given by [26, 29]:

$$\Delta f^{exc}(E) = A\left\{\sqrt{E-\hbar\omega_e}\,f_0(E-\hbar\omega_e)\,[1-f_0(E)]\right. \\ \left. -\sqrt{E+\hbar\omega_e}\,f_0(E)\,[1-f_0(E+\hbar\omega_e)]\right\}, \qquad (5.10)$$

where f_0 is the electron distribution before optical excitation (Fermi-Dirac distribution at temperature T_0) and A a constant defining the injected energy. Electron energy relaxation during the excitation process has been disregarded.

When interband absorption takes place, d-electron excitation leads to an excess electron population of conduction band states with energy around $E_F + \hbar\omega_e - \hbar\omega_{ib}$. The created d-band holes recombine in a few tens of femtoseconds via an Auger process leading to indirect excitation of electron-hole pairs in the conduction band [93, 97]. This translates into a increase of f in the energy range $[E_F, E_F + \hbar\omega_e]$ and a decrease in the range $[E_F - \hbar\omega_e, E_F]$. The difference between the created nonequilibrium distributions for intra and interband absorptions has to be taken into account only when processes taking place on the first tens of femtoseconds are studied, the subsequent electron kinetics being very similar. For the sake of simplicity, only intraband excitation will be considered in the following.

In bulk noble metals, the time evolution of the conduction electron energy distribution function f can be described by the Boltzmann equation [26, 29, 98, 99]. Assuming an isotropic conduction band it reads:

$$\frac{df(E,t)}{dt} = \left.\frac{\partial f(E,t)}{\partial t}\right|_{e-e} + \left.\frac{\partial f(E,t)}{\partial t}\right|_{e-ph} + \left.\frac{\partial f(E,t)}{\partial t}\right|_{exc}. \tag{5.11}$$

Homogeneous excitation has been assumed, which corresponds to optically thin samples (note that spatial homogeneity can also be assumed in thicker metal film due to fast electron transport in metal [100, 101]). Coupling with the surrounding environment has also been neglected as it usually takes place on longer time scales (few tens to few hundred picoseconds) as compared to electron kinetics processes described by Eq. 5.11 (up to few picoseconds). The first term describes e-e scattering, which, taking into account energy and momentum conservations reads [26, 29, 102]:

$$\left.\frac{\partial f(E(\mathrm{k}))}{\partial t}\right|_{e-e} = \frac{2\pi}{\hbar}\sum_{k_1,k_2,k_3} |M_{ee}(|k-k_2|)|^2 F(E, E_1, E_2, E_3)\delta_k\delta_E \tag{5.12}$$

where δk and δE stand for electron momentum and energy conservations: $k + k_1 - k_2 - k_3 = 0$ and $E(k) + E_1(k_1) - E_2(k_2) - E_3(k_3) = 0$. F includes the Pauli exclusion effect for electron scattering in and out the E state:

$$F = -f(E)\,f(E_1)\,[1-f(E_2)]\,[1-f(E_3)] + [1-f(E)]\,[1-f(E_1)] \times f(E_2)\,f(E_3)\,. \tag{5.13}$$

Assuming statically screened Coulomb electron interaction, the e-e scattering matrix element is:

$$M_{ee}(q) = \frac{e^2}{\varepsilon_0 \varepsilon^{ib}(0)} \quad \frac{1}{q^2 + q_S^2}. \tag{5.14}$$

The static description of screening overestimating reduction of the e-e scattering amplitude, a phenomenological screening reduction has been introduced using a screening wave vector $q_S = \beta q_{TF}$, instead of the Thomas Fermi one q_{TF} (with $\beta = 0.73$ in bulk silver and gold) [26, 29, 103].

The second term on the right hand side of Eq. 5.11 is the e-ph scattering rate [26, 99]:

$$\left.\frac{\partial f(E(\mathrm{k}))}{\partial t}\right|_{e-ph} = \frac{2\pi}{\hbar}\sum\nolimits_q \left|M_{eph}\right|^2 F^-(k,q)\cdot\delta(E(k)-E(k-q)-\hbar\omega_q) + \\ + \frac{2\pi}{\hbar}\sum\nolimits_q \left|M_{eph}\right|^2 F^+(k,q)\cdot\delta(E(k)-E(k+q)+\hbar\omega_q), \tag{5.15}$$

where $\hbar\omega_q$ is the energy of the q wave vector phonon and:

$$F^-(k,q) = -f(E(k))[1-f(E(|k-q|))][1+N(\hbar\omega_q)] + \\ + [1-f(E(k))]f(E(|k-q|))N(\hbar\omega_q), \tag{5.16}$$

and $F^+(k,q) = -F^-(k+q,q)$. $N(\hbar\omega_q)$ is the occupation number of the q phonon.

Assuming deformation potential coupling the e-ph interaction matrix element is:

$$\left|M_{eph}(q)\right|^2 = \frac{\hbar^2 \Xi^2}{2\rho V}\frac{q^2}{\hbar\omega_q}, \tag{5.17}$$

where Ξ is the deformation potential and ρ the material density. Though it is a rough approximation in metal, it has been shown that the exact nature of the e-ph coupling does not influence the computed electron dynamics for a lattice at room temperature. This is a consequence of the fact that T_L being then larger than the Debye temperature Θ_D [66], electron distribution changes on the energy scale of a phonon has a minor influence on the overall dynamics. The Debye model for the phonon dispersion is used: $\omega_q = v_s q$, v_s being the material sound velocity, the exact phonon dispersion having no impact on the computed f kinetics for T_L much larger than Θ_D.

The last term in Eq. 5.11 describes incoherent single electron excitation. It is identical to Δf^{exc} (Eq. 5.10, with replacing f_0 by f and A by $BI(t)$ to take into the finite duration of the excitation pulses (B is a constant and $I(t)$ is the time dependent incident pulse intensity). An important parameter to describe excitation of the electrons is their transient excess energy density Δu_e, i.e., their total energy at time t minus the one before excitation:

$$\Delta u_e(t) = \frac{\sqrt{2}m_e^{3/2}}{\pi^2\hbar^3}\int E^{3/2}\Delta f(E,t)dE = \frac{a}{2}\left[T_e^2(t) - T_0^2\right], \tag{5.18}$$

the second equality being only valid when the electron temperature T_e is established. The temperature dependence of the electron heat capacity has been taken into account assuming a quasi-free electron behavior $C_e(T_e) = aT_e$, a being a constant ($a = \pi^2 n_e k_B/2T_F$ for a free electron gas, T_F is the Fermi temperature,) [66]. This expression for C_e is valid in noble metals as long as electron heating involves only conduction band electrons, with an assumed parabolic band. This is valid for $\Delta T_e = T_e - T_0 \leq 3,000\,\mathrm{K}$, C_e increasing for larger ΔT_e due to thermal depopulation or population of other bands [104], an effect that will not be considered here assuming moderate electron heating.

It is convenient to define the parameter B via the total energy density injected by the pump pulse $u_e^{abs} = \int \Delta u_e^{exc}(t)dt$ where $\Delta u_e^{exc}(t)$ is given by Eq. 5.18, replacing Δf by Δf^{exc} or equivalently, by defining a maximum equivalent electron temperature rise, ΔT_e^{me}, as the temperature rise of a thermalized electron gas for the same energy increase:

$$\Delta T_e^{me} = \left[T_0^2 + 2u_e^{abs}/a\right]^{1/2} - T_0 \tag{5.19}$$

where T_0 is the initial temperature of the system. In a nanoparticle, electron excitation being usually much faster than energy transfer to the surrounding matrix (few tens to few hundred picoseconds [58, 59], a minimum ΔT_e^{me} is induced in each excited particle, corresponding to absorption of a single photon. This can be fairly large for

small sizes, reaching for instance about 450 K for a 3 nm diameter gold sphere and $\hbar\omega_e = 1.3$ eV, an effect that must be taken into account in interpreting experimental data [37].

5.3.2.1 Electron Gas Thermalization

The computed time dependent electron distribution function is illustrated in Fig. 5.3 in the case of gold for weak excitation, $\Delta T_e^{me} = 100$ K, and pulse duration $t_p = 25$ fs and 250 fs. In both cases, an athermal electron population is created, reflecting in a broad energy extension of the distribution change $\Delta f(E,t) = f(E,t) - f_0(E)$. Fast electron-electron energy redistribution subsequently leads to build up of Δf around E_F as the electron gas internally thermalizes, i.e., f reaches a Fermi-Dirac distribution with temperature T_e. This takes place concurrently with excitation by the pulse leading to a narrower athermal distribution when using longer pulses (Fig. 5.3). Internal thermalization kinetics takes place with characteristic thermalization times of about 500 fs and 350 fs in gold and silver respectively, this slow kinetics being determined by e-e collisions around the Fermi surface. Their probabilities are strongly reduced by the Pauli exclusion principle effects, making them the slowest scattering processes involved in the internal thermalization process [26, 29]. Experimental results have been found to be in quantitative agreement with the computed ones the reduced thermalization time in silver as compared to gold being due to larger screening by the bound electrons in the latter [26]. This kinetics is almost independent of the injected energy in the weak perturbation regime, i.e., for $\Delta T_e^{me} \leq 200 - 300$ K and becomes faster for larger excitations due to weakening of the effects of Pauli exclusion increased smearing of the electron distribution around the Fermi energy [26].

Internal electron gas thermalization has been shown to be faster in nanospheres with diameter smaller than 10 nm (the thermalization time being about 300 fs in 5 nm gold spheres) [51, 52]. Using a bulk-like model, this size dependence has been ascribed to confinement induced fastening of the electron-electron energy exchanges, due to less efficient screening of the e-e Coulomb interactions close to a surface [52]. However, other processes associated to quantum confinement of the electrons, such as relaxation of momentum conservation or electron state quantization, can play a role, especially in the very small size regime. For large excitation, other effects can also influence the observed kinetics, as resonant dynamic screening modification [105–107].

5.3.2.2 Electron-Lattice Energy Exchanges

Light being selectively absorbed by the electrons, they are out of equilibrium with the lattice and cools down by electron-lattice energy transfer. After establishment of an electronic temperature, the electron cooling kinetics can be simply described using the electron temperature and using the two-temperature model [25, 70, 108].

It is based on the assumption that both the electron and lattice are thermalized at different temperatures T_e and T_L, assumed to be homogeneous over the metal sample (note that the assumption that the lattice temperature is always maintained by phonon anharmonic interactions can certainly be questioned). This model can be generalized to include non-homogeneous metal heating using spatial dependent temperatures and adding a diffusion term in the metal. These extensions will not be considered here, where the same assumption of spatial homogeneity and slow metal-environment energy transfer will be assumed as for Eq. 5.11. The electron gas cooling dynamics can then be simply modeled using the rate equation system:

$$\begin{array}{l} C_e(T_e)\frac{\partial T_e}{\partial t} = -G(T_e - T_L) \\ C_L\frac{\partial T_L}{\partial t} = G(T_e - T_L) \end{array} \tag{5.20}$$

where G is the electron-phonon coupling constant. As C_e, G can be assumed constant for sufficiently small electron temperature rise $\Delta T_e \leq 2{,}000 - 3{,}000\,\mathrm{K}$, i.e., as long as only conduction band electronic states are involved. It increases for larger ΔT_e with increasing the density of available states for electron scattering due to intervention of other electronic states [104]. As before, only moderate excitation will be considered including only the conduction band electrons. The above equations are then a consequence of the Boltzmann equation Eq. 5.11, and are obtained computing the electron energy loss rate to the lattice in the thermalized regime (with $T_e, T_L > \Theta_D$):

$$C_e\frac{\partial T_e}{\partial t} = \frac{\partial \Delta u_e}{\partial t} = \frac{m_e^{3/2}\sqrt{2E}}{\pi^2\hbar^3}\int E\frac{\partial f(E)}{\partial t}\bigg|_{e-ph} dE = -G(T_e - T_L), \tag{5.21}$$

with

$$G = \Xi^2\frac{k_B m_e^2 q_D^2}{16\rho\pi^2\hbar^3}, \tag{5.22}$$

where q_D is the Debye wave vector [26, 66]. The above rate equation system can be solved analytically [109]:

$$T_{eq}\ln\left[\frac{T_e - T_{eq}}{T_{exc} - T_{eq}}\right] + \tilde{T}\ln\left[\frac{T_e - \tilde{T}}{T_{exc} - \tilde{T}}\right] = -G\frac{\tilde{T} + T_{eq}}{2C_L}t. \tag{5.23}$$

T_{exc} is the temperature at time t_{th} after which T_e can be defined. For the sake of simplicity $t_{th} = 0$ has been used, i.e., instantaneous internal electron thermalization is assumed and $T_{exc} = T_0 + \Delta T_e^{me}$. The final temperature, T_{eq}, of the thermalized electron-lattice system is then given by:

$$T_{eq} = \left[T_s^2 + T_{exc}^2 + 2T_s T_0\right]^{1/2} - T_s \approx T_0 + \frac{T_{exc}^2 - T_0^2}{2T_s}, \tag{5.24}$$

where $\tilde{T} = T_{eq} + 2T_s \approx 2T_s$, and $T_s = C_L/a$ is a metal dependent constant. The lattice heat capacity C_L being much larger than the electronic one, T_s is large ($T_s \approx 120T_0$ in gold). The final temperature rise $T_{eq} - T_0$ is thus much smaller than T_{exc} (Fig. 5.4). For moderate heating, i.e., for T_e, $T_L << T_s$, the approximated expression of T_{eq} and $\tilde{T}$ can be used as well as a simplified expression of Eq. 5.23:

$$\frac{T_{exc} - T_e}{T_{eq}} - \ln\left[\frac{T_e - T_{eq}}{T_{exc} - T_{eq}}\right] = \frac{G}{aT_{eq}}t. \tag{5.25}$$

For weak electron heating, $\Delta T_e^{me} << T_0$, the first term on the left hand side can be neglected and T_{eq} identified with T_0. The electron temperature rise then decays exponentially (Fig. 5.4):

$$\Delta T_e = T_e(t) - T_L(t) = (T_{exc} - T_0)\exp\left[-(t - t_{th})/\tau_{e-L}\right] \tag{5.26}$$

with the intrinsic electron-lattice energy exchange time [26, 29]:

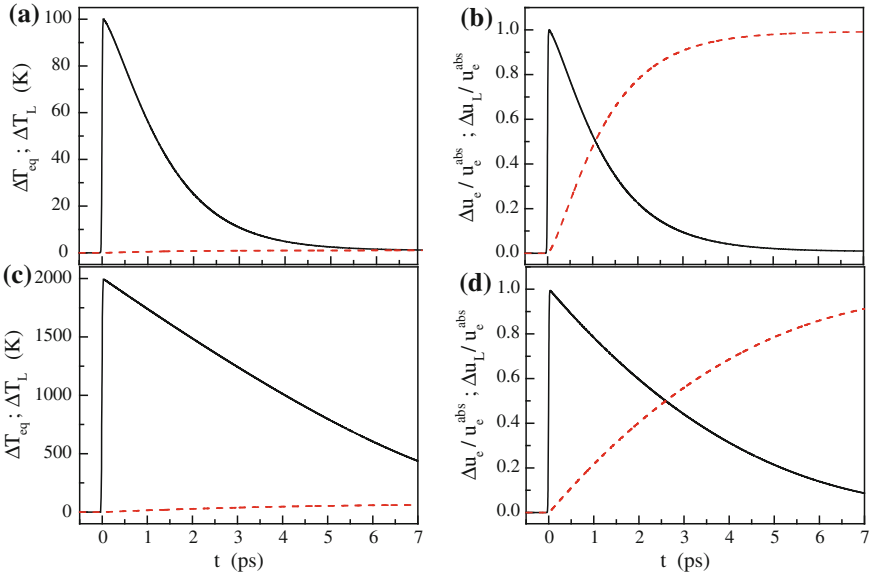

Fig. 5.4 Computed time dependence of the temperature rises of the conduction electrons (*full lines*) and lattice (*dashed lines*), ΔT_e and ΔT_L, and of their excess energy densities, Δu_e (Eq. 5.18) and $\Delta u_L = C_L \Delta T_L$, normalized to the total energy u_e^{abs} absorbed by the electrons in gold from a 25 fs pulse for $\Delta T_e^{me} = 100$ K. (**a**) and (**b**), and 2,000 K (**c**) and (**d**). Calculation are performed using Eq. 5.11 including lattice heating, identical results being obtained for long times with the two-temperature model Eq. 5.20 after internal thermalization of the conduction electrons ($t \geq 500$ fs)

$$\tau_{e-L} = \frac{C_e(T_0)C_L}{G(C_e(T_0)+C_L)} \approx C_e(T_0)/G = aT_0/G \tag{5.27}$$

In this regime, the electron excess energy is proportional to ΔT_e: $\Delta u_e \approx 2aT_0\Delta T_e$ (Eq. 5.18), and thus exhibits the same time-dependence (Fig. 5.4). The energy exchange time τ_{e-L} has been measured in different metal monitoring electron cooling in femtosecond pump-probe experiment [26, 28, 29, 110]. Values of about 1.1 ps in bulk gold and 850 fs in bulk silver were obtained. As for the electron thermalization time, acceleration of the electron-lattice energy exchanges has been demonstrated in metal nanospheres smaller than about 10 nm [33, 50]. It has to be noted that, on a short time scale, the electron distribution is athermal and the two-temperature model, Eq. 5.20, cannot be used. The electron energy loss rate to the lattice has been found to be slower in the athermal situation and to increase over a time scale of a few hundred femtoseconds (i.e., the internal thermalization time of the electrons), to reach the thermal regime value τ_{e-L} [26]. This evolution from a quasi-individual to a collective electron behavior leads to deviation from an exponential decay of the electron excess energy that has been observed experimentally [47, 110, 111].

For larger excitation, the T_e dependence of C_e has to be taken into account (the assumption leading to Eq. 5.26 being equivalent to neglect the temperature dependence of C_e over the T_e excursion and to identify it to $C_e(T_0)$). The electron temperature rise ΔT_e then decay non-exponentially, with a large perturbation dependent slowing down of its short time delay dynamics (Fig. 5.4). Exponential decay with the time constant $\tau_{e-L}T_L/T_0 \approx \tau_{e-L}$ is eventually recovered as the electron gas cools-down, in agreement with experimental results [26, 109, 112, 113].

In both cases, electron cooling is accompanied to lattice temperature rise to T_{eq} with the same kinetics (Fig. 5.4). Because of its large heat capacity as compared to the electronic one, energy is eventually mostly stored in the lattice as the metal reaches thermal electron-lattice equilibrium, with $\Delta u_e << \Delta u_L = C_L\Delta T_L$ in thermal equilibrium (Fig. 5.4). In nanoparticles the electron energy can also be damped to the surrounding solvent or matrix either directly or via the metal lattice, possibly modifying the observed relaxation. This coupling is frequently assumed to be sufficiently slow to be neglected on the scale of the metal electron-lattice energy exchange. However, it strongly increases with size reduction and may play a role in the observed electron cooling for large excitation [114–116].

The above approach describes the different steps of internal relaxation of a metal driven out of equilibrium by a light pulse. Though in nanoparticles, the electron kinetics is modified, this only shows-up for sizes smaller than about 10 nm. For larger sizes, the bulk like model can thus be directly used to describe electron relaxation, with a possible extension to smaller sizes taking into account increase of the electronic interactions [52].

5.3.2.3 Nanoparticle Cooling

After electron-lattice thermalization, the metal temperature T_{eq} is larger than the initial one. It subsequently cools-down by damping its energy to its environment via its interface, making T_{eq} time dependent on this time-scale. This effect is particularly important for small size nanoparticles which exhibit a large surface over volume ratio, increasing their interaction with their environment. The rate at which heat dissipates from a nanoparticle depends both on the thermal interface resistance which governs energy transfer at the interface between the nanoparticle and its surrounding, and on heat diffusion in the surrounding medium [58, 59, 117, 118]. Nanoparticle cooling can be described introducing the time and space dependent temperature T_m of its surrounding matrix, whose evolution is described adding a third rate equation to the two-temperature model, Eq. 5.20 [114]. Assuming electron-lattice thermalization in a nanoparticle is much faster than its cooling to its environment, T_e and T_L can be taken as identical (to T_{eq}, an assumption valid only after particle thermalization, i.e., after a few picoseconds). T_{eq} is also assumed to be uniform over the nanoparticle, which is justified by the high thermal conductivity of metals. In the case of nanospheres, T_m depends only on the distance from the particle centre r, assuming sufficient dilution to neglect matrix heating by other particles. Heat dissipation from a nanosphere of diameter D is then governed by a set of two equations describing heat flux at the particle-matrix interface and heat diffusion within the glass matrix [58, 59]:

$$\begin{aligned} \frac{\partial T_{eq}(t)}{\partial t} &= -\frac{6H}{Dc_p}\left(T_{eq}(t) - T_m(D/2,t)\right), \\ c_m \frac{\partial T_m(r,t)}{\partial t} &= \Lambda_m \frac{1}{r}\frac{\partial^2}{\partial r^2}\left(rT_m(r,t)\right) \end{aligned} \tag{5.28}$$

where $c_{p,m}$ is the particle and matrix specific heat per unit volume, Λ_m the thermal conductivity of the matrix, and H the interface thermal conductance. Solving the above equations, one obtains the following expression for the particle temperature [59, 119, 120]:

$$\Delta T_{eq}(t) = \frac{kD^2b^2\Delta T_{eq}^0}{2\pi} \int_0^{+\infty} \frac{u^2 \exp(-4\kappa u^2 t/D^2)}{\left[u^2(1+Db/2) - kDb/2\right]^2 + (u^3 - kDbu/2)^2} du, \tag{5.29}$$

where $\Delta T_{eq}(t) = T_{eq}(t) - T_0$, ΔT_{eq}^0 being the initial temperature increase of the particle (after electron-lattice thermalization), $\kappa = \Lambda_m/c_m$, $k = 3c_m/c_p$ and $b = H/\Lambda_m$. If one of the involved mechanisms, i.e., interface-resistance or heat-diffusion, limits the nanoparticle cooling kinetics, a much simpler expression is obtained. The former dominates in small nanoparticles and the latter in large ones, leading to exponential or non-exponential ΔT_{eq} decay, respectively. A similar approach can be used in 2D systems, i.e., a metal film, the problem being then unidimensional [58, 121].

5.4 Time Dependent Metal Dielectric Function Change

Modification of the distribution f (or temperature) of the electrons in the conduction band and subsequent lattice heating translate into modifications of the dielectric function ε of the metal and thus of its optical absorption [26, 29, 52, 61, 65]. These can be computed provided the induced change $\Delta\varepsilon$ is connected to the electron distribution change Δf (or ΔT_e) and to the lattice temperature rise ΔT_L. This is done analyzing their impacts on the interband (bound electrons) and intraband (quasi-free electrons) contributions to ε (Eqs. 5.1 and 5.5). The dominant mechanisms involved in modification of the former, $\Delta\varepsilon^{ib}$, and latter, $\Delta\varepsilon^{in}$, contributions are associated to electron and lattice heating, respectively. $\Delta\varepsilon^{ib}$, thus usually dominates when most of the excess energy is stored in the electrons, i.e., on a short time scale, while $\Delta\varepsilon^{in}$ is dominant on a long time-scale when energy has been transferred to the lattice, i.e., after electrons-lattice thermalization (Fig. 5.4). These different contributions are discussed in the following.

5.4.1 Electronic Contribution

The electronic contribution due to energy injection in the electrons is important only if energy is in the electron gas. It mostly impacts the interband term $\Delta\varepsilon^{ib}$, with a smaller intraband contribution due to the change of the electron scattering rates, both effects thus decaying with electron cooling to the lattice (Fig. 5.4).

5.4.1.1 Interband Dielectric Function

Change of the interband contribution $\Delta\varepsilon^{ib}$ is a consequence of modification of the interband absorption spectrum due to electron distribution smearing (Fig. 5.3), [26, 29, 110]. Its calculation requires connection of $\Delta\varepsilon_2^{ib}(\omega)$ to Δf, which can be done in gold and silver, using the band structure models of Rosei and co-workers (Eq. 5.9). In these models, the spectral width of the electronic states is neglected [122]. Estimation of its impact on $\Delta\varepsilon^{ib}$ is difficult, since its inclusion introduces an additional parameter when comparing experimental and theoretical results, which could compensate for deviation between the real and model band structures. As a first approximation we have neglected it, an approximation justified by the good agreement between the calculated and measured transient optical property spectra [26, 32, 52]. One has also to keep in mind that the Rosei models are valid for frequencies ω close to ω_{ib} and a quasi-thermalized electron gas. For strongly nonequilibrium electrons and frequency away from ω_{ib} significant deviations can take place and have to be taken into account to quantitatively compare the experimental and theoretical results. In this regime, the simple model of a parabolic conduction band and undispersed d-bands can be used,

where, in contrast to the Rosei's description, $\Delta\varepsilon_2^{ib}(\omega)$ is sensitive only to electron states with energy: $E = \hbar\omega + (E_F - \hbar\omega_{ib})$ [26].

Using these models (Eq. 5.9 for gold), $\Delta\varepsilon_2^{ib}$ can be calculated as a function of time t, frequency ω, and electron excitation amplitude ΔT_e^{me} using the computed Δf. As an example, the $\Delta\varepsilon_2^{ib}$ spectra and amplitude computed after intraband absorption of 25 fs pulse are shown in Figs. 5.5b and 5.6b at the time $t = 0$ (maximum of the pulse) and after 500 fs and 3 ps, for low and high excitation temperatures ($\Delta T_e^{me} = 100$ K and 2,000 K) in bulk gold. $\Delta\varepsilon_1^{ib}(\omega)$ is subsequently calculated by Kramers-Kronig transformation (Figs. 5.5a and 5.6a, note that this approach is valid as $\Delta\varepsilon_2^{ib}(\omega)$ is non-zero only over a limited range around ω_{ib}). The short time $\Delta\varepsilon_2^{ib}(\omega)$ and $\Delta\varepsilon_1^{ib}(\omega)$ exhibit very broad almost featureless spectra, reflecting change of f over a broad electron energy range (Fig. 5.3). The $\Delta\varepsilon_2^{ib}(\omega)$ and $\Delta\varepsilon_1^{ib}(\omega)$ amplitudes increase with time around ω_{ib} as electrons internally thermalize, and Δf mostly concentrates around E_F (Fig. 5.3). They show two distinct features associated to contribution around the X and L points of the Brillouin zone (Fig. 5.1, with maxima around 1.9 and 2.3 eV, respectively, for $\Delta\varepsilon_2^{ib}(\omega)$), the latter yielding as expected the largest contribution. These structures are much broader for large excitation as a consequence of increased smearing of the electron distribution around E_F with increasing T_e. The rise of $\Delta\varepsilon^{ib}$ as the electrons internally thermalize has been used to optically monitor this process in noble metal films and nanoparticles [26, 29, 52]. When the electrons are internally thermalized, after about 500 fs for weak excitation in gold, and faster for large excitation, their amplitudes, are mostly related to the electron excess energy $\Delta u_e(t)$ and subsequently decrease as electron energy is transferred to the lattice (with the time τ_{e-L} for weak excitation, and a longer time for large excitation, Fig. 5.4).

5.4.1.2 Intraband Dielectric Function

The intraband contribution to ε is also modified by electron excitation. It is a consequence of the dependence of the rate of all electron scattering processes on the electronic distribution (or temperature T_e when it is established), Eqs. 5.2 and 5.6. In the case of nanoparticles, taking into account electron-surface $\Delta\gamma_n$ can be written (Eqs.5.2 and 5.6):

$$\Delta\gamma_n(\omega, T_e, T_L) = \Delta\gamma_{e-ph}(\omega, T_e, T_L) + \Delta\gamma_{e-e}(\omega, T_e) + \Delta\gamma_S(\omega, T_e) \tag{5.30}$$

with a similar expression for $\Delta\gamma_{bulk}$. In a sphere: $\gamma_S = 2g(\omega, T_e)v_F/D$ and for not too small particles (larger than about 10 nm), $\Delta\gamma_{e-ph}$ and $\Delta\gamma_{e-e}$ can be identified to their bulk values.

Using Eq. 5.1 or 5.5, the real and imaginary parts of $\Delta\varepsilon^{in}$ are then given by:

$$\Delta\varepsilon_1^{in} \approx \frac{2\gamma\,\omega_p^2}{\omega^4}\Delta\gamma; \quad \Delta\varepsilon_2^{in} \approx \frac{\omega_p^2}{\omega^3}\Delta\gamma, \tag{5.31}$$

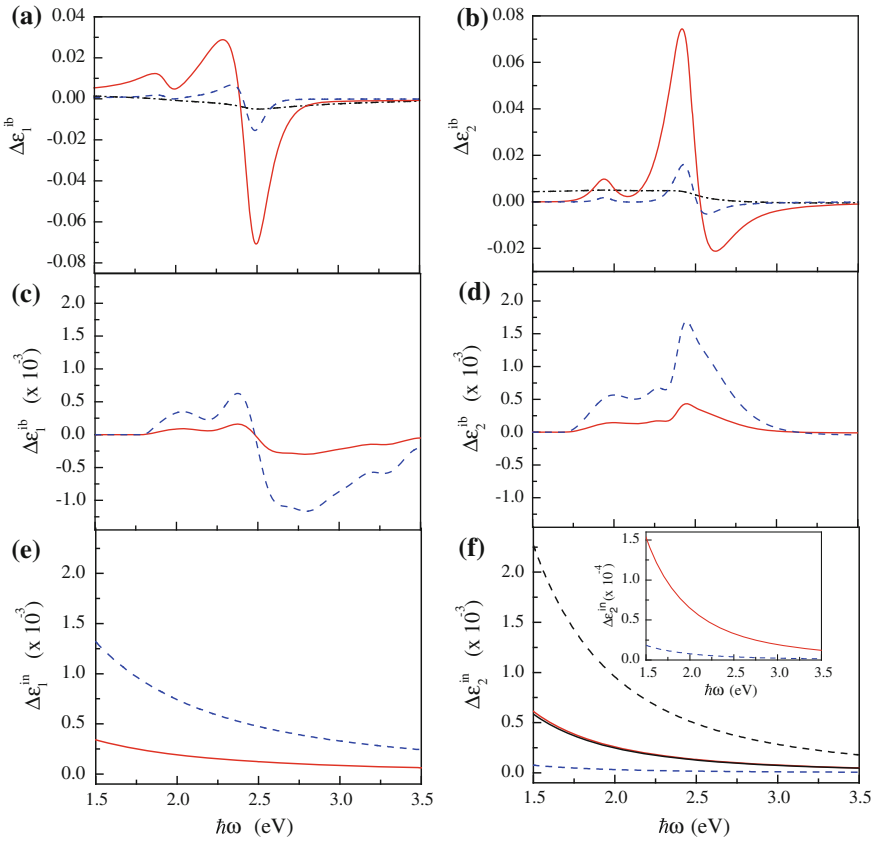

Fig. 5.5 Computed absolute values of the changes of the real (*left*) and imaginary (*right*) parts of the interband, ε^{ib}, and intraband, ε^{in}, contributions to the gold dielectric function after excitation with a 25 fs pulse with $\hbar\omega_e = 1.5$ eV and $\Delta T_e^{me} = 100$ K and time $t = 0$ fs (*dash-dotted line*), 500 fs (*full line*) and 3 ps (*dashed line*) after the maximum of the excitation pulse. Different mechanisms are considered: **a** and **b**: effect of electronic distribution change on ε^{ib} for $t = 0$ fs, 500 fs and 3 ps (Sect. 4.1.1); **c** and **d**: effect of the volume change on ε^{ib} for $t = 500$ fs and 3 ps (Eq. 5.33); effect of the volume change on ε^{in} **e**: for $t = 500$ fs and 3 ps (Eq. 5.35); **f**: effect of increase of electron-electron scattering γ_{e-e} for $t = 0$ fs (*lower dashed line*) and 500 fs (*upper full line*, almost overlapping that due to $\Delta\gamma_{e-ph}$) (Eqs. 5.31 and 5.32) and of electron-phonon scattering γ_{e-ph} for $t = 500$ fs (*lower full line*, almost overlapping that due to $\Delta\gamma_{e-e}$) and 3 ps (*upper dashed line*) (Eq. 5.34); insert of **f**: effect of the electron surface contribution for a 10 nm gold nanosphere for $t = 500$ fs and 3 ps (Eqs. 5.7 and 5.31). All the $\Delta\varepsilon$ amplitudes associated to mechanisms due to electronic or lattice heating decrease or increase with time, respectively. Note the different $\Delta\varepsilon$ scales for the different mechanisms

where $\Delta\gamma$ stand for $\Delta\gamma_{bulk}$ or $\Delta\gamma_n$ in film and nanoparticles, respectively. $\Delta\varepsilon_2^{in}$ is thus much larger than $\Delta\varepsilon_1^{in}$ ($\Delta\varepsilon_1^{in}/\Delta\varepsilon_1^{in} \approx 2\gamma/\omega << 1$). Only the former gives a significant contribution and will be considered in the following.

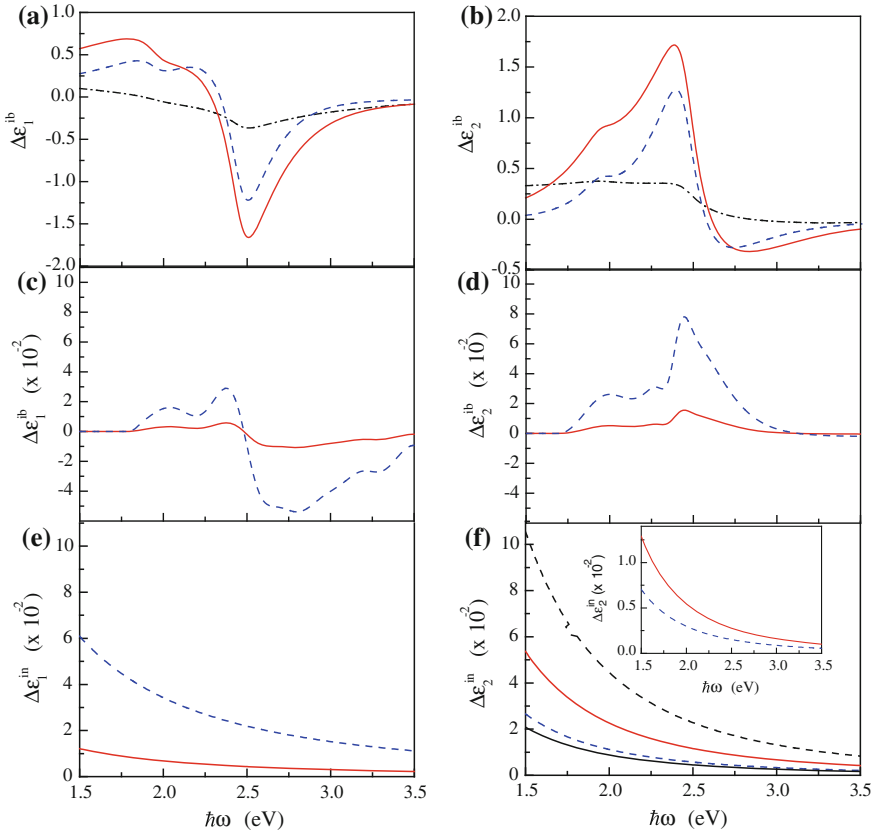

Fig. 5.6 Same as Fig. 5.5 for $\Delta T_e^{me} = 2,000\,\mathrm{K}$

The electron-phonon contribution $\Delta\gamma_{e-ph}$ varies very weakly with T_e (Eq. 5.3) conversely to the DC rates $\gamma_{e-ph}(\omega = 0)$ [123]. The electron-electron and electron-surface terms $\Delta\gamma_{e-e}$ and $\Delta\gamma_S$ rise and decay with the electron temperature change, or more generally with the changes of the electron distribution f (Eqs. 5.4 and 5.7). Using Eq. 5.4, the relative change of γ_{e-e} is given by (Fig. 5.1):

$$\frac{\Delta\gamma_{e-e}}{\gamma_{e-e}} \approx \left(\frac{2\pi k_B}{\hbar\omega}\right)^2 \left(T_e^2 - T_0^2\right). \tag{5.32}$$

Using Eqs. 5.31 and 5.32 and the computed time dependence of T_e (Fig. 5.4), one obtains $\Delta\varepsilon_2^{in}$ (Fig. 5.5f, with $\hbar\gamma_{e-e} \approx 15\,\mathrm{meV}$ [68]). For weak excitation, it only yields a small contribution as compared to the interband electronic one and to the lattice heating one (showing-up on for longer time). It becomes more significant for high electronic temperature rise (Fig. 5.6) as a consequence of the quadratic dependence of γ_{e-e} on T_e (Eqs. 5.4 and 5.32, Fig. 5.1).

The change of the surface term $\Delta\gamma_S$ is due to the electron temperature dependence of g that can be estimated using Eq. 5.7 (Fig. 5.1). It yields a relatively small contribution to $\Delta\varepsilon_2^{in}$ for not too small nanoparticles, as illustrated for 10 nm diameter gold nanospheres (inset of Fig. 5.5f, using Eqs. 5.6 and 5.31). As it increases with the particle size (Eq. 5.6), it can play a significant role in small nanoparticles as shown in the case of gold nanospheres [60]. It is the first manifestation of quantum confinement in their nonlinear optical response.

5.4.2 *Lattice Contribution*

In the equilibrium regime ($T_e = T_L = T_{eq}$), the electronic mechanisms are almost negligible, as $\Delta T_{eq} << \Delta T_e^{me}$ and most of the energy is in the lattice (Fig. 5.4). $\Delta\varepsilon$ then reflects lattice temperature rise and the concomitant metal dilation. Note that the latter effect, that impacts both the interband contribution, via electronic band shifting (i.e., deformation potential coupling), and the intraband one, via change of the electronic density, has permitted detection of coherent vibration of metal films and nanoparticles following the concomitant modulation of their volume [33, 86, 88, 124]. All the induced changes are proportional to ΔT_L and thus rise with lattice heating by the electrons (Fig. 5.4) and decay with metal cooling to its environment.

5.4.2.1 Interband Dielectric Function

Due to lattice anharmonicity, lattice heating leads to increase of the equilibrium inter-atomic distance a_L and to shift of the Fermi energy. This induces modification of the electronic band structure, shifting the energy position of the electronic bands and their filling, and thus of the metal interband absorption spectrum. ε^{ib} is thus modified, proportionally to ΔT_L. Assuming rigid band shift one gets:

$$\Delta\varepsilon^{ib}(\omega) = -\left.\frac{\partial\varepsilon^{ib}}{\partial\,\omega}\right|_{\omega}\left.\frac{\partial\,\omega_{ib}}{\partial T_L}\right|_{T_0}\Delta T_L. \tag{5.33}$$

Displacement of the interband transition threshold ω_{ib} with the T_L can be estimated from calculation of the Fermi energy and the electronic band structure of metal [80, 84]. For gold, one obtains around the L point of the Brillouin zone $(\partial\hbar\,\omega_{ib}/\partial T_L)_{T_0} \approx -5\times10^{-5}$eV/K comparable but smaller than the experimentally estimated value: $(\partial\hbar\,\omega_{ib}/\partial T_L)_{T_0} \approx -1.7\times10^{-4}$eV/K [82]. A different shift is estimated for the X point threshold, an effect that will not be included here as contribution of the X point transitions to ε^{ib} and $\Delta\varepsilon^{ib}$ is smaller than for the L point. The estimated changes of ε^{ib} are shown in Fig. 5.5c,d using the above experimental $(\partial\,\omega_{ib}/\partial T_L)_{T_0}$ and the $(\partial\varepsilon/\partial\,\omega)$ values computed from the ε data of Johnson and Christy. As expected, they show structures around the interband transition threshold and rise with the lattice temperature.

5.4.2.2 Intraband Dielectric Function

Lattice heating modifies the intraband contribution to ε both via increase of the electron scattering rate γ_{e-ph} and by reduction of the plasma frequency ω_p. The former effect is a direct consequence of increase of the phonon occupation number with the lattice temperature (Eq. 5.3). As for the electron temperature induced change of γ, it mostly affects the imaginary part of ε (Eq. 5.30).

$$\Delta\varepsilon_2^{in} \approx \frac{\omega_p^2}{\omega^3}\Delta\gamma_{e-ph} \approx \frac{\omega_p^2}{\omega^3}\frac{\partial\gamma_{e-ph}}{\partial T_L}\Delta T_L. \tag{5.34}$$

Its contribution obtained using the lattice temperature dependence of γ_{e-ph} estimated in gold films $\partial\hbar\gamma_{e-ph}/\partial T_L \approx 0.11\,\text{meVK}^{-1}$ [125], is shown in Fig. 5.5f. It increases as ω decreases (Eq. 5.34), $\partial\gamma_{e-ph}/\partial T_L$ being almost frequency independent, and gives the dominant contribution to $\Delta\varepsilon_2$ on a few picosecond time-scale, after electron-lattice thermalization [26, 38].

Increase of the metal volume due to lattice dilation reduces the electronic density n_e, and thus ω_p. It thus translates in increase of the Drude contribution to ε yielding for its real part:

$$\Delta\varepsilon_1^{in} \approx -\frac{\omega_p^2}{\omega^2}\frac{\Delta n_e}{n_e} = \frac{\omega_p^2}{\omega^2}\frac{\Delta V}{V} = \frac{\omega_p^2}{\omega^2}3\alpha_L\Delta T_L, \tag{5.35}$$

where α_L is the linear dilation coefficient of gold ($\alpha_L \approx 1.42\times10^{-5}\text{K}^{-1}$). The corresponding change of the imaginary part is much smaller than the contribution due to γ_{e-ph}, Eq. 5.34 (the relative contribution being of the order of $3\alpha_L T_L$), and will be disregarded. Volume change induce comparable amplitude for the interband and intraband contributions (Eqs. 5.33 and 5.35), the former showing-up mostly around the interband threshold ω_{ib}, while the latter increase in the red part of the spectrum (Figs. 5.5 and 5.6). Note that these two contributions permit detection of the vibration modes of metal nanoobjects associated to volume changes, an oscillatory behavior, signature of the volume change being thus obtained [33, 37, 55, 56, 126]. The direct impact of lattice temperature rise is more difficult to disentangle from other effect as environment heating [59], or other modifications of the electron band structure not included here as change of the electronic mass [61].

5.5 Ultrafast Nonlinear Optical Response

The changes of a metal dielectric function induced by electron excitation by a light pulse translate into changes of the optical properties of the system, i.e., its, absorption, scattering, transmission T, or reflection R, which are observed experimentally. Quite generally, the optical transmission or reflection of a sample for a light pulse of

frequency ω, $T(\omega)$ and $R(\omega)$, are determined by its geometry and dielectric function $\varepsilon(\omega)$. Their time-dependent changes after excitation by a short pulse of frequency ω_0 thus reflects that of ε. If the optical property changes are sufficiently weak, the relative transmission and reflection changes can be connected to those of the real, $\Delta\varepsilon_1$, and imaginary, $\Delta\varepsilon_2$, parts of $\Delta\varepsilon$, using a lowest order development:

$$\begin{aligned}\frac{\Delta T}{T}(\omega,t) &= t_1(\omega)\Delta\varepsilon_1(\omega,t) + t_2(\omega)\Delta\varepsilon_2(\omega,t)\\ \frac{\Delta R}{R}(\omega,t) &= r_1(\omega)\Delta\varepsilon_1(\omega,t) + r_2(\omega)\Delta\varepsilon_2(\omega,t)\end{aligned} \tag{5.36}$$

where $\Delta T(\omega,t) = T(\omega,t) - T(\omega)$ and $\Delta R(\omega,t) = R(\omega,t) - R(\omega)$, t being the time delay after the maximum of the excitation pulse. The coefficients $t_{1,2}(\omega) = \left(\partial \ln T/\partial\varepsilon_{1,2}\right)_\omega$ and $r_{1,2}(\omega) = \left(\partial \ln R/\partial\varepsilon_{1,2}\right)_\omega$ can be analytically or numerically computed from the dependence of $T(\omega)$ and $R(\omega)$ on the sample dielectric function. These general expressions will be used below for discussing the nonlinear response of different metal materials.

In the following, weak metal excitation will be assumed ($\Delta T_e^{me} = 100\,\mathrm{K}$), and only the dominant contributions to $\Delta\varepsilon$ due to modification of the interband term by electron heating (Sect. 4.1.1) and of the intraband one by lattice heating (Eq. 5.34) will be included. In particular, dilation effect will be disregarded, their inclusion also requiring to take into account the direct dependences of T or R on the metal object size, e.g., film thickness or nanoparticle volume (Eq. 5.44 or 5.46, for instance).

5.5.1 Metal Film

In the case of a homogeneous metal film deposited on a substrate, the coefficient linking $\Delta T/T$ and $\Delta R/R$ to $\Delta\varepsilon$ can be analytically computed using the expression $T(\varepsilon)$ and $R(\varepsilon)$ for a thin film of thickness L [127], ε being the metal dielectric function, assumed to be identical to the bulk one [83]. The dispersion of T, R, $t_{1,2}$, and $r_{1,2}$ are shown in Figs. 5.7a and b, in the case of an optically thin gold film ($L = 20\,\mathrm{nm}$). The temporal and spectral dependences of $\Delta T(\omega,t)$ and $\Delta R(\omega,t)$ calculated from the computed $\Delta\varepsilon$ (Fig. 5.5a, b and f) are also shown. They exhibit similar amplitudes with extrema for frequencies ω close to the interband threshold ω_{ib}, around the L point of the Brillouin zone (the X point yields smaller structures as for $\Delta\varepsilon^{ib}$, Fig. 5.5a and b). The spectral shapes are mostly set by the $\Delta\varepsilon^{ib}$ spectra modified by $t_{1,2}$ or $r_{1,2,}$ the $\Delta\varepsilon^{in}$ contribution being weaker.

The computed spectral profiles have been found to be in excellent agreement with the measured ones in optically thin films when the electronic response dominates [26, 29, 30, 61, 65]. Note that simultaneous measurement of $\Delta T(\omega,t)$ and $\Delta R(\omega,t)$ also permits experimental estimation of $\Delta\varepsilon_1^{bulk}(\omega,t)$ and $\Delta\varepsilon_2^{bulk}(\omega,t)$ using Eq. 5.36 [26]. Though this agreement validates the above theoretical modeling, one has to keep in mind that quantitative comparison, i.e., of the $\Delta T/T$ and $\Delta R/R$ amplitudes, is however limited by the experimental difficulty in estimating the temperature rise of the metal film.

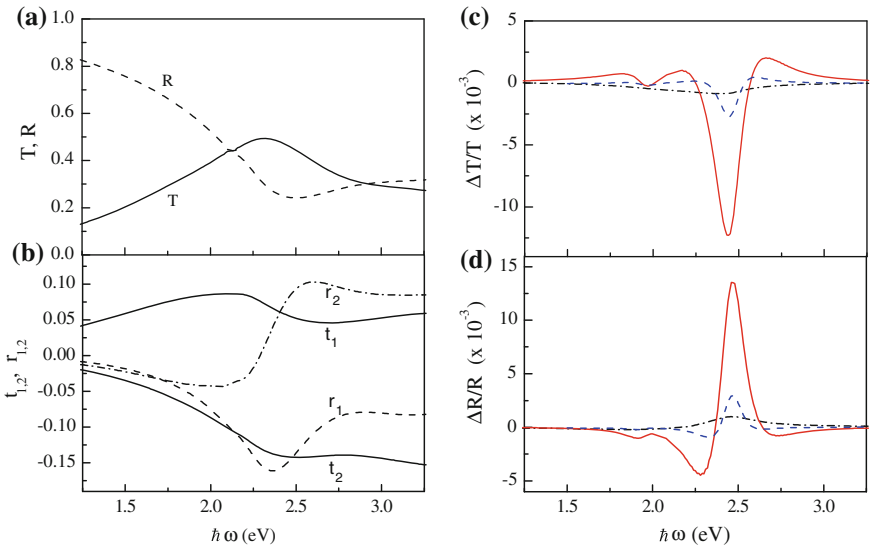

Fig. 5.7 **a** and **b**; Transmission T and reflection R of a 20 nm thick gold film deposited on silica, and corresponding coefficient linking ΔT and ΔR to $\Delta\varepsilon_{1,2}$ (Eq. 5.36). **c** and **d**; Computed relative change of transmission and reflection of the same film for t = 0 fs (*dash-dotted line*), 500 fs (*full line*)and 3 ps (*dashed line*) after excitation with a 25 fs pulse with $\eta\,\omega_e = 1.5$ eV and $\Delta T_e^{me} = 100$ K. The results are obtained using Eq. 5.36 and the $\Delta\varepsilon$ values shown in Fig. 5.5, considering only the electron induced interband contribution (Fig. 5.5a and b) and increase of the electron-phonon scattering (Fig. 5.5f)

Though consistent results have also been obtained on longer time-scales, for thermalized electron-lattice films, different results have been obtained in different films, stressing the important role played by the film structure and the film-substrate interaction in this regime. These variations are probably of similar origins as those observed in measurement of the dielectric function of thin metal films [83].

For optically thick films, only $\Delta R(\omega, t)$ can be measured and excitation cannot be assumed homogeneous anymore. Fast electronic energy transfer in the metal has to be included, lowering the actual sample excitation, i.e., signal amplitude, and modifying the short time scale kinetics as demonstrated comparing the responses in 20 nm and 1μm thick gold films [29, 113].

5.5.2 Single Plasmonic Nanoparticle

Interaction of a single nanoparticle with a light pulse leads to absorption and scattering of the incident optical power. These effects are described by the absorption and scattering cross-section $\sigma^i_{abs}(\omega)$ and $\sigma^i_{sca}(\omega)$ of the nanoparticle for light polarized along one of its main axis i. For light polarized along i with power P^i incident on a

particle of size much smaller than the beam diameter, the transmitted power P_t^i is, using the optical theorem [1]:

$$P_t^i = P^i - \sigma_{ext}^i I^i(x, y) + \delta P_{sca}^i. \tag{5.37}$$

where $I^i(x, y)$ is the beam intensity at the particle position (x, y) (z being the propagation direction). $\sigma_{ext}^i(\omega) = \sigma_{abs}^i(\omega) + \sigma_{sca}^i(\omega)$ is the nanoparticle extinction cross section and δP_{sca}^i the power scattered in the forward direction in the solid angle collected by the optical detector. Reflection or possible absorption by the substrate has been neglected. For a weak scattering and a small collecting solid angle, the last term can be neglected, P_t^i being then only set by the particle extinction. Assuming a Gaussian intensity profile $I^i(x, y)$ with a full width half maximum d, at the position of the nanoparticle, one can define the power transmission for a particle at the center of the beam:

$$T^i(\omega) = 1 - \frac{4Ln(2)}{\pi d^2}\sigma_{ext}^i(\omega). \tag{5.38}$$

The relative change of transmission can thus be connected to $\Delta\varepsilon$ using either the general expression (Eq. 5.36) or the above expression (Eq. 5.38), yielding:

$$\frac{\Delta T^i}{T^i}(\omega, t) = \frac{-4Ln(2)}{\pi d^2}\Delta\sigma_{ext}^i(\omega, t), \tag{5.39}$$

and:

$$\Delta\sigma_{ext}^i(\omega, t) = a_1^i(\omega)\Delta\varepsilon_1(\omega, t) + a_2^i(\omega)\Delta\varepsilon_2(\omega, t) \tag{5.40}$$

where the coefficients $a_{1,2}^i(\omega) = \partial\sigma_{ext}^i/\partial\varepsilon_{1,2}\big|_\omega$ are determined by the linear optical extinction of the nanoparticle for the incident beam polarization. Knowing the beam size d and the dielectric function change $\Delta\varepsilon$ of the metal forming the nanoparticle, nonlinear modification of its optical extinction σ_{ext} or transmission T^i can thus be fully computed and compared to experimental data [38]. Note that the substrate and environment nonlinearities are neglected.

Similarly the induced change of the scattering cross-section leads to a relative change of the scattering power P_s. For instance assuming the same incident and scattered light polarization, and light collection along the $\hat{s}$ direction:

$$\frac{\Delta P_s^i}{P_s^i}(\omega, t) = \frac{\Delta\sigma_{sca}^i(\hat{s}, \omega, t)}{\sigma_{sca}^i(\hat{s}, \omega)}. \tag{5.41}$$

This can be observed experimentally monitoring change of light scattering by a single nanoparticle [43].

The above approach can be generalized to individual nanoparticle of any shape or size, and formed by a single material or different ones, using the connection between its extinction or scattering cross-section with the dielectric function of the constituting materials. The simple cases of a small nanosphere and nanoellispoid

whose optical response can be computed analytically, as well as that of a nanorod, are illustrated below.

5.5.2.1 Small Metal Nanosphere and Nanoellipsoid

The optical response, absorption or scattering, of a sphere of dielectric constant ε and diameter D embedded in a dielectric medium of dielectric constant ε_d has been described by Mie using a multipolar expansion [1, 3]. For a nano-sphere much smaller than the optical wavelength λ only the dipolar term has to be retained [1, 128]. The sphere response can then be described as that of a dipole $\boldsymbol{p}_L$ at its center and oriented along the electric field $\boldsymbol{E}$ of the incident electromagnetic wave:

$$p_L(\omega) = \varepsilon_0 \varepsilon_d \alpha_L(\omega) E(\omega). \tag{5.42}$$

where α_L is the nanosphere linear polarizability:

$$\alpha_L(\omega) = 3V_{np} \frac{\varepsilon(\omega) - \varepsilon_d}{\varepsilon(\omega) + 2\varepsilon_d} \tag{5.43}$$

Its extinction cross-section can be identified with its absorption cross-section in this regime, scattering being negligible as compared to absorption in the dipolar approximation, $\sigma_{ext} \approx \sigma_{abs}. >> \sigma_{sca}$. It is given by the imaginary part of α_L and is independent of the polarization direction:

$$\sigma_{ext}(\omega) \approx \sigma_{abs}(\omega) = \omega\, \varepsilon_d^{1/2} Im(\alpha_L)/c = \frac{9\,\omega\, V_{np} \varepsilon_d^{3/2}}{c} \frac{\varepsilon_2(\omega)}{|\varepsilon(\omega) + 2\varepsilon_d|^2}, \tag{5.44}$$

where V_{np} is the nanoparticle volume. Similar calculations were performed for ellipsoidal shapes, yielding similar simple expression in the small size limit [1]. For light polarized along one of the ellipsoid main axis i the optical response is equivalent to that of a i direction dipole $p_L^i(\omega) = \varepsilon_0 \varepsilon_d \alpha_L^i(\omega) E^i(\omega)$ at the ellipsoid center with:

$$\alpha_L^i(\omega) = \frac{\mathrm{V}_{np}}{L_i} \frac{\varepsilon(\omega) - \varepsilon_d}{\varepsilon(\omega) + (1/L_i - 1)\varepsilon_d}, \tag{5.45}$$

yielding the extinction cross section for light polarized along the i direction

$$\sigma_{ext}^i(\omega) \approx \sigma_{abs}^i(\omega) = \omega\, \varepsilon_d^{1/2} Im(\alpha_L^i)/c = \frac{\omega\, V_{np} \varepsilon_d^{3/2}}{c L_i^2} \frac{\varepsilon_2(\omega)}{|\varepsilon(\omega) + (1/L_i - 1)\varepsilon_d|^2}, \tag{5.46}$$

where L_i are geometrical factors. For instance, for a prolate spheroid of length l_x along its long axis direction x, and $l_y = l_z$, along its short axis directions y,z, they are given by:

$$L_x = \frac{1-e^2}{e^2}\left(-1+\frac{1}{2e}\ln\left(\frac{1+e}{1-e}\right)\right), \tag{5.47}$$

where e is the ellipsoid eccentricity: $e^2 = 1-(l_y/l_x)^2$, and $L_y = L_z = (1-L_x)/2$.

The extinction cross-sections take similar forms in both types of nanoparticles, (with $L_i = 1/3$ for a sphere). For a weakly dispersed ε_2, it is enhanced close to the frequency minimizing the denominator in Eq. 5.44 or 5.46, which corresponds to the condition for the localized surface plasmon resonance (SPR). This is concomitant with enhancement of the electromagnetic field in the particle and its close environment as compared to the applied one, i.e., corresponds to a local field or dielectric confinement effect [5]. For a sphere, the field is uniform in the particle and enhanced as compared to the applied field by the plasmonic factor:

$$f_{pl}(\omega) = \frac{3\varepsilon_d}{\varepsilon(\omega)+2\varepsilon_d}. \tag{5.48}$$

For a nanosphere, the resonance condition is independent of the light polarization direction (Eq. 5.44) and is associated to resonant collective oscillation of the electrons driven by the electromagnetic field along its polarization direction. This degeneracy is lifted in an ellipsoid, three different resonance conditions being obtained along its three main axis (Eq. 5.46). It reduced to two in a spheroid, two SPR showing-up associated to electron oscillations along its long and short axis. The SPR frequency splitting depending of its aspect ratio $\eta = l_x/l_y$ [1, 5, 128].

The extinction cross-sections of a gold nano-sphere and of a gold prolate spheroid of long axis x and short axis y, z are shown in Figs. 5.8a and 5.9a and d, respectively (the bulk ε data [83] were corrected for surface effect in the sphere case using $g_{eff} = 0.7$, Eq. 5.8). The SPR of the sphere overlap the interband transition (Fig. 5.8a), while the longitudinal SPR (along its x axis) of the spheroid is strongly red shifted away from ω_{ib}, (Fig. 5.9a). Its transverse one (along its y or z axis) is slightly blue shifted (as compared to the sphere SPR) and overlaps with the interband transitions (Fig. 5.9d). The corresponding coefficients $a^i_{1,2}(\omega)$ computed using Eqs. 5.40, 5.44 and 5.46 are shown in Figs. 5.8b and 5.9b and e. The plasmonic effect is at the origin of their large amplitude and dispersion around the longitudinal SPR frequency ω^x_R. As for the linear response, it reflect local field effect enhancement. Similar effects show-up around the transverse SPR, but with weaker amplitude as expected because of smaller amplitude of this SPR.

Using these coefficients together with the computed changes of ε (Fig. 5.5a, b, and f), one obtains the amplitude and time and spectral dependence of the extinction cross-section change $\Delta\sigma^i_{ext}(\omega)$ for a given excitation ΔT^{me}_e (Figs. 5.8c, and 5.9c and f). Modification of the surface scattering term has been disregarded for the considered sizes [60]. For the gold nanosphere, the SPR being around ω_{ib}, the plasmonic effect only leads to modification of the spectral shape and enhancement of the amplitude of the nonlinear response as compared to the film one around ω_{ib} (Figs. 5.7 and 5.8).

These two effects are separated in a prolate spheroid for light polarized along its long axis. Two distinct spectral features around ω_{ib} and $\omega^x_R$are thus obtained.

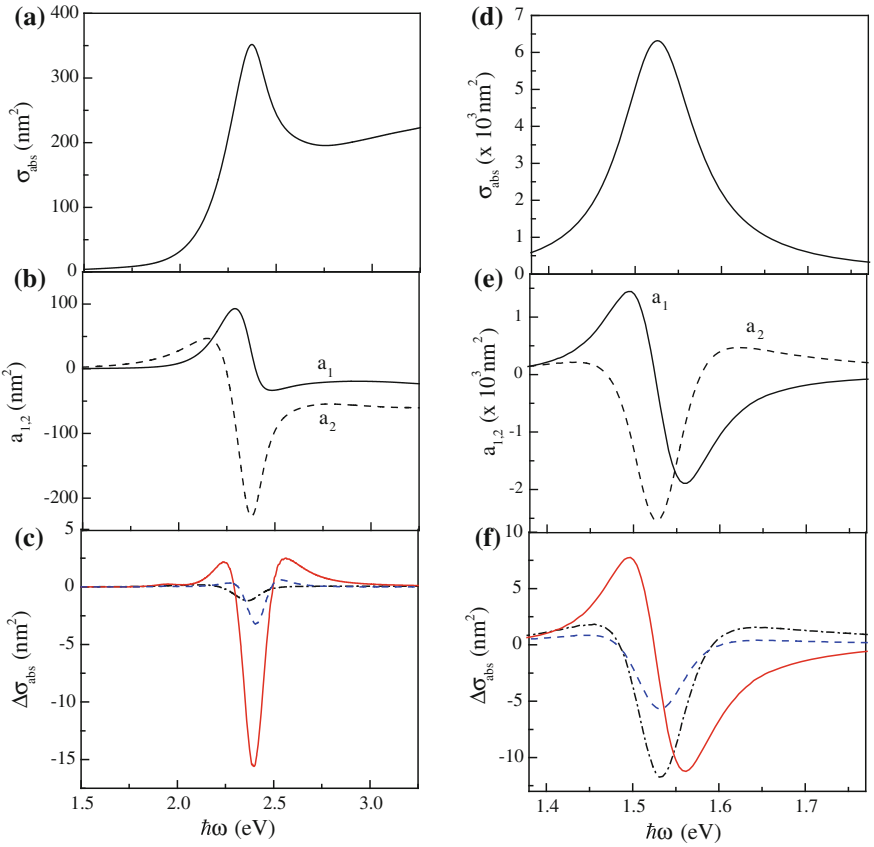

Fig. 5.8 Computed spectra of the absorption cross-section of a 20 nm diameter gold sphere in water around its SPR at 2.37 eV (**a**), and of a 43 nm long and 12 nm diameter gold nanorod only around its longitudinal SPR at about 1.52 eV (**d**)—note the different photon energy scales. The corresponding coefficient linking $\Delta\sigma_{ext}$ to $\Delta\varepsilon_{1,2}$ (Eq. 5.40) are shown in (**b**) and (**e**). They are computed using Eq. 5.44 for the sphere and numerically for the nanorod [38]. The computed absolute changes of the extinction cross-section are shown in (**c**) and (**f**) for the two individual particles for $t = 0$ fs (*dash-dotted line*), 500 fs (*full line*) and 3 ps (*dashed line*) after excitation with a 25 fs pulse with $\hbar\omega_e = 1.5$ eV and $\Delta T_e^{me} = 100$ K. The results are obtained using Eq. 5.40 and the $\Delta\varepsilon$ values shown in Fig. 5.5, considering only the electron induced interband contribution (Fig. 5.5a and b) and increase of the electron-phonon scattering (Fig. 5.5f)

The former is similar to that in bulk gold and reflects modification of the electron distribution around the Fermi energy (Fig. 5.5a and b). In this spectral region, a_1^x and a_2^x are small and almost undispersed and the $\Delta\sigma_{ext}^x$ spectral shape reflects the dispersion of $\Delta\varepsilon_{1,2}$. As the latter, it rises with internal electron thermalization and decay with electron cooling (Fig. 5.4) [37]. In contrast, the structure around ω_R^x is specific to plasmonic systems. It is much larger than the one around ω_{ib} as a consequence of plasmonic enhancement of the nonlinear optical response around the

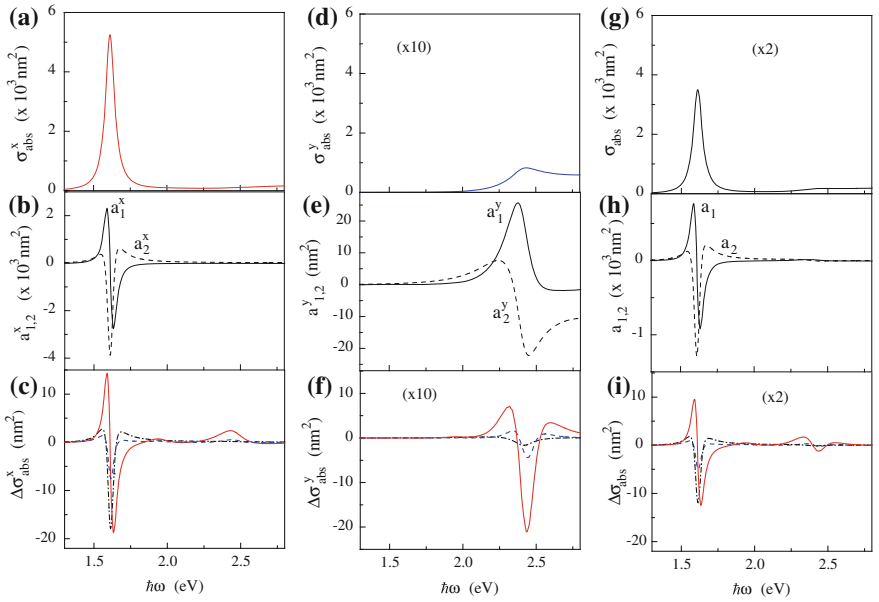

Fig. 5.9 Computed spectra of the absorption cross-section of a gold prolate spheroid with long and short axis lengths: $l_x = 40\,\text{nm}$ and $l_y = l_z = 10\,\text{nm}$ in water, for light polarized along its long axis (**a**) and short axis (**d**). The longitudinal SPR (along the long x axis) shows at about 1.6 eV and the transverse one (along the short y or z axis) at about 2.43 eV, overlapping with the interband transitions. The corresponding coefficient linking $\Delta\sigma^{x,y}_{ext}$ to $\Delta\varepsilon_{1,2}$ (Eq. 5.40) computed using Eq. 5.45 are shown in (**b**) and (**e**). The computed absolute changes of the extinction cross-section for the two light polarizations are shown in (**c**) and (**f**) for $t = 0\,\text{fs}$ (*dash-dotted line*), 500 fs (*full line*) and 3 ps (*dashed line*) after excitation with a 25 fs pulse with $\hbar\omega_e = 1.5\,\text{eV}$ and $\Delta T^{me}_e = 100\,\text{K}$. The results are obtained using Eq. 5.40 and the $\Delta\varepsilon$ values shown in Fig. 5.5, considering only the electron induced interband contribution (Fig. 5.5a and b) and increase of the electron-phonon scattering (Fig. 5.5f). The same results for an ensemble of randomly oriented identical nanoellipsoids are shown in (**g**)–(**h**)–(**i**). Identical excitation of the particles has been assumed for computing their nonlinear response (Eqs. 5.63 and 5.64). The different mean values are normalized to the number density of nanoellipsoids, i.e., correspond to a mean particle (Eqs. 5.56 and 5.63)

SPR [76, 129, 130]. Actually, ω^x_R being much smaller than ω_{ib}, $\Delta\varepsilon^{ib}_2(\omega \approx \omega^x_R, t)$ is nonzero only for very short times t and (for strongly out of equilibrium electrons, typically for $t \leq 50\,\text{fs}$, Fig. 5.5b). For the short excitation pulse assumed here (25 fs), it however give a significant contribution for very short times, leading to different spectral shapes for $t = 0\,\text{fs}$ and $t = 500\,\text{fs}$ (Fig. 5.9b, this effect almost washing out when longer pulses are assumed [38])). For longer delays, only $\Delta\varepsilon^{ib}_1$ is nonzero around ω^x_R and the $\Delta\sigma^x_{ext}$ spectral shape reflects that of a^x_1 ($\Delta\varepsilon^{ib}_1$ being almost undispersed away from ω_{ib}, Fig. 5.5a). Its time behavior essentially follows that of $\Delta\varepsilon^{ib}_1(\omega^x_R, t)$ which is almost identical to the time evolution of the electron gas excess energy (Fig. 5.4) [131, 37]. Consequently, in this spectral range $\Delta\sigma^x_{ext}$ rises

with energy injection in the electrons and decays with the electron energy losses to the lattice. On a longer time scale, after electron-lattice thermalization, the spectral profile of $\Delta\sigma_{ext}^{x}$ is strongly modified. The $\Delta\varepsilon_1^{ib}(\omega_R^x, t)$ contribution is then negligible as compared to the $\Delta\varepsilon_2^{in}(\omega_R^x, t)$ one due to heating of the lattice (Fig. 5.5f). $\Delta\sigma_{ext}^{x}$ then essentially reflects modification of the electron-phonon scattering rate (Eq. 5.34). Its spectral shape is set by the dispersion of a_2^x (Fig. 5.9b and c), $\Delta\varepsilon_2^{in}(\omega_R^x)$ being weekly dispersed on the relevant spectral range around ω_R^x (Fig. 5.5f).

For light polarized along the short direction of a prolate spheroid, the transverse SPR and interband transitions overlap leading to a small SPR amplitude (Fig. 5.9d). The situation is very similar to the gold sphere one, and $\Delta\sigma_{ext}^{y,z}$ around the transverse SPR frequency $\omega_R^{y,z}$ shows similar spectral and temporal features as $\Delta\sigma_{ext}^{x}$ in gold nanosphere (Figs. 5.9f and 5.8c).

It is interesting to note that the characteristic spectral shape of $\Delta\sigma_{ext}^{x}$ imposed by the a_1^x and a_2^x dispersion closely corresponds to that obtained for a SPR spectral shift and broadening, respectively (assuming $\Delta\varepsilon$ undispersed). This is simply related to the fact that the longitudinal SPR exhibits a quasi-Lorentzian shape with a frequency determined by $\varepsilon_1(\omega_R^x)$ and a width by $\varepsilon_2(\omega_R^x)$. The full approach used here, can then be reduced to a simple analysis in term of SPR frequency shift (for $t \approx 500$ fs) and broadening (for $t \geq 500$ fs), related to $\Delta\varepsilon_1(\omega_R^x, t)$ and $\Delta\varepsilon_2(\omega_R^x, t)$, respectively. This approach can be used as long as the SPR is away from the interband transitions, as for the longitudinal SPR of a prolate spheroid or nanorod or for the SPR of silver nanospheres [37, 60, 132]. In contrast, it cannot be used when the SPR overlap the interband transition as in gold or copper nanospheres or for the transverse SPR of a prolate spheroid, $\Delta\varepsilon_{1,2}^{ib}$ showing a large dispersion on the relevant frequency range around their SPR (Fig. 5.5, note that similarly because of the dispersion of ε^{ib}, Fig. 5.1a, the SPR width can also not be correctly defined). The $\Delta\sigma_{ext}$ spectral profile is then related to both $\Delta\varepsilon_1$ and $\Delta\varepsilon_2$ with contributions weighted by the enhancement of the nonlinear response around the SPR (Figs. 5.8c and 5.9f).

The above simulations have been performed assuming a given excitation of the nanoparticles, imposing the maximum electron temperature rise ΔT_e^{me} or, equivalently, the injected total energy u_e^{abs} (Eq. 5.19). More generally, ΔT_e^{me} or u_e^{abs} are imposed by absorption of the exciting pulse of frequency ω_e. Assuming it is polarized along the j direction with a time-dependent intensity $I_p^j(t)$, it is given by:

$$u_e^{abs} = \frac{\sigma_{abs}^{j}(\omega_e)}{V_{np}} \int_{-\infty}^{+\infty} I_p^j(t)dt = \frac{\sigma_{abs}^{j}(\omega_e)}{V_{np}} F_p^j(\omega_e), \tag{5.49}$$

where $F_p^j(\omega_e)$ is the pulse fluence. Assuming $\Delta\varepsilon$ linearly depends on u_e^{abs}, an approximation verified in the weak excitation regime, $\Delta T_e^{me} \leq 200-300$ K, $\Delta\sigma_{ext}^{i}(\omega)$ can thus be written:

$$\Delta\sigma_{ext}^{i}(\omega, t) = \left[a_1^i(\omega)\Delta\bar{\varepsilon}_1(\omega, t) + a_2^i(\omega)\Delta\bar{\varepsilon}_2(\omega, t)\right]\sigma_{abs}^{j}(\omega_e)F_p^j(\omega_e)/V_{np}. \tag{5.50}$$

where $\Delta\bar{\varepsilon}_{1,2} = \Delta\varepsilon_{1,2}/u_e^{abs}$. This expression yields the amplitude, spectral, and temporal dependence of the extinction cross section of a metal nanoparticle, i.e., its nonlinear response, in the presence of an excitation pulse of frequency ω_e.

For a small particle the nonlinearity can also be described in term of change of its dipolar response, introducing modification of its polarizability α_L due to that of the metal dielectric function. Retaining only the lowest order nonlinear term, one can write:

$$p^i = p_L^i + p_{NL}^i = \varepsilon_0 \varepsilon_d (\alpha_L^i + \alpha_{NL}^i) E^i, \tag{5.51}$$

with:

$$\alpha_{NL}^i(\omega, t) = \left.\frac{\partial \alpha_L^i}{\partial \varepsilon_1}\right|_\omega \Delta\bar{\varepsilon}(\omega, t) \sigma_{abs}^j(\omega_e) F_p^j(\omega_e)/V_{np}, \tag{5.52}$$

which yields the same expression as Eq. 5.50 using $\Delta\sigma_{abs}^i(\omega) = \omega\, \varepsilon_d^{1/2} Im(\alpha_{NL}^i)/c$. Using Eq. 5.51 one can define a time-dependent third-order hyperpolarizability characterizing the optical nonlinearity of a single nanoparticle (note that hyperpolarizability is correctly defined only in the frequency domain [133]). Plasmonic effects on the nonlinear response shows-up in the amplitude and spectral dependence of $\partial\alpha_L^i/\partial\varepsilon_1$ and σ_{abs}^j. In the case of a sphere, the former term is enhanced proportionally to the square of the local field enhancement factor at ω, $f_{pl}^2(\omega)$, and the latter to its modulus square at ω_e, $\left|f_{pl}(\omega_e)\right|^2$ (where f_{pl} is given by Eq. 5.48). This yields the usual dependence on the field enhancement factor $f_{pl}^2(\omega)\left|f_{pl}(\omega_e)\right|^2$ of the nonlinear response for a Kerr-type of nonlinear interaction $\omega = \omega + \omega_e - \omega_e$ [5, 130, 133].

5.5.2.2 Other Shapes and Sizes

Conversely to the case of small nanospheres and nanoellipsoids, simple expressions of the nanoparticle extinction or scattering cross-section are not available for other shapes or for large nanoparticles. Calculation of the nonlinear response then requires numerical computation of the coefficients linking their changes to that of $\Delta\varepsilon$, e.g., of a_1^i and a_2^i (Eqs. 5.40 and 5.50). This is done using:

$$a_1^i = \left[\left(\sigma_{ext}^i(\varepsilon + \delta) - \sigma_{ext}^i(\varepsilon)\right)/\delta\right]_{\delta\to 0}; \quad a_2^i = \left[\left(\sigma_{ext}^i(\varepsilon + i\delta) - \sigma_{ext}^i(\varepsilon)\right)/\delta\right]_{\delta\to 0}. \tag{5.53}$$

In the case of large nanospheres or nanoellipsoids, $\Delta\sigma_{ext}^i$ is computed using higher order expansion of the Mie theory [1] or of its generalization to ellipsoid [134]. For other shapes it is calculated with the fully numerical models, as Discrete Dipole Approximation (DDA) or Finite Element Method, used for computing their linear properties [38, 135]. It is illustrated in Fig. 5.8d and e using FEM in the case of a gold nanorod modeled by a cylinder end-capped by hemispheres [38]. As before, $\Delta\sigma_{ext}^i$ can then be computed from $\Delta\varepsilon$, as shown in Fig. 5.8f along its long axis x. It exhibits

similar features as that for a spheroid Fig. 5.9c, showing in particular the same time-dependent spectral features due to change with time of the dominant nonlinearity around its longitudinal SPR.

The spectral shape, temporal behavior, and amplitude of the nonlinearity are in excellent agreement with measurements performed in individual gold nanorod using time-resolved spectroscopy [38]. In these experiments, the investigated nanorod extinction cross-section and orientation on a substrate is first quantitatively determined monitoring the loss of energy of a tightly focused light beam while modulating the nanoparticle position (Spatial Modulation Spectroscopy, SMS) [131, 136]. The amount of energy absorbed by the particle, or equivalently the peak electron temperature rise ΔT_e^{me}, can thus be precisely determined, permitting quantitative comparison of the experimental and theoretical results using Eq. 5.50 [38].

5.5.3 Plasmonic Material: Ensemble of Metal Nanoparticles

Many plasmonic materials are formed by metal nanoparticles dispersed in a solid or liquid dielectric matrix. Assuming homogeneous properties over a size smaller than the optical wavelength, the linear optical response of the composite material can be described defining an effective linear dielectric function $\tilde{\varepsilon}_L(\omega)$ taking into account the polarizability of the nanoparticles and host material. The main difficulty is to properly define this connection, i.e., to link $\tilde{\varepsilon}_L$ to ε, ε_d, V_{np} and to the density of nanoparticle N_{np}. This can be easily done if N_{np} is sufficiently small to neglect particle interactions. For small nanoparticles whose individual response can be described in the dipolar approximation, the total polarisation $\mathbf{P}$ of the composite medium is the sum of the polarisation $\mathbf{P}_{np}$ due to the metallic particles and the polarisation $\mathbf{P}_d$ due to the dielectric matrix:

$$P = P_d + P_{np} = (1 - F_{np})\varepsilon_0(\varepsilon_d - 1)E + \frac{1}{V}\sum_j p_j. \tag{5.54}$$

where $\mathbf{p}_j$ is the dipole moment of the j particle and summation run over the nanoparticles in a unit volume. $F_{np} = \frac{1}{V}\sum_j V_{np,j}$ is the volume fraction occupied by the nanoparticles. If the particles are identical and randomly oriented in the matrix, the above expression simplifies into:

$$P = (1 - N_{np}V_{np})\varepsilon_0(\varepsilon_d - 1)E + N_{np}\varepsilon_0\varepsilon_d\bar{\alpha}_L\, E. \tag{5.55}$$

$\bar{\alpha}$ is the orientationally averaged polarizability of the particles:

$$\bar{\alpha}_L = \frac{1}{3}\sum_i \alpha_L^i, \tag{5.56}$$

where α_L^i is the linear polarizability of one particle along its main axis i (Eq. 5.51). The effective dielectric constant $\tilde{\varepsilon}$ is then obtained using $\tilde{\varepsilon}_L \varepsilon_0 E = \varepsilon_0 E + P$ yielding for small metal volume fraction [5]:

$$\tilde{\varepsilon}_L(\omega) = \varepsilon_d \left[1 + N_{np} \bar{\alpha}_L(\omega)\right]. \tag{5.57}$$

The nonlinear response can be calculated using the same approach introducing the nonlinear component of the polarizability α_{NL} of each particle (Eqs. 5.51 and 5.52). Taking into account the lowest order nonlinearity, one can define a time dependent effective dielectric constant $\tilde{\varepsilon}$ [38]:

$$\tilde{\varepsilon}(\omega, t) = \tilde{\varepsilon}_L(\omega) + \tilde{\varepsilon}_{NL}(\omega, t), \tag{5.58}$$

in the same approximation as for Eq. 5.57. Neglecting the third order nonlinear response of the matrix and depletion of the excitation pulse during its propagation in the material, averaging α_{NL} over the particle orientation yields:

$$\tilde{\varepsilon}_{NL}(\omega, t) = \frac{\varepsilon_d N_{np}}{15} \sum_i \left. \frac{\partial \alpha_L^i}{\partial \varepsilon_1} \right|_\omega \Delta\bar{\varepsilon}(\omega, t) \left[3\bar{\sigma}_{abs}(\omega_e) + 2\sigma_{abs}^i(\omega_e)\right] F_p(\omega_e)/V_{np}, \tag{5.59}$$

for identical polarization of the exciting pulse and ω pulse, and

$$\tilde{\varepsilon}_{NL}(\omega, t) = \frac{\varepsilon_d N_{np}}{15} \sum_i \left. \frac{\partial \alpha_L^i}{\partial \varepsilon_1} \right|_\omega \Delta\bar{\varepsilon}(\omega, t) \left[6\bar{\sigma}_{abs}(\omega_e) - \sigma_{abs}^i(\omega_e)\right] F_p(\omega_e)/V_{np}, \tag{5.60}$$

for perpendicular polarizations. $\bar{\sigma}_{abs} = \omega \varepsilon_d^{1/2} Im(\bar{\alpha}_L)/c$ is the mean absorption of one particle. The above expressions permit to describe the nonlinearity of the composite material introducing time-dependent modification of its dielectric function. Note that it is defined in the time domain which does not permit proper definition of a third-order susceptibility (defined in the frequency domain as the hyper-polarizability of a single nanoparticle [133]).

The change of transmission or reflection of a sample can then be simply computed using Eq. 5.36, replacing $\Delta\varepsilon$ by $\tilde{\varepsilon}_{NL}$. The $t_{1,2}$ and $r_{1,2}$ coefficients are computed using the expression $T(\tilde{\varepsilon}_L)$ and $R(\tilde{\varepsilon}_L)$ for a thin film of thickness L and dielectric constant $\tilde{\varepsilon}_L$ [127]. For a diluted material $\Delta T/T$ essentially reflects modification of the imaginary part of $\tilde{\varepsilon}$, or, equivalently, that of the sample absorption [37].

For polarization independent absorption of the excitation pulse (case of nanospheres or interband excitation of nanoellipsoids or nanorods, for instance [38]), Eqs. 5.59 and 5.60 are identical. This reflects the fact that all the particles are identically excited and one can then simply write:

$$\tilde{\varepsilon}_L(\omega, t_d) = \varepsilon_d \left[1 + N_{np} \bar{\alpha}_L(\omega) + N_{np} \bar{\alpha}_{NL}(\omega, t_d)\right], \tag{5.61}$$

with

$$\bar{\alpha}_{NL} = \frac{1}{3}\sum_i \alpha^i_{NL}. \tag{5.62}$$

The transmission change of a sample of thickness L is then given by:

$$\frac{\Delta T}{T}(\omega, t) \approx -\,\omega\, \varepsilon_m^{1/2} N_{np} Im\left\{\bar{\alpha}_{NL}(\omega, t)\right\} L/c = -N_{np}\Delta\bar{\sigma}_{abs}(\omega, t)L, \tag{5.63}$$

where $\Delta\bar{\sigma}_{abs}$ is the mean absorption change per particle. It can be rewritten:

$$\frac{\Delta T}{T}(\omega, t_d) \approx a_1(\omega)\Delta\varepsilon_1(\omega, t) + a_2(\omega)\Delta\varepsilon_2(\omega, t), \tag{5.64}$$

where the coefficients a_1 and a_2 are directly related to the equilibrium absorption coefficient of the sample: $A(\omega) = N_{abs}\bar{\sigma}_{abs}(\omega)$:

$$a_{1,2} = -\frac{\partial A}{\partial \varepsilon_i}(\omega)L, \tag{5.65}$$

and are entirely determined by the linear absorption properties.

Knowing the dielectric function change of a metal, the transmission change can thus be computed for different composite nanomaterials made of nanoparticles of different shapes dispersed in different environment using the relevant a_1 and a_2 coefficients (at least for not too small objects so that the bulk electron kinetics can be used). It is illustrated in Fig. 5.8f, in the case of an ensemble of randomly oriented identical gold ellipsoids (prolate spheroids with long and short axis 40 nm and 10 nm, respectively) dispersed in water. The same excitation temperature has been assumed in each particle with $\Delta T_e^{me} = 100\,\mathrm{K}$. The computed features are similar to those observed in single nanoellipsoids, the main difference lying in the absence of light polarization effect.

This approach permits comparison of the experimental and theoretical data obtained in ensemble of metal nanoparticles. In particular it has been extensively used in the case of nanospheres for which excellent agreement between the measured and computed spectral shapes have been obtained both for low and high excitation of the electrons [37, 52, 60, 137]. Note that in very diluted samples, the nonlinear response of the matrix can also contribute, yielding additional non-resonant contribution to the observed nonlinearity. Comparison of the amplitude of the signals are however more difficult as it requires taking into account the size and shape dispersions of the particles and to determine their absorbed energy. Though this can be done summing up the nonlinear contribution of the different particles, taking into account their possibly different absorption, the precision is limited by the knowledge of these dispersions. This problem is overcome performing experiments in single nanoparticle, whose morphology and size can be either optically characterized [136] or independently measured by electron microscopy [138, 139].

5.6 Conclusion

The third order nonlinear optical response of metals and plasmonic nanomaterials has been described focusing on the resonant incoherent mechanisms associated to energy absorption. Because of ultrafast dephasing of coherent electron-light polarization and of the presence of electronic absorption over a very broad spectral range, these mechanisms usually dominate the Kerr-type nonlinearity of metals. They are directly connected to electronic and vibrational excitation and relaxation of the material and are thus more conveniently modeled in the time-domain, describing the time-dependent changes of the metal dielectric function due to electron excitation and lattice heating. This time dependence reflects electron excitation and energy redistribution processes within the metal (i.e., between the electrons and between the electrons and the lattice) and to its environment (metal cooling). These processes can be reliably modeled in noble metals, of key interest for plasmonic applications, using an approach developed for bulk metals. After computing modifications of the metal dielectric function, the observable nonlinear optical response is obtained connecting the material linear optical responses to the constituting metal dielectric function and analyzing impact of its modification.

This modeling of the ultrafast nonlinear response has been successfully applied to nanoparticles and nanomaterials. For not too small particles, down to about 10 nm, the time and spectrally dependent nonlinear response can be fairly well reproduced using the computed nonlinearity of bulk metals and taking into account the plasmonic effects. Excellent agreement has also been found for individual metal nanoparticles, for which both the spectral shape and amplitude of the nonlinear response have been reproduced. As for their linear absorption, the fundamental mechanisms at the origin of the optical nonlinearity are identical in bulk and confined metals, the main differences lying in enhancement effects around specific wavelength due to plasmonic resonances. The dominant nonlinear mechanism depends on the investigated time scale. It is mostly due to modification of the interband transition when the electrons are out of equilibrium with the lattice, i.e., one to a few picoseconds, depending on the transient temperature of the electron gas. Modification of the lattice temperature yields the dominant contribution on a longer time-scale. These nonlinear mechanisms are associated to metal heating and thus to losses for the incident pulse.

For smaller sizes, down to 2-3 nm, a similar model can be used introducing modification of the electronic and vibrational kinetics [52]. Quantum effect and increased interaction with the environment are expected to deeply modify the above picture for even smaller sizes, with a transition from a solid state to a molecular type of behavior in the 2-3 nm size range as reported in thiol stabilized clusters [140].

Though we have focused on description of the nonlinear response of simple plasmonic systems, i.e., individual metal nanoparticle and diluted ensemble of nanoparticles, the above model can be extended to any kind of plasmonic materials and metamaterials, such as dense ensemble of nanoparticles, arrays of particles or holes, or waveguide stripes. The main point is then to properly connect the observable optical properties of the plasmonic system with the dielectric functions of the constituting

materials, i.e., calculate its linear optical response taking into account plasmonic effects.

Acknowledgments The authors wish to thank D. Mongin, H. Baida, D. Christofilos, G. Bachelier, A. Crut, P. Maioli, for their contributions to parts of this work. NDF acknowledges support by Institut Universitaire de France (IUF).

References

1. C.F. Bohren, D.R. Huffman, *Absorption and Scattering of Light by Small Particles* (John Wiley, New York, 1998)
2. A. Kawabata, R. Kubo, J. Phys. Soc. Jap. **21**, 1765 (1966)
3. U. Kreibig, M. Vollmer, *Optical Properties of Metal Clusters* (Springer, Berlin, 1995)
4. S.A. Maier, *Plasmonics: Fundamentals and Applications* (Springer, Berlin, 2007)
5. F. Vallée, in *Nanoscience: Nanomaterials and Nanochemestry*, ed. by C. Dupas, P. Houdy, M. Lahmani (Springer, Berlin, 2007), p. 197
6. R. Kubo, A. Kawabata, S. Kobayashi, Ann. Rev. Mater. Sci. **14**, 49 (1984)
7. A.M. El-Sayed, A.S. Majied, Colloids Surf. A **246**, 61 (2004)
8. K.L. Kelly, E. Coronado, L.L. Zhao, G.C. Schatz, J. Phys. Chem. B **107**, 668 (2003)
9. L.M. Liz-Marzan, Langmuir **22**, 32 (2006)
10. B. Luk'yanchuk, N. Zheludev, S. Maier, N. Halas, P. Nordlander, H. Giessen, C. Chong, Nat. Mater. **9**, 707 (2010)
11. J.J. Mock, D.R. Smith, S. Schultz, Nano Lett. **3**, 485 (2003)
12. J.A. Schuller, E.S. Barnard, W. Cai, Y.C. Jun, J.S. White, M.L. Bronger, Nat. Mat. **9**, 196 (2010)
13. K. Willets, R. Van Duyne, Ann. Rev. Phys. Chem. **58**, 267 (2007)
14. M.L. Brongersma, V.M. Shalaev, Science **328**, 440 (2010)
15. T.W. Ebbesen, H.J. Lezec, H.F. Ghaemi, T. Thio, P.A. Wolff, Nature **391**, 667 (1998)
16. J. Krenn, A. Dereux, J.C. Weeber, E. Bourillot, Y. Lacroute, J.P. Goudonnet, G. Schider, W. Gotschy, F.R. Aussenegg, C. Girard, Phys. Rev. Lett. **83**, 2590 (1999)
17. S.A. Maier, H.A. Atwater, J. Appl. Phys. **98**, 011101 (2005)
18. M. Aeschlimann, M. Bauer, D. Bayer, T. Brixner, F.J. García de Abajo, W. Pfeiffer, M. Rohmer, C. Spindler, F. Steeb, Nature **446**, 301 (2007)
19. A.S. Kirakosyan, M. Tong, T.V. Shahbazyan, Z.V. Vardeny, Appl. Phys. B **93**, 131 (2008)
20. K.F. MacDonald, Z.L. Sámson, M.I. Stockman, N.I. Zheludev, Nat. Photonics **3**, 55 (2009)
21. M. Pohl, V.I. Belotelov, I.A. Akimov, S. Kasture, A.S. Vengurlekar, A.V. Gopal, A.K. Zvezdin, D.R. Yakovlev, M. Bayer, Phys. Rev. B **85**, 081401(R) (2012)
22. C. Ropers, D.J. Park, G. Stibenz, G. Steinmeyer, J. Kim, D. Kim, C. Lienau, Phys. Rev. Lett. **94**, 113901 (2005)
23. N. Rotenberg, J.N. Caspers, H.M. van Driel, Phys. Rev. B **80**, 245420 (2009)
24. Z.L. Samson, K.F. MacDonald, N.I. Zheludev, J. Opt. A **11**, 114031 (2009)
25. S.I. Anisimov, B.L. Kapeliovitch, T.L. Perelman, Sov. Phys. JETP **39**, 375 (1974)
26. N. Del Fatti, C. Voisin, M. Achermann, S. Tzortzakis, D. Christofilos, F. Vallée, Phys. Rev. B **61**, 16956 (2000)
27. G.L. Eesley, Phys. Rev. Lett. **51**, 2140 (1983)
28. J.G. Fujimoto, J.M. Liu, E.P. Ippen, N. Bloembergen, Phys. Rev. Lett. **53**, 1837 (1984)
29. C.K. Sun, F. Vallée, L. Acioli, E.P. Ippen, J.G. Fujimoto, Phys. Rev. B **50**, 15337 (1994)
30. F. Vallée, C.R. Acad, Science **2**, 1469 (2001)
31. G.L. Eesley, Phys. Rev. B **33**, 2144 (1986)
32. N. Del Fatti, F. Vallée, C. R. Phys. **3**, 365 (2002)
33. G.V. Hartland, Chem. Rev. **111**, 3858 (2011)

34. M. Kiel, H. Möhwald, M. Bargheer, Phys. Rev. B **84**, 165121 (2011)
35. S. Link, M.A. El-Sayed, J. Phys. Chem. B **103**, 8410 (1999)
36. T. Tokizaki, A. Nakamura, S. Kavelo, K. Uchida, S. Omi, H. Tanji, Y. Asahara, Appl. Phys. Lett. **65**, 941 (1994)
37. C. Voisin, N. Del Fatti, D. Christofilos, F. Vallée, J. Phys. Chem B **105**, 2264 (2001)
38. H. Baida, D. Mongin, D. Christofilos, G. Bachelier, A. Crut, P. Maioli, N. Del Fatti, F. Vallée, Phys. Rev. Lett. **107**, 057402 (2011)
39. G.V. Hartland, Chem. Sci. **1**, 303 (2010)
40. T. Itoh, T. Asahi, H. Masuhara, Appl. Phys. Lett. **79**, 1667 (2001)
41. Y. Matsuo, K. Sasaki, Japan. J. Appl. Phys. **40**, 6143 (2001)
42. O.L. Muskens, N. Del Fatti, F. Vallée, Nano Lett. **6**, 552 (2006)
43. M. Pelton, M. Liu, S. Park, N. Scherer, P. Guyot-Sionnest, Phys. Rev. B **73**, 155419 (2006)
44. M.A. Van Dijk, M. Lippitz, M. Orrit, Phys. Rev. Lett. **95**, 267406 (2005)
45. H. Staleva, G.V. Hartland, Adv. Funct. Mater. **18**, 1 (2008)
46. A. Anderson, K.S. Deryckx, X.G. Xu, G. Steinmeyer, M.B. Raschke, Nano Lett. **10**, 2519 (2010)
47. C. Guillon, P. Langot, N. Del Fatti, F. Vallée, New J. Phys. **5**, 13 (2003)
48. T. Hanke, G. Krauss, D. Trautlein, B. Wild, R. Bratschitsch, A. Leitenstorfer, Phys. Rev. Lett. **103**, 257404 (2009)
49. B. Lamprecht, J.R. Krenn, A. Leitner, F.R. Aussenegg, Phys. Rev. Lett. **83**, 4421 (1999)
50. A. Arbouet, C. Voisin, D. Christofilos, P. Langot, N. Del Fatti, F. Vallée, J. Lermé, G. Celep, E. Cottancin, M. Gaudry, M. Pellarin, M. Broyer, M. Maillard, M.P. Pileni, M. Treguer, Phys. Rev. Lett. **90**, 177401 (2003)
51. C. Voisin, D. Christofilos, N. Del Fatti, F. Vallée, B. Prével, E. Cottancin, J. Lermé, M. Pellarin, M. Broyer, Phys. Rev. Lett. **85**, 2200 (2000)
52. C. Voisin, D. Christofilos, P.A. Loukakos, N. Del Fatti, F. Vallée, J. Lermé, M. Gaudry, E. Cottancin, M. Pellarin, M. Broyer, Phys. Rev. B **69**, 195416 (2004)
53. C. Voisin, D. Christofilos, N. Del Fatti, F. Vallée, Eur. Phys. J. D **16**, 139 (2001)
54. J. Burgin, P. Langot, N. Del Fatti, F. Vallée, W. Huang, M.A. El Sayed, J. Phys. Chem. C **112**, 11231 (2008)
55. N. Del Fatti, C. Voisin, D. Christofilos, F. Vallée, C. Flytzanis, J. Phys. Chem. A **104**, 4321 (2000)
56. G.V. Hartland, Annu. Rev. Phys. Chem. **57**, 403 (2006)
57. V. Juvé, A. Crut, P. Maioli, M. Pellarin, M. Broyer, N. Del Fatti, F. Vallée, Nano Lett. **10**, 1853 (2010)
58. D.G. Cahill, W.K. Ford, K.E. Goodson, G.D. Mahan, A. Majumdar, H.J. Maris, R. Merlin, S.R. Phillpot, J. Appl. Phys. **93**, 793 (2003)
59. V. Juvé, M. Scardamaglia, P. Maioli, A. Crut, S. Merabia, L. Joly, N. Del Fatti, F. Vallée, Phys. Rev. B **80**, 195406 (2009)
60. N. Del Fatti, F. Vallée, C. Flytzanis, Y. Hamanaka, A. Nakamura, Chem. Phys. **251**, 215 (2000)
61. D.T. Owens, C. Fuentes-Hernandez, J.M. Hales, J.W. Perry, B. Kippelen, J. Appl. Phys. **107**, 123114 (2010)
62. J. Butet, J. Duboisset, G. Bachelier, I. Russier-Antoine, E. Benichou, C. Jonin, P.-F. Brevet, Nano Lett. **10**, 1717 (2010)
63. M. Lippitz, M.A. van Dijk, M. Orrit, Phys. Rev. Lett. Nano Lett. **5**, 799 (2005)
64. S. Palomba, M. Danckwerts, L. Novotny, J. Opt. A **11**, 114030 (2009)
65. Y. Guillet, E. Charron, B. Palpant, Phys. Rev. B **79**, 195432 (2009)
66. N.W. Ashcroft, N.D. Mermin, *Solid State Physics* (Holt-Saunders, Tokyo, 1981)
67. R.N. Gurzhi, Sov. Phys. JETP **35**, 673 (1959)
68. J.B. Smith, H. Ehrenreich, Phys. Rev. B **25**, 923 (1982)
69. C.-Yi Tsai, C.-Yao Tsai , C.-H. Chen, T.-L. Sung, T.-Y. Wu, F.-P. Shih, IEEE J. Quant. Electr. **34**, 552 (1998)
70. P.B. Allen, Phys. Rev. Lett. **59**, 1460 (1987)
71. H. Hovel, S. Fritz, A. Hilger, U. Kreibig, M. Vollmer, Phys. Rev. B **48**, 18178 (1993)

72. F. Hache, D. Ricard, C. Flytzanis, J. Opt. Soc. Am. B **3**, 1647 (1986)
73. H. Baida, P. Billaud, S. Marhaba, D. Christofilos, E. Cottancin, A. Crut, J. Lermé, P. Maioli, M. Pellarin, M. Broyer, N. Del Fatti, F. Vallée, A. Sánchez-Iglesias, I. Pastoriza-Santos, L.M. Liz-Marzán, Nano Lett. **9**, 3463 (2009)
74. E.A. Coronado, G.C. Schatz, J. Chem. Phys. **119**, 3926 (2003)
75. J. Lermé, H. Baida, C. Bonnet, M. Broyer, M. Cottancin, A. Crut, P. Maioli, N. Del Fatti, F. Vallée, M. Pellarin, J. Phys. Chem. Lett. **1**, 2922 (2010)
76. C. Flytzanis, F. Hache, M.C. Klein, D. Ricard, P. Roussignol, in *Progress in Optics*, vol. XXIX, ed. by E. Wold (North Holland, Amsterdam, 1991), p. 321
77. R. Rosei, F. Antonangeli, U.M. Grassano, Surf. Sci. **37**, 689 (1973)
78. R. Rosei, Phys. Rev. B **10**, 474 (1974)
79. R. Rosei, C.H. Culp, J.H. Weaver, Phys. Rev. B **10**, 484 (1974)
80. N.E. Christensen, B.O. Seraphin, Phys. Rev B **4**, 3321 (1971)
81. M. Guerrisi, R. Rosei, P. Winsemius, Phys. Rev. B **12**, 557 (1975)
82. P. Winsemius, M. Guerrisi, R. Rosei, Phys. Rev. B **12**, 4570 (1975)
83. P.B. Johnson, R.W. Christy, Phys. Rev. B **6**, 4370 (1972)
84. N.E. Christensen, Phys. Stat. Solidi B **54**, 551 (1972)
85. D. Brorson, A. Kazeroonian, J.S. Modera, D.W. Face, T.K. Cheng, E.P. Ippen, M.S. Dresselhaus, G. Dresselhaus, Phys. Rev. Lett. **64**, 2172 (1990)
86. N. Del Fatti, C. Voisin, F. Chevy, F. Vallée, C. Flytzanis, J. Chem. Phys. **110**, 11484 (1999)
87. M. Nisoli, S. De Silvestri, A. Cavalleri, A.M. Malvezzi, A. Stella, G. Lanzani, P. Cheyssac, R. Kofman, Phys. Rev. B **55**, R13424 (1997)
88. C. Thomsen, H.T. Grahn, H.J. Maris, J. Tauc, Phys. Rev. B **34**, 4129 (1986)
89. T. Vartanyan, M. Simon, F. Träger, Appl. Phys. B **68**, 425 (1999)
90. J. Bosbach, C. Hendrich, F. Stietz, T. Vartanyan, F. Träger, Phys. Rev. Lett. **89**, 257404 (2002)
91. F. Stietz, J. Bosbach, T. Wenzel, T. Vartanyan, A. Goldmann, F. Träger, Phys. Rev. Lett. **84**, 5644 (2000)
92. T. Ziegler, C. Hendrich, F. Hubenthal, T. Vartanyan, F. Träger, Chem. Phys. Lett. **3**(86), 319 (2004)
93. A. Knoesel, A. Hotzel, M. Wolf, Phys. Rev. B **57**, 12812 (1998)
94. H. Petek, S. Ogawa, Progr. Surf. Sci. **56**, 239 (1997)
95. V.P. Drachev, E.N. Khaliullin, W. Kim, F. Alzoubi, S.G. Rautian, V.P. Safonov, R.L. Armstrong, V.M. Shalaev, Phys. Rev. B **69**, 035318 (2004)
96. R.A. Farrer, F.L. Butterfield, V.W. Chen, J.T. Fourkas, Nano Lett. **5**, 1139 (2005)
97. R. Matzdorf, A. Gerlach, F. Theilmann, G. Meister, A. Goldmann, Appl. Phys. B **68**, 393 (1999)
98. R. Knorren, K.H. Bennemann, R. Burgermeister, M. Aeschlimann, Phys. Rev. B **61**, 9427 (2000)
99. J.M. Ziman, *Principles of the Theory of Solids* (Cambridge University Press, Cambridge, 1969)
100. S.D. Brorson, J.G. Fujimoto, E.P. Ippen, Phys. Rev. Lett. **59**, 1962 (1987)
101. C. Suarez, W.E. Bron, T. Juhasz, Phys. Rev. Lett. **75**, 4536 (1995)
102. D. Pines, P. Nozières, *The Theory of Quantum Liquids* (Benjamin, New York, 1966)
103. J.I. Juaristi, M. Alducin, I. Nagy, J. Phys. Condens. Matter **15**, 7859 (2003)
104. Z. Lin, L.V. Zhigilei, Phys. Rev. B **77**, 075133 (2008)
105. T.V. Shahbazyan, I.E. Perakis, J.-Y. Bigot, Phys. Rev. Lett. **81**, 3120 (1998)
106. T.V. Shahbazyan, I.E. Perakis, Chem. Phys. **251**, 37 (2000)
107. T.V. Shahbazyan, I.E. Perakis, Phys. Rev. B **60**, 9090 (1999)
108. M.I. Kaganov, I.M. Lifshitz, L.V. Tanatarov, Sov. Phys. JETP **4**, 173 (1957)
109. N. Del Fatti, A. Arbouet, F. Vallée, Appl. Phys. B **84**, 175 (2006)
110. R. Groeneveld, R. Sprik, A. Lagendijk, Phys. Rev. B **51**, 11433 (1995)
111. N. Del Fatti, R. Bouffanais, F. Vallée, C. Flytzanis, Phys. Rev. Lett. **81**, 922 (1998)
112. R.W. Schoenlein, W.Z. Lin, J.G. Fujimoto, G.L. Eesley, Phys. Rev. Lett. **58**, 1680 (1987)
113. C.K. Sun, F. Vallée, L.H. Acioli, E.P. Ippen, J.G. Fujimoto, Phys. Rev. B **48**, 12365 (1993)
114. P. Grua, J.P. Morreeuw, H. Bercegol, G. Jonusauskas, F. Vallée, Phys. Rev. B **68**, 035424 (2003)

115. V. Halté, J.-Y. Bigot, B. Palpant, M. Broyer, B. Prével, A. Pérez, Appl. Phys. Lett. **75**, 3799 (1999)
116. Y. Hamanaka, J. Kuwabata, I. Tanahashi, S. Omi, A. Nakamura, Phys. Rev. B **63**, 104302 (2001)
117. Z.B. Ge, D.G. Cahill, P.V. Braun, J. Phys. Chem. B **108**, 18870 (2004)
118. M. Hu, G.V. Hartland, J. Phys. Chem. B **106**, 7029 (2002)
119. H.S. Carslaw, J.C. Jaeger, *Conduction of Heat in Solids* (Oxford University Press, Oxford, 1959)
120. A. Plech, V. Kotaidis, S. Gresillon, C. Dahmen, G. von Plessen, Phys. Rev. B **70**, 195423 (2004)
121. E.D. Swartz, R.O. Pohl, Rev. Mod. Phys. **61**, 605 (1989)
122. J.-Y. Bigot, J.-C. Merle, O. Cregut, A. Daunois, Phys. Rev. Lett. **75**, 4702 (1995)
123. R.N. Gurzhi, M. Ya.Azbel', H.P. Lin, Sov. Phys. Solid State **5**, 554 (1963)
124. C. Voisin, D. Christofilos, N. Del Fatti, F. Vallée, Physica B **316**, 89 (2002)
125. G.R. Parkins, W.E. Lawrence, R.W. Christy, Phys. Rev. B **23**, 6408 (1981)
126. A. Crut, P. Maioli, N. Del Fatti, F. Vallée, Phys. Chem. Chem. Phys. **11**, 5882 (2009)
127. F. Abelès, in *Optics of Thin Films*, ed. by A.C.S. Van Heel. Advanced Optical Techniques (North Holland, New York, 1967), p. 144
128. O. Muskens, D. Christofilos, N. Del Fatti, J. Opt. A **8**, S264 (2006)
129. R.F. Haglund, in *Handbook of Optical Properties*, vol. 2, ed. by R.E. Hummel, P. Wissmann (CRC Press, New York, 1997), p. 191
130. D. Ricard, in *Nonlinear Optical Materials: Principles and Applications*, ed. by V. Degiorgio, C. Flytzanis (IOS Press, Amsterdam, 1995), p. 289
131. A. Arbouet, D. Christofilos, N. Del Fatti, F. Vallée, J.-R. Huntzinger, L. Arnaud, P. Billaud, M. Broyer, Phys. Rev. Lett. **93**, 127401 (2004)
132. S. Park, M. Pelton, M. Liu, P. Guyot-Sionnest, N.F. Scherer, J. Phys. Chem. C **111**, 116 (2007)
133. Y.R. Shen, *The Principles of Nonlinear Optics* (Wiley-Interscience, Hoboken, New Jersey, 1984)
134. N.V. Voshchinnikov, V.G. Farafonov, Astrophys. Space Sci. **204**, 19 (1993)
135. O. Muskens, G. Bachelier, N. Del Fatti, F. Vallée, A. Brioude, X. Jiang, M.P. Pileni, J. Phys. Chem. C **112**, 8917 (2008)
136. O.L. Muskens, P. Billaud, M. Broyer, N. Del Fatti, F. Vallée, Phys. Rev. B **78**, 205410 (2008)
137. N. Del Fatti, F. Vallée, Appl. Phys. B **73**, 383 (2001)
138. P. Billaud, S. Marhaba, E. Cottancin, L. Arnaud, G. Bachelier, C. Bonnet, N. Del Fatti, J. Lermé, F. Vallée, J.-L. Vialle, M. Broyer, M. Pellarin, J. Phys. Chem. C **112**, 978 (2008)
139. P. Zijlstra, A.L. Tchebotareva, J.W.M. Chon, M. Gu, M. Orrit, Nano Lett. **8**, 3493 (2008)
140. M.Y. Sfeir, H. Qian, K. Nobusada, R. Jin, J. Phys. Chem. C **115**, 6200 (2011)

Chapter 6
Second-Order Nonlinear Optical Properties of Plasmonic Nanostructures

Martti Kauranen, Hannu Husu, Jouni Mäkitalo, Robert Czaplicki, Mariusz Zdanowicz, Joonas Lehtolahti, Janne Laukkanen and Markku Kuittinen

Abstract We review our work on second-order nonlinear optical properties of plasmonic nanostructures. In order to achieve the required non-centrosymmetry of the structures, our samples consist of arrays of L-shaped nanoparticles and T-shaped nanodimers. The samples are investigated by polarization-dependent second-harmonic generation to address the tensorial nonlinear response. We show that the response can be strongly modified by symmetry-breaking defects and other deviations of the samples from ideal. Nonlinear sources localized to defects can also give rise to higher-multipolar emission. The defect problem is overcome with a recent and significant improvement in sample quality, allowing the dipole limit of the nonlinear response to be reached. This achievement opens the path towards plasmonic metamaterials with tailorable nonlinear properties. As a demonstration of this possibility, we modify the nonlinear response by the mutual arrangement of the L-shaped particles in the array. We will also summarize our numerical boundary-element method to describe the nonlinear response of nanoparticles.

Keywords Surface plasmon · Nonlinear optics · Second harmonic generation

M. Kauranen (✉) · H. Husu · J. Mäkitalo · R. Czaplicki · M. Zdanowicz
Department of Physics, Tampere University of Technology, P.O. Box 692,
33101 Tampere, Finland
e-mail: martti.kauranen@tut.fi

H. Husu
Centre for Metrology and Accreditation (MIKES), P.O. Box 9, 02151 Espoo, Finland

M. Zdanowicz
National Institute of Telecommunications, Szachowa 1, 04894 Warsaw, Poland

J. Lehtolahti · J. Laukkanen · M. Kuittinen
Department of Physics and Mathematics, University of Eastern Finland, 80101 Joensuu, Finland

T. V. Shahbazyan and M. I. Stockman (eds.), *Plasmonics: Theory and Applications*,
Challenges and Advances in Computational Chemistry and Physics 15,
DOI: 10.1007/978-94-007-7805-4_6, © Springer Science+Business Media Dordrecht 2013

6.1 Introduction

The optical response of metal nanoparticles is dominated by particle plasmons, which are collective oscillations of the metallic conduction electrons in the particles [1, 2]. The resonance wavelengths of the particle plasmons depend on the size and shape of the particles as well as their dielectric environment [3]. When the particles are arranged in an array, as is often the case for metamaterials [4, 5], near-field or long-range coupling between the individual particles can further modify the resonances, giving rise to sharp spectral features [6–12]. All these mechanisms provide several degrees of freedom for tuning the resonances and optical properties of metal nanostructures over broad wavelength ranges [13–16].

The plasmon resonances are associated with strong local electromagnetic fields near the particles [17, 18]. Such "hot spots" can be used to enhance optical interactions, allowing for example surface-enhanced Raman scattering from individual molecules [19, 20]. The local-field enhancement is of particular interest for nonlinear optical effects, which scale with a high power of the local field. The nonlinear effects are therefore expected to be locally enhanced at the hot spots and, with judicious design, even when the response is averaged over the whole sample volume.

In this Chapter, we focus on second-order nonlinear optical properties of plasmonic nanostructures. Relatively strict symmetry rules constrain second-order effects to non-centrosymmetric material systems [21]. Such effects are therefore sensitive probes of symmetry breaking in the material structure. A well-known example of this is the fact that the symmetry of bulk materials is necessarily broken at surfaces, which justifies second-order techniques as probes of surfaces, interfaces, and molecular order in thin films [21–24]. Such responses can only be accessed when the optical fields couple with the direction of the sample normal. In the plane wave limit and planar samples, the experiments therefore need to be performed at oblique angle of incidence. In the context of metal nanostructures, possible sources of symmetry breaking are deviations of the overall features of the sample from design and nanoscale defects that can support their own highly-localized plasmonic modes [18, 25].

In our work, we have studied second-harmonic generation (SHG) from arrays of metal nano-objects on a dielectric substrate. SHG is the most common second-order process, which is easy to implement experimentally. In order to break their centrosymmetry, our objects have consisted of L-shaped nanoparticles and T-shaped nanodimers. More specifically, such objects look non-centrosymmetric even when investigated at normal incidence to avoid the coupling of the optical beams with the traditional surface nonlinearity with the out-of-plane character. Our work therefore addresses the nonlinear response arising from the shape of the particles, rather than uses the nanoparticles to enhance the coupling with the traditional surface nonlinearity.

The role of various multipole effects in the optical responses is an important aspect that needs to be considered when nanostructures are discussed. In addition to the traditional electric-dipole interaction, higher-multipole interactions, magnetic-dipole and electric-quadrupole interactions in particular, can become important in

the second-order nonlinear response, and they can arise from two complementary mechanisms. First, higher-multipole interactions on the atomic level give rise to new types of nonlinear responses that allow second-order effects even in the bulk of centrosymmetric materials [21]. Second, field retardation across nanoparticles may give rise to effective multipole effects, similar to the various multipole terms in the Mie scattering theory [26, 27].

To theoretically understand the optical properties of nanoparticles, one usually needs to solve an electromagnetic scattering problem. The geometry of the particles is often so complicated that closed form solutions cannot be found and approximate solutions must be sought numerically. Plasmonic structures pose challenges for numerical schemes, as resonances can make the problem sensitive to its mathematical formulation and the structures tend to give rise to sub-wavelength features in the local fields. Modeling nonlinear effects in nanoparticles can make these issues even more pronounced, as multiple frequencies are present and the associated wavelengths can be very short. The early approaches on modeling have focused on SHG in spheres or other simple geometries that can be treated analytically [24]. Recently, various, more general methods have been considered to address particles of arbitrary shapes.

This Chapter is structured as follows. In Sect. 6.2, we introduce a theoretical formalism based on effective multipole nonlinearities, which provides a convenient way to describe the experimental results. The sample fabrication and experimental setups for SHG measurements are described in Sect. 6.3. Section 6.4 then summarizes the early results on SHG from metal nanostructures where fabrication related defects were found to play a disproportionate role in the nonlinear response, giving rise to symmetry-forbidden signals and effective multipole effects in the response. Section 6.5 discusses the role of the local-field distribution and its symmetry in the nonlinear response. In Sect. 6.6, we show that recent progress in nanofabrication has led to a significant improvement in the sample quality, allowing the desired dipole limit in the nonlinear response to be reached. This result is an important milestone for the development of metamaterials with tailored nonlinear properties, an example of which is discussed in Sect. 6.7. We then discuss recent progress in the numerical modeling of the nonlinear response in Sect. 6.8 and provide an outlook for the future in Sect. 6.9.

6.2 Theoretical Background

6.2.1 Nonlinear Response Tensor

On the fundamental level, SHG arises from the interaction between light and matter characterized by the second-order susceptibility tensor, which is a material quantity that can be derived using microscopic theories of the light-matter interaction. In homogeneous media, the susceptibilities are spatially invariant over macroscopic length scales. Metal nanostructures, however, have spatial variations of the mater-

ial parameters in a scale that typically varies in the range of a few nm to 100s of nm. Hence, the susceptibility is a locally varying quantity. Furthermore, the local electromagnetic fields at the fundamental frequency are strongly varying in space in metal nanostructures. A detailed approach would therefore require taking into account the local-field variations, the spatially varying susceptibility tensors, the locally-generated nonlinear sources, and also, the coupling of the incoming and outgoing radiation fields to the local quantities. Such an approach would give detailed knowledge on the nonlinear response of the nanostructures, but it is very challenging even computationally.

We therefore use a simplified approach that allows us to treat the experiments in a convenient way. The sample is treated as a "black box", and only the input and output fields are considered. The relation between the incoming and outgoing fields is described by the nonlinear response tensor (NRT) components A_{jkl} defined as [28]

$$E_j(2\omega) = \sum_{kl} A_{jkl} E_k(\omega) E_l(\omega), \tag{6.1}$$

where $E_j(2\omega)$ is the outgoing field at the second-harmonic (SH) frequency, and $E_k(\omega)$ and $E_l(\omega)$ are the incoming fields at the fundamental frequency. The fields are assumed to be plane waves, which is the case also in all our experiments.

The nonlinear response tensor is a macroscopic parameter, which implicitly takes into account all the effects in the nanoscale, while avoiding the difficulties in their explicit treatment. The main disadvantage is that the tensor components can depend significantly on the experimental setup, however, even this can be used to advantage. Comparison of NRTs under different experimental conditions provides important insight to the nanoscopic origin of the nonlinear response of the sample. Another benefit is that, due to its macroscopic character, NRT includes implicitly contributions from different multipolar sources.

The nonlinear response tensor has in total $3^3 = 27$ complex valued components. In our measurements, the sample is always characterized at normal or near-normal incidence using plane waves. In consequence, only the in-plane field components need to be included in the analysis, which significantly reduces the number of components. The coordinate system is chosen so that the fields are polarized in the (x, y)-plane and the propagation is in the z direction. By using the described coordinate system, the x- and y-polarized second-harmonic fields can be written in terms of the fundamental field components as

$$E_j(2\omega) = A_{jxx} E_x^2(\omega) + A_{jyy} E_y^2(\omega) + 2A_{jxy} E_x(\omega) E_y(\omega), \tag{6.2}$$

where j is either x or y and the factor of two comes from the fact that for second-harmonic generation the latter two indices are interchangeable. Only six tensor components therefore need to be considered.

Second-harmonic generation, as well as other even-order processes, is very sensitive to the symmetry of the nanostructures [29]. A typical example is a

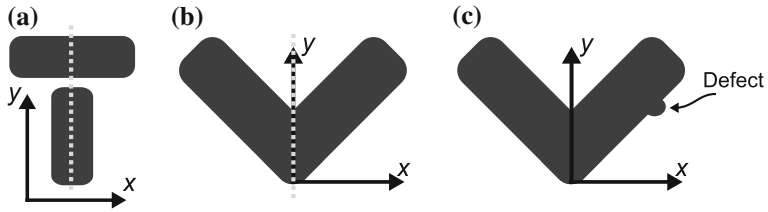

Fig. 6.1 **a** An ideal T-shaped and **b** L-shaped particle with a symmetry plane in *y* direction (*dashed gray line*). **c** An L-shaped particle with a defect breaking the symmetry

centrosymmetric particle, like a sphere, which does not produce any second-harmonic generation in the forward direction. Note, however, that second-harmonic signals can be generated to sideways directions even from a sphere [24, 30–32]. For non-centrosymmetric particles, electric-dipole-type selection rules can be applied to NRT in order to deduce the vanishing tensor components. The investigated L-shaped and T-shaped particles have a mirror plane along the *y* axis (Fig. 6.1a, b), which forbids half of the remaining tensor components. However, the ideal symmetry is easily broken by sample defects (Fig. 6.1c).

6.2.2 Extension to Multipole Effects

The NRT approach can be extended to account for effective electric-dipole and higher-multipole interactions. In the response of nanostructured materials, multipole effects arise from the light-matter interaction Hamiltonian [33] or are described by Mie scattering theory [3, 26, 27]. In order to take the higher multipoles into account more explicitly than in Eqs. (6.1) and (6.2), yet on the level of the measured far-field signals, we introduce three effective NRTs. The first includes electric-dipole interactions only, whereas the other two account for magnetic-dipole interactions at the fundamental frequency or the second-harmonic frequency. The magnetic tensors include both magnetic and quadrupole effects due to difficulties in their separation in coherent signals [34]. Emphasis on magnetic, rather than quadrupole effects, is beneficial because they are local with respect to magnetic quantities.

It is important to note that the components of the three tensors contribute in different ways to the total NRT components of Eqs. (6.1) and (6.2) that can be measured under different experimental conditions [35]. More specifically, the contributions of each tensor to the total components can be separated by comparing SHG signals in the reflected and transmitted directions and for metal- and substrate-side incidence of the fundamental beam. A consequence is that if the SHG response is dominated by the electric-dipole-only part, all four signals should behave identically. Any differences between the signals, on the other hand, provide evidence of higher-multipole effects, which can be quantified by a detailed tensor analysis of the response.

Independent of which multipole effects play a role, the tensor components forbidden by symmetry vanish for a perfectly ideal particle. The real samples, however, always have imperfections, which leads to nonvanishing of these ideally forbidden components. For high-quality samples, those components are expected to remain weak. The magnitude of the forbidden components can thus be used as a measure of sample quality.

6.3 Experimental Techniques

6.3.1 Samples and Fabrication

The samples studied in our work consist of square arrays of T- and L-shaped gold nanoparticles or nanodimers fabricated on a fused silica substrate by the common electron-beam lithography and lift-off techniques. The thickness of the nanoparticles is 20 nm and there is a thin (typically 5 nm) adhesion layer of chromium between the substrate and gold. In addition, the samples are covered by a 20 nm thick protective layer of silica. The other sample dimensions, such as the length and width of different parts of the particles, are varied between different samples, and the array period is either 400 or 500 nm.

The T-shaped gold nanodimers (Fig. 6.2a, b) consist of a horizontal and a vertical bar with the width of 125 nm and length of 250 nm. The gap separating the bars is varied in order to investigate its effect on the optical response of the dimers. The L-shaped gold nanoparticles (Fig. 6.2c, d) have two different arm widths: 50 or 100 nm. The arm length is varied from 100 to 300 nm.

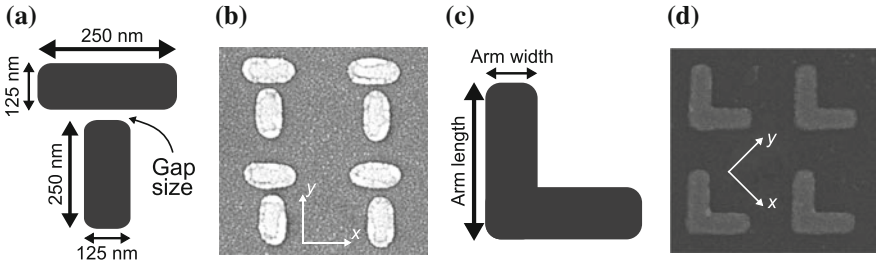

Fig. 6.2 **a** The geometry and dimensions of T-shaped nanodimers. **b** Scanning electron microscope image of T-dimers and the coordinate system. **c** The geometry of L-shaped nanoparticle and the definitions for the dimensions. **d** Scanning electron microscope image of L-particles and the coordinate system

6.3.2 Experimental Setup

The linear optical properties of the samples were determined by measuring their extinction spectra. These measurements were performed at normal incidence using a fiber-coupled halogen lamp as a light source. Microscope objectives were used to collimate light from the fiber and to focus the light into the pick-up fiber of the spectrometer. A calcite polarizer was used to set linear polarization state and a pinhole was placed in order to illuminate the desired sample area. Two spectrometers were used to cover a spectral range from 400 to 1700 nm.

In order to address the nonlinear properties of the samples, several different measurements were performed. All measurements are based on measuring polarization-dependent SHG from the samples, where the fundamental beam is applied to the sample, and transmitted only or transmitted and reflected second-harmonic signals are detected (Fig. 6.3). As a source of fundamental light, a Nd:glass laser (Time-Bandwidth Products GLX-200) was used, with 200 fs pulses at 1060 nm, 150 mW average power and 82 MHz repetition rate. The polarization state of the fundamental beam was cleaned with a high-quality Glan polarizer and modulated continuously during the experiments by rotating a half- or quarter-wave plate. For some experiments a Glan polarizer was used before the detector as an analyzer in order to select the measured SHG polarization. Before the sample, a long pass filter was used in order to block any second-harmonic radiation coming from optical components. Other filters, to block the fundamental wavelength, were placed after the sample in the transmission and reflection detection arms. For the detection, two photomultiplier tubes were used with a photon counting system.

When measurements in both transmission and reflection were performed, the sample was tilted off-normal with respect to the fundamental beam. However, the angle was sufficiently small (less than 1°) not to affect the results.

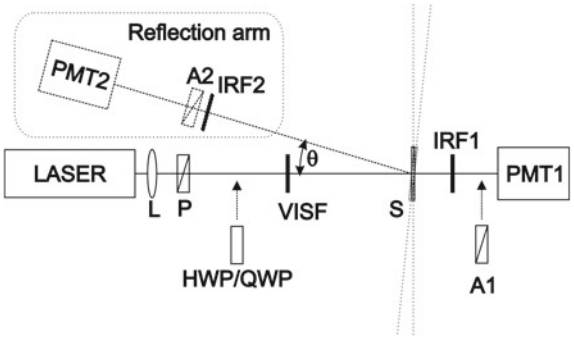

Fig. 6.3 Setup used for second-harmonic measurements. *L* lens, *P* polarizer, *HWP* half-wave plate, *QWP* quarter wave plate, *VISF* visible blocking filter, *S* sample (at normal incidence or tilted off-normal, θ less than 2°) *IRF1*, *IRF2* infrared blocking filters, *A1*, *A2* analyzers, *PMT1*, *PMT2* photomultiplier tubes

6.4 Early Work

6.4.1 Basic Results

The L-shaped nanoparticles for SHG were originally introduced for autocorrelation measurements of the plasmon dephasing time in metal nanoparticles [36]. The motivation for our studies, on the other hand, has been to prepare arrays of nanoparticles with tailorable nonlinear properties. Our very first results already showed that the efficiency of SHG depends sensitively on how the individual particles are ordered in the array [37].

Subsequent work, however, soon showed that the expected selection rules between the allowed and forbidden signals are not well obeyed. The forbidden signals were then traced to the broken symmetry of the actual samples compared to the ideal, which could arise from small-scale defects or the deviations of the overall shape from the ideal. The broken symmetry was found to lead to relatively strong SHG responses for tensor components forbidden by the ideal symmetry [25, 38, 39]. This was explained by the fact that small defects can attract very strong spatially confined fields which can modify local electric-field distribution and significantly affect the second-order response [40, 41]. In most cases, the forbidden signals were related to chiral symmetry breaking, i.e., the loss of mirror symmetry with respect to y axis (Fig. 6.1). More specifically, the SHG signals from nanoparticles with defects revealed strong chirality even from an array designed to be achiral [25].

6.4.2 Multipole Effects

Various multipole sources of radiation can be distinguished in the far-field by measuring their polarization dependent angular emission patterns. In the case of coherent SHG, however, strong signals are detected only in the transmitted and reflected directions, preventing the measurement of the full radiation pattern. The radiative properties of the various multipoles in the two opposite directions lead to differences in interference between electric dipoles and higher multipoles. In particular, the polarization-dependent SHG response allows different multipolar contributions to SHG signal to be distinguished [42].

Experimental evidence of multipole interference in the second-harmonic radiation from an array of metallic L-shaped nanoparticles (length 200 nm, width 100 nm, period 400 nm) suggested that the contribution of higher multipoles was up to 20 % of the total emitted SH field amplitude [42]. The NRT approach was used in order to confirm previous results and to separate the dipolar and higher multipole parts of all in-plane tensor components. The results showed that the nonlinear response was dominated by a tensor component associated with chiral symmetry breaking of the sample [41]. The same tensor component exhibited strong multipole character. The relation between chiral symmetry breaking and strong multipole effects was due to

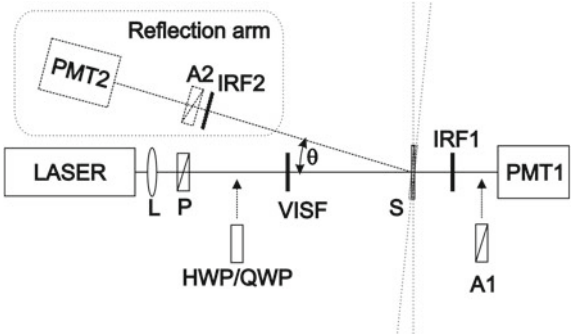

Fig. 6.4 Measured polarization line shapes for an array of L-shaped gold nanoparticles. The presence of higher multipoles leads to differences in the detected signals. The labels refer to metal incidence (*M*-), substrate incidence (*S*-), transmission (-*T*) and reflection (-*R*). Adapted with permission from Ref. [35]. Copyright 2011, Institute of Physics

defects located at two opposite sides of the particle, and dipolar and quadrupolar SH emission arising from interference between the retarded SH wavelets emitted by these small features.

More detailed tensor analysis, where electric and magnetic effects at the fundamental and second-harmonic frequencies were addressed, confirmed the important role of higher multipoles (see differences in the SH signals in Fig. 6.4) especially at the fundamental frequency [35]. The importance of higher multipole effects at the fundamental frequency was suggested to be related to plasmon resonances, and thus strong local fields, at the fundamental frequency. Furthermore, the tensor components related to higher-multipole effects were up to 50 % larger in magnitude compared to the dominant electric-dipole component.

6.4.3 Related Work

The nonlinear studies of metal nanostructures, of course, are not limited to our work. The early work on SHG from rough metal surfaces was motivated by the open questions regarding the possible enhancement mechanisms of SERS [43]. This work was subsequently extended to near-field [44, 45] and far-field microscopy [46]. These and more recent studies have confirmed the incoherent and depolarized character of SHG from rough surfaces [18, 47]. Related studies have also been extended to investigate the role of nanoparticle morphology on the SHG response [48, 49].

Individual nano-objects have also been investigated by SHG. Sharp tips can strongly influence the local-field enhancement, especially, when the field is polarized along the tip axis [50–53]. Furthermore, individual nanostructures and particles have been designed to give rise to an enhanced SHG response, including nanoapertures surrounded by a circular grating [54] and nanocups [55].

A large body of work also exists for arrays of nanoparticles and nanoapertures. Arrays of split-ring resonators (SRRs) were found to give rise to particularly strong SHG when the fundamental wavelength matched the magnetic resonance of the SRR [56–58]. However, more recent results suggested that the excitation of the magnetic resonance is not a prerequisite for a strong response [59]. These results have been interpreted by models based on free-electron approaches to the optical response of metals [60]. Finally, the role of resonance enhancement in SHG from SRRs has been addressed [61]. The interpretation was that a resonance at the fundamental frequency is advantageous, whereas a resonance at the harmonic frequency is just a loss mechanism, reabsorbing the generated SHG light.

Nanoapertures are interesting, because they can enhance light transmitted through them [62]. SHG has been used to investigate holes with high [63, 64] and low symmetry [65] as well as dimers consisting of two holes [66]. Careful inspection of these results on apertures and particles as well as other work [67, 68] reveals that the expected symmetry rules of SHG are only approximately fulfilled, suggesting that the results have also been influenced by defects and imperfections of the nanostructures.

Beyond results regarding nonlinear effects in coherent SHG, incoherent Hyper-Rayleigh scattering (HRS) has been used to characterize nanoparticles, including their multipolar nonlinear responses. For small (diameter below 50 nm) spherical gold and silver nanoparticles, imperfections in the particle shape give rise to a dominant dipolar contribution in HRS. For larger particles, the response has strong quadrupolar contribution due to retardation effects in the interaction of the electromagnetic fields with the particles [30, 69, 70]. These results were supported by theoretical calculations, using finite element method, for particles with noncentrosymmetric shape [31]. By using long acquisition times and signal statistics, single nanoparticle sensitivity has also been achieved [71, 72]. The technique has also been used for the discrimination of single particles from their aggregates [73]. Furthermore, the octupolar contribution to HRS has recently been observed [32], which can also be used to separate the surface and bulk contributions to the signal [74]. Recently, polarization resolved SH intensity measurements on arrays of gold nanocylinders showed that the incoherent SHG response arises from small defects present at the surface of nanocylinders [75, 76].

6.5 Local-Field Issues

6.5.1 Gap Dependence

The optical response of individual metal nanoparticles can be significantly modified by bringing the particles close to each other. Due to charge accumulation close to surfaces within each particle, a very strong local field can exist within the gap between the particles [77–80]. The consequences of this for nonlinear responses were first tested using a dimer consisting of two gold nanospheres and four-wave

mixing, a third-order process with no symmetry constraints [81]. One of the spheres was attached to a scanning arm, allowing the gap size to be varied. The four-wave-mixing signal was found to increase with decreasing gap size down to the ångstrom regime where quantum effects start limiting the local-field enhancement for nearly touching particles. For SHG, it has been predicted that a self-similar chain of nanodots of decreasing size, which results in a noncentrosymmetric structure, can channel the optical energy to the gap between the two smallest spheres, thereby enhancing SHG [82].

In order to test these ideas for SHG, we investigated T-shaped gold nanodimers (Fig. 6.2a, b) made of two bars, a vertical and horizontal, separated by a small gap [83]. In contrast to four-wave mixing, we observed a more complex gap dependence of the SHG signal. The smallest gap size did not always lead to the strongest response and a sample with a certain gap size gave rise to almost vanishing second-harmonic signal followed by an increase in the response for increased gap size (Fig. 6.5).

The counterintuitive behavior of the second-harmonic response could be explained by considering the symmetry of the local electric field distributions in the middle layer of the dimers (Fig. 6.5b, c). The local fields were calculated using the Fourier modal method (FMM). According to the simulations, the local fields were clearly affected by the coupling between the bars, and the symmetry properties of the local fields correlated qualitatively very well with the measured second-harmonic response. The main observation was that even very small structural differences in the dimer can lead to significant changes in the details of the local electric fields and thereby in the SHG response.

6.5.2 Chiral Symmetry Breaking of Dimers

It is evident from Fig. 6.6 that our T-dimers are not ideal either. More specifically, their mirror symmetry is broken by the non-orthogonal mutual orientations of the

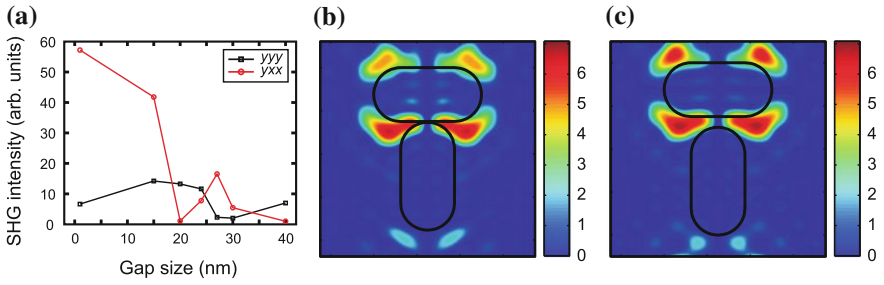

Fig. 6.5 **a** Gap dependence of the SHG signals for the allowed tensor components *yyy* and *yxx* from dimers of the type shown in Fig. 6.2. **b** An example of asymmetric field distribution for the sample with 2 nm gap. **c** An example of more symmetric field distribution for the sample with 25 nm gap. The distributions correspond to the local field *y*-component and for *x*-polarized excitation, which thus can explain the gap dependence of the *yxx* tensor component (*red* plot in Fig. 6.5a). Adapted with permission from Ref. [83]. Copyright 2007, American Chemical Society

vertical and horizontal bars [84]. This gives rise to chirality of the dimer, which can be addressed by SHG with circularly-polarized fundamental light. More specifically, chirality is expected to lead to different SHG responses for left- and right-hand circularly-polarized fundamental beams [34, 85]. This can be quantified by the SHG circular-difference (CD) response defined as

$$CDR = 2\frac{I_{LHC}(2\omega) - I_{RHC}(2\omega)}{I_{LHC}(2\omega) + I_{RHC}(2\omega)}, \tag{6.3}$$

where LHC and RHC refer to the circular polarizations of the fundamental beam.

In the experiments, we observed a general trend that the CD response decreases as the gap size increases, which is due to less coupling between the more separated bars (Fig. 6.6a). However, the sample with the smallest gap size did not fit to the trend as its CD-value was close to zero. The experimental results were explained by comparing the symmetry of the local field distributions for the two circular polarizations. It is important to note that for ideal structures, the local-field distributions for the two cases should be mirror images of each other.

For the sample with 2 nm gap, the distributions are very similar leading to small chiral signature (Fig. 6.6b,c). The field distributions for the sample with 15 nm gap, on the other hand (Fig. 6.6d,e), are clearly different for the two circular polarizations, which is experimentally observed as a large CD-value. According to our investigations even very small symmetry breaking can significantly affect the local-field distributions in the structure, which leads to a remarkable circular-difference in the second-harmonic response. Note that such an effect is not observable in the linear response.

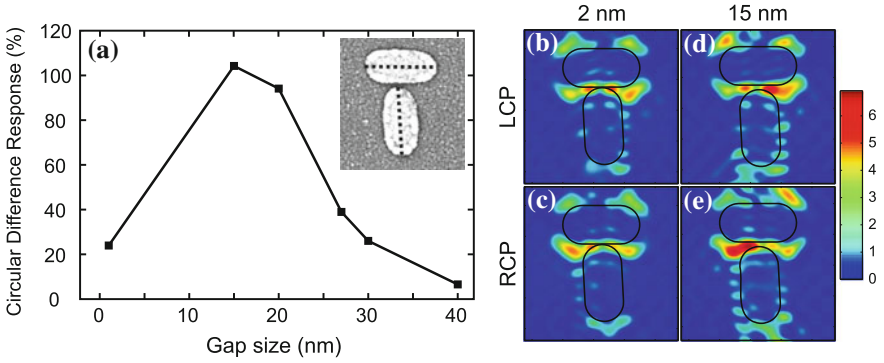

Fig. 6.6 **a** The gap dependence of the circular-difference response. The *inset* shows the scanning electron microscope image of the T-nanodimer with dashed lines illustrating the slant of the vertical bar. **b–e** The distribution of the local field *y*-component for left- and right-hand circular polarizations of the fundamental beam for samples with gap sizes of 2 and 15 nm. Adapted with permission from Ref. [84]. Copyright 2008, American Institute of Physics

6.6 Improved Samples

6.6.1 Key Improvement in Fabrication

It is evident from the results discussed so far that SHG is extremely sensitive to the nanoscale morphology and defects of metal nanostructures even when the linear response behaves as expected. In order to design nanostructures with the desired nonlinear response, samples with higher quality are needed. It is therefore quite fortunate to note that during the last few years, a huge improvement in fabrication methods has been achieved [86], resulting in high-quality nanostructures with parameters pushed up to the fabrication limit [87]. Such an improvement is also evident for our samples. Figure 6.7 shows two samples from different years. Both low- (Fig. 6.7a) and high-quality (Fig. 6.7b) samples were fabricated with the same method. The improvement in the fabrication process is mainly due to a new electron-beam lithography system with better accuracy and stability than the old one. The line quality is improved by smaller beam step size and the improvement of the shape control is due to higher acceleration voltage (100 kV) of the new system.

The effect of the sample quality is seen not only by comparing the scanning electron microscope images (Fig. 6.7), but also in the linear extinction spectra of the plasmon resonances. For the new samples, the extinction peaks are enhanced and their linewidths are narrowed compared to the old samples (Table 6.1). Such results are due to smaller variation in the sample dimensions, leading to less inhomogeneous broadening of the resonance for the new samples.

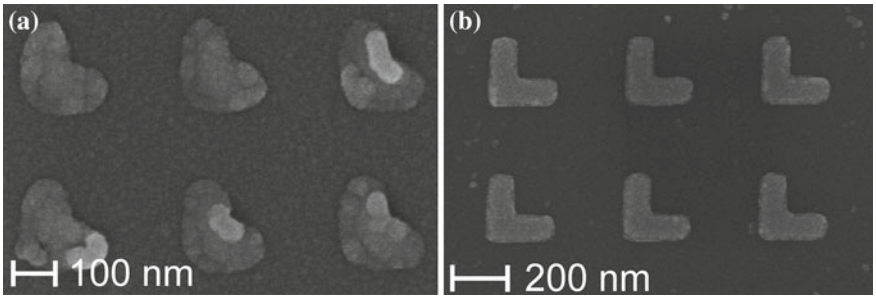

Fig. 6.7 Scanning electron microscope images of arrays of L-shaped nanoparticles of **a** low-quality (from 2004) and **b** high-quality samples (from 2009)

Table 6.1 The details of resonances for low and high-quality samples

Sample	Resonance wavelength (nm)	FWHM (nm)
Low-quality	1060	260
(length 200 nm, width 100 nm, period 400 nm)	1490	420
High-quality	1031	88
(length 250 nm, width 100 nm, period 500 nm)	1555	203

6.6.2 Dipole Limit

We have characterized the new samples of L-shaped particles using the technique described in Sect. 6.3, where the polarization-dependent SHG responses are compared in reflection and transmission and for the metal- and substrate-side incidence of the fundamental beam. The results for a given sample (arm length 250 nm, arm width 100 nm, array period 500 nm) are shown in Fig. 6.8. The four signals are seen to overlap almost completely, which suggests that the response is dominated by the electric-dipole-only part of the nonlinear response tensor [88]. This is in strong contrast to the results of the old samples shown in Fig. 6.4 [35].

Detailed tensor analysis of the results of Fig. 6.8 shows that all multipolar components are suppressed to below 2 % of the dominant electric-dipole component of NRT. Furthermore, due to sample improvement, the SH signals obey the selection rules extremely well and the forbidden signals are much weaker than the allowed ones. The quality of the sample also influences the strength of the second-harmonic radiation, which is enhanced for the case of high-quality samples compared to the low-quality ones.

6.7 Tailored Nonlinear Response

6.7.1 Resonance Domain Effects

The improved sample quality allows fabricating metal nanostructures with designable optical properties, which is a prerequisite for many nanophotonics applications of

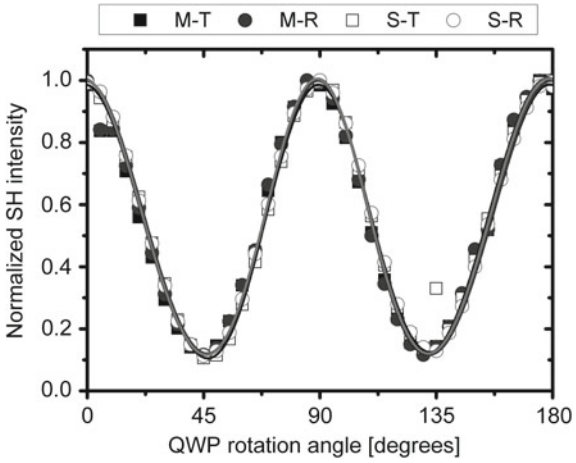

Fig. 6.8 SHG signals from an array of L-shaped gold nanoparticles as function of rotation angle of QWP. Reprinted with permission from Ref. [88]. Copyright 2011, Optical Society of America

the future. As a first demonstration of this possibility, we have utilized arrays of high-quality L-shaped gold nanoparticles and introduced a new concept for tuning the optical properties of plasmonic samples.

Our approach is based on so-called resonance-domain effects, where the period of the structure is of the order of wavelength. In contrast to effective medium samples, where the period must be much smaller than wavelength, the resonance-domain effects allow diffractive coupling between the individual units even when no diffraction orders propagate in free space. By proper design, such effects can be very useful as an additional parameter for tailoring the optical properties of plasmonic arrays. They can lead to spectral narrowing and enhancement of the plasmonic resonances [6–12]. Similar effect has been observed also for purely dielectric structures [89, 90].

We have taken the approach even further by introducing metamolecular samples, where the diffractive coupling between the unit cells depends on the relative orientation of the individual L-shaped gold nanoparticles in a 2 × 2-particle unit cell [91], as shown in Fig. 6.9. Sample A acts as a reference sample with all the L particles oriented in the same way (Fig. 6.9a inset). The coordinate system is based on the (x, y) coordinates of the individual particles. In Sample B, the particles in every other column are rotated by 90° (Fig. 6.9b inset), which implies new eigenpolarizations in a new (u, v) coordinate system. From Sample B to Sample C, the adjacent particles in every other row are interchanged, which appears as an inconsequential modification that does not change the symmetry properties of the sample (Fig. 6.9c inset).

The modifications in the sample layout, however, double its period in one or two directions, opening diffraction orders that match the wavelengths of the plasmon resonances. This is seen to affect the resonances in a significant way leading to either very narrow (Fig. 6.9c) or very broad (Fig. 6.9b) resonances. This approach therefore offers a new degree of freedom in the design of plasmonic arrays.

6.7.2 Tailored SHG Response

The modified properties of samples B and C also strongly influence their SHG properties. There are two reasons for this. First, the change in the mutual orientation of the

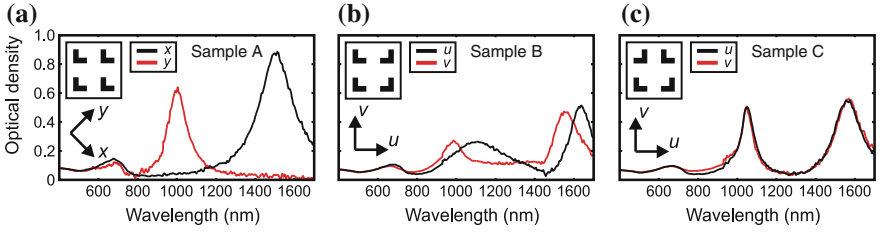

Fig. 6.9 The linear spectra of **a** Sample A, **b** Sample B and **c** Sample C. The *insets* show the layout of the particles in the 2 × 2-particle cells. The coordinate systems are also shown. Adapted with permission from Ref. [92]. Copyright 2012, American Chemical Society

particles is expected to modify the tensorial properties of the SHG response, which is obtained as the orientational average of the response of individual particles. By this approach, one should be able to predict the SHG response of samples B and C from that of the reference sample A.

However, the second reason proved to be even more important than the orientational distribution [92]. This arises from the fact that the efficiency of SHG depends strongly on the existence of a resonance close to the fundamental laser wavelength. The second-harmonic signal therefore depends both on the location of the resonance peak and the width of the resonance. Sample C with a very narrow resonance thus significantly enhances the second-harmonic signal, whereas the broadened resonance of Sample B leads to decrease in the signal (Fig. 6.10).

The difference between Samples B and C is quite significant, because the maxima of the black curves in Figs. 6.10a, b differ by a factor of 50. By combining the orientational issues and the resonance-domain effects, we have thus been able to significantly tailor the tensorial SHG properties of the samples by a minor change in the sample layout.

6.8 Numerical Modeling

6.8.1 Challenges in Modeling

Numerical simulations and modeling have become an indispensable aid in the study of optical properties of nanoparticles and metamaterials. Although the optical properties of plasmonic particles can often be modeled as a classical electrodynamical scattering problem, this must be done with extreme care in order to get reliable results [93, 94].

For the case of a spherical or an infinite cylindrical particle, the scattering problem can be solved in closed form as a series expansion of multipoles [27]. For SHG,

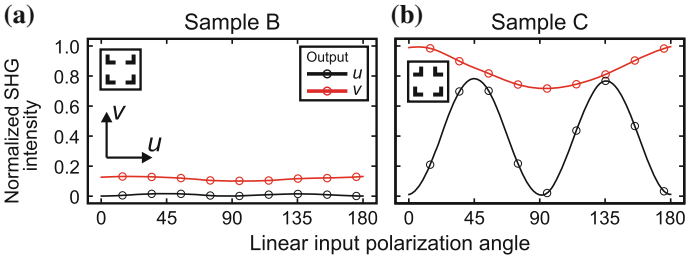

Fig. 6.10 Second-harmonic intensity from **a** Sample B and **b** Sample C as a function of the linear input polarization state for *u*- and *v*-polarized outputs. The polarization rotation starts from *u* polarization reaching the *v*-polarized input at 90°. Insets show the layouts of the samples. Adapted with permission from Ref. [92]. Copyright 2012, American Chemical Society

however, the particle geometry is usually more complicated [41, 59, 83] and such methods, relying on the separation of variables, are not feasible. Most numerical methods then divide the solution domain into simple primitives, such as n-simplexes, and represent the fields by some low-degree polynomials [95]. In addition, plasmon resonances usually lead to field variations on a sub-wavelength scale, which makes accurate field representation a necessity [83]. The resonances can also render the problem sensitive, so that small variations in the excitation (also due to round-off errors) can give rise to abrupt changes in the solution.

In plasmonic scattering problems, the division of methods into time-domain and frequency-domain methods is also crucial. This is because the material properties are highly frequency-dependent [1] and taking into account the dispersive material response in the time-domain requires either time-consuming evaluation of the response convolution or the use of simplified models obtained from first-principles description of the response. Most often, frequency-domain descriptions are more convenient, because they offer more flexibility. If desired, the frequency-dependent material parameters can be calculated from first principles. On the other hand, the parameters can also be described phenomenologically or obtained directly from experiments.

These challenges are further augmented for nonlinear problems. The second-order response can originate from the dipolar response at material surfaces [96], requiring accurate representation of the surfaces. The response, however, can also arise from the atomic-level higher multipoles in the bulk medium [97]. Consequently, a volume source may exist also in the case where the solution domain is divided into parts homogeneous in material properties. This source involves derivatives of the fields, which can be problematic for numerical schemes near the interfaces between different materials.

6.8.2 General Approach for Nonlinear Problems

The three-dimensional electromagnetic scattering problem is described in the frequency-domain by the vectorial Helmholtz equations for the electric and magnetic fields and by the Silver-Müller radiation conditions [98]. To study SHG in the undepleted-pump approximation, one can then first solve the fundamental fields described by source-free Helmholtz equations, and then solve the second-harmonic fields described by Helmholtz equations with a polarization source, which is related to the fundamental fields by the second-order susceptibility.

The nanostructure is often composed of piece-wise homogeneous media and it is most convenient to divide the domain of the boundary value problem accordingly. The electromagnetic interface conditions are posed at the resulting domain interfaces. In traditional linear problems, the tangential components of the electric and magnetic fields are continuous at the interfaces. In the presence of a dipolar second-order surface source, the tangential fields have jump discontinuities [24]. The nonlinear source is then invoked via the interface conditions.

In geometries, where the Helmholtz equation is not separable, more general, but in certain sense approximate, methods must be employed. The numerical methods can be divided into differential-operator and integral-operator methods. In the latter, the Helmholtz equations are first transformed into integral equations by the use of Green's functions [99, 100]. This allows one to impose the radiation conditions analytically and the solution can be represented in a compact subset of the original domain. Although the integral-operator approach is not generally applicable to nonlinear problems, it can be used to model harmonic generation within the undepleted pump approximation.

6.8.3 Recent Approaches for Modeling SHG

The second-harmonic scattering problem has been addressed only recently in general geometries, although it has been treated in simple geometries for a long time. SHG from plane surfaces and stratified media has been done using the plane-wave Green's function formalism [101]. Recently, SHG from nanodefects on a planar surface has also been modeled [102, 103]. Multipole solution of SHG from spherical particles has been derived for arbitrary size parameters and especially the properties of spheres with a small size parameter have been studied [104–106]. Multipole expansion has also been used to model sum-frequency generation in spheres [107] and to model SHG from collections of spheres [108]. The multiple scattering matrix method has been applied for modeling SHG from cylindrical nanowires and from photonic crystals [109, 110]. For particles whose permittivity is close to that of the surrounding medium, the Rayligh-Gans-Debye approximation provides a good approximation, also for modeling SHG [111].

SHG from metal nanostructure arrays has been modeled by using the finite-difference time-domain method [60, 112] and the Fourier modal method [113, 114]. The finite element method has been used to study second-harmonic scattering and multipolar response from particles that slightly differ from spheres [31, 32].

In recent years, the integral-operator methods have gained popularity due to rapid developments in the theory and since computational power has increased. The volume integral method has been applied to model second-harmonic microscopy of nanoparticles [115]. Recently it has also been applied to model SHG from nanowires, nanoantennas and from nano-resonator chains [116, 117]. We have recently applied the surface integral-operator boundary-element method (BEM) for modeling SHG from arbitrary nanoparticles [118], which will be described in the following section.

6.8.4 Boundary-Element Method

BEM has been widely used for modeling scattering from ideally conducting and dielectric bodies as well as in antenna problems. More recently, it has also gained

popularity in modeling the linear response of plasmonic structures [79, 119–122]. In our use, BEM has proven to be excellent in terms of accuracy, efficiency and versatility. For our present implementation, we assume that the local nonlinear response of the metal can be described by the surface susceptibility.

If a bounded domain consists of a homogeneous electromagnetic medium, it turns out that the electric and magnetic fields are uniquely determined by their tangential components on the domain boundary surface. Further, a linear mapping from these surface fields to fields in the whole domain exists. This is facilitated by the Stratton-Chu equations [123]. The mapping is given by integro-differential operators, which involve weakly and strongly singular kernels. The result holds even for unbounded domains, if the fields are required to satisfy the Silver-Müller radiation conditions. This motivates the use of these integral operators as a base for a numerical method for obtaining approximate solutions to the scattering problem. The operators are then used for each domain separately to formulate the problem entirely on compact boundary surfaces (Fig. 6.11a).

By using the integral operators for representing the fields, the Helmholtz equations and the radiation conditions are implicitly satisfied and we need to enforce a set of integral equations explicitly. This is usually done approximately by using, e.g., the Rao-Wilton-Glisson triangular patch basis functions illustrated in Fig. 6.11b [124] and the method of moments [125]. In the second-harmonic scattering problem, the representation of the fields remains the same as in the linear problem, but we then enforce the interface conditions involving the surface polarization source.

The most significant advantages of BEM are that the unknowns only appear over a compact surface and the surface is conveniently described for the SHG problem. It is possible to use any time-harmonic excitation source, such as a focused Gaussian beam or an electric dipole. Spatially periodic problems can be modeled by using the periodic Green's function, whose evaluation can be performed efficiently by the Ewald's method [126].

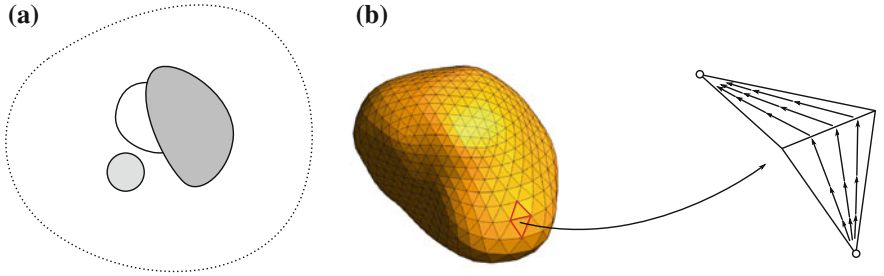

Fig. 6.11 **a** The solution domain decomposition characteristic to BEM. The *dashed line* represents the outer boundary, which can be taken infinitely far away from the scatterers. The *solid lines* represent interfaces between different subdomains, where material properties are homogeneous. Unknown fields appear only over the *solid lines*. **b** Illustration of a typical *triangulated* surface used in BEM. A Rao-Wilton-Glisson function, supported by a *triangle* pair, is shown, with *arrows* representing surface current density

A drawback of BEM is that the scheme results in a dense and, in general, non-Hermitian system matrix, which then leads to quadratic scaling in memory requirements and in the large electrical size limit to cubic scaling in solution time if direct solvers are used. These scalability issues can be well mitigated by the use of the fast multipole method [127] or the adaptive cross-approximation method [128], which can lead to $n\log(n)$ or even linear scaling with respect to the number of unknowns. A practical difficulty of BEM is that the singular integral kernels require special treatment, such as singularity subtraction or some regularization such as the Duffy transform, before the matrix elements can be evaluated accurately by numerical integration.

To illustrate second-harmonic scattering from plasmonic nanoparticles, we consider an L-shaped gold particle illustrated in Fig. 6.12a. The arm length is 250 nm, arm width is 100 nm and the particle thickness is 20 nm. As excitation, we use a plane wave propagating in the z-direction and polarized in x- or y-directions in the coordinate system of Fig. 6.12a. In Fig. 6.12b the extinction spectra are shown, and we can see two resonances for both polarizations. The long wavelength resonances at λ_1 and λ_3 are related to plasmon oscillations along the arms and the common resonance is related to plasmon oscillations along the width of the arms. In Fig. 6.12c the total scattered second-harmonic power is shown as a function of the fundamental wavelength. It shows that we always get some resonance enhancement. The field enhancement is strongest at resonances of high extinction and thus it is a rather non-trivial fact that we actually predict more second-harmonic signal at the weakest resonances. A similar behavior is observed for the second-harmonic intensity in the forward direction, although it is not shown. In this example, the enhancement results primarily from resonances at the fundamental wavelength, although slight

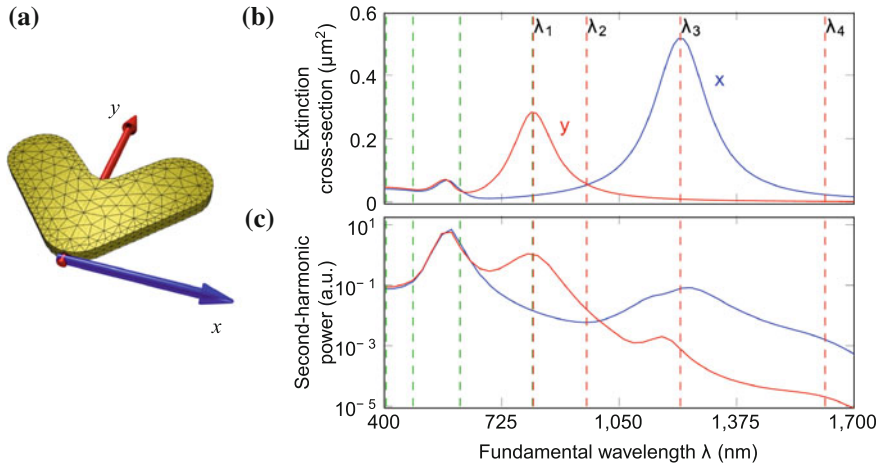

Fig. 6.12 **a** L-shaped gold nanoparticle with its coordinate system, **b** x- and y- polarized extinction spectra, **c** corresponding second-harmonic signal

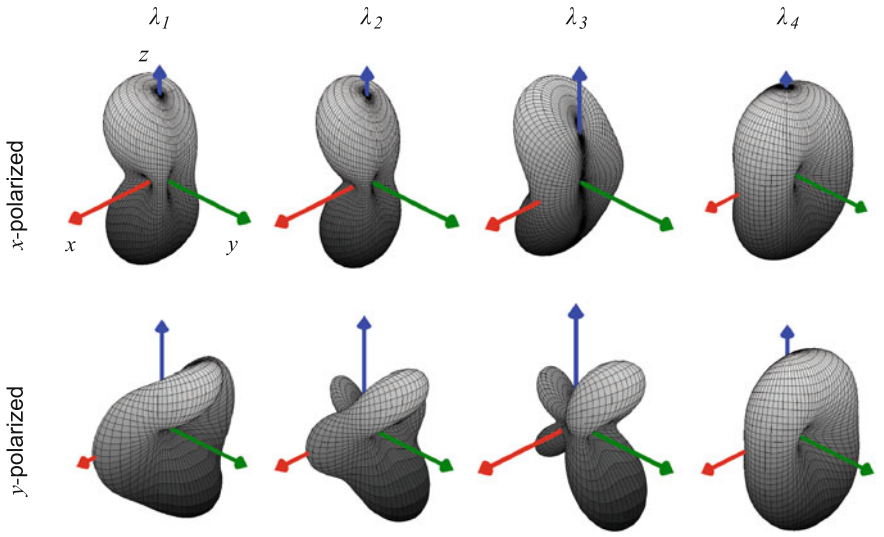

Fig. 6.13 Second-harmonic radiation patterns at resonance wavelengths λ_1, λ_2, $\lambda_3$and λ_4 for both incident wave polarizations (see Fig. 6.12)

enhancement due to resonances at the second-harmonic frequency can be seen in the logarithmic scale. To illustrate the multipolar nature of the second-harmonic scattering, the radiation patterns from a single particle are shown for different resonance wavelengths in Fig. 6.13.

6.9 Outlook

During the past 10–20 years there has been a growing interest in the optical properties of metal nanostructures and metamaterials, [5, 129], resulting in the birth of the field of nanoplasmonics. This development has been largely motivated by the possibility of enhancing local electromagnetic fields in the nanostructures and their future prospects in nanophotonics applications. It is therefore evident that after the great progress in understanding the linear optical properties of nanoplasmonic structures, their nonlinear properties will receive more and more attention.

In this Chapter, we have presented a comprehensive overview of our own work regarding second-order nonlinear properties of arrays of non-centrosymmetric nanoparticles. We have shown that the nonlinear response of such structures can exhibit extreme sensitivity to the smallest details of the structure, including surface defects and deviations of the shape from the ideal. However, recent improvements in sample quality have brought us to the point where the response can be described by effective electric-dipole nonlinearity with the expected symmetry rules fulfilled to a very good accuracy. We consider this achievement a significant milestone, which

opens the path towards metamaterials with truly tailorable nonlinear properties. We have also presented the first example of this possibility by modifying the nonlinear response by the detailed arrangement of the particles in the array.

In spite of this experimental progress, there are still several theoretical challenges in the understanding of the nonlinear properties of plasmonic metal nanostructures. For a proper approach, one would have to account for the locally varying fields, nonlinear responses, and nonlinear sources. However, it is not clear at present as to what the relative importance of the surface and bulk effects in the local second-order response are. Our experiments on planar metal films suggest that surface terms dominate [130]. Some theoretical approaches, on the other hand, have emphasized bulk terms [59, 131], whereas others indicate that the weight of surface and bulk effects depends on the experiment [117]. It is not even clear whether the various approaches are mutually compatible, representing different limiting cases of the same underlying approach.

The role of surface and bulk effects in the local nonlinear response may have significant implications for the optimization of the local-field distribution in the metal structure. The plasmonic resonances typically confine the strongest fields into small volumes at the ends of the nanoparticles. If the local response mainly arises from the local surface response, the present approaches poorly utilize the total surface area of the metal particles. It will be interesting to see whether completely new sample designs can be conceived, where the strong fields are spread over larger surface areas.

The role of resonance enhancement as such is better understood. As usual, a nonlinear response is enhanced when any combination of the interacting frequencies is resonant with the nonlinear material. In contrast to traditional atomic, molecular, and crystal systems, where resonant transition between the energy levels of the system play a role, the resonances of plasmonic systems arise mainly from the local-field factors [132]. It has recently been suggested that, for harmonic generation, a resonance at the fundamental frequency is beneficial, whereas a resonance at the harmonic frequency is just a loss mechanism [61]. However, this may also be due to fact that the strong local fields at the fundamental and second-harmonic frequency do not overlap spatially. In principle, a resonance at the harmonic output frequency should also be beneficial, as is the case for other cases where plasmonic systems are used to enhance radiation. It therefore remains to be seen whether the nonlinear responses could be further enhanced by simultaneous resonances at multiple wavelengths.

Losses are nevertheless a significant challenge for plasmonic systems. For now, the strongest nonlinear responses have been obtained at resonances with high losses. One approach to mitigate this may be to utilize diffractive coupling between the particles. It can lead to sharper resonances, which may allow optimizing the losses and resonance enhancement in an attractive way. Another possibility is to use the higher-order plasmon resonances, which can also enhance the nonlinear response without significantly increasing the losses.

Additional routes for optimizing the nonlinear optical properties of metal nanostructures can be found by combining several particles into more complex structures. We have demonstrated this by the T-nanodimers, where the coupling between the bars significantly affected the nonlinear response. In the future, the dimensions of

the bars need to be optimized for stronger coupling than so far. Also, completely new oligomeric structures provide unexplored avenues for optimizing the plasmonic resonances [129], which have not yet been explored for nonlinear optics.

It is fair to say that our recent achievements on the dipole limit of the second-harmonic response and on tailoring the nonlinear response by particle ordering represent only a starting point for future work on nonlinear plasmonics. Only now do the improved techniques allow the fabrication of nanostructures whose nonlinear properties can be designed by the structural features of the samples. Such control will be paramount when various new approaches are explored for the optimization of the nonlinear responses for various applications.

Acknowledgments We thank B. K. Canfield, G. Genty, K. Koskinen, S. Kujala, H. Pietarinen, R. Siikanen, S. Suuriniemi, Y. Svirko, and J. Turunen for fruitful discussions and/or help in measurements. This work was supported by the Academy of Finland (132438 and 134980), by the Graduate School of the Tampere University of Technology, by the Finnish Foundation for Technology Promotion, and by the Wihuri Foundation.

References

1. U. Kreibig, M. Vollmer, *Optical Properties of Metal Clusters. Springer Series in Materials Science* (Springer, New York, 1995)
2. S. Maier, *Plasmonics: Fundamentals and Applications* (Springer, New York, 2007)
3. K. Kelly, E. Coronado, L. Zhao, G. Schatz, The optical properties of metal nanoparticles: The influence of size, shape, and dielectric environment. J. Phys. Chem. B **107**, 668–677 (2003)
4. V.M. Shalaev, Optical negative-index metamaterials. Nat. Photon. **1**, 41 (2007)
5. C.M. Soukoulis, M. Wegener, Past achievements and future challenges in the development of three-dimensional photonic metamaterials. Nat. Photon. **5**, 523–530 (2011)
6. S. Linden, J. Kuhl, H. Giessen, Controlling the interaction between light and gold nanoparticles: Selective suppression of extinction. Phys. Rev. Lett. **86**, 4688–4691 (2001)
7. L. Zhao, K.L. Kelly, G.C. Schatz, The extinction spectra of silver nanoparticle arrays: Influence of array structure on plasmon resonance wavelength and width. J. Phys. Chem. B **107**, 7343–7350 (2003)
8. A. Christ, S.G. Tikhodeev, N.A. Gippius, J. Kuhl, H. Giessen, Waveguide-plasmon polaritons: Strong coupling of photonic and electronic resonances in a metallic photonic crystal slab. Phys. Rev. Lett. **91**, 183901 (2003)
9. A. Christ, T. Zentgraf, J. Kuhl, S.G. Tikhodeev, N.A. Gippius, H. Giessen, Optical properties of planar metallic photonic crystal structures: experiment and theory. Phys. Rev. B **70**, 125113 (2004)
10. Y. Chu, E. Schonbrun, T. Yang, K.B. Crozier, Experimental observation of narrow surface plasmon resonances in gold nanoparticle arrays. Appl. Phys. Lett. **93**, 181108 (2008)
11. B. Auguié, W.L. Barnes, Collective resonances in gold nanoparticle arrays. Phys. Rev. Lett. **101**, 143902 (2008)
12. K.D. Ko, A. Kumar, K.H. Fung, R. Ambekar, G.L. Liu, N.X. Fang, K.C. Toussaint, Nonlinear optical response from arrays of au bowtie nanoantennas. Nano Lett. **11**, 61–65 (2011)
13. E. Prodan, C. Radloff, N.J. Halas, P. Nordlander, A hybridization model for the plasmon response of complex nanostructures. Science **302**, 419–422 (2003)
14. T.D. Corrigan, P.W. Kolb, A.B. Sushkov, H.D. Drew, D.C. Schmadel, R.J. Phaneuf, Optical plasmonic resonances in split-ring resonator structures: An improved LC model. Opt. Express **16**, 19850–19864 (2008)

15. K. Aydin, I. Pryce, H. Atwater, Symmetry breaking and strong coupling in planar optical metamaterials. Opt. Express **18**, 13407–13417 (2010)
16. P. Ginzburg, N. Berkovitch, A. Nevet, I. Shor, M. Orenstein, Resonances on-demand for plasmonic nano-particles. Nano Lett. **11**, 2329–2333 (2011)
17. K. Li, M.I. Stockman, D.J. Bergman, Self-similar chain of metal nanospheres as an efficient nanolens. Phys. Rev. Lett. **91**, 227402 (2003)
18. M. Stockman, D. Bergman, C. Anceau, S. Brasselet, J. Zyss, Enhanced second-harmonic generation by metal surfaces with nanoscale roughness: Nanoscale dephasing, depolarization, and correlations. Phys. Rev. Lett. **92**, 057402 (2004)
19. K. Kneipp, Y. Wang, H. Kneipp, L.T. Perelman, I. Itzkan, R.R. Dasari, M.S. Feld, Single molecule detection using surface-enhanced Raman scattering (SERS). Phys. Rev. Lett. **78**, 1667–1670 (1997)
20. S. Nie, S.R. Emory, Probing single molecules and single nanoparticles by surface-enhanced Raman scattering. Science **275**, 1102–1106 (1997)
21. P. Guyot-Sionnest, W. Chen, Y. Shen, General considerations on optical second-harmonic generation from surfaces and interfaces. Phys. Rev. B **33**, 8254–8263 (1986)
22. T.F. Heinz, H.W.K. Tom, Y.R. Shen, Determination of molecular orientation of monolayer adsorbates by optical second-harmonic generation. Phys. Rev. A **28**, 1883–1885 (1983)
23. T. Rasing, Y.R. Shen, M.W. Kim, P. Valint, J. Bock, Orientation of surfactant molecules at a liquid-air interface measured by optical second-harmonic generation. Phys. Rev. A **31**, 537–539 (1985)
24. T.F. Heinz, in *Nonlinear Surface Electromagnetic Phenomena*, ed. by H.-E. Ponath, G.I. Stegeman. Second-Order Nonlinear Optical Effects at Surfaces and Interfaces (Elsevier, Amsterdam, 1991), pp. 353–416
25. B. Canfield, S. Kujala, K. Laiho, K. Jefimovs, J. Turunen, M. Kauranen, Chirality arising from small defects in gold nanoparticle arrays. Opt. Express **14**, 950–955 (2006)
26. G. Mie, Beiträge zur optik trüber medien, speziell kolloidaler metallösungen. Annal. der Phys. **330**, 377–445 (1908)
27. C.F. Bohren, D.R. Huffman, Absorption and Scattering by an Arbitrary Particle. Wiley-VCH Verlag GmbH, 2007)
28. B. Canfield, S. Kujala, K. Jefimovs, Y. Svirko, J. Turunen, M. Kauranen, A macroscopic formalism to describe the second-order nonlinear optical response of nanostructures. J. Opt. A **8**, S278–S284 (2006)
29. R.W. Boyd, *Nonlinear Optics*, 3rd edn. (Academic Press, San Diego, 2008)
30. J. Nappa, G. Revillod, I. Russier-Antoine, E. Benichou, C. Jonin, P.-F. Brevet, Electric dipole origin of the second harmonic generation of small metallic particles. Phys. Rev. B **71**, 165407 (2005)
31. G. Bachelier, I. Russier-Antoine, E. Benichou, C. Jonin, P.-F. Brevet, Multipolar second-harmonic generation in noble metal nanoparticles. J. Opt. Soc. Am. B **25**, 955–960 (2008)
32. J. Butet, G. Bachelier, I. Russier-Antoine, C. Jonin, E. Benichou, P.-F. Brevet, Interference between selected dipoles and octupoles in the optical second-harmonic generation from spherical gold nanoparticles. Phys. Rev. Lett. **105**, 077401 (2010)
33. L. Novotny, B. Hecht, Principles of Nano-optics, 1st edn. (Cambridge University Press, Cambridge, 2007)
34. M. Kauranen, T. Verbiest, S. Elshocht, A. Persoons, Chirality in surface nonlinear optics. Opt. Mater. **9**, 286–294 (1998)
35. M. Zdanowicz, S. Kujala, H. Husu, M. Kauranen, Effective medium multipolar tensor analysis of second-harmonic generation from metal nanoparticles. New J. Phys. **13**, 023025 (2011)
36. B. Lamprecht, A. Leitner, F. Aussenegg, SHG studies of plasmon dephasing in nanoparticles. Appl. Phys. B **68**, 419–423 (1999)
37. H. Tuovinen, M. Kauranen, K. Jefimovs, P. Vahimaa, T. Vallius, J. Turunen, N.-V. Tkachenko, H. Lemmetyinen, Linear and second-order nonlinear optical properties of arrays of noncentrosymmetric gold nanoparticles. J. Nonlinear Opt. Phys. Mater. **11**, 421–432 (2002)

38. B. Canfield, K. Kujala, K. Jefimovs, J. Turunen, M. Kauranen, Linear and nonlinear optical responses influenced by broken symmetry in an array of gold nanoparticles. Opt. Express **12**, 5418–5423 (2004)
39. B. Canfield, S. Kujala, K. Jefimovs, T. Vallius, J. Turunen, M. Kauranen, Polarization effects in the linear and nonlinear optical responses of gold nanoparticle arrays. J. Opt. A **7**, S110–S117 (2005)
40. B. Canfield, H. Husu, J. Kontio, J. Viheriälä, T. Rytkönen, T. Niemi, E. Chandler, A. Hrin, J. Squier, M. Kauranen, Inhomogeneities in the nonlinear tensorial responses of arrays of gold nanodots. New J. Phys. **10**, 013001 (2008)
41. S. Kujala, B. Canfield, M. Kauranen, Y. Svirko, J. Turunen, Multipolar analysis of second-harmonic radiation from gold nanoparticles. Opt. Express **16**, 17196–17208 (2008)
42. S. Kujala, B. Canfield, M. Kauranen, Y. Svirko, T. Turunen, Multipole interference in the second-harmonic optical radiation from gold nanoparticles. Phys. Rev. Lett. **98**, 167403 (2007)
43. C.K. Chen, A.R.B. de Castro, Y.R. Shen, Surface-enhanced second-harmonic generation. Phys. Rev. Lett. **46**, 145–148 (1981)
44. I.I. Smolyaninov, A.V. Zayats, C.C. Davis, Near-field second harmonic generation from a rough metal surface. Phys. Rev. B **56**, 9290–9293 (1997)
45. A.V. Zayats, T. Kalkbrenner, V. Sandoghdar, J. Mlynek, Second-harmonic generation from individual surface defects under local excitation. Phys. Rev. B **61**, 4545–4548 (2000)
46. S.I. Bozhevolnyi, J. Beermann, V. Coello, Direct observation of localized second-harmonic enhancement in random metal nanostructures. Phys. Rev. Lett. **90**, 197403 (2003)
47. C. Anceau, S. Brasselet, J. Zyss, P. Gadenne, Local second-harmonic generation enhancement on gold nanostructures probed by two-photon microscopy. Opt. Lett. **28**, 713–715 (2003)
48. R. Jin, J.E. Jureller, H.Y. Kim, N.F. Scherer, Correlating second harmonic optical responses of single Ag nanoparticles with morphology. J. Am. Chem. Soc. **127**, 12482–12483 (2005)
49. M. Zavelani-Rossi, M. Celebrano, P. Biagioni, D. Polli, M. Finazzi, L. Duò, G. Cerullo, M. Labardi, M. Allegrini, J. Grand, P.-M. Adam, Near-field second-harmonic generation in single gold nanoparticles. Appl. Phys. Lett. **92**, 093119 (2008)
50. S. Takahashi, A.V. Zayats, Near-field second-harmonic generation at a metal tip apex. Appl. Phys. Lett. **80**, 3479–3481 (2002)
51. A. Bouhelier, M. Beversluis, A. Hartschuh, L. Novotny, Near-field second-harmonic generation induced by local field enhancement. Phys. Rev. Lett. **90**, 013903 (2003)
52. C.C. Neacsu, G.A. Reider, M.B. Raschke, Second-harmonic generation from nanoscopic metal tips: Symmetry selection rules for single asymmetric nanostructures. Phys. Rev. B **71**, 201402 (2005)
53. J. Kontio, H. Husu, J. Simonen, M. Huttunen, J. Tommila, M. Pessa, M. Kauranen, Nanoimprint fabrication of gold nanocones with 10 nm tips for enhanced optical interactions. Opt. Lett. **34**, 1979–1981 (2009)
54. A. Nahata, R.A. Linke, T. Ishi, K. Ohashi, Enhanced nonlinear optical conversion from a periodically nanostructured metal film. Opt. Lett. **28**, 423–425 (2003)
55. Y. Zhang, N.K. Grady, C. Ayala-Orozco, N.J. Halas, Three-dimensional nanostructures as highly efficient generators of second harmonic light. Nano Lett. **11**, 5519–5523 (2011)
56. M. Klein, C. Enkrich, M. Wegener, S. Linden, Second-harmonic generation from magnetic metamaterials. Science **313**, 502–504 (2006)
57. M.W. Klein, M. Wegener, N. Feth, S. Linden, Experiments on second- and third-harmonic generation from magnetic metamaterials. Opt. Express **15**, 5238–5247 (2007)
58. M.W. Klein, M. Wegener, N.-A. Feth, S. Linden, Experiments on second- and third-harmonic generation from magnetic metamaterials: Erratum. Opt. Express **16**, 8055–8055 (2008)
59. N. Feth, S. Linden, M. Klein, M. Decker, F. Niesler, Y. Zeng, W. Hoyer, J. Liu, S. Koch, J. Moloney, M. Wegener, Second-harmonic generation from complementary split-ring resonators. Opt. Lett. **33**, 1975–1977 (2008)
60. Y. Zeng, W. Hoyer, J. Liu, S.W. Koch, J.V. Moloney, Classical theory for second-harmonic generation from metallic nanoparticles. Phys. Rev. B **79**, 235109 (2009)

61. F.B.P. Niesler, N. Feth, S. Linden, M. Wegener, Second-harmonic optical spectroscopy on split-ring-resonator arrays. Opt. Lett. **36**, 1533–1535 (2011)
62. T.W. Ebbesen, H.J. Lezec, H.F. Ghaemi, T. Thio, P.A. Wolff, Extraordinary optical transmission through sub-wavelength hole arrays. Nature **391**, 667–669 (1998)
63. J.A.H. van Nieuwstadt, M. Sandtke, R.H. Harmsen, F.B. Segerink, J.C. Prangsma, S. Enoch, L. Kuipers, Strong modification of the nonlinear optical response of metallic subwavelength hole arrays. Phys. Rev. Lett. **97**, 146102 (2006)
64. T. Xu, X. Jiao, G.-P. Zhang, S. Blair, Second-harmonic emission from sub-wavelength apertures: Effects of aperture symmetry and lattice arrangement. Opt. Express **15**, 13894–13906 (2007)
65. F. Eftekhari, R. Gordon, Enhanced second harmonic generation from noncentrosymmetric nanohole arrays in a gold film. IEEE J. Sel. Top. Quant. Electron. **14**, 1552–1558 (2008)
66. A. Lesuffleur, L.K. Swaroop Kumar, R. Gordon, Enhanced second harmonic generation from nanoscale double-hole arrays in a gold film. Appl. Phys. Lett. **88**, 261104 (2006)
67. M.D. McMahon, R. Lopez, R.F. Haglund, E.A. Ray, P.H. Bunton, Second-harmonic generation from arrays of symmetric gold nanoparticles. Phys. Rev. B **73**, 041401 (2006)
68. M. McMahon, D. Ferrara, C. Bowie, R. Lopez, Second harmonic generation from resonantly excited arrays of gold nanoparticles. Appl. Phys. B **87**, 256–265 (2007)
69. J. Nappa, I. Russier-Antoine, E. Benichou, C. Jonin, P. Brevet, Second harmonic generation from small gold metallic particles: From the dipolar to the quadrupolar response. J. Chem. Phys. **125**, 184712 (2006)
70. I. Russier-Antoine, E. Benichou, G. Bachelier, C. Jonin, P.F. Brevet, Multipolar contributions of the second harmonic generation from silver and gold nanoparticles. J. Phys. Chem. C **111**, 9044–9048 (2007)
71. J. Duboisset, I. Russier-Antoine, E. Benichou, G. Bachelier, C. Jonin, P.F. Brevet, Single metallic nanoparticle sensitivity with hyper Rayleigh scattering. J. Phys. Chem. C **113**, 13477–13481 (2009)
72. J. Butet, J. Duboisset, G. Bachelier, I. Russier-Antoine, E. Benichou, C. Jonin, P.-F. Brevet, Optical second harmonic generation of single metallic nanoparticles embedded in a homogeneous medium. Nano Lett. **10**, 1717–1721 (2010)
73. J. Butet, G. Bachelier, J. Duboisset, F. Bertorelle, I. Russier-Antoine, C. Jonin, E. Benichou, P.-F. Brevet, Three-dimensional mapping of single gold nanoparticles embedded in a homogeneous transparent matrix using optical second-harmonic generation. Opt. Express **18**, 22314–22323 (2010)
74. G. Bachelier, J. Butet, I. Russier-Antoine, C. Jonin, E. Benichou, P.-F. Brevet, Origin of optical second-harmonic generation in spherical gold nanoparticles: Local surface and nonlocal bulk contributions. Phys. Rev. B **82**, 235403 (2010)
75. C. Awada, C. Jonin, F. Kessi, P. Adam, S. Kostcheev, R. Bachelot, P. Royer, M. Samah, I. Russier-Antoine, E. Benichou, G. Bachelier, P. Brevet, Polarized second harmonic response of square, hexagonal and random arrays of gold metallic nanocylinders. Opt. Mater. **33**, 1440–1444 (2011)
76. C. Awada, F. Kessi, C. Jonin, P.M. Adam, S. Kostcheev, R. Bachelot, P. Royer, I. Russier-Antoine, E. Benichou, G. Bachelier, P.F. Brevet, On- and off-axis second harmonic generation from an array of gold metallic nanocylinders. J. Appl. Phys. **110**, 023109 (2011)
77. T. Atay, J.-H. Song, A. Nurmikko, Strongly interacting plasmon nanoparticle pairs: From dipole-dipole interaction to conductively coupled regime. Nano Lett. **4**, 1627–1631 (2004)
78. J. Aizpurua, G.W. Bryant, L.J. Richter, F.J.G. De Abajo, B.K. Kelley, T. Mallouk, Optical properties of coupled metallic nanorods for field-enhanced spectroscopy. Phys. Rev. B **71**, 235420 (2005)
79. I. Romero, J. Aizpurua, G.W. Bryant, F.J.G. De Abajo, Plasmons in nearly touching metallic nanoparticles: Singular response in the limit of touching dimers. Opt. Express **14**, 9988–9999 (2006)
80. A. Sundaramurthy, K.B. Crozier, G.S. Kino, D.P. Fromm, P.J. Schuck, W.E. Moerner, Field enhancement and gap-dependent resonance in a system of two opposing tip-to-tip Au nanotriangles. Phys. Rev. B **72**, 165409 (2005)

81. M. Danckwerts, L. Novotny, Optical frequency mixing at coupled gold nanoparticles. Phys. Rev. Lett. **98**, 026104 (2007)
82. K. Li, M.I. Stockman, D.J. Bergman, Enhanced second harmonic generation in a self-similar chain of metal nanospheres. Phys. Rev. B **72**, 153401 (2005)
83. B. Canfield, H. Husu, J. Laukkanen, B. Bai, M. Kuittinen, J. Turunen, M. Kauranen, Local field asymmetry drives second-harmonic generation in noncentrosymmetric nanodimers. Nano Lett. **7**, 1251–1255 (2007)
84. H. Husu, B. Canfield, J. Laukkanen, B. Bai, M. Kuittinen, J. Turunen, M. Kauranen, Chiral coupling in gold nanodimers. Appl. Phys. Lett. **93**, 183115 (2008)
85. J. Maki, M. Kauranen, A. Persoons, Surface second-harmonic generation from chiral materials. Phys. Rev. B **51**, 1425–1434 (1995)
86. P. Biagioni, J.-S. Huang, B. Hecht, Nanoantennas for visible and infrared radiation. Rep. Prog. Phys. **75**, 024402 (2012)
87. H. Duan, A.I. Fernandez-Dominguez, M. Bosman, S.A. Maier, J.K.W. Yang, Nanoplasmonics: Classical down to the nanometer scale. Nano Lett. **12**, 1683–1689 (2012)
88. R. Czaplicki, M. Zdanowicz, K. Koskinen, J. Laukkanen, M. Kuittinen, M. Kauranen, Dipole limit in second-harmonic generation from arrays of gold nanoparticles. Opt. Express **19**, 26866–26871 (2011)
89. M. Siltanen, S. Leivo, P. Voima, M. Kauranen, P. Karvinen, P. Vahimaa, M. Kuittinen, Strong enhancement of second-harmonic generation in all-dielectric resonant waveguide grating. Appl. Phys. Lett. **91**, 111109 (2007)
90. A. Saari, G. Genty, M. Siltanen, P. Karvinen, P. Vahimaa, M. Kuittinen, M. Kauranen, Giant enhancement of second-harmonic generation in multiple diffraction orders from sub-wavelength resonant waveguide grating. Opt. Express **18**, 12298–12303 (2010)
91. H. Husu, J. Mäkitalo, R. Siikanen, G. Genty, H. Pietarinen, J. Lehtolahti, J. Laukkanen, M. Kuittinen, M. Kauranen, Spectral control in anisotropic resonance-domain metamaterials. Opt. Lett. **36**, 2375–2377 (2011)
92. H. Husu, R. Siikanen, J. Mäkitalo, J. Lehtolahti, J. Laukkanen, M. Kuittinen, M. Kauranen, Metamaterials with tailored nonlinear optical response. Nano Lett. **12**, 673–677 (2012)
93. M. Karamehmedovic, R. Schuh, V. Schmidt, T. Wriedt, C. Matyssek, W. Hergert, A. Stalmashonak, G. Seifert, O. Stranik, Comparison of numerical methods in near-field computation for metallic nanoparticles. Opt. Express **19**, 8939–8953 (2011)
94. M.G. Araújo, J.M. Taboada, D.M. Solís, J. Rivero, L. Landesa, F. Obelleiro, Comparison of surface integral equation formulations for electromagnetic analysis of plasmonic nanoscatterers. Opt. Express **20**, 9161–9171 (2012)
95. R. Garg, *Analytical and Computational Methods in Electromagnetics. Artech House Electromagnetic Analysis Series* (Artech House, London, 2008)
96. Y.R. Shen, Surface properties probed by second-harmonic and sum-frequency generation. Nature **337**, 519–525 (1989)
97. N. Bloembergen, R. Chang, S. Jha, C. Lee, Optical second-harmonic generation in reflection from media with inversion symmetry. Phys. Rev. **174**, 813–822 (1968)
98. D. Colton, R. Kress, *Integral Equation Methods in Scattering Theory. Pure and Applied Mathematics Series* (Krieger Publishing Company, Malabar, 1991)
99. J.D. Jackson, *Classical Electrodynamics*, 2nd edn. (Wiley, New York, 1975)
100. W. Gibson, *The Method of Moments in Electromagnetics. Electrical Engineering* (Chapman and Hall/CRC, New York, 2008)
101. J. Sipe, New green-function formalism for surface optics. J. Opt. Soc. Am. B **4**, 481–498 (1987)
102. L. Cao, N.C. Panoiu, R.M. Osgood, Surface second-harmonic generation from surface plasmon waves scattered by metallic nanostructures. Phys. Rev. B **75**, 205401 (2007)
103. L. Cao, N.C. Panoiu, R.D.R. Bhat, R.M. Osgood, Surface second-harmonic generation from scattering of surface plasmon polaritons from radially symmetric nanostructures. Phys. Rev. B **79**, 235416 (2009)

104. J. Dewitz, W. Hübner, K. Bennemann, Theory for nonlinear Mie-scattering from spherical metal clusters. Zeits. Phys. D Atoms, Mol. Clusters **37**, 75–84 (1996)
105. J. Dadap, J. Shan, T. Heinz, Theory of optical second-harmonic generation from a sphere of centrosymmetric material: small-particle limit. J. Opt. Soc. Am. B **21**, 1328–1347 (2004)
106. Y. Pavlyukh, W. Hübner, Nonlinear Mie scattering from spherical particles. Phys. Rev. B **70**, 245434 (2004)
107. A.G.F. de Beer, S. Roke, Nonlinear Mie theory for second-harmonic and sum-frequency scattering. Phys. Rev. B **79**, 155420 (2009)
108. J. Xu, X. Zhang, Second harmonic generation in three-dimensional structures based on homogeneous centrosymmetric metallic spheres. Opt. Express **20**, 1668–1684 (2012)
109. E. Centeno, D. Felbacq, Second-harmonic emission in two-dimensional photonic crystals. J. Opt. Soc. Am. B **23**, 2257–2264 (2006)
110. C.G. Biris, N.C. Panoiu, Second harmonic generation in metamaterials based on homogeneous centrosymmetric nanowires. Phys. Rev. B **81**, 195102 (2010)
111. A.G.F. de Beer, S. Roke, J.I. Dadap, Theory of optical second-harmonic and sum-frequency scattering from arbitrarily shaped particles. J. Opt. Soc. Am. B **28**, 1374–1384 (2011)
112. W.L. Schaich, Second harmonic generation by periodically-structured metal surfaces. Phys. Rev. B **78**, 195416 (2008)
113. W. Nakagawa, R.-C. Tyan, Y. Fainman, Analysis of enhanced second-harmonic generation in periodic nanostructures using modified rigorous coupled-wave analysis in the undepleted-pump approximation. J. Opt. Soc. Am. A **19**, 1919–1928 (2002)
114. B. Bai, J. Turunen, Fourier modal method for the analysis of second-harmonic generation in two-dimensionally periodic structures containing anisotropic materials. J. Opt. Soc. Am. B **24**, 1105–1112 (2007)
115. S.I. Bozhevolnyi, V.Z. Lozovski, Self-consistent model for second-harmonic near-field microscopy. Phys. Rev. B **61**, 11139–11150 (2000)
116. A. Benedetti, M. Centini, C. Sibilia, M. Bertolotti, Engineering the second harmonic generation pattern from coupled gold nanowires. J. Opt. Soc. Am. B **27**, 408–416 (2010)
117. M. Centini, A. Benedetti, C. Sibilia, M. Bertolotti, Coupled 2D Ag nano-resonator chains for enhanced and spatially tailored second harmonic generation. Opt. Express **19**, 8218–8232 (2011)
118. J. Mäkitalo, S. Suuriniemi, M. Kauranen, Boundary element method for surface nonlinear optics of nanoparticles. Opt. Express **19**, 23386–23399 (2011)
119. J. Aizpurua, P. Hanarp, D.S. Sutherland, M. Käll, G.W. Bryant, F. Garcia de Abajo, Optical properties of gold nanorings. J. Phys. Rev. Lett. **90**, 057401 (2003)
120. G.W. Bryant, F.J. Garcia de Abajo, J. Aizpurua, Mapping the plasmon resonances of metallic nanoantennas. Nano Lett. **8**, 631–636 (2008)
121. A.M. Kern, O.J.F. Martin, Surface integral formulation for 3D simulations of plasmonic and high permittivity nanostructures. J. Opt. Soc. Am. A **26**, 732–740 (2009)
122. B. Gallinet, A.M. Kern, O.J.F. Martin, Accurate and versatile modeling of electromagnetic scattering on periodic nanostructures with a surface integral approach. J. Opt. Soc. Am. A **27**, 2261–2271 (2010)
123. J.A. Stratton, *Electromagnetic Theory*, 1st edn. (McGraw-Hill, New York, 1941)
124. S. Rao, D. Wilton, A. Glisson, Electromagnetic scattering by surfaces of arbitrary shape. IEEE Trans. Ant. Propag. **30**, 409–418 (1982)
125. R.F. Harrington, Field Computation by Moment Methods (Wiley-IEEE Press, New York, 1993)
126. G. Valerio, P. Baccarelli, P. Burghignoli, A. Galli, Comparative analysis of acceleration techniques for 2-D and 3-D Green's functions in periodic structures along one and two directions. IEEE Trans. Ant. Propag. **55**, 1630–1643 (2007)
127. R. Coifman, V. Rokhlin, S. Wandzura, The fast multipole method for the wave equation: A pedestrian prescription. IEEE Ant. Propag. Mag. **35**, 7–12 (1993)
128. M. Bebendorf, Approximation of boundary element matrices. Numerische Mathematik **86**, 565–589 (2000)

129. N.J. Halas, S. Lal, W.-S. Chang, S. Link, P. Nordlander, Plasmons in strongly coupled metallic nanostructures. Chem. Rev. **111**, 3913–3961 (2011)
130. F. Wang, F. Rodríguez, W. Albers, R. Ahorinta, J. Sipe, M. Kauranen, Surface and bulk contributions to the second-order nonlinear optical response of a gold film. Phys. Rev. B **80**, 233402 (2009)
131. Y. Zeng, J. Moloney, Volume electric dipole origin of second-harmonic generation from metallic membrane with noncentrosymmetric patterns. Opt. Lett. **34**, 2844–2846 (2009)
132. S. Tang, D.J. Cho, H. Xu, W. Wu, Y.R. Shen, L. Zhou, Nonlinear responses in optical metamaterials: theory and experiment. Opt. Express **19**, 18283–18293 (2011)

Chapter 7
Ultrafast and Nonlinear Plasmon Dynamics

Markus B. Raschke, Samuel Berweger and Joanna M. Atkin

Abstract The interaction of light with a metal mediated by surface plasmon polaritons provides for sub-diffraction limited optical confinement and control. While the relationship of the linear plasmon response to the underlying elementary electronic excitations of the metal is well understood in general, the corresponding ultrafast and nonlinear plasmon interactions could provide further enhanced functionalities. However, while the ultrafast and nonlinear optics of metals is an advanced field, the understanding of the related plasmonic properties is less developed. Here we discuss ultrafast and nonlinear wave-mixing properties of metals and metallic nanostructures in terms of the elementary optical interactions related to electronic band structure, plasmon resonances, and geometric selection rules. These properties form the fundamental basis of the nonlinear plasmonic light-matter interaction. The understanding of these fundamental properties, together with the ability to measure and control the typically fast femtosecond intrinsic and extrinsic dephasing times, is important for the development of applications such as enhanced nano-imaging, coherent control of individual quantum systems, strong light-matter interaction and extreme nonlinear optics, and nano-photonic devices.

Keywords Nonlinear optics · Metal optics · Plasmonics · Ultrafast dynamics

7.1 Electronic Excitation at Metal Surfaces: Surface Modes

7.1.1 Introduction

Optical excitations of electrons at metal surfaces play an important role in a wide range of fundamental and applied science applications. The elementary electronic

M. B. Raschke (✉) · S. Berweger · J. M. Atkin
Department of Physics, Department of Chemistry, and JILA, University of Colorado,
Boulder, CO 80302, USA
e-mail: markus.raschke@colorado.edu

T. V. Shahbazyan and M. I. Stockman (eds.), *Plasmonics: Theory and Applications*,
Challenges and Advances in Computational Chemistry and Physics 15,
DOI: 10.1007/978-94-007-7805-4_7, © Springer Science+Business Media Dordrecht 2013

excitations determine carrier and thermal transport, and surface photo-chemistry including photocatalysis, with distinct characteristics for planar and nanostructured metal surfaces. Collective excitations in the form of surface plasmon polaritons (SPPs) at the boundaries of metallic media permit the tailoring of optical fields for surface-enhanced spectroscopy and sub-wavelength resolution microscopy, and have attracted wide attention for their potential for the design of new micro- and nano-scale photonic devices. The near-field and optical antenna properties of surface plasmon polaritons, in particular, may even open the door for qualitatively new optical physics in the near-field. This includes new ways to control the light-matter interaction in quantum systems, negative-index and related meta-materials, or new nonlinear optical phenomena.

The possibilities and fundamental limitations associated with several of these proposed ideas are linked to the fundamental properties of surface plasmon polaritons. Excellent books have been devoted to their linear optical properties [1–3]. Here we will discuss in particular the ultrafast and nonlinear optical properties of surface plasmon polaritons, and how they relate to the elementary electronic properties of metals that ultimately determine the radiative and non-radiative evolution of the plasmon excitation.

We start with a brief overview of the basic properties of surface waves and plasmon polaritons and the relevant underlying physics. We then focus on the ultrafast and nonlinear behaviour, which just as for linear SPPs is a convolution of the *intrinsic* elementary electronic properties of metals with *extrinsic* size and geometry-dependent structural resonances. Ultrafast and nonlinear optics involving SPPs are particularly sensitive to the combination and relative roles of intrinsic and extrinsic effects. The goal here is to provide a microscopic discussion of the dynamic processes of SPPs and the parameters that govern their spectral, spatial, and temporal characteristics linked to the ultrafast electron dynamics of metals.

The nonlinear SPP response is of interest for the generation of optical frequency components by parametric generation or nonlinear wave-mixing, optical saturation and gain, and strong light-matter interaction, taking advantage of the nonlinearity of the medium in combination with resonant or non-resonant field enhancement and optical antenna effects. The study of the ultrafast dynamics of SPPs also opens new experimental approaches for controlling the light-matter interaction and super-resolution microscopy simultaneously on femtosecond time and nanometer length scales as determined by the elementary processes in (homogeneous and heterogeneous) media.

7.1.2 Linear Optical Polarization

We first discuss some basics of the light-matter interaction to define the relevant nomenclature. The induced optical polarization of a (nonmagnetic) medium subject to an incident electromagnetic field is given by

$$\boldsymbol{P}(\omega) = \varepsilon_0 \chi(\omega) \boldsymbol{E}(\omega) \tag{7.1}$$

in the frequency domain, where $\chi(\omega)$ is the dielectric susceptibility, with the frequency-dependence in general arising from material resonances. $\chi(\omega)$ is related to the relative dielectric permittivity by $\varepsilon(\omega) = 1 + \chi(\omega)$, and the complex index of refraction $\tilde{n}(\omega) = n(\omega) + i\kappa(\omega) = \sqrt{\varepsilon(\omega)}$. Both $\chi(\omega)$ and $\varepsilon(\omega)$ are tensor properties, but we will initially consider the medium to be isotropic.

Alternatively, the optical response can be described by an induced electrical current $\boldsymbol{j}(\omega)$ as

$$\boldsymbol{j}(\omega) = \sigma(\omega)\boldsymbol{E}(\omega) \tag{7.2}$$

with electrical conductivity $\sigma(\omega)$. The relationship between the typically complex $\sigma(\omega) = \sigma_1(\omega) + i\sigma_2(\omega)$ and $\varepsilon(\omega) = \varepsilon_1(\omega) + i\varepsilon_2(\omega)$ is given by

$$\sigma(\omega) = -i\varepsilon_0\omega[\varepsilon(\omega) - 1]. \tag{7.3}$$

7.1.3 Time Domain Description

The standard frequency domain description of linear optics and the induced polarization from above has an equivalent time domain formalism. In this case the optical polarization at time t and location $\boldsymbol{r}$ is the result of the interaction of the optical electic field $\boldsymbol{E}(\boldsymbol{r}, t)$ with the medium at earlier times and possibly different locations (non-local response):

$$P(\boldsymbol{r}, t) = \varepsilon_0 \int_{-\infty}^{\infty}\int R(\boldsymbol{r}, \boldsymbol{r}', t')E(\boldsymbol{r}', t - t')d^3\boldsymbol{r}'dt' \tag{7.4}$$

where $R(\boldsymbol{r}, \boldsymbol{r}', t')$ is the *response function* of the system. The response function encodes the memory of the system, with causality dictating that for $t < 0$, $R(\boldsymbol{r}, \boldsymbol{r}', t) = 0$. Additionally, time invariance means that the dynamical response of the system is unchanged by a time offset. For most situations discussed in this chapter, we can neglect the spatial dependence of the response function.[1] The linear susceptibility in the frequency domain can then be derived from the response function as

$$\chi(\omega) = \int_{-\infty}^{\infty} R(t')e^{i\omega t'}dt'. \tag{7.5}$$

[1] In general the dielectric function is wave vector dependent, $\varepsilon(\boldsymbol{k}, \omega)$. However, for the regime discussed here, we can apply the local approximation $\varepsilon(\boldsymbol{k} = 0, \omega) = \varepsilon(\omega)$. Non-local effects and the associated spatial dispersion become significant for $\omega = v_F k$, where v_F is the Fermi velocity. This corresponds to $k > 1\ \text{nm}^{-1}$, i.e. structure sizes of a few nanometers at optical frequencies [4]. Note, however, that this effect is different from the finite-size effect, which can also alter the dielectric function when structure sizes become less than the characteristic scattering length or the onset of quantum confinement.

The well known Kramers-Kronig relationship relates real and imaginary parts of the susceptibility to each other.

A medium is considered instantaneously responding when the excitation is far off-resonant, meaning that the polarization at $t = t_0$ depends only on the electric field at that point in time. Resonant interactions are associated with memory effects, and relaxation processes following the excitation.

The usual Fourier transform relationships hold between the time and frequency domains and the two descriptions are complementary. While the frequency-domain description is typically employed for monochromatic optical interactions, the time-domain provides a more convenient way of analyzing problems where the excitation is induced by a short optical transient. The time domain analysis is therefore useful in particular for the dynamical properties of SPPs.

7.1.4 Electronic Properties of Metals

The spectral and temporal characteristics of SPPs for a metal are ultimately determined by the intrinsic electronic structure of the supporting metal. Most typical metals have hybridized *sp* bands that are parabolic to first order, with a density of states (DOS) that varies weakly within the range of a few eV above and below the Fermi level. *sp* bands resemble the free electron behavior typical for an *s*-metal [4]. In the absence of other electronic states or for sufficiently small photon energies, the optical response of the metal is determined by indirect *intraband* excitations.

Transition metals are characterized by an occupied *d*-band a few eV below the Fermi level, and weak dispersion with high DOS. Figure 7.1 shows a schematic of the

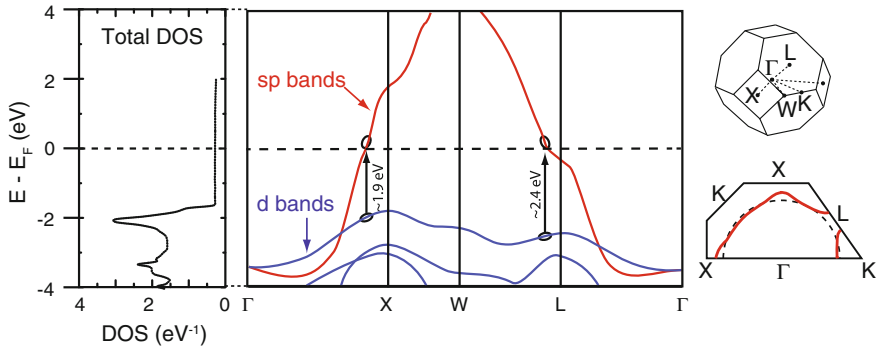

Fig. 7.1 Schematics of the calculated density of states, band structure, and Fermi surface of gold. Gold displays free-electron behavior for low photon energies. The absorption and color of the metal arise primarily due to the interband transition, from the occupied *d* band to the unoccupied *sp* band above the Fermi level. The onset is at ~1.9 eV near the X-point, which leads to a long tail in the experimentally observed absorption spectrum, and approximately 2.4 eV for the L-point, producing a sharp transition. The resulting dielectric function spectral response is shown in Fig. 7.2. DOS and band structure adapted from Ref. [5], and Fermi surface based on Ref. [6]

band structure for Au ([Xe] $4f^{14}5d^{10}6s$) as an example, near the high-symmetry X and Γ points. The dominant contributions to the *interband d-sp* transition are shown, with onset at ~1.9 eV and sharp rise at 2.4 eV.

The topology of the Fermi surface resembles the free electron sphere within the first Brillouin zone, except for the $\langle 111 \rangle$ direction (L neck). Near the Fermi level E_F the optical absorption is weak due to the absence of direct transitions, but is allowed for finite ω if translational symmetry is broken. This is the case for electrons with momenta $2\pi/l$, where l is the electron scattering length. With increasing wavelength this gives rise to an increase in absorption. The effect of the d band on the optical properties is discussed further in Sect. 7.1.6 after introducing the free electron response.

7.1.5 Drude-Sommerfeld Model

Classically the motion of carriers in a metal can be described as ballistic under the assumption of negligible Coulomb interaction. This is the so-called *free electron response* of metals, described by the Drude-Sommerfeld model [7]. Damping, which gives rise to ohmic resistance, can be introduced via the assumption of inelastic and instantaneous collisions with unspecified scattering centers. This leaves as the only key parameter the time τ_D between collision events, defining a relaxation rate $\Gamma = 1/\tau_D$. The equation of motion describing that *relaxor* behavior then corresponds to that of a damped harmonic oscillator without a restoring force term, giving rise to an apparent resonance at $\omega = 0\,\mathrm{s}^{-1}$. This is the Drude peak, describing the increasing absorption with decreasing frequency as mentioned above.

It is instructive to first consider the ideal Drude response without damping. From the equation of motion of free carriers of density n subject only to a driving external optical field $E(t)$, the induced optical polarization is given by

$$P(t) = -nex(t) = -\frac{ne^2}{m\omega^2}E(t), \tag{7.6}$$

with $x(t)$ the separation of electrons from the ions under the influence of the driving field, and m and e the electron mass and charge, respectively. Based on that expression the dielectric function of the charge plasma can be derived as

$$\varepsilon(\omega) = 1 - \frac{\omega_p^2}{\omega^2}, \quad \text{with } \omega_p = \sqrt{\frac{ne^2}{\varepsilon_0 m}} \tag{7.7}$$

termed the volume plasma frequency. This dielectric function is purely real, reflecting the absence of an energy dissipating term. The conductivity $\sigma(\omega)$ is then purely imaginary, indicating a 90° phase shift between an applied field and the induced

current. This reflects the hypothetical picture of a current that will persist infinitely long after a field is no longer applied.

Including damping in the form of scattering to describe the relaxation of the electron momentum with rate $\Gamma = 1/\tau_D$, the resulting dielectric function takes the form

$$\varepsilon(\omega) = 1 - \frac{\omega_p^2}{\omega^2 + i\omega\Gamma}, \tag{7.8}$$

that gives rise to an imaginary component of $\varepsilon(\omega)$, which describes the ohmic resistance.

At low frequencies $\omega \ll 1/\tau_D$, in the so called *Hagen-Rubens* regime, the polarization (current) is in phase with the driving field, hence real and purely dissipative. The conductivity is mostly real and frequency independent, and for $\omega \to 0$ converges to $\sigma_{DC} = ne^2\tau_D/m$. This conductivity is also used to describe radio frequency antenna resonance behavior. At intermediate frequencies, with the optical cycle period becoming comparable to τ_D at mid-infrared frequencies, the imaginary conductivity $\mathrm{Im}(\sigma(\omega))$ peaks at $\omega = 1/\tau_D$ and is equal to the real part $\mathrm{Re}(\sigma(\omega))$. Here, a phase lag appears between the applied field and current response due to the inertia of the electrons. Above $\omega = 1/\tau_D$ (into the near-IR) is the *relaxation* regime, where the response is characterized by decreasing real and imaginary parts with $\mathrm{Re}(\sigma(\omega))$ remaining larger than $\mathrm{Im}(\sigma(\omega))$, leading to large ohmic loss and phase lag, and consequently high damping of SPPs.

7.1.6 Interband Transition and Hybridization

Despite the fact that the electrons obey quantum statistics, the Drude model provides a satisfactory description for the observed dielectric function over a wide energy range well below the interband transitions.[2] However, as a purely phenomenological model it does not provide any physical insight into the damping mechanism, and requires modification for frequencies in the visible and near-IR as the optical frequencies approach d-band resonances.

Table 7.1 summarizes typical Drude and other parameters for Cu, Ag, and Au as representative free electron d-metals. From the Fermi velocity v_F and τ_D an effective electron mean free path $l = v_F\tau_D$ can be estimated between successive scattering events. To account for electron correlation effects in a heuristic manner, a correction to the electron rest mass via an effective mass m^* can be introduced.

The contribution of the positive ion cores to the dielectric function, which is not included in the Drude model, can be corrected for through an empirical, largely frequency independent term ε_∞, with typical values between 1 and 10 depending

[2] A quantum mechanical treatment of the electromagnetic response is provided in the form of the Kubo model. It is based on the fluctuation-dissipation theorem, and an interaction Hamiltonian to describe the interaction of the electromagnetic field with the charge carriers [8].

Table 7.1 Free carrier density n, plasma frequency ω_p, Drude relaxation time τ_D, effective mass m^*, correction term ε_∞, Fermi velocity v_f, band edge E_g, skin depth at 1 eV δ, and mean free path l for Cu, Ag, and Au. n and v_F from Ashcroft and Mermin [4], τ_D, ε_∞, and band edge from fitting to NIR-vis data in Johnson and Christy [9], and ω_p calculated from Eq. 7.9.

	n [cm^{-3}]	$\hbar\omega_p$ (eV)	$\tau_D = 1/\Gamma_0$ (fs)	v_F (nm/fs)	E_g (eV)	l (nm)	m^*/m	ε_∞	δ (nm)
Cu	8.47×10^{22}	8.85	6.9 ± 0.7	1.57	~2.4	~11	1.49	1.6	24
Ag	5.86×10^{22}	9.17	31 ± 12	1.39	~3.8	~43	0.96	3.7	22
Au	5.90×10^{22}	9.07	9.3 ± 0.9 to 14 ± 3	1.40	~2.15	~13	0.99	9.84	24

For Au, τ_D = 14 fs extracted from true Drude free electron behavior [10], with (9.3 ± 0.9) fs reflecting modifications in behavior due to polarization of core electrons at shorter wavelengths [9]. (Values for 300 K.)

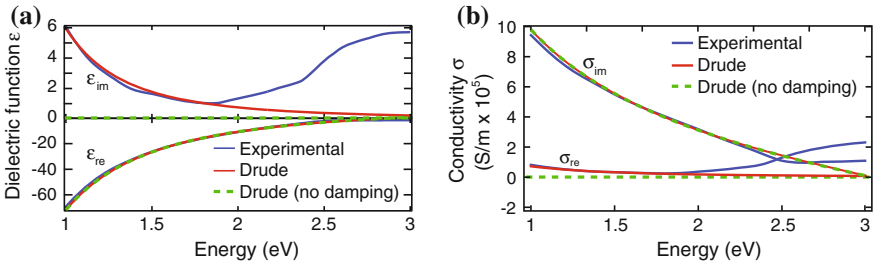

Fig. 7.2 Dielectric function $\varepsilon(\omega)$ for Au for ideal Drude behavior with (*red*) and without damping (*green*), in the near-IR to visible spectrum (**a**). The experimentally measured dielectric function for Au [9] (*blue*) shows the deviations at high frequencies, due to the contributions from interband transitions. **b** shows the corresponding conductivities $\mathrm{Im}(\sigma)$ and $\mathrm{Re}(\sigma)$

on, e.g., the degree of sp electron hybridization with ion core states (see Table 7.1). The dielectric function $\varepsilon(\omega)$ then takes the form

$$\varepsilon(\omega) = \varepsilon_\infty - \frac{\omega_p^2}{\omega^2 + i\omega\Gamma}, \quad \text{with plasma frequency } \omega_p = \sqrt{\frac{ne^2}{\varepsilon_0 m^*}}. \tag{7.9}$$

The theoretical Drude behavior of Au for the parameters from Table 7.1, with and without damping Γ, in comparison with experimentally measured values [9, 10], are shown for $\varepsilon(\omega)$ and $\sigma(\omega)$ at visible frequencies in Fig. 7.2a, b, respectively. The Drude model provides a good fit to the data for energies below ~2 eV, but diverges above that energy due to the onset of $sp - d$ interband transitions.

The absorption spectrum of d-electron metals is characterized by the direct *interband transition* from d to sp bands (Fig. 7.1), with the absorption proceeding largely from the top of the d-band due to its high DOS. The excitation of free carriers via intraband sp band absorption is weak in comparison, since it requires additional momentum scattering, primarily through phonon scattering, but also scattering with impurities, defects, the surface, or other electrons. However, even the behavior below the interband transition is strongly affected by the d-bands through the hybridization

of sp and d bands (copper ($3d-4sp$), silver ($4d-5sp$), and gold ($5d-6sp$)), which gives rise to mutual polarization of the s and d electrons and deviations from the ideal free electron behavior. The d-band is therefore an integral part of the collective electron excitation, even in the regime where the free electron model effectively describes the optical response.

The contribution of the d-bands can empirically be accounted for by writing $\varepsilon(\omega)$ in the form $\varepsilon(\omega) = \varepsilon_{Drude}(\omega) + \varepsilon_d(\omega)$. The Drude term is well described by the sp electron density behavior. The d-bands can then be described in an extended Drude or Drude-Lorentz type model, with the d-electrons assigned an effective Coulomb restoring force, and with a certain density of oscillators, to parametrize the response.

7.1.7 Optics at Metal Interfaces

Following the general discussion of the optical properties of basic metals expressed through their dielectric function, we proceed to the description of surface plasmon polaritons (SPPs) as a collective excitation. A unified description of optical surface wave phenomena, in particular the notion of SPPs, was developed from the work of Sommerfeld, Zenneck, and Wood at the beginning of twentieth century, with subsequent experimental studies by Ritchie, Stern, Kretschmann, and Raether, together with related work by Mie. The optical excitation of the free electrons at the interface of a metal with vacuum or a dielectric medium gives rise to a collective oscillation of the carriers. This surface charge density oscillation is associated with a time varying optical field, hence the notion of a surface plasmon polariton.[3]

The electron charge density at a metal surface decays to zero on a scale comparable to the Fermi wavelength λ_F (the de Broglie wavelength of electrons at the Fermi energy, ~0.5 nm for Au and Ag) (Fig.7.3). Despite being a dynamic surface response

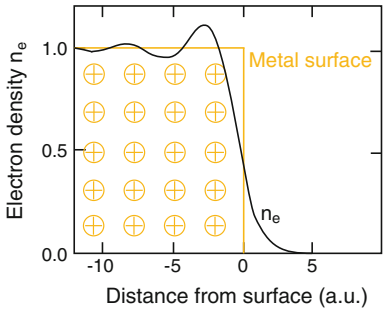

Fig. 7.3 Bulk normalized electron density n_e along the surface normal direction across the metal-vacuum interface, with distance. Friedel oscillations due to electron wavefunction scattering at the interface characterize the density behavior inside the metal, with decay into the vacuum. The decaying electron density can extend several tenths of a nanometer beyond the geometric interface

[3] Instead of an electronic excitation underlying a surface plasmon polariton, collective excitation of lattice vibrations can give rise to a surface phonon polariton. The scope of this chapter is limited to surface plasmon polaritons, but the concepts discussed can readily be extended to phonon polaritons.

the SPP is determined by the local dielectric properties of the bulk (for structures with dimensions above the onset of finite size effects).

This surface wave phenomenon manifests itself in two dis tinct ways: either in the form of *propagating* SPP modes, or as *localized* SPP oscillations.The former surface-bound wave allows for energy propagation and transport over distances at the dielectric-metal interface. In the latter, the additional restoring force introduced to the electron motion by geometric constraints of, for example, noble metal nanoparticles, results in spatially localized resonant charge density oscillations.These can lead to large optical polarizabilities and local optical field enhancement. Signatures of both propagating and localized SPP modes can be observed in random, percolated, or clustered media.

7.1.8 Propagating Surface Plasmon Polaritons

From the wave equation with appropriate boundary conditions at a metal/dielectric interface, the dispersion relationship for propagating SPPs is given by

$$k_{\parallel}^2(\omega) = \frac{\omega^2}{c^2}\frac{\varepsilon_m(\omega)\varepsilon_s}{\varepsilon_m(\omega)+\varepsilon_s} \tag{7.10}$$

with dielectric permittivity of the metal $\varepsilon_m(\omega)$ and its surrounding ε_s (assumed to be frequency independent in the spectral range of interest).[4] Specifically for the metal/vacuum interface the resonant condition $\varepsilon(\omega) = -1$ results in $\omega_{\mathrm{sp}} = \omega_p/\sqrt{1+\varepsilon_\infty}$ for the surface plasmon resonance for a Drude metal.[5]

Figure 7.4 shows the ω versus k dispersion relationship for the ideal Drude surface plasmon polariton with and without loss. The SPP is characterized by surface parallel wave vectors that are large compared to light at optical frequencies. Only in the region near $k_{\parallel} \approx \omega/c$ does the surface plasmon couple to free-space electromagnetic radiation. For higher frequencies, the excitation requires additional momentum via, for example, direct evanescent excitation, grating coupling, or increased index of refraction of the adjacent medium.

Momentum conservation relates the propagating in-plane and evanescent out-of-plane wavevectors to the incident free space wavevector via $k_{\perp,i}^2 + k_{\parallel,i}^2 = \varepsilon_i k_0^2$ for both the metal ($i = 1$) and adjacent dielectric ($i = 2$). Im ($k_{\parallel}$) describes the finite propagation length along the interface. Unlike localized SPP resonances discussed below, due to the large electric field component of propagating SPPs that penetrates into the dielectric medium, lifetimes generally exceed the Drude damping time. $k_{\perp,i}$ governs the spatial extent of the evanescent field in the surface normal

[4] A wide range of interesting phenomena result for the case of frequency dependent or resonant surrounding media, but are beyond the scope of this chapter.

[5] In treatments of this subject the contribution of core electrons is frequently neglected, using $\varepsilon_\infty = 1$. This results in $\varepsilon_{\mathrm{sp}} = \omega_p/\sqrt{2}$ and a plasmonic bandgap in the range of $\omega_{\mathrm{sp}} < \omega < \omega_p$.

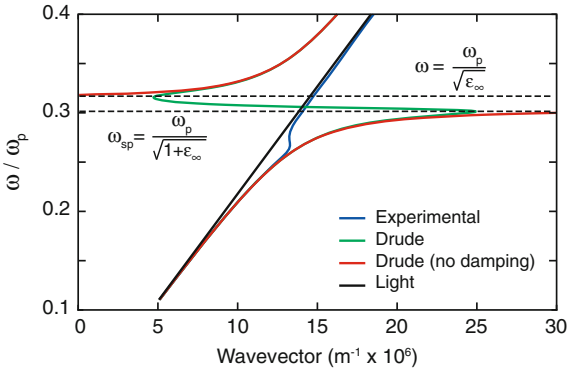

Fig. 7.4 Dispersion relation of surface plasmon polariton for the case of an ideal (undamped) Drude metal (*red*), and Au as an example of a real metal assuming both pure free electron Drude damping (*green*), and additional interband damping from experimental values (*blue*) [9, 10]. The frequency is normalized with respect to the plasma frequency ω_p

direction. The characteristic length $l_{\perp,i}$ is defined as the distance from the surface where $|E(z)/E(z=0)| = 1/e$. For medium i with complex dielectric function $\varepsilon_i = \varepsilon_i' + i\varepsilon_i''$, $l_{\perp,i}$ is given by

$$l_{\perp,i} = \frac{1}{|k_{\perp,i}|} = \frac{\lambda_0}{2\pi}\left(\frac{\varepsilon_1' + \varepsilon_2}{\varepsilon_i^2}\right)^{1/2}. \tag{7.11}$$

The penetration depth into the metal is related to the skin depth (the $1/e$ penetration depth of the optical field into the metal) $\delta = c/\kappa\omega$, with κ the imaginary part of refractive index $N = n + i\kappa$. For gold, $\delta \sim 22 - 25$ nm throughout the mid IR to visible spectral range (0.1–2 eV) [10]. The weak frequency dependence in that regime is due to the near linear dependence of $1/\kappa$ with ω.

The SPP is sensitive to a wide range of which affect surface modifications, including charge, contact to dielectrics, adsorbates, etc. which affect the surface dispersion relation through the modification of the dielectric function. This is closely related to the size and shape dependence of local SPPs in confined geometries (Mie and Rayleigh resonances) as discussed in the following section.

7.1.9 Localized SPP in Small Metal Particles

Localized SPPs are non-propagating modes that can be excited in structurally inhomogeneous environments of dimensions comparable to or smaller than the optical wavelength, i.e. where the translational invariance of the medium is lost on the length scale of the SPP wavelength. With R defining a characteristic structural dimension the parameter $1/R$ plays a role analogous to the parallel SPP wavevector for the case

of a flat surface. For a spherical particles discussed here as an example, R is the radius. In analogy to the wavelength of a surface wave of $\lambda = 2\pi/k$, with wavevector k, for a spherical particle the local mode can be described by an effective wavelength λ_{eff} given by the circumference as $\lambda_{\text{eff}} = 2\pi R$. This analogy implies $k \sim 1/R$.[6]

The optical response of a sphere of arbitrary radius can be solved exactly using (the albeit computationally intensive) *Mie theory* [11, 12], discussed here and also further below in the context of damping. Analyzing the limiting case of a spherical particle provides insight into the basic mechanisms underlying the particle response and its dependence on different input parameters. Many of the conclusions can be generalized to other simple geometries, such as rods, discs, etc.

For particles which are small compared to the wavelength, the response can be more simply described by an induced optical dipole in the lowest order approximation, when neglecting retardation. In that *quasistatic* limit ($R \ll \lambda$), provided the particle is still large enough to avoid finite size effects on the intrinsic dielectric properties,[7] the field distribution of the particle follows from the Laplace equation in spherical polar coordinates. The field outside the sphere is equivalent to the field of a point dipole at the center of the sphere with dipole moment $\boldsymbol{p} = \varepsilon_0 \varepsilon_s \alpha \boldsymbol{E}$. The (complex) polarizability α is given by the Clausius-Mossotti relation:

$$\alpha(\omega) = 4\pi R^3 \frac{\varepsilon_m(\omega) - \varepsilon_s(\omega)}{\varepsilon_m(\omega) + 2\varepsilon_s(\omega)}, \tag{7.12}$$

with $\varepsilon_m(\omega)$ the dielectric function of the metal and $\varepsilon_s(\omega)$ the dielectric function of the surrounding medium. The corresponding absorption cross section is given by $\sigma(\omega)_{\text{abs}} = k\text{Im}\alpha(\omega)$. Since $\sigma(\omega)_{\text{abs}}$ scales as R^3, it dominates for small radii over the scattering cross section $\sigma(\omega)_{\text{scat}} = (k^4/6\pi)|\alpha|^2$, which scales as R^6.

As seen from Eq. 7.12, for a particle in vacuum or air the Fröhlich resonance condition is given by $\text{Re}(\varepsilon_m(\omega)) = -2\varepsilon_s$, provided Im (ε_m) has a negligible frequency dependence. In a Drude metal the localized SPP resonance frequency is then given by $\omega_{\text{res}} = \omega_p/\sqrt{2 + \varepsilon_\infty}$. The resonance frequency redshifts with increasing index of refraction of the environment. Above $R \sim 50$ nm the onset of retardation and multipole excitation gives rise to spectral broadening and decrease in peak amplitude, which necessitates the application of the full Mie treatment.

The different dielectric properties of Au and Ag lead to pronounced differences in the spectral behavior close to the SPP resonance. For small spherical Au particles the plasmon resonance at $\lambda_{\text{SPP}} \sim 530$ nm is already superimposed on a pronounced increase in scattering and absorption due to the interband transition. In contrast, for Ag with the interband transition at ~4 eV, the SPP peak at 350 nm is dominated by

[6] $k \sim 1/R$ also describes to first order the wavevector distribution cut-off of the near-field modes of a structural element with characteristic dimension R, and their corresponding spatial localization.

[7] For particle size with radius $R \gg \lambda_{\text{TF}}$ with λ_{TF} the Thomas-Fermi screening wavelength, the response can be treated as that of the homogeneous bulk electron density. However, electron spillover, as depicted in Fig. 7.3, may become significant in sub-nanometer particles [12, 13]. In addition, surface scattering becomes relevant when particle sizes approach the effective mean free paths of the excited electrons. (See also footnote 1.)

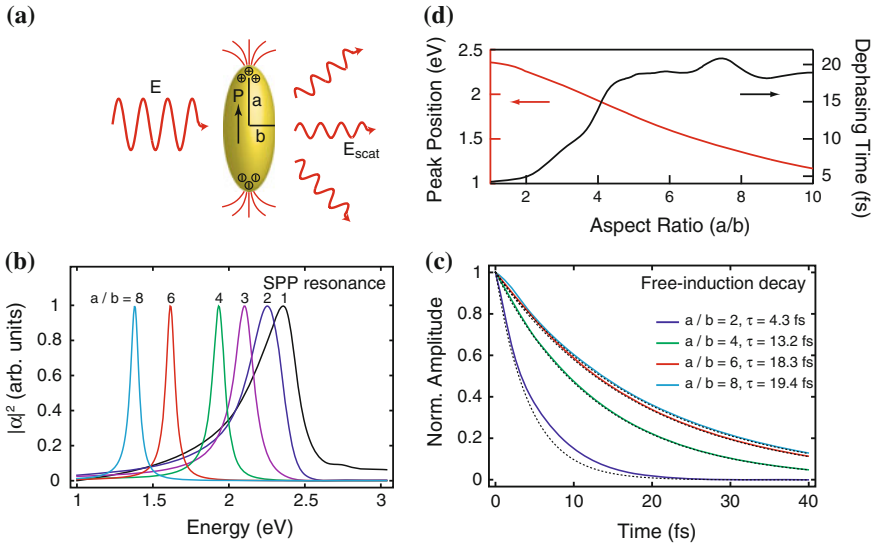

Fig. 7.5 Schematic of local SPP for a prolate spheroid with a/b for the aspect ratio of long to short principal axis (**a**). Normalized polarizability squared ($|\alpha|^2$) calculated using using experimental Au dielectric function [9] (**b**). The SPP resonance *red-shifts* with increasing aspect ratio starting with a spherical particle ($a = b$) with fixed major axis length. The interband continuum response increasing to high energies, has been subtracted for clarity. Fourier transform showing the underlying time domain evolution of the plasmon dynamics (**c**). SPP dephasing time as a function of aspect ratio and thus SPP energy exhibits a decrease from $T_2 \sim 20$ fs for the free electron behavior for energies above ~ 2 eV due to the interband contribution (**d**). *Dotted lines* in panel (**c**) show exponential fits for extracting dephasing times shown in (**d**)

the free electron response. Under otherwise identical conditions, the cross sections for Ag spheres are about one order of magnitude larger than those for Au.

A useful extension of the sphere model, also in the discussion of the damping of the plasmon response, is the SPP of an ellipsoid ($a \neq b \neq c$) or spheroid ($a = b \neq c$) shaped particle, treated in the quasistatic approximation. The longitudinal polarizability for a *prolate spheroid* (see Fig. 7.5a) with aspect ratio a/b is given by

$$\alpha(\omega) = \frac{4\pi ab^2}{3} \frac{\varepsilon_m(\omega) - \varepsilon_s(\omega)}{\varepsilon_s + L(\varepsilon_m(\omega) - \varepsilon_s)}, \tag{7.13}$$

where L is the so-called depolarization factor, an integral reflecting the particle aspect ratio. As shown in Fig. 7.5b the plasmon resonance shifts to lower energies with increasing aspect ratio. The red-shift can be viewed as a result of the increase in spatial charge separation and thus a decrease in effective restoring force. As we will see below this allows us to predict the frequency dependence of the plasmon dephasing and its correlation with the damping of the underlying dielectric function.

7.2 Damping of Surface Plasmon Polaritons

7.2.1 Theory of Radiative and Nonradiative Decay

The coherent electronic excitation of a medium is followed by fast electronic dephasing and the subsequent absorption and decay of the polarization into electron hole pairs.[8] Here we will discuss the radiative and non-radiative relaxation dynamics of SPPs as the fastest initial processes describing the light-matter interaction. We will restrict the discussion to the homogeneous SPP response, i.e., in the absence of ensemble effects and different inhomogeneities. We will discuss the basic physics of plasmon dephasing in this section, followed in subsequent sections by different frequency- and time-domain experimental linear and nonlinear spectroscopic results for its experimental determination.

Of primary interest is the electronic *dephasing*, that is, the eventual loss in phase coherence of the collective and initially phase coherent oscillation of the free electron gas (plasma oscillation). In contrast to semiconductors, which allow for a low and variable carrier density through controlled doping, the carrier density in metals is comparatively high and fixed (Table 7.1). Those high carrier densities immediately imply a high scattering and thus high dephasing rate. The SPP decoherence time is therefore fundamentally linked to the effective relaxation time in the Drude dielectric function as the response function that determines the temporal evolution of the induced optical polarization in response to an applied optical field. Consequently, to first order, the Drude relaxation time τ_D sets an upper limit for the dephasing time T_2 for a localized SPP.

The macroscopic optical response of metals in general, including the SPP resonance for plasmonic metal nanostructures, reflects the underlying elementary electron dynamics of the bound and conduction electrons involved. Specifically, the linewidth and shape of the SPP resonance in the frequency domain, or its Fourier transform in the form of the *free-induction decay* in the time domain, describes the loss in phase coherence, which in turn is directly linked to the dielectric function. In the following we discuss the ultrafast electron dynamics of spherical and spheroidal metal nanoparticles as model systems using analytical treatments. The results can readily be generalized for more complex geometries using numerical techniques. For small enough particles ($R \ll \lambda$) the excitation is dominated by the dipolar SPP response, with polarizability given by Eq. 7.12 for a sphere or Eq. 7.13 for a spheroid.

[8] Following the typically up to 10s fs coherent evolution of electronic excitations, different processes govern the incoherent carrier cooling and equilibration. The decay of the coherent excitation into electron-hole pairs gives rise to hot non-equilibrium and non-thermal carrier distributions. Electron–electron scattering leads to thermalization of the hot electrons within at most a few hundred fs and can often be described by the Fermi liquid theory. Electron–phonon interaction on 100 fs to ps time scales leads to the subsequent equilibration with the lattice degrees of freedom. Although not the subject of this review, these processes lead to transient variations of the dielectric function and its frequency dependence, ultimately due to the deposited energy in the form of heat. The processes need to be considered in time resolved experiments, especially with high pump intensities and large excitation densities, giving rise to a nonlinear response.

From the calculated spectra for a Au sphere or spheroids with different aspect ratios as shown in Fig. 7.5b, the corresponding time traces for the polarization decay are obtained by Fourier transform as shown in Fig. 7.5c. The associated SPP lifetimes can then either be directly deduced from the $1/e$ value of the maximum amplitude, or obtained from the FWHM (Γ) spectral line width by $T_2\Gamma = 2\hbar$. Note that the deviation from an ideal Lorentzian spectral or exponential time behavior in this model calculation is due to the use of the experimentally measured dielectric function $\varepsilon(\omega)$ as an input parameter and associated deviations from the ideal Drude behavior. The resulting *plasmon lifetimes* are then shown in Fig. 7.5d as a function of resonant energy (or aspect ratio). The dephasing times are found to be in the range of 18–22 fs for energies between 1.0 and 1.7 eV, i.e., the free electron regime. The dramatic decrease in lifetime at 2 eV is associated with the onset of the interband transition.

The interpretation of the dephasing time is complicated by the various possible mechanisms contributing to the loss of phase coherence in the plasmon oscillation. In general, the measured dephasing time T_2 is related to a population relaxation time T_1 of participating quantum states, and pure dephasing T_2^* by $1/T_2 = 1/2T_1 + 1/T_2^*$. The pure dephasing contribution T_2^* corresponds to elastic collisions of electrons, which destroy only the phase coherence. Because of the high carrier density and high electron scattering rate, this is expected to be negligible for SPPs. However, this relation has limited applicability in this case. The SPP classical polarization is described in terms of T_2, i.e. the polarization decay through inelastic electron scattering processes, but there is no associated population prior to the decay into electron-hole pairs after decoherence. Instead, the underlying momentum scattering, which gives rise to the loss in phase coherence, can be associated with the Drude scattering τ_D, with $T_2 \sim 2\tau_D$.

Drude scattering leads to electron-hole excitation and corresponding absorption effects, alternatively described via ohmic loss. It competes with radiative decay. The larger effective oscillator size and polarization with increasing particle size leads to an increase in the radiation damping contribution. For particles larger than ~20 nm this produces a monotonic trend of decreasing dephasing time with increasing particle diameter.

The quasistatic ellipsoid model discussed above and shown in Fig. 7.5 neglects radiative decay and thus provides only an upper limit for the dephasing time. In order to account for radiation damping, we use the rigorous solution for the scattering of a particle given by Mie theory [14, 11]. The scattering and extinction efficiencies for the m-th multipole order is related to the scattering and extinction cross sections $\sigma_{\mathrm{sca},m}$ and $\sigma_{\mathrm{ext},m}$, and the geometrical cross section $G = \pi R^2$, by

$$\begin{aligned} Q_{\mathrm{sca},m} &= \tfrac{\sigma_{\mathrm{sca},m}}{G} = \frac{2}{x^2}(2m+1)(|a_m|^2 + |b_m|^2), \text{ and} \\ Q_{\mathrm{ext},m} &= \tfrac{\sigma_{\mathrm{ext},m}}{G} = \frac{2}{x^2}(2m+1)Re(a_m + b_m), \end{aligned} \tag{7.14}$$

with $x = kR = \omega n_d(\omega)R/c$. The scattering coefficients a_n and b_n are given by

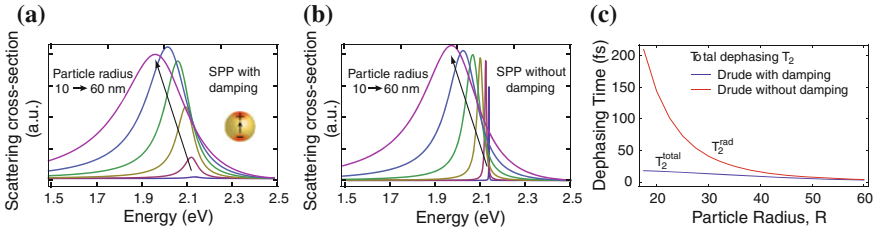

Fig. 7.6 Comparison of scattering cross-sections for the dipolar mode in spherical particles using Mie theory and the Drude model with (**a**) and without (**b**) intrinsic Drude damping of the metal electrons. The linewidths without that damping reveal the pure radiation damping contribution. Resulting dephasing times (**c**) based on linewidth analysis, demonstrating the relative contribution of radiative and nonradiative contributions with increasing particle radius [15]. Calculations utilize the Drude parameters for Au listed in Table 7.1, with $\varepsilon_\infty = 9.84$. The surrounding medium has index of refraction $n = 1.5$

$$a_m = \frac{N\psi_m(Nx)\psi_m'(x) - \psi_m(x)\psi_m'(Nx)}{N\psi_m(Nx)\xi_m'(x) - \xi_m(x)\psi_m'(Nx)}$$
$$b_m = \frac{\psi_m(Nx)\psi_m'(x) - N\psi(x)\psi_m'(Nx)}{\psi_m(Nx)\xi_m'(x) - N\xi(x)\psi_m'(Nx)} \tag{7.15}$$

with the relative refractive index $N = n_p(\omega)/n_d(\omega)$ of the particle (n_p) and the dielectric medium (n_d), and the Ricatti-Bessel functions ψ_m and ξ_m.

Shown in Fig. 7.6 is the result of the calculated spectral dependence of the scattering cross sections for spherical Au particles with increasing radius from Mie theory, using the Drude model parameters with (a) and without (b) damping (based on Eq. 7.9), and the resulting variation in dephasing times (c) [15]. The finite linewidths in the hypothetical absence of material damping (b) reveal the *radiation* contribution to the plasmon dephasing. The broader linewidths when including material damping (a) are due to contributions from both *radiative and nonradiative* dephasing, i.e.,

$$\frac{1}{T_2} = \frac{1}{T_2^{\text{rad}}} + \frac{1}{T_2^{\text{non-rad}}}, \tag{7.16}$$

with $T_2^{\text{non-rad}} \sim 18 - 22$ fs as discussed above. The increasing dephasing rate for larger particles is a result of the increasing contribution of radiation damping. As a result, the dephasing times for the damped and undamped Drude models converge for the case of large particles where the radiation damping due to the increasing dipole moment dominates over Drude scattering.

As SPPs oscillate in the visible spectral range with periods in the $\sim 2-4$ fs range, radiative decay times for electronic excitations in the 10 s of fs to sub 10 fs range thus imply a very good coupling of the optical dipole to the electromagnetic density of states in the far-field. The results can be compared to the emission of radiation from a classical dipole or the spontaneous emission from a quantum two level system.

In order to describe the radiative emission of a oscillating charge it must be recognized that the radiation field in turn influences the motion of the charge itself, termed *radiation reaction*. Assuming the radiation reaction force $\boldsymbol{F}_r$ as the only damping term, the equation of motion can be written as:

$$m\frac{\mathrm{d}^2\boldsymbol{r}}{\mathrm{dt}^2} + \omega_0^2 m\boldsymbol{r} = \boldsymbol{F}_r = -m\Gamma_0\frac{\mathrm{d}\boldsymbol{r}}{\mathrm{dt}} = \frac{q^2}{6\pi\varepsilon_0 c^3}\frac{\mathrm{d}^3\boldsymbol{r}}{\mathrm{dt}^3}, \tag{7.17}$$

with the Abraham-Lorentz equation to describe the reaction force coefficient:

$$\Gamma_0 = \frac{1}{4\pi\varepsilon_0}\frac{2q^2\omega_0^2}{3mc^3}. \tag{7.18}$$

This gives rise to radiative lifetimes $\tau = 1/\Gamma_0 \simeq 20$ ns for optical frequencies. An additional term, conventionally introduced to describe the damping of a Lorentzian oscillator of the form $\Gamma \mathrm{d}\boldsymbol{r}/\mathrm{d}t$, contains both radiative and non-radiative contributions.

Similarly to Eq. 7.17, one can start with the induced optical polarization of the form:

$$\boldsymbol{P}(\omega) = \chi(\omega)\left(\boldsymbol{E}_{inc} + i\frac{2k_0^3}{3}\boldsymbol{P}(\omega)\right) \tag{7.19}$$

with particle susceptibility $\chi(\omega)$. The second term corresponds to the radiation reaction field with:

$$\boldsymbol{F}_r = e\boldsymbol{E}_{rad} = \frac{2}{3}\frac{e^2}{c^3}\ddot{\boldsymbol{v}} = i\frac{2}{3}\frac{\omega^3}{c^3}e\boldsymbol{x} = i\frac{2}{3}k^3\boldsymbol{P}, \tag{7.20}$$

using $\boldsymbol{x} = \mathrm{e}^{-i\omega t}$ and $\ddot{\boldsymbol{v}} = i\omega^3\boldsymbol{x}$ for the harmonic oscillator. Hence, both approaches are equivalent, with the difference that the damping for the resonant denominator for $\chi(\omega)$ already contains the a priori indistinguishable radiative and non-radiative terms.

Interestingly, the quantum description for the spontaneous emission of a two level system provides a qualitative intuition for the high radiative emission rate as derived from Mie theory in the femtosecond regime. The transition rate follows from Fermi's golden rule as

$$\Gamma_{sp} = \frac{\pi\omega_0}{3\varepsilon_0\hbar}|\langle a|\hat{\boldsymbol{\mu}}|b\rangle|^2\rho_\mu(\boldsymbol{r}_0, \omega_0), \tag{7.21}$$

with transition dipole moment operator $\hat{\boldsymbol{\mu}}$ and ρ_μ the partial local density of states (LDOS) at the location $\boldsymbol{r}_0$ of the system, given by $\rho_v(\omega) = \omega_0^2/\pi^2c^3$ in vacuum. With $\boldsymbol{\mu_{ba}}^2 = |\langle a|\hat{\boldsymbol{\mu}}|b\rangle|^2 = q^2r_{21}^2$ the spontaneous emission rate becomes:

$$\Gamma_{sp} = \frac{\omega_0^3}{3\pi\varepsilon_0\hbar c^3}\boldsymbol{\mu_{ba}}^2. \tag{7.22}$$

For an atomic emitter with typically $\boldsymbol{\mu_{ba}}$ = (1 electron charge)·(0.1 nm) (or 1.602×10^{-29}C·m), and $\omega_0 = 2\,\text{eV}/\hbar = 3.04 \times 10^{15}$ rad/s, the corresponding spontaneous emission lifetime is $\tau = 1/\Gamma_{sp} = 33$ ns. Since the results in the weak perturbation regime are similar for the classical and quantum treatment (oscillator strength ~ 1), we can rewrite Eq. 7.22 in the following semi-classical form:

$$\Gamma_{sp} = \frac{8e^2\pi^2}{3\varepsilon_0\hbar}\left(\frac{r}{\lambda_0}\right)^2 \frac{1}{\lambda_0}. \tag{7.23}$$

This equation highlights the size mismatch r/λ_0 giving rise to the long ns radiative lifetimes for atomic emitters. Considering the SPP nanoparticles as an optical dipole with $r = 10...100$ nm, compared to the 0.1 nm of atomic dimensions, will increase the effective size of the dipole moment and thus reduce the radiative impedance mismatch. For a one-electron oscillator of that size the radiative rate would increase by $10^2 - 10^6$ and with that the dephasing time would decrease from the ns into the fs regime as seen for a localized SPP of a metal nano-particle. Note that this model merely qualitatively describes the general trend of an increase in radiative rate with increasing oscillating charge separation, with details depending sensitively on geometry.

7.2.2 Experimental Studies of Plasmon Lifetimes

A range of studies have investigated dephasing times from both time resolved and spectral line width analysis (see, e.g., [16, 17] and references therein). Here we discuss frequency-domain measurements of T_2, with further time-resolved experiments provided in Sect. 7.4. Since the time scales for plasmon dephasing are in the few femtosecond regime and the relative contributions of radiative and nonradiative decay pathways are size-dependent, accurate measurements of the intrinsic dephasing time usually require either a homogeneous sample or individual nanostructure, and various model assumptions are employed. Dark field scattering of individual particles or persistent spectral hole burning give access to the homogeneous sub-ensemble of an inhomogeneous sample. In hole burning, for example, the sub-ensemble with resonance close to that of the exciting laser frequency is bleached, and the linewidth of the spectral hole at different fluences is extrapolated to zero fluence to establish the dephasing time.

As shown in Figs. 7.5 and 7.6, the linewidth and related quality factor $Q = \omega_0/\Gamma$ can be derived with a particle SPP calculation using either the Drude model or experimental dielectric values. Most experimental results indicate 5–10 fs for dephasing time T_2, i.e. reduced from the theoretical maximum nonradiative value of $\sim$18 fs. While the limiting nonradiative case has been demonstrated [18], the shorter dephasing times often reported may result from structural inhomogeneities, surface scattering, and radiation damping. Measurements of the dephasing times of

Ag and Au particles as a function of their geometrical aspect ratio found that the dephasing times for higher aspect ratios are longer than for similarly sized spherical particles. Larger particles have shorter radiative dephasing times, consistent with observations from Mie theory and the quasistatic approximation. The SPP decay time for long rods approaches 20 fs, indicating that dephasing for these geometries is dominated by nonradiative Drude relaxation τ_D.

The different geometric behavior is important for applications of plasmonic structures. For mediating the coupling of nanoscopic emitters to far-field emission, increased radiation rates and spherical particles are preferred. However, the dephasing time is directly related to the field enhancement $T_2 \propto F$, so for many applications it is desirable to instead maximize the plasmon lifetime.

There are various *momentum scattering* contributions to the T_2 SPP dephasing discussed above. Electron–electron, electron–phonon, electron-defect, impurity, and surface scattering can all contribute, so that the total decay rate is the sum of these different contributions,

$$\Gamma = \sum_i \tau_i^{-1} = \tau_{e-e}^{-1} + \tau_{e-ph}^{-1} + \tau_{e-defect}^{-1} \tag{7.24}$$

All of these processes have been found to be largely temperature independent with the exception of electron–phonon scattering, which shows a linear increase with temperature, explained with a Debye model for the material-dependent electron–phonon interaction [19].

In addition to the extrinsic dependence of particle plasmon properties on size, with dielectric constant $\varepsilon = \varepsilon_{\text{bulk}}$, intrinsic *size effects* occur for particles where the size approaches the mean free path of the conduction electrons. This regime, relevant for few nanometer sized particles, is characterized by increased electron scattering from the particle surface and $\varepsilon \neq \varepsilon_{\text{bulk}}$. A radius-dependent correction to the Drude damping can be introduced empirically [12, 20]:

$$\Gamma(R) = \Gamma_\infty + \frac{A v_F}{R} \tag{7.25}$$

with the bulk Drude damping Γ_∞ and Fermi velocity v_F. A has a value near unity depending on particle geometry and the $1/R$-dependence follows from the ratio of the surface area to particle volume.

The short timescales and multiple relaxation processes involved in SPP dephasing lead to difficulty in interpreting results and separating the various effects in both frequency and time domain measurements. For time domain measurements, a challenge arises that for plasmon resonances in the visible to near-IR, the SPP dynamics on few femtosecond timescales are comparable to the shortest possible laser pulses in that energy range (e.g. ~2 fs optical cycle period at $\lambda_{\text{SPP}} = 600$ nm). In the following section as an application of the nonlinear SPP response we will also discuss nonlinear optical time-resolved techniques for the investigation of the ultrafast plasmon dynamics.

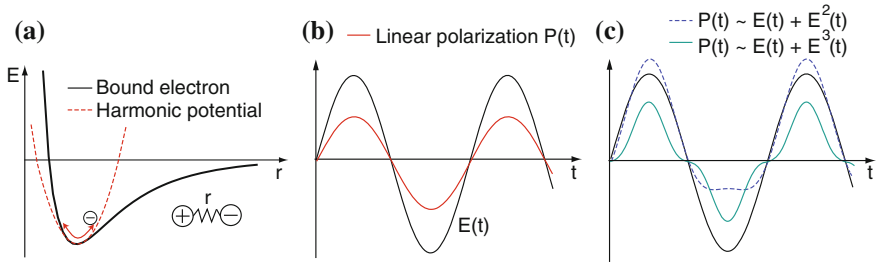

Fig. 7.7 **a** Interaction potential experienced by a bound electron in a medium. The deviation from a purely harmonic potential leads to a nonlinear optical polarization response under high driving fields. **b** The far off-resonant linear polarization $P(t)$ (*red*) in response to a weak driving field $E(t)$ (*black*). **c** The corresponding induced polarization incorporating a second-order response (i.e. $P(t) \propto E^2(t)$), for example in a non-centrosymmetric material (*blue*), and a third-order response (*green*), for large driving fields

7.3 Nonlinear Plasmon Optics

In this section we will first discuss the nonlinear optical response of metallic nanostructures, nonlinear resonant effects, and selection rules. We will then show how they can provide a means of separating the complex interaction of dephasing processes, for example from investigation of their relative phase, and also enable precise characterization of electric fields and response functions.

Thus far we have been assuming that the optical polarization P of the metal is linear with respect to the applied optical field, which applies for the case of a relatively weak driving field. However, if the incident driving field is comparable to electric fields within the medium a *nonlinear response* can result due to the deviation from a perfect harmonic oscillator potential experienced by the charge carriers coupling to the optical field. This anharmonic oscillator behavior is shown schematically in Fig. 7.7 for a bound electron in a medium. In metals, the polarization perpendicular to the surface is particularly important for second-order nonlinearities, since at the surface the electrons will experience an additional surface asymmetric potential.

A small nonlinearity can be treated *perturbatively*, so that the polarization is expressed as a power series expansion in the driving field:

$$\boldsymbol{P} = \varepsilon_0 \boldsymbol{\chi}^{(1)} \boldsymbol{E} + \varepsilon_0 \boldsymbol{\chi}^{(2)} \boldsymbol{E}^2 + \varepsilon_0 \boldsymbol{\chi}^{(3)} \boldsymbol{E}^3 ...., \tag{7.26}$$

with $\boldsymbol{\chi}^{(n)}$ the susceptibility tensor describing the material and its resonances for the n-th ($n \geq 2$) order optical process. In the following we employ explicit tensor notation due to the importance of anisotropy and symmetry considerations in studying the nonlinear response. The electric field $\boldsymbol{E}$ in this description is the local electric field experienced by atoms in the medium. The local field can be modified from the incident driving field due to the polarization of the medium itself. This local field correction and its importance for plasmonic antennas is discussed further below.

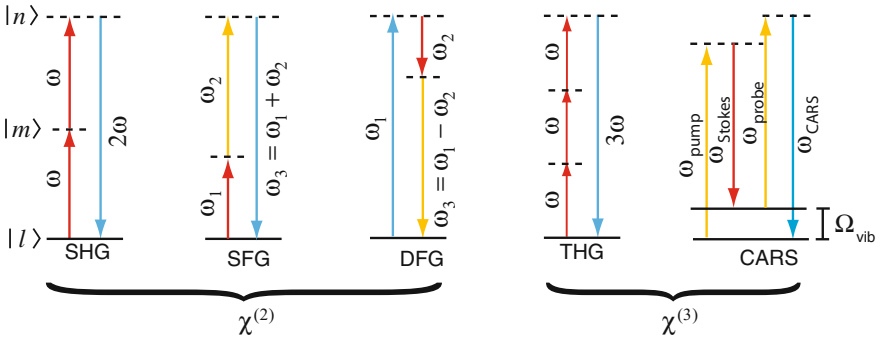

Fig. 7.8 Summary of common nonlinear optical processes with corresponding energy level diagrams. Second-harmonic generation (SHG), sum-frequency generation (SFG), and difference-frequency generation (DFG) are second-order processes. Third-harmonic generation (THG) is a third order process, in which three fundamental photons combine to produce a 3ω photon. Coherent anti-Stokes Raman scattering (CARS) is a resonant four-wave mixing process. The *dashed lines* represent the off-resonant excitation of a real state $|m\rangle$, $|n\rangle$, at a different energy

Just as in the linear case, the induced optical polarization can equivalently be described in terms of a current, but this approach is often less practical because there are typically several nonlinear source terms that may be difficult to separate in this treatment. Both basic harmonic generation wavemixing and more complex frequency conversion processes follow from Eq. 7.26, with relative efficiencies depending on the spectral and symmetry characteristics of the linear and nonlinear susceptibilities of the material.

Several representative nonlinear optical processes are summarized in Fig. 7.8. Metals typically have bulk *inversion symmetry* and therefore a vanishing $\boldsymbol{\chi}^{(2)}$, so that all even-order nonlinear responses in the bulk will vanish in the so-called *dipole approximation*, which neglects weaker higher-order, non-local contributions to the nonlinear response such as magnetic dipole and electric quarupole terms. The second-order nonlinear processes in metals are therefore dominated by the optical-surface interaction.[9] Second-harmonic generation (SHG) is the simplest second-order nonlinear process, where two photons with frequency ω combine to produce a single photon at 2ω. The material response is described by the nonlinear susceptibility $\boldsymbol{\chi}^{(2)}(-2\omega;\omega,\omega)$, which is a third rank tensor with symmetry reflecting the crystal symmetry and dependent on all frequencies $(\omega, 2\omega)$ in the nonlinear process. More generally, the second-order induced polarization can radiate at any frequency which is a linear combination of the frequencies of the incident waves (see Fig. 7.9a), allowing sum-frequency generation (SFG) with the energy conservation condition $\hbar\omega_3 = \hbar\omega_1 + \hbar\omega_2$, difference-frequency generation corresponding to

[9] The term surface is defined here with respect to the actual atomic layer surface boundary, extending over a region of only a few atomic layers in the surface normal direction, where electronic structure is distinct from translationally invariant bulk and possibly modified by surface electronic states.

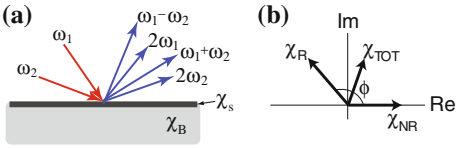

Fig. 7.9 **a** Schematic of interactions with two input fields, ω_1 and ω_2, producing output fields with different frequency, intensity, and emission direction for a planar surface. Both surface χ_s and bulk χ_B induced polarizations occur, with the nonlinear laws of reflection and refraction governing the momentum conservation of the in-plane wavevector. **b** Resonant (χ_R) and non-resonant (χ_{NR}) contributions to the second-order polarization in the complex plane and the sum χ_{TOT}, which may produce interference and asymmetric lineshapes depending on relative phase ϕ

$\hbar\omega_3 = \mid \hbar\omega_1 - \hbar\omega_2 \mid$, and the degenerate case ($\omega = \omega_1 = \omega_2$) of optical rectification giving rise to a DC field with the condition $0 = \hbar\omega - \hbar\omega$.

Third-harmonic generation (THG) produces a 3ω photon from three incident photons with frequencies ω, with a rank four susceptibility tensor $\boldsymbol{\chi}^{(3)}(-3\omega; \omega, \omega, \omega)$. The general third-order process of four wave mixing (FWM) is based on interactions of three photons, with frequencies ω_1, ω_2, and ω_3 combining to produce an output photon with frequency ω_4, with $\boldsymbol{\chi}^{(3)}(-\omega_4; \pm\omega_1, \pm\omega_2, \pm\omega_3)$. Since these are odd-order processes, they are permitted for all materials, including those with centrosymmetric point groups. The nonlinear Kerr effect is also a third-order process, but one with degenerate input and output frequencies, described by the susceptibility $\boldsymbol{\chi}^{(3)}(-\omega; \omega, \omega, -\omega)$. Here the negative sign indicates that the process involves the annihilation of a photon, instead of the simple additive combination seen in harmonic generation. This process is based on a change in the index of refraction and absorption of a material proportional to the incident intensity. Another type of four wave mixing is Coherent anti-Stokes Raman Scattering (CARS), a resonant third order interaction with $\omega_{CARS} = \omega_{pump} + \omega_{probe} - \omega_{Stokes}$ and $\boldsymbol{\chi}^{(3)}(-\omega_{CARS}; \omega_{pump}, \omega_{probe}, -\omega_{Stokes})$. Usually the pump and probe frequencies are identical, and ω_{Stokes} is typically chosen so the difference between the frequencies is resonant with a vibrational level of the material $\Omega_{vib} = \omega_{pump} - \omega_{Stokes}$. This is the coherent analog to incoherent Raman scattering, and as a vibrational spectroscopy technique provides chemical specificity.

The efficient generation of coherent nonlinear optical signals requires both energy conservation and *phase-matching* conditions, that is, momentum conservation between the nonlinear and fundamental k-vectors. In the bulk, this is achieved through the linear dispersion and associated wavelength-dependence of the index of refraction $n(\omega)$. At the interface, it arises from the selection of the input and output k-vector directions. For rough structures or particles on the order of or smaller than λ, the loss of translational invariance leads to changes in the momentum conservation conditions, giving rise to nonlinear light scattering and in certain situations allowing for, e.g. separation of non-local bulk and local surface susceptibilities, as discussed further below.

These nonlinear responses provide access to conduction electrons throughout the energy continuum, which allows probing of interband and intraband transitions. The

enhancement provided by both intrinsic material and extrinsic structural resonances can also lead to a significant increase in the efficiency of nonlinear processes. A discussion of plasmon-resonant metallic systems, where the nonlinear enhancement scales with the order of the process, can be found in Sect. 7.3.4. The coherent nature of the wavemixing processes leads to a strong dependence on the phase of the driving field and material response, which provides additional information for characterization and control. This is particularly useful for the study of the ultrafast dynamics in complex metallic nanostructures, where nonlinear techniques provide more degrees of freedom to probe multiple resonances and their coupling than linear optics. The multiple driving fields in nonlinear optics also enable probing of changes in the complex dielectric function and therefore propagation characteristics of SPPs under strong-pump illumination, an important consideration for active plasmonics.

7.3.1 Second-Order Nonlinear Optics

Here we will provide a more detailed discussion of the origins and theory associated with the lowest, second-order nonlinear response. Although the symmetry considerations associated with even-order responses are different from odd-order nonlinearities, much of what follows can be readily extended to third-order and higher nonlinear processes.

Using Einstein summation notation, the second-order optical response can be written as

$$P_i^{(2)}(\omega_1+\omega_2) = \varepsilon_0 \chi_{ijk}^{(2)}(-\omega_1-\omega_2;\omega_1,\omega_2)E_j(\omega_1)E_k(\omega_2) \tag{7.27}$$

with i, j, k denoting the Cartesian coordinates x, y, z. Within the classical theory of nonlinear optics, an expression for the nonlinear susceptibility can be derived from *perturbation theory* based on a driven, damped harmonic oscillator, analogous to the linear case, with the addition of a quadratic term as a first order perturbation. This approximation results in Lorentzian resonances at the fundamental and wavemixing frequencies,

$$\chi_{ijk}^{(2)}(-\omega_1-\omega_2;\omega_1,\omega_2) \tag{7.28}$$

$$= \frac{Ne^3a}{\varepsilon_0 m^2}\frac{1}{(\omega_0^2-(\omega_1+\omega_2)^2-2i(\omega_1+\omega_2)\Gamma)}\frac{1}{(\omega_0^2-\omega_1^2-2i\omega_1\Gamma)(\omega_0^2-\omega_2^2-2i\omega_2\Gamma)}$$

$$= \frac{\varepsilon_0^2 ma}{N^2e^3}\chi^{(1)}(\omega_1+\omega_2)\chi^{(1)}(\omega_1)\chi^{(1)}(\omega_2) \tag{7.29}$$

with resonance frequency ω_0 (for a single oscillator), nonlinear parameter a and number density of atoms N. This simple model provides an intuitive description of the optical nonlinearity, for the case of weak absorption in the material.

In the dipole approximation of the quantum mechanical description, by considering symmetry operations, the second-order susceptibility tensor can be written as a sum of terms of the form [21, 22]

$$\chi^{(2)}_{ijk}(-(\omega_1+\omega_2);\omega_1,\omega_2) = \frac{Ne^3}{2\varepsilon_0\hbar^2}\sum_{lmn}\rho_l\Big[\frac{\langle l|r_i|n\rangle\langle n|r_j|m\rangle\langle m|r_k|l\rangle}{(\Omega_{nl}+\omega_1+\omega_2)(\Omega_{ml}-\omega_2)}+ \frac{\langle l|r_i|m\rangle\langle m|r_k|n\rangle\langle n|r_j|l\rangle}{(\Omega_{nl}+\omega_1+\omega_2)(\Omega_{ml}-\omega_1)}\cdots\Big] \tag{7.30}$$

This expression describes transitions from state $|l\rangle$ (not necessarily the ground state), through two intermediate states $|m\rangle$ and $|n\rangle$, followed by the emission of a photon with the remaining net energy difference, e.g. $\hbar(\omega_1+\omega_2)$ when returning to the initial state. ρ_l is the population of the initial state, $\langle l|r_i|n\rangle$ is the transition dipole moment operator in the density matrix formalism, and $\hbar\Omega_{nl}$ is the energy difference for this transition. For driving fields with frequencies far off-resonance, all components of $\boldsymbol{\chi}^{(n)}$ are real and additive, corresponding to almost-instantaneous transitions involving "virtual" energy levels, as shown in Fig. 7.8. Close to resonance, $\Omega_{nl} = \omega_{nl} + i\Gamma_{nl}$, with Γ_{nl} describing the line width of the transition, arising from damping. Therefore, $\boldsymbol{\chi}^{(n)}$ is generally complex, with *resonant* (R) and *nonresonant* (NR) contributions to the nonlinear response,

$$\boldsymbol{\chi}^{(n)} = \boldsymbol{\chi}^{(n)}_{\mathrm{R}} + \boldsymbol{\chi}^{(n)}_{\mathrm{NR}} \tag{7.31}$$

As shown in Fig. 7.9b, the SHG signal then arises from the sum of these complex contributions. Since $\boldsymbol{\chi}^{(n)}_{\mathrm{R}}$ will have a strong frequency dependence, the interference of the two terms will produce dispersive lineshapes and even destructive interference depending on the relative phase.[10] The resonances that lead to this behavior can involve single or multiphoton processes, with different degrees of coupling [23].

Figure 7.10 shows possible resonant SHG interactions within the Au band structure, with a plasmon resonant process from the Fermi level and an electronic resonance from the d-band.The mixing of the two fundamental ω photons is essentially an instantaneous process if the intermediate $|1\rangle$ state is a virtual energy level, as shown for the 2ω electronic resonance. If the intermediate state is resonant with an eigenfrequency of the material, e.g. in the form of an extrinsic SPP resonance, it has a finite lifetime and the SHG process can accordingly involve fundamental pulses separated by a time interval, denoted τ.

[10] These asymmetric lineshapes resemble those observed in the case of the quantum interaction of two competing pathways connecting discrete and continuous energy levels, called Fano resonances. However, since the interference of the different nonlinear contributions does not arise from quantum interference, but rather from the classical interference of different linear and nonlinear, and resonant and non-resonant polarizations, the use of the Fano lineshape terminology for describing asymmetric linear or nonlinear lineshapes may only be seen as an analogy.

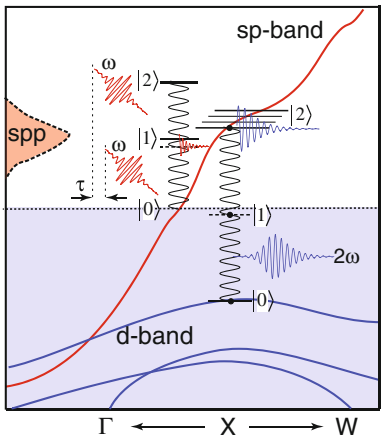

Fig. 7.10 Schematic representation of second-harmonic generation (SHG) in a three level system, superimposed on a band structure diagram for Au. Enhancement of the SHG response can occur when either ω or 2ω corresponds to an eigenfrequency of the material. As an example, resonant excitation can occur via an intermediate extrinsic SPP resonance at the 800 nm fundamental frequency, or a two-photon $sp-d$ resonance involving the d-bands

7.3.2 SHG Response at Metal Surfaces

Since the discovery of nonlinear optics, the nonlinear response of metals has received substantial attention. However, establishing and accurately modeling the microscopic signal sources has been difficult. The nonlinear response does not follow simply from the linear case and includes several contributions to the nonlinear polarization, which are typically hard to separate. These contributions, and the sensitivity of SHG to surface modifications, hampered efforts to quantify the magnitude of $\boldsymbol{\chi}^{(2)}$ in metals.

For centrosymmetric crystals, the lowest order, bulk dipole response is forbidden, since $\chi^{(2)} \equiv 0$ is the only solution to satisfy the inversion operation. The second-order response therefore originates from surfaces and interfaces where symmetry is broken in the sample normal direction, and higher order bulk contributions. The higher-order terms arise primarily from magnetic dipole and electric quadrupole interactions. They are usually small compared to the dipolar response, yet as a bulk response might overall be comparable to a pure surface dipole response. For a cubic crystal, the bulk polarization from these sources can be expressed as an isotropic and anisotropic term,

$$\boldsymbol{P}_B(2\omega) \propto \gamma(\omega)\nabla(\boldsymbol{E}\cdot\boldsymbol{E}) + \xi(\omega)\boldsymbol{E}\nabla\boldsymbol{E}. \tag{7.32}$$

In the free-electron model the anisotropic second term above is zero, but can appear if lattice effects are taken into account. The first description of SHG in metals therefore treated SHG as generated by the isotropic bulk term within the skin depth of the metal [24, 25]. However, this treatment neglects the broken inversion symmetry at the metal-dielectric interface, which leads to the additional dipole-allowed surface SHG.

The surface polarization arises due to the rapid change of the electric field at the metal-air interface, which produces a surface second-order polarization perpendicular and parallel with respect to the surface. The normal component of the electric field

at the surface varies over approximately the Thomas-Fermi screening length, which leads to the spatial confinement of the induced nonlinear current to a subnanometer region. Therefore, a classical electromagnetic description to model surface SHG fails and a quantum mechanical treatment is necessary in order to accurately incorporate the surface charge density and screening effects.

The nonlinear surface polarization is described by susceptibility tensor components, with $\chi^{(2)}_{zzz,s}$ describing the surface normal current, which is expected to be the largest contribution to surface SHG as it is the most sensitive to the structural and electric field change across the interface. The other components for the in-plane surface current are $\chi^{(2)}_{xxz,s}$, or equivalently $\chi^{(2)}_{yyz,s}$, $\chi^{(2)}_{xzx,s}$, etc., and $\chi^{(2)}_{zxx,s} = \chi^{(2)}_{zyy,s}$, due to the symmetries of the tensor.

Rudnick and Stern [26] parametrized three contributions to SHG in terms of the phenomenological constants $a(\omega) \propto \chi^{(2)}_{\perp,s}$, $b(\omega) \propto \chi^{(2)}_{\parallel,s}$, and $d(\omega) \propto \chi^{(2)}_{B}$. In the Drude model, $b(\omega) = -1, d(\omega) = 1$, and $a(\omega)$ was initially assumed to be close to 1. Several models for calculating the spatial distribution of the electron density close to the surface and deriving $a(\omega)$ were developed, chiefly using hydrodynamic arguments to derive the surface potential within a jellium framework, which treats the metal surface as a homogeneous gas of interacting free electrons in a background of uniform positive charge. These models provided an intuitive description of the system, but underestimated the magnitude of the SHG by an order of magnitude [27]. Subsequent models used density functional theory to describe the electron–electron interactions at the surface, which incorporates the screening of the external electric field [28]. While these models typically agree qualitatively with experimental observations, particularly in the long wavelength limit, other effects can also become significant and change the relative contributions of the different polarization terms. Additional susceptibility components may also appear when the lattice is considered. For example, close to resonances the bound electrons may contribute more strongly to the nonlinear polarization, producing a bulk response larger than the surface, even in centrosymmetric materials. Consistent with this, a strong enhancement in SHG has been observed in noble metals close to the interband transition, in addition to the usual off-resonant nonlinear signal [29, 30].

For noble metals, the k-dependence of the electronic structure is typically neglected in modeling the SHG response. The high density of states and overlapping d-bands allow for a continuum of transitions with different symmetries, as shown in Fig. 7.10, producing broad SHG peaks. When the excitation frequency is such that the band gap E_g is less than 2ω, the SHG response is generally dominated by transitions where both the initial and the intermediate states are in the d-band. This sensitivity of SHG to the d-band can provide spectroscopic material specificity.

The literature disagrees on quantitative measurements of the magnitude of the SHG signal and its components, due to the high sensitivity of SHG to surface structure and contamination. In particular for Ag and Al, accurate measurements require ultra high vacuum to ensure clean surfaces. The second-harmonic responses from Ag(111) and Au(111) surfaces, far off-resonant at $\hbar\omega = 0.81$ eV, were found to be dominated by the surface normal susceptibility, as expected [31]. Significant contributions were

also found for other susceptibility components, with their relative magnitude varying with fundamental frequency. In this early work, the nonlinear response of Au was measured to be $\chi^{(2)}_{s\perp\perp\perp} \sim 2 \times 10^{-8}$ m/V, approximately four times larger than that of Ag, close to 1 eV. Later measurements on thin films found that Ag has the strongest SHG intensity of the metals, with Au slightly smaller and Cu approximately 50 % of the Ag response [32]. With careful angle and polarization-dependent measurement enabling separation of the bulk and surface responses in the experiment, the $\chi^{(2)}_{s\perp\perp\perp}$ component was determined to be approximately 200 times larger than $\chi^{(2)}_B$ for Au, and ∼100 $\chi^{(2)}_B$ in Ag, at a fundamental photon energy of 1.55 eV. Interestingly, Al has an inherently high bulk nonlinear response, with $\chi^{(2)}_B$ values an order of magnitude higher than Au and Ag. However, it also suffers from a short skin depth and high losses in the visible and NIR, in addition to a tendency to oxidize, so is generally not considered as suitable for plasmonic applications.These experiments also demonstrated a wide variation in surface susceptibility values depending on surface roughness and growth conditions of the thin films, an effect that is the subject of Sect. 7.3.4. Hence, the development of both accurate quantitative experiments and an accurate quantitative theory has remained difficult.

While the discussion to this point has been limited to the nonlinear response of metal involving single particle excitations, the next section is concerned with nonlinear interactions involving SPPs, where the surface-sensitivity of the second-order response becomes particularly important for the enhancement of the nonlinear signal.

7.3.3 Nonlinear Wavemixing with Surface Plasmons

The momentum mismatch between the incident and emitted light and in plane SPP wavevectors as shown in Fig. 7.4 means that linear excitation of SPPs on planar surfaces typically requires an effective momentum change of the incident field in the form of a coupling element or increase in index of refraction, for example a grating or Kretschmann prism, respectively. However, the phase-matching conditions associated with the different wavevectors participating in a nonlinear wavemixing process provide additional flexibility, allowing free-space launching of SPPs via the generated nonlinear polarization, or SPPs as the source for the nonlinear output field, or both. While even-order processes are intrinsically surface-confined, interactions involving SPPs are also in practice limited to the near-surface region given by the skin-depth, even for odd-order processes. Any of the participating wavemixing fields can be an SPP, with a wavevector that is defined by the surface dispersion relation of the specific SPP frequency. Figure 7.11 shows a set of different possible configurations. The surface-parallel components of the free-space k-vectors $k_i = \omega_i n(\omega_i) \sin\theta_i / c$, where θ_i is the angle with respect to the surface normal and $n(\omega_i)$ is the index of refraction of the dielectric medium, can then be summed appropriately with the

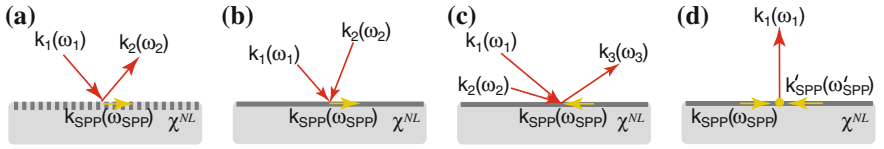

Fig. 7.11 Schematics for several examples of wavemixing processes involving SPPs. Launching of SPPs through the use of a grating or a modification of the index of refraction can lead to enhancement in the nonlinear response (**a**), with surface-parallel momentum conservation condition $k_1(\omega_1) + \frac{2\pi n}{a_0} = k_2(\omega_2) + k_{\mathrm{SPP}}(\omega_{\mathrm{SPP}})$, for integer n and grating period a_0. SPPs can also be generated through appropriate phase matching conditions between several input waves (**b**), e.g., $k_1(\omega_1) - k_2(\omega_2) = k_{\mathrm{SPP}}(\omega_{\mathrm{SPP}})$ for DFG. One or more of the free-space waves in a wavemixing process can also be substituted by an SPP, e.g. $k_1(\omega_1) + k_2(\omega_2) - k_{\mathrm{SPP}}(\omega_{\mathrm{SPP}}) = k_3(\omega_3)$ for FWM (**c**), or $k_{\mathrm{SPP}}(\omega_{\mathrm{SPP}}) - k_{\mathrm{SPP}}(\omega_{\mathrm{SPP}}) = k_{1,\parallel} = 0$ (**d**)

SPP wavevectors to achieve energy and momentum conservation for the desired wavemixing process.

Nonlinear SPP wavemixing can also provide enhanced efficiency of the nonlinear response. The field amplitudes of SPP modes that drive the wavemixing process are enhanced near the surface due to the spatial field confinement, thus enhancing the nonlinear polarization generated. An example of this process is the enhancement of SHG observed when an SPP is excited through prism coupling onto a silver film in the Kretschmann geometry [33]. Similar effects have been seen in third-harmonic generation (THG) with total internal reflection [34]. The plasmon-enhanced nonlinear response can interfere with other sources of nonlinear polarization in the system. Due to their different phase relationship with the driving field, this interference will also depend on the incident k-vector.

Early in the development of nonlinear optics, four-wave mixing (FWM) was proposed as a mechanism for launching surface waves such as exciton polaritons, phonon polaritons [35] or SPPs [36], by tuning the angle of illumination to achieve wavevector matching at the sample-air interface. The efficiency of this approach is determined by the local field enhancement and nonlinearity of the metal. While the nonlinearity of metals is high in general, the interaction volume is limited by the skin depth. This leads to a low efficiency in generating SPPs by wavemixing, compared to direct excitation of an SPP of the corresponding frequency. Another approach to achieve SPP coupling via a nonlinear process is create a transient temperature grating by interfering two incident waves on the surface. This is a incoherent pump induced, rather than a coherent wavemixing process. The resulting thermal gradient gives rise to a spatial variation in the index of refraction, and thus allows for launching SPPs. This process has a much higher efficiency than FWM with femtosecond pulses, but a much long timescale, given by thermal diffusion [37]. In order to maintain the ultrafast timescale of wavemixing, higher efficiencies could be possible with a second-order process such as DFG [38] rather than FWM. These and other combinations of free space and propagating SPP waves (examples shown in Fig. 7.11) have

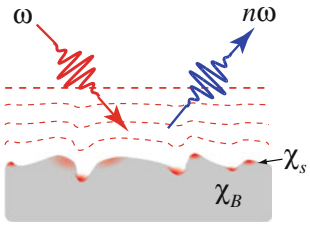

Fig. 7.12 Areas of local field enhancement on rough metallic surfaces lead to large enhancement in both the local and the overall nonlinear response, here for the example of harmonic generation $n\omega$, with $n = 2, 3$ etc

been considered for second and third order wavemixing SPPs, and recently received renewed attention [39].

SPPs can also act as one or more of the driving fields in a nonlinear optical process [40–42] (Fig. 7.11b, c). For the right conditions, SPPs contribute in a phase-matched fashion to the wavemixing process, e.g. SHG generation from two SPP fields [43].

7.3.4 Surface-Enhanced Nonlinear Processes

The sensitivity to symmetry-breaking of even-order nonlinear processes makes them an effective tool for the study of, e.g., surface electronic and vibrational resonances and their coupling. However, the nonlinear response is weak in general, and further limited by the small volume of surface material involved in the nonlinear interaction. Enhancement can arise from the localization and concentration of the optical fields near a surface or at a nanostructure. Localized plasmon resonances in noble metal nanoparticles, clusters, and rough metal surfaces can provide a further increase in nonlinear optical effects, and substantially change the relative bulk to surface contributions in a nonlinear response.[11] These "hot spots" provide enhancement in linear optical processes as well, but with regard to an aggregate bulk response are reduced, since energy conservation conditions require that enhancement of the field is balanced by lower local fields and thus reduced optical response in other regions. In nonlinear processes, in contrast, in one sample location the total signal enhancement can be much higher due to the nonlinear dependence of the response on the local optical field. The breaking of translational symmetry and spatial redistribution of the optical field is therefore beneficial to the higher order response (See Fig. 7.12).

The enhancement of an optical response is described phenomenologically in terms of a local field enhancement factor $L(\omega)$, which modifies the driving electric field, analogous to the Fresnel factors for planar interfaces in reflection or the bulk local field correction factor discussed earlier, as

[11] In random, fractal, or percolated media, a mixed mode between localized and propagating SPPs is possible. The interference of this collective mode of the local excitation and multiple scattering in the disordered media can give rise to Anderson localization for typically uncorrelated disorder with associated nonlinear optical effects [44].

$$E_{\mathrm{loc}}(\omega) = L(\omega)E(\omega). \tag{7.33}$$

A local field factor needs to be considered for all optical fields contributing to the nonlinear process, so that the total enhancement is the combination of all enhancement factors incorporating the order and coherence of the nonlinear process.[12]

Raman scattering is an incoherent, linear optical process, but the enhancement in the field is approximately proportional to $L^2(\omega)$ since the fundamental and Stokes shifted Raman signal have only a small frequency separation compared to the typical spectral variation of $L(\omega)$ for the supporting metal, and will both be enhanced.[13] This effect has been exploited for *surface-enhanced Raman scattering* (SERS), where the increase in the effective cross section by a rough metal film can provide single-molecule sensitivity [46], and is also the basis of *tip-enhanced Raman scattering* (TERS). In both cases, the additional sensitivity arises from the redistribution and near-field localization of the field in the surface normal direction. A higher-order, coherent process such as SHG also benefits from the *lateral* redistribution of the field, with areas of high field enhancement increasing the signal nonlinearly. For SHG, the enhancement in the polarization is given by

$$\boldsymbol{P}(2\omega) = L(2\omega)\boldsymbol{\chi}^{(2)}(-2\omega;\omega,\omega)L^2(\omega)\boldsymbol{E}^2(\omega) \tag{7.34}$$

where $L(\omega)$ and $L(2\omega)$ are the local field factors at the fundamental and SHG frequencies respectively. The total intensity enhancement is then $\propto L^2(2\omega)L^4(\omega)$. Both fields in this case might not simultaneously be enhanced due to their spectral separation, in which case either $L(\omega)$ or $L(2\omega)$ is typically approximately equal to 1. The same arguments apply to higher-harmonic generation processes, with the general field enhancement behavior

$$\boldsymbol{P}(n\omega) = L(n\omega)\boldsymbol{\chi}^{(n)}(-n\omega;\omega,\omega,...)L^n(\omega)\boldsymbol{E}^n(\omega). \tag{7.35}$$

In a spatially distributed nanoparticle system, the regions of highest local field enhancement for different wavemixing processes can be in different locations, depending on the resonant frequency and mode behavior. Degenerate four wave mixing in general displays higher enhancement on rough surfaces than third harmonic generation, due to more than one driving laser field being enhanced simultaneously. It has also been observed that harmonic generation tends to show lower enhancement than incoherent processes such as the nonlinear Kerr effect, since the coherence of the process can produce destructive interference in random metallic systems [44].

---

[12] Equivalently, the enhancement can be incorporated into a modification of the susceptibility tensor, but this description may be less intuitive for the case of, for example, surface-enhanced Raman scattering, where the susceptibility tensor is not the intrinsic metallic system but rather a coupled metal-molecule system.

[13] Because of symmetry considerations arising from the Raman tensor, this coupling of the incident and radiative fields is not rigorously accurate. In reality, the relative orientation of the local field and the molecular dipole or crystallographic orientation can lead to more complex enhancement behavior. For more details, see, e.g., Ref. [45].

The general principles of surface- and plasmon-enhanced nonlinear optical effects are well understood. However, details in terms of the relative surface and bulk modifications to the susceptibility, the interband and intraband transitions, finite size effects on band structure, plasmon mediated effects in the nanostructure, and interactions with the substrate are not yet well understood. Furthermore, the spectral dependence and magnitude of the field enhancement varies critically depending on the surface morphology, which is difficult to model. Grating structures can be useful for the treatment of surface-enhanced nonlinear processes, since they provide a model system for rough surfaces. Experimentally, the enhancement of nonlinear optical effects has been demonstrated on various samples, with roughness controlled to a certain extent through film thickness and growth conditions [47], and SHG enhancement of 10^4 on a roughened Ag surface was observed early on [48], in addition to surface-enhanced higher order processes [49]. However, just as for a planar geometry, the surface and bulk contributions to the SHG are difficult to separate, and both may be modified by the roughness [50].

7.3.5 Nonlinear Light Scattering

One of the complications of surface-enhanced nonlinear interactions is that the roughness can lead to extrinsic dephasing and depolarization. Similarly, nonlinear processes in particle systems, e.g. in gas and liquid phase, where there is a substantial spatial inhomogeneity in local fields and nonlinear susceptibilities, will be accompanied by scattering. For the small particle limit, where the particles can be treated as dipole sources (i.e. 5–10 nm for visible light), nonlinear light scattering is known as hyper-Rayleigh scattering, in analogy to Rayleigh scattering [11]. Some confusion in terminology exists in the literature, but according to the strict definition, the nonlinear response in particles larger than 10 nm arises from coherent effects, even when the contributions from the particles add incoherently, and so hyper-Rayleigh scattering can be a misleading term [51].

The change in momentum conservation rules in scattering processes compared to bulk media produces new and additional symmetry selection rules, which are described in the context of nonlinear Mie and Rayleigh scattering with an effective surface susceptibility $\chi_s^{(n)}$ [52–54]. In particular, the lack of translational invariance and $k \propto 1/r$ for a single nanoscopic system lifts the phase matching condition, so that the projection of the nonlinear k-vectors to the far field is not restricted to a particular direction. Of the different nonlinear interactions in individual nanoparticles, third-order processes such as THG behave similarly to linear scattering, while second-order processes such as SHG have additional sensitivity to the particle surface and geometric details. Furthermore, the susceptibilities for nanoparticles can be very strongly affected by grain size and crystallinity. Analogous to the linear case, if the particles are large enough to allow for retardation effects over the particle diameter, higher order multipolar contributions to the nonlinear polarization occur.

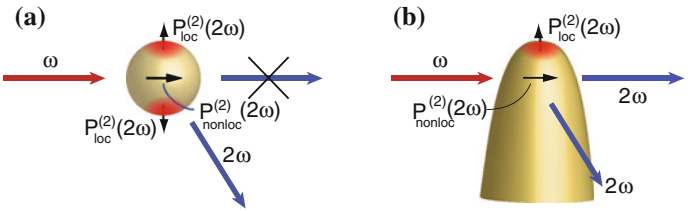

Fig. 7.13 Symmetry considerations for a sphere of centrosymmetric material (**a**) and a conical tip (**b**). No second-order response appears in the exact forward or backscattering directions for the sphere since the surface contributions are out of phase and interfere destructively, but a non-local response can produce SHG in other directions. For the conical tip, the broken symmetry along the tip axis allows both local dipolar forward- and back-scattering and non-local scattering

The case of SHG from a *spherical nanoparticle* of a centrosymmetric material is particularly interesting for reasons of symmetry of the second-order nonlinear response. Inversion symmetry is broken at the surface, but the usual linear dipole mode aligned in the direction of the pump polarization, as is responsible for linear Rayleigh scattering, will not produce SHG as the surface contributions are 180° out of phase and thus cancel (Fig. 7.13a. Instead, a non-local nonlinear polarization in the direction of the pump wavevector arises due to retardation in the phase across the particle diameter [55], in addition to a possible higher-order bulk response. The orientation of the dipole and bulk quadrupole sources is such that no SHG will radiate in the exact forward and backward directions, but radiates in non-collinear directions with spatial distribution determined by particle size.

A *conical tip*, such as those used in near-field optical experiments, while semi-infinite, can also be considered within the context of nanoscale particles. It possesses broken mirror symmetry along the tip axis (∞mm point group symmetry). This leads to fully *local dipole-allowed* SHG polarization $P^{(2)}_{\mathrm{loc}}(2\omega)$ along the tip axis [53]. This symmetry breaking produces different polarization selection rules for SHG in nanoscopic metal tips than for surfaces or spherical particles. In particular it is possible to distinguish the *non-local* bulk $P^{(2)}_{\mathrm{nonloc}}(2\omega)$ and *local* surface $P^{(2)}_{\mathrm{loc}}(2\omega)$ SHG response, since these two contributions are perpendicular (Fig. 7.14) and produce correspondingly cross-polarized SHG. As discussed above, this separation of local and non-local SHG contributions is typically difficult for planar surfaces due to nonlinear laws of reflection, which limit emission to the direction defined by the incident k-vector direction. The conical geometry therefore provides a model system for characterizing nonlinear enhancement and scattering effects, since it is a single element structure with well-defined symmetry and permits the separation of different SHG responses.

The symmetry-breaking behavior of a Au conical tip with apex radius ~20 nm is demonstrated in Fig. 7.14, for sagittal illumination of the tip exciting a local, purely dipolar surface nonlinear polarization $P^{(2)}_{\mathrm{loc}}(2\omega)$ oriented along the tip axis, leading to radiation of SHG in the forward direction. In addition, the non-local source perpendicular to the tip axis can radiate in the 90° direction. This arises from retarda-

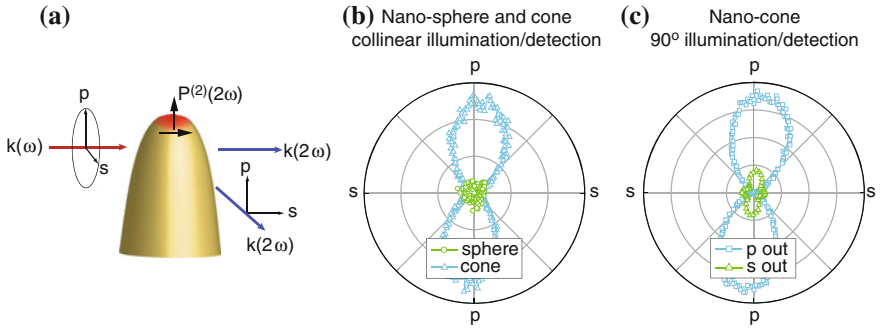

Fig. 7.14 Geometry of SHG scattering from a conical nano-tip (**a**), with forward scattering allowed for sagittal *p*-polarized illumination due to the broken symmetry along the tip axis (**b**). For 90° detection both a bulk non-local and dipolar response are possible (**c**). Input polarization dependence for collinear SHG (**b**) from a nano-sphere reference (*green*) and nano-cone (*blue*). No SHG is observed in this geometry for the sphere, but the cone demonstrates the expected dipolar response. SHG in 90° sagittal illumination/detection geometry, for *p* and *s* polarized output (**c**), demonstrating the separation of dipolar surface and bulk response

tion from spatially-distributed surface nonlinear polarizations and higher-order bulk contributions. Experimental results are shown, first with no SHG observed for a nano-sphere in the forward-scattering direction used as a reference (Fig. 7.14b, green). In contrast, for the tip, SHG in this geometry is dominated by the local dipole-allowed $p_{\text{in}} - p_{\text{out}}$ contribution (blue), with the expected two-fold anisotropy, i.e. intensity $I_{\text{SHG}} \propto \cos^4(\theta)$. Similar to a planar surface, the response is due to the strong $\chi^{(2)}_{s,\perp\perp\perp}$ tensor element. For the tip, the weak $s_{\text{in}} - p_{\text{out}}$ response (data not shown) suggests that the $\chi^{(2)}_{s,\perp\parallel\parallel}$ susceptibility component is negligible. With sagittal illumination and 90° detection for a tip (c), both the local dipolar $p_{\text{in}} - p_{\text{out}}$ and non-local (distributed) bulk $p_{\text{in}} - s_{\text{out}}$ and $s_{\text{in}} - s_{\text{out}}$ response appear.

These results provide a demonstration that the additional degrees of freedom that arise from the combination of *intrinsic* material response and *extrinsic* nanoscale geometric properties enables separation of bulk and surface SHG. The SHG properties again depend sensitively on the morphology and local environment of the nanostructure, but the symmetry selection rules derived above are generally applicable to asymmetric nanostructure systems. For example, the presence of a substrate will break symmetry and relax the polarization selection rules for metal particles, and the tip in a near-field optical experiment will have a similar effect on a local scale. With the capability to probe both surface and bulk properties on the nanoscale, the study of plasmonic behavior with high specificity can be achieved.

7.3.6 Nonlinear Optical Antennas

As discussed above, particles and rough surfaces can provide large field enhancements, but with the increasing interest in plasmonic applications such as imaging, sensing, cloaking, or harvesting, a need for controllable and reproducible linear and nonlinear responses has developed. Recent advances in chemical synthetic methods allow the production of crystalline metal nanostructures with a wide range of shapes and sizes with nanometer-scale structural control. Single-crystal nanoparticles and nanowires often exhibit strong plasmonic resonances due to their low defect density and well-defined shape. Additionally, lithographic techniques, focused ion beam milling, and template stripping now provide a means to generate arrays of nanoparticles and other more complex structures such as coupled nanowires and bowtie antennas, which have a large field enhancement in the nanogap region. For an antenna, the SHG polarization is again given by

$$\boldsymbol{P}^{(2)}(2\omega) = \boldsymbol{\chi}^{(2)}(-2\omega;\omega,\omega)L^2(\omega)L(2\omega)\boldsymbol{E}^2, \tag{7.36}$$

where the nonlinear response is given by the material susceptibility. The local field factor L now describes enhancements due to antenna resonances in addition to localized plasmon resonances, and so depends sensitively on geometrical and environmental properties and the coupling of plasmonic modes.

Similar to radio-frequency antennas, antenna resonances for plasmonic antennas such as rods occur when the length of the antenna is equivalent to an integer multiple of half the wavelength. However, the wavelength is modified from the free-space wavelength by the SPP dispersion on the surface of the metal [56]. The precise resonant behavior of the antenna depends sensitively on geometrical details such as diameter, cross-section, and shape, as well as roughness. For such simple antennas, the spectral dependence of the antenna resonances is often approximated by Lorentzian lineshapes,

$$L(\omega) \propto \sum_l \frac{A_l}{\omega_l - \omega + i\Gamma_l}, \tag{7.37}$$

where ω_l are the resonance frequencies, Γ_l is the damping of the antenna, and A_l the relative strength of the resonance.

The local field correction arising from optical antenna resonances can provide an enhanced nonlinear response, up to several orders of magnitude, arising from the enhancement of the linear electric field. However, the spectral dependence of the local field enhancement can lead to a shift in the emission spectrum, as represented in Fig. 7.15, and therefore also an apparent spectral shift in the nonlinear response. The nonlinear response may also not be accurately predicted by the linear far-field response, due to the different near-field spectral density of states distribution compared to the far-field [57].

For non-degenerate wavemixing processes, coupled antennas can be designed such that several input frequency components are simultaneously enhanced [58, 59].

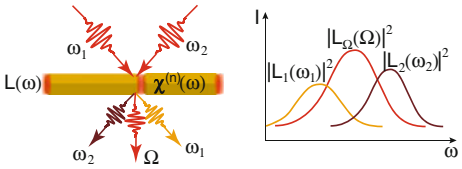

Fig. 7.15 Interaction of light with a rod antenna, showing the spectral shift in emission due to the local field enhancement associated with antenna and plasmon resonances at incident and wavemixing frequencies $L(\omega_1)$, $L(\omega_2)$, and $L(\Omega)$

The localization and concentration provided by optical antennas can also be utilized to couple to highly nonlinear media, such as GaAs, ZnO, or $BaTiO_3$, to generate a strong nonlinear response.

7.4 Femtosecond Time-Domain Measurement of Plasmon Dynamics

In this section we resume the discussion on plasmon dynamics from above (7.2), demonstrating the use of the nonlinear SPP response itself for the determination of the dynamic response underlying a localized SPP excitation, and with that the electron dynamics of the supporting metal. An SPP, as with any optical response, is defined in terms of both amplitude and phase, whether in the spectral or temporal domain. The characterization of SPP dynamics, however, is frequently incomplete, with only amplitude but no phase information obtained, e.g., in incoherent dark field scattering. The underlying dynamics inferred from these spectral measurements therefore rely on model assumptions such as a Lorentzian lineshape from a harmonic oscillator model with flat spectral phase, a transform limited driving laser pulse, or constant relative phase of the response with respect to the non-resonant background. In addition, in frequency space the fast initial dynamics of the plasmon evolution are encoded in the spectral wings, where the signal level is low and thus sensitive to background and noise. Consequently, the spectral wings are very susceptible to possible constructive or destructive interference with the background. Conventional techniques are therefore unsuitable for the study of complex, multi-resonance, or coupled plasmonic systems.

In contrast to incoherent techniques such as dark field scattering, nonlinear optical techniques such as harmonic generation provide access to full amplitude and phase for optical waveform characterization, enabling the direct measurement of plasmon dephasing time and other electron interaction and relaxation behavior. Access to the ultrafast nonlinear response is therefore important for developing an understanding of field enhancement and resonance effects, since a resonance with a plasmon excitation in a system can enhance the linear and nonlinear response, but will also lead to a prolonged dephasing time [60]. Ultrafast nonlinear measurements can ad-

ditionally provide insight into more complicated effects such as the interaction of the various resonance decay channels and interface relaxation time, and the effect of spatial confinement on scattering. Measurements of the temporal dynamics of plasmon resonances in the visible range are challenging, since the few-femtosecond resolution necessary is comparable to the shortest possible pulse duration in the desirable visible to near-IR local SPP resonance energy range. However, achieving the required temporal resolution is not necessarily limited by the shortest pulse available, but rather by the signal to noise ratio and precise characterization of the full optical transient in amplitude and phase.

Plasmonic interactions can be probed with interferometric homodyne or heterodyne techniques or electro-optic sampling to extract the response function defined in Eq. 7.4. These techniques can resolve the ultrashort dynamics of the plasmon response $R(t)$ with exact reconstruction of the response function by deconvolution from autocorrelation and cross-correlation measurements. Spectrally resolved nonlinear techniques can provide the simultaneous phase and amplitude information needed for the unambiguous reconstruction of both the driving field and the resonant polarization transient response, for example through a frequency resolved optical gating (FROG)-based technique [61].

FROG allows the determination of a pulse amplitude and phase through measurement of the self-gated pulse in the time-frequency domain. The most common implementation of FROG is based on the SHG response arising from two pulses interacting in a medium, given by $(X(t) + X(t-\tau))^2$, where $X(t)$ is the field transient of the pulse and τ is the time delay between the two pulses. In a non-collinear implementation, only the cross-term is detected, so that the FROG spectrogram corresponds to a spectrally-resolved intensity autocorrelation, i.e.,

$$S(2\omega, \tau) \propto \left| \int_{-\infty}^{\infty} X(t) X(t-\tau) e^{-i\omega t} dt \right|^2, \tag{7.38}$$

For a nonlinear medium which is far off-resonant, where the response is essentially instantaneous, the field transient $X(t)$ is simply proportional to the electric field of the driving laser pulse $E(t)$, gated by the time-delayed pulse $E(t-\tau)$. For a material close to resonance, the finite response time leads to an induced polarization transient, so that $X(t) = P(t)$, with free-induction decay behavior. From the spectrogram, the full electric field or polarization transient information can be reconstructed using an iterative algorithm. The resonant response function $R(t)$ can be extracted through deconvolution.

The spectrogram can be measured in a collinear geometry, producing additional terms and a spectrally resolved interferometric autocorrelation or IFROG:

$$S(2\omega, \tau) \propto \left| \int_{-\infty}^{\infty} (X(t) + X(t-\tau))^2 e^{-i\omega t} dt \right|^2 \tag{7.39}$$

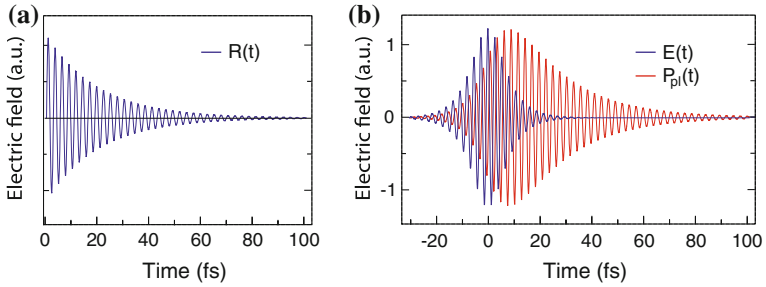

Fig. 7.16 Modeled plasmon response function $R(t)$ (**a**), with dephasing time $T_2 = 20$ fs, and resulting resonant polarization response $P(t)$ subject to driving electric field $E(t)$ (**b**). Incident pulse duration $\tau_0 = 10$ fs, and $\omega_0 = \omega_{\mathrm{pl}}$ corresponding to 800 nm wavelength (details in text)

A model of the effects of a finite response function $R(t)$ on the resulting induced polarization $P(t)$ transient in the time domain is shown in Fig. 7.16. The plasmonic response is modeled as a damped harmonic oscillator in the time domain,

$$R(t) = Ae^{i\omega_{\mathrm{pl}}t}e^{-\gamma t} \tag{7.40}$$

where A gives the effective oscillator strength, ω_{pl} is the plasmon resonant frequency, here taken to be resonant with the laser pulse, and the linewidth is given by $\gamma = 1/T_2 = \frac{1}{20}\ \mathrm{fs}^{-1}$. A sech^2 laser pulse with flat spectral phase is used to simulate the driving field $E(t)$, with full width at half-maximum $\tau_0 = 10$ fs and carrier frequency $\omega_0 = \omega_{\mathrm{pl}}$ corresponding to 800 nm center wavelength, i.e.,

$$E_{\mathrm{sim}} = E_0 \mathrm{sech}\frac{1.763t}{\tau_0}e^{i\omega_0 t}. \tag{7.41}$$

The resulting polarization arising from the driving field demonstrates the increased response time from relaxation of the damped harmonic oscillator model of the plasmon resonance, with its free-induction decay lasting past the end of the laser pulse.

A possible experimental geometry for measuring SPP dynamics in the time domain is shown in Fig. 7.17. A high quality, well-aligned parabolic mirror is used as the focusing element in order to minimize dispersion and maintain short pulses and a spatially well-defined Gaussian beam profile. Phase and amplitude of the driving laser pulse are determined using an instantaneously responding reference medium. The BBO acts as the non-resonant medium for pulse characterization, mounted interchangeably with the plasmonic system without further alignment. Results are shown in Fig. 7.18a for BBO, and the corresponding IFROG for a resonant plasmon tip response in b, with the characteristic spectrally narrowed and temporally broadened plasmon excitation [62]. The tip, as a resonant medium, shows spectral narrowing due to the temporal broadening from the finite response function, and a frequency shift in the spectrogram due to the difference between the plasmon resonance and

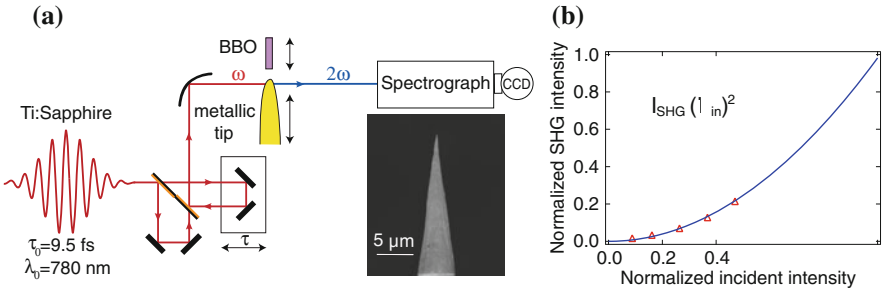

Fig. 7.17 Schematic of the experimental set-up for IFROG characterization of the plasmon dynamics in a single nanoscopic plasmonic structure, here with a plasmonic conical tip as an example of a localized SPP system (**a**). A Mach-Zehnder interferometer with special beamsplitter and parabolic mirror are employed to minimize dispersion and provide diffraction-limited excitation. *Inset* SEM image of a Au plasmonic tip. Power dependence of tip apex SHG, showing the expected quadratic behavior (**b**)

laser carrier frequencies. Figure 7.18c, d show the electric field $E(t)$ and polarization $P(t)$ amplitude and phase, reconstructed from a FROG retrieval algorithm, for the time and frequency domains. Panels (d) and (f) are the plasmon response function from deconvolution of $P(t)$ and $E(t)$, with comparison to the decay for a damped Lorentzian fit as given in Eq. 7.40. From $R(t)$ a dephasing time of 20 ± 5 fs can be directly determined without model assumptions, while for a tip with plasmon frequency not resonant within the bandwidth of the driving field, the tip response is essentially instantaneous (data not shown). The deviations from a flat phase behavior indicate possible inhomogeneities arising from structural imperfections in the nanoscale tip.

The value of T_2 is in agreement with the low-energy limit and energy-independent damping, i.e. $T_2 \sim 2\tau_D \sim 20$ fs for Au, as shown in Table 7.1. This corresponds to the non-radiative limit for decay of the plasmon response in the Drude model. Note that this value was directly extracted from the envelope of the reconstructed plasmon response function (green curve, Fig. 7.18) without any model assumptions.

Other nonlinear processes can also provide the necessary nonlinear polarization and pulse characterization, and may be required since SHG relies on a non-centrosymmetric structure. However, THG for example cannot distinguish bulk, surface, local and non-local effects and is therefore not ideal for extracting the pure plasmonic response. In addition to FROG-based measurements, time-resolved two-photon photoemission can also provide information on plasmonic dephasing. Here a two-pulse cross correlation measurement is used to measure the photoemission current from electrons excited above the vacuum level as a function of pump-probe delay, providing phase information, sub-femtosecond time resolution, and sub-100 nm spatial resolution in combination with photoemission electron microscopy (PEEM). As an early example, Ag nanoparticles on a grating were studied to determine both morphology and dynamics of the nanostructures, with dephasing times as short as 5 fs measured [63].

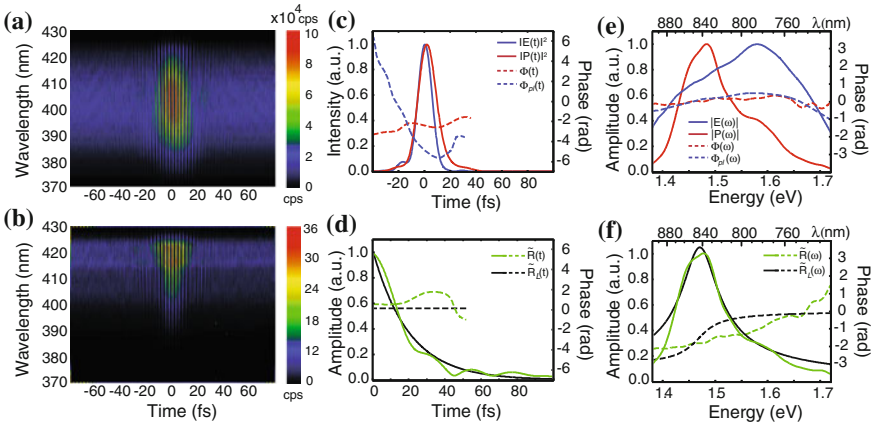

Fig. 7.18 Interferometric SHG FROG measurement of BBO (**a**) and a plasmon resonant Au tip (**b**). Phase (*dashed*) and intensity (*solid line*) of $\boldsymbol{E}(t)$ (*blue*) and $\boldsymbol{P}(t)$ (*red*) (**c**), derived from **a** and **b**. Corresponding Fourier transforms $\boldsymbol{E}(\omega)$ (*blue*) and $\boldsymbol{P}(\omega)$ in frequency domain (**e**). Response function $R(t)$ (**d**) and $R(\omega)$ (**f**) (*green*) from deconvolution of (**c**) and (**e**). Damped harmonic oscillator model response function fit $R_L(t)$ and $R_L(\omega)$ shown in *black*. Reprinted with permission from Ref. [62]. *Copyright 2010 American Chemical Society*

7.5 Ultrafast Spatio-Temporal Control with Plasmonic Antennas

The capability of optical antennas to generate high spatial localization and enhancement of optical fields is also important for characterization of nanoscale materials. While most implementations of optical antennas rely on planar geometries, spatial control of optical fields for nano-imaging can be realized using free-standing conical tip geometries, such as those used in scanning probe applications and discussed in Sect. 7.3.5 as individual nanoscopic nonlinear antennas.

The sensitivity and efficiency of optical antennas can be improved by reducing the *mode-mismatch* between the exciting far-field waveform and the near-field excitation, for example using wedges, grooves, or cascaded structures to achieve a continuous transformation from the micro- to the nano-scale. Taking advantage of the radius-dependent index of refraction experienced by SPP modes on a conical waveguide such as a noble metal tip is one approach for achieving high localization for background-free spectroscopy and imaging [64, 65]. This *adiabatic nanofocusing* approach has the advantage that scattering losses due to structural discontinuities and the decreasing SPP wavelength are minimized until the apex, where a nanoscale optical emitter is efficiently generated.

Furthermore, the nanofocusing mechanism does not rely on a resonant response and therefore is only weakly wavelength and phase dependent, unlike most optical antenna concepts which rely on the spectrally-limited plasmonic response. A broad bandwidth and thus short pulse delivery to the apex is possible. Other approaches to achieve localization rely on the interference of plasmon modes in an arbitrary

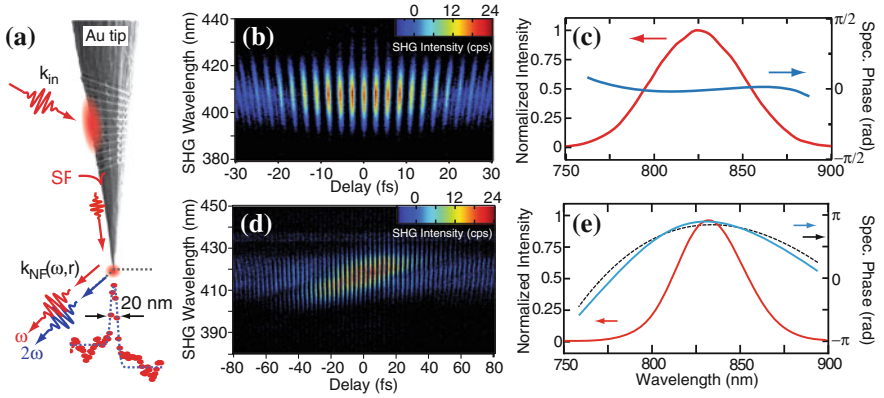

Fig. 7.19 SEM image of Au tip, illustrating grating coupling for SPP launching and nanofocusing to $\sim 20\,\text{nm}$, followed by localized apex emission (**a**). Interferometric spectrogram of apex-emitted SHG radiation (**b**) and corresponding spectral amplitude and phase (**c**) from reconstruction using a FROG algorithm, showing a transform limited pulse with bandwidth corresponding to a 16 fs pulse duration. Demonstration of deterministic pulse control at the tip-apex, with interferometric spectrogram of transform limited pulse and pulse with $200\,\text{fs}^2$ applied chirp (**d**). Corresponding reconstructed spectral amplitude and phase (**e**), showing the close agreement between the applied and extracted phase. After Ref. [67]. *Copyright 2011 American Chemical Society*

metallic structure [66]. This requires some combination of spatial, spectral, and phase pulse shaping of the driving laser field, and often uses *adaptive* algorithms in order to generate the desired nanofocus at a particular spatial location. However, the necessary local interference relies on a specific phase relationship between modes and therefore limits the spectral and temporal degrees of freedom available at the nanofocus. In contrast, the adiabatic nanofocusing process retains essentially all degrees of freedom to *deterministically* control the optical transient at the tip apex.

A demonstration of femtosecond-nanometer spatio-temporal control based on plasmonic nanofocusing on a tip is shown in Fig. 7.19. Femtosecond SPPs are launched onto an electrochemically etched Au tip using a grating structure formed by focused ion beam milling to overcome the photon-SPP momentum mismatch (a). The grating is spatially chirped for maximum coupling bandwidth. The SPPs then propagate along the tip towards the apex experiencing an increasing effective index of refraction, which leads to an increasing wavevector, decreasing group velocity, and increasing spatial confinement, thereby concentrating the electric field into the tip apex. Figure 7.19a shows the 20 nm spatial field localization at the tip apex. The efficiency of the process is high enough that, combined with the symmetry-breaking along the cone axis, SHG can be generated at the tip apex. This enables full characterization of the electric field transient at the apex, for example through IFROG, as discussed previously. Furthermore, frequency-domain pulse-shaping can be used to compensate dispersion with a multiphoton intrapulse interference phase scan (MIIPS) algorithm [68], and also to generate pulse pairs with controllable delay for the IFROG measurements themselves. The resulting spectrogram for a few-

femtosecond pulse at the apex is shown in Fig. 7.19b, with reconstructed amplitude and phase (c) corresponding to a 16 fs transform limited pulse. Arbitrary waveform generation and full deterministic control of the re-emitted apex radiation is possible through feedback on the nonlinear response of the tip. This capability is demonstrated here by applying a 200 fs^2 chirp to one of the pulses at the apex, as shown in Fig. 7.19 d) and e) with the reconstructed amplitude and phase characteristics from cross-correlation FROG (XFROG).

The localized plasmon resonance for the tips in these experiments was red-shifted relative to the laser bandwidth, so that the tips were non-resonant and had an almost instantaneous response. A tip with a plasmon resonance close to the laser wavelength would provide higher field enhancement, but with achievable minimum pulse duration now limited by the plasmon dephasing time to a few 10s of fs, rather than the SPP coupling bandwidth. The adiabatic nanofocusing process is necessarily accompanied by a decrease in the SPP group velocity on approaching the apex of the tip [69]. This SPP slow-down could provide a further increase in the nonlinear response of the tip-apex.

The grating-coupled tips demonstrate how the combination of the ultrafast optical properties of metals and intrinsic and geometry-related SPP behavior allow for spatio-temporal nano-imaging in a scanning probe configuration. Together with the nonlinear optical response of the tips and associated symmetry selectivity, this opens the door for deterministic few-femtosecond optical control on the nanoscale.

More generally, the design and optimization of optical antennas for nonlinear applications requires the ability to accurately characterize field enhancement and mode distribution properties within an antenna. Both electron-based techniques and photon-based techniques have been used for antenna characterization. Conventional far-field optical characterization can provide information about the interaction between an optical antenna and propagating light, such as the relationship between device geometry and resonant frequency. While this can be applied over a broad frequency range, it suffers from comparatively low spatial resolution, and the linear response of an antenna does not necessarily predict the nonlinear response, due to, for example, coupling between the driven plasmon and surrounding dielectric resonances. SHG, two-photon photoluminescence, or FWM can provide slightly higher spatial resolution and more accurate determination of nonlinear spectral properties, but do not provide knowledge of the underlying resonant modes and their associated spatial field distribution within an antenna. Electronic techniques, such as electron energy loss spectroscopy (EELS), transmission electron microscopy (TEM), and cathodoluminescence can facilitate the extraction of spatially detailed information, with nanometer resolution of modes and plasmonic field enhancement.

In recent years, near-field optical techniques such as scattering-scanning near-field optical microscopy (*s*-SNOM) have been utilized for high spatial resolution mapping of linear and nonlinear antenna properties, offering information about the local optical electric field magnitude and phase and interactions of modes in coupled nano-optical plasmonic and optical antenna structures. With these techniques it is possible to spatially and spectrally probe the microscopic electric field distribution, and correlate details of the field with geometrical features. Such measurements

have demonstrated spectral shifts between near-field and far-field, and confirmed that within nanoparticle geometries the nonlinear response remains sensitive to deviations in shape and other defects. These techniques are applicable to various antenna geometries and wavelengths, provide design criteria for more complex architectures and modeling, and can facilitate impedance matching of optical antennas to quantum systems [56].

The adiabatic focusing tips provide an avenue to extend ultrafast spectroscopic imaging from its conventional far-field spatial resolution limit to the nanoscale. Historically, the development of femtosecond pulsed lasers has enabled the investigation of ultrafast dynamics on the characteristic time scales of the elementary electronic and vibrational excitations in matter, with direct and selective spectroscopic access to the corresponding energy levels. The combination with spectral pulse shaping [70] provides the additional capability to control the coherent evolution of these quantum excitations (quantum coherent control), which allows steering of chemical reactions or control of optical and electronic material properties [71].

It would be highly desirable to extend the spatial resolution to the nanoscale to simultaneously access ultrafast dynamics on their associated natural length scales of the elementary electronic, visible, and spin excitations. The potential use of plasmonic properties to achieve this nanometer-femtosecond spatio-temporal control of optical excitations for imaging and spectroscopy has attracted much interest. With such a nano-optical technique, individual molecules, quantum dots, and plasmonic structures, for example, could be investigated even in dense inhomogeneous media, in addition to spatial and non-local dynamics to probe transport, propagation, and spatial coupling properties. The adiabatic focusing tips are one optical antenna concept for overcoming the diffraction limit and providing the desired high spatial field localization, with high bandwidth, and high off-resonant field enhancement thus supporting even the shortest possible few-fs optical pulses.

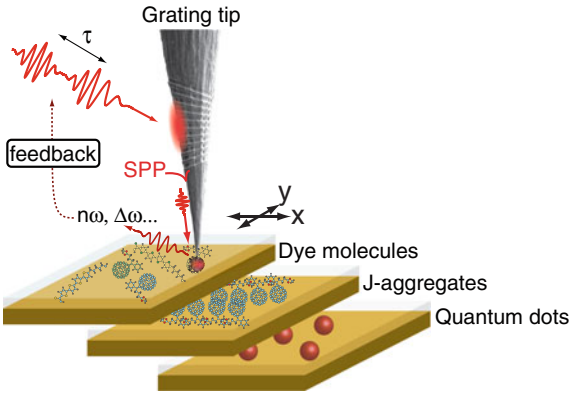

Fig. 7.20 Implementation of nanofocused, background-free coherent control and interaction dynamics experiments on single quantum emitter. Feedback for optimization is based on the luminescent or nonlinear response of the coupled tip-sample system

A possible implementation of adiabatic nanofocusing for imaging and quantum coherent control is shown in Fig. 7.20. Nanofocusing in combination with a pulse shaper can be used for linear, nonlinear, and ultrafast imaging of individual quantum systems or mesoscale variations in bulk and dense media. The ability to control pulse shape and phase enables pump-probe techniques including collinear FWM and 2D spectroscopy. With feedback on the nonlinear response $n\omega$, $\Delta\omega$, etc. of the coupled tip-sample system, the extension to quantum coherent control of the excitation pathways and evolution of the quantum system can also be realized.

7.6 Outlook

In spite of the importance of the nonlinear and ultrafast properties of metals in general, and metal surfaces and nanostructures in particular, for the understanding of phenomena such as enhancement and dephasing associated with plasmonic excitations, considerably less work has focused on these aspects compared to linear and continuous wave spectroscopies. Here we have attempted to summarize the fundamental properties of metals and their plasmonic excitations and their effect on nonlinear behavior in order to provide a guide for future extensions of plasmonic studies. Optimization and control of these properties will be important for increasing sensitivity and efficiency in a wide variety of sensing and optical switching applications, chemical spectroscopy, nano-scale imaging, or coherent control on the single quantum limit. Thus far little nanoscale imaging using a nonlinear response of a material system has been demonstrated [72], though there has been interest in further increasing the nonlinear response through engineered nanostructures with a bulk nonlinear material at the tip, which in combination with field enhancement could provide high wave-mixing conversion efficiencies and provide access to the additional spectroscopic and symmetry degrees of freedom enabled by nonlinear techniques.

In the ultrafast regime, recent work has demonstrated the control of mode coherence in plasmonic systems [73], in spite of the extremely short plasmon dephasing times. Control of coupled plasmonic-photonic modes, which have longer dephasing times and are therefore easier to direct, has been demonstrated, as well as nonlinear wavemixing in plasmonic-photonic waveguides [57]. Furthermore, taking advantage of SPP properties such as nanofocusing provides one of the most promising routes to achieving full spatio-temporal control of individual nanostructures and nanosystems. This would enable the investigation of ultrafast dynamics on the characteristic time scales of the elementary electronic and vibrational excitations in matter, and with direct and selective spectroscopic access to the corresponding energy levels.

Plasmonic field enhancement has also been proposed as a means to achieve the necessary peak intensities for high harmonic generation (HHG). However, the nanoscopic interaction volume for plasmonic structures in comparison to conventional intracavity HHG suggests that the HHG yield would be small [74]. Multiphoton or high field fluorescence processes can however be effective below the ionization threshold [75], in addition to electron emission [76]. Strong field gradients could

be utilized for nanomanipulation and trapping [77]. Additionally, strong coupling of quantum states to light can lead to qualitatively new nonlinear optics, beyond the perturbative regime discussed here. Structures based on molecular, quantum-dot, or quantum-wire exciton resonances coupled to plasmonic metal nanostructures can be optimized to form hybrid modes with large optical nonlinearities as a result of the quantum interference of the exciton dipole oscillation and the plasmonic modes, providing new quantum states and allowing new avenues for ultrafast control [78]. Further improvements in design and control or plasmonic structures could also provide access to non-local nonlinear effects.

Acknowledgments Funding was provided by the National Science Foundation (NSF CAREER Grant CHE 0748226). Part of the work was performed at the Environmental Molecular Sciences Laboratory (EMSL), a national scientific user facility from DOE's Office of Biological and Environmental Research at Pacific Northwest National Laboratory (PNNL). PNNL is operated by Battelle for the US DOE under the contract DEAC06-76RL01830.

References

1. H. Raether, *Surface Plasmons on Smooth and Rough Surfaces and on Gratings* (Springer, New York, 1987)
2. M. Kerker, *The Scattering of Light, and Other Electromagnetic Radiation* (Academic Press, New York, 1969)
3. S.A. Maier, *Plasmonics: Fundamentals and Applications* (Springer, New York, 2007)
4. N.W. Ashcroft, N.D. Mermin, *Solid State Physics* (Brooks Cole, Belmont, 1976)
5. F. Ladstädter, U. Hohenester, P. Puschnig, C. Ambrosch-Draxl, Phys. Rev. B **70**, 235125 (2004)
6. D.J. Roaf, Philos. T. R. Soc. A **255**(1052), 135 (1962)
7. A. Sommerfeld, Z. Phys. A **47**(1), 1 (1928)
8. M. Dressel, G. Grüner, *Electrodynamics of Solids: Optical Properties of Electrons in Matter* (Cambridge University Press, New York, 2002).
9. P. Johnson, R. Christy, Phys. Rev. B **6**, 4370 (1972)
10. R.L. Olmon, B. Slovick, T.W. Johnson, D. Shelton, S.H. Oh, G.D. Boreman, M.B. Raschke, Phys. Rev. B **86**, 235147 (2012)
11. C.F. Bohren, D.R. Huffman, *Absorption and Scattering of Light by Small Particles* (Wiley, New York, 2008)
12. U. Kreibig, M. Vollmer, *Optical Properties of Metal Clusters, Springer Series in Materials Science*, vol. 25 (Springer, Berlin, 1995)
13. C. Ciracì, R.T. Hill, J.J. Mock, Y. Urzhumov, A.I. Fernández-Domínguez, S.A. Maier, J.B. Pendry, A. Chilkoti, D.R. Smith, Science **337**(6098), 1072 (2012)
14. G. Mie, Ann. Phys. **330**, 377 (1908)
15. H.U. Yang, S. Berweger, J.M. Atkin, M.B. Raschke (in preparation)
16. S. Link, C. Burda, M.B. Mohamed, B. Nikoobakht, M.A. El-Sayed, Phys. Rev. B **61**(9), 6086 (2000)
17. G.V. Hartland, Chem. Rev. **111**(6), 3858 (2011)
18. C. Sönnichsen, T. Franzl, T. Wilk, G. von Plessen, J. Feldmann, O. Wilson, P. Mulvaney, Phys. Rev. Lett. **88**(7), 077402 (2002)
19. M. Liu, M. Pelton, P. Guyot-Sionnest, Phys. Rev. B **79**, 035418 (2009)
20. T.V. Shahbazyan, I.E. Perakis, J.Y. Bigot, Phys. Rev. Lett. **81**, 3120 (1998)
21. R. Boyd, *Nonlinear Optics* (Academic Press, New York, 2003)
22. Y.R. Shen, *The Principles of Nonlinear Optics* (Wiley, New York, 1984)

23. M.B. Raschke, M. Hayashi, S.H. Lin, Y.R. Shen, Chem. Phys. Lett. **359**(5–6), 367 (2002)
24. S. Jha, Phys. Rev. **140**(6A), 2020 (1965)
25. N. Bloembergen, R.K. Chang, S.S. Jha, C.H. Lee, Phys. Rev. **174**, 813 (1968)
26. J. Rudnick, E.A. Stern, Phys. Rev. B **4**, 4274 (1971)
27. J.E. Sipe, V.C.Y. So, M. Fukui, G.I. Stegeman, Phys. Rev. B **21**, 4389 (1980)
28. A. Liebsch, W.L. Schaich, Phys. Rev. B **40**, 5401 (1989)
29. C.M. Li, L.E. Urbach, H.L. Dai, Phys. Rev. B **49**, 2104 (1994)
30. G. Petrocelli, S. Martellucci, R. Francini, Appl. Phys. A Mater. Sci. Proces. **56**, 263 (1993)
31. E.K.L. Wong, G.L. Richmond, J. Chem. Phys. **99**(7), 5500 (1993)
32. D. Krause, C.W. Teplin, C.T. Rogers, J. Appl. Phys. **96**(7), 3626 (2004)
33. H.J. Simon, D.E. Mitchell, J.G. Watson, Phys. Rev. Lett. **33**, 1531 (1974)
34. T.Y.F. Tsang, Opt. Lett. **21**(4), 245 (1996)
35. F. De Martini, Y.R. Shen, Phys. Rev. Lett. **36**, 216 (1976)
36. K. Ujihara, Opt. Commun. **42**(1), 1 (1982)
37. N. Rotenberg, M. Betz, H.M. van Driel, Phys. Rev. Lett. **105**, 017402 (2010)
38. A.T. Georges, N.E. Karatzas, Phys. Rev. B **85**, 155442 (2012)
39. J. Renger, R. Quidant, N. van Hulst, S. Palomba, L. Novotny, Phys. Rev. Lett. **103**, 266802 (2009)
40. M. Fukui, J. Sipe, V. So, G. Stegeman, Solid State Commun. **27**(12), 1265 (1978)
41. G.I. Stegeman, J.J. Burke, D.G. Hall, Appl. Phys. Lett. **41**(10), 906 (1982)
42. Q. Zhang, K. Lin, Y. Luo, Opt. Express **19**(6), 4991 (2011)
43. N.B. Grosse, J. Heckmann, U. Woggon, Phys. Rev. Lett. **108**, 136802 (2012)
44. V.M. Shalaev, *Nonlinear Optics of Random Media: Fractal Composites and Metal-dielectric Films*, vol. 158 (Springer Tracts in Modern Physis, Heidelberg, 2000)
45. E.L. Ru, J. Grand, N. Felidj, J. Aubard, G. Levi, A. Hohenau, J. Krenn, E. Blackie, P. Etchegoin, J. Phys. Chem. C **112**, 8117 (2008)
46. M. Moskovits, Rev. Mod. Phys. **57**, 783 (1985)
47. A. Wokaun, J.G. Bergman, J.P. Heritage, A.M. Glass, P.F. Liao, D.H. Olson, Phys. Rev. B **24**, 849 (1981)
48. C.K. Chen, A.R.B. de Castro, Y.R. Shen, Phys. Rev. Lett. **46**, 145 (1981)
49. D.S. Chemla, J.P. Heritage, P.F. Liao, E.D. Isaacs, Phys. Rev. B **27**, 4553 (1983)
50. F.X. Wang, F.J. Rodriguez, W.M. Albers, M. Kauranen, New J. Phys. **12**, 063009 (2010)
51. S. Roke, G. Gonella, Ann. Rev. Phys. Chem. **63**(1), 353 (2012)
52. J.I. Dadap, J. Shan, T.F. Heinz, J. Opt. Soc. Am. B **21**, 1328 (2004)
53. C. Neacsu, G. Reider, M. Raschke, Phys. Rev. B **71**(20), 201402 (2005)
54. S. Roke, W.G. Roeterdink, J.E.G.J. Wijnhoven, A.V. Petukhov, A.W. Kleyn, M. Bonn, Phys. Rev. Lett. **91**, 258302 (2004)
55. J. Nappa, I. Russier-Antoine, E. Benichou, C. Jonin, P.F. Brevet, J. Chem. Phys. **125**(18), 184712 (2006)
56. R. Olmon, M. Raschke, Nanotechnology **23**, 444001 (2012)
57. T. Utikal, T. Zentgraf, T. Paul, C. Rockstuhl, F. Lederer, M. Lippitz, H. Giessen, Phys. Rev. Lett. **106**, 133901 (2011)
58. M. Danckwerts, L. Novotny, Phys. Rev. Lett. **98**, 026104 (2007)
59. M. Kauranen, A.V. Zayats, Nat. Photon. **6**(11), 737 (2012)
60. C. Timm, K.H. Bennemann, J. Phys. Condens. Matter. **16**(4), 661 (2004)
61. R. Trebino, *Frequency Resolved Optical Gating: The Measurement of Ultrashort Laser Pulses* (Kluwer, New York, 2002)
62. A. Anderson, K.S. Deryckx, X.G. Xu, G. Steinmeyer, M.B. Raschke, Nano Lett. **10**, 2519 (2010)
63. H. Petek, S. Ogawa, Prog. Surf. Sci. **56**(4), 239 (1997)
64. A.J. Babadjanyan, N.L. Margaryan, K.V. Nerkararyan, J. Appl. Phys. **87**(8), 3785 (2000)
65. M.I. Stockman, Phys. Rev. Lett. **93**, 137404 (2004)
66. M. Aeschlimann, M. Bauer, D. Bayer, T. Brixner, S. Cunovic, F. Dimler, A. Fischer, W. Pfeiffer, M. Rohmer, C. Schneider, F. Steeb, C. Strüber, D.V. Voronine, Proc. Nat. Acad. Sci. **107**, 5329 (2010)

67. S. Berweger, J.M. Atkin, X.G. Xu, R.L. Olmon, M.B. Raschke, Nano Lett. **11**, 4309 (2011)
68. B. Xu, J.M. Gunn, J.M.D. Cruz, V.V. Lozovoy, M. Dantus, J. Opt. Soc. Am. B **23**(4), 750 (2006)
69. V. Kravtsov, J.M. Atkin, M.B. Raschke, Opt. Lett. **38**(8), 1322 (2013)
70. A.M. Weiner, Rev. Sci. Intr. **71**, 1929 (2000)
71. A. Assion, T. Baumert, M. Bergt, T. Brixner, B. Kiefer, V. Seyfried, M. Strehle, G. Gerber, Science **282**(5390), 919 (1998)
72. C.C. Neacsu, B.B. van Aken, M. Fiebig, M.B. Raschke, Phys. Rev. B **79**(10), 100107 (2009)
73. A. Kubo, K. Onda, H. Petek, Z. Sun, Y.S. Jung, H.K. Kim, Nano Lett. **5**, 1123 (2005)
74. M.B. Raschke, Annalen der Physik **525**(3), 40 (2013)
75. M. Sivis, M. Duwe, B. Abel, C. Ropers, Nature **485**, 7397 (2012)
76. C. Ropers, D.R. Solli, C.P. Schulz, C. Lienau, T. Elsaesser, Phys. Rev. Lett. **98**, 043907 (2007)
77. M.L. Juan, M. Righini, R. Quidant, Nat. Photon. **5**, 349 (2011)
78. P. Vasa, R. Pomraenke, G. Cirmi, E. De Re, W. Wang, S. Schwieger, D. Leipold, E. Runge, G. Cerullo, C. Lienau, ACS Nano **4**(12), 7559 (2010)

Chapter 8
Controlling Thermal Radiation with Surface Waves

Philippe Ben-Abdallah, François Marquier and Jean-Jacques Greffet

Abstract The purpose of this chapter is to show that surface waves can be used to tailor radiative heat transfer. The first part of the chapter deals with the modification of radiative properties of surfaces. By taking advantage of surface waves, it is possible to design both the angular and the spectral characteristics of the emissivity/absorptivity. This paves the way to the design of smart incandescent IR sources with unprecedented properties. The second part of the chapter deals with the radiative heat transfer at the nanoscale. Here, the flux can be orders of magnitude larger than the flux given by Stefan-Boltzmann law. Surface waves can be used to enhance this flux and also to control its spectrum. Applications to heat flux modulators and thermophotovoltaics devices are discussed.

Keywords Plasmon · Thermal radiation · Surface waves

8.1 Surface-Waves Assisted Thermal Emission

8.1.1 Introduction to Thermal Emission

8.1.1.1 Radiometric Point of View

In this section we briefly introduce the definitions used to deal with emitted flux in the framework of radiometry. We then introduce an alternative point of view based

P. Ben-Abdallah · F. Marquier · J.-J. Greffet (✉)
Laboratoire Charles Fabry, Institut d'Optique, CNRS, 2 av Fresnel, 91127 Palaiseau, France
e-mail: pba@institutoptique.fr

F. Marquier
e-mail: francois.marquier@institutoptique.fr

J.-J. Greffet
e-mail: jean-jacques.greffet@institutoptique.fr

T. V. Shahbazyan and M. I. Stockman (eds.), *Plasmonics: Theory and Applications*,
Challenges and Advances in Computational Chemistry and Physics 15,
DOI: 10.1007/978-94-007-7805-4_8, © Springer Science+Business Media Dordrecht 2013

on stochastic electrodynamics where thermal emission is considered to be a radiation problem. This allows to introduce a simple picture of the thermal emission.

In radiometry, the power $\mathrm{d}Q$ emitted by an elementary opaque surface $\mathrm{d}S$ at temperature T in a elementary frequency range $\mathrm{d}\omega$ around the circular frequency ω in a solid angle $\mathrm{d}\Omega$ around a direction $\mathbf{u}$ making an angle θ with the normal to the surface is given by:

$$\mathrm{d}Q(\omega,\theta) = I^e_\omega(T)\mathrm{d}S\cos\theta\mathrm{d}\omega\mathrm{d}\Omega$$

where $I^e_\omega(T)$ is the specific intensity of the emitted radiation. As a body can only radiate less than a blackbody, it is useful to express the specific intensity emitted by a material as

$$I^e_\omega(T) = E(\omega,\theta)I_{BB,\omega}(T)$$

where $E(\omega,\theta)$ is the emissivity and $I_{BB,\omega}(T)$ is the specific intensity at thermodynamic equilibrium (also known as blackbody specific intensity) given by:

$$I_{BB,\omega}(T) = \frac{c}{4\pi}\times\frac{\omega^2}{\pi^2c^3}\times\frac{\hbar\omega}{\exp(\hbar\omega/k_BT)-1},$$

in which k_B is Boltzmann's and $2\pi\hbar$ is Planck's constant. The first term in the previous equation relates the specific intensity to the energy per unit volume, the second term is the density of states in vacuum and the third is the mean energy per mode. In what follows, we will be interested in the physical meaning of the emissivity and the different ways to engineer this quantity. Here, we note that the emissivity is a real number in the interval [0, 1] that depends on frequency and angle. It characterizes the ability of a material to produce thermal radiation. In radiometry, it is introduced as a phenomenological quantity. Using energy conservation arguments, it can be shown that it is related to the interface reflectivity [44].

8.1.1.2 Electrodynamic Point of View

The above formalism is a purely phenomenological description of the radiative fluxes. It is interesting to try to develop an alternative point of view where thermal radiation is viewed as an antenna problem. In classical electrodynamics, fields are radiated by time-dependent currents [110]. With this point of view, thermal emission appears to be the radiation of random dipoles induced by the thermal motion of charges in the emitter. These charges can be electrons in metals or ions in iono-covalent materials. Note that the mean value of these random currents is zero so that the mean value of the radiated fields is also zero. However, the power carried by the field fluctuations is not zero. The key quantity is therefore the current density fluctuation which is given at thermodynamic equilibrium by the fluctuation-dissipation theorem [72].

$$\langle j^{\mathrm{f}}_n(\mathbf{r},\omega)j^{\mathrm{f}}_m(\mathbf{r}',\omega')\rangle = 2\pi\omega\Theta(\omega,T)i\left[\varepsilon^*_{mn}(\omega)-\varepsilon_{nm}(\omega)\right]\delta(\omega-\omega')\delta(\mathbf{r}-\mathbf{r}'), \quad (8.1)$$

where $i^2 = -1$, $j_n^{\mathrm{f}}(\mathbf{r}, \omega)$ is a spatial component of the fluctuating current density at the frequency ω. The subscripts n or m stand for the x, y or z component of the vector. $\varepsilon_{nm}(\omega)$ is the dielectric tensor of the emitter and the function

$$\Theta(\omega, T) = \frac{\hbar\omega}{2} + \frac{\hbar\omega}{\mathrm{e}^{\hbar\omega/(k_B T)} - 1} \tag{8.2}$$

is the mean energy of a harmonic oscillator in thermal equilibrium. In Eq. (8.1), the delta-function $\delta(\mathbf{r} - \mathbf{r}')$ shows up because we have neglected spatial dispersion. The second delta function $\delta(\omega - \omega')$ reflects the fact that we assume a stationary system. Indeed, the fluctuation dissipation theorem is only valid in thermal equilibrium so that by applying this theorem we assume that the medium containing the fluctuating currents is in local thermal equilibrium at temperature T.

Computing the thermal emission by a body amounts to sum the contributions of all the volume elements in the material. The electric and magnetic field are then given by:

$$\mathbf{E}^{\mathrm{f}}(\mathbf{r}, \omega) = \mathrm{i}\omega\mu_0 \int_V \mathrm{d}\mathbf{r}'' \mathbb{G}^{\mathrm{E}}(\mathbf{r}, \mathbf{r}'', \omega) \cdot \mathbf{j}^{\mathrm{f}}(\mathbf{r}'', \omega), \tag{8.3}$$

$$\mathbf{H}^{\mathrm{f}}(\mathbf{r}, \omega) = \mathrm{i}\omega\mu_0 \int_V \mathrm{d}\mathbf{r}'' \mathbb{G}^{\mathrm{H}}(\mathbf{r}, \mathbf{r}'', \omega) \cdot \mathbf{j}^{\mathrm{f}}(\mathbf{r}'', \omega), \tag{8.4}$$

where the integrals are taken over the volume V which contains the fluctuating source currents; $\mathbb{G}^{\mathrm{E}}$ and $\mathbb{G}^{\mathrm{H}}$ are the electric and magnetic Green tensors [117]. Note in particular that each volume element can be characterized by a fluctuating dipole $\mathbf{p}_{\mathrm{f}}$ such that $-i\omega\mathbf{p}_{\mathrm{f}} = \mathbf{j}^{\mathrm{f}}(\mathbf{r}'', \omega)\mathrm{d}\mathbf{r}''$. It follows that thermal radiation can be reduced to the emission of a time-dependent dipole below an interface.

Let us consider the thermal emission in the upper half-space ($z > 0$) by a homogeneous material in the lower half-space ($z < 0$). With the electrodynamic point of view, it appears that the field thermally emitted is due to random dipoles below the interface. These dipoles radiate fields which decay upon propagation as the medium is absorbing. Nonetheless, dipoles located close enough to the interface radiate fields that can reach the interface. Then, these fields are either reflected or transmitted by the interface. This suggests that the emissivity introduced in the phenomenological description should be connected to the concept of transmission at an interface.

8.1.1.3 Kirchhoff's Law: Electrodynamic and Radiometric Point of View

Let us consider radiation impinging from vacuum on an absorbing half-space. Energy conservation of the incident beam imposes that the incident radiation is either reflected or transmitted by the interface. The part transmitted by the interface enters a thick absorbing medium so that it will be absorbed sooner or later. It follows that absorptivity is equal to the interface transmissivity. In the previous paragraph, we have pointed out the link between emissivity and interface transmissivity. In sum-

mary, this simple qualitative discussion shows that emissivity and absorptivity are two sides of the same coin: transmission by an interface. This discussion provides some physical ideas justifying Kirchhoff's law that states the equality between the emissivity and the absorptivity. Here, we do not elaborate any further on the foundations of Kirchhoff's law. We only note that it is valid for directional monochromatic polarized fields. A rigorous derivation of Kirchhoff's law can be found in Ref. [44]. It is based on the definition of the specific intensity (the fundamental radiometric quantity) in the framework of statistical electrodynamics (i.e. coherence theory). Let us also point out that a generalized form of Kirchhoff's law has been derived for non isothermal sources. This generalized relation establishes a link between local absorption rate and local emission rate. The local emission rate then depends on the local temperature [48, 125].

Kirchhoff's law is thus the corner stone of the modelling of thermal emission. We emphasize that it establishes a connection between the emissivity that characterizes the emission process by random currents with the absorptivity which can be computed using a coherent incident wave. This is important from a practical point of view as emissivity is a concept that belongs to radiometry and thermodynamics whereas absorptivity or transmissivity belong to coherent optics. Kirchhoff's law establishes a link between the two worlds. In summary, designing a thermal emitter with specific directional or spectral properties amounts to design an absorber with the same properties. The latter can be done using standard electromagnetic tools.

When designing absorbers, it is useful to design structures that can excite resonantly surface waves. Indeed, it is well known that absorption can be drastically modified when surface waves can be excited. It is the purpose of this section to review the potential applications to control the design of thermal sources.

8.1.1.4 Characteristics of Usual Thermal Sources, Limitations and Prospects

Incandescent sources relying on thermal emission have been the most commonly way of lighting with the tungsten filament bulb. Yet this type of radiation source suffers from a number of limitations.

It is usually taken for granted that thermal emission is incoherent as opposed to a laser which is coherent. More specifically, thermal radiation is usually *temporally incoherent* because the emitted spectrum is very broad. This is basically because all the available modes are thermally populated according to Bose-Einstein distribution. As shown by the fluctuation-dissipation theorem, the spectrum of the random currents is only limited by the absorption spectrum given by the imaginary part of the dielectric constant. In what follows, we will see that the emission spectrum can be changed dramatically by microstructuring the interface. Indeed, it is the absorptivity of the interface that matters, not the intrinsic absorption spectrum of the material.

It is also usually taken for granted that thermal sources are *spatially incoherent*. This amounts to say that they emit over many angles as opposed to a laser that can emit in a well-defined direction (or over a small area that can be located at the focus of a lens). This appears to be a reasonable assumption as the fluctuating current densities

are delta correlated as shown by the fluctuation-dissipation theorem. However, when these currents excite extended modes of the emitter such as a surface wave, a spatial correlation can be built in the source. It follows that the source can become directional as it was first demonstrated in Ref. [45].

Another basic property of thermal sources is the impossibility of modulating the emitted flux at high frequencies. Indeed, the standard approach relies in modulating the temperature. As cooling a source is a slow process, high speed modulation cannot be obtained. Typical modulation frequencies for available IR sources are on the order of tens of Hz. To go beyond this limitation, it has been proposed recently to modulate the emissivity instead of modulating the temperature [46]. This modulation can be performed without modifying the emitter temperature by using e.g. a phase material change or modulating the doping of an active absorber. These approaches are no longer limited by the cooling dynamics.

In summary, it is seen that many limitations of usual thermal sources such as a poor directivity, a broad spectrum and a low intensity frequency modulation can be overcome by using advanced concepts of nanophotonics. This paves the way towards the design of smart IR incandescent sources. This is all the more important as it is very difficult to produce efficient LEDs in the IR. This is due to a fundamental limit based on the spontaneous photon emission rate that scales as the cube of the frequency. When moving the wavelength from 1 to 10 μm, the rate of spontaneous emission is thus decreased by a factor of 1000. In what follows, we review several experiments showing how emissivity can be modified by taking advantage of the interplay between surface waves and surface microstructures.

8.1.1.5 Thermal Sources and Partial Coherence

A thermal source is often considered to be an incoherent source. The aim of this section is to briefly review the basic concepts of coherence in order to clarify how it is possible to design a partially coherent thermal source. Let us first remind what is a blackbody source. We start by reminding that the term blackbody is sometimes used to refer to the radiation at thermal equilibrium, sometimes used to refer to an isothermal cavity that can be used to experimentally produce radiation approaching the radiation field at thermodynamic equilibrium, and sometimes used to refer to a perfectly absorbing surface which can absorb incident radiation at any wavelength and from any direction and polarization. Only the last will be called blackbody hereafter. In other words, we use the term blackbody to refer to a material with an emissivity which is equal to 1 for any wavelength and angle.

The coherence properties of the electromagnetic field at thermodynamic equilibrium are well known [43]. They are characterized by the correlation function $\langle E_n(\mathbf{r}, t) E_m(\mathbf{r}', t')\rangle$. Field correlations are often called second-order coherence. Intensity correlations which are widely studied in quantum optics will not be considered here. It is customary to introduce spatial coherence and temporal coherence of a given electromagnetic field. The spatial coherence is characterized by the field correlation function at a given time $\langle E_n(\mathbf{r}, t) E_m(\mathbf{r}', t)\rangle$ whereas the temporal coherence

is characterized by the correlation function at the same point $\langle E_n(\mathbf{r},t)E_m(\mathbf{r},t')\rangle$ and two different times.

The time-correlation functions contain information on the spectral content of the fields. The Wiener-Khinchin theorem [43] shows that the Fourier transform of the time correlation function is the spectral density of the field. Hence, at thermodynamic equilibrium, we find the field correlation function:

$$\langle E_n(\mathbf{r},t+\tau)E_m(\mathbf{r},t)\rangle = \delta_{nm} Re\left[\int_0^\infty 4\mu_0 \frac{\omega^2}{6\pi c}\frac{\omega}{\exp(\hbar\omega/k_B T)-1}\exp(i\omega\tau)\frac{\mathrm{d}\omega}{2\pi}\right].$$

Here, we see that the broad spectrum entails a short correlation time. However, by filtering the spectrum in order to reduce the bandwidth, it is possible to increase the coherence time of a given source. Hence, designing temporally coherent sources amounts to design spectrally narrow sources.

A similar property exists for spatial coherence in a plane. We introduce a plane perpendicular to the propagation direction to analyse transverse spatial coherence. When dealing with homogeneous random processes, the Fourier transform cannot be defined for a function which is not square integrable. As usual, the spectral analysis is done using the concept of power spectral density. For the sake of convergence of the field Fourier transform, a new electric field $\mathbf{E}_A(\mathbf{r}_{/\!/},\omega)$ is defined to be equal to the random field in a square of area A and null outside. The spatial power spectral density is given by:

$$\lim_{A\to\infty}\frac{1}{A}\langle E_{n,A}(\boldsymbol{\kappa},\omega)E_{m,A}(-\boldsymbol{\kappa},\omega)\rangle.$$

Using again Wiener-Khinchin theorem, the spatial correlation function is given by [43]:

$$\langle E_n(\mathbf{r}_{/\!/},\omega)E_m(\mathbf{r}'_{/\!/},\omega)\rangle = \int \frac{\mathrm{d}^2\boldsymbol{\kappa}}{4\pi^2}\lim_{A\to\infty}\frac{1}{A}\langle E_{n,A}(\boldsymbol{\kappa},\omega)E_{m,A}(-\boldsymbol{\kappa},\omega)\rangle\exp[i\boldsymbol{\kappa}\cdot(\mathbf{r}'_{/\!/}-\mathbf{r}_{/\!/})].$$

It can be shown that the far-field intensity in a direction specified by $\boldsymbol{\kappa}$ is proportional to $\langle E_{n,A}(\boldsymbol{\kappa},\omega)E_{m,A}(-\boldsymbol{\kappa},\omega)\rangle$, so that it is seen that the directivity of the source is directly related to the transverse correlation function by a Fourier transform. Designing a transverse correlation function amounts to control the spatial spectrum of the field at the source plane. Again, it is seen that spatial coherence can be seen as a filtering issue in $\boldsymbol{\kappa}$-space.

In summary, the coherence of thermal sources can be controlled by filtering the directional and spectral emission properties. In what follows, we will show that by taking advantage of surface-waves resonances, it is indeed possible to engineer these properties.

8.1.1.6 Partially Coherent Sources: Emissivity as a Filter

In this section, we introduce a simple picture of the partially coherent emission by a single interface separating an opaque medium from vacuum. In order to derive this simple picture, we use two simple arguments introduced above. First, we have seen that the emissivity can be interpreted as the transmissivity of the interface. Second, we have seen that at local thermodynamic equilibrium all the modes are populated according to the Bose-Einstein distribution. In particular, radiation impinging on the interface from the emitter side is characterized by the emitter temperature as the body is in local thermodynamic equilibrium. Finally, we have seen that controlling the coherence amounts to control the direction of emission for spatial coherence and the emission spectrum for temporal coherence. Summarizing, we see that if we can design the angular and spectral dependence of the interface transmissivity, we can fully control the coherence of the thermally emitted field. For instance, a temporally coherent source requires a transmission factor (i.e. emissivity) which is zero almost everywhere and close to one in a narrow spectrum.

8.1.1.7 Early Results

A corner stone result is the first demonstration of total absorption by a shallow gold grating due to the resonant excitation of a surface plasmon. It has been predicted by D. Maystre and observed by Maystre and Hutley [81] in the 1970s. It is a remarkable result as the reflectivity of this shallow grating is essentially either 1 (as one would expect for a gold mirror) or zero (for a very limited range of frequencies and angle corresponding to the excitation of the surface plasmon). Later on, Hesketh and his group showed spectral measurements on doped-silicon deep gratings with varying periods heated at 400 °C [51]. They showed that the behavior of the emission in p-polarization depended strongly on the period, while in s-polarization the spectra did not change significantly. Since then, it has been shown that this was related to the surface plasmon thermally excited on doped silicon. In the late 1990s works were conducted on doped-silicon V-grooved gratings showing antireflection properties in p-polarization [5, 49]. In 1999, The first experiment on thermal emission by a metallic lamellar grating has been performed by Kreiter and coworkers [62]. A gold grating was heated at 700 °C and the angular emission at two wavelengths (710 and 810 nm) was observed. They showed a purely p-polarized peak emission for well-defined angles, attributed to surface plasmons.

Of particular relevance for thermal sources are surface phonon polaritons. Indeed, surface plasmons of common metals are in the near UV so that they cannot be effectively thermally excited close to the plasma frequency for achievable temperatures. Of course, the part of the dispersion relation that lies close to the light line at lower frequencies (see Fig. 8.1) can always be excited. By contrast, the surface phonon polaritons exist in the so-called reststrahlen region where optical phonon exists, in the infrared. This region exist between the so-called longitudinal optical frequency and transverse optical frequency. The polaritons are coupled electromagnetic and vibra-

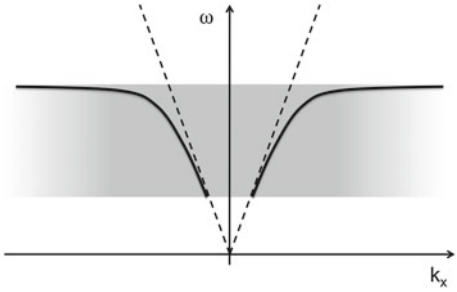

Fig. 8.1 Sketch of the dispersion relation of a surface wave. k_x is the x component of the wave vector. The *dotted line* represents the light cone $k_x = k_0 = \omega/c$. The *gray shaded area* corresponds to the frequency range in which the surface waves exists ($\mathrm{Re}[\varepsilon(\omega)] < -1$). The asymptote appears when $|\varepsilon(\omega) + 1|$ approaches 0

tion modes (i.e. half a photon and half a phonon) and can be thermally excited even at ambient temperature. Considering the particular case of a flat interface between a dielectric and vacuum, a surface wave can exist when the real part of the dielectric constant $\varepsilon(\omega)$ is less than -1. The surface wave is characterized by its dispersion relation seen on Fig. 8.1: the component k_x of the wave vector parallel to the interface is always larger than the wave vector in the surrounding medium, denoted by k_0, so that the wave is evanescent in the z-direction: the wave is confined close to the surface.

In the early 1980s, Zhizhin and coworkers studied the thermal emission of materials supporting surface phonons [129]. The surface waves were excited by heating the film at 150 °C and then coupled to propagating waves using periodic inhomogeneities on the surface. The emission spectra in p-polarization was changed with the direction of observation. Between 2002 and 2004, angularly and spectrally resolved experiments on SiC gratings were conducted and compared to numerical studies [45, 78], in which the role of surface phonons has been clearly demonstrated. Similar numerical and experimental studies have also been performed on materials supporting surface plasmons as doped-silicon gratings [66, 77] as well as tungsten [65].

In the next sections, we will mainly study the thermal emission of lamellar gratings. Figure 8.2 shows a typical grating characterized by its period, height and filling

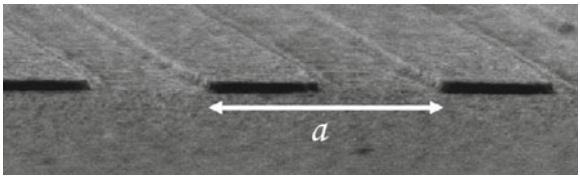

Fig. 8.2 Scanning electron microscope image of a shallow lamellar grating of tungsten with period $a = 3\,\mu m$, filling factor $F = 50\,\%$, and depth $h = 0.125\,\mu m$. This structure allows coupling surface plasmons to propagating waves at wavelengths around $4\,\mu m$ as shown in Sect. 8.1.4

factor. Thermal emission of lamellar gratings in the plane perpendicular to the lines of the gratings is studied first. Section 8.1.5 shows then how the p-polarized surface waves can be coupled to s-polarized propagating waves. The case of crossed gratings will be also discussed.

8.1.2 Spatially-Coherent Thermal Emission: Surface-Phonons Assisted Directional Thermal Emission

Surface waves and propagating waves are coupled here using a shallow periodic structuration of the surface. More precisely, this structuration is a lamellar grating. The x axis is chosen parallel to the mean surface and perpendicular to the lines of the grating. The period of this grating is denoted by a. An incident wave is diffracted by the structure in directions given by a phase matching condition: $k_{\text{diffracted},x} = k_{\text{incident},x} + nG$, where n is an integer and $G = 2\pi/a$ is the grating vector modulus. We consider thermally-excited surface waves, characterized by a frequency ω and a wave vector $k_x = \kappa_{\text{sw}}$. Figure 8.3 shows that phase matching conditions allow coupling this surface wave to a diffracted propagating wave if $k_{\text{diffracted},x} = \kappa_{\text{sw}} + nG$ is lower than $k_0 = \omega/c$.

Considering a given grating vector G (a given grating period a), two parts of the dispersion relation can be coupled to propagating waves. The linear part, close to the light cone, provides diffracted propagating waves with a well-defined wave vector at a given frequency. Hence, it yields directional absorption or emission. The flat asymptote of the dispersion relation corresponds to the condition $\varepsilon(\omega) + 1 = 0$. This is easily seen from the dispersion relation $\kappa_{sw} = k_0\sqrt{\varepsilon/(\varepsilon+1)}$. At the corresponding frequency, the surface wave can be excited for any wavevector so that it yields isotropic absorption or emission.

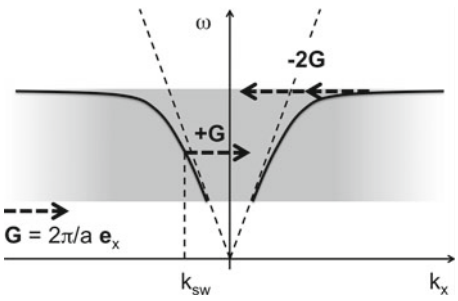

Fig. 8.3 Sketch of the dispersion relation of a surface wave. κ_{sw} is a surface-wave wave vector, a is the grating period and $\mathbf{G}$ is the grating vector. $\mathbf{e}_x$ is the unit vector along the x direction, perpendicular to the lines of the grating. When $\kappa_{\text{sw}} + nG$ is lower than k_0, there is a coupling between the surface wave and a propagating wave. Two cases are shown: $n = 1$ and $n = -2$

We take here the example of a silicon carbide sample. Silicon carbide is a polar material, which can support surface phonons in the range 10.5–12.5 μm. It can be described by the permittivity

$$\varepsilon_1(\omega) = \varepsilon_2(\omega) = \varepsilon_\infty \left(\frac{\omega_L^2 - \omega^2 - i\gamma\omega}{\omega_T^2 - \omega^2 - i\gamma\omega} \right) \equiv \varepsilon(\omega), \tag{8.5}$$

with the longitudinal phonon frequency $\omega_L = 1.827 \times 10^{14}$ rad/s, the transversal phonon frequency $\omega_T = 1.495 \times 10^{14}$ rad/s, the damping $\gamma = 0.9 \times 10^{12}$ rad/s and $\varepsilon_\infty = 6.7$.

A period $a = 6.25\,\mu m$ is chosen to permit the whole dispersion relation to be coupled to propagating waves. The filling factor of 50 % and the height $h = 285$ nm have been optimized to have the better efficiency in the coupling at a wavelength of 11.36 μm. Figure 8.4 gives the calculated emissivity of this grating for three directions of observation in *p*-polarization. It is shown that the emissivity reaches unity at a wavelength of 11.36 μm and in the direction 46°, with respect to the normal to the interface. When changing the direction of observation, the emissivity peak moves. These peaks are directly related to the surface-wave dispersion relation. A remarkable secondary peak appears around 10.9 μm for directions 46° and 60°, which is due to the contribution of the asymptotic part of the dispersion relation.

The predicted behaviour is well reproduced experimentally as shown in Fig. 8.5. Note that the peak emissivity is lower than in calculations. Besides, they appear at slightly different wavelengths (red-shift of the peaks). It has been shown that this effect is related to the temperature of the sample. Numerical simulations have been made using tabulated dielectric constant of silicon carbide measured at ambient temperature, whereas the experiment has been performed around 770 K. If the dielectric constant at 770 K is measured and used in the numerical simulations, a very good agreement can be found between experiments and numerical calculations [78]. It was found that when increasing the temperature in the range 300–700 K, the main effect is an increase of the parameter γ.

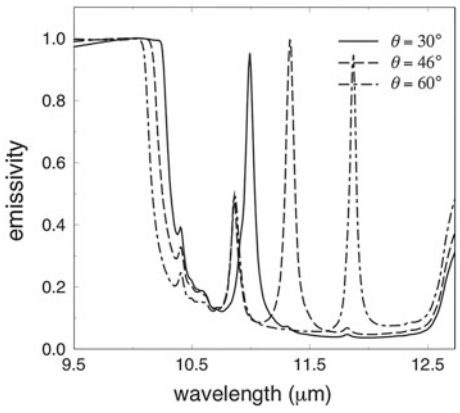

Fig. 8.4 Calculatedemissivity spectra of a SiC lamellar grating, whose features are period: 6.25 μm, filling factor: 50 % and height: 285 nm. Each spectrum corresponds to a given direction of observation (30, 46 and 60°)

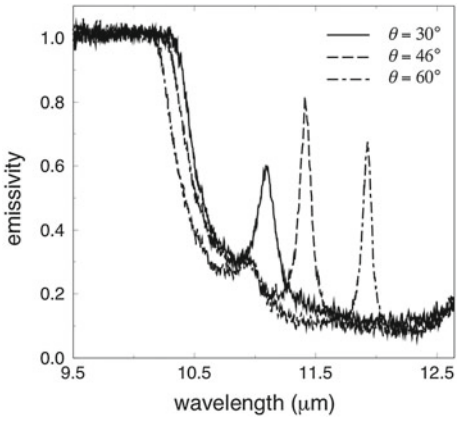

Fig. 8.5 Experimental emissivity spectra of a SiC lamellar grating, whose features are period: 6.25 μm, filling factor: 50 % and height: 288 nm. Each spectrum corresponds to a given direction of observation (30, 46 and 60°)

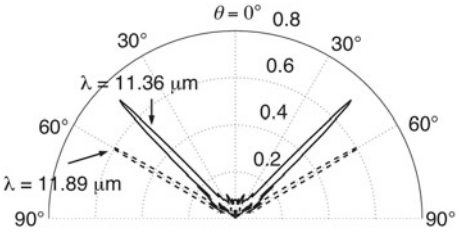

Fig. 8.6 Experimental emissivity diagram of a silicon carbide grating characterized by its period: 6.25 μm, filling factor: 50 % and height: 288 nm at two different wavelengths 11.36 and 11.89 μm

At a given wavelength, the emission of the silicon carbide structure is very directional. Figure 8.6 shows the experimental emissivity diagram of the previously-defined grating for two different wavelengths 11.36 and 11.89 μm. It is seen that the emission peaks are very narrow: the grating behaves like an antenna. This is a clear signature of the spatial coherence of the source at these wavelengths. That means that two distant dipole moments of the source are correlated, giving rise to constructive interferences in specific directions. The surface wave is correlated in the near field over distances of several wavelengths, corresponding to the decay length of the surface wave along the interface. It is possible to show that this decay length of the surface wave gives the spatial-coherence length of the source: two dipoles in the structure are correlated over distances of the order of the propagation length of the surface phonon. Such correlations have been studied in Ref. [21]. The near-field temporal coherence has been studied in Ref. [112].

8.1.3 Surface-Phonons Assisted Isotropic Thermal Emission

Spatially-coherent thermal emission due to surface phonons has been shown in the previous section. A periodic structuration of the surface has been used to couple

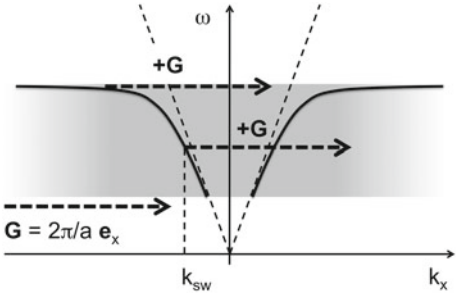

Fig. 8.7 Sketch of the dispersion relation of a surface wave. κ_{sw} is a surface-wave wave vector, a is the grating period and $\mathbf{G}$ is the grating vector. $\mathbf{e}_x$ is the unit vector along the x direction, perpendicular to the lines of the grating. When $|\boldsymbol{\kappa}_{sw} + n\mathbf{G}|$ is lower than k_0, there is a coupling between the surface wave and a propagating wave. In this case, only the surface waves whose frequency is close to the asymptote can be coupled to propagating waves

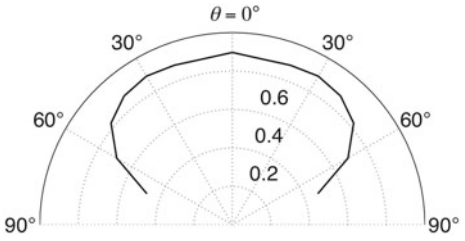

Fig. 8.8 Experimental emissivity diagram of a silicon carbide grating characterized by its period: 3 μm, filling factor: 40 % and height: 350 nm at a 10.88 μm wavelength

surface waves to the far field. When varying the period of the grating, the phase matching condition will change, so that the direction of emission will change at a given wavelength. This effect is however limited for smaller periods. Indeed, the smaller the period, the greater the grating vector modulus G. Figure 8.7 shows the surface-waves dispersion relation with a greater G. It is seen that the linear part of the dispersion relation cannot be coupled to a wave lying in the light cone, but only the asymptotic part. That means that for such a grating period, there is only one wavelength at which the coupling between surface waves and propagating waves occurs. At this wavelength, a large number of wave vectors fulfills the phase matching conditions. Hence, we expect a surface-wave assisted isotropic thermal emission.

Using the same material as in the previous section, a grating can be numerically optimized to obtain emissivity close to unity at the asymptote frequency. The period has been chosen to be $a = 3\,\mu$m. The calculated filling factor and height of the lamellar grating are respectively 40 % and 350 nm. A single peak appears in the emissivity spectrum at a wavelength around 10.88 μm. At this wavelength, the emissivity is experimentally as high as 0.9. Figure 8.8 shows the experimental emissivity diagram for this grating at this wavelength. In contrast with Fig. 8.6, the emission is almost isotropic.

8.1.4 Surface-Plasmons Assisted Thermal Emission

Results have been seen in the previous sections on silicon carbide structures, showing an efficient coupling between surface phonons and propagating waves. That leads to non-usual thermal emission characteristics, in particular spatial coherence. Similar results can be obtained using surface plasmons on metals instead of surface phonons on polar materials. Kreiter and coworkers studied thermal emission of a gold grating. Heating their sample at 700 °C, they observed narrow peaks of emission mediated by surface plasmons at 710 and 810 nm. The full width at half maximum (FWHM) of the peaks is of the order of 85 mrad. Dealing with thermal emission of metals, tungsten appears as a good candidate. It is indeed widely used in thermal light applications because of its high melting temperature. It is however not a very good emitter in the infra red and works have been done to enhance its thermal emission [50]. Tungsten does not support surfaces plasmons in the visible but in the near IR, there are modes with very large propagation length. This may be surprising at first glance because tungsten is a lossy metal. However, its dielectric constant is so large that the field of the surface plasmon is mostly in the vacuum where there are no losses. Very narrow peaks of emission are thus expected. A grating can be optimized to produce highly directional sources. Figure 8.9 shows calculated and experimental emission diagrams for a grating characterized by its period $a = 3\,\mu$m, filling factor F = 50 %, and depth $h = 125$ nm. The experiment has been performed at a temperature of 300 °C. The peak at 4.53 μm presents a FWHM of 15.7 mrad (0.9°), which is only twice the FWHM of a standard CO_2 laser (typically 7 mrad). In order to reduce further the angular width of the emission, it is necessary to use surface waves with longer propagation lengths. Dahan et al. have designed a structure consisting of coupled cavities with a longer propagation length [33]. An even larger coherence length of 10 mm has been obtained using a gold grating in the plasmonic bandgap edge [19].

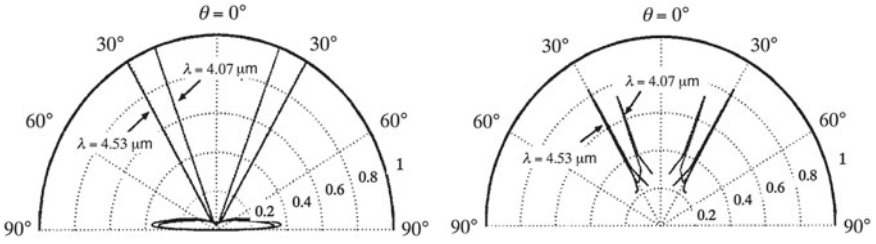

Fig. 8.9 Calculated (*left*) and experimental (*right*) emissivity diagram for a tungsten grating characterized by its period $a = 3\,\mu$m, filling factor F = 50 %, and depth $h = 125$ nm at two different wavelength 4.07 and 4.53 μm

8.1.5 Polarization Effects: Coupling of s-Polarized Propagating Waves and Surface Waves

Previous sections have been devoted to the study of the coupling between surface waves and propagating waves. It is well known that surface plasmons or phonons are p-polarized electromagnetic waves. It is thus tempting to think that propagating waves excited by surface waves through the grating are also p-polarized. That is true only in the emission plane perpendicular to the lines of the grating. Indeed, when observing in another plane, it is possible to couple s-polarized propagating waves to surface waves [79, 80]. Figure 8.10 presents the emissivity patterns of a silicon carbide grating ($a = 6.25\,\mu$m, filling factor 50 % and height $h = 285$ nm) as a function of the parallel components k_x and k_y of the emitted wave vector at a wavelength $\lambda = 11.36\,\mu$m. The pattern is limited by $k_0 = \omega/c$. Figure 8.10a, b, respectively in p- and s-polarization, shows the same circle-like pattern emissivity corresponding to the phase matching condition $k_{sw} \pm G$.

It is seen however on Fig. 8.10b that the maximum emissivity is very low comparing to the maximum emissivity seen on Fig. 8.10a, which is very close to unity. There is indeed a second condition in addition to the phase matching condition to couple surface waves and propagating waves. It deals with the polarization of the emitted wave. The emitted wave must have an electric field component along the wave vector of the surface wave. This is the origin of emissivity variations along the circles defined by the phase matching condition. Let us consider the case of absorption of a plane incident wave by coupling to a surface wave through a grating. A surface wave propagating along the interface with a wave vector $\boldsymbol{\kappa}_{sw}$ has two components of the electric field: one is parallel to $\boldsymbol{\kappa}_{sw}$ and the other is parallel to the normal of the surface. It follows that the surface current density associated with the surface plasmon in the material has a component parallel to $\boldsymbol{\kappa}_{sw}$. An external electric field can excite a surface wave provided that it has a component parallel to $\boldsymbol{\kappa}_{sw}$. A s-polarized propagating wave can fulfill these conditions as seen on Fig. 8.11.

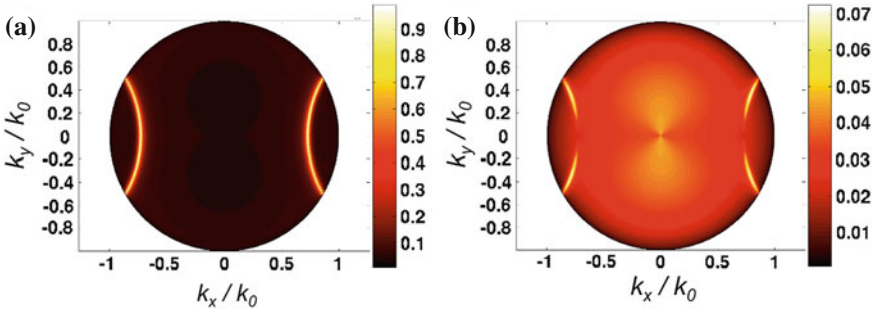

Fig. 8.10 Polar representation of the emissivity at $\lambda = 11.36\,\mu$m for the directional source (silicon carbide grating with period: 6.25 μm, filling factor: 50 % and height: 288 nm) in both p-polarization (**a**) and s-polarization (**b**) (numerical simulations)

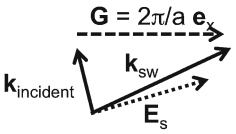

Fig. 8.11 Sketch of the phase matching and polarization condition in the case of a coupling between an incident propagating wave and a surface wave. The wave vector of the surface wave $\boldsymbol{\kappa}_{sw}$ is not colinear with the grating vector **G**. The order +1 is shown. The diffracted wave vector is not colinear with the surface-wave wave vector. The incident wave is s-polarized: the electric field $\mathbf{E}_s$ has a component parallel to $\boldsymbol{\kappa}_{sw}$, so that it can excite the surface wave

Conversely, a p-polarized surface wave can be coupled to a s-polarized emitted wave in the far field.

In the case of surface-wave assisted isotropic emission using a small-period grating, the phase matching condition between surface waves and propagating waves may be always fulfilled. The only condition is thus the polarization matching, as it can be seen on Fig. 8.12 for the previously-defined lamellar silicon carbide grating (period: 3 μm, filling factor: 40 % and height: 350 nm). The emitted waves can be s-polarized and the emissivity in this case could reach unity due to a very efficient coupling. A detailed discussion of the polarization properties of thermal emission by gratings can be found in Ref. [80].

So far, we have discussed periodic structures. However, it is possible to locally modify the orientation of the grating. This results in a local modification of the polarization of the emission. Experimental results have been reported in Refs. [30, 31]. The interplay between a surface wave propagating along a grating whose orientation varies along the surface has been studied by the group of E. Hasman [32].

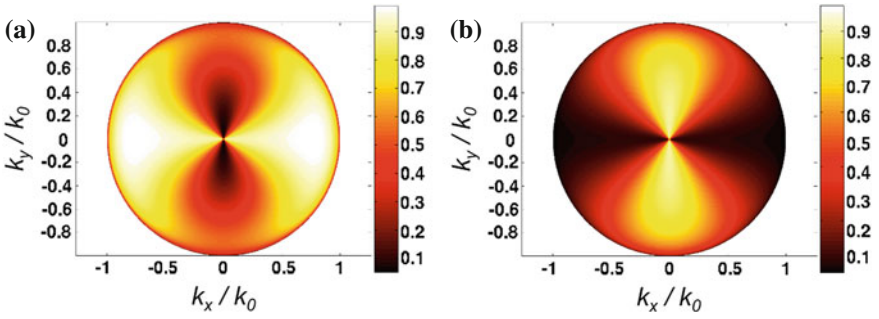

Fig. 8.12 Polar representation of the emissivity at $\lambda = 10.88\,\mu$m for the quasi-isotropic source (silicon carbide grating with period: 3 μm, filling factor: 40 % and height: 350 nm) in both p-polarization (**a**) and s-polarization (**b**) (numerical simulations)

8.1.6 Crossed Gratings

In this section, we discuss the possibility of designing a directional source using surface phonon polaritons. When using a single grating, it has been shown that emission can be directional provided that the emission frequency lies in the region where the dispersion relation is close to the light cone. However, light is emitted into a cone and not along a single direction. It is possible to design a two-dimensional grating in order to achieve vertical emission. Figure 8.13 displays the emission by a grating both in s-polarization and p-polarization. It is seen that the p-polarized emission is highly directional with an angular aperture of 2° [3].

8.1.7 Metamaterials with Controlled Emission Spectrum

The purpose of this section is to discuss the possibility of controlling the spectrum of a thermal source using metamaterials. A review paper summarizes the state of the art until 2009 [41]. While incandescent sources are often assumed to have a broad spectrum, it turns out that many groups have reported sources with narrow emission spectra. The basic strategy to design such a source is to start from a transparent or reflecting material such that its emissivity is close to zero. The second step consists in designing resonant absorbers. By controlling their spectrum, one can control the structure emissivity. The structure is chosen to be subwavelength so that it behaves as a metamaterial. Several results have been reported recently. A common approach is to rely on the excitation of guided modes in metal-insulator-metal (MIM) systems. For a thin insulator, it turns out that the effective index is large so that a subwavelength resonator can be resonant for the guided mode. A theoretical analysis of these struc-

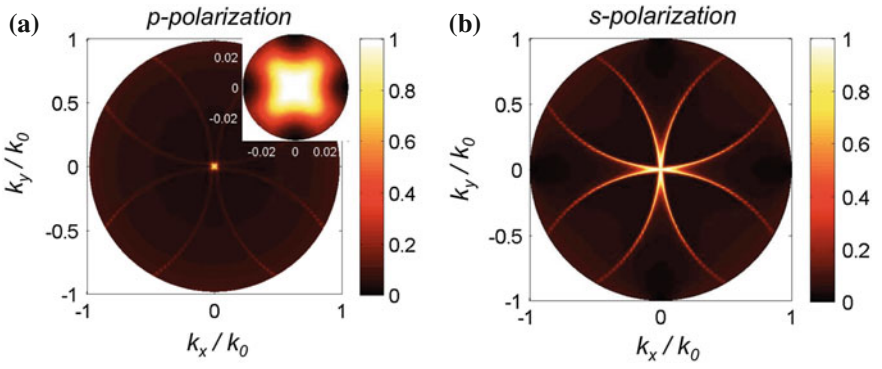

Fig. 8.13 Polar representation of the emissivity at $\lambda = 10.88\,\mu\text{m}$ for the quasi-isotropic source (silicon carbide grating with period: $3\,\mu\text{m}$, filling factor: 40% and height: 350 nm) in both p-polarization (**a**) and s-polarization (**b**) (numerical simulations)

tures can be found in Ref. [128]. Several groups have reported absorbers based on this idea [18, 20, 53, 74, 75]. In these systems, the absorption takes place predominantly in the upper metallic layer. A slightly different system has been developed for thermal emitters in the infrared [101]. Here, the insulator is silica and the device works in the IR by taking advantage of dielectric losses in silica. It is important to stress that although these systems are usually periodic arrays of absorbers, the periodicity does not play a significant role. Instead, the systems can be viewed as a collection of independent absorbers. The small interaction between scatterers can be understood by noting that the velocity mismatch between a surface plasmon propagating along the bare surface and the guided mode propagating in the structure is very large. A similar system has been reported recently. It consists in a periodic array of graphene disks deposited on a dielectric coated metal [119].

Based on the same general principle of absorption by subwavelength resonant structures, it is possible to use the absorption resonance of thin slits in a bulk metal. By controlling the slit width, it is possible to modify the effective index. The resonance frequency is therefore fixed by the depth and the width of the slit. Again, these slits are resonant absorbers. They can lead to total absorption. The resonances of these systems have been studied by a number of authors [70, 93]. As these slits can be periodically arranged with periods smaller than half a wavelength, these structures do not diffract and behave as metamaterials.

Another type of periodic structures has been designed to generate a controlled absorption. It can be described as a periodic array of rectangular slits in a thin metallic film. The structure can be considered to be analogous to a LC resonant cavity as discussed in Refs. [71, 124]. A similar structure with negative index properties has been also studied for resonant absorption [6]. Other schemes based on patterning metallic structures can also be used to control thermal emission [82, 111].

8.1.8 Multilayers and Photonic Crystals for Controlled Emission

In this section, we review tailoring emissivity using interferences. Although it is not based on surface waves, it is useful to briefly quote these works. We start with simple planar systems and we continue with photonic crystals. A simple approach is based on using multilayered systems, the simplest possible structure being an absorbing dielectric slab. The interferences lead to a non trivial angular and spectral dependence of the emission for a silicon slab as discussed in Ref. [63]. For thermophotovoltaics application, it is necessary to have a quasimonochromatic source in the near infrared. Rephaeli and Fan [104] have proposed to use a tungsten slab covered by a stack of Si/SiO_2 layers that act as an interferential filter. This system has an emissivity with low dependence on the angle and displays a peak at the desired frequency. As in this spectral range, Si and SiO_2 are transparent, emission is due to the tungsten and the stack plays the role of a filter. Drevillon et al. were able to design a layer stack emitting at a well-defined frequency over all angles [39] by using an optimization

algorithm. It has also been shown how to design spatially coherent sources with multilayered systems [10, 22, 69].

The potential of photonic crystals has been explored by many authors [24, 40, 42, 73, 100]. In Ref. [68] the authors take advantage of the fact that a surface wave exists at the interface between a truncated photonic crystal and a homogeneous dielectric. This surface wave is a leaky wave and exists in the photonic gap. It is thus possible to design a monochromatic directional source. In Ref. [59], the authors take advantage of a wave guided by a large refractive index dielectric layer on top of an absorbing substrate. Here, the guided wave plays the role of the surface mode. By properly designing a grating, it is possible to generate directional emission. A completely different approach has been taken by Noda's group [36]. Here, the photonic crystal is essentially a transparent medium. Several tens of quantum wells are inserted in the photonic crystal in order to produce an absorption band at a desired frequency. This frequency can be adjusted by engineering the intersubband transition. The photonic crystal is used to control the frequency and the direction of emission.

8.2 Radiative Heat Transfer at the Nanoscale

Two hot bodies (see Fig. 8.14) separated by a vacuum gap exchange heat through the thermal electromagnetic fields radiated by local fluctuating currents. At a separation distance larger than the Wien wavelength $\lambda_T = c\hbar/(k_B T)$ characteristic of the Planck's function, this energy exchange results exclusively from propagative waves emitted by a body and absorbed by the other. The limit given by the famous Stefan-Boltzmann's law sets the maximum heat flux these media can exchange at long separation distances (i.e. in far field). However, at subwavelength distances (i.e. in the near-field regime) the situation changes radically as anticipated by Planck [98] himself. It turns out that evanescent waves are the main contributors to heat transfer through tunneling across the vacuum gap. This phenomenon was first discovered experimentally by Cravalho et al. [29] while studying the radiative heat transfer between metals at low temperatures. A complete theory has been developed by

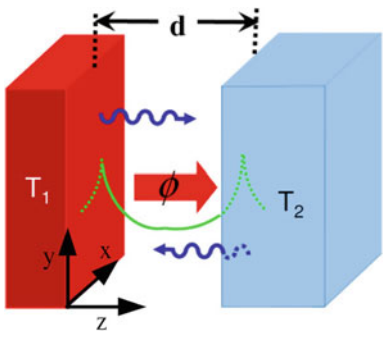

Fig. 8.14 Two hot bodies held at different temperatures T_1 and T_2 and separated by a vacuum gap of thickness d exchange heat through both radiative (i.e. propagative) and non-radiative (i.e. evanescent) photons

Polder and van Hove a few years later [99]. The experimental observation at ambient temperature remained difficult and some inconclusive results were reported [127].

A significant heat flux increase results from this tunneling. In presence of resonant surface modes such as surface polaritons, the radiative heat exchange can even surpass by several orders of magnitude the Stefan-Boltzmann law as first predicted in Refs. [84, 85]. These results have been experimentally confirmed [52, 60, 87, 90, 107, 113] and have opened new possibilities for the development of innovative technologies for nanoscale thermal management, near-field energy conversion (thermophotovoltaic conversion devices [8, 37, 67, 86], heating assisted data storage [23], plasmon assisted nanophotolithography [116]) or IR sensing and spectroscopy [56]. In what follows we will first introduce an appropriate theoretical framework to describe the radiative heat transfer between arbitrary media out of thermal equilibrium. Next we will establish a link between this theory and the Landauer theory of charge transport used in mesoscopic physics of electron transport. From this new formulation we will then derive the fundamental limits for heat exchanges both in far and near-field. Finally, we will present different practical applications of the near-field heat transfer theory for innovative technologies for nanoscale thermal management and near-field energy conversion. In this review, we focus on the heat transfer between two parallel flat surfaces with local dielectric constants. The effect of non-locality is discussed in Ref. [25], the effect of roughness is addressed in Refs. [13, 47, 76]. Heat transfer between a nanoparticle and a surface is analyzed in Refs. [14, 26, 35]. Two review papers have been recently published [38, 123].

8.2.1 Heat Flux Exchanged Between Two Planar Media

Equipped with the correlation function for the source currents in Eq. (8.1) and the linear relations in Eqs. (8.3) and (8.4) we can now determine the correlation functions of the electromagnetic fields between the bodies $\langle \tilde{E}_i^{\mathrm{f}}(\mathbf{r},\omega)\tilde{E}_j^{\mathrm{f}}(\mathbf{r}',\omega')\rangle$, $\langle \tilde{H}_i^{\mathrm{f}}(\mathbf{r},\omega)\tilde{H}_j^{\mathrm{f}}(\mathbf{r}',\omega')\rangle$, and $\langle \tilde{E}_i^{\mathrm{f}}(\mathbf{r},\omega)\tilde{H}_j^{\mathrm{f}}(\mathbf{r}',\omega')\rangle$ in terms of Green's functions and the bodies temperatures. Hence, if we know the classical electromagnetic Green functions $\mathbb{G}^{\mathrm{E}}$ and $\mathbb{G}^{\mathrm{H}}$ for a given geometry, we can evaluate the correlation functions of the fields allowing for determining heat fluxes. Although some purely quantum mechanical approaches exist [1, 55, 72], fluctuational electrodynamics has the advantage of being conceptually simple while giving the correct results for the correlation functions of the fields.

Now we want to determine the heat flux between two semi-infinite media (see Fig. 8.14) which are at local thermal equilibrium and have the temperatures T_1 and T_2. We assume that both media are separated by a vacuum gap of thickness d. In order to determine the heat flux, we first consider $T_2 = 0$, so that we consider only fluctuating currents $\mathbf{j}_1^{\mathrm{f}}$ in medium 1. The fluctuating fields $\mathbf{E}_1^{\mathrm{f}}$ and $\mathbf{H}_1^{\mathrm{f}}$ inside the vacuum gap generated by the fluctuating sources in medium 1 can be expressed in terms of the relations (8.3) and (8.4). From these expressions one can determine the

mean Poynting vector in the z direction:

$$\langle S_z^{1\to 2}\rangle = \langle \mathbf{E}_1^{\mathrm{f}} \times \mathbf{H}_1^{\mathrm{f}}\rangle \cdot \mathbf{e}_z \tag{8.6}$$

by means of the fluctuation dissipation theorem in Eq. (8.1). The resulting expression contains the dyadic Green's functions $\mathbb{G}^{\mathrm{E}}(\mathbf{r}, \mathbf{r}'', \omega)$ and $\mathbb{G}^{H}(\mathbf{r}, \mathbf{r}'', \omega)$ for that layered geometry with source points $\mathbf{r}''$ inside medium 1 and observation points $\mathbf{r}$ inside the vacuum gap. For the given layered geometry, the Green functions are well known and can for example be found in [64]. For determining the net heat flux one has also to consider the opposite case with $T_1 = 0$ so that only fluctuating currents inside medium 2 are taken into account. The expression for the transfered heat is given by

$$\mathrm{H_F}(T_1, T_2, a) = \int_A \mathbf{dA} \cdot \langle \mathbf{S}^{1\to 2} - \mathbf{S}^{2\to 1}\rangle = \int_{z=0} \mathrm{d}^2\mathbf{r}_\parallel \langle S_z^{1\to 2} - S_z^{2\to 1}\rangle, \tag{8.7}$$

where $\mathbf{r}_\parallel = (x, y)$ and $S_z^{1\to 2}$ is given by (8.6) and the integration can be performed over any surface A that completely separates the bodies. For convenience, (and with no loss of generality) we took it as the plane $z = 0$. By using the Green dyadic introduced in (8.3, 8.4), we can recast the integrand of the previous expression into

$$\langle S_z\rangle = \int_0^\infty \frac{\mathrm{d}\omega}{2\pi}\big[\Theta(\omega, T_1) - \Theta(\omega, T_2)\big]\langle S_\omega\rangle, \tag{8.8}$$

where [123]:

$$\langle S_\omega\rangle = 2\,\mathrm{Re\,Tr} \int \mathrm{d}\mathbf{r}'_\parallel \Big(\mathbb{G}(\mathbf{r}, \mathbf{r}')\partial_z\partial'_z\mathbb{G}^\dagger(\mathbf{r}, \mathbf{r}') - \partial_z\mathbb{G}^\dagger(\mathbf{r}, \mathbf{r}')\partial'_z\mathbb{G}(\mathbf{r}, \mathbf{r}')\Big)\Big|_{z'=z=0}, \tag{8.9}$$

and $\Theta(\omega, T_i)$ was defined in (8.2).

The conclusion that we draw from Eqs. (8.7)–(8.9) is that, in order to evaluate the heat transfer for a given geometry we have to determine the Green dyadic inside the gap region. In most cases this is surely a formidable task, but for planar homogeneous media, even if anisotropic, it is possible to simplify things enough so semi-analytic expressions are obtainable. This is not to say that everything was made easy - in fact even in this simplified case the calculations are fairly long [27, 120] or requires some indirect arguments as in Ref. [97], so we shall just quote the final result for the Green tensor

$$\begin{aligned}\mathbb{G}(\mathbf{r}, \mathbf{r}') = \frac{\mathrm{i}}{2}\int \mathrm{d}^2\boldsymbol{\kappa}\, \frac{e^{i\boldsymbol{\kappa}\cdot(\mathbf{r}_\parallel - \mathbf{r}'_\parallel)}}{k_{z0}}\Big[\mathbb{D}_{12}\Big(\mathbb{1}\mathrm{e}^{\mathrm{i}k_{z0}(z-z')} + \mathbb{R}_1\mathrm{e}^{\mathrm{i}k_{z0}(z+z')}\Big)\\ + \mathbb{D}_{21}\Big(\mathbb{R}_2\mathbb{R}_1\mathrm{e}^{\mathrm{i}k_{z0}(z'-z)}\mathrm{e}^{2\mathrm{i}k_{z0}d} + \mathbb{R}_2\mathrm{e}^{2\mathrm{i}k_{z0}d}\mathrm{e}^{-\mathrm{i}k_{z0}(z+z')}\Big)\Big],\end{aligned} \tag{8.10}$$

where $\mathbb{R}_i$ $(i = 1, 2)$ are the 2×2 reflection matrices characterizing interfaces (to be extensively discussed in the next section) and $\mathbb{D}_{ij}$ are defined by

$$\mathbb{D}_{ij} = (\mathbb{1} - \mathbb{R}_i \mathbb{R}_j \mathrm{e}^{2\mathrm{i}k_{z0}d})^{-1}. \tag{8.11}$$

We now derive an explicit form of the energy transfer between two surfaces using a scattering formalism that introduces reflection matrices between the bodies. Using this formalism, we will recover the result derived by Polder and van Hove for the particular case of two interfaces. We will then analyse in detail the maximum value of the heat transfer [11]. Finally, we will establish a link with the Landauer theory of charge transport commonly used in mesoscopic physics of electrons [12, 34].

When inserting Eq. (8.10) into the Poynting vector we find that [15]:

$$\langle S_\omega \rangle = \int \frac{\mathrm{d}^2\boldsymbol{\kappa}}{(2\pi)^2} \mathscr{T}(\omega, \boldsymbol{\kappa}, d), \tag{8.12}$$

where

$$\mathscr{T}(\omega, \mathbf{k}_\parallel, d) = \begin{cases} \mathrm{Tr}\big[(\mathbb{1} - \mathbb{R}_2^\dagger \mathbb{R}_2)\mathbb{D}_{12}(\mathbb{1} - \mathbb{R}_1^\dagger \mathbb{R}_1)\mathbb{D}_{12}{}^\dagger\big], & \kappa < \omega/c \\ \mathrm{Tr}\big[(\mathbb{R}_2^\dagger - \mathbb{R}_2)\mathbb{D}_{12}(\mathbb{R}_1 - \mathbb{R}_1^\dagger)\mathbb{D}_{12}{}^\dagger\big]\mathrm{e}^{-2|k_{z0}|d}, & \kappa > \omega/c \end{cases} \tag{8.13}$$

where Tr stands for the two-dimensional trace. From the previous equation we see that the whole problem is now reduced essentially to the calculation of the reflection matrices defined as

$$\mathbb{R}_j = \begin{bmatrix} r_j^{\mathrm{s,s}}(\omega, \boldsymbol{\kappa}) & r_j^{\mathrm{s,p}}(\omega, \boldsymbol{\kappa}) \\ r_j^{\mathrm{p,s}}(\omega, \boldsymbol{\kappa}) & r_j^{\mathrm{p,p}}(\omega, \boldsymbol{\kappa}) \end{bmatrix}. \tag{8.14}$$

where the $r_j^{\mathrm{i,k}}$ denote the cross reflection coefficients at the interface of medium j between the polarization i and k, respectively. In the particular case where both media are isotropic $r_j^{\mathrm{s,p}} = r_j^{\mathrm{p,s}} = 0$ and the energy transmission coefficient $\mathscr{T}_j(\omega, \boldsymbol{\kappa}, d)$ reduces to the usual expression [99]

$$\mathscr{T}_j(\omega, \kappa; d) = \begin{cases} (1 - |r_j^1|^2)(1 - |r_j^2|^2)/|D_j^{12}|^2, & \kappa < \omega/c \\ 4\mathrm{Im}(r_j^1)\mathrm{Im}(r_j^2)\mathrm{e}^{-2|k_{z0}|d}/|D_j^{12}|^2, & \kappa > \omega/c \end{cases} \tag{8.15}$$

for $j = \{\mathrm{s,p}\}$ where r_j^1 and r_j^2 are the usual Fresnel coefficients

$$r_{\mathrm{s}}^i(\omega, \kappa) = \frac{k_{z0} - k_{zi}}{k_{z0} + k_{zi}} \quad \text{and} \quad r_{\mathrm{p}}^i(\omega, \kappa) = \frac{\varepsilon_i(\omega)k_{z0} - k_{zi}}{\varepsilon_i(\omega)k_{z0} + k_{zi}} \tag{8.16}$$

for s- and p-polarized light, where $k_{zi} = \sqrt{\varepsilon_i(\omega)\omega^2/c^2 - \kappa^2}$. We have also introduced here the Fabry-Perot-like denominator D^{12}, defined by ($j = \{\mathrm{s,p}\}$)

$$D_j^{12} = (1 - r_j^1 r_j^2 \mathrm{e}^{2\mathrm{i}k_{z0}d}) \tag{8.17}$$

which results from multiple reflections inside the separation gap. As shown by Pendry [96], for any mode the energy transmission coefficient $\mathscr{T}_j$ is always smaller than one. The net heat flux inside the vacuum gap is given by the difference

$$\Phi = \langle S_z^{1\to 2} \rangle - \langle S_z^{2\to 1} \rangle. \tag{8.18}$$

Note that the term describing vacuum fluctuations $\hbar\omega/2$ in $\Theta(\omega, T)$ does not contribute to the flux Φ. A further discussion of this term can be found in Ref. [58].

For two arbitrary planar anisotropic media we find [99] by taking into account both polarization states s and p

$$\Phi = \int_0^\infty \frac{\mathrm{d}\omega}{2\pi} [\Theta(\omega, T_1) - \Theta(\omega, T_2)] \sum_{j=\{\mathrm{s,p}\}} \int \frac{\mathrm{d}^2\boldsymbol{\kappa}}{(2\pi)^2} \mathscr{T}_j(\omega, \boldsymbol{\kappa}; d) \tag{8.19}$$

The second integral of the energy transmission coefficient $\mathscr{T}_j(\omega, \boldsymbol{\kappa}; d)$ is carried out over all transverse wave vectors $\boldsymbol{\kappa} = (k_x, k_y)$ so that it includes propagating modes as well as evanescent modes. The splitting into propagating and evanescent modes stems from the fact that the electromagnetic waves inside the vacuum gap region are plane waves of the form $\exp[\mathrm{i}(k_x x + k_y y + k_{z0} z) - \mathrm{i}\omega t]$ with $k_{z0} = \sqrt{\omega^2/c^2 - \kappa^2}$, where c is the velocity of light in vacuum. k_{z0} is purely real for all lateral wave vectors $\kappa < \omega/c$ whereas k_{z0} is purely imaginary for all $\kappa > \omega/c$. The former modes are propagating waves whereas the latter are evanescent modes.

8.2.2 A Mesoscopic Analysis of the Heat Transfer at the Nanoscale

8.2.2.1 Büttiker-Landauer Formula

The expression in Eq. (8.19) together with the energy transmission coefficient in Eq. (8.15) is very general and allows finding the heat flux between two arbitrary planar bodies kept at fixed temperatures T_1 and T_2 for any distance d. Now, we are going to see that the heat flux transferred between two media can be discussed in the spirit of a Büttiker-Landauer approach. The Büttiker-Landauer approach is used to analyse the electron transport through nanowires in the mesoscopic regime. Mesoscopic physics deals with physics of systems whose size is smaller than the coherence length and the mean free path. Hence, electron transport through a nanowire cannot be viewed as a random walk of a classical particle but rather as a ballistic transport. The electron need to be described quantum mechanically using its wave function. Thus, the nanowire is a waveguide with a finite number of modes connecting two electrons reservoirs at different potentials. It can be shown that the intensity flowing through the nanowire is proportional to the applied voltage. A quantum of conductance $g_0 = e^2/h$ can be

associated to each mode. The nanowire conductance is proportional to the number of modes propagating through the nanowire weighted by a transmission factor.

We are now in a position to establish a link between the two systems as discussed in Ref. [11]. The temperature plays the role of the voltage, the energy $\hbar\omega$ plays the role of the quantized charge e, the thermal flux Φ plays the role of the current density. The electromagnetic modes propagating between the two half spaces play the role of the modes of the nanowire. Each electromagnetic mode is characterized by (ω, κ). In order to analyse Eq. (8.19) as a sum over modes, we start by writing the energy exchanged during a time interval Δt through an area L^2. It is given by

$$\Phi \Delta t L^2 = \int_0^\infty \frac{\mathrm{d}\omega}{(2\pi/\Delta t)} [\Theta(\omega, T_1) - \Theta(\omega, T_2)] \sum_{j=\{\mathrm{s,p}\}} \int \frac{\mathrm{d}^2\boldsymbol{\kappa}}{(2\pi/L)^2} \mathscr{T}_j(\omega, \boldsymbol{\kappa}; d). \tag{8.20}$$

Now, we recognize the spatial mode spacing $2\pi/L$ in κ-space. Indeed, applying periodic boundary conditions (also called Born von Karman conditions) to a system with size L, we get $\exp(ik_x L) = 1$ so that $k_x = p2\pi/L$ where p is an integer. Hence $L\mathrm{d}k_x/2\pi$ is the number of modes contained in $\mathrm{d}k_x$ in an interval L. Similarly, $\Delta t \mathrm{d}\omega/2\pi$ is the number of modes in $\mathrm{d}\omega$ in an interval Δt. Finally, it turns out that $\frac{\mathrm{d}\omega}{2\pi}\frac{\mathrm{d}^2\boldsymbol{\kappa}}{(2\pi)^2}$ is the density of modes per unit area and per unit time. We are now in a position of interpreting the Eq. (8.19) as a sum over modes. It has been shown in Ref. [96] that for a gap separating two identical interfaces, the factor $\mathscr{T}_j(\omega, \boldsymbol{\kappa})$ can be interpreted as a transmission factor and is always smaller than 1. This has been generalized to the case of a gap separating two arbitrary interfaces in Ref. [11]. We can thus obtain an estimate of the total number of channels per unit surface which effectively participate to the transfer of energy at a given frequency by summing over all channels with a weighting factor given by the transmission factor:

$$N(\omega, d) = \sum_{j=\{\mathrm{s,p}\}} \int \frac{\mathrm{d}^2\boldsymbol{\kappa}}{(2\pi)^2} \mathscr{T}_j(\omega, \boldsymbol{\kappa}, d). \tag{8.21}$$

In order to identify a linear conductance for each channel (j, κ), it is necessary to linearize, assuming a weak temperature difference, $\Theta(\omega, T_1) - \Theta(\omega, T_2) = \frac{\partial\Theta}{\partial T}(T_1 - T_2)$. Assuming that a channel has a transmission factor independent of the frequency, it is possible to find the thermal conductance g_0 associated to this channel [95, 103]:

$$\int_0^\infty \frac{\mathrm{d}\omega}{2\pi} [\Theta(\omega, T_1) - \Theta(\omega, T_2)] \approx g_0[T_1 - T_2], \tag{8.22}$$

where

$$g_0 = \int_0^\infty \frac{\mathrm{d}\omega}{2\pi} \frac{\partial\Theta}{\partial T} = \frac{\pi^2 k_B^2 T}{3h}, \tag{8.23}$$

is the quantum of thermal conductance [83]. We now analyse the linearized form of the flux:

$$\Phi = \sum_{j=\{\mathrm{s,p}\}} \int \frac{\mathrm{d}^2\boldsymbol{\kappa}}{(2\pi)^2} \int_0^\infty \frac{\mathrm{d}\omega}{2\pi} \mathscr{T}_j(\omega, \boldsymbol{\kappa}, d) \frac{\partial \Theta}{\partial T} [T_1 - T_2]. \tag{8.24}$$

This equation shows that we can attribute to each electromagnetic mode (j, κ) a contribution to the conductance which is bounded by the quantum of thermal conductance. It appears very clearly in this context that the enhancement of the flux in the near field is due to the increase of the number of modes $N(\kappa, d)$. We will clarify this point in the following paragraph. Let us first establish a rigorous form of the flux in the mesoscopic framework. To this end, we start with Eq. (8.24). Following Ref. [12], we can introduce a mean transmission factor weighted by $\frac{\partial \Theta}{\partial T}$ and averaged over frequencies:

$$\overline{\mathscr{T}}_j = \frac{\int_0^\infty \mathrm{d}u\, f(u) \mathscr{T}_j(u, \kappa; d)}{\int_0^\infty \mathrm{d}u\, f(u)} \tag{8.25}$$

with $f(u) = u^2 \mathrm{e}^u / (\mathrm{e}^u - 1)^2$ and $u = \hbar\omega/(k_\mathrm{B} T)$. This mean transmission factor is always smaller than 1. Using this quantity, we obtain a Landauer-like expression for the heat flux as derived in Ref. [12]:

$$\Phi = g_0 \left(\sum_{j=\mathrm{s,p}} \int \frac{\mathrm{d}^2\kappa}{(2\pi)^2} \overline{\mathscr{T}}_j \right) [T_1 - T_2]. \tag{8.26}$$

This equation shows that the thermal conductance is a sum over all the modes (j, κ). Each mode has a conductance which is given by the quantum of thermal conductance g_0 weighted by the transmission factor $\overline{\mathscr{T}}_j$ averaged over frequencies.

8.2.2.2 Fundamental Limits for the Heat Transfer

It follows from the linearized expression of heat flux (8.26) that two different strategies can be followed to enhance the heat flux between two media. The first one consists in increasing the number of modes (j, κ) while the second one consists in increasing their average transmission factor. Here, we will derive an estimate of the upper value of the heat flux both in far-field and in near-field regimes. These limits have been discussed in Refs. [9, 11, 12].

At large distances (ie. in far-field), only propagating waves are involved. We see from Eq. (8.19) that the maximum heat flux corresponds to a situation where $\mathscr{T} = 1$ for $\kappa < \omega/c$. This transmission factor corresponds to perfectly absorbing media also called blackbodies. For a semi-infinite body, this situation is realized, when the Fresnel reflection factors are exactly zero for both polarizations. The heat flux can then be computed from Eq. (8.19) yielding

$$\Phi_{\mathrm{BB}} = \int_0^\infty \left[\Theta(\omega, T_1) - \Theta(\omega, T_2) \right] \left(\frac{\omega^2}{c^3 \pi^2} \right) \frac{c}{4} = \sigma_{\mathrm{BB}} (T_1^4 - T_2^4), \tag{8.27}$$

which is the Stefan-Boltzmann law for the heat flux between two black bodies with the Stefan constant $\sigma_{\mathrm{BB}} = 2\pi^5 k_B^4/15h^3c^2 = 5.67 \times 10^{-8}\,\mathrm{W\,m^{-2}\,K^{-4}}$. This well-known equation can be cast in a different form in the spirit of a Landauer approach. By linearizing $(T_1^4 - T_2^4)$ in the form $4T^3(T_1 - T_2)$ with $T = (T_1 + T_2)/2$, we find

$$\Phi_{\mathrm{BB}} = g_0 \frac{2\pi}{5\lambda_T^2}(T_1 - T_2). \tag{8.28}$$

In other words, in the linearized regime, the usual Stefan-Boltzmann law is described by the quantum of thermal conductance g_0 times a number of modes per unit area roughly given by $\frac{1}{\lambda_T^2}$.

At close separation distance (i.e. in near-field) the modes located beyond the light line ($\kappa > \omega/c$) contribute to the energy transfer as well as the propagative modes. According to Eq. (8.26), the conductance seems to diverge. In practice, obviously, this is not the case. The transmission factor decays exponentially for wavevectors larger than $1/d$. It is thus the decay of the transmission factor that ensures the convergence of the flux. Let us discuss this issue in more detail. When studying analytically the upper value of the transmission factor, it can be shown that it is always smaller than 1 for arbitrary values of d. This factor of 1 certainly does not ensure convergence of the integral as pointed out in Ref. [96]. We now discuss in more detail the physics involved in this transmission factor. Upon inspection of Eq. (8.15), we see that the transmission factor has an exponential decay term $\exp(-2\kappa d)$ and a denominator $(1 - r_j^1 r_j^2 \mathrm{e}^{2\mathrm{i}k_{z0}d})$. It turns out that high quality factor resonances characterized by a zero of the denominator can compensate in theory arbitrary large damping factors. It is thus not easy to derive mathematically an upper bound of the transmission factor. However, we have to account for the fact that it is unphysical to assume that the denominator can be arbitrarily small as a quality factor will always be limited by losses and scattering losses in practice. It is thus clear that the exponential decay $\exp(-2\kappa d)$ cannot be compensated by a resonance for arbitrary large gap distances. It is thus reasonable to introduce a cutoff spatial frequency k_c on the order of the inverse of the gap thickness as suggested by the damping term. We now provide an estimate of the maximum conductance for a system with a gap d. Following Ref. [11], we assume that the transmission factor is unity below k_c and zero beyond k_c. Based on the previous qualitative discussion, we use a somewhat arbitrary cutoff $k_c = 2/d$. The number of modes is thus $2 \times \pi k_c^2/4\pi^2$ where a factor of 2 accounting for the sum over the two polarisations has been included. We finally get the result:

$$\Phi_{\max} = g_0 \frac{k_c^2}{2\pi}(T_1 - T_2) = g_0 \frac{2}{\pi d^2}(T_1 - T_2). \tag{8.29}$$

This simple result provides a very simple explanation of the divergence of the thermal conductance as $1/d^2$. It is a direct consequence of the increase of the number of modes. When comparing this result with the previous result in far field, it is seen that the increase of conductance when going into the near field is due to the increase

in the number of modes. Our rough estimate shows that the ratio of the number of modes is given by $(\lambda_T/d)^2$. This yields a factor 4×10^4 for $\lambda_T = 10\,\mu\text{m}$ and $d = 50\,\text{nm}$. Let us insist on the fact that we have assumed unit transmission factor for all the modes below cutoff. In what follows, we discuss this issue and show that in most cases, the transmission factors are much lower than 1.

We finally discuss the existence of a cutoff of fundamental nature. The macroscopic model of a dielectric constant does not include information on the microscopic structure of the material. Yet, it is well known that for polar materials, there is a cutoff value for the phonons spatial wave vectors given by π/a , where a is the lattice constant. This is the limit of the first Brillouin zone. This sets an ultimate limit to the heat flux and removes the $1/d^2$ divergence.

8.2.3 Heat Transfer Mediated by Photon Tunneling

8.2.3.1 Frustrated Modes

The first experiments demonstrating a flux larger than Stefan Boltzmann law were analysed in Ref. [29]. In this paper, the increase of the flux was attributed to the contribution of waves propagating in a dielectric but totally reflected at the interface. As shown in Fig. 8.15a, these waves can be partially transmitted when the gap distance d is smaller than the relevant wavelength which is given by $\lambda_T = \hbar c/(k_B T)$. This phenomenon is called frustrated total reflection or photon tunnelling. Radiation can therefore tunnel through the vacuum gap and hence contribute to the heat flux. Since these modes are propagating inside the material but evanescent in the vacuum region, they are defined by $\omega/c < \kappa < n'(\omega)\omega/c$ (where n′ is the real part of the refractive index and $\varepsilon = n^2$).

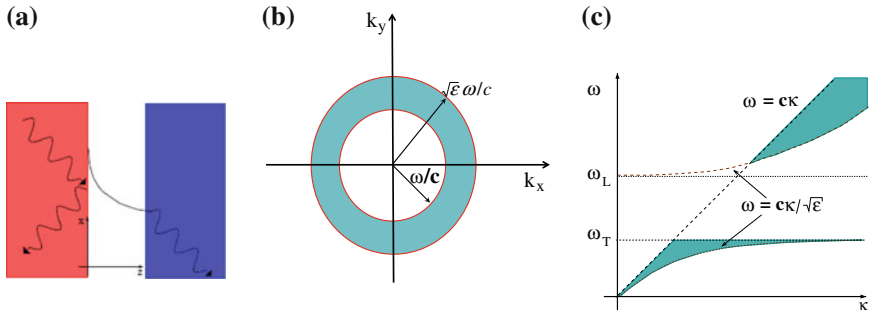

Fig. 8.15 Sketch of the frustrated modes in the real space (**a**), wave vector space (**b**) and the (ω, κ) plane (**c**). The modes which can propagate inside the dielectric are on the left of the polariton lines $\omega = c\kappa/\sqrt{\varepsilon}$. The modes totally reflected are within the *green* region between the light line and the polariton line

We illustrate schematically in Fig. 8.15b the regions for which one can expect frustrated modes. The discussion is performed using the real part of the index which is a fair approximation when dealing with low lossy materials. From Fig. 8.15b it is obvious that due to the frustrated internal reflection the number of contributing modes for the heat flux increases, but is still limited to $\kappa < n'\omega/c$. This discussion is valid for media with a real part of the refractive index and a small imaginary part responsible for the emission and absorption. For polar materials such as SiC for example, there is a frequency range in the IR where the dielectric permittivity can have a negative real part between the longitudinal and the transverse frequencies ω_L and ω_T. Note in Fig. 8.15c, that in the so-called *reststrahlen region* $\omega_{\mathrm{T}} < \omega < \omega_{\mathrm{L}}$ no optical phonons can be excited. Within this frequency band the permittivity is negative so that the material behaves effectively like a metal, i.e., the reflectivity is close to one.

8.2.3.2 Surface Modes

Another kind of evanescent mode is responsible for the tremendous increase of the heat flux at nanoscale, the so-called surface phonon polariton [61]. We now consider two SiC interfaces across a gap with a gap distance d smaller than the attenuation length of the surface mode i.e., $1/\mathrm{Im}\left(\sqrt{\omega^2/c^2 - \kappa_{\mathrm{SPhP}}^2}\right)$ where κ_{SPhP} is the surface phonon polariton wavevector. In that case, the two surface modes are coupled. This coupling removes the two-fold degeneracy and produces two branches. They can be found by solving the equation [102]

$$\left[-\mathrm{Im}(r_{\mathrm{p}})^2 + \mathrm{Re}(r_{\mathrm{p}})^2 + 2\mathrm{i}\mathrm{Im}(r_{\mathrm{p}})\mathrm{Re}(r_{\mathrm{p}})\right]\mathrm{e}^{-2\mathrm{Im}(k_{z0}d)} = 1. \tag{8.30}$$

It is of upmost importance in this context to realize that when this condition is satisfied, the denominator of the transmission factor approaches zero and therefore, the transmission factor for these modes is almost 1. In other words, the enhancement due to the resonance compensates the exponential decay across the gap. Hence, entails that these modes have a large contribution to the heat transfer. These modes are schematically illustrated in Fig. 8.16a. Figure 8.16b shows the dispersion relation of the surface phonon polariton. Here, the key feature is the fact that the dispersion relation becomes almost flat for very large values of the wavevector. This entails that the number of modes becomes very large at the asymptote frequency. It is important to clarify a technical point here. When plotting the dispersion relation, different choices can be made. A usual choice consists in taking κ complex and ω real. This choice leads to a dispersion relation where the flat asymptote has been replaced by a backbending. This suggests (incorrectly) that the density of states is no longer large in the presence of losses. It has been shown in [2] that when dealing with the density of states, the relevant choice is real κ and complex ω. This choice leads to a flat asymptote of the dispersion relation. This asymptote yields the divergence of

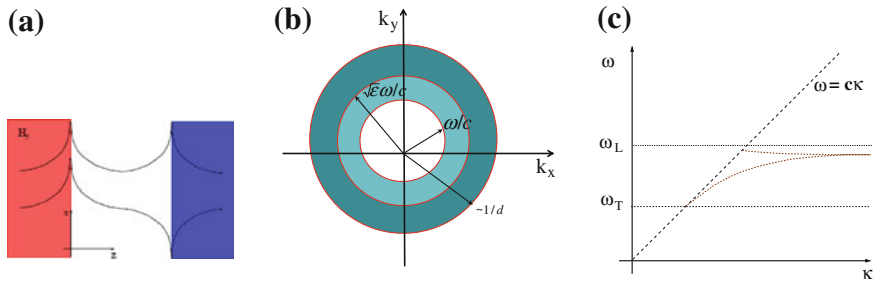

Fig. 8.16 Sketch in the real space (**a**), wave vector space (**b**) and (ω, κ) plane (**c**) of surface polariton modes (symmetric and antisymmetric). The first plot shows the exponential decay from the interface of the field associated with a surface polariton. Note that the dispersion relation extends toward large wavevectors

the local density of states in agreement with a direct calculation based on the Green tensor [57]. The reader is referred to Ref. [2] for further details.

In what follows, we simply plot the energy transmission factor as it is used in our formulas where both the circular frequency and the wavevector are real. We focus on the frequency range of this mode. We consider a permittivity with absorption, or $\gamma \neq 0$. For small absorption, more precisely for $\mathrm{Im}(r_\mathrm{p}) \ll \mathrm{Re}(r_\mathrm{p})$, the dispersion relation for the coupled surface modes coincides with the resonance condition of the energy transmission factor [96]

$$\left[-\mathrm{Im}(r_\mathrm{p})^2 + \mathrm{Re}(r_\mathrm{p})^2\right] \mathrm{e}^{-2\mathrm{Im}(k_{z0}d)} = 1. \tag{8.31}$$

The energy transmission factor for evanescent waves in Eq. (8.15) is almost one for the surface phonon polaritons as long as $\mathrm{Im}(r_\mathrm{p}) \ll \mathrm{Re}(r_\mathrm{p})$. Nonetheless, for very large wavevectors $\kappa \gg d^{-1} \gg \omega/c$ the energy transmission factor in Eq. (8.15) is damped exponentially due to the exponential $\exp(-2\mathrm{Im}(k_{z0})d) \approx \exp(-2\kappa d)$. Here, the exact damping of the energy transmission coefficient is determined by the losses of the material [12]. Hence, all modes κ such that $\kappa < 1/d$ contribute to the heat flux. It follows from Fig. 8.16c that the area in κ space is proportional to d^{-2}. This contribution to the heat flux eventually results in a larger contribution than that of the frustrated internal reflection modes.

To illustrate this, we discuss the energy transmission factor between two semi-infinite SiC plates assuming that $T_1 = 300\,\mathrm{K}$ and $T_2 = 0\,\mathrm{K}$ so that $\lambda_\mathrm{T} = 7.6\,\mu\mathrm{m}$. For this purpose we plot in Fig. 8.17 the energy transmission coefficient $\mathscr{T}_p(\omega, \kappa; d)$ in ω-κ space for distances (a) $d = 5\,\mu\mathrm{m}$, (b) $d = 500\,\mathrm{nm}$ and (c) $d = 100\,\mathrm{nm}$. In Fig. 8.17a as expected, we observe that for a relatively large distance the transmission factor is dominated by the propagating modes and is maximal for the Fabry-Perot modes inside the gap. For a distance of 500 nm we can see in Fig 8.17b that the surface modes and frustrated modes come into play.

The most important features are seen for 100 nm. First, it is seen that the energy transmission factor equals one for all modes which can exist inside the bulk SiC (on

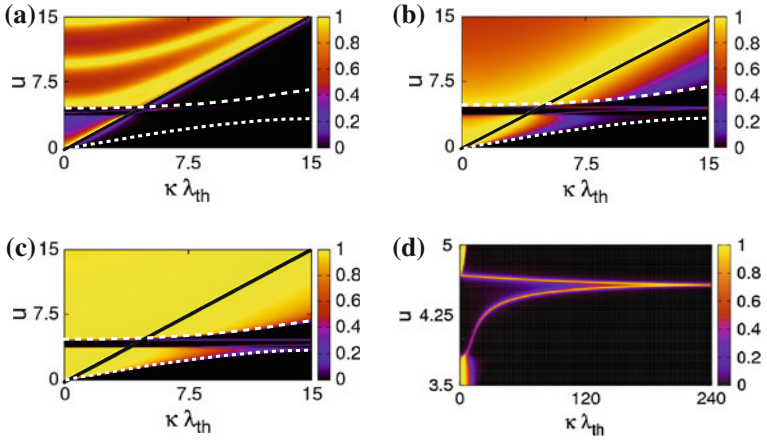

Fig. 8.17 Transmission coefficient $\mathscr{T}_{\mathrm{p}}(\omega, \kappa; d)$ between two SiC plates for different distances in ω-κ space. Note that (**d**) is the same as (**c**) but for a large κ range, showing that the number of contributing modes for the coupled surface modes is much larger than for the frustrated modes. The *dashed lines* are the phonon polariton lines for SiC. Here, $u = \hbar\omega/(k_{\mathrm{B}}T)$ is a rescaled frequency so that for $T = 300\,\mathrm{K}$ we have $\omega = u \times 4.14 \times 10^{13}\,\mathrm{rad/s}$: **a** $d = 5\,\mu\mathrm{m}$, **b** $d = 500\,\mathrm{nm}$, **c** $d = 100\,\mathrm{nm}$, **d** $d = 100\,\mathrm{nm}$

the left of the phonon polariton lines) and for the surface modes (see Fig. 8.17c). Second, the number of modes is very large as seen by inspection of the wavevector scale of Fig. 8.17d. A remarkable feature is that the transmission factor is very large for all the wavevectors. This is because the resonant excitation of the surface mode compensate the large decay factor $\exp(-2\kappa d)$. Hence, since the number of contributing modes is very large (see Fig. 8.17d), a very large heat flux is expected. Note however that the transmission factor is only large for a well defined value of the frequency. It is thus expected that the transmission factor averaged over frequencies is much smaller.

This is indeed what is seen in Fig. 8.18. We show a plot of the mean transmission coefficient $\overline{\mathscr{T}}_{\mathrm{p}}$ for two SiC slabs when varying the distance. It can be seen that the mean transmission coefficient for the surface modes is two orders of magnitude smaller than 1. Nonetheless, the coupled surface modes give the dominant heat transfer mechanism for small distances. This is due to the number of modes which increases dramatically (Note that the abscissa scale is logarithmic).

The resulting spectral heat flux Φ_ω is now plotted in Fig. 8.19a. It can be observed that for very small distances the spectrum becomes quasi monochromatic around the frequency of the surface mode resonance $\omega_{\mathrm{SPhP}} = 1.787 \times 10^{14}\,\mathrm{rad/s}$ which is defined through the implicit relation $\mathrm{Re}[\varepsilon(\omega_{\mathrm{SPhP}})] = -1$ and $\mathrm{Im}[\varepsilon(\omega_{\mathrm{SPhP}})] \ll 1$. The distance dependence is shown in Fig. 8.19b where the flux Φ is normalized to the heat flux between two black bodies $\Phi_{\mathrm{BB}} = 459.27\,\mathrm{W\,m^{-2}}$. The contributions are divided into the propagating, the frustrated, and the surface phonon polariton part. One can clearly see that the heat flux increases for distances smaller than the thermal

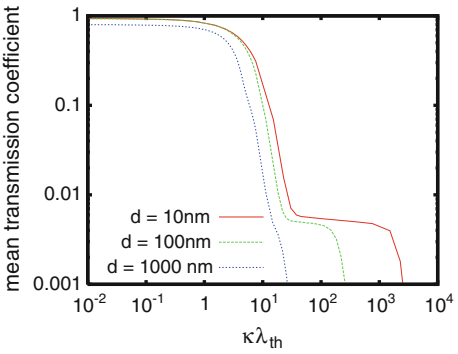

Fig. 8.18 Mean transmission coefficient $\overline{\mathscr{T}}_{\mathrm{p}}$ for two SiC slabs with varying distances d

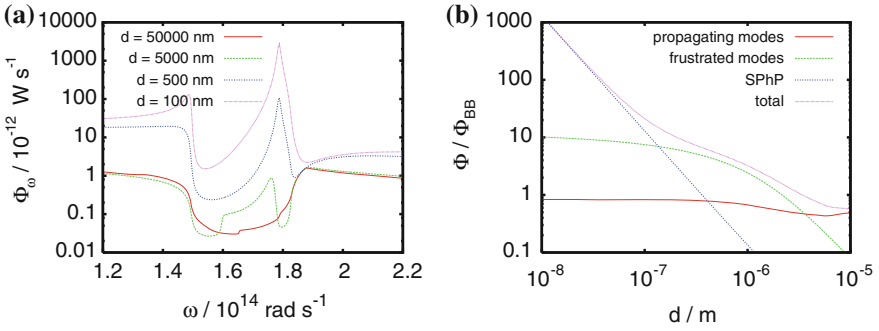

Fig. 8.19 **a** Spectral heat flux Φ_ω between two SiC halfspaces at $T_1 = 300\,\mathrm{K}$ and $T_2 = 0\,\mathrm{K}$ for different distances. **b** Total heat flux Φ over distance

wavelength $\lambda_{\mathrm{T}} = 7.6\,\mu\mathrm{m}$ due to the frustrated modes and exceeds the black body limit at $d \approx 3\,\mu\mathrm{m}$. For even smaller distances ($d < 100\,\mathrm{nm}$) the surface modes start to dominate the heat flux completely and give a characteristic $1/d^2$ dependence, since the number of contributing modes is for these modes proportional to $1/d^2$. Note, that on the nanoscale at a distance of $d = 10\,\mathrm{nm}$ the heat flux exceeds the black body limit by a factor of 1000! Asymptotic closed forms solutions of these contributions in different distance regimes can be found in Refs. [108, 109].

8.2.4 Beyond SPPs Coupling: Toward a Near-Field Analog of Blackbody

A blackbody is well known to be an ideal emitter of thermal radiation. No real hot body can radiate more energy. In this section, we analyse the possibility of achieving a near-field blackbody. From the previous discussion, it follows that the radiative heat flux is increased in the near field because the number of modes increases. We have

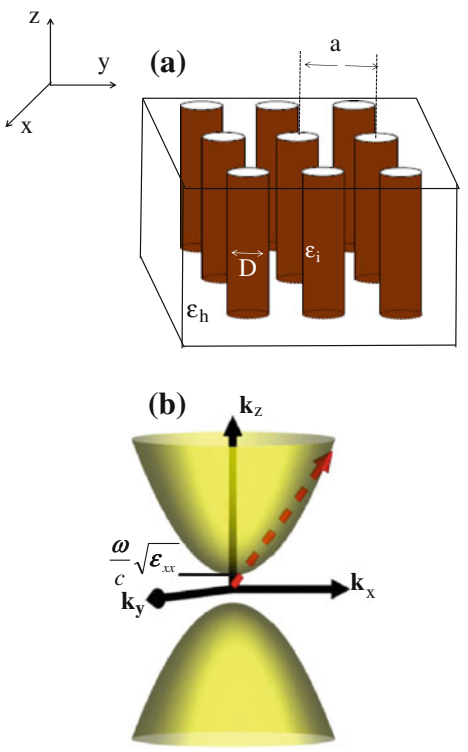

Fig. 8.20 **a** Sketch of a hyperbolic material consisting of a periodical array of nanowires embedded in a host matrix. **b** Hyperbolic dispersion relation (isofrequency mapping) in such materials for a fixed frequency

also shown that in practice, the number of modes is proportional to $1/d^2$ because the tunneling through the gap introduces a cutoff for the spatial wavevectors that is proportional to $1/d$. An important point is that in most cases, the frequency averaged transmission factor is much smaller than 1. If surface waves such as surface phonon polaritons exist, the transmission factor reaches the maximum value of 1 but only for a very limited range of frequencies. In order to obtain the near-field analog of a blackbody, transmission factors approaching 1 over a broad spectrum around λ_T are needed. This may be obtained using metamaterials.

With today nanotechnology it is possible to manufacture artificial materials to tailor the electromagnetic field. These artificial materials are generally structured at the length scale or below the length scale of the correlation length of thermal photons. Among these artificial media, a class of metamaterials called indefinite or hyperbolic media [54, 115] has turned out to be a promising material for realizing a perfect near-field emitter [17]. By approaching such two media, it is possible to have an efficient heat transport through the gap [17].

To analyse this behavior let us consider the structure as depicted on Fig. 8.20a made with a periodic array of SiC nanorods defined by a permittivity ε_i embedded within a host matrix of permittivity ε_h. When the characteristic sizes of such a structure is small enough compared with the thermal wavelength, this medium can be viewed as

an effective uniaxial medium [16] described by the effective dielectric tensor

$$\varepsilon_{eff} = \begin{pmatrix} \varepsilon_{xx} & 0 & 0 \\ 0 & \varepsilon_{yy} & 0 \\ 0 & 0 & \varepsilon_{zz} \end{pmatrix} \tag{8.32}$$

where the diagonal components are given by the Maxwell-Garnett relations [118])

$$\varepsilon_{xx} = \varepsilon_{yy} = \varepsilon_h \frac{\varepsilon_i(\omega)(1+f) + \varepsilon_h(1-f)}{\varepsilon_i(\omega)(1-f) + \varepsilon_h(1+f)}, \tag{8.33}$$

$$\varepsilon_{zz} = \varepsilon_h(1-f) + \varepsilon_i(\omega) f, \tag{8.34}$$

where ε_{xx} and ε_{yy} are the optical responses parallel to the surface and ε_{zz} perpendicular to the surface, i.e., along the nanowires. Here f denotes the volume filling fraction of the SiC wires. Since the optical axis of the considered material is perpendicular to the surface, the s- and p-polarized modes decouple and we have only extraordinary waves for p polarization [115]. The dispersion relation for extraordinary waves in uniaxial materials can be stated as [54, 115]

$$\frac{k_x^2 + k_y^2}{\varepsilon_{zz}} + \frac{k_z^2}{\varepsilon_{xx}} = \frac{\omega^2}{c^2}. \tag{8.35}$$

Hyperbolic materials are now defined by the fact that they have a band of frequencies where ε_{xx} and ε_{zz} have an opposite sign [115]. Hence, the dispersion relation defines a hyperboloid in the (κ, k_z) plane instead of an ellipse as illustrated in Fig. 8.20b. This means that in principle there is no upper bound for $|\kappa|$. In the following we will call such modes hyperbolic modes (HM). The HM are propagating inside the hyperbolic material and for $\kappa > \omega/c$ evanescent in the gap, i.e., for small distances $d \ll \lambda_{\text{th}}$ they are a special kind of frustrated internal reflection modes. As for usual frustrated modes, we can expect a large mean transmission factor for the HM up to $\kappa \approx 1/d$ if they exist in a broad frequency band. It follows that the heat flux due to the HM scales for small distances like $1/d^2$ as the contribution of the surface phonon polaritons.

In Fig. 8.21a we plot the transmission factor between two arrays of SiC nanowires with a filling factor $f = 0.1$ and a separation distance $d = 100\,\text{nm}$. In Fig. 8.21b we show the real part of the parallel $Re(\varepsilon_{\parallel})$ and the perpendicular $Re(\varepsilon_{\perp})$ components of the dielectric tensor in a frequency range around the transversal and longitudinal phonon frequency of SiC ($\omega_T = 1.495 \times 10^{14}\,\text{rad/s}$ and $\omega_L = 1.827 \times 10^{14}\,\text{rad/s}$). It clearly appears that the regions of high transmission indicated in the figures, corresponds to frequencies where both media support frustrated hyperbolic modes (HM). More importantly, it is seen in Fig. 8.21c that the heat flux due to HM can be larger than the flux due to surface phonon polaritons between two SiC media at the same distance. So far, the largest fluxes have been obtained with resonant surface phonon polaritons [107, 113]. Hence, the use of metamaterials paves the way to a novel class

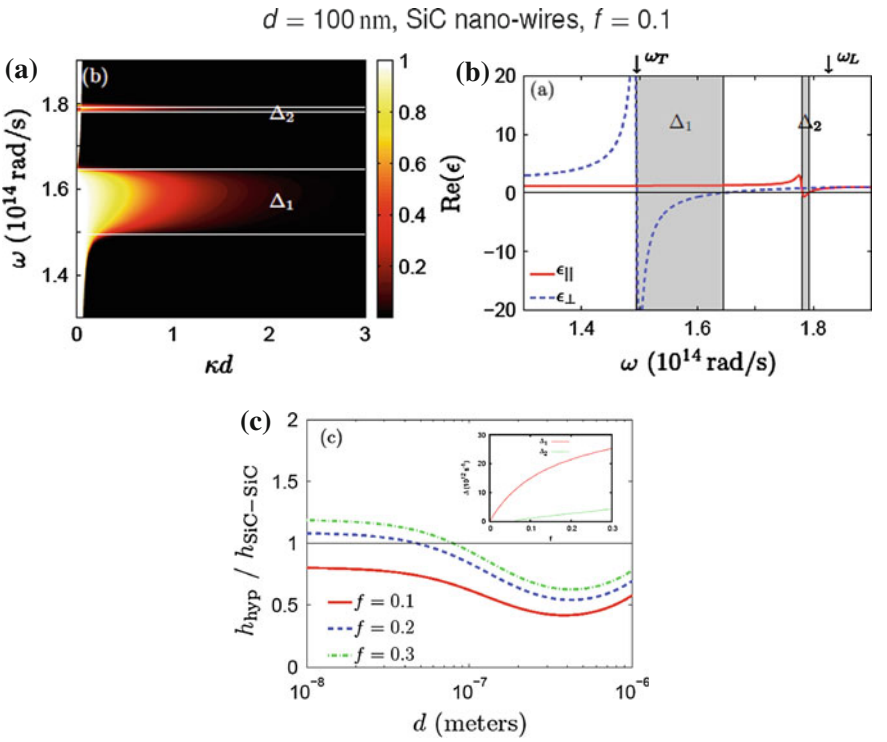

Fig. 8.21 **a** Transmission coefficient $T_p(\omega, \kappa)$ between two SIC periodic arrays separated by a distance d = 100 nm. **b** Real part of the parallel and orthogonal components of dielectric tensor. **c** Normalized heat transfer coefficient for two hyperbolic materials with $f = 0.1, 0.2, 0.3$

of materials for heat transfer at the nanoscale. Their efficiency is based on a broad range of frequencies where the transmission factor can be large. In practice, there is a cutoff in κ and therefore for d. It is due to the validity of the homogenization approximation. The order of magnitude of the cutoff is given by $1/a$ where a is the average nanorod spacing.

8.2.5 Applications

8.2.5.1 Thermal Management with Anisotropic Media

A proper understanding of near-field heat transfer naturally gives rise to new ideas on how to control the heat flux between closely separated structures, i.e., on *thermal management* at the micro/nanoscale. Such a control can be achieved, for instance, by thermal rectifiers [7, 89], thermal transistors [88] and thermal modulators [16,

121] for thermal photons. Here we present heat-flux modulation based on actively changing the relative orientation of electrically anisotropic materials while keeping a fixed (small) distance between them.

With the explicit expressions for the reflection matrices, we can calculate the transmission factor in (8.13) and therefore the heat transfer (8.8) with (8.12). In order to have a concrete situation in mind, let us consider the situation depicted in Fig. 8.22. Two grating structures are parallel with an arbitrary twist angle [16]. In the effective medium approximation, those gratings may be described as anisotropic media with different dielectric/conduction properties in y and x, z directions. Assuming a simple Maxwell-Garnett model [118] for the respective permittivities, we get

$$\varepsilon^i_{xx}(\omega) = \varepsilon^i_{zz}(\omega) = \varepsilon_{\mathrm{h}_i}(\omega)(1-f_i)+f_i\,, \quad \varepsilon^i_{yy}(\omega) = \frac{\varepsilon_{\mathrm{h}_i}(\omega)}{(1-f_i)+f_i\varepsilon_{\mathrm{h}_i}(\omega)}, \tag{8.36}$$

where $\varepsilon_{\mathrm{h}_i}$ is the permittivity of the i-th host medium, and f_i is the filling factor of the air inclusions in the i-th grating.

Substituting expressions (8.36) into (35)–(40) of Ref. [105] and then into (8.12) we get the heat transfer between the two gratings in the EMA. In Fig. 8.23a we plot the heat flux between two gold gratings as a function of the relative twist angle, for fixed distances. The flux is dramatically reduced as the gratings are twisted, up to almost 80 % at $\phi = \pi/2$ for distances as large as 1 μm. Unfortunately there is no simple physical picture that allows us to understand such effect, but it clearly indicates that symmetric configurations transmit heat more efficiently that asymmetric ones. This is further supported by Fig. 8.23b, where the heat flux between two SiC gratings is shown. The reduction in the flux is less impressive in this case (although still quite significant), but the upside is that here we have a more direct interpretation: for SiC gratings the surface modes give an important contribution to the flux. Hence, a

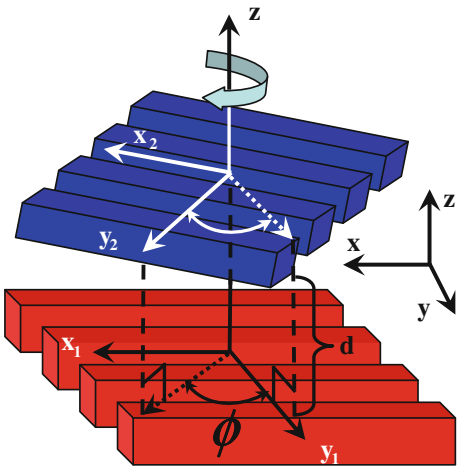

Fig. 8.22 Two gratings at different temperatures twisted with respect to each other. Reproduced with permission from Ref. [16]. Copyright [2011], American Institute of Physics

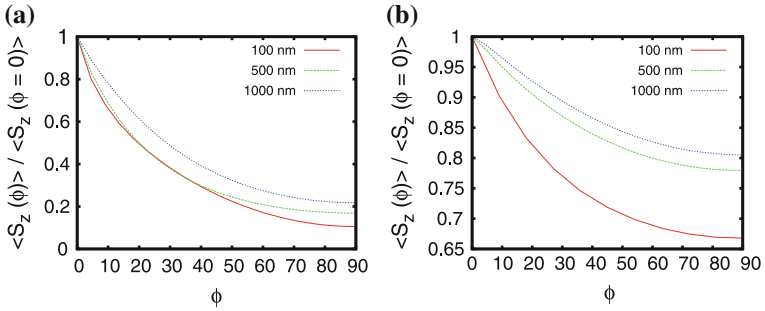

Fig. 8.23 The heat flux $\langle S_z \rangle(\phi)$ between two: **a** Au and **b** SiC gratings, normalized by the flux $\langle S_z \rangle(0°)$ when the gratings are aligned. The angle ϕ measures the relative twisting between the gratings, and the filling factor is fixed at $f = 0.3$

mismatch of the surface mode dispersion relations (for twisted structures) results in a smaller transmission factor as observed.

Going back to the *Au* gratings, we see that the large suppression obtained by just rotating the structures with respect to one another suggests that such a setup could be used as a thermal modulator controlled by the twist angle: in the parallel position there would be a heat flux (position "on"), in the orthogonal one there would not (position "off"). Such thermal modulators can for example be interesting for fast heat flux modulation and thermal management of nano-electromechanical devices [16].

8.2.5.2 Thermal Management with Phase Change Materials

More recently, it has been shown [121, 122] that the near-field heat transfer can be modulated by orders of magnitude upon inducing a phase transition of the materials. In this case, the optical properties of the materials may change so that a huge modulation of heat transfer becomes possible.

Different phase change materials (PCM) materials have been considered such as AIST [121] and VO2 [122]. VO2 has two distinct solid phases (see Fig. 8.24), one amorphous and the other crystalline. The material can be switched from one phase to the other in a sufficiently short time [126]. The switching typically goes through the liquid phase as well, and can be summarized in a series of three steps [126]. First we consider VO2 in the crystalline phase and heat it up quickly with an intense short pulse. The subsequent cooling is thus also very fast and leads to a quenching process, trapping the material in an amorphous state.

As seen in Fig. 8.24, a large radiative heat transfer contrast can be obtained through an active modulation of VO2 state. Both phases lead to a contrast of almost 2 orders of magnitude in the extreme near field. In order to understand the physics involved in these mechanisms, we have plotted in Fig. 8.25 the transmission coefficient $\mathscr{T}_p$ in the (ω, κ) plane of p-modes for both states at a separation distance $d = 500\,\text{nm}$. For insulating VO2 we see mainly a large magnitude of $\mathscr{T}_p$ in the region of coupled

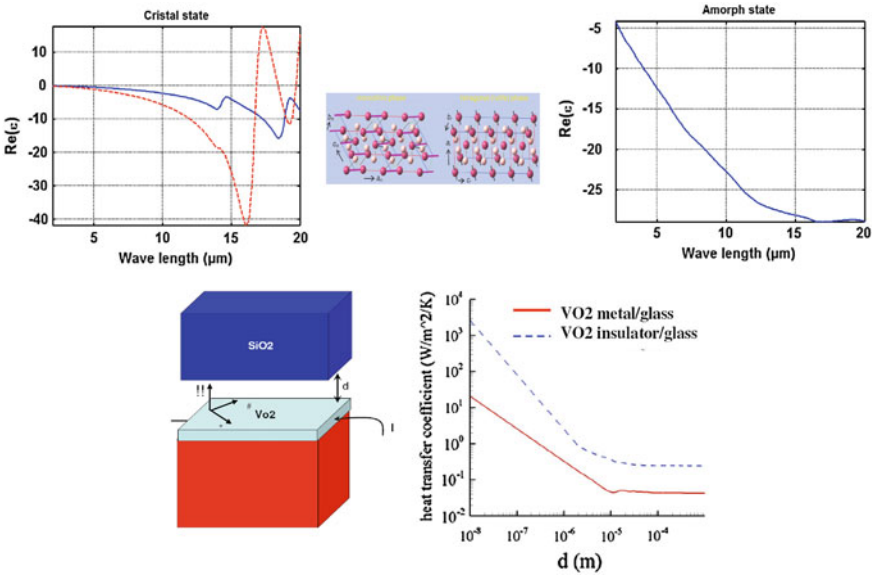

Fig. 8.24 *Top*: (Left) Real part of the dielectric permittivity of crystalline VO2 along the optical axis (red curve) and in the plane orthogonal to the optical axis (blue curve). (Right) Real part of the dielectric permittivity of amorphous (isotropic) VO2. *Bottom*: Heat transfer coef?cient at T = 300 K between two parallel plates VO2-glass as a function of the gap width.

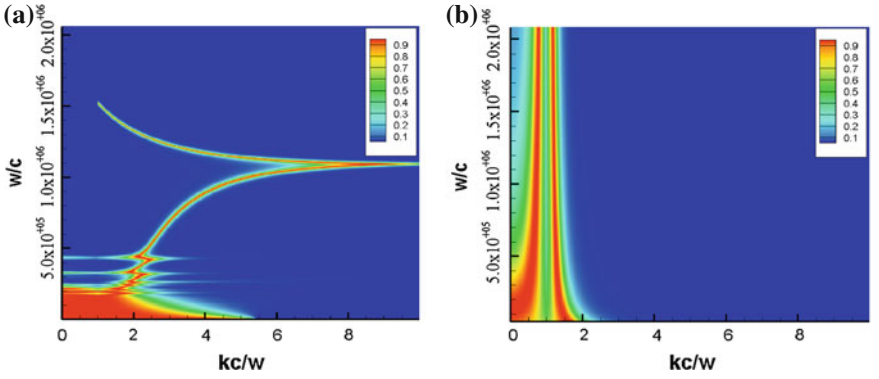

Fig. 8.25 *Left* Transmission coefficient (p polarized) between two insulating VO2 surfaces. *Right* Same for two metallic VO2 surfaces. Both graphs were obtained at a separation distance d = 500 nm

surface phonon polaritons. The mode coupling is rather efficient in this region and responsible for a large heat transfer ($\mathcal{T}_p$ is close to one over a large κ range). There are also discrete extraordinary surface modes at lower frequencies when $\varepsilon_{\parallel}\varepsilon_{\perp} = 1$ as well as frustrated modes due to total internal reflection (propagating waves inside VO2 become evanescent within the gap). Such modes give a non-negligible contribution to the heat transfer in the near field [15]. On the other hand, for metallic VO2 only

a thin region around the $\kappa = \omega/c$ over a broad spectral range contributes to the transfer. It corresponds to a spectral region where the real part of the permittivity is negative. In summary, VO2 can change from a metallic emitter to a dielectric emitter supporting surface phonon-polaritons.

The considerable difference in optical and electrical properties between the amorphous and crystalline states of some PCMs opens the door to several applications. For example, it is possible to actively control the heat flux by switching the PCM. This can be done as fast as 100 ns [126]. Note that not only the modulation is quick, but it was also shown [121] that for certain distances the switching changes the heat flux by one order of magnitude and that the cycle is fairly repeatable (10^7–10^{12} times), making it a good candidate for possible applications in thermal management and for designing thermal transistors.

8.2.5.3 Near-Field Energy Conversion

Thermophotovoltaic (TPV) devices [28] are energy conversion systems that generate electric power directly from thermal radiation. The basic principle (see Fig. 8.26) is similar to the usual photovoltaic conversion: illuminating a pn junction produces a current. There is one difference: the sun is replaced by a thermal source. As the temperature is obviously lower that the sun temperature, TPV devices operate in the near-infrared and not in the visible range. The efficiency of a photovoltaic cell is defined as the ratio $\eta = P_{el}/P_{rad}$ of the electric power P_{el} produced by the photovoltaic cell and the net radiative power P_{rad} exchanged between the hot source and the p-n junction.

The photovoltaic efficiency of a single junction photovoltaic cell is limited by the thermodynamic Shockley-Queisser limit [114] and is 30 % for a gap at 1.1 μm and a sun considered to be a blackbody at 6000 K. This limit is essentially due to the mismatch between the broad spectrum of the sun and the narrow spectrum of a single junction: photons with energy lower than the band gap cannot produce an

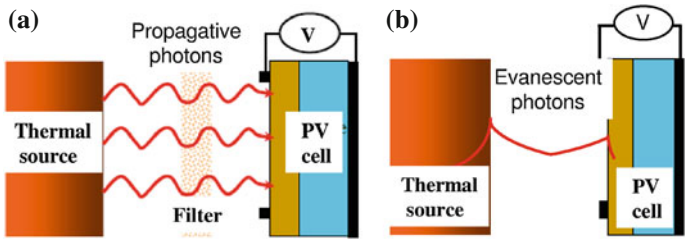

Fig. 8.26 Principle of thermophotovoltaic energy conversion devices. **a** In far field, the photovoltaic (PV) cell is located at a long distance (compared to the thermal wavelength) from a thermal source. Only propagative photons reach the cell. A filter can be used to select the photons with an energy matching the energy gap of the cell so that photons with different energies are recycled. **b** In near-field TPV the cell is located at subwavelength distance from the source. Evanescent photons are the main contributors to the radiative power transfered from the source to the cell

electron-hole pair whereas photons with energies $h\nu$ larger than the band gap E_g produce electron with an excess energy $h\nu - E_g$ which is lost when the electron relaxes to the bottom of the conduction band. This limit can be overcome with a monochromatic source if the emission frequency is slightly above with the gap energy of the semiconductor. In this case η approaches unity. To achieve this goal, it is necessary to design a filter that transmit the photons with the right energy and recycles the other photons. However, such a system is efficient only if the recycling process does not suffer from losses. In practice, the best efficiencies obtained are still below 15 %.

In the near-field, the heat flux can be several orders of magnitude larger than that of a black body, so that near-field TPV conversion [8, 67, 86, 92, 94] seems to be a promising technology for production of electricity as it can enhance the current generation per unit area. This may be of great interest for small portable generators. In addition, the efficiency should benefit from near-field for two reasons. On one hand, the near-field emitter can become spectrally selective, on the other hand, the fill factor is increased when the current is increased.

Generally speaking, in (far or near-field) TPV devices, the maximal power which can be extracted from the cell is given by [67]

$$P_{el} = F_{\text{fill}} I_{\text{ph}} V_{\text{oc}}, \tag{8.37}$$

where I_{ph} is the photogeneration current (which corresponds to photons that are effectively converted), V_{oc} is the open-circuit voltage (which correspond to a vanishing current into the diode). The factor F_{fill} is called fill factor and depends on I_{ph} and on the saturation current I_0 of the diode. When we assume that each absorbed photon with an energy higher than the gap energy E_{g} produces an electron-hole pair, the photogeneration current is [67]

$$I_{\text{ph}} = e \int_{E_{\text{g}}/\hbar}^{\infty} \mathrm{d}\omega \, \frac{P_{\text{rad}}(\omega)}{\hbar\omega}. \tag{8.38}$$

It immediately follows from this equation that an increase in the radiative power exchanged between the source and the cell leads to an enhancement of the photogeneration current. On the other hand, the fill factor is given by [67]

$$F_{\text{fill}} = \left[1 - \frac{1}{\ln(I_{\text{ph}}/I_0)}\right]\left[1 - \frac{\ln(\ln(I_{\text{ph}}/I_0))}{\ln(I_{\text{ph}}/I_0)}\right], \tag{8.39}$$

with the dark current [4]

$$I_0 = e\left(\frac{n_i^2 D_{\text{h}}}{N_{\text{D}} \tau_{\text{h}}^{1/2}} + \frac{n_i^2 D_{\text{e}}}{N_{\text{A}} \tau_{\text{e}}^{1/2}}\right). \tag{8.40}$$

In Eq. (8.40), n_i denotes the intrinsic carrier concentration, N_D (N_A) the donor (acceptor) concentration, D_{e} (D_{h}) the diffusion constant of electrons (holes) and τ_{e}

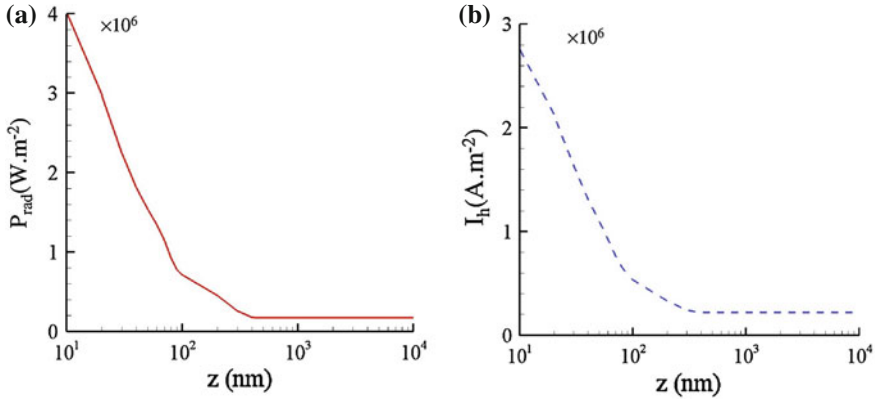

Fig. 8.27 **a** Radiative power exchanged between a tungsten source at 2000 K and a GaSb cell at 300 K. **b** Photocurrent in the GaSb cell with respect to the separation distance z of the thermal source. $N_A = N_D = 10^{-17}\,\mathrm{cm}^{-3}$; $n_i = 4.3 \times 10^{1}2\,\mathrm{cm}^{-3}$. Physical properties are taken from Ref. [106]

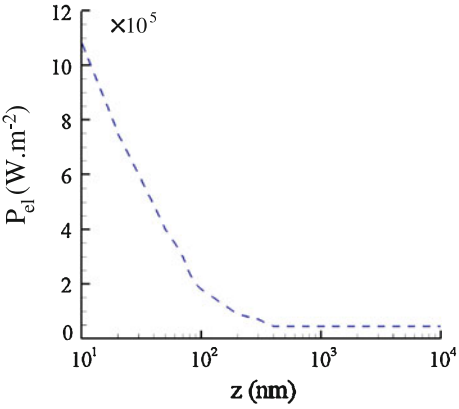

Fig. 8.28 Electric power generated by a Tungsten-GaSb cell with respect to the separation distance cell-source (same parameters as in Ref. [67])

and τ_h represent the electron-hole pair lifetime in the p-doped and n-doped domains of the cell. In Fig. 8.27 we see that for a plane tungsten thermal source in front of a GaSb cell (see [91] for optical properties) the radiative power exchanged increases dramatically at subwavelength distances compared to what we observe in far field. As a direct consequence, the photocurrent generated in the GaSb cell follows an analog behavior.

Once the photocurrent and the dark current are known, the electric power [see Eq. (8.37)] can be calculated using the open circuit voltage [67]

$$V_{oc} = \frac{k_B T}{e} \log\left(\frac{I_h}{I_0}\right). \tag{8.41}$$

Figure 8.28 clearly shows that the near-field TPV device produces much more electricity than a classical TPV conversion system. At a distance between the thermal

source and the cell of $z = 100\,\text{nm}$ the production is approximately enhanced by a factor of 5. At 10 nm this factor reaches a value of about 50 times the far-field value. These results show that the near-field TPV conversion is a promising technology that could offer new solutions for energy production.

References

1. G.S. Agarwal, Quantum electrodynamics in the presence of dielectrics and conductors. I. Electromagnetic-field response functions and black-body fluctuations in finite geometries. Phys. Rev. A **1**, 230–242 (1975)
2. A. Archambault, T.V. Teperik, F. Marquier, J.J. Greffet, Surface plasmons Fourier optics. Phys. Rev. B **79**, 195414 (2009)
3. C. Arnold, F. Marquier, M. Garin, F. Pardo, S. Collin, N. Bardou, J.L. Pelouard, J.J. Greffet, Coherent thermal infrared emission by two-dimensional silicon carbide gratings. Phys. Rev. B **86**, 035316 (2012)
4. N. Ashcroft, N.D. Mermin, *Solid-State Physics* (Saunders, Philadelphia, 1976)
5. M. Auslender, D. Levy, S. Hava, One-dimensional antireflection gratings in 100 silicon: a numerical study. Appl. Opt. **37**, 369 (1998)
6. Y. Avitzour, Y.A. Urzhumov, G. Shvets, Wide-angle infrared absorber based on a negative-index plasmonic metamaterial. Phys. Rev. B **79**, 045131 (2009)
7. S. Basu, M. Francoeur, Near-field radiative transfer based thermal rectification using doped silicon. Appl. Phys. Lett. **98**, 113106 (2011)
8. S. Basu, Z.M. Zhang, C.J. Fu, Review of near-field thermal radiation and its application to energy conversion. Int. J. Energy Res. **33**, 1203–1232 (2009)
9. S. Basu, Z.M. Zhang, Maximum energy transfer in near-field thermal radiation at nanometer distances. J. Appl. Phys. **105**, 093535 (2009)
10. A. Battula, S.C. Chen, Monochromatic polarized coherent emitter enhanced by surface plasmons and a cavity resonance. Phys. Rev. B **74**, 245407 (2006)
11. P. Ben-Abdallah, K. Joulain, Fundamental limits for noncontact transfers between two bodies. Phys. Rev. B **82**, 121419(R) (2010)
12. S.A. Biehs, E. Rousseau, J.J. Greffet, A mesoscopic description of radiative heat transfer at the nanoscale. Phys. Rev. Lett. **105**, 234301 (2010)
13. S.A. Biehs, J.J. Greffet, Influence of roughness on near-field heat transfer between two plates. Phys. Rev. B **82**, 245410 (2010)
14. S.A. Biehs, J.J. Greffet, Near-field heat transfer between a nanoparticle and a rough surface. Phys. Rev. B **81**, 245414 (2010)
15. S.A. Biehs, F.S.S. Rosa, P. Ben-Abdallah, K. Joulain, J.J. Greffet, Nanoscale heat flux between nanoporous materials. Opt. Express **19**, A1088–A1103 (2011)
16. S.A. Biehs, F.S.S. Rosa, P. Ben-Abdallah, Modulation of near-field heat transfer between two gratings. Appl. Phys. Lett. **98**, 243102 (2011)
17. S.A. Biehs, M. Tschikin, P. Ben-Abdallah, Hyperbolic metamaterials as an analog of a blackbody in the near-field. Phys. Rev. Lett. arXiv:1112.4966 (2012) (To appear)
18. G. Biener, A. Niv, V. Kleiner, E. Hasman, Metallic subwavelength structures for a broadband infrared absorption control. Opt. Lett. **32**, 994–996 (2007)
19. G. Biener, N. Dahan, A. Niv, V. Kleiner, E. Hasman, Highly coherent thermal emission obtained by plasmonic bandgap structures. Appl. Phys. Lett. **92**, 081913 (2008)
20. P. Bouchon, C. Koechlin, F. Pardo, R. Haidar, J.L. Pelouard, Wideband omnidirectional infrared absorber with a patchwork of plasmonic nanoantennas. Opt. Lett. **37**, 1038 (2012)
21. R. Carminati, J.-J. Greffet, Near-field effects in spatial coherence of thermal sources. Phys. Rev. Lett. **82**, 1660–1663 (1999)

22. I. Celanovic, D. Perreault, J. Kassakian, Resonant-cavity enhanced thermal emission. Phys. Rev. B **72**, 075127 (2005)
23. W.A. Challener, C. Peng, A.V. Itagi, D. Kams, W. Peng, Y. Peng, X. Yang, X. Zhu, N.J. Gokemeijer, Y.T. Hsia, G. Ju, E. Rottmayer, M.A. Seigler, E.C. Gage, Heat-assisted magnetic recording by a near-field transducer with efficient optical energy transfer. Nat. Photonics **3**, 220–224 (2009)
24. D.L.C. Chan, M. Soljacic, J.D. Joannopoulos, Thermal emission and design in 2D-periodic metallic photonic crystal slabs. Opt. Express **14**, 8785–8796 (2006)
25. P.O. Chapuis, S. Volz, C. Henkel, K. Joulain, J.J. Greffet, Effects of spatial dispersion in near-field radiative heat transfer between two parallel metallic surfaces. Phys. Rev. B **77**, 035431 (2008)
26. P.O. Chapuis, M. Laroche, S. Volz, J.J. Greffet, Near-field induction heating of metallic nanoparticles due to infrared magnetic dipole contribution. Phys. Rev. B **77**, 125402 (2008)
27. W.C. Chew, *Waves and Fields in Inhomogeneous Media* (IEEE Press, Piscataway, 1995)
28. T.J. Coutts, A review of progress in thermophotovoltaic generation of electricity. Renew. Sustain. Energy Rev. **3**, 77–184 (1999)
29. E. Cravalho, C. Tien, R. Caren, Effect of small spacings on radiative transfer between 2 dielectrics. J. Heat Transfer **89**, 351 (1967)
30. N. Dahan, A. Niv, G. Biener, V. Kleiner, E. Hasman, Space-variant polarization manipulation of a thermal emission by a SiO_2 subwavelength grating supporting surface phonon-polaritons. Appl. Phys. Lett. **86**, 191102 (2005)
31. N. Dahan, A. Niv, G. Biener, V. Kleiner, E. Hasman, Thermal image encryption obtained with a SiO_2 space-variant subwavelength grating supporting surface phonon-polaritons. Opt. Lett. **30**, 3195–3197 (2005)
32. N. Dahan, Y. Gorodetski, K. Frischwasser, V. Kleiner, E. Hasman, Geometric Doppler effect: spin-split dispersion of thermal radiation. Phys. Rev. Lett. **105**, 136402 (2010)
33. N. Dahan, A. Niv, G. Biener, Y. Gorodetski, V. Kleiner, E. Hasman, Enhanced coherency of thermal emission: beyond the limitation imposed by delocalized surface waves. Phys. Rev. B **76**, 045427 (2007)
34. S. Datta, *Electronic Transport in Mesoscopic Systems* (Cambridge University Press, Cambridge, 2002)
35. G.V. Dedkov, A.A. Kyasov, Thermal radiation of nanoparticles occurring at a heated flat surface in vacuum. Tech. Phys. Lett. **33**, 305–308 (2007)
36. M. De Zoysa, T. Asano, K. Mochizuki, A. Oskooi, T. Inoue, S. Noda, Conversion of broadband to narrowband thermal emission through energy recycling. Nat. Photonics **6**, 535–539 (2012)
37. R.S. DiMatteo, P. Greiff, S.L. Finberg, K.A. Young-Waithe, H.K.H. Choy, M.M. Masaki, C.G. Fonstad, Enhanced photogeneration of carriers in a semiconductor via coupling across a nonisothermal nanoscale vacuum gap. Appl. Phys. Lett. **79**, 1894 (2001)
38. I.A. Dorofeyev, E.A. Vinogradov, Fluctuating electromagnetic fields of solids. Phys. Rep. **504**, 75 (2011)
39. J. Drevillon, P. Ben-Abdallah, Ab initio design of coherent thermal sources. J. Appl. Phys. **102**, 114305 (2007)
40. S. Enoch, J.J. Simon, L. Escoubas, Z. Elalmy, F. Lemarquis, P. Torchio, G. Albrand, Simple layer-by-layer photonic crystal for the control of thermal emission. Appl. Phys. Lett. **86**, 261101 (2005)
41. C. Fu, Z.M. Zhang, Thermal radiative properties of metamaterials and other nanostructured materials: a review. Front. Energy Power Eng. China **3**, 11–26 (2009)
42. M. Garin, T. Trifonov, A. Rodrguez, R. Alcubilla, F. Marquier, C. Arnold, J.J. Greffet, Improving selective thermal emission properties of three-dimensional macroporous silicon through porosity tuning. Appl. Phys. Lett. **93**, 081913 (2008)
43. J. Goodman, *Statistical Optics* (Wiley, New York, 1985)
44. J.J. Greffet, M. Nieto-Vesperinas, Field theory for the generalized bidirectional reflectivity: derivation of Helmholtz's reciprocity principle and Kirchhoff's law. J. Opt. Soc. Am. A. **10**, 2735 (1998)

45. J.J. Greffet, R. Carminati, K. Joulain, J.P. Mulet, S.P. Mainguy, Y. Chen, Coherent emission of light by thermal sources. Nature (London) **416**, 61–64 (2002)
46. J.J. Greffet, Controlled incandescence. Nature (London) **478**, 191–192 (2011)
47. R. Guerout, J. Lussange, F.S.S. Rosa, J.P. Hugonin, D.A.R. Dalvit, J.J. Greffet, A. Lambrecht, S. Reynaud, Enhanced radiative heat transfer between nanostructured gold plates. Phys. Rev. B **85**, 180301(R) (2012)
48. S.E. Han, D.J. Norris, Control of thermal emission by selective heating of periodic structures. Phys. Rev. Lett. **104**, 043901 (2010)
49. S. Hava, J. Ivri, M. Auslender, Reflection of infrared radiation from lamellar gratings on a silicon wafer. J. Appl. Phys. **85**, 7893 (1999)
50. A. Heinzel, V. Boerner, A. Gombert, B. Blsi, V. Wittwer, J. Luther, Radiation filters and emitters for the NIR based on periodically structured metal surfaces. J. Mod. Opt. **47**, 2399 (2000)
51. P.J. Hesketh, J.N. Zemel, B. Gebhart, Organ pipe radiant modes of periodic micromachined silicon surfaces. Nature (London) **324**, 549 (1986)
52. L. Hu, A. Narayanaswamy, X. Chen, G. Chen, Near-field thermal radiation between two closely spaced glass plates exceeding Planck's blackbody radiation law. Appl. Phys. Lett. **92**, 133106 (2008)
53. K. Ikeda, H.T. Miyazaki, T. Kasaya, K. Yamamoto, Y. Inoue, K. Fujimura, T. Kanakugi, M. Okada, K. Hatade, S. Kitagawa, Controlled thermal emission of polarized infrared waves from arrayed plasmon nanocavities. Appl. Phys. Lett. **92**, 021117 (2008)
54. Z. Jacob, L.V. Alekseyev, E. Narimanov, Optical hyperlens: far-field imaging beyond the diffraction limit. Opt. Express **14**, 8247–8256 (2006)
55. M. Janowicz, D. Reddig, M. Holthaus, Quantum approach to electromagnetic energy transfer between two dielectric bodies. Phys. Rev. A **68**, 043823 (2003)
56. A.C. Jones, M.B. Raschke, Thermal infrared near-field spectroscopy. Nano Lett. **12**, 1475 (2012)
57. K. Joulain, R. Carminati, J.P. Mulet, J.J. Greffet, Definition and measurement of the local density of electromagnetic states close to an interface. Phys. Rev. B **68**, 245405 (2003)
58. K. Joulain, J.P. Mulet, F. Marquier, R. Carminati, J.J. Greffet, Surface electromagnetic waves thermally excited: radiative heat transfer, coherence properties and Casimir forces revisited in the near field. Surf. Sci. Rep. **57**, 59–112 (2005)
59. K. Joulain, A. Loizeau, Coherent thermal emission by microstructured waveguides. J. Quant. Spectrosc. Radiat. Transfer **104**, 208–216 (2007)
60. A. Kittel, W. Müller-Hirsch, J. Parisi, S.A. Biehs, D. Reddig, M. Holthaus, Near-field heat transfer in a scanning thermal microscope. Phys. Rev. Lett. **95**, 224301 (2005)
61. K.L. Kliewer, R. Fuchs, Theory of dynamical properties of dielectric surfaces. Adv. Chem. Phys. **27**, 355–541 (1974)
62. M. Kreiter, J. Oster, R. Sambles, S. Herminghaus, S. Mittler-Neher, W. Knoll, Thermally induced emission of light from a metallic diffraction grating, mediated by surface plasmons. Opt. Commun. **168**, 117–122 (1999)
63. O.G. Kollyukh, A.I. Liptuga, V. Morozhenko, V.I. Pipa, Thermal radiation of plane-parallel semitransparent layers. Opt. Commun. **225**, 349 (2003)
64. J.A. Kong, *Electromagnetic Wave Theory*, 2nd edn. (Wiley, New York, 2007)
65. M. Laroche, C. Arnold, F. Marquier, R. Carminati, J.J. Greffet, S. Collin, N. Bardou, J.L. Pelouard, Highly directional radiation generated by a tungsten thermal source. Opt. Lett. **30**, 2623 (2005)
66. M. Laroche, F. Marquier, R. Carminati, J.J. Greffet, Tailoring silicon radiative properties. Opt. Commun. **250**, 316–320 (2005)
67. M. Laroche, R. Carminati, J.J. Greffet, Near-field thermophotovoltaic energy conversion. J. Appl. Phys. **100**, 063704 (2006)
68. M. Laroche, R. Carminati, J.J. Greffet, Coherent thermal antenna using a photonic crystal slab. Phys. Rev. Lett. **96**, 123903 (2006)

69. B.J. Lee, Z.M. Zhang, Design and fabrication of planar multilayer structures with coherent thermal emission characteristics. J. Appl. Phys. **100**, 063529 (2006)
70. J. Le Perchec, P. Quemerais, A. Barbara, T. Lopez-Rios, Why metallic surfaces with grooves a few nanometers deep and wide may strongly absorb visible light. Phys. Rev. Lett. **100**, 066408 (2008)
71. B.J. Lee, L.P. Wang, Z.M. Zhang, Coherent thermal emission by excitation of magnetic polaritons between periodic strips and a metallic film. Opt. Express **16**, 11328 (2008)
72. E.M. Lifshitz, L.P. Pitaevskii, *Statistical Physics*, Part 2 (Butterworth-Heinemann, Oxford, 1980)
73. S.Y. Lin, J.G. Fleming, D.L. Hetherington, B.K. Smith, R. Biswas, K.M. Ho, M.M. Sigalas, W. Zubrzycki, S.R. Kurtz, J. Bur, A three-dimensional photonic crystal operating at infrared wavelengths. Nature (London) **394**, 251 (1998)
74. N. Liu, M. Mesch, T. Weiss, M. Hentschel, H. Giessen, Infrared perfect absorber and its application as plasmonic sensor. Nano Lett. **10**, 2342 (2010)
75. X. Liu, T. Tyler, T. Starr, A.F. Starr, N.M. Jokerst, W.J. Padilla, Taming the blackbody with infrared metamaterials as selective thermal emitters. Phys. Rev. Lett. **107**, 045901 (2011)
76. J. Lussange, R. Guerout, F.S.S. Rosa, J.J. Greffet, A. Lambrecht, S. Reynaud, Radiative heat transfer between two dielectric nanogratings in the scattering approach. Phys. Rev. B **86**, 085432 (2012)
77. F. Marquier, K. Joulain, J.P. Mulet, R. Carminati, J.J. Greffet, Engineering infrared emission properties of silicon in the near field and the far field. Opt. Commun. **237**, 379 (2004)
78. F. Marquier, K. Joulain, J.P. Mulet, R. Carminati, J.J. Greffet, Y. Chen, Coherent spontaneous emission of light by thermal sources. Phys. Rev. B **69**, 11 (2004)
79. F. Marquier, M. Laroche, R. Carminati, J.J. Greffet, Anisotropic polarized emission of a doped silicon lamellar grating. Trans. ASME J. Heat Transfer **129**, 11–16 (2007)
80. F. Marquier, C. Arnold, M. Laroche, J.J. Greffet, Y. Chen, Degree of polarization of thermal light emitted by gratings supporting surface waves. Opt. Express **16**, 5305 (2008)
81. D. Maystre, M.C. Hutley, The total absorption of light by a diffraction grating. Opt. Commun. **19**, 431 (1976)
82. S. Maruyama, T. Kashiwa, H. Yugami, M. Esashi, Thermal radiation from two-dimensionally confined modes in microcavities. Appl. Phys. Lett. **79**, 1393–1395 (2001)
83. R. Maynard, E. Akkermans, Thermal conductance and giant fluctuations in one-dimensional disordered systems. Phys. Rev. B **32**, 5440 (1985)
84. J.P. Mulet, K. Joulain, R. Carminati, J.J. Greffet, Nanoscale radiative heat transfer between a small particle and a plane surface. Appl. Phys. Lett. **78**, 2931–2933 (2001)
85. J.P. Mulet, K. Joulain, R. Carminati, J.J. Greffet, Enhanced radiative heat transfer at nanometric distances. Microscale Thermophys. Eng. **6**, 209–222 (2002)
86. A. Narayanaswamy, G. Chen, Surface modes for near field thermophotovoltaics. Appl. Phys. Lett. **82**, 3544–3546 (2003)
87. A. Narayanaswamy, S. Shen, G. Chen, Near-field radiative heat transfer between a sphere and a substrate. Phys. Rev. B **78**, 115303 (2008)
88. T. Ojanen, A.P. Jauho, Mesoscopic photon heat transistor. Phys. Rev. Lett. **100**, 155902 (2008)
89. C.R. Otey, W.T. Lau, S. Fan, Thermal rectification through vacuum. Phys. Rev. Lett. **104**, 154301 (2010)
90. R. Ottens, V. Quetschke, S. Wise, A. Alemi, R. Lundock, G. Mueller, D.H. Reitze, D.B. Tanner, B.F. Whiting, Near-field radiative heat transfer between macroscopic planar surfaces. Phys. Rev. Lett. **107**, 014301 (2011)
91. E.D. Palik, *Handbook of Optical Constants of Solids* (Academic Press, London, 1998)
92. J.L. Pan, H.K.H. Choy, C.G. Fonstad, Very large radiative transfer over small distances from a black body for thermophotovoltaic applications. IEEE Trans. Electron Devices **47**, 241–249 (2000)
93. F. Pardo, P. Bouchon, R. Haidar, J.L. Pelouard, Light funneling mechanism explained by magnetoelectric interference. Phys. Rev. Lett. **107**, 093902 (2011)

94. K. Park, S. Basu, W.P. King, Z.M. Zhang, Performance analysis of near-field thermophotovoltaic devices considering absorption distribution. J. Quant. Spectrosc. Radiat. Transfer **109**, 305–316 (2007)
95. J.B. Pendry, Quantum limits to the flow of information and entropy. J. Phys. A: Math. Gen. **16**, 2161–2171 (1983)
96. J.B. Pendry, Radiative exchange of heat between nanostructures. J. Phys.: Cond. Matt. **11**, 6621–6634 (1999)
97. T.G. Philbin, U. Leonhardt, Alternative calculation of the Casimir forces between birefringent plates. Phys. Rev. A **78**, 042107 (2008)
98. M. Planck, *The theory of heat radiation* (Forgotten Books, Leipzig, 2010)
99. D. Polder, M. Van Hove, Theory of Radiative Heat Transfer between Closely Spaced Bodies. Phys. Rev. B **4**, 3303–3314 (1971)
100. M.U. Pralle, N. Moelders, M.P. McNeal, I. Puscasu, A.C. Greenwald, J.T. Daly, E.A. Johnson, T. George, D.S. Cho, I. El-Kady, R. Biswas, Photonic crystal enhanced narrow-band infrared emitters. Appl. Phys. Lett. **81**, 4685–4687 (2002)
101. I. Puscasu, W.L. Schaich, Narrow-band, tunable infrared emission from arrays of microstrip patches. Appl. Phys. Lett. **92**, 233102 (2008)
102. H. Raether, *Surface Plasmons on Smooth and Rough Surfaces and on Gratings* (Springer, Heidelberg, 1988)
103. L.G.C. Rego, G. Kirczenow, Fractional exclusion statistics and the universal quantum of thermal conductance: a unifying approach. Phys. Rev. B **59**, 13080–13086 (1999)
104. E. Rephaeli, S. Fan, Absorber and emitter for solar thermophotovoltaic systems to achieve efficiency exceeding the Shockley-Queisser limit. Opt. Express **17**, 15145–15159 (2009)
105. F.S.S. Rosa, D.A.R. Dalvit, P.W. Milonni, Casimir interactions for anisotropic magnetodielectric metamaterials. Phys. Rev. A **78**, 032117 (2008)
106. E. Rosencher, B. Vinter, *Optoélectronique* (Dunod, Paris, 2002)
107. E. Rousseau, A. Siria, G. Jourdan, S. Volz, F. Comin, J. Chevrier, J.J. Greffet, Radiative heat transfer at the nanoscale. Nat. Photonics **3**, 514–517 (2009)
108. E. Rousseau, M. Laroche, J.J. Greffet, Radiative heat transfer at nanoscale mediated by surface plasmons for highly doped silicon. Appl. Phys. Lett. **95**, 231913 (2009)
109. E. Rousseau, M. Laroche, J.J. Greffet, Radiative heat transfer at nanoscale: closed-form expression for silicon at different doping levels. J. Quant. Spectrosc. Radiat. Transfer **111**, 1005–1014 (2010)
110. S.M. Rytov, Y.A. Kravtsov, V.I. Tatarskii, *Principles of Statistical Radiophysics*, vol. 3 (Springer, New York, 1989)
111. H. Sai, Y. Kanamori, K. Hane, H. Yugami, Numerical study on spectral properties of tungsten one-dimensional surface-relief gratings for spectrally selective devices. J. Opt. Soc. Am. A **22**, 1805–1813 (2005)
112. A.V. Shchegrov, K. Joulain, R. Carminati, J.J. Greffet, Near-field spectral effects due to electromagnetic surface excitations. Phys. Rev. Lett. **87**, 1548–1551 (2000)
113. S. Shen, A. Narayanaswamy, G. Chen, Surface phonon polaritons mediated energy transfer between nanoscale gaps. Nano Lett. **9**, 2909–2913 (2009)
114. W. Shockley, H.J. Queisser, Limit of efficiency of p-n junction solar cells. J. Appl. Phys. **32**, 510–519 (1961)
115. D.R. Smith, P. Kolinko, D. Schurig, Negative refraction in indefinite media. J. Opt. Soc. Am. B **21**, 1032–1043 (2004)
116. W. Srituravanich, N. Fang, C. Sun, Q. Luo, X. Zhang, Plasmonic nanolithography. Nano Lett. **4**, 1085 (2004)
117. C.T. Tai, *Dyadic Green's Functions in Electromagnetic Theory* (Intext Educational Publishers, Scranton, 1971)
118. R. Tao, Z. Chen, P. Sheng, First-principles Fourier approach for the calculation of the effective dielectric constant of periodic composites. Phys. Rev. B **41**, 2417 (1990)
119. S. Thongrattanasiri, F.H.L. Koppens, F.J. Garcia de Abajo, Complete optical absorption in periodically patterned graphene. Phys. Rev. Lett. **108**, 047401 (2012)

120. M.S. Tomaš, Casimir force in absorbing multilayers. Phys. Rev. A **66**, 052103 (2002)
121. P.J. van Zwol, K. Joulain, P. Ben-Abdallah, J.J. Greffet, J. Chevrier, Fast heat flux modulation at the nanoscale. Phys. Rev. B **83**, 201404(R) (2011)
122. P. van Zwol, K. Joulain, P. Ben-Abdallah, J. Chevrier, Phonon-polaritons enhance near-field thermal transfer across the phase transitions of VO2. Phys. Rev. B **84**, 161413(R) (2011)
123. A.I. Volokitin, B.N.J. Persson, Near-field radiative heat transfer and noncontact friction. Rev. Mod. Phys. **79**, 1291–1329 (2007)
124. L. Wang, Z.M. Zhang, Effect of magnetic polaritons on the radiative properties of double-layer nanoslit arrays. J. Opt. Soc. Am. B **27**, 2595 (2010)
125. L.P. Wang, S. Basu, Z.M. Zhang, Direct and indirect methods for calculating thermal emission from layered structures with non uniform temperatures. J. Heat Transfer **133**, 072701 (2011)
126. M. Wuttig, N. Yamada, Phase-change materials for rewritable data storage. Nat. Mater. **6**, 824 (2007)
127. J.B. Xu, K. Lauger, R. Moller, K. Dransfeld, I.H. Wilson, Heat transfer between two metallic surfaces at small distances. J. Appl. Phys. **76**, 7209–7216 (1994)
128. J. Yang, C. Sauvan, A. Jouanin, S. Collin, J.L. Pelouard, P. Lalanne, Ultrasmall metal-insulator-metal nanoresonators: impact of slow-wave effects on the quality factor. Opt. Express **20**, 16880 (2012)
129. G.N. Zhizhin, E.A. Vinogradov, M.A. Moskalova, V.A. Yakovlev, Applications of surface polaritons for vibrational spectroscopic studies of thin and very thin films. Appl. Spectrosc. Rev. **18**, 171 (1982)

Chapter 9
Aperiodic Order in Nanoplasmonics

Luca Dal Negro, Carlo Forestiere, Nathaniel Lawrence, Sylvanus Lee, Jacob Trevino and Gary Walsh

Abstract In this chapter, we review our work on the engineering of aperiodic order for nanoplasmonics device applications. In particular, we discuss the optical response of arrays of metallic nanoparticles with Fourier spectral features that interpolate in a tunable fashion between periodic crystals and disordered random media, referred to as Deterministic Aperiodic Nano Structures (DANS). These plasmonic structures, conceived by designing spatial frequencies in aperiodic Fourier space, give rise to characteristic scattering resonances and localized mode patterns enhancing the intensity of optical near fields over planar surfaces and broad frequency spectra. Moreover, the distinctive interplay between photonic diffraction and near field plasmonic localization in DANS provides novel opportunities to manipulate light-matter interactions on the nanoscale for device applications to optical biosensing, plasmon-enhanced light sources, solar cells, nonlinear frequency generation, and singular optics.

Keywords Surface plasmon · Aperiodic order · Quasiperiodic arrays

Order is not sufficient. What is required, is something much more complex. It is order entering upon novelty, so that the massiveness of order does not degenerate into mere repetition.
Alfred North Whitehead, Gifford lectures, 1927–1928

L. D. Negro (✉) · C. Forestiere · N. Lawrence · S. Lee · J. Trevino · G. Walsh
Department of Electrical and Computer Engineering, Boston University Photonics Center, Boston University, 8 Saint Mary's street, Boston, MA 02215, USA
e-mail: dalnegro@bu.edu

G. Walsh
Nanomaterials Science Team, U.S. Army NSRDEC, Kansas Street, Natic, MA 01760, USA

T. V. Shahbazyan and M. I. Stockman (eds.), *Plasmonics: Theory and Applications*, Challenges and Advances in Computational Chemistry and Physics 15,
DOI: 10.1007/978-94-007-7805-4_9, © Springer Science+Business Media Dordrecht 2013

9.1 Introduction

Engineering aperiodic order in arrays of metallic nanostructures offers a great and largely unexplored potential for tailoring electromagnetic interactions and enhancing the near field intensity and the optical cross sections (i.e, scattering, absorption, nonlinear processes) of plasmonic media and metamaterials. Fascinating new scenarios emerge when combining aperiodic geometries with resonant nanoparticles supporting surface oscillations of conduction electrons localized on the nanoscale, known as Localized Surface Plasmons (LSPs).

Analogously to the coupling of atomic and molecular orbitals in solid state and quantum chemistry, the LSPs resonances of individual nanoparticles resonantly couple by near-field (i.e., quasi-static) interactions enhancing the intensity of incident electromagnetic fields over nanoscale spatial regions referred to as "electromagnetic hot-spots". Additionally, arrays of nanoparticles separated by distances comparable or larger than the wavelength of light interact by radiative electromagnetic interactions (i.e., diffractive coupling and multiple scattering), giving rise to collective photonic modes largely tunable by the aperiodic array geometry.

Recently, roughened metal surfaces and random media have demonstrated dramatic enhancement of the linear and non-linear optical properties of semiconductor quantum dots and single molecules [1–3]. However, the technological appeal of disordered systems remains very limited. Random structures, while in fact providing a convenient path to electromagnetic field localization and enhancement, lack simple design rules for deterministic optimization. These difficulties have limited the ability to conceive, manipulate, and engineer optical resonances and scattering phenomena in deterministic nanoparticle systems that lack spatial periodicity.

In this chapter, we will review our research activities on the design, nanofabrication, and engineering applications of multi-scale nanoparticle arrays with a degree of structural complexity that interpolates in a tunable fashion between disordered random systems and regular periodic structures. We refer to this general class of artificial metal-dielectric materials as Deterministic Aperiodic Nano Structures (DANS). In contrast to disordered random systems, DANS are generated by deterministic algorithms rooted in computational geometry and crystallography [4–6], symbolic dynamics [7–9], number theory [10–12], and can be fabricated using conventional nano-lithographic or imprint techniques. Moreover, they are amenable to predictive theories. Importantly, the Fourier diffraction spectra of DANS can be tailored from purely discrete ones, such as for periodic and quasiperiodic crystals, to diffuse spectra as for amorphous and random systems. Moreover, DANS can support mixed diffraction spectra, and can additionally encode non-crystallographic point symmetries of arbitrary order (i.e., up to infinity-fold rotational symmetry) as well as more abstract mathematical symmetries [13]. However, differently from well-investigated fractal structures, DANS do not always exhibit scale-invariance symmetry (i.e., self-

similarity in direct space), and are typically characterized by a broader density of spatial frequencies in Fourier space.[1]

Deterministic aperiodic arrays of metal nanoparticles feature interparticle separations that fluctuate from the nanoscale to distances comparable or larger than the wavelength of light. As a result, they support a broad frequency spectrum of "structural resonances", or photonic–plasmonic coupled modes, which significantly enhance the intensity of localized plasmon fields, as we will show later.

This book chapter is organized as follows: Sect. 9.2 introduces general aspects of aperiodic order and the importance of aperiodic Fourier space for the manipulation of plasmonic excitations. Section 9.3 focuses on the fabrication and device applications of two-dimensional (2D) plasmonic DANS. Section 9.4 offers an outlook on complex aperiodic nanoplasmonics and draws general conclusions.

9.2 Fundamentals of Deterministic Aperiodic Order

Aperiodic optical media generated by deterministic mathematical rules have recently attracted significant attention in the optics and electronics communities due to their simplicity of design, fabrication, and full compatibility with current materials deposition and device technologies [13–17]. Initial work, mostly confined to the theoretical investigation of one-dimensional (1D) aperiodic systems [18–25], have succeeded in stimulating broader experimental/theoretical studies on photonic and plasmonic structures that leverage deterministic aperiodicity as a strategy to enable novel optical devices and functionalities.

In what follows, we will introduce the conceptual framework of aperiodic order for the manipulation of optical fields in complex nanoparticle arrays. Moreover, we will discuss the relation between the topological order of DANS, determined by their spectral measures (Fourier or diffraction spectra), and the general characteristics of their optical spectra and plasmonic wave excitations (i.e., structure–property relations). This section will also serve as an introduction to the various types of array geometries discussed in Sect. 9.3.

9.2.1 Periodic and Quasi-Periodic Order

Traditionally, optical media were simply classified as either periodic or non-periodic, without the need of further distinctions. However, the word "non-periodic" encompasses a very broad range of different concepts that describe complex structures characterized by varying degrees of order and correlations, ranging from

[1] However, inhomogeneous fractal structures (i.e., multi-fractals) described by a distribution of scaling exponents can support a higher density of spatial frequencies compared to traditional mono-fractals, similarly to DANS.

quasiperiodic crystals to more disordered "amorphous" materials with diffuse diffraction spectra. Moreover, structures featuring "mixed spectra", containing both discrete peaks and a diffuse background, also frequently occur in science and technology [13, 15]. Therefore, the rigid dichotomy between periodic and amorphous structures is inadequate and needs to be surpassed. More rigorously, non-periodic structures have been classified according to the nature of their Fourier and energy spectra, which correspond to mathematical measures [8, 13]. In optics, these spectral measures are often identified with the characteristics of diffraction patterns and optical mode spectra (i.e., Local Density of States).

According to the *Lebesgue's decomposition theorem* [26], any measure can be uniquely decomposed in terms of three primitive spectral components (or into a mixture of them), namely: pure-point (μ_P), singular continuous (μ_{SC}), and absolutely continuous spectral components (μ_{AC}), with: $\mu = \mu_P \cup \mu_{SC} \cup \mu_{AC}$. Based on this result, Maciá Barber [13, 15] recently proposed to classify different types of structures according to a matrix with nine entries, corresponding to all the combinations of the three fundamental types of spectral measures describing their spatial Fourier and energy spectra.

Random media are characterized by large structural fluctuations modeled by continuous (i.e., constant) spatial Fourier spectra. However, their energy spectra are ideally discrete (i.e., pure-point), since disorder-induced localized states appear at discrete resonant frequencies where the electronic/optical transport comes to a halt. On the other hand, the diffraction patterns of periodic structures contain well defined and sharp (i.e., δ-like) peaks in their spatial Fourier spectra corresponding to the presence of periodic long-range order. Therefore, the reciprocal Fourier space of periodic and multi-periodic lattices is discrete (i.e., pure-point), with peaks (i.e., Bragg peaks) positioned at rational multiples of primitive reciprocal lattice vectors. However, their energy or optical transmission spectra consist of continuous functions describing the different energy bands.

In between these two extremes lies the extremely rich spectral domain of deterministic aperiodic systems. It was recently realized that the presence of sharp peaks in the diffraction spectra of materials does not necessarily imply structural periodicity. In 1984, Dan Shechtman et al. [27] when studying the electron diffraction spectra from certain metallic alloys (Al_6Mn), discovered sharp diffraction peaks arranged with icosahedral point group symmetry, which cannot be reconciled with structural periodicity [6, 27]. However, the sharpness of the measured diffraction peaks, which indicates the coherence of the spatial interference patterns, turned out to be comparable with the one of ordinary periodic crystals. Stimulated by these findings, Levine and Steinhardt promptly formulated the notion of aperiodic crystals or quasicrystals in a seminal paper titled [28]: "*Quasicrystals: a new class of ordered structures*". The geometry of aperiodic crystals was already anticipated in the seminal work on aperiodic tilings by the mathematician Penrose, who discovered in 1974 the existence of two simple polygonal shapes (i.e., tilings) capable of exactly covering the infinite Euclidean plane *without spatial periodicity* [29]. In response to these breakthrough discoveries, the International Union of Crystallography (IUCr) reformulated the concept of crystal structures as "*any solid having an essentially discrete*

diffraction diagram", irrespective of spatial periodicity, thus shifting from direct to the reciprocal Fourier space the defining aspect of a crystal structure [13]. According to this new picture, the essential attribute of crystalline order, either periodic or quasiperiodic, is the presence of a discrete diffraction spectrum containing only isolated Bragg peaks, namely a pure-point spectrum.

It has also been realized after the breakthrough discovery of quasi-crystals and the fabrication of Fibonacci [22, 23] and Thue–Morse semiconductor heterostructures [30, 31], that physical systems can display singular-continuous energy spectra featuring an infinite hierarchy of narrow gaps with vanishingly small widths (in the limit of infinite-size systems), bridging a long standing gap between the theory of spectral operators and condensed matter physics.

9.2.2 Aperiodic Order and Substitutions

We will now discuss how to manipulate aperiodic order beyond traditional quasicrystals. In optics and electronics, a very efficient algorithmic approach to generate aperiodic structures with controlled Fourier spectral properties is provided by symbolic substitutions [7, 8, 13, 32]. Substitutions are an essential component of every recursive *symbolic dynamical system* formally defined on a finite symbolic alphabet $\mathrm{G} = (a, b, c, \ldots)$. In physical realizations, each letter in the alphabet can be associated to a different type of building block (e.g., metal nanoparticle, dielectric layer, etc). A specific substitution rule ω then replaces each letter in the alphabet by a finite word, starting from a given letter called an *axiom* or *initiator.* An aperiodic sequence is then obtained by iterating the substitution rule ω multiple times to any desired order, producing a symbolic string of arbitrary length. For instance, one-dimensional Fibonacci quasicrystal structures can be simply generated by the iteration of the rule $\omega_{\mathrm{F}} : a \to ab, b \to a$ with axiom a, as exemplified by the inflation process: $a \to ab \to aba \to abaab \to abaababa \to abaababaabaab \to \ldots$

A large number of substitution rules have been explored in the study of deterministic aperiodic optical systems [13, 16, 17], producing 1D structures with all three primitive spectral measures, as shown in Fig. 9.1.

The diffraction spectrum of a Fibonacci quasicrystal is pure-point, featuring a countable set of δ-like Bragg peaks at incommensurate intervals. More complex structures displaying singular-continuous spectra[2] can also be conveniently generated by the symbolic substitution approach [13]. In such media, individual Bragg peaks are no longer separated by well-defined gaps, but cluster to form "broad bands" in reciprocal space.

The chief example of a deterministic sequence with a singular-continuous diffraction spectrum is the Thue–Morse sequence [8, 33], which is generated by the substitution $\omega_{\mathrm{TM}} : a \to ab, b \to ba$. This binary sequence was first studied by

[2] Singular-continuous structures support Fourier spectra can be covered by an ensemble of open intervals with arbitrarily small total length.

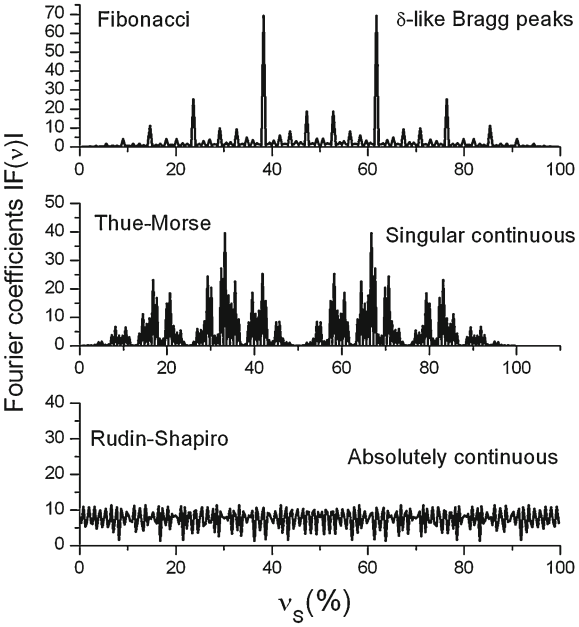

Fig. 9.1 Absolute value of the Fourier coefficients of a quasiperiodic (Fibonacci) structure, of an aperiodic Thue–Morse structure with singular-continuous spectrum, and of an aperiodic Rudin–Shapiro structure with absolutely continuous spectrum. From Ref. [32]

Prouhet in 1851, who applied it to number theory [34]. Thue in 1906 used it to found the study of combinatorics on words. The sequence was successively brought to worldwide attention by the differential topology work of Morse in 1921, who proved that the complex trajectories of a dynamical system whose phase space has negative curvature can be mapped into the Thue–Morse sequence [35]. Interestingly, pseudo-random structures with Fourier spectra of constant amplitude (i.e., in the infinite-size or thermodynamic limit) can also be generated deterministically by binary substitutions. As a result, the eigenmodes of such systems (e.g., optical modes, plasmon modes, etc) are expected to be more localized in space compared to the excitations supported by structures with pure-point spectra.

The chief example of deterministic structures with absolutely continuous Fourier spectrum is the Rudin–Shapiro sequence [8, 36, 37]. In a two-letter alphabet, the RS sequence can simply be obtained by the substitution: $aa \rightarrow aaab, ab \rightarrow aaba, ba \rightarrow bbab, bb \rightarrow bbba$ [38]. Rudin–Shapiro structures are expected to share most of their physical properties with disordered random systems, including the presence of localized optical states (i.e., Anderson-like states). However, the abundance of short-range correlations, whose main effect is to reduce the degree of disorder and localization, favors the existence of resonant extended states in their energy spectra, and significantly complicates the theoretical analysis of Rudin–Shapiro and other deterministic structures with absolutely continuous Fourier spectra [38, 39]. The

calculated Fourier spectra of one-dimensional Fibonacci, Thue–Morse, and Rudin–Shapiro symbolic sequences are displayed in Fig. 9.1.

The substitution approach described above can be rigorously generalized to higher dimensions using the theory of automatic sequences [40–42]. Alternatively, 2D quasi-periodic Fibonacci arrays can be easily generated by alternating two complementary Fibonacci substitution rules along the horizontal and the vertical directions [32]. This way, a square 2D Fibonacci matrix can be obtained. Extending this approach, our group recently introduced 2D generalizations of Thue–Morse and Rudin–Shapiro sequences for the design of planar metallic nanoparticle arrays of interest in nanoplasmonics device technology [43].

Figure 9.2 shows the direct and reciprocal Fourier space of Fibonacci, Thue–Morse and Rudin–Shapiro arrays of particles obtained using the 2D substitution method [32]. We notice that, differently from periodic structures, a Brillouin zones cannot be defined for aperiodic arrays (i.e., their diffraction diagrams are aperiodic). As a result, when displaying the diffraction spectra of aperiodic systems, we restrict the Fourier space vectors to spatial frequencies within the interval $\pm 1/\Delta$, where Δ is the minimum interparticle separation represented in the array.

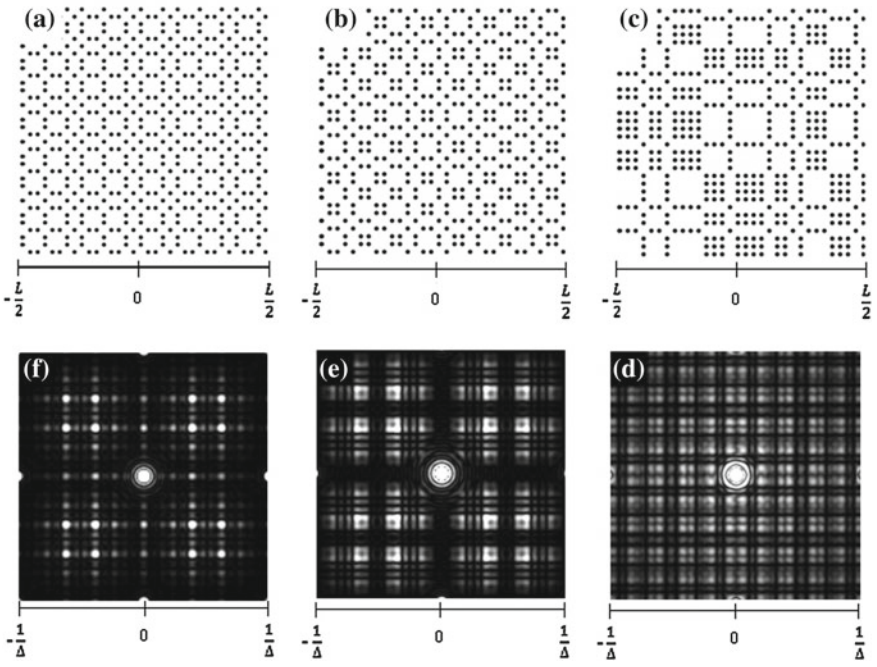

Fig. 9.2 **a** Fibonacci array, L = 13.4 μm, generation 7. **b** Thue–Morse array, L = 12.6 μm, generation 5. **c** Rudin–Shapiro array, L = 12.6 μm, generation 5. **d** Rudin–Shapiro reciprocal space. **e** Thue–Morse reciprocal space. **f** Fibonacci reciprocal space. In all cases $\Delta = 400$ nm is the minimum center-to-center particle distance

9.2.3 Plasmonic Chains: Collective Excitations and Energy Gaps

The advantage of the substitutional method is that relevant information on the nature of the diffraction spectra of aperiodic sequences can be obtained from the knowledge of the *substitution matrix*, whose elements indicate the number of times a given letter appears in the components of the substitution rules (irrespective of the order in which it occurs) [13]. This follows from the Bombieri–Taylor theorem, which unveils a fundamental connection between the arithmetical nature of substitutions and the presence/absence of Bragg peaks in the corresponding Fourier spectra [44–48]. According to the Bombieri–Taylor theorem [49, 50], if the spectrum of the substitution matrix $\boldsymbol{S}$ contains a so-called Pisot–Vijayvaraghavan (PV) number as an eigenvalue, then the sequence is quasiperiodic,[3] otherwise it is not.[4] A very important question in aperiodic systems research concerns the relation between their structural properties/topological order and the energy spectra of their elementary excitations and eigenmodes. Solving this difficult problem is of direct interest to aperiodic optics and plasmonics, as it will enable the formulation of powerful structural-property relations for predictive device modeling and engineering.

A fundamental result in this direction in known as the *gap-labeling theorem.* This theorem relates the positions of the diffraction Bragg peaks of substitutional sequences with the locations of the gaps in the energy spectra of the elementary excitations supported by the structures (e.g., plasmon modes) [44, 45, 51]. In general, a tight-binding analysis of the energy spectra or the density of states of aperiodic structures obtained by Pisot-type substitutions shows that both the position and the width of the gaps can be "labeled" by the singularities of the Fourier transform associated to the aperiodic sequence of scattering potentials (optical or electronic) [44, 51]. This approach, first introduced for the 1D Schrödinger equation [52], has also been applied to the optical wave equation in quasiperiodic and almost-periodic structures [21, 51]. Recently, Dal Negro et al. [53] developed an efficient transfer matrix approach, valid within the dipole approximation, for the calculation of the resonant eigenfrequencies, oscillation eigenvectors and the integrated density of states (IDS) of chains of metallic nanoparticles (i.e., dipolar chains) with Fibonacci, Thue–Morse and Rudin–Shapiro aperiodic modulation [32, 53, 54].

Aperiodically modulated plasmonic chains are constructed by letting $\mathrm{d_A} \equiv \mathrm{A}$ and $\mathrm{d_B} \equiv \mathrm{B}$ in the corresponding substitution rule, where $\mathrm{d_A} = 25\,\mathrm{nm}$ and $\mathrm{d_B} = 30\,\mathrm{nm}$ are two minimum interparticle separations. With this identification, we can readily map symbolic aperiodic sequences into chains of nanoparticles with deterministic aperiodic order, as sketched in Fig. 9.3 for a Fibonacci chain of Ag nanoparticles. This system can be modeled by considering the dynamical equation for an arbitrary Hertzian dipole in the chain [32, 53, 55], and recasting it into a matrix that connects

[3] This means that its spectrum can be expressed as a finite sum of weighted Dirac δ-functions, corresponding to Bragg peaks that are indexed by integer numbers.

[4] A PV number is a positive algebraic number larger than one and such that all of its conjugate elements (i.e., the other solutions of its defining algebraic equation) have absolute value less than one. For instance, the golden mean, satisfying the algebraic equation $\mathrm{x}^2 - \mathrm{x} - 1 = 0$ is a PV number.

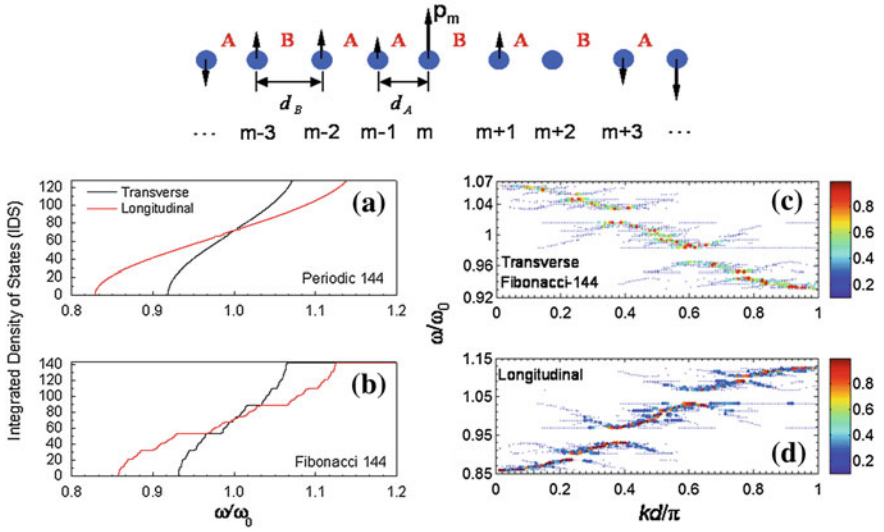

Fig. 9.3 Integrated density of states (IDS) for the **(a)** periodic and **(b)** quasiperiodic Fibonacci chains showing longitudinal and transverse branches. Dispersion diagrams for **(c)** quasiperiodic Fibonacci chain, transverse polarization; **(d)** quasiperiodic Fibonacci chain, longitudinal polarization. Adapted from Ref. [53]

the spectral oscillation amplitudes of neighboring dipoles in terms of unimodular transfer matrices T_n:

$$\begin{pmatrix} u_{n+1} \\ u_n \end{pmatrix} = T_n \begin{pmatrix} u_n \\ u_{n-1} \end{pmatrix} \tag{9.1}$$

where u_n is the Fourier transform of the oscillation amplitude of dipole n and the matrix T_n can be expressed as Ref. [53]:

$$T_n = \begin{pmatrix} \frac{\omega^2 - \omega_0^2 - i(\Gamma_e \omega - \Gamma_R \omega^3/\omega_0^2)}{\gamma_i \alpha_n^2} & -1 \\ 1 & 0 \end{pmatrix} \tag{9.2}$$

In the expression above ω_0 is the metal plasma frequency, Γ_e is the electronic relaxation frequency, Γ_R is the relaxation frequency due to radiation into the far-field, γ_i is a polarization-dependent term ($\gamma = 1$ for transverse modes and $\gamma = -2$ for longitudinal) and $\alpha\alpha_n^2 \propto 1/d_n^3$ is the near-field coupling term, which is aperiodically modulated because nearest neighbors of the nth dipole do not repeat regularly, but follow a deterministic aperiodic sequence.

Therefore matrices T_n depend on frequency and on the geometrical arrangement of the particles through the short-range dipole–dipole coupling [53], establishing the connection with the aperiodic geometry. The displacement of the Nth dipole with frequency ω and eigenvector $u_N(\omega)$, can be easily calculated by cascading the

individual transfer matrices:

$$\begin{pmatrix} u_{N+1} \\ u_N \end{pmatrix} = T_N T_{N-1} T_{N-2} \ldots T_2 T_1 \begin{pmatrix} u_1 \\ u_0 \end{pmatrix} = Q \begin{pmatrix} u_1 \\ u_0 \end{pmatrix} \tag{9.3}$$

Imposing the fixed boundary condition $u_0 = u_{\mathrm{N}+1} = 0$, which describes an N-particle chain, we finally obtain that the vibration frequencies of the plasmonic chain satisfy the following eigenvalue equation:

$$Q_{11}(\omega) = 0 \tag{9.4}$$

which can readily be solved numerically for an arbitrary aperiodic geometry to yield the oscillation amplitudes of the dipole chain (i.e., the eigenvectors) and the oscillation frequencies (i.e., the eigenvalues) [32, 53].

In addition, Dal Negro et al. [32, 53] have shown, based on the eigenmode statistics, that it is possible to calculate the Integrated Density of States (IDS) and the participation ratio of each dipolar eigenstate, which allows to quantify the degree of spatial localization of the plasmonic modes. Based on this approach, we have computed the pseudo-dispersion $\omega - k$ diagram of periodic and Fibonacci-modulated plasmonic chains of finite size (i.e., 144 nanoparticles) corresponding to longitudinal and transverse oscillation modes, and demonstrated the presence of large spectral gaps in one-dimensional Fibonacci structures, as summarized in Fig. 9.3. We subsequently extended this transfer matrix approach to the analysis of the spectral and localization properties of dipolar modes in nanoparticle chains based on Thue–Morse and Rudin–Shapiro aperiodic sequences [32]. We have shown that the aperiodic modulation of the particle positions leads to the formation of sub-wavelength plasmon band-gaps in Fibonacci and Thue–Morse structures, while Rudin–Shapiro structures are characterized by vanishingly small gaps and a singular density of states, akin to random systems. In addition, we have demonstrated a characteristic power-law scaling in the localization degree of the eigenstates of all the investigated deterministic aperiodic structures, which is a manifestation of the multifractal nature of their density of states spectra.

A more general approach for the calculation of dipolar modes and energy spectra of aperiodic arrays of metal nanoparticles with ellipsoidal shapes, which also includes their electromagnetic coupling with external fields, was developed by Forestiere et al. [54]. The equations governing the plasmon oscillations were formulated in such a way as to highlight the role of the geometrical arrangement of the particles on one side, the particles shape, the dielectric response, and the incoming field polarization on the other side, enabling the accurate design of aperiodic plasmonic devices with controlled sub-wavelength gaps and spectral positions of localized states. The work in Ref. [54] rigorously demonstrates that the spectral and localization properties of dipolar modes in aperiodic chains of resonant nanoparticles are determined by the mathematical spectral properties of a symmetric, positive-definite operator relating the electric field along the chain to the electric dipole moments, within the electric quasi-static approximation. In addition, Forestiere et al. [54] showed that

the spectrum of this operator, which is determined by the aperiodic geometry of the arrays for a given shape of the nanoparticles, explains the spectral positions of the plasmonic pseudo-band gaps in terms of the singularities of the aperiodic Fourier spectra. This analysis therefore establishes the validity of the gap-labeling theorem in the context of aperiodic nanoplasmonics. Therefore, the demonstration of controllable plasmonic band-gaps and sub-wavelength localized plasmon fields in finite-size chains of metal nanoparticles with aperiodic order suggests novel designs for the implementation of plasmonic devices and functionalities.

9.2.4 Rotational Symmetry: Aperiodic Tilings and Vogel Spirals

One of the main features of aperiodic planar arrays is the ability to encode forbidden rotational symmetries in their discrete or diffuse diffraction diagrams, displayed by their Fourier spectra [6, 56]. It was recently discovered that aperiodic tilings can be constructed with an arbitrary degree of rotational symmetry using a purely algebraic approach [57]. In addition, deterministic tilings with full rotational symmetry up to infinite order (i.e., circular symmetry) have been demonstrated [58] by a simple procedure that iteratively decomposes a triangle into five congruent copies. The resulting tiling, called Pinwheel tiling, has triangular elements (i.e., tiles) which appear in infinitely many orientations and, in the limit of arrays with infinite-size, the diffraction pattern displays continuous ("infinity-fold") rotational symmetry.

Radin has shown that there are no discrete components in the Pinwheel diffraction spectrum [58]. However, it is currently unknown if the spectrum is continuous or singular continuous.

We recently engineered [59] Pinwheel arrays of resonant metallic nanoparticles and reported on isotropic structural coloration of metal films using homogenized Pinwheel patterns. In particular, following this approach we demonstrated bright green coloration of Au films with greatly reduced angular sensitivity and enhanced spatial uniformity of coloration compared to both periodic and random arrays [59].

In Fig. 9.4, we show three different types of deterministic aperiodic arrays of particles with increasing degree of rotational symmetry in their diffraction spectra (Fig. 9.4d–f). In particular, Fig. 9.4a shows a particle array with tenfold rotational symmetry in the arrangement of its (interior) Bragg peaks. This array is obtained by positioning particles at the vertices of a planar Penrose tiling. A Danzer particle array [60] with sevenfold symmetry (Fig. 9.4b) and the Pinwheel array (Fig. 9.4c) are also shown along with the corresponding diffraction spectra (Fig. 9.4d–f).

We can appreciate in Fig. 9.4 how by increasing the degrees of rotational symmetry the different spectra acquire a more diffuse spectral character. This behavior is particularly evident in a broad class of finite-size deterministic aperiodic arrays, known as Vogel's spirals (Fig. 9.5), whose diffraction spectra do not posses any discrete component and display almost continuous circular symmetry.

Vogel's structures have been investigated by mathematicians, botanists, and theoretical biologists [61] in relation to the outstanding geometrical problems of

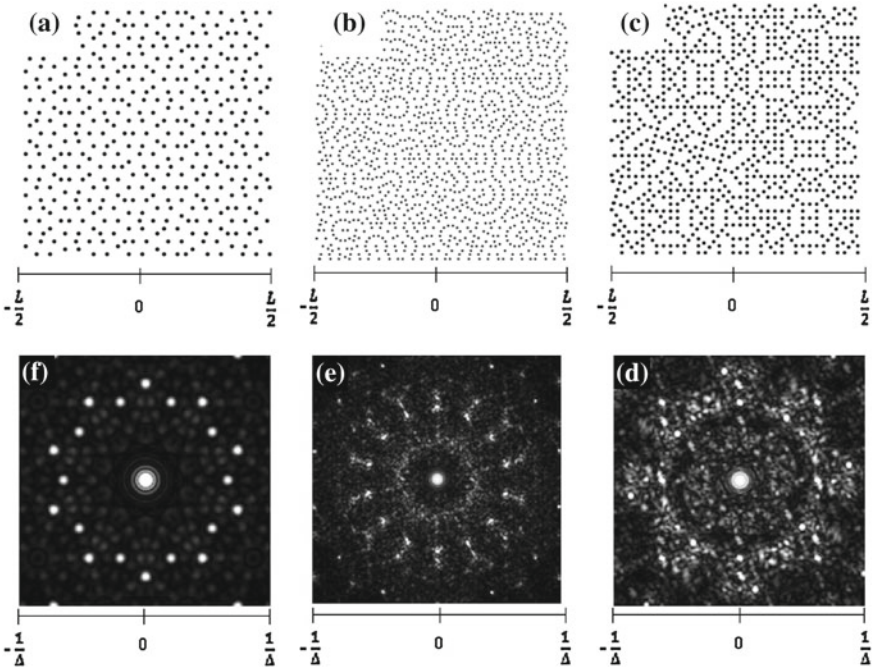

Fig. 9.4 **a** Penrose array, L = 11.9 μm, generation 12; **b** Danzer array, L = 26.6 μm; **c** Pinwheel array, L = 16.1 μm; **d** Pinwheel reciprocal space; **e** Danzer reciprocal space; **f** Penrose reciprocal space. In all cases Δ = 400 nm is the minimum center-to-center particle distance

phyllotaxis [62–64], which concerns the understanding of the spatial arrangement of leaves, bracts and florets on plant stems.

Aperiodic Vogel spiral structures are rapidly emerging as a powerful nanophotonics platform with distinctive optical properties of interest to a number of engineering applications [65–68]. This fascinating class of deterministic aperiodic media possess circularly symmetric scattering rings in Fourier space entirely controlled by simple generation rules inducing a very rich structural complexity described by multi-fractal geometry with a degree of local order in between amorphous and random systems [65].

Our group recently demonstrated Vogel spiral arrays of metallic nanoparticles and show that they give rise to polarization-insensitive, planar light diffraction across a broad spectral range, referred to as *circular light scattering* [69]. This interesting phenomenon originates from the circular symmetry of the reciprocal space of aperiodic spirals, and it can already be appreciated within standard Fourier optics (i.e., neglecting near-field interactions among neighboring particles). In fact, for radiation of wavelength λ normally incident on a generic arrays of particles, to be diffracted *into the plane of the array* its longitudinal wavevector component must vanish, i.e., $k_z = 0$. This requirement is equivalent to the well-known Rayleigh cut-off condition

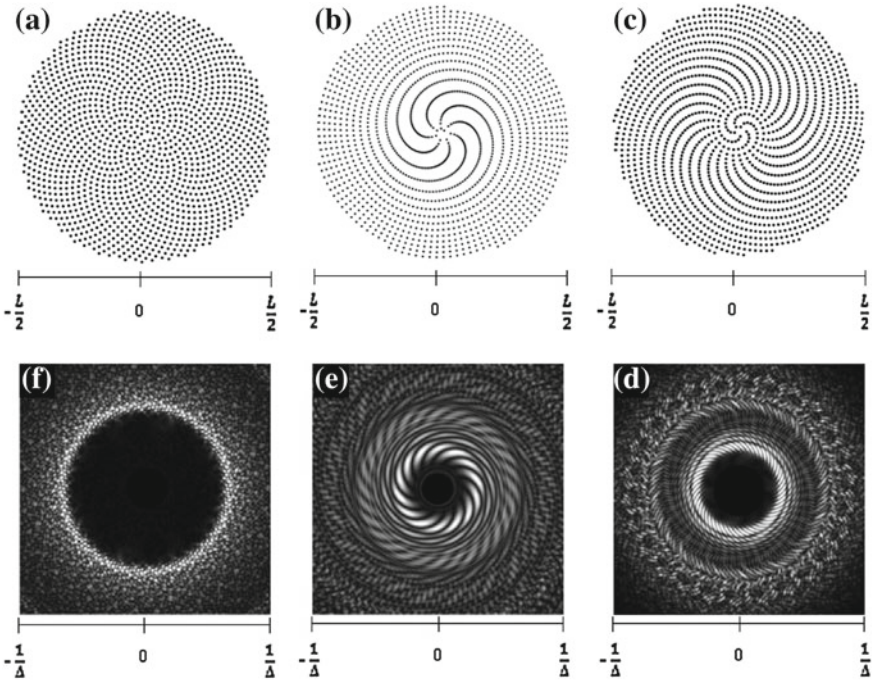

Fig. 9.5 **a** Golden angle spiral array, L = 23.2 μm, divergence angle $\theta \approx 137.508$; **b** π-spiral array, L = 34.9 μm, divergence angle $\theta \approx 50.973$; **c** μ-spiral array, L = 23.2 μm, divergence angle $\theta \approx 69.330$; **d** Golden angle spiral reciprocal space where Δ is the average minimum center-to-center particle distance (Δ = 308 nm); **e** π-spiral reciprocal space where Δ is the average minimum center-to-center particle distance (Δ = 403 nm); **f** μ-spiral reciprocal space where Δ is the average minimum center-to-center particle distance (Δ = 201 nm)

that determines the propagation of the first diffractive order of a periodic grating *on its planar surface* [70]. The Rayleigh condition depends on wavelength λ and on the transverse spatial frequencies ν_x and ν_y of the diffracting element, according to:

$$k_z = 2\pi\sqrt{(1/\lambda)^2 - \nu_x^2 - \nu_y^2} = 0 \tag{9.5}$$

Equation (9.5) is satisfied on a circle of radius $1/\lambda$ in reciprocal space, and therefore structures with circularly-symmetric Fourier space satisfy the Rayleigh cut-off condition strongly diffracting normal incident radiation into evanescent grating modes. We say that the resonant condition expressed by Eq. 9.5 induces "planar diffraction". It is important to notice that, differently from periodic crystals and quasicrystals with finite-order rotational symmetries, aperiodic spirals satisfy the condition for planar diffraction over a range of wavelengths uniquely determined by the *number and the width of the scattering rings in their reciprocal space*.

This property is ideal to enhance light-matter coupling on planar substrates [69], leading to thin-film solar cell enhancement [67], light emission enhancement [66, 71], and enhanced second harmonic generation [68], as further discussed in Sect. 9.3. Moreover, we recently discovered that Vogel spiral arrays of Au nanoparticles support distinctive scattering resonances carrying orbital angular momentum (OAM), potentially leading to novel applications in singular optics and cryptography [69, 72, 73].

Vogel spiral arrays can be obtained in polar coordinates (r, θ) by the relations [13, 74, 75]:

$$\begin{aligned} r_n &= a_0\sqrt{n} \\ \theta_n &= n\alpha \end{aligned} \tag{9.6}$$

where $n = 0, 1, 2, \ldots$ is an integer index, a_0 is a constant scaling factor, and α is an irrational number known as the divergence angle. This gives the constant angle between successive particles in the spiral array. When $\alpha \approx 137.5086°$, it approximates an irrational number known as the "golden angle", we obtain the so-called Fibonacci golden angle spiral (GA), shown in Fig. 9.5a. The golden angle α is related to the famous Fibonacci golden number $\varphi = (1 + \sqrt{5})/2 \approx 1.618$ by the relation $\alpha = 360/\varphi^2$.

The structure of a GA spiral can be decomposed into clockwise and counterclockwise families of out-spiraling lines of particles, known as *parastichies,* which stretch out from the center of the structures. Interestingly, the number of spiral arms in each family of parastichies is given by consecutive Fibonacci numbers [74]. Moreover, since the golden angle is an irrational number, the GA spiral lacks both translational and rotational symmetry. Accordingly, its spatial Fourier spectrum does not exhibit well-defined Bragg peaks, as for standard photonic crystals and quasicrystals, but rather features a diffuse circular ring whose spectral position is determined by the particles geometry (Fig. 9.5f). Interestingly, Vogel's spirals with remarkably different structural properties can be obtained by choosing only slightly different values of divergence angle, thus providing the opportunity to control and explore distinctively different degrees of aperiodic structural complexity. We show in Figs. 9.5b, c two examples of Vogel spirals, known as π and μ-spirals, obtained using the following divergence angles $\alpha_\pi = 309.03°$ and $\alpha_\mu = 290.67°$, respectively. These structures feature a rotationally symmetric Fourier space with remarkable structural complexity, as demonstrated by Fig. 9.5d, e.

Recently, Dal Negro et al. [73] developed an analytical model that captured in closed form solution the spectral properties of arbitrary Vogel spiral arrays. Within the framework of scalar Fourier optics, we showed that the complex Fourier spectrum (i.e., Fraunhofer diffraction pattern) of arbitrary Vogel spirals is described by the analytical expression [73]:

$$E_\infty(\nu_r, \nu_\theta) = E_0 \sum_{n=1}^{N} e^{j2\pi\sqrt{n}a_0\nu_r \cos(\nu_\theta - n\alpha)} \tag{9.7}$$

where the variables (ν_r, ν_θ) are Fourier conjugate of the direct-space cylindrical coordinates (r, θ) used to represent the Vogel spiral density, α is an irrational divergence angle, a_0 is a constant scaling factor, and N is the number of particles in the array [73].

A distinctive property of Vogel spiral nanoparticle arrays is that, when illuminated by optical beams, they give rise to scattered radiation carrying OAM [69, 73]. Modal decomposition can be used to analyze a superposition state of OAM carrying modes in the far field pattern and determine their relative contribution to the overall field [66, 72, 76]. Decomposition into a basis set with helical phase fronts, is accomplished through Fourier–Hankel decomposition (FHD) according to:

$$f(m, k_r) = \frac{1}{2\pi} \int_0^\infty \int_0^{2\pi} r dr d\theta \rho(r, \theta) J_m(k_r r) e^{im\theta} \tag{9.8}$$

where J_m is the mth order Bessel function. In this decomposition, the mth order function carries OAM with azimuthal number m, accommodating positive and negative integer values for m.

By analytically performing Fourier–Hankel Decomposition (FHD) analysis, Dal Negro et al. [73] demonstrated that diffracted optical beams by Vogel spirals carry OAM values arranged in aperiodic numerical sequences determined by the number-theoretic properties of the irrational angle α. In particular, wave diffraction by GA arrays generates a Fibonacci sequence of OAM values in the Fraunhofer far field region. More precisely, the OAM values transmitted in the far field region are directly related to the rational approximations of the continued fraction expansion of the irrational divergence angles of Vogel spirals [73].

It is important to realize that Vogel spiral arrays provide a very large spectrum of OAM values relying uniquely on light scattering phenomena. In Fig. 9.6, we show the calculated Fraunhofer far fields and the OAM azimuthal spectra of GA and μ-spirals. Since we are primarily concerned with the azimuthal component *f(m)* of OAM, we sum $f(m, k_r)$ over radial the wavenumbers k_r. Figures 9.6c, d demonstrate the very rich structure of OAM peaks of the scattered radiation by Vogel spirals. These peaks occur at azimuthal numbers (labeled in the figures) corresponding to the denominators of the rational approximations of the irrational divergence angles used to generate the spirals. The Fibonacci sequence of OAM values is coded in the far field region of the radiation scattered by the GA spiral.

This fascinating property of Vogel spirals can be understood clearly by considering the analytical solution of the FHD of the far field radiation pattern, which is given by [73]:

$$f(m, k_r) = \sum_{n=1}^{N} A(k_r) e^{imn\alpha} \tag{9.9}$$

where $A(k_r)$is a k_r-dependent coefficient, which can be ignored since we are concerned with the azimuthal dependence contained in *f(m)*.

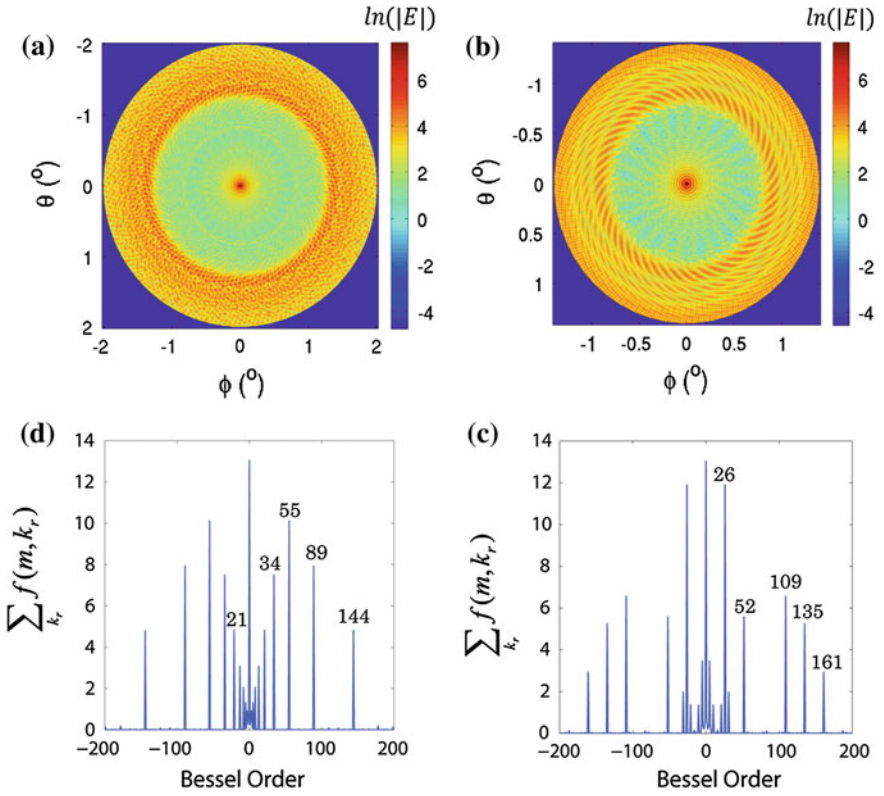

Fig. 9.6 **a**, **b** Analytically calculated far field radiation patterns of GA and μ-spiral with 2,000 particles at a wavelength of 633 nm for structures with $a_0 = 14.5\,\mu m$. The far field radiation patterns have been truncated with an angular aperture of 4° and 3°, respectively. **c**, **d** Fourier–Hankel transforms of far field scattered radiation by GA and μ-spiral, respectively, summed over the radial wavenumber k_r. The numbers in the figures indicate the azimuthal Bessel order of the corresponding FHD peaks

We see from the result in Eq. 9.9 that when $m\alpha$ is an integer, the N waves in the equation will be exactly in phase to produce an OAM peak with azimuthal number m. For an irrational angle α, this condition will never be exactly satisfied. However, any irrational α can be approximated by an infinite continued expansion of rational fractions, each approximately matching the integer condition for the $m\alpha$ product. Therefore, for spirals generated using an arbitrary irrational number α, azimuthal peaks of order m (i.e, Bessel order m) will appear in the FHD spectrum due to all the denominators q_n of the rational approximations (i.e., the convergents) of $\alpha \approx p_n/q_n$, resulting in a sequence of discrete azimuthal peaks in the OAM of scattered light simply determined by the aperiodic geometry.

Using phase delayed interferometric measurements, we have recently recovered the complex electric field distribution of scattered radiation by Vogel spirals and

demonstrated structured light carrying multiple values of OAM in the far field scattering region of arrays of metallic nanoparticles, in excellent agreement with analytical calculations [77].

The unique features of Vogel spirals provide exciting new opportunities for the engineering of OAM states using aperiodic nanostructures for a number of emerging engineering applications in singular optics, secure communication, optical cryptography, and optical sensing.

9.2.5 Aperiodic Order and Number Theory

Numerical sequences and geometric patterns with deterministic, though apparently haphazard behavior, have been deeply investigated in discrete mathematics and information theory [78, 79]. In particular, deterministic structures generated by number-theoretic numerical sequences with flat-Fourier spectra have found numerous technological applications in different research areas ranging from the engineering of acoustic diffusers to radar abatement (stealth surfaces), spread spectrum communication (jamming countermeasures, secure channel sharing), and the design of minimum redundancy antenna arrays (surveillance) in the RF regime [10]. However, aperiodicity in number theory is still largely unexplored in the domain of optical technologies.

Number theory is primarily concerned with the properties of integer numbers, but encompasses a large spectrum of advanced techniques from virtually all branches of mathematics [11, 12]. As a result, number theory provides numerous insights and algorithmic approaches for the generation of different types of *pseudo-random* systems, point sets, and aperiodic tilings with various degree of structural complexity and Fourier spectral properties [10, 12].

Figure 9.7 shows representative examples of aperiodic particle arrays deterministically generated based on number-theoretic concepts in the real and complex fields. In particular, we show a Gaussian prime array (Fig. 9.7a), a co-prime array (Fig. 9.7b), and a Galois field array (Fig. 9.7c), along with the calculated Fourier spectra (Fig. 9.7d–f).

Gaussian primes (GP) are Gaussian integers that are prime in the complex field, and are defined by $n+im$, where n and m are integers and i is the imaginary unit [10]. We notice that primes of the form $4k-1$ in the ring of conventional integer numbers are still primes in the complex field, but 2 and primes of the form $4k+1$ can be factored in the complex field (e.g., $2=(1+i)(1-i)$, $5=(2+i)(2-i)$, etc.). Moreover, if x is a Gaussian prime, the four numbers $\pm x, \pm ix$ are called the *associates* of x and are also Gaussian primes. As a result, Gaussian primes are symmetric about the real and imaginary axes.

By plotting the real and imaginary components of GP numbers as horizontal and vertical coordinates, we can represent Gaussian primes geometrically in the complex plane, and produce the highly symmetric pattern displayed in Fig. 9.7a. However, despite the remarkable symmetry of the pattern, GP arrays are non-periodic.

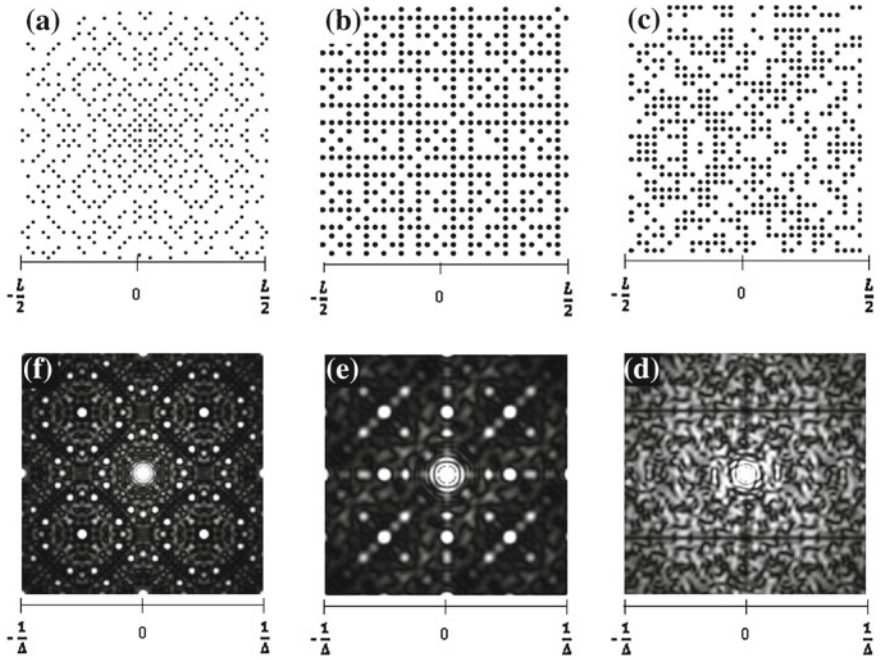

Fig. 9.7 **a** Array of Gaussian prime numbers, L = 19.4 μm. **b** Array of co-prime numbers, L = 11.4 μm. **c** Galois array, L = 12.8 μm. **d** Reciprocal space of the Galois array. **e** Reciprocal space of the co-prime array. **f** Reciprocal space of Gaussian prime array. Δ = 400 nm is the minimum center-to-center particle distance

Moreover, the presence a diffuse background along with well-defined peaks in the Fourier space of GP arrays (Fig. 9.7f) suggests the singular continuous nature of the spectrum. However, no rigorous mathematical results are known on the spectral character of GP arrays. Interestingly, GP aperiodic arrays with different degree of rotational symmetries can be obtained by considering primes defined by $n + \alpha m$, where α is a complex algebraic root of unity. When considering the complex cube root of unity, which is the solution of the algebraic equation $1 + \alpha + \alpha^2 = 0$, we obtain the two-dimensional pattern of Eisenstein primes, which displays hexagonal symmetry [10].

A co-prime array is shown in Fig. 9.7b. This array is obtained by positioning nanoparticles in correspondence to pairs of co-prime integers in the two-dimensional plane. We recall that two integers a and b are said to be co-prime ($a \perp b$) if their greatest common divisor GCD, denoted by (a,b), equals 1 (they have no common factors other than 1). Figure 9.7e shows the Fourier spectrum of the co-prime array. We notice that since the array is symmetric around the 45° diagonal, so is its Fourier spectrum. Furthermore, since in Fig. 9.7e we plot the *magnitude* of the Fourier transform of the array, an additional diagonal at −45° will appear as a symmetry axis. Compared to the spectrum of the GP array shown in Fig. 9.7f, the co-prime array features a

broader spectrum of spatial frequencies that are associated to several characteristic length scales. Interestingly, several peaks appear in Fourier space related to the most frequent distances between prime numbers [10, 80].

The discussion above makes us appreciate clearly the irreducible complexity that often arises from the simple arithmetic properties of integer numbers. To this regard, we notice that most number-theoretic functions (e.g., co-primality, discrete logarithm, Euler's ϕ, Möbius function, Riemann's zeta function, Dirichlet L-functions, etc) display apparent random behavior despite the large number of symmetry properties, easily detected when constructing the corresponding geometrical arrays. This aperiodic behavior, ubiquitous in number theory, is fundamentally related to intractable arithmetic problems (e.g., distribution of prime numbers, factorization, etc). The role of randomness in number theory has been deeply discussed in the framework of Algorithmic Information Theory (AIT) [78, 79].

Pseudo-random particle arrays with constant Fourier spectra can be conveniently designed based on the theory of finite Galois fields [10]. In abstract algebra, a field is a set of elements with addition, subtraction, multiplication and division (except by 0) operations that satisfy the usual commutative, associative, and distributive laws.

Galois fields, named after the French mathematician Évariste Galois, are fields with a finite number of elements (i.e., finite order fields) and have found numerous applications in physics, communication theory, error-correcting code, cryptography, and even artistic design [10]. As a simple example, a residue system modulo a prime p forms a finite field (i.e., a Galois field) of order p, which is indicated by GF(p). Of particular importance are finite number fields of order equal to a prime power p^m (i.e., with pm elements), where p is a prime number and m is a positive integer. A Galois field of order p^m is usually denoted as GF(p^m).

In particular, Galois sequences derived from GF(2^m) have unique correlation properties and possess flat Fourier spectra but, in contrast to other pseudo-random binary sequences (i.e., Legendre sequences), are efficiently generated by a linear recursion [10, 81–83]. Galois nanoparticle arrays can be constructed by generalizing Galois recursions in two spatial dimensions as detailed in Refs. [10, 84]. Figure 9.7c shows a calculated Galois particle array. The reciprocal Fourier space is shown in Fig. 9.7d, and features a broad distribution of spatial frequencies without any well-defined Bragg peak, similarly to the white spectrum of disordered random media.

Two-dimensional Galois arrays possess a high density of spatial frequencies, theoretically a flat measure for infinite-size arrays. This property has been used to improve the image resolution of X-ray sources in astronomy [10].

Aperiodic arrays of metal nanoparticles generated according to number-theoretic functions have been explored only recently in the context of plasmonic scattering and field localization for optical sensing device applications [80, 85, 86].

However, since number-theoretic methods mostly provide asymptotic results, their applicability to finite-size aperiodic structures remain fundamentally limited, with remarkable exceptions in cryptographic domains (e.g., pseudo-random generators, optical cryptography).

9.2.6 Hot Spot Engineering with Aperiodic Plasmon Arrays

In this section, we will discuss the distinctive features of local electromagnetic field engineering using aperiodic arrays of metal nanoparticles. Let us first recall that arbitrary arrays of resonant metallic nanostructures can resonantly couple at multiple length scales due to near-field (i.e., quasi-static) interactions and radiative electromagnetic interactions (i.e., multiple scattering). Nanoplasmonics is mostly concerned with the engineering of longitudinal near-fields around metallic nanostructures and near-field coupling between nanostructures in order to boost the intensity of incident electromagnetic fields over nanoscale regions, known as "electromagnetic hot spots" [87]. However, when the electromagnetic radiation is incident on multi-particle arrays with separations comparable or larger than the wavelength of light, nanoparticles additionally couple by radiative interactions and give rise to collective scattering resonances that are largely tunable by the array geometry. Therefore, when engineering multi-particle arrays, long-range photonic–plasmonic coupling effects must always be carefully accounted for. A simple example of "array driven" photonic–plasmonic coupling is provided by the Fano-type resonances observed in metal nanoparticle gratings [88–92]. Periodic gratings support a discrete spectrum of narrow photonic resonances, known as diffractive or grating modes that when spectrally/spatially overlapped with the broader LSP modes of individual nanoparticles, under appropriate excitation wavelengths and incidence angles, lead to more intense hot spots and larger optical cross sections.

On the other hand, in aperiodic multi-particle arrays a large number of spatial frequencies (wavenumbers) are available to match in-plane photonic scattering processes, resulting in photonic–plasmonic coupling effects distributed over a larger wavelength range [93]. Therefore, we can generally expect that aperiodic arrays featuring a large density of spatial frequencies will result in a higher density of enhanced hot spots over a broader frequency range compared to structures with more regular geometry.

Consistently, roughened metal surfaces and random media, characterized by delta-correlated white spectra, have demonstrated dramatic enhancement of hot spot intensities for single molecule detection [94]. We have recently confirmed the qualitative picture discussed above by coupled dipole and semi-analytical multiple scattering calculations of near-fields and scattering spectra in deterministic aperiodic arrays of varying structural complexity (i.e., Fourier spectral properties) [80, 93, 95]. It is important to notice that the ability to engineer aperiodic structures with structural complexity in between random and periodic media enables the optimization of hot spots in complex photonic–plasmonic media, and can unveil distinctive engineering design rules. This point is illustrated by Forestiere et al. [80], who systematically investigated the near-field plasmonic behavior and far-field scattering response of Ag nanoparticle arrays generated according to prime numbers distributions in two spatial dimensions. Using rigorous coupled dipole analysis for dipolar nanoparticles, this study demonstrates how the local intensity of plasmon fields can be strongly enhanced over broad frequency spectra by engineering closely packed (i.e., large

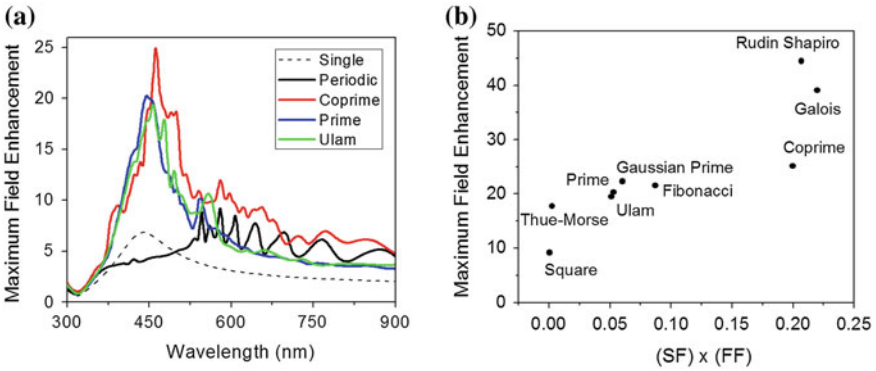

Fig. 9.8 **a** Maximum field enhancement versus the wavelength for an isolated Ag nanosphere (50 nm radius) and for periodic, coprime, prime, and Ulam spiral aperiodic arrays of nanospheres with 25 nm minimum interparticle separation. The arrays are exited by a circularly polarized plane wave at normal incidence. **b** Values of maximum filed enhancement versus the spectral flatness (SF) × filling fraction (FF) product for the different arrays indicated in the figure

particle filling fraction) arrays with large density of spatial frequencies, as shown in Fig. 9.8a. The case of a single Ag nanosphere of 50 nm radius is also shown for comparison. Figure 9.8b shows the maximum hot spot intensity, probed in the plane of the arrays, for a number of aperiodic deterministic structures (named in the figure) as a function of the product of the arrays filling fraction (FF) (or particles density) and spectral flatness[5] (SF). To better describe the influence of both the polarization states of the incident field, the arrays were excited by a circularly polarized plane wave at normal incidence. It is to be noted that aperiodic arrays have been found to perform better than closely packed periodic ones despite their substantially lower filling fractions (i.e., particle density). Therefore, the computational results in Fig. 9.8b demonstrate clearly that closely-packed aperiodic plasmonic arrays with a large density of spatial frequency are necessary in order to enhance hot spots intensity over a broader frequency range compared to optimized periodic and quasiperiodic structures [80].

Another very important aspect of aperiodic plasmonic arrays relates to the fraction of the total array area covered by strong plasmonic fields. In plasmonic sensing technology, the understanding of the area density of enhanced fields on a planar chip is of fundamental importance. In order to quantitatively understand this aspect, we studied the fraction of the total area of the arrays covered by plasmonic enhanced fields with values greater then a fixed threshold. This important feature is mathematically defined by the cumulative distribution of field enhancement (CDFE), which we have introduced in Ref. [80].

[5] The spectral flatness (SF) is a digital signal processing parameter that measures how spectrally diffused a signal is. In the case of plasmonic structures, the arrays are considered as digitized 2D spatial signals and the SF is calculated by dividing the geometric mean and the arithmetic mean of their Fourier power spectra [80].

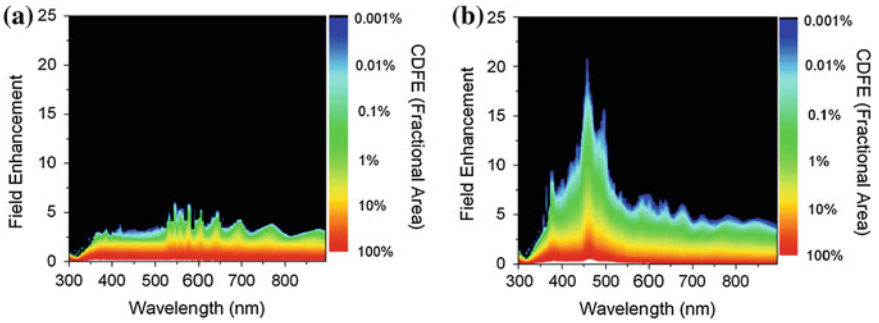

Fig. 9.9 The color-maps show the cumulative distributions of field enhancement (CDFE) (logarithmic scale) versus wavelength (x-axis) and field-enhancement (y-axis) for **(a)** periodic **(b)** coprime arrays. The arrays are excited by a circularly polarized plane wave at normal incidence

In Fig. 9.9a, b we show the CDFE calculated for a periodic and a co-prime array, respectively. The CDFE function describes the fraction of the total area of the arrays covered by plasmonic enhanced fields with values greater then a fixed value specified in the vertical axis. Although the CDFE does not give any information about the size of hot spot, it provides a quantitative measure of how the energy is spatially distributed, at each wavelength, over the entire surface of the array. The results in Fig. 9.9 demonstrate that aperiodic arrays with large spectral flatness and particle filling fraction support enhanced field states that are spatially distributed over larger array areas compared to periodic plasmonic structures, which is an important attribute for the engineering of scattering-based plasmonic sensors (e.g., SERS substrates).

We want to emphasize again that the characteristic behavior of aperiodic nanoplasmonic structures follows from the large number of supported photonic modes that enhance the coupling, over a broad spectral range, to the subwavelength plasmon modes of local particle clusters inhomogeneously distributed across the arrays. Broadband hot spots intensity enhancement with aperiodic plasmonic structures is therefore made possible by the long-range nature of the electromagnetic coupling in multi-scale arrays of resonant nanoparticles with positional fluctuations. However, we should notice that aperiodic designs with dense Fourier spectra come at the additional cost of a larger system's size compared to narrow-band periodic or multi-periodic structures, ultimately requiring engineering trade-offs between the intensity enhancement, the resonant frequency bandwidth, and the total size of plasmonic devices.

Another consequence of multi-scale electromagnetic coupling in aperiodic arrays of metallic nanoparticles is the distinctive scaling of their hot spots intensity with the total number of particles, which is a measure of the overall arrays dimension. This is best illustrated by the analytical multiple scattering results in Fig. 9.10 that illustrate the field intensity distribution and the maximum hot spots intensity, versus the number of particles, for periodic square arrays of Au nanospheres (100 nm radius, 25 nm separation) and Fibonacci, Thue–Morse, Rudin–Shapiro arrays (25 nm minimum

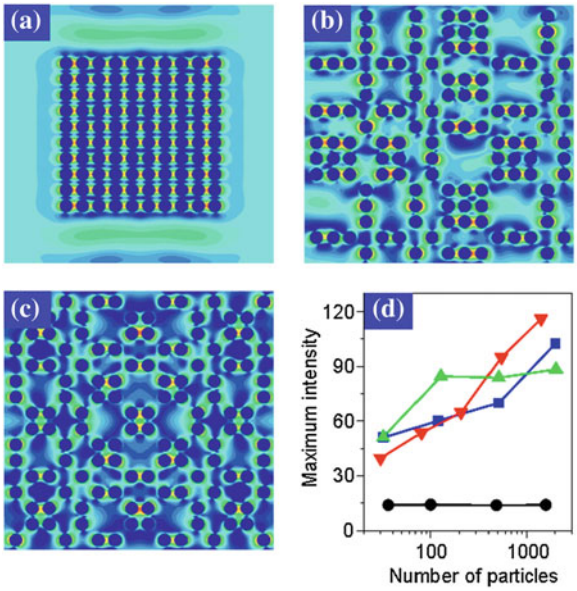

Fig. 9.10 Generalized Mie Theory (GMT) calculations of electromagnetic field scattered by plasmonic arrays of spherical Au nanoparticles arranged according to **(a)** a periodic array **(b)** a Rudin–Shapiro array **(c)** a Fibonacci array. All the particles in the arrays have a radius of 100 nm and a minimum separation of 25 nm. **d** Scaling of the calculated intensity enhancement for the different arrays as a function of the number of particles

interparticle separation). All the structures are illuminated at normal incidence by a plane wave at 785 nm. First, we can clearly appreciate from Fig. 9.10b, c that the nanospheres in the aperiodic arrays are coupled by both the near-field interactions responsible for hot spots formation and the multiple scattering of light occurring in the plane of the array, activated by the characteristic "photonic length scales" (i.e., lower spatial frequencies) of the aperiodic arrays. When scaling up the size of the arrays by increasing the particles number, new configurations of local particle clusters appear separated by wavelength-scale distances [96], thus increasing the total number of spatial frequencies in the plane and enhancing the maximum hot spots intensity in a size-dependent fashion.

The size dependent nature of the optical response of aperiodic systems is a well-known manifestation of multiple scattering in the mesoscopic regime [97]. On the other hand, since no photonic coupling occurs in subwavelength coupled periodic arrays (Fig. 9.10a), more delocalized plasmonic modes are formed across the entire periodic structure with reduced hot spot intensity. The lack of photonic-type coupling in closely packed periodic arrays therefore prevents the onset of size-dependent photonic–plasmonic resonances and enhancement effects, making the maximum hot spot intensity insensitive to the overall array size, as demonstrated in Fig. 9.10d. The distinctive size-dependence of the plasmonic near field response of aperiodic

arrays has direct implications for device engineering, since in addition to the particles composition/morphology and array geometry, the size of aperiodic arrays can be tailored to enhance the near field hot spots intensity. In the next section, after a discussion on the electron beam nanofabrication of DANS, we will introduce few selected device applications.

9.3 Engineering Applications of Aperiodic Plasmon Arrays

From the discussions in the previous sections, it should be clear that manipulating the interplay of coherent photonic scattering and near field plasmonic coupling in aperiodic Fourier space offers novel opportunities to design electromagnetic hot spots and to control light-matter coupling on the nanoscale for a number of engineering device applications.

We will discuss in the next sections the nanofabrication of plasmonic DANS and introduce some engineering device applications that leverage deterministic aperiodicity and metallic arrays of nanoparticles. The interested reader should consult the reference section for more device applications and in-depth discussions of specific structures.

9.3.1 Nanofabrication of Aperiodic Plasmon Arrays

In contrast to random media, DANS can be specifically tailored and fabricated using conventional nanolithographic techniques such as electron beam lithography (EBL) or Focused Ion Beam (FIB) milling followed by standard metal deposition and etching steps. Our group has recently developed a flexible process flow, as detailed below, for the nanofabrication of arbitrary arrays of metal nanoparticles for nanoplasmonic applications. In particular, we developed metallic nanoparticle arrays based on noble metals, typically Au and Ag, on quartz substrates with a 10 nm layer Indium Tin Oxide (ITO) to provide conduction. A 180-nm-thick layer of PMMA (PolyMethylMethAcrylate) is then spin coated on top of the cleaned substrate. Subsequently, the DANS patterns are defined using a Zeiss SUPRA 40VP SEM equipped with a Raith Beam Blanker and NPGS for nanopatterning.

After developing the resist in a 1:3 solution of MIBK (Methyl IsoButyle Ketone) and IPA (Isopropanol), a $\sim$30 nm thick Au/Ag film is deposited on the patterned surface by electron-beam evaporation. Finally, a liftoff process is performed using acetone, resulting in the definition of the targeted metal nanoparticle arrays. Within the same general process flow, nano-perforated metal/dielectric films can also be obtained using a Reactive Ion Etching (RIE) step immediately after EBL writing. The concept of our process flow for the fabrication of both metallic nanoparticle arrays and nano-hole patterns is summarized in Fig. 9.11.

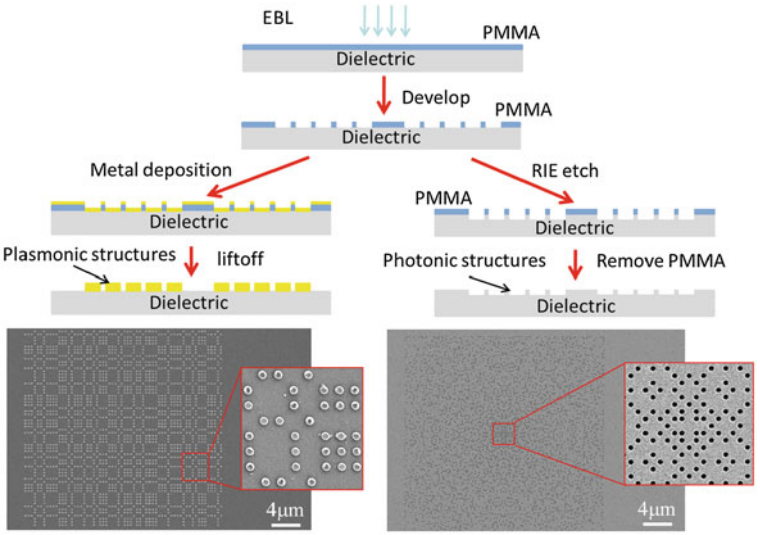

Fig. 9.11 Schematics of the fabrication process flow for the generation of aperiodic plasmonic nanoparticle arrays (*left*) and nano-hole arrays (*right*). The SEM pictures show a Rudin–Shapiro arrays of Au nanoparticles (*left*) and a Gaussian prime array of nano-holes in a quartz substrate. The particle/hole radius is 100 nm and the minimum interparticle separation is 200 nm

Typical dimensions of each fabricated array are about $100\,\mu m \times 100\,\mu m$ for nanoparticles with a diameter of 200 nm, 30 nm tall and variable separations that can range in between 25 and 400 nm, depending on the specific DANS geometry, device applications, and nanolithographic setup.

As an example of fabricated DANS, we show in Fig. 9.12 the Scanning Electron Microscopy (SEM) pictures of arrays of Au nanoparticles arranged in periodic (a), Fibonacci (b), Thue–Morse (c), and Ruden-Shapiro (d) geometry. The Au particles are cylindrical in shape and their height, as characterized by Atomic Force Microscopy (AFM) and SEM, was found to be $h = 30\,nm$. All the particles have a circular diameter of $d = 200\,nm$ and a minimum interparticle separation $a = 25\,nm$. Notice however, the additional length scales present in the aperiodic structures, which extend to scales comparable to the wavelength in the optical regime. DANS as shown in Figs. 9.12 and 9.13 have been successfully applied to Surface Enhanced Raman sensing technology, as it will be discussed in the following section.

To demonstrate the complete flexibility of the DANS fabrication process described above, we additionally show in Fig. 9.13 Au nanoparticle arrays fabricated with various types of deterministic aperiodic order on a Si substrate. These structures are Pinwheel (a), Danzer (b), Coprime arrays (c) and the three most investigated types of Vogel spirals (d–f). We can clearly appreciate from Figs. 9.12 and 9.13 the overall quality of the nanofabricated arrays, which excellently match the abstract geometrical patterns previously introduced in Sect. 9.2. However, current nanoscale writing techniques, such as EBL, focused ion beam lithography (FIB), and scanning

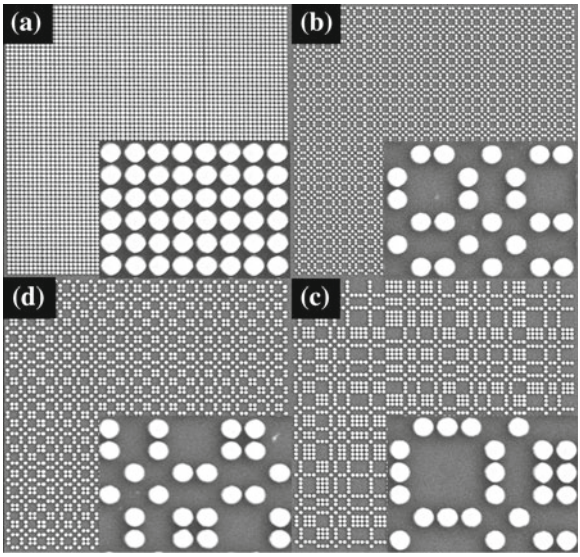

Fig. 9.12 SEM pictures of **(a)** Periodic, **(b)** Fibonacci, **(c)** Thue–Morse, **(d)** Rudin–Shapiro Au nanoparticle array. The individual particle sizes are 200 nm, and the minimum interparticle separations in the arrays shown are 25 nm

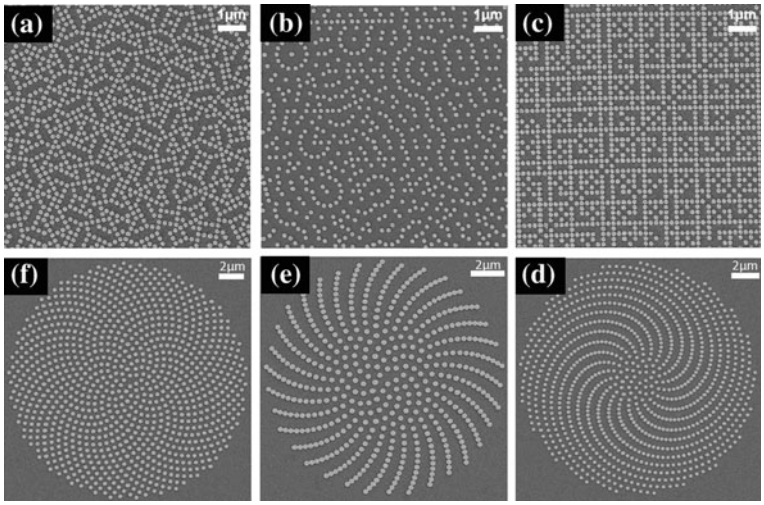

Fig. 9.13 SEM pictures of **(a)** Peenwheel, **(b)** Danzer, **(c)** Coprime, **(d)** Rudin–Shapiro Au nanoparticle array. The individual particle sizes are 200 nm, and the minimum interparticle separations in the arrays shown are 50 nm

probe microscopy (SPM), suffer from high operating costs and low throughput. On the other hand, shadow-mask patterning techniques, such as stencil-based methods, allow for the fabrication of plasmonic nanostructures but inherently suffer from edge blurring and cannot produce plasmonic films perforated with nano-holes, which play an important role in nanoplasmonics.

To solve these problems, we recently proposed and demonstrated a scalable and cost-effective direct transfer nanofabrication technique that utilizes a hard mold master and an inexpensive, commercially available flip-chip bonder, for the fabrication of large-scale metallic nanoparticles and perforated metallic films (plasmonic nano-hole arrays) directly atop silk fibroin films [98].

The process flow for the transfer imprint of plasmonic nano-dots and nano-holes, begins with the fabrication of the reusable master molds. As an example, we discuss in Fig. 9.14 the case of printing nano-hole arrays on a metal film. In the case of the nano-dot transfer process, the desired geometry is fabricated into a Si mold consisting of nanopillar arrays, while the nano-hole process requires a mold containing nano-holes, as shown in Fig. 9.14a.

The fabrication of the nano-hole master proceeds via EBL writing with a 260-nm-deep RIE step, using the PMMA as an etch mask. The remaining PMMA is removed by hot acetone bath, resulting in the Si nano-hole master. The Si master is first treated with a silanizing agent to reduce the adhesion of the Au to the Si surface. This surface treatment enables a higher yield in pattern transfer of the Au to the silk film in the subsequent steps. The process flow continues with the deposition of a 35nm-thick e-beam evaporated gold (Au) film, as shown in Fig. 9.14b. The Au coated master is now ready for transfer imprinting on the silk films. A commercial flip-chip bonder (Smart Equipment Technology FC150) was employed to transfer imprint from the fabricated master mold. The flip-chip bonder is used to align and bond one or more chips onto a substrate using pressure and heat as shown in Fig. 9.14c. The transfer

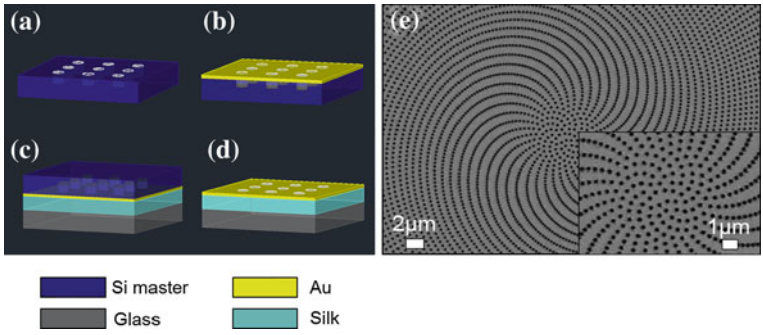

Fig. 9.14 Process flow of transfer nanoimprint of plasmonic nano-hole arrays using reusable masters. **a** Nano-hole structures are defined in a Si master by EBL and RIE processing. **b** E-beam evaporation of Au films to be transfered. **c** Transfer imprint utilizing commercial filp-chip bonder. **d** Removal of master, leaving nanohole arrays on the silk film surface. **e** example of nanofabricated plasmonic nanohole structures with aperiodic Vogel spiral geometry. Adapted from Ref. [98]

imprint process begins by heating the Au covered master to 90 °C, when it is then pressed onto the surface of the silk layer with a force of 50 kg (area of 16 mm^2) for 5 min. During the imprinting, the plasmonic nanostructures bind to the surface of silk layer. Upon completion of the bonding cycle, the master is removed, leaving the Au embedded on the surface of the silk layer as shown in Fig. 9.14d for nano-dots arrays. Nano-imprinted plasmonic hole arrays with Vogel spiral geometry are shown as an example in Fig. 9.14e.

A similar process has been successfully developed to imprint arrays of metallic nanoparticles atop polymer films. In this case, a Si mold consisting of nanopillar arrays needs to be utilized. More details on these novel high throughput and scalable fabrication processes can be found in Ref. [98]. These techniques enable the large-scale replication of arbitrarily complex nanostructures with deep sub-wavelength details down to 30 nm with a high throughput, as the mould is reusable. The inexpensive scalability of aperiodic nanoplasmonic structures over large areas is of great importance for device engineering as it offers the opportunity to abate fabrication costs and to develop aperiodic substrates into a mature technology. Some specific device applications of aperiodic nanoplasmonic substrates will be discussed in the next sections.

9.3.2 Applications to Surface Enhanced Raman Biosensing

Surface Enhanced Raman Scattering (SERS) spectroscopy is a well-established and highly sensitive technique for investigating the specific vibrational response of a variety of different analytes with fingerprinting accuracy. Recently, SERS spectroscopy has been successfully applied to label-free chemical and biological sensing [99–101], where it has proven to be an excellent method for sensing DNA hybridization [102], protein binding events [103], and even single molecules [104–107]. In addition, it bears great promises for rapid identification of viruses and bacteria [108–110], potentially enabling whole-organism fingerprinting. The dramatic enhancement of the Raman scattering efficiency observed in SERS experiments is mainly driven by the enhanced local electromagnetic fields in nanostructured metal surfaces [111–113]. In fact, despite that SERS enhancement can also be affected by the specific electronic resonances of Raman-active molecules (i.e., electronic enhancement) and by their direct contact with metal surfaces (i.e., chemical enhancement), the dominant factor originates from a resonant effect between the incident and the scattered radiation fields associated to the excitation of localized surface plasmon resonances. In particular, the Raman enhancement factor scales roughly as the fourth power of the local field [100, 111, 112]:

$$\eta_{SERS} \propto \left|E_{loc}(\omega_p)\right|^2 \left|E_{loc}(\omega_s)\right|^2 \tag{9.10}$$

where $E_{loc}(\omega_p)$ is the local electromagnetic field at the pumping frequency and $E_{loc}(\omega_s)$ is the local electromagnetic field at the scatted signal frequency. Because of this distinctive scaling, in SERS applications it is very important to engineer strong local fields at these two frequencies in order to obtain very high Raman enhancement factors, enabling optical sensing of few or even single molecules.

Currently, the best approaches to generate efficient SERS substrates rely on random roughening of metal surfaces by etching or by colloidal synthesis of nanoparticles resulting in aggregates statistically described by fractal morphologies [1, 3, 114, 115]. The giant fluctuations of the local fields characteristic of self-similar (fractal) structures leads to an efficient transfer of excitations towards progressively smaller length scales of the aggregates where the electromagnetic enhancement reaches the 10^{12} level needed to observe single molecule SERS [1, 116, 117]. However, while fractal aggregates and rough metal surfaces led to successful applications in single molecule spectroscopy [101, 105, 106], reproducibility of results can vary from sample to sample and engineering design rules are not easy to formulate. On the other hand, these approaches clearly demonstrated the importance of the morphology dependent "structural enhancement", which is characteristic of multi-scale complex systems where both electrodynamical interactions and electrostatic coupling (lightning rod effect, quasi-static plasmon coupling) contribute to the overall SERS enhancement.

In contrast to randomly roughened surfaces, it is possible to fabricate reproducible metal nanostructures using Electron beam lithography (EBL) to be used as efficient SERS substrates. Following the pioneering work of Wokaun et al. [118], it became possible to obtain SERS signals from lithographically defined metal nanostructures [119–123]. By using EBL, it is possible to fabricate uniform SERS substrates by controlling not only the shapes but also the positions of each particle at the nanoscale.

The SERS enhancement achievable using periodic arrays of metal nanoparticles can be further increased by reducing their inter-particle separations [122, 123]. However, the width of the inter-particle gaps achievable by EBL is limited to approximately 20 nm, which is much larger than the inter-particle separations typically obtained using random colloidal aggregates (1–5 nm). Therefore, in order to take full advantage from structural enhancement effects in highly reproducible EBL-based substrates, our group recently proposed to engineer the subtle interplay between diffractive long-range and near-field coupling interactions in nanoparticles arrays with complex, yet deterministic, morphologies [124, 125].

In particular, by developing DANS arrays of Au nanoparticles as a novel approach for the design and implementation of "engineered roughness" in SERS substrates, we demonstrated large values ($\sim 10^7$) of spatially averaged enhancement factors (i.e., defined over the entire excitation area) localized within 25 nm gaps using molecular pMA (p-mercaptoaniline) monolayers. In our studies, we used pMA as the Raman marker because of its ability to form reproducible saturation coverage on gold surfaces, which reduces the ambiguity associated with the experimental quantification of the SERS enhancement. Moreover, we introduced novel multi-scale aperiodic nanostructures, called "plasmonic nanogalaxies", which yield reproducible SERS enhancement (spatially averaged) values up to $\sim 10^8$ [124]. These deterministic ape-

riodic structures feature multiple length scales and produce cascade enhancement effects similar to arrays of nano-lenses [116, 117], which significantly boost the SERS enhancement values to almost single molecule sensitivity levels.

In our experimental analysis, Raman signal measurements were performed using a Renishaw Raman microscope (RM2000, Renishaw, IL). A 50× (N.A. = 0.55) objective was used to focus the laser beam on a nanostructured array and to collect the scattering light from the sample surface using a backscattering configuration. The SERS signal was typically acquired for 10 s using 785 nm laser wavelength at 1.7 mW excitation power. The dimension of the laser spot is constant (2.5 μm × 25 μm) ensuring that the SERS signal from the different arrays is comparable and unaffected by size variation.

In Fig. 9.15 we summarize the SERS results obtained using the DANS arrays of Au nanoparticles with different shapes (nano-cylinders and nano-triangles) and aperiodic geometry. The experimentally measured SERS enhancement factors are determined by the ratio of the Raman signal per molecule measured on the engineered substrates and the reference Raman signal per molecule originating from a pMA bulk crystal, as detailed elsewhere [124, 125]. The experimental results on pMa molecular monolayers demonstrate large ($\sim 10^7$), morphology-dependent values of average enhancement factors driven by the hot-spot formation in DANS arrays with 25 nm minimum separations (Figs. 9.15 and 9.16). Even larger values of enhancement factors ($\approx 10^8$) were recently obtained by Gopinath and collaborators [124] using plasmonic nano-galaxies. Aperiodic nano-galaxy structures are fabricated by a combination of top-down EBL, which serves to define DANS arrays of nano-cylinders with various geometries and bottom-up in-situ chemical Au reduction to attach smaller nanoparticles (satellites) to the EBL-defined template (see Fig. 9.16a). The dimensions and positions of the large nanoparticles are controlled precisely by e-beam lithography. The size of the nano-satellites can be tuned by modification of

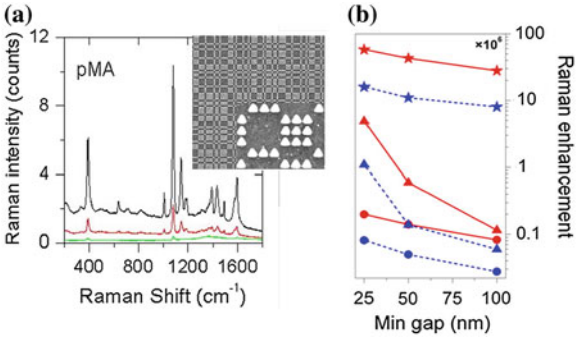

Fig. 9.15 SERS platforms based on deterministic aperiodic plasmonic arrays. Experimental SERS spectra of pMA on lithographically defined arrays of **(a)** Fibonacci nano-triangles shown in the SEM micrograph in the *inset* **(b)** scaling behavior of Raman enhancement factor calculated from experimental data in periodic (*dash blue*) and Fibonacci (*solid red*) nanoparticle arrays. *Circles*, *triangles* and *stars* correspond to the nanodisk, nanotriangles and nanogalaxy arrays, respectively

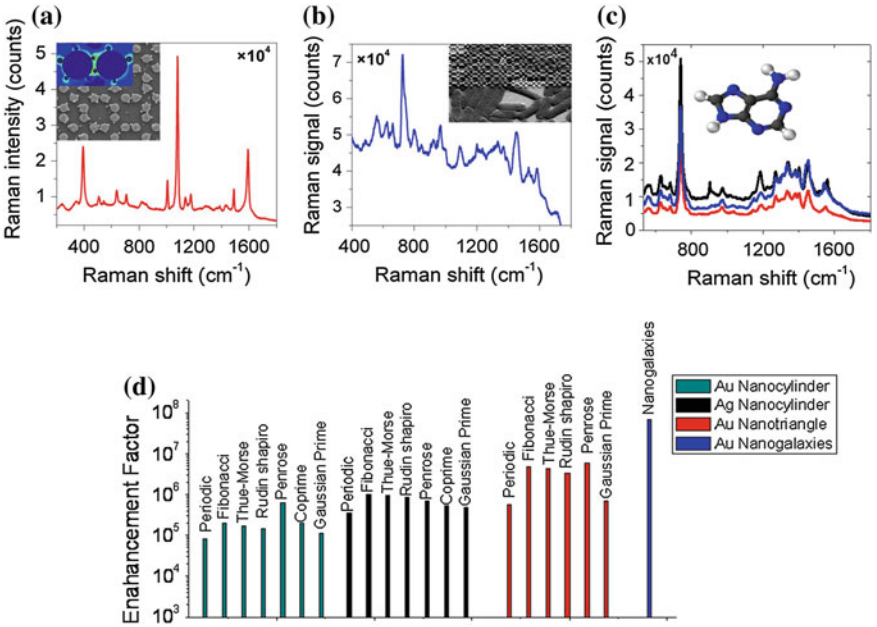

Fig. 9.16 **a** nanodisks decorated by small Au spheres (termed plasmonic nanogalaxy) with an SEM image of the device and a calculated electric field distribution shown in the inset. **b–c** SERS spectra of bacteria (E-coli, shown in the SEM inset) and DNA molecules on plasmonic nanogalaxies. Au particles are 200 nm in size and are separated by minimum interparticle gaps of 25 nm. **d** SERS enhancement factors experimentally obtained for various aperiodic Au (*green*) and Ag (*black*) nanocylinder arrays with 100 nm radius and minimum interparticle separation of 25 nm along with Au (*red*) nanotriangle arrays with sides = 200 nm and interparticle separation of 25 nm and Fibonacci Au nanogalaxy represented as *blue*

the in situ nanoparticle growth procedure. The data summarized in Fig. 9.15b and Fig. 9.16d demonstrate that the selective attachment of smaller satellite nanoparticles to pre-defined DANS leads to a dramatic increase of the SERS enhancement factors by more than three orders of magnitudes, without significantly perturbing the particle separation scaling associated to the underlying deterministic aperiodic template. We also note that the measured $\sim 10^8$ spatially-averaged SERS enhancement factors for Fibonacci nano-galaxy arrays should be considered a lower limit of the local enhancement values since we have assumed that all the pMA molecules are equally contributing to the measured SERS signal.

Additionally, due to the significant contribution of radiative coupling across the DANS arrays, these field enhancement effects can additionally be controlled and engineered by varying the geometry and the size of the aperiodic arrays. The fundamental role played by long-range diffractive coupling in aperiodic array geometry is demonstrated by the data summarized in Fig. 9.16d for a number of DANS arrays with Au and Ag nanoparticles of comparable sizes and average separations.

Presently, we are optimizing deterministic aperiodic SERS substrates for real-time detection and discrimination of different bacteria including Staphylococcus, E-Coli, and bacillus serus [126]. A representative SERS spectrum obtained from E-Coli bacteria is shown in Fig. 9.16b. The proposed SERS technology is also utilized for the optical identification of different DNA nucleobases. Fig 9.16c demonstrates the ability to detect, using aperiodic nanogalaxy substrates, SERS signal from 0.5 μM solution of adenine using 0.8 mW radiation at 785 nm and integrating for 10 s.

The bacterial and molecular Raman spectra shown in Figs. 9.15 and 9.16 demonstrate the potential and robustness of the DANS approach for real-time bio-chemical sensing and identification using reproducible and engineerable SERS substrates that leverage aperiodic order on a chip.

9.3.3 Applications to Colorimetric Optical Sensing

In current biosensing technology, two-dimensional periodic lattices, (i.e. 2D optical gratings) provide a well-established approach for biochemical colorimetric detection, which can yield label-free sensing of various molecular analytes and protein dynamics. Standard periodic grating biosensors provide a distinct change either in the intensity of diffracted light or in the frequency of optical resonances in response to variations in the refractive index of the surrounding environment. The physical mechanism at the basis of these optical signatures is the well-known phenomenon of Bragg scattering. While this process provides frequency selective responses that are useful for colorimetric detection, the ability of light waves to interact with adsorbed or chemically bound analytes present on the surface of these sensors is intrinsically limited. In fact, Bragg scattering is a first-order process in surface scattering perturbation theory [127], and scattered photons easily escape from a periodic surface within well-defined spectral bands and without prolonged interaction with the sensing layer. On the other hand, eengineering elastic light scattering in planar aperiodic structures provides novel opportunities for bio-chemical sensing applications. In particular, optical sensing platforms can be boosted by developing scattering elements that simultaneously provide high sensitivity to the environmental changes and high spectral resolution, as both factors contribute to the improvement on the sensor detection limit.

Detector sensitivity is conventionally defined as the magnitude of the wavelength shift induced by the change of the ambient refractive index (measured in nm/RIU), and can be improved by enhancing the light-matter interaction. In turn, the resolution in measuring wavelength shifts inversely depends on the linewidth of the resonant mode supported by the structure. It has recently been shown that aperiodic photonic structures provide the necessary balance between the resonant character of the quasi-localized critical modes, which simultaneously feature high quality factors and large field intensity over large sensing areas, resulting in largely improved sensitivity over periodic grating sensors and even photonic crystals cavities due to their smaller analyte-field overlap factors [128]. Building on these results, we have recently intro-

duced a novel approach to label-free optical biosensing based on micro-spectroscopy and spatial correlation analysis of structural color patterns excited by white light illumination in DANS metal-dielectric surfaces [85, 86]. In contrast to traditional photonic gratings or photonic crystals sensors (which efficiently trap light within small-volumes), aperiodic scattering sensors sustain distinctive resonances localized over larger surface areas. These structural resonances, known as *critical modes*, are described by highly fluctuating field profiles (i.e., best described by multi-fractal analysis) and have a dense spectrum, which result in efficient photon trapping and surface interactions through higher-order multiple scattering processes. These features thereby strongly enhance the sensitivity of DANS surfaces to small refractive index changes. The complex spatial patterns of critical modes in these structures offer the potential to engineer structural color sensing with spatially localized patterns at multiple wavelengths. Under white light illumination, DANS surfaces feature structured multi-color colorimetric patterns which are a phase sensitive fingerprints of their aperiodic geometries, known as *colorimetric fingerprints*.

When light is normally incident on aperiodic surfaces, distinct optical frequencies (i.e., colors) localize in different areas (resolution limited) of the device and can readily be observed in the object-plane or in the far-zone, as demonstrated in Fig. 9.17. Adding a thin layer of analyte on top of aperiodic arrays shifts the resonance wavelengths of their optical modes leading to a spatial rearrangement of the localized field intensity. This in turn triggers a global change in the colorimetric pattern of the scattered radiation.

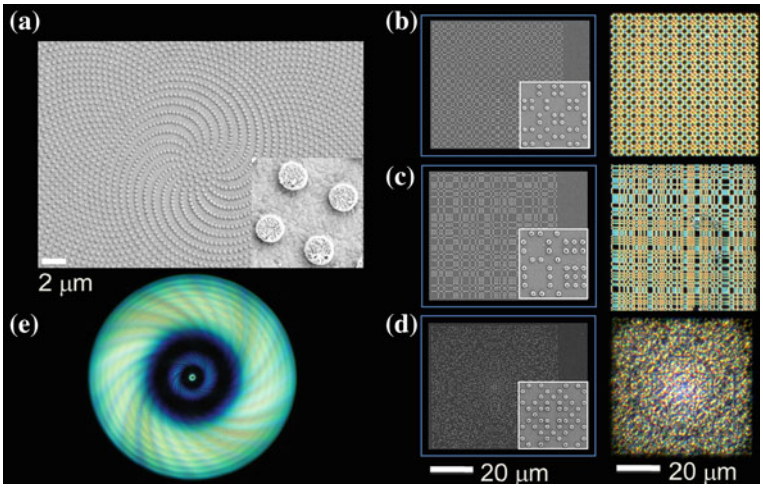

Fig. 9.17 SEM images of **a** aperiodic spiral array, **b** Fibonacci array, **c** Rudin–Shapiro array, and **d** Gaussian prime array of Au nano-cylinders with radius r = 100 nm, height h = 30 nm, and minimum interparticle separation d = 25 nm. Color figures in (**b**–**e**) are the corresponding "colorimetric fingerprints" measured with dark-field microscopy under white light illumination

Light scattering from nano-patterned deterministic aperiodic surfaces, which occurs over a broad spectral-angular range, leads to the formation of colorimetric fingerprints, in their near and far-field zones, which can be captured with conventional dark-field microscopy, as demonstrated in Fig. 9.17. The distinctive colorimetric fingerprints of aperiodic surfaces can be used as a transduction mechanism for novel types of highly sensitive label-free multiplexed sensors [86]. In particular, both the peak wavelength shifts (Fig. 9.18a, b) of the scattered radiation as well as the environment-dependent spatial structure of the colorimetric fingerprints (Fig. 9.17b–e) of aperiodic surfaces can be utilized to detect the presence of nanoscale protein layers at the surface of DANS. The proposed approach is intrinsically more sensitive to local refractive index modifications compared to traditional ones due to the enhancement of small phase variations, which is typical of the multiple light scattering regime.

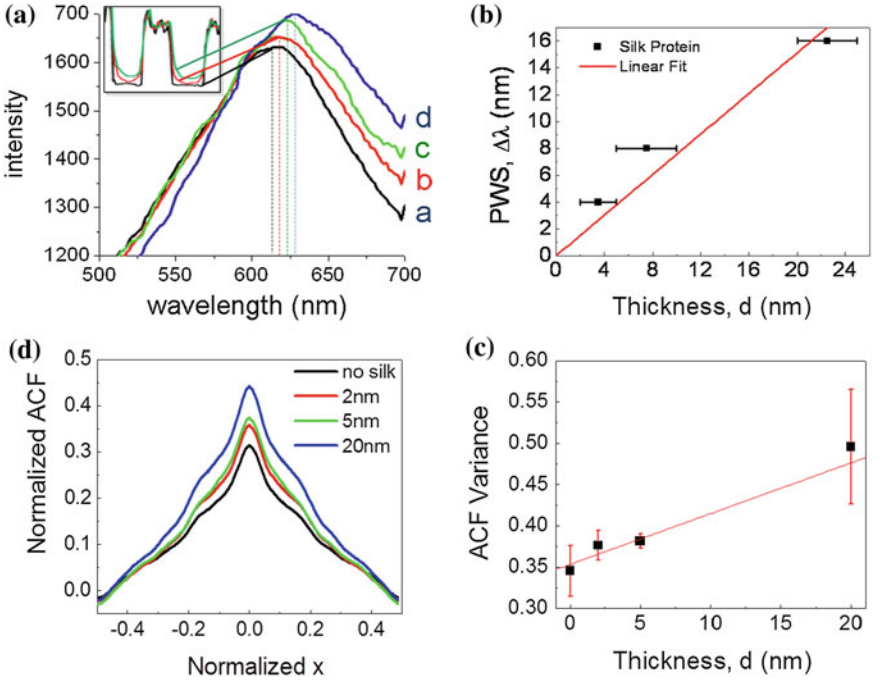

Fig. 9.18 **a** Coating of different thicknesses of silk protein monolayers were characterized by Atomic Force Microscopy (*inset*) and the colorimetric responses of the associated arrays were measured spectrally. Coating of different thicknesses of silk protein monolayers were characterized by Atomic Force Microscopy (*inset*) and the colorimetric responses of the associated arrays were measured spectrally. **b** The sensitivity of the arrays is quantified by the spectral shift of the scattered radiation peaks (PWS) per thickness variation of the protein layer. **c** The changes of patterns due to different thicknesses of silk protein monolayers are quantified by the normalized ACF variances. **d** 1D ACF profiles extracted from 2D normalized autocorrelation function along the x-axis of the middle of the images. Adapted from Ref. [86]

The spatial modifications of the structural color fingerprints induced by small refractive index variations can be readily quantified using image autocorrelation analysis performed on the scattered radiation [129], using polychromatic or single wavelength modalities, as shown in Fig. 9.18 for silk protein monolayers deposited on DANS surfaces. To construct the image autocorrelation function (ACF), the value of the field intensity at point (x, y) in the array plane is compared with that at another point (x′, y′) and mapped as a function of the distance between the two points. 1D profiles through the 2D autocorrelation function of the intensity images in Fig. 9.18d. The initial decay in the ACF reflects local short-range correlations in the aperiodic structure, and any long-range periodicities in the intensity pattern give rise to periodic oscillations in the ACF. To quantify the overall change in the colorimetric pattern induced by the presence of thin molecule layers, we calculate the variance of the fluctuations in the intensity distribution function, which can be found as the value of the properly normalized discrete ACF in the limit of zero lateral displacements. The proposed approach recently led to the demonstration of femto-molar detection of silk proteins adsorbed on DANS [86].

The refractive index modifications induced by the analytes (silk protein) can be detected by frequency shifts *and* a global structural color modification. Combining Electron Beam Lithography (EBL), dark-field scattering micro-spectroscopy, autocorrelation analysis and rigorous multiple scattering calculations based on the Generalized Mie Theory (GMT), Lee and collaborators [86] have engineered aperiodic arrays of metal nano-particles on quartz substrates, and showed that the information encoded in *both* the spectral and spatial distribution of structural resonances can be simultaneously utilized for sensitive bio-detection on the nanoscale. The potential of the proposed approach for rapid, label-free detection and recognition of biomolecular analytes in the visible spectral range was experimentally demonstrated by the distinct variation in the spectral and spatial colorimetric fingerprints in response to monolayer increments of protein layers sequentially deposited on the surface of aperiodic arrays of nanoparticles.

Finally, we remark that this DANS-enabled detection technique can be conveniently integrated into microfludics channels for optical liquid sensing applications. Our group is currently working to demonstrate full optofludics integration of spatial-spectral colorimetric detectors for liquid sensing based on sensitive multiple light scattering in DANS.

9.3.4 Applications to Light Emission Enhancement

Studies on the far-field and near-field optical behavior of two-dimensional Fibonacci-based lattices fabricated by EBL have demonstrated the presence of strongly localized plasmon modes whose exact location can be accurately predicted from purely structural considerations. In particular, Dallapiccola at al. [130], by performing near-field optical measurements in collection mode and three dimensional Finite Difference Time Domain (FDTD) simulations, showed that dimer coupling in a Fibonacci lat-

tice results in a deterministic quasi-periodic sub-lattice of localized plasmon modes which follow a Fibonacci sequence. In addition, stronger field enhancement was experimentally observed in Fibonacci structures compared to periodic arrays [130], demonstrating that quasiperiodic gold nanoparticle arrays can have a significant impact for the design and fabrication of novel nanoplasmonic devices. The potential of plasmonic DANS for the engineering of light emitting devices based on the silicon technology has been recently demonstrated by studying quasi-periodic Fibonacci Au nanoparticle arrays of varying interparticle separations fabricated on light emitting Erbium-doped silicon nitride films (Er:SiN_x) by electron beam lithography [131].

A 3.6 times enhancement of the photoluminescence (PL) intensity accompanied by a reduction of the Er^{3+} emission lifetime at 1.54 μm (see Fig. 9.19) has been observed and explained by the coupling with the near-infrared structural resonances of the Fibonacci structure. photonic–plasmonic hybrid modes were identified in a comparative transmission experiment between periodic plasmonic gratings and Fibonacci quasi-periodic structures by the spectral positions of their transmission minima, for a large range of fabricated structures.

The scaling behavior of the emission enhancement in Fibonacci and periodic gratings was discussed in relation to the modifications of the photonic LDOS at the Er emission wavelength [131]. The strongly reduced frequency sensitivity of the photonic–plasmonic scattering resonances in Fibonacci arrays prevented their detuning from the Er emission wavelength. As a result, when decreasing the interparticle separation in the Fibonacci arrays, their emission intensity was found to increase along with their emission rate, while an opposite behavior, indicative of non-radiative losses, was observed in periodic gratings. The coupling of light emission to the distinctive scattering resonances of photonic–plasmonic coupled aperiodic arrays makes these systems particularly attractive for radiative rate engineering applications where light extraction/enhancement is required over broad frequency spectra.

The distinctive features of circular light scattering in plasmonic Vogel's spirals, introduced in Sect. 9.2.4, also provides an alternative approach for broadband light emission enhancement in active thin films coupled to deterministic aperiodic structures. Our group has recently exploited planar light scattering for light emission enhancement [66, 71] and demonstrated the role of the inhomogeneous distribution of local spatial frequencies on the emission patter of Vogel's spirals [69]. We prepared a dye polymer solution by dissolving common laser dye molecules of DCM (Exciton Inc.), in toluene.

The dilute solution was then mixed with Polymethylmethacrylate (PMMA), spun onto samples and cured, resulting in 100 nm thick films of laser dye doped PMMA. This particular laser dye has maximum absorption at 480 nm and an emission peak at 640 nm, which overlaps the scattering resonances of the investigated α_2-spiral, leading to broadband emission enhancement, shown in Fig. 9.20b. Moreover, we demonstrate the ability to dramatically modify the angular emission of the sample by imaging the fluorescence in transmission under for different excitation conditions. In particular, the sample was pumped by positioning the laser spot at different locations onto the doped PMMA substrate at normal incidence (focused through a 10×

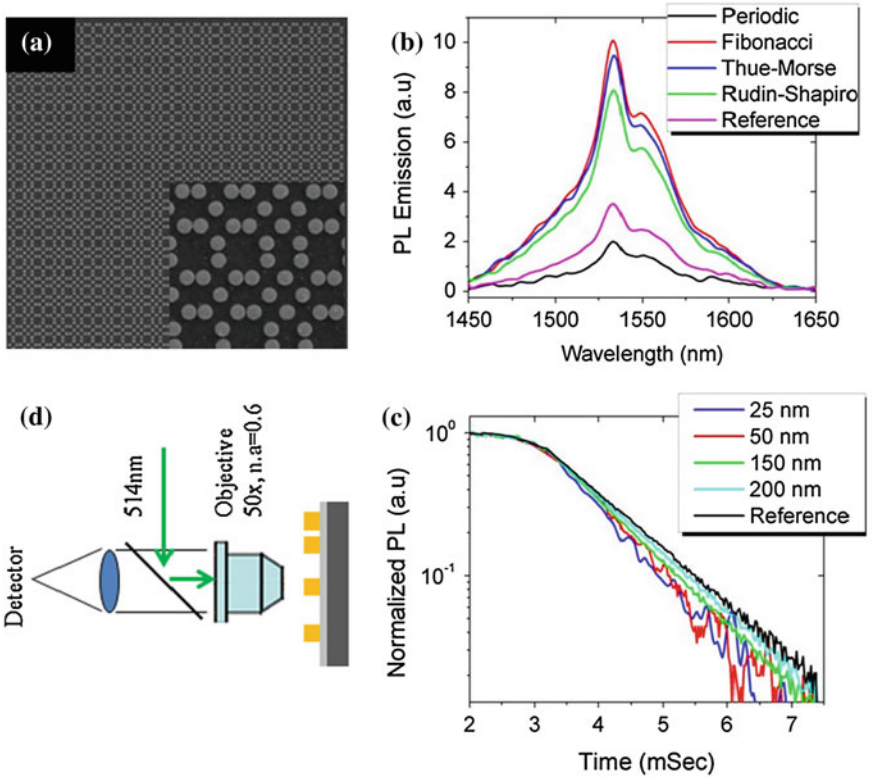

Fig. 9.19 Demonstration of light emission enhancement from Erbium atoms coupled to deterministic aperiodic plasmonic arrays of Au nanoparticles (200 nm diameters). **a** SEM picture of quasiperiodic Fibonacci Au nanoparticle array fabricated atop a light emitting Er:SiNx substrates of 80 nm thickness; **b** PL spectra excited at 488 nm through periodic and aperiodic nanoparticle arrays with 50 nm min interparticle separations; **c** PL time decay of Er atoms through unpatterned substrate (*black*) and Fibonacci arrays with varying interparticle separations indicated in the *legend*. **d** Schematics of the experimental photoluminescence setup. Adapted From Ref. [131]

objective) with a laser diode at 480 nm and the emitted light was collected in transmission configuration through the substrate using a lens of 100 mm focal length, and imaged by a CCD camera. In order to capture only the emission patterns, the pump laser light was blocked by a 514 nm high-pass filter. An identically prepared emitting layer was also coated on unpatterned quartz for reference. Figure 9.20c shows the CCD image of the fluorescence collected in transmission through the reference sample (i.e., with no spiral pattern), which indicates that the fluorescence is spatially confined to the pumped region in the absence of scattering structures. On the other hand, when pumping the samples with the plasmonic arrays, the fluorescence spreads laterally in the plane of the array and, when the sample is symmetrically pumped through its center, a significant fracton of the fluorescence is emitted along multiple directions due to the isotropic character of the Fourier space (i.e., circular

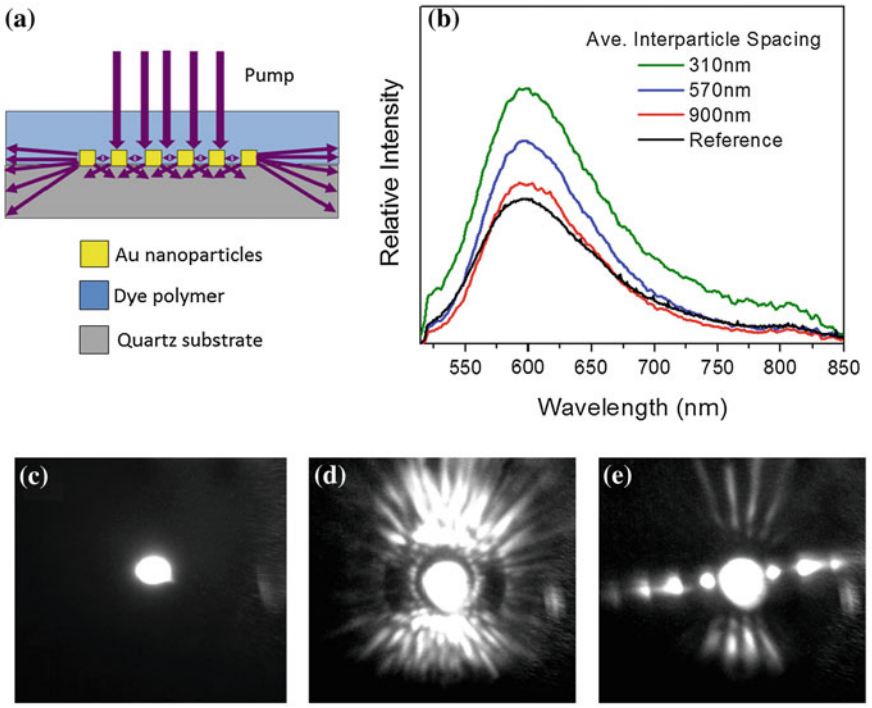

Fig. 9.20 **(a)** Schematic cross-section of Au spiral nanoparticle array on a quartz substrate, coated with DCM doped PMMA. Nanoparticles are cylindrical in shape with 200 nm diameter and 30 nm in thickness with array diameter of 100 μm. **(b)** Photoluminescence spectra of doped polymer form samples coupled to α_2-spiral arrays with varying average interparticle separations (310, 570, 900 nm and un-coupled film for reference). CCD image of light emission from a DCM dye layer deposited onto: **(c)** homogeneous quartz substrate **(d)** dye emission from scattered pump light by α_2-spiral with beam centered on the array and **(e)** dye emission from scattered pump light by α_2-spiral with beam ~20 μm off center horizontally

light scattering). On the other hand, when the position of the laser pumping spot is slightly misplaced from the centre of the sample (in the horizontal direction) by approximately 25 μm, the angular distribution of the radiation changes dramatically due to the very inhomogeneous distribution of local spatial frequencies associated to the surface of aperiodic spirals with circularly-symmetric Fourier space [65, 69].

These results demonstrate the potential of aperiodic arrays with Vogel spiral geometry to enhance and manipulate light emission in planar structures. While more work is be required to fully leverage aperiodic spiral order for active optical devices, we believe that our results motivate the development of novel optical devices that benefit from polarization insensitive, enhanced light-matter coupling on planar surfaces, such as plasmonic photodetectors and thin-film solar cells, which will be discussed in Sect. 9.3.5 .

9.3.5 Applications to Thin-Film Solar Cell Enhancement

The solar cell market is predominately based on crystalline silicon (c-Si) wafers with absorbing layer thickness in between 100 and 300 μm to guarantee complete light absorption and effective carrier collection. However, the increasing materials costs related to the fabrication of highly pure c-Si and the ever-growing efficiency demands of the solar industry have motivated novel approaches to increase light absorption in cells with reduced active thickness. In particular, promising approaches consist in the engineering of thin-films non-crystalline (amorphous or poly-crystalline Si) and nanocrystalline Si (Si-ncs) structures [132, 133].

Amorphous and nanocrystalline materials can be fabricated with strongly reduced thermal budgets, costs and with much larger volumes compared to traditional Si wafers. However, their shorter diffusion lengths (limited by defects and grain boundaries) restrict the active cell thicknesses to approximately a few hundreds of nanometers, severely decreasing the probability of photon absorption. This has recently spurred the search for advanced photon recycling and light-trapping schemes capable of increasing the optical paths of photons, and therefore the absorption probability, in ultra-thin film Si solar cells (<200 nm-thick) [134–138]. Recent studies have shown that metal nanostructures can lead to effective light trapping into thin-film solar cells improving the overall efficiency due to the enhancement of optical cross sections associated to the excitation of Localized Surface Plasmon modes (LSPs) [139–142].

One commonly utilized geometry consists of the fabrication of metal-dielectric nanoparticles on the front/bottom surface of the absorbing cell structure. When the nanoparticles shapes are correctly designed, incident light is preferentially scattered into the thin-film absorbing Si layer over an increased angular range, effectively enhancing the material absorption [143–146].

Plasmon-enhanced light absorption in thin-film Si solar cells has been demonstrated using periodic arrays of gold (Au) or silver (Ag) nanoparticles, which give rise to best enhancement in the spectral regions where evanescent diffraction grating orders spectrally overlap the broader LSP resonances characteristic of metallic nanoparticles. However, polarization sensitivity and the narrow frequency range for effective photonic–plasmonic coupling in periodic grating structures inherently limit these approaches. In order to broaden the spectral region of enhancement, it is crucial to engineer aperiodic nanoparticle arrays with a higher density of spatial frequencies without resorting to uncontrollable random systems, which have only limited engineering appeal. To overcome these limitations, recent studies have proposed to utilize plasmonic arrays with aperiodic quasicrystal structures, such as Penrose lattices, which exhibit non-crystallographic rotational symmetries [138, 147]. Such arrays, by virtue of their higher degree of rotational symmetry as compared to traditional periodic structures, give rise to enhanced scattering along multiple directions and over a broader wavelength range.

Our group has recently introduced plasmonic aperiodic spiral arrays as a viable strategy to engineer wide-angle light scattering for broadband and polarization insensitive absorption enhancement in thin-film Si solar cells [67].

We have previously discussed that aperiodic Vogel spiral arrays feature nearly continuous azimuthal symmetry in Fourier space and, when normally illuminated, satisfy the Rayleigh condition for planar light scattering over broad and controllable frequency bands, irrespective of the incident polarization of light [69]. A simple scalar Fourier optics picture already suggests that polarization-insensitive large-angle scattering of incident radiation can occur in GA spiral arrays at frequencies matching the radial position of the scattering ring in reciprocal space [69]. This property is ideal to engineer light trapping in thin-film Si solar cells. Following this approach, we recently designed and fabricated GA arrays of Au nanoparticles atop ultra-thin film (i.e., 50 nm-thick absorbing amorphous Si layer) Silicon On Insulator (SOI) Schottky photodetector structure, sketched in Fig. 9.21a, and demonstrated experimentally larger photocurrent enhancement in the 600–950 nm spectral range compared to optimized nanoparticle gratings [67]. The relation between the spatial Fourier spectrum of GA arrays of Au nanoparticles and the large angular distribution of scattered radiation in the forward scattering hemisphere has been rigorously discussed by calculating the angular radiation diagrams within our recently developed formulation of the Coupled Dipole Approximation (CDA) for particles with ellipsoidal shape [54].

This CDA approach is particularly suited to efficiently treat large-scale plasmonic systems made of small and well separated nanoparticles, and it has been previously validated against semi-analytical multiple scattering methods [95]. In our work, all nanoparticles were modeled by oblate spheroids with 100 nm diameter and 30 nm height. Moreover, the arrays are embedded in Si and normally excited by a linearly polarized plane wave. The parameter of interest for the understanding of angular scattering in complex plasmonic arrays is the differential scattering cross section, which describes the angular distribution of electromagnetic power density scattered at a given wavelength within a unit solid angle centered around an angular direction (θ, φ) per unit incident irradiance [59]. In the case of arrays composed of dispersive metal nanoparticles, the power scattered from a particular structure is in general a function of both the geometrical parameters of the array and the wavelength of the incident radiation. Full information on angular scattering is thus captured by calculating the averaged differential scattering cross section, where the average is performed on the azimuthal angle φ and the scattered intensity is normalized to the maximum value (i.e., forward scattering peak). By plotting the azimuthally averaged differential scattering cross section versus the inclination angle, we obtain the radiation diagrams of the arrays. In Fig. 9.21b we show (plotted in dB scale) the calculated radiation diagrams for the optimized GA arrays at three different wavelengths $\lambda_B = 480\,\text{nm}$, $\lambda_G = 550\,\text{nm}$ and $\lambda_R = 610\,\text{nm}$ (i.e corresponding to the blue, green, and red colors), respectively. Differently from the well-known case of periodic structures, where the scattered radiation is preferentially redistributed along the directions of coherent Bragg scattering, the radiation diagram of GA arrays is significantly broadened at large angles (i.e. $>30°$) for all the investigated wavelengths, demonstrating broadband wide-angle scattering behavior.

By combining experimental absorption enhancement and photocurrent measurements with CDA and full-vector 3D Finite Difference Time Domain (FDTD)

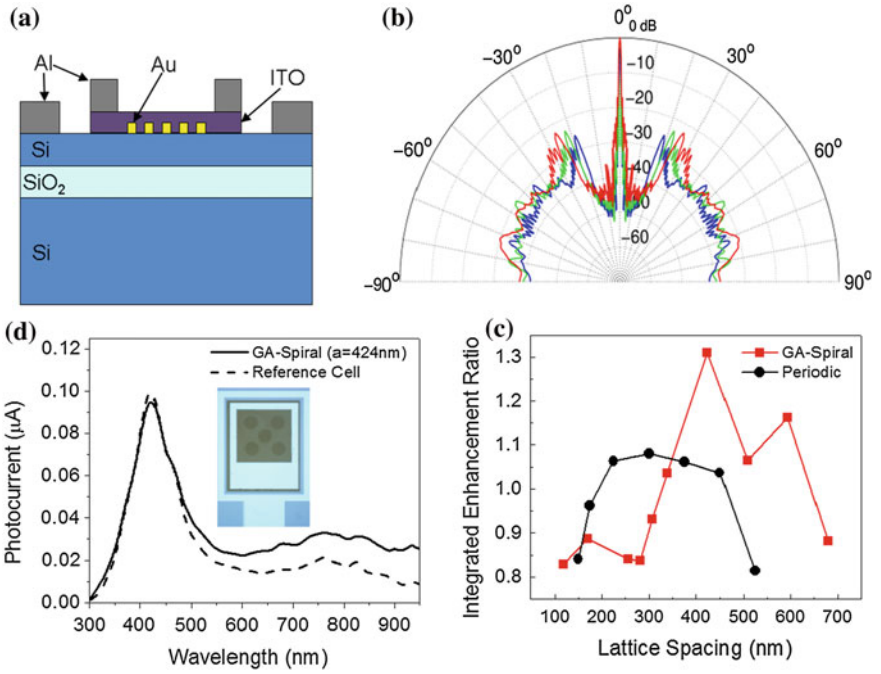

Fig. 9.21 **a** Device cross-section of the SOI Schottky photo-detector with plasmonic arrays integrated onto the absorbing surface. **b** Calculated radiation diagrams as a function of the inclination angle for a GA spiral with N = 1,810 particles and for three different wavelengths, namely 480 nm (*Blue*), 520 nm (*Green*), and 650 nm (*Red*). The GA spiral features an averaged minimum interparticle separation of 420 nm. **c** Integrated photocurrent enhancement ratio for GA spiral (*red*) and periodic (*black dashed*) arrays of different center-to-center particle spacings. **d** Spiral array photocurrent with average center-to-center spacing of 425 nm (*solid*) and reference cell device without the GA array (*dashed*). Adapted from Ref. [67]

simulations, we recently demonstrated [67] that broadband wide-angle scattering in GA spiral arrays redirects a larger fraction of the incident radiation into the absorbing Si substrate. Moreover, this effect increases the optical path of photons in the photodetector, as well as enhancing the coupling to LSPs in the array plane. In Fig. 9.21d we show the integrated photocurrent enhancement ratio, calculated by the ratio of the integrated photocurrent spectrum of the device with and without the plasmonic arrays. The ratios falling below the dotted line indicate devices with overall reduced performance when compared against their neighboring empty reference cells. We see in Fig. 9.21d that both GA spiral and periodic arrays exhibit an optimization trend with respect to the interparticle spacing, yielding maximum integrated enhancements of 8 and 31 % over reference cells, respectively. Fig. 9.21d show the measured photocurrent spectra for the best performing GA spiral photodetector. The dashed lines are the reference photocurrent spectra measured on the unpatterned devices in the nearest reference cells, respectively. The maximum photocurrent enhancement of

approximately a factor of 3 is measured for the GA spiral at 950 nm. The increase in photocurrent results from the interplay of plasmonic-photonic effects in GA spirals, which contribute to the overall enhancement as follows: by providing better coupling of incident radiation into the thin Si layer due to photonic wide-angle scattering; by enhancing the intensity of the nanoparticle near-fields at the Si interface owing to better LSP coupling in the plane of the array compared to periodic structures. A detailed comparison with optimized periodic grating structures in discussed in Ref. [67].

We observe finally that the experimentally measured 31 % integrated enhancement for GA spiral arrays has been demonstrated with only 25 % of the active photodetector device area covered by GA arrays (Fig 9.21d, inset). These results highlight the potential for even greater enhancement for complete device area coverage using GA spirals. Moreover, in the context of thin-films absorption enhancement, a large class of deterministic aperiodic spiral arrays with divergence angles different from the golden angle remains to be explored, promising additional flexibility due to the presence of multiple scattering rings in Fourier space [65].

9.4 Outlook and Conclusions

While light transport and localization phenomena in periodic and random structures have been investigated for decades, the study of deterministic aperiodic structures is still in its infancy. Deterministic aperiodic optical structures defines a novel, fascinating, and highly interdisciplinary research field with deep ramifications in different areas of mathematics and physical sciences, such as crystallography and computational geometry, dynamical systems, and number theory. Due to the unprecedented flexibility in their Fourier space, which can be designed to span across all possible spectral singularity measures, engineered aperiodic structures provide unprecedented opportunities to manipulate light states, scattering and localization phenomena for nanophotonics technologies.

In this chapter, we presented a comprehensive overview of our own work on the conceptual foundation, design, nanofabrication, and selected device applications of aperiodic arrays of metallic nanoparticles generated by algorithmic rules, referred to as Deterministic Aperiodic Nano-Structures. Specifically, we discussed relevant structure-property relations, hot spots engineering rules and near-field enhancement in a large number of nanoplasmonic arrays of Au nanoparticles with aperiodic Fourier space. Specific device applications were presented in relation to optical biosensing, plasmon-enhanced light sources, and solar cells, demonstrating that the distinctive interplay between photonic diffraction and near field plasmonic localization in DANS provides novel opportunities to manipulate light-matter interactions on the nanoscale. In addition, we reviewed the fascinating scattering properties of a novel plasmonic platform based on the engineering of aperiodic Vogel's spirals, which offer broadband planar diffraction, light emission enhancement and the generation and manipulation

of orbital angular momentum of light, potentially leading to novel applications in secure communications and singular optics.

The computational and experimental results presented in this chapter demonstrate the significance of aperiodic optics as a highly interdisciplinary field of optical engineering, and its potential for innovation in basic science and technological applications. However, our achievements on the design, fabrication and engineering of aperiodic optical nanostructures represent only a starting point for future work in aperiodic optics and nanoplasmonics, particularly in relation to the following: (a) nonlinear optical regime; (b) light-emitting and lasing structures; (c) theory of inverse design of aperiodic structures.

Despite our initial demonstration of enhanced second harmonic generation in plasmonic DANS [68], little is known on the solution of multiple light scattering problems in the nonlinear optical regime, especially in relation to the enhancement of localization and scattering phenomena (e.g., aperiodic discrete breathers). The fundamental interplay between aperiodic order and optical nonlinearity still needs to be investigated both theoretically and experimentally in photonic–plasmonic DANS, potentially leading to the discovery of novel physical effects.

The great flexibility of aperiodic Fourier space for the engineering of light emitting devices with tailored frequency and angular emission spectra also needs to be systematically addressed with respect to the lasing regime, potentially leading to novel concepts and discoveries in coherent generation from aperiodic environments.

Finally, we believe that more efficient numerical methods and specific approaches for theoretical and computational research of aperiodic deterministic systems need to be developed, especially in relation to the solution of inverse scattering problems in aperiodic geometry. Advances in multi-scale computational science for large systems with arbitrary Fourier spectral components are essential in order to properly optimize device structures that fully leverage the opportunities of aperiodic Fourier space for optical engineering applications.

To conclude, we believe that despite the many challenges still ahead, photonic–plasmonic deterministic aperiodic structures have a unique potential to become the platform of choice for the flexible manipulation of light-matter coupling on the nanoscale, potentially resulting in significant advances to both fundamental sciences and optical technology.

Acknowledgments We thank A. Gopinath and S. V. Boriskina for experimental and computational contributions that led to numerous developments. We thank G. Miano for many insightful discussions and for sharing his profound expertise on the computational modeling of electromagnetic systems. This work was supported by by the AFOSR program "Deterministic Aperiodic Structures for On-chip Nanophotonic and Nanoplasmonic Device Applications" under Award FA9550-10-1-0019, and partly by the NSF Career Award No. ECCS-0846651 and the U.S. Army Natick Soldier Center under contract W911NF-07-D-001, and the SMART Scholarship Program. This document has been approved for public release. NSRDEC PAO U12-414.

References

1. M.I. Stockman, Inhomogeneous eigenmode localization, chaos, and correlations in large disordered clusters. Phys. Rev. E **56**(6), 6494 (1997)
2. V.M. Shalaev, *Nonlinear Optics of Random Media: Fractal Composites and Metal-Dielectric Films* (Springer, New York, 1999)
3. V.M. Shalaev, *Optical Properties of Nanostructured Random Media* (Springer Verlag, Berlin, 2002)
4. M. Senechal, *Quasicrystals and Geometry* (Cambridge University Press, Cambridge, 1996)
5. T. Janssen, G. Chapuis, M. De Boissieu, *Aperiodic Crystals: From Modulated Phases to Quasicrystals* (Oxford University Press, Oxford, 2007)
6. M. De Graef, M.E. McHenry, V. Keppens, Structure of materials: an introduction to crystallography, diffraction, and symmetry. J. Acoust. Soc. Am. **124**(3), 1385–1386 (2008)
7. J.P. Allouche, J.O. Shallit, *Automatic Sequences: Theory, Applications, Generalizations* (Cambridge University Press, Cambridge, 2003)
8. M. Queffélec, *Substitution Dynamical Systems-Spectral Analysis* (Springer Verlag, Berlin, 2010)
9. D.A. Lind, B. Marcus, *An Introduction to Symbolic Dynamics and Coding* (Cambridge University Press, Cambridge, 1995)
10. M. Schroeder, *Number Theory in Science and Communication: With Applications in Cryptography, Physics, Digital Information, Computing, and Self-Similarity* (Springer Verlag, Berlin, 2009)
11. G.H. Hardy, E.M. Wright, D.R. Heath-Brown, J.H. Silverman, *An Introduction to the Theory of Numbers* (Clarendon press, Oxford, 1979)
12. S.J. Miller, R. Takloo-Bighash, *An Invitation to Modern Number Theory* (Princeton University Press, Princeton, 2006)
13. E. Maciá, *Aperiodic Structures in Condensed Matter: Fundamentals and Applications* (CRC Press Taylor and Francis, Boca Raton, 2009)
14. L. Dal Negro, S.V. Boriskina, Deterministic aperiodic nanostructures for photonics and plasmonics applications. Laser Photonics Rev. **6**(2), 178–218 (2012). doi:10.1002/lpor.201000046
15. E. Maciá, The role of aperiodic order in science and technology. Rep. Prog. Phys. **69**(2), 397–441 (2006)
16. W. Steurer, D. Sutter-Widmer, Photonic and phononic quasicrystals. J. Phys. D Appl. Phys. **40**(13), R229–R247 (2007)
17. A.N. Poddubny, E.L. Ivchenko, Photonic quasicrystalline and aperiodic structures. Physica E **42**(7), 1871–1895 (2010)
18. M. Kohmoto, L.P. Kadanoff, C. Tang, Localization problem in one dimension: mapping and escape. Phys. Rev. Lett. **50**(23), 1870 (1983)
19. M. Kohmoto, B. Sutherland, K. Iguchi, Localization of optics: quasiperiodic media. Phys. Rev. Lett. **58**(23), 2436 (1987)
20. M.S. Vasconcelos, E.L. Albuquerque, Transmission fingerprints in quasiperiodic dielectric multilayers. Phys. Rev. B **59**(17), 11128 (1999)
21. M. Dulea, M. Severin, R. Riklund, Transmission of light through deterministic aperiodic non-Fibonaccian multilayers. Phys. Rev. B **42**(6), 3680 (1990)
22. W. Gellermann, M. Kohmoto, B. Sutherland, P.C. Taylor, Localization of light waves in Fibonacci dielectric multilayers. Phys. Rev. Lett. **72**(5), 633 (1994)
23. R. Merlin, K. Bajema, R. Clarke, F.Y. Juang, P.K. Bhattacharya, Quasiperiodic GaAs-AlAs heterostructures. Phys. Rev. Lett. **55**(17), 1768 (1985)
24. E. Maciá, Optical engineering with Fibonacci dielectric multilayers. Appl. Phys. Lett. **73**(23), 3330–3332 (1998)
25. E. Maciá, Exploiting quasiperiodic order in the design of optical devices. Phys. Rev. B **63**(20), 205421 (2001)
26. A.N. Kolmogorov, S.V. Fomin, *Elements of the Theory of Functions and Functional Analysis (Dover Books on Mathematics)* (Dover, New York, 1999)

27. D. Shechtman, I. Blech, D. Gratias, J.W. Cahn, Metallic phase with long-range orientational order and no translational symmetry. Phys. Rev. Lett. **53**(20), 1951 (1984)
28. D. Levine, P.J. Steinhardt, Quasicrystals: a new class of ordered structures. Phys. Rev. Lett. **53**(26), 2477 (1984)
29. R. Penrose, The role of aesthetic in pure and applied mathematical research. Inst. Math. Appl. **7**(8), 10 (1974)
30. Z. Cheng, R. Savit, R. Merlin, Structure and electronic properties of Thue–Morse lattices. Phys. Rev. B **37**(9), 4375 (1988)
31. L. Dal Negro, M. Stolfi, Y. Yi, J. Michel, X. Duan, L.C. Kimerling, J. LeBlanc, J. Haavisto, Photon band gap properties and omnidirectional reflectance in Si/ SiO Thue–Morse quasicrystals. Appl. Phys. Lett. **84**, 5186 (2004)
32. L. Dal Negro, N.N. Feng, A. Gopinath, Electromagnetic coupling and plasmon localization in deterministic aperiodic arrays. J. Optics A. Pure Appl. Opt. **10**, 064013 (2008)
33. M. Kolar, M.K. Ali, F. Nori, Generalized Thue–Morse chains and their physical properties. Phys. Rev. B **43**(1), 1034 (1991)
34. M.E. Prouhet, Mémoire sur quelques relations entre les puissances des nombres. CR Acad. Sci. Paris **33**, 225 (1851)
35. H.M. Morse, Recurrent geodesics on a surface of negative curvature. J. Math. **42**, 84–100 (1920)
36. H.S. Shapiro, Extremal problems for polynomials and power series. M. Sc. Thesis, Massachusetts Institute of Technology, 1951
37. F. Axel, J. Allouche, On certain properties of high-resolution X-ray diffraction spectra of finite-size generalized Rudin–Shapiro multilayer heterostructures. J. Phys. Cond. Mat. **4**, 8713 (1992)
38. L. Kroon, E. Lennholm, R. Riklund, Localization-delocalization in aperiodic systems. Phys. Rev. B **66**(9), 094204 (2002)
39. L. Kroon, R. Riklund, Absence of localization in a model with correlation measure as a random lattice. Phys. Rev. B **69**(9), 094204 (2004)
40. A. Barbé, F. Haeseler, Correlation and spectral properties of higher-dimensional paperfolding and Rudin–Shapiro sequences. J. Phys. A Math. Gen. **38**, 2599 (2005)
41. A. Barbé, F. Von Haeseler, Correlation and spectral properties of multidimensional Thue–Morse sequences I. J. Bifurcat. Chaos **17**(4), 1265–1303 (2007)
42. A. Barbé, F. Haeseler, Correlation functions of higher-dimensional automatic sequences. J. Phys. A Math. Gen. **37**, 10879 (2004)
43. A. Gopinath, S.V. Boriskina, N.N. Feng, B.M. Reinhard, L. Dal Negro, Photonic-plasmonic scattering resonances in deterministic aperiodic structures. Nano Lett. **8**(8), 2423–2431 (2008)
44. J.M. Luck, Cantor spectra and scaling of gap widths in deterministic aperiodic systems. Phys. Rev. B **39**(9), 5834 (1989)
45. C. Godreche, J.M. Luck, Indexing the diffraction spectrum of a non-Pisot self-similar structure. Phys. Rev. B **45**(1), 176 (1992)
46. M. Kolar, F. Nori, Trace maps of general substitutional sequences. Phys. Rev. B **42**(1), 1062 (1990)
47. G. Gumbs, M.K. Ali, Dynamical maps, Cantor spectra, and localization for Fibonacci and related quasiperiodic lattices. Phys. Rev. Lett. **60**(11), 1081 (1988)
48. X. Wang, U. Grimm, M. Schreiber, Trace and antitrace maps for aperiodic sequences: extensions and applications. Phys. Rev. B **62**(21), 14020 (2000)
49. E. Bombieri, J.E. Taylor, Quasicrystals, tilings, and algebraic number theory: some preliminary connections. Contemp. Math. **64**, 241–264 (1987)
50. E. Bombieri, J.E. Taylor, Which distributions of matter diffract? An initial investigation. J. Phys. Colloques **47**(C3), C3-19–C13-28 (1986)
51. M. Dulea, M. Johansson, R. Riklund, Localization of electrons and electromagnetic waves in a deterministic aperiodic system. Phys. Rev. B **45**(1), 105 (1992)
52. M. Kohmoto, Localization problem and mapping of one-dimensional wave equations in random and quasiperiodic media. Phys. Rev. B **34**(8), 5043 (1986)

53. L. Dal Negro, N.-N. Feng, Spectral gaps and mode localization in Fibonacci chains of metal nanoparticles. Opt. Express **15**(22), 14396–14403 (2007)
54. C. Forestiere, G. Miano, G. Rubinacci, L. Dal Negro, Role of aperiodic order in the spectral, localization, and scaling properties of plasmon modes for the design of nanoparticle arrays. Phys. Rev. B **79**(8), 085404 (2009)
55. M.L. Brongersma, J.W. Hartman, H.A. Atwater, Electromagnetic energy transfer and switching in nanoparticle chain arrays below the diffraction limit. Phys. Rev. B **62**, 356–359 (2000)
56. C. Janot, *Quasicrystals: a primer* (Oxford University Press, Oxford, 1997)
57. N.G. De Bruijn, Algebraic theory of Penrose's non-periodic tilings of the plane. Kon. Nederl. Akad. Wetensch. Proc. Ser. A **43**, 84 (1981)
58. C. Radin, The pinwheel tilings of the plane. Ann. Math. **139**(3), 661–702 (1994)
59. S.Y. Lee, C. Forestiere, A.J. Pasquale, J. Trevino, G. Walsh, P. Galli, M. Romagnoli, L. Dal Negro, Plasmon-enhanced structural coloration of metal films with isotropic pinwheel nanoparticle arrays. Opt. Express **19**(24), 23818–23830 (2011)
60. L. Danzer, Three-dimensional analogs of the planar Penrose tilings and quasicrystals. Discrete Math. **76**(1), 1–7 (1989)
61. P. Prusinkiewicz, A. Lindenmayer, *The Algorithmic Beauty of Plants* (Springer-Verlag, New York, 1990)
62. P. Ball, *Shapes. Nature's Patterns* (Oxford University Press, New York, 2009)
63. R.V. Jean, *Phyllotaxis* (Cambridge University Press, Cambridge, 1995)
64. D.A.W. Thompson, *On Growth and Form* (Dover, New York, 1992)
65. J. Trevino, S.F. Liew, H. Noh, H. Cao, L. Dal Negro, Geometrical structure, multifractal spectra and localized optical modes of aperiodic Vogel spirals. Opt. Express **20**(3), 3015–3033 (2012)
66. N. Lawrence, J. Trevino, L. Dal Negro, Aperiodic arrays of active nanopillars for radiation engineering. J. Appl. Phys. **111**(11), 113101–113109 (2012)
67. J. Trevino, C. Forestiere, G. Di Martino, S. Yerci, F. Priolo, L. Dal Negro, Plasmonic-photonic arrays with aperiodic spiral order for ultra-thin film solar cells. Opt. Express **20**(S3), A418–A430 (2012)
68. A. Capretti, G.F. Walsh, S. Minissale, J. Trevino, C. Forestiere, G. Miano, L. Dal Negro, Multipolar second harmonic generation from planar arrays of Au nanoparticles. Opt. Express **20**(14), 15797–15806 (2012)
69. J. Trevino, H. Cao, L. Dal Negro, Circularly symmetric light scattering from nanoplasmonic spirals. Nano Lett. **11**, 2008 (2011)
70. U. Fano, The theory of anomalous diffraction gratings and of quasi-stationary waves on metallic surfaces (Sommerfeld's waves). JOSA **31**, 213–222 (1941)
71. E.F. Pecora, N. Lawrence, P. Gregg, J. Trevino, P. Artoni, A. Irrera, F. Priolo, L. Dal Negro, Nanopatterning of silicon nanowires for enhancing visible photoluminescence. Nanoscale **4**(9), 2863–2866 (2012)
72. S.F. Liew, H. Noh, J. Trevino, L.D. Negro, H. Cao, Localized photonic band edge modes and orbital angular momenta of light in a golden-angle spiral. Opt. Express **19**(24), 23631–23642 (2011)
73. L. Dal Negro, N. Lawrence, J. Trevino, Analytical light scattering and orbital angular mementum spectra of arbitrary Vogel spirals. Opt. Express **20**(16), 18209–18223 (2012)
74. M. Naylor, Golden, $\sqrt{2}$, and π flowers: a spiral story. Math. Mag. **75**(3), 163–172 (2002)
75. G.J. Mitchison, Phyllotaxis and the Fibonacci series. Science **196**(4287), 270–275 (1977)
76. S. Chavez-Cerda, M. Padgett, I. Allison, G.H.C. New, J.C. Gutierrez-Vega, A.T. O'Neil, I. MacVicar, J. Courtial, Holographic generation and orbital angular momentum of high-order Mathieu beams. J. Opt. B Quantum Semiclass. Opt. **4**, S52–S57 (2002)
77. N. Lawrence, J. Trevino, L. Dal Negro, Control of optical orbital angular momentum by Vogel spiral arrays of metallic nanoparticles. Opt. Lett. **37**, 5076 (2012)
78. C.S. Calude, *Randomness and Complexity: From Leibniz to Chaitin* (World Scientific, Singapore, 2007)
79. J.G. Chaitin, *Exploring Randomness* (Springer, London, 2001)

80. C. Forestiere, G.F. Walsh, G. Miano, L. Dal Negro, Nanoplasmonics of prime number arrays. Opt. Express **17**(26), 24288–24303 (2009)
81. W. Trappe, L. Washington, M. Anshel, K.D. Boklan, Introduction to cryptography with coding theory. Math. Intelligencer **29**(3), 66–69 (2007)
82. Ç.K. Koç, *Cryptographic Engineering* (Springer, US, 2009)
83. J. Hoffstein, J.C. Pipher, J.H. Silverman, *An introduction to mathematical cryptography* (Springer Verlag, New York, 2008)
84. F.J. MacWilliams, N.J.A. Sloane, Pseudo-random sequences and arrays. Proc. IEEE **64**, 1715–1729 (1976)
85. S.V. Boriskina, S.Y.K. Lee, J.J. Amsden, F.G. Omenetto, L. Dal Negro, Formation of colorimetric fingerprints on nano-patterned deterministic aperiodic surfaces. Opt. Express **18**(14), 14568–14576 (2010)
86. S.Y. Lee, J.J.S. Amsden, S.V. Boriskina, A. Gopinath, A. Mitropolous, D.L. Kaplan, F.G. Omenetto, L. Dal Negro, Spatial and spectral detection of protein monolayers with deterministic aperiodic arrays of metal nanoparticles. Proc. Natl. Acad. Sci. USA **107**(27), 12086–12090 (2010)
87. S.A. Maier, *Plasmonics: Fundamentals and Applications* (Springer Verlag, New York, 2007)
88. Y. Chu, E. Schonbrun, T. Yang, K.B. Crozier, Experimental observation of narrow surface plasmon resonances in gold nanoparticle arrays. Appl. Phys. Lett. **93**, 181108 (2008)
89. B. Auguié, W.L. Barnes, Collective resonances in gold nanoparticle arrays. Phys. Rev. Lett. **101**, 143902 (2008)
90. V.G. Kravets, F. Schedin, A.N. Grigorenko, Extremely narrow plasmon resonances based on diffraction coupling of localized plasmons in arrays of metallic nanoparticles. Phys. Rev. Lett. **101**, 087403 (2008)
91. S. Zou, G.C. Schatz, Silver nanoparticle array structures that produce giant enhancements in electromagnetic fields. Chem. Phys. Lett. **403**, 62–67 (2005)
92. B. Luk'yanchuk, N.I. Zheludev, S.A. Maier, N.J. Halas, P. Nordlander, H. Giessen, C. Tow Chong, The Fano resonance in plasmonic nanostructures and metamaterials. Nat. Mat. **9**, 707 (2010)
93. C. Forestiere, M. Donelli, G.F. Walsh, E. Zeni, G. Miano, L. Dal Negro, Particle-swarm optimization of broadband nanoplasmonic arrays. Opt. Lett. **35**(2), 133–135 (2009)
94. M. Moskovits, L.L. Tay, J. Yang, T. Haslett, SERS and the single molecule. Top. Appl. Phys. **82**, 215–227 (2002). in *Optical Properties of Nanostructured Random Media*. Springer, New York
95. C. Forestiere, G. Miano, S.V. Boriskina, L. Dal Negro, The role of nanoparticle shapes and deterministic aperiodicity for the design of nanoplasmonic arrays. Opt. Express **17**(12), 9648–9661 (2009)
96. S.V. Boriskina, A. Gopinath, L. Dal Negro, Optical gap formation and localization properties of optical modes in deterministic aperiodic photonic structures. Opt. Express **16**(23), 18813–18826 (2008)
97. P. Sheng, *Introduction to Wave Scattering, Localization and Mesoscopic Phenomena* (Springer Verlag, Berlin, 2006)
98. D. Lin, H. Tao, J. Trevino, J.P. Mondia, D.K. Kaplan, F.G. Omenetto, L. Dal Negro, Direct transfer of sub-wavelength plasmonic nanostructures on bio-active silk films. Adv. Mat. **24**, 6088–6093 (2012)
99. K.A. Willets, R.P. Van Duyne, Localized surface plasmon spectroscopy and sensing. Annu. Rev. Phys. Chem. **58**, 267–297 (2007)
100. M. Moskovits, Surface-enhanced spectroscopy. Rev. Mod. Phys. **57**, 783–826 (1985)
101. K. Kneipp, M. Moskovits, H. Kneipp, *Surface-Enhanced Raman Scattering* (Springer, Berlin, 2006)
102. Y.W.C. Cao, R.C. Jin, C.A. Mirkin, Nanoparticles with Raman spectroscopic fingerprints for DNA and RNA detection. Science **297**, 1536–1540 (2002)
103. I. Delfino, A.R. Bizzarri, S. Cannistraro, Single-molecule detection of yeast cytochrome c by surface-enhanced Raman spectroscopy. Biophys. Chem. **113**, 41–51 (2005)

104. D.R. Ward, N.K. Grady, C.S. Levin, N.J. Halas, Y.P. Wu, P. Nordlander, D. Natelson, Electromigrated nanoscale gaps for surface-enhanced Raman spectroscopy. Nano Lett. **7**, 1396–1400 (2007)
105. K. Kneipp, H. Kneipp, V.B. Kartha, R. Manoharan, G. Deinum, I. Itzkan, R.R. Dasari, M.S. Feld, Detection and identification of a single DNA base molecule using surface-enhanced Raman scattering (SERS). Phys. Rev. E **57**(6), R6281 (1998)
106. K. Kneipp, Y. Wang, H. Kneipp, L.T. Perelman, I. Itzkan, R.R. Dasari, M.S. Feld, Single molecule detection using surface-enhanced Raman scattering (SERS). Phys. Rev. Lett. **78**(9), 1667 (1997)
107. S.M. Nie, S.R. Emery, Probing single molecules and single nanoparticles by surface-enhanced Raman scattering. Science **275**, 1102–1106 (1997)
108. L. Yang, Y. Bo, R.W. Premasiri, L.D. Ziegler, L. Dal Negro, B. Reinhard, Engineering nanoparticle cluster arrays for bacterial biosensing: the role of the building block in multiscale SERS substrates. Adv. Funct. Mater. **20**, 2619 (2010)
109. R.M. Jarvis, A. Brooker, R. Goodacre, Surface-enhanced Raman scattering for the rapid discrimination of bacteria. Faraday Discuss. **132**, 281–292 (2006)
110. R.A. Tripp, R.A. Dluhy, Y. Zhao, Novel nanostructures for SERS biosensing. Nano Today **3**, 31–37 (2008)
111. F.J. García-Vidal, J.B. Pendry, Collective theory for surface enhanced Raman scattering. Phys. Rev. Lett. **77**, 1163–1166 (1996)
112. J. Gersten, A. Nitzan, Electromagnetic theory of enhanced Raman scattering by molecules adsorbed on rough surfaces. J. Chem. Phys. **73**, 3023–3037 (1980)
113. M. Kerker, D.-S. Wang, H. Chew, Surface enhanced Raman scattering (SERS) by molecules adsorbed at spherical particles. Appl. Opt. **19**, 3373–3388 (1980)
114. V.M. Shalaev, M.I. Stockman, Optical properties of fractal clusters: susceptibility, surface enhanced Raman scattering by impurities. Sov. Phys. JETP. **65**, 287–294 (1987)
115. Z. Wang, S. Pan, T.D. Krauss, H. Du, L.J. Rothberg, The structural basis for giant enhancement enabling single-molecule Raman scattering. PNAS **100**, 8636–8643 (2003)
116. J. Dai, F. Ccaronajko, I. Tsukerman, M.I. Stockman, Electrodynamic effects in plasmonic nanolenses. Phys. Rev. B **77**(11), 115419 (2008)
117. K. Li, M.I. Stockman, D.J. Bergman, Self-similar chain of metal nanospheres as an efficient nanolens. Phys. Rev. Lett. **91**(22), 227402 (2003)
118. A. Wokaun, J.G. Bergman, J.P. Heritage, A.M. Glass, P.F. Liao, D.H. Olson, Surface second-harmonic generation from metal island films and microlithographic structures. Phys. Rev. B **24**, 849 (1981)
119. Q. Yu, P. Quan, D. Qin, G. Golden, P.M. Wallace, Inverted size-dependence of surface-enhanced Raman scattering on gold nanohole and nanodisk arrays. Nano Lett. **8**(7), 1923–1928 (2008)
120. L. Gunnarsson, S. Petronis, B. Kasemo, H. Xu, J. Bjerneld, M. Käll, Optimizing nanofabricated substrates for surface enhanced Raman scattering. Nanostruct. Mater. **12**, 783 (1999)
121. M. Kahl, E. Voges, S. Kostrewa, C. Vietz, W.M. Hill, Periodically structured metallic substrates for SERS. Sens. Actuators B **51**, 285 (1995)
122. Y.J. Liu, Z.Y. Zhang, Q. Zhao, Y.P. Zhao, Revisiting the separation dependent surface enhanced Raman scattering. Appl. Phys. Lett. **93**, 173106 (2008)
123. L. Gunnarsson, E.J. Bjerneld, H. Xu, S. Petronis, B. Kasemo, M. Kall, Interparticle coupling effects in nanofabricated substrates for surface-enhanced Raman scattering. Appl. Phys. Lett. **78**, 802 (2001)
124. A. Gopinath, S.V. Boriskina, W.R. Premasiri, L. Ziegler, B.R.M. Reinhard, L. Dal Negro, Plasmonic nanogalaxies: multiscale aperiodic arrays for surface-enhanced Raman sensing. Nano Lett. **9**(11), 3922–3929 (2009). doi:10.1021/nl902134r
125. A. Gopinath, S.V. Boriskina, B.M. Reinhard, L. Dal Negro, Deterministic aperiodic arrays of metal nanoparticles for surface-enhanced Raman scattering (SERS). Opt. Express **17**(5), 3741–3753 (2009)

126. B. Yan, A. Thubagere, W.R. Premasiri, L.D. Ziegler, L. Dal Negro, B.M. Reinhard, Engineered SERS substrates with multiscale signal enhancement: nanoparticle cluster arrays. ACS Nano **3**, 1190–1202 (2009)
127. L. Tsang, J.A. Kong, K. Ding, *Scattering of Electromagnetic Waves: Theories and Applications* (Wiley, New York, 2000)
128. S.V. Boriskina, L. Dal Negro, Sensitive label-free biosensing using critical modes in aperiodic photonic structures. Opt. Express **16**(17), 12511–12522 (2008)
129. N.O. Petersen, P.L. Hoddelius, P.W. Wiseman, O. Seger, K. Magnusson, Quantitation of membrane receptor distributions by image correlation spectroscopy: concept and application. Biophys. J. **65**, 1135–1146 (1993)
130. R. Dallapiccola, A. Gopinath, F. Stellacci, L. Dal Negro, Quasi-periodic distribution of plasmon modes in two-dimensional Fibonacci arrays of metal nanoparticles. Opt. Express **16**(8), 5544–5555 (2008)
131. A. Gopinath, S.V. Boriskina, S. Yerci, R. Li, L. Dal Negro, Enhancement of the 1.54 μm Er^3+ emission from quasiperiodic plasmonic arrays. Appl. Phys. Lett. **96**(7), 071113–071113 (2010)
132. D. Song, E. Cho, G. Conibeer, C. Flynn, Y. Huang, M.A. Green, Structural, electrical and photovoltaic characterization of of silicon nanocrystals embedded in SiC matrix and Si nanocrystals/crystalline silicon heterojunction devices. Solar Energy Mater. Solar Cells **92**, 474–481 (2008)
133. M.A. Green, Third generation photovoltaics: solar cells for 2020 and beyond. Physica E **14**, 65 (2002)
134. C. Haase, H. Stiebig, Thin- film silicon solar cells with efficient periodic light trapping texture. Appl. Phys. Lett. **91**, 061116 (2007)
135. D. Shir, J. Yoon, D. Chanda, J.H. Ryu, J.A. Rogers, Performance of ultrathin silicon solar microcells with nanostructures of relief formed by soft imprint lithography for broad band absorption enhancement. Nano Lett. **10**, 3041–3046 (2010)
136. S.B. Mallick, M. Agrawal, P. Peumans, Optimal light trapping in ultra-thin photonic crystal crystalline silicon solar cells. Opt. Express **18**, 5691–5706 (2010)
137. R. Biswas, J. Bhattacharya, B. Lewis, N. Chakravarty, V. Dalal, Enhanced nanocrystalline silicon solar cell with a photonic crystal back-reflector. Sol. Energy Mat. Sol. Cells **94**, 2337–2342 (2010)
138. V.E. Ferry, M.A. Verschuuren, M.C. van Lare, R.E.I. Schropp, H.A. Atwater, A. Polman, Optimized spatial correlations for broadband light trapping nanopatterns in high efficiency ultrathin film a-Si:H solar cells. Nano Lett. **11**, 4239–4245 (2011)
139. V.E. Ferry, L.A. Sweatlock, D. Pacifici, H.A. Atwater, Plasmonic nanostructure design for efficient light coupling into solar cells. Nano Lett. **8**, 4391–4397 (2008)
140. C. Rockstuhl, S. Fahr, F. Lederer, Absorption enhancement in solar cells by localized plasmon polaritons. J. Appl. Phys. **104**, 123102 (2008)
141. K.R. Catchpole, A. Polman, Design principles for particle plasmon enhanced solar cells. Appl. Phys. Lett. **93**, 191113 (2008)
142. H.A. Atwater, A. Polman, Plasmonics for improved photovoltaic devices. Nat. Mat. **9**, 205 (2010)
143. C. Eisele, C.E. Nebel, M. Stutzmann, Periodic light coupler gratings in amorphous thin film solar cells. J. Appl. Phys. **89**, 7722 (2001)
144. K. Nakayama, K. Tanabe, H.A. Atwater, Plasmonic nanoparticle enhanced light absorption in GaAs solar cells. Appl. Phys. Lett. **93**, 121904 (2008)
145. F.J. Beck, A. Polman, K.R. Catchpole, Tunable light trapping for solar cells using localized surface plasmons. J. Appl. Phys. **105**, 114310 (2009)
146. H.R. Stuart, D.G. Hall, Island size effects in nanoparticle-enhanced photodetectors. Appl. Phys. Lett. **73**, 3815–3817 (1998)
147. A.E. Ostfeld, D. Pacifici, Plasmonic concentrators for enhanced light absorption in ultrathin film organic photovoltaics. Appl. Phys. Lett. **98**(11), 113112 (2011)

Chapter 10
Waves on Subwalength Metallic Surfaces: A Microscopic View Point

Philippe Lalanne and Haitao Liu

Abstract At a microscopic level, the electromagnetic properties of subwavelength metallic surfaces are due to two kinds of elementary distinct waves, the surface plasmon polaritons and the quasi-cylindrical waves. These waves are launched on the metal surface by the scattering of the incident field on the subwavelength indentations, and are subsequently scattered by adjacent indentations to ultimately form a complex surface charge pattern that is responsible of various fascinating phenomena. We review the fundamental properties that govern these waves and discuss their impacts in the Wood anomaly of metallic gratings, a phenomenon historically attributed to surface plasmon polaritons since the milestone work by U. Fano [10].

Keywords Wood anomalies · Surface plasmon · Extraordinary optical transmission · Theory of metallic grating · Quasi-cylindrical wave · Norton wave · Microscopic model · Plasmonic surfaces

10.1 Introduction

In 1902, R.W. Wood observed that the spectrum of a continuous light source reflected by a metallic surface etched by a periodic array of tiny grooves exhibits a rapid variation that occurs within a range of wavelengths not greater than the distance between the sodium lines. Since then, grating anomalies have fascinated specialists of optics

P. Lalanne (✉)
Laboratoire Photonique, Numérique et Nanosciences, Institut d'Optique d'Aquitaine, Allée Laroumagne, Univ Bordeaux 1 , CNRS, Talence 33405, , Talence Cedex, France
e-mail: philippe.lalanne@institutoptique.fr

H. Liu
Key Laboratory of Optical Information Science and Technology, Ministry of Education, Institute of Modern Optics, Nankai University, Tianjin 300071, China
e-mail: liuht@nankai.edu.cn

T. V. Shahbazyan and M. I. Stockman (eds.), *Plasmonics: Theory and Applications*, Challenges and Advances in Computational Chemistry and Physics 15,
DOI: 10.1007/978-94-007-7805-4_10, © Springer Science+Business Media Dordrecht 2013

and physics, and nowadays with the progress of nanofabrication, metallic surfaces patterned with subwavelength indentations are studied for a variety of interesting properties, with applications ranging from sensing, new photonic and metamaterial devices, to integrated circuits mixing photonics and electronics [9]. It is the purpose of this chapter to examine the concepts, to elucidate the underlying physics and to discuss recent results and current problems in relation with resonance of metallic gratings. Particular emphasis will be placed on work carried out in the last decade, in anticipating future directions and in assessing the relevance of the subject to other areas of science.

Section 10.2 provides a historical background on the waves that are launched on a conducting surface by a subwavelength indentation, recalling the pioneer works at the beginning of last century by Marconi, Sommerfeld, Norton … in relation with long-distance radio-wave communications. Note that the field radiated by a dipole source in the vicinity of an interface has been considerably studied in the context of molecule fluorescence and other optical processes, such as surface-enhance Raman scattering, energy transfer … An interface may alter the way an excited molecule loses energy through fluorescence in several ways. It may absorb part of the spontaneous decay, and may alter both the radiative decay rate and the spatial distribution of the emitted radiation. Such situations are completely out of the scope of the present survey. The interested reader may refer to the review article [3] and to other reviews quoted there.

At optical frequency, the field scattered by subwavelength indentations on metal surface has been first considered for understanding the spectacular Wood's anomalies. Well before the establishment of modern theories of gratings (Floquet-Bloch expansions, phenomenological models with the zeros and poles of scattering operators …) and before the discovery of surface plasmon polaritons (SPP) by Ritchie [27], microscopic theories of metallic gratings considered the SPP launched by the individual grating indentations as responsible for Wood anomalies. Section 10.3 summarizes the Fano's seminal ideas that, since 1941, have durably impacted the field of periodic metallic surfaces.

Section 10.4 describes what is presently known on the waves launched on metal surfaces by subwavelength indentations, which include the SPP mode and another contribution called the quasi-cylindrical wave (quasi-CW). A good knowledge of the properties of these waves is essential for understanding the rich physics of subwavelength metallic surfaces. Particular emphasis is put on 1D indentations such as ridges or grooves, 0D point defects such as holes being rapidly visited.

In Sects 10.5 and 10.6, we examine the scattering of SPPs and quasi-cylindrical waves by tiny indentations, emphasizing cross-conversion processes that convert quasi-CWs into SPPs and vice versa. Under the assumption that the indentations have subwavelength dimensions, scattering coefficients for the SPPs, quasi-CWs, and for a combination of theses waves can be consistently defined. The objective is to settle the foundation of a "microscopic" treatment of the electromagnetic properties of metallic subwavelength surfaces, which is accurate and intuitive. For that, the microscopic treatment should fit our current understanding and design recipes that all rely on a wavy description, which assume that surface waves are first generated by some illuminated indentations, then propagate on the metal surface and

interact with nearby indentations before being recovered as freely propagating light or detected. Note the large gap existing between such an intuitive wavy picture and state-of-the-art numerical tools (some are purely numerical like finite-element and finite-difference methods, some are more physically oriented like modal- or multipole-expansion methods …), that rarely consider the waves launched on the surface and that never directly calculate how those waves are scattered by the subwavelength indentations. The main physical ingredients of our understanding of subwavelength surfaces (the launching, absorption, propagation and scattering of surface waves) are only implicitly taken into account in standard modelisation by matching the continuous electromagnetic field components at the interface.

Section 10.7 concludes the chapter.

10.2 Waves on Metal Surfaces: Historical Background

The field scattered by subwavelength indentations or emitted by subwavelength emitters in the vicinity of interfaces has been of longstanding interest in electromagnetism. In the 1900s, the rapid development of radio-wave technology prompted theoretical studies to explain why very long-distance (over-ocean transmission have been achieved in 1907 by Marconi) transmission could be achieved with radio waves above the earth. The solution is indeed linked to guiding by the ionosphere layers, but at the beginning of the twentieth century, the explanation was thought to be due to the nature of the surface waves launched on the flat earth by the emitting antennas acting as a dipole. Sommerfeld was the first to determine the complete electromagnetic field radiated by a subwavelength antenna (a 0D vertical dipole) at the interface between two semi-infinite half spaces. He verified that his complicated solution [30] is composed of a "direct contribution" and of a bounded Zenneck mode [37], the analogue of the surface plasmon polariton (SPP) [25] for metals at optical frequencies, with an exponential damping. On the other hand, the amplitude of the direct contribution does not decay exponentially, but algebraically as $1/r^2$ at asymptotically long-distance from the antenna [21–23]. The direct contribution, known as the Norton wave [2, 6], was therefore believed to be responsible for long-distance radio transmission.

In nanophotonics, the field scattered on metallic surfaces by subwavelength indentations is also essential, since it is responsible for the electromagnetic interaction between nearby indentations on the surfaces. Since the initial milestone interpretation of Wood's anomalies [35] by U. Fano [10] who introduced the concept of bounded SPP modes, SPPs have been central in modern history of the research on the optical properties of metallic surfaces, which have recently enabled researchers to overcome the diffraction limit for applications in microscopy [31], nano-optical tweezing [28], integrated optics [8] and lasers [38]. From a mathematical point of view, the solution of this photonic problem is identical to that of the radio-wave problem [14, 19]. However, there are also differences. We are mainly concerned by short-distance (rather than long-distance) electromagnetic interactions, since the distance between two neighboring indentations on subwavelength optical surfaces is

of the order of λ and rarely exceeds 10λ. The second important difference concerns the fact that the dipole orientation cannot be chosen in nanophotonics. For instance, for a subwavelength 1D indentation under illumination of transverse-magnetic (TM) polarization, two coherent equivalent electrical dipoles of different polarizations are generally excited with different strengths.

Despite its importance for understanding the rich optics of subwavelength metallic surfaces, the field scattered by subwavelength indentations on a metal surface has been studied only recently. Lezec and his co-workers [11] were the first to recognize the importance of a "direct" wave other than the SPP. This initial finding has been followed by theoretical [5, 13, 20, 33] and experimental [1] works aiming at determining the main characteristics of this wave. It turns out that for intermediate distances of interest ($x < 10\lambda$), the direct wave is very different from the Norton wave; it looks like a cylindrical wave.

10.3 Fano's Microscopic Model of Wood Anomaly

In 1902, R.W. Wood, when observing the spectrum of a continuous light source reflected by an optical metallic diffraction grating when the incident wave is polarized with its magnetic vector parallel to the grooves (TM polarization), noticed a surprising phenomenon: "*I was astounded to find that under certain conditions, the drop from maximum illumination to minimum, a drop certainly of from 10 to 1, occurred within a range of wavelengths not greater than the distance between the sodium lines*" [35]. Wood's discovery drew immediately a considerable attention and the fascination of many specialists of optics for the so-called Wood's anomalies that never died.

By considering the metal as perfectly conducting and using a complicated mathematical derivation, Lord Rayleigh proposed the first explanation to the existence of the anomalies [26]: an anomaly in a given spectrum occurs at a wavelength corresponding to the passing-off of a spectrum of higher order, in other words, at the wavelength given by the grating equation for which a scattered wave emerges tangentially to the grating surface. Considering the imprecise knowledge of the grating period in Wood's experiment, the agreement between the grating equation and Wood's experimental results was considered as rather fair, and the Rayleigh conjecture remained unquestioned during almost two decades. However, the conclusions radically changed in 1936, with Strong's study of Wood's anomalies for various metallic gratings having the same period [32]. Strong evidenced that the anomalies occur at a wavelength systematically larger than that predicted by the grating equation.

To explain the red shift from the Rayleigh condition, U. Fano introduced a microscopic model of Wood's anomalies in his seminal article published in 1941 [10] (40 years after Wood's observation). Fano's model is much less mathematically involved than the theoretical work by Lord Rayleigh. It rather relied on a Huygens-type very intuitive interpretation, and importantly, it suggested that a surface mode with a parallel momentum greater than the free space momentum be involved in

the energy transport between adjacent grooves. It is retrospectively interesting and amazing to see how the surface wave, which is nothing else than the SPP of the flat interface, is introduced in Fano's model. U. Fano first considered the parallel propagation constants of the modes of a glass plate sandwiched between a metal and a vacuum and asks himself "*Is there left any mode when the thickness of the glass layer vanishes?*". By solving analytically the bi-interface problem, he showed that one and only one bound mode (the SPP) exists in the limit of vanishingly small glass thicknesses for TM polarization, with a complex propagation constant whose real part is always slightly larger than the modulus k_0 of the wave-vector in a vacuum. He therefore made the ansatz that Wood's anomaly originates from a collective resonance of the subwavelength surface (see Fig. 10.1), in which the part of the wave scattered by groove A excites the bound mode, travelling along the surface with a phase velocity smaller than the vacuum phase velocity, which gives a resonance whenever it reaches the neighboring groove B in phase with the incident wave (phase-matching condition). Denoting by k_{SP} (surprisingly Fano does not give any analytical expression) the complex propagation constant of the surface wave and assuming that the grooves are infinitely small and thus neglecting multiple scattering, the microscopic interpretation by Fano leads to the following phase matching condition,

$$\mathrm{Re}(k_{\mathrm{SP}}) = k_{\mathrm{x}} + 2\pi/a, \tag{10.1}$$

where the real part of the propagation constant is matched to the parallel wave vector k_{x} of the incident plane wave through a wave vector $2\pi/a$ of the 1D reciprocal lattice associated to the grating (a being the periodicity). In Rayleigh's theory, because perfect metals were considered, the wave on the perfectly-conducting surface propagates exactly with the vacuum phase velocity, and this causes the phase velocity difference that explains the red-shift for real metals.

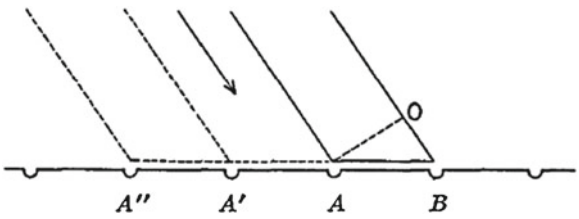

Fig. 10.1 Fano's microscopic model of Wood's anomaly (from [10]). In Rayleigh's interpretation derived by considering the metal as a perfect conductor, resonance occurs whenever the part of the wave that is scattered by groove A and that is traveling along the grating with the vacuum phase velocity reaches the neighboring groove B in phase with the incident wave and with the waves scattered by the grooves A', A''. What Fano proposes to explain the red-shifted Wood anomaly is to replace the free-space grazing wave of Rayleigh by a bounded mode with a smaller phase velocity. This bounded mode is nothing else than the SPP of the flat metallic surface, which will be discovered 16 years after by Ritchie [27]

The big success of introducing a bounded SPP mode to convincingly explain the experimental red shift is a milestone result, and since Fano's work our understanding of Wood's anomalies is intimately linked to the resonant excitation of SPPs. The last decade has proved that this vision is simplistic and that, although Fano's approach is remarkable in predicting the resonant wavelength, Rayleigh and Fano's interpretations should be actually "combined" to provide a quantitative analysis of Wood's anomalies.

10.4 Field Scattered on Metal Surfaces by Subwavelength Indentations

The waves scattered on the surface of a metal film by a tiny indentation are at the essence of the optical properties of metallic subwavelength surfaces. Provided that the indention is small enough (in practice, dimensions should be smaller than $\lambda/3$), it is convenient to consider asymptotically small indentations. For 1D indentations, such as grooves or ridges like in Wood's experiment, the equivalent sources are Dirac line sources. When the polarization of the incident wave is parallel to the indentation, the field radiated on the surface is nearly zero. In that case often referred to as TE polarization, the indentations are all independent and the field scattered by all indentations is simply the superposition of the field scattered by every indentation. This "trivial" case is not discussed hereafter. The TM polarization case is much more interesting. Two coherent electric line sources, one being polarized perpendicular to the surface and the second one being polarized parallel to the surface and perpendicular to the indentation, have to be considered. This case is discussed in Sect. 10.4.1. For 0D indentations such as holes, three dipole polarizations should be investigated. The properties of the associated radiated fields will be qualitatively discussed in Sect. 10.4.2.

10.4.1 The Quasi-Cylindrical Wave

The scattering of a 1D subwavelength indentation illuminated by a TM wave has been the subject of intense research [1, 5, 7, 11, 13, 33] over the last decade. Hereafter we simply summarize the main results, which are documented in a review article [14].

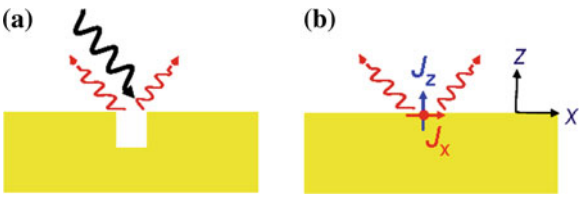

Fig. 10.2 Equivalence of a subwavelength indentation under TM illumination (**a**), to two electric line sources (**b**)

Referring to Fig. 10.2, a subwavelength indentation invariant along the y-axis (the z-axis being perpendicular to the surface) and illuminated with a plane wave polarized in the x-z plane (Fig. 10.2a), can be replaced by two electric line sources in the dipolar approximation (Fig. 10.2b), one J_z being polarized perpendicularly to the interface (along the z-axis) and the other one J_x parallel to the interface (along the x-axis). Concerning the field scattered on the surface (this is the field that is responsible for the electromagnetic interaction between the indentations on the surface), three important properties are worth mentioning here.

Property 1: *The field radiated on the surface by each individual line source can be decomposed into a SPP mode and a quasi-cylindrical wave (quasi-CW), which represents a "direct" contribution from the source.*

At optical frequencies, the amplitude of the quasi-cylindrical wave is initially damping as $x^{-1/2}$ (just as a cylindrical wave) in the vicinity of the line source, then is dropping at a faster rate for intermediate distances $\lambda < x < 10\,\lambda$, before reaching an asymptotic regime behavior with an $x^{-3/2}$ damping rate at large propagation distances.

Figure 10.3 illustrates the different contributions to the magnetic field radiated on an air/gold (permittivities $\varepsilon_d = 1$ and $\varepsilon_m = -46.8 + 3.5i$) interface ($z = 0$) by a line source vertically polarized. The results hold for gold at $\lambda = 1\ \mu$m. The dashed line is the SPP contribution, with an exponential damping $\exp[-Im(k_{SP})x]$, and the solid curve is the "direct" wave contribution. At very large propagation distances, the direct-wave decay rate asymptotically tends to $1/x^{3/2}$ and becomes

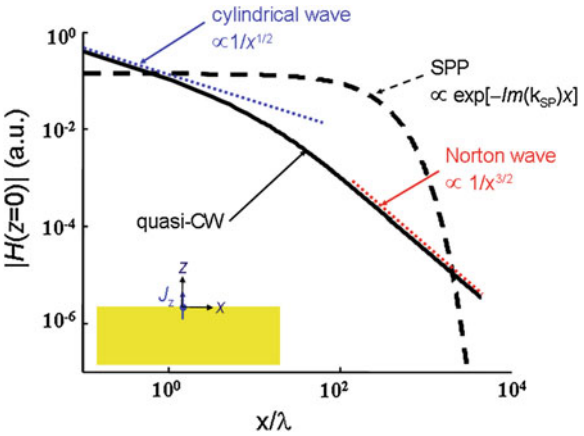

Fig. 10.3 Magnetic field radiated at $\lambda = 1\mu$m on an air/gold interface ($z = 0$) by a line source J_z polarized vertically. The field is composed of a SPP (*dashed curve*) and of a quasi-CW (*solid curve*). The latter takes two asymptotic forms. It is very intense and behaves as a cylindrical wave (*dotted blue line*) with a $1/x^{1/2}$ decay rate at small propagation distances. At very long propagation distances, it is very weak and decays as $1/x^{3/2}$. It is the analogue of the Norton wave (shown with the *dotted red line*) discovered for radio communication

the analogue of the Norton radio wave (shown with the dotted red line) at optical frequencies. For subwavelength propagation distances ($x < 2\lambda$), the direct wave contribution dominates. It is very different from the Norton wave as it looks like a cylindrical wave with a $1/x^{1/2}$ damping rate (dotted blue line). Consistently, the direct wave contribution has been called a quasi-cylindrical wave (quasi-CW) in the recent literature. The existence and importance of the quasi-cylindrical wave at optical frequencies on metals has been first observed with a very elegant slit-groove experiment [11], in which the groove acts as a line source and the slit as a local detector of the field scattered by the groove. By systematically varying the groove-slit separation-distance in a series of samples, the field pattern is recorded. The experimental data, which were probably contaminated by an undesired adlayer on the silver film, have been initially interpreted in a confusing manner as shown in [1, 13], but they had the merit to unambiguously reveal the existence and importance of a direct wave (different from the SPP) that is initially dominant for $|x| < 2\lambda$.

Property 2: *As one moves from the visible to longer wavelengths, the SPP is less attenuated, but it is also less and less efficiently excited, whereas the quasi-CWs are equally excited at all energies.*

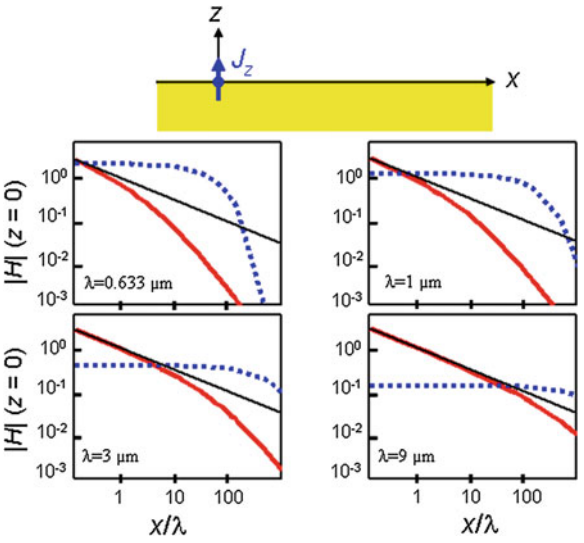

Fig. 10.4 Magnetic field, $H(x) = H_{SP}(x) + H_{CW}(x)$, radiated by a vertically-polarized line source J_z at an Ag/air interface (inset on the top) for wavelengths ranging from the visible to thermal infrared [13]. The *blue dashed curves* correspond to $|H_{SP}|$ and the *red-solid curves* to $|H_{CW}|$. Thin black lines show a damping scaling as $1/x^{1/2}$. The calculations are performed for silver but similar results have been obtained for gold. Note the logarithmic scales used in both the *horizontal* and *vertical* axes, which are all identical for the sake of comparison. The frequency-dependent value of Ag permittivity is taken from [24]

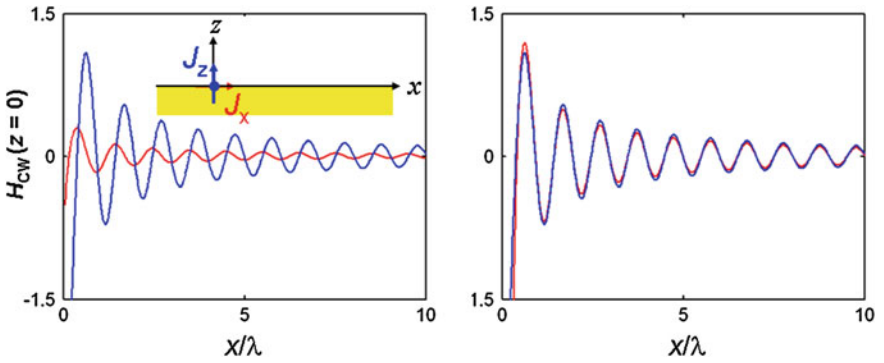

Fig. 10.5 Illustration of property 3 for a gold/air interface at $\lambda = 800$ nm. *Left* The *blue* and *red curves* represent the magnetic field of the quasi-cylindrical waves radiated on the surface by two line sources polarized vertically and horizontally, respectively, with $J_x = J_z = 1$. The two quasi-cylindrical waves seem completely different a priori. *Right* In reality, the two quasi-cylindrical waves are almost identical in shape and only differ by a constant, as show by the new red curves obtained for $J_x \approx 3i$. The frequency-dependent Au permittivity takes value from [24]

This property is illustrated in Fig. 10.4 for different wavelengths. More precisely, the figure represents the magnitude of the total magnetic field $H(x, z = 0)$ radiated on the interface ($z = 0$) by a z-polarized line source located at $x = z = 0$. The total field results from the sum of two contributions, $H(x) = H_{SP}(x) + H_{CW}(x)$, where H_{SP} (blue-dotted) and H_{CW} (red-solid) represent the SPP and quasi-CW contributions, respectively. We first note that the initial quasi-CW contribution at short distances is nearly independent of the metal dielectric properties, whereas the initial SPP contribution rapidly drops as the metal conductivity increases, $|H_{SP}| \propto |\varepsilon_m|^{-1/2}$. At visible wavelengths ($\lambda = 0.633\mu$m), the SPP contribution dominates even at relatively short distances, the SPP and quasi-CW being actually equal for $x_c \approx \lambda/6$. At thermal-infrared wavelengths ($\lambda = 9\mu$m), the quasi-CW is preponderant until distances as large as 100λ. It can be shown that the initial crossing distance x_c below which the quasi-CW wave dominates increases with the metal conductivity, $x_c \approx \lambda |\varepsilon_m|/(2\pi \varepsilon_d^{3/2})$ [14].

Property 3: *The quasi-cylindrical waves radiated on the surface by each individual line source, J_x or J_z although they differ in amplitude and phase, are almost identical in shape.*

Figure 10.5 illustrates the property. In the left graph, the magnetic fields of the quasi-cylindical waves radiated by vertical (blue curve) and horizontal (red curve) line sources ($J_x = J_z = 1$) are shown as a function of the distance x from the source. The calculation is performed for a gold substrate at $\lambda = 800$ nm. In the right panel, the source J_x has been optimized ($J_x \approx 3i$) so that its associated quasi-cylindrical wave is similar to that generated by the vertical source. It turns out that, although a slight difference remains, the two fields are almost superimposed. It can be shown

that this difference becomes smaller and smaller as the metal conductivity increases (or λ increases) [14].

This property has an important consequence if one neglects the small residual difference. When a subwavelength indentation is illuminated by a TM polarized light, the scattered field can be seen as the total field radiated by two line sources, J_x and J_z, and the relative amplitudes of the line sources are arbitrary: they for instance depend on the incident illumination (its angle of incidence for instance if it is a plane wave), on the actual geometry of the indentation, on the dielectric and metal permittivities… A priori two independent radiation problems should be considered, but since the quasi-cylindrical waves associated to the two line source polarizations are identical in shape, any arbitrary sub-indentation illuminated by any incident electromagnetic field will launch a unique field (the quasi-cylindrical wave) on a metallic surface, in addition to the SPP. Also note that the mixing ratio between the SPP and the quasi-CW radiated by the two line sources are approximately the same [14], and we finally conclude that this mixing ratio is fixed for the field scattered by any sub-indentation.

10.4.2 SPP and Quasi-CW Launched by a Dipole Point-Source on a Metal Surface (3D case)

The field radiated by point-source or sub-λ antennas in the vicinity of metallic surfaces has been of long-standing interest in classical electromagnetism. In particular for long-distance radio propagation and for remote sensing, the problem was analyzed in detail by Sommerfeld [29, 30], Norton [21–23] and others for a half-space conductor with a finite conductivity (the sea surface for instance). The conclusions were that the radiated field can be calculated as an integral along a contour in the complex plane and is composed of two contributions, the Zenneck mode (corresponding to the pole, the analog of the SPP at visible frequencies) and a "direct" wave (corresponding to branch integrals, the analog of the quasi-CW). In an intermediate region and near the surface, the field is well approximated by that of the cylindrical Zenneck mode; but then, as the distance increases further, the long-distance propagation is mainly due to the direct wave that is often referred to as the Norton wave. The latter, whose amplitude asymptotically decays as $1/r^2$, overcomes the Zenneck mode at large distances because of the additional exponential damping factor $\exp(\mathrm{i}k_{SP}r)$ of the Zenneck mode. These issues are discussed in great detail in the review article by R.E. Collin [6] or in the book by Baños [2].

Hereafter we simply show an example for the sake of illustration. For a vertical dipole, perpendicular to the interface, the in-plane component of the radiated field is radially polarized and isotropic. The situation is more interesting for an in-plane dipole (let us say parallel to the x-axis). Both the SPP and quasi-CW fields on the surface are anisotropic. Figure 10.6 shows the radial electric fields radiated by such a dipole. The SPP field is proportional to $r^{-1/2}\exp(\mathrm{i}k_{SP}r)$ and its electric

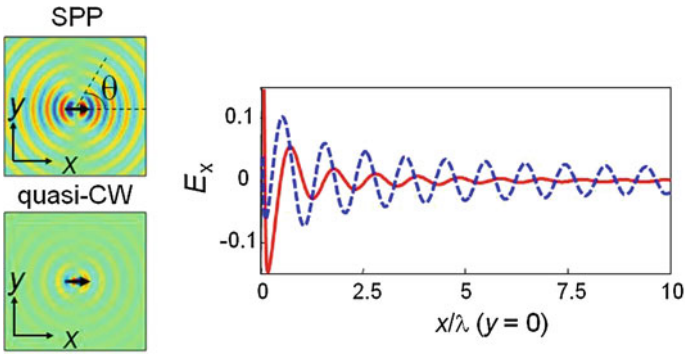

Fig. 10.6 Radial electric field radiated on an Au/air surface by a dipole point source polarized parallel to the surface (along x-axis) for $\lambda = 800$ nm. The *left panels* show a surface map for the SPP (*top*) and quasi-CW (*bottom*) fields. The same units are used in both plots. As the metal conductivity increases, the perfect-conductor limit is reached and the quasi-cylindrical wave becomes a spherical wave with a $r^{-2}\exp(ik_0 r)$ behavior. In the *right panel*, the radial field (E_x) is plotted as a function of x for $y = 0$. The *blue dashed curve* corresponds to the SPP mode and the *red-solid curve* to the quasi-CW. The frequency-dependent value of Au permittivity is taken from [24]

vector is mainly perpendicular to the surface with a small in-plane component. Along any direction (different from $\theta = \pi/2$) the in-plane SPP field tends to be radially polarized, as $E_\theta/E_r \approx \tan(\theta)/r$, where the subscript θ and r are used to denote the orthoradial and radial components of the fields. The quasi-CW wave initially varies as $r^{-1}\exp(ik_0 r)$ at small distances from the dipole, then at longer distances, its electric field amplitude decays algebraically with distance as $r^{-2}\exp(ik_0 r)$, like the Norton radio wave. The electric field of the quasi-CW points mainly along the direction perpendicular to the interface, and its in-plane components satisfy $E_\theta/E_r \approx \tan(\theta)$. However, for the vertical dipole the in-plane component of the quasi-CW field is radially polarized and isotropic.

10.5 Fano-Like Model of the Extraordinary Optical Transmission

The modes (SPP) and waves (the quasi-CW) scattered by individual subwavelength scatterers are at the essence of the electromagnetic properties of subwavelength metallic surfaces and in particular of subwavelength gratings. Every individual indentation that is illuminated launches SPPs and quasi-CWs on the surface. The launched fields further interact with the adjacent indentations, before being eventually radiated back into free space.

The electromagnetic interaction on the surface may lead to a complicated multiple scattering process, in which for instance the launched quasi-cylindrical waves may scatter and generate SPPs, or vice-versa. Before examining the multiple scattering process in details in Sect. 10.6, to simplify we will examine a simplified model,

assuming like Fano, that the electromagnetic interaction among the indentations is only mediated by the SPPs of the flat interfaces between the indentations, the quasi-CW contribution being neglected. There are two reasons for considering such a pure-SPP model that only considers SPPs. First the model allows us to define the SPP scattering coefficients for the individual indentations, and these scattering coefficients are fundamental to understand the multiple scattering process (since the same scattering coefficients apply to the quasi-CWs as well, as shown in Sect. 10.6). Second, by comparing the predictions of the model with fully-vectorial computational results, one may directly determine the role of SPP in the electromagnetic property of subwavelength surfaces [16].

To illustrate our purpose, we consider the text-book case of the extraordinary optical transmission (EOT). The EOT was first observed in the near infrared with subwavelength hole arrays perforated in opaque gold and silver films [9], and is an emblematic example in plasmonics that has sparked a huge amount of research trying to apply the phenomenon and to unveil the underlying mechanisms, and especially to unveil the role of SPPs in the transmission. The analysis is performed for a self-supported membrane (thickness d) in air for the sake of simplicity (the upper and lower grating interfaces are identical, see Fig. 10.7a).

At a microscopic level, the basic mechanism enabling the EOT is a coherent diffraction by all the individual holes acting as elementary scatterers. However, it is more convenient to consider isolated 1D arrays of holes (a periodic hole chain with periodicity a in the y-direction, see the bottom panels in Fig. 10.7) perforated in a metal substrate as the elementary scatterers. Provided that the hole separation distance is subwavelength, the 1D hole chains act as 1D indentations, like in classical metallic gratings.

The elementary SPP-scattering events used in a pure-SPP model of the EOT are shown in Fig. 10.7b–d for classical diffraction geometries (the y-component k_y of the in-plane wave vector momentum is zero). Upon interaction with the chain, the SPP modes are partly excited, transmitted, reflected or scattered into the chain mode and into a continuum of outgoing plane waves. The interaction defines four elementary SPP scattering coefficients. Two coefficients, see Fig. 10.7b, namely the SPP modal reflection and transmission coefficients, ρ_{SP} and τ_{SP}, correspond to in-plane scattering. The other two, α_{SP} and β_{SP}, correspond to the transformation of the SPPs into aperture modes or radiation waves, and vice versa. They allow us to link the local field on the surface to the far field that is transporting light away from the metal film.

From these elementary SPP scattering coefficients, a coupled-mode model that provides closed-form expressions for the transmittance and reflectance coefficients of the fundamental supermode of the 2D hole array, t_A and r_A, is readily derived [16]. For instance, the reflection coefficient r_A of the fundamental supermode, a very important physical quantity of the EOT phenomenon [18], can be written

$$r_A = r + \frac{2\alpha_{SP}^2}{u^{-1} - (\rho_{SP} + \tau_{SP})}. \tag{10.2}$$

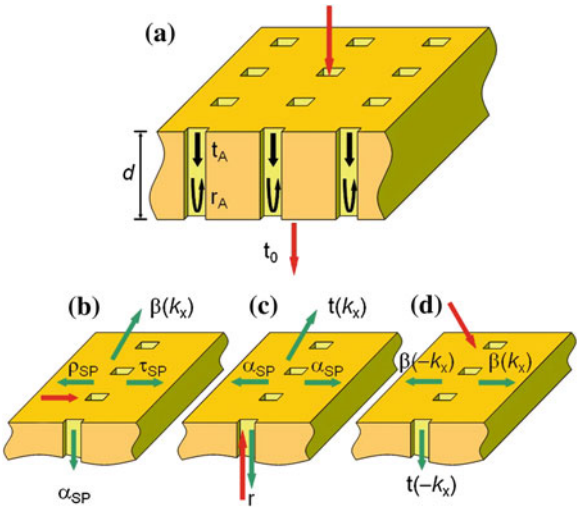

Fig. 10.7 Pure-SPP model of the EOT. **a** Self-supported geometry in air considered for the sake of simplicity. The transmission coefficient of the membrane (from the incident plane wave to the (0,0)th-order transmitted plane wave) is denoted by t_0. Similarly we denote by t_A and r_A the transmission and reflection coefficients of the fundamental supermode of the 2D hole array. The membrane thickness is denoted by d. **b–d** SPP elementary scattering processes involved in the EOT. They are all associated to a single 1D hole chain of infinite depth under illumination by **b** the SPP mode, **c** the fundamental supermode of the hole chain, and **d** an incident TM-polarized (magnetic vector along the chain direction) plane wave impinging at an oblique incidence defined by its in-plane wave-vector component k_x. The *red* and *green arrows* refer to the incident and scattered modes, respectively. The processes in **b–d** define six independent elementary scattering coefficients, ρ_{SP} (reflection coefficient of the SPP mode), τ_{SP} transmission coefficient of the SPP mode), α_{SP} (scattering coefficient from the SPP mode to the fundamental supermode and vice versa according to the reciprocity theorem), $\beta(k_x)$ (scattering coefficient from the SPP mode to the outgoing plane wave with an in-plane wave-vector component k_x and vice versa), $t(k_x)$ (scattering coefficient from the fundamental supermode to the plane wave and vice versa) and r (reflection coefficient of the fundamental supermode)

In Eq. 10.2 that holds for normal incidence ($k_x = 0$), $u = \exp(ik_{SP}a)$ is the phase delay accumulated by the SPP over a grating period and r is the reflection coefficient of the fundamental mode of the hole chain, see Fig. 10.7c.

It is crucial to realize that the SPP scattering coefficients in Eq. 10.2 are not related to the periodicity of the structure and that the coupled-mode model can be applied to aperiodic structures as well [16]. Indeed, the essence of Eq. 10.2, and in particular of the denominator that results from a geometric summation over all chain contributions, is a multiple scattering process that involves the excitation of SPP modes by the incident field and the further scatterings of the excited SPPs onto the infinite set of periodically-spaced hole chains. The same denominator would be obtained for the groove geometry in Fig. 10.1, and would explain the Wood anomaly in Fano's interpretation.

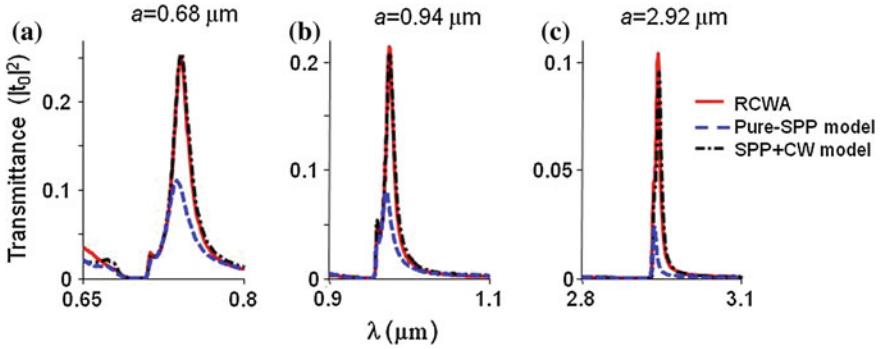

Fig. 10.8 The role of SPPs in the EOT. Three spectral bands are covered, from visible to near-infrared frequencies: **a** $a = 0.68\,\mu$m, **b** $a = 0.94\,\mu$m and **c** $a = 2.92\,\mu$m, a being the grating pitch. The *red-solid curves* represent fully-vectorial data of the EOT and the *blue-dashes* are predictions obtained with the pure-SPP model. The *black dash-dot curves* (almost superimposed with the fully-vectorial results) are obtained with a microscopic model that takes into account SPPs and quasi-CWs (see Sect. 10.6.2). The data are obtained for a gold membrane in air perforated by a periodic array of square holes illuminated by a normally incident plane wave. The hole side length is $0.28a$ (hole filling fraction 8 %) and the membrane thickness is $d = 0.21a$

The question arises on how accurate is the pure-SPP model in predicting the EOT phenomenon. The answer is provided in Fig. 10.8, which compares the pure-SPP model predictions (blue dashed curves) with fully-vectorial computational results (red solid curves). The comparison is performed for three spectral intervals, from the visible ($a = 0.68\mu$m) to the near-infrared ($a = 2.92\mu$m). The SPP model quantitatively predicts all the salient features of the EOT, and especially the Fano-type spectral profile with the antiresonance transmission dip followed by the resonance peak. Importantly, there are also some discrepancies that are due to the model assumption of a pure SPP electromagnetic interaction between the hole chains. As deduced from Fig. 10.8, the SPPs account for only half of the total transmitted energy at peak transmittance at visible frequencies, and only one fifth at longer wavelength in the near-infrared. The reason comes from the presence of the quasi-CW, which becomes more and more predominant as the wavelength increases, see Fig. 10.4.

This theoretical prediction has been recently confirmed experimentally by measuring the transmissions of a set of metal hole arrays with varying hole densities. More specifically, Beijnum and his coworkers have varied the size of the unit cell along the x-axis, choosing $a_x = qa_(a = 450\,\text{nm})$ and $a_y = a$, where q is an integer ranging from 1 to 7 [4]. When the measured transmissions are rescaled to correct for the reduced density of holes, all the arrays, $q = 2 - 7$, except the $q = 1$ array exhibit almost identical transmission spectra. Remarkably, all those rescaled spectra are reproduced with high accuracy by the pure-SPP model. In comparison, the $q = 1$ array differs by a two-fold increase of the scaled transmission peaks, a distinct effect that is attributed to the impact of the short-range-interaction provided by the quasi-CW.

10.6 Generalized Microscopic Model with Surface Plasmon Polaritons and Quasi-Cylindrical Waves

The pure-SPP microscopic model captures most of the important features of the EOT at visible frequencies, but it is largely inaccurate at longer wavelengths. In this Section, we keep on elaborating on an intuitive microscopic description of multiple scattering phenomena occurring on metallic subwavelength surfaces. By incorporating the quasi-CW into the pure SPP model, we obtain a more accurate model that provides quantitative predictions well above the visible wavelengths. In the first Sect. 10.6.1, a key scattering process of surface waves, the cross conversion from quasi-CWs to the SPPs is investigated. In the second Sect. 10.6.2, the quasi-CW contribution is incorporated into the pure-SPP model, and a generalized wavy model, similar to the pure-SPP model (actually it is much more accurate as shown by the black dash-dot curves in Fig. 10.8), is presented.

10.6.1 Cross Conversion from Quasi-Cylindrical Wave to Surface Plasmon Polariton

For a metal surface patterned with a set of 1D indentations under external illumination by TM-polarized light, several scattering processes of surface waves may exist: the SPP-to-SPP scattering that has been considered in the pure-SPP description, the possible CW-to-SPP or SPP-to-CW cross conversions, and the CW-to-CW scattering. The cross conversion between different surface waves plays a key role in the physical multiple-scattering picture. Demonstration of its existence along with a quantitative description of its scattering coefficient appear to be a heuristic step in incorporating quasi-CWs to build up an accurate microscopic description of subwavelength metallic surfaces.

The importance of the cross conversion has been demonstrated in [36], by considering a groove doublet and by calculating its SPP excitation efficiency on the outer sides as a function of the groove separation-distance. The interpretation of the computational results has led the authors to conclude that the SPP excitation efficiency dependence on the separation distance cannot be explained if one does not consider a CW-to-SPP cross conversion. Additionally, the authors have proposed a method to directly extract, from the SPP excitation efficiency, the scattering coefficients associated to the cross-conversion process and have argued and verified that the cross-conversion scattering coefficients are simply related to SPP scattering coefficients,

$$\rho_c \approx \rho_{SP}, \tag{10.3a}$$

$$\tau_c \approx \tau_{SP} - 1, \tag{10.3b}$$

where τ_c and ρ_c are the cross-conversion coefficients from an incident CW to a transmitted and a reflected SPP (Fig. 10.9a), and τ_{SP} and ρ_{SP} are the elastic transmis-

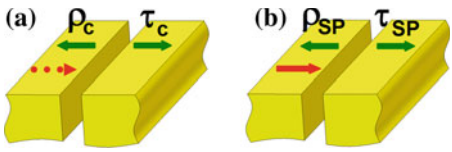

Fig. 10.9 Mapping from the cross conversion to the SPP scattering for a slit. **a** Cross conversion coefficients ρ_c and τ_c from an incident CW (*red dotted arrow*) to a reflected and a transmitted SPP (*green solid arrows*). **b** SPP scattering coefficients ρ_{SP} and τ_{SP} from an incident SPP (*red solid arrow*) to a reflected and a transmitted SPP (*green solid arrows*)

sion and reflection coefficients of the SPP (Fig. 10.9b). Equations 10.3a and 10.3b originate from a map of the scattering of an incident CW to the scattering of an incident SPP by a subwavelength indentation. Although the two incident fields are different in nature, their distributions are similar within the subwavelength region of the indentation, which yields an equality between the two scattered fields with the use of the causality principle. Note that in Eq. 10.3b, $\tau_{SP} - 1$ represents the transmitted SPP amplitude that is scattered by the indentation.

10.6.2 Multiple-Scattering Model with Surface Plasmon Polaritons and Quasi-Cylindrical Waves

In addition to providing closed form expressions, the main force of the pure-SPP model is to propose an intuitive and physical wavy description of the multiple scattering processes involved at metallic subwavelength interfaces. In order to make the model more accurate, one should introduce the quasi-CW into the pure-SPP formalism, and define scattering coefficients for quasi-CWs, including the CW-to-CW scattering and the cross conversion as discussed in the Sect. 10.6.1.

To derive a generalized formalism, it is convenient to introduce the concept of hybrid waves (HWs) [17]. For 1D subwavelength indentations, the generalized wavy formalism relies on two main ingredients. The first ingredient is related to the overall shape of the field scattered by subwavelength indentations on metallic surfaces. This shape is always composed of a known mixing ratio of SPP and quasi-CW waves at a given frequency, and the respective contributions are fixed, independently of the excitation field and of the exact geometry of the indentation (provided that the indentation is subwavelength, indeed). The property is illustrated in Fig. 10.10, which shows the fields scattered on the metal interface for several subwavelength indentations and for various incident illuminations. The fields are calculated with a fully vectorial method and are normalized so that their amplitude are all equal at a distance $|x| = \lambda$ from the indentation. Remarkably, it is found that for every frequency, all the scattered fields are identical, except for a proportionality factor.

This important property comes from the fact that under TM-polarized illumination, any 1D subwavelength indentation can be approximated by two coherent

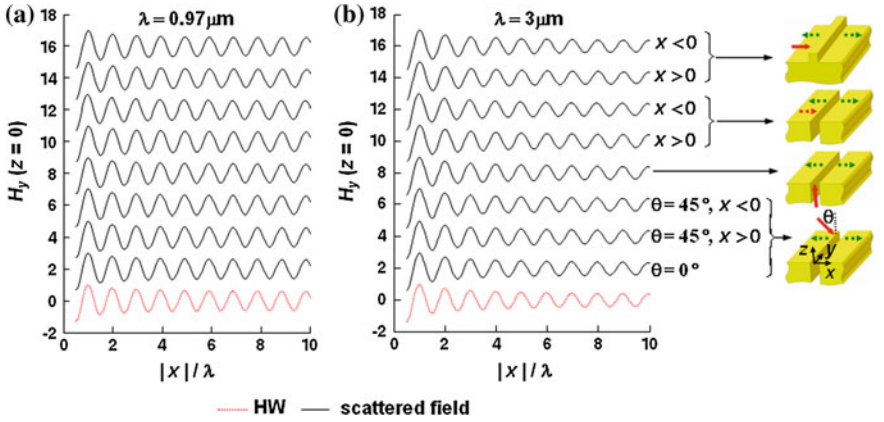

Fig. 10.10 Field scattered by a single 1D subwavelength indentation on a metallic surface under TM-polarized illumination [17]. **a–b** Magnetic fields H_y scattered on the surface (at $z = 0$) for $\lambda = 0.97$ and 3 μm. They are vertically shifted by 2 and normalized such that $H_y(|x| = \lambda) = 1$. The *black solid curves* are data calculated with the fully vectorial method and the two *red dashed curves* show the HW calculated as the radiation of a y-polarized magnetic line source on the surface. The results are gathered for gold slits and ridges with widths 0.27λ and ridge height 0.27λ. From bottom to top, the illuminations are a plane wave, the fundamental slit TEM_{00} mode, a HW generated by a magnetic line source located on the surface at $x = -\lambda$, and a SPP mode. The *dashed* and *solid arrows* on the surface represent HWs and SPPs, respectively, the *arrows* in the slit represent fundamental slit modes, and other *arrows* in free space represent plane waves. The *arrows* denoting incident and scattered waves are in *red* and in *green*, respectively. This notation of *arrows* is consistently used throughout the chapter

electric line sources, one with a polarization parallel to the surface and the other with a polarization perpendicular, and that the radiations of these two sources are *approximately* equal (they are strictly equal in the limit of large metal conductivity). This has been shown in [14] by an analytical treatment. In particular, the scattered fields are composed of a SPP and of a quasi-CW with a fixed mixing ratio, and thus this mix forms a new wave with universal properties [we call a hybrid wave (HW) hereafter]. Note that the HW is nothing else than the Green function of a metal-dielectric interface for a dipole line source on the interface. The only new point we stress here is that the Green function is *almost* independent of the line source polarization (it is "degenerate").

Therefore, in the multiple scattering processes of any subwavelength metallic surfaces, SPPs and quasi-CWs only appear in a fixed proportion at a given frequency, or in another word, only HWs exist on the surface. This property largely simplifies the introduction of the quasi-CW into the pure-SPP model, since the four scattering processes, the SPP-to-SPP, CW-to-SPP, SPP-to-CW and CW-to-CW, may be combined into a single HW-to-HW scattering process.

The second ingredient of the generalized wavy formalism is the definition of scattering coefficients for HW. Although HWs are not normal modes (just like quasi-CWs, they are not exponentially damped, they do not possess phase or group

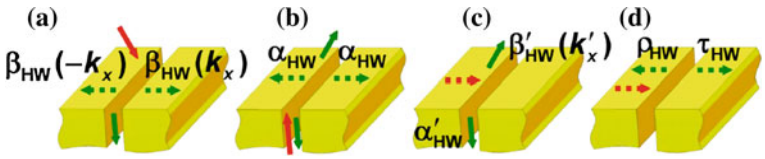

Fig. 10.11 HW Scattering coefficients for a slit. **a**–**b** Scattering coefficients $\beta_{HW}\, k_x)$ or α_{HW} corresponding to HW excitations under illumination either by a TM-polarized incident plane wave with an in-plane parallel wave vector k_x or by the fundamental slit mode. **c** Reciprocal scattering coefficients $\beta'_{HW}(k'_x)$ and α'_{HW} under illumination by HWs, where k'_x denotes in-plane parallel wave vectors of scattered plane waves. **d** In-plane scattering coefficients τ_{HW} and ρ_{HW} that characterize the transmission and the reflection of HWs by the slit

velocities …), it can be shown that it is possible to define scattering coefficients for HWs, in the same way as scattering coefficients have been defined for the bound SPP modes in Sect. 10.5 (see Fig. 10.7), and that the scattering coefficients are equal to those of the SPP. For instance, if we refer to the HW scattering coefficients in Fig. 10.11 for a semi-infinite slit, all the HW scattering coefficients can be related to the classical SPP scattering coefficients, and as shown in [17], we may write

$$\beta_{HW}(k_x) = \beta_{SP}(k_x),\ \alpha_{HW} = \alpha_{SP}, \tag{10.4a}$$

$$\beta'_{HW}(k'_x) = \beta'_{SP}(k'_x),\ \alpha'_{HW} = \alpha'_{SP}, \tag{10.4b}$$

$$\rho_{HW} = \rho_{SP},\ \tau_{HW} = \tau_{SP} - 1, \tag{10.4c}$$

where the subscripts HW and SP refer to HW and SPP, respectively. Equations (10.4a–c) are remarkably simple and readily relate non-intuitive HW scattering coefficients to much classical SPP coefficients that are routinely calculated with various numerical tools. Additionally, they allow us to preserve the intuitive picture of a microscopic wave progression, and to explicitly analyze the macroscopic properties of metallic surface in terms of a multiple scattering process. The equalities between the HW scattering coefficients and their associated SPP ones are justified in [17]. Although the HW scattering coefficients may be directly extracted from the calculated scattered field, this calculation cannot benefit from classical normal-mode theory [34] since the HW is not a mode. Equations (10.4 a–c) render the calculations of the HW scattering coefficients much simpler, since the coefficients can be obtained directly from the scattering coefficients of SPPs, and therefore reciprocity arguments (under proper normalization [17]) may be applied even if the HWs are not normal modes.

From the elementary HW scattering coefficients, it is easy to derive a coupled-wave model that provides closed-form expressions for the transmittance and reflectance (thus absorbance) of subwavelength metallic surfaces. In [17], the model has been tested for various geometries such as grooves and ridges, or mix of grooves and ridges. In all cases, comparisons with fully vectorial computational results have

revealed that the generalized formalism is highly accurate, even when the indentation dimensions are as large as $\lambda/3$. Similar results have been reported in [12, 15] for other geometries. The generalized formalism has also been successfully applied for the EOT, see [17] for details. In the generalized formalism, the reflection coefficient r_A of the fundamental supermode of the hole array is given by

$$\mathbf{r}_A = r + \frac{2\alpha_{SP}^2}{(1/\Sigma H_{HW} + 1) - (\rho_{SP} + \tau_{SP})}. \tag{10.5}$$

Actually Eq. 10.5 is very similar to that obtained with the pure-SPP model, see Eq. 10.2, except that the SPP phase-term u^{-1} is replaced by $(1/\Sigma H_{HW} + 1)$, where ΣH_{HW} is a lattice summation of the HW fields that is known analytically [17]. As shown with the black dash-dot curves in Fig. 10.8, the HW model accurately predicts the EOT from visible to middle-infrared bands. Other computations have shown that the reflectance and the absorbance are also predicted with a high accuracy. It is important to realize that the HW model does not require additional computations, in comparison to the pure-SPP model. Importantly, it relies on the same SPP scattering coefficients, which are therefore found to play a fundamental role in the electromagnetic properties of subwavelength metallic surfaces.

10.7 Conclusion

Many optical phenomena related to subwavelength metallic surfaces, which are observed with metallic nanostructures at visible frequencies, can be "reproduced" at longer wavelengths by scaling the geometrical parameters. At an elementary level, these phenomena are due to the electromagnetic fields that are scattered by the indentations and that interact with the neighbor indentations. For visible wavelengths, the analysis promotes an interaction mediated by surface-plasmon-polaritons (SPPs) and supplemented at distances up to a few wavelengths by an additional scattered near-field, the quasi-cylindrical wave (quasi-CW). At longer wavelength, because they spread far away into the dielectric medium, the delocalized SPPs are marginally excited by the indentations and the quasi-CWs are dominant (Sect. 10.4).

The two-wave picture represents a helpful microscopic view to comprehend the rich physics of subwavelength metallic surfaces. The SPP and quasi-CW scattering involves SPP-to-SPP and CW-to-CW scatterings, CW-to-SPP and SPP-to-CW cross conversions, and scattering into radiation modes. All those scattering coefficients, some of them being non trivial, are quantitatively equal to SPP-scattering coefficients (Sect. 10.6). This places SPP scatterings at the root of the physics of subwavelength metallic surfaces, even when quasi-CWs are dominantly excited like in the infrared. The important fact that quasi-CWs and SPPs essentially scatter identically is at the core of the concept of hybrid-waves (Sect. 10.6.2).

After 100 years or more, research in the area of subwavelength metallic surfaces and gratings continues unabated. This reflects the underlying importance of metal to manipulate light. It is likely that this situation will continue. The use of interfaces possessing complex subwavelength textures is really only beginning and the microscopic point of view presented here may help to understand and to design the surfaces. It is hoped that this review will stimulate new ideas and lead to new research.

Acknowledgments Haitao Liu acknowledges financial supports from the National Natural Science Foundation of China (No. 10804057), from the Cultivation Fund of the Key Scientific and Technical Innovation Project, Ministry of Education of China (No. 708021), from the 973 Project (No. 2007CB307001), and from the Natural Science Foundation of Tianjin (No. 11JCZDJC15400). Jean Claude Rodier, Lionel Aigouy, Xiaoyan Yang, Jacques Giérak, Eric Bourhis, Christophe Sauvan, Stéphane Collin, Lionel Jacobowiez and Jean Paul Hugonin are acknowledged for fruitful discussions.

References

1. L. Aigouy, P. Lalanne, J.P. Hugonin, G. Julie, V. Mathet, M. Mortier, Near-field analysis of surface waves launched at nanoslit apertures. Phys. Rev. Lett. **98**, 153902 (2007)
2. A. Banos, *Dipole Radiation in the Presence of a Conducting Half-Space* (Pergamon Press, Oxford, 1966)
3. W.L. Barnes, Topical review: fluorescence near interfaces: the role of photonic mode density. J. Mod. Opt. **45**, 661–699 (1998)
4. F. van Beijnum, C. Rétif, C.B. Smiet, H.T. Liu, P. Lalanne, M.P. van Exter, Quasi-Cylindrical Wave Contribution in Experiments on Extraordinary Optical Transmission, Nature. **492**, 411–414 (2012)
5. L. Chen, J.T. Robinson, M. Lipson, Role of radiation and surface plasmon polaritons in the optical interactions between a nano-slit and a nano-groove on a metal surface. Opt. Express **14**, 12629 (2006)
6. R.E. Collin, Hertzian dipole radiating over a lossy earth or sea: some early and late 20th century controversies. IEEE Antennas Prop. Mag. **46**, 64 (2004)
7. W. Dai, C. Soukoulis, Theoretical analysis of the surface wave along a metal-dielectric interface. Phys. Rev. B **80**, 155407 (2009)
8. H. Ditlbacher, J.R. Krenn, G. Schider, A. Leitner, F.R. Aussenegg, Two-dimensional optics with surface plasmon polaritons. Appl. Phys. Lett. **81**, 1762–1764 (2002)
9. T.W. Ebbesen, H.J. Lezec, H.F. Ghaemi, T. Thio, P.A. Wolff, Extraordinary optical transmission through subwavelength hole arrays. Nature **391**, 667–669 (1998)
10. U. Fano, The theory of anomalous diffraction gratings and of quasi-stationary waves on metallic surfaces (Sommerfeld's waves). J. Opt. Soc. Am. **31**, 213–222 (1941)
11. G. Gay, O. Alloschery, B. Viaris de Lesegno, C. O'Dwyer, J. Weiner, and H.J. Lezec, The optical response of nanostructured surfaces and the composite diffracted evanescent wave model. Nat. Phys. **2**, 262–267 (2006)
12. X. Huang, M.L. Brongersma, Rapid computation of light scattering from aperiodic plasmonic structures. Phys. Rev. B **84**, 245120 (2011)
13. P. Lalanne, J.P. Hugonin, Interaction between optical nano-objects at metallo-dielectric interfaces. Nat. Phys. **2**, 551–556 (2006)
14. P. Lalanne, J.P. Hugonin, H.T. Liu, B. Wang, A microscopic view of the electromagnetic properties of sub-λ metallic surfaces. Surf. Sci. Rep. **64**, 453–469 (2009)
15. G.Y. Li, F. Xiao, L. Cai, K. Alameh, A.S. Xu, Theory of the scattering of light and surface plasmon polaritons by finite-size subwavelength metallic defects via field decomposition. New J. Phys. **13**, 073045 (2011)

16. H.T. Liu, P. Lalanne, Microscopic theory of the extraordinary optical transmission. Nature **452**, 728–731 (2008)
17. H.T. Liu, P. Lalanne, Light scattering by metallic surfaces with subwavelength patterns. Phys. Rev. B **82**, 115418 (2010)
18. L. Martín-Moreno, F.J. García-Vidal, H.J. Lezec, K.M. Pellerin, T. Thio, J.B. Pendry, T.W. Ebbesen, Theory of extraordinary optical transmission through subwavelength hole arrays. Phys. Rev. Lett. **86**, 1114–1117 (2001)
19. A.Y. Nikitin, S.G. Rodrigo, F.J. Garcìa-Vidal, L. Martìn-Moreno, In the diffraction shadow: Norton waves versus surface plasmon polaritons in the optical region. New J. Phys. **11**, 123020 (2009)
20. A.Y. Nikitin, F.J. Garcìa-Vidal, L. Martìn-Moreno, Surface electromagnetic field radiated by a subwavelength hole in a metal film. Phys. Rev. Lett. **105**, 073902 (2010)
21. K.A. Norton, Propagation of radio waves over a plane earth. Nature **135**, 954 (1935)
22. K.A. Norton, The propagation of radio waves over the surface of the earth and in the upper atmosphere. Proc. IRE **24**, 1367–1387 (1936)
23. K.A. Norton, The propagation of radio waves over the surface of the earth and in the upper atmosphere. Proc. IRE **25**, 1203–1236 (1937)
24. E.D. Palik (ed.), in *Handbook of Optical Constants of Solids*, Part **II**(1) (Academic Press, New York, 1985)
25. H. Raether, *Surface Plasmons on Smooth and Rough Surfaces and on Gratings* (Springer, Berlin, 1988)
26. L. Rayleigh, On the Dynamical Theory of Gratings. Proc. R. Soc. (London) A. **79**, 399–416 (1907)
27. R.H. Ritchie, Plasma losses by fast electrons in thin films. Phys. Rev. **106**, 874–881 (1957)
28. M. Righini, A.S. Zelenina, C. Girard, R. Quidant, Parallel and selective trapping in a patterned plasmonic landscape. Nat. Phys. **3**, 477–480 (2007)
29. A. Sommerfeld, The broadening of the waves and the wireless telegraph. Ann. der Physik **28**, 665–736 (1909)
30. A. Sommerfeld, The propagation of waves in wireless telegraphy. Ann. der Physik **81**, 1135–1153 (1926)
31. M. Specht, J.D. Pedarning, W.M. Heckl, T.W. Hänsch, Scanning plasmon near-field microscope. Phys. Rev. Lett. **68**, 476–479 (1992)
32. J. Strong, Effect of evaporated films on energy distribution in grating spectra. Phys. Rev. **49**, 291–296 (1936)
33. B. Ung, Y.L. Sheng, Optical surface waves over metallo-dielectric nanostructures. Opt. Express **16**, 9073–9086 (2008)
34. C. Vassallo, *Optical Waveguide Concepts* (Elsevier, Amsterdam, 1991)
35. R.W. Wood, On a remarkable case of uneven distribution of light in a diffraction grating spectrum. Philos. Mag. **4**, 396–402 (1902)
36. X.Y. Yang, H.T. Liu, P. Lalanne, Cross conversion between surface plasmon polaritons and quasicylindrical waves. Phys. Rev. Lett. **102**, 153903 (2009)
37. I. Zenneck, Propagation of plane electromagnetic waves along a plane conducting surface and its bearing on the theory of transmission in wireless telegraphy. Ann. Phys. **23**, 846 (1907). http://web.mit.edu/redingtn/www/netadv/zenneck.html
38. N.I. Zheludev, S.L. Prosvirnin, N. Papasimakis, V.A. Fedotov, Lasing spaser. Nat. Photon. **2**, 351 (2008)

Chapter 11
Plasmonic Functionalities Based on Detuned Electrical Dipoles

Anders Pors, Michael G. Nielsen and Sergey I. Bozhevolnyi

Abstract We introduce and demonstrate the concept of detuned electrical dipoles (DED) that originates from the plasmonic realization of the dressed-state picture of electromagnetically induced transparency in atomic physics. Numerically and experimentally analyzing DED metamaterials consisting of unit cells with two and three differently sized gold nanorods, we show the possibility of optical transparency characterized by enhanced transmission, reduced group velocity and propagation loss. The concept of DED is further applied to plasmonic sensing of the environment, demonstrating unprecedented sensitivity to refractive index changes by the utilization of scattering asymmetry. By the similar concept, DED metamaterials are designed to function as nanometer-thin wave plates in reflection.

11.1 Introduction

In recent years there has been an explosive growth in research activities devoted to investigating and designing new artificial materials, called metamaterials, with strikingly new optical properties. Metamaterials are made of conventional (natural) materials that are structured on a scale considerably smaller than the wavelength of light used. Consequently, one can introduce effective material parameters reducing

A. Pors (✉)
Mads Clausen Institute (MCI), University of Southern Denmark, Alsion 2,
DK-6400 Sønderborg, Denmark
e-mail: pors@mci.sdu.dk

M. G. Nielsen · S. I. Bozhevolnyi
Institute of Technology and Innovation (ITI), University of Southern Denmark, Niels Bohrs Allé 1, DK-5230 Odense M, Denmark
e-mail: mgni@iti.sdu.dk

S. I. Bozhevolnyi
e-mail: seib@iti.sdu.dk

T. V. Shahbazyan and M. I. Stockman (eds.), *Plasmonics: Theory and Applications*, Challenges and Advances in Computational Chemistry and Physics 15,
DOI: 10.1007/978-94-007-7805-4_11, © Springer Science+Business Media Dordrecht 2013

nanostructured heterogeneous (composite) materials to homogeneous metamaterials, whose effective parameters exhibit new optical properties that can even be inaccessible with natural materials. An interesting application of metamaterial dispersion engineering, is the imitation of electromagnetically induced transparency (EIT), which has attracted much attention [1–5] due to the possibility of slowing light down, enhancing nonlinear interactions and improving the sensitivity of metamaterial-based nanosensors. Similarly, the classical realization of electromagnetically induced absorption, which is the complementary phenomenon of EIT, has also received some attention [6], though the less apparent usage within applications has limited the general interest.

The phenomenon of EIT is based on the laser induced coherence of atomic states leading to quantum interference between the excitation pathways controlling the optical response, which is thereby modified exhibiting enhanced transmission [7, 8]. The strongly enhanced transmission within the absorption band results in strong dispersion and consequently in a significant reduction in the group velocity (see e.g. [8] and references therein). Slowing down the propagation of light pulses enhances light-matter interactions, allowing one, for example, to boost optical nonlinearities and to tackle the tantalizing problem of an all-optical buffer [9].

The phenomenon of EIT can be considered in two alternative ways: as resulting from the destructive interference between two pathways involving either the bare, dipole-allowed and metastable states or, equivalently, the doublet of dressed states (created by strong pump radiation) representing two closely spaced resonances decaying to the same continuum [7, 8]. While these two physical pictures are equivalent when dealing with EIT in atomic systems, their realization with plasmonic nanostructures, whose responses are determined by their configurations and not electromagnetically induced as in EIT, depends on the EIT mechanism that is imitated. The first picture suggests employing radiative and subradiant (dark) plasmonic elements that are strongly coupled by being closely placed and appropriately oriented [1–3, 5]. Note that the strong-coupling condition imposes rather stringent requirements on the fabrication accuracy for the plasmonic structures to be operated at optical wavelengths [1]. Alternatively viewed, EIT is achieved due to the cancellation of opposite contributions from two resonances, which are equally spaced but with opposite signs of detuning from the probe frequency, due to the Fano-like interference of the decay channels. Fundamentally, the dressed-state picture of EIT is equivalent to the case of interference between two closely spaced lifetime broadened resonances decaying to the same continuum [7]. The underlying physics of the cancellation of absorption in EIT is also similar to that involved in the phenomenon of coherent population trapping [8]. Metamaterials utilizing trapped-mode resonances and featuring the EIT-like transmission spectra have been realized in the cm-wavelength range using fish-scale patterns [2] and concentric ring resonators [10]. In both configurations, electrical currents induced (at the trapped-mode resonance frequency) in different parts of a unit cell oscillate with opposite phases, resulting in scattering suppression and enhanced transmission.

It should be emphasized that the EIT realization with plasmonic nanostructures is fundamentally different from EIT in atomic systems with respect to the linewidths of

resonances involved: while atomic resonances are lifetime broadened, the linewidth of plasmonic resonances is determined not only by radiation damping but also by absorption, i.e. by direct loss of photons. In this case, the EIT phenomenon manifests itself as the *scattering suppression*, whereas the absorption (becoming progressively more important and even dominant at optical frequencies) is mainly determined by the fundamental material properties and is impossible to eliminate no matter which EIT realization approach is chosen [11]. For this reason, one should not expect to achieve complete transparency when dealing with plasmonic nanostructures, as also seen from the reported simulations [1, 12] and experiments [5].

We investigate in detail the optical properties of periodic arrays of paired gold nanorods having different lengths. Essentially, the nanorod pairs represent two or three dipolar scatterers resonating at different frequencies, i.e. detuned electrical dipoles (DED), whose detuning is simply determined by their difference in length. We demonstrate that the transmission spectra exhibit windows of enhanced transmission surrounded on both sides by transmission minima, a phenomenon that we have attributed to the effect of optical transparency that emulates the dressed-state picture of EIT [13]. We consider this intriguing effect from different viewpoints in detail by numerical simulations and experiments. Additionally, we also demonstrate that DED arrays can advantageously be used for very sensitive monitoring of environmental refractive index, i.e. for plasmonic sensing [14] and as ultrathin metamaterial wave retarders in reflection [15].

11.2 Detuned Electrical Dipole Metamaterials: Optical Transparency and Slow Light

The concepts of optical transparency and slow light with DEDs can be illustrated by considering a metamaterial with the unit cell consisting of two nearly identical and non-interacting electric dipolar scatterers, whose resonances are equally detuned from the central frequency ω_0 so that their dipole polarizabilities can be represented as

$$\alpha_{1(2)}(\omega) = \frac{A\omega_0^2}{(\omega_0 \pm \Delta)^2 - \omega^2 - i\Gamma\omega}, \tag{11.1}$$

where Δ is the DED detuning frequency, Γ is the damping factor and A characterizes their strength [14]. This type of polarizabilities can readily be implemented in plasmonics for optical frequencies, e.g. with metal nanoshells or nanorods whose resonances can be adjusted by tuning the shell inner-to-outer radius ratio [16] or the rod aspect ratio [17], respectively. In the effective medium theory (EMT) with the unit cell being much smaller than the light wavelength (see, e.g., [18] and references therein), the response of the unit cell is determined (irrespective of the dipole positions) by the sum of two polarizabilities, $\alpha_1 + \alpha_2$. For frequencies close to the central frequency, $\delta = \omega - \omega_0 \ll \omega_0$, and weak detuning ($\omega_0 \gg \Delta, \Gamma \gg \delta$), the DED response can then be expressed with the first-order approximation as [see Eq. (11.1)]

$$\alpha_1 + \alpha_2 \simeq 2A\omega_0 \left[\delta \frac{2(4\Delta^2 - \Gamma^2)}{(4\Delta^2 + \Gamma^2)^2} + i \frac{\Gamma}{4\Delta^2 + \Gamma^2} \right], \tag{11.2}$$

implying strong suppression of scattering, i.e. a regime of optical transparency, at the central frequency ω_0 ($\delta = 0$).

In the EMT framework [18], the effective dielectric susceptibility of metamaterials consisting of DED pairs in vacuum (with sufficiently low concentrations N) can be approximated within the transparency window by that of non-interacting unit cells,

$$\epsilon_{eff} \simeq 1 + N(\alpha_1 + \alpha_2). \tag{11.3}$$

We have recently shown [13], that the total polarizability expressed by Eq. (11.2) is directly comparable with the susceptibility of an effective medium consisting of plasmonic molecules, in which a radiative element is coupled with a subradiant (dark) element (see Eq. (11.3) in [1]). One notices that both expressions are similar in form, becoming quantitatively similar if $2\Delta = \kappa$ and $\Gamma^2 \simeq \gamma_a \gamma_b$, where κ is the coupling between the two elements with their damping factors being γ_a and γ_b. Note that the electrostatic limit for quality factors of localized plasmon resonances [19], which is difficult to exceed [20], implies that the latter condition becomes progressively more realistic for optical frequencies because of the dominance of absorption in extinction of plasmonic nanostructures [21].

The aforementioned similarity has a deep physical meaning related to the *equivalence* of the bare- and dressed-state pictures of the EIT [7, 8]. Mathematically, transformation from the former to the latter occurs by the transition to another (rotating) coordinate system, in which the interaction operator is diagonal. In classical optics, similar equivalence is found, for example, when considering the power exchange between two waveguides in a directional coupler to be a result of the coupling between two modes of individual waveguides or due to the interference of two super-modes of a two-waveguide system [22]. In any case, splitting between eigenvalues of super-modes is proportional to the coupling between two individual oscillators (e.g. in our case: $2\Delta = \kappa$), a feature that is found in many classical and quantum mechanical systems. It is, however, important, from the viewpoint of EIT realization with plasmonic nanostructures, that the strong-coupling condition with its stringent fabrication requirements [1, 5] can be traded for the detuning condition requiring dipolar scatterers to resonate at different frequencies. The latter seems more amenable to being implemented in practice.

Slowing light down within the transparency window is probably the most striking effect associated with EIT [8]. Using the EMT approach described above [Eq. (11.3)] and the condition $N\mathrm{Re}(\alpha_1 + \alpha_2) \ll 1$ (that can be satisfied near the central frequency [Eq. 11.2]), the group index determining the light slowdown can be expressed as

$$n_g \simeq 1 + \frac{\omega N}{2} \frac{\mathrm{dRe}(\alpha_1 + \alpha_2)}{\mathrm{d}\omega}. \tag{11.4}$$

An increase in the group index can thereby be traced to the dispersion of the real part of cell polarizability, resulting in [see Eq. (11.2)]

$$\left.\frac{\mathrm{d}[\mathrm{Re}(\alpha_1+\alpha_2)]}{\mathrm{d}\omega}\right|_{\omega_0} \simeq 4A\omega_0\frac{4\Delta^2-\Gamma^2}{(4\Delta^2+\Gamma^2)^2}. \tag{11.5}$$

It should be borne in mind that the group velocity is generally not a useful concept in regions of anomalous dispersion [23] and that the above relation should therefore be considered only for relatively large detuning: $\Delta > 0.5\Gamma$. In the case of normal dispersion at the probe frequency, one can show that the group refractive index exhibits a broad maximum at $\Delta_{opt} = \sqrt{0.75}\Gamma$. A similar condition of the detuning to be close to the broadening of two resonances is also found in the dressed-state picture of the EIT for atomic media [7, 8]. Finally, the above condition [Eq. (11.5)] being obtained in the approximation of non-interacting dipolar scatterers should be considered only as an estimate of the optimum DED detuning, with a careful optimization yet to be conducted for a given DED configuration designed to operate in a given frequency range. In the following, we therefore study a realistic DED configuration consisting of two differently-sized and weakly-interacting gold nanorod antennas numerically, and address the intriguing phenomena of optical transparency and slow light.

11.2.1 The Two-Nanorod System

The DED concept deals, in principle, with any imaginable configuration that displays scattering suppression in between the detuned resonances. In this section, however, the concept will be further elucidated by considering the simplest DED configuration: two detuned nanorods (Fig. 11.1a). At first, the optical properties of a single two-nanorod configuration will be discussed with emphasis on the electric and magnetic responses, followed by a discussion of two-nanorod metamaterials and its ability to slow down light near the central frequency.

In the following we consider gold nanorods with cross-sections of $w \times w = 25 \times 25\,\mathrm{nm}^2$, lengths (i) L_1 and (ii) $L_2 = 150\,\mathrm{nm}$, respectively, and a center-to-center distance d. The surrounding medium is assumed to be glass with refractive index 1.45. It should be emphasized that when d and L_1 are not explicitly mentioned in this section, the configuration is considered with nominal values $d = 120\,\mathrm{nm}$ and $L_1 = 125\,\mathrm{nm}$. All modeling results presented throughout this chapter are conducted with the finite-element method implemented in the commercial software Comsol Multiphysics in which the dielectric function of gold is described by interpolation of tabular values [25]. In the simulations, all corners of the nanorods are rounded with a radius of 3 nm for numerical as well as physical reasons.

If a z-propagating x-polarized incident wave is considered, the individual nanorods [(i) and (ii)] exhibit fundamental plasmonic resonances at $\lambda \simeq 1065\,\mathrm{nm}$ and $\lambda \simeq 1190\,\mathrm{nm}$, respectively (Fig. 11.1b). These resonances are related to standing waves of short-range surface plasmon polaritons (SR-SPPs) [21] making it easy to control

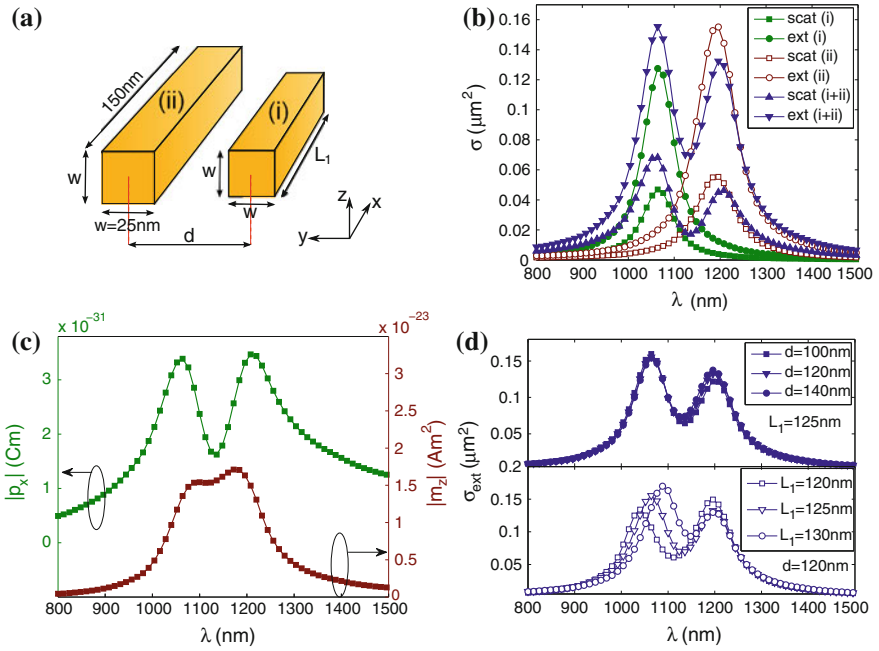

Fig. 11.1 **a** Sketch of the DED system consisting of two gold nanorods with square cross sections $w \times w$ but different lengths. The separation between the nanorods is denoted d. The surrounding medium is assumed to be glass with refractive index 1.45. **b** Scattering and extinction cross sections for DED system with nominal values $w = 25\,\text{nm}$, $L_1 = 125\,\text{nm}$ and $d = 120\,\text{nm}$. **c** The total electric and magnetic dipole moments for the nominal DED configuration. **d** Extinction spectra for varying separation d and length L_1. In all calculations the incident wave is x-polarized and propagates along the z-axis. Reproduced with permission from Ref. [24]. ©American Physical Society 2011

the resonance wavelengths as they scale to a good approximation linearly with the length of the nanorod [26, 27]. It can be seen that the extinction is significantly higher than the scattering implying that a significant fraction of the total loss in the nanorods is due to absorption. This is a consequence of the small geometrical cross section of the nanorods giving rise to a tightly bound SR-SPP mode with a high propagation loss [28]. From the point of view of EIT this is an undesirable effect as plasmonic EIT is *only* capable of suppressing scattering and not absorption [11]. For this more conceptual discussion, however, the choice of cross section is less relevant; the light will still be slowed down, although with a propagation loss that is higher than for larger cross sections. That said, the EIT effect is still evident for the nominal DED configuration (Fig. 11.1b) clearly displaying the transparency region at $\lambda \simeq 1130\,\text{nm}$ in which the out-of-phase (detuned) plasmonic currents in the nanorods suppress the total electric dipole moment ($|\mathbf{p}| = |p_x|$) and create a magnetic dipole moment along the z-direction (Fig. 11.1c). The electric and magnetic dipole moments are obtained by a multipole expansion of the induced current in the nanorods [29]. Importantly, the generated magnetic dipole moment and the magnetic

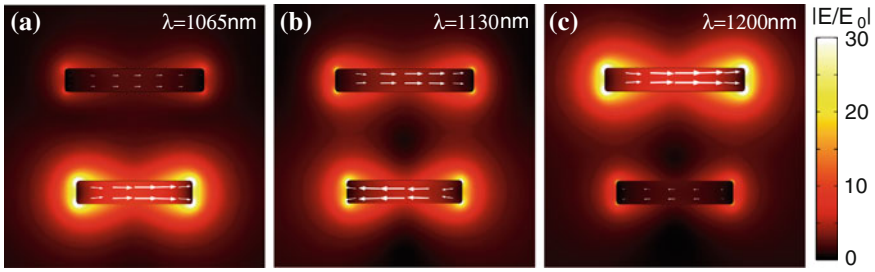

Fig. 11.2 Field plots of the eletric field enhancement for the nominal DED configuration with x-polarized incident wave that propagates along the z-axis. The arrows depict the induced plasmonic current at an representative time. The relative length of the arrows in the two nanorods represents the ratio in the current magnitude

field of the incident wave (pointing along the y-axis) are orthogonal to each other, which demonstrates that DED metamaterials consisting of two-nanorod unit cells must have a bianisotropic response as it is the incident electric field that generates the magnetic response. The presence of bianisotropy for the achiral DED structure implies that a metasurface of DED metamaterial would possess *optical activity* for oblique incident light; a property known a *extrinsic chirality* [30–32] that could be used to, e.g., design ultrathin polarization rotators. For a detailed discussion of the chirality parameter of the two-nanorod metamaterial, one should consult [24].

The underlying electrodynamics involved in the scattering suppression by the DED structure was originated from the reduction in the total electric dipole moment at the transparency wavelength (Fig. 11.1c). This fact is further illustrated by the electric field distributions in the x-y plane cutting through the middle of the nanorods calculated for different wavelengths (Fig. 11.2). It is seen that at the wavelengths of 1065 and 1200 nm associated with the resonances of the individual nanorods, electromagnetic excitations are almost exclusively located at the corresponding nanorods (Fig. 11.2a and c). At the transparency wavelength of 1130 nm, however, both nanorods are excited featuring oppositely induced plasmonic currents (Fig. 11.2b). The total electric dipole moment is thereby greatly reduced, resulting in suppression of scattering.

An important property of any nanostructure is the sensitivity to parameter variation due to the inevitable fabrication tolerances present in all techniques. Here, the dependence of d and L_1 on the extinction spectrum has been studied (Fig. 11.1d) demonstrating that the coupling between the nanorods is weak as the extinction is almost independent of the separation $d \in [100; 140]$ nm. This is indeed the main advantage of the DED configuration compared to the dipole-quadrupole antenna approach that relies on strong coupling [1, 5], and a consequence of the relatively large separation and detuning of the resonances. Similarly, the DED configuration is rather robust with respect to variations in $L_1 \in [120; 130]$ nm. The extinction spectra do show dependence on L_1, but for all considered lengths the spectra possess a transparency region within the broader extinction band.

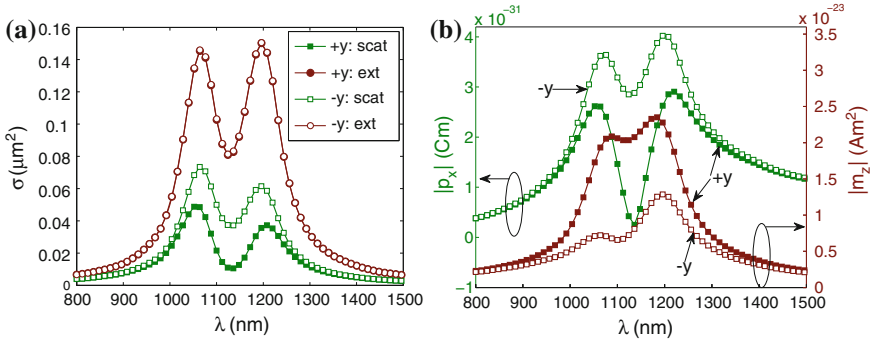

Fig. 11.3 **a** Scattering and extinction cross sections and **b** total electric and magnetic dipole moments for the nominal DED configuration. In the calculations the incoming plane wave is x-polarized and propagates along $\pm y$-axis. Reproduced with permission from Ref. [24]. ©American Physical Society 2011

If the direction of the incident wave is instead along the y-direction (still x-polarized), the optical properties of the DED configuration are strongly influenced whether the wave propagates in the ±y-directions (±y in Fig. 11.3). In accordance with the reciprocity principle,the extinction is the same for both propagation directions [coinciding curves in Fig. 11.3a] whereas the scattering, and consequently the absorption, depends on the propagation direction within the extinction band. In fact, at $\lambda = 1130\,\text{nm}$ the ratio of the scattered power for the two directions, i.e., $\sigma_{sc}^{(-y)}/\sigma_{sc}^{(+y)}$, is ∼3.5. The effect on the propagation direction is further elucidated by a multipole expansion (keeping only the electric and magnetic dipoles) of the induced plasmonic polarization current (Fig. 11.3b) clearly showing a stronger suppression (creation) of the electric (magnetic) dipole for the +y-direction. The origin of this effect is due to the phase change of the incident wave by kd (k being the wave number) across the DED structure, which enhances the phase difference between the plasmonic currents in the nanorods for the +y-direction, but in contrast reduces the phase difference for the −y-direction.

The remaining part of this section will be devoted to two-nanorod metamaterials for which the DED configuration constitutes the unit cell. The unit cell is chosen to be cubic with side length $\Lambda = 300\,\text{nm}$, and we will consider x-polarized light propagating along the z-axis. If a light pulse propagates through a DED metamaterial (or another dispersive medium), its group velocity will be slowed down by a factor equivalent to the group refractive index n_g, defined as

$$n_g = n - \lambda \frac{\partial n}{\partial \lambda}, \tag{11.6}$$

where n is the real part of the effective refractive index, $\tilde{n} = n + i\kappa$, and λ is the vacuum wavelength. It should be stressed that the group refractive index is only a

well-defined quantity in regions of normal dispersion ($\partial n/\partial\lambda < 0$) with relatively small absorption [23].

Another important parameter that characterizes the DED metamaterial is the loss associated with wave propagation through the medium. In the following we define the loss per unit cell (in dB) as

$$\text{Loss} = -10\log\left[\exp(-2k_0\kappa\Delta_z)\right], \tag{11.7}$$

where k_0 is the vacuum wave number, and Δ_z is the periodicity in the propagation direction. In order to evaluate the group refractive index and the loss, we must calculate the effective refractive index of the DED metamaterial. This is done by applying the eigenvalue-based homogenization method in [24], which computes the effective refractive index by calculating dispersion curves of Bloch modes in the DED metamaterial. The resulting refractive index is shown in Fig. 11.4(a), displaying strong dispersion near the central frequency with a minimum in κ. The group refractive index and the loss (per cell thickness) are then straightforwardly evaluated within the region of normal dispersion (Fig. 11.4b), demonstrating a group index of $\simeq$10 and loss of $\simeq$2.5 dB per 300-nm-thick unit cell.

Another important metamaterial characteristic relevant for EIT is the bandwidth-delay product (BDP) [9]. The BDP is a figure of merit for the ability of a structure to simultaneously delay a propagating pulse effectively while maintaining a large operation bandwidth. The delay time τ and the bandwidth $\delta\lambda$ are, in general, two opposing quantities, which is why their product is a descriptive measure of the performance. We define the transparency bandwidth as the increase in loss by 1 dB while the delay is defined as $\tau = L(n_g - n_d)/c$, where c is the speed of light in vacuum, L is the propagation length limited by the e^{-1}-level, and n_d is the refractive index of the surrounding medium ($n_d = 1.45$ in our case). Consequently, the BDP may be calculated as

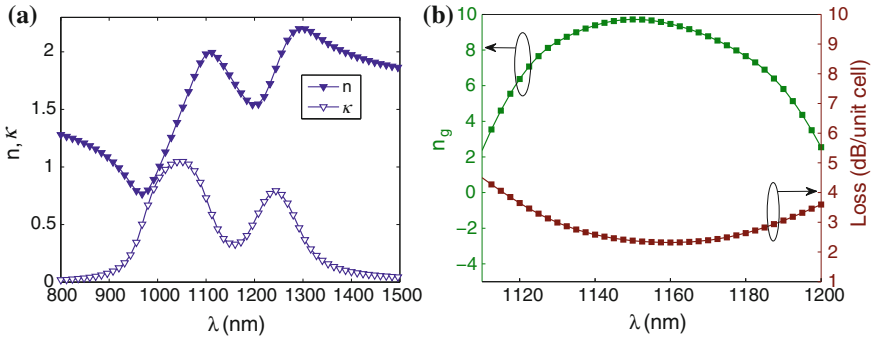

Fig. 11.4 **a** Dispersion of the effective refractive index of the nominal DED system experienced by a x-polarized and z-propagating incident wave and calculated using the eigenvalue-based homogenization method. The unit cell size is $300 \times 300 \times 300\,\text{nm}^3$. **b** The corresponding dispersion of the group refractive index and loss per unit cell for the same configuration as in **a**

$$\mathrm{BDP} = \tau\delta f = \frac{\delta\lambda L(n_g - n_d)}{\lambda^2}. \tag{11.8}$$

For the two-nanorod configuration (Fig. 11.4) we obtained $\delta\lambda \simeq 70\,\mathrm{nm}$ centered at the wavelength $\lambda \simeq 1150\,\mathrm{nm}$ and $L \simeq 0.55\,\mu\mathrm{m}$, which results in $\mathrm{BDP} \simeq 0.25$. It should be noted that a comparison of the main characteristics of the two plasmonic EIT realizations has been conducted in [13], demonstrating a *fundamental equivalence* between the two approaches, even though they are very different with respect to the fabrication tolerances required.

11.2.2 The Three-Nanorod System

The DED configuration considered above consists of two nanorods of different length and, consequently, polarizabilities of different strength. At the same time, as follows from the qualitative arguments in Sect. 11.2 [Eq. (11.2)], a prominent EIT effect depends on the cancellation of at least the real part of the *total* polarizability of the unit cell. This criteria might be easier to achieve by using *two* small nanorods resonating at a shorter wavelength being placed on both sides of the large nanorod resonating at a longer wavelength. The resulting structure is termed the three-nanorod configuration (Fig. 11.5a), and the EIT characteristics of the corresponding metamaterial is the subject of this section. The configuration is also included to illustrate the *versatility* of the DED concept. The configuration under study is made of two smaller gold nanorods of size $105 \times 40 \times 50\,\mathrm{nm}^3$ separated by a distance $d = 100\,\mathrm{nm}$ to the larger gold nanorod of size $150 \times 60 \times 50\,\mathrm{nm}^3$ (Fig. 11.5a). It should be noted that, to balance the scattering strengths of the longer nanorod and the two shorter nanorods, the latter was designed to be narrower. Also, the induced currents in the three-nanorod configuration do *not* induce a magnetic dipole at the central frequency, which suggests a relatively weak dependence of the transmission properties on the angle of incidence [10].

The EIT-properties of the three-nanorod DED metamaterial will be considered for x-polarized light propagating along the z-axis and a parallelepiped unit cell of size $300 \times 300 \times 150\,\mathrm{nm}^3$. In contrast to the previous section, the effective refractive index will be computed using the S-parameter method for which the retrieval procedure is based on transmission and reflection coefficients [33]. Figure 11.5b shows transmission and reflection spectra calculated for one layer of unit cell, exhibiting the EIT-like transmission spectra with window of transparency at $\sim$870 nm and a quite strong reflection away from the central wavelength, at which it is strongly suppressed. The fact that the reflection suppression is virtually complete at the central wavelength while the transparency is not agrees well with our general consideration of EIT realization with plasmonic nanostructures.

The transmission and reflection spectra calculated for three layers of unit cells were used to determine the dispersion of the corresponding metamaterial effective refractive index (Fig. 11.5c). Note the similarity of the dispersion of real and imaginary parts of the effective index to that obtained for the metamaterial using two

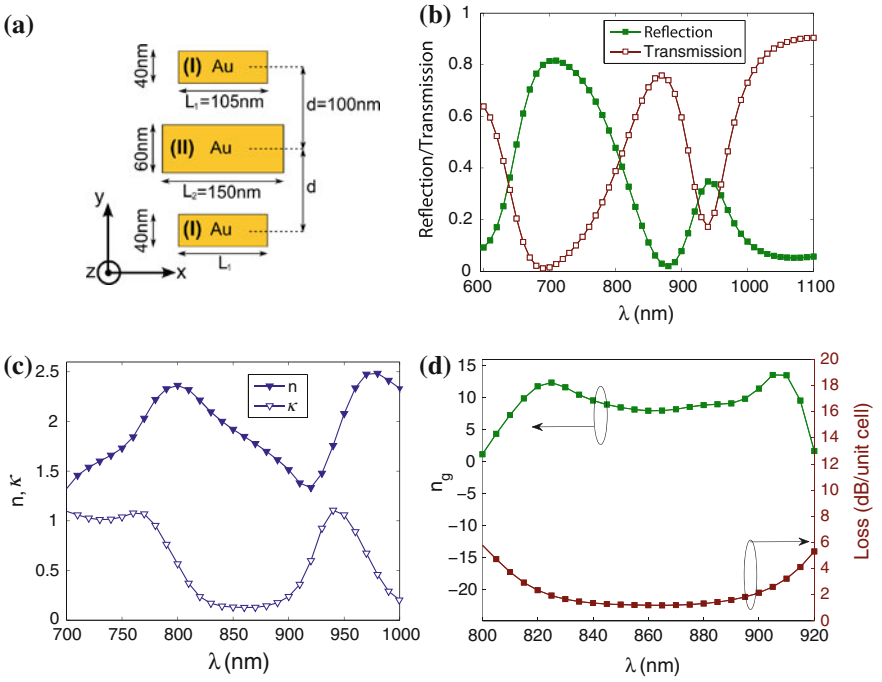

Fig. 11.5 **a** Top-view sketch of the three-nanorod DED system with the height of the nanorods (i.e., the dimension along the z-axis) being 50 nm. The nanorods are surrounded by glass with refractive index $n_d = 1.45$. **b** Transmission and reflection spectra calculated for one layer of unit cell with size $300 \times 300 \times 150\,\text{nm}^3$ for a x-polarized incident wave propagating along the z-axis. **c** Dispersion of the effective refractive index for the system in **a** calculated directly from the transmission and reflection by three layers of unit cells. **d** The corresponding dispersion of the group refractive index and loss per unit cell derived from **c**. Adapted with permission from Ref. [13], DOI: 10.1088/1367-2630/13/2/023034. ©Institute of Physics 2011

nanorods (Fig. 11.4a). The group refractive index and loss (per cell thickness) were computed from the corresponding refractive index dispersion, limited to the wavelength range of normal dispersion (Fig. 11.5d). The relevant metamaterial characteristics for EIT can now be evaluated, yielding a group refractive index $n_g \simeq 8$, bandwidth of $\delta\lambda \simeq 70\,\text{nm}$ centered at the wavelength $\lambda \simeq 860\,\text{nm}$, and propagation loss of 1 dB per 150-nm-thick unit cell resulting in a propagation length $L \simeq 0.65\,\mu\text{m}$. Using these data, the BDP takes on the value $\simeq 0.40$ which is noticeably higher than for the two-nanorod metamaterial, although the transparency region is at shorter wavelengths. The main reason for this difference is related to two facts: (i) the larger nanorod cross sections for the three-nanorod configuration imply that a larger part of the extinction is related to scattering (less bound SR-SPP modes) compared to the two-nanorod configuration, and (ii) the three-nanorod configuration is slightly better at suppressing the scattering at the central wavelength. Finally, it is worth

noting that both the two- and three-nanorod metamaterials show BDPs that are favorably comparable to other EIT realizations using coupled split-ring resonators [3] or waveguide-coupled plasmonic antennas [12].

11.2.3 Experimental Study of Detuned Electrical Dipole Metamaterials

In this section we investigate the DED metamaterials comprised of two and three gold nanorods experimentally. Specifically, the investigated samples consist of a silica substrate with DEDs defined by electron-beam lithography (EBL) and fabricated by lift-off of a 55 nm thick gold film, deposited by electron beam evaporation on top of a 5 nm thick titanium adhesion layer. DED arrays comprised of two nanorods are fabricated with a 300 nm period (Fig. 11.6a), whereas the DEDs comprised of three nanorods are fabricated with a 400 nm period (Fig. 11.6d). Furthermore, in order to ensure a nearly symmetric environment (phase matching) the sample is covered with a $\sim$15 μm thick layer of polymethyl methacrylate (PMMA) by spin coating.

In order to measure the transmission spectra (Fig. 11.6b and e), light from a broad band halogen light source with a fiber output, whose (weakly divergent) radiation is directed (at normal incidence) through a polarizer, is incident upon the sample with the electric field aligned to the axes of the gold nanorods in the array. After transmission through the sample the transmitted light is collected by an objective with 60x magnification and 0.85 numerical aperture, sent through an analyzer (parallel to the polarizer) and finally collected by an optical fiber connected to a VIS/NIR spectrometer. Reflection spectra (Fig. 11.6b and e) of the DED arrays are measured in a similar manner, where the incident polarized light is focused onto the sample with the aforementioned objective, collected by the same objective, sent through the analyzer and collected by the fiber connected to the VIS/NIR spectrometer. The transmission spectra are afterwards normalized by the transmission measured outside the DED arrays whereas the reflection spectra are normalized using the reflection measurements from a 300 nm thick gold sample and afterwards weighted with the reflectivity calculated from tabular values of the gold optical constants [25].

Along with the experimental investigations, the transmission and reflection spectra for one layer of DED unit cells, with dimensions similar to those in the experiment, are simulated. In the simulation, the gold nanorods are embedded in a lossless dielectric with refractive index $n_d = 1.5$, i.e. in a homogeneous dielectric with optical properties similar to those of PMMA. The choice of PMMA in the simulations rather than silica ($n_d = 1.45$) is due to the fact that in the experiment the DEDs are situated on top of the silica and covered with PMMA. It is therefore expected that a larger part of the electric field of the plasmonic resonances are concentrated at the high index side of the sample. The transmission and reflection spectra (Fig. 11.6c and f), exhibit two resonances separated by a window of enhanced transmission and, correspondingly, reduced reflection, i.e. EIT-like behavior due to scattering suppression in between the resonances. In general, there is quite good

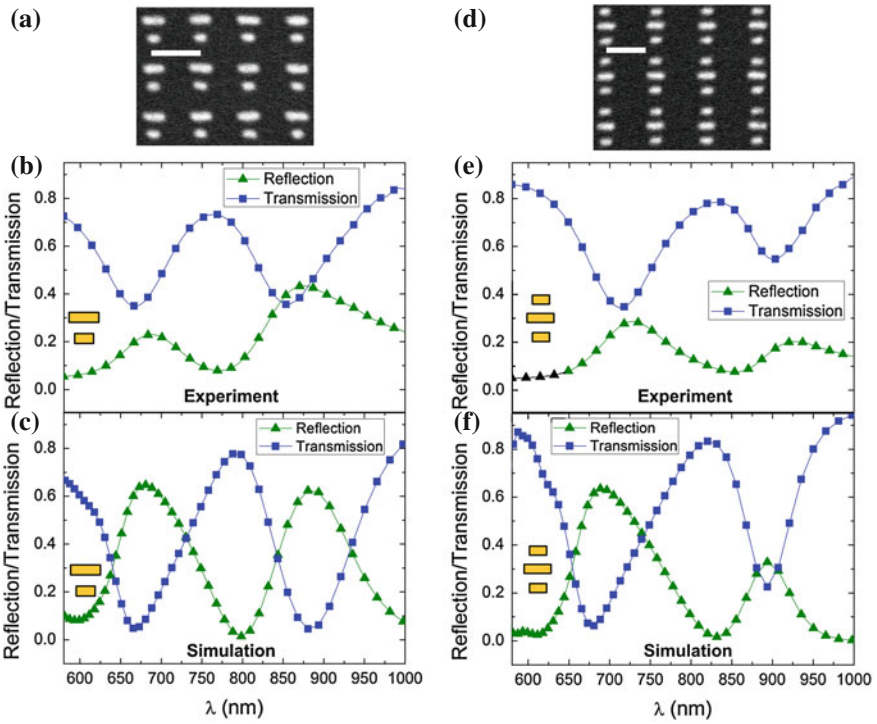

Fig. 11.6 Representative SEM-images (scale bars: 300 nm) along with experimental and simulated reflection and transmission spectra of the DED metamaterial consisting of unit-cells with **a**–**c** two nanorods positioned with a period of 300 nm and **e**–**f** three nanorods positioned with a period of 400 nm. For the two nanorod metamaterial, the nanorod center-to-center distance is 110 nm, whereas the widths and lengths are 55 and 85 nm, respectively, of the short nanorod and 55 and 140 nm, respectively, of the long nanorod. For the three nanorod metamaterial, the nanorod center-to-center distances are 110 nm, whereas the widths and lengths are 50 and 90 nm, respectively, of the two short nanorods and 60 and 135 nm, respectively, of the long nanorod. Reproduced with permission from Ref. [34], DOI: 10.1088/2040-8978/13/5/055106. ©Institute of Physics 2011

agreement between the experimental and simulated spectra in terms of the positions of the resonance wavelengths. The strengths and widths, however, are smaller and larger, respectively, in the experiment compared to the simulations. This is, however, not unexpected since the DEDs in the realized metamaterial vary slightly due to the incomplete reproducibility of EBL and lift-off technique which inevitably introduces a variation in lengths and widths as well as rough edges in the nanorod ensemble comprising the DED metamaterials. These structural variations manifest themselves as inhomogeneous broadening and reduced resonance strengths in the spectra.

We have also investigated the DED metamaterial dispersions by estimating the metamaterial complex refractive indexes $\tilde{n}$ experimentally in the wavelength range corresponding to the transparency windows. Our procedure for experimental retrieval of $\tilde{n}$ is based on diffraction [34] and, specifically, $\tilde{n}$ is retrieved indirectly

by minimizing a function $\xi(n, \kappa)$ which describes the error between the experimental and theoretical metamaterial transmission and metamaterial grating diffraction efficiency, respectively. For a specific wavelength, the error function exhibits distinct minima (Fig. 11.7a) corresponding to solutions of n and κ, thereby enabling experimental access to the DED metamaterial wavelength dispersions (Figs. 11.7b and 11.7c). Comparison of the experimental and simulated real and imaginary parts of the metamaterial refractive index of the DEDs comprised of two (Fig. 11.7b) and three (Fig. 11.7c) nanorods reveals reasonably consistent trends regarding the wavelength dispersion of the refractive index. However, there is in general a substantial difference in the actual value of the real part. Nevertheless, this is not unexpected, when taking into account the evident differences in resonance strengths and widths in the experimental and simulated transmission and reflection spectra (Fig. 11.6), and

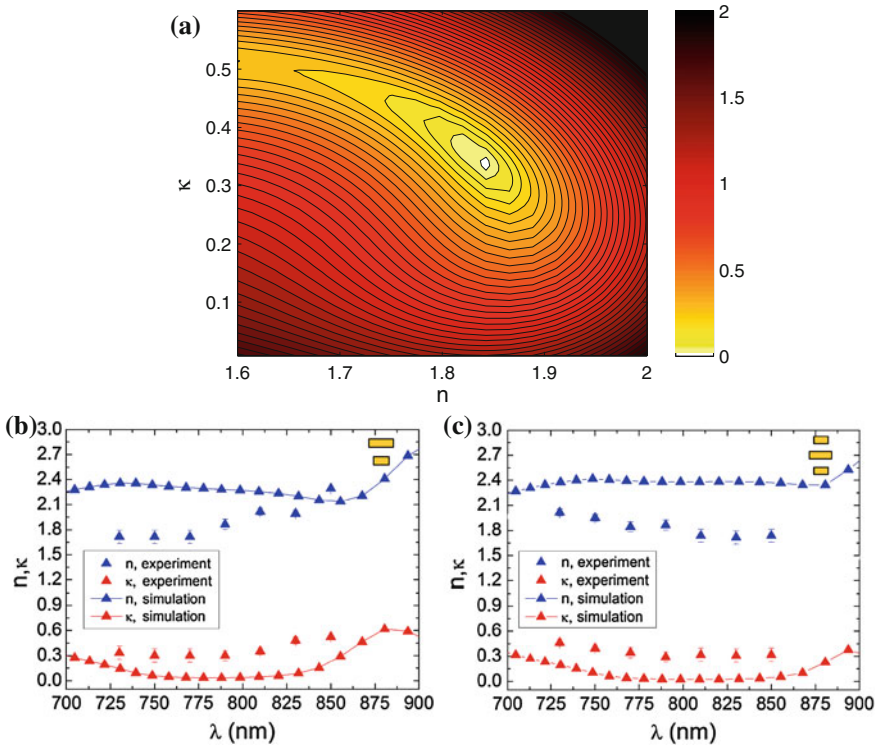

Fig. 11.7 **a** Contour plot showing the error $\xi(n, \kappa)$ in the case of a DED metamaterial consisting of three nanorods at the wavelength 770 nm, which is used for retrieval of $n \simeq 1.84$ and $\kappa \simeq 0.34$ corresponding to the minimum in $\xi(n, \kappa)$. **b**, **c** Experimental and simulated real (n) and imaginary (κ) parts of the complex refractive index for the DED metamaterial consisting of **b** two nanorods and **c** three nanorods. In the simulations and experiment, the metamaterial thickness is 150 nm, which corresponds to 50 nm of gold embedded in 50 nm PMMA above and below the nanorod antennas. Reproduced with permission from Ref. [34], DOI: 10.1088/2040-8978/13/5/055106. ©Institute of Physics 2011

the fact that the refractive index is directly related to the amplitude and phase of the transmitted and reflected fields [33]. Importantly, for the case of the DED metamaterial consisting of three nanorod antennas, n decreases in the experiment from $\simeq$1.9 to $\simeq$1.7 in the wavelength range $\simeq$750 to 850 nm, thereby indicating normal dispersion in the transparency window. The group refractive index, which is estimated from the slope of the linear fit to $n(\lambda)$, is, however, only $n_g = 3.6$ in the experiment and $n_g = 2.7$ in the simulations, i.e. the light slow-down is quite moderate. The imaginary part κ is approximately two times larger in the experiment compared to the simulated results, which is reasonable due to the surface scattering and grain boundary effects leading to increased damping in the gold nanorod antennas compared to bulk gold [35, 36].

11.3 Applications

Despite the fact that the DED concept follows naturally from the plasmonic realization of the dressed state picture of EIT, featuring DED metamaterials with wavelength regions of slow light and enhanced transmission, the concept shows broader applicability. Based on DED configurations, we suggest in this section a new approach to the design of a plasmonic sensor for refractive index sensing and a novel type of ultrathin plasmonic quarter-wave plate.

11.3.1 Plasmonic Sensing

Recent developments have greatly improved the sensitivity of optical sensors that are based on metal nanoparticles and the exploitation of their localized plasmon resonances [37]. The resonance wavelenght is determined by the susceptibilities of constituent materials as well as by the nanoparticle size and geometry. The former feature provides the possibility of monitoring environmental changes by tracking the resonance wavelength, whereas the latter allows one to adjust the LSPR position across the visible and near-infrared spectral regions. The overall sensing performance of a plasmonic nanostructure is typically characterized by the *figure of merit* (FOM)

$$\text{FOM} = \frac{s}{\Delta\lambda}, \tag{11.9}$$

where $s = \partial\lambda_{res}/\partial n_d$ is the sensitivity (measured in nm/RIU) of the resonance wavelength λ_{res} to changes in the environmental refractive index n_d, and $\Delta\lambda$ is the resonance spectral width at half-maximum (FWHM) [38]. Both characteristics are rather difficult to improve, especially for *single* nanoparticle configurations [37, 39]. For example, the resonance quality (Q) factor is problematic to increase over the electrostatic limit imposed by the Ohmic losses in metals [19]. In fact, one can reach this limit only with ultrasmall metal particles, whose scattering (radiation)

losses are negligibly small with respect to the absorption losses. On the other hand, environmental sensing relies on the detection of scattered light so that, for practical purposes, nanoparticles have to be chosen large enough to obtain measurable signals.

In order to boost the FOM, alternative ways have been investigated to create sharp spectral features that are sensitive to the surrounding medium. For example, one may take advantage of diffractive coupling present in periodic arrays of nanoparticles [40] or in complementary hole structures [41] when the period is on the order of the wavelength. Especially at the onset of diffraction it is possible to excite the so-called Rayleigh anomaly. The Rayleigh anomaly corresponds to light that is diffracted parallel to the grating, and it appears in reflection and transmission measurements as a sharp spectral feature that is sensitive to the surroundings. As a prominent example, the coupling of SPPs and the Rayleigh anomaly in multiscale patterned hole arrays in gold films demonstrates FOM as large as 23.3 [42]. The diffractive coupling approach, however, does not allow for measuring local changes in nanoscale volumes or for a high integration density of sensing devices.

A second approach that alleviates the above problems, yet with a high-Q resonance, involves interference between coupled nanostructures and the creation of *Fano resonances*. The Fano resonance occurs due to the interference between radiant and subradiant plasmonic modes resulting (typically) in asymmetric resonances with narrow linewidths [43]. For this reason, a multitude of complex plasmonic nanostructures exhibiting Fano resonances have been investigated in relation to plasmonic sensing, though the FOM, generally, never exceeds 10 [5, 44, 45]. Note that Fano resonances have also been advantageously exploited within biosensing [46].

Our approach still rely on DED configurations exhibiting an EIT-like response. However, this time we take advantage of the *scattering asymmetry* present near the central frequency [47]. The idea can be elaborated by considering scattering in $\pm$y-direction for two non-interacting point scatterers placed similarly to the nanorods in (Fig. 11.1a) with their electric dipole moment along the x-axis. If each scatterer is described by the polarizability in Eq. (11.1), it is straightforward to show that in the limit of weak detuning ($\omega_0 \gg \Delta$) the mutual phase difference at the central frequency is

$$\Delta\Phi(\omega_0) = \pi - 2\tan^{-1}\left[\Gamma/(2\Delta)\right]. \tag{11.10}$$

The scattering asymmetry along the line connecting the scatterers (y-direction) can then be maximized by requiring $\Delta\Phi \pm k_0 n_d d = \pi(0)$ (k_0 is the wavenumber in vacuum), which implies complete scattering cancellation in one direction and constructive interference in the other. By satisfying the two equations one finds that the separation d and frequency detuning Δ must be chosen as follows

$$d = \frac{\lambda}{4n_d}, \Delta = \frac{\Gamma}{2}. \tag{11.11}$$

Although these parameter choices can only be seen as a guide to a realistic optimal configuration, they still underline the possibility of pronounced scattering asymmetry along the y-direction for which the *ratio* can be used as a sensitive probe for

environmental changes. Note that in a related study the scattering asymmetry of a bimetallic DED configuration has been used as a nanoscale-sized directional color router [48]

The above conceptual discussion has been cooperated further in [14] by considering two interacting ellipsoids with detuned resonance wavelengths in the point-dipole limit. Here, we consider full-wave simulations of the two-nanorod configuration consisting of nanorods of size (i) $120 \times 50 \times 50\,\text{nm}^3$ and (ii) $135 \times 40 \times 40\,\text{nm}^3$ separated by a distance $d = 85\,\text{nm}$. The nanorods are made of gold and embedded in glass ($n_d = 1.45$) with the x-polarized incident wave propagating along the z-axis [see Fig. 11.1a]. The scattering cross sections reveal individual nanorod resonances with the same scattering strength and a DED configuration showing an EIT-like behavior with a minimum at $\lambda = 941\,\text{nm}$ (Fig. 11.8a). The expected strong scattering asymmetry at this wavelength can be elucidated by studying the angular distribution of the scattering (Fig. 11.8b). It is seen that even at the resonance of the short nanorod

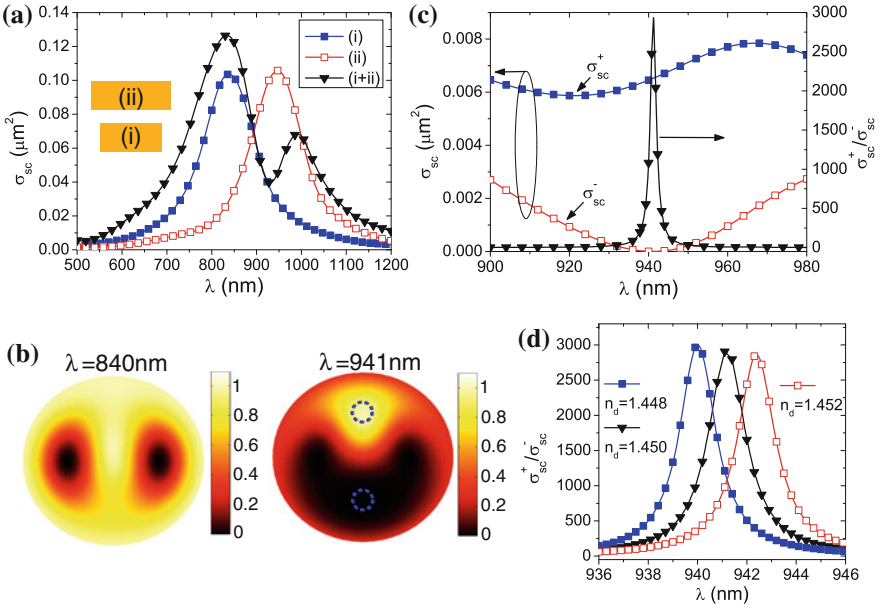

Fig. 11.8 **a** Scattering cross section of the individual nanorods of size (i) $L_1 = 120 \times 50 \times 50\,\text{nm}^3$ and (ii) $135 \times 40 \times 40\,\text{nm}^3$, respectively, and the DED configuration with $d = 85\,\text{nm}$ for x-polarized incident wave propagating along the z-axis. **b** Normalized differential scattering cross section of the DED configuration displayed in spherical coordinates for the wavelengths $\lambda = 840\,\text{nm}$ and $\lambda = 941\,\text{nm}$. The polar angle θ measured from the z-axis is represented by the radial distance, whereas the azimuthal angle ϕ (counted in the xy-plane from the x-axis) is displayed in the figure plane with the x-axis being horizontal. **c** Spectra of cross sections of scattering into the directions of constructive (σ_{sc}^{+}) and destructive (σ_{sc}^{-}) interference and their ratio calculated for x-polarized incident wave with propagation along z-axis. The solid angle of integration is $\Delta\theta = 22.5°$, and it is indicated by *dashed circles* in **b**). **d** Sensitivity of the scattering ratio $\sigma_{sc}^{+}/\sigma_{sc}^{-}$ on the refractive index of the surrounding medium

($\lambda = 840\,\text{nm}$) one observes asymmetry in scattering due to interference between light from the two detuned nanorods. However, at the central wavelength ($\lambda = 941\,\text{nm}$) the asymmetry is maximized with a vanishing amount of power scattered into the $-$y-direction due to destructive interference.

For practical realization of environmental sensing, it is necessary to collect the scattered light within a solid angle along the $\pm$y-directions [see dashed circles in Fig. 11.8b]. Figure 11.8c displays the amount of power scattered into a cone angle of $\Delta\theta = 22.5°$ in the +y-direction (σ_{sc}^{+}), $-$y-direction (σ_{sc}^{-}), and their ratio in the neighborhood of the central wavelength. Clearly, the scattering ratio is an eminent probe for environmental changes as it features a FWHM of $\sim$2 nm. At the same time, the scattering ratio demonstrates a sensitivity of $s \simeq 600\,\text{nm/RIU}$ to the refractive index of the surrounding medium (Fig. 11.8d), which results in a FOM as large as $\sim$300. Importantly, the configuration is quite robust towards fabrication tolerances. As an example, if the separation d is changed to 90 nm the FWHM increases to $\sim$2.5 nm (not shown) which, of course, lowers the FOM but still keeps the value remarkably high compared to conventional sensing techniques. It should be stressed that it is possible to detect the scattered light from a single DED configuration. To give an example, for the configuration in Fig. 11.8 ($\Delta\theta = 22.5°$) illuminated with the intensity of $1\,\text{mW}/\mu\text{m}^2$, the scattered powers at the central wavelength would amount to $P^{+} \simeq 6.5\,\mu\text{W}$ and $P^{-} \simeq 2.3\,\text{nW}$ that should be possible to reliably detect.

The scattered power available for the detection can be significantly increased if the same idea is implemented using a periodic array of DED pairs. In this case, the scattering directions with constructive and destructive interference can be chosen to coincide with the directions of light diffraction into $\pm$first orders. Considering non-interacting point dipoles again, the corresponding retardation phase should, in this case, be considered in the direction of light diffraction determined by the array period Λ_y along the line connecting DED scatterers. The retardation phase $k_0 n_d d$ should therefore be changed onto $k_0 n_d d \sin\theta_1$, where θ_1 is the diffraction angle given by the grating equation: $\sin\theta_1 = \lambda/(n_d \Lambda_y)$. This modification results in the following conditions required to extinguish one and maximize another diffraction order

$$d = \frac{\Lambda_y}{4}, \Delta = \frac{\Gamma}{2}, \tag{11.12}$$

which are again strictly valid only for noninteracting scatterers. The periodicity in the other direction, Λ_x, should be as small as possible to increase the density of DED pairs but large enough so as to not result in the strong coupling between the neighbor DED pairs. In contrast, Λ_y should be on the order of the wavelength so that the array does not act as a metasurface with only zero-order diffraction.

The idea of using the ratio of scattering in the first diffraction orders as a sensitive probe has been investigated experimentally as a *proof-of-principle* study. In these experiments, we fabricated periodic ($\Lambda_x = 400\,\text{nm}$ and $\Lambda_y = 750\,\text{nm}$) arrays ($50 \times 50\,\mu\text{m}^2$) consisting of individual and double gold nanorods (of different lengths) on a silica substrate using electron-beam lithography and lift-off applied to a 50 nm thick gold film (Fig. 11.9a). Transmission spectra were measured using a

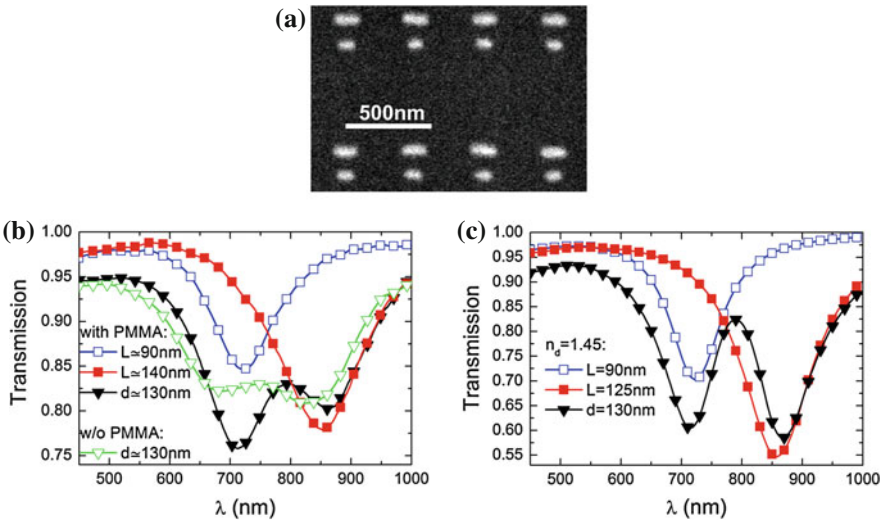

Fig. 11.9 **a** Representative SEM-image of the DED grating with Λ_x=400 nm and Λ_y=750 nm along with **b** experimental and **c** simulated transmission spectra of individual nanorod arrays (*blue* and *red curves*) and arrays with pairs of nanorods (*black curves*). The experimentally obtained spectra of the array with pairs of nanorods were measured before and after deposition of a PMMA phase-matching layer, whereas the simulated spectra was obtained with the nanorods embedded in glass. The gold nanorods have 50 nm × 50 nm cross sections and lengths 90 and 140 nm, respectively. Adapted with permission from Ref. [14]. ©2011 American Chemical Society

broad band halogen light source with a fiber output whose (weakly divergent) radiation was directed (at normal incidence) through a polarizer on the fabricated arrays of nanorods aligned so that their axes were parallel to the light polarization. The transmitted radiation was collected with an objective and fed into an optical fiber connected to a spectrometer. The transmission spectra were measured before and after depositing a thick (several micrometers) layer of PMMA. The latter was used to form a homogeneous dielectric environment for gold nanorods. The transmission spectra obtained with arrays of nanorod pairs before and after the deposition of the PMMA layer feature local maxima located at ∼755 and ∼790 nm, respectively, each being surrounded by two local minima (Fig. 11.9b). These maxima indicate the suppression of scattering achieved at the wavelengths that are intermediate with respect to the resonance wavelengths of individual nanorods. The effect of enhanced transmission is especially pronounced and documented in detail for the arrays covered with the PMMA layer: the transmission spectra obtained with the arrays of individual short and long nanorods exhibit the effect of detuning in their resonances located at wavelengths ≃720 nm and 860 nm, while the transmission spectrum of the array consisting of pairs of corresponding nanorods (Fig. 11.9a) shows the effect of increased transmission at the intermediate wavelength of ≃790 nm (Fig. 11.9b). Note also a significant red shift in the transmission spectrum of the DED array after the deposition of the PMMA layer (due to a change in the dielectric environment of nanorods), as well as an improvement in the contrast. We have attempted to model

the response of the fabricated arrays. Individual and double gold nanorods being $\simeq 50 \times 50\,\mathrm{nm}^2$ in the cross section with the lengths of $\simeq 90\,\mathrm{nm}$ and $\simeq 125\,\mathrm{nm}$ and the center-to-center distance of $\simeq 130\,\mathrm{nm}$ were considered to be embedded in dielectric with the refractive index of 1.45. Transmission spectra were then calculated using their computed extinction cross sections and the corresponding size ($400 \times 750\,\mathrm{nm}^2$) of unit cell (Fig. 11.9c). It is seen that the positions of local minima and maximum in the transmission spectra correspond well to the experimental results (Fig. 11.9b), albeit for a slightly shorter length of the long nanorod, but the contrast obtained in simulations is much better than that achieved in the experiment. It should be borne in mind that the use of divergent illumination and detection of focused radiation as well as inhomogeneous broadening (due to fabrication-induced deviations of nanorod dimensions in the fabricated arrays) could definitely contribute to smearing out the spectral features in these preliminary experiments.

The fabricated DED array (Fig. 11.9a) covered with the PMMA layer was further characterized in the setup for leakage-radiation microscopy (LRM) [49] using a continuous-wave-operated tunable Ti:sapphire laser, whose radiation polarized parallel to the nanorod axes was slightly focused and directed at normal incidence on the sample (Fig. 11.10a) with the incident light powers being on the level of a few milliwatts. The $\pm$ first diffraction orders observed in the back focal plane of an LRM objective exhibited strong asymmetry (Fig. 11.10b) in their wavelength-dependent behavior as expected [cf. Fig. 11.8c]. Wavelength dependencies of the corresponding diffraction efficiencies measured with a calibrated photodetector resulted in a very sharp peak of their ratio at the wavelength of $\simeq 785\,\mathrm{nm}$ with the FWHM of $\simeq 20\,\mathrm{nm}$ (Fig. 11.10c), a value which is significantly smaller than the FWHM of plasmonic resonances for individual nanorods (Fig. 11.9b). Such a drastic narrowing of the system response at resonance constitutes the main forte of the DED-based plasmonic nanostructures. Since the sensitivity (nm/RIU) of plasmonic resonances is difficult to appreciably increase, the FOM can radically be increased only by narrowing the resonance line width [37]. Note that the fabricated and characterized DED array was *not* optimized with respect to the nanorod parameters and their separation, resulting in a significantly smaller maximum ratio as compared to the model case (Fig. 11.8c). The balance between the strengths, resonance positions, and spatial separation of individual nanorods (that should also be related to the array periodicity) is quite delicate: one should achieve the same scattering strength of interacting DED scatterers simultaneously while fulfilling the optimum conditions [Eq. (11.12)] in order to ensure the highest ratio between the diffraction efficiencies. Still, the effect of destructive interference of DED pairs is rather robust as demonstrated with our proof-of-principle experiments (Fig. 11.10b and c). It should be mentioned that we characterized also similar arrays of DED pairs with a smaller center-to-center separation ($\simeq 100\,\mathrm{nm}$) and found a similarly sharp system response with the maximum ratio (between the diffraction efficiencies) of $\simeq 40$ and the FWHM of $\simeq 30\,\mathrm{nm}$. Finally, assuming that the sensitivity of the fabricated array is on the same level as that obtained in our simulations, i.e., $\simeq 600\,\mathrm{nm/RIU}$, one obtains the FOM of $\simeq 30$, a value which exceeds the record one obtained with multiscale patterned hole arrays in gold films fabricated by soft interference lithography [42].

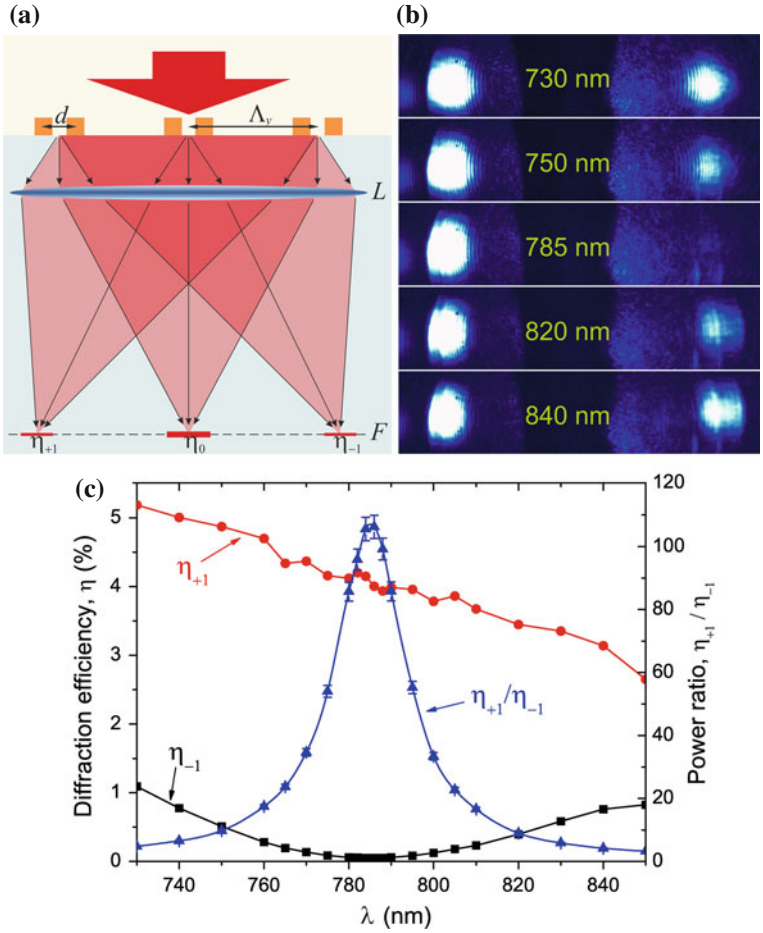

Fig. 11.10 **a** Experimental leakage-radiation microscopy configuration used to detect radiation diffracted by the DED array shown in Fig. 11.9**a** after the deposition of the PMMA phase-matching layer. The lens L denotes a high-numerical-aperture objective (N.A. = 1.25). The back focal plane F of the objective represents the location of a Fourier-transformed image of the radiation emerging from the sample. **b** Images taken in the Fourier plane F with the sample being illuminated at different wavelengths. The *left* and *right spots* correspond to the ±first diffraction orders with the (*brightest*) zeroth diffraction order being blocked to enhance the contrast of images. **c** Wavelength dependencies of the corresponding diffraction efficiencies, η, together with their ratio. Reprinted with permission from Ref. [14]. ©2011 American Chemical Society

11.3.2 Metamaterial Wave Retarders in Reflection

Materials exhibiting linear birefringence are of crucial importance in modern optics, providing necessary control of the polarization state of light. For example, uniaxial crystalline materials (e.g., quartz) are characterized with two different refractive

indexes that result in a phase difference between orthogonally polarized waves traveling through the crystal, thereby permitting the construction of wave retarders, e.g., half- and quarter-wave plates. An alternative method for obtaining birefringence is to introduce a periodic anisotropy in the (nonbirefringent) material so that transverse electric and transverse magnetic waves experience different effective refractive indexes. Their difference, Δn, is known as form birefringence [50–52]. Generally, a high Δn is desired as it can lead to more compact optical components that can be used in on-chip photonics [53]. Although difficult to achieve at optical wavelengths (typically, $\Delta n \simeq 0.1 - 0.2$ [54]), it has recently been shown that the waveguide dispersion of surface plasmon polaritons (SPPs) in gold nanoslits can be used to create giant form birefringence $\Delta n \simeq 2.7$ at $\lambda = 632.8\,\text{nm}$ [55], facilitating sub-wavelength-thin wave plates. In a different approach [56], a subwavelength circular aperture in a gold film surrounded by an elliptical grating was used to introduce a phase shift between SPPs traveling along the ellipse axes, influencing the polarization of transmitted light.

Based on our DED concept, we demonstrate theoretically and experimentally a new method to construct a nanometer-thin quarter-wave plate that in contrast to previous studies [55, 56] works in reflection mode. Also, the quarter-wave plate relies on anisotropic detuned electric resonant scattering and not form birefringence as in grating-based circular polarizers (see, e.g., [51, 57]). Furthermore, the proposed nanostructures, constituting a unit cell in the metamaterial wave retarders, are not related to the optically active extrinsic chiral metamaterials [30] as they only display an electric response (no magnetic response), eliminating the possibility of extrinsic chirality.

Our approach can be illustrated by considering two *perpendicular* noninteracting electric dipolar scatterers centered at the origin of the coordinate system with electric dipole moments in the x- and y-direction, respectively, and the observation region being in the far field close to the z-axis ($z \gg x, y$). Assuming that the resonances of the noninteracting dipole scatterers are equally detuned from the central frequency ω_0, their dipole polarizabilities can be represented by Eq. (11.1), and for weak detuning ($\omega_0 \gg \Delta$) their polarizability phase difference, $\Delta\Phi$, is equivalent to Eq. (11.10) implying that for $\Delta = \Gamma/2$ the scattered light close to the z-axis will be circularly polarized ($\Delta\Phi = \pi/2$). Consequently, a metamaterial consisting of subwavelength noninteracting DED unit cells will work as a circular polarizer as the polarizability of each cell, $\alpha_1 + \alpha_2$, adds coherently in this limit [58] [see Eq. (11.3)]. The above condition for circular polarized light is strictly valid only for noninteracting scatterers with the same strength and damping factor, but, as we will see below, the simplified description is still valid as a guideline for more realistic cases due to very weak dipole-dipole interaction for *orthogonal* dipoles [59]. Note that even though we focus on the quarter-wave plate structure, the same idea can be used to construct a wave plate with arbitrary retardation by adjusting the detuning Δ and/or slightly displacing two scatterers along the propagation direction. Furthermore, based on a similar concept, recent studies have shown that orthogonally oriented nanoslits of different lengths in a metal surface, i.e. complementary structures to the perpendic-

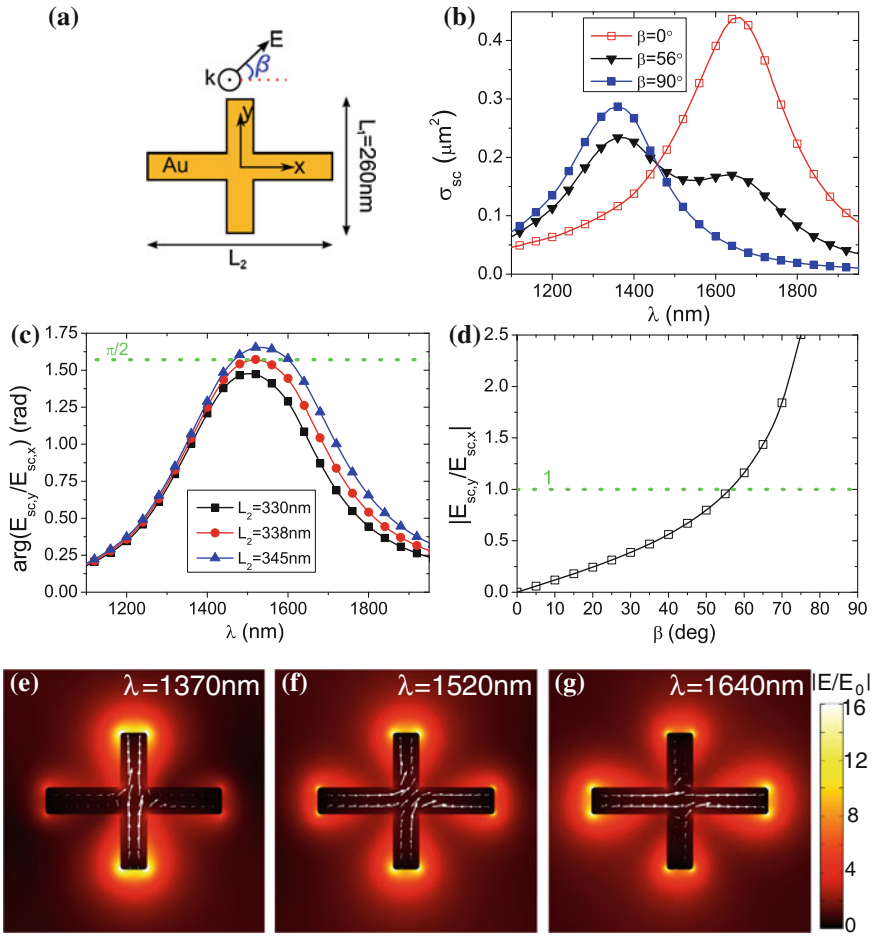

Fig. 11.11 **a** Sketch of nanocross system. **b** Scattering cross section at three angles β for $L_2 = 338$ nm. **c** The phase difference between x- and y-component of scattered E-field along the $-$z-axis in the far field at $\beta = 45°$. **d** The amplitude ratio along $-$z-axis in the far-field as a function of angle β for $L_2 = 338$ nm and $\lambda = 1520$ nm. **e**–**g**: Color map shows the electric field enhancement while the arrows depict the induced plasmonic current at an representative time. The relative length of the arrows in the two nanorod arms represents the ratio in the current magnitude. **a**–**c**: Reproduced with permission from Ref. [15]. ©The Optical Society Of America 2011

ular nanorod antennas, have proven to work as ultrathin waveplates at terahertz [60] and visible frequencies [61–63].

Our approach is further demonstrated numerically with full three-dimensional finite element calculations. In this study, we focus on two different DED configurations (Figs. 11.11a and 11.12a) in which both nanostructures are made of gold and embedded in a surrounding medium with refractive index $n = 1.45$ (glass). The first configuration (Fig. 11.11a) is a nanocross consisting of two perpendicular

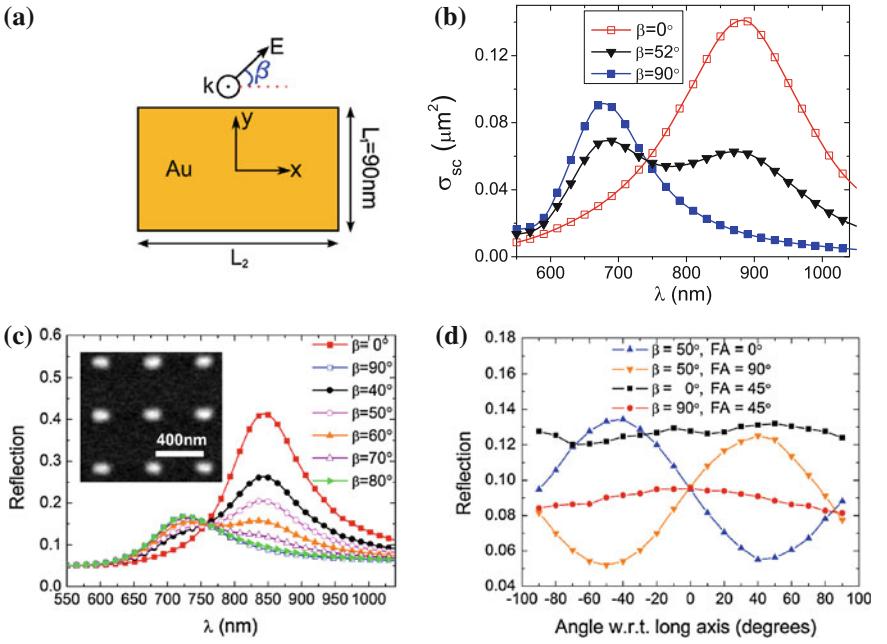

Fig. 11.12 **a** Sketch of nanobrick system. **b** Scattering cross section at three angles β for $L_2 = 140\,\text{nm}$. **c** Normalized experimental reflection spectra for seven difiifferent values of β. The inset shows an electric microscopy image of the fabricated 400 nm-period array consisting of ∼50 nm high gold bricks with short and long axes of ∼100 nm and 150 nm, respectively. **d** Normalized reflection from the array as a function of analyzer angle w.r.t. the long axis of the brick for $\lambda = 780\,\text{nm}$. The reflection in **c** and **d** was normalized using the reflectivity from a ∼300 nm-thick gold film and weighted with the calculated reflectivity by using gold optical constants. Reproduced with permission from Ref. [15]. ©The Optical Society Of America 2011

nanoantennas with the same cross section of $50 \times 50\,\text{nm}^2$ but of different length (i.e., orthogonal DEDs). Note that it is possible to excite individual plasmonic resonances by choosing the angle of polarization, β, of the incident linearly polarized wave to either $\beta = 0°$ or $\beta = 90°$ (Fig. 11.11b). For intermediate angles, both resonances are excited, which allows us to construct a quarter-wave plate by properly choosing the length of the nanoantennas (detuning) and β (influencing the relative strength of DEDs). The right choice of length is illustrated in Fig. 11.11c for $\beta = 45°$ when the short axis is fixed at $L_1 = 260\,\text{nm}$ and the long axis, L_2, is slightly varied. The figure depicts the phase difference between the y- and x-component of the scattered electric field ($E_{sc,y}$ and $E_{sc,x}$) along the -z-axis in the far field showing that for $L_2 = 338\,\text{nm}$ the phase difference is $\simeq \pi/2$ at $\lambda = 1520\,\text{nm}$. At this wavelength, the minimum observed in the scattering cross section is related to plasmonic currents induced in both nanoantennas (Fig. 11.11f), whereas the scattering cross section maxima at wavelengths $\lambda = 1370\,\text{nm}$ and $\lambda = 1640\,\text{nm}$ are related to plasmonic currents induced only in the vertical (Fig. 11.11e) and horizontal (Fig. 11.11g)

nanoantenna, respectively. Interestingly, simulations show that the induced current at $\lambda = 1520\,\text{nm}$ (Fig. 11.11f) makes a full rotation within one cycle; a property related to scattered light with elliptical/circular polarization. In order to get circular polarized light at $\lambda \simeq 1520\,\text{nm}$, we should require $|E_{sc,x}| = |E_{sc,y}|$ that can be satisfied at $\beta = 56°$ (Fig. 11.11d). Note that in the simplified case of Eq. (11.1), we would expect circular polarization at $\beta = 45°$, but a lower dipole strength of the short nanoantenna requires $\beta > 45°$. Also importantly, the configuration has the wavelength range 1475–1560 nm where the phase difference variation is less than 2 %, implying a relatively broadband operation of the proposed wave plate.

As an example of versatility of our approach, we construct a quarter-wave plate from a gold nanobrick of 50 nm thickness (Fig. 11.12a) exhibiting two orthogonal plasmonic resonances [see the scattering cross section in Fig. 11.12b]. This time, however, we choose the short axis to be $L_1 = 90\,\text{nm}$ satisfying the criteria for a quarter-wave plate at $\lambda \simeq 770\,\text{nm}$ when $L_2 = 140\,\text{nm}$ and $\beta = 52°$ (not shown). The wavelength range in which the phase difference deviates with less than 2 % is 748–796 nm. For further details on the nanobrick configuration, we refer to [15].

Using electron-beam lithography and lift-off technique, a 400 nm-periodic ($50 \times 50\,\mu\text{m}^2$) array of the nanobrick configuration has been fabricated on a silica substrate [see inset in Fig. 11.12c] and subsequently covered with $\simeq 15\,\mu\text{m}$ PMMA to create (almost) homogeneous surroundings. Reflection spectra are measured using a broadband halogen light source with a fiber output whose radiation is directed through a Glan-Thompson polarizer and focused onto the fabricated array by a x60-objective (NA = 0.85). The reflected light is collected by the same objective and fed into an optical fiber connected to a spectrometer. The reflection spectra (Fig. 11.12c) show that for $\beta = 0°$ and $\beta = 90°$ the individual resonances along the brick long and short axis, respectively, are being excited, whereas both resonances are excited when using an intermediate β.

In order to verify experimentally that the reflected light from the fabricated array is circularly polarized, β is fixed to an angle of 50° and the radiation from a Ti:sapphire laser at 780 nm is focused onto the array with a x10-objective (NA = 0.25), collected by the same objective and sent through an achromatic quarter-wave plate (690–1200 nm) followed by a Glan-Thompson analyzer with varying analyzer angle with respect to (w.r.t.) the long axis of the brick (Fig. 11.12d). If the reflected light from the fabricated array is circularly polarized it must be converted into linearly polarized light with an angle of 45° w.r.t. the fast axis (FA) of the quarter-wave plate. When fixing the FA w.r.t. the long axis of the brick at 0° and 90°, respectively, the output of the Glan-Thompson analyzer reveals linear polarization at angles −45° and 45°, respectively. Therefore, in this case, the criteria of equal strengths and a phase difference of $\simeq \pi/2$ between the two resonances of the brick are approximately met, and the reflected light is circularly polarized. Note that the minimum reflection is ≃5 % due to the presence of linearly polarized light reflected at the glass/PMMA interface. On the other hand, when $\beta = 0°$ or $\beta = 90°$ and the FA is fixed at 45° w.r.t. to the long axis of the brick, the individual resonances are excited, and the commercial quarter-wave plate converts the reflected (linearly polarized) light into circularly polarized light as evidenced by the analyzer output when varying the analyzer angle.

Note that the reflection as a function of the analyzer angle is not perfectly flat when $\beta = 0°$ and $\beta = 90°$ due to the commercial quarter-wave plate not providing a retardance of exactly one quarter at 780 nm. That said, it is clear from the measurements that the nanobrick metamaterial functions as a quarter-wave plate in reflection.

11.4 Conclusion

The concept of detuned electrical dipoles (DED) have emerged from the plasmonic realization of the dressed-state picture of the electromagnetically induced transparency (EIT) in atomic physics. The DED concept shows *versatility* in the sense that it covers any plasmonic configuration consisting of two dipole resonances that are oppositely detuned from the central frequency. Importantly, the detuning must be weak so that the line shapes of the individual resonances overlap, hereby creating *scattering suppression* at the central frequency. Furthermore, as the scattering suppression also occurs in the limit of noninteracting resonators, DED configurations display *robustness* with respect to mutual positioning of individual scatterers. A fact that amounts in less stringent fabrication requirements compared to the other EIT realization mimicking the bare-state picture.

By employing gold nanorod antennas as dipolar scatterers, we have demonstrated that two- and three-nanorod configurations constituting a unit cell in a DED metamaterial exhibit enhanced transmission (i.e., optical transparency) at the central frequency with the possibility of slowing down light. Specifically, the numerically studied two-nanorod system demonstrates slow down factors of ~ 10 with propagation loss of ~ 2.5 dB per 300-nm-thick unit cell at the central wavelength $\simeq 1150$ nm, whereas the three-nanorod system features a group refractive index of ~ 8 with loss ~ 1 dB per 150-nm-thick cell at the central wavelength $\simeq 860$ nm. DED metamaterials and their associated effective refractive indexes have also been studied experimentally, showing consistent trends with simulations.

Although the DED concept was presented in relation to slow-light metamaterials, it has proven a much larger applicability. Here, we demonstrated that the *scattering asymmetry* along the line connecting the two nanorods at the central wavelength can be advantageously exploited for plasmonic sensing of the environment, both as an individual subwavelength-sized sensor and as a unit cell of a periodic array. Simulations of a single two-nanorod configuration revealed that the ratio of the scattering asymmetry produces spectral peaks at the central wavelength $\lambda = 941$ nm with a FWHM of $\sim$2 nm and a sensitivity of $\simeq$600 nm/RIU resulting in a record high figure of merit (FOM) of $\sim$300. Experimental proof-of-principle studies of lithographically fabricated gold nanorod arrays demonstrate FWHM of $\simeq$20 nm, a value which is significantly smaller than the FWHM of plasmonic resonances of individual nanorods.

Finally, we showed that a metasurface with unit cells consisting of *perpendicular* dipolar scatterers can be designed to function as a nanometer-thin quarter-wave plate in reflection, meaning that the reflected light is circularly polarized for a lin-

early polarized incident wave. The quarter-wave plate functionality has been verified numerically for nanocross and nanobrick configurations in the near-infrared. Additionally, a metasurface of nanobrick unit cells has been fabricated and optically characterized, revealing quarter-wave plate behavior at $\lambda \simeq 780\,\text{nm}$.

Despite the already widespread work on and utilization of the DED concept, there is still room for improvements and new applications. For example, the EIT-response of DED metamaterials depends on a large number of parameters such as the frequency detuning, the size and composition of the unit cell. For this reason, it is a complicated task to find an optimal configuration. The word 'optimal' also depends on the objective; in some cases a large group refractive index might be of more importance than a large bandwidth-delay product. Similarly, the extrinsic chirality present for two-nanorod metasurfaces (see Sect. 11.2.1) ought to be investigated in more detail, possibly opening a new way to create ultrathin polarization rotators. The sensing capabilities of the DED array can also be improved by a proper optimization of the structural dimensions, which potentially could experimentally verify FOM exceeding 100. Moreover, as indicated in Sect. 11.3.1, it should be possible to reliably detect the light scattered from a *single* DED configuration, opening up the possibility to detect environmental changes in nanometer-sized volumes with unforeseen sensitivity. Likewise, we envision a considerable improvement in the reflection strength of the DED quarter-wave plate [the current configuration shows a reflection of ~ 0.15, see Fig. 11.12c] by placing the nanobricks on a nanometer-thin ($\sim 20\,\text{nm}$) dielectric spacer pinned to a thin metal film. The overall thickness of the structure would still be subwavelength, but the mirror-like properties of the metal film ensures a predominant scattering in the reflection direction.

References

1. S. Zhang, D.A. Genov, Y. Wang, M. Liu, X. Zhang, Phys. Rev. Lett. **101**, 047401 (2008)
2. N. Papasimakis, V.A. Fedotov, N.I. Zheludev, S.L. Prosvirnin, Phys. Rev. Lett. **101**, 253903 (2008)
3. P. Tassin, L. Zhang, T. Koschny, E.N. Economou, C.M. Soukoulis, Phys. Rev. Lett. **102**, 053901 (2009)
4. P. Tassin, L. Zhang, T. Koschny, E.N. Economou, C.M. Soukoulis, Opt. Express **17**, 5595 (2009)
5. N. Liu, L. Langguth, T. Weiss, J. Kästel, M. Fleischhauer, T. Pfau, H. Giessen, Nat. Mater. **8**, 758 (2009)
6. R. Taubert, M. Hentschel, J. Kästel, H. Giessen, Nano Lett. **12**, 1367 (2012)
7. K.J. Boller, A. Imamolu, S.E. Harris, Phys. Rev. Lett. **66**, 2593 (1991)
8. M. Fleischhauer, A. Imamoglu, J.P. Marangos, Rev. Mod. Phys. **77**, 633 (2005)
9. T.F. Krauss, Nat. Photonics **2**, 448 (2008)
10. N. Papasimakis, Y.H. Fu, V.A. Fedotov, S.L. Prosvirnin, D.P. Tsai, N.I. Zheludev, Appl. Phys. Lett. **94**, 211902 (2009)
11. S. Maier, Nat. Mater. **8**, 699 (2009)
12. R.D. Kekatpure, E.S. Barnard, W. Cai, M.L. Brongersma, Phys. Rev. Lett. **104**, 243902 (2010)
13. S.I. Bozhevolnyi, A.B. Evlyukhin, A. Pors, M.G. Nielsen, M. Willatzen, O. Albrektsen, New J. Phys. **13**, 023034 (2011)

14. A.B. Evlyukhin, S.I. Bozhevolnyi, A. Pors, M.G. Nielsen, I.P. Radko, M. Willatzen, O. Albrektsen, Nano Lett. **10**, 4571 (2010)
15. A. Pors, M.G. Nielsen, G.D. Valle, M. Willatzen, O. Albrektsen, S.I. Bozhevolnyi, Opt. Lett. **36**, 1626 (2011)
16. E. Prodan, C. Radloff, N.J. Halas, P. Nordlander, Science **302**, 419 (2003)
17. C. Sönnichsen, T. Franzl, T. Wilk, G. von Plessen, J. Feldmann, O. Wilson, P. Mulvaney, Phys. Rev. Lett. **88**, 077402 (2002)
18. L. Jylhä, I. Kolmakov, S. Maslovski, S. Tretyakov, J. Appl. Phys. **99**, 043102 (2006)
19. F. Wang, Y.R. Shen, Phys. Rev. Lett. **97**, 206806 (2006)
20. G.D. Valle, T. Søndergaard, S.I. Bozhevolnyi, Phys. Rev. B **80**, 235405 (2009)
21. A. Pors, M. Willatzen, O. Albrektsen, S.I. Bozhevolnyi, J. Opt. Soc. Am. B **27**, 1680 (2010)
22. A. Yariv, *Quantum Electronics*, 3rd edn. (Wiley, New York, 1989)
23. J.D. Jackson, *Classical Electrodynamics*, 3rd edn. (Wiley, New York, 1999)
24. A. Pors, M. Willatzen, O. Albrektsen, S.I. Bozhevolnyi, Phys. Rev. B **83**, 245409 (2011)
25. P.B. Johnson, R.W. Christy, Phys. Rev. B **6**, 4370 (1972)
26. L. Novotny, Phys. Rev. Lett. **98**, 266802 (2007)
27. G.D. Valle, T. Søndergaard, S.I. Bozhevolnyi, Opt. Express **16**, 6867 (2008)
28. J. Jung, T. Søndergaard, S.I. Bozhevolnyi, Phys. Rev. B **76**, 035434 (2007)
29. A. Pors, M. Willatzen, O. Albrektsen, S.I. Bozhevolnyi, J. Comput. Theor. Nanosci. **8**, 1619 (2011)
30. E. Plum, X.X. Liu, V.A. Fedotov, Y. Chen, D.P. Tsai, N.I. Zheludev, Phys. Rev. Lett. **102**, 113902 (2009)
31. E. Plum, V.A. Fedotov, N.I. Zheludev, J. Opt. A: Pure Appl. Opt. **11**, 074009 (2009)
32. A. Alù, Y. Zhao, X.X. Liu, in *URSI Proceedings* (2011)
33. D.R. Smith, S. Schultz, P. Markoš, C.M. Soukoulis, Phys. Rev. B **65**, 195104 (2002)
34. M.G. Nielsen, A. Pors, O. Albrektsen, M. Willatzen, S.I. Bozhevolnyi, J. Opt. **13**, 055106 (2011)
35. N. Liu, M. Mesch, T. Weiss, M. Hentschel, H. Giessen, Nano Lett. **10**, 2342 (2010)
36. S. Zhang, W. Fan, K.J. Malloy, S.R.J. Brueck, J. Opt. Soc. Am. B **23**, 434 (2006)
37. J.N. Anker, W.P. Hall, O. Lyandres, N.C. Shah, J. Zhao, R.P.V. Duyne, Nat. Mater. **7**, 442 (2008)
38. L.J. Sherry, S.H. Chang, G.C. Schatz, R.P.V. Duyne, Nano Lett. **5**, 2034 (2005)
39. L.J. Sherry, R. Jin, C.A. Mirkin, G.C. Schatz, R.P.V. Duyne, Nano Lett. **5**, 2060 (2006)
40. V.G. Kravets, F. Schedin, A.N. Grigorenko, Phys. Rev. Lett. **101**, 087403 (2008)
41. J.M. McMahon, J. Henzie, T.W. Odom, G.C. Schatz, S.K. Gray, Opt. Express **15**, 18119 (2007)
42. J. Henzie, M.H. Lee, T.W. Odom, Nat. Nanotechnol. **2**, 549 (2007)
43. B. Luk'yanchuk, N.I. Zheludev, S.A. Maier, N.J. Halas, P. Nordlander, H. Giessen, C.T. Chong, Nat. Mater. **9**, 707 (2007)
44. J.B. Lassiter, H. Sobhani, J.A. Fan, J. Kundu, F. Capasso, P. Nordlander, N.J. Halas, Nano Lett. **10**, 3184 (2010)
45. N. Verellen, P.V. Dorpe, C. Huang, K. Lodewijks, G.A.E. Vandenbosch, L. Lagae, V.V. Moshchalkov, Nano Lett. **11**, 391 (2011)
46. C. Wu, A.B. Khanikaev, R. Adato, N. Arju, A.A. Yanik, H. Altug, G. Shvets, Nat. Mater. **11**, 69 (2012)
47. T. Pakizeh, M. Käll, Nano Lett. **9**, 2343 (2009)
48. T. Shegai, S. Chen, V.D. Miljković, G. Zengin, P. Johansson, M. Käll, Nat. Commun. **2**, 481 (2011)
49. I.P. Radko, A.B. Evlyukhin, A. Boltasseva, S.I. Bozhevolnyi, Opt. Express **16**, 3924 (2008)
50. F. Xu, R.C. Tyan, P.C. Sun, Y. Fainman, Opt. Lett. **20**, 2457 (1995)
51. G.P. Nordin, P.C. Deguzman, Opt. Express **5**, 163 (1999)
52. W. Yu, A. Mizutani, H. Kikuta, T. Konishi, Appl. Opt. **45**, 2601 (2006)
53. S.H. Yang, M.L. Cooper, P.R. Bandaru, S. Mookherjea, Opt. Express **16**, 8306 (2008)
54. L.H. Cescato, E. Gluch, N. Streibl, Appl. Opt. **29**, 3286 (1990)
55. S.Y. Hsu, K.L. Lee, E.H. Lin, M.C. Lee, P.K. Wei, Appl. Phys. Lett. **95**, 013105 (2009)

56. A. Drezet, C. Genet, T.W. Ebbesen, Phys. Rev. Lett. **101**, 043902 (2008)
57. G.F. Brand, Am. J. Phys. **71**, 452 (2003)
58. W. Cai, V. Shalaev, *Optical Metamaterials: Fundamentals and Applications* (Springer, New York, 2009)
59. S.K.N. Liu, H. Giessen, Adv. Mater. **20**, 4521 (2008)
60. F.I. Baida, M. Boutria, R. Oussaid, D.V. Labeke, Phys. Rev. B **84**, 035107 (2011)
61. E.H. Khoo, E.P. Li, K.B. Crozier, Opt. Lett. **36**, 2498 (2011)
62. Y. Zhao, A. Alù, Phys. Rev. B **84**, 205428 (2011)
63. A. Roberts, L. Lin, Opt. Lett. **37**, 1820 (2012)

Chapter 12
Plasmonics with a Twist: Taming Optical Tornadoes on the Nanoscale

Svetlana V. Boriskina

Abstract This chapter discusses a hydrodynamics-inspired approach to trap and manipulate light in plasmonic nanostructures, which is based on steering optical powerflow around nano-obstacles. New insights into plasmonic nanofocusing mechanisms are obtained by invoking an analogy of the 'photon fluid' (PF). By proper nanostructure design, PF kinetic energy can be locally increased via convective acceleration and then converted into 'pressure' energy to generate localized areas of high field intensity. In particular, trapped light can be molded into optical vortices–tornado-like areas of circular motion of power flux–connected into transmission-like sequences. In the electromagnetic theory terms, this approach is based on radiationless electromagnetic interference of evanescent fields rather than on interference of propagating waves radiated by the dipoles induced in nanoparticles. The resulting ability to manipulate optical powerflow well beyond the diffraction limit helps to reduce dissipative losses, to increase the amount of energy accumulated within a nanoscale volume, and to activate magnetic response in non-magnetic nanostructures. It also forms a basis for long-range on-chip energy transfer/routing as well as for active nanoscale field modulation and switching.

Keywords Plasmon · Optical tornado · Light scattering

12.1 Introduction

Noble-metal nanostructures known for their unique ability to squeeze light into subwavelength volumes enable a broad range of fascinating applications in optoelectronics, biomedical research, energy harvesting and conversion [1–5]. Most of these

S. V. Boriskina (✉)
Mechanical Engineering Department, Massachusetts Institute of Technology,
77 Massachusetts Avenue, Cambridge, MA, USA
e-mail: sboriskina@gmail.com

T. V. Shahbazyan and M. I. Stockman (eds.), *Plasmonics: Theory and Applications*,
Challenges and Advances in Computational Chemistry and Physics 15,
DOI: 10.1007/978-94-007-7805-4_12, © Springer Science+Business Media Dordrecht 2013

applications–Raman and fluorescence sensing being the most widespread–make use of the electric field enhancement and high local density of states provided by plasmonic nanostructures to amplify weak molecular signals such as Rayleigh [6–8] or Raman [9–13] scattering efficiency, absorption efficiency [14], fluorescence rate [15–18], etc.

The electric field enhancement is a manifestation of the resonant excitation of collective oscillations of free charge carriers in some materials (e.g., free electrons in metals) by the external light sources or embedded emitters. In the language of quantum mechanics, this process can be explained as the excitation of plasmons (quanta of plasma oscillations). The collective dynamics of plasmons is driven by the long-range correlations caused by Coulomb forces, and can be drastically modified by engineering the boundaries of the spatial region filled by electron plasma. In particular, bulk plasmons confined in thin metal films can couple with photons to create surface plasmon-polariton (SPP) waves [22]. On the other hand, illumination-induced collective response of plasmons confined in nanoparticles is manifested in the excitation of quantized localized surface plasmon (LSP) modes with different angular momenta [23].

Although being quantum in nature, many plasmonic effects can be well described in the frame of the classical electromagnetic theory by using a semi-classical Drude-Lorentz-Sommerfeld model to define the frequency-dependent permittivity of metals. As a result, many fundamental principles and engineering solutions established in the electromagnetic modeling of radio-frequency (RF) antennas, microwave transmission lines, circuit elements, etc. can be applied to study and design plasmonic nanostructures. These include the concepts of antenna resistance, directivity and efficiency [24] and the principle of impedance matching [25, 26] just to name a few. Overall, the striking analogies with RF and microwave engineering–which focus on reversible interfacing of the propagating radiation with the fields localized inside sub-wavelength-size components–cemented the use of the design framework that treats plasmonic nanostructures as nanoscale analogs of RF antennas [17, 24, 27–29] and waveguides [2, 26, 30–32]. Alternative yet closely-related formulations are based on the treatment of plasmonic components as lumped circuit elements [33, 34] and resonators for plasmons [35–37].

The concept of an optical antenna is a very straightforward and visual analogy to describe a plasmonic nanoparticle, which can serve as both electromagnetic transmitter and receiver capable of converting the incoming radiation into localized surface plasmon modes, subsequently re-radiating it into the far-field, or modifying emission properties of embedded molecules. The oscillating dipole moments in individual particles induced by external sources can in turn be treated as secondary sources of electromagnetic radiation, i.e., dipole antennas (Fig. 12.1a). Dimer-gap nanoantenna configuration, which provides larger radiation efficiency as well as higher spectral tunability than an individual nanoparticle, can be constructed by analogy with a classical radio-frequency radiator, the Hertzian dipole (Fig. 12.1b) [27, 38]. The RF technology analogies so deeply penetrated the field of plasmonics research, that the terms ‘noble-metal nanoparticle(s)’ and ‘optical nanoantenna(s)’ became almost interchangeable. Furthermore, since the collective response of multi-particle struc-

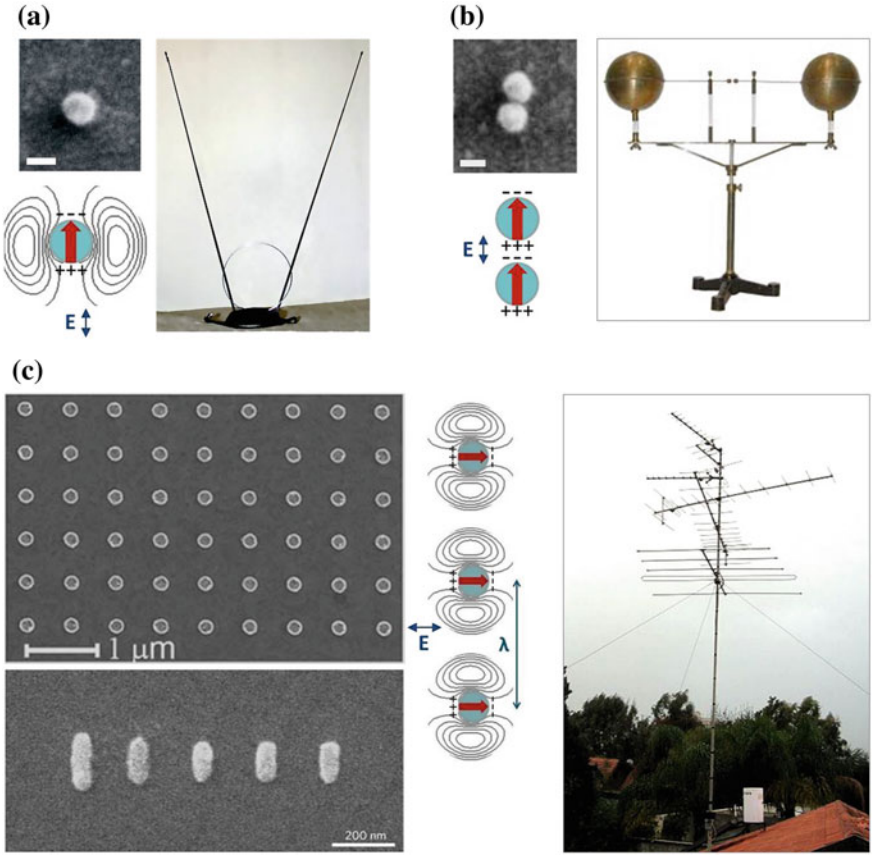

Fig. 12.1 Noble-metal nanoparticles as optical nanoantennas. **a** A single metal nanoparticle with an oscillating electric dipole moment induced by an external light source serves as an analog to an RF dipole antenna. The scale bars in SEM images here and in **b** are 50 nm (adapted with permission from [19], ©ACS). **b** Dimer-gap nanoantenna as an analog to a classical Hertzian dipole radio-frequency radiator. **c** Ordered metal nanoparticle arrays (adapted with permission from: *top left* [20] ©AIP, *bottom left* [21] ©NPG) as optical analogs to phased periodic antenna arrays and Yagi-Uda antennas. The insets show schematics of the charge distribution and emission patterns of dipole LSP modes of individual nanoparticles. Antennas images *source* wikimedia commons

tures is governed by the long-range interactions between individual dipoles (as long as the interparticle spacing is large enough so that the contribution of higher order resonances is negligible), various phased RF antenna array configurations have been successfully replicated on the nanoscale (Fig. 12.1c) [20, 21, 39–42].

On the other hand, for closely-packed nanoparticle clusters–where short-range interactions play the major role–a theoretical framework drawing analogies with chemistry has been successfully used. Owing to the similarities between the properties of confined quantized plasmonic states in nanoparticles and confined elec-

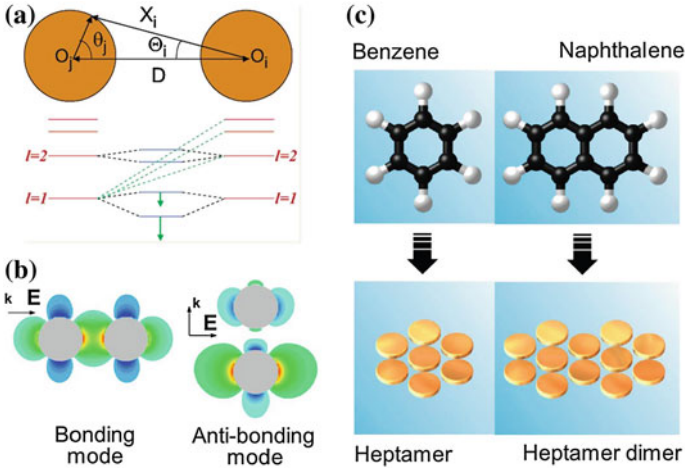

Fig. 12.2 Noble-metal nanoclusters as plasmonic molecules. **a** Splitting of the energy levels of LSP resonances in the nanoparticle dimer (reproduced with permission from [43], ©ACS). **b** Spatial distributions of the electric fields of the bonding (often referred to as longitudinal) and anti-bonding (often referred to as transverse) coupled-dipole modes. **c** Individual and coupled nanoparticle heptamers as plasmonic analogs of aromatic chemical molecules (adapted with permission from [44] ©ACS)

tron states in atoms, the former can be dubbed 'plasmonic atoms'. Just as atomic wavefunctions added together produce molecular orbitals, in-phase and out-of-phase overlaps of electromagnetic fields of LSP modes in plasmonic atoms result in the splitting of their energy levels [43] (Fig. 12.2a) and hybridization into bonding and anti-bonding modes of plasmonic molecules (shown in Fig. 12.2b for the lowest-energy modes of a diatomic molecule—nanoparticle dimer). The in-phase overlap combination (a bonding mode, Fig. 12.2b, left) produces a build-up of electromagnetic energy density in the gap between the nanoparticles, while the out-of-phase overlap results in the decrease in energy density down to a zero value in the gap center for the anti-bonding mode (Fig. 12.2b, right). Also, in perfect analogy with the molecular orbitals, the anti-bonding mode is higher in energy (has a shorter wavelength), while bonding mode is lower in energy than the dipole mode of an isolated plasmonic nanoparticle (see Fig. 12.2a [13]). More complex nature-inspired plasmonic molecule structures–such as aromatic plasmonic molecules shown in Fig. 12.2c) have been proposed [44, 45], offering a natural extension to the concept of plasmonic crystals and quasicrystals [46, 47]. It should also be noted that this chemical analogy has been previously exploited to study coupling of confined optical states in 'photonic molecules' [48].

In this chapter, I discuss in detail an alternative approach to the plasmonic design that does not cast the problem in the conventional terms of a sequence of scattering events but treats it as continuous energy flow process. This approach draws inspiration from hydrodynamics, which studies how the flow of fluids can be manipulated

by obstacles strategically positioned in the flow path. Accordingly, the focus shifts to the studies of the Poynting vector (which is a direct analog of a fluid flux) rather than the electromagnetic field behavior under the influence of nanostructures. Many interesting hydrodynamic effects can be engineered by a proper design of the obstacles pattern, including convective acceleration or deceleration even in the case of steady flow, formation of flow vortices–areas of spinning flow of fluid—as well as flows collisions accompanied by the formation of 'shock waves'. Electromagnetic analogies of these effects can be invoked in the plasmonic design, offering new insights into routing, re-circulation, and concentration of optical energy within nanostructures. In particular, optical energy flow can be molded into optical vortices–tornado-like areas of circular motion of energy flux–'pinned' to nanostructures (see Fig. 12.3). In the following, I will demonstrate that unique optical effects can be achieved by coupling multiple nanoscale vortices into complex structures resembling multiple-gear transmissions. Furthermore, it will be revealed that some previously

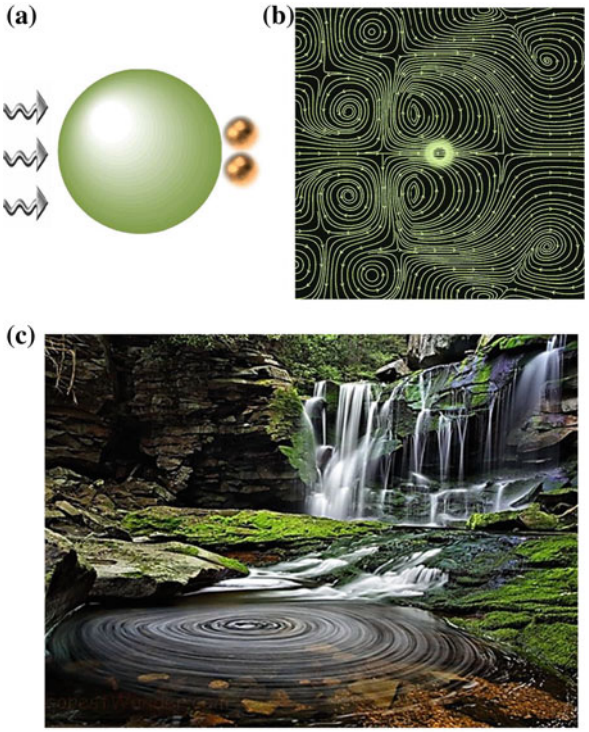

Fig. 12.3 Hydrodynamical modeling of plasmonic nanostructures: nanoparticles as the obstacles modifying the powerflow path. **a** An example of a photonic-plasmonic structure that molds optical powerflow into coupled counter-rotating vortices (shown in (**b**), see [49] for details). **c** An example of a complex trajectory of the fluid motion through the obstacle course, which features formation of the areas of convective flow acceleration and flow vortices [50]

observed strong light focusing effects can be attributed to nanostructure-induced formation and manipulation of optical powerflow vortices. Finally, I will discuss application of these new design principles to the development of multi-functional phase-operated plasmonic machinery, including light-trapping and biosensing platforms, SERS substrates, spectrally-tunable directional nanoantennas, strain sensors, waveguides, and metamaterial building blocks.

12.2 Energy Transport and Dissipation in Plasmonic Materials

The time- and space evolution of the electromagnetic field vectors **E** and **H** can be obtained by solving Maxwell equations with the problem-specific initial and/or boundary conditions:

$$\begin{aligned} &\nabla \cdot \mathbf{E} = \rho/\varepsilon \\ &\nabla \cdot \mathbf{H} = 0 \\ &\nabla \times \mathbf{E} = -\mu \cdot \partial \mathbf{H}/\partial t \\ &\nabla \times \mathbf{H} = \mathbf{J} + \varepsilon \cdot \partial \mathrm{E}/\partial t \end{aligned}, \tag{12.1}$$

However, it is "*more physically satisfying and visually appealing–as well as pedagogically more effective*" [23] to consider the evolution of the dc component of the power density flux, which is given by the time-averaged Poynting vector **S**:

$$\mathbf{S} = 1/2\mathrm{Re}[\mathbf{E} \times \mathbf{H}^*]. \tag{12.2}$$

Eq. 12.1 has a form applicable in the case of an isotropic linear medium, with ε and μ being permittivity and permeability, and ρ and **J**—charge and current density, respectively. The Poynting vector specifies the magnitude and direction of the energy flow, and the integral of the power flux through a closed surface gives the rate of the energy loss from the surrounded volume by leakage through its surface. Flow of the electromagnetic energy through absorbing media (such as metals) is accompanied by its irreversible dissipation, which represents a major bottleneck in the engineering of high-efficiency plasmonic devices.

The energy carried by the electromagnetic wave through a dissipative medium is stored partially in the electromagnetic field and partially in the excited charge oscillations in the host medium. In the frame of the semi-classical Drude-Lorentz-Sommerfeld approach, electromagnetic properties of materials with high concentration of free charge carriers that move against the background of positive ion cores can be captured within the well-known expression for the Drude dielectric permittivity. Assuming the excitation by a harmonic field with $\exp(-i\omega t)$ time dependence, the Drude permittivity function derived from the equation of motion of carriers with charge e, mass m, density n, and collision frequency γ takes the following complex form:

$$\varepsilon(\omega) = \varepsilon_r(\omega) + i\varepsilon_i(\omega) = 1 - \frac{\omega_p^2}{\omega^2 + \gamma^2} + i\frac{\omega_p^2 \gamma}{\omega(\omega^2 + \gamma^2)}, \tag{12.3}$$

where ω is the light angular frequency, $\omega_p = \sqrt{ne^2/\varepsilon_0 m}$ is the plasma frequency, and the effects of interband transitions and quantum size effects for particles much smaller than the carrier mean free path are neglected. Accordingly, the energy density of a harmonic field propagating through a non-magnetic, dispersive and absorptive medium characterized by the Drude permittivity can be written as [37, 51, 52]:

$$W = \varepsilon_0/4 \cdot (\varepsilon_r + 2\omega\varepsilon_i/\gamma) \cdot |\mathbf{E}|^2 + \mu_0/4 \cdot |\mathbf{H}|^2 . \tag{12.4}$$

The energy conservation law in this case reflects the rate of the energy change within the metal volume V due to leakage across its surface σ as well as due to volume dissipation:

$$-\int_V \dot{W} dV = \int_\sigma \mathbf{S} d\sigma + \frac{1}{2}\int_V \omega\varepsilon_0\varepsilon_i |\mathbf{E}|^2 dV . \tag{12.5}$$

One rarely-discussed yet important consequence of Eqs. 12.4–12.5 is that while a plasmonic nanostructure may provide light concentration in the volume below the diffraction limit in the host medium, the effective mode volume–which accounts for the portion of the electric field energy stored inside the metal–can in principle exceed this limit [37]. Furthermore, the energy dissipation rate grows with the increase of the imaginary part of permittivity, and also with the amount of energy stored in the electric rather than magnetic field. Typically, for electromagnetic fields confined in the vicinity of sub-wavelength plasmonic nanostructures, magnetic energy is just a tiny portion of the electric energy. This results in the fast energy dissipation and low degree of temporal coherence of localized SP modes [53]. Typical approaches to alleviate or compensate for dissipation losses include loss compensation with gain [4, 54, 55]–which however may require high pump rates and complicates local heat management in sub-wavelength plasmonic components–and the search for new materials with high charge carriers mobility yet reduced dissipative losses [56–59]. In the following, I will discuss an alternative approach to reducing the dissipative losses by modifying the pattern of the nanoscale powerflow through plasmonic nanostructures.

12.3 How can a Particle Absorb more than the Light Incident on it?

The above question was famously posed and answered by Craig Bohren [23] to explain the physics of the strong energy concentration on metal nanoparticles by studying the modification of the optical powerflow in the electromagnetic field due to the presence of a single nanoparticle. The Poynting vector field lines—which otherwise would have been parallel lines along the propagation direction of the plane wave–become drastically distorted in the vicinity of the particle at the frequencies corresponding to the real parts of the particle eigenmodes frequencies [23, 60, 61]. This effect is illustrated in Fig. 12.4a, which shows the optical powerflow behavior

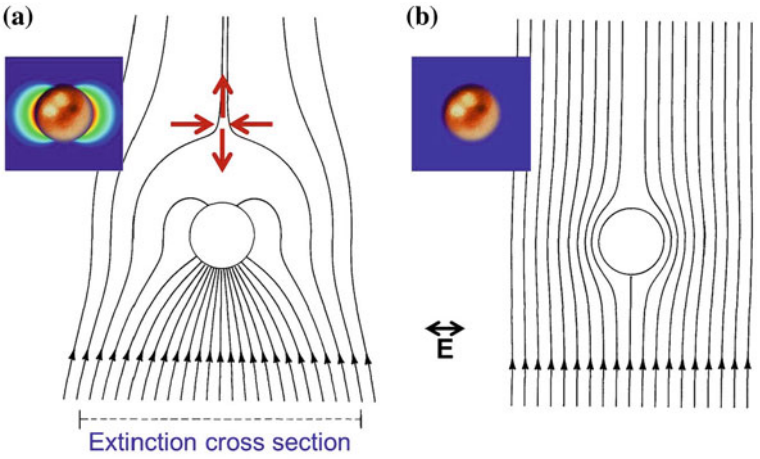

Fig. 12.4 Optical powerflow underlying the dipole LSP resonance in the plane wave scattering by a metal nanoparticle. Field lines of the Poynting vector in the E-plane around an aluminum nanosphere illuminated by a plane wave at the frequency of its dipole LSP resonance (**a**) and away from it (**b**) (adapted with permission from [23] ©AIP). The *insets* show the corresponding electric field intensity distributions around the particle

at the wavelength of the dipole LSP mode in an aluminum nanosphere [23]. Far from the sphere, the field lines are still parallel, but they strongly converge to the sphere surface in close vicinity to the particle, increasing the effective particle cross-section, as 'seen' by light. This ability of the particle to harvest light from the area much larger that the particle cross-section translates into the strong field concentration on the particle surface (see inset to Fig. 12.4a). It was initially assumed that away from the LSP resonances, the Poynting vector field lines just bend around the particle, resulting in the absence of the strong field enhancement off resonance (Fig. 12.4b).

In general, the ability of the particle to scatter and absorb light can be characterized by its scattering/absorption cross sections, or scattering/absorption efficiencies (cross-sections normalized to the particle volume). For a nanosphere of radius a and complex-valued permittivityε immersed in air, these efficiencies can be found by analytically solving the Maxwell equations in the quasi-static approximation, and have the following form [23]:

$$Q_{abs} \approx 4\left(\frac{2\pi a}{\lambda}\right) \mathrm{Im}\left(\frac{\varepsilon - 1}{\varepsilon + 2}\right), \; Q_{sca} \approx \frac{8}{3}\left(\frac{2\pi a}{\lambda}\right)^4 \left|\frac{\varepsilon - 1}{\varepsilon + 2}\right|^2. \tag{12.6}$$

Not surprisingly, both, the scattering and the absorption cross-sections grow with increase of the sphere size (although the scattering efficiency clearly prevails for larger particles), and their values resonantly peak at the frequency where $\varepsilon_r = -2$. A somewhat less-expected result is that not only the scattering efficiency and localized field intensity (see e.g. [62]) but also the absorption efficiency is inversely proportional to the ε_i value at the resonant frequency.

The most striking feature of the on-resonance powerflow pattern shown in Fig. 12.4a is the reversal of the energy flow in the particle shadow area, with a portion of energy entering the particle from behind. This powerflow reversal is driven by the formation of a topological feature in the Poynting vector field—a saddle node. The direction of the powerflow around the saddle node is highlighted with red arrows in Fig. 12.4a. A presence of another saddle node inside the particle volume drives the exchange of the electromagnetic energy between the E- and H-planes. As the energy re-circulation occurs through the volume of the metal–where energy dissipation takes place (12.5)–the LSP resonance is accompanied by high absorption losses. The saddle nodes observed in Fig. 12.4a are the local topological features in the Poynting vector field at which the intensity of the time-averaged Poynting vector is zero, and thus its phase cannot be defined [63–67]. The powerflow lines around the saddle points are hyperbolas (see Fig. 12.4a). It has previously been observed that the decrease of the material dissipation losses results in even more complex picture of the powerflow through the particle [61, 68]. This effect may explain the inverse dependence of the absorption efficiency on the imaginary part of the dielectric function due to more efficient light re-circulation through the metal volume.

The scattering efficiency as well as the intensity of the local electric field concentrated on the particle surface can be further enhanced by combining the individual particles into ordered arrays and making use of the constructive interference of the scattered partial fields. The scattering, absorption and emission spectra of such arrays exhibit sharp resonant peaks [20, 41, 42, 46, 69–71] corresponding to the well-known Rayleigh anomalies associated with the opening of new array diffraction orders. For discrete values of array periods proportional to the wavelength of the incident field, the dipoles induced in individual particles oscillate in phase, inducing coherent correlations across the array. This collective effect – known as superradiance–was initially predicted by Dicke for a system of two-level atoms [72] and results in the generation of a signal proportional to the square of the number of dipoles in the directions of their constructive interference.

A complex picture of energy flow through a periodic chain of gold nanoparticles at the frequency of the chain superradiant collective mode resulting from the spectral overlap of a particle dipole LSP resonance and a chain Rayleigh anomaly is illustrated in Fig. 12.5b. It can be seen that–similarly to the case of individual nanoparticles–the field lines strongly deflect towards particles, and the energy is re-circulated through their metal volumes. Furthermore, formation of a collective mode is associated with appearance of additional topological features around the particle chain (the direction of powerflow around additional saddle nodes is indicated with red arrows in Fig. 12.5b). The net result of this effect is a more efficient light trapping and re-circulation through the particle chain, which increases its collective scattering, absorption, and field enhancement efficiency over that of a sum of efficiencies of individual nanoparticles.

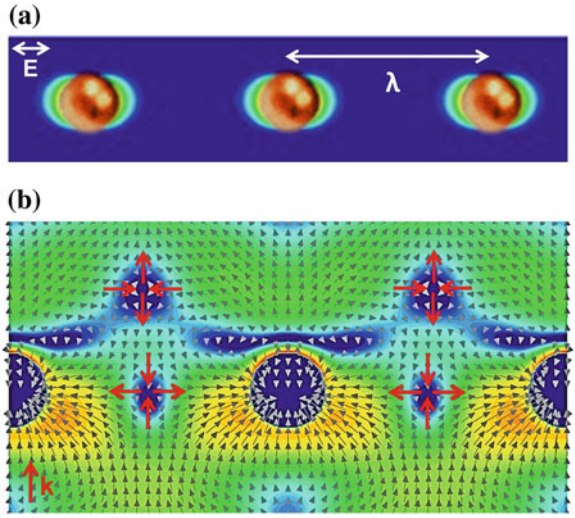

Fig. 12.5 Energy flow underlying the Dicke superradience effect in a periodic nanoparticle array. **a** Electric field intensity distribution in the E-plane of the periodic chain of Au nanoparticles separated by distances close to the wavelength of the illuminating plane wave. **b** Powerflow pattern (*small arrows*) and the spatial intensity map of the Poynting vector in the plane cutting through the centers of the nanoparticles in the chain. The direction of the powerflow around the additional array-induced saddle nodes is highlighted with *red arrows*

12.4 Nanoparticle-Generated Optical Tornadoes

Saddle nodes are not the only type of topological features that can emerge as a result of the interference of several waves (or–in the alternative hydrodynamic picture–collision of several flows). Perhaps the most intriguing flow features are flow vortices—singular nodes of the Poynting vector (points in 2D and lines in 3D)—that are the centers of circulating powerflow (i.e., the field lines surrounding a vortex are circles) [63, 65, 73]. These optical analogs of whirlpools and tornadoes can be created by superposition of three (or more) waves, e.g., plane waves, partially scattered fields, pulses, or fields generated by point sources. Understanding the origins and exploiting flow effects associated with these topological features have been proven to be of high relevance for many branches of physics, including hydrodynamics, acoustics, quantum physics, and singular optics [73, 74].

Formation of vortices is known to significantly affect the properties of superfluids, superconductors, and optical components; however, without proper engineering their effect can be detrimental. In particular, electromagnetic vortices form in the interference field of the waves propagating through random, turbulent and chaotic media and are manifested as dark points in the speckle fields. However, their presence causes trouble in the measurement and interpretation of scattered fields for remote sensing applications. Formation of vortices in the interference field of light

scattered by sub-wavelength slits can also be detrimental as it results in the phenomenon of the frustrated transmission [66]. Likewise, the motion of 'Abrikosov vortices' –nanoscale tubes of magnetic flux that form inside superconductors upon exposure to magnetic fields–decreases the current-carrying capability of superconductors and requires vortex immobilization (or 'pinning') by the material artificial defects [75, 76]. To pin vortices effectively, in-depth understanding of the pinning strength of individual defects as well as the collective effects of many defects interacting with many vortices is required.

In a perfect analogy, developing a general design strategy of pinning optical vortices to properly-designed plasmonic nanostructures would offer an unprecedented degree of control over light trapping in sub-wavelength volumes and in dynamical manipulation of nanoscale powerflow patterns. We already saw in the previous sections that resonant scattering of light from noble-metal nanoparticles creates a complex spatial distribution of the time-averaged Poynting vector in their near-field. An even more interesting nanoscale powerflow features can be observed in at the frequencies just around the LSP resonant frequency in the nanoparticle, as illustrated in Figs. 12.6 and 12.7. Fig. 12.6a shows frequency spectra of the electric and magnetic

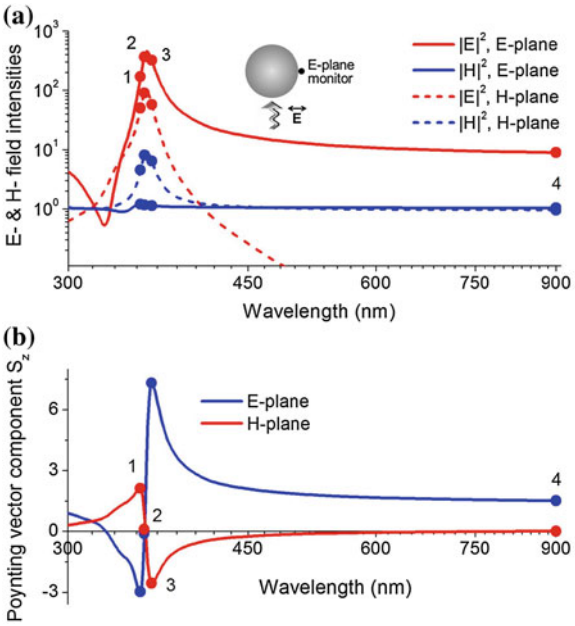

Fig. 12.6 Optical powerflow around a plasmonic nanoparticle: off-resonance effects. Wavelength spectra of the electromagnetic field intensities (**a**) and the energy flow direction (**b**) around a 30 nm-diameter Ag nanosphere in a wide spectral window enclosing the particle LSP resonance. The particle is illuminated by a linearly-polarized plane wave propagating upwards along the z-axis. The *inset* in (**a**) shows the spatial position of the field monitor in the E-plane (the H-plane monitor is located at the same position in the H plane). The dots indicate the discrete wavelengths at which the spatial distributions of the field intensity and powerflow patterns are calculated (see Fig. 12.7)

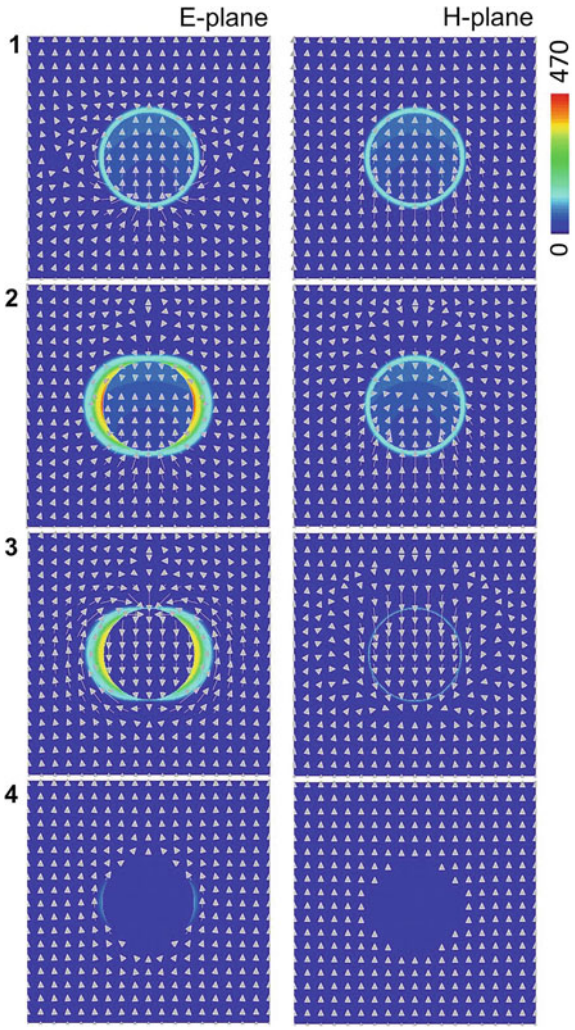

Fig. 12.7 Optical powerflow (arrows) and E-field intensity patterns on a 30 nm-diam Ag sphere at the frequencies around its dipole LSP resonance (positions 1–4 are marked in Fig. 12.6)

field intensities generated on the particle surface by a plane wave propagating along the z-axis and linearly polarized along the x-axis. The intensity values are probed at intersections of the particle equatorial plane with the E- and H-planes (see inset to Fig. 12.6a). The excitation of the dipole LSP resonance in the nanoparticle is marked by the pronounced peaks in the E-field intensity spectra (with the E-plane intensity value being an order of magnitude higher). The magnetic field intensity probed in the H-plane also features a weak resonant feature in the same frequency range.

To reveal the direction and density of the optical power flux around the nanoparticle on and off its LSP resonance, the frequency spectra of the z-component of the Poynting vector (pointing in the direction of the plane wave propagation) are plotted in Fig. 12.6b. The Poynting vector (12.2) is a 3D real-valued vector field, which in the Cartesian coordinate system is defined by three orthogonal components: $\mathbf{S} = \{S_x, S_y, S_z\}$. The plots in Fig. 12.6b show that the direction of the powerflow around the particle changes abruptly from forward (characterized by positive S_z values) to backward (negative S_z) at the wavelength of the LSP resonance. The phase change by π at a resonance is a manifestation of the delay between the action of the driving force and the oscillator response. It is a characteristic feature of any resonant structure driven by the external field, including classical forced oscillators [77, 78]. However, the spatial distributions of the Poynting vector field around the particle on and off resonance shown in Fig. 12.7 reveal an intricate picture of local powerflow. In particular, a pair of saddle nodes can be observed in the on-resonance powerflow pattern 2, while at the frequencies just around the LSP resonance, the powerflow forms pairs of coupled counter-rotating vortices (patterns 1 and 3 in Fig. 12.7). Only far away from the resonant frequency (pattern 4) the flow resembles the one discussed by Bohren (compare to Fig. 12.4b). Hereafter, the arrows point into the direction of the local powerflow, and the length of each arrow is proportional to the local value of the Poynting vector amplitude.

First predicted theoretically several years ago [68, 81], the effect of formation of optical whirlpools in individual nanoparticles initially did not attract a lot of attention because it does not translate into efficient field enhancement (see Fig. 12.6a). However, the situation changes when the particles are deposited on a high-refractive-index dielectric substrate as illustrated in Fig. 12.8 [79]. In particular, resonant illumination of an Au particle by a focused laser beam may cause formation of coupled counter-rotating vortices at the interface between the particle and the substrate (shown in Fig. 12.8a). The strong light re-circulation through a nanoscale area underneath the

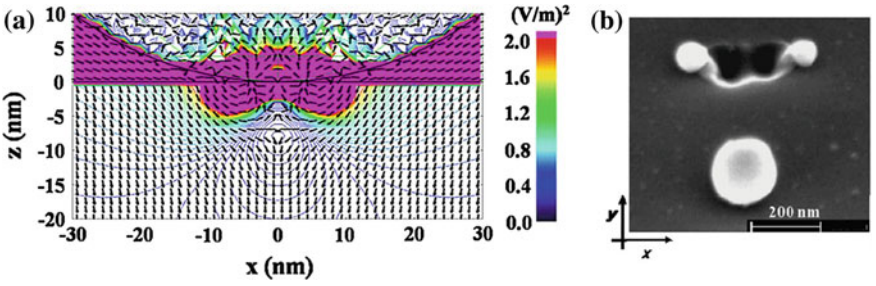

Fig. 12.8 Near-field nanopatterning with plasmonic particles. **a** Optical powerflow (arrows) and the electric field intensity distribution (color) around a 100 nm-diameter Au nanosphere deposited on a silicon substrate (reproduced with permission from [79], ©Springer). **b** SEM image of the nanohole fabricated by the particle-enhanced near-field under the laser illumination (reproduced with permission from [80], ©Elsevier)

particle creates localized temperature gradient in the substrate material, and can be used for efficient nanohole processing (Fig. 12.8b) [80].

12.5 Molding the River of Light in Vortex Nanogear Transmissions

As shown in the previous sections, nanostructure-induced interference of the evanescent-field components of the electromagnetic field may generate complex spatial distributions of the time-averaged Poynting vector in the near-field region, including creation of nanoscale vortices of optical powerflow. This mechanism of light trapping offers a new way to efficiently focus and store light within nanoscale volumes. However, it calls for more work to formulate rational strategies for vortex-pinning nanostructures engineering and to predict new physical effects. It has long been realized that variations of amplitude and phase of interacting *propagating waves* can be used to create and control *free-space vortex fields*. Experimental techniques for the free-space vortices generation include the use of "forked" holograms, lenses and spiral phase plates as well as their recently proposed plasmonic analogs [82–84]. Complex vortex topologies such as loops and knots can be created by superposing waves with correctly-weighted amplitudes and phases [85, 86]. A similar theoretical framework for generation and manipulation of the powerflow vortices via the interference of evanescent waves in plasmonic nanostructures is still under development [49, 67, 87], and below I will review several successful realizations of the vortex-pinning nanostructures.

The first example to be discussed is a celebrated silver nanolens design for efficient light focusing in the gap between the particles arranged into a showman-like structure (shown in Fig. 12.9a). This configuration was theoretically introduced over a decade ago by Li, Stockman and Bergman [89], and has generated over 500 follow-up papers since publication. However, the origin of the observed phenomenon has not been understood until recently [67], and can be revealed through the concept of coupled-vortex formation. To illustrate the underlying physical effects of light focusing in the nanolens, in Fig. 12.9b the on-resonance optical powerflow pattern is overlapped with the electric field intensity distribution. The structure is illuminated by a linearly-polarized plane wave (propagating from bottom up in Fig. 12.9b). Figure 12.9b reveals a complex picture of powerflow through the nanolens focal point, with the reversal of flow direction at the near-field intensity resonance, which is caused by the formation of coupled counter-rotating vortices inside the nanoparticles. The powerflow pattern in Fig. 12.9b resembles a multiple-gear transmission (schematically illustrated in Fig. 12.9c), which is composed of coupled vortex nanogears made of light and arranged into a linear sequence. To reflect this analogy, the nanostructures engineered to couple counter-rotating optical vortices into transmission-like sequences have been termed *Vortex Nanogear Transmissions* (VNTs) [67, 87]. As seen in Fig. 12.9b, light circulation through VNT drives

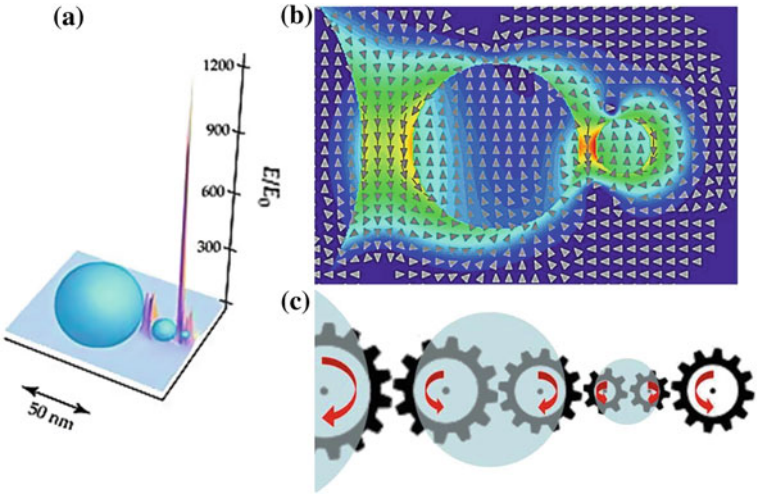

Fig. 12.9 Silver nanolens as a vortex nanogear tansmission. **a** Schematic of a nanolens and an electric field intensity distribution generated by an incoming plane wave (reproduced with permission from [88] ©APS). **b** Optical powerflow pattern underlying the nanolens focusing mechanism. **c** Schematic of the nanogear transmission generated in the nanolens. Power flux in each nanogear is looped through nanoparticles (adapted with permission from [67] ©RSC)

the increased backward powerflow through the inter-particle gaps, resulting in the dramatic local field enhancement.

The nanolens in Fig. 12.9 re-circulates optical power through the volume of nanoparticles, which results in the strong energy dissipation on every pass through the metal. Accordingly, engineering VNTs capable of weaving the powerflow *away from* the volume of metal nanoparticles would go long way in overcoming the problem of high dissipative losses in plasmonics even without using gain compensation mechanism. Physically, there are no restrictions on creating optical vortices outside of the nanostructure. Vortices–as well as saddle nodes–are characterized by the zero energy absorption ($\nabla \cdot \mathbf{S}(\mathbf{r}) = 0$) and thus can exist in the non-absorbing medium [63–67]. Indeed, various configurations of the VNTs capable of folding light into nanogears threaded through the inter-particle gaps have been predicted theoretically [49, 67, 87] and subsequently realized experimentally [87]. One such design is shown in the inset to Fig. 12.10a, and consists of a regular linear chain of identical Ag nanoparticle dimers separated by sub-wavelength gaps [67, 87]. This VNT can generate localized light intensity in the gap of the central dimer, which significantly exceeds that in a stand-alone dimer (Fig. 12.10a).

Note that the reduced powerflow through the metal results in the significant narrowing of the resonance linewidth, reflecting the increase of the quality (Q) factor of the collective VNT mode over that of a single dimer LSP mode. The Q-factor is inversely proportional to the energy loss rate of the mode. It can be interpreted as the number of field oscillations that occur coherently, during which the mode is able to

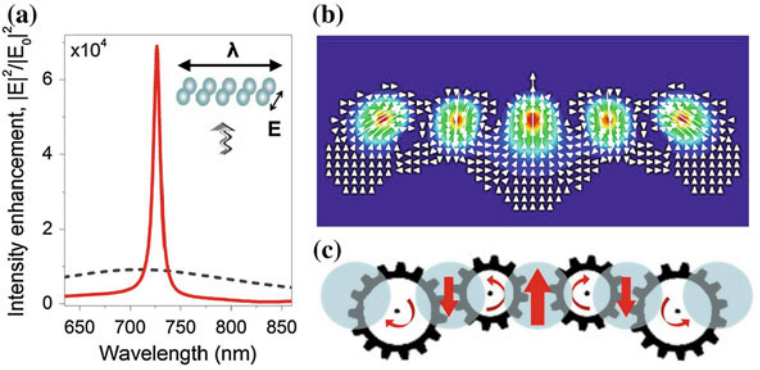

Fig. 12.10 Vortex nanogear transmission re-circulating optical energy outside of the nanoparticles metal volume. **a** Wavelength spectrum of the electric field intensity enhancement in the center of a chain of Ag nanosphere dimers of 50 nm sphere radii, 3 nm intra-dimer gaps and 10 nm inter-dimer gaps in water, as shown in the inset. The corresponding spectrum of a single dimer is shown as *dashed line*. The structures are illuminated by a plane wave with the electric field polarized along the dimers axes. **b** Poynting vector intensity distribution and powerflow through the chain (plotted in the plane cutting through the centers of the dimer gaps) at its resonant wavelength. **c** Schematic of the VNT generated in the dimer chain. Power flux in each nanogear is looped between the particles (adapted with permission from [67] ©RSC)

sustain its phase and accumulate energy. Accordingly, local fields can be enhanced by a factor of Q (as seen in Fig. 12.10a). Other important characteristics of the mode interaction with its material environment also scale with Q, including spontaneous and stimulated emission rates, absorption rates, and the strength of resonant Coulomb interaction between distant charges [37, 90, 91].

Metal nanoparticle structures capable of pinning optical vortices and combining them into nanogear transmissions can be easily fabricated by standard techniques such as electron beam lithography [87, 92] or template-assisted self-assembly [13]. Furthermore, their spectral properties can be tuned in a wide frequency range by varying the nanoparticle sizes as well as the separations between adjacent dimers (see Fig. 12.11). In particular, the possibility of tuning the resonant frequency of a linear VNT by stretching has the potential for developing mechanically- and optofluidically-tunable devices. Note that the optical spectrum of a single nanodimer can also be tuned by pulling the two nanoparticles away from each other by stretching the substrate. However, the increase of the gap size has a severe detrimental effect on the dimer near-field intensity. To the contrary, the spectra of linear VNTs can be tuned by stretching the substrate in the direction along the VNT long axis (see Fig. 12.11c, d). This deformation does not result in the increase of the intra-dimer gaps (and for sufficient deformations can even shrink the gaps). This is reflected in the very slight variations in the peak intensity for a significant (over 100 %) VNT stretching (Fig. 12.11c).

Although the position of each optical vortex pinned to the nanostructure is sensitive to changes in the structure geometry, vortices are structurally stable and typically

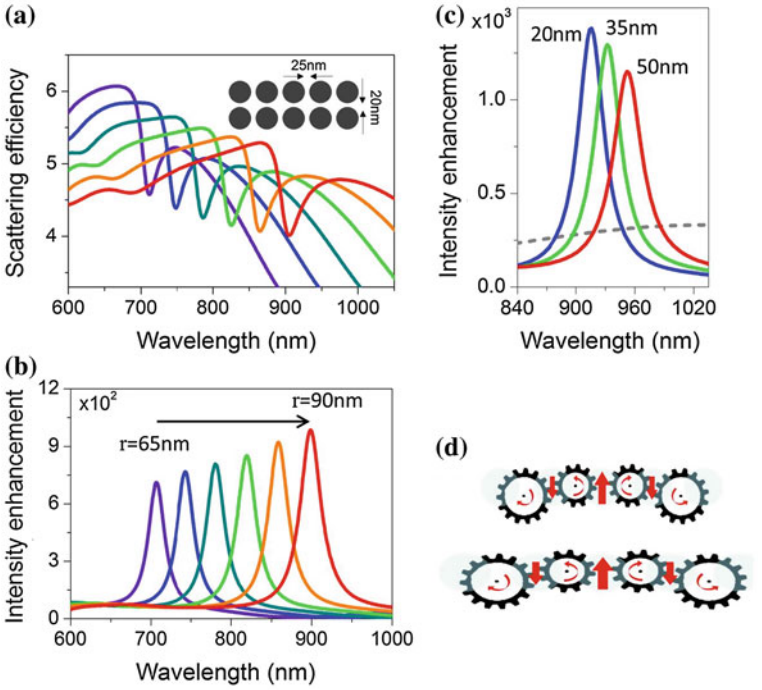

Fig. 12.11 Rainbow trapping in spectrally-tunable VNTs. Red-shifting of the spectral features in the scattering efficiency (**a**) and the localized electric field intensity (**b**) of the linear VNT shown in the *inset*. Au nanoparticles radii are varied from 65–90 nm with 5 nm increment. (**c**) Tuning of the VNT spectrum via the increase of the inter-dimer gaps, which amounts to 'stretching' the vortex nanogears, as schematically illustrated in (**d**)

only continuously migrate upon small perturbations of field parameters [63, 65]. This opens the way–exploited in the designs shown in Fig. 12.11–to continuously tune the VNT characteristics in a controllable fashion by changing the nanostructure design. On the other hand, large perturbations of the controllable external parameters (such as e.g. wavelength of incident field) can be introduced to force vortices of opposite sign either to approach and annihilate, or to nucleate as a pair. The above effects form the basis for realizing active spatio-temporal control of powerflow and the field intensity redistribution on the nanoscale, as illustrated in Fig. 12.12.

In particular, Fig. 12.12 shows a design of a 'vortex nanogate', in which optical powerflow though an Au nanodimer gap coupled to a dielectric microsphere (as shown in Fig. 12.3a) can be dynamically switched on/off and even reversed by tuning the frequency of the excitation [49]. As seen in Fig. 12.12a, under the resonant excitation by the plane wave, pairs of coupled counter-rotating optical vortices form both inside the microsphere and around the Au nanodimer gap. Their combined effect yields enhanced backward powerflow through the dimer gap (Fig. 12.12a). With the wavelength shift, the vortices migrate away from the nanodimer gap area,

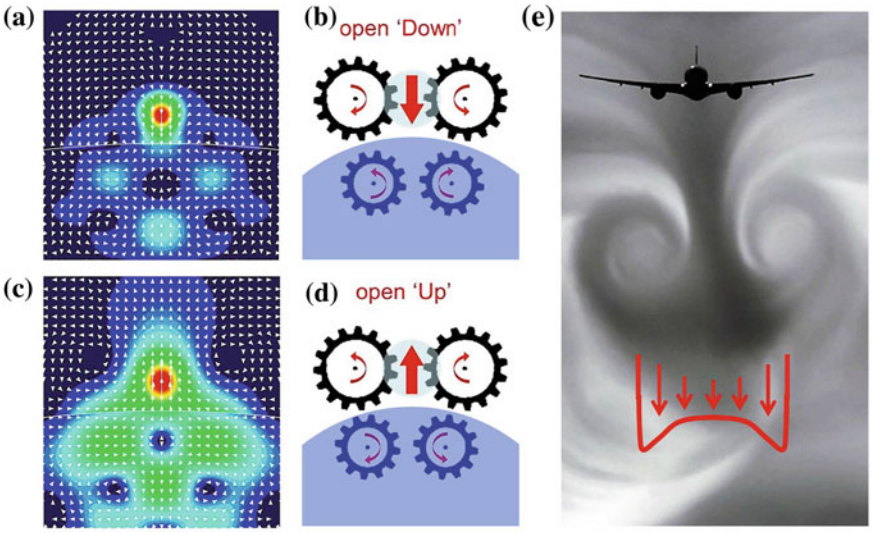

Fig. 12.12 Operation of the optoplasmonic vortex nanogate. **a**,**c** Poynting vector intensity maps and the optical powerflow through the gap of a microsphere-coupled Au nanodimer at the frequencies around the resonance of the structure shown in Fig. 12.3a. Spatial maps are shown in the plane cutting through the dimer gap center. **b**,**d** Schematics of the vortex-operated nanogate in the 'open Down' and 'open Up' positions (reproduced with permission from [49] ©OSA). **e** Coupled vortices forming behind a flying airplane (*source* [94]), with a vortex-driven downwash velocity profile shown as the *inset*

while oppositely-rotating vortices form there and help to drive the enhanced forward powerflow through the nanogate as shown in Fig. 12.12(c). Various arrangements of vortex nanogear configurations corresponding to different regimes of the nanogate operation (i.e., 'open up' or 'open down') are schematically visualized in Figs. 12.12b, d. The proposed strategy of re-configuring powerflow through plasmonic nanostructures opens the way to developing chip-integrated plasmonic and optoplasmonic switching architectures, which is crucial for implementation of quantum information nanocircuits. It should also be noted that vortex-driven enhanced or blocked powerflow through sub-wavelength gaps was revealed [66] to be behind the phenomenon of extraordinary transmission through nanohole arrays [93].

Overall, a rational design strategy based on creation and coupling of areas of circulating powerflow offers a new level of control over tailoring optical properties of plasmonic nanocircuits, possibly providing a better insight into their behavior than traditional approaches based on antenna design concepts. Furthermore, owing to the similarities between optical, hydrodynamic and superfluidic vortices, many concepts can be directly borrowed or adapted from other branches of physics. In particular, enhanced vortex-driven powerflow through the dimer gap shown in Figs. 12.12a,c remarkably resembles a picture of coupled vortex flows that combine to provide a downwash velocity profile behind a flying airplane (Fig. 12.12e). The fundamental

mechanisms underlying this intuitive picture can be revealed by using the mathematical isomorphism between the hydrodynamic equations and the electromagnetic wave equations separated into phase and amplitude variables, as will be discussed in the following section.

12.6 Hydrodynamics of Light Flow in Plasmonic Nanostructures

Maxwell famously pointed out defending his theory of molecular vortices–which aimed at explaining electromagnetic phenomena mechanically in terms of the interacting vortices in the imaginary fluid ether–that "*it is a good thing to have two ways of looking at a subject and to admit that there are two ways of looking at it*" [95]. It has long been recognized that hydrodynamics offers an alternative way of looking at electromagnetic waves propagation even in a very general case of dispersive, lossy and nonlinear media [96–101]. For example, a nonlinear Schrödinger equation that governs the amplitude of the wave trains propagating through nonlinear medium in a paraxial approximation can be re-cast in a hydrodynamic form via the Madelung transformation $\psi(\mathbf{r}, t) = \sqrt{\rho(\mathbf{r}, t)} \exp\{i\Phi(\mathbf{r}, t)\}$:

$$\begin{aligned} &\frac{\partial \rho}{\partial \tau} + \nabla'(\rho \mathbf{v}) = 0 \\ &\frac{\partial \mathbf{v}}{\partial \tau} + (\mathbf{v} \cdot \nabla')\mathbf{v} = -\frac{1}{\rho}\nabla'\left(\frac{\rho^2}{2}\right) + \nabla' Q \end{aligned} . \tag{12.6}$$

Eqs. 12.6 have a well-known form of the Navier-Stokes equations of the fluid dynamics for inviscid, compressible and irrotational flow, with the field intensity $|\psi|^2$ regarded as the 'photon fluid' (PF) density ρ, and the phase gradient $\nabla'\Phi$ as the PF velocity $\mathbf{v}$. Note that to arrive to the familiar form of (12.6), the time is treated as the third spatial coordinate: $\nabla' = \hat{\boldsymbol{x}}\partial/\partial x + \hat{\boldsymbol{y}}\partial/\partial y + \hat{\boldsymbol{t}}\partial/\partial t$, and the space coordinate in the propagation direction–as a generalized time coordinate τ: $\partial/\partial z \equiv \partial/\partial\tau$. The first equation in (12.6) has the same form as the continuity (mass conservation) equation of the fluid dynamics. The right hand side of the momentum conservation equation (second line in (12.6)), however, features not only the term analogous to the fluid pressure but also a term $Q = \nabla'^2\sqrt{\rho}/2\sqrt{\rho}$ known as 'quantum pressure', which has no analog in hydrodynamics.

The availability of the hydrodynamic form (12.6) of the nonlinear Schrödinger equation helps to draw parallels between the properties of lasers, superfluids and superconductors. A similar, but rarely invoked analogy can be drawn between the electromagnetic Maxwell equations and the hydrodynamics equations. In particular, the Helmholtz wave equation for a monochromatic plane wave propagating in a piece-wise homogeneous linear nonmagnetic medium with complex permittivity $\varepsilon(\mathbf{r}) = \varepsilon_r(\mathbf{r}) + i\varepsilon_i(\mathbf{r})$ can be cast in a from similar to that of the Schrödinger equation with the external potential $V(\mathbf{r}) = k_0^2/2\,(1 - \varepsilon_r(\mathbf{r}))$ ($V(\mathbf{r}) = 0$ in the free space) and the total energy $E_0 = k_0^2/2$ [78]. Subsequent application of the

Madelung transformation $\mathbf{E}(\mathbf{r}) = \sum_{m=1}^{3} \hat{e}_m U_m(\mathbf{r}) \exp\{i(\Phi(\mathbf{r}) - \omega t)\}$ brings the wave equation to the hydrodynamic form for the steady flow ($\partial\rho/\partial t = 0$) of 'photon fluid' in the presence of sources and sinks $\alpha(\mathbf{r}) = -k_0^2 \varepsilon_i(\mathbf{r})$ [67, 102]:

$$\begin{array}{l} \nabla(\rho(\mathbf{r})\mathbf{v}(\mathbf{r})) = \alpha(\mathbf{r})\rho(\mathbf{r}) \\ (\mathbf{v}(\mathbf{r}) \cdot \nabla)\mathbf{v}(\mathbf{r}) = -\nabla(V(\mathbf{r}) + Q(\mathbf{r})) \end{array}. \tag{12.7}$$

Similarly to Eq. 12.6, here the intensity plays the role of a 'photon fluid' density $\rho(\mathbf{r}) = \mathbf{U}(\mathbf{r}) \cdot \mathbf{U}(\mathbf{r})$, and the phase gradient–the role of the fluid velocity, $\mathbf{v} = \nabla\Phi(\mathbf{r})$. However, the local pressure term does not appear in the absence of non-linearity, and the internal quantum potential has the following form: $Q(\mathbf{r}) = 1/(8\rho(\mathbf{r})) \sum_{m=1}^{3} (\nabla\rho_m(\mathbf{r}) \cdot \nabla\rho_m(\mathbf{r})/\rho_m(\mathbf{r})) - \nabla^2\rho(\mathbf{r})/(4\rho(\mathbf{r}))$, where $\rho_m(\mathbf{r}) = U_m^2(\mathbf{r})$. Accordingly, the optical flux defined by the Poynting vector transforms into the analog of a fluid flux (the momentum density): $\mathbf{S} = 1/(2\mu_0\omega) \cdot \rho(\mathbf{r})\mathbf{v}(\mathbf{r})$. One important difference between conventional fluids and the PF is that photon 'mass' can be created owing to the linear gain $\varepsilon_i(\mathbf{r}) < 0$ and dissipated through material losses $\varepsilon_i(\mathbf{r}) > 0$. The 'photon mass' reduction due to dissipative losses results in the decrease of the PF density (i.e., field intensity).

In the case of PF steady flow, the field patterns are constant in time, yet local accelerations/decelerations of the flow can occur between different parts of the plasmonic nanostructure, governed by the convective term $(\mathbf{v}(\mathbf{r}) \cdot \nabla)\mathbf{v}(\mathbf{r})$ in the momentum conservation equation. This situation is analogous to e.g. local variations of the velocity of the fluid flow passing through pipes of varying diameters. In the structures shown in Figs. 12.10–12.11, these local changes of flow rate are driven by the formation of vortices, with each vortex line inducing a velocity field given by the Biot-Savart formula [103] (compare to the vortex-driven airplane downwash velocity profile shown as the inset of Fig. 12.12e). In particular, the tangential velocity of an optical vortex varies inversely with the distance from its center, and the angular momentum is thus uniform everywhere throughout the vortex-induced circulating flow.

A change in the fluid's momentum can generate pressure, and this hydrodynamic effect is utilized in hydraulic pumps and motors, which increase the fluid kinetic energy (angular momentum) and then convert it into usable pressure energy. Accordingly, the problem of wave scattering by the VNT in Fig. 12.10 can be cast in new light by invoking the fluid dynamic analogy. Fig. 12.13 follows the evolution of the PF velocity and density along the z-axis, which passes from the bottom up through the gap of the VNT central dimer. At the VNT center, the flows generated by adjacent counter-rotating vortices collide and form a 'shock wave' in the form of a region of high PF density. In the situation depicted in Fig. 12.13, the PF gets convectively accelerated by the potential forces and impacts onto the narrow interparticle gaps of the VNT dimers. The threading of the PF through the gaps leads to a sudden change in the flow regime and results in the dramatic increase of the PF local density driven by the conversion of the PF kinetic energy into pressure energy. In effect, VNTs shown in Figs. 12.10–12.11 operate as plasmonic analogs of hydraulic pumps that exploit the convective acceleration of the PF caused by its circulation

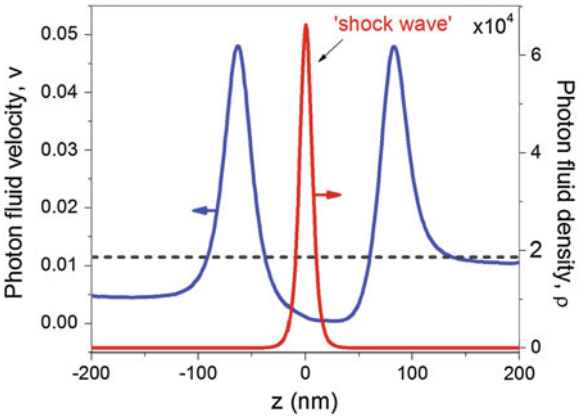

Fig. 12.13 VNT as an analog of a hydraulic pump. Velocity and density of the 'photon fluid' along the line parallel to the incident plane wave propagation direction and passing through the center of the linear VNT in Fig. 2.10. The *dash line* corresponds to the constant fluid velocity in the absence of the nanostructure. Formation of the 'shock wave' accompanied by the spatially-localized increase of the fluid density in the central dimer gap is observed (reproduced with permission from [67] ©RSC)

through the vortices 'pinned' to the nanostructure to generate localized areas of high PF density [67].

12.7 Applications of Plasmonically-Integrated Tornadoes

As demonstrated in the previous sections, nanostructure-generated fine features of the electromagnetic energy flow–which may not be apparent from the near-field intensity patterns–can, however, be controllably manipulated to tailor local properties of the electromagnetic field. The logical next step is the conversion of these theoretical insights into useful practical applications. It is expected that the new approach to light trapping in nanoscale volumes by the generation of optical tornadoes pinned to plasmonic nanostructures may lead to novel device solutions in light generation, harvesting and processing. Here are some specific application areas where this new plasmonic engineering concept offers advantages.

The most obvious advantages are envisioned in making use of the VNTs ability to generate high field intensity for Raman and fluorescence spectroscopy. The first surface-enhanced Raman sensing (SERS) platforms have already been successfully fabricated by e-beam lithography on planar dielectric substrates (Fig. 12.14a, c). They have been characterized by elastic scattering spectroscopy (Fig. 12.14b), and used to detect Raman spectra of para-mercaptoaniline (pMA) molecules [87] (Fig. 12.14d). To generate a multi-frequency response, different light trapping techniques can be combined within a single platform [7, 49, 69, 104, 105], e.g., Dicke effect in a periodic arrays and light re-circulation through VNTs [87]. Furthermore, it was

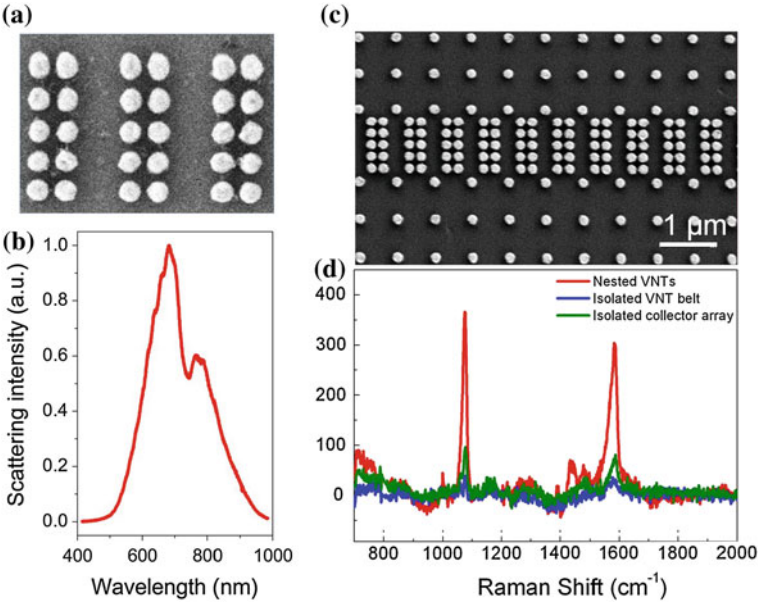

Fig. 12.14 Elastic and inelastic scattering characterization of fabricated VNTs. **a** SEM image of planar Au VNT structures fabricated by e-beam lithography on a quartz substrate (particle diameters 139.2 nm, intra-dimer gaps 30.0 nm and inter-dimer gaps 46.4 nm). **b** Experimental dark-field scattering spectrum of VNTs shown in **a**. **c** SEM image of a SERS platform that combines two mechanisms of field enhancement–Dicke effect in a periodic array and light re-circulation through VNTs. **d** Experimental SERS spectra of pMA on the platform shown in **c** (adapted with permission from [87] ©ACS)

theoretically predicted that embedding of dipole emitters in VNTs can result in the manifold resonant enhancement of their radiative rates over those of emitters embedded in the gaps of isolated dimers [67]. VNTs can also strongly modify the angular distribution of light emitted by the embedded dipole. This offers opportunities for surface-enhanced fluorescence microscopy and vortex-mediated radiative engineering [67].

As already discussed in previous sections, the new way to manipulate powerflow by creating, moving and annihilating nanoscale optical vortices offers tremendous opportunities for intensity switching and energy transfer in plasmonic nanocircuits. Just as mechanical gears and hydrodynamic turbines form the basis of complex machinery, vortex nanogears can be combined into complex reconfigurable networks to enable dynamical light routing. One possible realization of a reconfigurable plasmonic VNT with a footprint of $\sim 320\,\mathrm{nm}^2$ is shown in Fig. 12.15 [67]. It consists of six Ag nanodimers arranged into a symmetrical ring-like structure and features several resonances in its optical spectra. The vector fields of the powerflow evaluated at two different resonant wavelengths show drastically different pictures of energy circulation through the nanostructure (Fig. 12.15a, c). In particular, formation of a

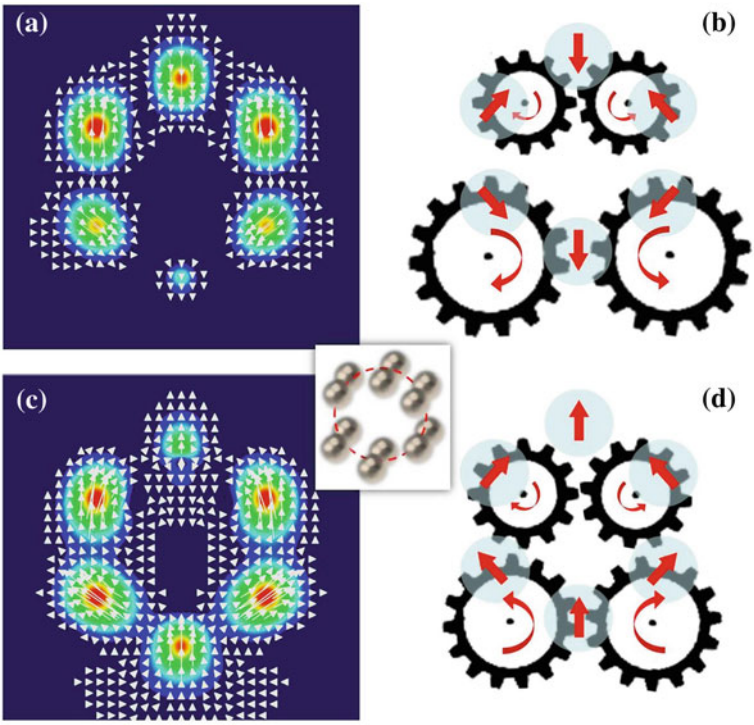

Fig. 12.15 Re-configurable looped nanogear transmission. **a**, **c** Poynting vector intensity distribution and powerflow pattern through the looped dimer chain shown in the inset at different wavelengths. The inset shows a schematic of a ring-like arrangement of Ag nanoparticle dimers of 50 nm radii, 3 nm intra-dimer gaps, and 10 nm inter-dimer gaps in water. **b**, **d** Schematics of the coupled and uncoupled VNTs generated by the structure at different resonant wavelengths. Power flux in each nanogear is looped through the gaps between the particles (reproduced with permission from [67] ©RSC)

looped VNT composed of four coupled vortex nanogears is observed in Fig. 12.15c, d. In contrast, when the same structure is illuminated by light of a slightly shifted wavelength, it behaves as a pair of uncoupled two-gear transmissions, thus reversing the powerflow direction as shown in Fig. 12.15b, d.

Another field that can benefit from the hydrodynamics-inspired high-Q plasmonic components is bio(chemical) sensing. High Q-factors of surface plasmon modes in VNTs translate into high spectral resolution of sensors. In particular, Fig. 12.16 demonstrates that novel bio(chemical) sensors based on the plasmonically-integrated tornadoes may offer at least an order of magnitude improvement in the figure-of-merit values as compared to current designs. In Fig. 12.16, the performance of the VNT in Fig. 12.15 as a refractive index sensor is evaluated by using the standard figure of merit: $FoM = sensitivity/linewidth$ [106, 107]. Sensor sensitivity is defined as the resonance shift resulting from the ambient refractive index change:

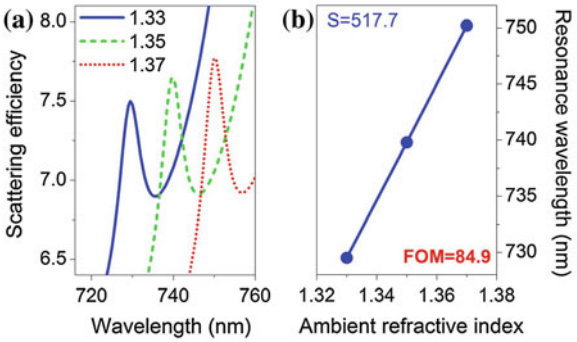

Fig. 12.16 Refractive index sensing with vortex nanogear transmissions. **a** Shift of the far-field scattering efficiency spectrum of the looped VNT in Fig. 12.15 with the change of the refractive index of the ambient medium. **b** The positions of the resonant peaks as a function of the refractive index. The calculated values of the refractive index sensitivity (S) and the corresponding figure of merit (FOM) are also shown

$S\,[nm/RIU] = \Delta\lambda/\Delta n$. The 'linewidth' of an asymmetrical resonant feature is measured as the wavelength difference between the resonant peak and the closest neighboring dip [106]. The VNT scattering spectrum shows pronounced redshifts with the refractive index increase (Fig. 12.16a). The linear regression slope for the resonance shift plotted in Fig. 12.16b yields the sensitivity value 518 nm/RIU, on par with those reported for other plasmonic nanosensors. However, owing to the narrow linewidths of the resonant features, the resulting FoM value of 85 is almost an order of magnitude larger than those predicted and measured in single particles (from ~1 to ~5.5) [107, 108] and nanoclusters (up to ~11) [106, 108]. Using low-loss nanoshells [109] and optimizing VNT configurations could enable even higher FoM values. Furthermore, the strong localized fields generated in VNTs provide optical trapping potentials strong enough to capture low-index particles and biological macromolecules. This offers novel solutions for background-free sensing of optically-trapped nano-objects, potentially reaching single-molecule sensitivity. It should also be noted that the high sensitivity of the VNTs optical spectra to the substrate stretching (Fig. 12.11c, d) makes them ideal candidates for nanoscale stress and strain sensors.

The proposed approach also offers the promise of a broad impact on nanoplasmonic-based renewable energy applications as it helps to eliminate the mismatch between the electronic and photonic length scales in thin-film photovoltaic devices. Most importantly, the expected increase of the efficiency and spectral bandwidth of light absorption can be achieved with the simultaneous reduction of the dissipative losses in metals. Light harvesting platforms based on folding optical powerflow into nanoscale vortices may help to minimize the thickness of semiconductor needed to absorb light completely and to amplify the signal via plasmonic enhancement mechanism. They will also be compatible for integration with either

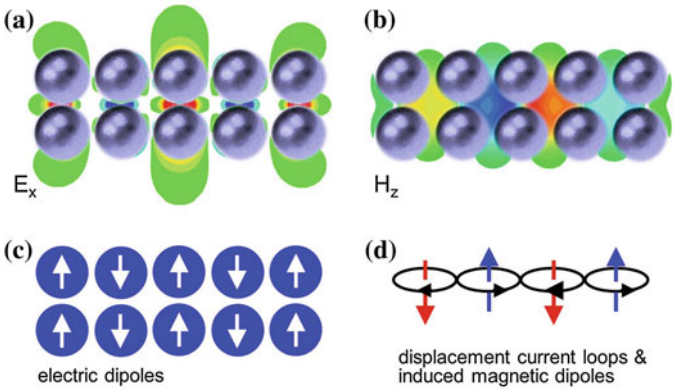

Fig. 12.17 Magnetic effects in vortex nanogears transmissions. Electric (**a**) and magnetic (**b**) field distributions in the plane of the VNT shown in Fig. 12.10 at the frequency of its collective mode resonance. Schematics of the induced electric dipoles (**c**), oscillating displacement currents and magnetic dipole moments (**d**)

silicon electronics or flexible substrates such as those based on organic and polymer materials.

Finally, excitation of collective coupled-vortex resonances in VNTs is accompanied by the generation of circulating displacement currents (Fig. 12.17). These currents, according to Maxwell's equations (12.1), induce magnetic moments (Fig. 12.17d) in the same way as circulating conducting currents in wire loops generate time-varying magnetic fields [33, 109, 110]. This effect can be clearly seen in Fig. 12.17, where the electric and magnetic field distributions are shown in the VNT plane. As schematically shown in Fig. 12.17d, antiphase magnetic moments are generated in the adjacent loops of displacement current, and their mutual coupling along the chain gives rise to an artificial "antiferromagnetic" behavior. We can now conclude that, according to Eqs. (12.4,12.5) the observed reduction of dissipative losses in VNTs in comparison to conventional plasmonic designs is achieved because (i) the electromagnetic energy is re-circulated outside of metal volume and thus does not get converted in to the kinetic energy of electrons, and (ii) noticeable portion of the energy is stored in the magnetic rather than electric field. Excitation of magnetic plasmons has also been observed in fused heptamer plasmonic molecules shown in Fig. 12.2c [44], however, in that case the energy is re-circulated through the metal volume, which increases dissipative losses. We have also recently demonstrated magnetic response in hybrid metal-dielectric vortex-pinning structures [111].

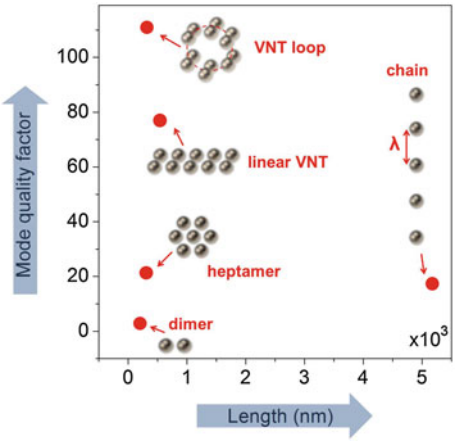

Fig. 12.18 Design roadmap for achieving high-Q modes in sub-wavelength plasmonic nanostructures composed of 100 nm silver nanoparticles

12.8 Conclusions and Outlook

A new hydrodynamics-inspired approach to plasmonic nanocircuit design is discussed. It helps to alleviate major setbacks to their practical applications, such as high radiative and/or dissipative losses of noble-metal nanostructures in the visible frequency range. In the frame of the new approach, basic building blocks of plasmonic nanocircuits are designed to feature phase singularities in the optical near fields. This results in the creation of areas of circulating electromagnetic energy flow–optical vortices–at pre-defined positions. As the examples discussed in this chapter demonstrate, the individual vortex-pinning building blocks may not exhibit any interesting electromagnetic behavior (such as high field intensity or narrow frequency linewidths). As such, they would have been discarded in the frame of the traditional design approaches. However, tailored coupling of individual nanoscale vortices into vortex nanogear transmissions may yield dramatic optical effects never observed before. The data presented in Fig. 12.18 summarize the advantages offered by the proposed rational design strategy. It offers a comparison between the optical performance of several popular designs of plasmonic components, including a nanodimer, a heptamer plasmonic molecule, and a periodic nanoparticle chain with the VNT structures shown in Figs. 12.10 and 12.14. For consistency, all the nanostructures in Fig. 12.18 are composed of identical 100 nm Ag nanoparticles and have the same minimum inter-particle gaps of 3nm. Fig. 12.18 shows that rationally-designed VNTs offer the way to achieve previously unattainable high-Q plasmonic modes within sub-wavelength footprints.

The advantages of the new vortex-pinning plasmonic platforms for sensing and spectroscopy having been demonstrated, other applications can be explored in the future. These include renewable energy generation (i.e., photovoltaic and photocatalytic platforms), metamaterials design, and reconfigurable nonlinear plasmonic nanocircuits [112, 113]. Another future exciting application for plasmonically-

integrated nanoscale tornadoes is in optical trapping of small particles (viruses, bacteria, etc.) and guiding them through on-chip nanoscale 'conveyor belts' [114]. The insights into the underlying physical mechanisms and analogies with the well-studied hydrodynamic effects are expected to help in developing additional design rules for complex plasmonic nanocircuitries. The hydrodynamics analogy also paves the road to using well-developed methods of computational fluid dynamics to facilitate simulation and optimization of plasmonic VNTs.

Acknowledgments I would like to thank Dr. Anton Desyatnikov from Australian National University and my colleagues at Boston University and MIT for useful discussions.

References

1. W.E. Moerner, New directions in single-molecule imaging and analysis. Proc. Natl. Acad. Sci. **104**, 12596 (2007)
2. S. Lal, S. Link, N.J. Halas, Nano-optics from sensing to waveguiding. Nat. Photonics **1**, 641–648 (2007)
3. J.A. Schuller, E.S. Barnard, W. Cai, Y.C. Jun, J.S. White, M.L. Brongersma, Plasmonics for extreme light concentration and manipulation. Nat. Mater. **9**, 193–204 (2010)
4. M.I. Stockman, Nanoplasmonics: past, present, and glimpse into future. Opt. Express **19**, 22029–22106 (2011)
5. H.A. Atwater, A. Polman, Plasmonics for improved photovoltaic devices. Nat. Mater. **9**, 205–213 (2010)
6. A.D. McFarland, R.P. Van Duyne, Single silver nanoparticles as real-time optical sensors with zeptomole sensitivity. Nano Lett. **3**, 1057–1062 (2003)
7. M.A. Santiago-Cordoba, S.V. Boriskina, F. Vollmer, M.C. Demirel, Nanoparticle-based protein detection by optical shift of a resonant microcavity. Appl. Phys. Lett. **99**, 073701 (2011)
8. S.I. Shopova, R. Rajmangal, S. Holler, S. Arnold, Plasmonic enhancement of a whispering-gallery-mode biosensor for single nanoparticle detection. Appl. Phys. Lett. **98**, 243104–243103 (2011)
9. M. Moskovits, L.L. Tay, J. Yang, T. Haslett, *SERS and the Single Molecule in Optical Properties of Nanostructured Random Media* (Springer, Berlin, 2002), pp. 215–226
10. K.A. Willets, R.P. Van Duyne, Localized surface plasmon resonance spectroscopy and sensing. Annu. Rev. Phys. Chem. **58**, 267–297 (2007)
11. F.J. Garcia-Vidal, J.B. Pendry, Collective theory for surface enhanced Raman scattering. Phys. Rev. Lett. **77**, 1163 (1996)
12. K. Kneipp, Y. Wang, H. Kneipp, L.T. Perelman, I. Itzkan, R.R. Dasari, M.S. Feld, Single molecule detection using surface-enhanced Raman scattering (SERS). Phys. Rev. Lett. **78**, 1667 (1997)
13. B. Yan, S.V. Boriskina, B.M. Reinhard, Theory, fabrication, and applications of nanoparticle cluster arrays in plasmon enhanced biosensing. J. Phys. Chem. C **115**, 24437–24453 (2011)
14. R. Adato, A.A. Yanik, J.J. Amsden, D.L. Kaplan, F.G. Omenetto, M.K. Hong, S. Erramilli, H. Altug, Ultra-sensitive vibrational spectroscopy of protein monolayers with plasmonic nanoantenna arrays. Proc. Natl. Acad. Sci. **106**, 19227 (2009)
15. P. Anger, P. Bharadwaj, L. Novotny, Enhancement and quenching of single-molecule fluorescence. Phys. Rev. Lett. **96**, 113002 (2006)
16. A. Kinkhabwala, Z. Yu, S. Fan, Y. Avlasevich, K. Mullen, W.E. Moerner, Large single-molecule fluorescence enhancements produced by a bowtie nanoantenna. Nat. Photonics **3**, 654–657 (2009)

17. S. Kühn, U. Håkanson, L. Rogobete, V. Sandoghdar, Enhancement of single-molecule fluorescence using a gold nanoparticle as an optical nanoantenna. Phys. Rev. Lett. **97**, 017402 (2006)
18. J.R. Lakowicz, Radiative decay engineering. Part 5: Metal-enhanced fluorescence and plasmon emission. Anal. Biochem. **337**, 171–194 (2005)
19. B. Yan, S.V. Boriskina, B.M. Reinhard, Optimizing gold nanoparticle cluster configurations (n <=7) for array applications. J. Phys. Chem. C **115**, 4578–4583 (2011)
20. Y. Chu, E. Schonbrun, T. Yang, K.B. Crozier, Experimental observation of narrow surface plasmon resonances in gold nanoparticle arrays. Appl. Phys. Lett. **93**, 181103–181108 (2008)
21. L. Novotny, N. van Hulst, Antennas for light. Nat. Photonics **5**, 83–90 (2011)
22. W.L. Barnes, A. Dereux, T.W. Ebbesen, Surface plasmon subwavelength optics. Nature **424**, 824–830 (2003)
23. C.F. Bohren, How can a particle absorb more than the light incident on it? Am. J. Phys. **51**, 323–327 (1983)
24. P. Bharadwaj, B. Deutsch, L. Novotny, Optical antennas. Adv. Opt. Photonics **1**, 438–483 (2009)
25. P. Spinelli, M. Hebbink, R. de Waele, L. Black, F. Lenzmann, A. Polman, Optical impedance matching using coupled plasmonic nanoparticle arrays. Nano Lett. **11**, 1760–1765 (2011)
26. P. Ginzburg, M. Orenstein, Plasmonic transmission lines: from micro to nano scale with lambda/4 impedance matching. Opt. Express **15**, 6762–6767 (2007)
27. A. Alu, N. Engheta, Tuning the scattering response of optical nanoantennas with nanocircuit loads. Nat. Photonics **2**, 307–310 (2008)
28. E. Cubukcu, Y. Nanfang, E.J. Smythe, L. Diehl, K.B. Crozier, F. Capasso, Plasmonic laser antennas and related devices. IEEE J. Sel. Top. Quantum Electron. **14**, 1448–1461 (2008)
29. P. Muhlschlegel, H.J. Eisler, O.J.F. Martin, B. Hecht, D.W. Pohl, Resonant optical antennas. Science **308**, 1607–1609 (2005)
30. Y. Fang, Z. Li, Y. Huang, S. Zhang, P. Nordlander, N.J. Halas, H. Xu, Branched silver nanowires as controllable plasmon routers. Nano Lett. **10**, 1950–1954 (2010)
31. A.W. Sanders, D.A. Routenberg, B.J. Wiley, Y. Xia, E.R. Dufresne, M.A. Reed, Observation of plasmon propagation, redirection, and fan-out in silver nanowires. Nano Lett. **6**, 1822–1826 (2006)
32. V.S. Volkov, S.I. Bozhevolnyi, E. Devaux, J.-Y. Laluet, T.W. Ebbesen, Wavelength selective nanophotonic components utilizing channel plasmon polaritons. Nano Lett. **7**, 880–884 (2007)
33. N. Engheta, Circuits with light at nanoscales: Optical nanocircuits inspired by metamaterials. Science **317**, 1698–1702 (2007)
34. A. Alu, N. Engheta, All optical metamaterial circuit board at the nanoscale. Phys. Rev. Lett. **103**, 143902 (2009)
35. E. Cubukcu, F. Capasso, Optical nanorod antennas as dispersive one-dimensional Fabry-Perot resonators for surface plasmons. Appl. Phys. Lett. **95**, 201101–201103 (2009)
36. K.B. Crozier, A. Sundaramurthy, G.S. Kino, C.F. Quate, Optical antennas: Resonators for local field enhancement. J. Appl. Phys. **94**, 4632–4642 (2003)
37. S.A. Maier, Plasmonic field enhancement and SERS in the effective mode volume picture. Opt. Express **14**, 1957–1964 (2006)
38. A. Alu, Andrea, and N. Engheta, Hertzian plasmonic nanodimer as an efficient optical nanoantenna. Phys. Rev. B **78**, 195111 (2008)
39. A.G. Curto, G. Volpe, T.H. Taminiau, M.P. Kreuzer, R. Quidant, N.F. van Hulst, Unidirectional emission of a quantum dot coupled to a nanoantenna. Science **329**, 930–933 (2010)
40. J. Li, A. Salandrino, N. Engheta, Shaping light beams in the nanometer scale: a Yagi-Uda nanoantenna in the optical domain. Phys. Rev. B **76**, 245403–245407 (2007)
41. S. Zou, N. Janel, G.C. Schatz, Silver nanoparticle array structures that produce remarkably narrow plasmon lineshapes. J. Chem. Phys. **120**, 10871–10875 (2004)
42. G. Pellegrini, G. Mattei, P. Mazzoldi, Tunable, directional and wavelength selective plasmonic nanoantenna arrays. Nanotechnology **20**, 065201 (2009)

43. P. Nordlander, C. Oubre, E. Prodan, K. Li, M.I. Stockman, Plasmon hybridization in nanoparticle dimers. Nano Lett. **4**, 899–903 (2004)
44. N. Liu, S. Mukherjee, K. Bao, L.V. Brown, J. Dorfmuller, P. Nordlander, N.J. Halas, Magnetic plasmon formation and propagation in artificial aromatic molecules. Nano Lett. **12**, 364–369 (2012)
45. M. Hentschel, M. Saliba, R. Vogelgesang, H. Giessen, A.P. Alivisatos, N. Liu, Transition from isolated to collective modes in plasmonic oligomers. Nano Lett. **10**, 2721–2726 (2010)
46. G. Vecchi, V. Giannini, J. Gómez Rivas, Shaping the fluorescent emission by lattice resonances in plasmonic crystals of nanoantennas. Phys. Rev. Lett. **102**, 146807 (2009)
47. L. Dal Negro, S.V. Boriskina, Deterministic aperiodic nanostructures for photonics and plasmonics applications. Laser Photonics Rev. **6**, 178–218 (2012)
48. S. Boriskina, Photonic molecules and spectral engineering, in *Photonic MicroresonatorRresearch and Applications*, ed. by I. Chremmos, O. Schwelb, N. Uzunoglu (Springer, Berlin, 2010), pp. 393–421
49. S.V. Boriskina, B.M. Reinhard, Adaptive on-chip control of nano-optical fields with optoplasmonic vortex nanogates. Opt. Express **19**, 22305–22315 (2011)
50. http://www.forestwander.com/2011/11/alluring-cascades-pirouette
51. R. Ruppin, Electromagnetic energy density in a dispersive and absorptive material. Phys. Lett. A **299**, 309–312 (2002)
52. R. Loudon, The propagation of electromagnetic energy through an absorbing dielectric. J. Phys. A **3**, 233 (1970)
53. J.B. Khurgin, G. Sun, Scaling of losses with size and wavelength in nanoplasmonics and metamaterials. Appl. Phys. Lett. **99**, 211103–211106 (2011)
54. M.A. Noginov, V.A. Podolskiy, G. Zhu, M. Mayy, M. Bahoura, J.A. Adegoke, B.A. Ritzo, K. Reynolds, Compensation of loss in propagating surface plasmon polariton by gain in adjacent dielectric medium. Opt. Express **16**, 1385–1392 (2008)
55. I. De Leon, P. Berini, Amplification of long-range surface plasmons by a dipolar gain medium. Nat. Photonics **4**, 382–387 (2010)
56. G.V. Naik, J. Kim, A. Boltasseva, Oxides and nitrides as alternative plasmonic materials in the optical range. Opt. Mater. Express **1**, 1090–1099 (2011)
57. M. Jablan, H. Buljan, M. Soljacic, Plasmonics in graphene at infrared frequencies. Phys. Rev. B **80**, 245435 (2009)
58. A. Vakil, N. Engheta, Transformation optics using graphene. Science **332**, 1291–1294 (2011)
59. J.C. Ginn, J.R.L. Jarecki, E.A. Shaner, P.S. Davids, Infrared plasmons on heavily-doped silicon. J. Appl. Phys. **110**, 043110–043116 (2011)
60. B.S. Lukyanchuk et al., Peculiarities of light scattering by nanoparticles and nanowires near plasmon resonance frequencies. J. Phys.: Conf. Ser. **59**, 234 (2007)
61. A. Alù, N. Engheta, Higher-order resonant power flow inside and around superdirective plasmonic nanoparticles. J. Opt. Soc. Am. B **24**, A89–A97 (2007)
62. L. Novotny, B. Hecht, *Principles of Nano-Optics* (Cambridge University Press, Cambridge, 2006)
63. M.R. Dennis, K. O'Holleran, M.J. Padgett, Singular optics: optical vortices and polarization singularities. Prog. Opt. **53**, 293–363 (2009)
64. M.R. Dennis, Y.S. Kivshar, M.S. Soskin, A.S. Grover Jr, Singular optics: more ado about nothing. J. Opt. A **11**, 090201 (2009)
65. M.S. Soskin, M.V. Vasnetsov, Singular optics. Prog. Opt. **42**, 219–276 (2001)
66. H.F. Schouten, T.D. Visser, D. Lenstra, Optical vortices near sub-wavelength structures. J. Opt. B **6**, S404 (2004)
67. S.V. Boriskina, B.M. Reinhard, Molding the flow of light on the nanoscale: from vortex nanogears to phase-operated plasmonic machinery. Nanoscale **4**, 76–90 (2012)
68. Z.B. Wang, B.S. Luk'yanchuk, M.H. Hong, Y. Lin, T.C. Chong, Energy flow around a small particle investigated by classical Mie theory. Phys. Rev. B **70**, 035418 (2004)
69. S.V. Boriskina, L. Dal Negro, Multiple-wavelength plasmonic nanoantennas. Opt. Lett. **35**, 538–540 (2010)

70. T.V. Teperik, A. Degiron, Superradiant optical emitters coupled to an array of nanosize metallic antennas. Phys. Rev. Lett. **108**, 147401 (2012)
71. D.M. Natarov, V.O. Byelobrov, R. Sauleau, T.M. Benson, A.I. Nosich, Periodicity-induced effects in the scattering and absorption of light by infinite and finite gratings of circular silver nanowires. Opt. Express **19**, 22176–22190 (2011)
72. R.H. Dicke, Coherence in spontaneous radiation processes. Phys. Rev. **93**, 99–110 (1954)
73. M. Berry, Making waves in physics. Nature **403**, 21–21 (2000)
74. J.F. Nye, M.V. Berry, Dislocations in wave trains. Proc. R. Soc. Lond. A Math. Phys. Sci. **336**, 165–190 (1974)
75. S. Gustafson, F. Ting, Dynamic stability and instability of pinned fundamental vortices. J. Nonlinear Sci. **19**, 341–374 (2009)
76. Y. Strauss, I.M. Sigal, Effective dynamics of a magnetic vortex in a local potential. J. Nonlinear Sci. **16**, 123–157 (2006)
77. Y.S. Joe, A.M. Satanin, C.S. Kim, Classical analogy of Fano resonances. Phys. Scr. **74**, 259 (2006)
78. B.R. Johnson, Theory of morphology-dependent resonances: shape resonances and width formulas. J. Opt. Soc. Am. A **10**, 343–352 (1993)
79. Y. Tanaka, N. Nedyalkov, M. Obara, Enhanced near-field distribution inside substrates mediated with gold particle: optical vortex and bifurcation. Appl. Phys. A **97**, 91–98 (2009)
80. P.A. Atanasov, H. Takada, N.N. Nedyalkov, M. Obara, Nanohole processing on silicon substrate by femtosecond laser pulse with localized surface plasmon polariton. Appl. Surf. Sci. **253**, 8304–8308 (2007)
81. M. Bashevoy, V. Fedotov, N. Zheludev, Optical whirlpool on an absorbing metallic nanoparticle. Opt. Express **13**, 8372–8379 (2005)
82. N. Yu, P. Genevet, M.A. Kats, F. Aieta, J.-P. Tetienne, F. Capasso, Z. Gaburro, Light propagation with phase discontinuities: generalized laws of reflection and refraction. Science **334**, 333–337 (2011)
83. L. Byoungho, L. Seung-Yeol, Plasmonic beam shaping and hot spot generation, in *Advances in Optoelectronics and Micro/Nano-Optics (AOM), 2010 OSA-IEEE-COS* (2010), pp. 1–2
84. H. Kim, J. Park, S.-W. Cho, S.-Y. Lee, M. Kang, B. Lee, Synthesis and dynamic switching of surface plasmon vortices with plasmonic vortex lens. Nano Lett. **10**, 529–536 (2010)
85. J. Leach, M.R. Dennis, J. Courtial, M.J. Padgett, Vortex knots in light. New J. Phys. **7**, 55 (2005)
86. J. Leach, M.R. Dennis, J. Courtial, M.J. Padgett, Laser beams: knotted threads of darkness. Nature **432**, 165–165 (2004)
87. W. Ahn, S.V. Boriskina, Y. Hong, B.M. Reinhard, Electromagnetic field enhancement and spectrum shaping through plasmonically integrated optical vortices. Nano Lett. **12**, 219–227 (2012)
88. M.I. Stockman, Nanoplasmonics: the physics behind the applications. Phys. Today **64**, 39–44 (2011)
89. K. Li, M.I. Stockman, D.J. Bergman, Self-similar chain of metal nanospheres as an efficient nanolens. Phys. Rev. Lett. **91**, 227402 (2003)
90. D.J. Bergman, M.I. Stockman, Surface plasmon amplification by stimulated emission of radiation: quantum generation of coherent surface plasmons in nanosystems. Phys. Rev. Lett. **90**, 027402 (2003)
91. M. Durach, A. Rusina, V.I. Klimov, M.I. Stockman, Nanoplasmonic renormalization and enhancement of Coulomb interactions. New J. Phys. **10**, 105011 (2008)
92. A. Gopinath, S.V. Boriskina, N.-N. Feng, B.M. Reinhard, L.D. Negro, Photonic-plasmonic scattering resonances in deterministic aperiodic structures. Nano Lett. **8**, 2423–2431 (2008)
93. T.W. Ebbesen, H.J. Lezec, H.F. Ghaemi, T. Thio, P.A. Wolff, Extraordinary optical transmission through sub-wavelength hole arrays. Nature **391**, 667–669 (1998)
94. www.airliners.net.
95. J.C. Maxwell, On physical lines of force. Philos. Mag. **21**, 11–23 (1861)

96. E. Madelung, Quantentheorie in hydrodynamischer form. Zeitschrift für Physik A Hadrons and Nuclei **40**, 322–326 (1926)
97. T.C. Wallstrom, Inequivalence between the Schrodinger equation and the Madelung hydrodynamic equations. Phys. Rev. A **49**, 1613 (1994)
98. M. Tsang, D. Psaltis, Metaphoric Optical Computing for Fluid Dynamics, in *Advanced Optical, Quantum Memories and Computing II*, ed. by H.J. Coufal, Z.U. Hasan, A.E. Craig (SPIE, San Jose, 2005)
99. K. Staliunas, V. Sánchez-Morcillo, Zero Detuning: Laser Hydrodynamics and Optical Vortices, ed. by K. Staliunas, V. Sánchez-Morcillo, in *Transverse Patterns Nonlinear Optical Resonators* (Springer, Berlin, 2003)
100. W. Wan, S. Jia, J.W. Fleischer, Dispersive superfluid-like shock waves in nonlinear optics. Nat. Phys. **3**, 46–51 (2007)
101. C.O. Weiss, M. Vaupel, K. Staliunas, G. Slekys, V.B. Taranenko, Solitons and vortices in lasers. Appl. Phys. B **68**, 151–168 (1999)
102. M. Fernández-Guasti, J.L. Jiménez, F. Granados-Agustín, A. Cornejo-Rodríguez, Amplitude and phase representation of monochromatic fields in physical optics. J. Opt. Soc. Am. A **20**, 1629–1634 (2003)
103. E.B. Sonin, Vortex oscillations and hydrodynamics of rotating superfluids. Rev. Mod. Phys. **59**, 87 (1987)
104. R. Blanchard, S.V. Boriskina, P. Genevet, M.A. Kats, J.-P. Tetienne, N. Yu, M.O. Scully, L. Dal Negro, F. Capasso, Multi-wavelength mid-infrared plasmonic antennas with nanoscale single focal point. Opt. Express **19**, 22113–22124 (2011)
105. S.V. Boriskina, B.M. Reinhard, Spectrally and spatially configurable superlenses for optoplasmonic nanocircuits. Proc. Natl. Acad. Sci. U.S.A. **108**, 3147–3151 (2011)
106. N.A. Mirin, K. Bao, P. Nordlander, Fano resonances in plasmonic nanoparticle aggregates. J. Phys. Chem. A **113**, 4028–4034 (2009)
107. L.J. Sherry, S.-H. Chang, G.C. Schatz, R.P. Van Duyne, B.J. Wiley, Y. Xia, Localized surface plasmon resonance spectroscopy of single silver nanocubes. Nano Lett. **5**, 2034–2038 (2005)
108. J.B. Lassiter, H. Sobhani, J.A. Fan, J. Kundu, F. Capasso, P. Nordlander, N.J. Halas, Fano resonances in plasmonic nanoclusters: geometrical and chemical tunability. Nano Lett. **10**, 3184–3189 (2010)
109. J.A. Fan, C. Wu, K. Bao, J. Bao, R. Bardhan, N.J. Halas, V.N. Manoharan, P. Nordlander, G. Shvets, F. Capasso, Self-assembled plasmonic nanoparticle clusters. Science **328**, 1135–1138 (2010)
110. J.B. Pendry, A.J. Holden, D.J. Robbins, W.J. Stewart, Magnetism from conductors and enhanced nonlinear phenomena. IEEE Trans. Microw. Theory Tech. **47**, 2075–2084 (1999)
111. Y. Hong, M. Pourmand, S.V. Boriskina, B. M. Reinhard, Enhanced light focusing in self-assembled optoplasmonic clusters with subwavelength dimensions. Adv. Mater. **25**, 115–119 (2013)
112. D. Leykam, A.S. Desyatnikov, Discrete multivortex solitons. Opt. Lett. **36**, 4806–4808 (2011)
113. D. Leykam, A.S. Desyatnikov, Vortex switching with discrete multivortex solitons. Phys. Rev. A **86**, 043812 (2012)
114. K. Ladavac, D. Grier, Microoptomechanical pumps assembled and driven by holographic optical vortex arrays. Opt. Express **12**, 1144–1149 (2004)

Chapter 13
Spinoptics in Plasmonics

Erez Hasman and Vladimir Kleiner

Abstract We review our work on effects of spin-symmetry breaking in nanoscale structures caused by spin-orbit interaction. The spin-based effects offer an unprecedented ability to control light and its polarization state in nanometer-scale optical devices, thereby facilitating a variety of applications related to nano-photonics. The polarization-dependent effects are considered as result of a geometric phase arising from the interaction of light with an anisotropic and inhomogeneous nanoscale structure. The discussed phenomena inspire one to investigate other spin-based plasmonic effects and to propose a new generation of optical elements for nano-photonic applications, as a constituent of a new branch in optics—*spinoptics*.

Keywords Plasmon · Spin-orbit interaction · Spinoptics

13.1 Introduction

The interaction of light with metallic subwavelength structures exhibits various anomalous effects such as extraordinary optical transmission [1] and beaming [2]. These effects have been elegantly explained by a mechanism involving the coupling of light to collective surface-confined electronic oscillations known as surface plasmon-polaritons (SPPs). Extensive research has been carried out in the field of electromagnetic surface waves due to its technological potential and fundamental implications. Additional exciting phenomena were studied such as unidirectional plasmon coupling [3], plasmon focusing [4, 5], waveguiding and interferometry

E. Hasman (✉) · V. Kleiner
Micro and Nanooptics Laboratory, Faculty of Mechanical Engineering, and Russell Berrie Nanotechnology Institute, Technion-Israel Institute of Technology, 32000 Haifa, Israel
e-mail: mehasman@technion.ac.il

V. Kleiner
e-mail: vkleiner@technion.ac.il

T. V. Shahbazyan and M. I. Stockman (eds.), *Plasmonics: Theory and Applications*, Challenges and Advances in Computational Chemistry and Physics 15,
DOI: 10.1007/978-94-007-7805-4_13, © Springer Science+Business Media Dordrecht 2013

[6, 7], enhanced coherent thermal emission [8, 9], surface-enhanced Raman scattering [10], planar optical chirality [11, 12] and super-resolution [13, 14]. Apparently, the handedness of the light's polarization (optical spin up/down) may provide an additional degree of freedom in nanoscale photonics. The dynamics of spinning light was recently investigated, and the effect of spin on the trajectories of polarized light beams (spin-orbit coupling) was experimentally observed [15], with results that agree with the predictions of Berry's phase theory. In this chapter we examine the spin-orbit coupling effects that appear when a wave carrying intrinsic angular momentum (spin) interacts with a nanoscale structures which support SPP. The Berry's phase is shown to be a manifestation of the Coriolis effect in noninertial reference frame attached to the wave. A variety of experiments demonstrate spin-dependent effects in the electromagnetic waves coupling via an anisotropic inhomogeneous nanostructure. In the Sect. 13.2 we present and discuss the observation of spin-dependent surface-plasmon phenomena in anisotropic nanostructures on metal surface. In the Sect. 13.3 we consider plasmonic nanoapertures which exhibit a crucial role of an angular momentum (AM) selection rule in a light-surface plasmon scattering process, which is accompanied by a spin symmetry breaking effect due to spin-orbit interaction. Section 13.4 is devoted to properties of plasmonic nanoapertures which demonstrate behavior that is analogous to the Aharonov-Bohm effect. In Sect. 13.5 properties of the nanoapertures as topological defects are considered in relation with potential spinoptical devices having a spiral point spread function. An optical spin Hall effect in this system due to spin-orbit coupling which can be observed in the far-field is then studied in detail in Sect. 13.6. In the final Sect. 13.7 observation of an optical Rashba effect—spin degeneracy breaking due to spin-orbit interaction—in thermal radiation emitted from an inhomogeneous anisotropic 2D lattice composed of coupled antennas is presented. The spin split dispersion arises from the inversion symmetry violation in the lattice.

13.2 Spin-Based Plasmonic Effect in Nanoscale Structures

In this section we will describe a spin-dependent behavior of SPPs that was experimentally found in the interaction of light with metallic anisotropic and inhomogeneous nanoscale structures [16]. The anisotropic plasmonic structure under consideration is produced on top of a thin metal film evaporated onto a glass plate (Fig. 13.1a, b). The element consists of a spiral Bragg grating with a central defect, surrounded by a coupling grating, both of which were etched to a depth of 50 nm by a focused ion beam (FIB). The thickness of the metal (Au) was chosen to be 100 nm in order to prevent any direct transmission of light. The grating provides coupling with normally incident light at $\lambda_0 = 532$ nm to a surface-plasmon wave, while the Bragg grating with a central defect serves as a plasmonic microcavity for the surface wave. Therefore, the actual coupler period and the Bragg period were chosen to be 0.5 and 0.25 μm, respectively. The outer diameter of the structure of 10 μm and the small radius of the spiral cavity $r_0 = 1.32$ μm are consistent with the surface plasmon propagation length [17] $L_c \propto 1/\mathrm{Im}\left(k_p\right)$, which is about 3 μm for gold at this wavelength.

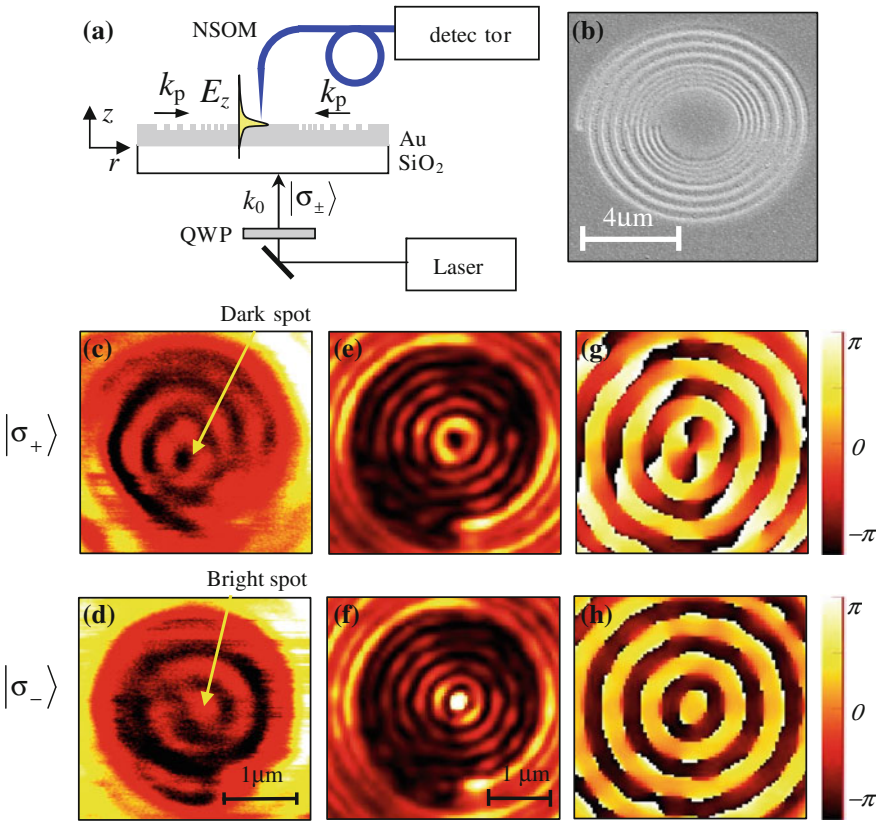

Fig. 13.1 Spin-dependent geometric phase in the spiral plasmonic structure. **a** The geometry of the structure (*side view*) and the optical setup. The Quarter Wave Plate (QWP) was used to generate a circularly polarized illumination, which was partially coupled to the SPP mode in the cavity—E_z. **b** Scanning electron microscope (SEM) picture of the spiral plasmonic cavity. **c**, **d** Intensity distribution in the cavity measured by a NSOM for $|\sigma_+\rangle$ and $|\sigma_-\rangle$ illumination, respectively. **e**, **f** Calculated intensity in the cavity for $|\sigma_+\rangle$ and $|\sigma_-\rangle$ illumination. **g**, **h** Calculated phase in the cavity for $|\sigma_+\rangle$ and $|\sigma_-\rangle$ illumination. Reprinted with permission from Ref. [16]. Copyright 2008 American Physical Society

The structure was illuminated by circularly polarized light which is denoted henceforth with a spin state$|\sigma_\pm\rangle$, where $|\sigma_+\rangle = 2^{-1/2}\begin{pmatrix}1 & -i\end{pmatrix}^T$ stands for right-handed circularly polarized light and $|\sigma_-\rangle = 2^{-1/2}\begin{pmatrix}1 & i\end{pmatrix}^T$ for left-handed circularly polarized light. Figure 13.1a demonstrates the intensity in the near-field of the plasmonic cavity that was measured by a near-field scanning optical microscope (NSOM) in a non-contact mode. The captured intensity distribution is presented in Fig. 13.1c, d. The near-field intensity distribution which calculated by a finite difference time domain (FDTD) algorithm is depicted in Fig. 13.1e, f. Surprisingly, the measured as well as the calculated intensity distribution exhibits a strong

dependence on the incident spin. An annular ring structure with a dark spot in the center for $|\sigma_+\rangle$ illumination and with a bright spot for $|\sigma_-\rangle$ illumination indicates coupling to different spiral plasmonic modes. The origin of the spin-dependent change in the near-field intensity distributions lies in the phase of the excited plasmonic mode. This phase has been verified by FDTD calculation (see Fig. 13.1g, h) and was found to correspond to a spiral mode $\exp(il\varphi)$, where φ is the azimuthal angle, with topological charge $l = -2$ for $|\sigma_+\rangle$ and $l = 0$ for $|\sigma_-\rangle$ illumination. The origin of the spin-dependent phase could be elucidated by use of a simpler structure with full rotational symmetry (see Fig. 13.2a). This structure consisted of concentric rings with the same depth and pitch as before and a central circular microcavity ($r_0 = 1.2\,\mu m$). The eigenmodes of such a circular plasmonic cavity are given by,

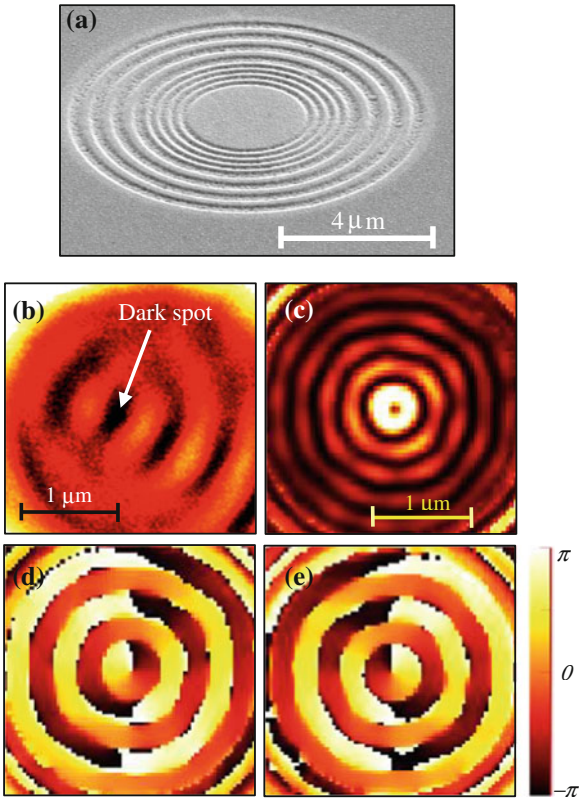

Fig. 13.2 Plasmonic field distribution in the circular cavity. **a** SEM picture of the *circular* structure. **b** Measured intensity distribution in the near-field for $|\sigma_+\rangle$ illumination. An identical intensity distribution was obtained for $|\sigma_-\rangle$. **c** Calculated intensity distribution for $|\sigma_+\rangle$. **d**, **e** Calculated E_z field phase inside the cavity for $|\sigma_+\rangle$ and $|\sigma_-\rangle$ illumination, respectively. Reprinted with permission from Ref. [16]. Copyright 2008 American Physical Society

$$\mathbf{E}_{l,p}(\varphi, r) = E_0 \exp(ik_z z) \exp(il\varphi)\ \boldsymbol{J}_l\left(k_p r\right)\ \hat{\mathbf{z}}, \tag{13.1}$$

where k_z is the wavenumber perpendicular to the surface direction, k_p is the radial wavenumber; φ, r and z are the cylindrical coordinate set, l is the topological charge and E_0 is a constant. The notation $\boldsymbol{J}_l$ stands for the l-order Bessel function of the first kind. The plasmonic in-plane wavenumber is given approximately by $k_p \sim k_0\sqrt{\varepsilon/(1+\varepsilon)}$, where ε is the dielectric constant of the metal ($\mathrm{Re}(\varepsilon) < -1$) and $k_0 = 2\pi/\lambda_0$ is the wavenumber of the incident light. The wavenumber in the z direction is expressed by $k_z^2 + k_p^2 = k_0^2$ and consequently is purely imaginary ($k_p > k_0$). Equation (13.1) represents an optical scalar vortex with a topological charge, l, which is associated with the optical angular momentum of the mode and corresponds to appropriate phase boundary conditions. The experimental near-field intensity distribution presented in Fig. 13.2b indicates a non-zero topological charge, which corresponds to a helical phase distribution for both $|\sigma_+\rangle$ and $|\sigma_-\rangle$ illumination. The FDTD calculation presented in Fig. 13.2d, e clear indicates that helicity of the phase equals to $l = -\sigma_\pm$, where $\sigma_+ = 1$, ($\sigma_- = -1$) stands for the spin state $|\sigma_+\rangle$, ($|\sigma_-\rangle$), respectively. This is evidence of a selective spin-dependent coupling to a single cavity mode induced by the structure. The existence of a spin-dependent spiral phase can be elucidated by analyzing the coupling mechanism between incident light with a specific spin and a surface plasmon cavity mode.

In plasmonic systems, when a coupling structure is illuminated by an arbitrarily polarized beam, the surface waves are excited via transverse magnetic (TM) polarization, corresponding to the magnetic field parallel to the grooves direction [17]. The propagation direction of the resulting plasmonic surface wave is perpendicular to the grooves whereas its polarization is linear in the vertical direction, E_z. If the direction of the grating's grooves varies azimuthally, the coupling of an incident plane wave to a surface wave takes place within a space-variant local direction. This non-trivial simultaneous manipulation in the space of polarizations and in the space of directions one can describe using geometric representation upon the Majorana sphere [18, 19]. In this scheme, polarized light is characterized by two dots on a unit sphere in the direction space (x, y, z), i.e., by two vectors, $\mathbf{u}$ and $\mathbf{v}$, which point to these dots from the origin. Their bisector unit vector, $\mathbf{n}$, coincides with the propagation direction of the wave, while its sign corresponds to the helicity of the polarization ellipse. For pure circular polarizations the bisector can be denoted as $\sigma_\pm\mathbf{n}$. The projections of the dots onto the plane perpendicular to $\mathbf{n}$ denote the two foci of the corresponding polarization ellipse. The physical significance of this representation is that it provides a method to evaluate a geometric Berry phase [20–22] for complex fields whose polarization and direction have been modified.

Let us consider right-handed circularly polarized illumination $|E_{ext}\rangle = E_0\,|\sigma_+\rangle$ impinging upon the element depicted in Fig. 13.2a from the bottom. Here E_0 is the amplitude of the field, which can be taken as one for brevity purposes. The circularly polarized incident beam, propagating along the z direction, can be depicted on the Majorana sphere by vectors $\mathbf{u}$ and $\mathbf{v}$, which coincide at the north pole (see Fig. 13.3). The evanescent vertically polarized electric field that propagates on the metal surface in a radial direction is consequently represented by a vector $\mathbf{u}'$, which still points to the

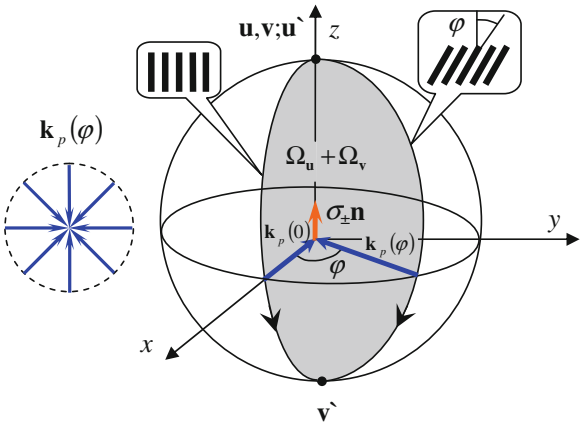

Fig. 13.3 Graphical representation of the geometric phase on the Majorana sphere. Geometric phase induced by the interaction of light with an anisotropic inhomogeneous structure is equal to half of the area enclosed by the two geodesics that correspond to different propagation directions, k_p of the excited SPPs (*gray area*). The variation of the propagation wavevector $\mathbf{k}_p(\varphi)$ along the element is depicted in the small picture by *blue arrows*. Reprinted with permission from Ref. [16]. Copyright 2008 American Physical Society

north pole, and a vector $\mathbf{v}'$ which now points to the south pole. The interaction of light with a coupling grating whose local orientation is φ can then be defined by a geodesic arc connecting the north pole with the south pole that intersects the *xy* plane at angle φ (see Fig. 13.3). The Berry phase in our specific case is geometrically associated with the area enclosed on the Majorana sphere by the paths of vectors $\mathbf{u}$ and vector $\mathbf{v}$, explicitly, $\phi_g = -(\Omega_{\mathbf{u}} + \Omega_{\mathbf{v}})/2$. Since the vector $\mathbf{u}$ is static, the Berry phase between the fields at two different azimuthal locations will be given simply as half of the area between two corresponding geodesics, which yields $\phi_g = -\varphi$. In the opposite case, when left-handed circularly polarized light is applied, i.e., $|E_{ext}\rangle = E_0\,|\sigma_-\rangle$, the picture on the sphere will be reversed. The initial state will be denoted by vectors $\mathbf{u}$ and $\mathbf{v}$ both pointing to the south pole, and the final state will be defined by $\mathbf{u}'$ pointing to the south pole and $\mathbf{v}'$ pointing to the north pole. In the second case, the path traversed on the Majorana sphere is in the reverse direction, which corresponds to the positive geometric phase, $\phi_g = \varphi$. The general case, therefore, can be given by $\phi_g = -\sigma_\pm\varphi$. Note that this phase results from the spin-orbit angular momentum coupling due to the space-variant polarization state and directional manipulations and is therefore geometric in nature. The appearance of the geometric phase in our experiment resulted from the SPP excitation by a spatially rotated grating and resembles the phase delay that arises when circularly polarized light is transmitted through a rotated polarizer [21, 22]. This phase is linear with φ and spirals around the center of the structure, giving rise to a phase singularity with a topological charg $l = -\sigma_\pm$; these properties explain the results presented in Fig. 13.2.

The intensity distributions in the cavity described above for incident spins σ_+ and σ_- are indistinguishable, as opposed to the experimental results obtained in the spiral cavity (see Fig. 13.1). In the latter, in addition to the geometric phase of the SPPs due to a polarization-dependent coupling, a dynamic phase arises as a result of a space-variant path difference. This dynamic phase is induced by the grooves' spiral pitch. The overall phase in the spiral cavity is the sum of the geometric and dynamic phases, $\phi = \phi_g + \phi_d$ and the total topological charge of the plasmonic vortex is $l = -(\sigma_\pm + m)$, where m is the spiral pitch in the units of SPP wavelength. For the specific case when $m = 1$, the microcavity mode obeys the form of $\boldsymbol{J}_0\left(k_p r\right)$ for $|\sigma_-\rangle$ and of $\exp(-i2\varphi)\ \boldsymbol{J}_2\left(k_p r\right)$ for $|\sigma_+\rangle$. Consequently, for $|\sigma_-\rangle$ illumination the resultant field distribution possesses no phase singularity in the center, as opposed to the $|\sigma_+\rangle$ illumination case, which agrees with the experimental results presented in Fig. 13.1. The formation of the geometric phase is, therefore, the origin of the spin-dependent intensity distribution in the spiral cavity, and may lead to other spin-based phenomena in plasmonic systems.

One of the possible implementations of the plasmonic geometric phase could be a spin-dependent plasmonic focusing lens. Figure 13.4e presents an appropriate structure that consisted of a 150 nm-thick gold film with a hemi-circular coupling grating with the inner radius of $r_0 = 1.64\,\mu\text{m}$ followed by a Bragg grating on the outer side. In experiment the structure was illuminated from the bottom with $|\sigma_+\rangle$ and $|\sigma_-\rangle$ plane waves and the intensity distribution was collected by the NSOM tip. The measured intensity of the plasmonic wave is shown in Fig. 13.4a, b. The most interesting feature

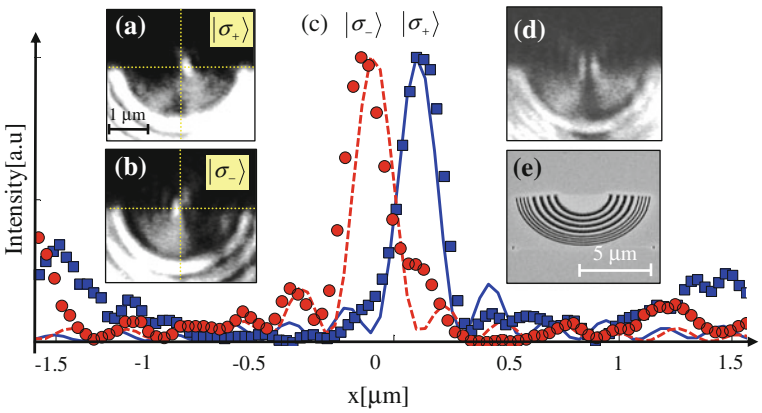

Fig. 13.4 Spin-dependent plasmonic lens based on a geometric phase. **a**, **b** The intensity distributions measured by a NSOM for $|\sigma_+\rangle$, and $|\sigma_-\rangle$ illumination, respectively. **c** The transverse cross-sections of the measured intensity distributions in the focal plane of the lens for $|\sigma_+\rangle$ (*blue squares*) ,$|\sigma_-\rangle$ (*red circles*) illumination, respectively. FDTD calculation is plotted for each polarization (*solid blue line*—$|\sigma_+\rangle$; *dashed red line*—$|\sigma_-\rangle$). The cross-sections in **c** were measured along the horizontal dashed lines depicted in **a** and **b**. **d** The intensity distribution measured by NSOM for $|\sigma_+\rangle + |\sigma_-\rangle$ (linearly polarized) illumination. **e** The SEM picture of the element. Reprinted with permission from Ref. [16]. Copyright 2008 American Physical Society

in this intensity distribution is a spin-dependent transverse shift of the focus which one can easily observe by comparing the cross-sections of the spots (Fig. 13.4c). This shift can be regarded as a manifestation of the optical Magnus effect [23, 24] and the optical spin Hall effect [25, 26] which arises in the system due to a spin-orbit coupling producing a spiral geometric phase. The experimental results are supported by the FDTD numerical simulation which are also depicted in the Fig. 13.4c. The focal shift corresponds to the spin-dependent spiral phase modification due to the Berry phase and can be estimated by $\Delta x \approx r_0 \left|k_p^{-1}\right| \nabla(\sigma_{\pm}\varphi) = \sigma_{\pm}\left|k_p^{-1}\right|$, ($\Delta x \approx 160\,\text{nm}$). The observed shift of the focal intensity distribution is about 200 nm which is in good agreement with the above estimation as well as with the FDTD results (see Fig. 13.4c). The slight deviation of the measured results from the simulation can be attributed to the modified dispersion relation of the SPPs due to impurities caused by the fabrication process. This geometric effect is exceptionally pronounced when linearly polarized light (the superposition of spin $|\sigma_+\rangle$ and $|\sigma_-\rangle$ beams) is incident upon the structure. In this case, the focal spot is split in the lateral direction (see Fig. 13.4d) and clearly reminds us the effect of spin-dependent electron beam splitting in the classic Stern-Gerlach experiment [27, 28].

13.3 Optical Spin Symmetry Breaking in Nanoapertures

The dynamics of various physical systems, including optical systems, are substantially characterized by their AM. The AM of an optical beam comprises the spin component, associated with the handedness of the circular polarization, and the orbital angular momentum (OAM), associated with a spiral phase front [29–32]. In a paraxial beam with a spiral phase distribution $\phi \propto l\varphi$, the total AM per photon, in units of $\hbar$ (normalized AM), was shown to be $j = (\sigma + l)$, where $\sigma = 1$ stands for the spin state $|\sigma_+\rangle$ and $\sigma = -1$ stands for the spin state $|\sigma_-\rangle$ [33]. In accordance with fundamental physical principles, resonant excitation of an electromagnetic eigenmode requires that the exciting wave match the excited mode both with its linear and angular momentum. This required matching imposes certain restrictions on the excitation process—selection rules. Likely the simplest plasmonic nanoscale structure, which demonstrates these common rules is a nanoaperture in a thin metal film. Let consider a matrix consisted of annular apertures surrounded by a shallow spiral periodic corrugation. In the experiment [34] a structure with the inner and the outer radii of the ring slit apertures of 250 and 350 nm, respectively, spiral corrugation with a period of 500 nm and a pitch of 2 periods, and depth of 70 nm was milled by a FIB into a 200 nm thick gold film evaporated onto a glass wafer (see Fig. 13.5b). Transmission of circularly polarized light through the structure is strongly affected by relationship between helicity of illuminating light and handedness of the spirals. A picture of the transmitted light for the spin states $|\sigma_+\rangle$ and $|\sigma_-\rangle$, and for the linear polarization $2^{-1/2}(|\sigma_+\rangle + |\sigma_-\rangle)$is presented in Fig. 13.5a. The experimental results show that when the incident spin is opposite to the handedness of the spiral grating,

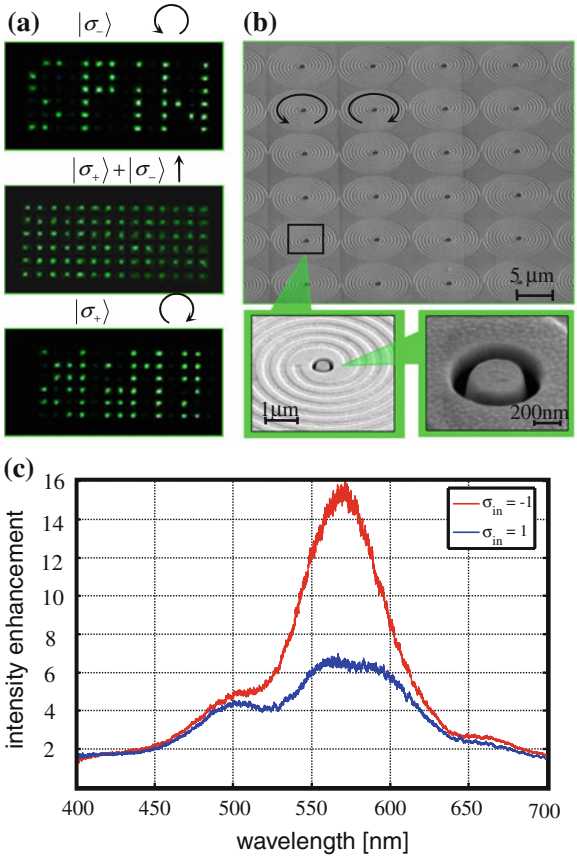

Fig. 13.5 Spin-dependent transmission through annular nanoapertures. **a** light transmission measured from the element for $|\sigma_-\rangle$, $|\sigma_+\rangle + |\sigma_-\rangle$ and $|\sigma_+\rangle$ illuminations. **b** SEM picture of the element used in the experiment. Spiral corrugations are either *left-handed* or *right-handed*, depicted with a counterclockwise or clockwise *arrow*, respectively. The magnified SEM pictures of a single element and a coaxial nanoaperture are also presented. **c** spectral transmission enhancement for $|\sigma_-\rangle$ (*red line*) and $|\sigma_+\rangle$ (*blue line*). The spectrum was normalized by the transmission measured for annular apertures without corrugations. Reprinted with permission from Ref. [34]. Copyright 2009 American Chemical Society

the intensity of the transmitted light is enhanced. Accordingly, the word "SPiN" written with right-handed spirals is lit up when illuminated by $|\sigma_-\rangle$ light. For $|\sigma_+\rangle$ illumination, the contrast is reversed. A spectral transmission through a similarly structured array of only right-handed spirals, normalized by transmission through a annular aperture array with-out corrugations manifest a clearly observed resonant peak for $|\sigma_-\rangle$ illumination around 570 nm. The light transmission at the peak was found to be enhanced by factor of 16 relative to an uncorrugated aperture array. The spectral transmission of a $|\sigma_+\rangle$ illumination does not exhibit any substantial resonance.

The excitation of electromagnetic eigenmodes inside a nanoaperture by surface waves is constrained by the AM selection rule, which is given by

$$l_{SM} = l_{GM}, \tag{13.2}$$

where l_{SM} and l_{GM} are the normalized OAM of the surface mode and guided mode inside the annular structure, respectively. A conceptual scheme of the transmission mechanism is depicted in Fig. 13.6. The annular nanoapertures can be designed to be a single mode system; for example, as in this case possessing a single allowed excitation for $l_{GM} = \pm 1$. This is a useful advantage of the annular apertures. The spiral corrugation couples the incident light into a plasmonic wave and induces a dynamic spiral phase according to the spiral grating pitch, l_S. In the described structure the spiral corrugation adds to the surface mode a spiral phase with $l_S = 2$. Experiment shows that *only* $l_S = 2$ provides spin-dependent transmission enhancement through the apertures. The observed exceptional transmission enhancement indicates that the eigenmode of the annular waveguide is properly excited by a surface mode. The apparent difference between $l_{GM} = \pm 1$ and the spiral charge $l_S = 2$ of the surface mode leads one to assume that another mechanism induced an additional spin-dependent spiral phase that compensated the excess of AM on the left side of the selection rule in Eq. (13.2). This phase modifies the complete OAM of the surface mode to be $l_{SM} = \sigma_{in} + l_S$, ($\sigma_{in}$ is the incident spin) which now perfectly satisfies the AM selection rule of the system. Thus, the incident spin is converted into the OAM, conserving the total AM of the system. The process by which an intrinsic property of light is coupled to an extrinsic property of a plasmonic field will be referred here to *plasmonic spin-orbit interaction*. This interaction occurs in anisotropic and inhomogeneous structures and is manifested by a geometric Berry phase arising in the system [15, 16, 35–37].

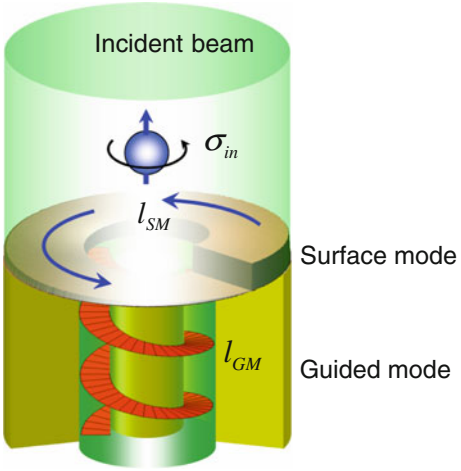

Fig. 13.6 The mechanism of the nanoaperture's excitation controlled by the AM selection rules. The incident beam bears the intrinsic angular momentum of σ_{in}. The excited surface mode acquires the orbital angular momentum of l_{SM} as a result of the plasmonic spin-orbit interaction. The guided mode with l_{GM} is excited only if the selection rule is satisfied. Reprinted with permission from Ref. [34]. Copyright 2009 American Chemical Society

The above effect can be regarded as a spatial angular Doppler effect (ADE) [38]. In analogy with a *temporal* ADE, where an observer at a reference frame rotating with a rate Ω_t registers a spin-dependent temporal frequency shift [39], here a spatial rotation of the periodic surface corrugation with a rate of Ω_ξ induces a spin-dependent *spatial* frequency shift. Accordingly, the geometric phase arising from this spatial frequency modulation can be easily calculated to be $\phi_g = -\sigma_{in} \int \Omega_\xi d\xi$, where the rotation of the grating is given by $\Omega_\xi = d\theta/d\xi$, the angle θ indicates the local groove's orientation, and ξ stands for a spatial coordinate. In the structure presented in Fig. 13.5b where $\xi = \varphi$, the geometric phase is simply given by the spin-dependent spiral phase $\phi_g = -\sigma_{in}\varphi$ producing the required additional OAM for the surface wave to satisfy the AM selection rule (Eq. (13.2)). Note that while polarization and chirality effects in anisotropic inhomogeneous nanoscale structures were investigated previously [40–43], the mechanism of spin-orbit interaction was not distinguished.

It is very helpful to compare the behavior of the spiral structure discussed above with properties of the annular aperture fitted with in a circularly symmetric (achiral) corrugation using incident beam with OAM . The circular symmetry of the coupling corrugation does not induce a dynamic phase, which means that $l_S = 0$. However, due to the spin-orbit interaction, the incident spin induces a spiral Berry phase, and, as before, is converted to the OAM component of the surface mode. The external spiral phase modifies the complete OAM of the surface mode to be $l_{SM} = \sigma_{in} + l_{ext}$. Therefore, when the external OAM is zero, the resulting surface mode AM is $l_{SM} = \pm 1$, in which case the selection rule is *always* satisfied and the transmission of the element is undistinguished for distinct spin states. Moreover, providing an external spiral phase of $l_{ext} = 2$, the AM of the surface mode will be either 1 or 3 for an incident spin $|\sigma_-\rangle$ or $|\sigma_+\rangle$, respectively. For $l_{ext} = -2$ the surface mode AM will be correspondingly, -3 for $|\sigma_-\rangle$ and -1 for $|\sigma_+\rangle$. As before, the best overlapping of the surface mode and the guided mode is obtained for $l_{SM} = \pm 1$; therefore, the transmitted intensity will be strongly dependent upon the incident spin.

Figure 13.7b shows the measured transmissions of a laser light at wavelength 532 nm by use of a spatial light modulator (SLM) generating a beam with OAM for various combinations of l_{ext} and σ_{in}. The transmission ratio of the two spin states is shown to be approximately 3 which is close to the ratio measured with the spiral corrugations. Thus, the suggested AM selection rule is verified for systems of substantially different symmetry.

Additional understanding of the AM evolution in the enhanced resonant transmission can be obtained by analyzing the AM of the light scattered from the nanoaperture. To do this, one should investigate the scattered light far behind the element. The transverse electric field component of the guided mode [44] with $l_{GM} = 1$, can be described by the Jones vector $\mathbf{E}_r^{GM} = \begin{pmatrix} E_x & E_y \end{pmatrix}^T = E_0(r) \begin{pmatrix} \cos\varphi & \sin\varphi \end{pmatrix}^T e^{i\varphi}$, where $E_0(r)$ is the radial field dependence. Note that the guided mode in a circular basis is given by $\mathbf{E}_r^{GM} = 2^{-1/2} E_0(r)[|\sigma_-\rangle + e^{i2\varphi}|\sigma_+\rangle]$. This field distribution corresponds to a vectorial vortex (see Fig. 13.8a) with a Pancharatnam topological charge of 1, resulting in a total AM of $j = 1$. As was shown [45], such vectorial vortices are unstable and collapse upon propagation. The guided mode can be verified by propa-

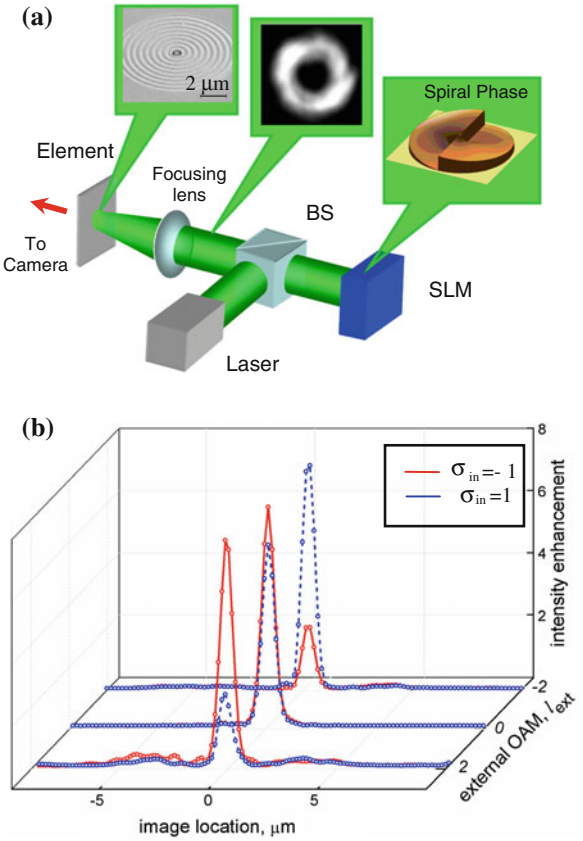

Fig. 13.7 The removal of the spin-degeneracy in circular corrugation by use of externally induced OAM. **a** Experimental setup. A laser beam is modulated by a spatial light modulator (SLM) to obtain a spiral phase and then incident through a beam splitter (BS) onto a coaxial aperture with circular corrugation. The transmitted light is captured in the image plane by the camera. The spiral phase with $l_{ext}= 2$, the measured intensity distribution across the incident beam, and the SEM picture of the element are presented in the figure. **b** Intensity distribution cross-sections captured by the camera for different l_{ext}. The *blue dashed lines* correspond to $|\sigma_+\rangle$ illumination and *red solid lines* correspond to $|\sigma_-\rangle$ illumination. The intensity is normalized by the transmission measured via a annular aperture without the surrounding corrugation (the horizontal dimension is scaled according to the optical magnification). Reprinted with permission from Ref. [34]. Copyright 2009 American Chemical Society

gating it to the far-field and it was done in experiment (see Fig. 13.8b–e). As expected from the far-field of $\mathbf{E}_r^{GM}$, a bright and a dark spot have been observed for the left and right circular polarization components, respectively, with a good agreement between calculation and measurement. Thus, the total AM of light in the system is conserved also for the scattered light ($j = 1$).

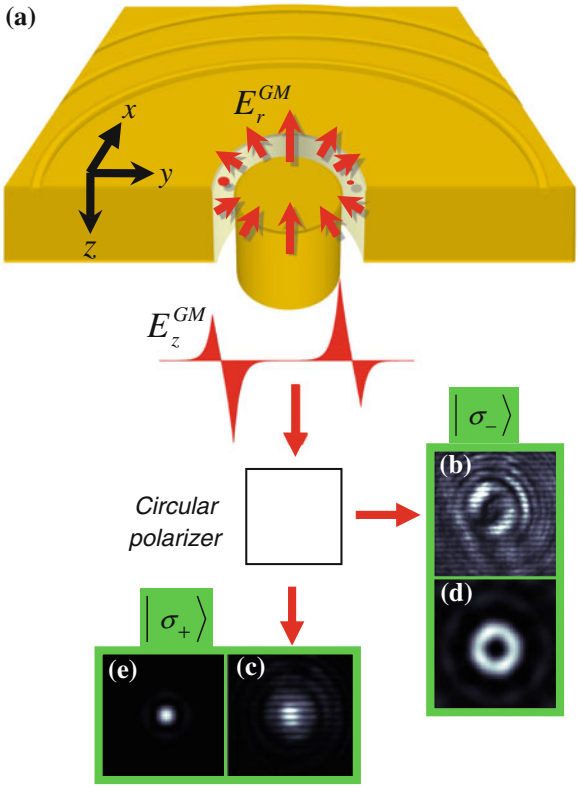

Fig. 13.8 Far-field analysis of the light scattered from the element. **a** The E_z component distribution of the guided mode and the instantaneous transverse vectorial field (E_r). **b**, **c** measured and **d**, **e** calculated intensity distributions of the light scattered to the far-field, for light transmitted through *right-handed* **b**, **d** and *left-handed* **c**, **e** circular polarizer. Reprinted with permission from Ref. [34]. Copyright 2009 American Chemical Society

13.4 Plasmonic Aharonov-Bohm Effect

As it was showed in previous section the rotation of the local anisotropy axis related to the slit curvature entails correction of the momentum term in the wave equation, which results in a spiral geometric phase. The geometric phase of the surface plasmons can be directly observed via the interference pattern in the near-field by means of near-field scanning optical microscope (NSOM) [46]. The observed effect will be analyzed using the analogy of the scattering of electrons from a topological defect in the Aharonov-Bohm (AB) effect [47]. In order to observe the surface plasmon interference in the near-field a structure onto glass substrate was chosen consisting of thin (120 nm) gold film with annular aperture (inner and outer radii of the aperture are 365 and 525 nm, respectively). The 320 nm-wide slit has been milled in the proximity of the annular aperture to provide a reference wavefront for the interference

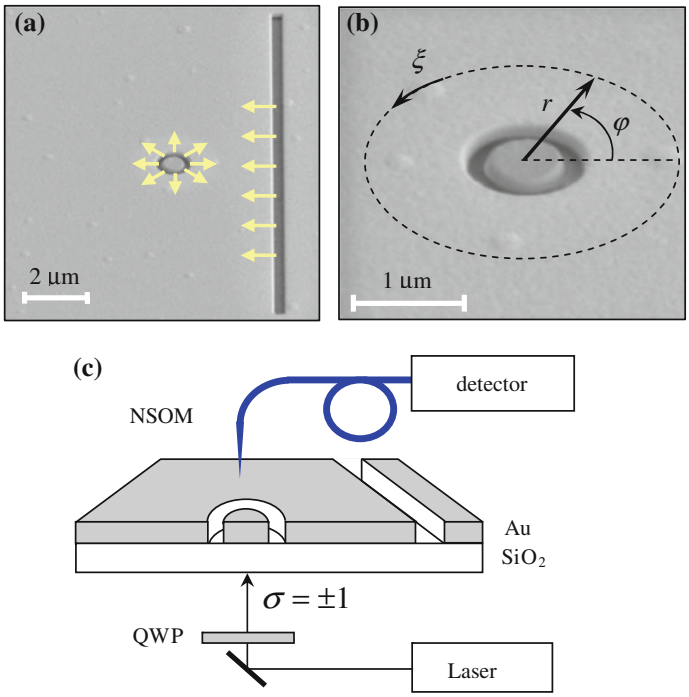

Fig. 13.9 **a** SEM image of the investigated element. **b** A magnified SEM image of the circular nanoslit. **c** Experimental set-up. The element is illuminated from the bottom by the laser beam whose polarization was switched by a quarter-wave plate (QWP) to be $\sigma = \pm 1$. The near-field intensity distribution was measured by the NSOM tip. Reprinted with permission from Ref. [46]. Copyright 2008 American Physical 2582 Society

measurement (see Fig. 13.9a, b). The structure was illuminated by a tunable laser and excited surface plasmon wave was directly probed by the 150 nm aperture NSOM tip. The measured fringe pattern for incident right- and left-handed circularly polarized light ($\sigma = \pm 1$) at $\lambda_0 = 800$ nm is presented in Fig. 13.10a, b. The resulting pictures appear to be asymmetric in that an additional fringe emerge above or below the coaxial aperture according to the incident spin (see fringe analysis in Fig. 13.10c, d). It can be concluded that a plasmonic wave scattered by the cylindrical defect acquires a phase front dislocation [46] analogous to the one obtained in a AB wavefunction [47–49]. A phase dislocation is a singular point of the field where the phase is indeterminate; therefore the field amplitude must vanish there. Such a dislocation is evidence of a spiral phase front obtained by the scattered surface plasmons. In the experiment, the additional fringe appearing in the interference pattern indicates that the topological charge of the spiral phase is ± 1, depending on the incident spin; therefore, the corresponding phase distribution is given by $\phi = -\sigma\varphi$, where φ, is the azimuthal angle (Fig. 13.9b). This phenomenon can be elucidated by considering the effect of spin-orbit coupling.

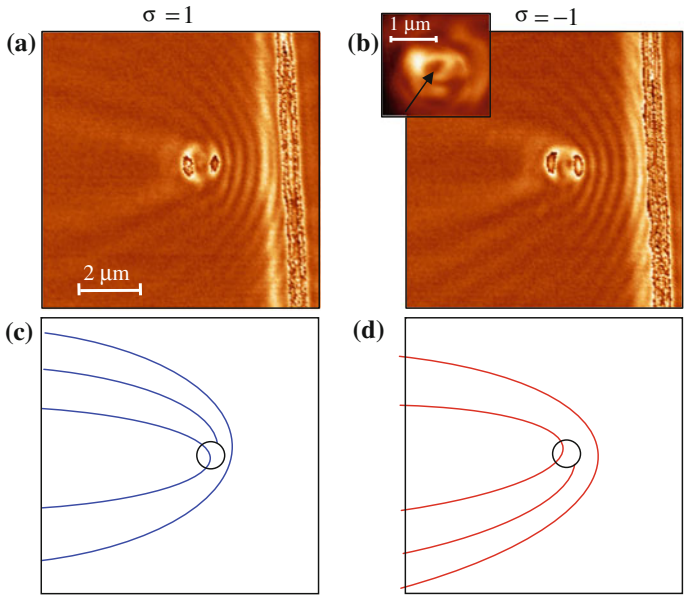

Fig. 13.10 Measured near-field intensity. **a** for $\sigma = 1$ polarization and **b** for $\sigma = -1$ polarization, at $\lambda = 800\,\text{nm}$. The observed fringe maxima are presented in **c** for $\sigma = 1$ and in **d** for $\sigma = -1$ states. The *black circle* in **c** and **d** represents the location of the annular nanoslit. The inset in **b** with a *dark spot* in the *center* (marked with an *arrow*) is the measured intensity distribution inside the circular slit. Reprinted with permission from Ref. [46]. Copyright 2008 American Physical Society

The coupling of light to non-radiative surface modes is achieved via momentum modification by a surface defect, such as a nanoaperture [50, 51]. In particular, a nanoslit introduces a momentum modification (matching) in perpendicular direction, exciting a surface wave with a phase front parallel to the slit. Moreover, only TM polarized incident waves (with an electric field perpendicular to the slit) can be efficiently coupled by the slit to surface plasmons. This polarization selectivity in SPP excitation implies highly anisotropic interaction. Due to the circular shape of the annular slit, it is convenient to analyze the wave propagation in a rotating reference frame attached to a local anisotropy axis [46, 52, 53]. For the observer moving along a path with radius r the local structure (slit) orientation appears to be rotated with the rate $\Omega = d\theta/d\xi = 1/r$ where $\theta\,(\xi)$ is the slit orientation, and ξ is the path parameter (see Fig. 13.10b). The Helmholtz equation in a non-inertial reference frame rotating with $\Omega\,(\xi)$, is $(\nabla^2 + k^2 - 2\sigma\Omega k)E_\sigma = 0$, where $E_\sigma = 2^{-1/2}\left(E_x + i\sigma E_y\right)$ are the eigenvectors of circular polarizations. Note that a spin-dependent Coriolis term appears in the corrected Helmholtz equation. This equation can be written as $\left(\nabla^2 + K^2\right)E_\sigma = 0$, where $K(\omega) \approx k(\omega) - \sigma\Omega$ is the *generalized momentum* [47, 48, 53]. A similar term also appears in the time-independent Schrödinger equation in the presence of a vector potential. This spin-dependent wavevector modification

is a manifestation of the optical spin-orbit interaction similar to the spin-Hall and the Stern-Gerlach effects. The additional momentum leads to a geometric phase accumulation of,

$$\phi_g = -\int \sigma \Omega d\xi = -\sigma\theta. \tag{13.3}$$

Accordingly, the phase of the scattered plasmonic wave will be continuous up to the factor of 2π everywhere excluding the point $r = 0$, where the phase dislocation appears. The phase in Eq. (13.3) is analogous to the phase arising in a AB wavefunction, $\psi(\mathbf{r})$ [48, 49]. The latter effect appears when a beam of particles with charge of q is scattered from an infinite impenetrable cylinder containing a magnetic flux $\Phi = \oint \mathbf{A}(\mathbf{r}) \cdot d\mathbf{r} = \iint \mathbf{B}(\mathbf{r}) d\mathbf{S}$, where $\mathbf{A}(\mathbf{r})$ is the vector potential and $\mathbf{B}(\mathbf{r})$ is the magnetic field. The suitable vector potential is given by $\mathbf{A}(\mathbf{r}) = (\Phi/2\pi r)\hat{\boldsymbol{\varphi}}$, where $\hat{\boldsymbol{\varphi}}$ is the unit vector in the azimuthal direction. The corresponding time-independent Schröedinger equation is then given by, $\frac{1}{2m}(-i\hbar\nabla - q\mathbf{A}(\mathbf{r}))^2 \psi(\mathbf{r}) = \frac{\hbar^2 k^2}{2m}\psi(\mathbf{r})$, where m is the particle's mass and $\hbar$ is Plank's constant. Note that the expression in parentheses is the generalized momentum term. In the linear approximation in $\mathbf{A}$, the above equation can be written as, $\left(\nabla^2 + k^2 - \frac{2iq}{\hbar}\mathbf{A} \cdot \nabla\right)\psi(\mathbf{r}) = 0$. The resulting equation resembles the Helmholtz equation in the rotating frame, where the third term in the parentheses stands for the Coriolis term. In our system, the momentum correction term along the ξ coordinate is $(\Delta k)_\xi = \sigma/r$, and is analogous to the $q\mathbf{A}$ term in the AB effect. The main result of the AB experiment is a spiral phase $\phi = \alpha\varphi$ acquired by the particles scattered from the cylinder, where the topological charge $\alpha = q\Phi/(2\pi\hbar)$ is the magnetic flux parameter. The topological charge of the phase obtained in our experiment can be found as, $l = \frac{1}{2\pi}\oint (\Delta k)_\xi d\xi = \sigma$. Therefore, one can conclude that the intrinsic spin in our experiment corresponds to the flux parameter α in the AB effect. Due to the non-zero topological charge ($\sigma = \pm 1$) a singularity of the plasmonic field appears in the center of the defect, resulting in a dark spot (see inset Fig. 13.10b). The vanishing electromagnetic field in the center corresponds to the impenetrability of the cylinder proposed in the AB experiment. Accordingly, the geometry of our system affects the resulting plasmonic phase front in a similar way as a vector potential affects the electrons' wavefunction. In contrast to the original AB effect, here the topological charge of the plasmonic spiral phase is spin-dependent, therefore it can be regarded as the intrinsic AB effect similar to the Aharonov-Casher effect [54].

A peculiarity of the observed effect lies in its geometric nature. The spiral phase of the plasmonic waves arises solely due to a rotation of the local anisotropy and is not the result of an optical path difference. Therefore, the phase dislocation will be independent of the wavelength or the size of the defect. This is confirmed experimentally on several elements with apertures of different sizes. Figure 13.11a, b presents the observed fringe patterns for circular slit with a diameter of 1.8 μm and width of 320 nm illuminated with $\lambda = 800$ nm. Moreover, a FDTD simulation for the same defect size, but for $\lambda = 532$ nm incident illumination is presented in Fig. 13.11(c, d). In the measured as well as in the calculated near-field intensity distributions, same

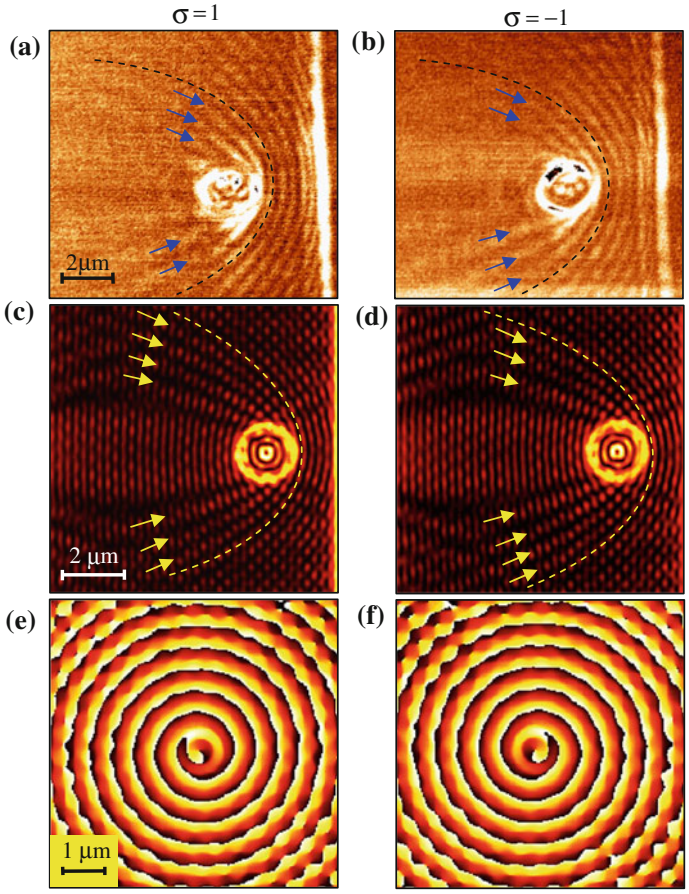

Fig. 13.11 **a** and **b** Measured intensity distribution of the SPPs scattered from a larger diameter defect compared to Fig. 13.10 (see text for details) for $\sigma = 1$ and $\sigma = -1$ polarizations, respectively, at $\lambda = 800$ nm. **c** and **d** The calculated interference intensity distribution for $\sigma = 1$ and $\sigma = -1$, respectively, with the same defect as in **a**, now with $\lambda = 532$ nm. To guide the eye, the *dashed lines* in **a**–**d** indicate one solid fringe and the *arrows* indicate the fringes appearing to the *left* of the *dashed line*. **e** and **f** The calculated phase distributions of the SPPs scattered from the same circular slit as in **c** and **d**. Reprinted with permission from Ref. [46]. Copyright 2008 American Physical Society

spin-dependent phase dislocations are clearly observed. A phase distribution of the scattered plasmonic field (without interfering with a reference wave) calculated by FDTD for $\lambda = 532$ nm illumination is presented in the Fig. 13.11e, f. The topological charge of the calculated spiral phase is equal to the incident spin and is not dependent upon the incident wavelength or the defect size, emphasizing the geometric nature of the observed effect. In the next section we will study the collective behavior of the defects upon the surface plasmon supporting media.

13.5 Spin-Dependent Plasmonics: Interfering Topological Defects

The results of the previous section show that the electromagnetic field scattered from subwavelength nanoaperture has an essential property of a topological defect (TD). The TD is a singular spatial configuration of a vector field which cannot unwind under continuous deformations [55]. Topological defects (TDs) are among the most intriguing signatures of symmetry breaking in the laws of physics [54]. TDs have attracted extensive attention in various realms such as condensed matter physics [56–58], superfluidics [59], hydrodynamics [60], cosmology [61], liquid crystals [62], and optics [63]. The optical TDs are termed vortices and they carry an OAM of $l\hbar$ per photon manifested by the spiral phase $l\varphi$ of the beam, where the integer number l is the topological charge and φ is the azimuthal angle. Observation of TDs in plasmonic systems is possible via the spin-orbit interaction (SOI), which provides a suitable mechanism to couple the optical spin to an OAM carried by the surface plasmons (SPs). Moreover, a measurement of a wavefront phase dislocation due to the scattering of SPs from a macro-wavelength TD was recently presented [64].

When a linearly polarized light illuminates a local scatterer, a typical dipolar SP polariton emission pattern is observed, aligned with the incident polarization direction [65, 66], and comprises a perpendicular dislocation line. The scattering of the SP waves propagating away from the point scatterer is described as a source of spherical (Huygens) wave [66], with π-phase retardation between the two sections intersected by the dislocation line (Fig. 13.12c). In this section we consider a spin-dependent plasmonics as result of scattering the circularly polarized wave from local defect on surface maintaining SP [67]. We choose an annular nanoslit as a source for a propagating plasmonic wavefront.

A FDTD simulation gives the near-field electromagnetic fields distribution for annular nanoantenna (Fig. 13.12a, inset), illuminated with a circular polarization. Figure 13.12a shows the horizontal cross sections of the electric field components. In the vicinity of the slit, all the field components have comparable amplitudes, while those components in the out-launching plasmonic wave decay in a different manner. After propagation to a distance of half a plasmonic wavelength, the contribution of the normal E_z component to the intensity distribution is an order of magnitude larger than those of the E_x and E_y components. Hence, for multi-wavelength propagation distances, the complex plasmonic wavefront launched from the nanoantenna mainly contains the E_z signature. Figure 13.12b shows the spin-degenerated magnitude of the electric field component E_z with zero-field amplitude in the origin. Moreover, the phase of the E_z field is spiral and its helicity is spin-dependent (Fig. 13.12d, e), resulting from the optical SOI. Due to the SOI, the excited SPs acquire an OAM which is equal to the incident spin, resulting in a nanoscale TD: a plasmonic vortex source.

We give below the analytical evaluation result for the E_z field launched from an annular nanoantenna—infinitely thin circular slit with a radius r_0, in a medium supporting SPs. The selected shape of the nanoantenna as a circular nanoslit originates

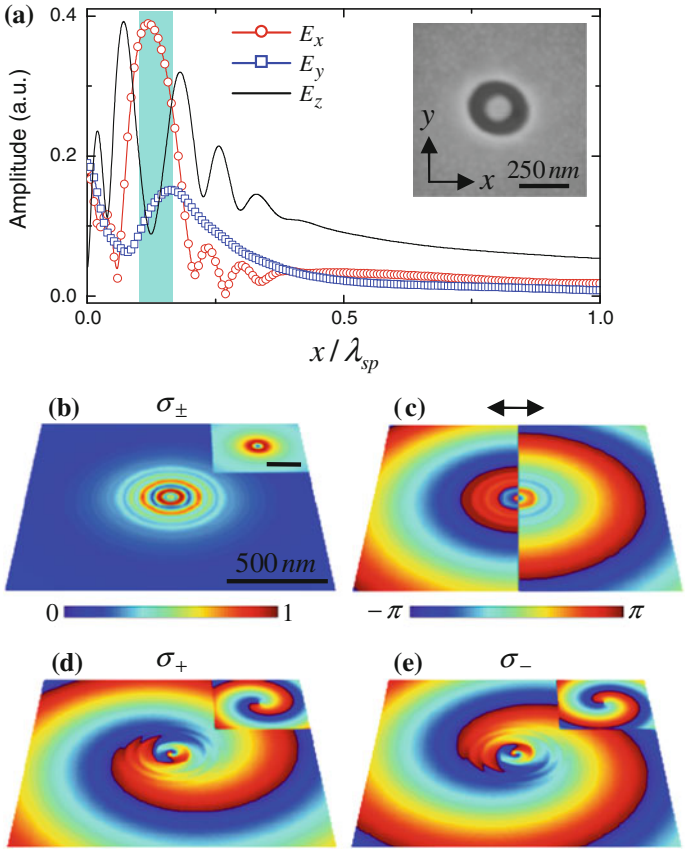

Fig. 13.12 Plasmonic vortex source. **a** Horizontal cross sections of the near-field electromagnetic fields of the nanoantenna, normally illuminated with circularly polarized light, at a wavelength of 780 nm; the *blue area* corresponds to the width of the etched circular nanoslit. The inset shows a SEM image of an annular nanoantenna with inner and outer radii of 75 and 125 nm, respectively, upon a 200 nm thick Au film. **b** FDTD simulation of the E_z magnitude for $\sigma_\pm$. **c** FDTD simulation of the E_z phase for horizontally linear polarization. **d**, **e** FDTD simulations of the E_z phases for $\sigma_\pm$, respectively. The insets in panels **b**, **d** and **e** shows the corresponding analytical calculation. Reprinted with permission from Ref. [67]. Copyright 2012 American Chemical Society

from the simple boundary conditions formulation. A one-dimensional nanoslit provides a momentum modification in the perpendicular direction, which is essential for the coupling of light to non-radiative surface modes, thereby exciting a surface wave with a phase front parallel to the slit. Moreover, only transverse magnetic polarized incident waves with an electric field perpendicular to the slit are efficiently coupled by the slit to SPs. If we consider a circularly polarized light as a rotating in time linear polarization, the maximal coupling efficiency along a circular nanoslit follows the local polarization selectivity of the one-dimensional slit [46]. The phase delay due

to the varying polarization state results in a geometric phase, leading to a plasmonic field $E_z(r_0, \varphi) = \exp(-i\sigma\varphi)$, where σ is the incident spin. Two additional boundary conditions are required: zero-field amplitude at the origin and at infinity, arising from the spiral phase and a single point source, respectively.

The two-dimensional Helmholtz equation, with the SP wave vector k_{sp}, is separable in polar coordinates (r, φ), where r is the radius and φ is the azimuthal angle. The different boundary conditions for the internal and external regions dictate different solutions for the in- and out-propagating plasmonic fields. The resulting solution of the in- and out-propagating plasmonic fields are

$$E_z(r, \varphi) = \begin{cases} J_{-\sigma}(k_{sp}r)[J_{-\sigma}(k_{sp}r_0)]^{-1}e^{-i\sigma\varphi}, \, in-wave \\ H_{-\sigma}(k_{sp}r)[H_{-\sigma}(k_{sp}r_0)]^{-1}e^{-i\sigma\varphi}, \, out-wave \end{cases}$$

Here, J_m and H_m are the mth-order of the Bessel and Hankel functions of the first kind, respectively. The analytical results, presented in the insets of Fig. 13.12b, d, e, confirm the scattering dynamics of the SPs from the localized vortex source obtained by the FDTD simulations.

The described mechanism of spin degeneracy removal in a single nanoantenna paves the way for consideration of spin-dependent plasmonic devices based on multiple plasmonic vortex sources. In conventional optics, the point spread function (PSF) is given by the spherical wave $h \propto \exp(ikr)$, and it links between the input and output of a space-invariant system via the superposition (convolution) integral. We herein propose the spin-orbit PSF—a spiral wavefront $h_\sigma \propto \exp(-i\sigma\varphi)$—where the incident spin is a degree of freedom. Hence, for a system consisting of multiple TD sources with an input g_1, the system output g_2 is spin-dependent and is described by the convolution relation $g_2(\sigma) = g_1 \otimes h_\sigma$. This concept encourages one to demonstrate different configurations of sources arrangements to observe *spinoptical* effects.

The experimental observation of multiple TD plasmonic field was completed on a circular chain of nanoscale TDs, etched by FIB at a thin Au film deposited on a glass substrate (Fig. 13.13a). The element was illuminated by a laser via a circular polarizer, and the excited SP wave was directly probed by the 150 nm aperture near-field scanning optical microscopy (NSOM) tip. The measured spin-degenerated intensity distribution is presented in Fig. 13.13b; the inset of Fig. 13.13a shows a horizontal cross section of the measured intensity and analytically calculated interference pattern of isolated TDs, at the center of the chain. A plasmonic interference pattern with a dark spot in the center (Fig. 13.13b, inset) is observed for the distinct spin states; such a singularity indicates a non-zero OAM, corresponding to a spiral phase. The calculated phase distributions by the model for multiple plasmonic vortex sources are presented in Fig. 13.13c, d and verified its spin-dependent helicity. Moreover, this calculation provided the quantitative value of the OAM per photon, shown to be equal to the incident optical spin; therefore, the superposition of vortex sources in a circular symmetry results in an intensity-enhanced plasmonic vortex with a higher total OAM. Note that if spherical waves from point sources are considered, a bright spot at the center would be expected.

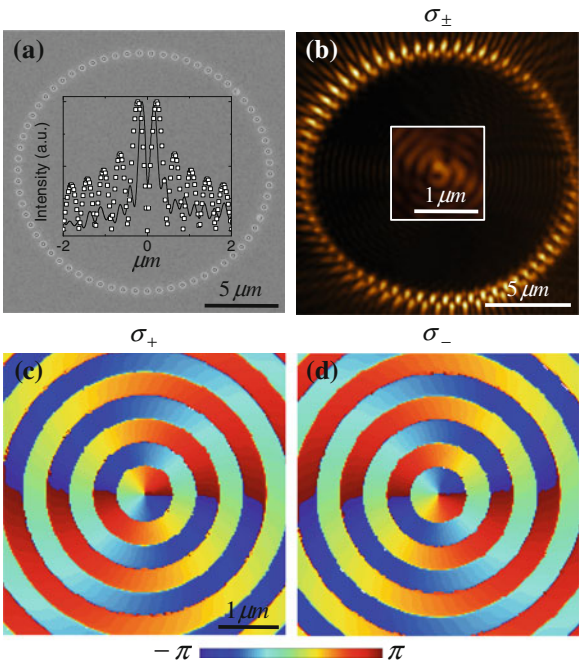

Fig. 13.13 Circular plasmonic chain of TDs. **a** SEM image of the chain consisting of annular nanoapertures arranged in a circular path with a radius of 8 μm, and with a period of 760 nm. The inset shows a horizontal cross section of the intensity at the center of the chain; the *curve* and the *squares* represent the measured and analytically calculated intensities, respectively. **b** Measured near-field intensity distribution for normally incident $\sigma_{\pm}$ at a wavelength of 780 nm; the inset represents a magnification of the *dark spot*. **c**, **d** Analytical calculations of the phase distributions of the plasmonic fields for $\sigma_{\pm}$, respectively. Reprinted with permission from Ref. [67]. Copyright 2012 American Chemical Society

The total field of uncoupled plasmonic nanoantennas, separated by a distance of the SP wavelength, is the coherent summation of all the elemental fields. The absence of a collective coupling between TDs in the proposed plasmonic device was verified by FDTD simulations of the same geometry with a random distribution of nanoantennas; the similar spin-based effect observed in ordered and disordered chains (not shown) is a signature for the non-collective behavior of the localized modes in the near-field. The isolated nature of TDs in the near-field is the basis for the multi-source consideration as the interference of vortex sources, and shows a good agreement with the spin-dependent experimental results

Another interesting spin-dependent plasmonic device based on the interference of TDs is a plasmonic focusing lens. A semicircular plasmonic chain consisted of annular nanoapertures with the previous parameters is shown in Fig. 13.14a. Figure 13.14c, d presents the measured intensities of the focusing plasmonic waves for $\sigma_{\pm}$, respectively. A spin-dependent transverse shift of the focal spot is easily observed from the

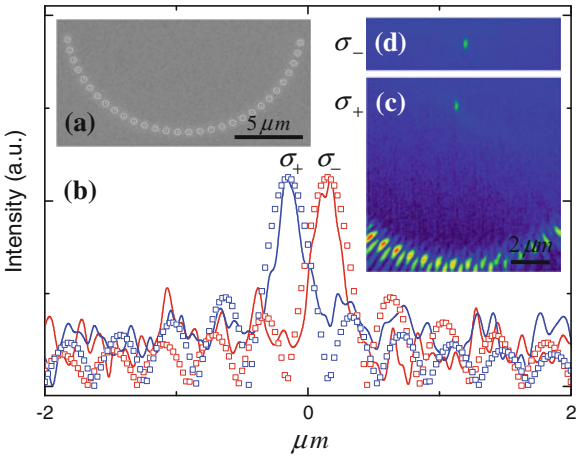

Fig. 13.14 Spin-dependent plasmonic focusing lens. **a** SEM image of the plasmonic lens consisting of annular nanoapertures arranged in a semicircular path. **b** Transverse cross sections of the intensity distributions in the focal plane; the *blue* and *red curves* (*squares*) represent the measured (analytically calculated) intensities for $\sigma_{\pm}$, respectively. **c**, **d** Measured near-field intensity distributions of the plasmonic lens, at a wavelength of 780 nm for normally incident $\sigma_{\pm}$, respectively. Reprinted with permission from Ref. [67]. Copyright 2012 American Chemical Society

compared cross sections (Fig. 13.14b). The obtained focal shift is a manifestation of the *optical spin-Hall effect* [15, 16, 35, 68], associated with the SOI, inducing the plasmonic vortex sources. The relocation of the spot can be calculated using the optical path condition with a spiral wavefront $k_{sp}r_i - \sigma\varphi_i = 2\pi m$, where r_i is the distance between the i th source and the shifted spot, φ_i is the corresponding azimuthal angle, and m is an integer. Using this formalism, we estimate the spin-dependent deflection by σ/k_{sp} ($\sim$120 nm), and it evidently supports the experimental results as well as the analytical calculations (Fig. 13.14b). Moreover, the calculation of the plasmonic fields reveals π-phase retardation between the spin-dependent focusing waves. Hence, when the superposition of the spin states $2^{-1/2}(|\sigma_+\rangle + |\sigma_-\rangle)$—a horizontal linear polarization—is illuminated, the focal spot splits in the lateral direction [64, 35]; however, for the superposed excitation $i2^{-1/2}(|\sigma_+\rangle - |\sigma_-\rangle)$—a vertical linear polarization—the retardation is compensated, and as a result the plasmonic wave homogeneously converges without a focal spot splitting [64].

In the next section we will introduce the optical spin-Hall effect induced by nanoapertures chain which observed in the far-field [35].

13.6 Optical Spin-Hall Effect from Plasmonic Nanoapertures

In contrast to the results of the previous section here we consider collective interaction [69] within periodic plasmonic chains, which play a crucial role in the recoupling of

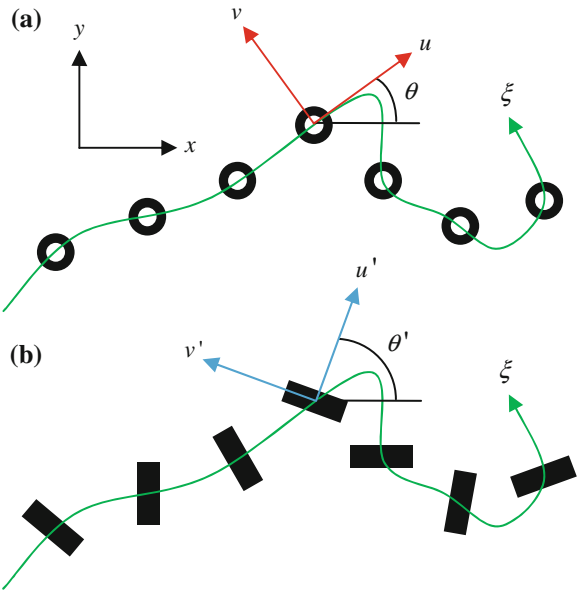

Fig. 13.15 Coupled localized plasmonic chains. **a** A plasmonic chain with isotropic unit cell and rotating reference frame (u, v) which follows the path ξ. **b** An anisotropy unit cell chain with a frame (u', v') attached to the local anisotropy axis of the unit cell. The lab reference frame is indicated by (x, y). Reprinted with permission from Ref. [35]. Copyright 2011 American Chemical Society

SPs to a propagating mode via the momentum-matching condition, as was recently presented [35].

One can distinguish between two types of optical spin-Hall effect (OSHE) [35]. The *locally isotropic* optical spin-Hall effect (OSHE-LI) is regarded as the interaction between the optical spin and the path ξ of the plasmonic chain with an isotropic unit cell (Fig. 13.15a). In contrast, the *locally anisotropic* optical spin-Hall effect (OSHE-LA) occurs due to the interaction between the optical spin and the local anisotropy of the unit cell, which is independent on the chain path (Fig. 13.15b). This resembles two types of spin-Hall effects in electron 2D systems—intrinsic (due to Rashba coupling) and extrinsic (due to the spin-orbit-dependent scattering of electrons from impurities).

The OSHE-LI can be observed on a chain of scatterers whose local orientation with respect to the selected x coordinate $\theta = \tan^{-1}(dy/dx)$ varies linearly with x, explicitly, $\theta(x) = \pi x/a$ where a is the period of the structure (Fig. 13.16b). This demand leads to a chain with a route $\{x(\xi), y(\xi)\}$ given by the function

$$\xi = (a/2\pi) \ln \left[\left(1 + \sin \frac{\pi x}{a}\right) \Big/ \left(1 - \sin \frac{\pi x}{a}\right) \right]. \tag{13.4}$$

The transmission spectrum of the coupled plasmonic chain, immersed in an index-matching oil to obtain symmetric configuration, bears a signature of two modes centered at the wavelengths of 700 and 780 nm corresponding to transversal and longitudinal polarization excitations [70], respectively (Fig. 13.16a).

Figure 13.16c shows the measured OSHE-LI observed from the chain corresponding to Eq. (13.5). In experiment the structure was sandwiched between circular polarizers and illuminated with a laser beam at a wavelength of 780 nm in order to excite the longitudinal mode. The intensity distribution is measured in the far-field, which corresponds to the momentum space.

Polarization analysis reveals that the scattering from the curved chain comprising two components: ballistic and spin-flip. The ballistic component doesn't experience any diffraction and maintains the polarization state of the incident beam, while the spin-flip component, with an opposite spin state, undergoes diffraction.

Spin-dependent beam deflection is observed in the experiment via orthogonal circular polarizers, corresponds to a momentum shift of $\Delta k_x = -2\sigma\pi/a$, where σ is the incident spin state. The peculiarity of the observed effect lies in its geometric nature. Light scattering by a system with spatially non-uniform anisotropy has a close analogy with a scattering from a revolving medium [39], as was shown recently [38]. Hence, the scattering by the bent chain is most conveniently studied using a rotating reference frame [52, 38] (u, v), which is attached to the axis of the local anisotropy of the chain and follows the chain's route $\xi\ (x, y)$ (Fig. 13.15a). This is accompanied by spatial rotation of the frame with a rate $\Omega_\xi = d\theta\,(\xi)/d\xi$, where $\theta\,(\xi)$ is the orientation angle. As a result, a spin-dependent momentum deviation $\Delta k_\xi = -2\sigma\,\Omega_\xi$ which corresponds to an additional phase of $\phi = \int \Delta k_\xi d\xi = -2\sigma\theta$, appears in the spin-flip scattered component. The experimentally observed spin-Hall momentum deviation concurs with the expected correction of $\Delta k_x = \nabla_x \phi = -2\sigma\pi/a$. This effect is regarded as the OSHE-LI.

When the chain unit cell is anisotropic itself, the local anisotropy is also allowed to be arbitrarily oriented along the path. The reference frame attached to the unit cell anisotropy is presented as the system $\left(u', v'\right)$ in Fig. 13.15b. It was previously shown that plasmonic structures consisting of nanorods exhibit a high polarization anisotropy that follows the orientation of the rods [71, 72]. An element consisting of randomly arranged but similarly oriented rectangular apertures with dimensions of 80×220 nm (Fig. 13.17a, top inset) demonstrates the localized mode resonance at a wavelength of 730 nm by measuring the transmission spectrum with linear polarization excitation parallel to its minor axis. High anisotropy is clearly observed between the two orthogonal linear polarization excitations, which results from the local anisotropy of the nanorod (Fig. 13.17a). A straight chain of subwavelength nanorods with a period of 430 nm (Fig. 13.17a, bottom inset) gives a narrow resonant line shape of the transmitted light in correspondence with the momentum matching condition, when the structure is illuminated by a linear polarization parallel to the nanorod's minor axis (Fig. 13.17a). When the orientation of the nanorods is varied linearly along the x-axis to obtain a spatial rotation rate of $\Omega = d\theta\prime/dx = \pi/a$ (Fig. 13.17b), the beam deflection of the spin-flip component corresponding to the spin-Hall momentum deviation of $\Delta k_x = -2\sigma\Omega$ arises (Fig. 13.17c). This beam

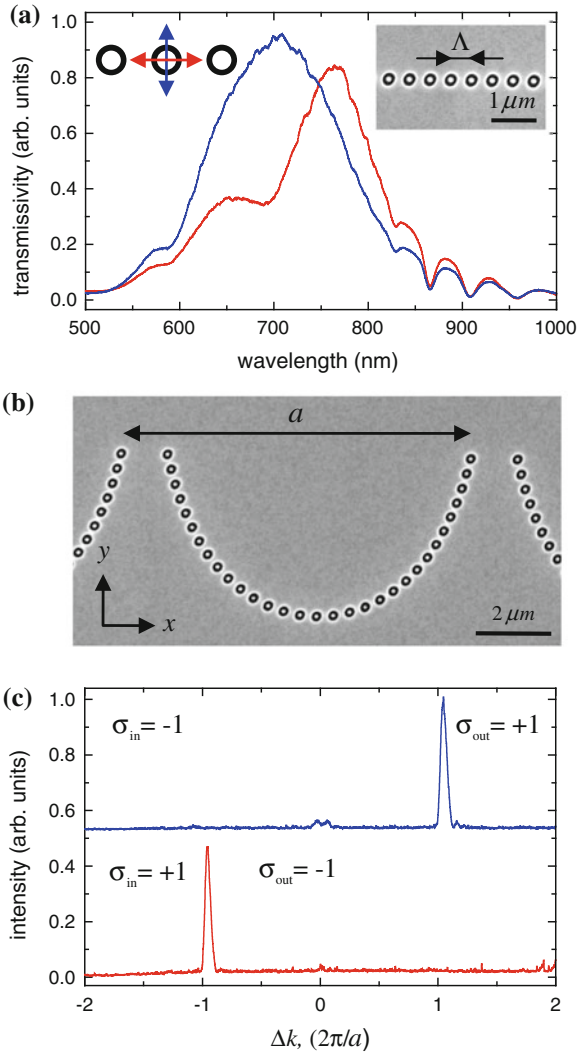

Fig. 13.16 **a** Transmission spectra of the plasmonic chain consisting of coaxial nanoapertures with inner/outer radii of 75/125 nm, with period of $\Lambda = 470$ nm and a length of 84.6 μm. The *blue* and *red lines/arrows* correspond to transversal and longitudinal polarization excitations, respectively. The inset shows SEM image of the chain. **b** SEM image of a curved chain whose local orientation θ is varied linearly along the x-axis with a rotation period of $a = 9$ μm, and a structure length of 135 μm. **c** The spin-dependent momentum deviation for the OSHE-LI, at a wavelength of 780 nm. The *red* and *blue lines* stand for incident *right-* and *left-handed* circularly polarized light, respectively ($\sigma_{in} = \pm 1$). σ_{out} denotes the spin state of the scattered light. Reprinted with permission from Ref. [35]. Copyright 2011 American Chemical Society

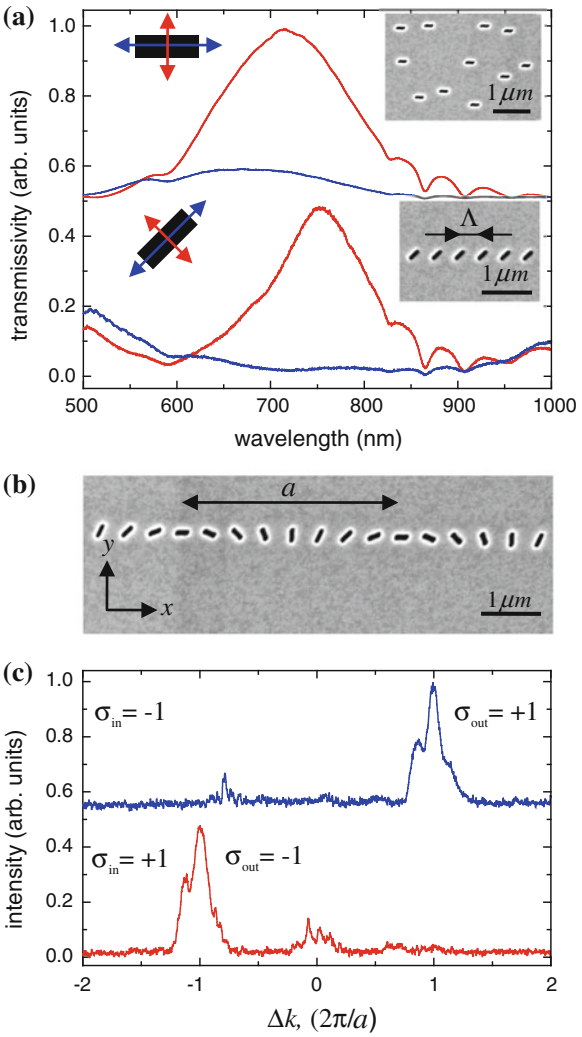

Fig. 13.17 **a** Transmission spectra of randomly arranged identically oriented *rectangular* apertures with dimensions of 80 × 220 nm in 86 μm *square* array, and of a homogeneous chain with period $\Lambda = 430$ nm, local orientation $\theta' = 45°$ and a length of 86 μm. The *red* and *blue lines/arrows* correspond to linear polarization excitations parallel and perpendicular to the nanorod's minor axis, respectively. The insets show SEM images of the structures described above. **b** SEM image of a chain in which the nanorods' orientation θ' varies linearly along the *x*-axis with a rotation period of $a = 3.44$ μm, and a structure length of 86 μm. **c** The spin-dependent momentum deviation for the OSHE-LA, at a wavelength of 730 nm. The *red* and *blue lines* stand for incident spin states $\sigma_{in} = \pm 1$, respectively. Reprinted with permission from Ref. [35]. Copyright 2011 American Chemical Society

deflection is regarded as the OSHE-LA and it arises due to the rotation of the local unit cell's anisotropy rather than the chain path curvature.The described mechanism paves the way for one to consider other path symmetries. According to Noether's theorem, for every symmetry in dynamical system there is a corresponding dynamical conservation law [73].

When the structure symmetry, or more explicitly the chain path $\xi\ (x, y)$, is circular, the corresponding conservation rule is for the angular momentum (AM). The AM of an optical beam can have two components: an intrinsic component that is associated with the handedness of the optical spin, and an extrinsic (orbital) component that is associated with its spatial structure. In an optical paraxial beam with a spiral phase distribution ($\phi = -l\varphi$, where φ is the azimuthal angle in polar coordinates, and the integer number l is the topological charge), the total AM per photon, in units of $\hbar$ (normalized AM), was shown to be $j = \sigma + l$ [33]. Let's consider circular chains with a path parameter $\xi = r_o\varphi$ (r_o is the chain radius) of annular apertures and rotating nanorods with a rotation rate $\Omega = m/r_o$, so the local anisotropy orientation is $\theta' = m\varphi$ (m is an integer). The far-field intensity distributions of the scattered spin-flip components are presented in Fig. 13.18a, b for annular apertures and rotating nanorods with $m = 2$, respectively. A characteristic dark spot in the center is clearly seen in the images which is a signature of orbital AM. Moreover, it is evident that the radius of the dark spot for the nanorod chain of $m = 2$ is larger than the one for the annular apertures, corresponding to a higher orbital AM. The observed OSHEs and specifically the orbital AM obtained from circular chains are due to the collective interaction of the localized modes within the periodic plasmonic chains. The role of the interaction can be elucidated by comparing the spin-flip component of the scattered light from a circular chain with random distribution of annular apertures.

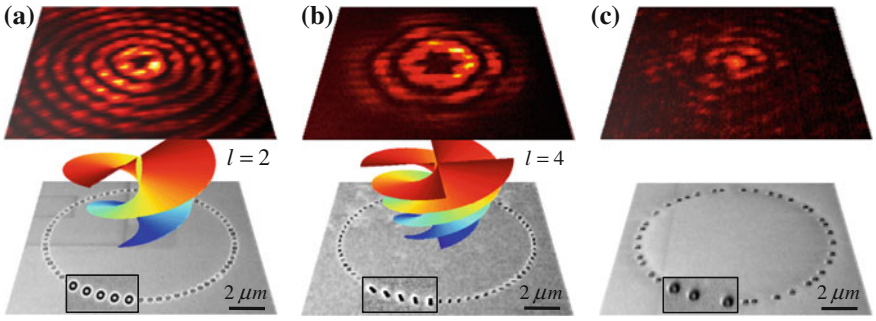

Fig. 13.18 The OSHE-LI and OSHE-LA for circular chains. The measured far-field intensity distribution of the spin-flip component scattered from a circular chain of ordered (**a**) and disordered (**c**) coaxial apertures at a wavelength of 780 nm, and rotating nanorods with $m = 2$ at a wavelength of 730 nm (**b**); *bottom*, SEM images of the chains with radii of $r_o = 5\ \mu$m. The spin-Hall momentum deviation is accompanied by a spiral phase-front with $l = 2$ and $l = 4$, for the OSHE-LI (**a**) and OSHE-LA (**b**), respectively. Note that no spin-Hall momentum deviation is observed from the disordered chain (**c**). Reprinted with permission from Ref. [35]. Copyright 2011 American Chemical Society

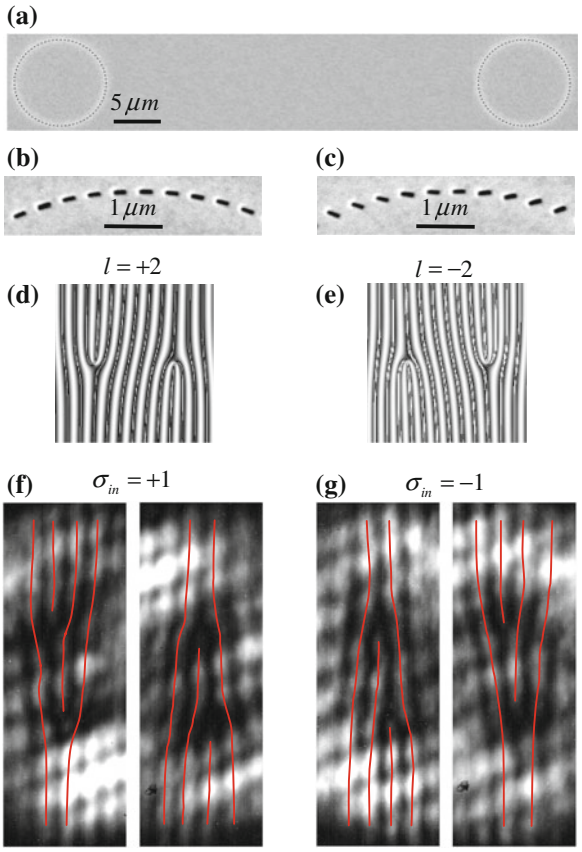

Fig. 13.19 Dislocation's strength measurement. **a** SEM image of two separated identical chains of nanorods rotated along a circular path with $m = 1$. **b**, **c** Magnified segments of SEM images of circular chains with $m = \pm 1$, respectively. **d**, **e** Calculated interference patterns for a pair of identical optical vortices with topological charges of $l = \pm 2$, respectively. **f**, **g** Measured interference patterns of the spin-flip components for $m = 1$ (regions of interest), at a wavelength of 730 nm and incident spin states $\sigma_{in} = \pm 1$, respectively. The additional fringes emerge *above* or *below* indicate the two generic phase dislocations and the *red guiding lines* emphasize their locations. Reprinted with permission from Ref. [35]. Copyright 2011 American Chemical Society

As evident from Fig. 13.18c a bright spot was obtained, indicating zero orbital AM in a disordered plasmonic chain. The orbital AM of the spin-flip component scattered from a circular chain is characterized by the strength of the dislocation and its helicity. Phase dislocations are singular field points such that the phase obtains a 2π-fold jump when making a closed loop around them. The dislocation's strength is the number of wave-fronts that end at the phase dislocation point. Its absolute value and sign (helicity) can be measured simultaneously by the interference of two optical vortices [74, 75]. For this purpose, one can use a system consisting of two separated identical chains of nanorods rotated along a circular path with $m = 1$ (Fig. 13.19a, b). The two chains, which behave as twin sources, give rise to intensity fringes, as shown in

Fig. 13.19f, g. In the observed interference patterns of the spin-flip components, two additional fringes emerge, indicating two phase dislocations (see the guiding lines in Fig. 13.19f, g). When the incident spin state alters , the antisymmetric fork-like picture is reversed. The experimental patterns with an incident spin of $\sigma = \pm 1$ are similar to the calculated patterns resulting from the scalar interference of two identical optical vortices with topological charges of $l = \pm 2$, respectively (Figs. 13.19d, e). The spin-dependent fringe patterns of a similar element with $m = -1$ (Fig. 13.19c) were also observed (not shown) to verify that the helicity of the phase dislocation corresponds to the rotation handedness of the nanorods. Moreover, the interference pattern of the ballistic component did not comprise a phase dislocation, indicating zero orbital AM. Each of the phase dislocations of the spin-flip components predicted by the calculated patterns (triple fork, see Figs. 13.19d, e), breaks in the experiment into a pair of fundamental phase dislocations (double fork, see Figs. 13.19f, g). The non-generic vortex collapse to generic vortices is in accordance with the prediction in Ref. [76]; therefore, the topological charge of the beam in this experiment is given by the number of the fundamental phase dislocations, resulting in $l = \pm 2$. As the orbital AM is directly linked to the azimuthal momentum correction Δk_φ via $l = -(1/2\pi) \oint \Delta k_\varphi d\xi$, the observed optical field with $l = 2m\sigma$ provides the evidence for a spin-Hall momentum deviation of $\Delta k_\varphi = -2m\sigma / r_o$. Since the unit cell anisotropy of the chain for $m = 1$ follows its curvature ($\theta' = \varphi$), the OSHE-LA in this case is equivalent to the OSHE-LI one. However, by m-fold rotation of the nanorods' orientation one can obtain m-fold magnification of the OSHE. Circular chains of annular apertures and rotating nanorods with $m = \pm 2$ were analyzed using the same interference method to experimentally demonstrate that the topological charge of the spin-flip component equals $l = 2\sigma$ and $2m\sigma$ for the OSHE-LI and OSHE-LA, respectively.

Finally, the topological charge's magnitude of the spin-flip component scattered from the circular chains can be verified by an interference, which results from a linear polarization projection of the ballistic and the spin-flip components [35]. For this purpose it is enough to measure the intensity distribution immediately behind the element via a linear polarizer. The interference patterns obtained by circular

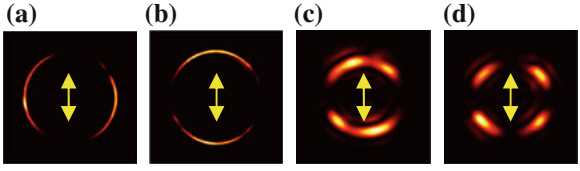

Fig. 13.20 Interference patterns resulting from linear polarization projections of the ballistic and spin-flip components scattered from single circular chains of coaxial apertures (**a**, **b**), rotating nanorods with $m = 1$ (**c**) and $m = 2$ (**d**). The *arrows* indicate the direction of the linear polarizer-analyzer. The coaxial chain was illuminated at wavelengths of 780 and 700 nm to excite the longitudinal (**a**) and transversal (**b**) plasmonic modes, respectively. The nanorod chain was illuminated at 730 nm. Reprinted with permission from Ref. [35]. Copyright 2011 American Chemical Society

chains of annular apertures and rotating nanorods with $m = 1, 2$ are visualized in Fig. 13.20. Propeller-like images confirm the orbital AM of l, which is expected from the obtained interference profile of $1 + \cos(l\varphi)$, for the OSHE-LI and OSHE-LA.

13.7 Coupled Thermal Antenna Lattices and Rashba-like Spin Degeneracy Violation

The spin state of elementary particles, atoms and molecules plays a key role in fundamental effects in physics. An external magnetic field causes energy separation of electrons (Zeeman effect) [77]. Spin-dependent momentum separation of charge carriers can occur due to structural inversion asymmetry in a material as result of spin-orbit interaction (Rashba and Dresselhaus effects) [78–80]. These two mechanisms show distinct patterns of energy dispersion, see Fig. 13.21. The photonic analogy of spin-orbit interaction is well known, wherein, the spin of the photons (helicity state of circularly polarized light) plays the role of the spin of charge carriers. Spin-dependent deflection of light was observed for propagation in gradient-index media [15, 53, 68] and with the scattering of surface plasmon polaritons (SPPs) from metallic nanostructures [34, 35, 46].

When light is emitted or scattered from a revolving medium, it exhibits a dispersion splitting—angular Doppler effect (ADE)—which depends on the circular polarization handedness (the photon's spin) [39]. The dispersion splitting is attributed to a spin-dependent correction of the momentum term in the wave equation due to rotation of the emitting medium. In this section we will describe a spin-dependent dispersion splitting of *thermal radiation* emitted from a structure whose local anisotropy is rotated along selected x-axis. The observed effect is attributed to the dynamics of the thermally excited surface wave propagating along the structure [81, 82].

For experiments the deepenings ("thermal antennas") with the subwavelength size of $1.2 \times 4.8\,\mu$m (Fig. 13.22a, right inset) were etched to a depth of $1\,\mu$m on a SiC substrate forming isolated thermal antenna and coupled thermal antenna

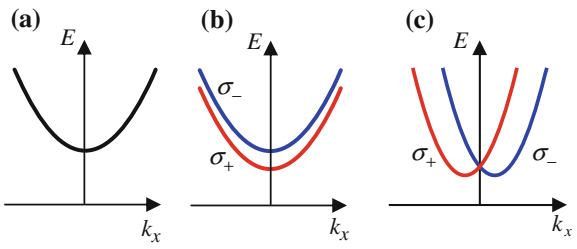

Fig. 13.21 Energy dispersion schemes of **a** spin-degenerated system, **b** energy splitting of the dispersion associated with Zeeman effect, **c** spin-dependent shift of the dispersion in the momentum space. Reprinted with permission from Ref. [82]. Copyright 2011 American Optical Society

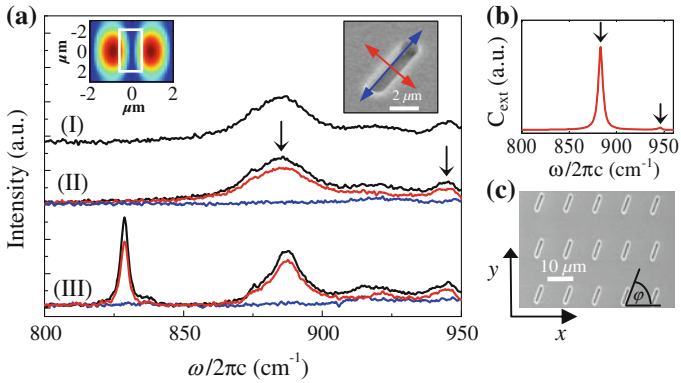

Fig. 13.22 **a** Spectral emission from the isolated thermal antenna, measured at $\theta = 6°$ (I) and $\theta = 0°$ (II) [SEM image of the antenna, *right inset*], and for antenna array at $\theta = 0°$ (III) [SEM image in **c**)]; *red* and *blue curves* correspond to polarization along the short axis and long axis of the antenna, respectively, and the black for the total intensity. *Left inset* presents FDTD simulation of the intensity distribution in vicinity of an isolated antenna at 883.7 cm^{-1}, *white square* indicates the location of the antenna. *Black arrows* point to the local resonances. **b** Calculated extinction cross section of an isolated antenna attained for polarization along the short axis of the antenna. Reprinted with permission from Ref. [82]. Copyright 2011 American Optical Society

array (Fig. 13.22c) with a period of $\Lambda = 11.6\,\mu m$. Two distinct resonances on isolated antenna, attributable to the local modes at $\omega_1/2\pi c = 885.7\,cm^{-1}$ and $\omega_2/2\pi c = 944.7\,cm^{-1}$, were observed at the temperature 773 K (Fig. 13.22a, curves I and II). These parameters find good agreement with calculations by the modified long wavelength approximation (MLWA) theory [83] resulting in $\omega_1^{(MLWA)}/2\pi c = 883.7\,cm^{-1}$ and $\omega_2^{(MLWA)}/2\pi c = 946.1\,cm^{-1}$ (Fig. 13.22b). Unlike the isolated antenna, the thermal antenna array manifest an additional narrow resonance peak at $830\,cm^{-1}$, attributed to collective antennas excitation (see Fig. 13.22a, curve III). The local resonances exhibit strong linear polarization along the direction of the small axis of the antenna. The emission dispersion measurement showed that the narrow spectral peak contains two propagating dispersive modes—a fast mode and a slow mode, (Fig. 13.23a) and the polarization direction of the slow mode follows the antennas' orientation (Fig. 13.23b).

The polarization properties of the thermal antenna array dramatically and intriguingly change if orientation of antennas is gradually rotated along the x-axis. In Fig. 13.24a the such antennas array with a distance along x-axis between neighboring antennas of $\Lambda = 11.6\,\mu m$ is presented. The antennas' angle with respect to the x direction, $\varphi(x) = (\pi/a)x$, changes at a spatial rotation rate of $\Omega = d\varphi(x)/dx = \pi/a$, where a is the distance along the x direction for a π rotation. Figure 13.24b represents a spin-projected dispersion (in the k_x momentum direction) for a lattice with $\Omega = 0.17(\pi/\Lambda)$ obtained by measuring the S_3 component of the Stokes vectors, which represents the circular polarization portion within the emitted light.

In the measured dispersion of thermal radiation [82], the slow mode exhibits a clear spin-controlled splitting in the momentum of the emitted waves. The degree of splitting of these modes, $2\Delta k$, grows linearly with Ω, so as $\Delta k = \sigma\Omega$, (Fig. 13.24c, d). The observed effect of the spin symmetry breaking is due to a spin-orbit interaction resulting from the dynamics of the surface waves propagating along the structure whose local anisotropy axis is rotated in space. The spin symmetry breaking is caused by the absence of inversion symmetry (IS) in the system. In general, time reversal symmetry (TRS) in a system results in energy relation $E(\mathbf{k}, \sigma_+) = E(-\mathbf{k}, \sigma_-)$. If the crystal lattice has inversion symmetry, i.e., the operation $\mathbf{r} \rightarrow -\mathbf{r}$ does not change the lattice, one will obtain $E(\mathbf{k}, \sigma_\pm) = E(-\mathbf{k}, \sigma_\pm)$. Consequently, if both TRS and IS are present, the band structure should satisfy the condition $E(\mathbf{k}, \sigma_+) = E(\mathbf{k}, \sigma_-)$. One can see that the inhomogeneous antenna lattice (Fig. 13.24a), has a broken inversion symmetry along the x direction, $\varphi(x) \neq \varphi(-x)$, resulting in $E(k_x, \sigma_+) \neq E(k_x, \sigma_-)$. However, from the dispersion depicted in Fig. 13.24b, it is evident that $E(k_x, \sigma_+) = E(-k_x, \sigma_-)$. Therefore, while the system has broken IS, it preserves TRS. Such behavior is similar to the Rashba spin splitting in electron bands of heterostructures which stems from inversion asymmetry in the structure [79]. The momentum offset Δkin the Rashba effect is proportional to the Rashba parameter α_R, ($\Delta k = m^*\alpha_R/\hbar^2$, m^* representing the effective mass of electrons), so in the observed photonic effect, the spatial rate of the lattices' inhomogeneity, Ω, resembles $m^*\alpha_R/\hbar^2$. In the same manner, one can define a Rashba-like energy, E_{R-L}, ($E_{R-L} = \hbar\Delta\omega_{R-L}$, see Fig. 13.24c) that is proportional to Ω^2, in accordance with approximately parabolic shape of the slow modes.

The peculiarity of the observed effect lies in its geometric nature. Surface waves scattered to radiation by a structure with spatially non-uniform anisotropy has a close analogy with emission from a revolving medium, as was recently shown [81]. Hence, the emission is most conveniently studied using a rotating reference frame that is attached to the axis of the local anisotropy of the antennas. The Helmholtz equation in a non-inertial reference frame revolving with rate $c\Omega << \omega$ is

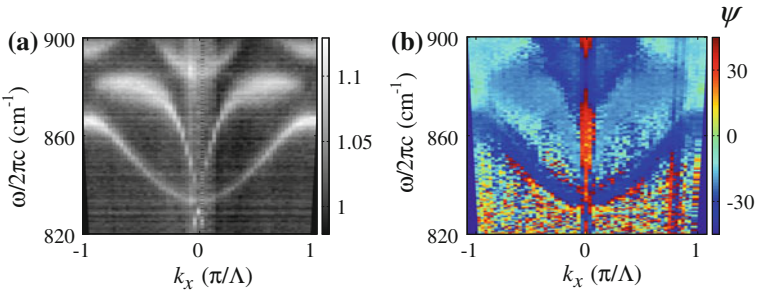

Fig. 13.23 **b** Dispersion of thermal emission from the parallel antenna array ($\varphi = 60^o$); *gray scale*—intensity, a.u. **b** Measured orientation angle of the polarization ellipse, $\psi^{(o)}$, for the dispersion in **a**. Reprinted with permission from Ref. [82]. Copyright 2011 American Optical Society

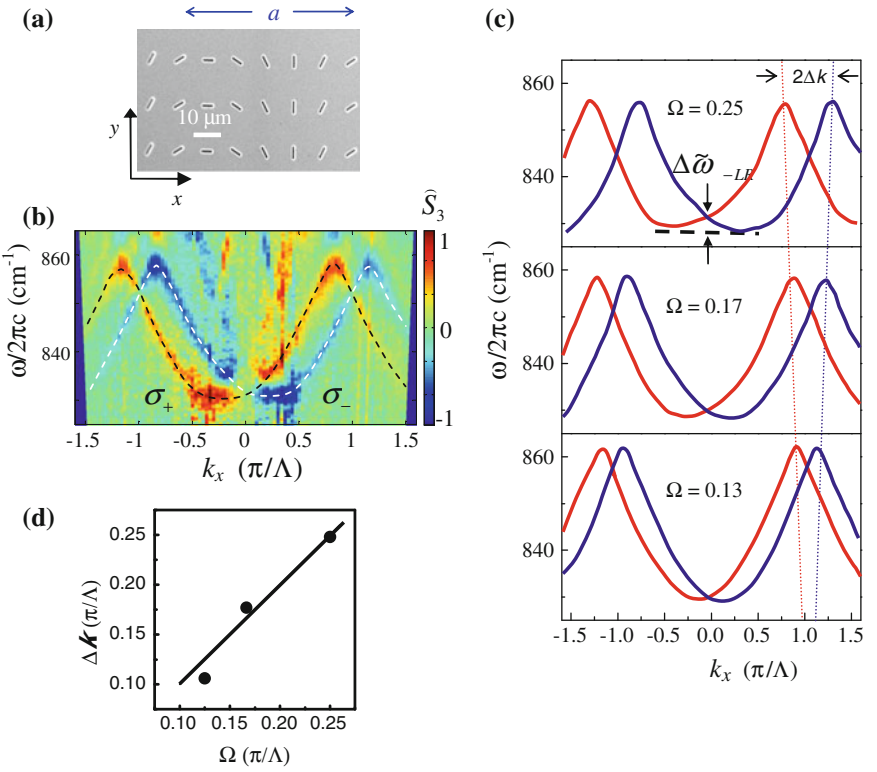

Fig. 13.24 **a** SEM image of the lattice composed of antennas rotating along the x-axis with spatial rotation rate $\Omega = 0.17(\pi/\Lambda)$. **b** Measured spin-projected dispersion of emission from the lattice obtained by the Stokes parameter S_3 measurement; *blue/red color* corresponds to a negative/positive spin projection. *Dashed white* and *black lines* highlight the spin-split dispersion. **c** Measured spin-projected dispersion of the split modes for various Ω (in units of (π/Λ)); *red* and *blue lines* correspond to σ_+ and σ_- spin states, respectively; $\Delta\tilde{\omega}_{R-L}$ denotes the Rashba-like energy normalized by $\hbar/2\pi c$. **d** Observed spin-controlled momentum displacement (*circles*), compared with the predicted dependence (*solid line*). Reprinted with permission from Ref. [82]. Copyright 2011 American Optical Society

$$(\nabla^2 + k^2 + 2\sigma\Omega k)E_\sigma = 0, \tag{13.5}$$

where E_σ are the eigenvectors of circular polarizations; note that $2\sigma\Omega k$ is the Coriolis term. This equation similar to the Schrödinger equation $(\nabla^2 + k^2 + 2m^*\alpha_R\sigma_y(-i\nabla)/\hbar^2)\Psi(r) = 0$ for the confined 1D Rashba system. The term $2m^*\alpha_R\sigma_y(-i\nabla)/\hbar^2$ corresponds to the Coriolis term $2\sigma\Omega k$, in accordance with our interpretation that Ω resembles $m^*\alpha_R/\hbar^2$. The Eq. (13.5) can be written as $\left(\nabla^2 + K^2\right)E_\sigma = 0$, where $K(\omega) \approx k(\omega) + \sigma\Omega$ is the generalized momentum, and the dispersion relation then becomes $\omega = \omega(k_x + \sigma\Omega)$. Therefore, due to rotation of the local anisotropy axis, the original dispersion of the homogeneous lattice

is now split into two modes with opposite spin states, each shifted by $\Delta k = \sigma\Omega$ on the momentum axis. The corresponding generalized momentum is the manifestation of the spin-orbit interaction, which is responsible for effects such as the optical spin-Hall, Magnus, and Coriolis effects, and the Berry phase shift.

References

1. T.W. Ebbesen, H.J. Lezec, H.F. Ghaemi, T. Thio, P.A. Wolff, Extraordinary optical transmission through sub-wavelength hole arrays. Nature **391**, 667–669 (1998)
2. H.J. Lezec, A. Degiron, E. Devaux, R.A. Linke, L. Martin-Moreno, F.J. Garcia-Vidal, T.W. Ebbesen, Beaming light from a subwavelength aperture. Science **297**, 820–822 (2002)
3. F. López-Tejeira, S.G. Rodrigo et al., Efficient unidirectional nanoslit couplers for surface plasmons. Nat. Phys. **3**, 324–328 (2007)
4. L. Yin, V.K. Vlasko-Vlasov et al., Subwavelength focusing and guiding of surface plasmons. Nano Lett. **5**, 1399–1402 (2005)
5. W. Nomura, M. Ohtsu, T. Yatsui, Nanodot coupler with a surface plasmon polariton condenser for optical far/near-field conversion. Appl. Phys. Lett. **86**, 181108–181111 (2005)
6. S.I. Bozhevolnyi, V.S. Volkov, E. Devaux, J.Y. Laluet, T.W. Ebbesen, Channel plasmon subwavelength waveguide components including interferometers and ring resonators. Nature **440**, 508–511 (2006)
7. G. Gay, O. Alloschery, B. Viaris de Lesegno, J. Weiner, H. J. Lezec, Surface wave generation and propagation on metallic subwavelength structures measured by far-field interferometry. Phys. Rev. Lett. **96**, 213901–213904 (2006)
8. J.-J. Greffet, R. Carminati, K. Joulain, J.-P. Mulet, S. Mainguy, C. Yong, Coherent emission of light by thermal sources. Nature **416**, 61–64 (2002)
9. N. Dahan, A. Niv, G. Biener, Y. Gorodetski, V. Kleiner, E. Hasman, Enhanced coherency of thermal emission: beyond the limitation imposed by delocalized surface waves. Phys. Rev. B **76**, 045427–045425 (2007)
10. F.J. Garcia-Vidal, J.B. Pendry, Collective theory for surface enhanced Raman scattering. Phys. Rev. Lett. **77**, 1163–1166 (1996)
11. S.L. Prosvirnin, N.I. Zheludev, Polarization effects in the diffraction of light by a planar chiral structure. Phys. Rev. E **71**, 037603–037604 (2005)
12. A.V. Krasavin, A.S. Schwanecke, N.I. Zheludev, Polarization conversion and "focusing" of light propagating through a small chiral hole in a metallic screen. Appl. Phys. Lett. **86**, 201105–201103 (2005)
13. N. Fang, H. Lee, C. Sun, X. Zhang, Sub-diffraction-limited optical imaging with a silver superlens. Science **308**, 534–537 (2005)
14. I.I. Smolyaninov, Y. Hung, C. Davis, Magnifying superlens in the visible frequency range. Science **315**, 1699–1701 (2007)
15. K.Y. Bliokh, A. Niv, V. Kleiner, E. Hasman, Geometrodynamics of spinning light. Nat. Photonics **2**, 748–753 (2008)
16. Y. Gorodetski, A. Niv, V. Kleiner, E. Hasman, Observation of spin-based plasmonic effect in nanoscale structures. Phys. Rev. Lett. **101**, 043903–043904 (2008)
17. W.L. Barnes, A. Dereux, T.W. Ebbesen, Surface plasmon subwavelength optics. Nature **424**, 824–830 (2003)
18. E. Majorana, Atomi orientati in campo magnetico variabile. Nuovo Cim. **9**, 43 (1932)
19. J.H. Hannay, The Majorana representation of polarization, and the Berry phase of light. J. Mod. Opt. **45**, 1001–1008 (1998)
20. M.V. Berry, The adiabatic phase and Pancharatnam's phase for polarized light. J. Mod. Opt. **34**, 1401–1407 (1987)

21. Z. Bomzon, V. Kleiner, E. Hasman, Pancharatnam-Berry phase in space-variant polarization state manipulations with subwavelength gratings. Opt. Lett. **26**, 1424–1426 (2001)
22. Z. Bomzon, V. Kleiner, E. Hasman, Formation of radially and azimuthally polarized light using space-variant subwavelength metal stripe gratings. Appl. Phys. Lett. **79**, 1587–1589 (2001)
23. N.B. Baranova, A.Y. Savchenko, B.Y. Zel'dovich, Transverse shift of a focal spot due to switching of the sign of circular polarization. JETP Lett. **59**, 232–235 (1994)
24. B. Zel'dovich, Ya, N.D. Kundikova, L.F. Rogacheva, Observed transverse shift of a focal spot upon a change in the sign of circular polarization. JETP Lett. **59**, 766–769 (1994)
25. A. Kavokin, G. Malpuech, M. Glazov, Optical spin hall effect. Phys. Rev. Lett. **95**, 136601–136604 (2005)
26. C. Leyder, M. Romanelli, JPh Karr, E. Giacobino, T.C.H. Liew, M.M. Glazov, A.V. Kavokin, G. Malpuech, A. Bramati, Observation of the optical spin Hall effect. Nature **3**, 628–631 (2007)
27. W. Gerlach, O. Stern, Das magnetische moment des silberatoms. Z. Phys. **9**, 353–355 (1922)
28. F. Zhou, Topological spin pumps: the effect of spin rotation on quantum pumps. Phys. Rev. B **70**, 125321–18 (2004)
29. J.H. Poynting, The wave motion of a revolving shaft, and suggestion as to the angular momentum in the beam of circularly polarised light. Proc. Roy. Soc. A **82**, 560–567 (1909)
30. R.A. Beth, Mechanical detection and measurement of the angular momentum of light. Phys. Rev. **50**, 115–125 (1936)
31. S.J. Van Enk, G. Nienheuis, Eigenfunction description of laser beams and orbital angular momentum of light. Opt. Commun. **94**, 147–158 (1992)
32. A.T. O'Neil, I. MacVicar, L. Allen, M.J. Padgett, Intrinsic and extrinsic nature of the orbital angular momentum of a light beam. Phys. Rev. Lett. **88**, 053601–4 (2002)
33. L. Allen, M.W. Beijersbergen, R.S. Spreeuw, J.P. Woerdman, Orbital angular momentum of light and the transformation of Laguerre-Gaussian laser modes. Phys. Rev. A **45**, 8185–8190 (1992)
34. Y.N. Gorodetski, I. Shitrit, V. Bretner, E. Kleiner, Hasman, Observation of optical spin symmetry breaking in nanoapertures. Nano Lett. **9**, 3016–3019 (2009)
35. N. Shitrit, I. Bretner, Y. Gorodetski, V. Kleiner, E. Hasman, Optical spin hall effects in plasmonic chains. Nano Lett. **11**, 2038–2042 (2011)
36. V.S. Liberman, B. Zel'dovich, Ya. Spin-orbit interaction of a photon in an inhomogeneous medium. Phys. Rev. A **46**, 5199–5207 (1992)
37. A. Niv, Y. Gorodetski, V. Kleiner, E. Hasman, Topological spin-orbit interaction of light in anisotropic inhomogeneous subwavelength structures. Opt. Lett. **33**, 2910–2912 (2008)
38. K.Y. Bliokh, Y. Gorodetski, V. Kleiner, E. Hasman, Coriolis effect in optics: unified geometric phase and spin-hall effect. Phys. Rev. Lett. **101**, 030404–4 (2008)
39. B.A. Garetz, Angular Doppler effect. J. Opt. Soc. Am. **71**, 609–611 (1981)
40. A.S. Schwanecke, V.A. Fedotov, V.V. Khardikov, S.L. Prosvirnin, Y. Chen, N.I. Zheludev, Nanostructured metal film with asymmetric optical transmission. Nano Lett. **8**, 2940–2943 (2008)
41. M. Kuwata-Gonokami, N. Saito, Y. Ino, M. Kauranen, K. Jefimovs, T. Vallius, J. Turunen, Y. Svirko, Giant optical activity in quasi-two-dimensional planar nanostructures. Phys. Rev. Lett. **95**, 227401–4 (2005)
42. A. Drezet, C. Genet, J.-Y. Laluet, T.W. Ebbesen, Optical chirality without optical activity: how surface plasmons give a twist to light. Opt. Express **16**, 12559–12570 (2008)
43. T. Ohno, S. Miyanishi, Study of surface plasmon chirality induced by Archimedes' spiral grooves. Opt. Express **14**, 6285–6290 (2006)
44. M.J. Lockyear, A.P. Hibbins, J.R. Sambles, C.R. Lawrence, Microwave transmission through a single subwavelength annular aperture in a metal plate. Phys. Rev. Lett. **94**, 193902 (2005)
45. A. Niv, G. Biener, V. Kleiner, E. Hasman, Manipulation of the Pancharatnam phase in vectorial vortices. Opt. Express **14**, 4208–4220 (2006)
46. Y. Gorodetski, S. Nechayev, V. Kleiner, E. Hasman, Plasmonic Aharonov-Bohm effect: optical spin as the magnetic flux parameter. Phys. Rev. B **82**, 125433–4 (2010)

47. Y. Aharonov, D. Bohm, Significance of electromagnetic potentials in the quantum theory. Phys. Rev. **115**, 485–491 (1959)
48. M.V. Berry, R.G. Chambers, M.D. Large, C. Upstill, J.C. Walmsley, Wavefront dislocations in the Aharonov-Bohm effect and its water wave analogue. Eur. J. Phys. **1**, 154–162 (1980)
49. C. Coste, F. Lund, M. Umeki, Shallow water scattering of dislocated wave fronts by vertical vorticity and the Aharonov-Bohm effect. I. Phys. Rev. E. **60**, 4908–4916 (1999)
50. F. López-Tejeira, S.G. Rodrigo, L. Martin-Moreno, F.J. Garcia-Vidal, E. Devaux, T.W. Ebbesen, J.R. Krenn, I.P. Radko, S.I. Bozhevolnyi, M.U. González, J.C. Weeber, A. Dereux, Efficient unidirectional nanoslit couplers for surface plasmons. Nat. Phys. **3**, 324–328 (2007)
51. L. Aigouy, P. Lalanne, J.P. Hugonin, G. Julié, V. Mathet, M. Mortier, Near-field analysis of surface waves launched at nanoslit apertures. Phys. Rev. Lett. **98**, 153902–4 (2007)
52. S.G. Lipson, Berry's phase in optical interferometry: a simple derivation. Opt. Lett. **15**, 154–155 (1990)
53. K.Y. Bliokh, Geometrodynamics of polarized light: berry phase and spin hall effect in a gradient-index medium. J. Opt. A: Pure Appl. Opt. **11**, 094009–14 (2009)
54. Y. Aharonov, A. Casher, Topological quantum effects for neutral particles. Phys. Rev. Lett. **53**, 319–321 (1984)
55. R. Pugatch, M. Shuker, O. Firstenberg, A. Ron, N. Davidson, Topological stability of stored optical vortices. Phys. Rev. Lett. **98**, 203601–4 (2007)
56. N.D. Mermin, The topological theory of defects in ordered media. Rev. Mod. Phys. **51**, 591–648 (1979)
57. H. Saito, Y. Kawaguchi, M. Ueda, Topological defect formation in a quenched ferromagnetic Bose-Einstein condensates. Phys. Rev. A **75**, 013621–10 (2007)
58. F. de Juan, A. Cortijo, M.A.H. Vozmediano, A. Cano, Aharonov-Bohm interferences from local deformations in graphene. Nature. Phys. **7**, 810–815 (2011)
59. R. Blaauwgeers, V.B. Eltsov, M. Krusius, J.J. Ruohio, R. Schanen, G.E. Volovik, Double-quantum vortex in superfluid ^{3}He-A. Nature **404**, 471–473 (2000)
60. G. Goren, I. Procaccia, S. Rasenat, V. Steinberg, Interactions and dynamics of topological defects: theory and experiments near the onset of weak turbulence. Phys. Rev. Lett. **63**, 1237–1240 (1989)
61. R.L. Davis, Texture: a cosmological topological defect. Phys. Rev. D **35**, 3705–3708 (1987)
62. E. Brasselet, C. Loussert, Electrically controlled topological defects in liquid crystals as tunable spin-orbit encoders for photons. Opt. Lett. **36**, 719–721 (2011)
63. J.F. Nye, M.V. Berry, Dislocations in wave trains. Proc. R. Soc. London, Ser. A, **336**, 165–190 (1974)
64. L. Yin, V.K. Vlasko-Vlasov, J. Pearson, J.M. Hiller, J. Hua, U. Welp, D.E. Brown, C.W. Kimball, Subwavelength focusing and guiding of surface plasmons. Nano Lett. **5**, 1399–1402 (2005)
65. J.-Y. Laluet, A. Drezet, C. Genet, T.W. Ebbesen, Generation of surface plasmons at single subwavelength slits: from slit to ridge plasmon. N. J. Phys. **10**, 105014–9 (2008)
66. R. Zia, M.L. Brongersma, Surface plasmon polariton analogue to Young's double-slit experiment. Nature. Nanotechnol. **2**, 426–429 (2007)
67. N. Shitrit, S. Nechayev, V. Kleiner, E. Hasman, Spin-dependent plasmonics based on interfering topological defects. Nano Lett. **12**, 1620–1623 (2012)
68. O. Hosten, P. Kwiat, Observation of the spin hall effect of light via weak measurements. Science **319**, 787–790 (2008)
69. M. Hentschel, M. Saliba, R. Vogelgesang, H. Giessen, A.P. Alivisatos, N. Liu, Transition from isolated to collective modes in plasmonic oligomers. Nano Lett. **10**, 2721–2726 (2010)
70. S.A. Maier, M.L. Brongersma, P.G. Kik, H.A. Atwater, Observation of near-field coupling in metal nanoparticle chains using far-field polarization spectroscopy. Phys. Rev. B **65**, 193408–4 (2002)
71. R. Gordon, A.G. Brolo, A. McKinnon, A. Rajora, B. Leathem, K.L. Kavanagh, Strong polarization in the optical transmission through elliptical nanohole arrays. Phys. Rev. Lett. **92**, 037401–4 (2004)

72. K.J.K. Koerkamp, S. Enoch, F.B. Segerink, N.F. van Hulst, L. Kuipers, Strong influence of hole shape on extraordinary transmission through periodic arrays of subwavelength holes. Phys. Rev. Lett. **92**, 183901–4 (2004)
73. J.D. Koralek, C.P. Weber, J. Orenstein, B.A. Bernevig, S.-C. Zhang, S. Mack, D.D. Awschalom, Emergence of the persistent spin helix in semiconductor quantum wells. Nature **458**, 610–613 (2009)
74. H.I. Sztul, R.R. Alfano, Double-slit interference with Laguerre-Gaussian beams. Opt. Lett. **31**, 999–1001 (2006)
75. E. Brasselet, N. Murazawa, H. Misawa, S. Juodkazis, Optical vortices from liquid crystal droplets. Phys. Rev. Lett. **103**, 103903–4 (2009)
76. M.S. Soskin, V.N. Gorshkov, M.V. Vasnetsov, J.T. Malos, N.R. Heckenberg, Topological charge and angular momentum of light beams carrying optical vortices. Phys. Rev. A **56**, 4064–4075 (1997)
77. P. Zeeman, On the influence of magnetism on the nature of the light emitted by a substance. Phil. Mag. **43**, 226–239 (1897)
78. E.I. Rashba, Properties of semiconductors with an extremum loop. 1. Cyclotron and combinational resonance in a magnetic field perpendicular to the plane of the loop. Sov. Phys. Solid State **2**, 1109 (1960)
79. K. Ishizaka, M.S. Bahramy, H. Murakawa, M. Sakano, T. Shimojima, T. Sonobe, K. Kiozumi, S. Shin, H. Miyahara, A. Kimura, K. Miamoto, T. Okuda, H. Namatame, M. Taniguchi, R. Arita, N. Nagaosa, K. Kobayashi, Y. Murakami, R. Kumai, Y. Kaneko, Y. Onose, Y. Tokura, Giant Rashba-type spin splitting in bulk BiTel. Nat. Mater. **10**, 521–526 (2011)
80. G. Dresselhaus, Spin-orbit coupling effects in zinc blende structures. Phys. Rev. **100**, 580–586 (1955)
81. N. Dahan, Y. Gorodetski, K. Frischwasser, V. Kleiner, E. Hasman, Geometric doppler effect: spin-split dispersion of thermal radiation. Phys. Rev. Lett. **105**, 136402–4 (2010)
82. K. Frischwasser, I. Yulevich, V. Kleiner, E. Hasman, Rashba-like spin degeneracy breaking in coupled thermal antenna lattices. Opt. Express **19**, 23475–23482 (2011)
83. K.D. Ko, C.K. Toussaint Jr, A simple GUI for modeling the optical properties of single metal nanoparticles. J. Quant. Spectrosc. Radiat. Transfer **110**, 1037–1043 (2009)

Chapter 14
Plasmonics and Super-Hydrophobicity: A New Class of Nano-Bio-Devices

F. Gentile, M. L. Coluccio, A. Toma, A. Alabastri, R. Proietti Zaccaria, G. Das, F. De Angelis, P. Candeloro, C. Liberale, G. Perozziello, L. Tirinato, M. Leoncini and E. Di Fabrizio

Abstract Early detection of diseases has great importance in terms of success of the disease treatment. In fact, it has a profound positive influence on the response provided by the patient, leading to shorter and less invasive treatment regimes. We consider here the Raman detection of low (atto-molar) concentrates of molecules by applying nanofabrication techniques in the fabrication of plasmonic devices fulfilling the requirement of superhydrophobicity. Plasmonic resonances will have the effect of substantially increasing the local electric field around the fabricated nanodevice which, in turn, will positively affect the Raman signal. Similarly, the superhydrophobicity will play the crucial role in localizing the few molecules of the analyte around the plasmonic device, therefore allowing their detection in a manner otherwise impossible in diffusion-based devices. We will theoretically explain the concept of superhydrophobicity by providing also a roadmap for defining the optimal superhydrophobic device, then we will introduce the fabrication process to realize such a device and, finally, we will provide the Raman counting of a series of analytes together with electromagnetic simulations illustrating the role of the electric field in the formation of the Raman signal.

Keywords Plasmon · Hydrophobicity

F. Gentile · M. L. Coluccio · P. Candeloro · G. Perozziello · L. Tirinato · E. Di Fabrizio (✉)
BioNEM (Bio Nano Engineering and Technology for Medicine), University Magna Graecia of Catanzaro, 88100 Catanzaro, Italy
e-mail: enzo.difabrizio@kaust.edu.sa

F. Gentile · A. Toma · A. Alabastri · R. Proietti Zaccaria · G. Das · F. De Angelis · C. Liberale · M. Leoncini · E. Di Fabrizio
Istituto Italiano di Tecnologia, Via Morego 30, 16163 Genova, Italy

E. Di Fabrizio
King Abdullah University of Science and Technology, 4086,Bld g. 3, 3rd floor, Office 3235, Thuwal 23955-69 00, Kingdom of Saudi Arabia

T. V. Shahbazyan and M. I. Stockman (eds.), *Plasmonics: Theory and Applications*, Challenges and Advances in Computational Chemistry and Physics 15,
DOI: 10.1007/978-94-007-7805-4_14, © Springer Science+Business Media Dordrecht 2013

14.1 Introduction

Plasmonics is a branch of Physics extremely promising for its applications in electronics, chemistry, computer science, solar energy harvesting and biology. In particular, it is dedicated to the investigation of confined electromagnetic waves originating by the combination of free electrons with the light source. Besides noble metals, artificial materials are at the basis of Plasmonics. This aspect strictly relates it to *Nanotechnology*, a growing science aiming to investigate both the theoretical and fabrication aspects of devices with dimensions in the nanometer range [1]. The strong appeal of these systems is their capacity of fundamentally changing the way biomedical sciences are practiced, in that they feature characteristic length scales that are of the same order of magnitude of biological objects (from cells, as large as ten microns, to bio molecules sizing few nanometers or less), and can accordingly interact with these in a fashion that new physical/biological laws, strategies or possibilities emerge [2]. Many are the examples where nanotechnology is applied to biology and include, for instance, surfaces patterned with random, rather than periodic, micro- nano- fabricated themes, to guide cells attachment and proliferation [3]; needles, holes or micro- nano- based microfluid channels for transdermal drug administration, protein sorting and cell analysis [4]; microstuctured, three dimensional scaffolds for tissue engineering [5]; the nano particles toolbox for the smart delivery of drugs and imaging [6, 7]; devices for molecular detection, identification and diagnostics. The latter comprise a variety of different systems, including nanowires and nano-cantilevers, microarrays [8], and nanoporous silicon surfaces, whereby the species of interest can be selectively adsorbed and detected using MALDI TOF mass spectroscopy techniques [9].

Early detection is particularly important in the case of cancer and other pathologies, in that the early stages of disease are typically treated with the greatest probability of success [10, 11]. Albeit the large variety of systems listed above, surface enhanced Raman scattering (SERS) substrates are among the most promising in terms of sensitivity, reproducibility and reliability [12]. These nano geometry based devices are capable to detect biological moieties in the limits of very low abundance ranges, and offer the most effective way for the diagnosis of few, or single, molecules.

SERS effects stem from the combination of subwavelength nanoscale features and noble metals, and particularly from the excitation of localized surface *plasmons* at the interface with a metallic surface, and thus they strongly depend upon the topology of the active substrate. It is very well understood that certain regular geometries, with a convenient design, induce giant electric fields, with an enhancement of up to 10^9 in the Raman signal. Recent advances in SERS technology produced, for instance, periodic arrays of metallic nano dots [13]; adiabatic nanofocusing cones [14–20]; or groups of three hierarchical metallic hemi spheres, where the ratio between the diameters or, equivalently, the distances of the spheres is chosen with high precision, and these are called nano lenses [21]. Interestingly, randomly rough surfaces, with a roughness in a nanometric scale, also exhibit superior sensing capabilities [22] but, differently from regular geometries, they retain the advantages of short fabrication

time and lower process costs. In 2008, Coluccio et al. [23] devised a SERS sensor constituted by electroless grown random assemblies of silver nanograins, where electroless growth is a process whereby metal ions are reduced and deposited as metals upon a silicon surface. Metal grains are obtained with an average size as small as few nanometers, with an overall shape and dimension that can be regulated with an extremely high precision and reproducibility. Despite the extremely high enhancement factors that are achievable *in theory*, devices like this suffer from a practical and serious limitation, that is, the huge time that the species of interest would take to reach and interact with the active sites of the substrate. In a solution at rest and under the effect of diffusion solely, a bio molecule with a Brownian diffusion coefficient $D = 10^{-9} m^2/s$, would take some 60 h to travel the distance of 1 cm, that is the typical length side of the device. And thus the performance of conventional, 2d SERS substrates would be dramatically limited by the bottleneck of diffusion.
To overcome this limit we have performed the integration of nano-photonic devices, such as the ones previously described, with *super-hydrophobic* surfaces (SHSs). By doing so, novel multifunctional systems were obtained with high selectivity, resolution, and very low detection limits. SHSs are artificial, micro- or nano- fabricated surfaces, with a texture given by a regular array of cylindrical pillars. The top of the pillars was conveniently modified to incorporate random assemblies of silver nanograins (Fig. 14.1). In sight of a dramatically low friction coefficient, this innovative family of devices offers realistic possibilities for the detection of extremely low concentrated solutions of analytes, and this discloses terrific opportunities in

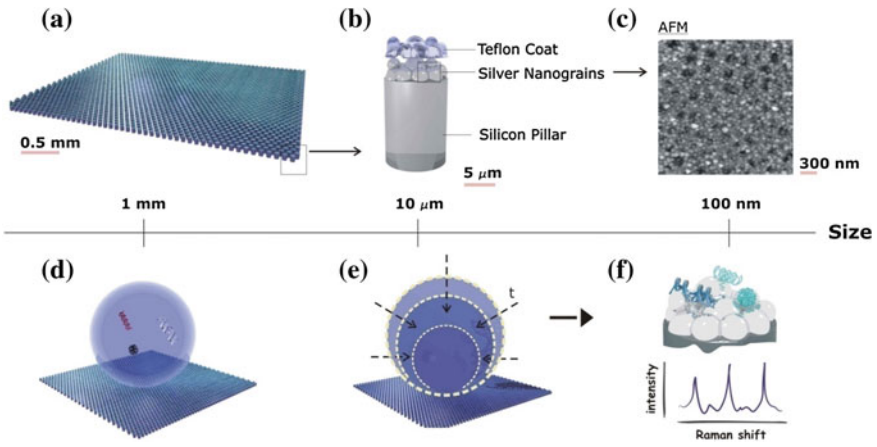

Fig. 14.1 The device features hierarchically different scales and, at each scale, different functions are revealed. On a large scale the superhydrophobic substrate looks continuous, millimetric drops are repelled and solutions can be easily manipulated (**a**, **d**). On a meso scale, that is micrometric, micro pillars (**b**) permit the evaporation of the solution whereby the solute is concentrated into small areas (**b**, **e**). On a nano scale, silver nano particles assemblies, conveniently positioned upon the pillars (**c**), induce SERS effects and permit the identification analytes in the single molecule regime (**f**). Published with permission from ACS Appl. Mat. Interf. 4, 3213 (2012)

medicine. A mathematical description of SHSs was provided, on the basis of which the devices could be designed and fabricated; extremely diluted biological solutions were therefore analyzed, and Rhodamine molecules were detected in the very low abundance range of 10^{-18} M.
The working principle is based on the use of small drops of de-ionized water, containing the moieties at study, which have to be positioned upon the substrate and there let to evaporate. In sight of a simple balance of forces, the line of contact at the solid interface would recede with time, and thus the footprint of the drop would also gradually reduce. When the drop gets sufficiently small, a transition to more a stable state occurs, whereby the drop is firmly attached to the substrate, and the scale-down of the area of contact is prevented. Thereupon, few molecules would be accumulated into a very small region, assuring an increased density and, accordingly, the attainment of the limits of detection (Fig. 14.1).

14.2 Super-Hydrophobicity: The Physical Model

Nature has endowed the leafs of some plants with the noticeable capability of repelling water, and thus if a drop is positioned upon these, it would assume a shape that resembles that of a sphere [24]. Conventionally we say that all the surfaces that behave like these leaves are super hydrophobic. The most practical property of SHSs is a reduced friction coefficient on account of which they can be used for a number of different applications, including, on the medical side, the manipulation and control of diluted solutions of biological interest [25, 26]. SHSs typically feature two distinguishing ingredients, that are (i) a quasi periodic hierarchical structure with dimensions comprised in the micro to nano meter range (and thus the geometry), and (ii) a superficial, chemical or physical, modification of the surface. Understanding the mechanisms whereby the combination of these reduces wettability is essential for the rational design of artificial SHSs, as those described later in the text. In the following sections, the laws describing the wetting phenomena are briefly recapitulated (I); why an hexagonal lattice of pillars would mimic natural SHSs better than other configurations is explained (II); the dynamics of slowly evaporating droplets and the influence of certain parameters on that is discussed (III); and, lastly, the parameters describing the lattice above are optimized on the basis of a mathematical criterion (IV).

14.2.1 The Physics of Drops and Surfaces

It is well known that the physics of micrometric or sub millimetric drops is correctly governed by surface tension solely. The angle of contact θ at the solid/air/liquid interface indicates the propensity of a droplet of whether wetting or not a surface. Surfaces where $\theta > 150°$ are super-hydrophobic. Interestingly, perfectly flat sur-

faces may have, via chemical modifications, a contact angle that is 120° at most [27, 28]. Artificial super hydrophobic states are possible solely for surfaces that also incorporate a regular pattern or texture [29]. Super hydrophobic states are very well described by the models of Wenzel [30] and Cassie Baxter [31]. In 1936, Wenzel explained the increased contact angle in terms of geometrical effects only and especially as a function of the solid roughness r (r is the real interfacial area over projected area, and it is always larger than one),

$$\cos\theta_w = r\cos\theta \tag{14.1}$$

and thus the effect of surface roughness is to amplify the wetting. Differently from Wenzel, Cassie described super hydrophobicity on account of the pockets of air that get trapped between the drop and the substrate

$$\cos\theta_c = -1 + \phi\,(\cos\theta + 1) \tag{14.2}$$

where ϕ is the fraction of solid in contact with the drop (and notice that ϕ is always smaller than one). The less ϕ the larger the apparent contact angle. At the limit of $\phi \to 0$, the drop would paradoxically float in air. The Cassie model is intuitive in that predicts that a drop upon a patterned surface develops a contact angle that is proportional to the fraction of air in contact with the drop. In spite of the fact that they do both induce hydrophobicity, these situations are very different from their adhesive properties, in that Wenzel drops are strongly pinned. On the contrary, in the Cassie state the drop sits mainly upon air, and this dramatically reduces the contact angle hysteresis thus favouring the self cleaning properties of the surface. On comparing Eq. 14.1 and 14.2, one can notice that a transition from Cassie to Wenzel occurs when

$$\cos(\theta) = \left(\frac{\phi - 1}{r - \phi}\right) \tag{14.3}$$

Equation 14.3 claims that the Cassie state is assured provided that the contact angle of the flat, unmodified material θ is sufficiently large; that is, larger than a certain, non linear combination of the geometrical parameters of the substrate. In particular, large ϕ's prompt a non wetting behaviour of the substrate [29–32]. In other terms, if the forest of posts or pillars is sufficiently dense on the surface, a Cassie state is assured. Notice though that large ϕ would induce small contact angles, and thus the choice for the best parameters in Eq. 14.3 is not trivial, and it is indeed a matter of optimization. Equation 14.3 holds on average. Situations are widely reported in literature where Cassie holds albeit ϕ is small, meaning that it is a metastable state. Practically this means that, if positioned with sufficient care upon a surface, a drop would not collapse even if it is supposed to, in that an energy barrier inhibits the spontaneous transition of the droplet to the level of lower energy content [33, 34].

14.2.2 Lattice Packings and SHSs

(Where it is introduced the mathematical representation of lattices. This is important because SHSs may be artificially mimicked by a discrete subset of cylindrical micro pillars, whose centers are placed in the plane as to recover a 2D lattice, as described in the following sections of the text. In brief, here we translate the problem from being expressed in terms of the sole ϕ, to a geometrical form.) A point lattice Λ, in a bi-dimensional space, is a regularly spaced array of points. The mathematical form of Λ is

$$\Lambda = \left\{ \sum_{i=1}^{d} a_i v_i | a_i \in \mathrm{Z} \right\} \tag{14.4}$$

where $\mathrm{d} = 2$ and $\{v_1, v_2\}$ is a basis for $\mathbf{R}^2$. Every lattice in $\mathbf{R}^2$ is completely determined given the fundamental parallelotope, that is the region of the plane that would reproduce the original lattice by simple translations. The fundamental parallelotope is thus the elementary cell there from the whole space can be reconstructed. Its volume is uniquely determined by Λ, and the square of this volume is called determinant of the lattice [35]. Here, a representation of 2d lattices in a complex plane is discussed. A lattice is defined by a pair of unit vector s, consider the first of these with coordinates $v_1 = (1, 0)$ or, in a complex notation, simply $v_1 = 1$. The position of the second vector in the plane is thus sufficient for describing the whole lattice geometry. The circumference in Fig. 14.2a describes all the configurations that are isotropic, that is, the lengths in the v_1 and v_2 directions are the same. Thus, for instance, a regular square pattern is the complex number $v_2 = \mathbf{i} = e^{\mathrm{i}\pi/2}$ (where $\mathbf{i}$ is the imaginary unit, and the Euler formula has been used), while an hexagonal lattice finds adequate formalisation in the number $v_2 = e^{\mathrm{i}\pi/3}$. In the realm of this structure, the multiplication of a lattice by another holds the meaning of a rotation, and thus, for instance, $\mathrm{e}^{\mathrm{i}\pi/2} \times \mathrm{e}^{\mathrm{i}\pi} = \mathrm{e}^{\mathrm{i}3\pi/2}$, and notice that $\mathrm{e}^{\mathrm{i}3\pi/2}$ is still a square lattice. Considering that, with [35], the area of the parallelotope may be written as the determinant of the generator matrix $\mathrm{M} = [v_1, v_2]$, for the present configuration it follows that

$$A_p{}^2 = \det \Lambda = (\det M)^2 = \begin{vmatrix} v_{12} & v_{12} \\ v_{21} & v_{22} \end{vmatrix}^2 = \begin{vmatrix} 1 & 0 \\ \cos\varphi & \sin\varphi \end{vmatrix}^2 = \sin^2\varphi \tag{14.5}$$

and thus the determinant of the lattice is the square of the imaginary part of v_2. The consequence of this is that the diagram of Fig. 14.2a finds a direct interpretation, that is, all the points that are equally distant from the real axis describe the same pattern. For instance, $\mathrm{e}^{i\pi/3}$, $\mathrm{e}^{i2/3\pi}$, $\mathrm{e}^{i4/3\pi}$ and $\mathrm{e}^{i5/3\pi}$ are equivalent and all represent the hexagonal lattice (Fig. 14.2b). This representation may be of some help in deriving ϕ as a function of the architecture of the pillars. Consider an isotropic periodic array of cylinders, the non dimensional diameter d of the cylinders, rescaled to the pitch, is a number comprised between 0 and 1. The solid fraction ϕ may be accordingly derived as $\pi/2^2\ \mathrm{d}^2/\mathrm{A_p} = \pi/2^2\ \mathrm{d}^2/\sin^2\varphi$.

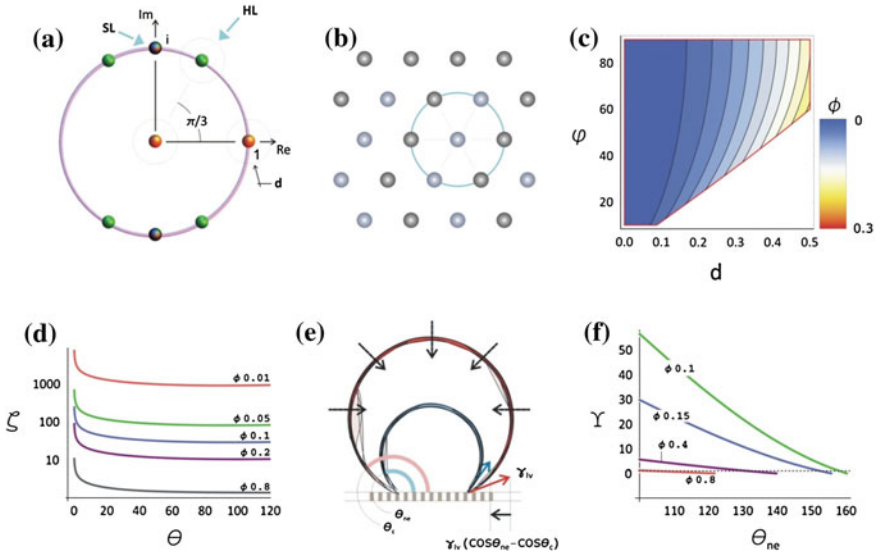

Fig. 14.2 Lattice representation in the complex plane (**a**). The hexagonal lattice reveals, in the plane, the largest coordination number n=6 (**b**). Contour plot of the solid fraction ϕ as a function of the normalized pillars' diameter d, and the angle φ that defines the lattice type (**c**). The augmented ability of a drop to slide over a textured surface ($\phi < 1$) with respect to a flat plane ($\phi = 1$), as a function of the equilibrium contact angle θ (**d**). Cartoon representing the evaporation process over a textured surface (**e**). The non dimensional force Υ that pushes the contact line inward during evaporation, as a function of the non equilibrium contact angle θ_{ne}, if $\Upsilon > 1$ sliding dominates over pinning (**f**). Published with permission from ACS Appl. Mat. Interf. 4, 3213 (2012)

The contour plot in Fig. 14.2c reports ϕ as a function of d and φ, and the smaller d, or the larger φ, the smaller ϕ. That is, small pillars, organized in non slanted geometries, are super-hydrophobic. The area in white in the diagram recovers the combinations of d and φ whereby the pillars would interfere and are, accordingly, impossible geometries. Notice that ϕ varies with d to a much more extent than with φ, while it is important choosing d with accuracy (using a mathematical criterion as explained later in the text), hexagonal tilings are preferred (and have been used in this work) in that they are optimal in the sense that solve the (i) densest packing and (ii) highest kissing number problems in the plane [35]. The kissing number (or coordination number) n is the number of circles, in 2 dimensions, which can touch an equivalent circle without any intersections. It is important because large kissing numbers would guarantee that the distances between a pivot pillar and the neighbouring is the same, and thus the problem is highly symmetric. For an hexagonal lattice, $n = 6$.

14.2.3 Vanishingly Small Friction Coefficients of SHSs and Evaporation Dynamics

Consider a drop sitting upon a surface and experiencing an arbitrary equilibrium contact angle θ. The radius r of the circumference at the solid liquid interface can be written as [36]:

$$r = \left(\frac{4}{\beta}\right)^{\frac{1}{3}} R \sin\theta, \quad \beta = (1-\cos\theta)^2 (2+\cos\theta) \tag{14.6}$$

The net adhesive force F_a acting along x may be therefore estimated [37–39], being

$$F_a = \int_{-\frac{\pi}{2}}^{\frac{\pi}{2}} \gamma_{lv} (\cos\theta_r - \cos\theta_a) r \cos\varphi \, d\varphi = 2r\gamma_{lv} (\cos\theta_r - \cos\theta_a) \tag{14.7}$$

And thus the adhesion force F_a would depend upon the width of the contact line (2r), the liquid-vapor surface tension (γ_{lv}) and the term ($\cos\theta_r - \cos\theta_a$) that is proportional to the contact angle hysteresis (CAH). Assume now to deposit the same drop upon a micro textured, artificial surface. In revisiting Eq. 14.7, it should be considered that (i) the radius r of the solid liquid contact is reduced due to the increased contact angle and (ii) the CAH the drop *senses* is not unique in view of the composite, heterogeneous surface it is placed upon (the CAH is maximum at the solid fraction, zero otherwise). Relation (7) can be thus rewritten as

$$F_a^c = 2r^c \langle \gamma_{lv} (\cos\theta_r - \cos\theta_a) \rangle = 2r^c \gamma_{lv} (\cos\theta_r - \cos\theta_a) \phi \tag{14.8}$$

where $< | >$ is the spatial average taken on the surface of contact of the drop, and it is here assumed that the radius of contact is large compared to the pillars' dimension. From this, it follows that tiling the surface increases hydrophobicity and dramatically reduces adhesion. Equation 14.8 can be expanded, reading

$$F_a^c = 4^{5/6} R \, \gamma_{lv} \frac{\sqrt{1-(\phi(\cos\theta+1)-1)^2}}{\left((1+\phi\cos(1+\theta))(2-\phi\cos(1+\theta))^2\right)^{1/3}} (\cos\theta_r - \cos\theta_a) \phi \tag{14.9}$$

The ratio $\zeta = F_a^C(\phi = 1)/F_a^C(\phi)$ gives a measure of the increased ability of a drop to slip or slide over SHSs (Fig. 14.2d). ζ is a function of ϕ, and the less ϕ, the less friction matters. A solid fraction of one percent ($\phi = 0.01$) would induce adhesion forces that are some 10^3 times less important than for a continuous surface. Also notice that ζ decreases with the initial contact angle θ, albeit ζ is practically constant for sufficiently large values of θ. Consider now a droplet positioned upon a SHS. The solvent evaporates over time and thus the volume of the drop decreases. On account of this, also the contact angle decreases. This fact unbalances the forces acting upon the drop and would generate a radial pressure that tends to recall the contact line

towards the center of the drop, thus recovering the initial equilibrium contact angle θ_c (Fig. 14.2e). The total force along x that is generated is

$$F_p = 2r^c \gamma_{lv} (\cos\theta_{ne} - \cos\theta_c) \tag{14.10}$$

and accordingly the condition for depinning is $F_p > F_a^c$. If $F_p \leq F_a^c$, the drop is stuck on the surface. (This condition may be valid, strictly speaking, in close proximity of θ_c) The ratio $\Upsilon = F_p/F_a^c$ indexes the propensity of a drop to slide upon a surface. When $\Upsilon > 1$ depinning dominate over friction, and thus the drop is recalled toward its centre during evaporation. In Fig. 14.2f, Υ is plotted against θ_{ne}, that is the non equilibrium contact angle as in Fig. 14.2e, at different ϕ's. At the initial time, $\Upsilon < 1$, and this means that the drop is sticky. As evaporation keeps on, θ_{ne} decreases. The depinning force augments with time, and so does Υ. When Υ is sufficiently large, that is $\Upsilon >> 1$, the contact line of the drop would recede, and the contact angle would again coincide with the expected equilibrium contact angle θ_c. Under these conditions, $\Upsilon = 0$. The process would then starts over again with the repetition of the same mechanism. Notice that the drop would experience a different story line on changing ϕ. When ϕ is small, Υ varies more rapidly with θ_{ne}, and the condition for radius downturn is met at earlier stages of evaporation. In any case, at each cycle, the contact radius is reduced by a quantity that is the distance between two lines of pillars. When r goes down below the critical radius of impalement, an irreversible transition to Wenzel occurs, whereby the drop is stuck. For sufficiently high pillars the minimum contact radius achievable is limited by energetic considerations being [40–42]

$$r_{\min} \propto \frac{\delta}{\cos\theta} \tag{14.11}$$

where δ is the distance between a spot and another.

14.2.4 Consideration for an Optimal Design

The models above predict that the contact angle is large, and thus the contact area is limited, provided that the pillars are diluted or, equivalently, that ϕ is small (Eq. 14.2). Unfortunately, the collateral effect of small ϕ is that a drop would collapse at the early stage of evaporation (Eq. 14.11). In this case, the drop would stick on the surface and, upon the continuance of evaporation, the solute would eventually redistribute as to form a ring like structure along the water-solid line of contact, therefore being spread over a large area, with no or few concentration effects. The coffee ring effect is very well understood and it is attributed to a fixed contact line and to an outward flow within the drop [43, 44]. Here, a criterion is discussed that would guarantee the best trade off between sufficiently dense forests of pillars, that prevent the early collapse of the drop and avoid the dispersion, and diluted structures, that instead assure large contact angle.

Let the surface be patterned as to reproduce a regular lattice described by d and δ, where the significance of these symbols is given above. If d is fixed, then the system would be determined given the sole δ. The aim here is to determine the optimal δ^0 that would induce large θ_c still retaining the advantages of a small r_{min}. To do this, we introduce the function Ψ as the sum of the two non dimensional contributions Ψ_1 and Ψ_2, $\Psi = \Psi_1 + \Psi_2$.

Ψ_1 accounts for the effects of the micro structure on the contact line. It is derived from the radius of contact r as in Eq. 14.4, being $\Psi_1 = r/R$. Ψ_1 depends upon θ_c and thus, through Eq. 14.2, ϕ. The smaller ϕ, the smaller Ψ_1 (Fig. 14.3a).

Ψ_2 instead accounts for the effects of the micro structure upon the smallest radius of contact prior the drop collapse. It is derived by the minimum contact radius r_{min} as in Eq. 14.9, being

$$\Psi_2 = \frac{r_{\min}}{d} = \frac{\delta}{d\cos\theta} = \frac{1}{\cos\theta}\frac{1-\sqrt{\phi}}{\sqrt{\phi}} \tag{14.12}$$

Differently from Ψ_1, Ψ_2 is inversely proportional to ϕ (Fig. 14.3a). While Ψ_1 and Ψ_2 are monotonic, their sum is not. A value of ϕ, and accordingly δ, exists where Ψ attains a minimum (Fig. 14.3a), and this would be the optimal gap for a fixed d. The optimal values of δ were calculated for d ranging from 0 to 30 μm. This region of best design is represented in the diagram of Fig. 14.3b. In the same diagram, a number of points is also reported. These represent evaporation experiments, where an excess of Rhodamine in D.I. water (concentration 10^{-4} M) was used to verify the concentration capabilities of different patterns. When the pillars are sufficiently dense, the drop successfully slips upon the posts and the solute gets concentrated, in accordance with the model. When the pillars are diluted, collapse occurs. This is a remarkable result in that the concentration process of a solute over a micro patterned substrate can be predicted and controlled with good accuracy. In general, d should be small to consent a sufficiently large number of pillars to interact with the drop.

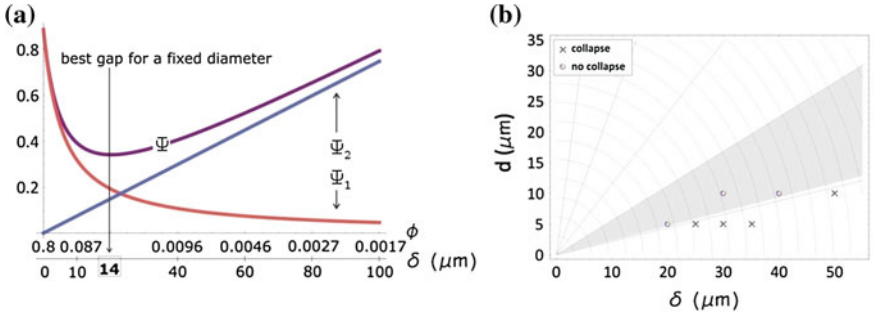

Fig. 14.3 The non dimensional function Ψ as a function of ϕ or, equivalently, δ. By minimizing Ψ, the optimal gap is found for a fixed diameter (**a**). The stability region, in light gray in the diagram, recovers all the combinations of optimal design, and this is confirmed by a number of different experiments (**b**). Published with permission from ACS Appl. Mat. Interf. 4, 3213 (2012)

14.3 Materials and Methods

Rhodamine R6G, myoglobin, ribonuclease B, lysozyme and sodium chloride was purchased from Sigma. De-ionized (D.I.) water (Milli-Q Direct 3, Millipore) was used for all experiments. All chemicals, unless mentioned otherwise, were of analytical grade and were used as received. Rhodamine6G is an organic compound and is used extensively in biotechnology applications. It is a dye which can be observed very clearly by fluorescence microscopy. Its absorption and emission wavelength are 530 and 556 nm, respectively.
Small drops ($V < 10\mu l$, $R < 1.35$mm) of D.I. water containing infinitesimal amounts of analytes were gently posted upon the surfaces and the entire process of evaporation followed over time. An automatic contact angle meter (KSV CAM 101, KSV INSTRUMENTS LTD, Helsinki, Finland) was used at room temperature. Please notice that the energy of adhesion γ per unit area at the gas/water interface is $\sim 72.8\text{mJ/m}^2$ at 20°C. The process enabled to concentrate very tiny amounts of agents over micrometric areas. The evaporation processes were performed in a clean room to reduce the presence of external contaminants and lasted approximately 30 min. The residual solute was observed using scanning electron microscope (SEM), fluorescent microscopy and Raman spectroscopy techniques.

14.3.1 Fabrication of the Devices

Artificial super hydrophobic surfaces were fabricated. These are textures comprising a periodic hexagonal lattice of cylindrical Si micro pillars with a certain diameter and pitch. Nano-sized geometries appropriately positioned upon the pillars would assure giant SERS enhancement. (100) silicon wafers (from Jocam, Milan, Italy) were cleaned with acetone and isopropanol to remove possible contaminant and then etched with a 4 % wet HF solution. The wafers were then rinsed with DI water and dried with N2. Standard optical lithography techniques (Karl Suss Mask Aligner MA 45, Suss MicroTec GA, Garching, Germany) were employed to dig regular arrays of disks within a layer of positive resist (S1813, from Rohm and Haas) that was spin-coated onto clean silicon wafers (Fig. 14.4a). Electroless deposition techniques were employed to grow silver nanograins within the holes (Fig. 14.4b). Upon removal of the residual resist with acetone, a Bosch Reactive Ion Etching (MESC Multiplex ICP, STS, Imperial Park, Newport, UK) process was utilized whereby the final structures were obtained in the form of cylindrical pillars with an aspect ratio greater than 2 (Fig. 14.4c). The electroless grown Ag layer served as mask during the RIE process, while its characteristic granular structure allowed for the enhancement of the SERS signal. The substrates, as a whole, were then covered with a thin (few nm) film of a Teflon like (C_4F_8) polymer to assure hydrophobicity (Fig. 14.4d). The masks necessary for optical lithography were fabricated using standard Electron Beam Lithography (Crestec CABL-9000C Electron beam lithography system) methods.

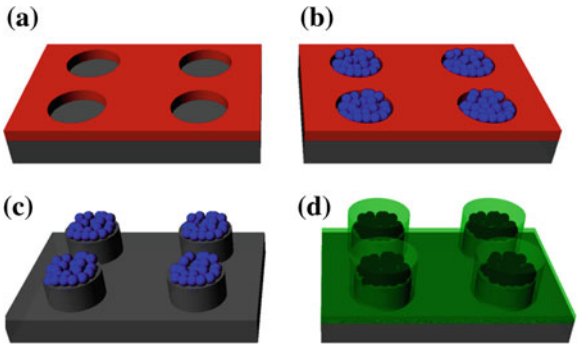

Fig. 14.4 Fabrication process of a super-hydrophobic surface. The four main steps are shown: **a** digging of disks followed by spin-coating, **b** electroless for growing grains of Ag, **c** resist removal, **d** Teflon layer deposition

The electroless deposition on a substrate is based on an autocatalytic or a chemical reduction of aqueous metal ions. This process consists of an electron exchange between metal ions and a reducing agent. In this work, Si substrate was used itself as reducing agent. A fluoridric acid (HF) solution containing silver nitrate ($AgNO_3$) was used, where Ag was reduced to metal form by the Si substrate oxidation. In particular, the patterned silicon wafer was dipped in a 0.15 M HF solution containing 1 mM silver nitrate for 60 s at a constant temperature T = 313 K. After the growth process the silicon wafer was rinsed with water and dried under nitrogen flux. The driving force in this process is the difference between redox potentials of the two half-reactions, which depends on the solution temperature, concentration and pH. Consequently, these parameters influence the particle size and density.

14.3.2 Samples SEM Characterization

SEM images of the samples were captured using a Dual Beam (SEM-FIB)-FEI Nova 600 NanoLab system. During the acquisitions beam energies of 5 and 15 keV, and corresponding electron currents of 0.98 pA and 0.14 nA, were used. In some cases, the mode 2 configuration was used, whereby images can be magnified over 2500 k× and ultra-high resolution may be achieved. In this modality the immersion lens was switched on, and the TLD detector in Secondary Electron operation was used.

14.3.3 Samples AFM Characterization

An atomic force microscopy (Veeco MultiMode with NanoScope V controller) was used for the measurements of the silver nanograin assemblies. The measurements were performed in a dry environment in intermittent contact mode over a sampling area of $6000 \times 6000 nm^2$. The room temperature was hold fixed for all the acquisitions. Ultra-sharp Si probes (ACLA-SS, AppNano) with a nominal tip radius less than 5 nm

were used for high resolution imaging. Multiple measurements were done in different scan directions to prove the avoidance of artifacts. The images had a resolution of 1024 × 1024 points and were acquired at a scanning rate of 1 Hz. The images obtained were processed with the WSxM© software, using either flattening or plane fit according to the relief characteristics, with the minimal polynomial order needed. Using conventional mathematical procedures implemented in Mathematica®, the roughness and fractal dimension of the samples were derived.

14.3.4 Fluorescence Microscopy Characterization of Rhodamine deposits.

Fluorescence microscopy measurements were performed using an inverted microscope, with infinity-corrected optics (Nikon-ECLIPSE TE 2000-U). The microscope objectives used were a Plan Fluor 40x and a Plan Apo 60x, with 0.75 and 0.95 numerical apertures. For probe excitation a violet diode laser source emitting at 408 nm, an Argon source emitting at 488 nm, Helium Neon laser source emitting at 543 nm were used. A Nikon D-Eclipse C1 scanning head with three channels was utilized for the measurements.

14.3.5 Raman Characterization of Rhodamine Deposits

Micro-probed Raman spectra were obtained using Renishaw inVia Raman microscope at room temperature through 20x objective of a Leica microscope. The Raman spectra were excited by the 514.0 nm line of an Ar^+ laser in backscattering geometry. The laser power was 0.18 mW with an integration time of 20 s. Mapping Raman measurements were carried out with the step size 19.50 μm and 34.60 μm in x and y-axis direction, respectively.

14.4 Results

Several SEM micrographs of the SHSs were taken over different samples to assess uniformity and reproducibility.
In Fig. 14.5a–b, silicon pillars are arrayed over large square areas sizing up to some millimeters per side, with few or no defects in the structures which thus recover a perfect hexagonal lattice. This would verify the fabrication process capability to attain extreme control over the key characteristics of the micropillars such as shape and size, at least on a large scale. On a smaller scale, as in Fig. 14.5c–d, the exposed top surface of the pillars is wrapped by silver nanograin assemblies. The AFM image of Fig. 14.5e shows the grains randomly distributed with an average grain size of about 50 nm and

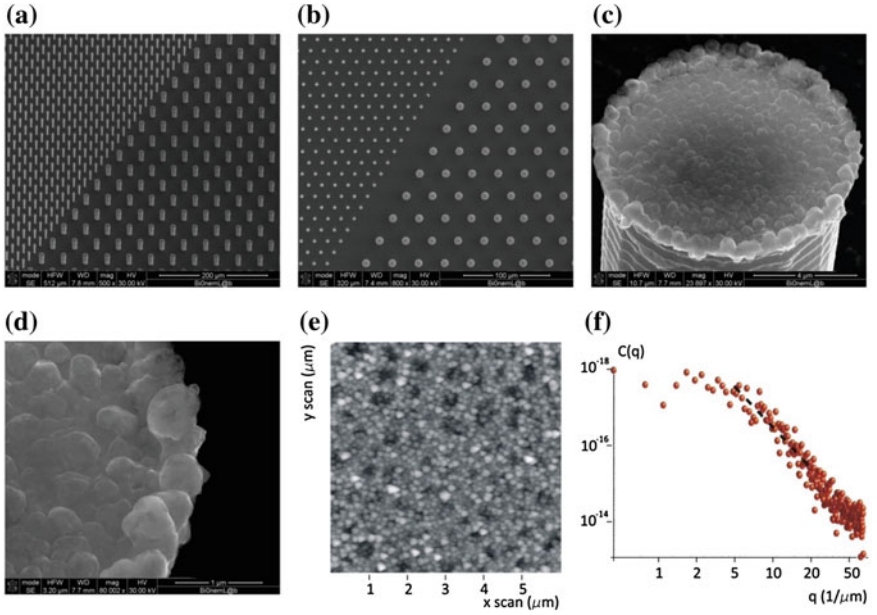

Fig. 14.5 Micro pillars are arrayed to form regular geometries over several hundreds of microns (**a**, **b**). Larger zoom reveals silver nano aggregates at the nano scales (**c**, **d**). AFM image of the silver nano grain assemblies (**e**) and characteristic power spectrum (**f**). Published with permission from ACS Appl. Mat. Interf. 4, 3213 (2012)

a small standard deviation Sd = 20 nm. From this, using custom made algorithms, a power spectrum can be deconvoluted and the average roughness Ra and the fractal dimension Df consequently derived, being Ra $\sim$ 34 nm and Df $\sim$ 2.34. Notice that the average grain size and roughness are consistent with a local enhancement of the Raman signal in the order of 10^6 [45]. Interestingly, albeit in a number of different works the influence of surface profile, and especially roughness, upon Raman signal has been reported, no works have been focusing on the effect of more sophisticated parameters such fractal dimension, that instead deserves to be investigated even further.

These devices were verified against the deposition, concentration and detection of few molecules of Rhodamine6G (R6G). R6G was used for the evaluation of the devices in that its utilization in biotechnology applications is very well assessed; it is a supplement to fluoresceins, as if offers longer wavelength emission maxima; and it is conveniently and extensively used for standard and non standard labelling essays. Solutions were prepared containing R6G molecules with a concentration as low as 10^{-18} M. Evaporation processes of small drops of solution were followed over time until an irreversible transition to a pinning state occurred. Few molecules were conveniently enforced to be confined into a small area, at the limit upon a single pillar.

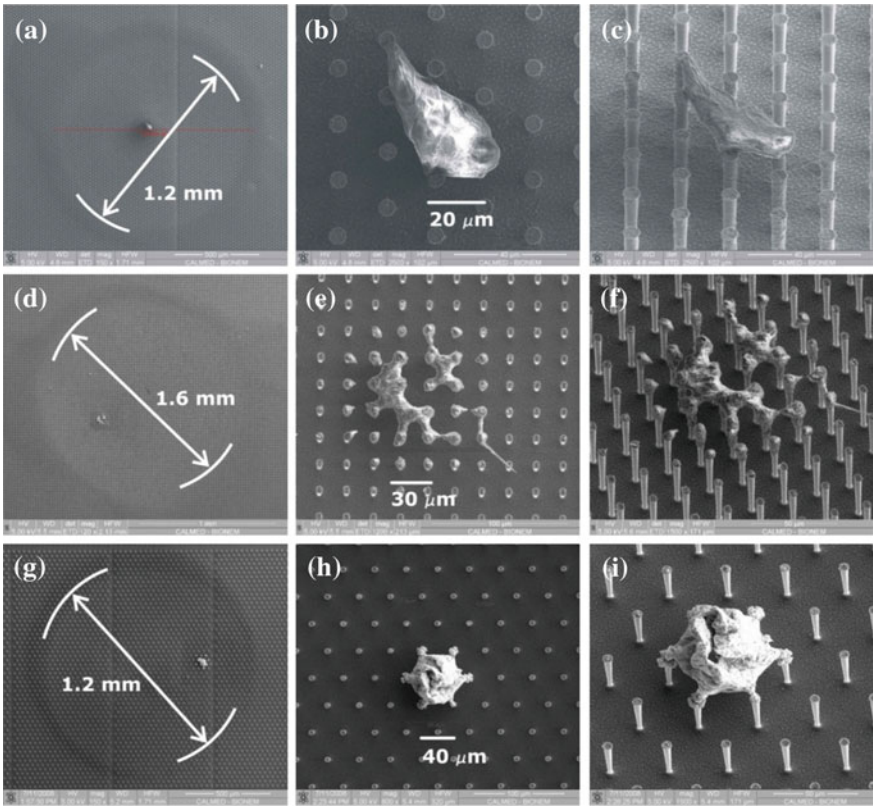

Fig. 14.6 SEM micrographs of the residual solute of R6G at magnifications ranging from 150× to 2500×. The initial footprint of the drop measures up to about 1.6 mm (**d**), and on average 1.2 mm (**a**, **g**), while the solution, at the final stage of the process, sediments in a bounded region sizing few tens of microns or less (**b**, **e**, **h**). The tilted images demonstrate that the solute was accumulated entirely upon the pillars (**c**, **f**, **i**). Published with permission from ACS Appl. Mat. Interf. 4, 3213 (2012)

Figure 14.6 shows an array of SEM images of the residual solute of R6G at different magnifications ranging from 150× to 2500×. The initial footprint of the drop measures up to about 1.6 mm (Fig. 14.6d), and on average 1.2 mm (Fig. 14.6a, g), while the solution, at the final stage of the process, sediments in a bounded region sizing few tens of microns or less. Considering bidimensional scale effects solely, the device is capable of concentrating a solution some $(1200/40)^2 \sim 10^3$ times. More importantly, all the deposits are suspended upon the pillars (Fig. 14.5c, f, i), the residual R6G is arranged in complex forms or agglomerates that wrap the pillars, connecting them one to the other, without touching the bottom of the substrate.
Fluorescent images in Fig. 14.7 would prove that identification of the residue as R6G is correct, and it is not instead constituted by debris or other refuses. The intensity of fluorescence is directly proportional to the quantity of substance deposited upon

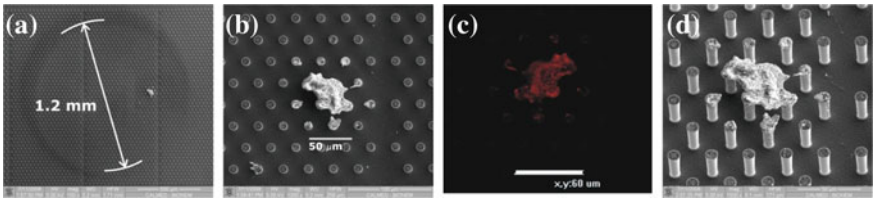

Fig. 14.7 SEM images of a Rhodamine deposit upon evaporation (**a**, **b**, **d**), and confocal fluorescence fingerprint of the residue (**c**). Published with permission ACS Appl. Mat. Interf. 4, 3213 (2012)

the pillars, and thus in the central part of the substrate the amount of R6G is higher and it diminishes as we move towards the sides. Notice the high degree of precision whereby the intensity of the signal of fluorescence relates to the mass of the solute distributed on the substrate.

Micro-Raman mapping measurements (Figs. 14.8 and 14.9) were performed to further substantiate the method. While conventional Raman intensity is directly proportional to the number of molecules probed, in the case of SERS, if the molecules are not in close proximity of the nano-metallic substrate ensuring the enhancement of the electric field, the resulting spectral amplitude would dramatically drop off, and thus, the thicker the layer of Rhodamine, paradoxically the lower the signal. This would explain why the intensity signals in some regions of the diagrams are not consistent with SEM or fluorescence imaging. The mapping analysis was performed by referring the band centred at 1650cm^{-1}. In the figures, mapping images in surface mode are overlapped onto the scanning area and this would clearly highlight the variation of intensity as a function of the position within the area of interest.

Fig. 14.8 shows SEM and Raman measurements for an initial concentration of 10^{-18} M and, in the present case, the Raman signal comes prevalently from the central region of the deposit, as expected. Figure. 14.9 completes a sequence comprising SEM, confocal fluorescence and Raman imaging of the excess of R6G upon evaporation.

Numerical simulations were also performed for three specific super-hydrophobic surfaces: i) pillars showing a metallic rough top surface, iii) metallic cone with grating coupler embedded in a super-hydrophobic surface and, finally, ii) matrix of metallic dimers fabricated on pillars heads. These structures were indeed implemented inside super-hydrophobic surfaces as shown by the SEM images in Fig. 14.10.

For all the three configurations the gold material was described through the Drude-Lorentz model [46]. Convergence analysis of the results was conducted for all the simulations. Fig. 14.11 illustrates the simulation results of a golden pillar with a top average rough surface of 3 nm. It corresponds to the SEM image in Fig. 14.10a. In particular, Fig. 14.11a shows the meshed structure. Sub-nanometer resolution was chosen to describe the surface roughness.

Figure 14.11b is the field distribution ought to the local roughness when a source wavelength of 633 nm impinges normally on the head of the pillar. The field enhancement reaches a value of about 80 with respect to the source amplitude of 1V/m.

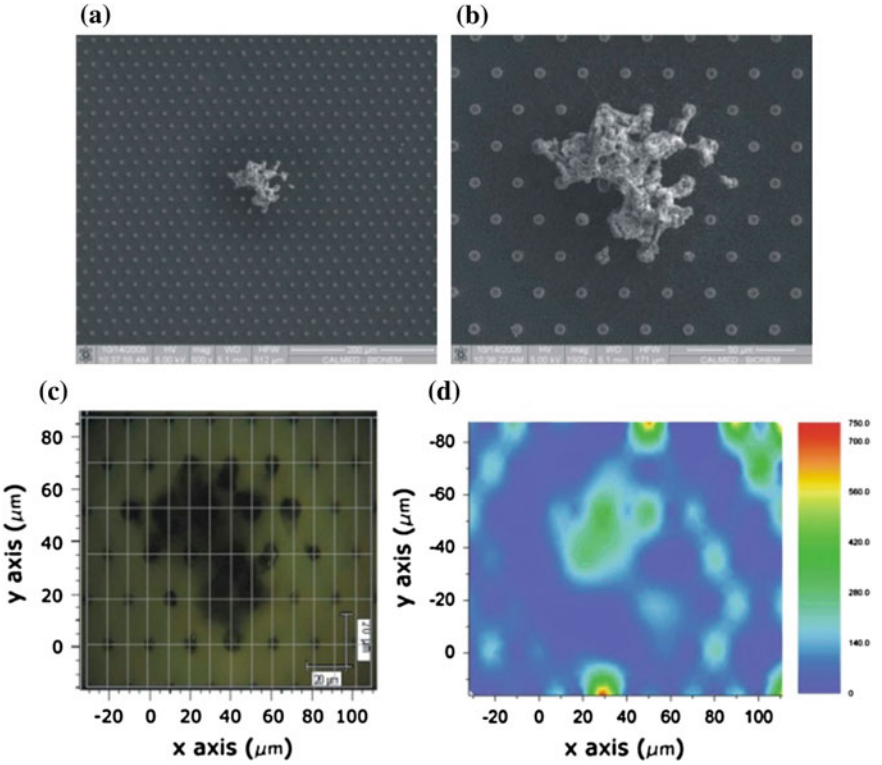

Fig. 14.8 SEM images of a Rhodamine deposit upon evaporation (**a**, **b**), and Raman mapping measurement of the residue (**c**, **d**). Initial concentration = 10^{-18} M. Published with permission from ACS Appl. Mat. Interf. 4, 3213 (2012)

Figure 14.12 describes the numerical results when a golden cone with a coupling grating is illuminated at different angles of incidence (see Fig. 14.10b). The source is a linearly polarized wave with wavelength 633 nm while the geometrical characteristics of the cone are: an height of 2.5μm, a radius of the base of 150 nm and a radius of curvature at the apex of 5 nm. The periodicity of the grating is 359 nm while the grove width is 180 nm. As expected, the grating improves the coupling between the incoming radiation and the surface plasmon plaritons leading to a field at the apex (5 nm off the apex) of the cone about 4 times higher than in case of no grating.

The last simulated device is a super-hydrophobic surface comprised of metallic pillars having a matrix of metallic dimers antennas at their top face. In particular, Fig. 14.13 shows the numerical results associated to the structure as in Fig. 14.10c. Figure. 14.13a represents the mesh profile for a single dimer antenna. The chosen gap was equal to 10 nm. Figure. 14.13b is the 3-dimensional field distribution on a single structure when a matrix of dimers with periodicity around 600 nm in y direction and 800 nm in x direction was considered. The single gold antenna is 100 nm long (x

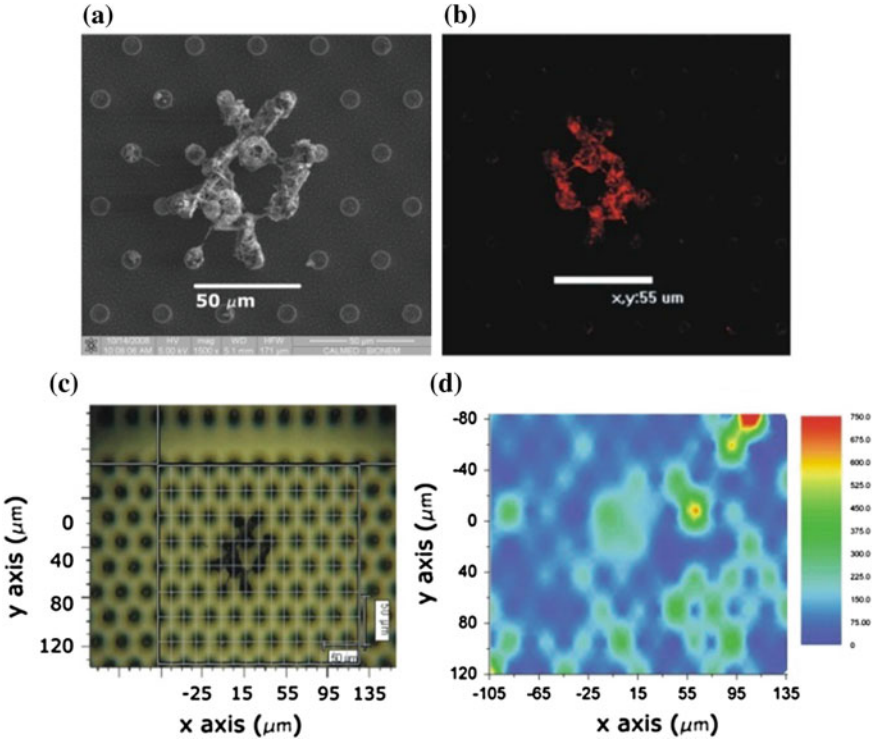

Fig. 14.9 SEM image (**a**), confocal fluorescence fingerprint (**b**) and Raman mapping measurement (**c**, **d**) of a Rhodamine deposit upon evaporation. Initial concentration = 10^{-18} M. Published with permission from ACS Appl. Mat. Interf. 4, 3213 (2012)

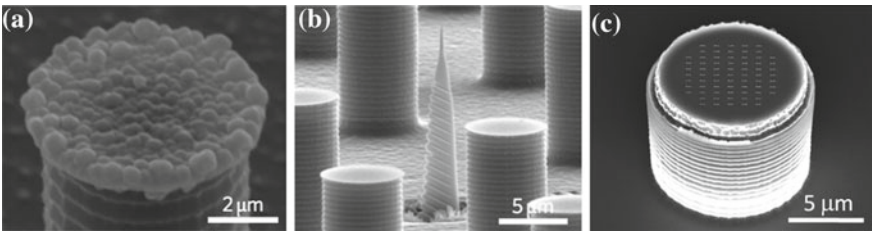

Fig. 14.10 SEM images for three SHS configurations: **a** golden pillar showing a top rough surface, **b** golden cone showing a coupling grating, **c** golden pillar with a matrix of dimers fabricated at its top face

direction) , 60 nm wide (y direction) and 60 nm thick (z direction). Also in this case the chosen source wavelength was 633 nm. The incoming field was directed along z direction and linearly polarized along y direction (short axis of the dimer). The field shows its maximum (around 20 V/m) at the edges of the antennas.

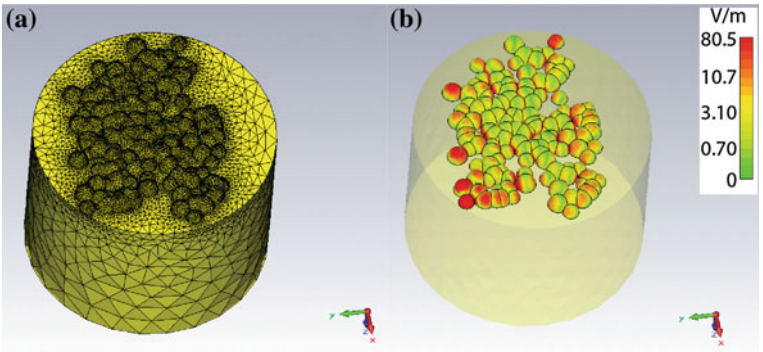

Fig. 14.11 Numerical results of a golden pillar showing an average top roughness of 3 nm. **a** Mesh resolution of the simulated structure. **b** Electric field distribution. The maximum field enhancement is about 80

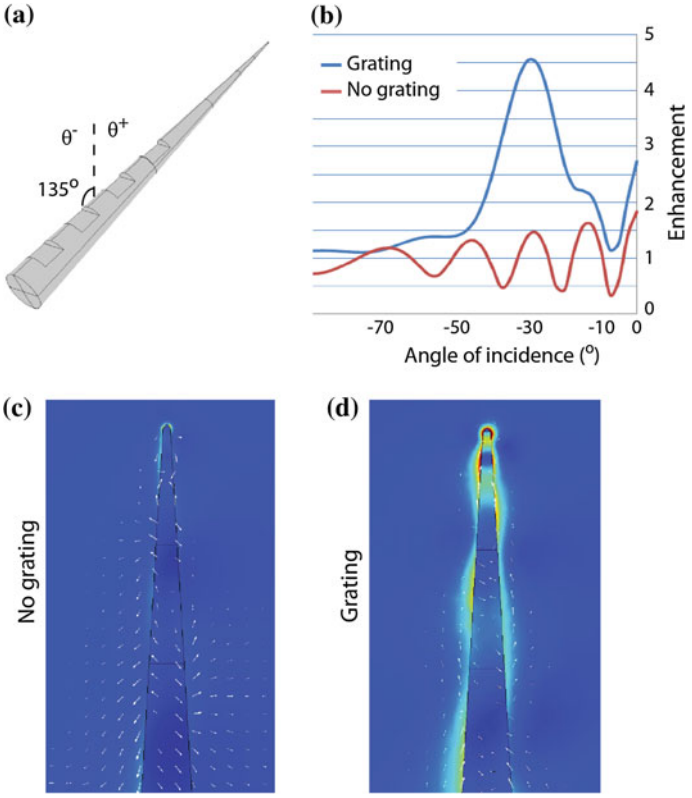

Fig. 14.12 Numerical results of a conical golden structure with grating coupler. **a** Scheme of the device. **b** Electric field calculated 5 nm off the tip apex for two situations: grating and no grating. The maximum value is found at about 30 incident angle when the grating is used. **c** and **d** electric field distribution in proximity of the cone apex when no grating or grating is used, respectively. The wavelength is 633 nm

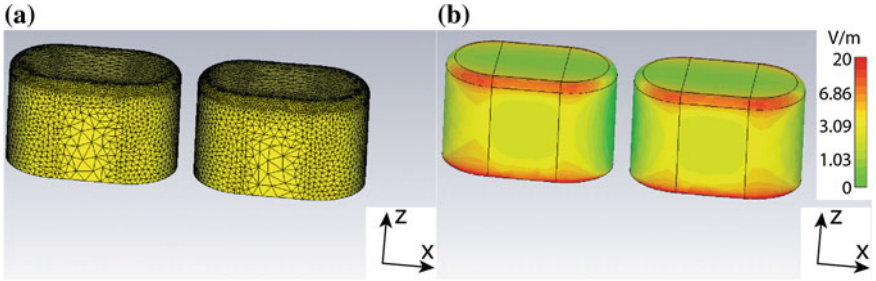

Fig. 14.13 Numerical results of a metal cylindrical structure with a matrix of dimers antennas at its top. **a** Mesh resolution of a single dimer. The gap is 10 nm. **b** Electric field calculated on the dimer. The wavelength is 633 nm with incident wave normal to the xy-plane and polarized along y direction

14.5 Discussion

Treatment of cancer patients is greatly facilitated by detection of the cancer prior to metastasis; nevertheless, the effective early detection of precancerous and neoplastic lesions remains an elusive goal. Advanced clinical cancer imaging technologies, including MRI (magnetic resonance imaging), PET (positron emission tomography), C-T (computerized tomography) scans, or medical ultrasonography, do not possess sufficient spatial resolution for early detection based on lesion anatomy and are, besides, very expensive, and thus not accessible to large scale. An effective evaluation of malignancies may be instead addressed basing on their molecular expression profiles. It is very well understood that blood contains a treasure trove of biomarkers that could reflect the ongoing pathological state of tissues or organs. Every cell in the body leaves a record of its physiological state in the products it sheds to the blood, either as waste or as signals to neighbouring cells. This hidden signature of diseases waits just to be decoded and revealed. In sight of this understanding, microbiologic, immunologic, and molecular analysis of tissue and cells are becoming indispensable clinical platforms for rendering pathologic evaluation. Collectively, these diagnostic modalities are critical for determining the appropriate medical treatment. Conventional immunoassay methods, including enzyme-linked immunosorbent assay (ELISA), fluorescence immunoassay, magnetic bead-based electro chemi lumincence (ECL), chemiluminescence, liquid chromatograpy-mass spectrometry (LC-MS) and immuno-polymerase chain reaction (PCR) assay allow reliable protein detection. However, these approaches are yet to meet all requirements for point-of-care diagnosis which require the sensor to be rapid, operationally simple, low cost and highly sensitive to address both levels of the biomarkers in normal and cancer patient serum. In particular, the primary challenge that still waits to be faced, is the severe dilution of the peptides of interest, being practically invisible, at the early stages of diseases, to the majority of these technologies. And thus blood serum is not yet used as a routinely screening procedure. To date, and rather

surprisingly, surgical biopsy remains the 'gold standard' for the clinical assessment of the pathologic basis of disease. The morphologic presentation of tissue specimens continues to be the backbone of diagnostic pathology; stills, this practice inherently suffers from being predominately a qualitative art. The quality of diagnoses is still entrusted with the pathologist's experience and knowledge.

The past decade has seen tremendous progress in the development of original strategies, technologies, or both, that promise to overcome the limitations discussed above. These include (i) the use of super-hydrophobicity for biological sample handling and manipulation; (ii) the analysis of molecules, bio molecules or individual peptides using mass spectrometry, Raman or other spectroscopies; (iii) micro and nano scale devices with advanced sensing capabilities, and especially SERS devices. Although, individually, the technologies above fostered important changes and progresses, the latter were mostly limited to their specific, and often limited, fields of application.

The major advance, here, is that at least three different technologies are conveyed into a single platform. From the combination of (i) to (iii) (and particularly from the introduction of super hydrophobic devices), new properties and opportunities arise. Biology does a lot with a little. Learning from nature, and inspired by the lotus effect, we developed a new nanotechnology that, mimicking the morphology of the lotus leaf, offer realistic possibilities to diagnosis tumours at their early stage. Our bio-devices are hybrid systems that incorporate hierarchically features at the micro- and nano- scales. On account of their multi scale nature, they permit to transporting target molecules in extremely dilute solutions to nano plasmonic sensors, surpassing the impractical timescales that these devices typically suffer from. In tests with rhodamine molecules, we found that these devices provide concentration factor of several orders of magnitude over a conventional, flat plasmonic substrate, and in fact we could detect molecules in the dramatically low concentration range of 10^{-18} M. Beyond bare numbers, this scheme provides the capability of localization and immobilization of molecules where and, possibly, when we want. And this is the result of an unprecedented blend of physics and chemistry, for the fabrication of the surfaces, and mathematics, for the correct design of these surfaces.

Still, certain problems remain unsolved, including how to bind the target biomolecules to the sensor surface, what factors determine the probability of binding, or how to deplete the solution of interest from abundant, interfering proteins. A detailed investigation of the droplet-collapsing process may provide clues to the first two questions. The integration, optimization and assessment of high tech bio/chemical procedures for separation from serum, purification, segmentation and enrichment of individual biomarkers, using methods that involve, for example, SISCAPA (stable isotope standards and capture by anti-peptide antibodies) procedures, or nano porous silicon filters, would address the third node. Again, the correct integration of pioneering (nano) technologies and biological and proteomic methods would boost the development of bio-sensors with exceptional sensibility and selectivity.

The single detection issue is a worthwhile aim in itself, nevertheless the introduction of super hydrophobicity in life sciences opens up a number of different applications and opportunities. Micro-drops provide environmental characteristics which are difficult to obtain otherwise. Using these conditions to investigate life processes affords

opportunities for discovery and development of applications which enhance research and the probability for pathfinding mechanisms in life processes. The physics of drops, where gravity has minor effects, and interfacial forces dominate over volume, affords a new window through which to observe life processes. It is a probe which can reveal novel mechanisms that are fundamental to cell processes, disease process, and the adaptation of living systems to changes in physical forces.
Moreover, SHSs provide an opportunity to better understand interfacial phenomena, such as the wetting and spreading of immiscible liquids or the spreading of fluid across a solid surface. Given the sizes of interest, which are small, wetting determines the configuration and location of fluid interfaces, thus greatly influencing, if not dominating, the behavior of multiphase fluid systems. Phenomena, processes and procedures that may be investigated in this context include cell culture, formation and stability of nanoemulsions, transportation phenomena, self-organization phenomena, advancement of analytical devices, protein crystal growth, formation and organization.

14.6 Conclusion

On account of the intrinsic limitations of conventional bio photonic devices, a novel procedure was conceived at the forefront of SERS and superhydrophobicity. Silicon substrates were conveniently patterned to include regular lattices of micro pillars, while the top of the pillars was further modified to incorporate silver nanograins assemblies. On account of its micro structure the substrate is superhydrophobic, while, on account of the silver grains, it reveals superior SERS capabilities. The micro and nano scales were conveniently combined to yield a family of bio sensors featuring new functions that can boost the detection of few molecules. The substrates were correctly designed on the ground of mathematical models, therefore nanotechnologies were employed to fabricate these devices. Different tests with R6G solutions showed that (i) a diluted solution can be largely concentrated, (ii) the solute can be conveyed towards the active sites of the device with high precision and very short times, (iii) few molecules can be detected and recognized. Using this pioneering procedure, an access is provided to precious information that are otherwise inaccessible with conventional methods. The major application of this technology is the early detection of cancers or other pathologies, in these regards further investigations and the integration with assessed biological and proteomic methods are necessary. Nevertheless, the door to a new frontier for the treatment of cancers is open up.

Acknowledgments This work was funded under European Project SMD FP7-NMP 2800-SMALL-2 (proposal no. CP-FP 229375-2), Italian project FIRB 'Rete Nazionale di Ricerca sulle Nanoscienze ItalNanoNet' (cod. RBPR05JH2P-010) and by the EU Commission, the European Social Fund and the Calabria Region (POR Calabria FSE 2007-2013).

References

1. nan'o tech nol'o gy n., Nature nanotechnology **1**, 8 (2006).
2. G.M. Whitesides, The right size in nanobiotechnology. Nat. Biotechnol. **10**, 1161 (2003)
3. F. Gentile, L. Tirinato, E. Battista, F. Causa, C. Liberale, E.M. di Fabrizio, P. Decuzzi, Cells preferentially grow on moderately rough substrates. BioMaterials **31**, 7205–7212 (2010)
4. F. Perennes et al., Sharp beveled tip hollow microneedle arrays fabricated by LIGA and 3D soft lithography with polyvinyl alcohol. J. Micromech. Microeng. **16**, 473–479 (2006)
5. T. Calimeri, E. Battista, F. Conforti, P. Neri, M.T. Di Martino, M. Rossi, U. Foresta, E. Piro, F. Ferrara, A. Amorosi, N. Bahlis, K.C. Anderson, N. Munshi, P. Tagliaferri, F. Causa, P. Tassone, A unique 3-D SCID-polymeric scaffold (SCID-synth-hu) model for in vivo expansion of human primary multiple myeloma cells. LEUKEMIA ISSN 0887–6924 (2011). doi:10.1038/leu.2010.300
6. E. Tasciotti, X. Liu, R. Bhavane, K. Plant, A.D. Leonard, B.K. Price, M.M. Cheng, P. Decuzzi, J.M. Tour, F. Robertson, M. Ferrari, Mesoporous silicon particles as a multistage delivery system for imaging and therapeutic applications. Nature Nanotechnol. **3**, 151–157 (2008)
7. F. De Angelis, A. Pujia, C. Falcone, E. Iaccino, C. Palmieri, C. Liberale, F. Mecarini, P. Candeloro, L. Luberto, A. de Laurentiis, G. Das, G. Scala, E. Di Fabrizio, Water soluble nanoporous nanoparticles for in vivo targeted drug delivery and controlled release in b cells tumor context. Nanoscale **2**, 2230–2236 (2010)
8. M. Ferrari, Cancer nanotechnology: opportunities and challenges. Nat. Rev. Cancer **5**, 161–171 (2005)
9. M. Gaspari et al., Nanoporous surfaces as harvesting agents for mass spectrometric analysis of peptides in human plasma. J. Proteome Res. **5**, 1261–1266 (2006)
10. L.A. Liotta, M. Ferrari, E. Petricoin, Clinical proteomics: written in blood. Nature **425**, 905 (2003)
11. E.M. Posasadas et al., Proteomic analysis for the early detection and rational treatment of cancer–realistic hope? Ann. Oncol. **16**, 16–22 (2005)
12. G. Das, F. Mecarini, F. Gentile, F. De Angelis, M. Kumar, P. Candeloro, C. Liberale, G. Cuda, E. Di Fabrizio, Nano-patterned SERS substrate: application for proteinanalysis vs. temperature. Biosens. Bioelectron. **24**, 1693–1699 (2009)
13. F. De Angelis, M. Patrini, G. Das, I. Maksymov, M. Galli, L. Businaro, L.C. Andreani, E. Di Fabrizio, A hybrid plasmonic photonic nanodevice for label-free detection of a few molecules. Nano Lett. **8**, 2321–2327 (2008)
14. A.J. Babadjanyan, N.L. Margaryan, KhV Nerkararyan, J. Appl. Phys. **87**, 3785 (2000)
15. M.I. Stockman Phys, Rev. Lett. **93**, 137404 (2004)
16. F. De Angelis, G. Das, P. Candeloro, M. Patrini, M. Galli, A. Bek, M. Lazzarino, I. Maksymov, C. Liberale, L.C. Andreani, E. Di Fabrizio, Nanoscale chemical mapping using three-dimensional adiabatic compression of surface plasmon polaritons. Nature Nanotech. **5**, 67–72 (2010)
17. F. De Angelis, C. Liberale, M.L. Coluccio, G. Cojoc, E. Di Fabrizio, Emerging fabrication techniques for 3D nano-structuring in plasmonics and single molecule studies. Nanoscale **3**, 2689–2696 (2011)
18. F. De Angelis, R. Proietti Zaccaria, M. Francardi, C. Liberale, E. Di Fabrizio, Multi-scheme approach for efficient surface plasmon polariton generation in metallic conical tips on AFM-based cantilevers. Opt. Exp. **19**, 22268 (2011)
19. R. Proietti Zaccaria, F. De Angelis, A. Toma, L. Razzari, A. Alabastri, G. Das, C. Liberale, E. Di Fabrizio, Surface plasmon polariton compression through radially and linearly polarized source. Opt. Lett. **37**, 545 (2012)
20. R. Proietti Zaccaria, A. Alabastri, F. De Angelis, G. Das, C. Liberale, A. Toma, A. Giugni, L. Razzari, M. Malerba, H.B. Sun, E. Di Fabrizio, Fully analytical description of adiabatic compression in dissipative polaritonic structures. Phys. Rev. B **86**, 035410 (2012)
21. K. Li, M.I. Stockman, D.J. Bergman, Phys. Rev. Lett. **91**, 227402 (2003)

22. D.A. Weitz, T.J. Gramila, A.Z. Genack, J.I. Gersten, Anomalous low-frequency Raman scattering from rough metal surfaces and the origin of surface-enhanced Raman scattering. Phys. Rev. Lett. **45**(5), 355–358 (1980)
23. M.L. Coluccio, G. Das, F. Mecarini, F. Gentile, A. Pujia, L. Bava, R. Tallerico, P. Candeloro, C. Liberale, F. De Angelis, E. Di Fabrizio, Silver-based surface enhanced Raman scattering (SERS) substrate fabrication using nanolithography and site selective electroless deposition. Microelectron. Eng. **86**, 1085–1088 (2009)
24. R. Blossey, Self-cleaning surfaces-virtual realities, Nat. Mater. **2**, 301–306 (2003).
25. G. McHale, N.J. Shirtcliffe, M.I. Newton, Super-hydrophobic and super-wetting surfaces: analytical potential? Analyst **129**, 284 (2004)
26. F. De Angelis, F. Gentile, F. Mecarini, G. Das, M. Moretti, P. Candeloro, M.L. Coluccio, G. Cojoc, A. Accardo, C. Liberale, R. Proietti Zaccaria, G. Perozziello, L. Tirinato, A. Toma, G. Cuda, R. Cingolani, E. Di Fabrizio, Breaking the diffusion limit with super hydrophobic delivery of few molecules to plasmonic nanofocusing structures. Nat. Photonics **5**, 682 (2011)
27. F. Gentile, M. L. Coluccio, N. Coppedè, F. Mecarini, G. Das., C. Liberale, L. Tirinato, M. Leoncini, G. Perozziello, P. Candeloro, F. De Angelis, E. Di Fabrizio, ACS Appl. Mat. Interf. **4**, 3213 (2012).
28. E.G. Shafrin, W.A. Zisman, in *Contact Angle, Wettability and Adhesion Advances in Chemistry Series*, vol. 43, ed. F. M. Fowkes (American Chemical Society, Washington D.C., 1964) , pp. 145–167
29. A. Lafuma, D. Quéré, Superhydrophobic states. Nat. Mater. **2**, 457–460 (2003)
30. R.N. Wenzel, Resistance of solid surfaces to wetting by water. Ind. Eng. Chem. **28**, 988–994 (1936)
31. A.B.D. Cassie, S. Baxter, Wettability of porous surfaces. Trans. Faraday Soc. **40**, 546–551 (1944)
32. J. Bico, U. Thiele, D. Quéré , Wetting of textured surfaces, Colloids Surf.A **206**, 41–46 (2002)
33. A.N. Patankar, Transition between superhydrophobic states on rough surfaces, Langmuir **20**, 7097–7102 (2004)
34. M. Nosonovsky, B. Bhushan, Energy transitions in superhydrophobicity: low adhesion, easy flow and bouncing. J. Phys.: Condens. Matter **20**, 395005 (2008)
35. I.R. Conway, N.J.A. Sloane, *Sphere Packings, Lattices and Groups* (Springer-Verlag, New York Inc, 1999, 1998, 1993)
36. L. Mahadevan, Y. Pomeau, Rolling droplets. Phys. Fluids **11**, 2449 (1999)
37. E.B. Dussan, T.P.R. Chow, On the ability of drops or bubbles to stick to non-horizontal surfaces of solids. J. Fluid Mech. **137**, 1–29 (1983)
38. D. Quéré, A. Lafuma, J. Bico, Slippy and sticky microtextured solids, Nanotechnology **14**, 1109–1112 (2003)
39. P.G. De Gennes, Rev. Mod. Phys. **57**, 827 (1985)
40. H. Kusumaatmaja, M.L. Blow, A. Dupuis, J.M. Yeomans, The collapse transition on superhydrophobic surfaces. Eur. Phys. Lett. **81**, 36003 (2008)
41. S. Moulinet, D. Bartolo, Life and death of a fakir droplet: impalement transitions on superhydrophobic surfaces. Eur. Phys. J. E **24**, 251–260 (2007)
42. M. Reyssat, J.M. Yeomans, D. Quéré, Impalement of fakir drops. Eur. Phys. Lett. **81**, 26006 (2008)
43. D. Deegan et al., Capillary flow as the cause of ring stains from dried liquid drops. Nature **389**, 827–829 (1997)
44. D. Deegan et al., Contact line deposits in an evaporating drop. Phys. Rev. E **62**, 756–765 (2000)
45. F.J. Garcia-Vidal, J.B. Pendry, Collective theory of surface enhanced Raman scattering. Phys. Rev. Lett. **77**, 1163–1166 (1996)
46. A.D. Rakic, A.B. Djurisic, J.M. elazar, M.L. Majewski, Optical properties of metallic films for vertical-cavity optoelectronic devices. Appl. Opt. **37**, 5271 (1998)

Chapter 15
Cooperative Effects in Plasmonics

Vitaliy N. Pustovit and Tigran V. Shahbazyan

Abstract In this chapter, we present our results on cooperative effects in hybrid plasmonic system involving a large number of fluorophores, e.g., dye molecules or semiconductor quantum dots, situated near a plasmonic nanostructure, e.g., metal nanoparticle. The optical properties of such complex systems are governed by the plasmon-mediated coupling between the fluorophores that leads to drastic changes in the system optical properties. Specifically, we consider in some detail two manifestations of plasmon-assisted cooperative behavior near a spherical nanoparticle: (a) superradiance by an ensemble of emitters and (b) cooperative energy transfer from an ensemble of donors to an acceptor.

Keywords Plasmon · Superradiance · Cooperative effects · Energy transfer

15.1 Plasmon-Mediated Superradiance Near Metal Nanostructures

15.1.1 Introduction

Superradiance of an ensemble of dipoles confined within a limited region in space has been discovered in the pioneering work by Dicke [1]. The underlying physical mechanism can be described as follows. Suppose that a large number, N, of dipoles with frequency ω_0 are confined in a volume with characteristic size L much smaller

V. N. Pustovit
Materials and Manufacturing Directorate, Air Force Research Laboratory,
Wright Patterson Air Force Base, Dayton, OH 45433, USA

T. V. Shahbazyan (✉)
Department of Physics, Jackson State University, Jackson, MS 39217, USA
e-mail: shahbazyan@jsums.edu

T. V. Shahbazyan and M. I. Stockman (eds.), *Plasmonics: Theory and Applications*,
Challenges and Advances in Computational Chemistry and Physics 15,
DOI: 10.1007/978-94-007-7805-4_15, © Springer Science+Business Media Dordrecht 2013

than the radiation wavelength $\lambda_0 = 2\pi/\omega_0$. Then radiation of the ensemble is a cooperative process in which the emission of a photon is accompanied by virtual photon exchange between individual emitters. This near field radiative coupling between the dipoles leads to formation of new system eigenstates, each comprised of *all* individual dipoles. The eigenstates with angular momentum $l = 1$ that are coupled to far field are *superradiant*, i.e., their radiative lifetimes are very short, $\sim \tau/N$, where τ is radiative lifetime of an individual dipole; the remaining states are *subradiant* with much longer decay times, $\sim \tau(\lambda_0/L)^2 \gg \tau$.

Since the appearance of Dicke paper, cooperative effects based on Dicke radiative coupling mechanism have been extensively studied in atomic and semiconductor systems (see, e.g., reviews in Refs. [2–4]). Two different decay times corresponding to superradiant and subradiant states were observed in a system of two laser-trapped ions [5] and, more recently, in laterally arranged quantum dots with sizes randomly distributed in a narrow interval [6]. In the later case, suparradiance takes place from an ensemble of emitters with weak disorder in excitation energies [7, 8]. Other examples of cooperative behavior analogous to the Dicke effect include, e.g., electron tunneling through a system of quantum dots [9, 10] and spontaneous phonon emission by coupled quantum dots [4, 11].

Recently, we have extended the Dicke effect to plasmonic systems comprised of N dipoles located in the vicinity of a metal nanostructure, e.g., metal nanoparticle (NP), supporting localized surface plasmon (SP) [12, 13]. In such systems, the dominant coupling mechanism between dipoles is *plasmonic* rather than radiative, i.e., it is based on virtual plasmon exchange (see Fig. 15.1). This plasmonic coupling leads to formation of collective states, similar to Dicke superradiant states, which dominate photon emission. Furthermore, the nanostructure acts as a *hub* that couples nearby and remote dipoles with about equal strength and hence provides a more efficient hybridization of dipoles as compared to radiative coupling. In general, since the dipoles orientations in space are non-uniform, there are three superradiant states with total angular momentum $l = 1$, each having radiative decay rate $\sim N\Gamma^r/3$, where Γ^r is radiative decay rate of a *single* dipole near a nanostructure (i.e., *with* plasmon enhancement) [12, 13].

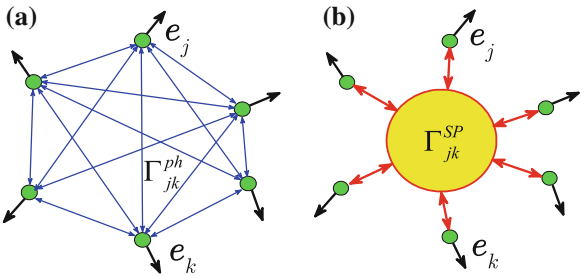

Fig. 15.1 Radiative coupling of emitters in free space (**a**), and plasmonic coupling of emitters near a metal nanoparticle (**b**)

The principal difference between plasmonic and usual (photonic) dipole coupling stems from the presence of non-radiative energy transfer between the dipoles and the nanostructure in the former case. Let us first outline its role for the case of a *single* dipole near metal NP. When an excited emitter is located close to metal surface, its energy can be transferred to optically inactive excitations in the metal and eventually dissipated (Ohmic losses). This is described by the *non-radiative decay* rate, $\Gamma^{nr} \propto d^{-3}$, where d is the dipole–surface separation [14]. Note that very close to metal surface ($\sim$1 nm), this dependence changes to $\propto d^{-4}$ due to surface-assisted generation of electron–hole pairs out of the Fermi sea [15, 16], although the non-local effects can change this behavior significantly [17]. As a result, the radiation of a coupled dipole–NP system is governed by a competition between non-radiative losses and plasmon enhancement [18] that determines system quantum efficiency, $Q = \Gamma^r/\Gamma$, where $\Gamma = \Gamma^r + \Gamma^{nr}$ is the *full* decay rate. Indeed, the radiated energy is $W = (\hbar kc/2)Q$, k and c being wave vector and speed of light, and its distance dependence follows that of Q. Namely, with decreasing d, the emission first increases due to the plasmon enhancement, and then, at several nm from metal surface, it is quenched due to the suppression of Q by non-radiative losses. Both enhancement and quenching were observed in recent experiments on fluorescing molecules attached to a metal NP [19–23], and, not too close to NP surface, the distance dependence of *single-molecule* fluorescence [21, 22] was found in excellent agreement with single dipole–NP models [24–27].

When radiation takes place from an *ensemble* of emitters near a metal nanostructure, there are *two* distinct types of plasmon-induced couplings between the emitters. The first is *plasmon-enhanced radiative coupling*, described by radiative decay matrix Γ^r_{jk}, where indexes $j, k = 1, \ldots, N$ refer to emitters, that is a straightforward extension of Dicke radiative coupling obtained by incorporating SP local field. Correspondingly, the eigenstates of Γ^r_{jk} are superradiant and subradiant states characterized by the strength of their coupling to radiation field. In the ideal case of "point sample," i.e., $kL \ll 1$, the subradiant decay rates are negligibly small and Γ^r_{jk} essentially has just three non-zero eigenvalues, corresponding to superradiant decay rates, each scaling with N as $\sim N\Gamma^r/3$ [12, 13].

The second coupling mechanism is *non-radiative energy transfer* between dipoles that takes place in two steps: an excited dipole first transfers its energy to the plasmons in a nanostructure via its near field, and then this energy is transferred to another dipole. This process involves plasmons with *all* angular momenta l, and it is described by non-radiative decay matrix, Γ^{nr}_{jk}. Importantly, due to plasmons with angular momenta $l > 1$, the eigenstates of *full decay matrix*, $\Gamma_{jk} = \Gamma^r_{jk} + \Gamma^{nr}_{jk}$, are *not* superradiant and subradiant states, but their admixtures. Close to metal surface where non-radiative processes are dominant, Γ^{nr}_{jk} prevails over Γ^r_{jk}, and no cooperative behavior is expected. However, when dipoles are separated from the surface by more than several nm, the coupling takes place primarily via dipole ($l = 1$) SP and so superradiance remains intact.

This observation is confirmed by numerical calculation of eigenvalues of Γ_{jk}, i.e., full decay rates of system eigenstates, for ensemble of N dipoles near a spherical

NP [12, 13]. Namely, in a wide range of dipole–NP distances, three eigenvalues corresponding to superradiant states are found to be well separated from the rest and scaled with N according to $\sim N\Gamma/3$. Since the radiative decay rate of superradiant states also scales as $\sim N\Gamma^r/3$, their quantum efficiencies essentially *coincide* with Q of single dipole–NP system. Therefore, in the cooperative regime, the ensemble quantum efficiency, Q_{ens}, is thrice that of the single dipole–NP system,

$$Q_{ens} \simeq 3Q \tag{15.1}$$

regardless of the ensemble size. Thus, the total radiated energy of the ensemble, $W_{ens} = (\hbar kc/2)Q_{ens}$, is reduced to just $3W$. The remaining energy is *trapped* by $N - 3$ subradiant states and eventually dissipated in the metal or radiated with a much slower rate than that of a single emiter near NP. On the other hand, at several nm from metal surface, cooperative behavior is destroyed by higher l plasmons, i.e., all system eigenstates have comparable quantum efficiencies so that $Q_{ens} \propto N$. Therefore, with increasing distance to surface, Q_{ens}, first exhibits a sharp rise with its slope $\propto N$, and then switches to a more slower $3Q$ dependence.

An obvious application of plasmon-mediated cooperative emission is related to fluorescence of a large but uncertain number of molecules at some average distances from metal nanostructure. For single-molecule case, fluorescence intensity variation with distance was proposed to serve as nanoscopic ruler [28] owing to the excellent agreement of measured distance dependences with single-dipole models [24–27]. In the case of an ensemble, the ambiguities caused by fluctuations of molecules numbers or their separations from the metal surface prevent, in general, the determination of system characteristics from fluorescence variations. However, in cooperative regime, these ambiguities are removed, and fluorescence intensity is essentially determined by Eq. (15.1) with *distance-averaged* single-molecule quantum efficiency.

Indications of a crossover from regular to cooperative regime were reported in Ref. [20] and, more recently, in Ref. [30]. Plasmon-mediated coupling between two dipoles near plasmonic nanowaveguides was studied in Ref. [31]. Coherent emission of excitons in disordered semiconductors due to coupling to surface plasmon-polaritons in metal films was reported in Ref. [32].

15.1.2 Plasmonic Coupling of Radiating Dipoles

We consider a system of N emitters, such as fluorescing molecules or quantum dots, with dipole moments $\mathbf{d}_j = d_j\mathbf{e}_j$, where d_j and $\mathbf{e}_j$ are magnitude and orientation, respectively, located at positions $\mathbf{r}_j$ near a metal NP with radius R. Throughout this chapter, we assume that characteristic size of the system (NP + dipoles) is much smaller than the radiation wavelength, $|\mathbf{r}_j - \mathbf{r}_k| \equiv |r_{jk}| \ll \lambda_0$. We also assume that emission events by individual molecules are uncorrelated, i.e., after excitation each molecule relaxes through its own internal nonradiative transitions before emitting a photon. Then the ensemble emission can be described within classical approach

by treating the dipoles as identical Lorentz oscillators with random initial phases driven by the common electric field. The frequency-dependent electric field, $\mathbf{E}(\mathbf{r}, \omega)$, satisfies Maxwell's equation

$$\frac{\varepsilon(\mathbf{r}, \omega)\omega^2}{c^2}\mathbf{E}(\mathbf{r}, \omega) - \nabla \times \nabla \times \mathbf{E}(\mathbf{r}, \omega) = -\frac{4\pi i\omega}{c^2}\mathbf{j}(\mathbf{r}, \omega), \tag{15.2}$$

where dielectric permittivity $\varepsilon(\mathbf{r}, \omega)$ is that of the metal inside NP, $\varepsilon(\omega)$ for $r < R$, and that of outside dielectric, ε_0 for $r > R$. Here $\mathbf{j}(\mathbf{r}, \omega)$ is the Laplace transform of dipole current,

$$\mathbf{j}(\mathbf{r}, \omega) = -i\int_0^\infty e^{i\omega t}\mathbf{j}(t)dt, \quad \mathbf{j}(t) = q\sum_j \dot{d}_j(t)\mathbf{e}_j\delta(\mathbf{r} - \mathbf{r}_j), \tag{15.3}$$

where dipole displacements $d_j(t)$ are driven by the common electric field at dipoles' positions (dot stands for time derivative)

$$\ddot{d}_j + \omega_0^2 d_j = \frac{q}{m}\mathbf{E}(\mathbf{r}_j, t)\cdot\mathbf{e}_j \tag{15.4}$$

with the initial conditions (at $t = 0$): $\mathbf{d}_j = d_0\mathbf{e}_j \sin\varphi_j$, $\dot{\mathbf{d}}_j = \omega_0 d_0\mathbf{e}_j\cos\varphi_j$, and $\mathbf{E} = 0$. Hereafter, ω_0, q, m, and φ_j are oscillators' excitation frequency, charge, mass, and initial phase, respectively ($\omega_0 = \hbar/md_0^2$). Closed equations for $d_j(\omega)$ can be obtained by using Laplace transform of Eq. (15.4) with the above initial conditions and eliminating $\mathbf{E}$ from Eqs. (15.2) and (15.4). Laplace transform of Eq. (15.2) has the form

$$\frac{\varepsilon(\mathbf{r}, \omega)\omega^2}{c^2}\mathbf{E}(\mathbf{r}, \omega) - \nabla \times \nabla \times \mathbf{E}(\mathbf{r}, \omega) = \frac{4\pi q}{c^2}\sum_j \delta(\mathbf{r} - \mathbf{r}_j)\big[i\omega_0 d_0\mathbf{e}_j\cos\varphi_j - \omega^2 d_j(\omega)\mathbf{e}_j + \omega d_0\mathbf{e}_j\sin\varphi_j\big]. \tag{15.5}$$

At this time, it is convenient to introduce normalized displacements

$$v_j(\omega) = d_j(\omega)/d_0 - i\left(\omega_0/\omega^2\right)\cos\varphi_j - \omega^{-1}\sin\varphi_j \tag{15.6}$$

and the solution of Eq. (15.5) reads

$$\mathbf{E}(\mathbf{r}, \omega) = \frac{4\pi d_0 q\omega^2}{c^2}\sum_j \mathbf{G}(\mathbf{r}, \mathbf{r}_j, \omega)\cdot\mathbf{e}_j v_j, \tag{15.7}$$

where $\mathbf{G}(\mathbf{r}, \mathbf{r}', \omega)$ is the electric field Green diadic *in the presence of* NP. From Eq. (15.4), for photon frequency close to dipoles frequency, $\omega \approx \omega_0$, we obtain a coupled system of equations for normalized displacements,

$$\sum_k \Big[(\omega_0 - \omega)\delta_{jk} + \Sigma_{jk}\Big] v_k = \frac{-i}{2} e^{-i\varphi_j}, \tag{15.8}$$

where $\Sigma_{jk} = \Delta_{jk} - \frac{i}{2}\Gamma_{jk}$ is the complex *self-energy matrix*, given by

$$\Sigma_{jk}(\omega) = -\frac{2\pi q^2 \omega_0}{mc^2}\, \mathbf{e}_j \cdot \mathbf{G}(\mathbf{r}_j, \mathbf{r}_k; \omega) \cdot \mathbf{e}_k. \tag{15.9}$$

The system Eq. (15.8) determines eigenstates of the ensemble of N dipoles in common radiation and plasmon field, while complex eigenvalues of the self-energy matrix give eigenstates frequency shifts with respect to ω_0 and their decay rates. In the absence of NP, real and imaginary parts of the self-energy matrix are dipole-dipole interaction and radiation coupling between dipoles j and k, given by (in lowest order in kr_{jk})

$$\Delta^0_{jk} = \frac{3\Gamma^r_0}{4(kr_{jk})^3}\left[(\mathbf{e}_j \cdot \mathbf{e}_k) - \frac{3(\mathbf{e}_j \cdot \mathbf{r}_{jk})(\mathbf{e}_k \cdot \mathbf{r}_{jk})}{r^2_{jk}}\right], \qquad \Gamma^0_{jk} = \Gamma^r_0\, \mathbf{e}_j \cdot \mathbf{e}_k, \tag{15.10}$$

where

$$\Gamma^r_0 = \frac{2kq^2\omega_0}{3mc^2} = \frac{2\mu^2 k^3}{3\hbar\varepsilon_0}, \tag{15.11}$$

is the radiative decay rate of a dipole in a dielectric medium, $\mu = qd_0$ is the dipole moment, and $k = \sqrt{\varepsilon_0}\omega/c$ is the wave vector. The eigenstates of *photonic* decay matrix Γ^0_{jk} are superradiant and subradiant states. In the case when all dipoles are aligned, there is only one superradiant state that couples to radiation field with decay rate $N\Gamma^r_0$, while for general dipole orientations there are three superradiant states with angular momentum $l = 1$. Note that in the longwave approximation used here, the decay rates of subradiant states vanish ("point sample").

In the presence of metal nanostructure, the system eigenstates are determined by the full Green diadic in self-energy matrix Eq. (15.9). In the case of spherical NP, the longwave approximation for $\mathbf{G}(r_j, r_k; \omega)$ can be easily found [25, 27]. The details are given in the Appendix, and the result reads

$$\Sigma_{jk}(\omega) = \Delta^0_{jk} - \frac{3\Gamma^r_0}{4k^3}\sum_l \alpha_l T^{(l)}_{jk} - \frac{i}{2}\Gamma^r_0\Big[(\mathbf{e}_j \cdot \mathbf{e}_k) - \alpha_1\big[K^{(1)}_{jk} + h.c.\big] + |\alpha_1|^2 T^{(1)}_{jk}\Big], \tag{15.12}$$

where

$$\alpha_l(\omega) = \frac{R^{2l+1}\,[\varepsilon(\omega) - \varepsilon_0]}{\varepsilon(\omega) + (1 + 1/l)\varepsilon_0} \tag{15.13}$$

is NP l-pole polarizability. The matrices $K_{jk}^{(l)}$ and $T_{jk}^{(l)}$ are defined as

$$K_{jk}^{(l)} = \frac{4\pi}{2l+1} \sum_{m=-l}^{l} [\mathbf{e}_j \cdot \boldsymbol{\psi}_{lm}(\mathbf{r}_j)][\mathbf{e}_k \cdot \boldsymbol{\chi}_{lm}^*(\mathbf{r}_k)], \tag{15.14}$$

$$T_{jk}^{(l)} = \frac{4\pi}{2l+1} \sum_{m=-l}^{l} [\mathbf{e}_j \cdot \boldsymbol{\psi}_{lm}(\mathbf{r}_j)][\mathbf{e}_k \cdot \boldsymbol{\psi}_{lm}^*(\mathbf{r}_k)], \tag{15.15}$$

where independent basis functions $\boldsymbol{\chi}_{lm}$ and $\boldsymbol{\psi}_{lm}$ are given by

$$\boldsymbol{\psi}_{lm}(\mathbf{r}) = \nabla \left[\frac{Y_{lm}(\hat{\mathbf{r}})}{r^{l+1}} \right], \qquad \boldsymbol{\chi}_{lm}(\mathbf{r}) = \nabla \left[r^l Y_{lm}(\hat{\mathbf{r}}) \right], \tag{15.16}$$

and $Y_{lm}(\hat{\mathbf{r}})$ are spherical harmonics. For $l = 1$, these matrices can be evaluated as

$$K_{jk}^{(1)} = \frac{1}{r_j^3} \Big[(\mathbf{e}_j \cdot \mathbf{e}_k) - 3(\mathbf{e}_j \cdot \hat{\mathbf{r}}_j)(\hat{\mathbf{r}}_j \cdot \mathbf{e}_k) \Big], \tag{15.17}$$

$$\begin{aligned} T_{jk}^{(1)} = \frac{1}{r_j^3 r_k^3} \Big[& (\mathbf{e}_j \cdot \mathbf{e}_k) - 3(\mathbf{e}_j \cdot \hat{\mathbf{r}}_j)(\mathbf{e}_k \cdot \hat{\mathbf{r}}_j) \\ & - 3(\mathbf{e}_j \cdot \hat{\mathbf{r}}_k)(\mathbf{e}_k \cdot \hat{\mathbf{r}}_k) + 9(\mathbf{e}_k \cdot \hat{\mathbf{r}}_k)(\mathbf{e}_j \cdot \hat{\mathbf{r}}_j)(\hat{\mathbf{r}}_j \cdot \hat{\mathbf{r}}_k) \Big], \end{aligned} \tag{15.18}$$

where we have used identities

$$\begin{aligned} \sum_{m=-1}^{1} \boldsymbol{\psi}_{1m}(\mathbf{r}_k) Y_{1m}^*(\hat{\mathbf{r}}) &= \frac{3}{4\pi r_k^3} \big[\hat{\mathbf{r}} - 3\hat{\mathbf{r}}_k (\hat{\mathbf{r}} \cdot \hat{\mathbf{r}}_k) \big], \\ \sum_{m=-1}^{1} \boldsymbol{\chi}_{1m}(\mathbf{r}_k) Y_{1m}^*(\hat{\mathbf{r}}) &= \frac{3}{4\pi} \hat{\mathbf{r}}. \end{aligned} \tag{15.19}$$

For dipoles oriented normally with respect to NP surface ($\mathbf{e}_j = \hat{\mathbf{r}}_j$), we obtain

$$K_{jk}^{(1)} = -\frac{2}{r_j^3} (\mathbf{e}_j \cdot \mathbf{e}_k), \qquad T_{jk}^{(1)} = \frac{4}{r_j^3 r_k^3} (\mathbf{e}_j \cdot \mathbf{e}_k), \tag{15.20}$$

and for parallel orientation ($\mathbf{e}_j \cdot \hat{\mathbf{r}}_j = 0$), we similarly get

$$K_{jk}^{(1)} = \frac{1}{r_j^3} (\mathbf{e}_j \cdot \mathbf{e}_k), \qquad T_{jk}^{(1)} = \frac{1}{r_j^3 r_k^3} (\mathbf{e}_j \cdot \mathbf{e}_k). \tag{15.21}$$

The *decay matrix*, $\Gamma_{jk} = -2\mathrm{Im}\,\Sigma_{jk}$, can be decomposed into radiative and nonradiative terms, $\Gamma_{jk} = \Gamma_{jk}^r + \Gamma_{jk}^{nr}$, as follows

$$\Gamma^r_{jk} = \Gamma^r_0\Big[(\mathbf{e}_j\cdot\mathbf{e}_k) - \alpha_1'\big[K^{(1)}_{jk} + h.c.\big] + |\alpha_1|^2 T^{(1)}_{jk}\Big],$$

$$\Gamma^{nr}_{jk} = \frac{3\Gamma^r_0}{2k^3}\sum_l \alpha_l'' T^{(l)}_{jk}. \tag{15.22}$$

The diagonal elements Γ^r_{jj} and Γ^{nr}_{jj} describe, respectively, plasmon-enhanced radiative decay rate of an *isolated* dipole near a NP, and nonradiative transfer of its energy to electronic excitations in metal. The non-diagonal elements of Γ^r_{jk} describe *plasmon-enhanced radiative coupling* that generalizes the Dicke coupling responsible for cooperative emission by incorporating local field enhancement into near field radiative coupling. On the other hand, the non-diagonal terms in Γ^{nr}_{jk} describe plasmon-mediated *near field* coupling between the dipoles. The latter coupling is absent in the photonic Dicke effect, but it plays important role in the plasmonic Dicke effect, as we will see below.

Since the numerical calculations below are carried for normal dipoles orientations, we provide here the corresponding expressions for self-energy matrix Σ_{jk}. The decay matrix has the form

$$\Gamma^r_{jk} = \Gamma^r_0\left[1 + 2\alpha_1'\left(\frac{1}{r_j^3} + \frac{1}{r_k^3}\right) + \frac{4|\alpha_1|^2}{r_j^3 r_k^3}\right]\cos\gamma_{jk},$$

$$\Gamma^{nr}_{jk} = \frac{3\Gamma^r_0}{2k^3}\sum_l \frac{\alpha_l''(l+1)^2}{r_j^{l+2} r_k^{l+2}} P_l(\cos\gamma_{jk}), \tag{15.23}$$

where P_l is Legendre polynomial and γ_{jk} is the angle between positions of dipoles j and k measured from NP center (i.e., $\cos\gamma_{jk} = \mathbf{e}_j\cdot\mathbf{e}_k$). The real part of self-energy matrix has the form

$$\Delta_{jk} = \Delta^0_{jk} + \Gamma^r_0\left[\alpha_1''\left(\frac{1}{r_j^3} + \frac{1}{r_k^3}\right)\cos\gamma_{jk} - \frac{3}{4k^3}\sum_l \frac{\alpha_l'(l+1)^2}{r_j^{l+2} r_k^{l+2}} P_l(\cos\gamma_{jk})\right], \tag{15.24}$$

where the second term describes NP-induced interactions. The latter in turn consists of two terms, first coming from plasmon-enhanced radiative coupling and second coming from non-radiative coupling.

Both NP-induced terms in Eq. (15.24) are weaker than their counterparts in Γ_{jk}, while having same symmetry, and hence are not expected to significantly alter the eigenstates. On the other hand, the dipole–dipole interaction term, Eq. (15.10), has different symmetry and can become large for two dipoles in a close proximity to each other. The effect of interactions on cooperative emission is studied in Sect. 15.2.4.

15.1.3 Radiated Energy of an Ensemble of Dipoles Near Nanoparticle

The radiated energy of an ensemble of dipoles in the unit frequency interval is obtained by integrating the far field ($r \to \infty$) spectral intensity over solid angle [33]

$$\frac{dW(\omega)}{d\omega} = \frac{c\varepsilon_0}{4\pi^2}\int |\mathbf{E}(\mathbf{r},\omega)|^2 r^2 d\Omega, \tag{15.25}$$

and then averaging the result over initial random phases of individual dipoles, φ_j. The electric field $\mathbf{E}(\mathbf{r},\omega)$ is given by Eq. (15.7), where v_j is the solution of Eq. (15.4). Then the energy density takes the form

$$\frac{dW}{d\omega} = \frac{4r^2\varepsilon_0\mu^2\omega_0^4}{c^3}\sum_{jk}\int d\Omega v_j v_k^*\big[\mathbf{G}(\mathbf{r},\mathbf{r}_j)\cdot\mathbf{e}_j\big]\cdot\big[\mathbf{G}^*(\mathbf{r},\mathbf{r}_k)\cdot\mathbf{e}_k\big]. \tag{15.26}$$

The Green dyadic consists of contributions from free space and scattered parts, $\mathbf{G}(\mathbf{r},\mathbf{r}_j,\omega) = \mathbf{G}^0(\mathbf{r},\mathbf{r}_j,\omega) + \mathbf{G}^s(\mathbf{r},\mathbf{r}_j,\omega)$, and can be replaced by its far field asymptotics (see Appendix),

$$\begin{aligned} G_{\mu\nu}(r,r_j) = \frac{e^{ikr}}{4\pi r}\Big[\delta_{\mu\nu} - \frac{4\pi}{3}\sum_m \hat{\mathbf{r}}_\mu Y_{1m}(\hat{\mathbf{r}})\chi_{1m}^{\nu *}(\mathbf{r}_j) \\ - \frac{4\pi}{3}\tilde{\alpha}_1 r\sum_m\big[\nabla_\mu Y_{1m}(\hat{\mathbf{r}})\big]\psi_{1m}^{\nu *}(\mathbf{r}_j)\Big], \end{aligned} \tag{15.27}$$

where the first two terms come from the free space part, $\mathbf{G}^0$, and the last term comes from the scattered part, $\mathbf{G}^s$. The angular integral in Eq. (15.25) can be performed using the relations Eq. (15.19). The free space contribution yields

$$4\pi r^2\int d\Omega\big[\mathbf{G}^0(\mathbf{r},\mathbf{r}_j)\cdot\mathbf{e}_j\big]\cdot\big[\mathbf{G}^{0*}(\mathbf{r},\mathbf{r}_k)\cdot\mathbf{e}_k\big] = \frac{2}{3}(\mathbf{e}_j\cdot\mathbf{e}_k). \tag{15.28}$$

The other integrals in the product Eq. (15.26) are evaluated using the relations

$$\left(\frac{4\pi r}{3}\right)^2\sum_{mm'}\big[\boldsymbol{\psi}_{1m}^*(\mathbf{r}_j)\cdot\mathbf{e}_j\big]\big[\boldsymbol{\psi}_{1m'}(\mathbf{r}_k)\cdot\mathbf{e}_k\big]\int\frac{d\Omega}{4\pi}\nabla Y_{1m}(\hat{\mathbf{r}})\cdot\nabla Y_{1m'}^*(\hat{\mathbf{r}}) = \frac{2}{3}T_{jk}^{(1)}, \tag{15.29}$$

and

$$\frac{4\pi r}{3}\sum_m\int\frac{d\Omega}{4\pi}\big[\mathbf{e}_k\cdot\nabla Y_{1m}(\hat{\mathbf{r}})\big]\big[\boldsymbol{\psi}_{1m}^*(\mathbf{r}_j)\cdot\mathbf{e}_j\big] = \frac{2}{3}K_{jk}^{(1)}, \tag{15.30}$$

yielding

$$\int \frac{d\Omega}{4\pi}\left[\mathbf{G}(\mathbf{r},\mathbf{r}_j)\cdot\mathbf{e}_j\right]\cdot\left[\mathbf{G}^*(\mathbf{r},\mathbf{r}_k)\cdot\mathbf{e}_k\right] = \frac{1}{(4\pi r)^2}\frac{2}{3}\left[(\mathbf{e}_j\cdot\mathbf{e}_k) - \alpha_1 K_{jk}^{(1)} - \alpha_1^* K_{kj}^{(1)} + |\alpha_1|^2 T_{jk}^{(1)}\right]. \tag{15.31}$$

The energy density then takes the form

$$\frac{dW(\omega)}{d\omega} = \frac{\sqrt{\varepsilon_0}\hbar\omega_0}{\pi}\sum_{jk} v_j v_k^* A_{jk}, \tag{15.32}$$

where $A_{jk} = \Gamma_0^r\left[(\mathbf{e}_j\cdot\mathbf{e}_k) - \tilde{\alpha}_1 K_{jk}^{(1)} - \tilde{\alpha}_1^* K_{kj}^{(1)} + |\tilde{\alpha}_1|^2 T_{jk}^{(1)}\right]$. Matrix A_{jk} is not symmetrical, however only its symmetrical part, equal to Γ_{jk}^r, contributes to the final expression. The solution of Eq. (15.8) can be presented as

$$v_j = -\frac{i}{2}\sum_k \left[\frac{1}{\omega_0 - \omega + \hat{\Sigma}}\right]_{jk} e^{-i\varphi_k}, \tag{15.33}$$

and after averaging out over the initial random phases φ_j, we finally obtain

$$\frac{dW(\omega)}{d\omega} = \frac{\hbar kc}{4\pi}\,\mathrm{Tr}\left[\frac{1}{\omega - \omega_0 - \hat{\Sigma}^\dagger}\hat{\Gamma}^r\frac{1}{\omega - \omega_0 - \hat{\Sigma}}\right], \tag{15.34}$$

where trace is taken over the indexes (jk).

15.1.4 Discussion and Numerical Results

We consider a common situation when emitters, e.g., fluorescent molecules or quantum dots, are attached to NP surface via flexible linkers. Typically, fluorophores bound to linker molecules have certain orientation of their dipole moments with respect to NP surface and, due to repulsive interactions, their angular positions are ordered rather then random [20]. Therefore, we assume here that angular positions of emitters coincide with the sites of spherical lattice, such as fullerenes. Specifically, we perform our numerical simulations for C20, C60, and C80 configurations for respective number N of dipoles; we also study the effect of deviations from ideal lattice. We find that not too close to metal surface, the system eigenstates fall into three groups, each dominated by a particular coupling mechanism: three superradiant states dominated by plasmon-enhanced radiative coupling, one state dominated by direct dipole–dipole interactions, and the rest dominated by non-radiative coupling via NP. Importantly, superradiant states are *not* significantly affected by dipole-dipole

interactions whose main effect is a large frequency shift of subradiant state with the smallest decay rate.

Let us start with a *single* dipole located at r_0 near a metal NP. In this case, the self-energy is a complex number, $\Sigma = \Delta - \frac{i}{2}\Gamma$, where $\Delta = \Delta_{jj}$ and $\Gamma = \Gamma^r + \Gamma^{nr} = \Gamma_{jj}$ are single-dipole energy shift and decay rate, respectively. For normal ($s = \perp$) and parallel ($s = \parallel$) dipole orientations, using Eqs. (15.20) and (15.21), these are given by [24]

$$\Gamma^r = \Gamma_0^r \left| 1 + \frac{a_s \alpha_1}{r_0^3} \right|^2, \quad \Gamma^{nr} = \frac{3\Gamma_0^r}{2k^3} \sum_l \frac{b_s^{(l)} \alpha_l''}{r_0^{2l+4}},$$
$$\Delta = \Gamma_0^r \left(\frac{a_s \alpha_1''}{r_0^3} - \frac{3}{4k^3} \sum_l \frac{b_s^{(l)} \alpha_l'}{r_0^{2l+4}} \right), \tag{15.35}$$

with $a_\perp = 2$, $b_\perp^{(l)} = (l+1)^2$ and $a_\parallel = -1$, $b_\parallel^{(l)} = l(l+1)/2$. Note that both terms in Δ are smaller than their counterparts Γ^r and Γ^{nr} due to plasmon pole in the imaginary part of NP polarizability α_l''. Radiated energy of single dipole–NP system, obtained by frequency integration of Eq. (15.34), is given by

$$W = \frac{\hbar kc}{2} \frac{\Gamma^r}{\Gamma + \Gamma_0^{nr}} = \frac{\hbar kc}{2} Q, \tag{15.36}$$

where we included the *intrinsic* molecular relaxation rate, Γ_0^{nr}, into quantum efficiency Q. For N *uncoupled* dipoles, i.e., for purely diagonal $\Sigma_{jk} = \delta_{jk}\left(\Delta - \frac{i}{2}\Gamma\right)$, Eq. (15.34) decouples into sum of N independent terms, yielding $W_{ens} = NW$.

In the presence of inter-dipole coupling, the system eigenstates, $|J\rangle$, are those of the self-energy matrix, Eq. (15.12). The corresponding eigenvalues are complex, $\hat{\Sigma}|J\rangle = (\Delta_J - \frac{i}{2}\Gamma_J)|J\rangle$, where Δ_J is frequency shift of collective eigenstate $|J\rangle$ relative to ω_0 and Γ_J is its decay rate. The molecular relaxation can be accounted for by adding to Σ_{jk} a diagonal term, $-\frac{i}{2}\delta_{jk}\Gamma_0^{nr}$. Then, after frequency integration of Eq. (15.34), the ensemble radiated energy takes the form

$$W_{ens} = \frac{\hbar kc}{2} Q_{ens}, \quad Q_{ens} = \sum_J \frac{\Gamma_J^r}{\Gamma_J + \Gamma_0^{nr}}, \tag{15.37}$$

where $\Gamma_J^r = \langle J|\hat{\Gamma}^r|J\rangle$ is radiative decay rate of state $|J\rangle$.

In the photonic Dicke effect, superradiant and subradiant states are eigenstates of the radiative decay matrix Γ_{jk}^0 obtained from the free space Green diadic. Similarly, in the plasmonic Dicke effect, superradiant states are eigenstates of *plasmon-enhanced* radiative decay matrix Γ_{jk}^r. Let us illustrate the emergence of plasmon-mediated superradiance for a simple case when all dipoles are at the same distance from NP surface and are oriented normal or parallel to it. Then it is easy to see that the corresponding decay matrix, $\Gamma_{jk}^r = \Gamma^r \mathbf{e}_j \cdot \mathbf{e}_k$ with Γ^r given by Eq. (15.35), has just three nonzero eigenvalues. Indeed, let us introduce new decay matrices as

$$\gamma^r_{\mu\nu} = \frac{N\Gamma^r}{3} B_{\mu\nu}, \tag{15.38}$$

where

$$B_{\mu\nu} = \frac{3}{N} \sum_j e^\mu_j e^\nu_j \tag{15.39}$$

is 3×3 matrix in coordinate space with $\mathrm{Tr}\hat{B} = 3$. It is easy to see that $\mathrm{Tr}\left[(\hat{\Gamma}^r)^n\right] = \mathrm{Tr}\left[(\hat{\gamma}^r)^n\right]$ for any integer n, i.e., the $N \times N$ matrix Γ^r_{jk} has only three non-zero eigenvalues coinciding with those of matrix $\gamma^r_{\mu\nu}$

$$\Gamma^r_\mu = \frac{N\Gamma^r}{3} \lambda_\mu, \tag{15.40}$$

where $\lambda_\mu \sim 1$ are eigenvalues of $B_{\mu\nu}$. Note that the decay rates of the remaining $N-3$ subradiant states vanish in the long wave approximation used here; they acquire finite values in the next order in $(kr_0)^2$.

Let us turn to non-radiative coupling, described by matrix Γ^{nr}_{jk}. Its diagonal elements, Γ^{nr}_{jj}, describe nonradiative energy exchange between excited dipole and NP plasmon modes with all angular momenta, as indicated by polarizabilities α''_l in Eq. (15.23). The non-diagonal elements of Γ^{nr}_{jk} describe a process by which a plasmon nonradiatively excited in the NP by dipole k transfers its energy to another dipole j. In general, due to high-l plasmons involved in nonradiative coupling, the eigenstates of Γ^{nr}_{jk} are *different* from those of plasmon-enhanced radiative coupling Γ^r_{jk} which contains only dipole ($l = 1$) plasmon mode. Therefore, the eigenstates of full decay matrix $\Gamma_{jk} = \Gamma^{nr}_{jk} + \Gamma^{nr}_{jk}$ are *not* pure superradiant and subradiant states but their admixtures. However, the high-l plasmon contribution to Γ^{nr}_{jk} is significant only at very small d [see, e.g., Eq. (15.23)] while for d larger than several nm Γ^{nr}_{jk} is dominated by the $l = 1$ term. In fact, in a wide range d, nonradiative coupling between dipoles is mainly through the optically active *dipole* plasmon mode that does not cause mixing between superradiant and subradiant states. Namely, it can be easily seen from Eq. (15.23) that the eigenstates of the $l = 1$ term in Γ^{nr}_{jk} are the same as those of Γ^r_{jk} so the corresponding eigenvalues are similarly given by $\Gamma^{nr}_\mu = (N\Gamma^{nr}/3)\,\lambda_\mu$. Thus, the superradiant quantum efficiency

$$Q_\mu = \frac{\Gamma^r_\mu}{\Gamma_\mu + \Gamma^{nr}_0} = \frac{\Gamma^r}{\Gamma + 3\Gamma^{nr}_0/N\lambda_\mu} \tag{15.41}$$

only weakly depends on N. Therefore, the sum in Eq. (15.37) includes just three terms, yielding

$$W_{ens} = \frac{\hbar kc}{2} Q_{ens} = \frac{\hbar kc}{2} \sum_{\mu=1}^{3} \frac{\Gamma^r}{\Gamma + 3\Gamma_0^{nr}/N\lambda_\mu}. \tag{15.42}$$

For high-yield (small Γ_0^{nr}) emitters, we obtain Eq. (15.1) and hence $W_{ens} \approx 3W$. In contrast, the radiated *power*,

$$P_{ens} = \frac{\hbar kc}{2} \sum_{\mu=1}^{3} Q_\mu \Gamma_\mu^r \simeq N \left(\frac{\hbar kc}{2} Q \Gamma^r \right) = NP, \tag{15.43}$$

scales with the ensemble size due to the shorter (by factor $N/3$) radiative lifetime of superradiant states.

For low-yield emitters (large Γ_0^{nr}), the relation Eq. (15.1) holds only approximately. However, it is evident from comparison of Eqs. (15.36) and (15.42) that here the relative effect of internal relaxation is much weaker than for usual cooperative emission. Numerical results for both high-yield and low-yield emitters are presented below.

Let us now turn to the role of interactions between dipoles in the ensemble. Interactions play critical role in cooperative emission since they introduce a disorder into system energy spectrum by causing random shifts of individual dipole frequencies [7, 8, 34]. In the conventional cooperative emission, the main disorder effect is to split the narrow subradiant peak in the ensemble emission spectra [8]. In the presence of metal nanostructure, radiation of subradiant states is expected to be quenched by much faster nonradiative losses in the metal. The crucial question is, however, whether interactions between closely spaced individual dipoles can significantly alter the structure of collective eigenstates. Below we present the results of our numerical simulations of cooperative emission fully incorporating both direct and plasmon-mediated interactions.

We consider an ensemble of N molecular dyes attached to an Ag spherical particle with radius $R = 20$ nm via molecular linkers with approximately same length. The system is embedded in aqueous solution with dielectric constant $\varepsilon_0 = 1.77$, and two types of dyes with quantum efficiencies $q = 0.3$ and $q = 0.95$ are used in the calculations. A distinguishing feature of this system is a strong effect of interactions on its geometry [20]. The flexible linker molecules hold the attached dyes with certain orientation of their dipole moments, so that repulsive inter-molecule interactions compel the dyes to form a spatially ordered structure on spherical surface. In our simulations, the dyes with normal dipole orientations were located at the sites of spherical lattice, specifically, fullerenes C20, C32, C60, and C80, and, in some calculations, we included random deviations from the ideal lattice positions. The system eigenstates are found by numerical diagonalization of self-energy matrix, $\Sigma_{jk} = \Delta_{jk} - \frac{i}{2}\Gamma_{jk}$, with its real and imaginary parts given by Eqs. (15.24) and (15.23), respectively. Calculations were carried at the SP energy of 3.0 eV, the size-dependent Landau damping was incorporated for all plasmon modes, and NP

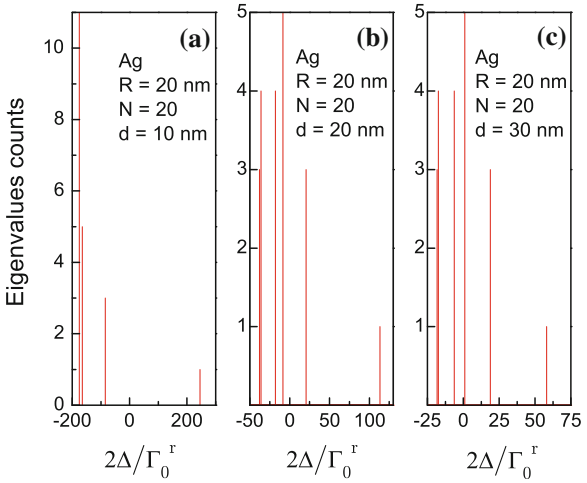

Fig. 15.2 Distribution of energy shifts for 20 dipoles in C20 configuration around Ag NP at several distances to its surface

polarizabilities, Eq. (15.13), with angular momenta up to $l = 30$, were calculated using the experimental bulk Ag complex dielectric function.

Figures 15.2 and 15.3 show distribution of real and imaginary parts of complex eigenvalues of Σ_{jk} for $N = 20$ molecules at the sites of C20 fullerene at three different molecule-surface distances. The system spectrum represents several sets of degenerate eigenvalues indicating a high degree of lattice symmetry. For all distances,

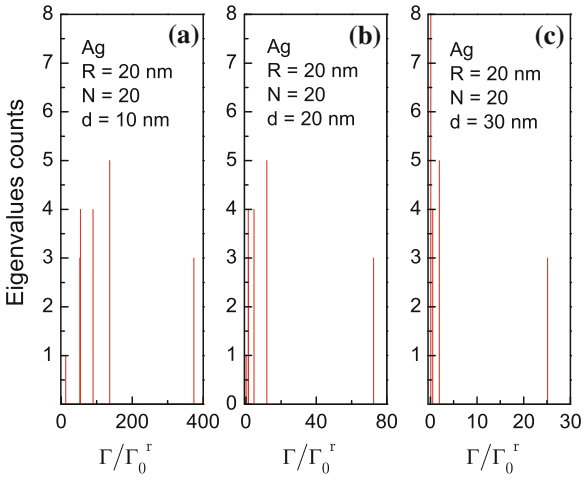

Fig. 15.3 Distribution of decay rates for 20 dipoles in C20 configuration around Ag NP at several distances to its surface

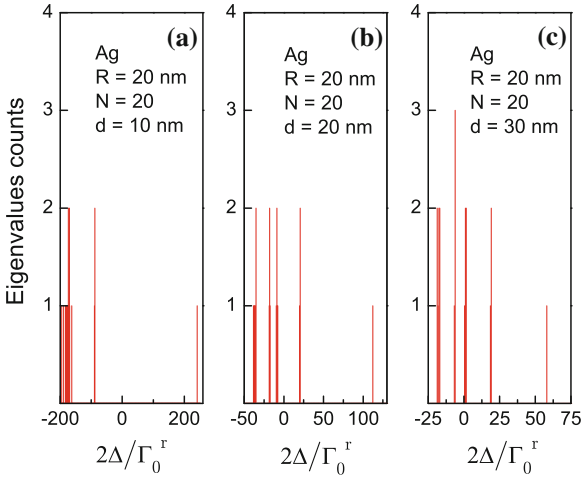

Fig. 15.4 Distribution of energy shifts for 20 dipoles in C20 configuration around Ag NP at several average (with 10 % fluctuations) distances to its surface

the histograms show a *single* eigenvalue with a large positive energy shift (Fig. 15.2), which corresponds to the direct dipole–dipole interaction between nearest-neighbor molecules. On the other hand, there are *three* degenerate eigenvalues with the largest decay rate, corresponding to predominantly *superradiant* states while the smaller decay rates are those of predominantly subradiant states (Fig. 15.3). With increasing distance, the mixing between superradiant and subradiant states decreases and, for $d = 30$ nm, decay rates of all but three eigenstates nearly vanish; note that in our approximation, pure subradiant states should have zero decay rate. Such behavior is due to diminishing contribution of higher-l plasmons at larger distances (see Eqs. (15.23) and (15.24)). Importantly, direct interactions between close molecules result only in energy shift of subradiant states, without affecting superradiant states. We therefore conclude that dipole–dipole interactions do *not* destroy cooperative emission in plasmonic systems.

This main conclusion remains unchanged when fluctuations (up to 10 %) of molecules positions in radial direction are included into simulations (Figs. 15.4 and 15.5). The spatial disorder lifts lattice symmetry, so that superradiant states now have different, however close, decay rates. Note that without interactions, i.e., when molecules angular positions are completely random, the spread of superradiant decay rates is considerably higher.

To elucidate the structure of collective states, we calculate the distance dependencies of complex eigenvalues, $\Delta_J - \frac{i}{2}\Gamma_J$, for C20, C60, and C80 configurations of dyes, as shown in Figs. 15.6, 15.7, and 15.8, respectively. For C20 configuration (Fig. 15.6), there are five sets of eigenvalues with three-, four-, four-, seven-, and onefold degeneracies, in descending order of Γ_J magnitudes. Down to the distance of $d = 5$ nm, the largest decay rates, corresponding to three predominantly superra-

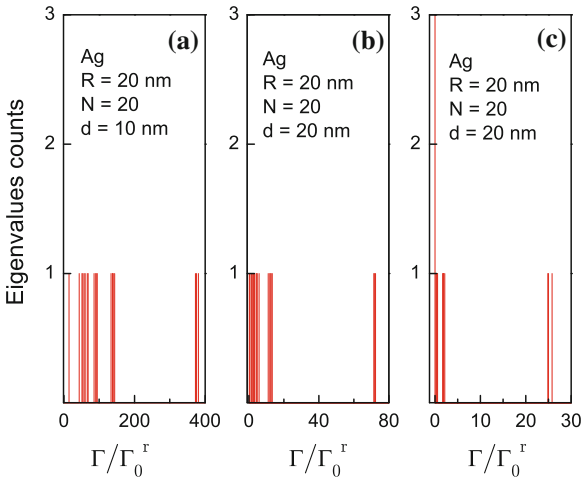

Fig. 15.5 Distribution of decay rates for 20 dipoles in C20 configuration around Ag NP at several average (with 10 % fluctuations) distances to its surface

diant states, are well separated from the rest. The steep rise of Γ_J at small distances is due to increasing contribution of high-l plasmon modes close to NP surface (see Eqs. (15.23) and (15.24)). The interplay between various coupling mechanisms is especially revealing when comparing the plots for Δ_J and Γ_J (curves for same eigenvalue sets have similar patterns). By their d dependence, the eigenvalues fall into three main groups. The superradiant states have the largest decay rate Γ_J for all d and relatively small mainly *positive* frequency shift for $d \gtrsim R/2$; these states are dominated by *plasmon-enhanced radiative coupling*. The non-degenerate state with large *positive* energy shift and smallest decay rate is dominated by direct nearest-neighbor dipoles interaction; this state is least affected by the presence of NP and does not participate in the emission. The third group of states with mostly *negative* Δ_J and small Γ_J is dominated by *nonradiative plasmon coupling*. Closer to NP surface, this coupling becomes dominant for all states due to high-l plasmons causing large decay rates and negative energy shifts. Note that down to $d \gtrsim R/4$, the admixture between superradiant and subradiant modes is still relatively weak; below $R/4$, the non-radiative coupling dominates the spectrum and the admixture is strong.

For larger ensembles, the eigenstates have similar structure, as illustrated in Figs. 15.7 and 15.8 which show calculated eigenvalues for dipoles in C60 and C80 configurations, respectively. Importantly, even with decreasing distance between the emitters in large ensembles, the dipole–dipole interactions still do not destroy cooperative emission. This can be understood from the following argument [8]. Mixing of superradiant and subradiant states takes place if the interactions between them are sufficiently strong. The latter requires that the electric field of a collective state is strongly inhomogeneous in space since, e.g., subradiant states couple only weakly to homogeneous field. On the other hand, such a field is comprised of individual fields

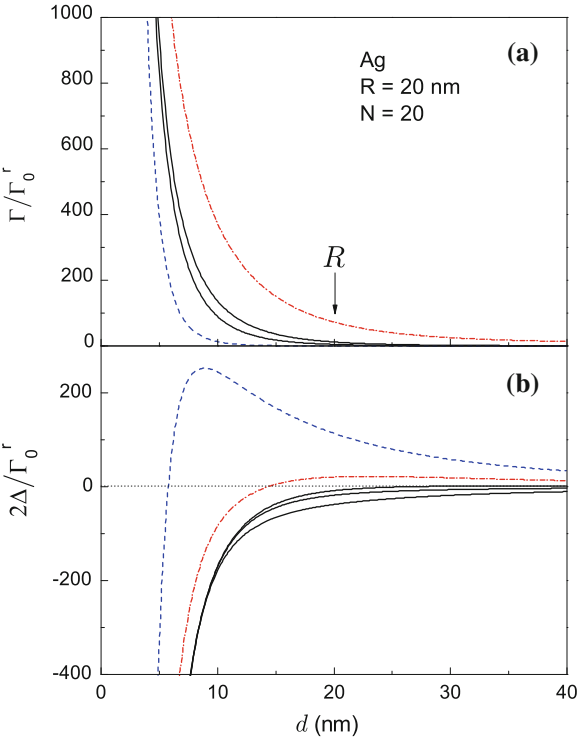

Fig. 15.6 **a** Decay rates and **b** energy shifts versus distance for 20 dipoles in C20 configuration around Ag NP. Each line corresponds to a system eigenstate and is similarly marked in both graphs. The *dash-dotted line* corresponds to three degenerate superradiant states, the *dashed line* is the darkest subradiant states dominated by dipole–dipole interactions, and *solid lines* correspond to the rest of subradiant states

of all the constituent dipoles so the resulting field's spatial fluctuations are weak if no two dipoles approach too close to each other; i.e., deviations of nearest-neighbor separations from their average, $\bar{s} = LN^{-1/3}$, L being characteristic system size, are small. However, if deviations from $\bar{s}$ are large, i.e., two dipoles can be separated by a much closer distance, $s \ll LN^{-1/3}$, thus causing a strong spatial field fluctuation, then the eigenstates are no longer superradiant and subradiant states so that cooperative emission is destroyed. This argument was confirmed numerically here by finding system eigenstates for both cases—dipoles on a spherical lattice with some fluctuations (see Figs. 15.4 and 15.5), and a completely random angular distribution with *fixed* dipole–NP distance with no minimal separation between two dipoles (not shown). In the latter case, the absence of superradiant states was traced to configurations with extremely close dipoles. Note, however, that with both radial and angular distributions being random, these are rare events and for *ensemble-averaged* case cooperative emission remains intact.

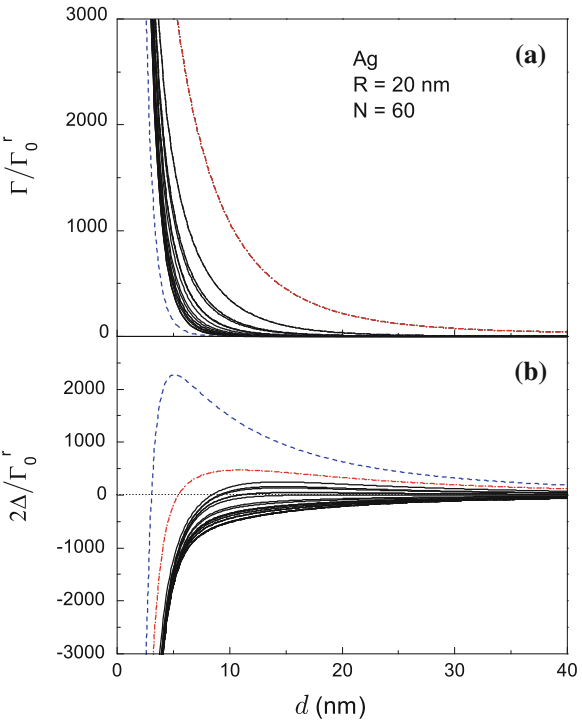

Fig. 15.7 Same as in Fig. 15.6, but for 60 dipoles in C60 configuration

Another sharp contrast between plasmonic and photonic Dicke effects is the fate of subradiant states. In the latter, the energy trapped in subradiant states is eventually radiated, albeit with a much slower rate, resulting in sharp spectral features of emission spectrum [2, 3]. Instead, in plasmonic systems, the trapped energy is dissipated in the NP and only a small fraction of total energy leaves the system via superradiant states. Thus, the net effect of plasmonic Dicke effect is to drastically *reduce* the emission as compared to same number of individual dipoles. Remarkably, as the eigenvalues scale *uniformly* with N, the *quantum efficiencies* of superradiant states are nearly independent of the ensemble size, leading to the simple relation (15.1) that holds in the cooperative regime.

This is illustrated in Figs. 15.9 and 15.10, which show *ensemble* quantum efficiencies Q_{ens} (see Eq. (15.37)) for two types of dyes with quantum yields $q = 0.95$ and 0.3, respectively. Two regimes can be clearly distinguished in the distance dependence of Q_{ens}: it first shows a sharp rise with its slope proportional to N (non-cooperative regime) followed by a slower d dependence (cooperative regime). The crossover between two regimes takes place at $d \simeq 5$ nm due to diminished high-l plasmons contribution to nonradiative coupling for larger distances. In the cooperative regime, the precise behavior of Q_{ens} is affected by molecules' quantum yield. For high-q molecules, all Q_{ens} dependences collapse onto a single curve, $Q_{ens} = 3Q$,

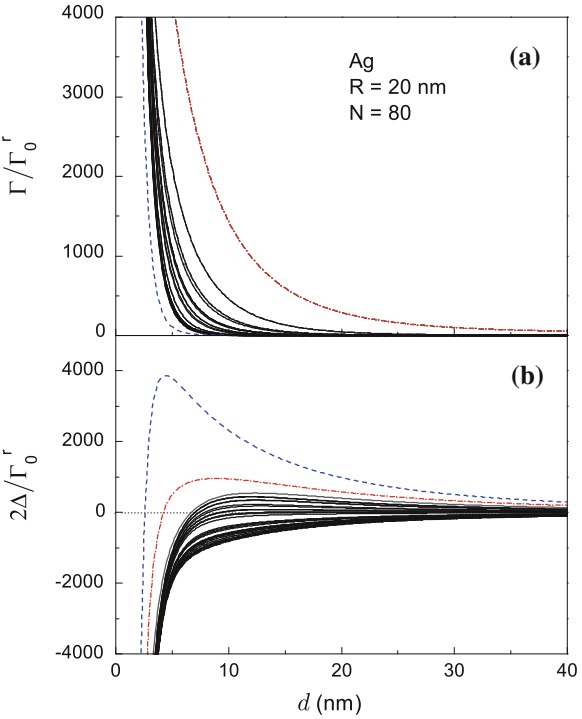

Fig. 15.8 Same as in Fig. 15.6, but for 80 dipoles in C80 configuration

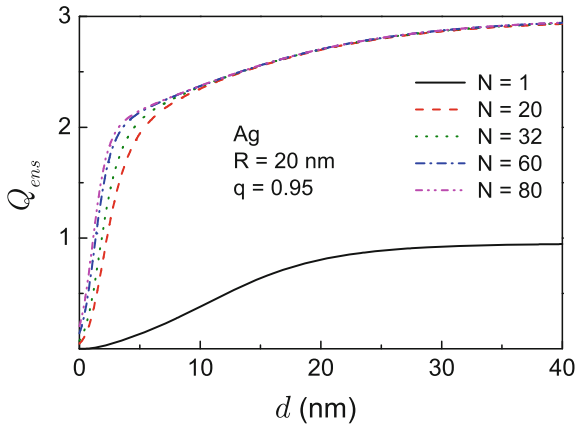

Fig. 15.9 Fluorescence quantum efficiency versus distance for several ensembles of high-yield emitters on spherical lattices around AG NP

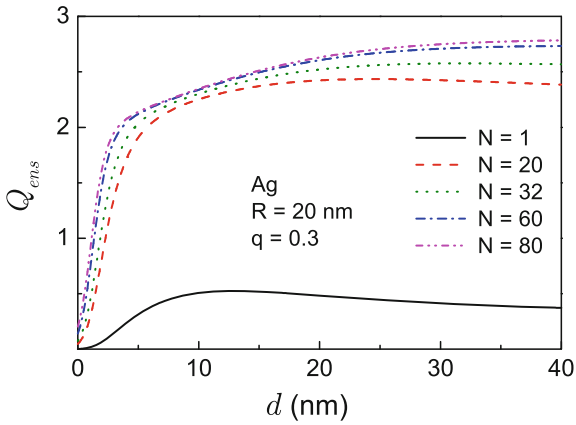

Fig. 15.10 Fluorescence quantum efficiency versus distance for several ensembles of low-yield emitters on spherical lattices around AG NP

while for low-q molecules, Q_{ens} shows a weak dependence on N. In both cases, this behavior can be easily understood from Eq. (15.42). Indeed, for degenerate superradiant eigenvalues we have $\lambda_\mu = 1$, and for large distances, as $\Gamma \to \Gamma_0^r$, we obtain

$$Q_{ens} \simeq \frac{3}{1 + 3(q^{-1} - 1)/N}, \tag{15.44}$$

i.e., for large ensembles, the role of molecular quantum yield is diminished.

15.2 Resonance Energy Transfer Near Metal Nanostructures Mediated by Surface Plasmons

15.2.1 Introduction

Efficient energy transfer at the nanoscale is one of the major goals in the rapidly developing field of plasmonics. Fluorescence resonance energy transfer (FRET) [35, 36] between spatially separated donor and acceptor fluorophores, such as dye molecules or semiconductor quantum dots (QD), underpins diverse phenomena in biology, chemistry and physics. Among prominent example are photosynthesis, exciton transfer in molecular aggregates, interaction between proteins [37, 38], and, more recently, energy transfer between QDs and in QD–protein assemblies [39–41]. FRET spectroscopy has been widely used, e.g., in studies of protein folding [42, 43], live cell protein localization [44, 45], biosensing [46, 47], and light harvesting [48]. During past decade, significant advances were made in FRET enhancement and control by placing molecules or QDs in microcavities [49–51] or near plasmonic materials such as metal films and nanoparticles (NPs) [52–60]. While the Förster transfer is

efficient only for relatively short distances ∼10 nm between a donor and an acceptor [37], the plasmon-mediated energy transfer channels provided by NPs [29, 62–66], metal films and waveguides [31, 65] or doped monolayer graphene [67] can lead to a significant increase of FRET efficiency and range.

The efficiency of plasmon-mediated FRET between a donor and an acceptor situated near a metal nanostructures is determined in a competition between the plasmonic enhancement and the losses due to radiation and dissipation in metal. Close to the metal surface, the dissipation largely prevails and only a fraction of donor's energy is transferred to the acceptor, while for intermediate distances the transfer efficiency significantly exceeds Förster's one [29, 62–66]. In a closely related phenomenon of plasmon-enhanced fluorescence, quantum efficiency of a fluorophore near a plasmonic nanostructure is determined by its distance to the metal surface, d, and the measured fluorescence [20–23] shows that, with decreasing d, plasmonic enhancement is replaced by quenching due to energy transfer to the metal [24, 25]. In a FRET configuration, an acceptor placed nearby will absorb some fraction of excited donor fluorophore energy via three main channels: Förster channel due to direct Coulomb interaction, non-radiative plasmon-mediated channel, and plasmon-enhanced radiative channel, the latter being dominant for intermediate distances [66]. Note, however, that the enhancement of individual donor's fluorescence will now contribute to the *losses* in FRET which is thus determined by an intimate interplay between transfer, radiation and dissipation channels [66].

Here we describe a highly efficient *cooperative* mechanism of energy transfer from an *ensemble* of donors to acceptors near a plasmonic nanostructure that takes advantage of the subtle balance between energy flow channels in the system. In a typical experimental setup, the energy transfer takes place from a large number of donors, e.g., deposited on top of silica shell around gold or silver core, to acceptors attached to NP surface via linker molecules. If the distance separating excited donors from metal is not too small, so that dissipation is not the dominant channel, then donors' coupling through NP plasmons gives rise to new system eigenstates—plasmonic superradiant and subradiant states, which, in the presence of a NP, are considerably more robust due to a strong plasmonic enhancement of radiative coupling [12, 13]. In this case, the energy transfer takes place from these collective states rather than from many individual donors coupled to the NP. Although the energy stored in a superradiant state is only a small fraction of the entire system energy, its large matrix element with external electric fields, e.g., leads to a huge decay rate that scales with the system size. In fact, in a similar manner, the large coupling of superradiant states with the electric field of an acceptor spatially separated from donor layer ensures, as we below demonstrate, a much more efficient plasmon-assisted FRET than from the same number of individual donors.

On the other hand, the multitude of subradiant states which carry almost the entire system energy are characterized by a much lower decay rate (radiative and nonradiative) than individual donors coupled to a NP [12, 13]. This gives rise to yet another plasmon-assisted FRET scenario that relies on the reduction of radiative and dissipative losses that naturally occurs in cooperative regime. Indeed, as show below, the FRET from plasmonic subradiant states is considerably larger than from

individual donors and is comparable to FRET from superradiant states. These two cooperative FRET mechanisms are easily distinguishable since they work in different energy regions; the superadiant FRET is most efficient within the dipole ($l = 1$) surface plasmon spectral band, while the subradiant states are formed due to plasmons with higher angular momenta ($l > 1$), and so FRET takes place in higher energy domain.

15.2.2 Energy Transfer from a Single Donor to an Acceptor Near Plasmonic Nanostructure

We start by recalling the famous Förster's formula for energy W_{ad}^F transferred from a donor to an acceptor [35–38]

$$\frac{W_{ad}^F}{W_d} = \frac{9}{8\pi} \int \frac{d\omega}{k^4} f_d(\omega)\sigma_a(\omega)\left|D_{ad}^0\right|^2, \tag{15.45}$$

where W_d is the donor's radiated energy, $f_d(\omega)$ is its spectral function, $\sigma_a(\omega)$ is the acceptor's absorption crosssection, D_{ad}^0 is the dipoles' electromagnetic coupling at distance r_{ad} and k is the wavevector of light. In the near field ($kr_{ad} \ll 1$), we have $D_{ad}^0 = q_{ad}/r_{ad}^3$ (q_{ad} is the orientational factor) and FRET changes with distance as $(r_F/r_{ad})^6$, where r_F is Förster's radius. In the far field ($kr_{ad} \gg 1$), FRET is dominated by radiative coupling $|D_{ad}^0| \propto k^2/r_{ad}$ leading to weaker r_{ad}^{-2} dependence [38, 61]. Eq. (15.45) is derived from first-order transition probability under the perturbation D_{ad}^0.

For molecules near a plasmonic nanostructure, Eq. (15.45) must be modified. The early model by Gersten and Nitzan [62, 63] and its extensions to planar and composite systems [29, 64, 65] incorporate SP in the transition's intermediate states, and thus Eq. (15.45) still holds albeit with new coupling D_{ad} which now includes plasmon-mediated channels. This model, however, does not account consistently for neither dissipation in metal nor plasmon-enhanced radiation channels and, as a result, yields enormous (up to 10^5) FRET enhancement that contrasts sharply with the much more modest ($\sim$10) increase [53–56, 58–60] and even reduction [52, 57] of measured RET rates.

Below we describe a unified model for FRET near metal nanostructures based on the classical approach that accounts accurately for all energy flow channels in the system [66]. We show that, in a wide parameter range, the dominant FRET mechanism near a plasmonic nanostructure is plasmon-enhanced radiative transfer (PERT) rather than nonradiative transfer. In the far field, a general formula for PERT from remote donors to an acceptor near the metal surface is derived that extends radiative FRET theory [38, 61] to plasmonic systems. In the near field, our numerical calculations of FRET near Ag NP (see inset in Fig. 15.11) show that PERT is the dominant mechanism here as well. Depending on system geometry, FRET can either

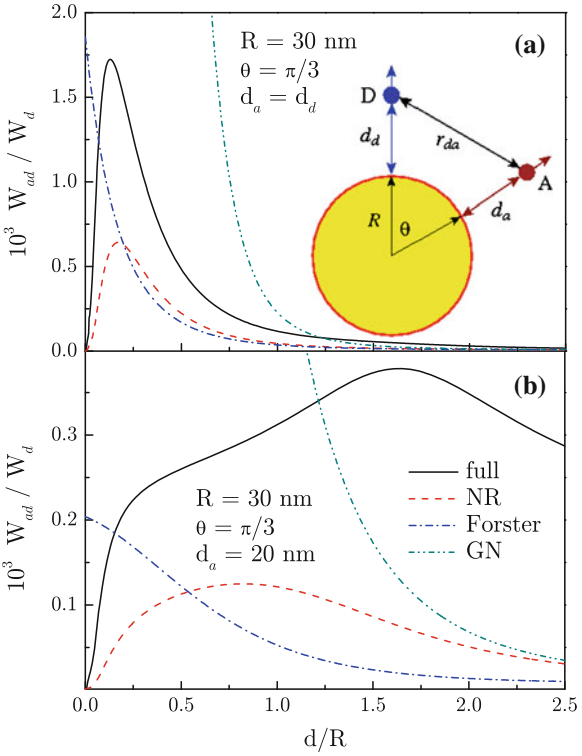

Fig. 15.11 RET versus distance for $R = 30$ nm Ag NP is shown at $\theta = \pi/3$ with **(a)** $d_a = d_d = d$ and **(b)** $d_a = 20$ nm, $d_d = d$ using the full Eq. (15.61), the nonradiative (NR) channel only, Förster's transfer Eq. (15.45), and the Gersten–Nitzan (GN) model [62, 63]

be enhanced or reduced as compared to Förster's transfer, consistent with experiment [52–60].

We consider a donor and an acceptor near the surface of a metal NP (see inset in Fig. 15.11) which are represented by pointlike dipoles located at $\mathbf{r}_j$ with induced moments $\mathbf{p}_j(\omega) = p_j(\omega)\mathbf{e}_j$ oriented along $\mathbf{e}_j$ $(j = a, d)$. The dipoles are driven by the common electric field,

$$\mathbf{p}_j(\omega) = \alpha_j(\omega)\mathbf{E}(\mathbf{r}_j, \omega) + \delta_{jd}\mathbf{p}_d^0(\omega), \tag{15.46}$$

where $\alpha_j(\omega) = \alpha_j'(\omega) + i\alpha_j''(\omega)$ is complex polarizability assumed here isotropic, $\mathbf{p}_d^0(\omega) = \alpha_d(\omega)\mathbf{e}_d E_0$ is the donor's initial dipole moment with some constant E_0 depending on excitation, and δ_{jk} is Kroniker's symbol. The electric field $\mathbf{E}$ is, in turn, the solution of Maxwell's equation with dipole sources [33]:

$$\mathbf{E}(\mathbf{r},\omega) = \frac{4\pi\omega^2}{c^2}\sum_j \mathbf{G}(\mathbf{r},\mathbf{r}_j;\omega)\cdot\mathbf{p}_j(\omega), \tag{15.47}$$

where $\mathbf{G}(\mathbf{r},\mathbf{r}';\omega)$ is Maxwell's equation Green's dyadic, satisfying $\boldsymbol{\nabla}\times\boldsymbol{\nabla}\times\hat{\mathbf{G}} - \varepsilon(\mathbf{r},\omega)(\omega/c)^2\hat{\mathbf{G}} = \hat{\mathbf{I}}$, and $\varepsilon(\mathbf{r},\omega)$ equals metal permittivity, $\varepsilon(\omega)$, inside the metal region, and that of the outside medium, ε_0, otherwise. The quantity of interest is energy absorbed by the acceptor in the unit frequency interval,

$$\frac{dW_{ad}}{d\omega} = -\frac{\omega}{\pi}\mathrm{Im}\left[\mathbf{p}_a^*(\omega)\cdot\mathbf{E}(\mathbf{r}_a,\omega)\right] = \frac{\omega\alpha_a''}{\pi}\left|\frac{p_a}{\alpha_a}\right|^2, \tag{15.48}$$

where we used $\mathbf{E}(\mathbf{r}_a,\omega) = \mathbf{p}_a(\omega)/\alpha_a(\omega)$ from Eq. (15.46). A closed system for $p_j(\omega)$ is obtained by using Eq. (15.47) to eliminate the electric field from Eq. (15.46),

$$p_j(\omega) + \alpha_j\sum_k D_{jk}(\omega)p_k(\omega) = \delta_{jd}p_d^0(\omega), \tag{15.49}$$

where we introduce the frequency-dependent matrix

$$D_{jk}(\omega) = -\frac{4\pi\omega^2}{c^2}\mathbf{e}_j\cdot\mathbf{G}(\mathbf{r}_j,\mathbf{r}_k;\omega)\cdot\mathbf{e}_k. \tag{15.50}$$

Expressing p_a from Eq. (15.49), we obtain

$$\frac{dW_{ad}}{d\omega} = \frac{\omega E_0^2}{\pi}\frac{|\tilde{\alpha}_d|^2\,\alpha_a''}{|1+\alpha_a D_{aa}|^2}\left|\tilde{D}_{ad}\right|^2, \tag{15.51}$$

where $\tilde{D}_{ad} = D_{ad}\left[1-\tilde{\alpha}_d D_{da}\tilde{\alpha}_a D_{ad}\right]^{-1}$ is donor–acceptor coupling that includes high-order transitions, and

$$\tilde{\alpha}_j(\omega) = \frac{\alpha_j(\omega)}{1+D_{jj}(\omega)\alpha_j(\omega)} \tag{15.52}$$

is the molecule's dressed polarizability satisfying the relation

$$\tilde{\alpha}_j'' + D_{jj}''|\tilde{\alpha}_j|^2 = \frac{\alpha_j''}{\left|1+D_{jj}\alpha_j\right|^2}, \tag{15.53}$$

which expresses the energy balance between total extinction described by $\tilde{\alpha}_j''$, external losses such as radiation and dissipation in metal encoded in $D_{jj}''(\omega)$, and absorption in the presence of environment (right-hand side).

To gain more insight, recover first Förster's FRET from Eq. (15.51). For a high-yield donor ($\alpha_d'' = 0$), Eq. (15.53) yields the optical theorem $\tilde{\alpha}_{d0}'' = \frac{2}{3}k^3|\tilde{\alpha}_{d0}|^2$,

where

$$\tilde{\alpha}_{j0} = \frac{\alpha_j}{1 - i\frac{2}{3}k^3\alpha_j} \tag{15.54}$$

is polarizability in radiation field and we use free space expression for $D^0_{jj} = -i\frac{2}{3}k^3$. The near field coupling is

$$D^0_{ad} = \left[\mathbf{e}_a \cdot \mathbf{e}_d - 3(\mathbf{e}_a \cdot \hat{\mathbf{r}}_{ad})(\mathbf{e}_d \cdot \hat{\mathbf{r}}_{ad})\right]/r^3_{ad} \tag{15.55}$$

with $\hat{\mathbf{r}} = \mathbf{r}/r$, while $\alpha_a D^0_{aa} \sim \alpha_a k^3$ is negligible. The radiated energy of an isolated donor can be derived in a similar manner as

$$W_d = \frac{E_0^2}{\pi}\int d\omega\omega\tilde{\alpha}''_{d0}(\omega). \tag{15.56}$$

Using the optical theorem, Eq. (15.51) leads to Eq. (15.45) with

$$\sigma_a(\omega) = \frac{4\pi}{3}k\alpha''_a(\omega), \quad f_d(\omega) = \frac{\omega\tilde{\alpha}''_{d0}(\omega)}{\int d\omega\omega\tilde{\alpha}''_{d0}(\omega)}, \tag{15.57}$$

where the free space donor's spectral function $f_d(\omega)$ is integral-normalized to unity.

Turning to the general case, we note that for a high-yield donor, the energy balance relation Eq. (15.53) implies the optical theorem in an absorptive environment,

$$\tilde{\alpha}''_d = -D''_{dd}|\tilde{\alpha}_d|^2 = \frac{2}{3}k^3|\tilde{\alpha}_d|^2\frac{\Gamma_d}{\gamma^r_d}, \tag{15.58}$$

where $\Gamma_j = -\mu_j^2 D''_{jj}$ is the molecule's *full* decay rate [33] and $\gamma^r_j = \frac{2}{3}k^3\mu_j^2$ is its radiative decay rate (μ_j is the dipole matrix element). Using this relation and normalizing Eq. (15.51) to the radiated energy of an isolated donor (Eq. (15.56)), we obtain

$$\frac{1}{W_d}\frac{dW_{ad}}{d\omega} = \frac{9}{8\pi k^4}\frac{\gamma^r_d}{\Gamma_d(\omega)}\tilde{f}_d(\omega)\tilde{\sigma}_a(\omega)\left|\tilde{D}_{da}\right|^2, \tag{15.59}$$

where

$$\bar{\sigma}_a = \frac{4\pi k}{3}\frac{\alpha''_a}{|1+\alpha_a D_{aa}|^2}, \quad \tilde{f}_d(\omega) = \frac{\omega\tilde{\alpha}''_d(\omega)}{\int d\omega\omega\tilde{\alpha}''_{d0}(\omega)} \tag{15.60}$$

are the acceptor's absorption cross section and the donor's spectral function modified by the environment [compare to Eq. (15.57)]. Note that, in the presence of metal, $\tilde{f}_d(\omega)$ is no longer integral-normalized to unity. After frequency integration, we finally obtain

$$\frac{W_{ad}}{W_d} = \frac{9}{8\pi}\int\frac{d\omega}{k^4}\frac{\gamma^r_d}{\Gamma_d(\omega)}\tilde{f}_d(\omega)\tilde{\sigma}_a(\omega)\left|\tilde{D}_{da}(\omega)\right|^2, \tag{15.61}$$

Equation (15.61) includes *all* relevant energy flow channels in the system. Interactions of the molecules with the metal alter the positions and shapes of the optical bands. While the coupling D_{ad} is enhanced due to plasmon-mediated channels, the factor γ_d^r/Γ_d accounts for FRET quenching due to the donor's energy transfer to the metal followed by dissipation and radiation. The absence of this factor leads to spuriously large FRET [29, 62–65]. Note that Eq. (15.61) was obtained for a high-yield donor with no assumptions on molecules' emission or absorption spectral bands, which are usually broad and asymmetric due to vibrational and rotational modes. Rigorous treatment of molecules' internal relaxation processes would require fully quantum-mechanical consideration which is beyond our scope. However, if we assume Lorenzian lineshape for the donor's effective polarizability $\tilde{\alpha}_d(\omega)$, which is a reasonable approximation in most cases, then it is easy to show that Eq. (15.61) is valid for low-yield donors as well upon replacing γ_d^r with the free space fluorescence rate γ_d.

To highlight the role of PERT in the far field FRET, consider energy transfer from remote donors to an acceptor located *near* the metal surface. In this case, the donor's decay rate and spectral function are unaffected by metal and FRET is dominated by the following process: A donor first radiatively excites a plasmon in the metal which then nonradiatively transfers its energy to the acceptor. The coupling D_{ad} can be derived from Dyson's equation for Green's dyadic,

$$\mathbf{G}(\mathbf{r},\mathbf{r}') = \mathbf{G}^0(\mathbf{r},\mathbf{r}') + k^2\bar{\varepsilon}\int dV_m \mathbf{G}^0(\mathbf{r},\mathbf{r}_m)\cdot\mathbf{G}(\mathbf{r}_m,\mathbf{r}'), \tag{15.62}$$

where integration is restricted to metal region and $\bar{\varepsilon}(\omega) = \varepsilon(\omega)/\varepsilon_0 - 1$. For remote donors, using the far field limit ($kr \gg 1$ and $kr' \ll 1$) of the free Green's dyadic [33], $\mathbf{G}^0(\mathbf{r},\mathbf{r}') = \frac{e^{ikr}}{4\pi r}(\delta_{\mu\nu} - \hat{\mathbf{r}}_\mu\hat{\mathbf{r}}_\nu)$, and averaging out over donors angular positions and their dipoles' orientations, we obtain PERT per donor

$$\frac{W_{ad}^r}{W_d} \approx \frac{1}{4\pi r_{ad}^2}\int d\omega f_d(\omega)\bar{\sigma}_a(\omega)A(\omega), \tag{15.63}$$

where

$$A = \left|\mathbf{e}_a + k^2\bar{\varepsilon}\int dV_m \mathbf{G}(\mathbf{r}_m,\mathbf{r}_a)\cdot\mathbf{e}_a\right|^2 \tag{15.64}$$

is the plasmon enhancement factor for a metal nanostructure of general shape. If the acceptor is located at distance r_a from the center of a spherical NP, we get $A = A^\perp\cos^2\phi + A^\parallel\sin^2\phi$, where

$$A^\perp = \left|1 + 2\frac{\alpha_1}{r_a^3}\right|^2, \quad A^\parallel = \left|1 - \frac{\alpha_1}{r_a^3}\right|^2 \tag{15.65}$$

are enhancement factors for normal and parallel dipole orientations[24], $\alpha_1(\omega)$ is the NP dipole polarizability, and $\cos\phi = \hat{\mathbf{r}}_a\cdot\mathbf{e}_a$. Equation (15.63) extends the far field

radiative FRET theory [38, 61] to plasmonic systems. In fact, the PERT mechanism can dominate FRET even in the *near field*, as our numerical calculations below demonstrate.

15.2.3 Numerical Results for Plasmon-Assisted Single-Donor Energy Transfer Near Metal Nanoparticle

As an example, consider a donor and acceptor near spherical Ag NP in water with normal dipole orientations (see Fig. 15.1). The near field matrix D_{jk} is readily obtained from the Mie's theory Green's dyadic [25] as $D_{jk} = D^0_{jk} + D^r_{jk} + D^{nr}_{jk}$, where [13]

$$D^r_{jk} = -\,i\frac{2}{3}k^3\left[1 + 2\alpha_1\left(\frac{1}{r_j^3} + \frac{1}{r_k^3}\right) + \frac{4|\alpha_1|^2}{r_j^3 r_k^3}\right](\hat{\mathbf{r}}_j \cdot \hat{\mathbf{r}}_k),$$
$$D^{nr}_{jk} = -\sum_l \frac{\alpha_l (l+1)^2}{r_j^{l+2} r_k^{l+2}} P_l(\hat{\mathbf{r}}_j \cdot \hat{\mathbf{r}}_k) \tag{15.66}$$

are NP-induced radiative and nonradiative terms, $\alpha_l = R^{2l+1}\frac{l(\varepsilon-\varepsilon_0)}{l\varepsilon+(l+1)\varepsilon_0}$ is NP polarizability, $P_l(x)$ is a Legendre polynomial, $D^0_{ad} = (1+\sin^2\theta/2)/r^3_{ad}$, $\hat{\mathbf{r}}_a \cdot \hat{\mathbf{r}}_d = \cos\theta$, and angular momenta up to $l = 50$ are included. Full decay rates are $\Gamma_j = -\left(3/2k^3\right)\gamma^r_j D''_{jj}$. We consider, for simplicity, a high-yield donor with a broad emission band due to the vibrational modes. Molecules optical bands are Lorentzians of width 0.05 eV centered at 2.95 eV and 3.2 eV with maximal overlap at about SP energy of 3.08 eV (see inset in Fig. 15.12a), $\sigma_a(\omega)$ was normalized to its total $\int d\omega\sigma_a(\omega)$, and modified $\bar{\sigma}_a$, $\tilde{f}_d$, and $\tilde{D}_{ad}$ were found using Eq. (15.66).

In Fig. 15.11, we plot W_{ad} versus the molecule's distance d from the $R = 30$ nm NP surface at $\theta = \pi/3$ with equal $d_a = d_d = d$ and with changing $d_d = d$ at fixed d_a. Three models—the full Eq. (15.61), its nonradiative part only, and the Gersten–Nitzan model [62, 63]—are compared to Förster's transfer Eq. (15.45). For $d_d = d_a$, W_{ad} is about three times larger than W^F_{ad} and rapidly decays with d, while for $d/R \ll 1$ it is quenched by metal. There is no enhancement if only the nonradiative channel is included in Eq. (15.61). In contrast, the Gersten-Nitzan model yields much greater enhancement (up to 10^5) for $d/R \ll 1$ since it includes no quenching effects. However, at fixed d_a and $d_d/R \gtrsim 1$, the full W_{ad} is the largest one (see Fig. 15.11b) due to the dominant role of the PERT mechanism, as discussed above.

The interplay of different FRET contributions is shown in Fig. 15.12 featuring spectral density Eq. (15.59) together with quenching factor γ^r_d/Γ_d and coupling $|D_{ad}|^2$ at fixed d. $dW_{ad}/d\omega$ has a sharp plasmon peak which disappears if only the nonradiative channel is included (see Fig. 15.12a). PERT channel *reduces* γ^r_d/Γ_d due to SP-enhanced radiation but it strongly *enhances* D_{ad} (see Fig. 15.12b), the net result being FRET increase, while in the nonradiative channel the enhancement

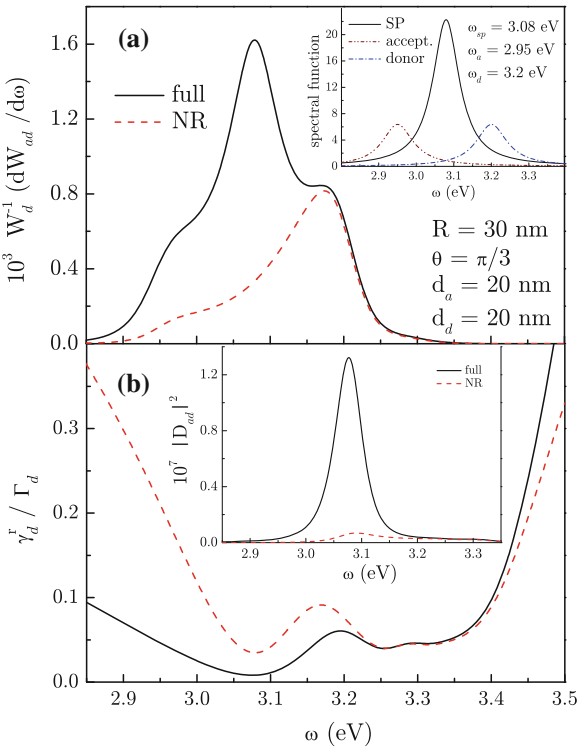

Fig. 15.12 **a** Spectral function Eq. (15.59) and molecules' optical bands relative to SP band α_1/R^3 (*inset*) are shown together with **b** quenching factor γ_d^r/Γ_d and coupling $|D_{ad}|^2$ (*inset*) using full and nonradiative (NR) models

and quenching effects nearly cancel out. Weak high-frequency oscillations are due to high-l plasmons.

The relative rates of plasmon-assisted FRET and Förster's transfer are highly sensitive to the system's geometry. RET is quenched if both molecules are close to the NP surface (see Fig. 15.13a) but it becomes enhanced if donor–NP distance increases (inset). For $\theta = \pi/3$ RET is enhanced if $d_d \gtrsim R$ (see Fig. 15.13b), but for $\theta = \pi$ it is strongly enhanced for nearly all d (inset). In fact, NP acts as a *hub* that couples equally well nearby and remote molecules with different θ while Förster's transfer drops for large r_{ad}. For smaller NP sizes, the role of PERT becomes less pronounced yet remains dominant for larger donor-NP distances.

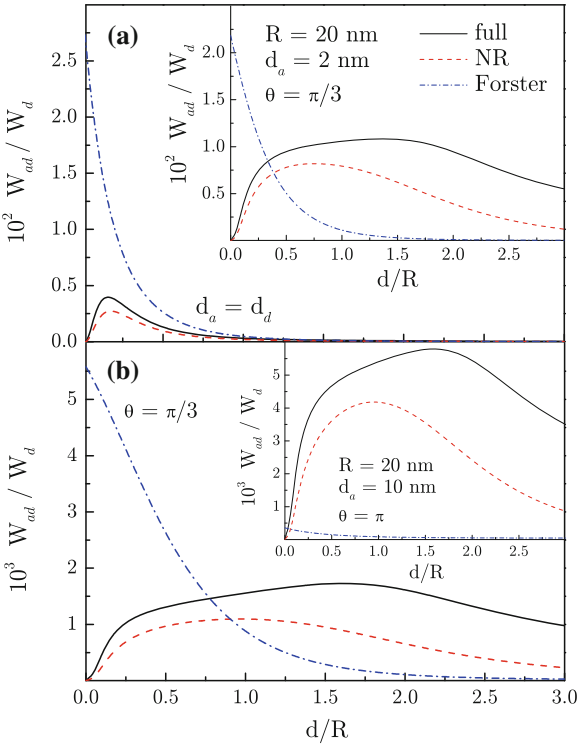

Fig. 15.13 FRET versus distance for $R = 20$ nm Ag NP is shown **a** at $\theta = \pi/3$ with $d_a = d_d$ and $d_a = 2$ nm (*inset*) and **b** with $d_a = 10$ nm at $\theta = \pi/3$ and $\theta = \pi$ (*inset*) using full, nonradiative (NR), and Förster models

15.2.4 Cooperative Plasmon-Assisted Resonance Energy Transfer from an Ensemble of Donor to an Acceptor

We now generalize the formalism developed in the previous section to the case of N donors and an acceptor near the surface of a metal nanostructure and represented as point-like dipoles located, respectively, at $\mathbf{r}_j$ ($j = 1, \ldots, N$) and $\mathbf{r}_a$ with induced moments $\mathbf{p}_j(\omega) = p_j(\omega)\mathbf{e}_j$ and $\mathbf{p}_a(\omega) = p_a(\omega)\mathbf{e}_a$ oriented along $\mathbf{e}_j$ and $\mathbf{e}_a$. The dipoles are driven by the common electric field,

$$\begin{aligned} \mathbf{p}_a(\omega) &= \alpha_a(\omega)\mathbf{E}(\mathbf{r}_a, \omega), \\ \mathbf{p}_j(\omega) &= \alpha_j(\omega)\mathbf{E}(\mathbf{r}_j, \omega) + \mathbf{p}_j^0(\omega), \end{aligned} \tag{15.67}$$

where $\alpha_a(\omega) = \alpha_a'(\omega) + i\alpha_a''(\omega)$ and $\alpha_j(\omega) = \alpha_j'(\omega) + i\alpha_j''(\omega)$ are aceptor's and donors' complex polarizabilities, $\mathbf{p}_d^0(\omega) = \alpha_d(\omega)\mathbf{e}_j E_0 e^{i\varphi_j}$ are donors initial dipole moments with some constant E_0 and random phases φ_j. The electric field $\mathbf{E}$ is, in

turn, the solution of Maxwell's equation with dipole sources [33]

$$\mathbf{E}(\mathbf{r},\omega) = \frac{4\pi\omega^2}{c^2}\sum_{\beta}\mathbf{G}(\mathbf{r},\mathbf{r}_\beta;\omega)\cdot\mathbf{p}_\beta(\omega), \tag{15.68}$$

where index $\beta = (a, j)$ runs over *all* dipoles positions, $\mathbf{G}(\mathbf{r},\mathbf{r}';\omega)$ is Maxwell's equation Green's dyadic, satisfying $\nabla\times\nabla\times\hat{\mathbf{G}} - \varepsilon(\mathbf{r},\omega)(\omega/c)^2\hat{\mathbf{G}} = \hat{\mathbf{I}}$, and $\varepsilon(\mathbf{r},\omega)$ equals metal permittivity, $\varepsilon(\omega)$, inside the metal region and that of outside medium, ε_0, otherwise. The quantity of interest is energy absorbed by the acceptor in unit frequency interval,

$$\frac{dW_{ad}}{d\omega} = -\frac{\omega}{\pi}\mathrm{Im}\left[\mathbf{p}_a^*(\omega)\cdot\mathbf{E}(\mathbf{r}_a,\omega)\right] = \frac{\omega\alpha_a''}{\pi}\left|\frac{p_a}{\alpha_a}\right|^2, \tag{15.69}$$

where we used $\mathbf{E}(\mathbf{r}_a,\omega) = \mathbf{p}_a(\omega)/\alpha_a(\omega)$ from Eq. (15.67). A closed system for $p_j(\omega)$ is obtained by using Eq. (15.68) to eliminate the electric field from Eq. (15.67),

$$\begin{aligned} p_a + \alpha_a D_{aa} p_a + \alpha_d \sum_j D_{aj} p_j &= 0, \\ p_j + \alpha_d D_{ja} p_a + \alpha_d \sum_k D_{jk} p_k &= p_j^0, \end{aligned} \tag{15.70}$$

where we introduced frequency-dependent matrix

$$D_{\beta\beta'}(\omega) = -\frac{4\pi\omega^2}{c^2}\mathbf{e}_\beta\cdot\mathbf{G}(\mathbf{r}_\beta,\mathbf{r}_{\beta'};\omega)\cdot\mathbf{e}_{\beta'}. \tag{15.71}$$

Expressing p_a from Eq. (15.70),

$$p_a = -\frac{\alpha_a}{1+\alpha_a\tilde{D}_{aa}}\sum_{jk} D_{aj}S_{jk}p_k^0, \tag{15.72}$$

where

$$S_{jk}^{-1}(\omega) = \delta_{jk} + \alpha_d D_{jk}(\omega) \tag{15.73}$$

and

$$\tilde{D}_{aa} = D_{aa} - \alpha_d\sum_{jk} D_{aj}S_{jk}D_{ka}. \tag{15.74}$$

Averaging over random phases φ_j, we obtain

$$\frac{dW}{d\omega} = \frac{\omega E_0^2}{\pi}\frac{|\alpha_d|^2\,\alpha_a''}{\left|1+\alpha_a\tilde{D}_{aa}\right|^2}\sum_{jkl} D_{aj}S_{jk}S_{kl}^\dagger D_{la}^\dagger. \tag{15.75}$$

The energy transfer to the acceptor takes place from system eigenstates rather than from individual donors. The eigenstates are determined by diagonalizing the matrix D_{jk}. We define the eigenstates $|J\rangle$ as $\hat{D}|J\rangle = D_J|J\rangle$, where the eigenvalues D_J can be presented as

$$D_J = \frac{2}{3}k^3 \left(\Delta_J - i\Gamma_J\right)/\gamma_d^r. \tag{15.76}$$

Here Δ_J and Γ_J are, respectively, frequency shift and full decay rate in the presence of metal and $\gamma_d^r = \frac{2}{3}k^3\mu_d^2$ is donors free space radiative decay rate (μ_d is dipole matrix element). We now introduce the acceptor coupling to the eigenstates,

$$D_{aJ} = \sum_j D_{aj}\langle j|J\rangle, \tag{15.77}$$

where $\langle j|J\rangle$ stands for jth element of eigenvector J, and dressed acceptor and eigenstates polarizabilities,

$$\tilde{\alpha}_J = \frac{\alpha_d}{1 + D_J\alpha_d}, \quad \tilde{\alpha}_a = \frac{\alpha_a}{1 + D_{aa}\alpha_a}, \tag{15.78}$$

satisfying the relation

$$\tilde{\alpha}_J'' + D_J''|\tilde{\alpha}_J|^2 = \frac{\alpha_d''}{|1 + D_J\alpha_d|^2}, \tag{15.79}$$

which expresses energy balance of an *eigenstate* between total extinction described by $\tilde{\alpha}_j''$, external losses such as radiation and dissipation in metal encoded in $D_{jj}''(\omega)$, and absorption in the presence of environment (r.h.s.). For high-yield donors ($\alpha_d'' = 0$), Eq. (15.79) implies the optical theorem in absorptive environment for each system eigenstate,

$$\tilde{\alpha}_J'' = -D_J''|\tilde{\alpha}_J|^2 = \frac{2}{3}k^3|\tilde{\alpha}_J|^2\frac{\Gamma_J}{\gamma_d^r}. \tag{15.80}$$

The radiated energy of an isolated donor, W_d, can be derived in a similar manner as

$$W_d = \frac{E_0^2}{\pi}\int d\omega\omega\tilde{\alpha}_{d0}''(\omega), \tag{15.81}$$

where $\tilde{\alpha}_{d0} = \alpha_d\left(1 - i\frac{2}{3}k^3\alpha_d\right)^{-1}$ is donor's polarizability in radiation field. Using the optical theorem and normalizing Eq. (15.75) to W_d, we obtain

$$\frac{1}{W_d}\frac{dW_{ad}}{d\omega} = \frac{9\tilde{\sigma}_a(\omega)}{8\pi k^4}\sum_J \frac{\gamma_d^r}{\Gamma_J(\omega)}\left|\tilde{D}_{aJ}\right|^2 \tilde{f}_J(\omega), \tag{15.82}$$

where

$$\tilde{D}_{aJ} = \frac{D_{aJ}}{1 - \tilde{\alpha}_a \sum_J D_{aJ} \tilde{\alpha}_J D_{Ja}} \tag{15.83}$$

is acceptor–eigenstate coupling that includes high-order transitions, and

$$\bar{\sigma}_a = \frac{4\pi k}{3} \frac{\alpha_a''}{|1 + \alpha_a D_{aa}|^2}, \quad \tilde{f}_J(\omega) = \frac{\omega \tilde{\alpha}_J''(\omega)}{\int d\omega \omega \tilde{\alpha}_{d0}''(\omega)} \tag{15.84}$$

are acceptor's absorption crossection and eigenstates's spectral function. Note that the latter is not integral-normalized to unity.

Expression (15.82) generalizes the FRET from a single donor, Eq. (15.61), to the case of an ensemble. The energy transfer now takes place from each system eigenstate independently and the full transferred energy is obtained by summing up over all eigenstates' contributions. As we show below, in cooperative regime, superradiant and subradiant eigenstates provide significantly more efficient transfer than individual donors.

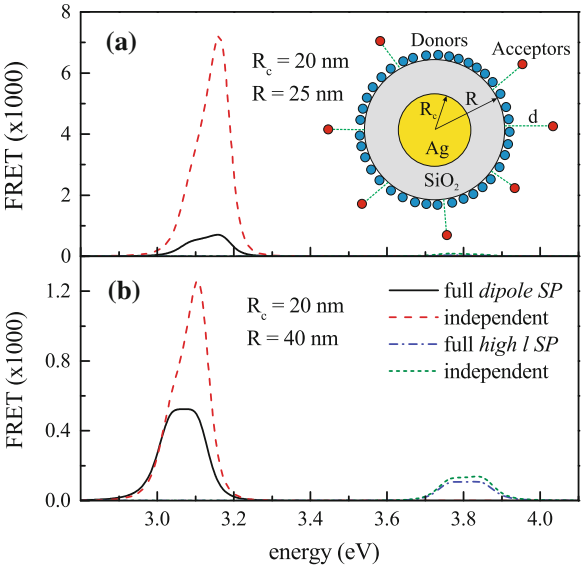

Fig. 15.14 FRET for $N = 100$ donors on top of spherical core-shell NP with Ag core radius $R_c = 20$ nm and SiO_2 shell thickness 5 nm (**a**) and 20 nm (**b**) with acceptor at $d = 10$ nm from NP surface. Full calculations for two sets of donors and acceptors with their emission and absorption bands tuned to dipole and high-l SP resonances are compared to independent donors approximation

15.2.5 Numerical Results for Cooperative Energy Transfer

As an example, consider an ensemble of N donors randomly distributed on surface of spherical core-shell NP of radius R submerged in water, with Ag core radius R_c and Silica shell thickness $L = R - R_c$, and a single acceptor separated from the NP surface by distance d (see inset in Fig. 15.14). We assume that the donors' and acceptor's dipole orientations are all normal to the NP surface and their respective emission and absorption bands are Lorentzians of width 0.1 eV centered at energies ω_d and ω_a which we chose depending on particular FRET mechanism we wish to study (see below). The dipole surface plasmon (SP) spectral band is centered at about 3.15 eV and weakly depends on shell thickness, while energies of higher angular momenta ($l \geq 2$) SPs are distributed in the interval 3.75 and 4.0 eV. Note that high-l SPs with energies above 4.0 eV are damped by electronic interband transitions in Ag.

The coupling matrix $D_{\beta\beta'}$ can be decomposed into free space and NP-induced radiative and nonradiative parts, $D_{\beta\beta'} = D^0_{\beta\beta'} + D^r_{\beta\beta'} + D^{nr}_{\beta\beta'}$, which, in long-wave limit and for normal dipole orientations (i.e., $\mathbf{e}_\beta = \hat{\mathbf{r}}_\beta$), can be readily obtained from Mie's theory Green's dyadic as [13]

$$
\begin{aligned}
D^0_{\beta\beta'} &= \left[1 + \sin^2\left(\theta_{\beta\beta'}/2\right)\right]/r^3_{\beta\beta'},\\
D^r_{\beta\beta'} &= -\,i\frac{2}{3}k^3\left[1 + 2\alpha_1\left(\frac{1}{r^3_\beta} + \frac{1}{r^3_{\beta'}}\right) + \frac{4|\alpha_1|^2}{r^3_\beta r^3_{\beta'}}\right](\hat{\mathbf{r}}_\beta \cdot \hat{\mathbf{r}}_{\beta'}),\\
D^{nr}_{\beta\beta'} &= -\sum_l \frac{\alpha_l (l+1)^2}{r^{l+2}_\beta r^{l+2}_{\beta'}} P_l(\hat{\mathbf{r}}_\beta \cdot \hat{\mathbf{r}}_{\beta'}),
\end{aligned}
\tag{15.85}
$$

where α_l is core-shell NP polarizability, $P_l(x)$ is Legendre polynomial, $\hat{\mathbf{r}}_\beta$ is the unit vector along radial direction pointing at βth molecule, and $\theta_{\beta\beta'}$ is the angle between βth and β'th molecules positions ($\hat{\mathbf{r}}_\beta \cdot \hat{\mathbf{r}}_{\beta'} = \cos\theta_{\beta\beta'}$). In all calculations, we used experimental Ag dielectric function and included angular momenta up to $l_{\max} = 75$.

We expect that in cooperative regime, the superradiant states are dominant at energies near the dipole SP resonance, while subradiant states are best developed at energies close to those of $l = 2$ and 3 SPs (note that, at a given distance, dipole–NP interaction rapidly falls with increasing l). Accordingly, we use two sets of donors and acceptors with energies tailored to interact with dipole SP and with high-l SPs. For the first set, the donors's energy is chosen to coincide with dipole SP resonance, while for the second set we chose $\omega_d = 3.85$ eV; in both cases, acceptor's energy is redshifted from donor's energy by $\omega_d - \omega_a = 0.1$ eV.

In Figs. 15.14 and 15.15 we plot calculated energy dependence of normalized FRET, given by Eq. (15.82), for core-shell NP with Ag core radius $R_c = 20$ nm and silica shell thickness in the range from 5 to 50 nm (i.e., overall NP radius R between 25 and 70 nm). The acceptor distance to NP surface was set at $d = 10$ nm and all curves were normalized *per donor*. Each panel shows dependencies for two donor–acceptor sets which are compared to those of independent donors near NP,

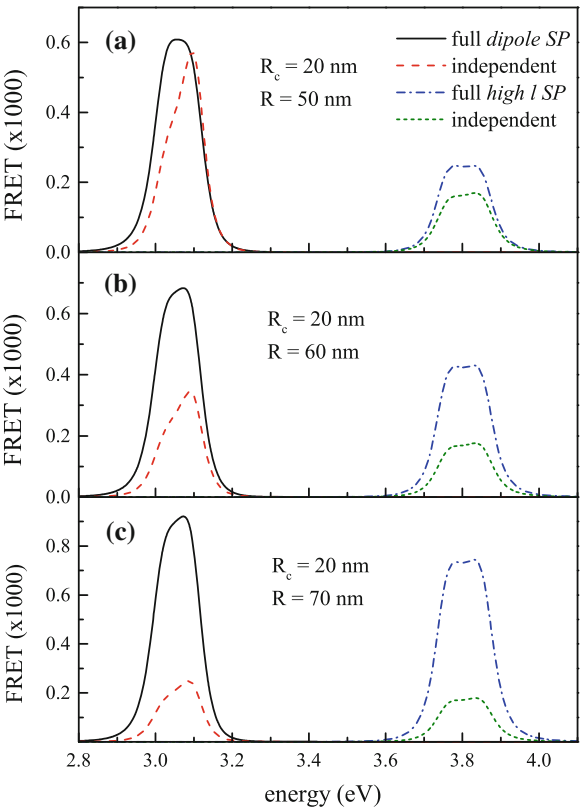

Fig. 15.15 FRET for $N = 100$ donors on top of spherical core-shell NP with Ag core radius $R_c = 20$ nm and SiO_2 shell thickness 30 nm (**a**), 40 nm (**b**), and 50 nm (**c**) with acceptor at $d = 10$ nm from NP surface. Full calculations for two sets of donors and acceptors with their emission and absorption bands tuned to dipole and high-l SP resonances are compared to independent donors approximation

i.e., without plasmon-induced coupling between them (this is achieved by setting to zero nondiagonal matrix elements of D_{ij}).

For relatively thin shells (i.e., donors close to metal core), the independent donor approximation substantially (by factor ~ 10) overestimates FRET (see Fig. 15.14). For the first donor–acceptor set (dipole SP region), the full calculation yields much smaller fraction of transferred since it accounts for significant energy dissipation in metal during multiple NP-induced transitions between the donors. The dissipation is much stronger in the high-l SP energy range, and no significant transfer takes place within the second donor–acceptor set.

With increasing shell thickness, as donors move away from the metal core, the system transitions into cooperative regime [12, 13]. In the dipole SP region, the transfer from *superradiant* state becomes increasingly larger than from individual

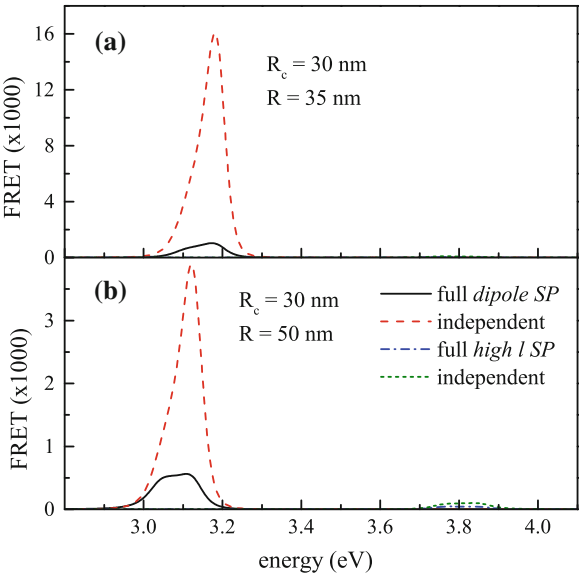

Fig. 15.16 FRET for $N = 100$ donors on top of spherical core-shell NP with Ag core radius $R_c = 30$ nm and SiO_2 shell thickness 5 nm (**a**) and 20 nm (**b**) with acceptor at $d = 10$ nm from NP surface. Full calculations for two sets of donors and acceptors with their emission and absorption bands tuned to dipole and high-l SP resonances are compared to independent donors approximation.

donors due to much stronger coupling of the supperadiant state to the acceptor (see Fig. 15.15). At the same time, with reduced dissipation in metal, the energy transfer assisted by high-l SPs sharply increases. Remarkably, cooperative FRET from *subradiant* states mediated by high-l SPs significantly exceeds FRET from independent donors and, for thicker shells, becomes comparable to FRET from superradiant states. Here FRET amplification is due to much weaker dissipation of subradiant states with energies lying in high-l SP region. In other words, the energy trapped in subradiant states can be transferred out of the system (to the acceptor) to be utilized.

With increasing metal core radius, the plasmon-enhanced radiative coupling and hence cooperative effects increase as well [12, 13], leading to stronger FRET amplification. This is illustrated in Figs. 15.16 and 15.17 where we show normalized FRET for a larger system; Ag core radius $R_c = 30$ and shell thickness changing between 5 and 80 nm. For relatively thin shells 5 and 20 nm (see Fig. 15.16), the donors' coupling through the NP results in a greater energy fraction that dissipates in the metal as compared to independent donors and, therefore, in a smaller fraction of energy transferred to the acceptor. With increasing shell thickness (see Fig. 15.17), as the cooperative regime is established, the FRET from both superradiant and subradiant states significantly exceeds FRET from independent donors. A larger metal core leads to stronger cooperative amplification of FRET which now reaches factor of 10 for the largest NP (see Fig. 15.17c). Importantly, the evolution of cooperative

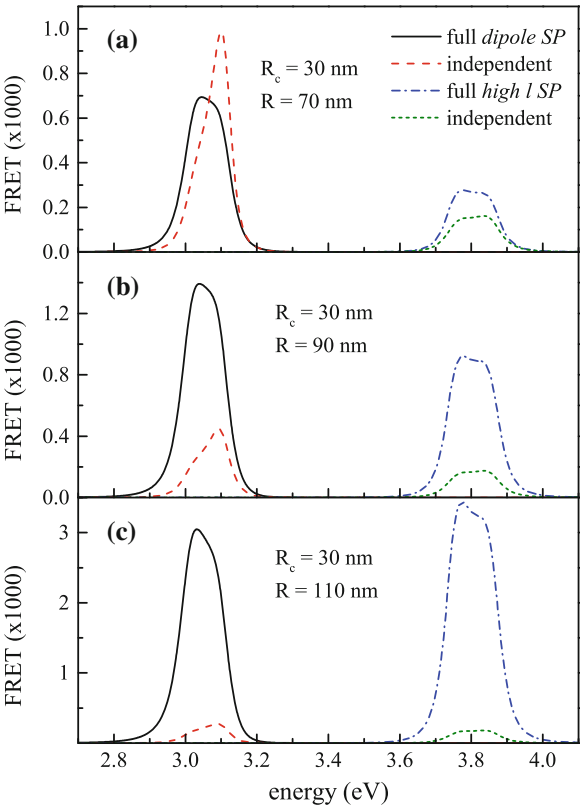

Fig. 15.17 FRET for $N = 100$ donors on top of spherical core-shell NP with Ag core radius $R_c = 30$ nm and SiO_2 shell thickness 40 nm (**a**), 60 nm (**b**), and 80 nm (**c**) with acceptor at $d = 10$ nm from NP surface. Full calculations for two sets of donors and acceptors with their emission and absorption bands tuned to dipole and high-l SP resonances are compared to independent donors approximation.

FRET and of FRET from independent donors with increasing shell thickness show opposite trends: the normalized cooperative FRET *increases* for thicker shells while energy transfer from independent donors is reduced (see Fig. 15.17).

Acknowledgments This work was supported in part through NSF under Grant DMR-1206975, CREST Center, and EPSCOR program.

Appendix

Here we collect relevant some formulas for the electric field Green dyadic in the presence of metal NP. The Green dyadic satisfies Maxwell equation

$$\boldsymbol{\nabla} \times \boldsymbol{\nabla} \times \hat{\mathbf{G}} - k^2 \varepsilon(r) \hat{\mathbf{G}} = \hat{\mathbf{I}}, \tag{15.86}$$

where $\varepsilon(r) = \varepsilon(\omega)\theta(R - r) + \varepsilon_0 \theta(r - R)$ is local dielectric function ($\theta(x)$ is the step-function). The Green dyadic can be split into free space and Mie-scattered parts, $G_{\mu\nu}(\mathbf{r}, \mathbf{r}') = G^0_{\mu\nu}(\mathbf{r}, \mathbf{r}') + G^s_{\mu\nu}(\mathbf{r}, \mathbf{r}')$, where the free-space Green dyadic is

$$G^0_{\mu\nu}(\mathbf{r} - \mathbf{r}') = \left(\delta_{\mu\nu} - \frac{\nabla_\mu \nabla'_\nu}{k^2}\right) g(\mathbf{r} - \mathbf{r}'), \tag{15.87}$$

with

$$g(\mathbf{r}) = \frac{e^{ikr}}{4\pi r} \tag{15.88}$$

satisfying a scalar equation

$$(\triangle + k^2) g(\mathbf{r}) = -\delta(\mathbf{r}). \tag{15.89}$$

Consider first the free space part. Its near field expression can be obtained in the long wave approximation, i.e. by expanding in $kr \ll 1$. In the first order,

$$G^0_{\mu\nu}(\mathbf{r}) = \frac{1}{4\pi k^2 r^3}\left[\frac{3\mathbf{r}_\mu \mathbf{r}_\nu}{r^2} - \delta_{\mu\nu}\right] + \frac{ik}{6\pi}\delta_{\mu\nu}. \tag{15.90}$$

In the far field limit, i.e., $kr \gg 1$ and $kr' \ll 1$, the free-space part can be expanded via Bessel functions,

$$\frac{e^{ik|r-r'|}}{4\pi|r - r'|} = ik \sum_{lm} j_l(kr') h_l(kr) Y_{lm}(r) Y^*_{lm}(r'), \tag{15.91}$$

which are approximated as

$$j_l(kr') = \frac{(kr')^l}{(2l+1)!!}, \quad h_l(kr) = (-i)^{l+1} \frac{e^{ikr}}{kr}, \tag{15.92}$$

yielding

$$G^0_{\mu\nu}(\mathbf{r},\mathbf{r}') = \left(\delta_{\mu\nu} - \frac{1}{k^2}\nabla_\mu\nabla'_\nu\right)\frac{e^{ikr}}{r}\left[\frac{1}{4\pi} - \frac{ikr'}{3}\sum_m Y_{1m}(\hat{\mathbf{r}})Y^*_{1m}(\hat{\mathbf{r}}')\right]. \tag{15.93}$$

After differentiation, the far field asymptotics takes the form

$$G^0_{\mu\nu}(\mathbf{r},\mathbf{r}') = \frac{e^{ikr}}{4\pi r}\left[\delta_{\mu\nu} - \frac{4\pi}{3}\sum_m \hat{\mathbf{r}}_\mu Y_{1m}(\hat{\mathbf{r}})\chi^{\nu *}_{1m}(\mathbf{r}')\right], \tag{15.94}$$

where we introduced $\chi^\mu_{lm}(\mathbf{r}) = \nabla_\mu[r^l Y_{lm}(\hat{\mathbf{r}})$ and $\psi^\mu_{lm}(\mathbf{r}) = \nabla_\mu[r^{-l-1}Y_{lm}(\hat{\mathbf{r}})]$.

Now turn to the scattered part of the Green dyadic derived from solution of Mie problem for electromagnetic wave scattered on single sphere,

$$G^s_{\mu\nu}(\mathbf{r},\mathbf{r}',\mathbf{k}) = ik\sum_{lm}\left[a_l N^\mu_{lm}(\mathbf{r})N^\nu_{lm}(\mathbf{r}') + b_l M^\mu_{lm}(\mathbf{r})M^\nu_{lm}(\mathbf{r}')\right], \tag{15.95}$$

where the first and second terms are electric and magnetic contributions and a_l and b_l are the Mie coefficients. In the long wave approximation, $kR \ll 1$, the magnetic contribution in Eq.(15.95) can be neglected as $b_l \ll 1$ [24–27]. The Mie coefficient a_l has a form

$$a_l = \frac{\varepsilon_0 j_l(\rho_0)[\rho j_l(\rho)]' - \varepsilon j_l(\rho)[\rho_0 j_l(\rho_0)]'}{\varepsilon_0 h_l(\rho_0)[\rho j_l(\rho)]' - \varepsilon j_l(\rho)[\rho_0 h_l(\rho_0)]'} \tag{15.96}$$

where $\rho_i = k_i R$, $k_i = \frac{\omega}{c}\sqrt{\varepsilon_i}$, and $i = (\varepsilon, \varepsilon_0)$. For $kR \ll 1$, it becomes

$$a_l = -is_l\tilde{\alpha}_l k^{2l+1}, \quad s_l = \frac{l+1}{l(2l+1)[(2l-1)!!]^2}, \tag{15.97}$$

where

$$\tilde{\alpha}_l = \frac{\alpha_l}{1 - is_l k^{2l+1}\alpha_l}, \tag{15.98}$$

is NP multipolar polarizability that accounts for plasmon radiative decay, and

$$\alpha_l = R^{2l+1}\frac{l(\varepsilon - \varepsilon_0)}{l\varepsilon + (l+1)\varepsilon_0}, \tag{15.99}$$

is the standard NP polarizability. The function $\mathbf{N}_{lm}(\mathbf{r})$ is given by

$$\mathbf{N}_{lm}(\mathbf{r}) = \frac{1}{k\sqrt{l(l+1)}}\nabla \times \left[h^{(1)}_l(kr)\mathbf{L}Y_{lm}(\hat{\mathbf{r}})\right], \tag{15.100}$$

where $\mathbf{L} = -i(\mathbf{r} \times \boldsymbol{\nabla})$ is angular momentum operator. Using the following identity,

$$\begin{aligned}\boldsymbol{\nabla} \times \left[h_l^{(1)}(kr)\mathbf{L}Y_{lm}(\hat{\mathbf{r}})\right] &= i\mathbf{r}k^2 h_l^{(1)}(kr)Y_{lm}(\hat{\mathbf{r}}) \\ &+ i\boldsymbol{\nabla}\left[[krh_l^{(1)\prime}(kr) + h_l^{(1)}(kr)]Y_{lm}(\hat{\mathbf{r}})\right],\end{aligned} \tag{15.101}$$

prime standing for derivative, and expanding $h_l^{(1)}(kr) = j_l(kr) + in_l(kr)$ in kr as

$$h_l^{(1)}(kr) = \frac{(kr)^l}{(2l+1)!!} - i\frac{(2l-1)!!}{(kr)^{l+1}}, \tag{15.102}$$

we obtain

$$\mathbf{N}_{lm}(kr) = -\frac{1}{k\sqrt{s_l(2l+1)}}\boldsymbol{\nabla}[\varphi_l(kr)Y_{lm}(\hat{\mathbf{r}})], \tag{15.103}$$

where

$$\varphi_l(kr) = \frac{1}{(kr)^{l+1}} - is_l(kr)^l. \tag{15.104}$$

Thus, for $kr \ll 1$ and $kr' \ll 1$, the scattered part of the Green dyadic has the form

$$\begin{aligned}G^s_{\mu\nu}(\mathbf{r},\mathbf{r}',\mathbf{k}) &\approx ik\sum_{lm}\left[a_l N^{\mu}_{lm}(kr)N^{\nu}_{lm}(kr')\right] \\ &\approx \sum_{lm}\frac{k^{2l}\tilde{\alpha}_l}{2l+1}\nabla_\mu\left[\varphi_l(kr)Y_{lm}(\hat{\mathbf{r}})\right]\nabla'_\nu\left[\varphi_l(kr')Y^*_{lm}(\hat{\mathbf{r}}')\right].\end{aligned} \tag{15.105}$$

This expression can be further simplified by substituting $\tilde{\alpha}_l = \bar{\alpha}_l + is_l k^{2l+1}|\tilde{\alpha}_l|^2$, where $\bar{\alpha}_l = \alpha_l|1 - is_l k^{2l+1}\alpha_l|^{-2}$, and keeping the first two powers of k

$$\begin{aligned}G^s_{\mu\nu}(\mathbf{r},\mathbf{r}') =& \frac{1}{k^2}\sum_{lm}\frac{\bar{\alpha}_l}{(2l+1)}\psi^{\mu}_{lm}(\mathbf{r})\psi^{\nu *}_{lm}(\mathbf{r}') \\ &- i\frac{ks_1}{3}\sum_{m=-1}^{1}\Big[\tilde{\alpha}_1\left[\psi^{\mu}_{1m}(\mathbf{r})\chi^{\nu *}_{1m}(\mathbf{r}') + \chi^{\mu}_{1m}(\mathbf{r})\psi^{\nu *}_{1m}(\mathbf{r}')\right] \\ &- |\tilde{\alpha}_1|^2\psi^{\mu}_{1m}(\mathbf{r})\psi^{\nu *}_{1m}(\mathbf{r}')\Big],\end{aligned} \tag{15.106}$$

which, after adding the free-space part of the Green dyadic and neglecting plasmon radiative decay, leads to Eq. (15.12).

For $kr \gg 1$, with help of Eqs. (15.92), (15.100), and (15.101), we easily obtain

$$\mathbf{N}_{lm}(\mathbf{r}) = -\frac{(-i)^{l+1}e^{ikr}}{k\sqrt{l(l+1)}}\boldsymbol{\nabla}Y_{lm}(\hat{\mathbf{r}}), \tag{15.107}$$

and combining this expression with Eq. (15.103), we obtain the far field Green dyadic (i.e., $kr \gg 1$ and $kr' \ll 1$)

$$G^s_{\mu\nu}(\mathbf{r}, \mathbf{r}') = -\frac{\tilde{\alpha}_1}{3} \sum_{m=-1}^{1} e^{ikr} \left[\nabla_\mu Y_{1m}(\hat{\mathbf{r}})\right] \psi^{\nu *}_{1m}(\mathbf{r}'), \tag{15.108}$$

where we set $l = 1$.

References

1. R.H. Dicke, Phys. Rev. **93**, 99 (1954)
2. M. Gross, S. Haroche, Phys. Rep. **93**, 301 (1982)
3. A.V. Andreev, V.I. Emel'yanov, Y.A. Il'inskii, *Cooperative Effects in Optics* (IOP Publishing, London, 1993)
4. T. Brandes, Phys. Rep. **408**, 315 (2005)
5. R.G. DeVoe, R.G. Brewer, Phys. Rev. Lett. **76**, 2049 (1996)
6. M. Scheibner, T. Schmidt, L. Worschech, A. Forchel, G. Bacher, T. Passow, D. Hommel, Nat. Phys. **3**, 106 (2007)
7. F.C. Spano, S. Mukamel, J. Chem. Phys. **91**, 683 (1989)
8. T.V. Shahbazyan, M.E. Raikh, Z.V. Vardeny, Phys. Rev. B **61**, 13266 (2000)
9. T.V. Shahbazyan, M.E. Raikh, Phys. Rev. B **49**, 17123 (1994)
10. T.V. Shahbazyan, S.E. Ulloa, Phys. Rev. B **57**, 6642 (1998)
11. T. Brandes, B. Kramer, Phys. Rev. Lett. **83**, 3021 (1999)
12. V.N. Pustovit, T.V. Shahbazyan, Phys. Rev. Lett. **102**, 077401 (2009)
13. V.N. Pustovit, T.V. Shahbazyan, Phys. Rev. B **82**, 075429 (2010)
14. R.R. Chance, A. Prock, R. Silbey, Adv. Chem. Phys. **37**, 1 (1978)
15. B.N.J. Persson, N.D. Lang, Phys. Rev. B **26**, 5409 (1982)
16. I.A. Larkin, M.I. Stockman, M. Achermann, V.I. Klimov, Phys. Rev. B **69**, 121403(R) (2004)
17. V.N. Pustovit, T.V. Shahbazyan, J. Chem. Phys. **136**, 204701 (2012)
18. M. Moskovits, Rev. Mod. Phys. **57**, 783 (1985)
19. E. Dulkeith, A.C. Morteani, T. Niedereichholz, T.A. Klar, J. Feldmann, S.A. Levi, F.C.J.M. van Veggel, D.N. Reinhoudt, M. Moller, D.I. Gittins, Phys. Rev. Lett. **89**, 203002 (2002)
20. E. Dulkeith, M. Ringler, T.A. Klar, J. Feldmann, A.M. Javier, W.J. Parak, Nano Lett. **5**, 585 (2005)
21. P. Anger, P. Bharadwaj, L. Novotny, Phys. Rev. Lett. **96**, 113002 (2006)
22. S. Kühn, U. Hakanson, L. Rogobete, V. Sandoghdar, Phys. Rev. Lett. **97**, 017402 (2006)
23. F. Tam, G.P. Goodrich, B.R. Johnson, N.J. Halas, Nano Lett. **7**, 496 (2007)
24. J. Gersten, A. Nitzan, J. Chem. Phys. **75**, 1139 (1981)
25. R. Ruppin, J. Chem. Phys. **76**, 1681 (1982)
26. A. Pineda, D.J. Ronis, J. Chem. Phys. **83**, 5330 (1985)
27. H. Chew, J. Chem. Phys. **87**, 1355 (1987)
28. J. Seelig, K. Leslie, A. Renn, S. Kluhn, V. Jacobsen, M. van de Corput, C. Wyman, V. Sandoghdar, Nano Lett. **7**, 685 (2007)
29. M. Durach, A. Rusina, V.I. Klimov, M.I. Stockman, New J. Phys. **10**, 105011 (2008)
30. L.N. Tripathi, M. Praveena, J.K. Basu, Plasmonics **8**, 657 (2013)
31. D. Martin-Cano, L. Martin-Moreno, F.J. Garcia-Vidal, E. Moreno, Nano Lett. **10**, 3129 (2010)
32. S.A. Guebrou, C. Symonds, E. Homeyer, J.C. Plenet, YuN Gartstein, V.M. Agranovich, J. Bellessa, Phys. Rev. Lett. **108**, 066401 (2012)

33. L. Novotny, B. Hecht, *Principles of Nano-Optics* (Cambridge University Press, New York, 2006)
34. M.I. Stockman, Phys. Rev. Lett. **79**, 4562 (1997)
35. T. Förster, Ann. Phys. **437**, 55 (1948)
36. D.L. Dexter, J. Chem. Phys. **21**, 836 (1953)
37. J.R. Lakowicz, *Principles of Fluorescence Spectroscopy* (Springer, New York, 2006)
38. D.L. Andrews, A.A. Demidov (eds.), *Resonance Energy Transfer* (Wiley, New York, 1999)
39. D.M. Willard, L.L. Carillo, J. Jung, A. Van Orden, Nano Lett. **1**, 469 (2001)
40. S.A. Crooker, J.A. Hollingsworth, S. Tretiak, V.I. Klimov, Phys. Rev. Lett. **89**, 186802 (2002)
41. S.W. Clark, J.M. Harbold, F.W. Wise, J. Phys. Chem. C **111**, 7302 (2007)
42. A.A. Deniz, T.A. Laurence, G.S. Beligere, M. Dahan, A.B. Martin, D.S. Chemla, P.E. Dawson, P.G. Schultz, S. Weiss, Proc. Natl. Acad. Sci. USA **97**, 5179 (2000)
43. E.A. Lipman, B. Schuler, O. Bakajin, W.A. Eaton, Science **301**, 1233 (2003)
44. P.R. Selvin, Nat. Struct. Biol. **7**, 730 (2000)
45. R.B. Sekar, A. Periasamy, J. Cell Biol. **160**, 629 (2003)
46. J. Gonzalez, R. Tsien, Biophys. J. **69**, 1272 (1995)
47. I.L. Medintz, A.R. Clapp, H. Mattoussi, E.R. Goldman, J.M. Mauro, Nat. Mater. **2**, 630 (2003)
48. D.L. Andrews, C. Curutchet, G.D. Scholes, Laser Photonics Rev. **5**, 114 (2011)
49. M. Hopmeier, W. Guss, M. Deussen, E.O. Göbel, R.F. Mahrt, Phys. Rev. Lett. **82**, 4118 (1999)
50. P. Andrew, W.L. Barnes, Science **290**, 785 (2000)
51. C.E. Finlayson, D.S. Ginger, N.C. Greenham, Chem. Phys. Lett. **338**, 83–87 (2001)
52. A. Leitner, H. Reinisch, Chem. Phys. Lett. **146**, 320–324 (1988)
53. J.R. Lakowicz, J. Kusba, Y. Shen, J. Malicka, S. D'Auria, Z. Gryczynski, I. Gryczynski, J. Fluoresc. **13**, 69 (2003)
54. P. Andrew, W.L. Barnes, Science **306**, 1002 (2004)
55. J. Zhang, Y. Fu, J.R. Lakowicz, J. Phys. Chem. C **111**, 50 (2007)
56. J. Zhang, Y. Fu, M.H. Chowdhury, J.R. Lakowicz, J. Phys. Chem. C **111**, 11784 (2007)
57. F. Reil, U. Hohenester, J.R. Krenn, A. Leitner, Nano Lett. **8**, 4128 (2008)
58. V.K. Komarala, A.L. Bradley, Y.P. Rakovich, S.J. Byrne, Y.K. Gunko, A.L. Rogach, Appl. Phys. Lett. **93**, 123102 (2008)
59. K.Y. Yang, K.C. Choi, C.W. Ahn, Opt. Express **17**, 11495 (2009)
60. K.H. An, M. Shtein, K.P. Pipe, Opt. Express **18**, 4041 (2010)
61. D.L. Andrews, G. Juzeliunas, J. Chem. Phys. **96**, 6606 (1992)
62. J.I. Gersten, A. Nitzan, Chem. Phys. Lett. **104**, 31 (1984)
63. X.M. Hua, J.I. Gersten, A. Nitzan, J. Chem. Phys. **83**, 3650 (1985)
64. S.D. Druger, S. Arnold, L.M. Folan, J. Chem. Phys. **87**, 2649 (1987)
65. H.T. Dung, L. Knöll, D.-G. Welsch, Phys. Rev. A **65**, 043813 (2002)
66. V.N. Pustovit, T.V. Shahbazyan, Phys. Rev. B **83**, 085427 (2011)
67. K.A. Velizhanin, T.V. Shahbazyan, Phys. Rev. B **86**, 245432 (2012)

Index

A

Ab initio quantum-chemical approach, 14
Abraham-Lorentz equation, 252
Acoustic echoes, 172
Active Raman spectroscopy. *See* Surface enhanced coherent anti-Stokes Raman scattering (SECARS)
Adaptive algorithms, 275
Adiabatic nanofocusing
  approach, 274
  cones, 502
  implementation, 278
  process, 275, 276
  waveguide, 9
Aharonov-Bohm (AB) effect, 464
  plasmonic, 475–479
Aharonov-Casher effect, 478
Algorithmic Information Theory (AIT), 347
Aluminium, 116
Anderson localization, 18, 21, 88, 264n11
Angular Doppler effect (ADE), 473, 492
Angular momentum (AM), 450, 464, 470, 489, 530, 563
  eigenstates with, 526
  optical, 467
Anisotropic particles, polarization-dependent resonances in, 138–139
Antennas, 8. *See also* Nanoantennas; Nonlinear optical antennas; Optical antennas; Plasmonic antennas; Thermal antennas
Aperiodic order, deterministic, 331
  aperiodic order and substitutions, 333–335
  and number theory, 345–347
  periodic and quasi-periodic order, 331–333
Aperiodic plasmon arrays, engineering applications of, 352
  to colorimetric optical sensing, 360–363
  to light emission enhancement, 363–366
  nanofabrication of, 352–356
  to surface enhanced Raman biosensing, 356–360
  to thin-film solar cell enhancement, 367–370
Aperiodic Vogel spiral structures, 340
Atomic layer deposition (ALD), 136
Autocorrelation function, 63
  2D, 362, 363
Azimuthal angle, 368, 466, 476, 480, 482, 489
Azimuthal number, 343, 344

B

Bandwidth delay product (BDP), 409
Beer's law, 137
Berry phase shift, 496
Berry's phase, 464, 467, 468, 470, 472, 473
Berry's phase theory, 464
Bessel functions, 343, 467, 482, 561
Bessel order, 344
Bistable spasers, 75, 76–77
Blackbodies, 284, 306, 319,
  near-field analog of, 312–315
  source, 287
  specific intensity, 284
Bloch equations. *See* Optical Bloch equations
Bloch modes, 409
Bloch theorem, 88

T. V. Shahbazyan and M. I. Stockman (eds.), *Plasmonics: Theory and Applications*, Challenges and Advances in Computational Chemistry and Physics 15,
DOI: 10.1007/978-94-007-7805-4, © Springer Science+Business Media Dordrecht 2013

Boltzmann distribution, 114
Boltzmann equation, 175, 179
Boltzmann factor, 110
Boltzmann's constant, 284
Boltzmann's law, 300
Bombieri–Taylor theorem, 336
Born von Karman conditions, 305
Bose-Einstein distribution, 286, 289
Boundary-element method (BEM), 224–227
Bragg grating, 464, 469
Bragg peaks, 332, 333, 336, 336n3, 339, 342, 347
Bragg period, 464
Bragg reflection, 88
Bragg scattering, 360, 368
Brillouin formula, 4, 83
Brillouin zone, 171, 182, 184, 187, 189, 241, 308, 335
Büttiker-Landauer formula, 304–306

C
Cathodoluminescence, 276
CdS/Ag nanolasers, 60
Chemical first layer effects, 107
Chemiluminescence, 520
Circular light scattering, 340, 364
Cluster-cluster aggregates (CCA), 18, 19, 26, 27
Coherent anti-Stokes Raman Scattering (CARS), 111, 112, 120, 256, 257
Collectively enhanced IR absorption (CEIRA), 118
Collinear FWM spectroscopy, 278
Colorimetric fingerprints, 361, 362, 363
COMSOL, 162
Continuous wave (CW) regime, 59
  equations for, 67–69
  spacers in, 69–72
Cosmol Multiphysics, 405
Contact angle hysteresis (CAH), 508
Controlled emission, multilayers and photonic crystals for, 299–300
Controlled emission spectrum, metamaterials with, 298–299
Cooperative effects, in plasmonics. *See* Plasmon-mediated superradiance near metal nanostructures; Resonance energy transfer near metal nanostructures
Co-prime arrays, 345, 346, 350
Coriolis effect, 464, 496
Coulomb forces, 432
Coupled dipole approximation (CDA), 368
Coupled thermal antenna lattices, 492–496
Coupler period, 464
Cross conversion, 380, 393–394
Cross-correlation FROG (XFROG), 276
Crossed gratings, 298
Cumulative distribution of field enhancement (CDFE), 349, 350

D
Damping of surface plasmon polaritons
  experimental studies of plasmon lifetimes, 253–255
  theory of radiative and nonradiative decay, 249–253
Dark modes, 21
Dark-field scattering micro-spectroscopy, 363
De Broglie wavelength, 244
Debye model, 177, 254
Debye temperature, 170, 177
Debye wave vector, 179
Density of states (DOS), 21, 240, 261, 269, 284, 309, 310, 338, 432
Detector sensitivity, 360
Deterministic aperiodic nano-structures (DANS), 330, 352, 353, 359, 360, 361, 362, 363, 364, 370
  developing DANS arrays, 357, 358
  two-dimensional (2D) plasmonic, 331
Deterministic aperiodic order, fundamentals of, 331
  aperiodic order and number theory, 345–347
  aperiodic order and substitutions, 333–335
  hot spot engineering with aperiodic plasmon arrays, 348–352
  periodic and quasi-periodic order, 331–333
  plasmonic chains, 336–339
  rotational symmetry, aperiodic tilings and Vogel spirals, 339–345
Detuned electrical dipoles (DED) metamaterails, applications, 415
  metamaterial wave retarders, 421–426
  plasmonic sensing, 415–421
Detuned electrical dipoles (DED) metamaterials, optical transparency and slow light, 403–405
  experimental study, 412–415
  three-nanorad system, 410–412

two-nanorod system, 405–410
Dicke effect, 451, 452, 526, 532, 535, 542
Dipole approximation, 256, 336
discrete, 140
Dipole–dipole coupling, 337
Dipole–dipole interaction, 442, 530, 532, 534–535, 539, 540, 541
Dipole-radiation rate, 10
Dirac δ-function, 22, 336n3
Direct band-gap semiconductors (DBGS), 70, 87
Dirichlet L-functions, 347
Dirichlet-Neumann boundary conditions, 17
Discrete dipole approximation (DDA), 140, 197
Discrete logarithm, 347
Divergence angle, 341, 342, 343, 370
Donor–acceptor coupling, 548
Drude behavior, 243, 250
Drude contribution, 133, 171, 172, 188
Drude damping, 245, 246, 251, 254
Drude dielectric permittivity, 436
Drude expression, 169, 173
Drude-Lorentz model, 516
Drude model, 242, 243, 251, 253, 261, 273
Drude scattering, 250, 251
Drude-Lorentz-Sommerfeld model, 432
Duffy transform, 226
Dye-sensitized solar cells (DSSCs), 126, 127, 128
plasmon enhanced. *See* Plasmon enhanced dye-sensitized solar cells
Dyson's equation, 550

E
Effective medium theory (EMT), 403, 404
Eigenstates, 338, 526, 527, 528, 530, 532, 534, 535, 536, 537, 539, 545, 555, 556
Einstein summation notation, 258
Eisenstein primes, 346
Electromagnetic hot spots, 348, 352
Electromagnetic properties, 389, 397, 436
microscopic treatment, 380
Electromagnetically induced transparency (EIT), 402, 403, 404, 405, 406, 409, 411, 415
in atomic physics, 426
effect, 406, 410
like behavior, 412, 417
like response, 416, 427
like transmission, 402, 410
plasmonic, 410
Electromechanical energy, 3, 4
Electron beam lithography (EBL), 161, 352, 353, 355, 357, 358, 363, 412, 413
Electron energy loss spectroscopy (EELS), 13, 276
Electron gas thermalization, 178
Electron kinetics, 172–173
ultrafast electron kinetics, 174–182
Electron-beam lithography (EBL), 161, 352, 353, 355, 357, 358, 363, 412, 413
Electronic dephasing, 249
Electronic excitation at metal surfaces, 237–238
Drude-Sommerfeld model, 241–242
electronic properties of metals, 240–241
interband transition and hybridization, 242–244
linear optical polarization, 238–239
localized SPP in small metal particles, 246–248
optics at metal interfaces, 244–245
propagating surface plasmon polaritons, 245–246
time domain description, 239–240
Electron-lattice energy, 168, 172, 173
exchanges, 178–181
Electron-lattice thermalization, 182, 188, 196
Electron-light interaction, 172–173
coherent electron-light coupling, 173–174
Energy transfer. *See* Resonance energy transfer near metal nanostructures
Enzyme-linked immunosorbent assay (ELISA), 520
Euler formula, 506
Euler function, 82, 347
Extraordinary optical transmission (EOT), 389–392
Extrinsic chirality, 407, 427

F
Fabry-Perot cavity, 3
Fabry-Perot-like denominator, 303
Fano lineshape, 259n10
Fano resonances, 11, 12, 259n10, 416
Fano-like model, 389–392
Fermi energy, 169, 171, 173, 174, 187, 194
Fermi liquid theory, 249n8
Fermi surface, 4, 29, 178, 240, 241
Fermi temperature, 177

Fermi velocity, 7, 170, 239n1, 242, 243, 254
Fermi's rule, 252
Fibonacci arrays, 335, 351, 361, 364, 365
Fibonacci golden number, 342
Fibonacci quasicrystal, 333
Fibonacci sequence, 343, 364
Fibonacci structures, 338, 364
Figure of merit (FOM), 409, 415, 426, 453, 454
Finite-difference methods, 381
Finite-difference time domain (FDTD)
  algorithm, 465
  calculations, 466, 467, 469
  method, 116
  numerical simulations, 370
  simulations, 363, 368–369, 378, 480, 481, 482, 483, 493
Finite-element methods, 197, 216, 224, 381, 405, 423
Floquet-Bloch expansion, 380
Fluctuation-dissipation theorem, 242n2, 284, 286, 287
Fluorescence immunoassay, 520
Fluorescence resonance energy transfer (FRET), 544, 546, 553
  amplification, 559
  efficiency, 545
  Förster's FRET, 548
  mechanism, 557
  plasmon-assisted transfer, 552
  quenching, 550
  theory, 551
Fluorescence sensing, 432
Focused ion beam (FIB), 352, 353, 464, 470, 482
Form birefringence, 422
Förster's transfer, 547, 551, 552
Fourier space, 331, 340, 346, 347, 365, 368, 370
  aperiodic, 352, 371
  circularly-symmetric, 341, 366
  reciprocal, 332, 333, 335, 347,
  rotationally symmetric, 342
Fourier transforms, 40, 50, 143, 240, 248, 249, 250, 274, 288, 336, 337, 346, 421
Fourier–Hankel decomposition (FHD), 343
Fourier–Hankel transform, 344
Free-induction decay, 248, 249, 271, 272
Free-space vortex fields, 444
Frequency resolved optical-gating (FROG)-based technique, 271, 272
  algorithm, 275
  characterization, 273
  measurements, 274
  retrieval algorithm, 273
Fresnel coefficient, 303
Fresnel reflection factors, 6, 264, 306
Frustrated modes, 308–309, 310, 311, 312, 314, 318
Full width at half maximum (FWHM), 142, 143, 272, 295

G

Galois field array, 345
Gap-labeling theorem, 336
Gaussian beam profile, 272
Gaussian prime array, 345, 346, 353, 361
Gaussian primes (GP), 345
Gaussian pulse, 49
Generalized Mie theory (GMT), 141, 351, 363
Generation threshold, 69, 70, 72, 73, 76, 77
Gersten–Nitzan model, 551
Glan polarizer, 213
Glan-Thompson analyzer, 425
Glan-Thompson polarizer, 425
Gold nanoaggregates, 119
Gold nanospheres, 5, 60, 87, 114, 185, 187, 193, 216
Golden angle, 341, 342, 370
Green dyadic (Green's dyadic), 302, 530, 533, 535, 548, 550, 551, 554, 557, 561, 562, 563, 564
Green function (Green's function), 2, 22, 23, 24, 25, 26, 27, 36, 38, 40, 224, 225, 301, 302, 395,
  dyadic, 39302
  periodic, 225
  retarded, 22–24
  retarded dyadic, 24, 39
Green tensor, 285, 302, 310
Gyration radius, 19, 20

H

Hagen-Rubens regime, 242
Hankel function, 482
Heat transfer. *See also* Radiative heat transfer at nanoscale; Surface-waves assisted thermal emission
  fundamental limits for, 306–308
Helmholtz equation, 223, 224, 225, 449, 477, 478, 482, 494
  two-dimensional, 482
Hermite-Gaussian (HG) beams, 52, 53

Hermitian operation, 18
Hertzian dipole, 336, 432, 433,
High harmonic generation (HHG), 278
Harmonic generation (technique), 270
Hole arrays, 397, 416
  Al, 116
  metal, 392
  nano-hole arrays, 353, 355, 448
  nano-imprinted plasmonic, 356
  near-infrared with subwavelength, 390
  2D, 390, 391
Hot spot engineering, 348–352
Hot spots, 16–18, 38, 39–40, 44, 56, 69, 80, 82, 87, 88, 114, 208, 264.330, 348, 349, 350, 351
  electromagnetic, 352
  engineering, 370
  inhomogeneous localization of SPs and, 18–22
  local fields, examples of, 26–28
  nanoplasmonic, examples of, 29–33
  retarded Green's function, 22–24
  SP modes, 24–26
Hybrid waveguide, 154, 155
Hybrid waves (HWs), 394, 395, 397
Hydrophobicity. *See* Super-hydrophobicity, model; Super-hydrophobicity, physical model
Hyper Raman scattering (HRS), 104
Hyperbolic modes (HM), 314
Hyper-Rayleigh scattering (HRS), 216

I
Immuno-polymerase chain reaction (PCR) assay, 520
Indium tin oxide, 51, 52, 158, 352
InGaN-core, 61, 62
InN-shell, 61
Integrated circuit technology, 150
  silicon integrated, 151
Interband dielectric function, 183–184
  electronic contribution, 183–184
  lattice contribution, 187
Interband transition, 243
Internal photoemission (IPE) process, 159
International Union of Crystallography (IUCr), 332
Intraband dielectric function
  electronic contribution, 184–187
  lattice contribution, 188
Irradiation, 135, 142

J
Joule losses, 59

K
Kerr effect
  optical, 174
  nonlinear, 257, 265
Kerr-type nonlinearity, 168, 201
Kramers-Kronig causality, 23, 84
Kramers-Kronig relations, 11, 240
Kretschmann coupling, 87
Kretschmann geometry, 263
Kroniker's symbol, 547
Kubo model, 242n2

L
Laguerre-Gaussian (LG) beams, 52
Lamb mode vibration, 172
Landau damping, 7, 13, 14, 173, 537
Landau decay, 174
Landauer approach, 307
Landauer theory, 301, 303
Landauer-like expression, 306
Laplace equation, 16, 247
Laplace transform, 529
Lattice, 2D, 464, 506
Leakage-radiation microscopy (LRM), 420, 421
Lebesgue's decomposition theorem, 332
Legendre polynomial, 532, 551, 557
Legendre sequences, 347
Light scattering, 191, 343, 360, 486
  circular, 340, 364, 365–366
  multiple, 371
  from nano-patterned deterministic aperiodic surfaces, 362
  nonlinear, 257, 266–268
  planar, 364, 368
  wide-angle, 367
Liquid chromatograpy-mass spectrometry (LC-MS), 520
Local density of states (LDOS), 252, 364
Local dipole-allowed SHG polarization, 267
Local oxidation of silicon (LOCOS), 151, 154, 155, 161
Local-field issues
  gap dependence, 216–217
  chiral symmetry breaking of dimmers, 217–218
Localized SPPs, 82, 253
  excitation, 270
  oscillations, 245

in small metal particles, 246–248
Localized surface plasmon (LSP) modes, 348, 367, 432, 433, 434, 438, 445
Localized surface plasmon resonances (LSPRs), 128
dielectric function of metals, 133
Localized surface plasmons (LSPs), 330
Locally anisotropic optical spin-Hall effect (OSHE-LA), 485
Locally isotropic optical spin-Hall effect (OSHE-LI), 485
LOCOS technique, 154, 155
Lorentzian lineshapes, 269, 270
Lorentzian oscillators, 252
Lorentzian resonances, 258
Lorentzian spectral time behavior, 250
Low-pressure chemical vapor deposition (LPCVD), 154

M
Magnetic bead-based electro chemiluminescence, 520
Magnus effect, 470, 496
Majorana sphere, 467, 468
MALDI TOF mass spectroscopy techniques, 502
Maxwell equations, 16, 436, 438, 529
Metal cooling, 187, 201
Metal surfaces
dipole point-source on, 388–389
field scattered on, 384
quasi-cylindrical wave, 384–388
SPP and quasi-CW, 388–389
waves on, 381–382
Metal-insulator-metal (MIM) structures, 150
Metal-oxide-semiconductor (MOS) geometry, 157, 158
Metals and metal nanoparticles, dielectric function of, 169–172
Micro-Raman mapping, 516
Microscopic model, Fano's, 382–384
Microscopic model, generalized, 393
cross conversion, 393–394
multiple-scattering model, 394–397
Mie coefficients, 562
Mie resonances, 246
Mie scattering, 266
Mie scattering theory, 211
Mie theory, 130, 197, 247, 250, 251, 252, 254
generalized (GMT). *See* Generalized Mie theory (GMT)
Möbius function, 347
Modal decomposition, 343
Monostable spasers, 73–75
Moore's law, 149
Multiphoton intrapulse interference phase scan (MIIPS), 275
Multiple-scattering model, 394–397
Multipole effects, 214–215
extension to, 211–212

N
Nanoantennas, 8–9
Nanoellipsoid, 192
Nanomirrors, 6
Nanoparticle cooling, 182
Nanoparticle-generated optical tornadoes, 439–444
Nanoplasmonic metamaterials, 78–79
Nanoplasmonic systems, 2, 4, 7, 9, 10, 16, 18, 26, 36
mechanical forces in, 13
nanoantenna effect, 8
Nanoplasmonics, 2
experimental examples, 29–33
fundamentals, 3–8
issues, 12–14
nanoantennas, 8–9
nonlinear photoprocesses in, 15–16
radiative loss, 9–12
Nanospasers, 61–64
Nanotechnology, 87, 127, 313, 502, 521
Near-field scanning optical microscope (NSOM), 21, 31, 153, 465, 475. *See also* Scanning near-field optical microscope (SNOM)
Non-Hermitian system matrix, 226
Nonlinear Kerr effect, 257, 265
Nonlinear optical antennas, 269–270
Nonlinear optics, second-order, 258–260
Nonlinear plasmon optics, 255–258
nonlinear light scattering, 266–268
nonlinear optical antennas, 269–270
nonlinear wavemixing with surface plasmons, 262–264
second-order nonlinear optics, 258–260
SHG response at metal surfaces, 260–262
surface-enhanced nonlinear processes, 264–266
Nonlinear response tensor (NRT), 209–211
Nonlocalized SPs
as eigenmodes, 16–18

inhomogeneous localization of, 18–22
local fields, 26–28
retarded Green's function, 22–24
SP modes as resonances, 24–26
Non-radiative decay rate, 527
Nonradiative plasmon coupling, 540
Norton wave, 381, 385, 386, 388
Number theory, 330, 334, 345, 370
aperiodic order and, 345–347
Numerical modeling
boundary-element method, 224–227
challenges, 222–223
modeling SHG, recent approaches for, 224
nonlinear problems, general approach for, 223–224
Numerical simulations, 516

O

Ohmic losses, 415
One-photon photoemission PEEM (1PP-PEEM), 29
Optical activity, 407
Optical antenna, 8, 9, 432
Optical Bloch equations, 64–66
Optical gratings, 2D, 360
Optical Magnus effect, 470
Optical spin Hall effect (OSHE), 470, 484, 485, 496
from plasmonic nanoapertures, 485–492
Optical spin symmetry breaking, in nanoapertures, 470–475
Optical tornado, nanoparticle generated, 440–444
Orbital angular momentum (OAM), 342, 343, 344, 470, 472, 473, 474, 480, 482

P

Para-mercaptoaniline (pMA) molecules, 451
Parastichies, 342
Perturbation theory, 59, 258, 360
Phase modulation, 34, 41, 47, 53, 55, 157
Photoemission electron microscope (PEEM), 29, 30, 31, 42, 50, 51, 273
Photon tunneling, 308
frustration modes, 308–309
surface modes, 309–312
Photonic molecules, 434
Photonic–plasmonic coupled modes, 331
Photonic–plasmonic coupling, 348
Photovoltaics (PVs), 126, 137, 319, 456
efficiency, 319
thermophotovoltaics (TPVs), 299, 301
thin-film, 454
Pinwheel tiling, 339
Pisot-type substitutions, 336
Planar diffraction, 341
Planck's constant, 284
Plasmon dynamics, femtosecond time-domain measurement of, 270–274
Plasmon enhanced dye-sensitized solar cells, 128
calculating solar enhancement, 130–132
mechanism of enhanced dye absorption, 129–130
Plasmon-enhanced radiative coupling, 527, 531, 540
Plasmon-enhanced radiative transfer (PERT), 546
Plasmonic Aharonov-Bohm effect, 475–479
Plasmonic antennas, ultrafast spatio-temporal control with, 274–278
Plasmonic atoms, 434
Plasmonic Dicke effect, 531, 535
Plasmonic eigenmodes and effective resonant permittivity of metamaterials, 79–80
Plasmonic in-plane wavenumber, 467
Plasmonic materials, energy transport and dissipation in, 436–437
Plasmonic nanogalaxies, 357
Plasmonic nanostructures
hydrodynamics of light flow in, 449–451
for supporting vibrational spectroscopy, 113–116
Plasmonically enhanced dye-sensitized solar cells, challenges, 139–140
ensembles, 140–141
excited state lifetime of plasmons, 142
metal losses, 142–143
Plasmonically-integrated tornadoes, applications of, 451–456
Plasmonics. *See* Nanoplasmonics; Plasmonics and coherent control; Quantum nanoplasmonics; Silicon plasmonics components; Spinoptics, in plasmonics
Plasmonics and coherent control, 33–36
coherent control by spatiotemporal pulse shaping, 46–50
experimental demonstrations of, 50–55

time-reversal coherent control, numerical results for, 40–46
time-reversal coherent control, qualitative description of, 37–40
time-reversal solution for coherent control, 36–37
Plasmon-mediated superradiance near metal nanostructures, 525–528
plasmonic coupling of radiating dipoles, 528–532
radiated energy of, dipoles near nanoparticle, 532–533
PlasMOStor, 157
Point spread function (PSF), 482
Polarization effects, coupling of s-polarized propagating waves and surface waves, 296–297
Polarization pulse shaping, 50
Polarization-dependent coupling, 469
Polymethyl methacrylate (PMMA), 352, 355, 364, 412, 419, 421, 425
Post CMOS era, 150
Poynting vector, 435
field lines, 437
Primality, 347
Propagating SPP modes, 245–246
Pump-probe techniques, 278
Pure-point spectrum, 333

Q

Quantum density matrix equations, 64–66
Quantum dots (QDs), 54, 86
Quantum efficiencies, 542
Quantum nanoplasmonics. *See* Spasers; Spasing
Quantum plasmonics, 14. *See also* Spasers; Spasing
Quantum-mechanical expression, 10
Quasi-cylindrical wave (quasi-CW), 380
Quasistatic approximation, 16

R

Rabi frequency, 65
Radiation reaction, 252
Radiative heat transfer at nanoscale, 300–301
with anisotropic media, 315–317
beyond SPPs coupling, 312–315
heat flux exchanged between two planar media, 301–304
mediated by photon tunneling, 308–312
mesoscopic analysis of, 304–308
near-field energy conversion, 319–322
with phase change materials, 317–319
Raman scattering, 104, 265
Raman sensing, 432
Raman Stokes light, 106
Random planar composite (RPC), 19, 27
Rao-Wilton-Glisson triangular patch basis functions, 225
Rashba and Dresselhaus effects, 492
Rashba-like spin degeneracy violation, 492–496
Rayleigh anomaly, 416
Rayleigh condition, 382
Rayleigh cut-off condition, 340
Rayleigh-Gans-Debye approximation, 224
Rayleigh resonances, 246
Rayleigh scattering, 173, 266
Reactive ion etching (RIE), 151, 161, 352
Resonance energy transfer near metal nanostructures, 544–546
cooperative energy transfer, 557–560
cooperative plasmon-assisted resonance energy transfer, 553–556
near plasmonic nanostructure, 546–551
plasmon-assisted single-donor energy transfer, 551–553
Resonance Raman scattering (RRS), 105–106
Reststrahlen region, 309
Retarded Green's function, 22–24
Rhodamine6G (R6G), 511, 514
Ricatti-Bessel functions, 251
Riemann's zeta function, 347
Rose bengal dye-sensitized TiO_2 cell, 135
Rotating wave approximation (RWA), 64
Rudin–Shapiro sequence, 334, 335, 339

S

Scanning near-field optical microscope (SNOM), 31. *See also* Near-field scanning optical microscope (NSOM)
Scattering-scanning near-field optical microscopy (*s*-SNOM), 276
Schawlow-Townes theory, 66, 71
Schottky barrier (SB) photodetector, 159, 160, 162
Schottky diodes, 14
Second harmonic generation (SHG), 208–209, 256
circular-difference (CD) response, 218
Shock waves, 172
Shockley-Queisser limit, 319

Short-range surface plasmon polaritons (SR-SPPs), 403
Silicon carbide, 292
Silicon plasmonic detectors (SPDs), 157–163
Silicon plasmonic modulators (SPMs), 157–158
Silicon plasmonics components
  active devices, 156–163
  motivation, 151
  passive devices, 151–156
Silver aggregates, 119
Singular-continuous spectra, 333, 333n2
Small metal nanosphere, 192
Solar spectrum, enhancing, 132–133
  dielectric core, metal shell particles, 138
  metal composition, 133–135
  other geometries, 139
  polarization-dependent resonances in anisotropic particles, 138–139
  polarization-independent resonances, 135–137
  shape, 135
Spasers, 55–56
  bistable spasers, 75, 76–77
  in CW mode, 69–70
  equations of, 64–65
  fundamentals, 56–58
  latest progress in, 59–64
  monostable spasers, 73–75
  nanospasers, 61–64
  as ultrafast quantum nanoamplifier, 72–73
Spasing, 55–56
  conditions of loss compensation by gain, 81–82
  loss compensation by gain, 77–81, 83–85
Spatial modulation spectroscopy (SMS), 198
Spatial signals, 2D, 349n5
Spatially-coherent thermal emission, 291–293
Spatio-temporal coherent control, 34–35
Spatiotemporal pulse shaping, 46–47
Spectroscopy. *See also* Surface enhanced vibrational spectroscopy, applications of; Vibrational spectroscopy, normal and surface-enhanced
  2D, 278
Spherical (Huygens) wave, 480
Spherical nanoparticle, 267
SPIDER, 14
Spin-based plasmonic effect in nanoscale structures, 464–470
Spin-dependent plasmonics, 480–484
Spin-Hall effects, 478
Spinoptics, in plasmonics
  coupled thermal antenna lattices, 492–496
  optical spin symmetry breaking, in nanoapertures, 470–475
  plasmonic Aharonov-Bohm effect, 475–479
  plasmonic nanoapertures, 485–492
  Rashba-like spin degeneracy violation, 492–496
  spin-based plasmonic effect in nanoscale structures, 464–470
  spin-dependent plasmonics, 480–484
Spin-orbit interaction, 460, 472, 473, 478, 480, 492, 494, 496
Split-ring resonators (SRRs), 216, 412
Stefan constant, 307
Stefan-Boltzmann law, 300, 301, 307, 308
Stern-Gerlach effects, 478
Stimulated emission, 59, 60, 65, 70, 74, 81, 82
Stimulated Raman scattering, 105
  surface enhanced femtosecond, 120
Stimulated Raman spectroscopy (SRS), 105, 111, 112
Stokes frequency, 104
Structural resonances, 331
Substitution matrix, 336
Sum-frequency generation (SFG), 256
Super-hydrophobic surfaces (SHSs), 503
  lattice packings and, 506–507
  small friction coefficients of, and evaporation dynamics, 508–510
Super-hydrophobicity, model
  fabrication of devices, 511–512
  fluorescence microscopy characterization of Rhodamine deposits, 513
  Raman characterization of Rhodamine deposits, 513
  samples AFM characterization, 512–513
  samples SEM characterization, 512
Super-hydrophobicity, physical model, 504
  lattice packings and SHSs, 506–507
  optimal design, consideration for, 509–510
  physics of drops and surfaces, 504–505
  small friction coefficients of SHSs and evaporation dynamics, 508–509
Superradiance, 439

Surface enhanced coherent anti-Stokes Raman scattering (SECARS), 105, 111–112
Surface enhanced hyper Raman scattering (SEHRS), 105
Surface enhanced infrared absorption, 108
  using two-photon excitation, 108–110
Surface enhanced pumped anti-Stokes Raman scattering (SEPARS), 105, 110–111
Surface enhanced Raman scattering (SERS), 1, 77, 105, 106–107, 265
Surface enhanced Raman sensing (SERS), 451
  SERS labels, 119
Surface enhanced stimulated Raman scattering (SESRS), 105, 111–113
Surface enhanced vibrational spectroscopy, applications of
  linear and non-linear vibrational probing and imaging, 119–120
  SERS for probing catalytic reactions, 116–117
  vibrational spectroscopy of protein monolayers using SEIRA, 118
Surface modes, 309–312
Surface phonon polariton, 309
Surface plasmon polaritons (SPPs), 46, 47, 77, 238, 245, 380, 463
  SPP waves, 432
Surface plasmon polaritons and quasi-cylindrical waves, generalized microscopic model, 393
  cross conversion, 393–394
  multiple-scattering model, 394–397
Surface plasmon resonance (SPR), 168, 193, 194, 196
Surface plasmons (SPs), 3, 5
  dipole limit, 220
  and electrons, 13–14
  improvement in fabrication, 219
  nonlocalized. *See* Nonlocalized SPs
  radiative decay, 9
Surface-phonons assisted directional thermal emission, 291–293
Surface-phonons assisted isotropic thermal emission, 293–294
Surface-plasmons assisted thermal emission, 295
Surface-waves assisted thermal emission
  characteristics of usual thermal sources, limitations and prospects, 286–287
  early results, 289–291
  electrodynamic point of view, 284–285
  Kirchhoff's law, 285–286
  partially coherent sources, 289
  radiometric point of view, 283–284
  thermal sources and partial coherence, 287–288
Symbolic dynamical system, 333

T

Tailored nonlinear response
  resonance domain effects, 220–221
  tailored SHG response, 221–222
TD-DFT, 14
Theory of finite Galois fields, 347
Theory of metallic grating, 380
Thermal antennas, 492–496
Thermal management
  with anisotropic media, 315–317
  with phase change materials, 317–319
Thermal radiation. *See* Radiative heat transfer at the nanoscale; Surface-waves assisted thermal emission; Thermal management
Thermophotovoltaic (TPV), 299, 301
  devices, 319
Third-harmonic generation (THG), 257, 263
Thomas-Fermi screening length, 261
Three-dimensional (3d) material, 86
  metamaterials, 78, 85, 87
3d optics, 31
3D real-valued vector field, 443
Thue–Morse sequence, 333, 334, 335, 339
Time dependent metal dielectric function change, 183
  electronic contribution, 183–187
  lattice contribution, 187–188
Time reversal symmetry (TRS), 494
Tip-enhanced Raman scattering (TERS), 265
Topological defect (TD), 480
Total reflection, 308
Transmission electron microscopy (TEM), 276
Transverse magnetic (TM) polarization, 467
T-shaped gold nanodimers, 212
Tungsten, 299
Two-dimensional (2D) systems, 485
  electron, 485
Two-photon luminescence (TPL) map, 53
Two-photon photoemission PEEM (2PP-PEEM), 29

U
Ultrafast dynamics, 34, 75, 238, 258, 277, 278
Ultrafast nonlinear optical response, 188–189
  metal film, 189–190
  plasmonic material: ensemble of metal nanoparticles, 198–200
  single plasmonic nanoparticle, 190–198
Ultraviolet (UV) wavelength photons, 126

V
Vibrational spectroscopy, normal and surface-enhanced, 105–106
  surface enhanced coherent anti-Stokes Raman scattering (SECARS), 105, 111–112
  surface enhanced infrared absorption, using two-photon excitation, 108–110
  surface enhanced pumped anti-Stokes Raman scattering (SEPARS), 105, 110–111
  surface enhanced Raman scattering (SERS), 105, 106–107
  surface enhanced stimulated Raman scattering (SESRS), 105, 111–113
Visible wavelength photons, 126
Vogel's structures, 339–340
Vortex nanogear transmissions (VNTs), 444–449

W
Wentzel-Kramers-Brillouin (WKB) method, 48
Wiener-Khinchin theorem, 288
Wood anomalies, 380
  Fano's microscopic model of, 382–384

X
XFROG. *See* Cross-correlation FROG

Z
Zeeman effect, 492
Zenneck mode, 381, 388